New AIE luminogens from the naphthalimide and peryleneimide series: Assembly on nanostructured materials for explosive detection

PhD THESIS

ANDREA REVILLA CUESTA

Supervisor:

Dr. Tomás Torroba Pérez

Burgos, September 2023

UNIVERSIDAD DE BURGOS
DEPARTAMENTO DE QUÍMICA
FACULTAD DE CIENCIAS

Dr. TOMÁS TORROBA PÉREZ, Professor of Organic Chemistry at the Organic Chemistry Department of the University of Burgos,

HEREBY CERTIFIES:

That the research work included in the dissertation: "New AIE luminogens from the naphthalimide and peryleneimide series: Assembly on nanostructured materials for explosive detection", performed by Mrs. Andrea Revilla Cuesta, in order to apply for the degree of Doctor in Chemistry by the University of Burgos, has been developed under my supervision and I give my approval for its submission to be defended as a PhD Thesis.

Burgos, 22th June 2023

TORROBA PEREZ TOMAS - 12233812C

Firmado digitalmente por TORROBA PEREZ TOMAS - 12233812C
Nombre de reconocimiento (DN): c=ES, serialNumber=IDCES-12233812C, givenName=TOMAS, sn=TORROBA PEREZ, cn=TORROBA PEREZ TOMAS - 12233812C
Fecha: 2023.06.22 12:02:25 +02'00'

SGD: Tomás Torroba Pérez

"La cantidad de entropía del universo tiende a incrementarse con el tiempo"

Segundo Principio de la Termodinámica

"Al final, yo soy el arquitecto de mi propio ser, mi propio carácter y destino.
No sirve de nada aparentar lo que podría haber sido,
porque yo soy lo que he hecho, y nada más"

Jean-Paul Sartre

"The amount of entropy in the universe tends to increase with time"

Second Principle of Thermodynamics

"In the end, I am the architect of my own being, my own character and destiny.
It is no use to pretend what I could have been,
for I am what I have made myself, and nothing more"

Jean-Paul Sartre

AGRADECIMIENTOS/ACKNOWLEDGEMENTS

Cuando te planteas hacer una Tesis Doctoral de cuatro años, en un primer momento parece mucho tiempo, pero, cuando vuelves la vista atrás, te percatas de que todo ese tiempo ha transcurrido en un plumazo. A pesar de que el orden no ha sido nunca uno de mis puntos fuertes, trataré de hacer unos agradecimientos ordenados.

En primer lugar, agradecer a mi director de Tesis, Dr. D. Tomás Torroba Pérez, la oportunidad de realizar esta Tesis Doctoral en su laboratorio, la confianza depositada en mí a lo largo de estos años y darme la libertad para poder intentar todas las ideas que se me ocurrían. Agradecer también su apoyo y preocupación por los pequeños avances diarios, su enorme disponibilidad para discutir/resolver cualquier duda y su paciencia a pesar de mi "ocasional" cabezonería. Gracias por animar a una perdida estudiante de máster a adquirir este compromiso con la investigación y ayudarla a descubrir, lo que ha acabado siendo, una gran pasión.

From September to December 2022, I had the opportunity to carry out a stay at the Department of Chemistry "*Ugo Schiff*" of the University of Florence. Therefore, secondly, I would like to thank Professor Stefano Cicchi for the opportunity to perform this stay in his laboratory, for his constant concern both for the research and for my situation in Florence and for his encouragement even though things sometimes did not work out as planned. Thanks to this stay, I got to know Lab 90: Francesco Bagni, "The Boss", who answered all my questions, from chemistry to music, Elisa Guerra, who recommended a thousand places to visit and taught me the secrets of tiramisu, Mattia Capecchi and Ginevra Santioli, who taught me the "*best of Italian"* and, outside the lab, Giuditta Pecori, for all those talks, meals and mornings in the sun. Grazie a tutti voi per quei giorni in laboratorio e per avermi fatto sentire quasi a casa.

Regresando a casa, me toca agradecer a mis compañeros de batallas. Al Dr. José García, por iniciarme en el mundo de la química y enseñarme que la única forma de saber si algo puede funcionar es intentarlo. A Irene Abajo, que me ha acompañado a lo largo de todos estos años y con la que he llevado a cabo muchos proyectos, concluyendo que, aunque la primera vez las cosas salgan mal y la segunda vez salgan raro, a la tercera siempre acaban saliendo bien. Gracias por tu inestimable ayuda durante todo este tiempo, por todas esas medidas interminables, por haber soportado mi desorden y por todas esas risas aseguradas cualquier día de laboratorio. Sin ti esta tesis no habría sido posible. Al Dr. Mateo Martín, una de las personas que más sabe de química y que más me ha enseñado de todas las que conozco. Siempre serás mi general. Su disponibilidad, compañerismo y ayuda en cualquier momento y para cualquier cosa han sido tremendamente valiosos. A la Dra. María Medrano por transmitirme esas pequeñas dosis de sabiduría, como la receta del "*café máximo*" o que muchas cosas pueden ser bonitas pero inútiles. Gracias también por todos los consejos, todas las medidas y todo el apoyo que me has proporcionado a lo largo de este tiempo. Lógicamente, Pin no podría estar sin su Pon, así que agradezco a María Merino las extracciones y los infrarrojos realizados, así como las charlas, risas y cotilleos esos eternos días de columna. A Miguel Rodríguez, maestro del PMI y experto danzarín, por el inimaginable número horas que se pasó delante de las columnas. Tu perseverancia y tesón son admirables. A Carla Hernando, especialmente en los últimos meses de esta Tesis, por todas esas imágenes de SEM. La lista era larga, pero tú has conseguido dejarla a cero. A Ángel Sáez, por atreverse a trabajar con esos compuestos imposibles con los que yo ya estaba quemada, así como por iluminar un poco los días más grises. Junto con Mateo, hicisteis mucho más amenas, e incluso divertidas, todas esas horas en el kindergarden. Y, finalmente, a Cristian Almeida, una persona que sabe trabajar duro y siempre tiene una sonrisa para los demás. Sé que esa charla sobre la Transferencia de Energía de Förster no la olvidarás en mucho tiempo.

En resumen, agradeceros a todos esos buenos momentos cualquier día de trabajo, tanto montando un spin-coater, como haciendo columnas o yendo a buscar disolventes a portería, lo mucho que me habéis ayudado a lo largo de los años y las risas que acompañaban los almuerzos y las comidas. No podría haber tenido unos mejores compañeros a lo largo de esta Tesis.

También me gustaría agradecer a los estudiantes de grado o máster que han pasado por este laboratorio y, aunque haya sido durante un breve tiempo, han acabado siendo compañeros, como Lidia Xanthakos, Lorenzo Marchi, Lorenzo Quadrini, Sara Failli y, los últimos en incorporarse, Valeria Alonso, Karl Tilmann Schuppe y Alejandro Elam García. También me gustaría agradecer a los demás compañeros con los que he pasado horas de trabajo y han estado disponibles para ayudarme y aconsejarme: Andrea Sancho, Javier Gómez, Daniel Alonso, Israel Carreira o José Vicente Cuevas.

Finalmente, me gustaría agradecer esta Tesis a las personas más cercanas, que siempre están ahí y, muchas veces, no se les reconoce ni se les da la importancia que merecen. No quiero cometer un error así.

De forma muy especial, gracias a mis padres, Begoña y Candi, y mi hermano Víctor. Visteis una química donde nadie más lo hizo y, gracias a vosotros y a vuestro apoyo, hoy he llegado hasta aquí. Habéis sido los mejores maestros que he podido tener, enseñándome que con perseverancia y esfuerzo es posible lograr todos los objetivos que uno se propone y, también, enseñándome a ser una adulta sin que, a día de hoy, deje de ser vuestra niña. Gracias simplemente por estar ahí todos los días, sin vosotros nunca habría llegado al final de este camino. Sois esenciales y espero que jamás me faltéis.

Y Johnny, a pesar de te incorporaste a mitad de camino, te has implicado activamente, tanto de una forma personal como profesional. Gracias por esforzarte en comprender la química y en entenderme a mí, por cuidarme y aplacar mi carácter, por aligerar mis preocupaciones y demostrarme que no gano nada con ellas. A lo largo de este tiempo, has conseguido sacar el color a mis días grises y has mejorado mis días tristes haciéndome reír. Eres el Kernel de mi Linux y espero que seas mi compañero de viaje mucho tiempo más.

Para acabar, me gustaría agradecer esta Tesis Doctoral a mis queridas perilenomonoimidas. Aunque no seáis los compuestos centrales de mi trabajo, para mí, siempre ocupareis un lugar especial.

Sin vosotros, ni yo ni esta Tesis habríamos llegado hasta aquí. Muchísimas gracias.

Andrea

Financiación: Agradezco al Ministerio de Ciencia, Innovación y Universidades la financiación destinada a la elaboración de la presente Tesis Doctoral a través de la convocatoria de 2018 de las Ayudas para la Formación de Profesorado Universitario, FPU18/03225. Sin esta beca, mi Tesis Doctoral no habría existido. También agradezco al Ministerio de Universidades la financiación a través de la convocatoria de 2022 de las Ayudas a la movilidad para estancias breves y traslados temporales para beneficiarios del programa de Formación de Profesorado Universitario, EST22/00518, gracias a la cual pude realizar la estancia en el Departamento "*Ugo Schiff*" de la Universidad de Florencia.

GENERAL INDEX

INDEX OF ABBREVIATIONS ..... **VII**

INTRODUCCIÓN GENERAL Y OBJETIVOS **1**

1. Contexto general 3
2. Antecedentes del grupo de investigación 4
3. Objetivos generales 6
4. Esquema organizativo de la Tesis Doctoral 6

GENERAL INTRODUCTION AND OBJETIVES **9**

1. General context 11
2. Background of the research group 12
3. General objectives 14
4. Organisational diagram of the Doctoral Thesis 14

CHAPTER 1. Introduction to fluorescent probes **17**

1. Chemical sensors: types and properties 19
   - 1.1. Optical sensors 21
   - 1.2. Luminescent sensors 22
2. Characteristics of fluorescence 23
   - 2.1. Fluorescence mechanism 23
   - 2.2. Factors affecting fluorescence 25
   - 2.3. Advantages of fluorescence 27
   - 2.4. Fluorescence quenching 27
3. Fluorescent probes 28
   - 3.1. Photoinduced electron transfer (PET) 29
   - 3.2. Photoinduced charge transfer (PCT) 30
   - 3.3. Excitation energy transfer (EET): excimer formation and FRET 32
   - 3.4. Characteristics of an ideal fluorescent sensor 33
     - 3.4.1. Photophysical characteristics 33
     - 3.4.2. Analytical characteristics 35
4. General operating procedure for fluorescent probes 36
   - 4.1. Solvatochromism 37
   - 4.2. Detection tests 38

4.2.1. Environmental studies 39
4.2.2. Ionic-addition studies 40
4.3. Microscopic studies 42
4.3.1. Scanning Electron Microscopy (SEM) 42
4.3.2. Atomic Force Microscopy (AFM) 42
4.4. Work concentration 43
4.5. Previous solvent test 44
4.6. Kinetic study 45
4.7. Titration methods 46
4.7.1. Calculation of detection limits (LODs) 47
4.8. Other fluorescence parameters 49
4.8.1. Fluorescence quantum yield ($Ø_F$) 49
4.8.2. Fluorescence lifetime (τ) 50

CHAPTER 2. NMI derivatives: synthesis and properties 53
1. NMI: starting material and reactivity 55
1.1. Imidization of the NMA to NMI 58
1.2. Introduction of groups by Suzuki-Miyaura coupling 58
1.3. Introduction of groups by Sonogashira coupling 59
1.4. Introduction of groups by Stille coupling 60
1.5. Deprotection of tert-butoxycarbonyl group 60
2. Properties and π-π stacking 60
2.1. Modulating NMIs properties: the stacking of NMIs 62
2.2. Aggregation Induced Emission of NMIs 65
2.2.1. Applications of AIEgens 68
3. Origins and applications of NMI 69
3.1. NMIs as probes 70
3.2. NMIs as semiconductors 71
3.3. NMIs as building blocks 72

CHAPTER 3. NMI derivatives for detection 73
CHAPTER 3A. NMI derivatives for TATP detection 77
1. Introduction 79
1.1. Explosives: TATP 80
1.2. Methods for detection of TATP 82
1.3. Naphthalimides for detection 83

2. Objectives 84
3. Synthesis of NMIs derivatives sensitive to TATP 85
3.1. Synthesis of silica materials with NMI derivates adsorbed 87
3.2. Characterization of the functional materials 88
4. Qualitative and quantitative measurements with oxidizing reagents 90
4.1. Probe in solution: solvent selection 90
4.2. Work concentration 96
4.3. Measures in dissolution: AR82s vs TATP/*m*-CPBA 98
4.3.1. TATP titration 98
4.3.2. *m*-CPBA titration 99
5. TATP detection in modified silica nanoparticles using a recirculation system 100
5.1. Experimental system 100
5.2. Study of fluorescence changes as a colour code 100
5.3. Fluorescence study by quantum yields 101
5.4. Titration in gas phase: AR82s·SiO_2 vs TATP 102
6. Validation in real-life scenarios 103
6.1. Experimental system 103
6.2. Experiments at different temperatures 104
6.3. Validation of the robustness of the detection system 105
7. Phone APP 108
7.1. Validation in real-life conditions 111
8. Detection mechanism 112
9. Conclusions 116

CHAPTER 3B. NMI derivatives for TNT detection 117
1. Introduction 119
1.1. Explosives: TNT 120
1.2. Methods for detection of TNT 121
2. Objectives 122
3. General procedure for probe synthesis and TNT detection 123
4. Detection of TNT in dissolution 124
4.1. Synthesis. Absorbance and fluorescence interpretation 124
4.2. Preliminary qualitative test 126
4.3. Probe in solution: solvent selection 127
4.4. Work concentration 129
4.5. Detailed quantitative studies 130

4.5.1. TNT/TNB kinetic study 130
4.5.2. TNT titration 130
4.5.3. TNB titration 132
4.5.4. Other experiments 132
4.5.5. Application under real-life conditions 136
4.5.6. Interferents analysis 138
4.5.7. Detection mechanism 142
5. Detection of TNT on surfaces 143
5.1. Synthesis. Absorbance and fluorescence interpretation 144
5.2. Sylgard synthesis 146
5.3. Synthesis of the fluorescent material 146
5.4. Contact test with TNT 147
6. Conclusions 149

CHAPTER 4. NMI derivatives: aggregation 151
1. Introduction 153
2. Objectives 155
3. Aggregation according to structure 156
3.1. Synthesis on NMI derivatives 156
3.2. Absorbance and fluorescence interpretation 157
3.2.1. Solvatochromism of the AR82 series 158
3.2.2. Solvatochromism of the AR83 series 160
3.3. Water acceptance test and aggregation analysis 162
3.3.1. Aggregation analysis of the AR82 series 162
3.3.2. Aggregation analysis of the AR83 series 165
4. Aggregation of other NMIs derivatives 168
4.1. Conjugation extension analysis: AR56 168
4.1.1. Aggregation analysis using THF as organic solvent 170
4.1.2. Aggregation analysis using acetone as organic solvent 171
4.2. Conjugation extension analysis: AR65 173
4.3. Analysis of a primary amine-phenyl derivative: AR52 176
4.4. Analysis of a primary amine-pyrimidine derivative: AR55 178
4.5. Analysis of derivatives with an indole-carbazole substituent: AR67 182
5. Conclusions 184

CHAPTER 5. PMI derivatives: properties and aggregation 187

1. PMI: starting material and applications 190
1.1. Applications of PMI 191
2. Objectives 192
3. π-π stacking: study of aggregation in terms of structure 193
3.1. Reactivity of PMI derivatives 197
3.1.1. Imidization of PDA to PMI 197
3.1.2. Bromination of PMI 198
3.1.3. Borylation of PMI 198
3.1.4. Carbon-carbon coupling reactions of the PMI 199
3.1.5. Reimidization of PMI 200
3.2. Aggregation as a function of concentration 201
4. Fluorescence redshift: aggregation analysis 202
4.1. Derivatives with triple bonds: AR20 202
4.2. Spiro derivatives: AR34 and AR35 205
5. AIE in PMI derivatives 212
6. Conclusions 219

FINAL CONCLUSIONS AND FUTURE RESEARCH LINES 221
1. Conclusions 223
2. Future research lines 224

SCIENTIFIC PRODUCTIVITY DURING THE PhD THESIS 227
1. Scientific research articles 229
2. Book chapters 230
3. Scientific presentations at national and international congresses and conferences 230
4. Patents 234
5. Participation in projects 234
6. PhD thesis funding 235

ANNEX I: Apparatus, reagents and solvents 237
1. Apparatus 239
2. Reagents and solvents 240

ANNEX II: NMI derivatives 241

ANNEX III: PMI derivatives 543

INDEX OF ABBREVIATIONS

SOLVENTS:

Acet.: acetone.

DCM: dichloromethane.

DMF: *N,N*-dimethyformamide.

DMSO: dimethyl sulfoxide.

Et_3N: triethylamine.

EtO_2: diethyleter.

EtOAc: ethyl acetate.

Hex.: hexane.

MCH: methylcyclohexane.

MeCN: acetonitrile.

MeOH: methanol.

***n*-BuOH:** 1-butanol.

NMP: *N*-methyl-2-pyrrolidone.

^{t}BuOH: *tert*-butyl alcohol.

THF: tetrahydrofurane.

Tol.: toluene.

REAGENTS:

BuLi: n-butyllithium.

DCTB: trans-2-[3-(4-tert-butylphenyl)-2-methyl-2-propenylidene]malononitrile.

DIT: dithranol.

DNT: 2,4-dinitrotoluene.

HEPES: 4-hydroxyethylpiperazineethanesulfonic acid.

HMTD: hexamethylene triperoxide diamine.

Hz.: hidrazine.

KOAc: potassium acetate.

***m*-CPBA:** 3-chloroperoxybenzoic acid.

NB: nitrobenzene.

NDI: naphthalenediimida.

NMA: 4-bromo-1,8-naphthalic anhydride.

NMI: naphthalenemonoimide.

Oxn.: oxone or potassium peroxymonosulfate.

PDA: perylenedianhydride.

PDI: perylenediimide.

PDMS: polydimethylsiloxane.

PMI: perylenemonoimide.

TATB: 2,4,6-triamino-1,3,5-trinitrobenzene or triaminotrinitrobenzene.

TATP: triacetone triperoxide.

TFA: trifluoroacetic acid.

TMSA: trimethylsilylacetylene.

TNB: 1,3,5-trinitrobenzene.

TNP: trinitrophenol.

TNT: trinitrotoluene.

TECHNIQUES:

^{1}H-NMR: Proton Nuclear Magnetic Resonance.

^{13}C-NMR: Carbon Nuclear Magnetic Resonance.

AFM: Atomic Force Microscopy.

ATR: Attenuated Total Reflection.

DEPT: Distortionless Enhancement by Polarization Transfer.

ESI: Electrospray ionization.

FT-IR: Fourier-Transform infrared spectroscopy.

HRMS: High resolution mass spectrometry.

ICP: Inductively Coupled Plasma.

LIBS: laser-induced plasma spectroscopy.

MALDI: Matrix-Assisted Laser Desorption/Ionization.

m.p.: melting point.

SEM: Scanning Electron Microscopy.

TEM: Transmission Electron Microscopy.

TOF: Time-of-Flight.

OTHER ABBREVIATIONS:

ACQ: Aggregation Caused Quenched.

AIE: Aggregation-Induced Emission.

AIEgens: Aggregation-Induced Emission luminogens.

C_{Ar}: aromatic Carbon.

Cq: quaternary Carbon.

EET: Excitation Energy Transfer.

ESIPT: Excited-State Intramolecular Proton Transfer.

FRET: Förster Resonance Energy Transfer.

ICT: Intramolecular Charge Transfer.

IED: Improvised Explosive Device.

H_{Ar}: aromatic Proton.

HOMO: Highest Occupied Molecular Orbital.

LOD: Limit of Detection.

LUMO: Lowest Unoccupied Molecular Orbital.

NIR: Near Infrared Spectroscopy.

PCT: Photoinduced Charge Transfer.

PET: Photoinduced Electron Transfer.

R: reference.

TICT: Twisted Intramolecular Charge Transfer.

τ = FLD: Fluorescence Lifetime Decay.

$Ø_F$ = FQY: Fluorescence Quantum Yield.

INTRODUCCIÓN GENERAL Y OBJETIVOS

La presente Tesis Doctoral se desarrolla por compendio de cuatro capítulos más uno en el que se detalla la base teórica y los procedimientos experimentales seguidos en los demás. A partir de cada uno de ellos se pretende publicar un artículo científico (alguno de los cuales se encuentra, actualmente, en este proceso), de modo que, cada uno es un documento independiente que puede ser leído y comprendido sin necesidad de los demás. Todos los capítulos se engloban dentro de un mismo campo de investigación: la química orgánica y el fenómeno de la fluorescencia. Por tanto, cada uno de los capítulos aborda un aspecto diferente de varias familias de compuestos de nafalenomonoimidas (NMI) y perilenomonoimidas (PMI), pero con múltiples características comunes. Así pues, aunque cada capítulo pueda considerarse como un elemento independiente de los demás, todos ellos constituyen un conjunto cuya lectura permite obtener una visión amplia y completa de la investigación realizada y de los aspectos estudiados.

En la presente introducción se incluye la justificación de la investigación realizada, así como el establecimiento de los objetivos y novedades alcanzados durante su elaboración. También incluye el contexto y los logros previos del grupo de investigación en el campo de desarrollo de la presente Tesis y las necesidades de la sociedad actual que han indicado la dirección a seguir a lo largo de la investigación.

1. CONTEXTO GENERAL

La fluorescencia fue observada por primera vez en el año 1560 por el misionero franciscano Bernardino de Sahagún y, cinco años después, fue observada en una infusión de *lignum nephriticum* por el médico y botánico español Nicolás Monardes. Esta fluorescencia fue debida a la matlalina, un producto de oxidación procedente de los flavonoides de la madera de un árbol de origen mejicano.[1] En el año 1852, el matemático y físico irlandés George Gabriel Stokes escribió el artículo "*On the change of refrangibility of light*" (Sobre el cambio de refrangibilidad de la luz),[2] donde acuñó el término de fluorescencia y la describió de la siguiente manera:

> *"Fue ciertamente curioso ver el tubo iluminado instantáneamente cuando se sumergió en los rayos invisibles: era visible literalmente la oscuridad. En conjunto, el fenómeno tenía una apariencia sobrenatural".*

Pocos años después, el físico polaco Aleksander Jablonski fue el primero en describir el ciclo "suelo-excitación-emisión" como un diagrama de energía de tres niveles, que quedó plasmado en su tesis doctoral "*Sobre la influencia del cambio de la longitud de onda de la luz de excitación en los espectros de fluorescencia*", defendida en la Universidad de Varsovia en el año 1930, y que pasó a la historia como el "Diagrama de Jablonski".

A lo largo de las décadas, la fluorescencia ha sido exhaustivamente estudiada en diversas áreas de uso. Uno de los más destacados ha sido las múltiples aplicaciones que presenta en el campo de la biología. La primera sustancia verde fluorescente en un organismo vivo fue encontrada por D. Davenport y J. A. C. Nicol,[3] en el año 1955, en el tejido fotogénico de los eosinófilos de una subclase de medusas (*Aequorea victoria*). Años después (1962), O. Shimomura determinó que esta fluorescencia verde era debida a una proteína que se denominó como "*Green Fluorescent Protein*" (GFP). Durante los años siguientes, numerosos investigadores se dedicaron a estudiar dicha proteína hasta que, en 1992, D.C. Prasher *et al.*[4] consiguieron clonar por primera vez el gen

[1] A. U. Acuña, F. Amat-Guerri, P. Morcillo, M. Liras, B. Rodríguez, *Org. Lett.*, **2009**, *11*, 3020-3023.
[2] G. G. Stokes, *Philos. Trans. Royal Soc. A*, **1852**, *142*, 463-562.
[3] D. Davenport, J. A. C. Nicol, *Proc. R. Soc. Lond. B.*, **1955**, *144*, 399-411.
[4] D. C. Prasher, V. K. Eckenrode, W. W. Ward, F. G. Prendergast, M. J. Cormier, *Gene.*, **1992**, *111*, 229-233.

responsable de producir la GFP. Así pues, este es un claro ejemplo de la gran utilidad de la fluorescencia en el avance y desarrollo de otros campos de la ciencia.

A lo largo de los años, la fluorescencia se ha empleado en otras muchas aplicaciones de muy variada naturaleza, tanto cotidianas como tecnológicas y entre las que destacan:

- Para el análisis en mineralogía, gemología, geología o medicina forense.
- Elaboración de pigmentos y tintas.
- En el laboratorio de química analítica, por ejemplo, en el inmunoensayo de polarización fluorescente (FPIA).[5]
- Desarrollo de detectores biológicos y otros aspectos de la medicina, por ejemplo, bioimagen,[6] microscopía fluorescente o citometría.
- Lámparas fluorescentes, inicialmente los conocidos tubos fluorescentes y actualmente en el desarrollo de LEDs.[7]
- Desarrollo de sensores químicos basados en espectroscopía de fluorescencia.[8]

Esta última aplicación es una de las más desarrolladas a lo largo de la presente Tesis Doctoral mediante el diseño y análisis de sondas fluorescentes empleadas en la detección de sustancias oxidantes y explosivos, más concretamente TATP (Capítulo 3A) y TNT (Capítulo 3B), debido al creciente aumento de artefactos explosivos caseros que ha tenido lugar durante los últimos años. Además, esta Tesis Doctoral ha profundizado en características relativamente novedosas provocadas por ciertos compuestos fluorescentes, como el fenómeno de Emisión Inducida por la Agregación (AIE). Este es un fenómeno muy habitual en los derivados de NMI (Capítulo 4) pero considerablemente extraño en los derivados de PMI (Capítulo 5), ambas familias de compuestos englobadas dentro de los rilenos, con unas propiedades de fluorescencia muy conocidas y estudiadas.

2. ANTECEDENTES DEL GRUPO DE INVESTIGACIÓN

La sociedad actual presenta diversos problemas en lo que respecta a bioseguridad y biodetección. Muchos de ellos han conseguido resolverse, pero aún no se ha conseguido encontrar una solución para muchos otros. Por tanto, los esfuerzos del grupo de investigación SUPRABUR están orientados a la preparación de sondas fluorogénicas que puedan ser empleadas en la detección de contaminantes de alto impacto ambiental y que puedan ocasionar importantes daños a nivel personal y material, como los explosivos o los agentes CBR.

A lo largo de los últimos años, el grupo de investigación ha formado parte de numerosos proyectos que han tratado de solventar diferentes problemas relacionados con la seguridad en la sociedad actual debido al, cada vez mayor, desarrollo de artefactos explosivos improvisados. Esto ha generado una creciente necesidad de métodos capaces de detectar de forma rápida y fiable dichos artefactos explosivos en entornos militares y civiles antes de que causen daños de distinta índole. Las técnicas convencionales actualmente disponibles han tenido éxito en la detección de

[5] a) C. Duan, H. Zhang, Y. Zhang, Q. Li, P. Li, G. M. Mari, S. A. Eremin, J. Shen, Z. Wang, *Foods*, **2023**, *12*, 1581. b) O. D. Hendrickson, L. I. Mukhametova, E. A. Zvereva, A. V. Zherdev, S. A. Eremin, *Biosensors*, **2023**, *13*, 477. c) P. Qiu, Z. Song, *Anal. Lett.*, **2023**, 1-11.

[6] S. Kaloyanova, Y. Zagranyarski, S. Ritz, M. Hanulova, *J. Am. Chem. Soc.*, **2016**, *138*, 2881-2884.

[7] a) R. Arunchai, T. Sudyoadsuk, N. Prachumrak, S. Namuangruk, V. Promarak, M. Sukwattanasinitt, P. Rashatasakhon, *New J. Chem.*, **2015**, *39*, 2807–2814. b) S. Luo, J. Lin, J. Zhou, Y. Wang, X. Liu, Y. Huang, Z. Lu, C. Hu, *J. Mater. Chem. C.*, **2015**, *3*, 5259–5267.

[8] a) T. Anand, S. K. A. Kumar, S. K. Sahoo, *SAA*, **2018**, *204*, 105–112. b) C. Zhang, Y. Wang, X. Li, S. Nie, C. Liu, Y. Zhang, J. Guo, *Anal. Biochem.*, **2023**, *670*, 115131. c) C. Shi, J. Luo, Y. Wang, L. Ding, Q. Liang, Z. Yang, J. Lu, A. Wu, *Spectrochim. Acta A Mol. Biomol. Spectrosc.*, **2023**, *289*, 122245.

explosivos, sin embargo, implican considerables costes en bienes de equipo y mantenimiento, consumo de energía, muestreo, así como una supervisión continua y la ausencia de resultados inmediatos. Por tanto, para tratar de solucionar estos inconvenientes y desarrollar sensores portátiles que monitoricen continuamente el entorno, el grupo de investigación ha trabajado a través de los siguientes proyectos:

- Proyecto "*Desarrollo de nuevos sensores químicos para la detección rápida y selectiva de dispositivos explosivos improvisados*" (PID2019-111215RB-I00, CHEMSIED). El foco de este proyecto fue la investigación básica en el campo de la defensa para producir sensores portátiles que monitorizasen continuamente el entorno, detectasen la presencia de compuestos explosivos y alertasen al usuario, así como el uso de sondas químicas combinadas para proporcionar redundancia en respuesta para la identificación positiva de explosivos TATP, HMDT y convencionales.
- Proyecto "*Development of new chemical sensors and optical technologies for fast and sensitive detection of improvised explosives*" (Desarrollo de nuevos sensores químicos y tecnologías ópticas para la detección rápida y sensible de explosivos improvisados, SPS G5536). El principal objetivo desarrollado a lo largo de este proyecto fue la elaboración de sondas fluorescentes y portátiles que vigilasen el entorno de forma continua, detectando la presencia de explosivos y alertando al usuario. También pretendió aunar esfuerzos entre varias organizaciones internacionales para hacer frente a los nuevos retos de seguridad en la lucha contra el terrorismo mediante la aplicación de novedosas tecnologías de detección.
- Proyecto "*Sistema colorante AIE en nanopartículas de sílice para la detección ultrasensible de TATP en aire: un prototipo de nariz química para detectar IEDs en almacenes de equipajes*" (PDC2022-133955-I00, IED-CHEMDOG). Se trata de un proyecto en vigor en el que se pretende desarrollar un sistema de detección automática de los explosivos caseros empleados en los artefactos explosivos actuales.

Paralelamente, el grupo de investigación ha llevado a cabo otros proyectos de índole biológica, en los que el transporte de sustancias y su liberación en una zona concreta del organismo pueden resultar de especial interés para el tratamiento de determinadas dolencias. Esto justifica la síntesis de compuestos que den lugar a vesículas bajo determinadas condiciones y su optimización para tratar de favorecer su obtención y control, lo que se ha llevado a cabo a través de proyectos como los que figuran a continuación:

- Proyecto "*Nuevas estrategias en el tratamiento de la obesidad y diabetes mellitus empleando el factor de preimplantación (PIF) en modelos preclínicos murinos*" (DIABO-PIF). El foco principal de este proyecto ha sido el empleo de familias de compuestos fluorescentes como marcadores celulares y su posible acción fisiológica sobre células vivas. Esto ha sido posible debido a que los derivados de los rilenos, individualmente o unidos a péptidos fisiológicos, pueden ser empleados como marcadores celulares de retículo endoplasmático, mostrando una acción citotóxica sobre ciertos tipos de células.
- Proyecto "*El factor de preimplantación (PIF) en el tratamiento de la diabetes mellitus tipo 2*" (UBU20-04, PIF-T2DM). A lo largo de este proyecto se desarrolló una nueva metodología de trabajo para producir nanovesículas huecas, robustas y estables en agua o en mezclas de agua y disolventes orgánicos. Se pretendió que la combinación de AIEgens y cadenas de depsipéptidos diesen lugar a vesículas con el tamaño suficiente para transportar moléculas voluminosas, como péptidos fisiológicos, moléculas sintéticas o complejos metálicos de coordinación.

Por tanto, trabajando en el marco de los distintos proyectos del grupo de investigación, se han conseguido avances tanto en el campo de la detección de sustancias explosivas como en el desarrollo de nanovesículas de forma controlada.

3. OBJETIVOS GENERALES

Se establece como principal objetivo de la presente Tesis Doctoral la síntesis y caracterización de nuevos compuestos fluorescentes derivados tanto del naftaleno como del perileno, todos ellos comprendidos dentro de los rilenos, así como su análisis para ser empleados en aplicaciones de distinta naturaleza: bien en la detección de explosivos y agentes oxidantes o bien para la formación de nanoestructuras destinadas al transporte de moléculas. Sin embargo, esta Tesis Doctoral recoge otros aspectos que permiten identificar una serie de objetivos específicos (OE):

- OE01: Explicar los diferentes tipos de sensores químicos existentes y establecer un protocolo de actuación orientado al desarrollo de sondas fluorescentes.
- OE02: Definir las carencias de la sociedad actual en lo que respecta a la detección de explosivos empleados en la fabricación de artefactos explosivos improvisados.
- OE03: Establecer pautas para el diseño de nuevas sondas fluorescentes en base a los compuestos ya existentes recogidos en la bibliografía.
- OE04: Diseñar y elaborar un sistema para la detección de vapores de explosivos y sustancias oxidantes bajo condiciones perfectamente controladas.
- OE05: Desarrollar un sistema de detección de trazas de explosivos en fase gaseosa que pueda ser empleado en circunstancias de vida real.
- OE06: Analizar el comportamiento y capacidad de detección de las sondas ancladas a distintas superficies para llevar a cabo el desarrollo de un sistema conocido como “algodón mágico”.
- OE07: Desarrollar una aplicación telefónica (APP) que nos permita determinar la presencia o ausencia de trazas de vapores explosivos de forma rápida y sencilla mediante la realización de una fotografía.
- OE08: Validar las sondas fluorescentes sintetizadas y los sistemas de detección desarrollados mediante la comparación de los límites de detección inferiores obtenidos con los que presentan los métodos y sensores actualmente disponibles.
- OE09: Estudiar los fenómenos de agregación de múltiples derivados de NMI y PMI al añadir cantidades crecientes de agua a un disolvente orgánico mediante diversas técnicas de microscopía.
- OE10: Establecer un sistema de control de la agregación para AIEgens derivados de NMIs.

Cada uno de estos objetivos específicos se abordan en uno o varios de los capítulos que constituyen esta Tesis Doctoral. El esquema de desarrollo de los distintos capítulos, así como la vinculación entre ellos y los objetivos enunciados, se muestra en el siguiente apartado.

4. ESQUEMA ORGANIZATIVO DE LA TESIS DOCTORAL

La presente Tesis Doctoral, como ya se ha comentado, está constituida por cinco capítulos diferentes. En el primer capítulo, aparte de introducir el fundamento teórico de los sensores químicos y de las propiedades de fluorescencia, se establecen de las bases generales del procedimiento a seguir para el empleo de los compuestos sintetizados como sondas fluorescentes.

Además, también se determinan las bases para el análisis de las distintas propiedades de los compuestos fluorescentes obtenidos, como los distintos estudios de microscopía o el análisis del fenómeno de AIE.

El segundo capítulo de la Tesis Doctoral es una revisión bibliográfica de las características, propiedades y aplicaciones de los NMI, que sirve de introducción para los derivados analizados en los siguientes capítulos. El tercer capítulo es el más extenso de la tesis doctoral y se centra en el análisis de las propiedades de detección de una serie de derivados de NMI. Por tanto, el capítulo 3A está enfocado en el estudio de una serie de sondas fluorescentes para llevar a cabo la detección de TATP en disolución y en forma de gas, bien mediante un sistema desarrollado a escala de laboratorio en condiciones perfectamente controladas o bien en escenarios y condiciones cercanas a la realidad, desarrollándose una APP que permita la obtención de resultados *in situ* y de manera instantánea. El capítulo 3B se centra, por un lado, en el desarrollo de una nueva sonda fluorescente empleada en la detección de TNT en disolución, capaz de diferenciar los demás explosivos nitrados existentes (DNT, NB, TNP…), y, por otro lado, la obtención de un sensor de TNT en superficies, lo que se consiguió anclando la sonda fluorescente a la superficie de un polímero de PDMS.

En el cuarto capítulo se inician los estudios de la agregación de los derivados de rileno. Este capítulo comienza con una breve explicación del fenómeno de AIE, seguido de un exhaustivo estudio del control del fenómeno de AIE en función del número de grupos amino-protectores presentes en el compuesto para acabar con el estudio de la influencia de la extensión de la conjugación o de determinados sustituyentes en las nanoestructuras formadas. Finalmente, el quinto y último capítulo de esta Tesis Doctoral se centra en los derivados de PMI, por lo que comienza con una breve revisión de las características y propiedades de este tipo de compuestos para terminar centrándose en el análisis de la agregación. Por un lado, se estudiaron las nanoestructuras formadas por aquellos compuestos que experimentaban un desplazamiento hacía la región del rojo del espectro electromagnético a medida que se incrementaba la cantidad de agua añadida a un disolvente orgánico y, por otro lado, se estudió el infrecuente fenómeno de AIE que tiene lugar en raros derivados de PMI. A lo largo de estos dos últimos capítulos se observó la formación de vesículas en ciertos derivados de PMI y de NMI, por lo que también se trató de establecer las condiciones más favorables para su formación.

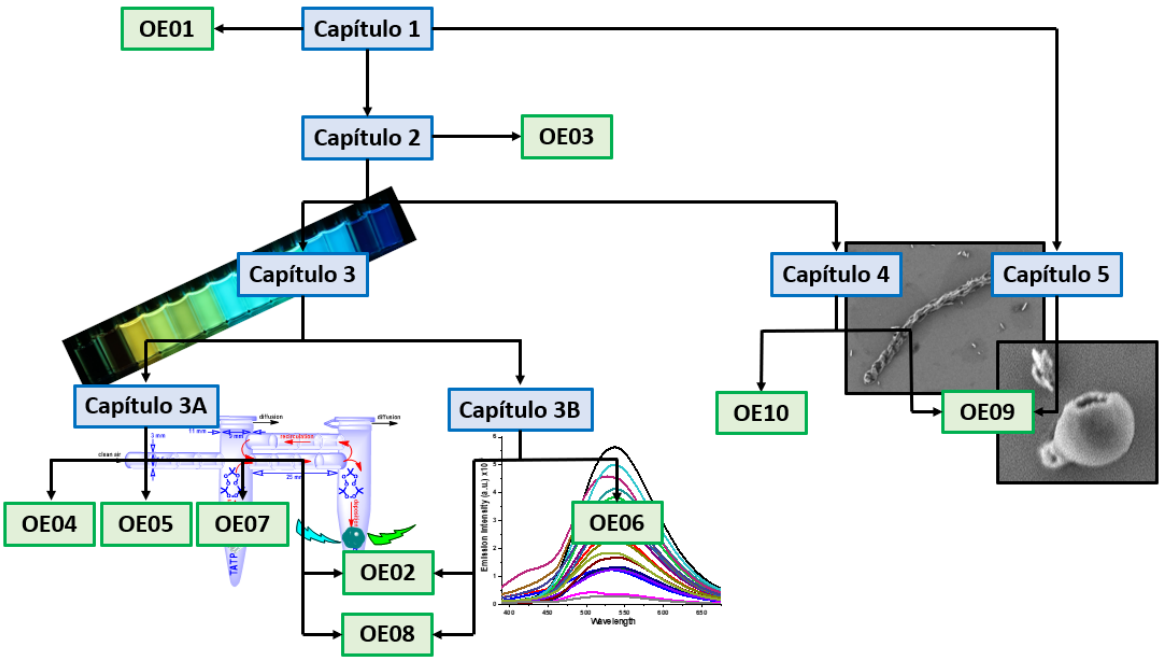

Figura 1. Esquema organizativo de la Tesis Doctoral.

General Introduction and Objetives

This Doctoral Thesis is a compendium of four chapters plus one in which the theoretical basis and the experimental procedures followed in the others are detailed. From each of them, a scientific article (some of which are currently in the process of being published) will be intended to publish, so that each one is an independent document that can be read and understood without the need for the others. All the chapters fall within the same field of research: organic chemistry and the phenomenon of fluorescence. Therefore, each chapter deals with a different aspect of several families of naphthalenemonoimide (NMI) and perylenemonoimide (PMI) compounds, but with many common features. Thus, although each chapter can be considered as an independent element of the others, all of them constitute a whole whose reading allows to obtain a broad and complete view of the research carried out and the aspects studied.

This introduction includes the justification for the research carried out, as well as the establishment of the objectives and developments achieved during its elaboration. It also includes the context and previous achievements of the research group in the field of development of this Thesis and the needs of today's society that have indicated the direction to be followed throughout the research.

1. GENERAL CONTEXT

Fluorescence was first observed in 1560 by the Franciscan missionary Bernardino de Sahagún and, five years later, it was observed in an infusion of *lignum nephriticum* by the Spanish physician and botanist Nicolás Monardes. This fluorescence was due to matlalin, an oxidation product from the flavonoids in the wood of a tree of Mexican origin.[1] In 1852, the Irish mathematician and physicist George Gabriel Stokes wrote the article "*On the change of refrangibility of light*",[2] where he introduced the concept of fluorescence and described it as follows:

> *"It was indeed curious to see the tube instantly illuminated when it was immersed in the invisible rays: it was literally visible darkness. Altogether, the phenomenon had a supernatural appearance."*

A few years later, the Polish physicist Aleksander Jablonski was the first to describe the "ground-excitation-emission" cycle as a three-level energy diagram, which was set out in his doctoral thesis "*On the influence of the change of the wavelength of excitation light on fluorescence spectra*", defended at the University of Warsaw in 1930, and which went down in history as the "Jablonski Diagram".

Over the decades, fluorescence has been extensively studied in various areas of use. One of the most important of which has been its many applications in the field of biology. The first green, fluorescent substance in a living organism was found by D. Davenport and J.A.C. Nicol,[3] in 1955, in the photogenic tissue of eosinophils of a subclass of jellyfish (*Aequorea victoria*). Years later (1962), O. Shimomura determined that this green fluorescence was due to a protein called "*Green Fluorescent Protein*" (GFP). In the following years, numerous researchers studied this protein until, in 1992, D. C. Prasher *et al.*[4] succeeded in cloning the gene responsible for producing GFP for the first time. Thus, this is a clear example of the great usefulness of fluorescence in the advancement and development of other fields of science.

[1] A.U. Acuña, F. Amat-Guerri, P. Morcillo, M. Liras, B. Rodríguez, *Org. Lett.*, **2009**, *11*, 3020-3023.
[2] G. G. Stokes, *Philos. Trans. Royal Soc. A*, **1852**, *142*, 463-562.
[3] D. Davenport, J. A. C. Nicol, Proc. *R. Soc. Lond. B.*, **1955**, *144*, 399-411.
[4] D. C. Prasher, V. K. Eckenrode, W. W. Ward, F. G. Prendergast, M. J. Cormier, *Gene.*, **1992**, *111*, 229-233.

Over the years, fluorescence has been used in many other applications of a very varied nature, both every day and technological, among which the following stand out:

- For analysis in mineralogy, gemmology, geology or forensic medicine.
- To produce pigments and dyes.
- In the analytical chemistry laboratory, for example, in fluorescence polarisation immunoassay (FPIA).[5]
- Development of biological detectors and other aspects of medicine, including bioimaging,[6] fluorescence microscopy and cytometry.
- Fluorescent lamps, initially the well-known fluorescent tubes and currently in the development of LEDs.[7]
- Development of chemical sensors based on fluorescent spectroscopy.[8]

This last application is one of the most developed throughout this Doctoral Thesis through the design and analysis of fluorescent probes used in the detection of oxidising substances and explosives, more specifically TATP (Chapter 3A) and TNT (Chapter 3B), due to the growing increase in home-made explosive devices that has occurred in recent years. In addition, this Doctoral Thesis has examined relatively novel characteristics caused by certain fluorescent compounds, such as the phenomenon of Aggregation Induced Emission (AIE). This is a very common phenomenon in NMI derivatives (Chapter 4) but considerably unusual in PMI derivatives (Chapter 5), both families of compounds grouped within the rylenes, with well-known and well-studied fluorescence properties.

2. BACKGROUND OF THE RESEARCH GROUP

The current society presents several problems in terms of biosafety and biosecurity. Many of these problems have been solved, but for many others a solution has not yet been found. Therefore, the efforts of the SUPRABUR research group are oriented towards the preparation of fluorogenic probes that can be used for the detection of contaminants with high environmental impact and that can cause significant personal and material damage, such as explosives or CBR agents.

Over the last few years, the research group has been involved in numerous projects that have tried to solve different problems related to security in modern society due to, the ever-increasing, development of improvised explosive devices. This has led to a growing need for methods capable of rapidly and reliably detecting IEDs in military and civilian scenarios before they cause damage of various kinds. Currently available conventional techniques have been successful in detecting explosives; however, they involve considerable costs in equipment and maintenance, energy consumption, sampling as well as continuous monitoring and lack of immediate results. Therefore, to address these drawbacks and to develop portable probes that continuously monitor the environment, the research group has worked through the following projects:

[5] a) C. Duan, H. Zhang, Y. Zhang, Q. Li, P. Li, G. M. Mari, S. A. Eremin, J. Shen, Z. Wang, *Foods*, **2023**, *12*, 1581. b) O. D. Hendrickson, L. I. Mukhametova, E. A. Zvereva, A. V. Zherdev, S. A. Eremin, *Biosensors*, **2023**, *13*, 477. c) P. Qiu, Z. Song, *Anal. Lett.*, **2023**, 1-11.

[6] S. Kaloyanova, Y. Zagranyarski, S. Ritz, M. Hanulova, *J. Am. Chem. Soc.*, **2016**, *138*, 2881-2884.

[7] a) R. Arunchai, T. Sudyoadsuk, N. Prachumrak, S. Namuangruk, V. Promarak, M. Sukwattanasinitt, P. Rashatasakhon, *New J. Chem.*, **2015**, *39*, 2807–2814. b) S. Luo, J. Lin, J. Zhou, Y. Wang, X. Liu, Y. Huang, Z. Lu, C. Hu, *J. Mater. Chem. C.*, **2015**, *3*, 5259–5267.

[8] a) T. Anand, S. K. A. Kumar, S. K. Sahoo, *SAA*, **2018**, *204*, 105–112. b) C. Zhang, Y. Wang, X. Li, S. Nie, C. Liu, Y. Zhang, J. Guo, *Anal. Biochem.*, **2023**, *670*, 115131. c) C. Shi, J. Luo, Y. Wang, L. Ding, Q. Liang, Z. Yang, J. Lu, A. Wu, *Spectrochim. Acta A Mol. Biomol. Spectrosc.*, **2023**, *289*, 122245.

- Project *"Desarrollo de nuevos sensores químicos para la detección rápida y selectiva de dispositivos explosivos improvisados"* (Development of new chemical sensors for the rapid and selective detection of improvised explosive devices, PID2019-111215RB-I00, CHEMSIED). The focus of this project was basic research in the field of defence to produce wearable sensors that continuously monitor the environment, detect the presence of explosive compounds and alert the user, as well as the use of combined chemical sensors to provide redundancy in response to positive identification of TATP, HMDT and conventional explosives.
- Project "*Development of new chemical sensors and optical technologies for fast and sensitive detection of improvised explosives*" (SPS G5536). The main aim developed during this project was the development of fluorescent and portable probes that continuously monitor the environment, detecting the presence of explosives and alerting the user. It also attempted to join forces between several international organisations in order to confront the new security challenges in the fight against terrorism through the application of novel detection technologies.
- Project "*Sistema colorante AIE en nanopartículas de sílice para la detección ultrasensible de TATP en aire: un prototipo de nariz química para detectar IEDs en almacenes de equipajes*" (AIE dye system in silica nanoparticles for ultra-sensitive detection of TATP in air: a prototype chemical nose to detect IEDs in luggage stores, PDC2022-133955-I00). This is an ongoing project to develop a system for the automatic detection of home-made explosives used in present-day explosive devices.

In parallel, the research group has carried out other projects of a biological nature, in which the transport of substances and their release in a specific area of the organism may be of particular interest for the treatment of certain ailments. This justifies the synthesis of compounds that form vesicles under certain conditions and their optimisation to try to favour their production and control, which has achieved through projects such as those listed below:

- Project "*Nuevas estrategias en el tratamiento de la obesidad y diabetes mellitus empleando el factor de preimplantación (PIF) en modelos preclínicos murinos*" (New strategies in the treatment of obesity and diabetes mellitus using preimplantation factor (PIF) in preclinical murine models, DIABO-PIF). The focus of this project has been the use of families of fluorescent compounds for cell markers and their possible physiological action on living cells. This has been possible because rylene derivatives, individually or linked to physiological peptides, can be used as endoplasmic reticulum cell markers, showing a cytotoxic action on certain types of cells.
- Project "*El factor de preimplantación (PIF) en el tratamiento de la diabetes mellitus tipo 2"* (Pre-implantation factor (PIF) in the treatment of type 2 diabetes mellitus, UBU20-04, PIF-T2DM). During this project, a new methodology was developed to produce hollow, robust and stable nanovesicles in water or in mixtures of water and organic solvents. The combination of AIEgens and depsipeptide chains was intended to produce vesicles of enough size to transport bulky molecules, such as physiological peptides, synthetic molecules or metal coordination complexes.

Thus, working within the framework of the research group's various projects, advances have been made both in the field of detection of explosive substances and in the development of nanovesicles in a targeted manner.

3. GENERAL OBJETIVES

The main goal of this Doctoral Thesis is the synthesis and characterisation of new fluorescent compounds derived from both naphthalene and perylene, all of them included in the rylenes as well as their analysis to be used in different applications: either in the detection of explosives and oxidising agents or for the formation of nanostructures for the transport of molecules. However, this Doctoral Thesis includes other aspects that allow us to identify a series of specific objectives (SO):

- SO01: To explain the different types of chemical sensors and to establish a protocol for the development of fluorescent probes.
- SO02: To define the shortcomings of the current society in terms of the detection of explosives used in the manufacture of IEDs.
- SO03: Establish guidelines for the design of new fluorescent probes based on existing compounds in the literature.
- SO04: Design and develop a system for the detection of explosive vapours and oxidising substances under perfectly controlled conditions.
- SO05: Develop a system for the detection of traces of explosives in the gaseous phase that can be used in real-life circumstances.
- SO06: To analyse the behaviour and detection capability of probes attached to different surfaces to carry out the development of a system known as “magic swab”.
- SO07: Develop a telephone application (APP) that allows us to determine the presence or absence of traces of explosive vapours quickly and easily by taking a photograph.
- SO08: Validate the synthesised fluorescent probes and detection systems developed by comparing the lower detection limits obtained with those of currently available methods and sensors.
- SO09: To study the aggregation phenomena of multiple NMI and PMI derivatives by adding increasing amounts of water to an organic solvent using a variety of microscopy techniques.
- SO10: Establish an aggregation control system for AIEgens derived from NMIs.

Each of these specific objectives is addressed in one or more of the chapters that make up this Doctoral Thesis. The scheme of development of the different chapters, as well as the link between them and the enunciated objectives, is shown in the following section.

4. ORGANISATIONAL DIAGRAM OF THE DOCTORAL THESIS

This Doctoral Thesis, as already mentioned, is made up of five different chapters. In the first chapter, apart from introducing the theoretical background of chemical sensors and fluorescence properties, the general bases of the procedure to be followed for the use of the synthesised compounds as fluorescent probes are established. In addition, the fundamentals for the analysis of the different properties of the obtained fluorescent compounds, such as the different microscopy studies or the analysis of the AIE phenomenon, are also determined.

The second chapter of the Doctoral Thesis is a bibliographical review of the characteristics, properties and applications of NMIs, which introduces the derivatives analysed in the following chapters. The third chapter is the longest chapter of the PhD Thesis and focuses on the analysis of the detection properties of a few NMI derivatives. Therefore, chapter 3A is focused on the study of a series of fluorescent probes to perform the detection of TATP in solution and in gas form, using a

system developed at laboratory scale under perfectly controlled conditions or in scenarios and conditions close to reality, developing an APP that allows obtaining results in situ and instantaneously. Chapter 3B is centred on the one hand, on the development of a new fluorescent probe used in the detection of TNT in solution, capable of differentiating the other nitrated explosives (DNT, NB, TNP...), and, on the other hand, on obtaining a TNT sensor on surfaces, which was achieved by attaching the fluorescent probe to the surface of a PDMS polymer.

The fourth chapter begins the studies of the aggregation of rylene derivatives. This chapter begins with a brief explanation of the AIE phenomenon, followed by an exhaustive study of the control of the AIE phenomenon as a function of the number of amino-protecting groups present in the compound, and ends with the analysis of the influence of the extent of conjugation or of certain substituents on the nanostructures formed. Finally, the fifth and last chapter of this Doctoral Thesis focuses on PMI derivatives, beginning with a brief review of the characteristics and properties of this type of compounds and ending with the analysis of aggregation. On the one hand, the nanostructures formed by those compounds that underwent a shift to the red region of the electromagnetic spectrum as the amount of water added to an organic solvent increased and, on the other hand, the infrequent AIE phenomenon that occurs in unusual PMI derivatives was studied. During these last two chapters, the formation of vesicles in certain PMI and NMI derivatives was observed, and the most favourable conditions for their formation were also investigated.

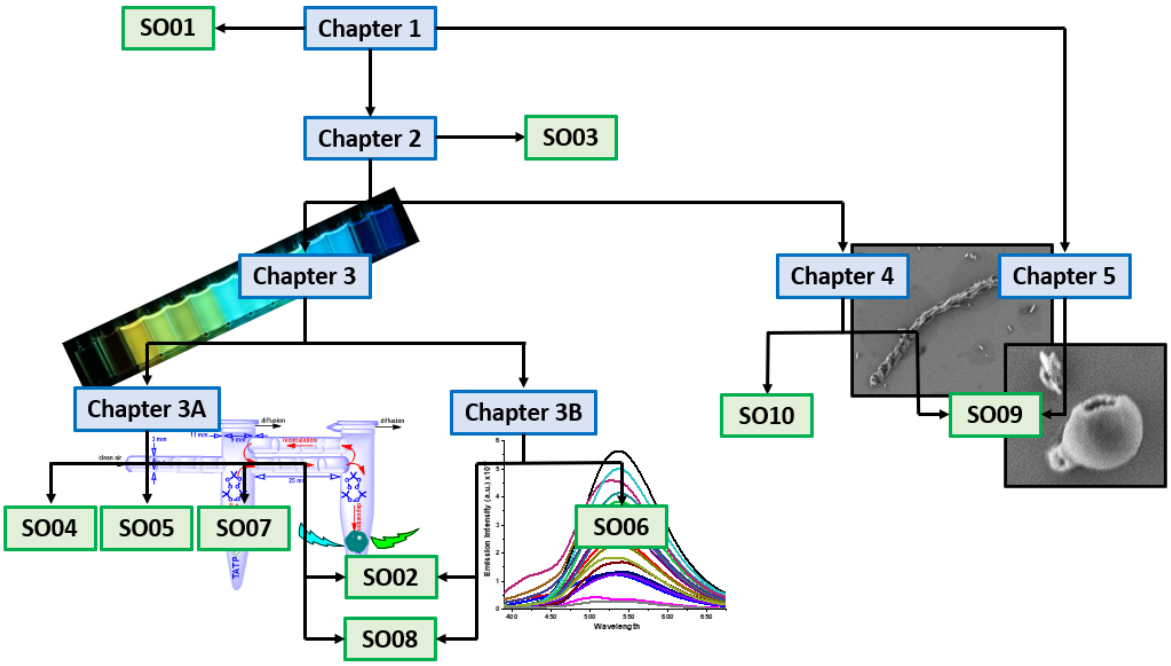

Figure 1. Organisational scheme of the Doctoral Thesis.

CHAPTER 1

INTRODUCTION TO FLUORESCENT PROBES

In general terms, a sensor can be defined as a device that receives and responds to a stimulus by generating a useful signal that can be measured or interpreted. Sensors can be classified into two main groups:[1]

- Physical sensors: these are those that determine changes in physical parameters such as temperature or pressure.
- Chemical sensors: devices that transform chemical information, ranging from the concentration of a specific component of the sample to the total analysis of its composition, into a useful signal. The chemical information may originate from a chemical reaction of the analyte or from a physical property of the system under investigation.

Therefore, a molecular sensor[2] is a system capable of detecting the presence of a species on a molecular level by generating a signal that can be measured.

The development and applications of sensors[3] have grown exponentially in recent years in a wide range of fields, and they can be used in all areas of daily life. One of the fields where the demand for the use of sensors is important is the environmental quality control. The increase in industrial activity has had a damaging effect on the quality of the environment in many cases, which has led to an awareness on the part of the population and to the development of programmes aimed at environmental protection. In this situation, the need has arisen to obtain rapid, and even continuous, data directly at source on the contents of different pollutants. Other fields in which continuous and *in situ* monitoring of various parameters has become important are medicine and industry, leading to greater efficiency in production and quality in manufacturing.

On the other hand, few techniques used in chemical analysis are specific to a definite species, which results in interferences that may attenuate the analyte signal or produce a confusing signal. The lack of specificity in the analytical signal is incompatible with in situ measurements that do not require pre-treatment.

Thus, many of the molecular sensors developed are aimed to reduce this lack of selectively and, in some cases, to eliminate it completely. In addition, these sensors allow *in situ* measurements, providing fast responses, with low detection limits and much lower costs than other equipment, such as chromatographs or ICP-MS.

1. CHEMICAL SENSORS: TYPES AND PROPERTIES

There is a broad variety of chemical sensors, however, they all consist of three distinct parts,[4] shown in Figure 1.

- Receptor: molecular or ionic recognition element that selectively interacts with a certain component of the sample (analyte), generating a primary signal carrying the chemical information, which can be thermal, optical, electrochemical, etc.
- Transducer: instrumental element that translates the interaction into a processable signal. Both parts can be more or less integrated, but always connected, since the

[1] A. Hulanicki, S. Glab, F. Ingman, *Pure & App. Chem.*, **1991**, *63*, 1247-1250.
[2] J. X. J. Zhang, K. Hoshino. Molecular sensors and nanodevices: principles, designs and applications in biomedical engineering, Elsevier, **2014**, ISBN: 978-0-12-814862-4.
[3] a) C. Pérez-Conde. Sensores ópticos, University of Valencia, **1996**, ISBN: 978-84-370-2326-7. b) D. A. Skoog. Química Analítica, McGraw-Hill, **2001**, ISBN: 978-6075193779.
[4] a) S. Alegret, M. Valle, A. Merkoçi. Sensores electroquímicos: Introducción a los quimiosensores y biosensores: curso teórico-práctico. University of Barcelona, **2004**, ISBN: 84-490-2361-0. b) J. Wu, B. Kwon, W. Liu, E. V. Anslyn, P. Wang, J. S. Kim, *Chem. Rev.*, **2015**, *115*, 7893-7943.

primary signal generated in the recognition reaction will be converted by the transducer into a secondary signal that is much easier to process, generally in the electrical domain.

- Signal processor: the system also has an electronic signal amplification and processing system.

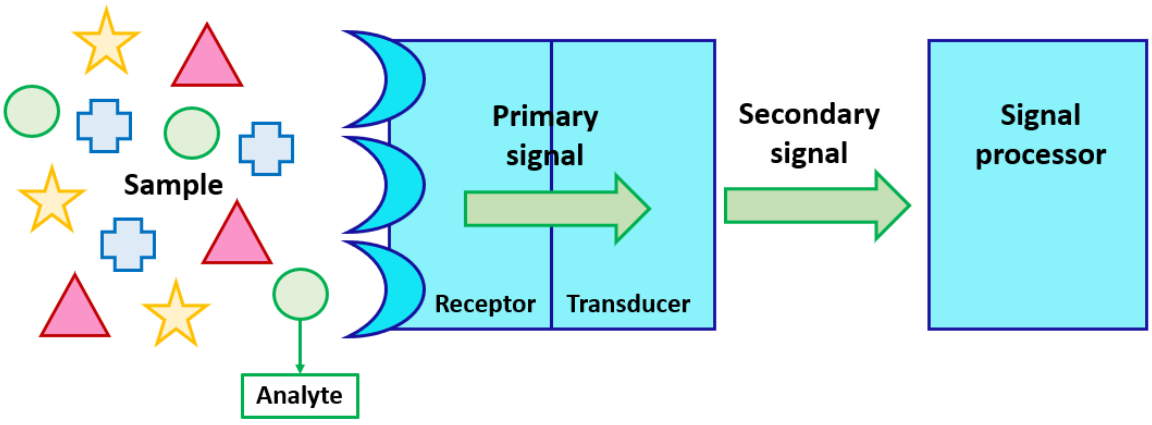

Figure 1. Schematic diagram of the components of a chemical probe.

Based on the elements that make up the chemical probes, different classifications can be made. One of the most commonly used classification criteria is the transduction system,[5] and four types can be distinguished:

- Piezoelectric sensors:[6] based on the generation of electrical currents in a vibrating crystal. The vibration frequency varies with the mass of the material adsorbed on its surface, which can be modified due to a chemical reaction.
- Thermal sensors: based on the measurement of the heat involved in certain chemical reactions, which is used to quantify certain analytes.
- Electrochemical sensors:[7] are those that transform the effect of the electrochemical interaction between the analyte and the electrode into a useful electrical signal. They can be subdivided into voltammetric sensors (measuring the current between the electrode and the medium), constant potential sensors or potentiometric sensors (measuring the change in potential between the electrode and a reference).
- Optical sensors: sensors that transform changes in optical phenomena, resulting from the interaction between the analyte and the receptor, into useful signals.

Apart from those mentioned, there are many other chemical sensors. However, from now on we will focus on optical sensors.

[5] B. R. Eggins. Biosensors: an introduction, Wiley, **1996**, ISBN: 978-0471981435.
[6] P. Gründler. Chemical sensors: an introduction for scientists and engineers, Springer-Verlag Berlin, **2007**, ISBN: 978-3-540-45742-8.
[7] E. Bakker, Y. Qin, *Analytical Chem.*, **2006**, *78*, 3965-3984.

1.1. Optical sensors

Optical sensors are based on the interaction of electromagnetic radiation with material systems.[8] This interaction usually happens in a specific way and over a wide wavelength range and is evaluated through the change in some optical property related to the concentration of the analyte.

Optical sensors are widely used in chemical analysis because of their advantages over other types of chemical probes, including the following:

- They do not require a reference signal.
- They allow analysis in the presence of electrical interference.
- They allow the determination of analytes that cannot be measured by electrochemical detection.
- Ease of miniaturization and versatility of transduction systems.

Optical sensors can be classified based on a few criteria such as the function performed by the optical fibre, the type of configuration selected to develop the sensor or the type of interaction between electromagnetic radiation and material.[9] Based on the last criteria, the sensors in Figure 2 can be distinguished.

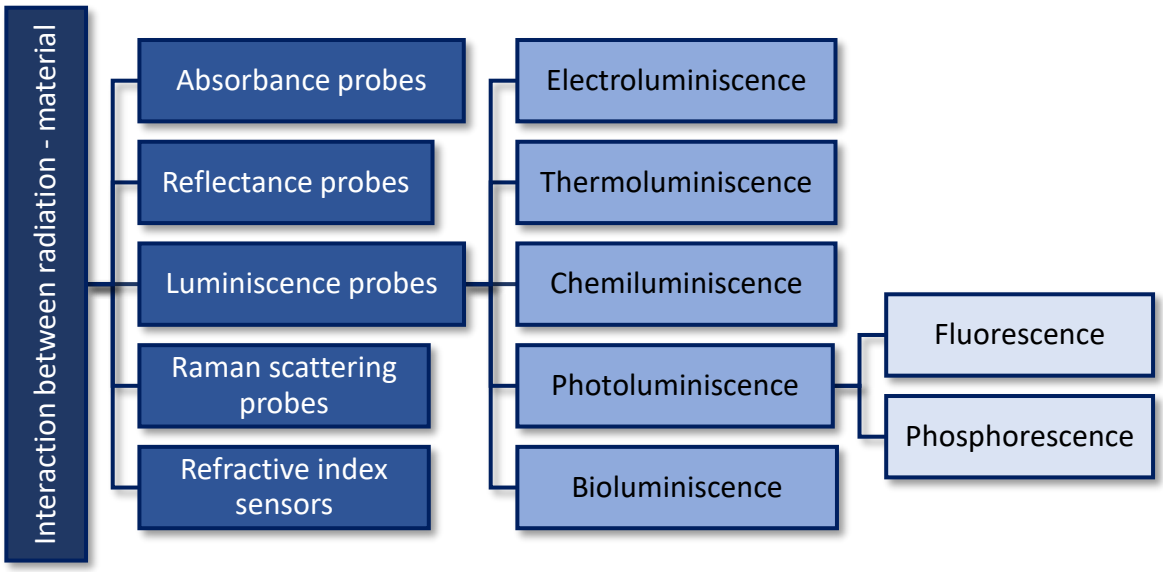

Figure 2. Classification of optical sensors.

As can be seen in Figure 2, among the optical sensors are photoluminescent probes, which are those based on the measurement of electromagnetic radiation emitted by molecules that have previously absorbed characteristic radiant energy or other types of energy. Of all the possible options, this thesis focuses on the study of probes that work by luminescence processes. Optical sensors can be used in a range of areas, such as the environment, clinical chemistry, or the agro-food industry. For example, optical sensors can be used in the development of pH sensors, based on the use of an acid-base indicator that modifies its optical properties, absorbance, reflectance, or fluorescence, by varying the concentration of protons in the medium. They can also be used in the manufacture of oxygen sensors, based on the effect that this gas has on the luminescent reagents, as well as glucose, nitrogen oxide or ion probes.

[8] a) D. C. Harris. Análisis químico cuantitativo, Reverté, **2007**, ISBN: 84-291-7224-6. b) J. M. García, F. C. García, F. Serna, J. L. Peña, *Polym. Rev.*, **2011**, *51*, 341-390.
[9] J. Janata. Principles of chemical sensors, Springer, **2009**, ISBN: 978-1-4757-6257-0.

1.2. Luminiscent sensors

Photoluminescent sensors [10] are based on measuring the ultraviolet, visible, or infrared emissions of electronically excited species. The electrons involved in the bonds pass to an excited electronic state (A*) and subsequently return to their ground state (A) emitting electromagnetic radiation of characteristic energy (Figure 3).

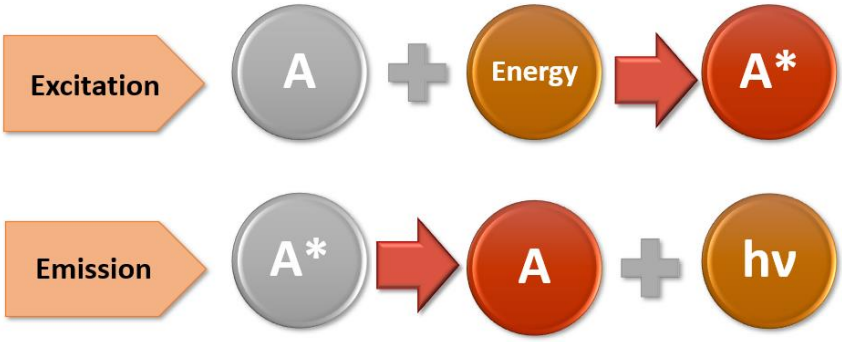

Figure 3. Scheme of the luminescence process.

Depending on the source of the excitation energy, there are different types of phenomena and, therefore, different types of probes. For example, if the excitation energy comes from a chemical or biochemical reaction, the phenomenon is called chemi or bioluminescence, respectively, while if it comes from an electromagnetic radiation source, it is called fluorescence or phosphorescence.

Luminescent detection methods are more selective than those based on the absorption of electromagnetic radiation. This fact, together with the higher sensitivity of the technique, has led to the development of numerous sensors based on fluorescence measurements in which the intensity of emitted radiation is proportional to the concentration of the analyte:

$$I_F = K \cdot C \cdot I_0$$

Where I_F is the fluorescent intensity, C is the concentration of the analyte and I_0 is the intensity of the incident radiation.

Another possibility of this technique is the indirect quantification of other analytes present in the medium that can modify the fluorescence of the luminescent reagent (receptor). In this type of detector, the concentration of the analyte (C) is directly proportional to the ratio of the fluorescence intensities in the absence (I) and in the presence (I_Q) of the analyte:

$$I/_{I_Q} = 1 + K \cdot C$$

The main problem with luminescent probes is the possibility of photodecomposition of the reagent due to the high intensity of the sources used. This fact, in addition to reducing the life of the sensor, causes drift in the analytical signal, which can be avoided by replacing the measurement of the intensity with that of the lifetime. The lifetime is often determined by exciting the sample with a short pulse of radiation and then measuring the decay of the intensity of the emitted radiation as a function of time. However, despite this problem, photoluminescent sensors have several advantages over other optical sensors:[11]

- High specificity: the number of false positives and false negatives is very low.

[10] D. A. Skoog, F. J. Holler, S. R. Crouch. Principios de análisis instrumental, **2008**, ISBN: 978-970-686-829-9.
[11] D. A. Skoog, F. J. Holler, T. A. Nieman. Principios de análisis instrumental, McGraw-Hill, **2000**, ISBN: 978-607-481-390-6.

- High sensitivity: as already mentioned, fluorescence sensors have lower detection limits than other optical sensors, being until 3 orders of magnitude lower than absorbance (colorimetric) sensors.
- Reusability: photoluminescent detection processes are generally non-destructive techniques that do not require destructive pre-treatment or high-energy sources.
- Fast operating mechanisms that allow the probe to provide a response in short periods of time.
- Low cost of operation and inexpensive maintenance.
- Portability: miniaturisation of devices is possible, usually by optical fibre.

On the other hand, although lifetime-based sensors require more sophisticated instrumentation, they are characterised by two important advantages over intensity-based sensors:

- They are not affected by the photo-decay processes of the receptor.
- They are not affected by source or detector fluctuations.

These characteristics can be extrapolated to sensors based on the phenomenon of phosphorescence. However, it is a characteristic that is present in a small group of molecules and is normally deactivated in the presence of oxygen. The development of such a sensor is much more complex, but more cost-effective due to the more restrictive conditions of use. However, although it was tested for all the materials synthesised, none of them showed phosphorescence, so throughout this thesis we worked mainly with fluorescent probes.

2. CHARACTERISTICS OF FLUORESCENCE

The concept of fluorescence was first introduced in 1852 by the British scientist Sir George G. Stokes when he observed the blue luminescence of the mineral fluorite. Over the years, this phenomenon has been explored further and has been used in a wide variety of applications, including the development of fluorescent sensors.

Fluorescence has very attractive and better aspects than absorption spectroscopy methods, such as high sensitivity or large linearity intervals, which makes it necessary to study its characteristics in more detail.

2.1. Fluorescence mechanism

The fluorescence process is defined as one of the mechanisms available to molecules to return to the minimum energy state after being excited. Unlike phosphorescence, the probability of a fluorescence transition is very high, but the half-life of the excited electron stays between 10^{-5} and 10^{-10} seconds, such as, fluorescence is rapidly depleted once the source of excitation is removed.

Fluorescence is usually explained by the Jablonski diagram (Figure 4).[12] If a species in its fundamental electronic state (S_0) absorbs a photon of light, it increases its energy by switching to a higher energy excited singlet state (S_1, S_2...). The half-life of the excited species is short because there are several mechanisms by which it releases its excess energy and relaxes to its ground state.[13] On the one hand, there are the radiative deactivation processes, which are those relaxation processes that lead to the emission of radiation:

[12] P. Elumalai, P. Atkins, J. Paula, Atkins' Physical Chemistry, Oxford University Press, **2002**, ISBN: 0-7167-8759-8.
[13] A. M. Braun, M. T. Maurette, E. Oliveros. Photochemical Technology, John Wiley & Sons, **1991**, ISBN: 978-0471926528.

- Fluorescence: is a relaxation process from the excited electronic state (S_1) to any of the vibrational levels of the ground state (S_0). Both states have the same spin multiplicity.
- Phosphorescence: is a relaxation process that takes place from an excited triplet state (T_1) to the ground state (S_0). This is a process in which the states have different multiplicity, so it takes place after a crossover of systems. This is the least likely deactivation mechanism, but it competes with fluorescence.

On the other hand, there are non-radiative deactivation processes, which are characterized as:

- Internal conversion: this is a relaxation process that takes place between two electronic states of the same multiplicity.
- Vibrational relaxation: a non-radiative relaxation process in which energy dissipation occurs between vibrational levels within the same excited electronic state.
- Intersystem crossing: energy deactivation takes place between two excited electronic states with different spin multiplicity. Transitions between electronic states with different spin multiplicity are in principle forbidden, however, they can occur due to the process known as spin-orbital coupling.
- Bimolecular deactivation or quenching: is a non-radiative deactivation process in which the excited species is deactivated by interacting with another species called a quencher or fluorescence inhibitor.

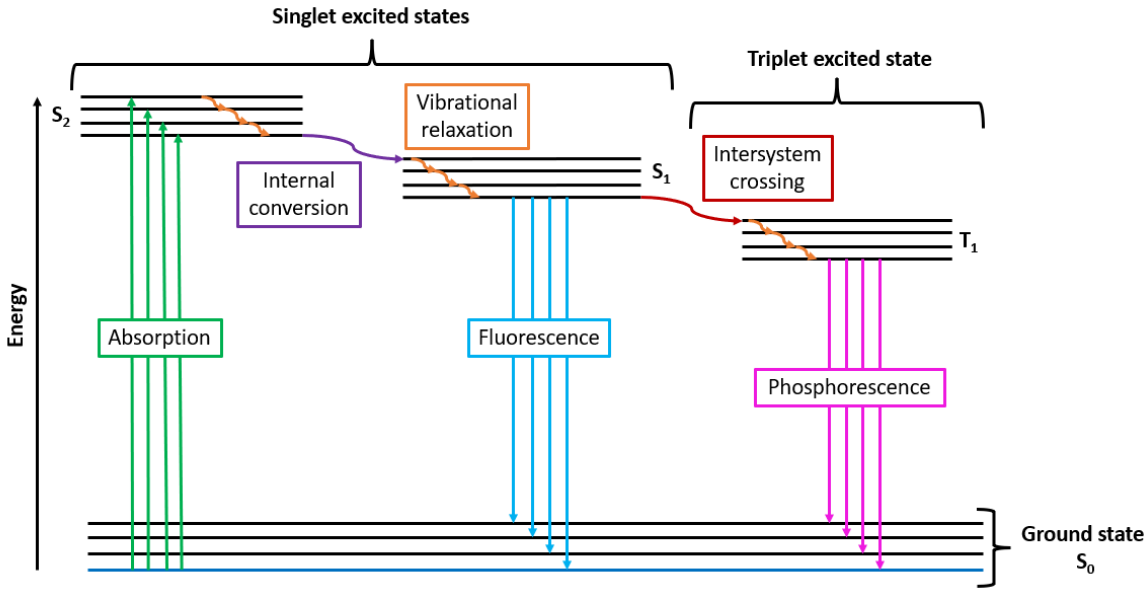

Figure 4. Jablonski diagram.

Since internal conversion and intersystem crossing will compete with fluorescence in deactivating the lower energy excited state, not all molecules will return to the ground state by fluorescence emission. The fraction of excited molecules that emit fluorescence is known as the fluorescence quantum yield ($Ø_F$), which is a physical constant that depends on the temperature and environment of the excited molecular species.

Fluorescence bands are normally observed at longer wavelengths, and therefore at lower energies, than the band of radiation responsible for their excitation (absorption band). This shift to longer wavelengths is called the Stokes shift.

2.2. Factors affecting fluorescence

Apart from the processes that can compete with fluorescence, that have been discussed in the previous section (internal conversion, intersystem crossing, vibrational relaxation, phosphorescence...), there are other parameters that influence the fluorescence. Both the molecular structure and the medium (physical and chemical factors) will determine whether a compound is luminescent or not, as well as the intensity of the emission once it has taken place.[14]

In the majority of fluorescent compounds, radiation is produced by an n→π* or π→π* transition. This condition virtually eliminates saturated organic compounds, while compounds with conjugated double bonds, especially those with a high degree of resonance stabilisation, are very promising. Thus, many unsubstituted aromatic hydrocarbons tend to fluoresce, with increasing quantum efficiency as the number of rings and their degree of condensation increases. Other important factors favouring fluorescence emission are structural rigidity and the presence of electron-donating groups.

The medium significantly influences the intensity of the fluorescent emission, being affected by a few factors, which are listed in Figure 5. In solution, for example, the concentration of the fluorophore, the polarity of the solvent, the viscosity or the pH are very important factors, while other factors such as the presence of ions, the aggregation of species, the probability of hydrogen bonding, the temperature or the pressure have a direct influence on the signal.

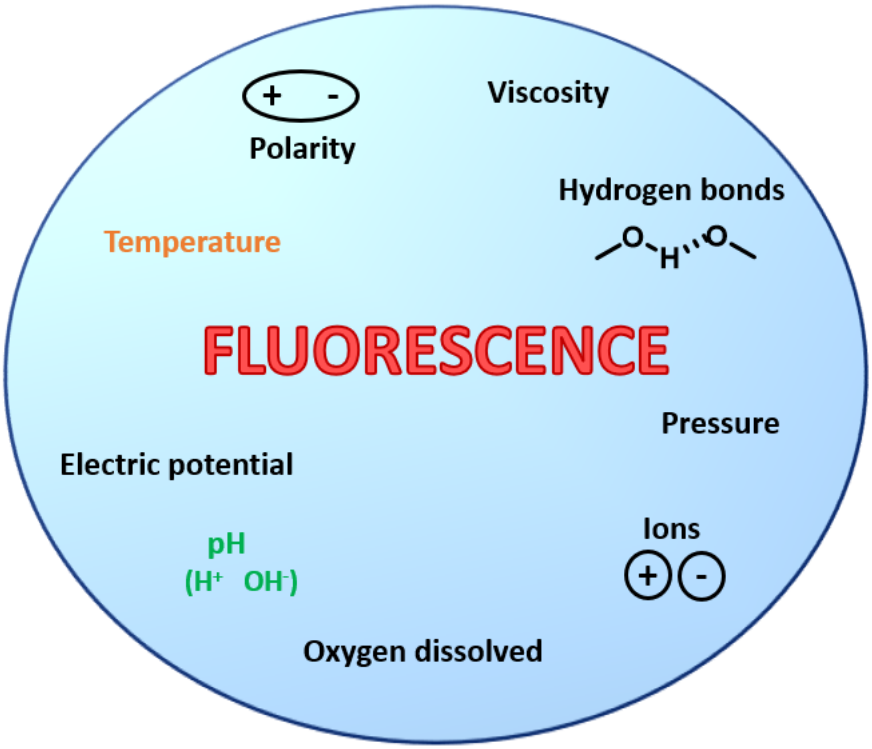

Figure 5. Medium parameters influencing fluorescence.

- Solvent: the study of fluorescent response as a function of solvent polarity is known as solvatochromism. Thus, depending on the solvent, variations in polarity can lead to intermolecular (aggregation) and fluorophore-solvent (solvation sphere) interactions. The fluorescent response is also often very different in protic or aprotic solvents, and it is strongly influenced by pH. Fluorescence is reduced in the presence of solvents containing heavy atoms in their structure, such as carbon tetrabromide and ethyl iodide.

[14] a) D. A. Skoog. Fundamentos de química analítica, Thomson, **2005**, ISBN: 978-0-495-55828-6. b) L. Hernández-Hernández, C. González-Pérez. Introducción al análisis instrumental, Ariel Ciencia, **2005**, ISBN: 84-344-8043-3.

- Viscosity: the fluorescence quantum efficiency decreases as the viscosity of the solvent decreases because the frequency of collisions and the probability of relaxation by internal conversion increases.
- pH: The fluorescence of an aromatic compound with acidic or basic substituents on the ring is pH-dependent. Both wavelength and emission intensity are likely different for the ionised and non-ionised forms of the compound. Changes in the emission of compounds of this type arise from the different number of resonant species associated with the acidic and basic forms of the molecules. The greater the number of resonant forms, the greater the stability of the first excited state, resulting in fluorescent emission.
- Temperature and pressure: these are directly related to mobility, internal vibration and interaction between molecules, as well as influencing all the other parameters considered. An example of the influence of these factors is observed when there is an increase in temperature, which causes an increase in the frequency of collisions and, therefore, an increase in the probability of deactivation by non-radiative processes.
- Dissolved oxygen: [15] its presence usually reduces the fluorescence intensity of a dissolution. This effect may be the result of photochemically induced oxidation of fluorescent species. More often, however, quenching occurs because of the paramagnetic properties of molecular oxygen, which is in the triplet state in the ground state, favouring intersystem crossing and conversion of excited molecules to the triplet state. The paramagnetic nature of oxygen favours spin-orbital coupling with electronically excited molecules, which is considered to form a transitory charge-transfer complex.
- Species in solution: all species in contact with a fluorophore influence the final fluorescence of the solution. However, if the species in solution have no specific interaction with the fluorophore and are dilute (typically $<10^{-5}$ M), their influence on the fluorescence is considered negligible. The interaction between the fluorophore and the species present can be of three types:
    - Static interactions: the interaction between the fluorophore and the analyte occurs by direct electrostatic forces, which modify the electronic properties and, consequently, the fluorescence.
    - Reaction: the interaction between the fluorophore and the other species in the solution gives rise to a new molecule, which alters the fluorescence.
    - Dynamic quenching: interaction by collision or proximity of molecules when not working at infinite dilution is always more likely. This type of interaction depends to a large extent on the parameters discussed so far: fluorophore concentration, temperature, viscosity, or pressure.

Therefore, the conditions under which fluorescence experiments are carried out must be thoroughly controlled. In a typical laboratory experiment, the parameters that are usually controlled are the temperature and pressure, which normally remain constant and are usually equal to the ambient ones, the solvent, which implies a certain polarity, pH and viscosity, and the species present in the solution, for example ions.

[15] A. Ríos-Castro, M. C. Moreno, B. M. Simonet. Técnicas espectroscópicas en química analítica, Editorial Síntesis, S.A., **2012**, ISBN: 978-84-995893-2-9.

2.3. Advantages of fluorescence

Fluorescence spectroscopy has become very popular in the study of changes at the molecular level in all kinds of systems. This is due to the advantages offered by this technique compared to other more conventional methods:[16]

- It presents high selectivity and sensitivity, due to the high molar extinction coefficient of the fluorophores.
- The response times are very short, in the order of 10^{-9} s.
- It is a non-destructive technique.
- Large amounts of sample are not necessary.
- Processes occurring on different time scales can be studied in real time.

2.4. Fluorescence quenching

The intensity of the fluorescent emission can decrease or even disappear (quenching) due to the deactivation of the excited state by interaction of the fluorophores with other species present in the medium, which has been briefly discussed in Section 2.2. Quenching[17] is caused by species with low ionisation potential or low electronic affinity, such as molecular oxygen, transition metal ions and other paramagnetic or highly conjugated species. On the other hand, quenching by interaction with the solvent or with molecules capable of forming hydrogen bonds proceeds by vibrational relaxation mechanisms: the interaction between the fluorophore and the solvent provides a vibrational coupling that favours internal conversion. Quenching processes can be divided into two broad categories: dynamic and static quenching (Figure 6).

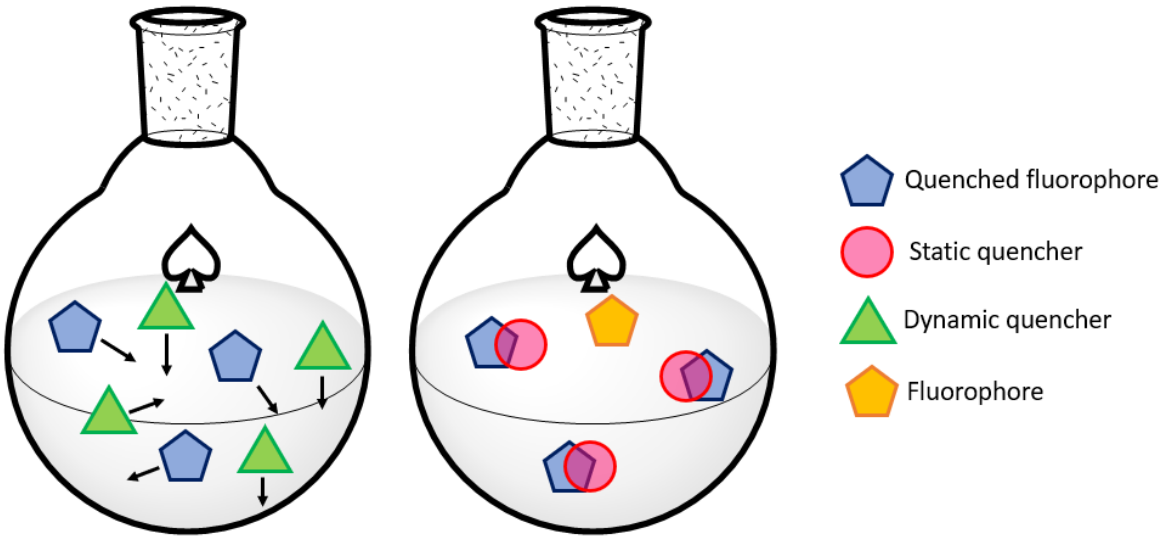

Figure 6. Scheme of the different types of fluorescence quenching.

Dynamic or diffusional quenching is where the interaction between the fluorophore and quencher occurs within the lifetime of the excited state. As a consequence, this quenching is limited

[16] a) W. Retting, B. Strehmel, S. Schrader, H. Seifer. Applied fluorescence in chemistry, biology and medicine, Springer, **1999**, ISBN: 978-3-642-59903-3. b) A. Sharma, S. G. Schulman. Introduction to fluorescence spectroscopy, John Wiley & Sons, **1999**, ISBN: 978-0-471-11098-9.

[17] A. B. Schvval, Influencia de la morfología y el efecto de filtro interno en la eficiencia de películas de polímeros conjugados segmentados como quimiosensores de compuestos nitroaromáticos en medio acuoso, PhD Thesis, Universidad Nacional del Sur, Bahía Blanca, Argentina, **2018**.

by the lifetime of the excited state and the concentration of the quencher. Complexation between the quencher and the excited molecule results in electronic transfer, forming a non-fluorescent oxidised or reduced species. In this type of quenching, the emission intensity is related to the quencher concentration by the Stern-Volmer[18] equation:

$$\frac{\emptyset_{F,0}}{\emptyset_F} = \frac{I_0}{I} = 1 + \tau_0 k_Q [Q]$$

$$k_Q = \frac{8RT}{3\eta}$$

Where $\emptyset_F$ is the fluorescence quantum yield, I is the emission intensity, τ is the fluorescence decay lifetime, $[Q]$ is the quencher concentration and k_Q is a quenching constant, directly proportional to temperature and inversely proportional to viscosity (η).

Static quenching is characterised by complexation in the ground state between the quencher species and the fluorophore. A typical example of this type of quenching is the decrease in fluorescence of *o*-phenanthroline upon complexation with Fe^{2+}. It is important to note that, while in dynamic quenching the fluorescence quantum yield is governed by the diffusion rate of the fluorescent species and the quencher, in static quenching it is governed by the stability of the complex formed between the quencher and the fluorophore in the ground state.[19]

Another factor leading to reduced fluorescence is the presence of heavy atoms or paramagnetic species because they facilitate spin-prohibited processes and increase the rate at which intersystem crossover occurs.

3. FLUORESCENT PROBES

Applying the properties of fluorescence discussed in the previous Section to the field of sensors results in fluorescent probes, which are defined as those in which the detection of the analyte is produced by variations in fluorescence. This detection can be carried out by means of two different procedures:

- Fluorescence quenching (ON-OFF or turn-off): this method is based on the specific quenching of fluorescence by interaction with the analyte of interest, which is what was previously mentioned as static quenching. However, this is a non-selective process, so it is necessary to take into account other species present that may be responsible for dynamic quenching, such as cationic and anionic species.
- Fluorescence enhancement (OFF-ON or turn-on): this is an increase in fluorescence due to interaction with a particular analyte. This increase in fluorescence can occur by different mechanisms: an increase in fluorescence from an initially non-fluorescent species or an increase in fluorescence of a specific wavelength either by decreasing the fluorescence of the initial wavelength or of a totally different wavelength. This is the most reliable method because it can be clearly differentiated from quenching procedures.

There are a variety of photophysical phenomena that produce the electron transfers responsible for fluorescence variations. The most relevant of these are photoinduced electron transfer (PET) and photoinduced charge transfer (PCT).

[18] a) J. R. Lakowicz, G. Weber, *Biochem.*, **1973**, *12*, 4161-4170. b) Y. A. Fuentes-Rubio, R. F. Domínguez-Cruz, O. Baldovino-Pantaleón, C. Ruiz-Zamarreño, F. J. Arregui, *IEEE Sens. J.*, **2020**, 1-4.
[19] H. Wang, S. Ma, Y. Sun, M. Gao, X. Wang, *Microchem. J.*, **2023**, *190*, 108720.

3.1. Photoinduced electron transfer (PET)

Photoinduced electron transfer, abbreviated as PET,[20] involves the transfer of an excited electron from a donor to an acceptor. This process can take place intramolecularly when the donor and acceptor coexist in the same molecule, but it can also take occur intermolecularly when both are in different molecules.

The following scheme shows the mechanism for an intramolecular PET (Figure 7), which causes fluorescence quenching. However, the addition of an analyte blocks the electron transfer, resulting in fluorescence.

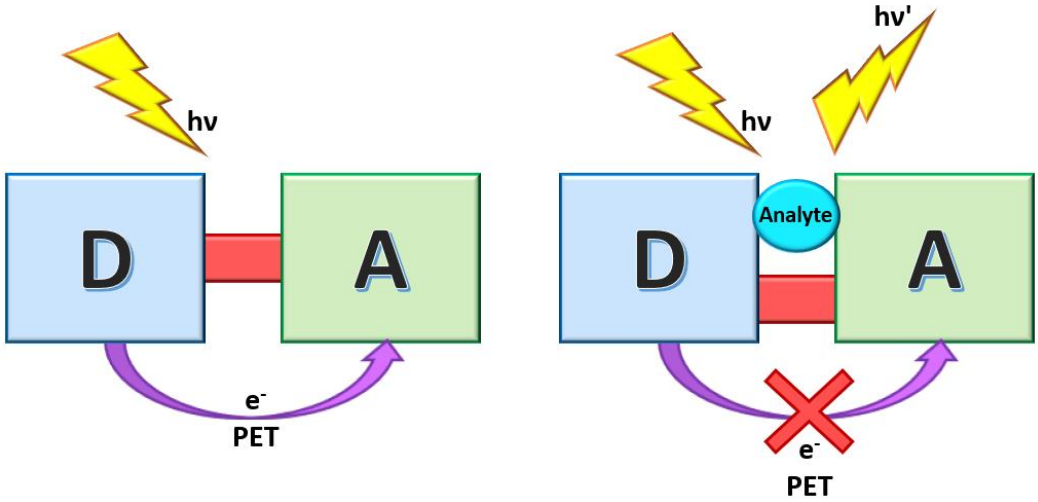

Figure 7. Mechanism of an intramolecular PET fluorescent probe.

Through the PET process, both turn-on and turn-off switching can occur.[21] The turn-on process is observed in receptors with non-bonding electron pairs, such as N or O. As can be seen in Figure 8, when the fluorophore is excited, it promotes an electron from the HOMO to the LUMO. The non-bonding electron pair, which is at an intermediate energy level between the HOMO and LUMO orbitals of the fluorophore, transfers an electron to the HOMO orbital of the fluorophore, resulting in a deactivation of the fluorescence. The excited fluorophore transfers the electron from the LUMO to the intermediate energy orbital, restoring the ground state. Upon coordination with the analyte, the intermediate orbital between the HOMO and the LUMO of the fluorophore drops in energy so that electron transfer is no longer possible and an increase in fluorescence intensity occurs.

On the other hand, the turn-off process occurs when the energy level of the LUMO of the analyte is between the HOMO and the LUMO of the fluorophore. Therefore, after the interaction between the receptor and the analyte, a non-radiative pathway is provided to dissipate the excitation energy, resulting in fluorescence quenching, as depicted in Figure 9.

It should be noted that even if a PET process is thermodynamically feasible, it does not imply its occurrence because it may not be fast enough to compete with other photodeactivation processes.[22]

[20] a) D. Escudero, *Acc. Chem. Res.*, **2016**, *49*, 1816–1824. b) P. Panchenko, O. Fedorova, Y. Fedorov, *Russ. Chem. Rev.*, **2014**, *83*, 155-182.

[21] S. Fernández-Alonso, Sensores sólidos fluorescentes obtenidos por funcionalización con derivados de 1,8-naftalimida de copolímeros de etileno-acrilato de butilo y de membranas acrílicas fotoentrecruzadas, PhD Thesis, Autonomous University of Madrid, **2018**.

[22] L. J. Fan, Y. Zhang, C. B. Murphy, S. E. Angell, M. F. L. Parker, B. R. Flynn, W. E. Joner, *Coord. Chem. Rev.*, **2009**, *253*, 410-422.

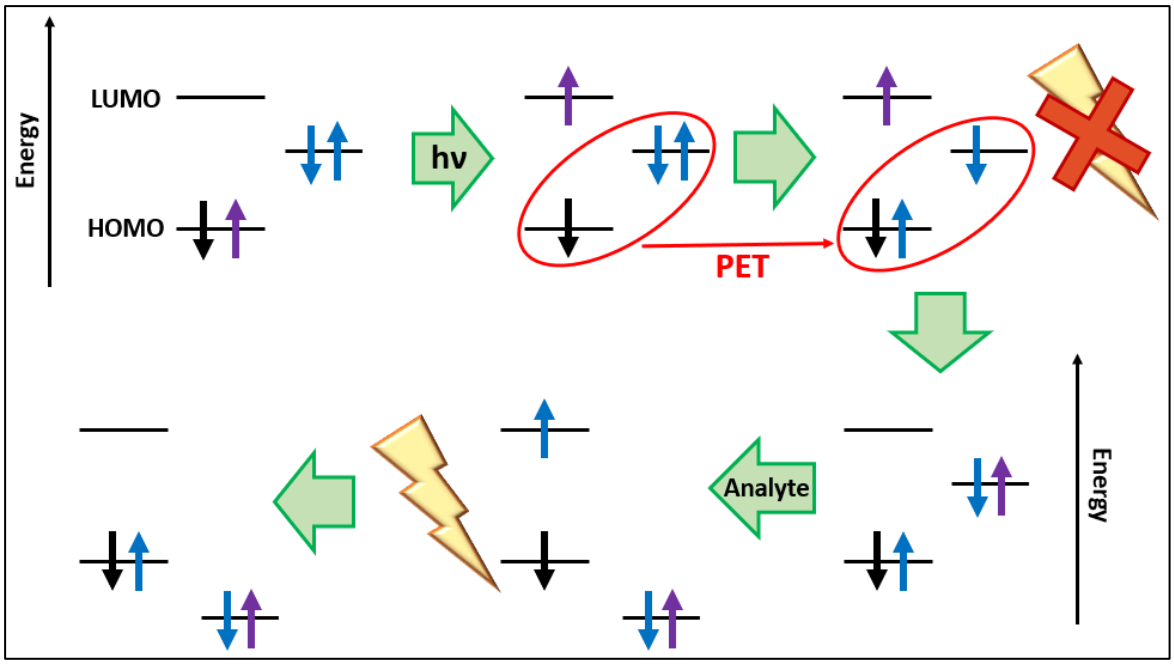

Figure 8. Orbital diagram of the PET process in a turn-on sensor.

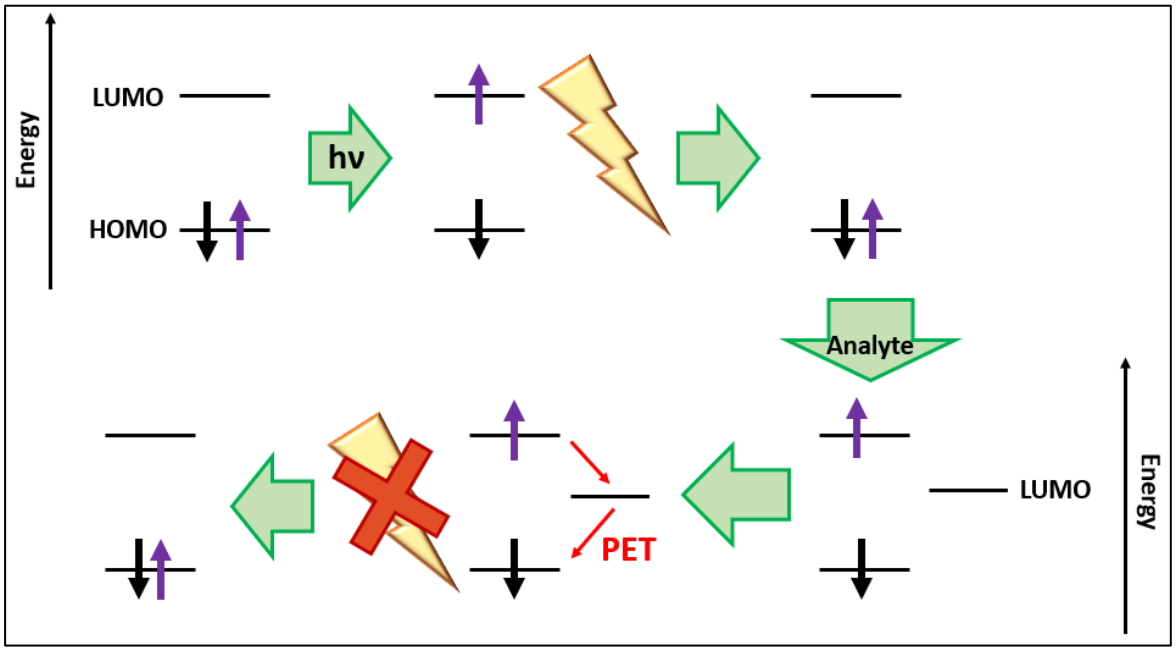

Figure 9. Orbital diagram of the PET process in a turn-off sensor.

3.2. Photoinduced charge transfer (PCT)

Photoinduced charge transfer, abbreviated as PCT,[23] happens in molecular sensors in which the recognition unit is part of the fluorophore. Normally, the fluorophore contains the electron donor group conjugated to an electron acceptor group. Once photoexcitation occurs, the transfer of a high-energy electron from the donor to the LUMO of the acceptor takes place (Figure 10). This electron transfer process involves 5 steps:[24]

[23] X. Li, S. Surendran, J. Yu, P. Deria, *Dalton Trans.*, **2020**, *49*, 12892.
[24] N. S. Sariciftci, L. Smilowitz, A. J. Heeger, F. Wudl, *Science*, **1992**, *258*, 1474–1476.

1. Photoexcitation of the donor from HOMO to a higher energy level.
2. Delocalisation of excited states in the donor-acceptor pair.
3. Separation of the charges of the donor-acceptor pair, leading to the formation of a dipole moment.
4. Formation of a pair of radical ions depending on the oxidation potential of the donor and the reduction potential of the acceptor.
5. Formation of the electron transfer state.

The change in dipole moment when a species is recognised by the receiver unit produces a fluorophore-dependent Stokes shift, allowing this type of charge transfer to be used in probe design.[25]

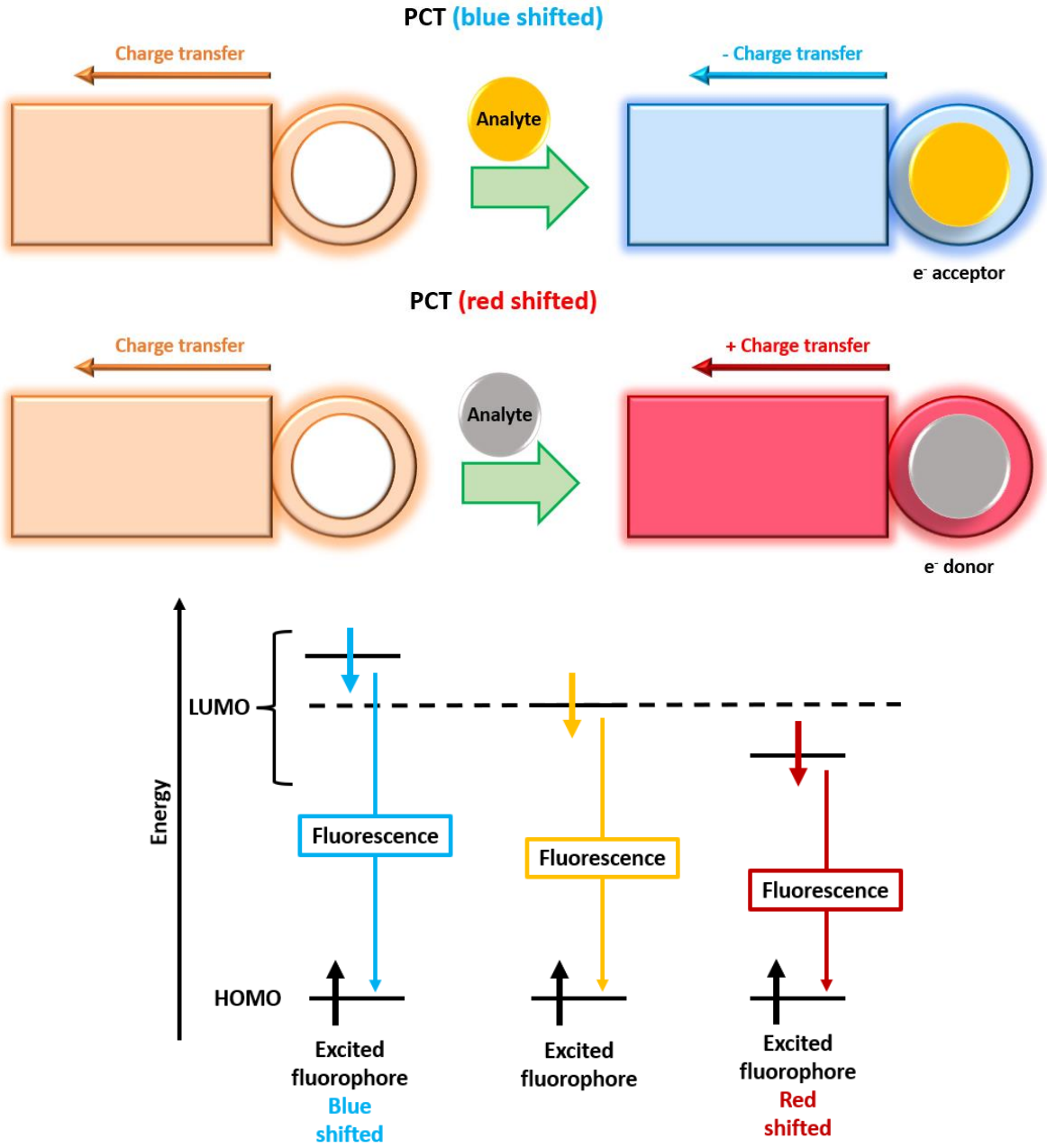

Figure 10. PCT mechanism when different analytes are added (up) and energy levels diagram (down)

[25] M. K. Homer, D. Y Kuo, F. Y. Dou, B. M. Cossairt, *J. Am. Chem. Soc.*, **2022**, *144*, 14226-14234.

3.3. Excitation energy transfer (EET): excimer formation and FRET

Excitation energy transfer, abbreviated as EET,[26] is a bimolecular process that occurs between two different fluorophores, where one is the donor and the other is the acceptor. In this case, the excited fluorophore can accept or donate electrons to another fluorophore in the ground state, resulting in a reduction of fluorescence. The factor controlling the existence of EET is the redox potential of the donor fluorophore. Generally, the rate of energy transfer in these processes can be described by theories derived from Fermi golden rule:

$$k_{EET} = \frac{2\pi}{\hbar} \cdot |V|^2 \cdot J$$

Where *V* is the electronic coupling and *J* is the density of states weighted by the Frank-Condon factor.

Excimer formation[27] is a special case of energy transfer between identical fluorophores. Normally, the fluorophores bound to the recognition unit via their side chains, interact with each other by π-π stacking or other polarity-related forces (Figure 11). The fluorophores bound by the recognition unit and the presence of the analyte modifies the interaction between them, modifying the fluorescence.

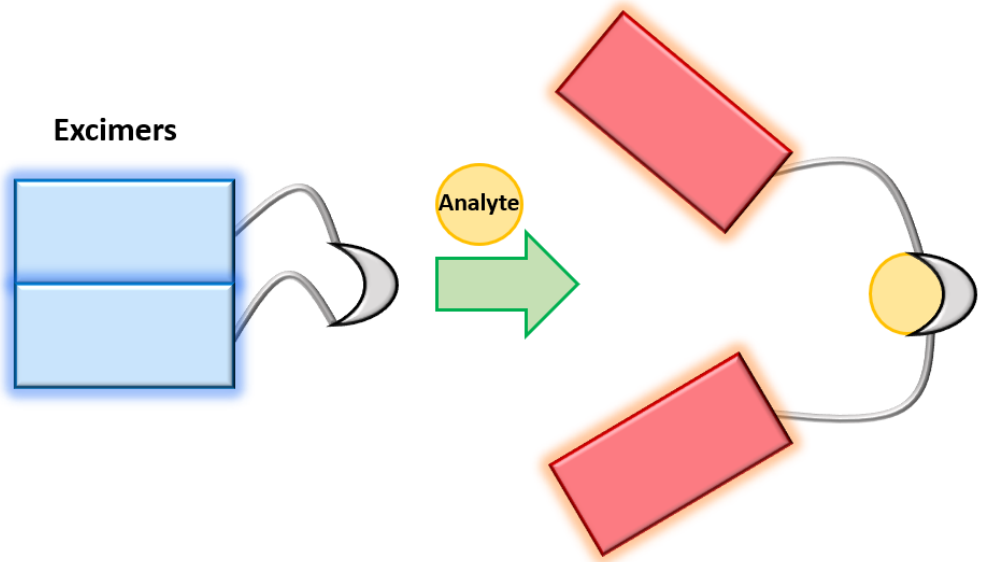

Figure 11. Mechanism of excimer separation when an analyte is added.

In emission spectra, both monomer and excimer signals are usually observed. This feature can be used for radiometric measurements, in which the intensity ratio between the bands is used to determine the ion concentration. Radiometric measurements eliminate distortions in the data caused by photobleaching and variations in indicator concentration, as well as those due to instrumental factors, such as changes in lamp intensity.

The Förster resonance energy transfer process, abbreviated as FRET,[28] can also be found in this group. It is a distance-dependent physical process by which non-radiative energy is transferred from an excited molecular fluorophore (donor) to another fluorophore (acceptor) via long-range intermolecular dipole-dipole coupling (Figure 12). FRET can be an accurate measure of molecular proximity at distances on the order of angstroms.

[26] C. P. Hsu, *Acc. Chem. Res.*, **2009**, *42*, 509-518.
[27] K. V. Balakin, V. A. Korshun, I. I. Mikhalev, G. V. Maleev, A. D. Malakhov, I. A. Prokhorenko, A. Y. Berlin, *Biosensors Bioelectron.*, **1998**, *13*, 771-778.
[28] R. B. Sekar, A. Periasamy, *J. Cell Biol.*, **2003**, *160*, 629-633.

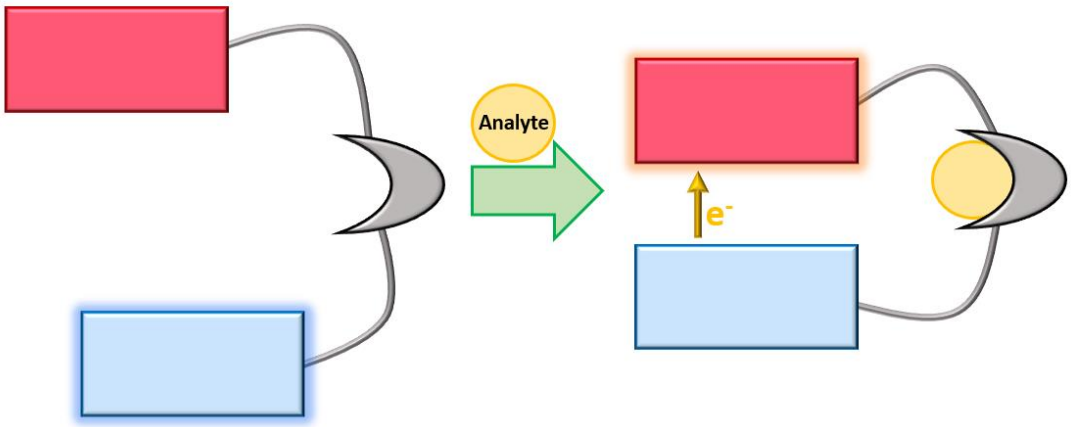

Figure 12. Mechanism of FRET when an analyte is added.

The presence of the recognition unit between the two fluorophores can change the conformation and, therefore, the response.

3.4. CHARACTERISTICS OF AN IDEAL FLUORESCENT SENSOR

There is a wide variety of fluorophores, of widely varying sizes and structures, and there are several practical aspects that can help in their selection. These standards are also used in the evaluation of new dyes and include both photophysical and analytical aspects.[29]

3.4.1. Photophysical characteristics:

The most important photophysical characteristics of fluorescent probes are the following:

- High molar absorptivity (ε). The molar extinction coefficient, also known as molar absorptivity, is a measure of the intensity with which a chemical species absorbs light of a determined wavelength. High molar absorptivities represent symmetry-allowed transitions, such as π-π*, where electron promotion from the ground state can easily occur, resulting in high fluorescence and high sensitivity.
- High fluorescence quantum yield ($Ø_F$). It is defined as the ratio of the number of photons emitted to the number of photons absorbed. The higher the value of $Ø_F$, the lower the probability of fluorescence quenching by non-radiative quenching methods or thermal relaxation and the more accurate and less noisy the measurements are. This factor is favoured with dyes that have flat and aromatic structures, such as perylene or naphthalene rings.
- Optimal excitation wavelength. Generally, the excitation wavelength should be longer than 400 nm to avoid degradation of molecules by high-energy radiation, which is especially important for molecules used for biological purposes.
- Optimal emission wavelength. Emission detectors are much more sensitive to radiation in the visible region, that is, between 400 and 750 nm. For fluorophores used in biological applications, emission bands beyond 450 nm are necessary to be distinguishable from the blue background.
- Large Stokes shift. The Stokes shift is defined as the difference (in wavelength or frequency units) between the position of the absorption maximum and the emission

[29] M. D. Heagy, *Chemosensors*, **2011**, *13*, 253–273.

maximum of a fluorophore. This will make it possible to avoid FRET, homo-FRET and reabsorption processes between fluorophores. It will also facilitate data processing as there is no band overlapping.

- Fluorescence lifetime (τ) between 0.5 and 20 ns. The fluorescence lifetime refers to the average time a molecule remains in its excited state before emitting a photon, however, it is highly dependent on the solvent used. Long lifetimes are usually associated with high quantum yields and are easy to detect and analyse.
- High photostability. This avoids photodegradation, to which most organic dyes are very susceptible.

Figure 13 summarises all the above photophysical characteristics.

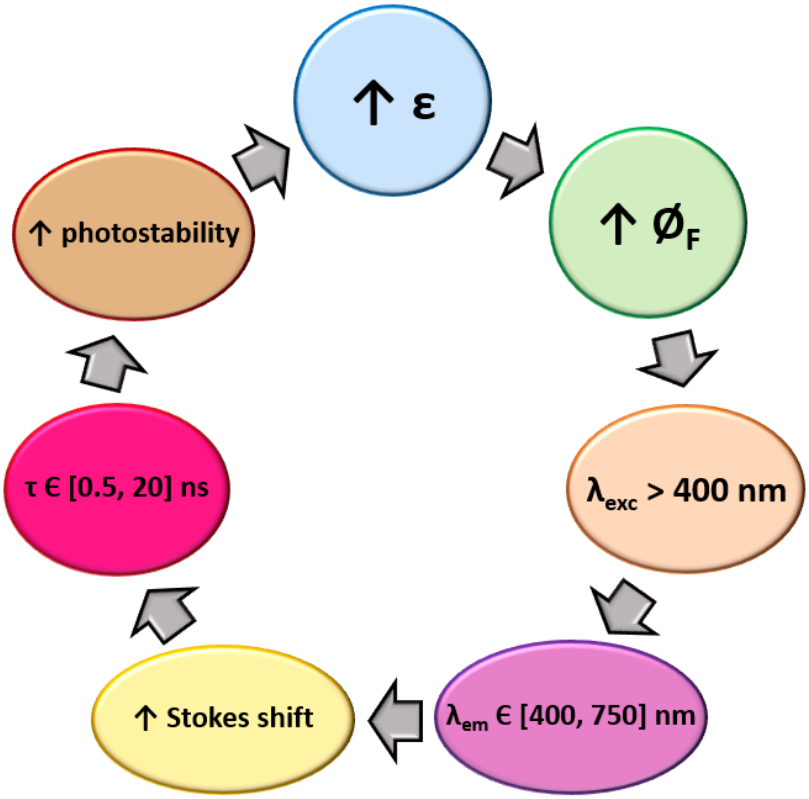

Figure 13. Summary scheme of photophysical properties of an ideal fluorescent probe.

In the literature, it is very common to find publications in which only the increase in fluorescence is considered without examining any of the other parameters mentioned. In fact, multiplying fluorescence by 3 or by 35 is indifferent if the additional data are not taken into account.

An example of this situation is shown in Figure 14. State 1 shows a probe with a blue fluorescence and very low fluorescence quantum yield ($Ø_F$ = 0.1%). When the analyte is added, the fluorescence quantum yield increases to 5%, about 50 times, but the fluorescence is still very low, so the experimental error in the measurements is likely to be very high, as well as the possibility of interferents.

In contrast, State 2 shows an orange fluorescence that triples its fluorescence quantum yield (from 7% to 21%) when the analyte is added. As can be observed, the increase in fluorescence is much smaller but, by working with higher quantum yields, the experimental error will be much smaller. In addition, a yellow-orange fluorescence is much more attractive than a blue fluorescence for probes with biological applications.

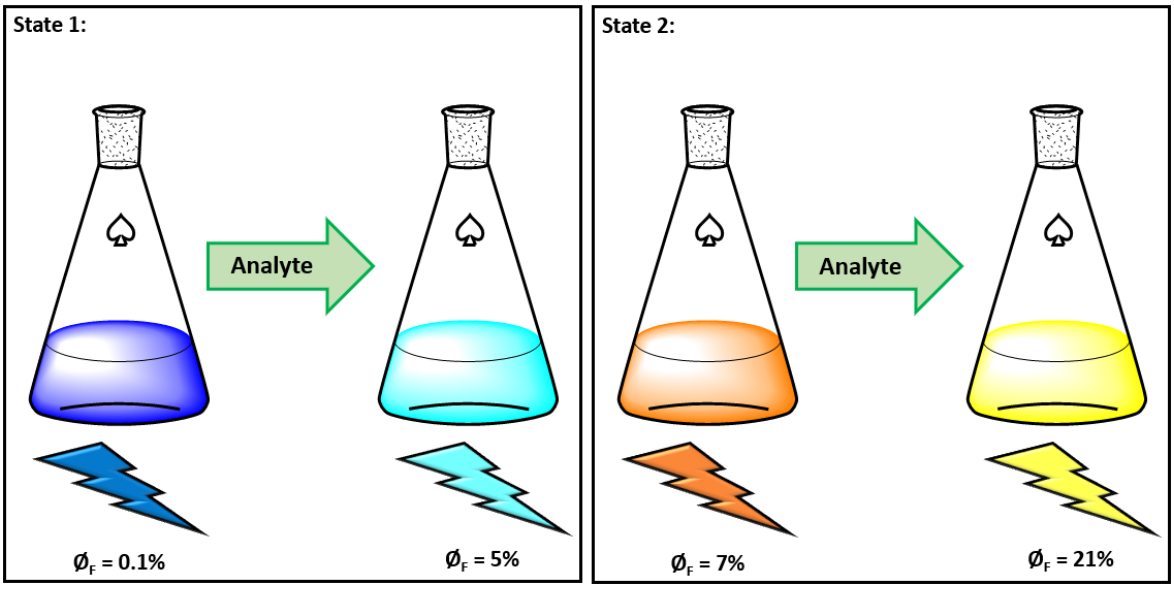

Figure 14. Illustrative example of the increase in fluorescence. In State 1 there is a 50-fold increase while in State 2 the increase is only 3-fold.

3.4.2. Analytical characteristics:

The most important analytical properties that a fluorescent probe must exhibit are the following:

- Good solubility in the selected solvent. The solubility of the fluorophore in the chosen solvent has to be high to prevent aggregation or precipitation processes. It is also desirable that the sensors are soluble in water to allow the detection of contaminants in the environment, such as cations in river water, or also to carry out *in vivo* cell studies.
- Direct measurements. Measurements that are carried out after a direct analyte-fluorophore interaction are more reliable than those that require the intervention of a third species. A three-species equilibrium, apart from reducing reliability, makes interpretation of the results more difficult.
- Turn-on probes. Fluorescence turn-on sensors are more reliable and selective than turn-off sensors because they are clearly differentiated from quenching processes, as seen in previous sections.
- High selectivity. Achieving 100% selectivity is impossible for any sensor, but the most suitable conditions must be studied in which the highest possible selectivity is achieved.
- High sensitivity, reflected in a low detection limit.
- Recyclability. It is most desirable to obtain probes that can be reused, which is the case when the interaction with the analyte occurs through a complexation process. On the other hand, for those interactions that are produced by a reaction, reusability is impossible.

Figure 15 below summarises all the above-mentioned analytical characteristics.

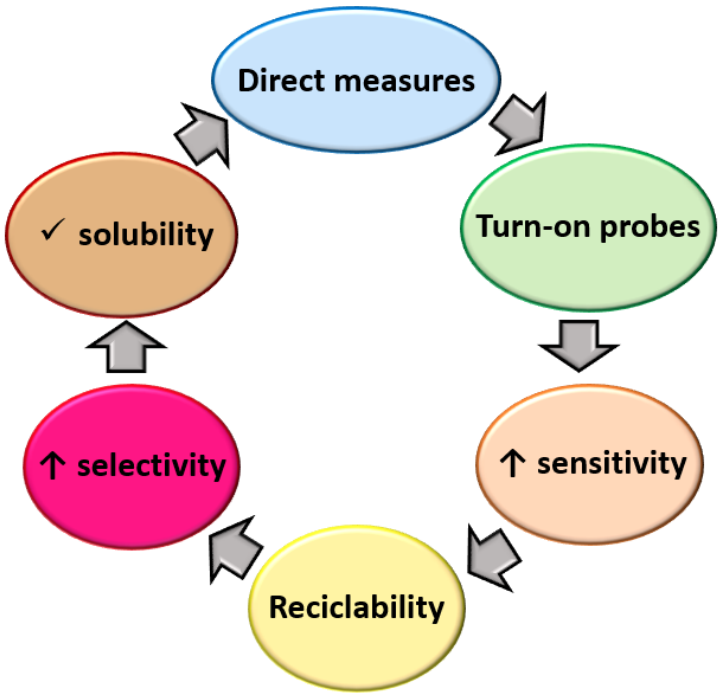

Figure 15. Summary scheme of analytical properties of an ideal fluorescent probe.

4. GENERAL OPERATING PROCEDURE FOR FLUORESCENT PROBES[30]

In this thesis, different fluorogenic sensors have been developed. The procedure followed to obtain them can be summarised in the following steps:

1. Synthesis of the fluorescent probes. This involves the synthesis of both the fluorescent skeleton (such as NMI or PMI) and the synthesis of the recognition part and the union of both fragments to give rise to the sensor itself.
2. Characterisation of the compounds synthesised. This is done using different techniques such as NMR, IR, high resolution mass spectrometry, melting point and certain fluorescence parameters such as lifetime and fluorescence quantum yield.
3. Search for a suitable support. If necessary, the probe obtained is attached to a material that acts as a support.
4. Fluorescence studies. This part depends on the purpose for which the synthesised molecule is to be used. In general, the sensors work well in solution, so the process starts with solvatochromism and qualitative detection tests for different species. Subsequently, for those probes that give a positive result, a solvent study, calculation of the working concentration and kinetic studies are carried out. Finally, quantitative studies are carried out for the calculation of detection limits.

Each of the fluorescence studies carried out for the molecules developed will be detailed below.

[30] J. García-Calvo, Fluorescent probes and nanostructured materials for the detection of environmental toxins and catalysts development, PhD thesis, University of Burgos, **2018**.

4.1. Solvatochromism

Solvatochromism is defined as the study of the variation of the absorption and emission bands of a compound as a function of the polarity of the solvent. The main objective of this study is to find a suitable solvent for the subsequent experiments. The requirements for selecting a good solvent are as follows:

- The solvent must be miscible with water because the analyte solutions of the detection tests are prepared in water. This is especially important if the probe is destined for use in biological applications.
- High solubility of the molecule in the selected solvent, so that the concentration of the solutions can be close to 0.1 mM. A lower solubility would imply difficulties in performing subsequent titrations.
- The fluorophore has to exhibit an intermediate emission intensity, so that variations in both increasing and decreasing fluorescence can be observed. However, detection may not only occur in these ways, but may also occur by the appearance of a new emission band at a different wavelength from the initial one.

The general procedure developed for solvatochromism is as follows:

For each compound studied, a mother solution was prepared, normally using chloroform as solvent, because it is a volatile solvent in which the compounds usually have good solubility and stability. An aliquot of this mother solution was then poured into different vials, one for each solvent to be used, in this case, fourteen. Once the chloroform has evaporated, the sensor is redissolved in each of the chosen solvents (Figure 16), working with a final concentration of the sensor between 5 and 100 µM, depending on the characteristics of the probe. Finally, absorption and emission spectra were recorded and photos of the solutions were taken under visible light and under 366 nm UV light.

1. Water	**8.** THF
2. MeOH	**9.** $CHCl_3$
3. DMSO	**10.** DCM
4. DMF	**11.** Toluene
5. MeCN	**12.** Et_2O
6. Acetone	**13.** Hexane
7. EtOAc	**14.** Methycyclohexane

Figure 16. Solvents used in solvatochromisms ordered according to the Snyder index.

An example of solvatochromism is shown below for compound AR94p (Figure 17) where photographs taken under visible and UV light as well as absorption, emission and normalised plots are shown.

	H_2O MeOH DMSO DMF MeCN Acet. EtOAc THF $CHCl_3$ DCM Tol. Et_2O Hex MCH
Visible light	

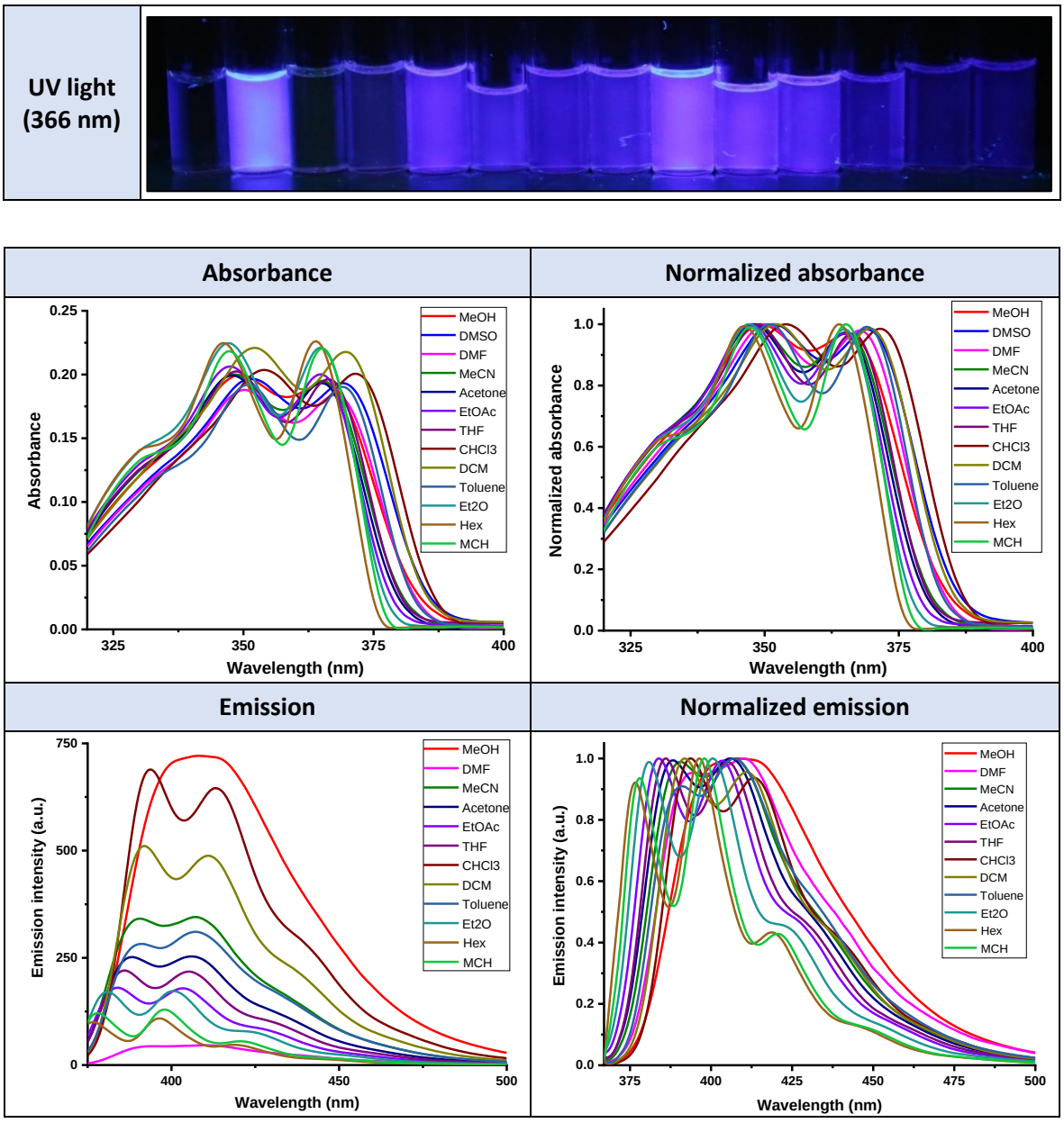

Figure 17. Solvatochromism of AR94p. Photographs under visible and 366 nm UV light (upper table) and absorption and emission plots (lower table) of a 10 µM solution of the probe in 14 different solvents. λ_{exc} = 360 nm.

4.2. Detection tests

Once the adequate solvent has been selected by solvatochromism, the detection tests are carried out, which can be defined as an initial qualitative study of the detection capacity of a new compound, for which different anionic, cationic, oxidising and reducing species are used. However, before carrying out these tests, a study of the influence of the medium on the fluorescence behaviour of the compounds is carried out.

Regardless of which test is carried out, the procedure followed was the same. A mother solution of the sensor to be studied was prepared in the solvent previously chosen. The concentration of the probe normally varied between 0.01 and 0.1 µM depending on its solubility and fluorescence. The species to be studied or the different amounts of water were added from a concentrated solution, usually 10 microlitres of the stock solution. Colour and fluorescence changes were

photographed under white light and 366 nm UV light both at the time of preparation and 24 hours later.

4.2.1. Environment studies

First, a water acceptance test is carried out in which increasing amounts of water are added and the changes in both colour and fluorescence are studied. The amount of water varies between 0 and 90%. An example of this test is shown in Figure 18 below.

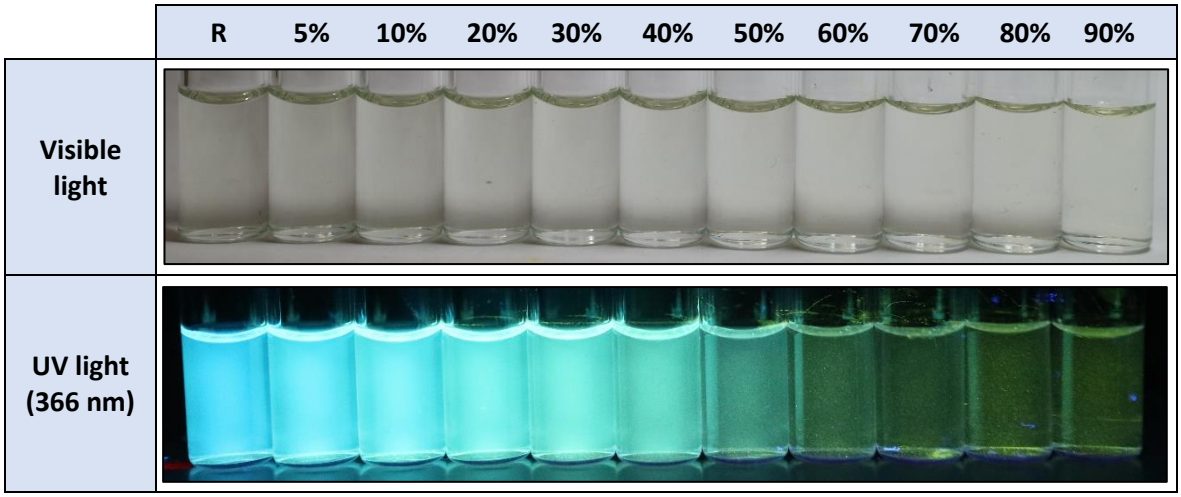

Figure 18. Water acceptance test of a 20 µM dissolution of AR27 in acetone under visible light and 366 nm light.

In this case, an aggregation caused quenching phenomenon (ACQ) was observed. However, in many of the synthesised compounds, the AIE phenomenon was observed so that the aggregates formed were studied using different microscopy techniques (Section 4.3).

This test determines the maximum amount of water admissible for each compound. Figure 18 shows that from 30% water, fluorescence quenching began to occur. This amount of water was replaced by buffer solutions of different pH (20 mM of HEPES). Figure 19 shows the influence of pH on the fluorescence of compound AR27.

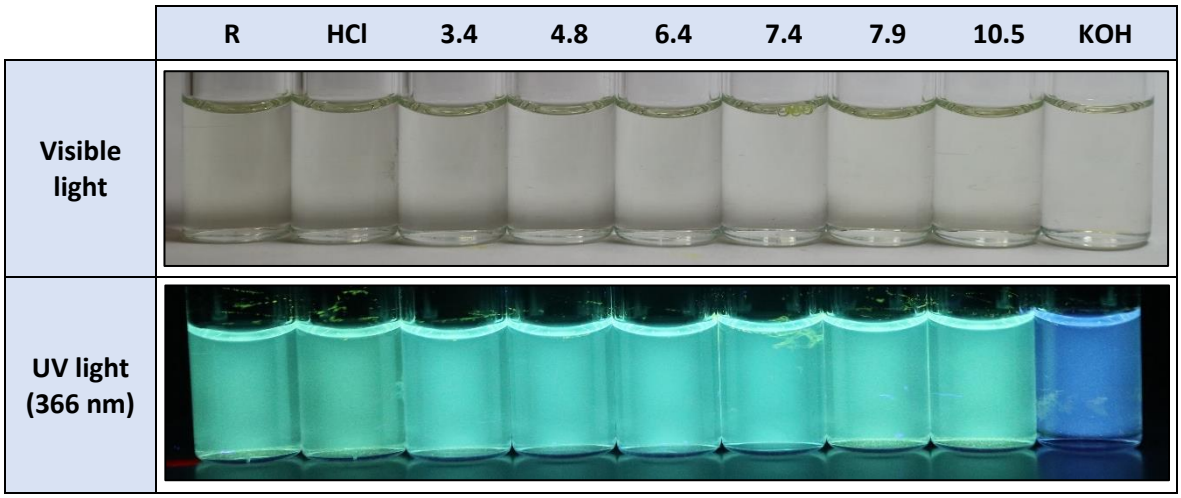

Figure 19. pH test of a 20 µM solution of AR27 in acetone under visible light and 366 nm light.

As can be seen in the Figure above, this product only exhibited fluorescence changes at very basic pH.

4.2.2. Ionic-addition studies

Once the study of the influence of the medium on the fluorescence of the sensor has been completed, the addition of different anionic, cationic, oxidising and reducing species is carried out. The compounds used to prepare the solutions used in the cation test are shown in Figure 20. An example of this type of test is shown in Figure 21 for compound AR85. As can be seen, only a quenching of fluorescence was observed upon exposure to Au^{3+}.

1. $AgClO_4 \cdot xH_2O$	**10.** $Al(ClO_4)_3 \cdot 9H_2O$
2. $Ni(ClO_4)_2 \cdot 6H_2O$	**11.** $Hg(ClO_4)_2 \cdot H_2O$
3. $Sn(CF_3SO_3)_2$	**12.** $HAuCl_4 \cdot 3H_2O$
4. $Cd(ClO_4)_2 \cdot H_2O$	**13.** $Co(BF_4)_2 \cdot 6H_2O$
5. $Zn(CF_3SO_3)_2$	**14.** $PdCl_2 \cdot H_2O$
6. $Pb(ClO_4)_2 \cdot 3H_2O$	**15.** $IrCl_3$
7. $Cu(ClO_4)_2 \cdot 6H_2O$	**16.** $Cu(MeCN)_4PF_6$
8. $Fe(ClO_4)_3 \cdot xH_2O$	**17.** $RuCl_3$
9. $Sc(CF_3SO_3)_3$	**18.** $PtCl_2$

Figure 20. Compounds used in the preparation of cation solutions.

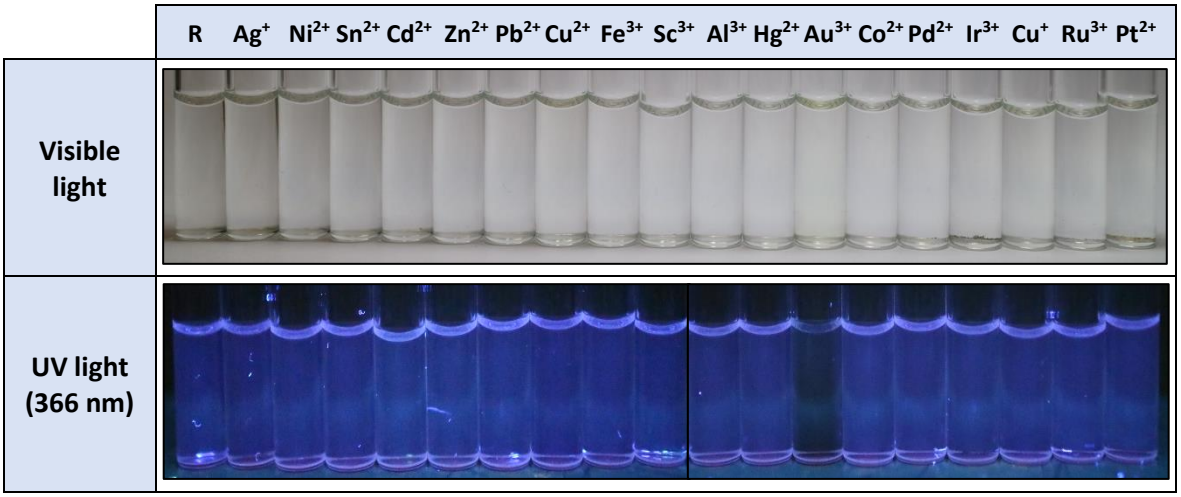

Figure 21. Cation test of a 10 µM dissolution of AR85 in THF under visible light and 366 nm light.

In the same way, the anion tests were carried out with the compounds of Figure 22 for the preparation of the solutions. An example of this type of test is shown in Figure 23 for compound AR80, where no change was observed for any of the added analytes.

1. $NBu_4F \cdot 3H_2O$	**7.** $NBu_4H_2PO_4$
2. NBu_4Cl	**8.** NBu_4HSO_4
3. NBu_4Br	**9.** NBu_4AcO
4. NBu_4I	**10.** NBu_4CN
5. NBu_4BzO	**11.** NBu_4SCN
6. NBu_4NO_3	

Figure 22. Compounds used in the preparation of anion solutions.

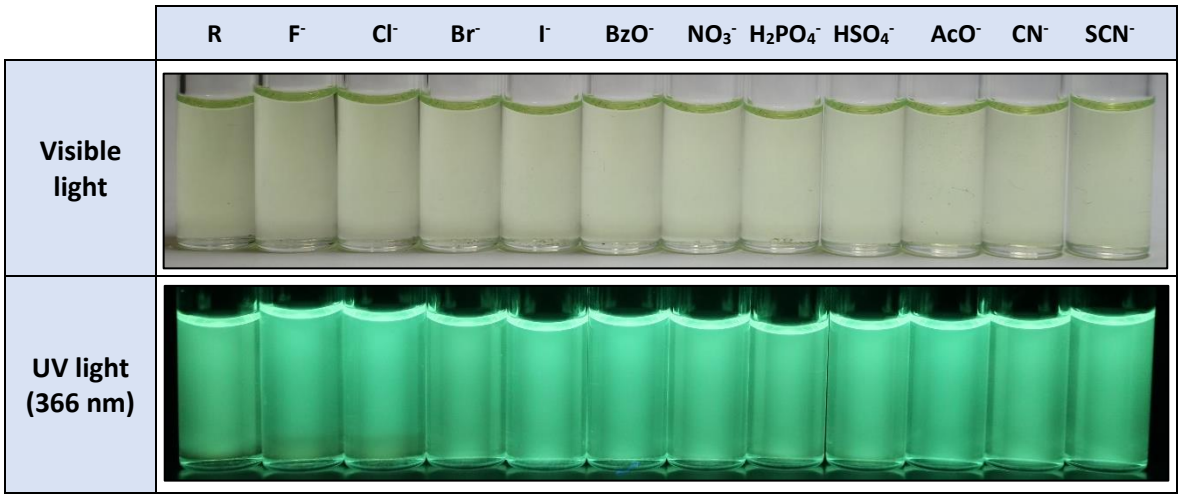

Figure 23. Anion test of a 20 µM dissolution of AR80 in THF under visible light and 366 nm light.

Finally, the test is carried out using different species of oxidants and reductants as analytes. The different species used are listed in Figure 24 below.

R.A. Reference with H_2O	**R.B.** Reference with MeOH	**R.C.** Solvent-free reference
1.A. HCl	**1.B.** *m*-CPBA	**1.C.** *m*-CPBA
2.A. HNO_3	**2.B.** TNB	**2.C.** TATP
3.A. Oxone	**3.B.** TNT	**3.C.** HMTD
4.A. Hidrazine		
5.A. H_2O_2		

Figure 24. Compounds used in test for oxidants and reducing agents.

As can be seen in Figure 24, the different analytes were classified into three different groups according to the solvent used in the preparation of the solutions. The solutions of group A had been prepared using water as the solvent, while the solutions of group B had been prepared in methanol, since these analytes were not soluble in water. Group C, on the other hand, used the solvent selected in solvatochromism in which the different analytes were added as a solid (spatula tip). An example of this type of test is shown in Figure 25.

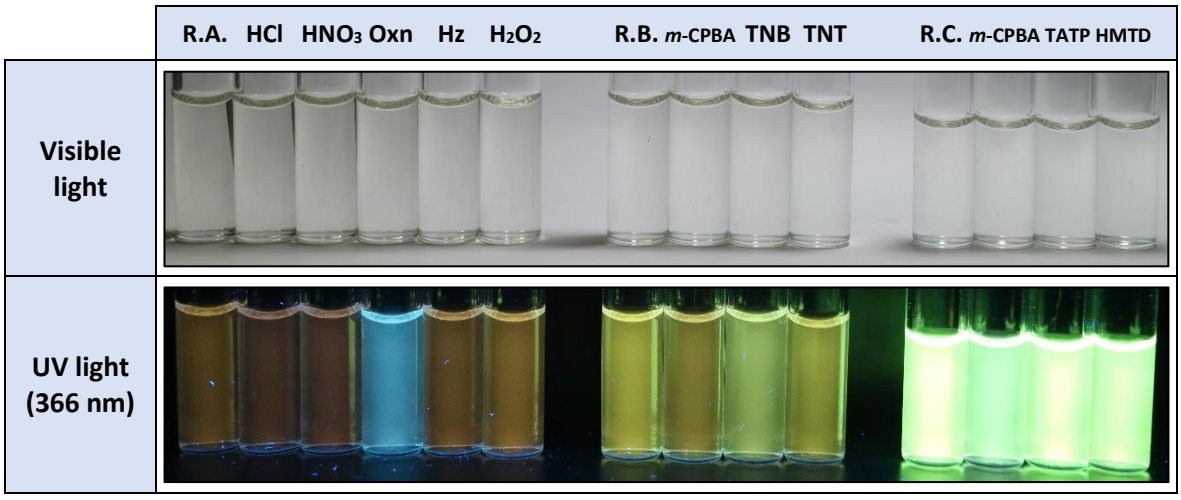

Figure 25. Test for oxidants and reducing agents of a 20 µM solution of AR82s in acetone under visible light and 366 nm light.

Compounds giving a positive result, in other words, a variation in fluorescence against any of the species of interest analysed in these tests, are submitted to the other experiments to study the observed variation in fluorescence emission.

4.3. Microscopic studies

As mentioned above, the compounds that exhibited the AIE phenomenon in the water acceptance test were studied using different microscopy techniques, such as SEM and AFM. This phenomenon is very common in NMI derivatives, as is the case of compound AR52, which is the one shown in Figure 26. In this Figure, it can be seen how from 60% water the fluorescence becomes more intense due to the formation of nanoaggregates.

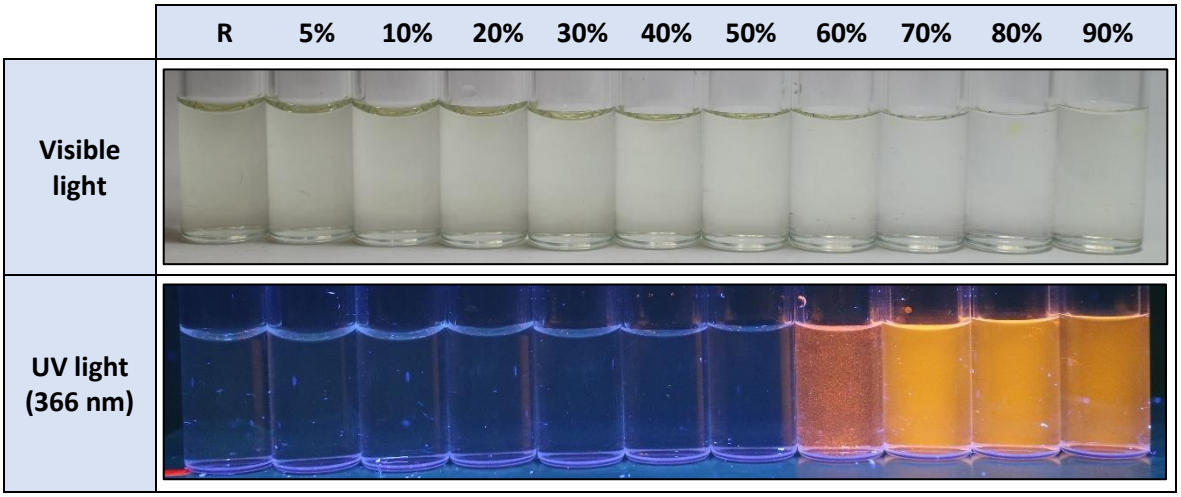

Figure 26. Water acceptance test of a 20 µM solution of AR52 in MeOH under visible light and 366 nm light. AIE was observed from 60% of water.

4.3.1. Scanning Electron Microscopy (SEM)

Scanning electron microscopy, abbreviated as SEM, is performed by emitting a beam of electrons that interacts with the surface of the sample, producing different types of signals that are picked up by the detectors. This technique can be used to study samples of diverse nature, such as metals, ceramics, polymers, composites, or organic samples.

Sample deposition was carried out by evaporation, that is, by depositing a drop of 20 - 25 µl on a silicon disc. This disc was placed on an aluminium holder, bonded with colloidal solution of graphite in aqueous base. Although samples of an organic nature were studied, it was not necessary to metallise them, so the voltage of the electron beam was 1.2 kV and a high vacuum was used. The distance from the sample to the detector varied between 4 and 6 mm, depending on the magnification used to acquire the images.

4.3.2. Atomic Force Microscopy (AFM)

Atomic force microscopy, abbreviated AFM,[31] is a technique based on the measurement of the interaction forces between the sample surface and the tip, which is a probe placed at the end of a flexible cantilever (Figure 27).[32]

[31] T. Witko, Z. Baster, Z. Rajfur, K. Sofńska, J. Barbasz, *Nature*, **2021**, *11*, 509.
[32] NanoWorld: Innovative Technology. NanoWorld: SPM and AFM probes. Obtained from: https://www.nanoworld.com/NanoWorld_AFM_Probes_Brochure_Spanish.pdf, accessed: 03/05/2023.

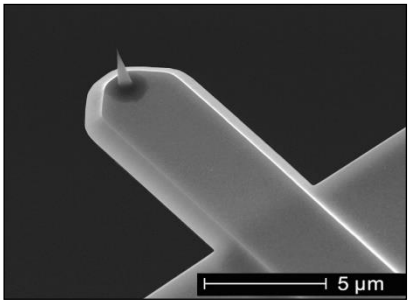

Figure 27. 3D view of a tip on an AFM cantilever.

The most important advantage of AFM is the possibility of obtaining three-dimensional images of electrically conductive, semiconducting, or electrically insulated samples without the need for pre-treatment. However, the main disadvantages include the smaller scanning area and the long time required to obtain an image.

Sample deposition was carried out by evaporation, that is, by depositing a drop on a mica plate. Measurements were made through contact mode working at constant force. A 2.4 $N \cdot m^{-1}$ tip and a 532 nm laser were used to study the organic nanoaggregates.

4.4. Work concentration

Before making any calculations or measurements, it is necessary to verify the behaviour of the probe at different concentrations. The reasons for this check are the following:

- Working at "high concentrations" may induce errors in the calculation of some characteristic parameters of the probe due to competitive processes, such as dynamic quenching or association effects, which may occur.
- Working at "low concentrations" there may be problems with signal resolution due to the signal-to-noise ratio, influenced by the absence of probe signals or the display of signals corresponding to impurities.

Therefore, to avoid extra parameters and undesirable secondary processes, the working conditions are usually high dilution and constant ionic strength. Thus, small variations in concentration will result in slight and linear changes in absorption where the ordinate at the origin is 0 or close to it. All this can be summarised in that, at low concentrations, the Lambert-Beer Law is fulfilled:

$$A = \log \frac{I - I_0}{I_0} = \varepsilon \cdot c \cdot l$$

Where A is the absorbance at a specific wavelength, I_0 is the intensity of radiation of a determined wavelength, I is the intensity of that radiation reaching the detector, ε is the molar extinction coefficient, c is the concentration of the solution and l is the width of the cuvette.

In the specific case of working with absorbance-fluorescence probes, the response to different concentrations has to be evaluated between 0.1 and 10 µM. After measuring the absorbance values in a spectrophotometer, they were plotted and fitted to a linear regression around a chosen value. Thus, the region in which the signal change with varying concentration is linear is considered the working range. This working range will allow variations in probe concentration without changes in signal other than those associated with interaction with the analyte. An example of a working concentration calculation is shown in Figure 28 for compound AR82d in DCM. As can be seen, the absorbance should be 0.1 or less, which means that the concentration of the probe should not be higher than 7 µM, thus avoiding inner filter effects, dynamic quenching or stacking processes, that is, complying with Lambert-Beer's Law.

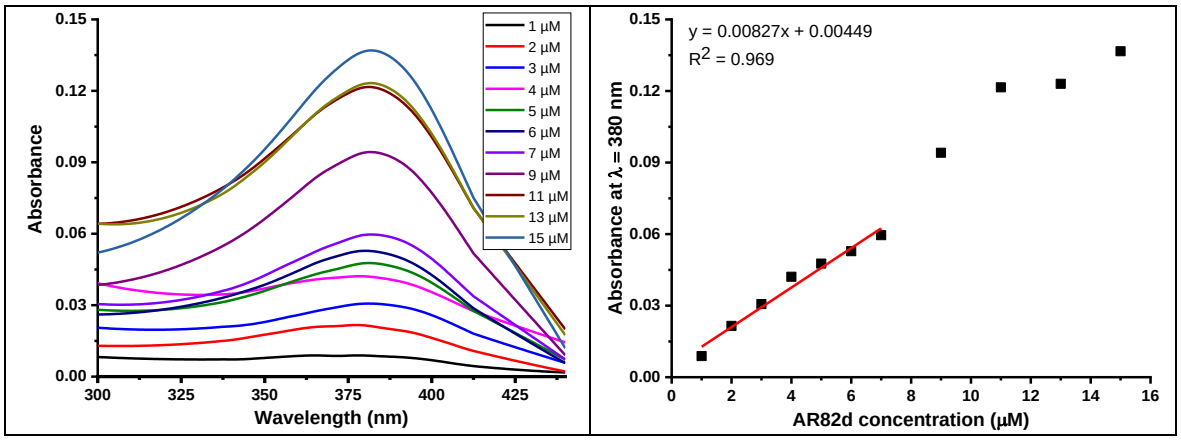

Figure 28. Calculation of the working concentration for compound AR82d in DCM. Absorbance spectrum (left) and absorbance profile at 380 nm (right).

For the selected solvents, it is possible to calculate the molar extinction coefficient (ε) by fitting the above formula to the linear regression obtained for the solvent considered, which is useful for determining the radiation absorbed by the probe in the solution.

In addition, when fluorescent probes are used, this same test can be carried out with fluorescence, known as the pseudo-Lambert-Beer Law, which is characterised by being more sensitive. An example of this test is shown in Figure 29.

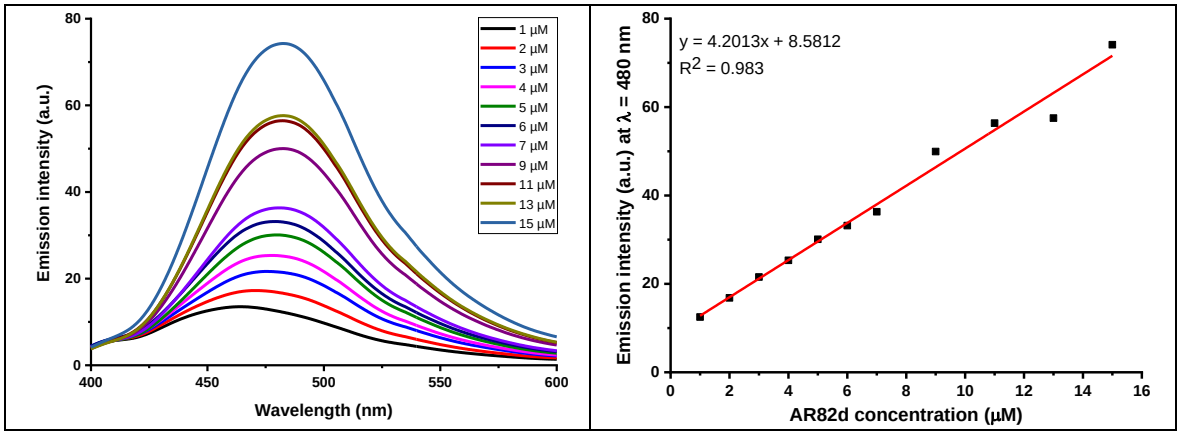

Figure 29. Calculation of the working concentration according to pseudo-Lambert-Beer Law for compound AR82d in DCM. Fluorescence spectrum (left) and fluorescence profile at 480 nm (right). λ_{exc} = 360 nm.

4.5. Previous solvent test

Those probes that provided a positive response to any of the analytes used in the screening test are subjected to a preliminary solvent test. For this qualitative test, a probe solution containing an excess of the analyte was compared with a reference, which only contains the probe dissolved in the corresponding solvent. Photographs are taken immediately after the addition of the analyte and 24 hours later.

The solvents and mixtures normally used in this test are those shown in Figure 30, but may be modified depending on the solubility of the probe.

1. MeOH	**6.** $CHCl_3$
2. DMF	**7.** DCM
3. MeCN	**8.** Toluene
4. EtOAc	**9.** $CHCl_3$:MeOH (9:1)
5. THF	**10.** DCM:MeOH (9:1)

Figure 30. Solvents used in the test.

An example of this experiment was performed with compound AR83d, which will be discussed in more detail in Chapter 3A and is shown in Figure 31 as follows. As can be seen, the most obvious changes occur in DMF, MeCN, $CHCl_3$:MeOH (9:1) and DCM:MeOH (9:1), so kinetics and titrations in these solvents will be performed below.

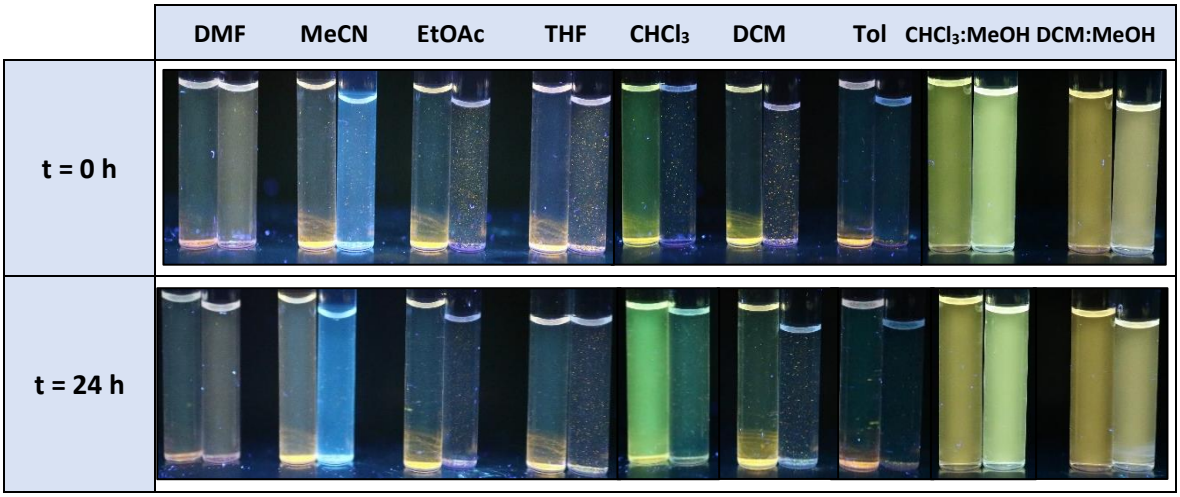

Figure 31. Preliminary solvent study of a 2.5 µM solution of AR83d under UV light of 366 nm.

4.6. Kinetic study

When detection is performed with molecular probes, time is a crucial parameter. Normally, in solution, the complexation equilibrium is reached very quickly, even in the order of seconds, which simplifies the probe study by titration.

A 1:1 equilibrium can be represented as follows:

$$A + P \leftrightarrows AP$$

This equilibrium is governed by the kinetic constants of association (k_1) and dissociation (k_2), so the thermodynamic equilibrium constant is formulated as follows:

$$K_{eq} = \frac{k_1}{k_2}$$

Thus, to perform a titration with calculations made in an equilibrium situation, it is necessary to determine the rate at which equilibrium is reached before giving data on stoichiometry, thermodynamic constants, or any other factor. If such calculations are necessary, the methods to be followed for the calculation of kinetic constants and other parameters are detailed in the literature.[33]

[33] J. I. Steinfeld, J. S. Francisco, W. L Hase, Chemical Kinetics and Dynamics, Prentice Hall, New Jersey, **1999**, ISBN: 0-13-737123-2.

In general, the performance of these calculations is usually quite complicated but should be recorded when carrying out such experiments because the detection limits or fluorescence quantum yields depend on them to a significant degree.

4.7. Titration methods

Once the different variables, such as the solvent or the working concentration, have been set, it is possible to carry out a titration by either of the two existing methods (Figure 32) and the results obtained can be extrapolated to any of the spectrophotometric or spectrometric measurements (absorption, fluorescence, NMR titration...).

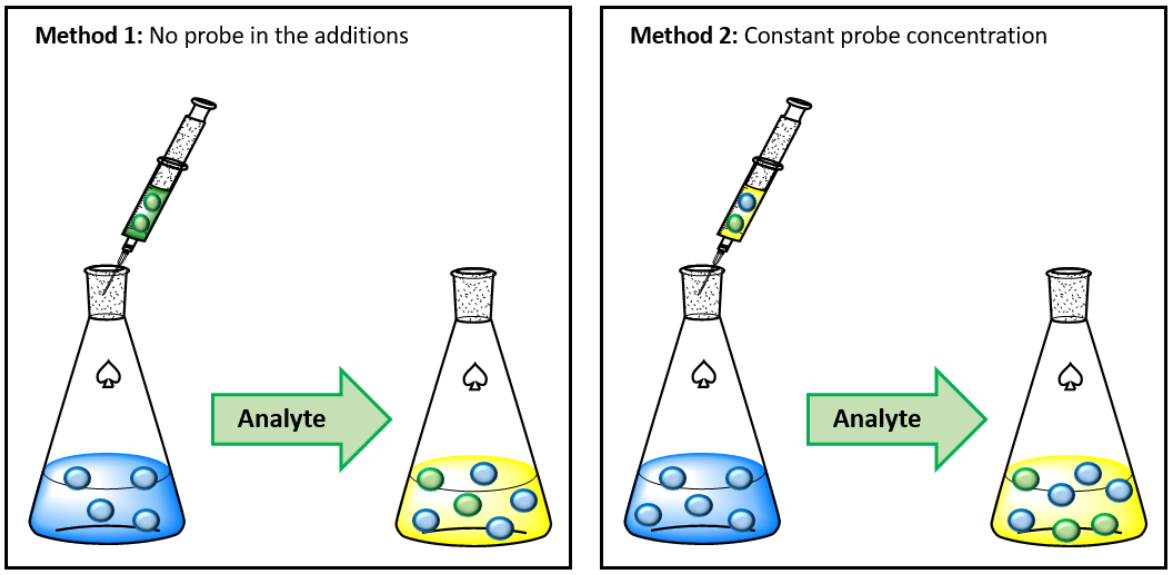

Figure 32. Summary of the methods used to carry out a titration.

- Method 1: addition of analyte to a dilute probe solution. In a titration of this kind, the analyte is usually added dissolved in the same solvent as the probe (it is possible not to do so, but this would add more variability factors to the titration) and always within the range in which the Lambert-Beer Law is fulfilled.

  However, this method is criticised by many authors in the literature due to the dilution effect, so it is very important to check whether the conditions of Lambert-Beer's Law for absorbance or pseudo-Lambert-Beer for fluorescence are fulfilled in the concentration range in which the titration is performed. Some other titrations, like NMR titrations, do not show a strong concentration dependence of both probe and analyte, but may present side effects such as increased signal amplitude or signal-to-noise ratio.

- Method 2: addition of the analyte previously dissolved in a probe solution. This is the most standardised method because it eliminates the problem of modifying the concentration of the probe (dilution), reducing the errors derived from it and facilitating the analysis of the data. When performing such a titration, the analyte is pre-concentrated in the probe dilution, so many factors require consideration:

  - It is not possible to use this titration method if a reaction is to be studied because the onset would occur in the moment when the probe and the analyte come into contact.
  - Although the concentration of the probe remains constant, there is the possibility of secondary processes occurring, such as association effects or other processes.

- The amount of probe consumed is high, which is a very important criterion when the quantity is limited, so it may be more convenient to use as little product as possible for the tests to be performed.

Despite the consequences of performing the titration using one or the other procedure, other factors, such as the probe-analyte kinetic response or solubility changes in the probe upon addition of the analyte, have to be considered.

4.7.1. Calculation of detection limits (LODs)

The limit of detection can be defined, according to IUPAC, as the smallest amount of an analyte that can be detected with certainty for any analytical procedure, being perfectly distinguishable from the blank.

There are three different methods that can be used for the calculation of LODs, which will be detailed below using the detection of 2,4-dinitrotoluene (DNT) by AR85 as an example. Therefore, Figure 33 shows the titration performed for the detection of DNT and the adjustment made (Chapter 3B). However, the explanation of how the expressions used for the calculation of the LODs work is very detailed and discussed in the literature, so it will not be an aspect mentioned in this thesis.

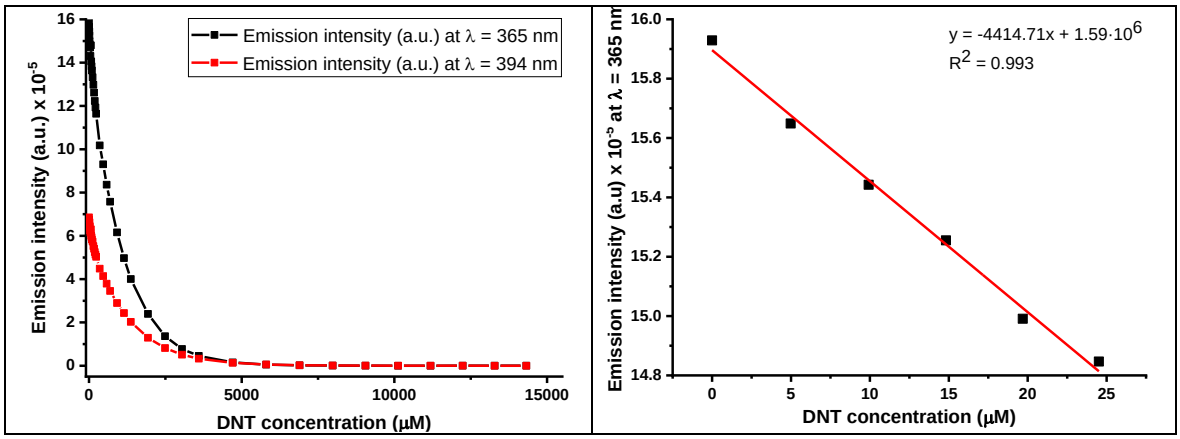

Figure 33. Fluorescence profile at 365 nm and 400 nm (right) and calibration for the LOD calculation using emission values at 365 nm (left) of a AR85 solution in toluene under increasing concentrations of DNT.

The blank, which contained only one probe dilution, was measured three times, giving an intensity value of 1631892.87 a.u. with a standard deviation of 38787.91 a.u.

- Method 1: calculation of the LOD based on measurements of the blank. This method is based on the IUPAC standard equation for the calculation of the LODS:

$$LOD = x_b + k \cdot s_b$$

Where x_b is the mean of the measured emission intensity of the targets, k is a constant that depends on the reliability of the method (usually takes a value of 3) and s_b is the standard deviation in the low concentration region of the analyte.

$$LOD = 1631892.87 + 3 \cdot 38787.91 = 1748256.61$$

This equation gives us an LOD in the units of emission intensity, in this case a.u., so it is necessary to transform it into units of concentration by means of the equation obtained in the linear regression adjusted with the analyte.

$$1748256.61 = |-4414.70|x + 1589607.43$$

$$x = LOD = 35.94\ \mu M$$

- Method 2: calculation of the LOD by using a linear regression at low concentrations of the analyte. It is a very common method in literature[34] in which the LOD is given by the following expression:

$$LOD = 3.3 \cdot {}^{SD}/_{S}$$

Where SD is the standard deviation of the blank and s is the slope of the calibration curve obtained at low analyte concentration. Depending on the paper considered, SD can also be the standard deviation of the fit.

  - SD as the standard deviation of the blank:

$$LOD = 3.3 \cdot {}^{38787.91}/_{|-4414.70|}$$

$$LOD = 29.00\ \mu M$$

  - SD as standard deviation of linear regression:

$$LOD = 3.3 \cdot {}^{165.86051}/_{|-4414.70|}$$

$$LOD = 0.12\ \mu M$$

There are also some authors in the literature who calculate the limit of quantification instead of the limit of detection, which implies replacing the factor 3.3 by 10, in order to make the calculations more reliable.

- Method 3: calculation of the LOD by linear regression + false positive and negative. According to the results obtained by other authors in the literature,[35] the procedure to be followed for the calculation of the LOD is the following:

  1. Fitting to a mean square linear regression.
  2. Eliminate the outliers, being those that are significantly different from the rest, considering a 95% probability.
  3. Fit a linear regression to the remaining values and check that the slope is significantly different from 0, considering a 95% probability.
  4. Calculate the limit of detection considering a probability of false positives (α) and false negatives (β) equal to or less than 5%.

In practice, all this is carried out using the "R" software,[36] providing for the case under consideration:

$$LOD = 2.16\ nM$$

Despite the different existing methods, the calculation of detection limits is a hotly debated field. Comparison of the different methods reveals some differences between them:

- The high dependence on the blank by some of the methods. This is because the standard deviation of the blank may vary when the analyte is added. In addition, repeated measurements of the blank make it possible to obtain lower values, which would make the LOD lower than it actually is.
- Many authors argue that the LOD has to be a quantity that has been measured by the probe in the laboratory under controlled conditions. They claim that the LOD of a

[34] S. Ahuja, M. Dong, Handbook of Pharmaceutical Analysis by HPLC, Elsevier, **2005**, ISBN: 0-12-088547-6.
[35] M. C. Ortiz, L. A. Sarabia, M. S. Sánchez, *Anal. Chim. Acta*., **2010**, *674*, 123-142.
[36] R Studio, Version 1.4.1103, 2009-2021 R Studio, 250 Northern Ave, Boston, MA 02210.

method corresponds to the second or third point of the linear regression used for the calculation.

- In the articles, the criteria used to calculate the LOD are not usually stated, which means that they do not specify the number of times they have measured the blank or the standard deviation values used.

Apart from all this, there are other drawbacks of a different nature, such as using the IUPAC as a guide, when it has not been updated for more than 70 years, establishing values for the constants without any justification (the formula on which Method 1 is based establishes "*k*" as 3 without any argument) or accepting previous results found in the literature without carrying out any checks.

Therefore, existing methods for LOD calculation are very controversial and complex, particularly for fluorogenic probes. The development of more reliable methods would be the first step towards the establishment of new standardised processes that provide more data about the calculations performed. However, one has to start by rejecting current techniques that are outdated and provide unreliable information.

4.8. Other fluorescence parameters

Apart from the fluorescence study carried out with those compounds that give a positive response to one of the analytes considered, there are other parameters that are used to characterise the products, such as the fluorescence quantum yield ($Ø_F$) and the fluorescence lifetime (τ), which have already been mentioned above.

4.8.1. Fluorescence quantum yield ($Ø_F$)

The fluorescence quantum yield is defined as the fraction of excited molecules that return to the ground state (S_0) accompanied by fluorescence emission. In other words, it is the ratio of photons emitted in fluorescence to photons absorbed.[37] When no phosphorescence processes occur, can be expressed by the speed constants:

$$Ø_F = \frac{Emitted\ photons}{Absorbed\ photons} = \frac{k_r^S}{k_r^S + k_{nr}^S} = k_r^S \cdot \tau_S$$

Where k_r^S is the radiative rate constant, k_{nr}^S is the non-radiative rate constant and τ_S is the fluorescence decay time. This value gives an idea of the fluorescence efficiency of the system, allowing an objective comparison of the fluorescence of the products.

There are numerous parameters that influence the fluorescence quantum yield, such as the increase in temperature that causes a decrease in quantum yield due to the rise in non-radiative relaxation processes (intramolecular vibrations and rotations, collisions with solvent molecules...). To avoid this, the quantum yield calculation requires to be performed at controlled temperature, in the absence of interferents and working at low concentrations.

Currently, there are two methods for calculating the fluorescence quantum yield: the absolute method and the relative method. While the absolute method allows the determination of the quantum yield both for species in solution and for compounds in the solid state, the relative method is only applicable to species in solution. However, the absolute method requires specific equipment which is not necessary for the relative method.

[37] a) A. Parker, W. T. Trees, *Analyst*., **1960**, *85*, 587-600. b) D. M. Alzate, R. Rodríguez, C. A. Sierra, *Rev. Colomb. Quim*., **2010**, *39*, 309-319. c) C. Würth, M. Grabolle, J. Pauli, M. Spieles, U. Resch-Genger, *Nat. Prot*., **2013**, *8*, 1535–1550.

- Absolute method.[38] The emission of fluorescence by a species is not a polarised process, that is, it does not occur in only one direction, but the radiation is emitted in all directions, which is why an integration sphere is used, which allows radiation from all angles to be collected. When this methodology is applied, it is necessary to carry out a spectral correction of the values obtained using a blank, in other words, only the solvent. As this is the system followed throughout this thesis, an example is shown in Figure 34 below.

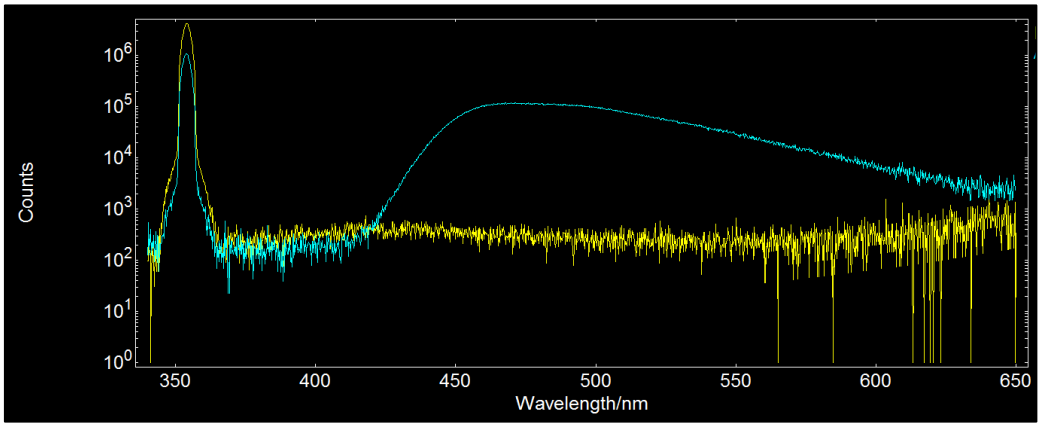

Figure 34. Calculation of fluorescence quantum yield by integration sphere of a 20 µM solution of AR56 in hexane. λ_{exc} = 355 nm.

- Relative or indirect method.[39] The determination of the fluorescence quantum yield is based on a comparison of the fluorescence emitted by the sample with standard materials, whose quantum yield is well known. Hence, this method is based on comparing the intensity of the light emitted with respect to the absorbance at the excitation maximum for both an unknown sample and a standard.

  This method is widely used because of its simplicity and low technological requirements and is expressed by the following equation:

$$\phi_F = \phi_{F,R} \cdot \frac{n^2}{n_R^2} \cdot \frac{1 - 10^{-A} \cdot R}{1 - 10^{-A}} \cdot \frac{F}{F_R}$$

  Where $\emptyset_F$ is the fluorescence quantum yield, *n* is the refractive index of the solvent, *A* is the absorbance, *F* corresponds to the integral of all fluorescent emission and *R* indicates that the calculated parameter is associated with a reference sample.

4.8.2. Fluorescence lifetime (τ)

The fluorescence decay lifetime is defined as the time between a system absorbing a photon and emitting it by fluorescence, returning to its ground state. This is one of the most important characteristics of fluorophores as it represents the experimental interval of time for the observation of any dynamic process.

Typically, this parameter is calculated using a time-correlated single photon counting instrument with several pulsed LEDs and then processed by software provided by the fluorometer. This processing is carried out by iterative reconvolution of the instrument source time profile (IRF) or by iterative adjustment of the sample tail avoiding overlap between the IRF and the sample lifetime,

[38] A. García-Suárez, Determinación de rendimientos cuánticos de fluorescencia por métodos indirectos, Master's Thesis, University of Oviedo, **2015**.
[39] A. M. Brouwer, *Pure Appl. Chem.*, **2011**, *83*, 2213–2228.

which is necessary when lifetimes are low.[40] From a theoretical point of view, the mean lifetime can be adjusted to the following expression:

$$F(t) = \sum_i A_i \cdot e^{-\frac{t}{\tau_i}}$$

Where A_i is a pre-exponential factor referring to the weighted amplitude (fractional value between 0 and 1) and τ_i is the lifetime of the i-th fluorescence component. The IRF is recorded using a non-fluorescing scattering sample (in this case LUDOX was used). Both *F(t)* and IRF were recorded with a sampling frequency adapted to the repetition frequency of the pulsed source, thus avoiding non-linear phenomena in the acquisition. The convolution of *F(t)* is fitted to the experimental decay curve using the least squares method to optimise the fitting parameters. The quality of the fit is determined by the χ^2 parameter statistic, which needs to be between 1 and 1.3, meaning that there is no deviation or trend in the residuals.

An example of the calculation of the mean lifetime is shown in Figure 35 below:

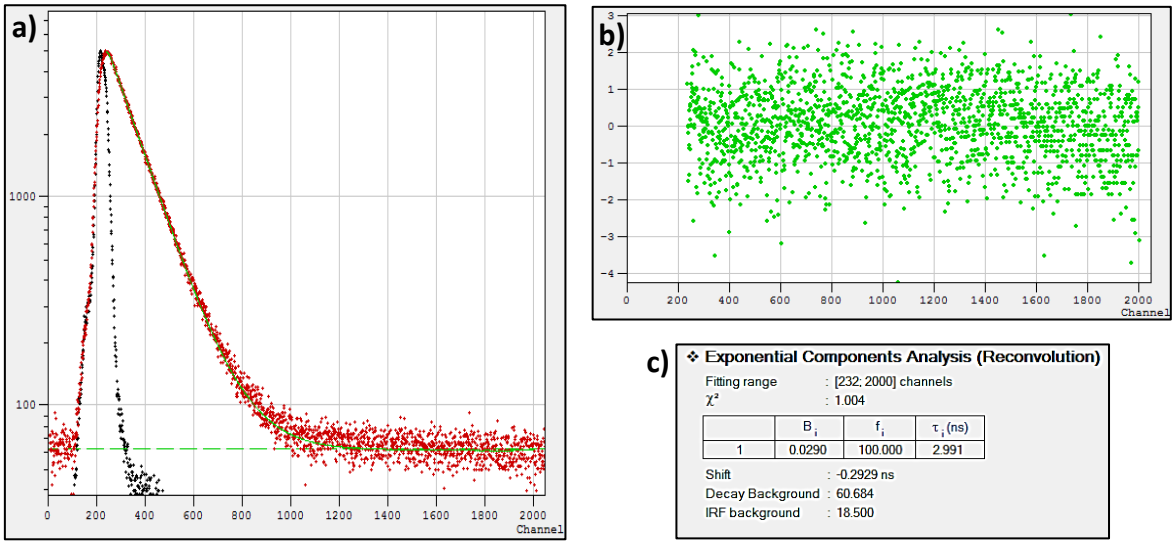

Figure 35. Calculation of the lifetime of a 20 µM solution of AR56 in hexane. Fluorescence decay plot for τ calculation (a), scatter plot of the residuals (b) and interpretation of the results (c). λ_{exc} = 355 nm.

This parameter provides a great deal of information about the system and the processes that occur:

- It makes it possible to determine which phenomenon is underway depending on the order of the value obtained. If the lifetime is in the order of microseconds or less, a fluorescence phenomenon is occurring, but if it has higher values, in the order of milliseconds or seconds, then it is phosphorescence.
- It allows the properties of the system to be compared, making it possible to determine the radiative and non-radiative decay constants.
- This parameter allows differentiation between dynamic and static quenching,[41] which is useful in the development of quenching probes or for photodynamic studies.[42]

[40] a) W. R. G. Baeyens, D. Keukeleire, K. Korkidis, Luminescence techniques in chemical and biochemical analysis, M. Dekker, New York, **1991**, ISBN: 0-82-478369-7. b) B. Valeur, Molecular fluorescence: principles and applications, Wiley-VCH, Weinheim, **2002**, ISBN: 978-35.2732837-6.
[41] J. H. Gutow, *J. Chem. Educ.*, **2005**, *82*, 302-305.
[42] A. Kamkaew, S. H. Lim, H. B. Lee, L. V. Kiew, L. Y. Chung, K. Burgess, *Chem. Soc. Rev.*, **2013**, *42*, 77-88.

CHAPTER 2

NMI DERIVATIVES: SYNTHESIS AND PROPERTIES

Naphthalene is the simplest known polycyclic aromatic hydrocarbon (PAH),[1] as shown in Figure 1a. It is an organic molecule consisting of two condensed benzene rings and is made up of only carbon and hydrogen atoms. It is characterised by a planar structure in which the carbon-carbon bonds are of different lengths, 136 and 142 pm. This compound can be found in many ways in the environment, as it is a component of crude oil and is a widespread pollutant due to its common presence in industrial waste or combustion residues, being toxic to human health and aquatic organisms, as well as dangerous for the environment. It is also used as an intermediate in the production of surfactants, phthalic anhydride and pesticides.[2]

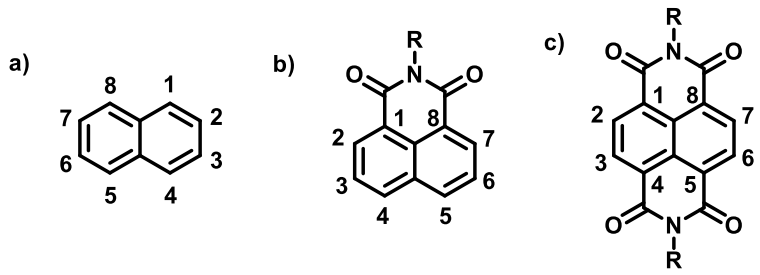

Figure 1. Structure of naphtalene (a), NMI (b) and NDI (c).

Naphthalimides are a type of heteroaromatic polycyclic amides obtained by functionalisation of different positions of naphthalene.[3] Depending on the functionalised positions, two types can be distinguished:

- Naphthalenomonoimides (NMI): obtained by functionalisation of positions 1 and 8 of the naphthalene ring with an *N*-imide group (Figure 1b).
- Naphthalenediimides (NDI): obtained by functionalisation of positions 1 and 8 and positions 4 and 5 of naphthalene ring with an *N*-imide group (Figure 1c).[4]

However, throughout this chapter, we will focus only on the properties and characteristics of 1,8-naphthalimides or NMIs.

1. NMI: STARTING MATERIAL AND REACTIVITY

Despite the remarkable reactivity of naphthalene, NMIs were obtained using 1,8-naphthalic anhydride as starting material. This compound was obtained from the oxidation of acenaphthene.[5] This is followed by a bromination reaction, which can occur at either the 3-position and the 4-position, leading to a conversion of the anhydride to an imide (Figure 2).

[1] D. Tsifakis, C. Charles, R. Boswell, *Front. Phys.*, **2020**, 389.

[2] a) A. V. Gildebranta, I. S. Sazykina, M. A. Sazykina, *Appl. Biochem. Microbiol.*, **2022**, *58*, 1036-1042. b) B. Manzanilla, Z. Domínguez, J. M Domínguez-Esquivel, M. Salas-Reyes, M. H. Matus, *J. Mol. Struct.*, **2020**, *1207*, 127846. c) J. J.Treviño-Reséndez, P. Mijaylova-Nacheva, J. D. García-Espinoza, *Rev. Int. Contam. Ambie.*, **2020**, *36*, 21-32.

[3] a) Y. Huang, C. Wu, Y. Song, M. Huang, D. Tian, X. Yang, Y. Fan, *Molecules*, **2018**, *23*, 266-277. b) F. Xin, J. Zhao, X. Wang, H. Wang, H. Wang, M. Xing, Y. Fu, Y. Tian, Y. Tian, *SAA.*, **2023**, *296*, 122621.

[4] a) P. Ledwon, D. Ovsiannikova, T. Jarosz, S. Gogoc. P. Nitschke, W. Domagala, *Electrochim. Acta.*, **2019**, *307*, 525-535. b) L. M. Svirskaite, S. Mandati, N. Spalatu, V. Malinauskiene, S. Karazhanov, V. Getautis, T. Malinauskas, *Synth. Met.*, **2022**, *291*, 117214. c) S.K. Nandi, D. Díaz-Díaz, D. Haldar, *J. Phys. Chem. C.*, **2022**, *126*, 675−682. d) D. Rosas-Villalva, S. Singh, L. A. Galuska, A. Sharma, J. Han, J. Liu, A. Haque, S. Jang, A. Hami-Emwas, L. J. Anton-Koster, X. Gu, B. C. Schroeder, D. Baran, *Mater. Horiz.*, **2022**, *9*, 500.

[5] S. Haremsa, *Ullmann's encycl. ind. chem.*, **2012**, *23*, 725-732.

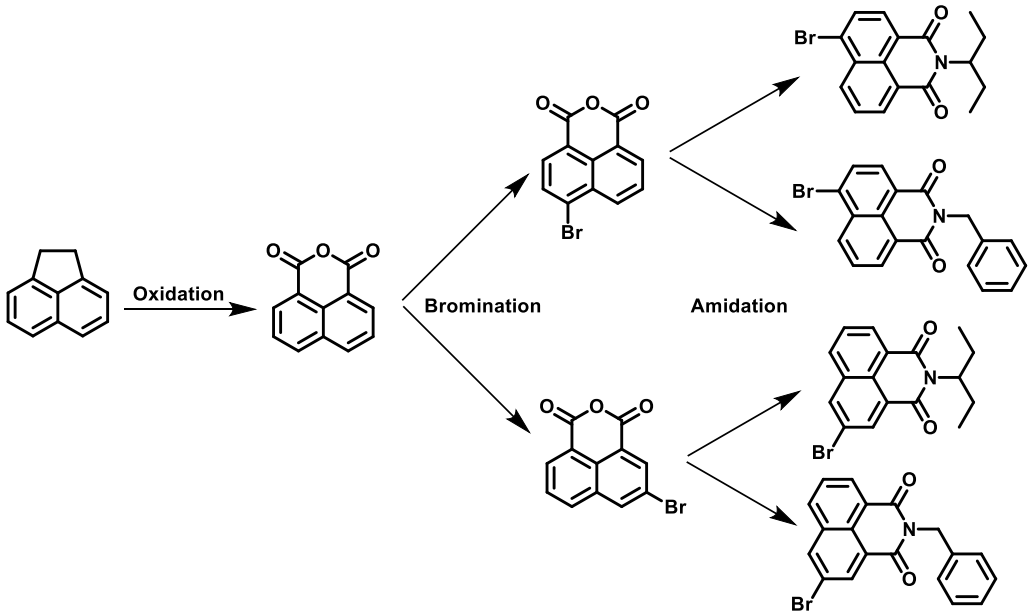

Figure 2. Experimental procedure of starting materials.

As can be seen in the previous Figure 2, a wide variety of substituents can be introduced at the *N*-imide position.[6] The presence of a hydrogen atom on the imidic nitrogen substituent causes the NMIs obtained to exhibit fungicidal and antibacterial properties.[7] The introduction of bulky and branched substituents in the *N*-imide positions prevents π-π stacking, a very common phenomenon in this type of structures due to their planar core, and improves the solubility of the resulting naphthalimides.[8] On the other hand, the introduction of small and unbranched substituents favours π-π stacking.

Naphthalimides become of interest in the field of detection once the functionalisation, usually with electron-attracting groups, of the 4- and 5-positions of the naphthalene core is carried out. However, although less common, functionalisation of NMIs can also be carried out at the 3 and 6 positions.[9] Figure 3 compares the solvatochromisms of two naphthalimides with the same substituent but, in the case of compound AR83p, at position 4 and, in the case of compound AR110p, at position 3.

In general, the emission spectra of the two compounds were very similar. In both cases, the emission is between 450 and 575 nm, that was, in the blue region, being more intense in the less polar solvents of all those used, and both showed a bathochromic shift of the emission maximum. However, the appearance of a shoulder was observed in the less polar solvents, hexane and methylcyclohexane. In the case of the absorption spectra, the absorption band was shifted to shorter wavelengths, from, approximately, 385 nm for the compound substituted at position 4 to 315 nm for the compound substituted at position 3. However, a second band at 385 nm was observed for compound AR110p. In addition, compound AR83p showed a small bathochromic shift of the absorption maximum, which compound AR110p lacked.

[6] A. Martínez Sanz. Síntesis y estudio de la relación estructura-actividad de una serie de naftalimidas sustituidas con acción citostática. Doctoral thesis, Complutense University of Madrid, **2015**.

[7] a) M. K. Hargreaves, J. G. Pritchard, H. R. Dave, *Chem. Rev.*, **1970**, *70*, 439-469. b) G. Mohr, K. Niethammer, S. Lust, G. Schneider, *Pat. S. Afr.*, **1968**, *67*, 305.

[8] R. Qin, D. Guo, T. Y. Gopalakrishna, G. Li, J. Yang, Y. Jiang, H. Ma, *Dyes Pigm.*, **2019**, *160*, 540-545.

[9] a) S. Kotowicz, M. Korzec, J. G. Małecki, S. Golba, M. Siwy, S. Mackowski, E. Schab-Balcerzak, *Mater.*, **2022**, *15*, 7043. b) X. Zhang, Y. Song, M. Liu, H. Li, H. Sun, M. Sun, H. Yu, *Dyes Pigm.*, **2019**, *160*, 799–805.

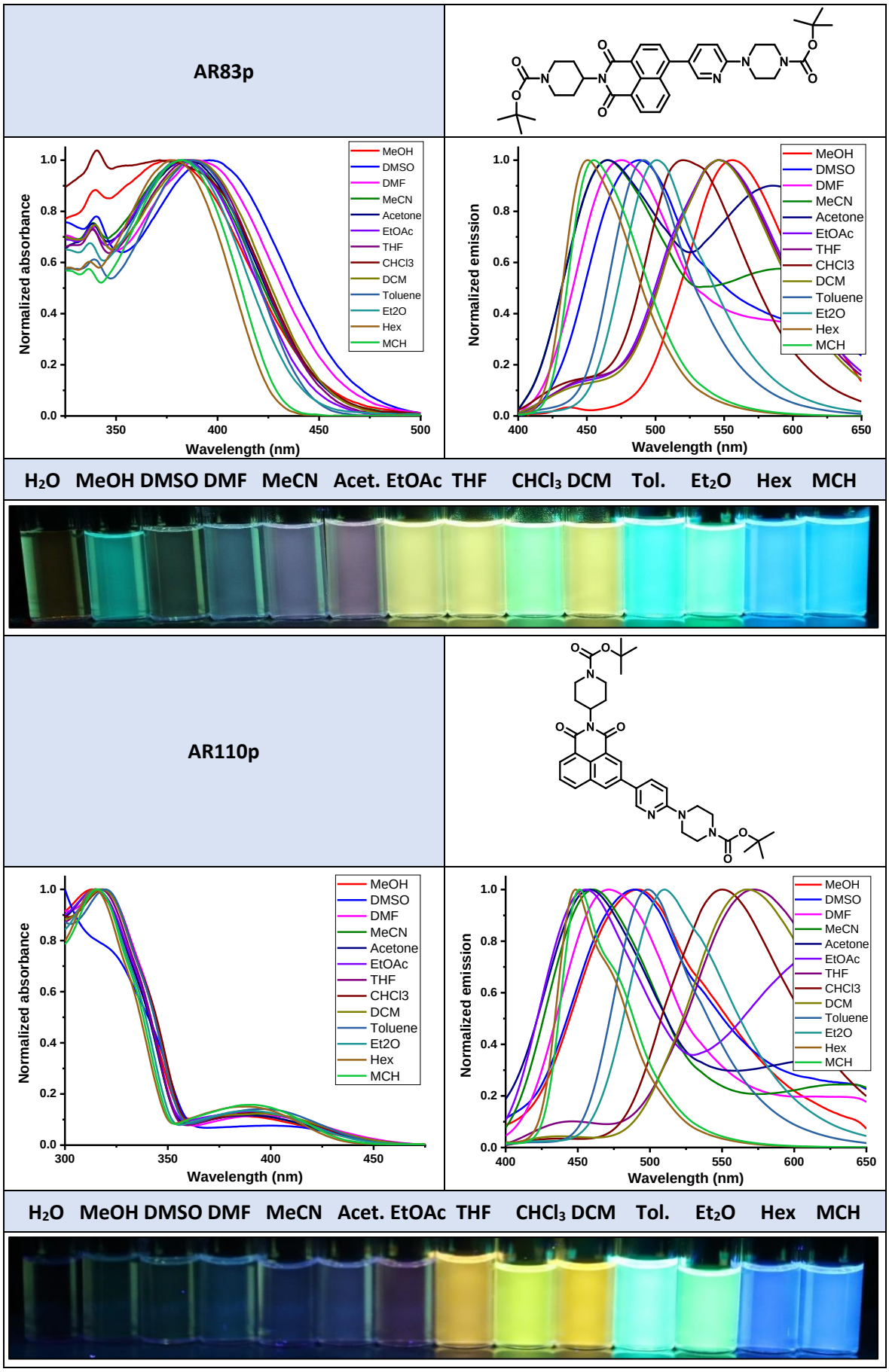

Figure 3. Solvatochromism comparison of 20 µM solutions of AR83p and AR110p.

1.1. Imidization of the NMA to NMI

Naphthalenomonoimides (NMI) functionalised at the 4-position were obtained using 4-bromo-1,8-naphthalic anhydride (NMA) as starting material. A bulky substituent was introduced at the *N*-imide position using 4-amino-piperidine-1-carboxylic acid *t*-butyl ester by stirring in hot ethanol. The experimental procedure is shown in Figure 4.

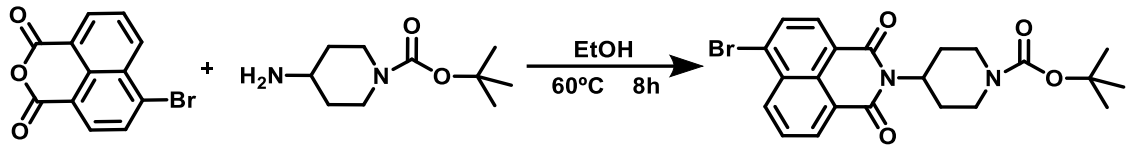

Figure 4. Synthesis scheme for starting material of NMIs.

Optimisation of this reaction was achieved by doubling the amount of amine added, bringing the yield from 54% to 95% (Figure 5).

Amount of NMA (eq)	Amount of amine (eq)	Solvent	Temperature (ºC)	Time (h)	Yield (%)
1	1.05	Ethanol	60	8	54
1	2	Ethanol	60	8	95

Figure 5. Optimisation of starting material

Using this compound as starting material, reactions of different nature were carried out. However, this compound has a lower reactivity than other starting materials used by the research group, such as PMIs or PDIs.[10] An example of this was the borylation reaction (Figure 6), which did not occur for NMI despite the different experimental conditions under which it was attempted.[11]

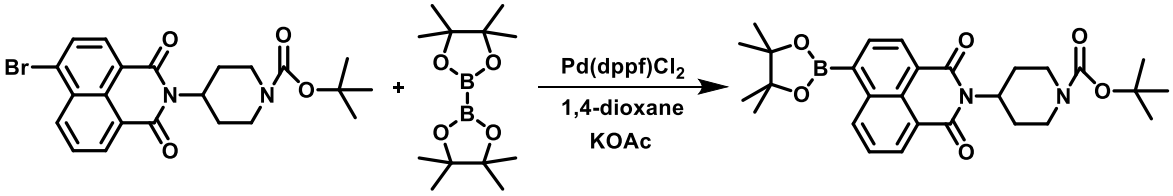

Figure 6. Synthesis scheme for borylation reaction of NMIs.

This was the reason why part of the chemistry with NMIs had been carried out through Stille coupling reactions.

1.2. Introduction of groups by Suzuki-Miyaura coupling

Suzuki reactions had been performed under the classical conditions previously described in the literature.[12] One of the main issues with the products obtained by this reaction might is their insolubility in some solvent mixtures. However, in this case, it is not necessary to take this into consideration because the amine introduced was sufficiently bulky. An example of the reaction and the conditions used for its development is shown in Figure 7.

[10] a) N. Busto, D. C. Romero, A. Revilla-Cuesta, I. Abajo, J. V. Cuevas, T. Rodríguez, B. García, T. Torroba, *Dyes Pigm.*, **2022**, *205*, 110557. b) N. Busto, J. García-Calvo, J. V. Cuevas, A. Herrera, J. L. Mergny, S. Pons, T. Torroba, B. García, *Bioorg. Chem.*, **2021**, *108*, 104660. c) J. García-Calvo, J. A. Robson, T. Torroba, J. Wilton-Ely, *Chem. Eur. J.*, **2019**, *25*, 14214–14222.
[11] P. Shao, M. Bai, *Chem. Commun.*, **2012**, *48*, 9498-9500.
[12] M. C. D'Alterio, E. Casals-Cruañas, N. V. Tzouras, G. Talarico, S. P. Nolan, A. Poater, *Chem. Eur. J.*, **2021**, *27*, 13481–13493.

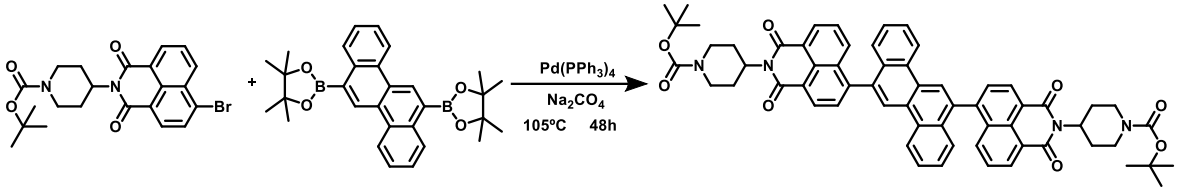

Figure 7. Reaction example for a Suzuki-Miyaura coupling for NMIs.

In a general reaction procedure, the brominated derivative (1 equiv.), boronic acid derivative (1 equiv.), palladium catalyst (1-5 mol%) and the base (Na_2CO_4, 4 equivalents) were dissolved in a mixture of solvents under nitrogen or argon atmosphere until a concentration 1-5 mM and left under reflux for 16-48 hours, depending on the reaction and the reagents used. The product was purified by column chromatography (by using DCM:MeOH from 0 to 5% as eluent) to obtain products from yellow to orange.

There are multiple solvent mixtures available for use in this type of reaction[13] but the most commonly used has been a mixture of toluene:*n*-BuOH:H_2O (4:1:0.3). This mixture has been developed by our research group and works for a wide variety of reagents, giving acceptable yields.[14]

1.3. Introduction of groups by Sonogashira coupling

Sonogashira reactions had been performed under the classic conditions previously describe in the literature.[15] An example of this kind of reactions and the conditions under which it was developed are shown in Figure 8.

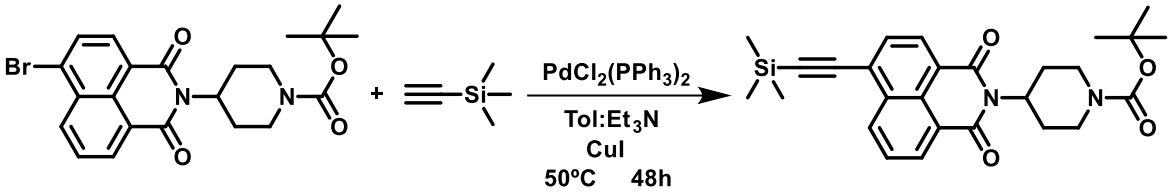

Figure 8. Reaction example for a Sonogashira coupling for NMIs.

The brominated derivative (1 equiv.), TMSA (1 equiv.), palladium catalyst and cooper iodine in catalytic amounts (1-5 mol%), were dissolved in a mixture of solvents under nitrogen or argon atmosphere until a concentration 5-10 mM and stirred at 50ºC for 48 hours. The product was purified by column chromatographic (DCM:MeOH from 0 to 5% as eluent) to obtain yellow products.

Under classical conditions, the solvent used for the reaction is a mixture of THF with 33% triethylamine. However, our research group has demonstrated that the yields improve if the reaction is carried out in toluene with 20% triethylamine. Nevertheless, the yield obtained was less than 20%, which was improved by obtaining the same product by the Stille coupling reaction.

[13] a) X. Luo, Y. Qu, Y. Zhang, Y. Wu, W. Yuan, L. Wuan, *J. Chem. Eng.*, **2021**, *415*, 129095. b) Y. Wang, B. Xu, R. Sun, Y. J. Xub, J. F Ge, *J. Mater. Chem. B.*, **2020**, *8*, 7466. c) E. Jang, T. Ding, M. Xie, H. Cao, *J. Photochem. Photobiol. A.*, **2018**, *364*, 145-150. d) R. Arunchai, T. Sudyoadsuk, N. Prachumrak, S. Namuangruk, V. Promarak, M. Sukwattanasinitta, P. Rashatasakhon, *New J. Chem.*, **2015**, *39*, 2807.

[14] a) B. Díaz de Greñu, D. Moreno, T. Torroba, A. Berg, J. Gunnars, T. Nilsson, R. Nyman, M. Persson, J. Pettersson, I. Eklind, P. Wästerby, *J. Am. Chem. Soc.*, **2014**, *136*, 4125–4128. b) J. García-Calvo, P. Calvo-Gredilla, M. Ibáñez-Llorente, T. Rodríguez, T. Torroba, *Chem. Rec.*, **2016**, *16*, 810-824.

[15] a) V. Bakthavachalam, M. d'Alarcao, N. J. Leonard, *J. Org. Chem.*, **1984**, *49*, 289-295. b) L. Turunen, N. K. Beyeh, F. Pan, A. Valkonen, K. Rissanen, *Chem. Commun.*, **2014**, *50*, 15920

1.4. Introduction of groups by Stille coupling

Stille coupling reactions had been performed using different conditions to those described in the literature.[16] An example of such a reaction is shown in Figure 9.

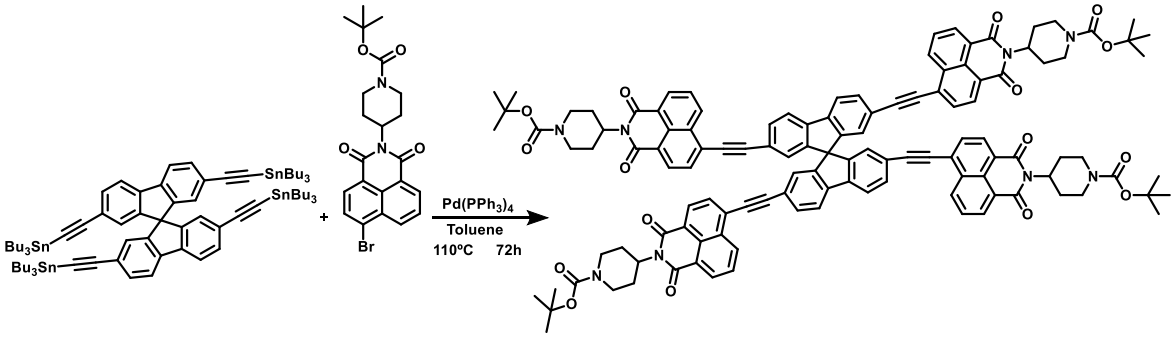

Figure 9. Reaction example for a Stille coupling for NMIs.

For these reactions, the brominated derivative and organostannane derivative were dissolved under nitrogen or argon atmosphere until a concentration 0-2 mM and stirred at 110ºC for 72 hours. The product was purified by column chromatography (DCM:MeOH from 0 to 5% as eluent) obtaining the products as yellow solids.

In the literature, most of the Stille coupling reactions are carried out in THF, though the research group carries out the same reactions in toluene due to the increased yield obtained.

1.5. Deprotection of *tert*-butoxycarbonyl group

The elimination of the *tert*-butoxycarbonyl (Boc) group was carried out by adding TFA to a solution of the amino-protected derivative in chloroform and the resulting mixture was stirred 4 hours at room temperature. The mixture was neutralized with 40% sodium hydroxide solution in water and the product was extracted with chloroform, obtaining solids from white to yellow. A scheme of the experimental procedure and reaction conditions is shown in Figure 10.

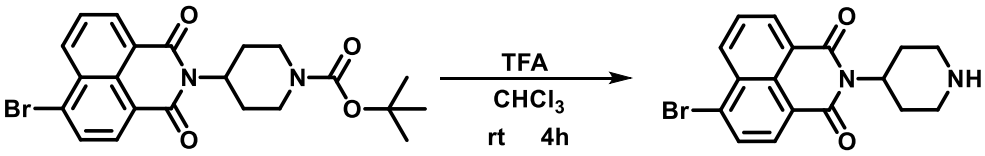

Figure 10. Reaction example for deprotection for NMIs.

2. PROPERTIES AND π-π STACKING

1,8-naphthalimides exhibit excellent spectroscopic properties which are conditioned by the functionalisation of the naphthalene ring and the nature of the substituents introduced. In general, NMIs are characterised by photostability and chemostability as well as high temperature resistance, excellent durability and a tunable emission band (from blue to yellow, green or red). The emission band shift can be observed in the solvatochromism tests of the NMI derivatives AR80 and AR90p (Figure 11), usually associated with a bathochromic shift of the emission maximum from the blue region to the orange or green region as the polarity of the medium increases.

[16] a) K. Kiyokawa, N. Tachikake, M. Yasuda, A. Baba, *Angew. Chem. Int. Ed.*, **2011**, *50*, 10393–10396. b) Y. Horino, M. Murakami, A. Aimono, J. H. Lee, H. Abe, *Org. Lett.*, **2019**, *21*, 476–480.

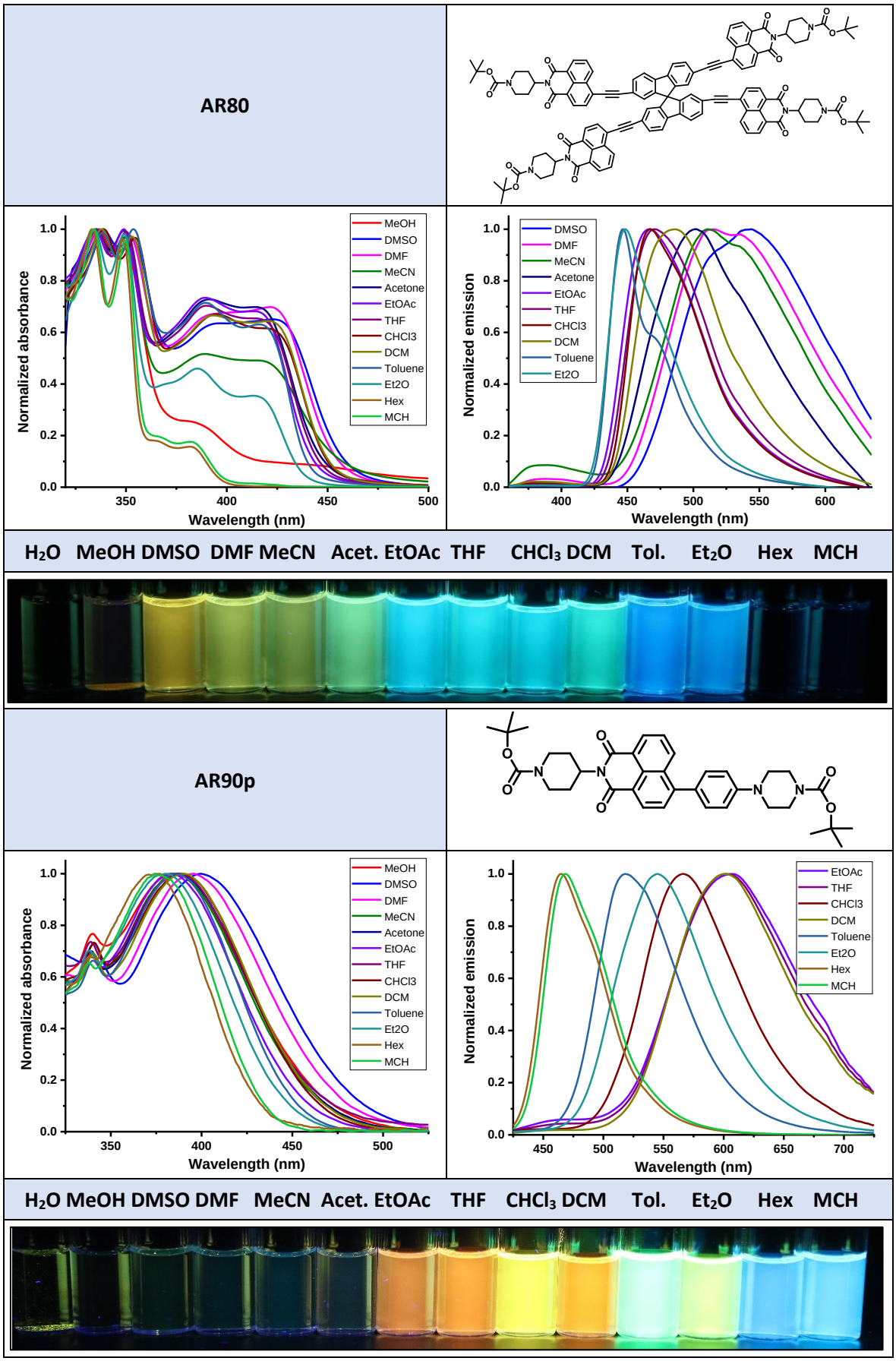

Figure 11. Solvatochromism of 20 µM dilutions of AR80 and AR90p. In AR80 the emission band is shifted towards the green region while in AR90p it is shifted towards orange.

Moreover, these compounds show exceptionally high fluorescence quantum yields, close to 100% on many occasions[17] and are therefore very suitable for use as fluorescent probes.

2.1. Modulating NMIs properties: the stacking of NMIs

To fully understand the properties, and thus the applications, of NMIs, it is necessary to explain to some extent one of their most important properties, which is their strong tendency to produce intermolecular π-π stacking.[18] The aggregates formed are important not only for the aggregation-solubility relationship but also for the optoelectronic properties, which directly affect the absorbance-emission wavelength (energy levels) and fluorescence quantum yields because more aggregation implies more possible non-radiative relaxation pathways.

A review of the literature on naphthalimide stacking shows that it is a phenomenon that depends on a large number of factors; Figure 12 shows schematically the consequences of different forms of aggregation and intermediate situations.[19]

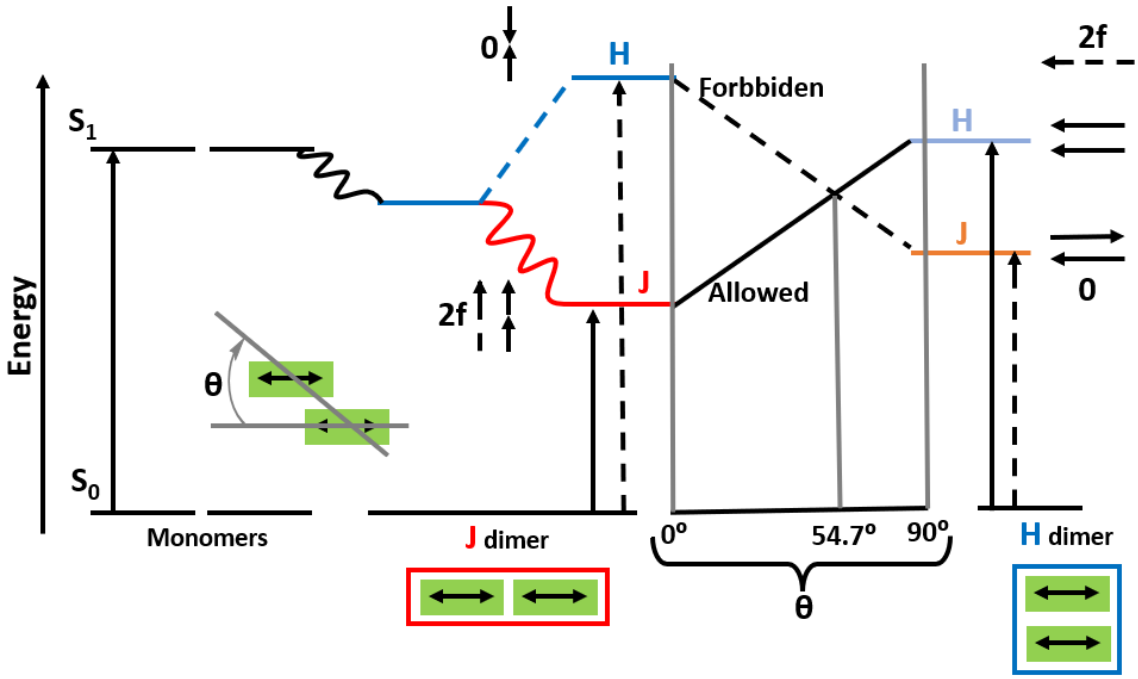

Figure 12. Schematic energy level diagram for formation of dimers and the effect over the energy levels.

To try to simplify this situation, it will be explained from the point of view of NMI derivatives. Figure 12 considers the effect of having a monomer and the different interaction between two molecules in a two-dimensional model. Thus, the relationship between aggregation and luminescent properties can be explained by this diagram:

- Monomers: fluorescence exhibited by an individual molecule of a naphthalimide derivative.
- J-aggregates (θ = 0°): occurs when NMI molecules are aggregated in the same plane, resulting in an excited energy level that is more easily accessible to electrons. Therefore, less energy is required for fluorescent emission, resulting in a bathochromic shift.

[17] A. Saini, K. R. J. Thomas, *RSC Adv*. **2016**, *6*, 71638-71651.
[18] X. Cao, L. Meng, Z. Li, Y. Mao, H. Lan, L. Chen, Y. Fan, T. Yi, *J. Am. Chem. Soc.* **2014**, *30*, 11753–11760.
[19] F. Würthner, C. R. Saha-Möller, B. Fimmel, S. Ogi, P. Leowanawat, D. Schmidt, *Chem. Rev.*, **2016**, *116*, 962–1052.

- H-aggregates (θ = 90º): occurs when naphthalimide molecules are aggregated on top of each other, which makes the excited energy level less accessible to electrons, causing the emission wavelength to increase. Consequently, a hypsochromic shift occurs.

This interpretation is based on the Kasha model, which is a qualitative explanation from the point of view of the interaction of the transition dipole moments of the chromophores with respect to the spatial arrangement when photoexcitation takes place. Intermediate situations also appear depending on the angle θ at which aggregation takes place. Situations between J-H aggregates are not only possible but the most common situation. In particular, it is possible to have a very similar emission wavelength compared to the monomer if the correct angle between molecules is achieved (θ = 54.7º).

According to a three-dimensional classification model,[20] stacking can be divided into two groups:

- π-π face-to-face stacking: this is the stacking that takes place in a plane parallel to the molecule. The alignment of stacked units does not have to be perfect, usually one unit is offset from another. This stacking is favoured when the two units are electron-poor, while the presence of electron-releasing groups disfavours this geometry. It is necessary to point out that it is the one produced in solution, being strongly conditioned by the solvent.
- π-π edge-to-face, point-to-face or "*T-shaped*" stacking: this is the stacking that takes place in a plane perpendicular to the molecule. This stacking takes place with both charge-releasing and charge-accepting groups. This geometry occurs mainly in the solid state.

Regardless of the stacking classification method used, stacks can be parallel or antiparallel (Figure 13).[21]

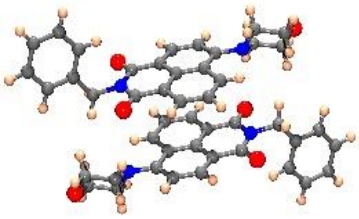

Figure 13. Example of π-π face-to-face antiparallel stacking of NMIs.

Apart from what has been discussed above, there are many possible and more complex variations. Some of these properties are briefly discussed in this section, so that the complexity of the subject can be understood. However, most interactions are explained by focusing on the molecule under study.

To explain the stacking that occurs in NMI derivatives, the influence of the substituents in media of different polarity is analysed below:

[20] a) A. S. Shetty, J. Zhang, J. S. Moore, *J. Am. Chem. Soc.*, **1996**, *118*, 1019-1027. b) M. A. Martínez. Estudio de las interacciones débiles presentes en sólido y en disolución en complejos de paladio y platino. Doctoral thesis, University of Burgos, **2005**. c) S. K. Burley, G. A. Petsko, *J. Am. Chem. Soc.*, **1986**, *108*, 7995-8001. d) E. G. Cox, D. W. Cruickshand, J. A. S. Smith, *Proc. R. Soc. London, Ser. A*, **1958**, *247*, 1. e) M. Egli, V. Tereshko, G. N. Mushudov, R. Sanishvili, X. Liu, F. D. Lewis, *J. Am. Chem. Soc.*, **2003**, *125*, 10842-10849.

[21] a) J. I. Lovitt, T. Gorai, E. Cappello, J. M. Delente, S. T. Barwich, M. E. Möbius, T. Gunnlaugsson, C. S. Hawes, *Mater. Chem. Front.*, **2021**, *5*, 3458–3469. b) A. Jamadar, C. Karan, L. Roy, A. Das, *Langmuir*, **2020**, *36*, 3089−3095. c) A. Jamadar, A. Singh, L. Roy, A. Das, *J. Mater. Chem. C.*, **2021**, *9*, 11893−11904. d) A. Das, B. Maity, D. Koley, S. Ghosh, *Chem. Commun.*, **2013**, *49*, 5757.

- Substituents with low polarity (for example, aliphatic chains or triple bonds): the polarity of the naphthalene core is higher than the polarity of the substituents. Consequently, in high polar solvents, such as methanol or DMSO, the core should be oriented towards the solvent (J-aggregate), because it interacts with the most polar part of the molecule, resulting in a bathochromic shift. On the other hand, in solvents of lower polarity, such as (hexane or diethyl ether, the substituents will be oriented to the solvent and the naphthalene rings will tend to aggregate (H-aggregate), giving rise to a hypsochromic shift. An example of this arrangement is shown in Figure 14.

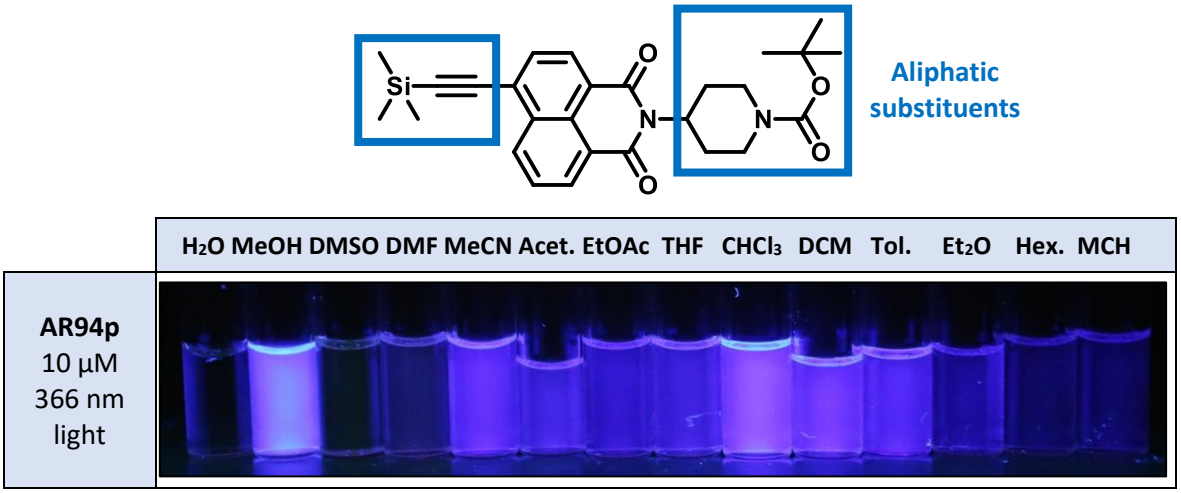

Figure 14. AR94p NMI derivative solvatochromism in different solvents.

- Substituents with high polarity (for example amino or hydroxyl groups): if the polarity of the substituents is high enough, the behaviour can be the opposite of that detailed in the previous case. Thus, H-aggregates would form when the solvent is more polar whereas J-aggregates would form in non-polar solvents. An example is shown in Figure 15.

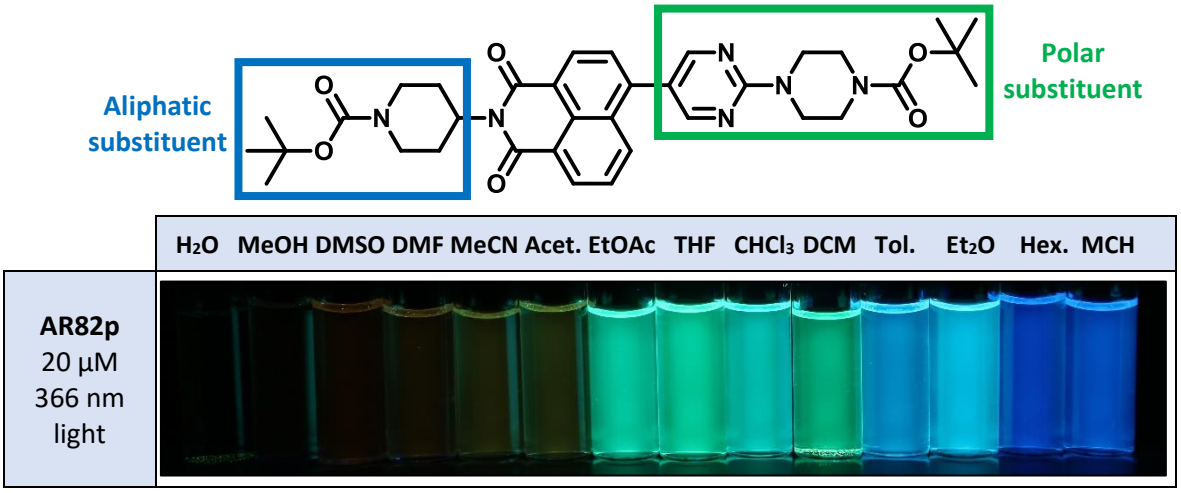

Figure 15. AR82p NMI derivative solvatochromism in different solvents.

- Conjugation extension: the increase in the number of aromatic rings causes a shift of the emission band and the formation of aggregates according to the criteria detailed in the two previous points: the polarity of the substituents and the polarity of the medium. An example is shown in Figure 16.

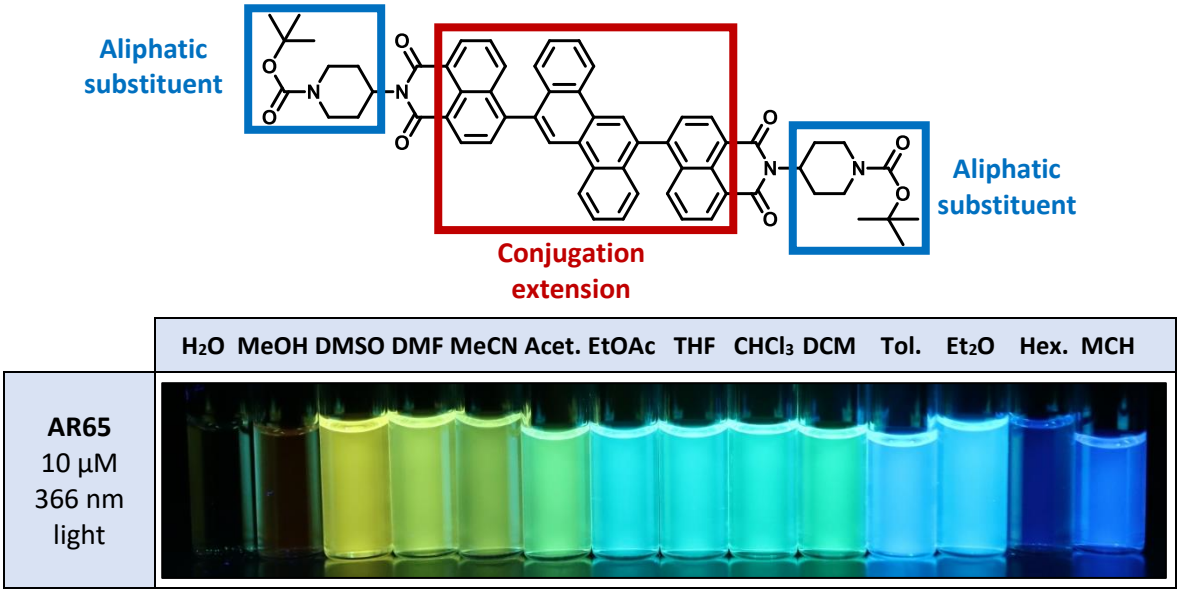

Figure 16. AR65 NMI derivative solvatochromism in different solvents.

Apart from this, it is important to remark that stacking does not only depend on the polarity of the substituents on the naphthalene core, also other factors, such as the position or the bulkiness of the substituents, can be crucial in forming aggregates.

The size of the substituents introduced is a vital factor in terms of aggregation. Bulky and branched substituents reduce stacking and give the products dye properties instead of just pigment. In addition, this kind of substituents in the *N*-imide position considerably increases the solubility of the NMIs, improving reactivity. It has been experimentally proven that the introduction of substituents at other positions of the naphthalene core (Figure 3) does not significantly change the optical and aggregation properties of the products.

2.2. Aggregation Induced Emission of NMIs

1,8-Naphthalimides, like many other compounds with aromatic cores, have a strong tendency to produce intermolecular π-π stacking, as discussed in the previous section, capable of causing fluorescence quenching through a very common phenomenon called "aggregation-caused quenching" (ACQ).[22] This is a feature that prevents molecules from achieving better performance in the solid state or in aggregation in terms of light emission, although it may benefit other applications associated with non-radiative decay processes, such as photothermal therapy or photoacoustic imaging.[23]

Diametrically opposed to ACQ is the phenomenon whereby an enhancement of fluorescence properties is achieved after a process of molecular aggregation, which is known as "aggregation-induced emission" (AIE). This term was first introduced in 2001 by Tang and co-workers[24] and has since been studied by multiple research groups due to its diverse applications for industry. Luminogens that emit weakly in the molecular state but can be induced to emit efficiently in the aggregated state are called AIEgens.

[22] a) M. Li, S. Zhang, P. Zhang, K. Qin, Q. Chen, Q. Cao, Y. Zhang, J. Zhang, C. Yuan, H. Xiao, *J. Environ. Manage.*, **2023**, *338*, 117773. b) T. Förster, K. Kasper, *Z. Phys. Chem.*, **1954**, *1*, 275-277.
[23] S. Xu, Y. Duan, B. Liu, *Adv. Mater.*, **2019**, 1903530.
[24] J. Luo, Z. Xie, J. W. Y. Lam, L. Cheng, H. Chen, C. Qiu, H. S. Kwok, X. Zhan, Y. Liu, D. Zhu, B. Z. Tang, *Chem. Commun.*, **2001**, 1740-1741.

The AIE is attributed to the mechanism of restriction of intramolecular motion (RIM)[25] that combines the restriction of intramolecular rotation (RIR), due for example to the presence of aromatic rings, with the restriction of intramolecular vibration (RIV). In dilute solutions, the free molecular motions of the flexible segments of the AIEgens can consume energy through non-radiative pathways while, once aggregation occurs, intramolecular motions are restricted, blocking non-radiative deactivation pathways in favour of radiative decay pathways.[26]

A typical example of this phenomenon occurs in tetraphenylethene (TPE), where the absence of intramolecular movements favours fluorescence (Figure 17),[27] which increases with rising polarity of a THF-water mixture.

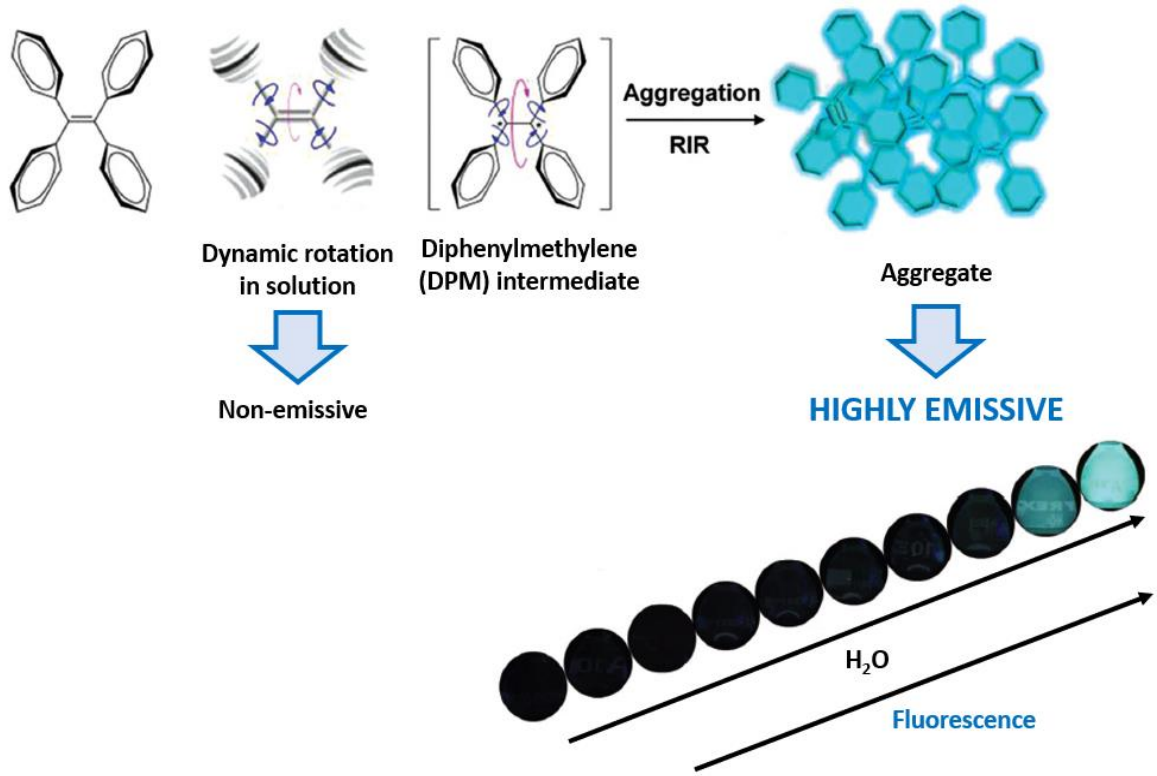

Figure 17. AIE scheme for TPE.

Materials that exhibit this phenomenon usually have a rotor structure, which is usually a benzene ring or some derivative. Such structures include derivatives of TPP, tetraphenylsilole (TPS),[28] distyrylananthracene or the aforementioned TPE. Today, AIEgens can be synthesised almost on demand. Derivatives of 1,8-naphthalimides are also materials that exhibit this property,[29] that is an enhancement of fluorescence by increasing the polarity of a mixture of water and organic solvent. An example of this can be seen in Figure 18.

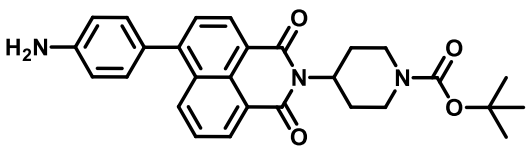

[25] J. Qi, C. Chen, D. Ding, B. Z. Tang, *Adv. Healthcare Mater.*, **2018**, *7*, 1800477
[26] Z. Wang, X. Guo, L. Jia, Z. Zhao, R. Yang, Y. Zhang, *J. Mol. Liq.*, **2023**, *381*, 121796.
[27] H. Gao, X. Zhang, C. Chen, K. Li, D. Ding, *Adv. Biosys.*, **2018**, *2*, 1800074.
[28] Y. N. Hong, J. W. Y. Lam, B. Z. Tang, *Chem. Soc. Rev.*, **2011**, *40*, 5361-5388.
[29] a) L. He, Q. Li, Y. Zhang, K. Huang, B. Du, L. Liang, *Spectrochim. Acta A Mol. Biomol. Spectrosc.*, **2023**, *296*, 122672. b) F. Xin, J. Zhao, X. Wang, H. Wang, H. Wang, M. Xing, Y. Fu, Y. Tian, Y. Tian, *Spectrochim. Acta A Mol. Biomol. Spectrosc.*, **2023**, *296*, 122621. c) S. Sharma, S. Srinivas, S. Rakshit, S. Sengupta, *Org. Biomol. Chem.*, **2022**, *20*, 9422-9430.

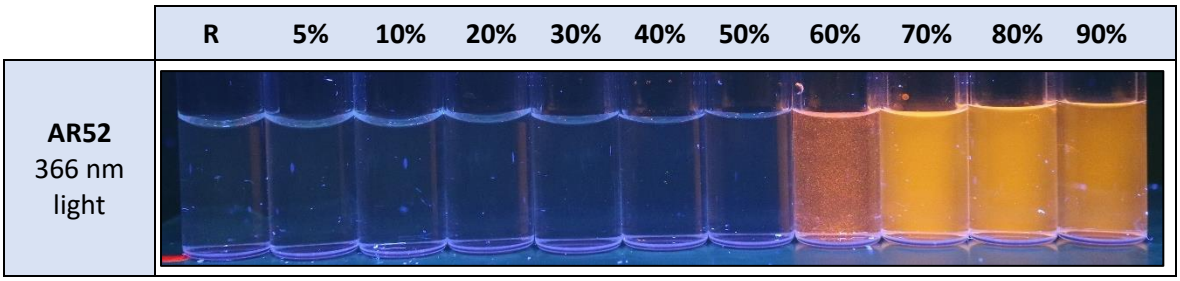

Figure 18. Water acceptance test of a 20 µM solution of AR52 in a mixture of MeOH and increasing amounts of water under UV (366 nm) light.

As can be noted in Figure 18, there was no emission until 60% water was reached, at which point an orange fluorescence started to be emitted. This can also be confirmed in the following graphs (Figure 19), where the large increase in emission intensity and the shift of the emission maximum from the blue region (about 430 nm) to orange (above 600 nm) could be observed.

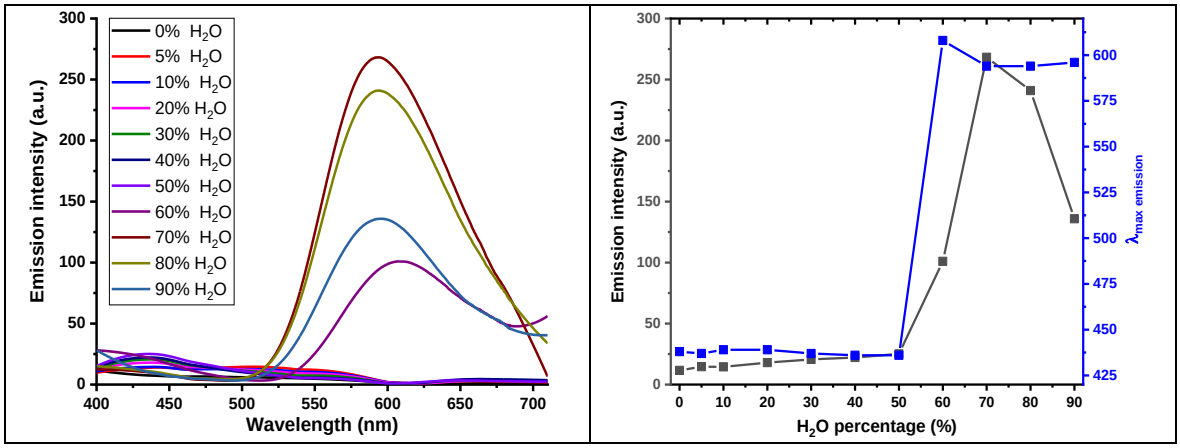

Figure 19. Emission intensity graph (left) and graph of relationship between the emission intensity and the wavelength of the maximum of emission (right) as a function of the amount of water added for AR52. λ_{exc} = 380 nm.

Once the AIE phenomenon was confirmed, the aggregates formed were studied by SEM and the result is shown in Figure 20.

At lower percentages of water, nanoparticles of different geometries, spherical and cubic, as well as small aggregates were found. The size of the nanoparticles did not exceed 130 nm. However, at 60% water, which was the amount at which emission occurred, needle-shaped nanoparticles and fibres formation were observed, while at 70% water the nanoparticles were larger, with some vesicles. At 70%, the size of the nanoparticles was approximately 700 nm.

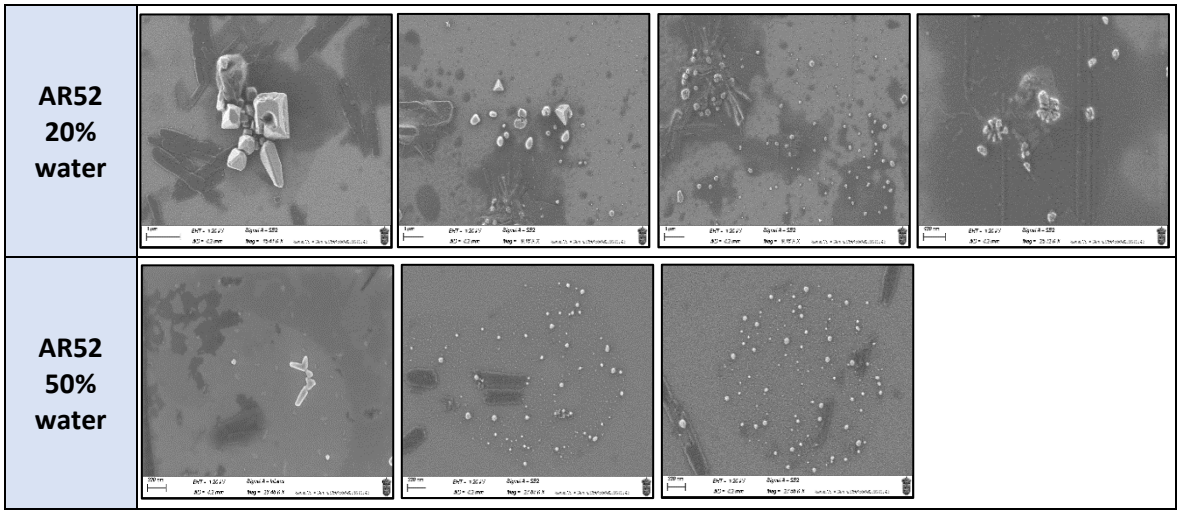

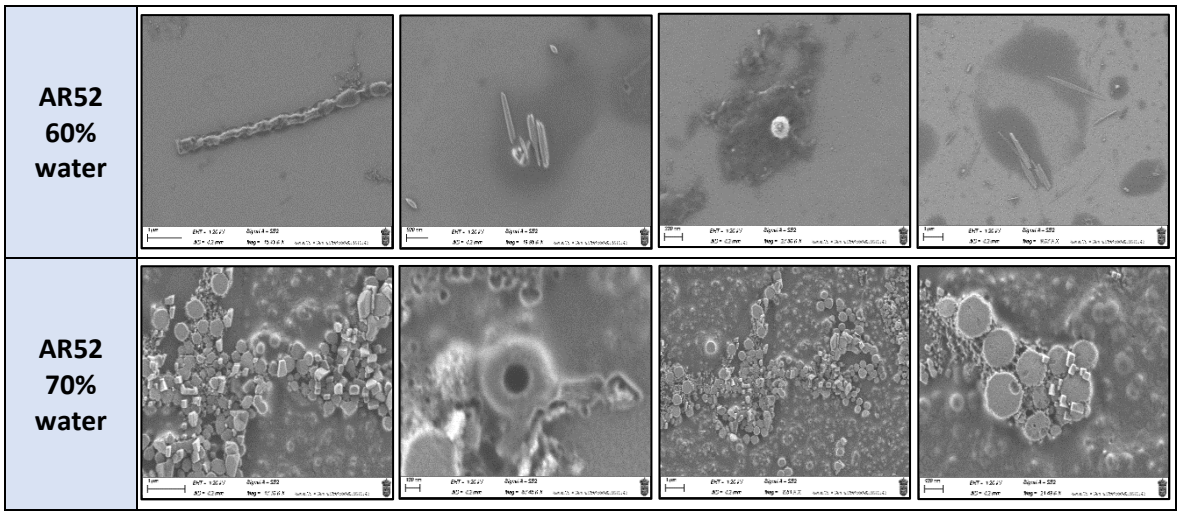

Figure 20. SEM nanoparticles of AR52 in different mixtures of MeOH and increasing amount of water.

By varying the working conditions, such as concentration, temperature or the solvent mixture used, the π-π intermolecular interactions responsible for the aggregates are modified, resulting in nanostructures of perfectly controlled morphology and size, which can be used in multiple applications.

2.2.1. Applications of AIEgens:

Numerous AIEgens have been designed for use in optical systems, luminescent sensors, bioimaging and phototherapy.[30] The results of theoretical and experimental studies revealed that the AIE mechanism, based on the restriction of intramolecular motions, has favoured the design of multiple high-performance materials, such as the development of organic AIE nanoparticles, with brighter luminescence and better physical stability than inorganic quantum dots, or noble metal nanoclusters.[31]

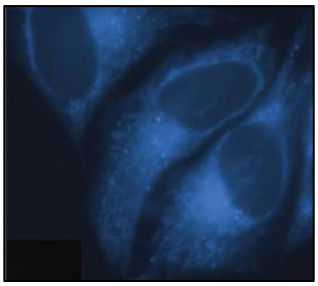

Figure 21. Confocal microscopy of HeLa cells.

Luminogens with a long absorption/emission wavelength have been used in biomedical applications because long wavelength light is less damaging to tissues and cells (Figure 21),[32] allowing deeper penetration and *in vivo* and *in vitro* imaging with a higher signal-to-background ratio.[33] In addition, such AIEgens can be used in applications for secure information display and night vision devices.[34]

Other important characteristics of AIEgens are, on the one hand, high quantum yields of photoluminescence (PLQY) to ensure good performance in fields such as the development of OLEDs[35] and, on the other hand, high molar extinction coefficients, a parameter that measures the efficiency with which the chemical species attenuates light of a specific wavelength, which makes them suitable for use in photodynamic therapy, light-emitting diodes or solar cells.

[30] X. Huang, F. Chen, Y. Ma, F. Zheng, Y. Fang, B. Feng, S. Huang, H. Zeng, W. Zeng, *Biomater. Res.*, **2023**, *27*, 20.
[31] X. Kang, S. Wang, M. Zhu, *Chem. Sci.*, **2018**, *9*, 3062-3068.
[32] Z. Song, W. Zhang, M. Jiang, H. H. Y. Sung, R. T. K. Kwok, H. Nie, I. D. Williams, B. Liu, B. Z. Tang, *Adv. Funct. Mater.*, **2016**, 26, 824-832.
[33] A. L. Antaris, H. Chen, K. Cheng, Y. Sun, G. Hong, C. Qu, S. Diao, Z. Deng, X. Hu, B. Zhang, X. Zhang, O. K. Yaghi, Z. R. Alamparambil, X. Hong, Z. Cheng, H. Dai, *Nat. Mater.*, **2016**, *15*, 235-242.
[34] a) G. Qian, Z. Y. Wang, *Chem. Asian J.*, **2010**, *5*, 1006-1029. b) J. O. Escobedo, O. Rusin, S. Lim, R. M. Strongin, *Curr. Opin. Chem. Biol.*, **2010**, 14, 64-70. c) K. Kiyose, H. Kojima, T. Nagano, *Chem. Asian J.*, **2008**, *3*, 506-515.
[35] Q. Yan, R. Yao, G. Li, J. Guo, B. Zhao, J. Li, R. Hang, H. Wang, *Dyes Pigm.*, **2023**, *215*, 111290.

Among many AIEgens, naphthalimides are very versatile chromophores which, together with their photophysical properties, make them suitable for a wide variety of applications. Some that have been developed thanks to the AIE phenomenon are the following:

- Xia *et al*. synthesised a thermoresponsive fluorescent rotor and used it as a viscometer and a viscosity-related thermometer.[36]
- Wang *et al*. described a thermometer, also based on naphthalimide derivatives, which changed its fluorescence as a function of temperature.[37]
- Song and co-workers synthesised fluorophores using naphthalimides and indoles as starting materials and used them to detect thiophenol[38] and biothiol[39] in living cells.

3. ORIGINS AND APPLICATIONS OF NMI

In 1972, Braña *et al*. began a line of research with the aim of synthesizing new compounds with cytostatic activity. For the design of the new molecules, they considered cycloheximide (1), CG-603 (2), aristolochic acid (3) and tilorone (4) as models. The structure of these compounds can be seen in Figure 22.[40]

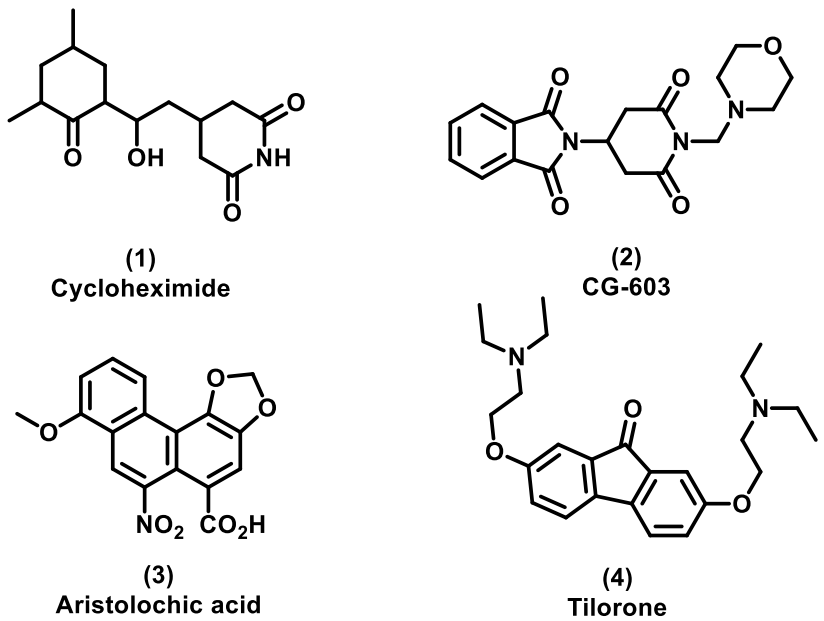

Figure 22. Structure of the models used by Braña and his co-workers.

With these structures in mind, they were interested in synthesising a compound that had the β-nitronaphthalene system of compound (3), the six-linked cyclic imide of compounds (1) and (2), and the side chain present in compound (4). The simplest solution was to obtain derivatives using 3-nitro-1,8-naphthalimide as starting material. The products obtained were studied for their biological activity and an outstanding inhibitory action on cell replication.[41]

[36] T. Xia, L. Wang, Y. Qu, Y. Rui, J. Cao, Y. Hu, J. Yang, J. Wu, J. Xu, *J. Mater. Chem. C*., **2016**, *4*, 5696–5701.
[37] S. Wang, J. Cao, C. Lu, *New J. Chem*., **2020**, *44*, 4547–4553.
[38] S. Zhou, Y. Rong, H. Wang, X. Liu, L. Wei, X. Song, *Sens. Actuators B*., **2018**, *276*, 136–141.
[39] Y. Rong, C. Wang, P. Chuai, Y. Song, S. Zhou, P. Hou, X. Liu, L. Wei, X. Song, *New J. Chem*., **2019**, *43*, 13212–13216.
[40] F. M. Braña, *Ars Pharmaceutica*, **1995**, *36*, 377-415.
[41] M. F. Braña, J. M. Castellano, C. M. Roldán, *Pat. Esp*., **1973**, *410*, 740.

From this time on, 1,8-naphthalimide derivatives began to be used in fields such as human medicine and veterinary medicine due to their antiparasitic, fungicidal, antidepressant, antiviral and anticarcinogenic properties.[42]

Subsequently, NMIs and their derivatives substituted at the C4 position turned into compounds of special interest due to their excellent properties and they continued to be used in medicine and biology, as fluorescent markers, because fluorescence techniques allow real-time, non-invasive imaging with high spectral resolution of living objects.[43] They are also used, for example, in synthetic membrane transporters or in selective catalysis.[44] However, they also began to be used in other applications of a much more technological nature, such as environmental sensors, solar energy collectors, chemical probes for the detection of metal ions and protons or in semiconductors.[45]

3.1. NMIs as probes

The development of fluorescent probes derived from 1,8-naphthalimide derivatives has many advantages, including immediate response or the use of cheap and affordable equipment suitable for use even in field analysis. Most NMI-derived sensors are based on one of the following photophysical phenomena:[46]

- Intramolecular charge transfer (ICT).
- Twisted intramolecular charge transfer (TICT).
- Photoinduced electron transfer (PET).
- Förster resonance energy transfer (FRET).
- Excited-state intramolecular proton transfer (ESIPT).
- Aggregation-induced emission (AIE).

Among them, the PET model developed by A. P. de Silva, consisting of "fluorophore-spacer-receptor", became the most popular approach to fluorescence design.[47] The main feature of this design is the easy communication between the receptor (recognition part) and the fluorophore (signalling part). An example of an NMI sensor based on this system is shown in Figure 23,[48] which was used in the detection of acid vapours.

[42] M. K. Hargreares, J. G. Pritchard, M. R. Dave, *Chem. Rev.*, **1970**, *70*, 439-469.
[43] a) J. Huang, Y. Chen, J. Qi, X. Zhou, L. Niu, Z. Yana, J. Wang, G. Zhao, *Spectrochim. Acta A Mol. Biomol. Spectrosc.*, **2018**, *201*, 105-111. b) X. Yang, J.F. Lovell, N. Murthy, Y. Zhang, *Top. Med. Chem.*, **2020**, *34*, 33–53. c) N. Georgiev, A. Said, R. Toshkova, R. Tzoneva, V. Bojinov, *Dyes Pigm.*, **2019**, *160*, 28–36.
[44] a) S. K. Nandi, D. Díaz Díaz, D. Haldar, *J. Phys. Chem. C.*, **2022**, *126*, 675−682. b) A. V. Jentzsch, A. Hennig, J. Mareda, S. Matile, *Acc. Chem. Res.*, **2013**, *46*, 2791−2800.
[45] a) A. Takai, T. Yasuda, T. Ishizuka, T. Kojima, M. A. Takeuchi, *Angew. Chem., Int. Ed.*, **2013**, *52*, 9167−9171. b) D. X. Wang, M. X. Wang, *J. Am. Chem. Soc.*, **2013**, *135*, 892−897. c) D. K. Maiti, A. A. Banerjee, *Chem. Commun.*, **2013**, *49*, 6909−6911.
[46] a) H. Zhang, Z. Xu, F. Tao, W. W. Yu, Y. Cui, *Anal. Chim. Acta.*, **2021**, *1186*, 339076. b) P. Zheng, A. Abdurahman, Z. Zhang, Y. Feng, Y. Zhang, X. Ai, F. Li, M. Zhang, *J. Hazard. Mater.*, **2021**, *409*, 124500. c) T. Anand, S. K. A. Kumar, S. K. Sahoo, *Spectrochim. Acta A Mol. Biomol. Spectrosc.*, **2018**, *204*, 105–112. d) S. Li, B. Zhao, W. Kan, L. Wang, B. Song, S. Chen, *Res. Chem. Intermed.*, **2018**, *44*, 491–502. e) A. L. García, A. Ochoa-Terán, A. Tirado-Guízar, J. Jara-Cortés, G. Pina-Luis, H. Santacruz-Ortega, V. Labastida-Galván, M. Ordoñez, J. Peón, *RSC Adv.*, **2022**, *12*, 6192-6204. f) M. Ozdemir, *Chem. Select.*, **2020**, *5*, 14340-14348. g) V. Bakov, N. I. Georgiev, V. B. Bojinov, *Molecules*, **2022**, *27*, 7556.
[47] a) S. Seraj, S. Rouhani, F. Faridbod, *RSC Adv.*, **2019**, *9*, 17933–17940. b) C. Yao, H. Lin, H. Crory, A. P. de Silva, *Mol. Syst. Des. Eng.*, **2020**, *5*, 1325–1353. c) N. Georgiev, P. Krasteva, V. Bakov, V. Bojinov, *Molecules*, **2022**, *27*, 4229.
[48] N. I. Georgiev, V. V. Bakov, V. B. Bojinov, *Photonics*, **2022**, *9*, 994.

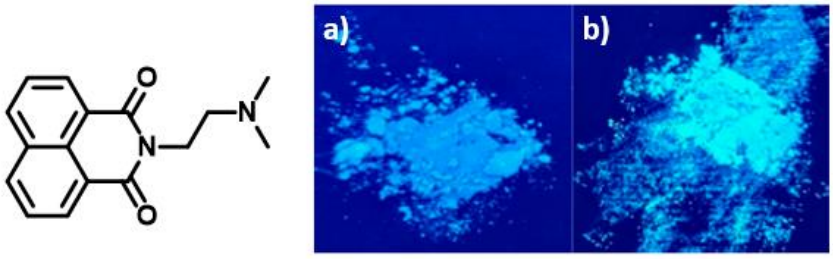

Figure 23. Powder of the NMI derivative probe before (a) and after (b) exposure to HCl vapours. Detection takes place through the PET phenomenon.

1,8-naphthalimide derivatives can be used as sensors due to, besides other properties, their ability to respond to a variety of external stimuli, such as heat, pH, light, ultrasound, or ions. This results in a reversible gel-solution phase transition that can be used to monitor, for example, the presence of CO_2.[49]

In addition, NMI derivatives can be used for the fluorescent detection of a wide range of species such as formaldehyde in food samples,[50] hypochlorite[51] or Cu^{2+} in cells,[52] nitrobenzene in the medium[53] or environmental pollutants such as $Cr_2O_7^{2-}$ or Fe^{3+}.[54]

3.2. NMIs as semiconductors

A very relevant feature of the naphthalimide derivatives is their chemical versatility since they can be functionalised both in the *N*-imide position and in different positions of the carbocyclic backbone.[55] This allows their electronic properties to be modified depending on the functionalisation, making them suitable for use as organic semiconductors.

Naphthalimide derivatives are classified as *n*-type semiconductor materials, that is, materials that present charge transport in the form of electrons. This makes it possible for them to be used in the development of OLEDs of different colours (blue, yellow-green or even red) depending on the functionalisation of the naphthalene core (Figure 24).[56] They have also been exploited in the development of field-effect transistors (OFET) and photovoltaic cells.[57]

[49] X. Zhang, Y. Song, M. Liu, H. Li, H. Sun, M. Sun, H. Yu, *Dyes Pigm.*, **2019**, *160*, 799–805.
[50] H. Du, H. Zhang, Y. Fan, Y. Zheng, S. Yuan, T. T. Jia, M. Li, J. Hou, Z. Li, Y. Li, Z. Ma, Y. Wang, H. Niu, Y. Ye, *Food Chem.*, **2023**, *411*, 135483.
[51] C. Zhang, Y. Wang, X. Li, S. Nie, C. Liu, Y. Zhang, J. Guo, *Anal. Biochem.*, **2023**, *670*, 115131.
[52] Z. Meng, Z. Wang, Y. Liang, G. Zhou, X. Li, X. Xu, Y. Yang, S. Wang, *Int. J. Biol. Macromol.*, **2023**, *239*, 124261.
[53] S. Khadija, H. Irshad, S. Rafique, A. M. Khan, S. Nawazish, H. Rehman, M. Imran, S. A. Shahzad, U. Farooq, *Spectrochim. Acta A Mol. Biomol. Spectrosc.*, **2023**, *290*, 122273.
[54] C. Shi, J. Luo, Y. Wang, L. Ding, Q. Liang, Z. Yang, J. Lu, A. Wu, *Spectrochim. Acta A Mol. Biomol. Spectrosc.*, **2023**, *289*, 122245.
[55] I. Arrechea, Estudio químico-físico de propiedades intra- e intermoleculares que afectan al transporte de carga en transistores orgánicos de efecto campo, PhD. Thesis, University of Málaga, **2019**.
[56] a) R. Arunchai, T. Sudyoadsuk, N. Prachumrak, S. Namuangruk, V. Promarak, M. Sukwattanasinitt, P. Rashatasakhon, *New J. Chem.*, **2015**, *39*, 2807–2814. b) E. R. Triboni, M. R. Fernandes, J. R. Garcia, M. C. Carreira, R. G. S. Berlinck, P. B. Filho, L. S. Roman, I. A. Hümmelgen, R. Reyes, M. Cremona, *J. Taibah Univ. Sci.*, **2015**, *9*, 579–585. c) S. Luo, J. Lin, J. Zhou, Y. Wang, X. Liu, Y. Huang, Z. Lu, C. Hu, *J. Mater. Chem. C.*, **2015**, *3*, 5259–5267.
[57] S. Kotowicz, M. Korzec, J. Grzegorz-Małecki, S. Golba, M. Siwy, S. Máckowski, E. Schab-Balcerzak, *Mater.*, **2022**, *15*, 7043.

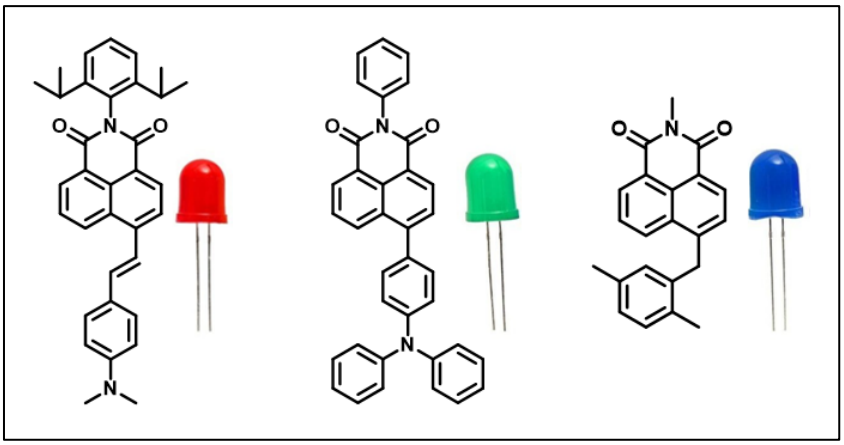

Figure 24. Scheme of NMI derivatives giving rise to different coloured OLEDs.

3.3. NMIs as building blocks

Finally, NMI derivatives substituted at the C4 position can be used as monomers in the field of supramolecular polymers, due to the growing interest in the development of supramolecular polymers with π-conjugated systems.[58] The polymerisation process can be carried out in various ways, for example by applying heat or by radiation of a certain wavelength.[59]

As demonstrated by Khanra *et al.*, homopolymerisation of two NMI-derived monomers with different heteroatoms (oxygen vs sulphur) results in very different nanostructures, which can be seen in Figure 25.[60]

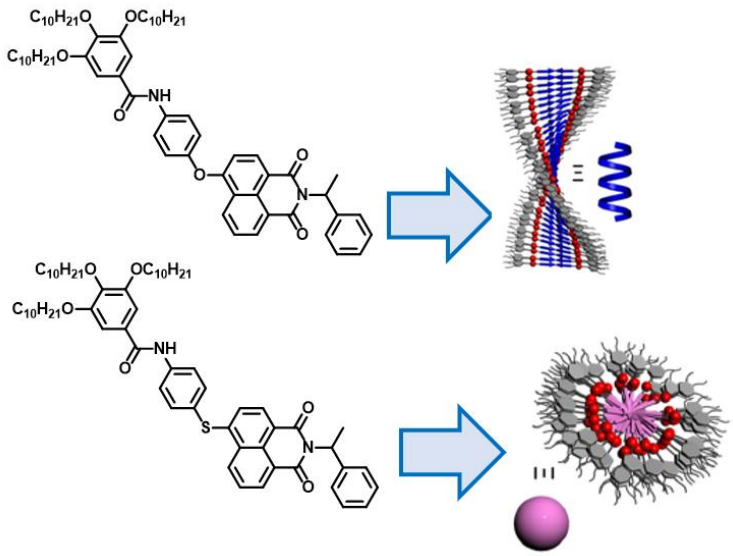

Figure 25. Scheme of different types of polymerisations of NMI derivatives.

The polymers and gels obtained can be used in a variety of fields, such as information encryption processes, smart devices, or LEDs with a long emission wavelength. Thin layers used in the development of field effect transistors, semiconductors or transistors can also be obtained.[61]

[58] A. Das, B. Maity, D. Koley, S. Ghosh, *Chem. Commun.*, **2013**, *49*, 5757 -5759.
[59] S. Liu, N. Giacoletto, B. Graff, F. Morlet-Savary, M. Nechab, P. Xiao, F. Dumur, J. Lalevee, *Mater. Today Chem.*, **2022**, 26, 101137.
[60] P. Khanra, A. K. Singh, L. Roy, A. Das, *J. Am. Chem. Soc.*, **2023**, *145*, 5270–5284.
[61] S. V. Bhosale, C. H. Janiab, S. J. Langford, *Chem. Soc. Rev.*, **2008**, *37*, 331-342.

CHAPTER 3

NMI DERIVATIVES FOR DETECTION

As we have discussed in the previous chapter, NMI derivatives substituted at the 4-position of the naphthalene ring can be used, among a large number of applications, in the development of luminescent sensors. This type of probes allows the detection of species of a very diverse nature, such as oxidants, cations that can act as environmental pollutants or various nitrated species, such as TNT. Therefore, this Chapter 3 is a compendium of different NMI derivatives that have applications in the field of detection, both in solution and deposited on the surface of other materials.

Chapter 3A focuses on the detection of TATP, a very common explosive used in the development of IEDs. This detection was carried out in solution, in the vapour phase using a system designed in the laboratory and in real conditions, such as in an office. In doing so, an APP was performed to determine the presence and amount of TATP that had come into contact with the detection system.

Chapter 3B focuses on the detection of another very common explosive, TNT. Throughout the chapter, different compounds were detailed for detection in both solution and solid form, in the form of magic swab.

One of the main objectives of the research is to publish the results obtained. As a result, an article published in the framework of this thesis, entitled "*Dye-modified silica-anatase nanoparticles for the ultrasensitive fluorogenic detection of the improvised explosive TATP in an air microfluidic device*" (DOI: 10.1039/d1qm01041g), carried out in collaboration with the Latvian Institute of Organic Synthesis, has not been developed in these chapters. The reason for this is that the compound used for the detection was synthesised by the Latvian Institute of Organic Synthesis, while the research group of the University of Burgos was in charge of the design, anchoring to surfaces and development of the detection tests. Therefore, the system for gas-phase TATP detection detailed in this article is the same as the one described in Section 5 of Chapter 3A of this PhD thesis.

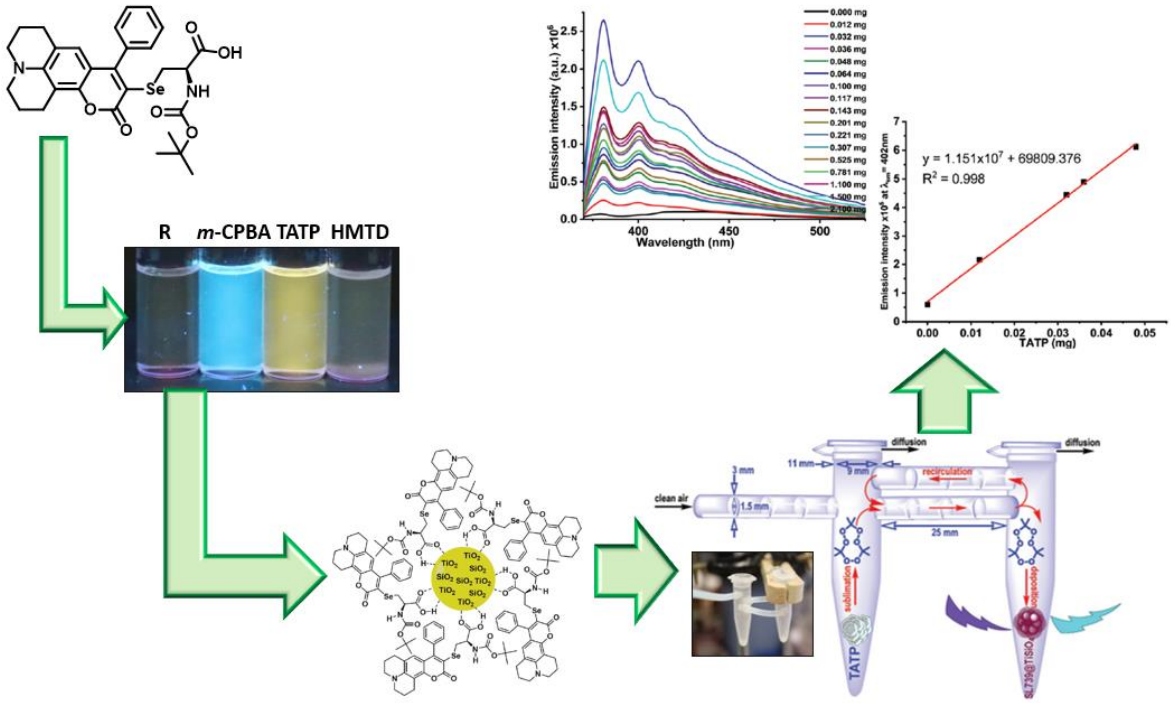

Figure 1. Schematic summary of the procedure described in the article with DOI: 10.1039/d1qm01041g.

CHAPTER 3A

NMI DERIVATIVES FOR TATP DETECTION

This chapter describes the proof of concept of a portable testing setup for the detection of triacetone triperoxide (TATP), a common component in improvised explosive devices. The system allows for field-testing and in real conditions, leading to real-time results to test for TATP vapor traces in air by simply using circulation of air samples through the sensing mechanism under the air conditioning system of an ordinary room. In this way, the controlled trapping of the analyte in the chemical sensor gives reliable results at extremely low concentrations of TATP in air under conditions suitable for daily use in luggage storage for airlines or the locker room for a major sporting event. The reported fluorescent methodology is very sensitive and selective, allowing for the trapping of TATP in the chemical sensor to give reliable results at very low concentrations in air under ambient conditions, by comparing the fluorescence of the material before and after exposition to TATP traces in air.

1. INTRODUCTION

A major threat in modern society is constituted by the so-called improvised explosive devices (IEDs).[1] The explosives contained in IEDs were commonly used in war sceneries but some years ago they were also beginning to use in sceneries of everyday life,[2] therefore constituting a threat for the lives of countless people.

To minimize or even cancel out the damage caused by such devices, rapid detection methods are necessary, that provide responses within minutes.[3] However, such detection methods are, currently, very scarce.[4] Indeed, the most advanced spectroscopy devices are very sensitive and selective to identify the chemicals used in IEDs, but they are typically too heavy and bulky to be used as portable devices, too much expensive for widespread use and required specialized personnel to handle them.[5]

Another cheaper technology is the cotton swab[6] (Figure 1a)[7] that requires physical access to the substance that might be hidden or not easily accessible, which makes them more dangerous or, in some instances, impossible to use. A widespread method of detection is the use of animals, particularly trained dogs (Figure 1b),[8] in the detection of explosives[9] but some explosives without a characteristic smell gone undetected by animals, which makes it not a very efficient method. The same problem is presented by electronic noses (Figure 1c),[10] a system allows different volatile organic substances to be differentiated based on their characteristic smell. It made up of artificial

[1] a) Improvised explosive devices: Past, present and future action on armed violence. 15/10/2020. Obtained from: https://reliefweb.int/report/world/improvised-explosive-devices-past-present-and-future, accessed 20/05/2022. b) IED attack, improvised explosive devices, national academies and the department of homeland security, 15/12/2020 Obtained from: https://www.dhs.gov/xlibrary/assets/prep_ied_fact_sheet.pdf, accessed 20/05/2022. c) Reducing the threat of improvised explosive device attacks by restricting access to explosive precursor chemicals, national academies of sciences, engineering, and medicine. **2018**, *The National Academies Press*, Washington DC.

[2] Improvised explosive device (IED): Guidelines for crowded places. Commonwealth of Australia, **2017**, ISBN: 978-1-925593-95-2.

[3] K. C. To, S. Ben-Jaber, I. P. Parkin, *ACS Nano*, **2020**, *14*, 10804−10833.

[4] a) T. Wasilewski, J. Gębicki, *Microchem. J.*, **2021**, *164*, 106025. b) T. P. Forbes, S. T. Krauss, G. Gillen, *Trends Anal. Chem.*, **2020**, *131*, 116023.

[5] A. Ostrinskaya, R. R. Kunz, M. Clark, R. P. Kingsborough, T. H. Ong, S. Deneault, *J. Forensic Sci.*, **2019**, *64*, 223-230.

[6] J. M. E. Glackin, R. N. Gillanders, F. Eriksson, M. Fjällgren, J. Engblom, S. Mohammed, I. D. W. Samuel, G. A. Turnbull, *Analyst*, **2020**, *145*, 7956–7963.

[7] Lab Tips: Bastoncillo de muestreo grande. Obtained from: https://berkshire.com.es/tienda/hisopo-bastoncillos-limpieza-sala-limpia/bastoncillo-de-muestreo/lab-tips-sampling-swabs/, accessed 14/03/2023.

[8] ¿Cómo entrenan a los perros detectores de droga? Obtained from: https://www.expertoanimal.com/como-entrenan-a-los-perros-detectores-de-droga-23387.html, accessed 14/03/2023.

[9] T. H. Ong, T. Mendum, G. Geurtsen, J. Kelley, A. Ostrinskaya, R. Kunz, *Anal. Chem.*, **2017**, *89*, 6482−6490.

[10] Peres es la primera nariz electrónica especializada en alimentos. Obtained from: https://www.afuegolento.com/articulo/peres-es-primera-nariz-electronica-especializada-alimentos/10820/, accessed 14/03/2023.

sensor arrays, are a consequential solution to replace the natural senses [11] for reliable monitorization of diverse environments.

Figure 1. Current methods for detection of IEDs: Cotton swap (a), detection with animals (b) and electronic nose (c).

1.1. Explosives: TATP

Explosives are defined as chemicals which give rise to a rapid and exothermic chemical reaction initiated by the application of a small pulse of energy. These processes are usually carried out with the release of gaseous products.[12] They are usually classified by their easiness of their ignition and their use (Figure 2). Primary explosives are the most sensitive because they are initiated by low-intensity mechanical stimuli, but they are normally used as initiators of secondary explosives, which are more powerful than primary explosives. Secondary explosives include triacetone triperoxide (TATP), which is the focus of this work. Finally, there are also propellants, which are those whose structure contains all the oxygen necessary for their combustion.[13]

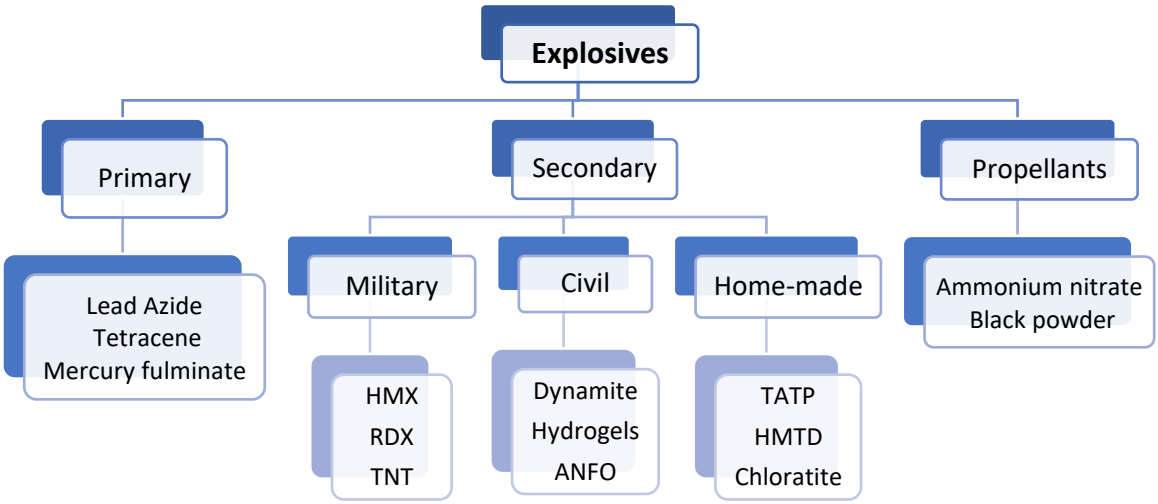

Figure 2. Explosives classification.

One of the most frequently used explosives in the preparation of IEDs is TATP (Figure 3a). TATP is a non-military explosive, classified in the group of peroxide explosives, 88% more powerful than trinitrotoluene (TNT) and synthesized from readily available starting materials.[14] TATP sublimes easily at room temperature but, due to the lack of aromatic nitro groups, its presence in the vapor phase is not detected by using common methods for explosives.[15] Common explosives containing

[11] a) Z. Li, J. R. Askim, K. S. Suslick, *Chem. Rev.*, **2019**, *119*, 231–292. b) Z. Li, K. S. Suslick, *Acc. Chem. Res.*, **2021**, *54*, 950–960.
[12] Y. Qi, W. Xu, N. Ding, X. Chang, C. Shang, H. Peng, T. Liu Y. Fang, *J. Mater. Chem. C.*, **2013**, *4*, 1-7.
[13] J. P. Agrawal, R. D. Hodgson, Organic chemistry of explosives, *Wiley*, England, **2007**.
[14] M. A. C. Härtel, T. M. Klapötke, B. Stiasny, J. Stierstorfer, *Propellants Explos. Pyrotech.*, **2017**, *42*, 623–634
[15] F. Dubnikova, R. Kosloff, J. Almog, Y. Zeiri, R. Boese, H. Itzhaky, A. Alt, E. Keinan, *J. Am. Chem. Soc.*, **2005**, *127*, 1146-1159.

nitro groups, such as TNT or 1,3,5-trinitrobencene (TNB), have a large variety of fluorescent methods for their detection, including the contribution of our research group to the field[16] and from other groups.[17] Another important explosive, within the group of peroxides, employed in IEDs is hexamethylene triperoxide amine (HMTD, Figure 3b), obtained by the addition of a hexamine to a hydrogen peroxide (H_2O_2) solution under acid catalysis. This explosive is characterized by low thermal and chemical stability and a much lower vapor pressure than TATP, which, unfortunately, makes vapours phase detection not possible.[18]

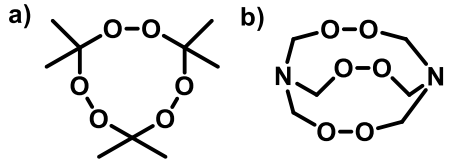

Figure 3. Explosives based in peroxide: TATP (a) and HMTD (b).

TATP is easily synthesised from acetone and hydrogen peroxide under acid catalysis, such as hydrochloric acid, tin (IV) chloride or nitric acid. However, the presence of other species, such as methanesulphonic, perchloric or sulphuric acid, as catalysts causes TATP to undergo spontaneous degradation to DADP. The putative mechanism of TATP synthesis is as shown in Figure 4.[19]

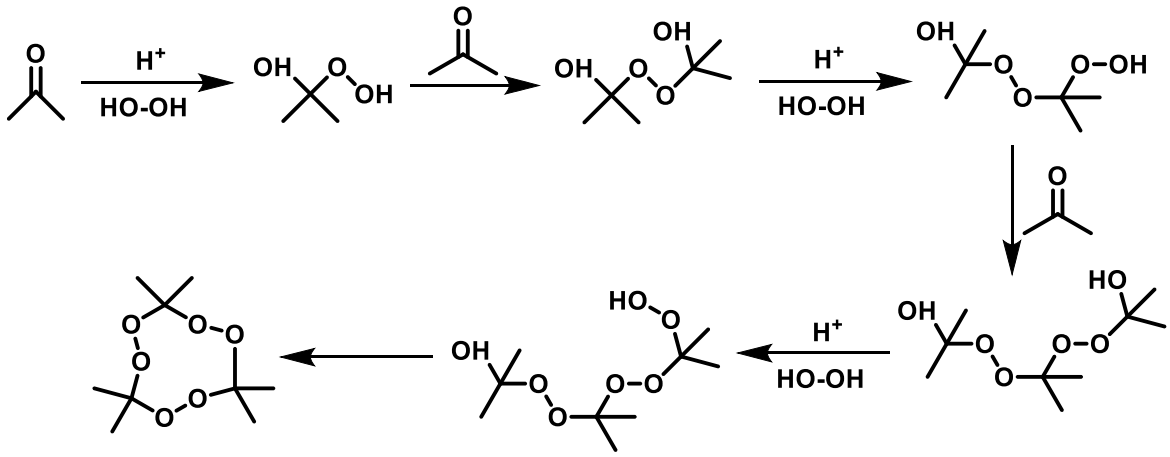

Figure 4. Presumed mechanism of TATP synthesis.

The breakdown of TATP gives rise to many of the current detection methods. However, there is controversy as to what these products are. Keinan *et al*.[20] and Oxley *et al*.[21] agree that TATP gives rise mainly to acetone and ozone, with secondary products such as dioxygen, methyl acetate, ethane and carbon dioxide. In contrast, Hiyosi and Nakamura have shown that heating degradation of TATP gives rise to carbon dioxide and water.[22]

[16] D. C. Romero, P. Calvo-Gredilla, J. García-Calvo, A. Diez-Varga, J. V. Cuevas, A. Revilla-Cuesta, N. Busto, I. Abajo, G. Aullón, T. Torroba, *Org. Lett*., **2021**, *23*, 8727–8732.

[17] a) W. M. Wan, D. Tian, Y. N. Jing, X. Y. Zhang, W. Wu, H. Ren, H. L. Bao, *Angew. Chem. Int. Ed*., **2018**, *57*, 15510–15516. b) S. Kim, H. Kim, T. Qiao, C. Cha, S. K. Lee, K. Lee, H. J. Ro, Y. Kim, W. Lee, H. Lee, *ACS Appl. Mater. Interfaces*, **2019**, *11*, 14354–14361. c) Z. Zhang, S. Chen, R. Shi, J. Ji, D. Wang, S. Jin, T. Han, C. Zhou, Q. Shu, *Talanta*, **2017**, *166*, 228–233. d) N. Tripathi, R. Kumar, P. Singh, S. Kumar, *Sens. Actuators B*, **2017**, *246*, 1001–1010.

[18]] K. Colizza, A. Yevdokimov, L. McLennan, J. L. Smith, J. C. Oxley, *J. Am. Soc. Mass Spectrom.*, **2018**, *29*, 675-684.

[19] R. Matyas, J. Pachman, H. G. Ang, *Propellants Explos. Pyrotech*., **2008**, *33*, 89 - 91. b) K. Betlz, The development of calibrants through characterization of volatile organic compounds from peroxide based explosives and a non-target chemical calibration compound, Ph.D. Thesis, Florida International University, **2013**.

[20] F. Dubnikova, R. Kosloff, J. Almog, Y. Zeiri, R. Boese, H. Itzhaky, E. Keinan, *J. Am. Chem. Soc*., **2005**, *127*, 1146-1159.

[21] J. C. Oxley, J. L. Smith, H. Chen, *Propellants Explos. Pyrotech*., **2002**, *27*, 197 - 246.

[22] R. I. Hiyoshi, J. Nakamura, *Propellants Explos. Pyrotech.*, **2007**, *32*, 127-134.

1.2. Methods for detection of TATP

The most common methods for the TATP detection are mass spectrometry,[23] ion mobility spectrometry or related technologies[24] and multiphoton spectroscopy.[25] Other methods more sophisticated are chemically modified nanosensor arrays[26] or portable optical methods based on colorimetric sensor arrays, in this case to detect the H_2O_2 produced by decomposition of the TATP.[27] There are also alternative indirect detection methods, for example by detecting of H_2O_2 or the oxidative processes linked to them, fluorescent detection methods are used for this purpose,[28] as well as detection of acetone from decomposition of TATP.[29] The direct detection of TATP has also been achieved by fluorescence quenching of chemical probes.[30] Analytical methods for the detection of TATP (or HMTD) in different scenarios must be selective for peroxides, appropriate for immediate analysis and safe sampling process by a qualified operator.[31] They are expected to have very low limits of detection and high selectivity, in this way they can detect peroxides in confined public places to prevent explosions and further damage.[32] An extremely low limit of detection is easier to achieve with the TATP because it is more volatile than HMTD.[33] Most physicochemical analytical methods for peroxide-based explosives are designed in this way.[34] Trace detection of TATP in the vapor phase by colorimetric (Figure 5)[35] or fluorometric methods, taking into account its volatility, continues to be an attractive approach for the development of chemical sensors for peroxide explosives. Some characteristics such as sensitivity and selectivity are still not well addressed.

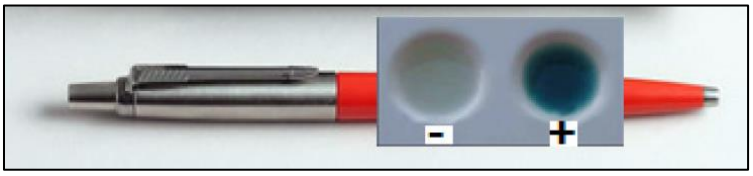

Figure 5. ACRO-P.E.T: pen used like device for colorimetric detection of peroxide derivates explosives.

[23] M. Makinen, M. Nousiainen, M. Sillanpaa, *Mass Spectrom. Rev.*, **2011**, *30*, 940-973.
[24] a) D. Jiang, L. Peng, M. Wen, Q. Zhou, C. Chen, X. Wang, W. Chen, H. Li, *Anal. Chem.*, **2016**, *88*, 4391–4399. b) D. N. Correa, J. J. Melendez-Perez, J. J. Zacca, R. Borges, E. M. Schmidt, M. N. Eberlin, E. C. Meurer, *Propellants Explos. Pyrotech.*, **2017**, *42*, 370–375. c) S. Hagenhoff, J. Franzke, H. Hayen, *Anal. Chem.*, **2017**, *89*, 4210–4215.
[25] S. Tang, N. Vinerot, D. Fisher, V. Bulatov, Y. Yavetz-Chen, I. Schechter, *Talanta*, **2016**, *155*, 235–244.
[26] A. Lichtenstein, E. Havivi, R. Shacham, E. Hahamy, R. Leibovich, A. Pevzner, V. Krivitsky, G. Davivi, I. Presman, R. Elnathan, Y. Engel, E. Flaxer, F. Patolsky, *Nat. Commun.*, **2014**, *5*, 4195.
[27] a) H. Lin, K. S. Suslick, *J. Am. Chem. Soc.*, **2010**, *132*, 15519-15521. b) Z. Li, W. P. Bassett, J. R. Askim, K. S. Suslick, *Chem. Commun.*, **2015**, *51*, 15312-15315. c) J. R. Askim, Z. Li, M. K. LaGasse, J. M. Rankin, K. S. Suslick, *Chem. Sci.*, **2016**, *7*, 199-206.
[28] a) M. Xu, J.M. Han, C. Wang, X. Yang, J. Pei, L. Zang, *ACS Appl. Mater. Interfaces*, **2014**, *6*, 8708-8714. b) Q.-H. Zhu, G.-H. Zhang, W.-L. Yuan, S.-L. Wang, L. He, F. Yong, G.-H. Tao, *Chem. Commun.*, **2019**, *55*, 13661-13664. c) X. Yu, Y. Gong, W. Xiong, M. Li, J. Zhao, Y. Che, *Anal. Chem.*, **2019**, *91*, 6967–6970.
[29] a) Y. Qi, W. Xu, N. Ding, X. Chang, C. Shang, H. Peng, T. Liu, Y. Fang, *Mater. Chem. Front.*, **2019**, *3*, 1218-1224. b) Y. An, X. Xu, K. Liu, X. An, C. Shang, G. Wang, T. Liu, H. Li, H. Peng, Y. Fang, *Chem. Commun.*, **2019**, *55*, 941-944.
[30] M. R. Rao, Y. Fang, S. De Feyter, D. F. Perepichka, *J. Am. Chem. Soc.*, **2017**, *139*, 2421–2427.
[31] K. Liu, Z. Wang, C. Shang, X. Li, H. Peng, R. Miao, L. Ding, J. Liu, T. Liu, Y. Fang, *Adv. Mater. Technol.*, **2019**, *4*, 1800644.
[32] Analysis of explosives reference list, OSAC, **2020**. Obtained from: https://www.nist.gov/topics/ organization-scientific-area-committees-forensic-science/fire-debris-explosives-subcommittee, accessed 20/05/2022.
[33] Characteristics of improvised explosive devices containing chemical substances in the context of the international airports protection, EU-SENSE, **2021**. Obtained from: https://eu-sense.eu/characteristics-of-improvised-explosive-devices-containing-chemical-substances-in-the-context-of-the-international-airports-protection/, accessed 20/05/2022.
[34] a) A. González-Calabuig, X. Cetó, M. del Valle, *Talanta*, **2016**, *153*, 340–346. b) V. Krivitsky, B. Filanovsky, V. Naddaka, F. Patolsky, *Anal. Chem.*, 2019, 91, 5323–5330.
[35] Z. C. Caron, D. J. Meekins, M. J. Platek, O. J. Gregory, *Nanomat. Synth*, **2016**, *1*, 1531-1537.

The previous approaches of our research group consisted of solid fluorogenic sensors for the sensitive and selective detection of TATP[36] or the microwave detection of wet-TATP,[37] both in the vapor phase. On the other hand, we developed a system for detection of TATP gas in an air microfluidic device (Figure 6).[38]

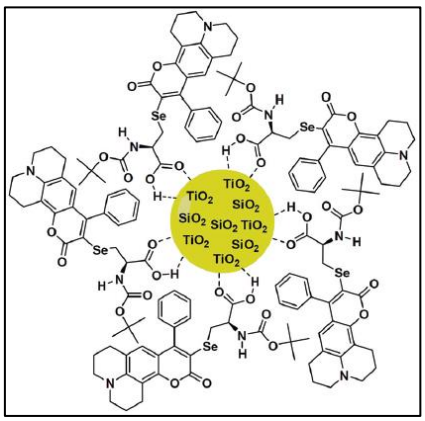

Figure 6. System develop for TATP detection in air microfluidic device.

After that, we have been looking for more selective and sensitive materials specifically tailored for the unambiguous detection of TATP traces in air.[39] For that purpose, we searched among diversely structured dyes, mainly naphthalimide derivatives, those in which an oxidation event could modulate the aggregation-induced emission (AIE) of dyes for the detection of oxidizing species.

1.3. Naphthalimides for detection

Naphthalimides are a kind of polycyclic amides derived from naphthalene that exhibit aggregation-induced emission (AIE) characteristics.[40] We selected a collection of new naphthalimides with donor and accepting groups in their structure and amino-protecting substituents, in which the variation of the substituents permitted the control of the AIE characteristics.

In this way, a new naphthalimide derivative dye was achieved, with optimum features for TATP detection, in which the AIE-gen fluorescent emission mechanism could be triggered via oxidation by only hydrophobic oxygen-containing oxidants. The subsequent study of the dye, supported on the surface of silica nanoparticles by adsorption process, permitted the construction of a new material with optimum performance for the selective and ultrasensitive detection of traces of TATP in the air. The system was tested at the interior of an ordinary office room by simply putting the sensor in the room aeration stream, and with positive results. In this way, it functioned as an IED-targeted chemical sniffing system.

[36] a) P. Calvo-Gredilla, J. García-Calvo, J. V. Cuevas, T. Torroba, J. L. Pablos, F. C. García, J. M. García, N. Zink-Lorre, E. Font-Sanchis, A. Sastre-Santos, F. Fernández-Lázaro, *Chem. Eur. J.*, **2017**, *23*, 13973–13979. b) J. García-Calvo, P. Calvo-Gredilla, M. Ibáñez-Llorente, D. C. Romero, J. V. Cuevas, G. García-Herbosa, M. Avella, T. Torroba, *J. Mater. Chem. A*, **2018**, *6*, 4416-4423.

[37] S. Blanco, A. Macario, J. García-Calvo, A. Revilla-Cuesta, T. Torroba, J. C. López, *Chem. Eur. J.*, **2021**, *27*, 1680-1687.

[38] S. Lapcinska, A. Revilla-Cuesta, I. Abajo-Cuadrado, J. V. Cuevas, M. Avella, P. Arsenyan, T. Torroba, *Mater. Chem. Front.*, **2021**, *5*, 8097–8107.

[39] T. Torroba, I. Schechter, J. G. Calvo, A. Revilla-Cuesta, Multi-year project: Development of new chemical sensors and optical technologies for fast and sensitive detection of improvised explosives, NATO Science for Peace and Security Series-B: Physics and Biophysics: Explosives Detection, Sensors, Electronic Systems and Data Processing, L. Capineri and E.K. Turmus, Eds., Springer, The Netherlands, **2019**, pp. 208-247

[40] P. Gopikrishna, N. Meher, P. K. Iyer, *ACS Appl. Mater. Interfaces*, **2018**, *10*, 12081−12111.

2. OBJECTIVES

As demonstrated in Chapter 2, naphthalenomonoimides (NMIs) are a good option in the search for new fluorescent sensors for the detection of oxidant species or for environmental purposes.[41] Due to their stability, NMIs are suitable for carrying out different chemical modifications in their structure, both with donor and acceptor groups, as well as for carrying out detection studies against diverse analytes, including different oxidising agents, most notably TATP.

Therefore, the main objective of this chapter is to modify an NMI core to give rise to a fluorescent compound that allows the sensitive and selective detection of TATP, both in solution and in gas phase. It is also intended to detection test of traces of TATP in air in real-life environment in a closed room by adsorbing the sensor on the surface of silica nanoparticles (Figure 7), demonstrating that it is a suitable system for the detection of TATP in everyday circumstances. On the other hand, from the initial tests, it was discovered that the several donor groups with which the naphthalene core is modified, as well as the presence of amino-protecting groups, had a direct influence on both the modulation of fluorescence and the detection capabilities against TATP.

Finally, the results obtained in the research are intended to be patented and published as a novel system for the detection of TATP vapours to lay the foundations for the detection of TATP in gas, a problem unsolved so far, also allowing the improvement of the developed system.

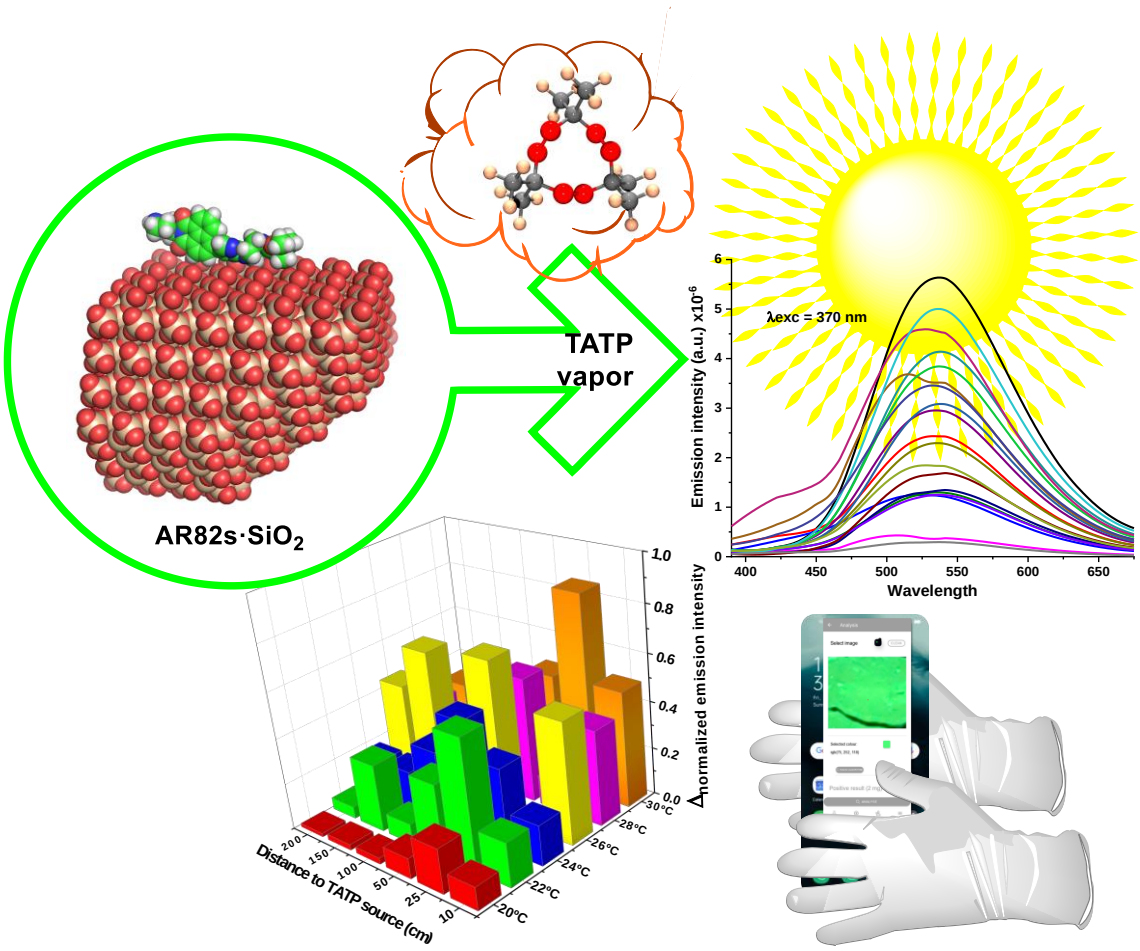

Figure 7. Summary of the experiments performed for TATP detection: adsorption on silica nanoparticles surface, exposure of the AR82s·SiO_2 system to TATP and results obtained in a titration against TATP vapours and in a real environment.

[41] a) J. Zhao, J. Zhang, B. Hu, C. Gao, Z. Li, Z. Sun, J. You, *Spectrochim. Acta A Mol. Biomol. Spectrosc.*, **2023**, *286*, 121965. b) Y. Cha, L. Gopala, M. H. Lee, *Spectrochim. Acta A Mol. Biomol. Spectrosc.*, **2023**, *291*, 122385.

3. SYNTHESIS OF NMIs DERIVATIVES SENSITIVE TO TATP

A number of fluorogenic probes was synthesized and they were tested against several types of analytes. The experimental procedure was performed by using Suzuki-Miyaura reactions, following previous experiences in developing fluorogenic probes by carbon-carbon coupling chemistry[42] to obtain the amino-protected (AR82p, AR83p and AR90p) and semi-protected products (AR82s, AR83s and AR90s). The new fluorogenic probes are shown in the Figure 8.

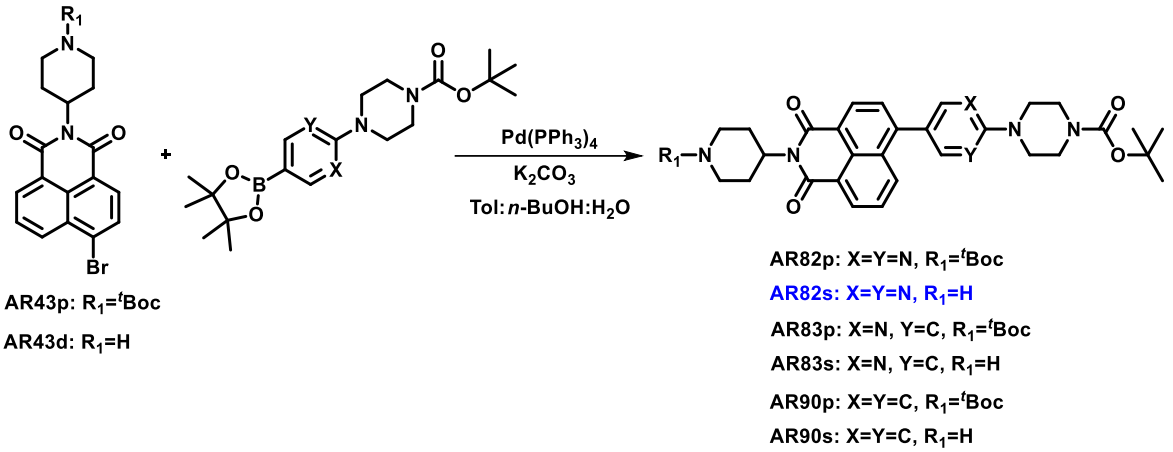

Figure 8. Synthesis of NMI amino-protected and semi-protected products.

Although the six different compounds, containing either a pyridine or a pyrimidine or a phenyl group and one or two amino-protecting groups, were synthetized, not all of them were a good option for being used as sensor.

As can be seen in Figure 9, the fluorescence of the pyridine derivatives (AR83p and AR83s) were very high for amino-protected and semi-protected products ($Ø_F$ > 85%). The phenyl derivatives (AR90p and AR90s) exhibited very different fluorescence, the amino-protected derivative showed a very high fluorescence ($Ø_F$ = 93%) but the semi-protected product had a very low fluorescence ($Ø_F$ < 5%), which would make it impossible to distinguish the changes due to a decrease in fluorescence. The pyrimidine derivatives showed a lower fluorescence and, among them, the semi-protected product had an intermediate emission intensity ($Ø_F$ = 73%) and was, therefore, the best option for use as a sensor.

	H_2O MeOH DMSO DMF MeCN Acet. EtOAc THF $CHCl_3$ DCM Tol. Et_2O Hex. MCH
AR82p	

[42] a) B. Díaz de Greñu, D. Moreno, T. Torroba, A. Berg, J. Gunnars, T. Nilsson, R. Nyman, M. Persson, J. Pettersson, I. Eklind, P. Wästerby, *J. Am. Chem. Soc.*, **2014**, *136*, 4125–4128. b) B. Díaz de Greñu, J. García-Calvo, J. Cuevas, G. García-Herbosa, B. García, N. Busto, S. Ibeas, T. Torroba, B. Torroba, A. Herrera, S. Pons, *Chem. Sci.*, **2015**, *6*, 3757-3764. c) J. García-Calvo, S. Vallejos, F. C. García, J. Rojo, J. M. García, T. Torroba, *Chem. Commun.*, **2016**, *52*, 11915-11918. d) J. García-Calvo, P. Calvo-Gredilla, M. Ibáñez-Llorente, T. Rodríguez, T. Torroba, *Chem. Rec.*, **2016**, *16*, 810-824. e) J. García-Calvo, J. A. Robson, T. Torroba, J.D.E.T. Wilton-Ely, *Chem. Eur. J.*, **2019**, *25*, 14214-14222. f) V. García-Calvo, J. V. Cuevas, H. Barbero, S. Ferrero, C. M. Álvarez, J. A. González, B. Díaz de Greñu, J. García-Calvo, T. Torroba, *Org. Lett.*, **2019**, *21*, 5803–5807. g) N. Busto, P. Calvo, J. Santolaya, J. M. Leal, A. Guédin, G. Barone, T. Torroba, J. L. Mergny, B. García, *Chem. Eur. J.*, **2018**, *24*, 11292-11296. h) J. García-Calvo, T. Torroba, V. Brañas-Fresnillo, G. Perdomo, I. Cózar-Castellano, Y. H. Li, Y. M. Legrand, M. Barboiu, *Chem. Eur. J.*, **2019**, *25*, 9287–9294. i) N. Busto, J. García-Calvo, J. V. Cuevas, A. Herrera, J. L. Mergny, S. Pons, T. Torroba, B. García, *Bioorg. Chem.*, **2021**, *108*, 104660.

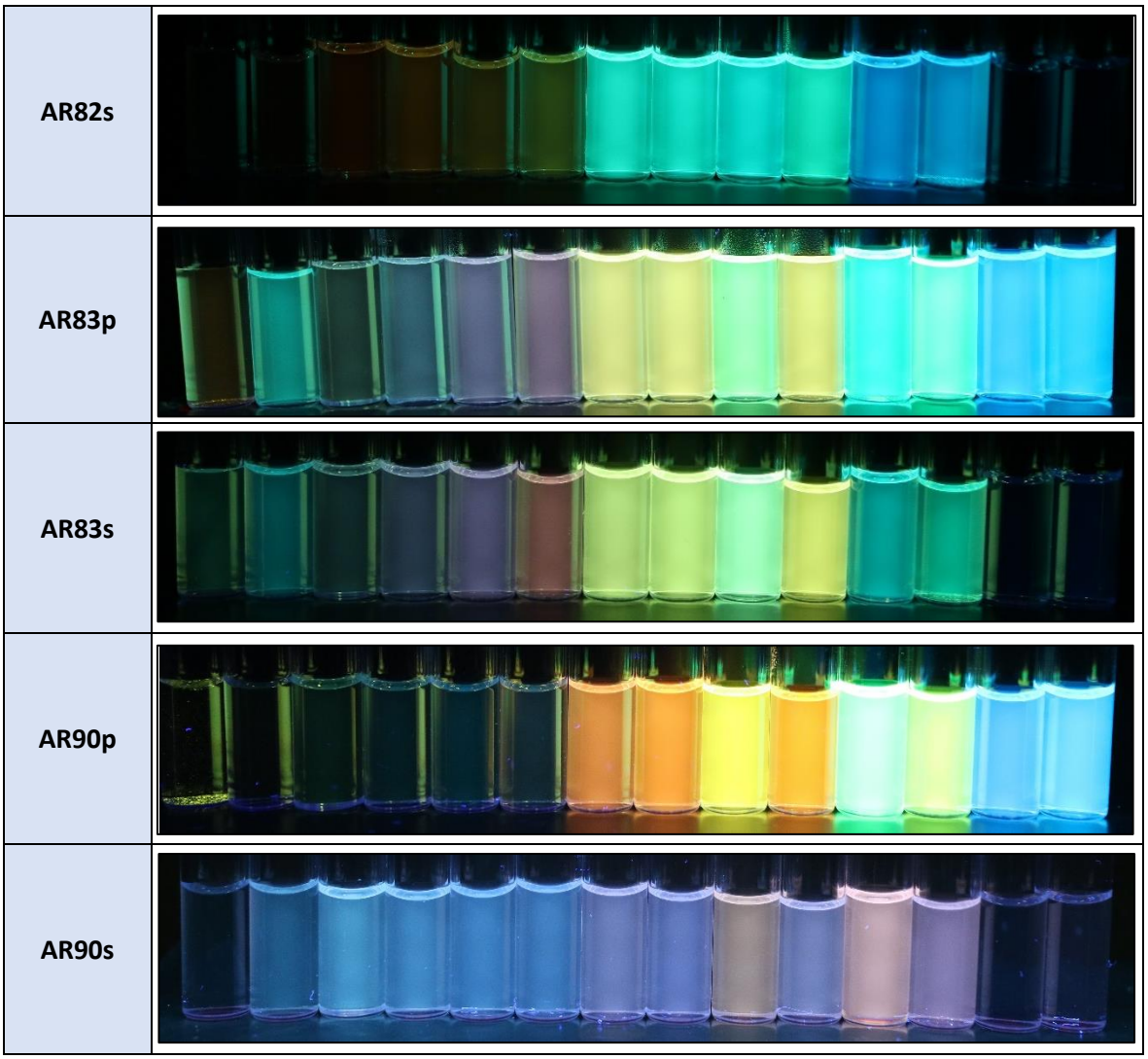

Figure 9. Fluorescent emission of 20 µM solutions of NMI derivatives in different solvents under 366 nm light.

The deprotected products (AR82d, AR83d and AR90d) were synthesised by adding TFA to a solution of the corresponding amino-protected product in chloroform (Figure 10).

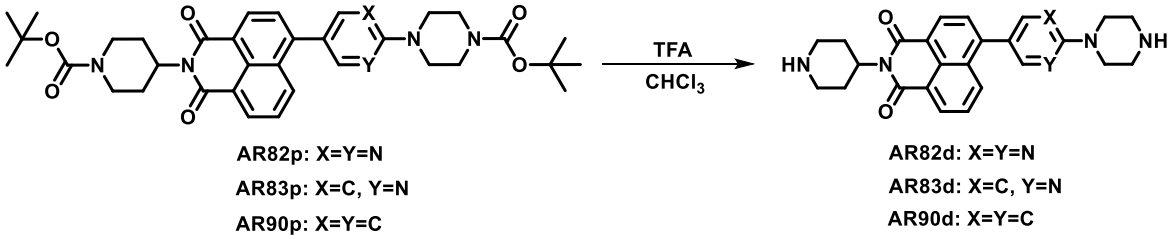

Figure 10. Synthesis of NMI unprotected products.

The amino-protected NMIs showed an increase of fluorescence in mixtures of organic solvents with increasing amounts of water (AIE). This phenomenon disappeared when the structures contained unprotected amino groups.

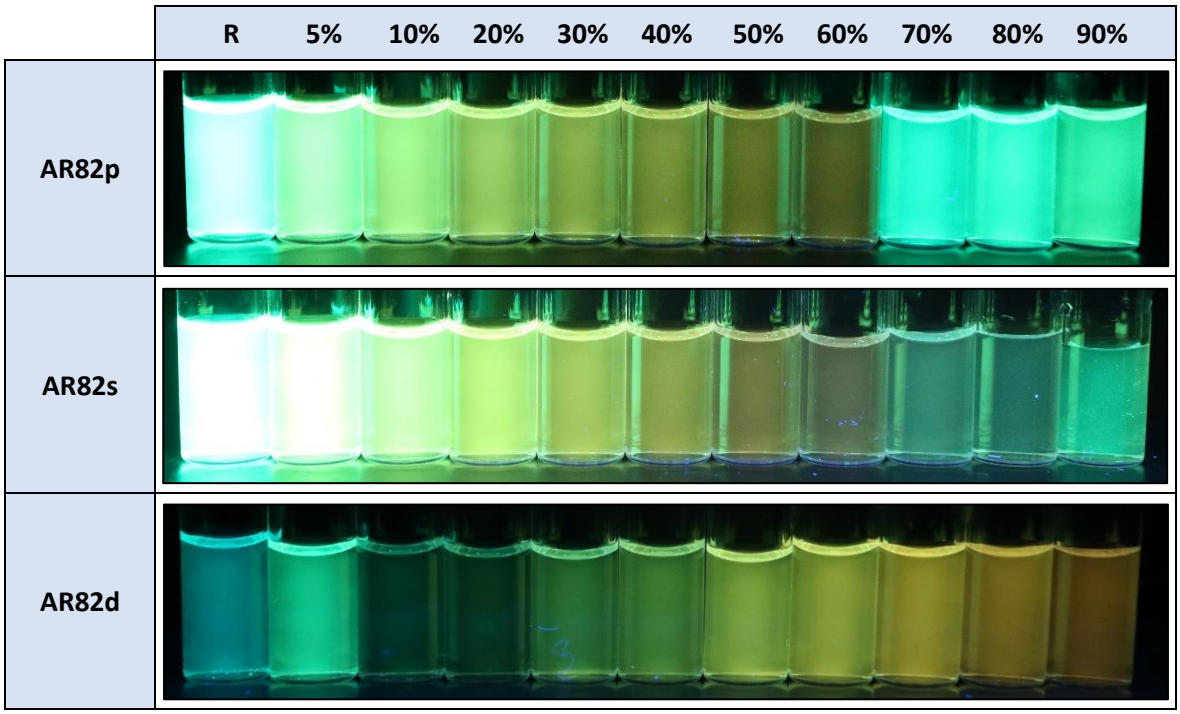

Figure 11. Water acceptance study of 20 µM solutions of amino-protected (up), semi-protected (middle) and unprotected (down) AR82 in THF under 366 nm light.

An example of this can be noted in Figure 11, where the fluorescence variation for the amino-protected, semi-protected and unprotected AR82 compound in mixtures of water and THF are observed. Previous examples have shown these characteristics.[43]

3.1. Synthesis of silica materials with adsorbed NMI derivatives

We prepared an experimental design for this part of the work that was applied to fluorescent probes that gave the best positive response in terms of sensitivity to trace amounts of oxygen-based explosives. Probes AR82s and AR82d, both bearing the same structure, NMI derivatives with a pyrimidine, and different number of protective groups in the periphery, resulted sufficiently sensitive to the presence of TATP, which will be demonstrated in the following section. Furthermore, the stability of both probes was checked and found that AR82s was much more stable than AR82d, therefore we used only AR82s for the preparation of sensing material.

For this purpose, the sensitivity of NMI derivatives on different solid supports was analysed in the presence of gaseous traces of home-made explosive TATP, so the fluorogenic materials were capable of discriminate the presence and the nature of the most important oxygen-based explosive. From previous experience in solid-supporting materials,[44] we performed initial experiments by supporting the fluorescent probes on thin layers of polydimethylsiloxane (PDMS) but the low detection limit (LOD) was not good enough. Instead, silica nanoparticles afforded much better results. Modified silica nanoparticles (AR82s·SiO_2, Figure 12) were prepared by adsorption process in which stirring under nitrogen stream, in the dark, 1 mg of AR82s product and 100 mg of silica nanopowder (10-20 nm particle size) in 5 ml chloroform for 30 minutes until there was no trace of dye in the solvent. Afterwards, the solvent was evaporated, the solid was washed three times with

[43] a) K. Tajima, N. Fukui, H. Shinokubo, *Org. Lett.*, **2019**, *21*, 9516–9520. b) Y. Wang, Y. Teng, H. Yang, X. Li, D. Yin, Y. Tian, *Chem. Commun.*, **2022**, *58*, 949-952.

[44] a) J. García-Calvo, P. Calvo-Gredilla, S. Vallejos, J. M. García, J. V. Cuevas-Vicario, G. García-Herbosa, M. Avella, T. Torroba, *Green Chem.*, **2018**, *20*, 3875-3883. b) J. García-Calvo, V. García-Calvo, S. Vallejos, F. C. García, M. Avella, J. M. García, T. Torroba, *ACS Appl. Mater. Interfaces*, **2016**, *8*, 24999–25004.

hexane (3 ml each) and then subjected to centrifugation and drying under nitrogen stream to get the material.

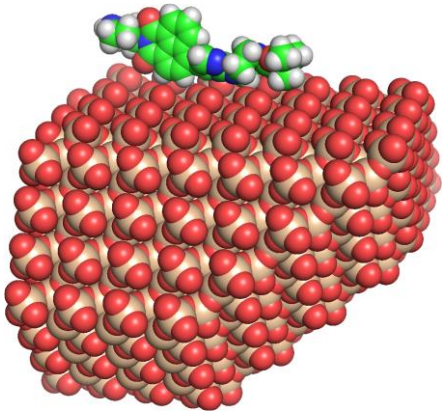

Figure 12. Model of the chemical probe AR82s on silica nanoparticles surface.

3.2. Characterization of the functional materials

The AR82s·SiO_2 system was characterized with different techniques: registering fluorescent profiles, TEM images and elemental composition analysis.

Nanoparticles with the AR82s compound adsorbed on their surface were characterized by recording the fluorescence profiles, both emission and excitation, before and after exposure to TATP vapours (Figure 13).

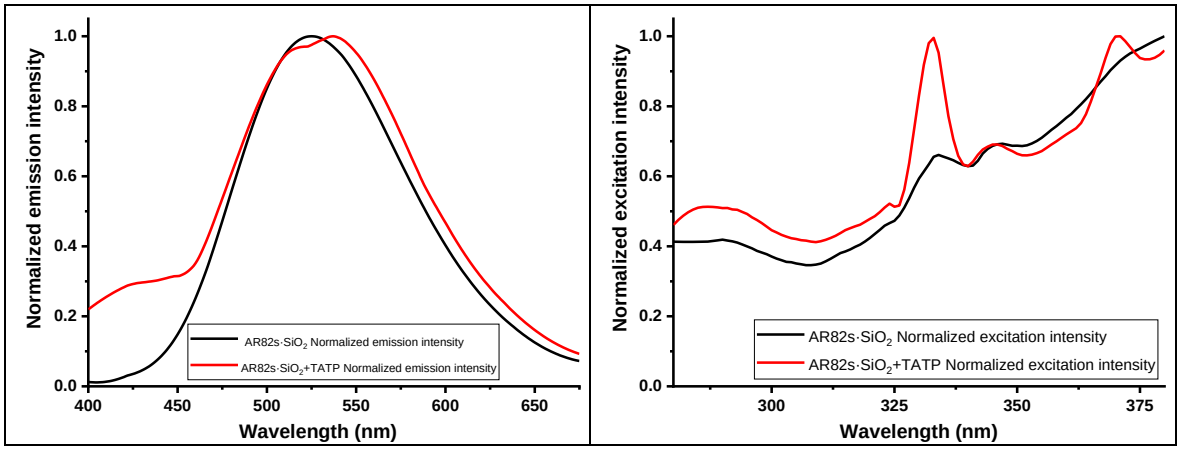

Figure 13. Fluorescence (left) and excitation (right) profiles of AR82s adsorbed in SiO_2 nanoparticles.

It was observed that, both before and after exposure to TATP vapours, the profile of the AR82s·SiO_2 system is very similar.

The proportion of carbon/silicon of the AR82s·SiO_2 were checked by elemental composition analysis, shown in Figure 14. From this profile, the proportion of C/Si obtained were around 6% for this silica nanoparticles. The presence of heavy metals traces, such as copper, was also observed.

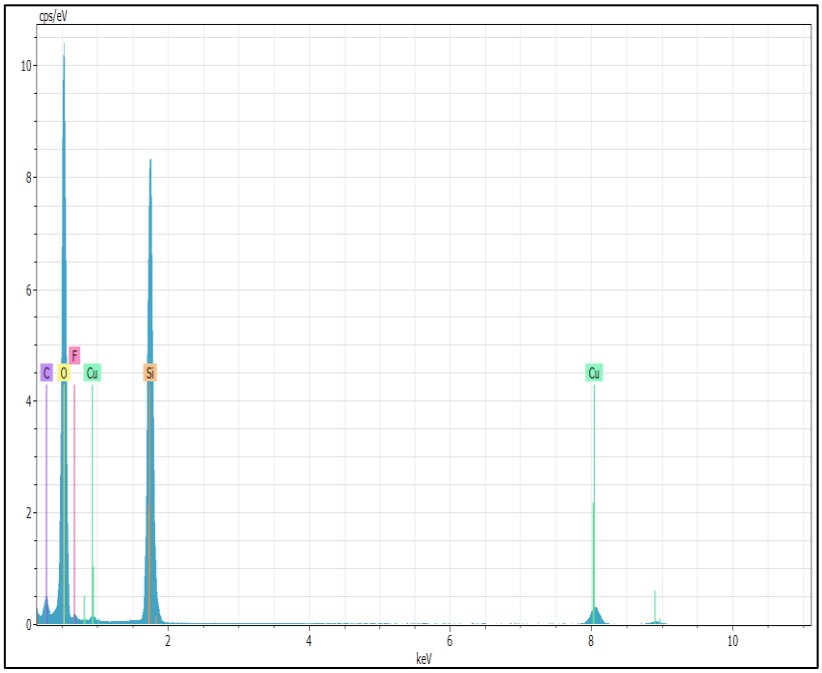

Figure 14. Elemental composition analysis of the AR82s·SiO_2 nanoparticles.

Finally, TEM images were also registered, to determine the structure and composition of AR82s·SiO_2 (Figure 15, upper and middle images respectively). The nanometric and micrometric structure of this nanoparticles was demonstrated with high resolution TEM images (Figure 15, images below).

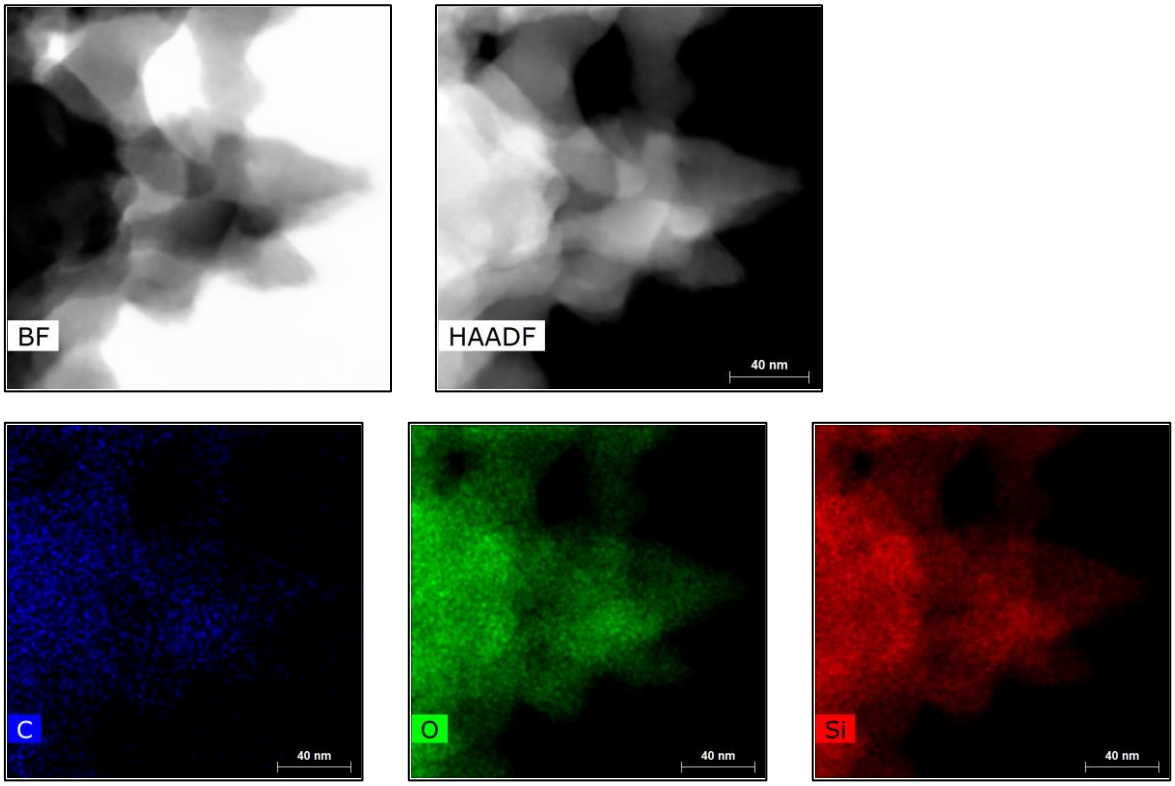

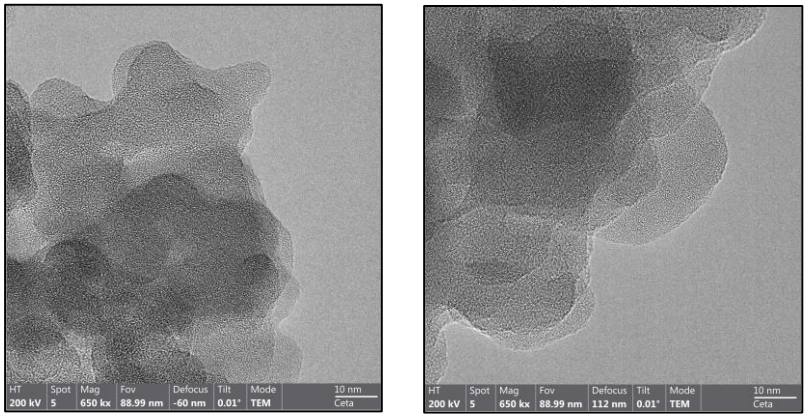

Figure 15. Structural (up) and elemental (middle) TEM images of AR82s·SiO_2 nanoparticles. High resolution (down) TEM images of AR82s·SiO_2 nanoparticles.

4. QUALITATIVE AND QUANTITATIVE MEASUREMENTS WITH OXIDIZING REAGENTS

The selectivity of each fluorogenic probe against the most important oxygen-based oxidizing reagents was addressed in mixtures of organic solvent and water, with the aim to select the best candidates for fluorogenic probes for oxygen-based explosives. With the new fluorogenic probes we performed a complete characterization and a battery of preliminary tests about selectivity and sensitivity with target explosives and several expected interferents. The sensitivity of the collection of fluorogenic probes was checked in the presence of TATP and HMTD.

4.1. Probe in solution: solvent selection

The selection of the appropriate dye for TATP detection consisted of an iterative process. Preliminary tests were carried out both on the probe individually and in the presence of TATP, in order to select the best solvent for subsequent studies.

First, a solvent study was carried out to determine in which solvents the most notable changes occurred. As shown in Figure 16, there were a large number of solvents in which changes were observed, being mainly a quenching of fluorescence when the addition of an excess of TATP was carried out. In the unprotected compounds, changes occurred in more solvents than in the semi-protected compound, where changes were only observed in four solvents: DMF, MeCN, toluene and DCM.

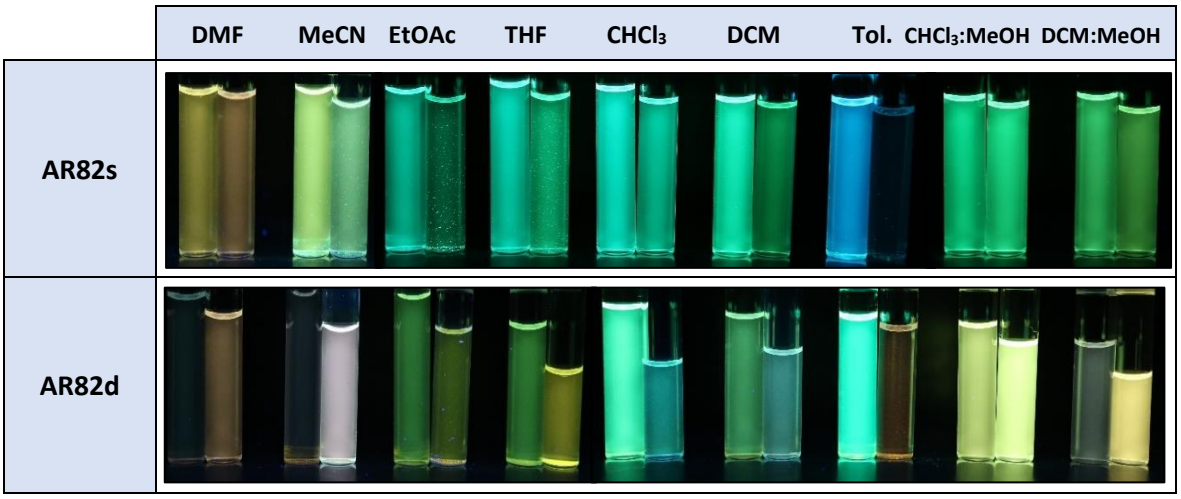

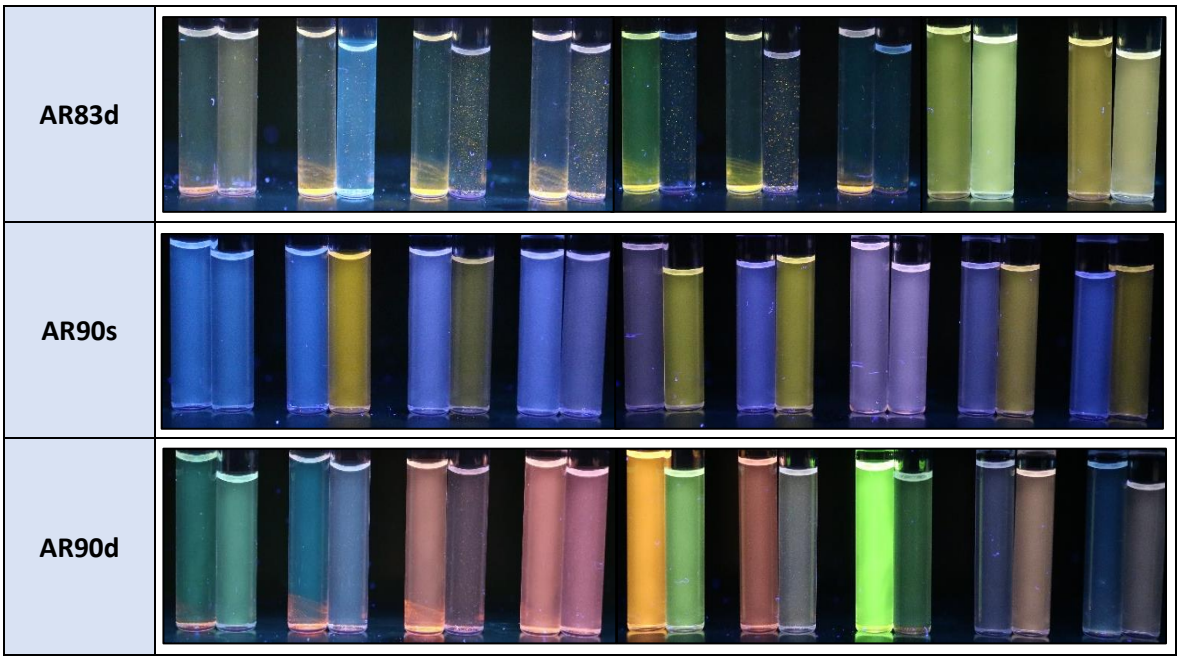

Figure 16. Solvent test. Pairs of 20 µM solutions of NMI derivative probe (left vial of each pair) and probe solution with excess of TATP (right vial of each pair) in different solvents under 366 nm light.

AR82s, AR82d, AR83d, AR90s and AR90d were showed an utmost performance in terms of sensitivity and selectivity to the presence of peroxide-carried oxidants (except hydrogen peroxide). Thereafter, kinetic behaviour studies and titration experiments were performed, first in different solvents, then by accurate titration in the best solvent, selected from previous experiments.

Therefore, the following figures (Figure 17, Figure 18, Figure 19, Figure 20 and Figure 21) show the profiles at the emission maximum wavelength of the titrations that were performed with the NMI derivatives versus TATP in the different solvents. The main objective of this test was to select the solvent in which the change in fluorescence occurs at the lowest concentration of TATP.

As can be seen in Figure 17, the best solvent in which the semi-protected AR82s product can detect TATP is DCM, because the fluorescence decrease occurred immediately after the addition of TATP, so the LOD is between 0 and 250 µM. On the other hand, in Figure 18 it was observed that the best solvents for AR82d are toluene and DCM, because the LOD is also, in both cases, between 0 and 250 µM. Finally, the products AR83d, AR90s and AR90d present very high LODs for all the solvents in which the study was carried out (Figure 19, Figure 20 and Figure 21 respectively).

In addition, the stability of compounds AR82s and AR82d was also studied, obtaining that compound AR82s was much more stable than AR82d, so only more detailed titrations were performed for AR82s.

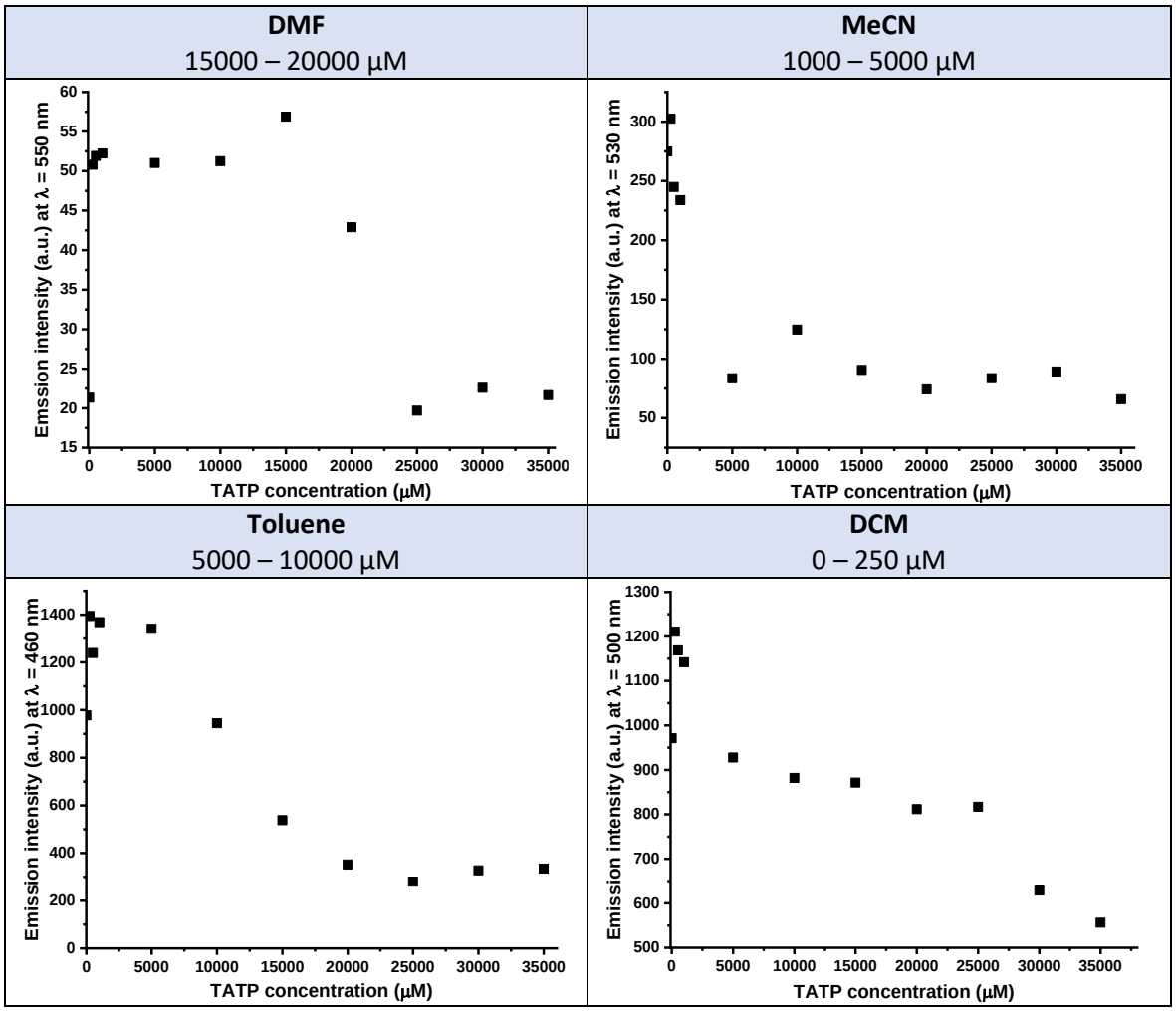

Figure 17. Study of 2.5µM of AR82s with TATP in different solvents. Fluorescence profile at maximum emission wavelength under increasing concentrations of TATP.

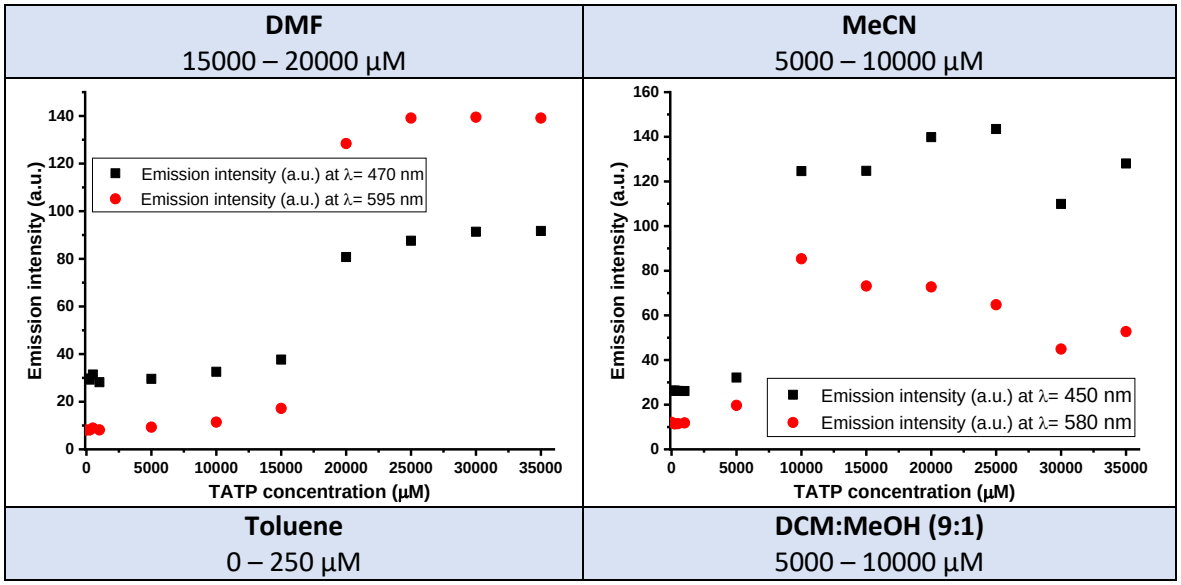

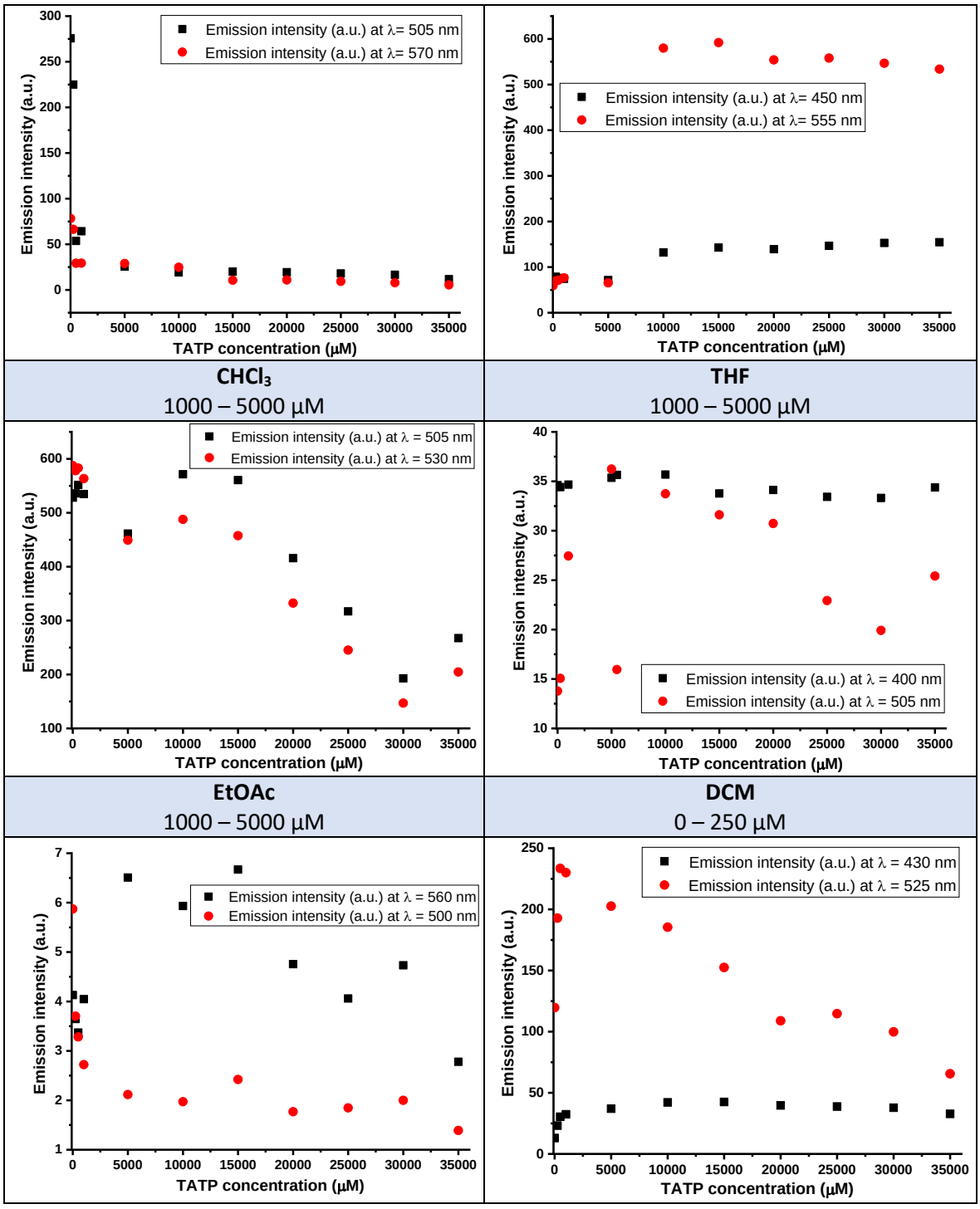

Figure 18. Study of 2.5μM of AR82d with TATP in different solvents. Fluorescence profile at maximum emission wavelength under increasing concentrations of TATP.

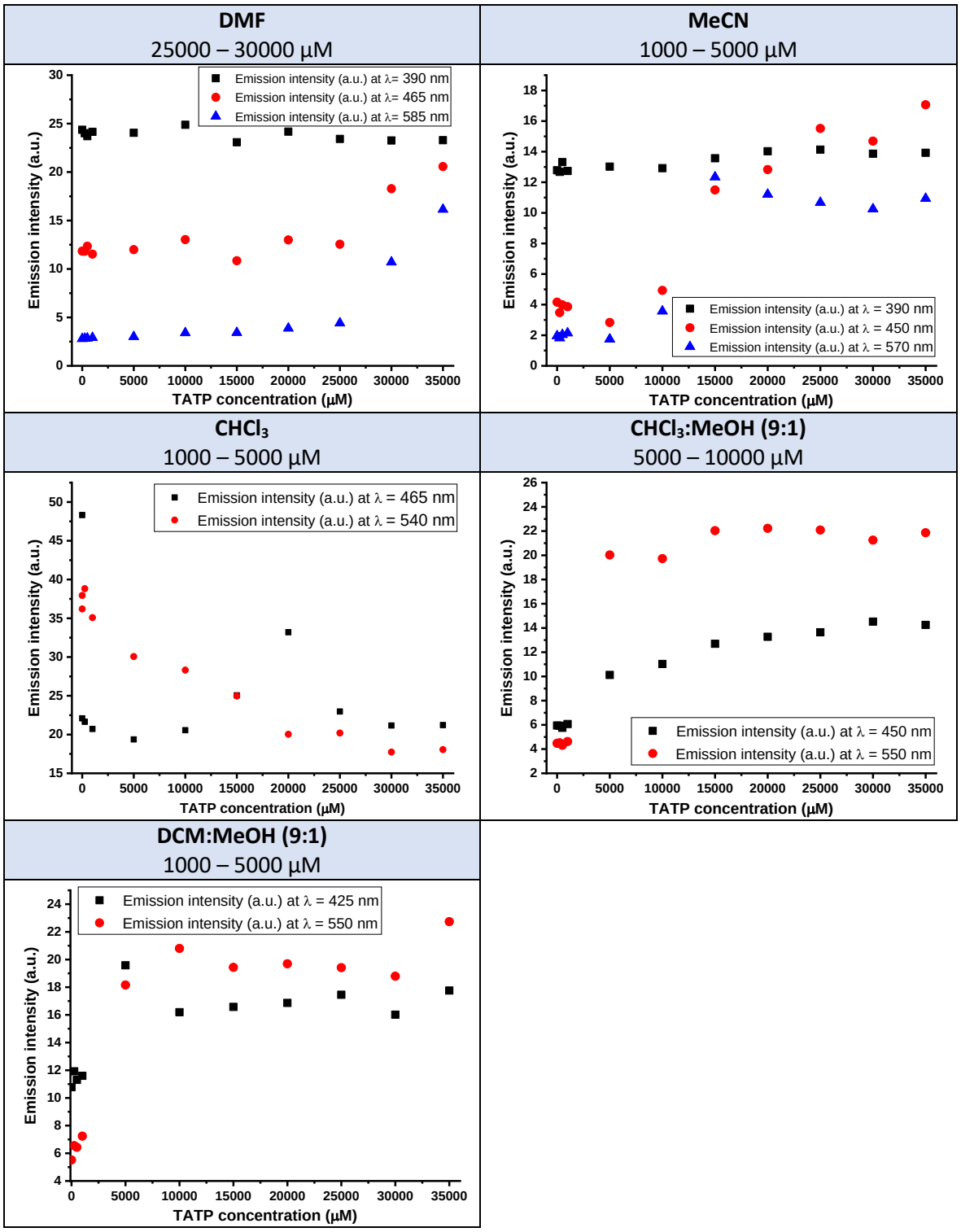

Figure 19. Study of 2.5µM of AR83d with TATP in different solvents. Fluorescence profile at maximum emission wavelength under increasing concentrations of TATP.

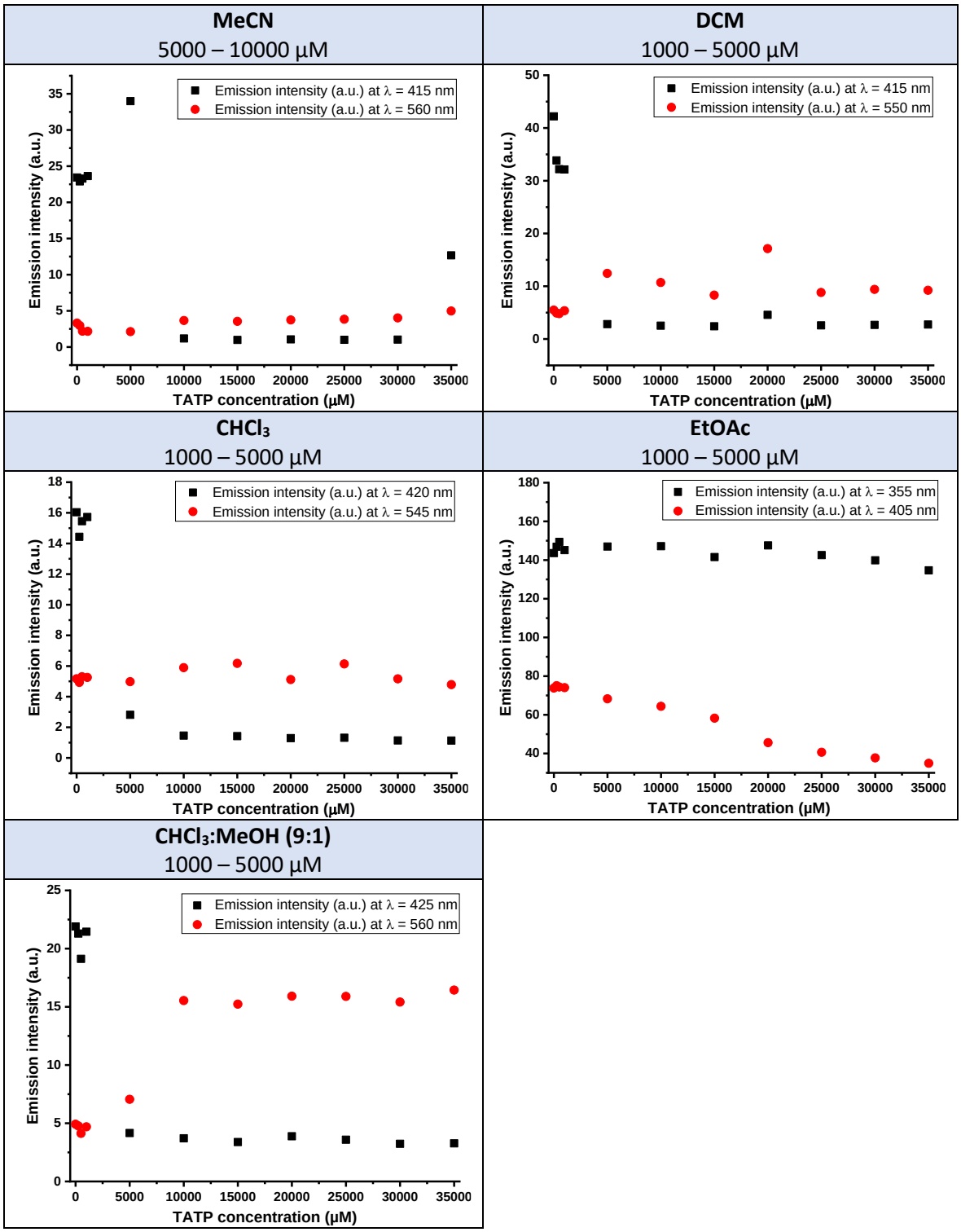

Figure 20. Study of 2.5µM of AR90s with TATP in different solvents. Fluorescence profile at maximum emission wavelength under increasing concentrations of TATP.

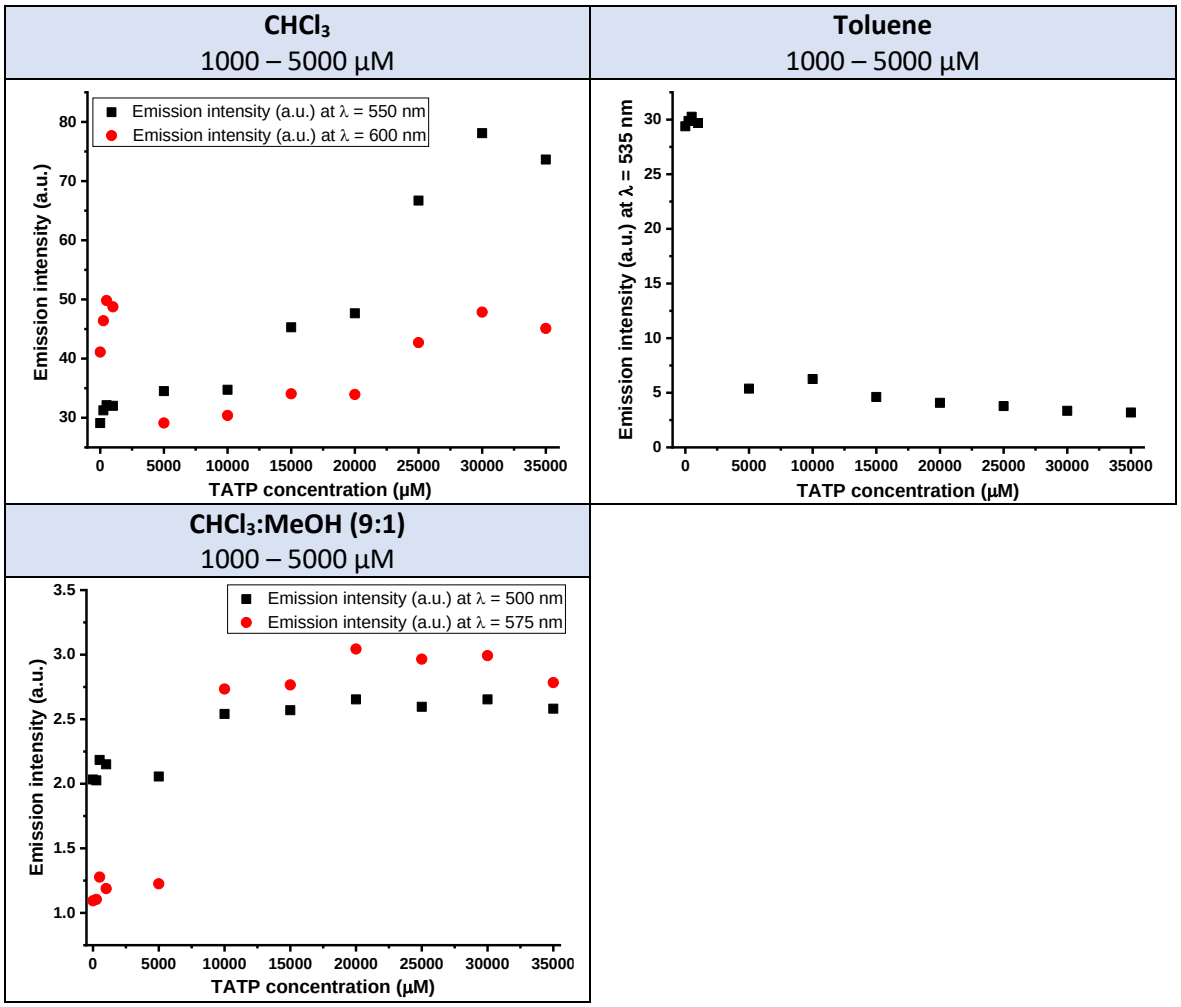

Figure 21. Study of 2.5µM of AR90d with TATP in different solvents. Fluorescence profile at maximum emission wavelength under increasing concentrations of TATP.

4.2. Work concentration

In order to choose an optimum concentration for the following quantitative studio, the absorbance and fluorescence of the probe were checked to be linear while concentration changes were small (Figure 22 and Figure 23). The solvent for this study was DCM.

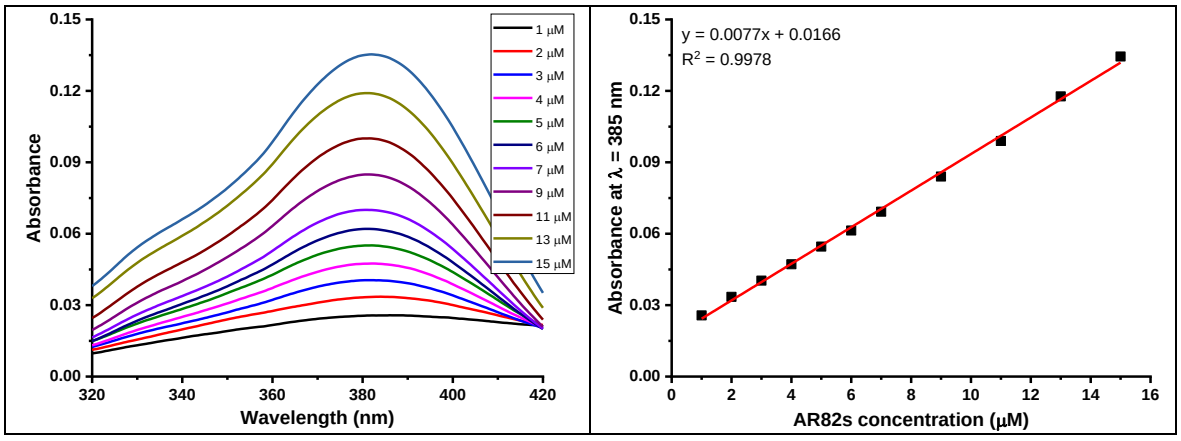

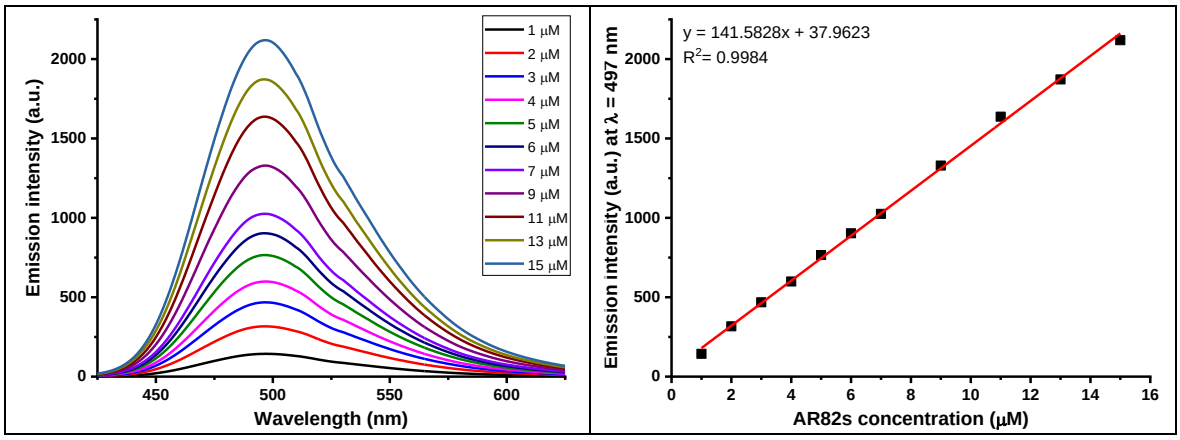

Figure 22. Absorbance spectrum (up left), absorbance profile at 385 nm (up right), fluorescence spectrum (down left) and fluorescence profile at 497 nm (down right) of increasing concentrations of AR82s solution in DCM. λ_{exc}=370 nm.

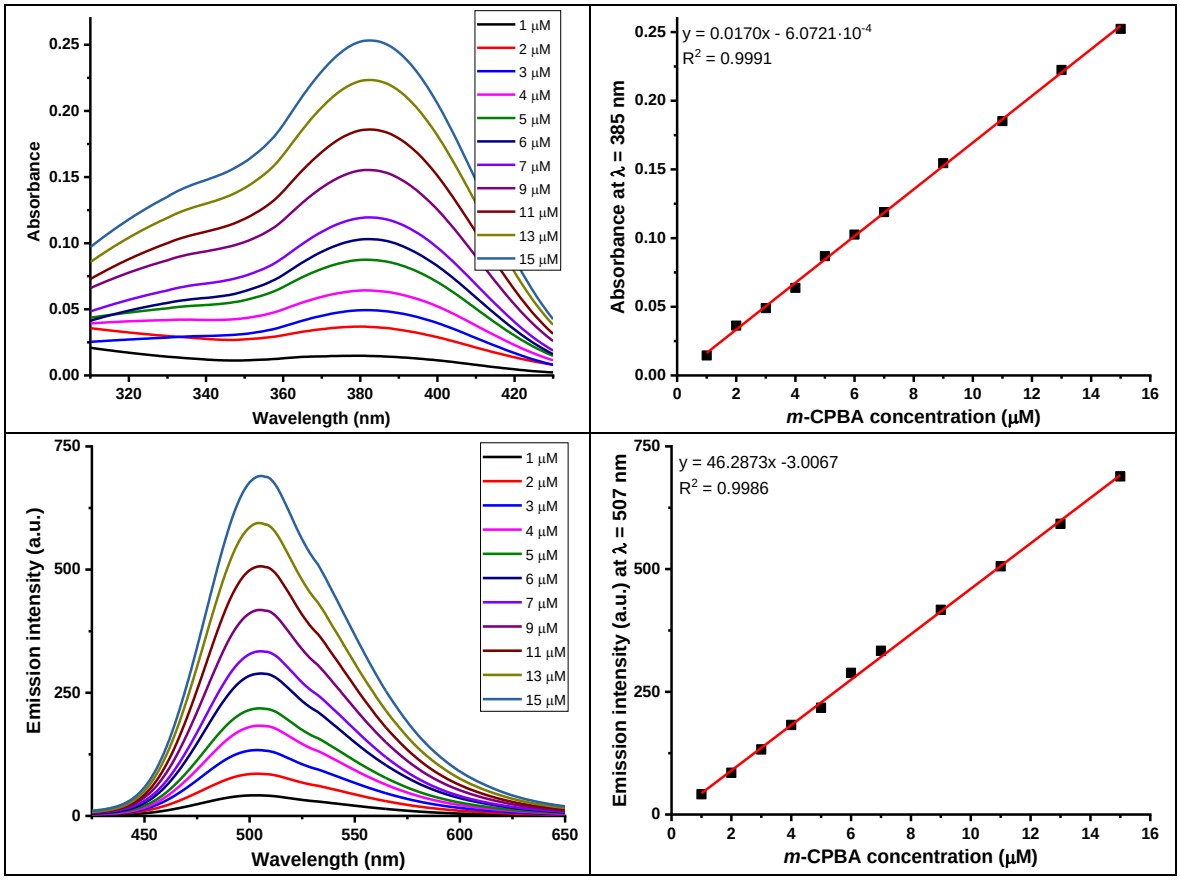

Figure 23. Absorbance spectrum (up left), absorbance profile at 385 nm (up right), fluorescence spectrum (down left) and fluorescence profile at 507 nm (down right) of increasing concentrations of AR82s with a excess of m-CPBA solution in DCM. λ_{exc}=370 nm.

The ideal working concentration should stay at 0.1 of absorbance or less, to avoid possible dynamic quenching, stacking processes or inner filter effects. It was implied a concentration below 11 µM. Taking the results into account, the chosen concentration was 2.5 µM, suitable value because, with this, the Lambert-Beer Law (or pseudo-Lambert-Beer linear behaviour for fluorescence) was fulfilled. In both cases, the excitation wavelength was the same, 370 nm, there were no changes with the addition of *m*-CPBA.

4.3. Measures in dissolution: AR82s vs TATP/*m*-CPBA

The mechanism of detection of TATP was carefully studied in solution by comparison of the action of TATP and *m*-CPBA, a strong oxidant, under the hypothesis that TATP acts as a mild oxidant. LODs for both analytes were also calculated, using the methods described in Chapter 1.

The conditions for the performance of both titrations are as follows:

- AR82s solutions (2.5 µM) in DCM was prepared.
- The fluorescence changes were registered at 25°C and immediately after the addition of the oxidizing agent.
- λ_{exc} = 370 nm.

4.3.1. TATP titration:

For the TATP titration, a point-to-point titration was performed of AR82s in the presence of increasing amounts of TATP by preparing several dissolutions of AR82s in DCM were prepared and then, TATP was added as a solid to each of them, resulting in 33 solutions of concentrations between 0 and 23724 µM.

In this titration, λ_{em} = 500 nm.

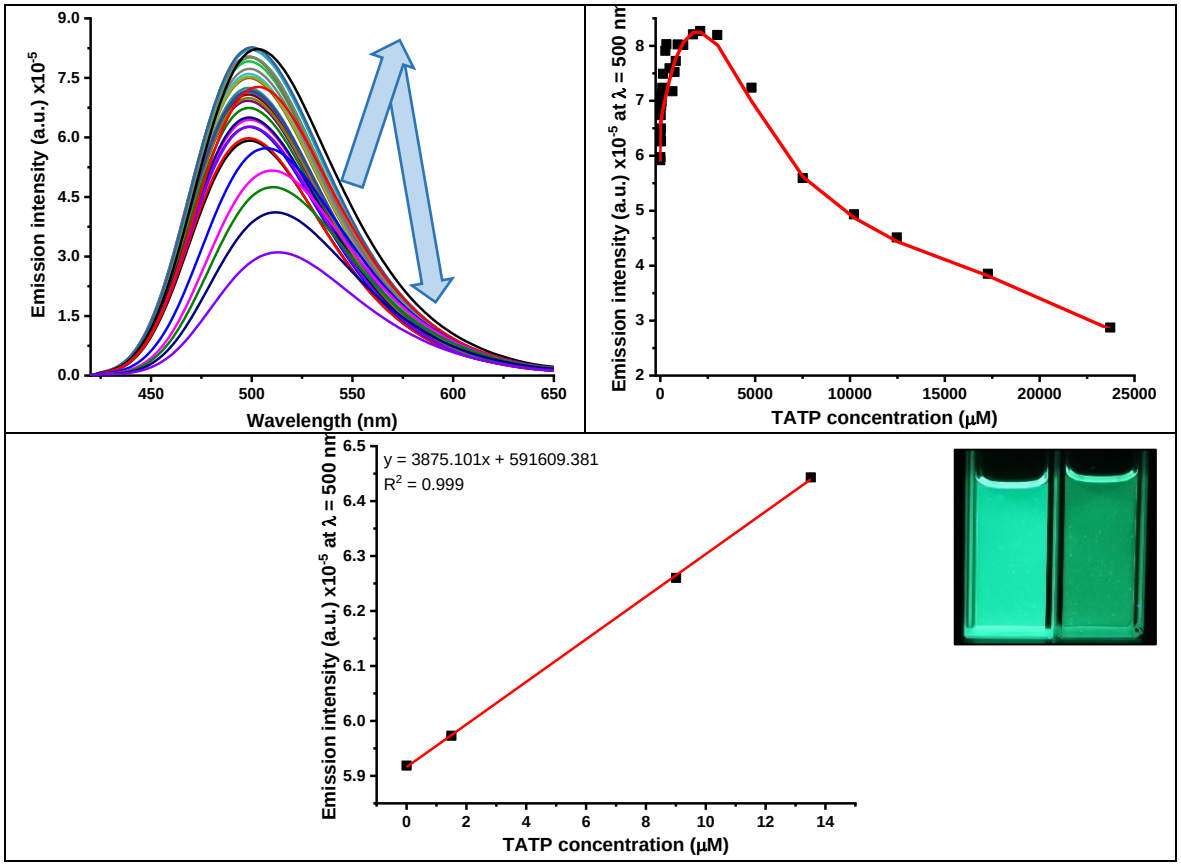

Figure 24. Titration curves (up left), fluorescence profile at 500 nm (up right) and calibration for the LOD calculation using emission values at 500 nm (down left) of a 2.5 µM of AR82s solution in DCM under increasing concentrations of TATP. Image of solutions before and after TATP titration (down right).

As seen in Figure 24, the TATP titration plot showed an increase in fluorescence at low concentrations of TATP and a decrease at higher concentrations. The LOD was calculated from the

initial titration plot values by IUPAC-consistent methods.[45] In this case, we calculated the LOD within the values measured (different than 0) by adjusting the initial values to a mean square linear regression and using the R program.[46] In this way, linear regression at low concentrations of TATP led to a **LOD of 0.87 µM or 0.19 µg of TATP in 1 ml**, which is suitable for practical purposes.

4.3.2. *m*-CPBA titration:

Analogously, a titration of AR82s in DCM was performed and increasing amounts of *m*-CPBA (the oxidant concentration maintained between 0 and 20 mM) from analyte solutions prepared in the same solvent.

In this titration: λ_{em} = 430 and 500 nm.

The detailed titration is shown in Figure 25. The *m*-CPBA titration plot showed a decrease in fluorescence of the green emission at 500 nm at low concentrations of *m*-CPBA and an increase at higher concentrations, followed by further decrease.

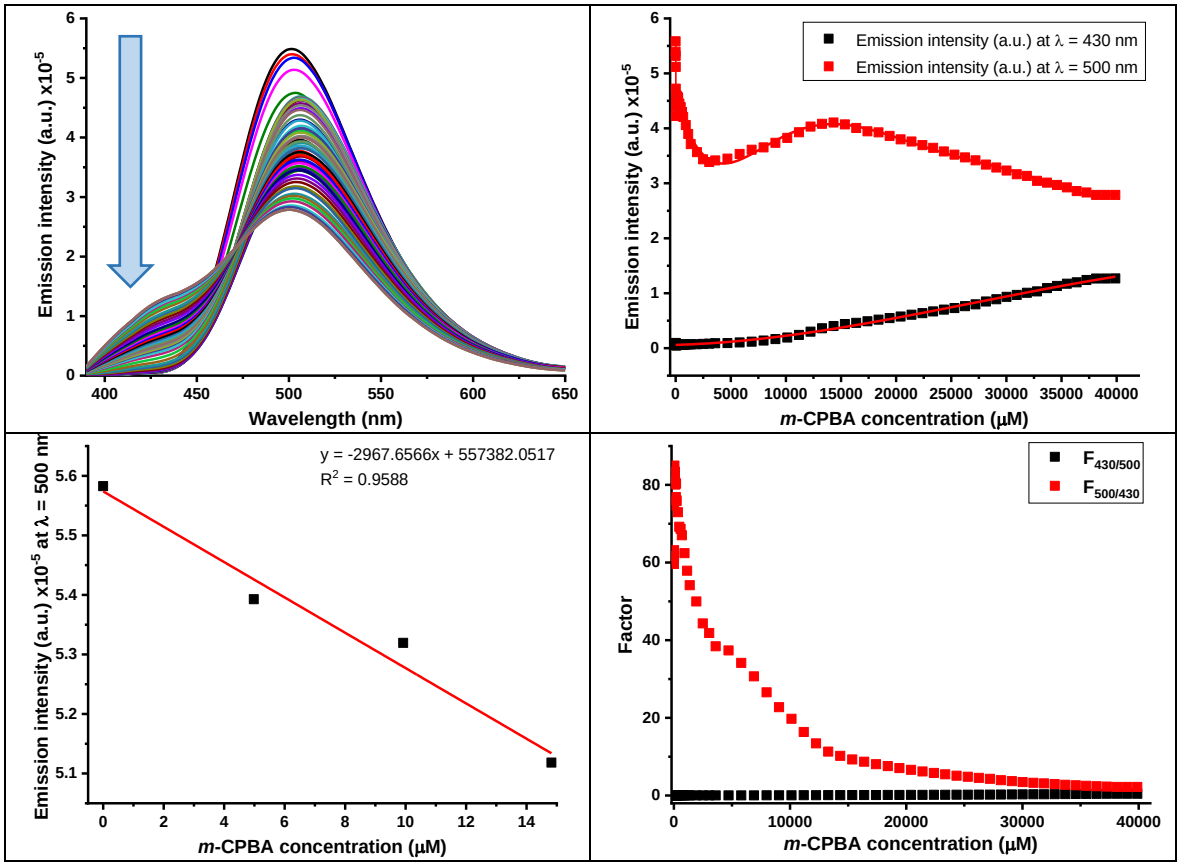

Figure 25. Titration curves (up left), fluorescence profile at 430 nm and 500 nm simultaneously (up right), calibration for the LOD calculation using emission values at 500 nm (down left) and fluorescence profile at the corresponding working curves of the ratiometric probe (down right) of a 2.5 µM of AR82s solution in DCM under increasing concentrations of m-CPBA.

LOD was calculated from the initial titration plot values by IUPAC-consistent methods.[41] In this case, we calculated the LOD within the values measured (different than 0) by adjusting the initial values to a mean square linear regression and using the R program.[42] In this way, linear regression

[45] F. Allegrini, A. C. Olivieri, *Anal. Chem.*, **2014**, *86*, 7858–7866.
[46] a) M. C. Ortiz, L. A. Sarabia, M. S. Sánchez, *Anal. Chim. Acta.*, **2010**, *674*, 123-142. b) RStudio, Version 1.4.1103, 2009-2021 RStudio, 250 Northern Ave, Boston, MA 02210.

at low concentrations of *m*-CPBA led to a **LOD of 2.1 nM or 0.3 ng·of m-CPBA in 1 mL**, which is only interesting for comparison purposes.

The blue emission at 430 nm showed instead a slow increase in intensity. The ratios of fluorescence intensities at 500 and 430 nm (F_{500}/F_{430}) exhibited good linearity with increasing m-CPBA concentration in the range from 0 to 20 µM (Figure 22). The linear regression equation was:

$$\frac{F_{500}}{F_{430}} = 0.1744x + 59.8340$$

5. TATP DETECTION IN MODIFIED SILICA NANOPARTICLES USING A RECIRCULATION SYSTEM

When the detection limit of titration in solution was sufficiently low, the study of detection of TATP in the gas phase was subsequently performed with the colorant adsorbed on the surface of silica nanoparticles. The experiments of sensitivity to TATP in the gas phase by solid supported dyes were developed by comparing the increase of the quantum yield of the samples in presence or in absence of TATP under controlled conditions (Section 3.2.). Compound AR82s showed the best performance in previous tests, so it was selected for the experiments of TATP detection in the gas phase under close to real conditions in the open air.

5.1. Experimental system

Several nanoparticles samples were modified by adsorption of the probe and tested as potential TATP sensors. In all three cases, 100 mg of the SiO_2 nanoparticles (5-15 µm particle size, 99.5% trace metal basis, Aldrich Chemistry) and 1 mg of the probe were added to a 5 ml of chloroform and thin foil was used to cover the vial to avoid degradation of the nanoparticles by the action of light. The resulting suspension was stirred at 60°C under a stream of nitrogen until complete evaporation of solvent (approximately 30 minutes). After that, nanoparticles with the adsorbed compound (AR82s·SiO_2) were washed with hexane (3×3 ml) and the solvent residues were dried with a stream of nitrogen, working in the dark throughout the process. AR82s·SiO_2 was evaluated by several techniques that gave complementary information. In a first instance, the detection process was evaluated as a code of colour under UV light. Afterwards, the capacity of detection of the system was studied by registering changes in the position of emission maximum and in fluorescence intensity by a more quantitative approach, comparing the fluorescence quantum yield for higher precision. Finally, a titration for the specific detection of TATP vapours was also carried out.

5.2. Study of fluorescence changes as a colour code

The initial evaluation of the AR82s adsorbed on SiO_2 nanoparticles against TATP in vapor was carried out by placing, at the bottom of an Eppendorf, 30 mg of the corresponding nanoparticles and 4 mg of TATP in the upper part of the Eppendorf, which was placed horizontally. The Eppendorf was covered with tin foil to prevent the degradation of the nanoparticles by action of light and was heated, at a temperature not higher than 60°C, until the complete evaporation of TATP. Once evaporated, the probe and the TATP were kept in contact for ten minutes more before proceeding to measure the emission and the excitation spectrums and the quantum yield of the nanoparticles, both exposed to the TATP and before the exposure, with an Edinburg Instrument FLS-980 fluorometer at an excitation wavelength of 370 nm an at 25°C. The presence of TATP could be qualitatively detected by comparing the fluorescence emitted by a sample before exposure to TATP and after exposure to TATP in gas phase (Figure 26).

Figure 26. Colour comparation between the nanoparticles with the probe before and after the exposure to TATP.

As shown in Figure 26, exposure to TATP vapours resulted in a marked decrease in fluorescence intensity and a shift from green region to yellow.

5.3. Fluorescence study by quantum yields

The fluorescence changes of AR82s·SiO_2 nanoparticles were recorded by measuring the emission and the excitation of the solids and determining the increase in fluorescence quantum yield ($Ø_F$), Figure 27. The fluorescence of the nanoparticles is directly related to the ratio [probe]/silica. Hence, providing that the amount of probe was not too high or too low, the fluorescence variations will be proportional to the analyte detected.

The most straightforward way to detect the presence of the analyte was the decrease in fluorescence of the modified nanoparticles. However, they are powder samples, so the measures were dependent most often on the position of the solid in the fluorometer and these factors were difficult to control. Consequently, fluorescence quantum yields were the most trustworthy way to measure it due to it is a parameter that provides errors less 2% if several replicas were performed.

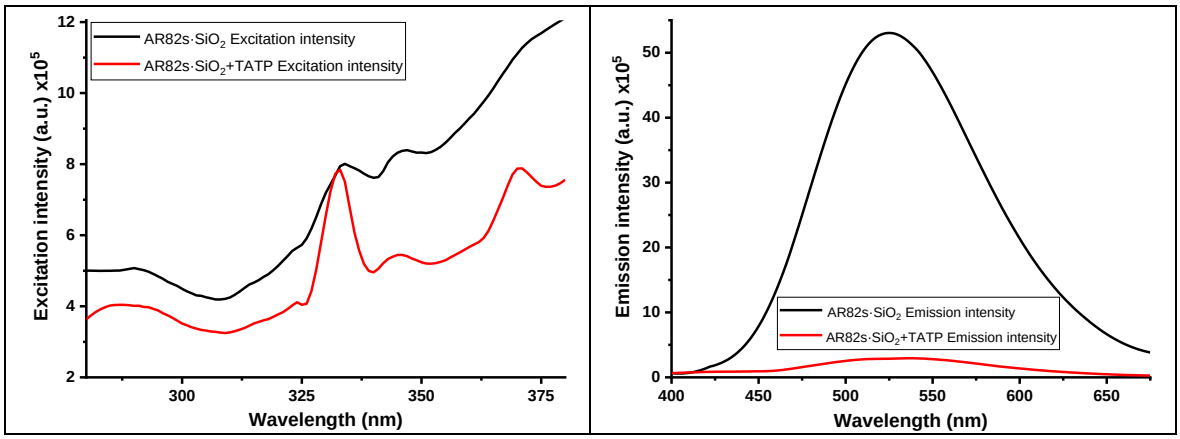

Figure 27. Response of fluorescence (right) and excitation (left) of AR82s·SiO_2.

Figure 27 shows how there was a noticeable decrease in the fluorescent emission intensity after exposing of AR82s·SiO_2 system to TATP vapours, as well as a slight shift of the emission maximum from the green to the yellow region. All of this agrees with what was observed qualitatively in section 5.2.

Fluorescence quantum yields were measured by placing an integration sphere in the equipment. The results obtained are shown in Figure 28.

$Ø_F$ AR82s·SiO_2 (%)	39.83
$Ø_F$ AR82s·SiO_2 + TATP (%)	3.22

Figure 28. Fluorescence quantum yields of AR82s·SiO_2 before and after the exposure to TATP vapours.

The variation of quantum yields between the probe before and after the exposure to TATP vapours was 0.081. A significant decrease in the emission intensity could be observed, about 12 times lower than the sensor before exposure to TATP vapours.

5.4. Titration in gas phase: AR82s·SiO_2 vs TATP

The titration of AR82s adsorbed onto SiO2 nanoparticles was carried out by placing 15 mg of nanoparticles in an Eppendorf, covered with tin foil to avoid degradation of the nanoparticles by the action of light, and increasing amounts of TATP (from 0.025 to 2 mg) in another Eppendorf. Both were connected to each other and to an air stream, air flow, 100 cm3/min, provided by a compressor. Working in the absence of light, TATP was heated, to a temperature below 50°C, until its complete evaporation, keeping probe and TATP under recirculation in the system for 10 additional minutes after the complete TATP evaporation. After this time, the emission measurements of the nanoparticles exposed to TATP were carried out in an Edinburg Instrument FLS-980 fluorometer at an excitation wavelength of 370 nm at 25°C (Figure 29).

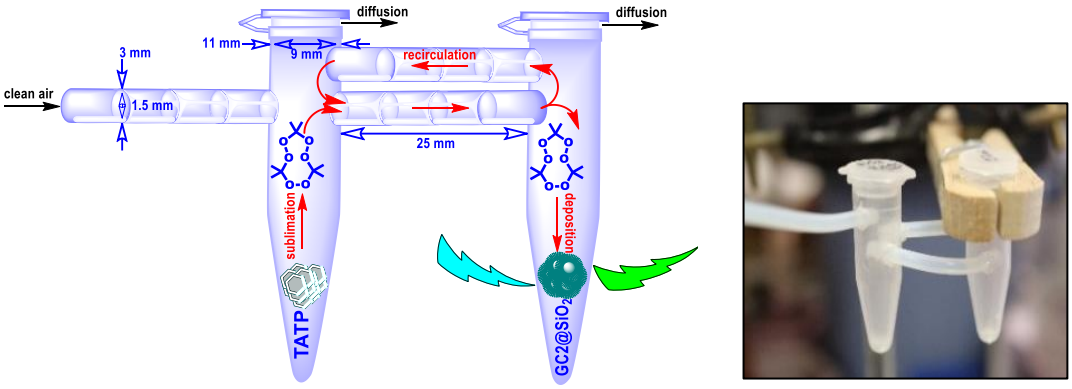

Figure 29. Microfluidic device used for titrations in vapour phase (left) and the actual aspect of the system[34] (right); reproduced with permission.

The results are displayed in the following Figures as qualitative (Figure 30) and quantitative fluorescent emission measurements (Figure 31).

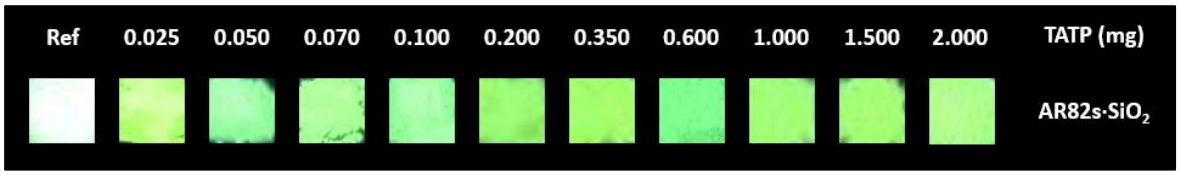

Figure 30. Fluorescent changes with TATP gas.

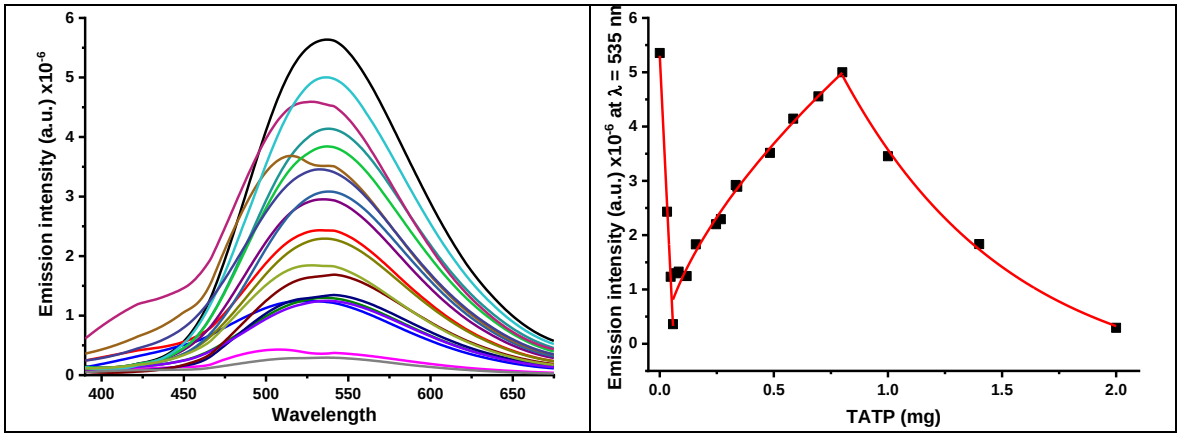

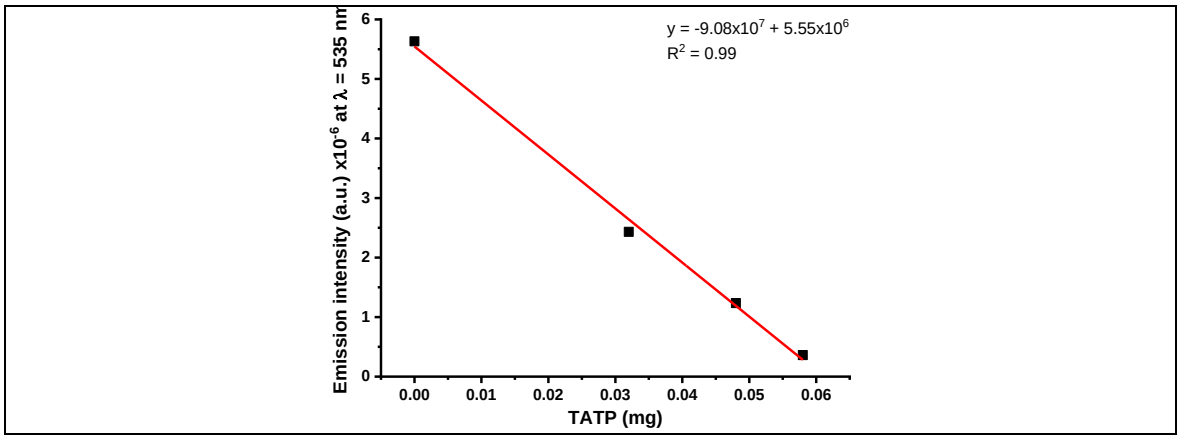

Figure 31. Titration curves (up left), fluorescence profile at 535 nm (up right) and calibration for the LOD calculation using emission values at 535 nm (down) of AR82s·SiO_2 under increasing concentrations of TATP in vapour phase.

The titration plot showed an initial decrease of fluorescence in the presence of very low amounts of TATP, then an increase in fluorescence and, finally, a decrease at higher concentrations.

The LOD was calculated from the initial titration plot values by IUPAC consistent methods.[41] In this case, the LOD was calculated within the values measured (different than 0) by adjusting the initial values to a mean square linear regression and using the R program.[42] In this way, linear regression at low concentrations of TATP vapours led to a LOD of **13.03 ng of TATP** in absolute value or, taking into account the time of measurement and air efflux, a LOD of **13.3 ng·L^{-1} (57 pM)**. Assuming that the best LOD values were found in the ppb to ppm range for TATP sensing in the gas phase,[47] the reported method competes favourably in terms of sensitivity and simplicity with the best-known methods, with a LOD value of 1.4 ppb in air, the lowest get so far by artificial olfaction.[4]

6. VALIDATION IN REAL-LIFE SCENARIOS

The validation of the fluorescent device to detect TATP explosive was studied in real life scenarios. Under close to realistic conditions, the TATP sensor material was tested by placing in a small room, at different temperatures, a few milligrams of solid TATP and some samples of the dye-silica nanoparticles at different distances, leaving it for some time. In every case, the experiment was previously performed without TATP to have a set of comparison values. In all tests, there was a neat change of the fluorescence between the signal obtained with the nanomaterial in the presence of TATP at a certain distance, in comparison to the nanomaterial without the presence of TATP. Therefore, tests were performed under the mildest conditions for the system to have a positive signal, under typical ambient temperatures and at increasingly longer distances from the vapor source.

6.1. Experimental system

The experiments were carried out in an office with dimensions 3.07 × 3.54 × 2.15 m (height × length × width). Inside the room, appropriate air heaters were placed to maintain constant temperature and, additionally, an air compressor (Figure 32), which was generated a gentle stream of clean air that passed over the TATP sample in the direction of the locations where the nanoparticles were positioned, entraining the TATP vapours towards the sensing material. The office had also its own central heating and ventilation system, so the airflow was not steady but subjected to the inherent small turbulences while it was in operation.

[47] J. H. Fujiyama-Novak, C. K. Gaddam, D. Das, R. L. V. Wal, B. Ward, *Sens. Actuators B,* **2013**, *176*, 985–993.

Figure 32. Arrangement of the elements inside the room.

A fixed amount of TATP (250 mg) was placed at a distance of 30 cm from the source of the airflow (100 cm^3/min, 0.8 cm internal diameter of the tube, Figure 33a). A fixed amount of AR82s·SiO_2 nanoparticles (0.75 mg) was placed on the surface of a cover glass, adhered to it with the help of a small amount of adhesive tape (Figure 33b and Figure 33c). This process was repeated 6 times by experiment and the cover glasses were placed at increasing distances from the point where the TATP was located (10 – 25 – 50 – 100 – 150 – 200 cm) (Figure 33d).

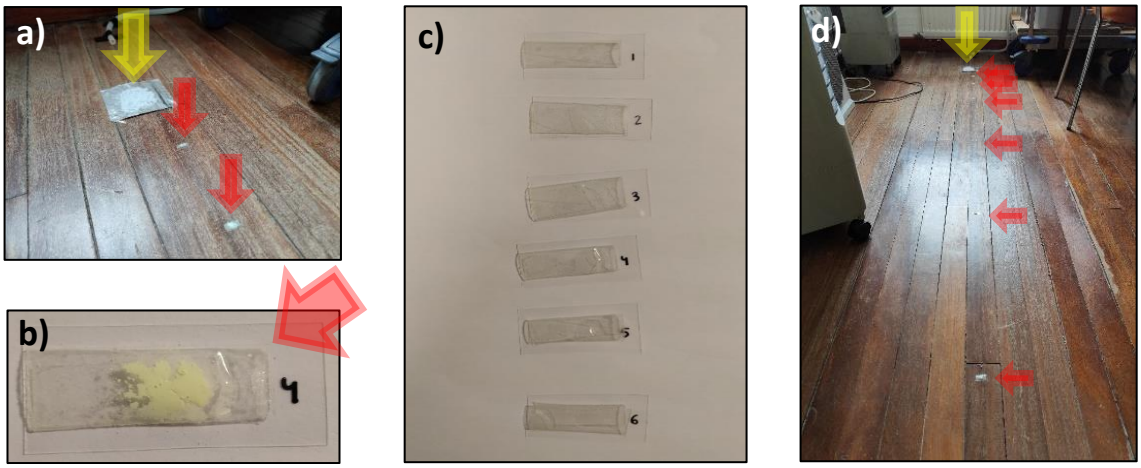

Figure 33. Distribution of samples and TATP source of in the office. a) Close view of the arrangement of the TATP source (yellow arrow) in front of the airflow outlet and the sensing material samples (red arrows). b) One single sample of sensing material. c) Assembly for the measurement of the nanoparticles. d) Distribution of TATP sample (yellow arrow) and sensor samples (red arrows) in the room.

6.2. Experiments at different temperatures

The experiments were performed at different temperatures between 20 and 30 degrees Celsius. To find the best working conditions, the fluorescence changes of all experiments were normalized to the highest value and compared with the non-exposed nanomaterial samples subjected to the same room conditions, the differences were represented together for comparison purposes. To compare the effect of TATP on time, the values were adjusted to 30 minutes in all cases.

In a representative experiment, 252.3 mg TATP were weighed and placed in the room at 26°C for 30 minutes. Of the 252.3 mg of TATP initially weighed, only 38.6 mg were evaporated under the temperature and time conditions used in this experiment, remaining 216.7 mg of TATP as solid in the original sample. This gave a maximum concentration of 1.65 mg/m^3 in the air of the room,

supposing that all TATP evaporated during the experiment remained in the room, which was not a sealed system.

Comparative photographs taken under UV light (366 nm) before and after exposure to TATP vapours are shown below (Figure 34).

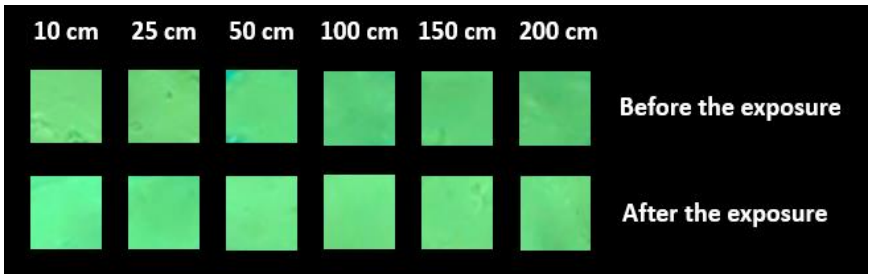

Figure 34. Comparative photographs taken under 366 nm light before and after exposure to TATP vapours in a typical experiment (26ºC).

For all the experiments performed, a 3D histogram of the differences in intensity emission was plotted, before and after exposure to TATP vapours, as a function of distance from the TATP source and temperature of the room, normalized to the top and reference signals. An excitation wavelength of 370 nm was used (Figure 35).

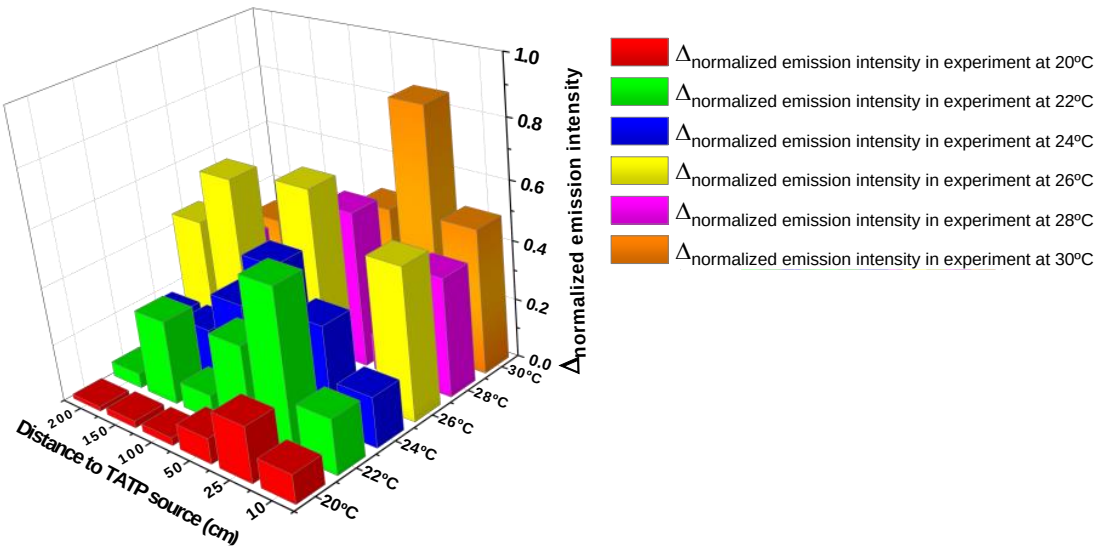

Figure 35. Histogram plotting the differences in intensity emission in all cases before and after exposure to TATP vapors as a function of distance from the TATP source and temperature of the room, normalized to the top and reference signals.

Generally speaking, there is a clear increase in fluorescence from the solid probe samples, with several variations related to the inherent turbulence of the air stream, combined to the air heating system and the variable sensitivity of the nanoparticles to the amounts of TATP detected. The detection of TATP in air is well assured in quantities of about one milligram per cubic meter of air in an ordinary room where there is air exchange, central heating, and consequently inherent air turbulence; this means that not all samples receive proportional amounts of TATP in gas phase.

Positive detection is therefore guaranteed by at least three neat increases in the fluorescence within ten centimetres to two meters from the TATP source. Hence, the detection system is suitable for practical measurements in standard real-life scenarios.

6.3. Validation of the robustness of the detection system

The robustness of a method is defined as the capacity of a procedure to remain unaffected by small deviations in method parameters. Robustness is characterized by providing information on the reliability of the procedure with respect to the control of the variables that define the operating conditions during normal routine use. It also expresses the resistance to change in the results generated when the variables of influence are modified.[48] Therefore, in order to test the robustness of the developed detection system, from the results of the previous series of experiments, we checked that the best temperature to perform the experiment was around 26ºC.

For that reason, a series of six experiments were carried out where the sensing material was exposed to TATP for 30 minutes at 26ºC in a room similar to the one described above with an analogous experimental design (Figure 36).

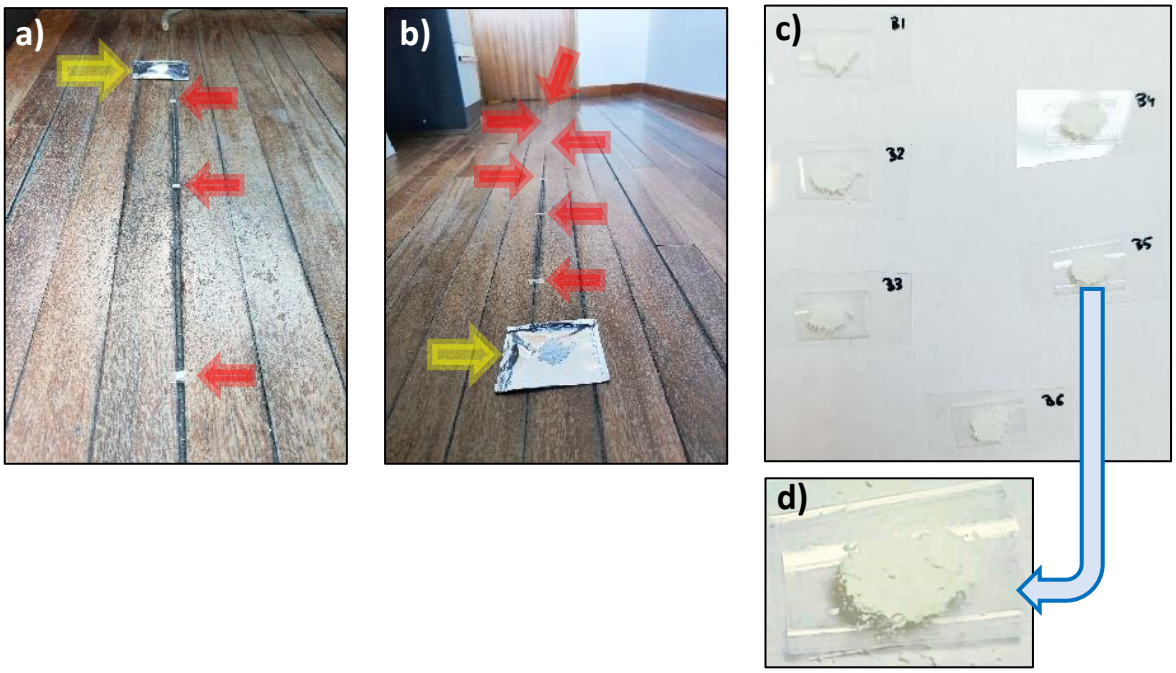

Figure 36. Distribution of the samples and TATP source in the room for robustness experiments. a) Arrangement of the TATP in front of the airflow outlet (yellow arrow). b) Distribution of sensing nanoparticles in the room (red arrows). c) Assembly of the nanoparticles for measurements. d) Detail of one sample of AR82·SiO_2.

To conduct every experiment, blank measurements of pristine nanoparticles left for 30 minutes in the room, with no presence of TATP, were performed and used as reference. Then, about 250 mg of TATP were placed at 30 cm distance from the source of the airflow. Once TATP and nanoparticles were placed, the system was left for a period of 30 minutes, so the measurements were made for each group of nanoparticles before and after the exposure to TATP vapours. In one hand, the remaining amount of TATP was weighed. From the initial 250 mg samples of TATP, only a small amount evaporated in every case: 23 – 23 – 36 – 36 – 32 – 32 mg, an average of 30.3 mg of TATP involved in all the experiments, 1.30 mg/m^3 average, in a range of 0.98 to 1.54 mg/m^3. In the other hand, the fluorescence of nanoparticles was measured using an excitation wavelength of 370 nm. To carry out the measurements in the fluorometer, each sample was covered with a quartz sheet to ensure that the nanoparticles remained in a fixed position. This sheet was removed to leave the particles exposed to TATP vapours during the experiment.

[48] L. Cuadros-Rodríguez, L. Gámiz-Gracia, A. Carraco-Pancorbo, C. Ruiz-Samblás. Glosario de términos analíticos, Spain, **2013**, ISBN: 978-84-616-4720-0.

For an easier visualization of the whole data, the normalized emission intensity variation before and after exposure to TATP vapours with respect to distance to the TATP source was graphically represented (Figure 37). This time, the tendency of the data showed a clear decrease of the fluorescence intensity or the proportionality factor of fluorescence variation in each case from short to long distances from the TATP source, but again the number of fluctuations from the similarly performed experiments was high.

In the 2D graphs of the Figure 38, the maximum emission intensity data from the experiments were organized according to the distance to the TATP source. The emission values before and after contact with TATP vapours were also normalized with respect to the maximum of emission from each experiment. After this, a common initial emission level was established using the lowest value measured for the nanoparticles prior to the exposure to TATP vapours. And finally, the subtraction was made between the final and initial emission values.

Figure 39 shows the summary of experiments as a 3D representation of the variation of the normalized emission intensity as a function of the distance to the TATP source.

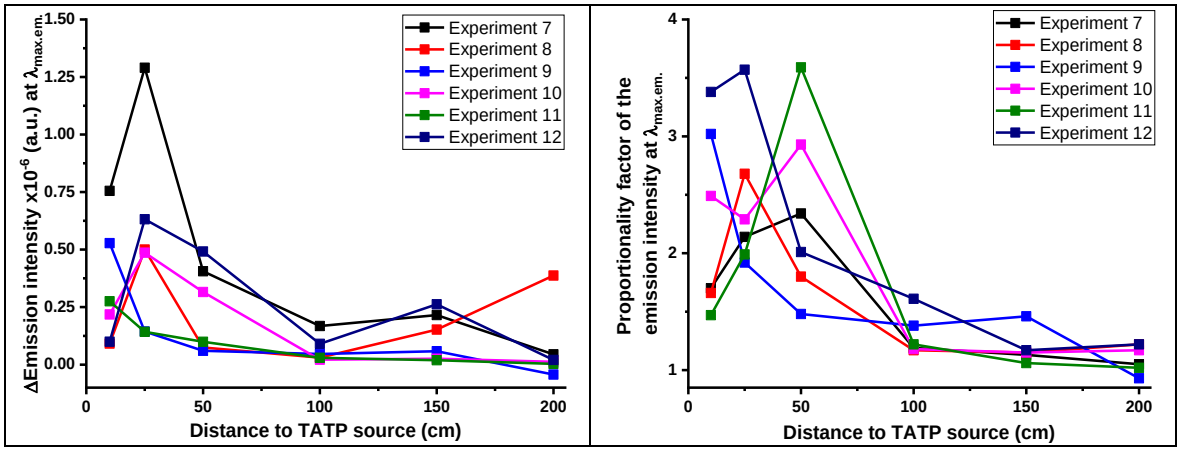

Figure 37. Summary of robustness experiments against TATP vapour at 26ºC. Emission intensity variation before and after exposure to TATP (left) and emission intensity proportionality factor (divided between the target, right) versus distance to the TATP source in both cases.

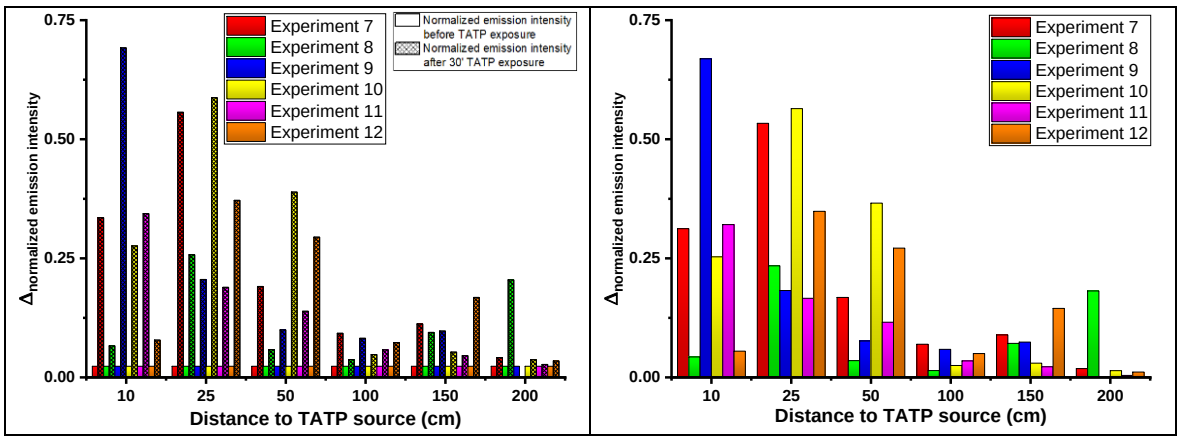

Figure 38. Summary of robustness experiments. Normalized emission intensity setting a common initial particulate emission level before and after exposure to TATP vapours (left) and variation of the normalized emission intensity (right) as a function of the distance to the TATP source in both cases.

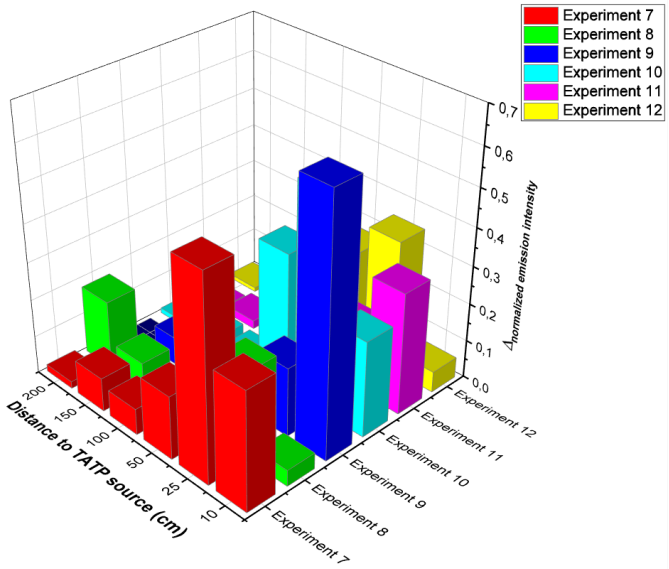

Figure 39. Histogram plotting the differences in intensity emission before and after exposure to TATP vapours as a function of distance from the TATP source at 26ºC.

With the aim to extract the tendency of the described experiments, a selection of the measurements was made, discarding outliers and selecting only 3 measurements for every one of the distances to the TATP source. Using these measurements, the average and standard deviation of the normalized variation of the emission intensity for each point were calculated and represented (Figure 40).

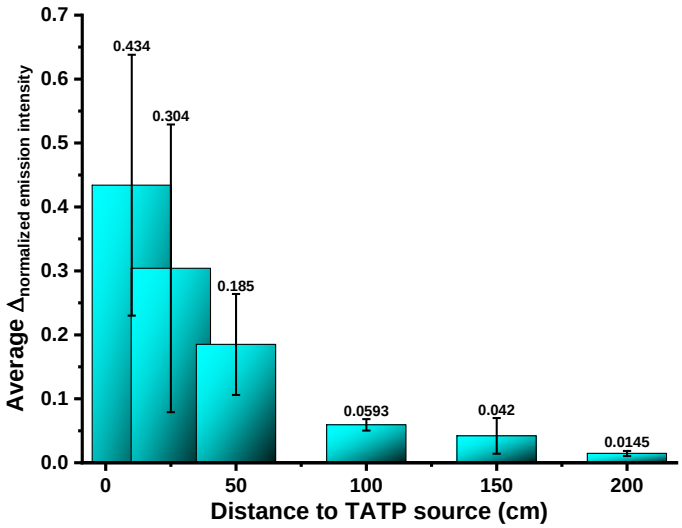

Figure 40. Average and standard deviation of normalized emission variation as a function of the distance to the TATP source.

Albeit the considerable fluctuations, represented by the large deviations from the normalized emission variations, it is clear that there is a marked tendency to stronger variations of the fluorescence as the detecting material is closer to the source of TATP vapor and the system is strong enough to work under close to real conditions appropriate to any environment where TATP vapor with a concentration of at least one milligram per cubic meter is suspected to be found, in a non-sealed environment suitable for life scenarios that could be sensitive to terrorism attack.

7. PHONE APP[49]

A dedicated mobile phone to the application was developed to detect the presence of TATP in a vapor flow. The purpose of the application was to detect the number of milligrams of TATP from a photo of a AR82s·SiO_2 sample exposed to TATP vapours. The user had to configure the system correctly in order to obtain a suitable result. The application has two systems for determining the amount of TATP by RGB:

- Interval search: each sample exposed to a known amount of TATP was configured with several colours, in which the target could be included. To detect the amount of TATP to which the nanoparticles were exposed, a colour was selected and an interval search was carried out.

  For example, suppose we have a target colour 50, 240, 70 and we have the following intervals [40, 130, 60], [10,250, 60] and [55, 244, 71]. The comparison algorithm will detect that the target 50, 240, 70 is in the interval [40, 230, 60] 50, 240, 70 [55, 244, 71].

- Radio search: the compare algorithm will detect a target within the radius of the interval.

  Suppose we have a target colour 50, 240, 70 and we work with a radius of 10. The intervals we have are [40, 230, 60], [10, 250, 60] and [85, 244, 41]. Then the compare algorithm will detect that the target 50, 240, 70 is in the radius of the interval [40, 230, 60] since if we add the radius ±10 we would have this radius [40, 230, 60] or [60, 250, 80].

The system of the application (Figure 41) was composed of the following components:

- Mobile application: it was developed with IONIC technology with which we have the possibility of generating an APK for Android or IPA for IOS. It was based on https://ionicframework.com.
- Laravel api: communication with the backend where queries were made from the mobile application to the database. It was based on https://laravel.com/docs/8.x/eloquent-resources.
- Database: system of tables designed to be able to store colours dynamically and to meet the needs of the application. It was based on https://www.mysql.com.

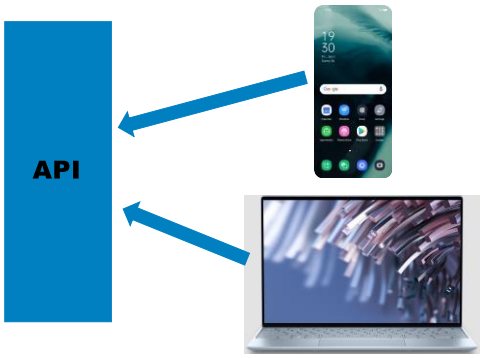

Figure 41. System structure of the application for a mobile phone.

The application is made up of different configurable sections:

- Login: to be able to enter the system, access credentials are required.
- Menu: allows the user to view and access to the different options of the application.

[49] The APP was performed by Jhonniffer R. Santana Tejada, from Movilmática.

- Users: the list of users authorised to access the application is displayed, as well as the option to delete them.
- User settings: personal data (name, email, password…) can be changed from this screen.
- New user: it allows the user to create new users by filling in the required information. The data will be verified before granting access to the application.
- Colour list: list of the different nanoparticle colours for each amount of TATP in vapour phase, accessed from "menu" and then "my colours". In this screen, colours can be deleted and update the data at any time as well as watch the rest of the stored colours.
- New colour: to add a new colour to a TATP measurement, we click on "add colour" and select the TATP quantity and add an RGB colour, manually or by selecting it on an image. The latter is the fastest method as it allows the user to save and continue adding colours.
- Colour detection: once the system is configured with the different TATP measurements, in the "analysis" screen you can take a picture or select an image from the gallery and choose the point where the user wants to detect how much TATP it has been exposed to. The images are very important because the higher the quality, the higher the accuracy in detecting RGB colour.

The app was a part of an autonomous system (Figure 42) for capturing and quantitative evaluation of fluorescent probe images based on mobile telephony composed of a customized display box, a 360° metal support, a personalized phone APP and a OPPO Find X3 Pro 5G.

Figure 42- Autonomous system for evaluation of fluorescent probes made up of customized box (left) and 360° metal support (right).

The system allows photographs to be taken with a mobile camera from very short distances of a sensor material previously exposed to an explosive atmosphere. For this, the sensing material was placed in a custom-made dark box with a metal holder and a UV lamp (366 nm) to illuminate the material. The mobile phone with the application subsequently compared the photo with a database of images of the material exposed to different quantities of TATP in vapour phase, therefore from the comparison and the calculated calibration curve from the application, the amount of the explosive in contact with the material AR82s·SiO_2 could be extracted.

Initially, the system was trained and tested by using the experiments described in Section 5 of this Chapter. In this way, the system worked as a quick preliminary test for detecting TATP in air from samples with quantitative TATP treatment under controlled conditions, in which giving accurate results. The following Figure is an example of how to use the APP in one of these situations (Figure 43).

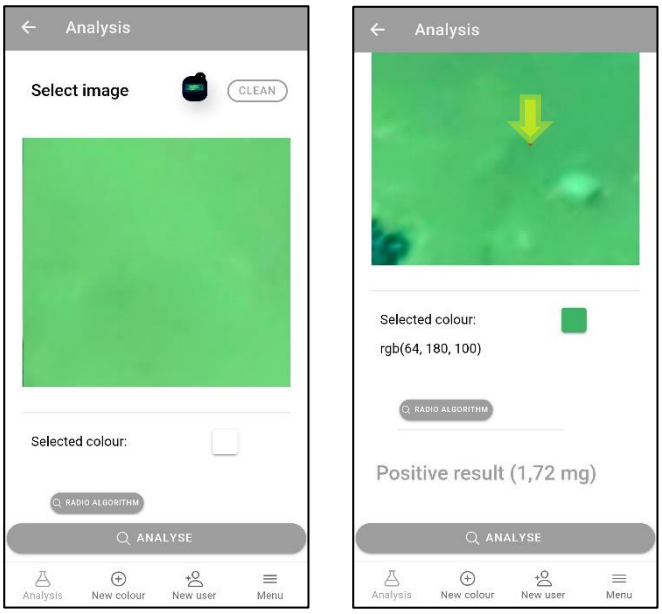

Figure 43. Example of APP use: select image for an exposure to 1.720 mg of TATP in the system (left) and a positive result (right). The yellow arrow indicate the point where the selected color was measured.

7.1. Validation in real-life conditions

The application was validated under close to real conditions from samples obtained in experiments 7 to 12 (experiments described in Section 6.3). The selected images corresponded to non-discarded measurements used for Figure 40 to allow the measurements to be compared with previous results obtained in those experiments. For maximal randomization one sample from each experiment series was measured.

Positive results gave a value in milligrams that was converted to TATP concentrations by using the table of evaporation times obtained from experiments described in Section 5 (Figure 44) under the air stream flow (100 cm^3/min).

TATP (mg)	Time required for complete evaporation
0.032	1’41”
0.048	1’45”
0.083	2’14”
0.114	2’42”
0.158	3’10”
0.203	3’21”
0.247	3’57”
0.333	4’26”
0.483	5’03”
0.800	7’45”
1.000	11’23”
1.400	13’13”
2.100	19’37”

Figure 44. Time required for total evaporation of the different amounts of TATP used in the experiments of Section 5.

Thus, the TATP concentrations to which the AR82s·SiO_2 nanoparticles were exposed using the evaporation times in the previous Figure 44 are as shown in Figure 45 below.

Number of experiment	Concentration (mg of TATP/m^3 of air)
7	0.70
8	0.70
9	0.24
10	0.24
11	0.06
12	0.24

Figure 45. TATP concentrations per cubic metre of air from the experiments described in Section 5.

On the other hand, non-exposed sample references from experiment 7 at 10 cm and from experiment 10 at 100 cm of the TATP source gave in both cases a negative result, thus providing roughly approximate values of existence, or confirming inexistence, of TATP in the room, with the only assistance of the sensing material, a black box with a UV lamp and a customized app installed in a mobile phone. An example of the tests performed is shown in Figure 46 below.

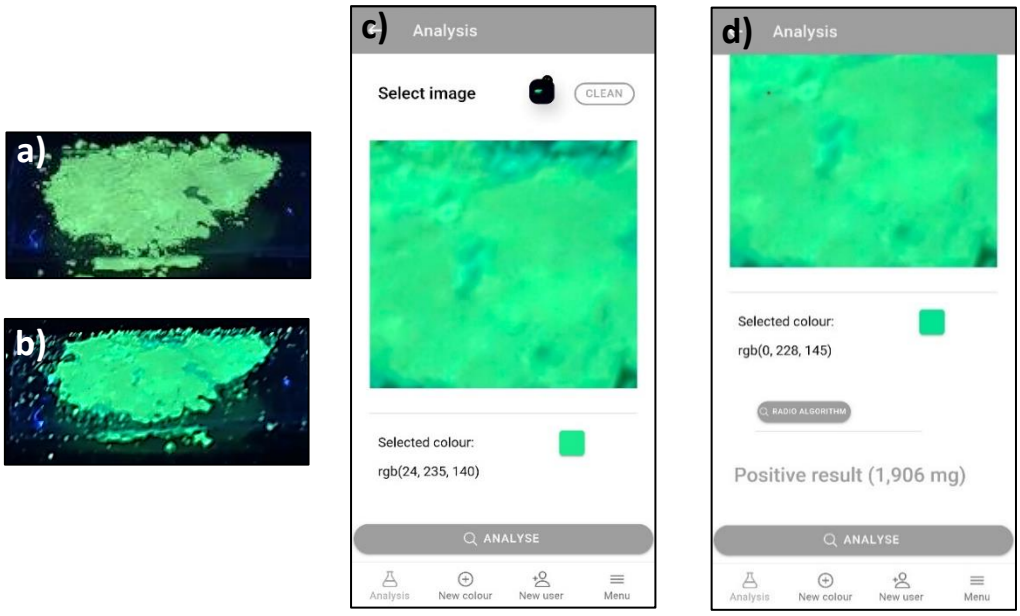

Figure 46. APP validation under real-life conditions. Pictures of the sensing material placed at 25 cm from the TATP source under a UV lamp, before (a) and after (b) being exposed to TATP. c) Picture captured by the mobile phone app. d) APP assigned a positive value after comparing the RGB values in the selected point with the customized database.

8. DETECTION MECHANISM

The mechanism of oxidation of AR82s (3 mg in 0.5 ml in $CDCl_3$) was studied by ^{1}H-NMR titration by using increasing amounts of TATP in the presence of Amberlite (1.5 mg) to prevent the accumulation of TATP in the NMR tube. The amounts of TATP used in the NMR titration were as shown in Figure 47.

Addition number	TATP mass added (µg)	Total mass of TATP added (µg)	Addition number	TATP mass added (µg)	Total mass of TATP added (µg)
1	0	0	**10**	60	150
2	5	5	**11**	150	300
3	5	10	**12**	200	500
4	5	15	**13**	300	800
5	5	20	**14**	600	1400
6	10	30	**15**	1800	3200
7	10	40	**16**	3600	6800
8	20	60	**17**	3600	10400
9	30	90	**18**	5400	15800

Figure 47. Additions of TATP to the ^{1}H-NMR titration of AR82s.

The extensions of two interesting regions of this ^{1}H-NMR titration are shown in Figure 48 below:

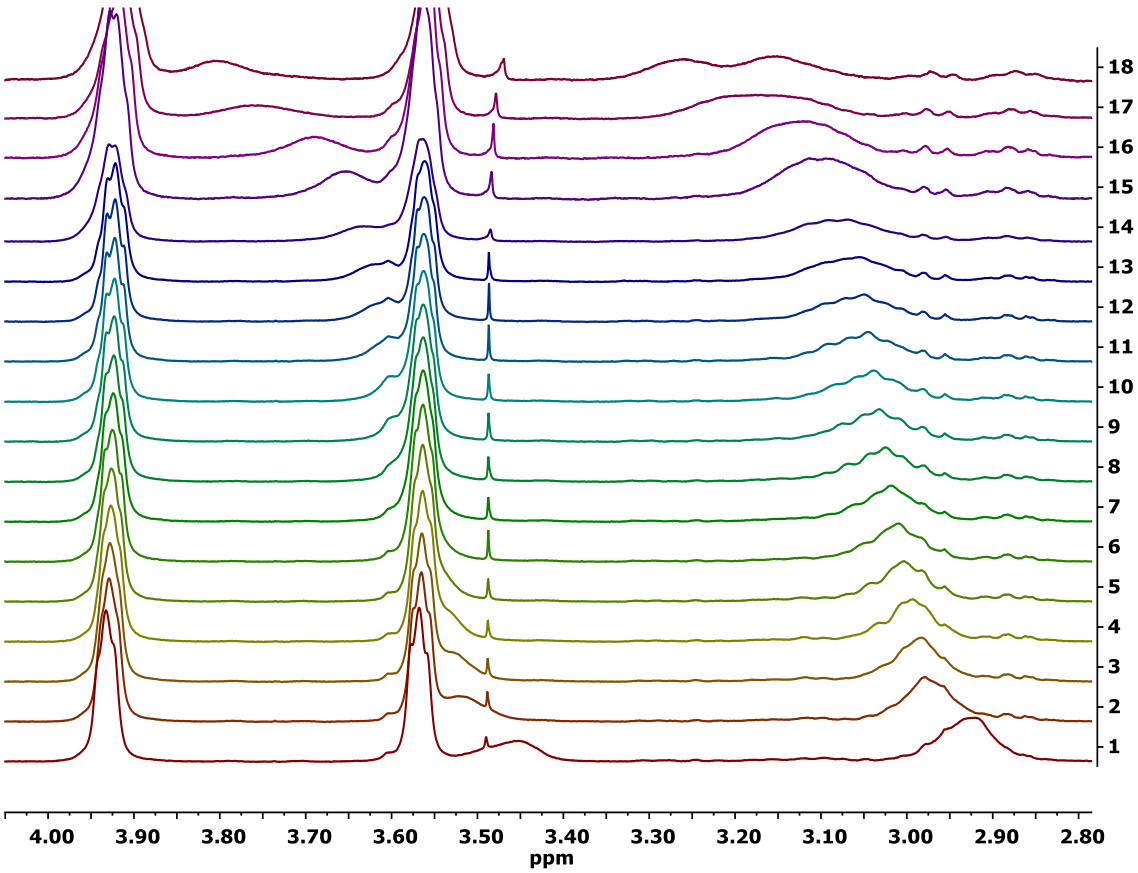

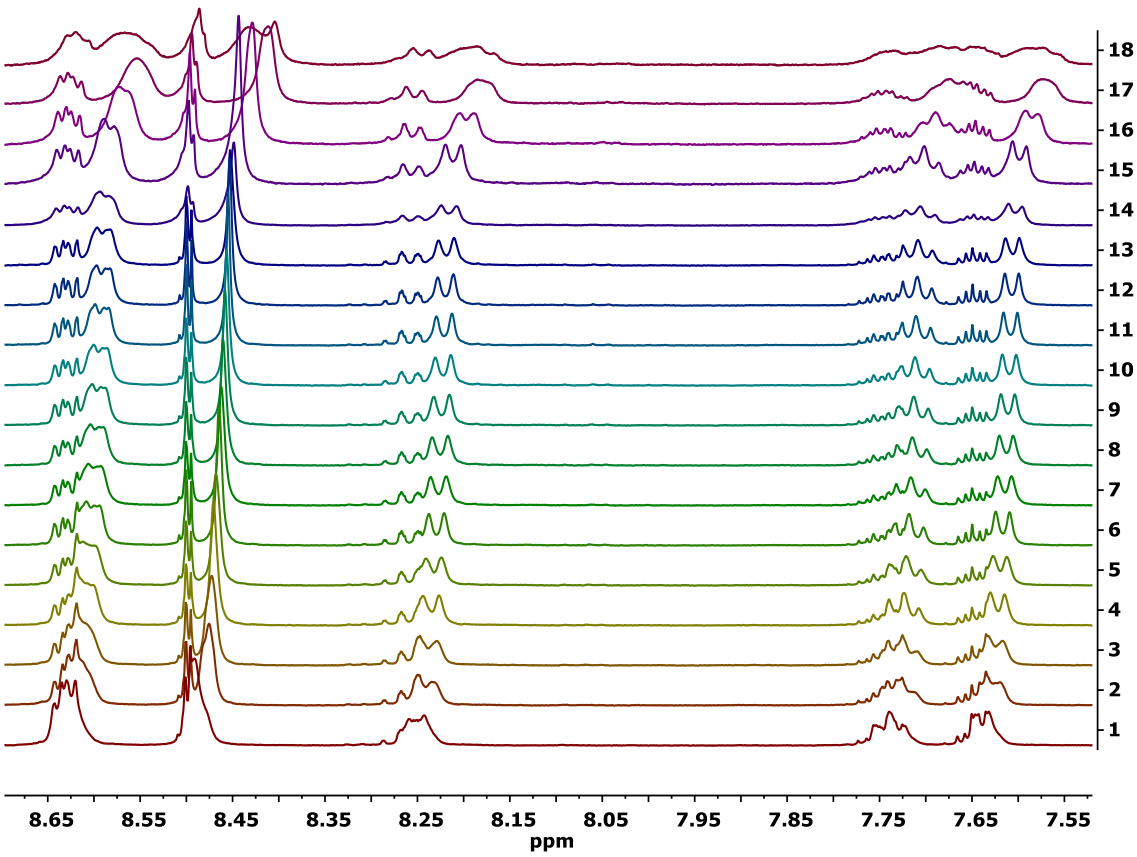

Figure 48. ^{1}H-NMR ($CDCl_3$, 500 MHz) titration of AR82s (3 mg in 0.5 ml of $CDCl_3$) with increasing amounts of TATP in presence of amberlite. The upper image is from the 2.8 to 4 ppm region and the lower image is from 7.5 to 8.7 ppm.

The titration showed a chemical shift of the signals of protons in the vicinity of the unprotected secondary amino group, signals at 2.93 and 3.46 ppm, accompanied by splitting of the signal at 2.93 at high amounts of TATP. There were no changes on the piperazine proton signals at 3.58 and 3.93 ppm. On the aromatic region, there was a clear splitting of all aromatic signals with changes in the coupling patterns between the signals, indicating a desymmetrization of the molecule.

Apparently, oxidation of the unprotected secondary amino group triggered the chemical shift of the methylene groups of the oxidized piperidine group as well as the association between molecules in dissolution with a concomitant change in fluorescence, either by suppressing the charge transfer from the amine group or by modifying the aggregation induced effect when in solution, because of the modification of the structure in relation to the variation in the AIE effect already observed for the rest of examples.

Then, the mechanism of oxidation of AR82s by ^{1}H-NMR titration in the presence of increasing amounts of *m*-CPBA was studied (Figure 49). The titration of the Figure 50 showed only oxidation of the unprotected secondary amino group with progressive disappearance of the proton signal of the amine group and chemical shift of the methylene groups of the oxidized piperidine group (the signals between 1.8 and 3.7 ppm), therefore confirming the oxidation mechanism. There was also splitting of the aromatic signals but, in this case, the changes in the aromatic region were obscured by the presence of the signals of the *m*-CPBA protons.

Addition number	*m*-CPBA mass added (µg)	Total mass of *m*-CPBA added (µg)	Addition number	*m*-CPBA mass added (µg)	Total mass of *m*-CPBA added (µg)
1	0	0	**9**	30	90
2	5	5	**10**	60	150
3	5	10	**11**	150	300
4	5	15	**12**	200	500
5	5	20	**13**	300	800
6	10	30	**14**	600	1400
7	10	40	**15**	1800	3200
8	20	60			

Figure 49. Additions of m-CPBA to the ^{1}H-NMR titration of AR82s.

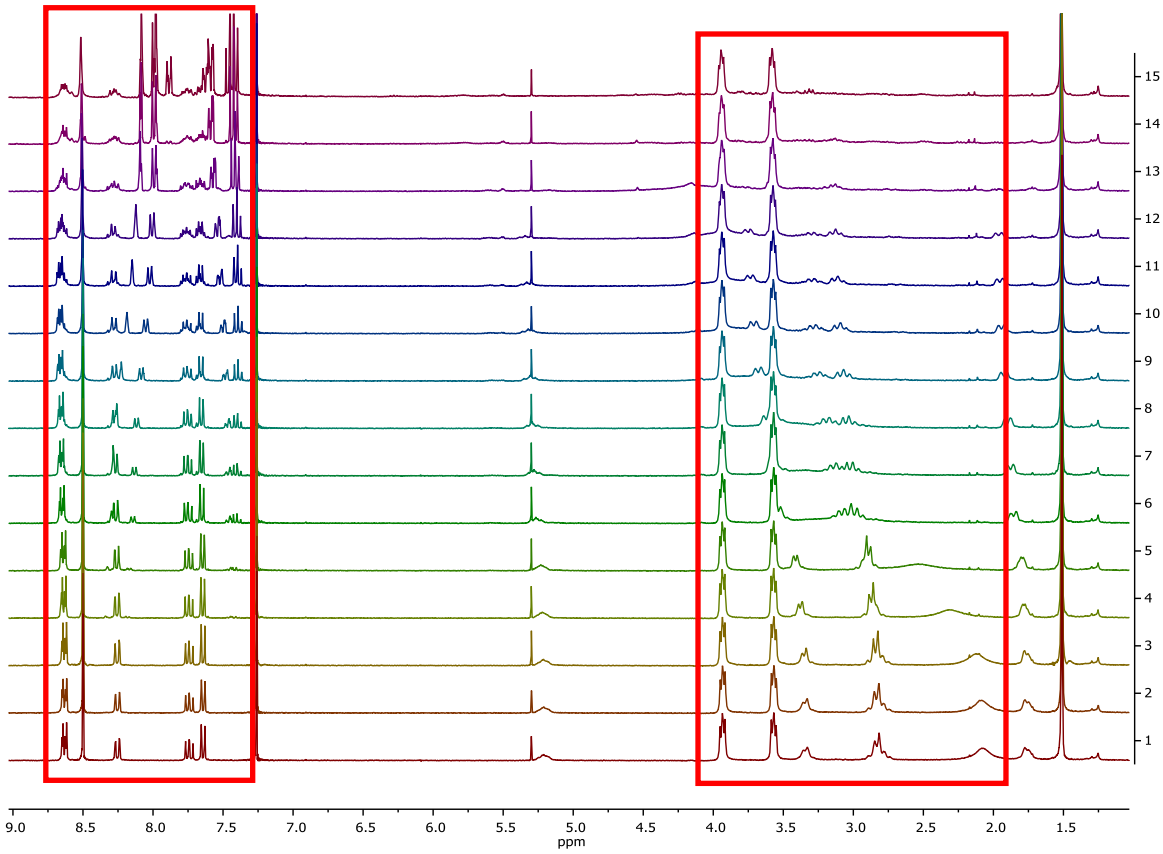

Figure 50. ^{1}H-NMR ($CDCl_3$, 500 MHz) titration of AR82s (10 mg in 0.5 ml of $CDCl_3$) with increasing amounts of m-CPBA

9. CONCLUSIONS

The proof of concept of a portable testing setup for the detection of triacetone triperoxide (TATP), also known as "mother of Satan", has been described in this chapter. This explosive is a common component in improvised explosive devices. TATP is a homemade explosive widely used in terrorist attacks and a very common component of improvised explosive devices. Its extreme volatility and difficult handling make any application requiring a controlled explosion impossible. Chemically, TATP is a peroxide derivative synthesized from readily available starting materials,

mainly acetone, and its very structure makes it very difficult to detect due to the absence of aromatic rings.

Currently, the most reliable detection methods, such as ICP, are difficult to access, costly, slow and require specialized personnel to operate. In contrast, the system developed allows for field-testing and generation of real-time results to test for TATP vapor traces in air by simply using circulation of the gas samples through the sensing material under the air conditioning system of a common room. In this way, the controlled trapping of the analyte in the chemical sensor gives reliable results at extremely low concentrations of TATP in air under real life conditions.

The system may have immediate applications in everyday use. Air samples at airports, government buildings, sports arenas or large concert halls where many people gather should be checked for IED-containing peroxide explosives in order to prevent terrorist acts. The system provides for an extremely low limit of detection of traces of peroxide in air, practically no interferents and an immediate response, as it is required to be of practical use. Vapor detection, as we have shown here, is a useful and non-invasive method suitable for explosive detection among current explosive detection technologies. TATP still goes largely unnoticed in many densely populated places, where permanent monitorization is needed. The results are suitable to convert the current knowledge in everyday useful technology that can be applied whenever it is necessary for the detection of traces of IEDs in luggage storage, sports depots, headquarters, locker rooms, or restricted public accesses, before they can cause any harm.

CHAPTER 3B

NMI DERIVATIVES FOR TNT DETECTION

This chapter describes the proof of concept of a portable testing setup for the detection of trinitrotoluene (TNT), a common component in hidden explosive devices frequently used in terrorist attacks. The system allows for field-testing and generation of real-time results to test for TNT traces in surfaces by simply using a filter paper and a fluorescent reporter. In this way, the controlled trapping and detection of the analyte by a chemical sensor gives reliable results at extremely low concentrations of TNT on surfaces under real life conditions suitable for daily use in ordinary sampling at airlines luggage storage or sport locker rooms. The reported fluorescent methodology is very sensitive and selective, allowing for the trapping and detection of TNT by fluorescent probes to give reliable results at very low concentrations.

1. INTRODUCTION

A major threat in modern society is constituted by the so-called improvised explosive devices (IEDs).[1] The explosives contained in IEDs were easily obtained from readily available source materials and commonly used in war scenarios but some years ago they were also used in situations of everyday life, therefore constituting a threat in the lives of countless people. In order to detect these explosives before they cause damage to property or personal injury, methods for the quick detection of explosive devices are needed, but there are very few methods for the detection of some explosives used in IEDs.[2]

The most advanced spectroscopy devices are very sensitive and selective to identify the chemicals used in IEDs, but they are typically too heavy to be used as portable devices and too much expensive for widespread use.[3] The cheap technology of the cotton swab[4] requires physical access to the substance that might be hidden or not easily accessible, which makes its use doubtful in certain cases. There is a long tradition in the use of animals in the detection of explosives, particularly trained dogs[5] but training and maintaining animals makes the method quite expensive. Electronic noses, made up of artificial sensor arrays, constitute a significant solution to replace the natural senses[6] for reliable monitorization of diverse environments.

Therefore, the methods of detection of explosive charge traces that currently exist are those shown in Figure 1 below. However, there are also IEDs detection methods based on the trigger mechanism, such as electromagnetic or mechanical detection systems, systems based on the

[1] a) Improvised explosive devices: past, present and future, action on armed violence. 15/10/2020. Obtained from: https://reliefweb.int/report/world/improvised-explosive-devices-past-present-and-future, accessed 20/02/2023. b) IED attack, improvised explosive devices, National Academies and the Department of Homeland Security, 15/12/2020. Obtained from: https://www.dhs.gov/xlibrary/assets/prep_ied_fact_sheet.pdf, accessed 20/02/2023. c) Reducing the threat of improvised explosive device attacks by restricting access to explosive precursor chemicals, national academies of sciences, engineering, and medicine. **2018**, *The National Academies Press*, Washington DC. d) Improvised explosive device (IED): guidelines for crowded places, Commonwealth of Australia, **2017**, ISBN: 978-1-925593-95-2. e) United Nations mine action service: improvised explosive device lexicon. Obtained from: https://unmas.org/sites/default/files/un-mas_ied_lexicon_0.pdf, accessed 20/02/2023. f) European union terrorism situation and trend report 2019, *European Union Agency for Law Enforcement Cooperation*, **2019**.

[2] a) K. C. To, S. Ben-Jaber, I. P. Parkin, *ACS Nano*, **2020**, *14*, 10804−10833. b) T. Wasilewski, J. Gębicki, W. Kamysz, *Trends Anal. Chem*., **2021**, *142*, 116330. c) T. P. Forbes, S. T. Krauss, G. Gillen, *Trends Anal. Chem.*, **2020**, *131*, 116023. d) R. Liu, Z. Li, Z. Huang, K. Li, Y. Lv, *Trends Anal. Chem.*, **2019**, *118*, 123-137. e) R. Apak, S. D. Çekiç, A. Uzer, E. Çapanoglu, S. E. Çelik, M. Bener, Z. Can, S. Durmazel, *Anal. Methods,* **2020**, *12*, 5266-5321.

[3] A. Ostrinskaya, R. R. Kunz, M. Clark, R. P. Kingsborough, T. H. Ong, S. Deneault, *J. Forensic Sci*., **2019**, *64*, 223-230.

[4] J. M. E. Glackin, R. N. Gillanders, F. Eriksson, M. Fjällgren, J. Engblom, S. Mohammed, I. D. W. Samuel, G. A. Turnbull, *Analyst*, **2020**, *145*, 7956–7963.

[5] T. H. Ong, T. Mendum, G. Geurtsen, J. Kelley, A. Ostrinskaya, R. Kunz, *Anal. Chem*., **2017**, *89*, 6482−6490.

[6] a) Z. Li, J. R. Askim, K. S. Suslick, *Chem. Rev.,* **2019**, *119*, 231−292. b) J. R. Askim, Z. Li, M. K. LaGasse, J. M. Rankin, K. S. Suslick, *Chem. Sci.*, **2016**, *7*, 199–206.

detection of metallic components, such as active or passive metal detection, and systems based on the appearance of the device, such as imaging technologies (for example X-rays).[7]

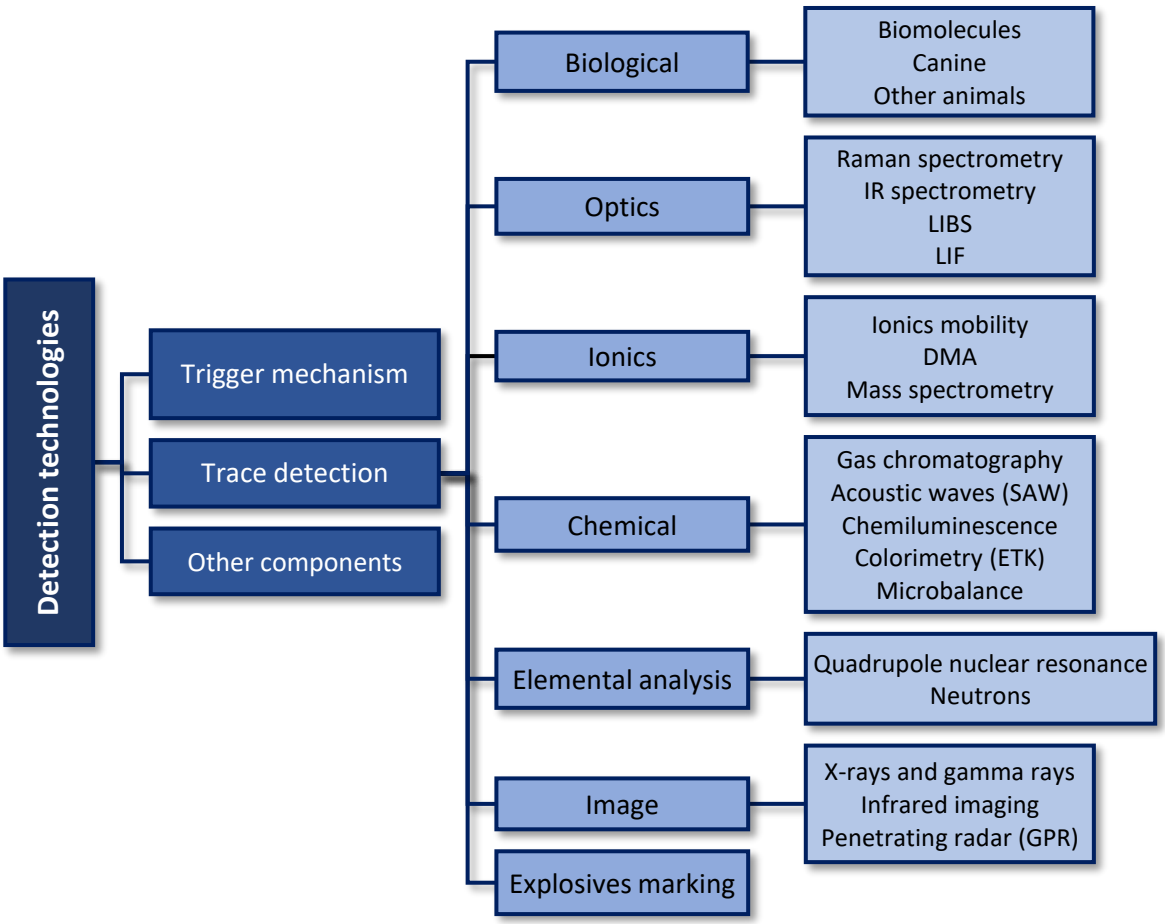

Figure 1. Technologies applicable to IEDs detection.

Appropriate portable devices for explosives detection used in the preparation of IEDs should alert to the presence of explosives within minutes.[8]

1.1. Explosives: TNT

2,4,6-Trinitrotoluene (TNT, Figure 2a) is a secondary explosive for military use, as described in Chapter 3A. This explosive was first prepared by Wilbrand in 1868 but its structure was not established until 1883 thanks to Claus and Becker. In 1902, TNT was adopted by the German Army to replace picric acid (Figure 2c) and, in 1912, the US Army also began to use it. Around 1914, TNT became the standard explosive for all the armies involved in the World War I.

During the war, TNT production was limited by the availability of toluene from coal tar. The pure TNT obtained was insufficient to meet the demand for munitions production, so a mixture of TNT with ammonium nitrate, called amatol, was used. Underwater explosives used the same mixture with the addition of aluminium, giving rise to aminal. Subsequently, TNT was used as a component of most of the explosives used in World War II, such as baronal, Torpex and picratol.[9]

[7] Documentos de seguridad y defensa: la seguridad frente a artefactos explosivos. Obtained from: https://publicaciones.defensa.gob.es/media/downloadable/files/links/P/D/PDF231.pdf, accessed: 27/03/2023.

[8] A. V. Kuznetsov, O. I. Osetrov, Meeting Proceedings RTO-MP-SET-117, **2007**, Paper 14. Obtained from: https://www.sto.nato.int › MP-SET-117-14, accessed 20/02/2023.

[9] J. Akhavan, The chemistry of explosives. RSC Paperbacks, **2004**, ISBN: 0-85404-640-2.

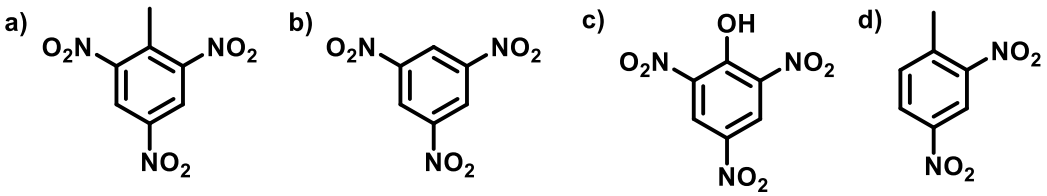

Figure 2. Nitro-derivative explosives: TNT (a), TNB (b), TNP (c) and DNT (d).

Currently, TNT is obtained by nitration of 2,4-dinitrotoluene (DNT, Figure 2d), which requires the use of mixed nitric acid and oleum at elevated temperatures, which produce its own pollutants and impurities, such as tetranitromethane and nitrogen oxides.

TNT is characterised by being insoluble in water and sparingly soluble in alcohols, with a melting temperature of approximately 80°C, while the ignition temperature is 300°C. This explosive can be obtained from cheap raw materials and by a low-cost manufacturing process. It is characterised by low sensitivity to impact and friction as well as good chemical and thermal stability and low volatility, making it a fairly safe explosive to handle.

Compared to 1,3,5-trinitrobenzene (TNB, Figure 2b), TNT has less explosive power. TNB is much more expensive and complicated to manufacture, so it is much better to synthesise TNT instead. Currently, TNB is used as a starting material in the synthesis of other explosives, such as TATB.[10]

1.2. Methods for detection of TNT

Common methods for explosives detection containing nitro groups, such as TNT in air, are known.[11] In solution, some turn-on fluorescent methods for their detection, including our contribution to the field[12] and from other research groups,[13] have been developed, but the most common methods are based on fluorescence quenching[14] and selected biosensing methods,[15] with very few specially dedicated methodologies.[16]

Analytical methods (Figure 3)[17] for TNT detection in different scenarios must be selective for nitroaromatics compounds, appropriate for immediate analysis and safe sampling by a qualified

[10] J. P. Agrawal, R. D. Hodgson, Organic chemistry of explosives. Wiley, **2007**. ISBN: 978-0-470-02967-1.

[11] C. Ferrari, G. Attolini, M. Bosi, C. Frigeri, P. Frigeri, E. Gombia, L. Lazzarini, F. Rossi, L. Seravalli, G. Trevisi, R. Lolli, L. Aversa, R. Verucchi, N. Musayeva, M. Alizade, S. Quluzade, T. Orujov, F. Sansone, L. Baldini, F. Rispoli, *Nanomaterials*, **2022**, *12*, 1278.

[12] D. C. Romero, P. Calvo-Gredilla, J. García-Calvo, A. Diez-Varga, J. V. Cuevas, A. Revilla-Cuesta, N. Busto, I. Abajo, G. Aullón, T. Torroba, *Org. Lett.*, **2021**, *23*, 8727–8732.

[13] a) S. Kim, H. Kim, T. Qiao, C. Cha, S. K. Lee, K. Lee, H. J. Ro, Y. Kim, W. Lee, H. Lee, *ACS Appl. Mater. Interfaces*, **2019**, *11*, 14354−14361. b) Z. Zhang, S. Chen, R. Shi, J. Ji, D. Wang, S. Jin, T. Han, C. Zhou, Q. Shu, *Talanta*, **2017**, *166*, 228–233. c) N. Tripathi, R. Kumar, P. Singh, S. Kumar, *Sens. Actuators B*, **2017**, *246*, 1001–1010. d) J. Y. Lee, H. D. Root, R. Ali, W. An, V. M. Lynch, S. Bähring, I. S. Kim, J. L. Sessler, J. S. Park, *J. Am. Chem. Soc*. **2020**, *142*, 19579−19587. e) M. Bener, F. B. Sen, R. Apak, *Spectrochim. Acta A: Mol. Biomol. Spectrosc.*, **2022**, *279*, 121462

[14] a) W. M. Wan, D. Tian, Y. N. Jing, X. Y. Zhang, W. Wu, H. Ren, H.L . Bao, *Angew. Chem. Int. Ed*., **2018**, *57*, 15510–15516. b) K. K. Kartha, S. S. Babu, S. Srinivasan, A. Ajayaghosh, *J. Am. Chem. Soc.,* **2012**, *134*, 4834−4841. c) A. S. Tanwar, R. Parui, R. Garai, M. A. Chanu, P. K. Iyer, *ACS Meas. Sci. Au.,* **2022**, *2*, 23−30. d) X. S. Ma, Y. Z. Cui, Y. Q. Ding, F. R. Tao, B. Zheng, R. H. Yu, W. Huang, *Sens. Actuators B Chem.,* **2017**, *238*, 48–57. e) H. Nie, Y. Lv, L. Yao, Y. Pan, Y. Zhao, P. Li, G. Sun, Y. Ma, M. Zhang, *J. Hazard. Mater.,* **2014**, *264*, 474– 480. f) B. Zhu, L. Zhu, Y. Wan, S. Deng, C. Zhang, J. Luo, *Sens. Actuators B Chem.,* **2021**, *341*, 130011. g) H. Zhou, X. Wang, T.T. Lin, J. Song, B. Z. Tang, J. Xu, *Polym. Chem.,* **2016**, *7*, 6309–6317..

[15] a) M. Paul, G. Tscheuschner, S. Herrmann, M. G. Weller, *Biosensors,* **2020**, *10*, 89. b) T. Komikawa, M. Tanaka, K. Yanai, B. R. G. Johnson, K. Critchley, T. Onodera, S. D. Evans, K. Toko, M. Okochi, *Biosens. Bioelectron.,* **2020**, *153*, 112030. c) H. Bai, G. Wen, A. Liang, Z. Jiang, *Biosens. Bioelectron.,* **2022**, *217*, 114743.

[16] a) S. Tang, N. Vinerot, D. Fisher, V. Bulatov, Y. Yavetz-Chen, I. Schechter, *Talanta,* **2016**, *155*, 235–244. b) A. Lichtenstein, E. Havivi, R. Shacham, E. Hahamy, R. Leibovich, A. Pevzner, V. Krivitsky, G. Davivi, I. Presman, R. Elnathan, Y. Engel, E. Flaxer, F. Patolsky, *Nat. Commun.,* **2014**, *5*, 4195.

[17] Secuplus. Obtained from: https://spanish.alibaba.com/product-detail/Airport-Security-check-Explosive-Detector-SPE3000-62205583414.html, accessed 29/03/2023.

operator. Very low limits of detection and high selectivity are expected, in this way they can detect explosives in confined public places to prevent explosions and further damage.[18]

Figure 3. TNT detector used in an airport.

Trace detection of TNT traces by fluorometric methods continues to be an attractive approach for the development of chemical sensors for hidden explosive devices.[19] The research group have some previous experience in fluorogenic sensors for the selective detection of explosive oxidants, such as TATP.[20] This time, new fluorescent dyes were looked for in which a stacking event allow regulate AIE characteristics of dyes for the detection of nitroaromatic species.

2. OBJECTIVES

Within the diverse range of applications for which they can be used, NMIs can detect a wide variety of analytes, including environmental pollutants or oxidizing species (Chapter 3A). NMIs are known to exhibit the AIE effect,[21] so some of them have been used for detection of trinitrophenol, an environmental contaminant and potential explosive.[22]

Therefore, a collection of new naphthalimide structures with some classic donor or accepting groups in their structures, such as carbazole or phenantroline, were selected with the aim to maximize the expected interactions with classic nitroaromatic derivatives. These new compounds were tested for TNT detection, as well as checking for the absence of interferers. In this way, a new naphthalimide dye with optimum features for the selective and ultrasensitive detection of traces of TNT was achieved.

On the other hand, other compound obtained was anchored on solid supports, such as a polymer, giving rise a new material for solvent-free, fast and easy detection of TNT on surfaces. In this way, the materials functioned as useful alternatives to known chemical tracking systems of traces of TNT.

Finally, the novel results obtained in this research are published as a simple system for the TNT detection on different surfaces and media, providing results in a rapid manner, which would make it suitable for in-situ analysis.

---

[18] A. González-Calabuig, X. Cetó, M. del Valle, *Talanta.,* **2016**, *153*, 340–346.

[19] X. Sun, Y. Wang, Y. Lei, *Chem. Soc. Rev.,* **2015**, *44*, 8019-8061.

[20] a) P. Calvo-Gredilla, J. García-Calvo, J. V. Cuevas, T. Torroba, J. L. Pablos, F. C. García, J. M. García, N. Zink-Lorre, E. Font-Sanchis, A. Sastre-Santos, F. Fernández-Lázaro, *Chem. Eur. J.,* **2017**, *23*, 13973–13979. b) J. García-Calvo, P. Calvo-Gredilla, M. Ibáñez-Llorente, D. C. Romero, J. V. Cuevas, G. García-Herbosa, M. Avella, T. Torroba, *J. Mater. Chem. A.,* **2018**, *6*, 4416-4423. c) S. Blanco, A. Macario, J. García-Calvo, A. Revilla-Cuesta, T. Torroba, J. C. López, *Chem. Eur. J.,* **2021**, *27*, 1680-1687. d) S. Lapcinska, A. Revilla-Cuesta, I. Abajo-Cuadrado, J. V. Cuevas, M. Avella, P. Arsenyan, T. Torroba, *Mater. Chem. Front.,* **2021**, *5*, 8097-8107.

[21] a) P. Gopikrishna, N. Meher, P. K. Iyer, *ACS Appl. Mater. Interfaces,* **2018**, *10*, 12081−12111. b) K. Tajima, N. Fukui, H. Shinokubo, *Org. Lett.,* **2019**, *21*, 9516−9520. c) Y. Wang, Y. Teng, H. Yang, X. Li, D. Yin, Y. Tian, *Chem. Commun.,* **2022**, *58*, 949-952.

[22] a) H. Ma, C. He, X. Li, O. Ablikim, S. Zhang, M. Zhang, *Sens. Actuators B Chem.,* **2016**, *230*, 746–752. b) X. Jiao, H. Li, X. Cheng, *Mater. Today Chem.,* **2021**, *22*, 100615.

3. GENERAL PROCEDURE FOR PROBE SYNTHESIS AND TNT DETECTION

The fluorogenic probes synthesized were tested for several types of analytes, such as anions, cations or oxidizing species. The synthesis was performed by using carbon-carbon coupling chemistry, following previous experiences in developing fluorogenic probes by the research group.[23] The new fluorogenic probes are shown in the Figure 4.

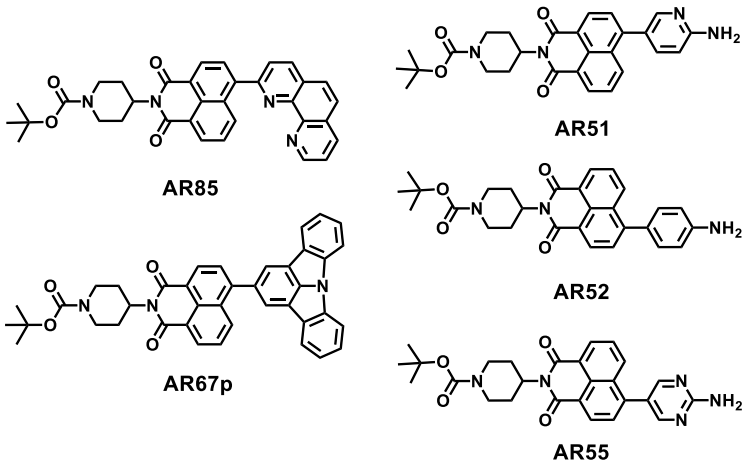

Figure 4. Structure of chemical probes used for the study.

The selectivity of each fluorogenic probe against the most important nitroaromatic derivatives was addressed in a mixture of water and organic solvents, with the aim to select the best candidates for explosives detection. With the new fluorogenic probes, a complete characterization were performed and a battery of preliminary tests about selectivity and sensitivity with target explosives and several expected interferents. The sensitivity of the collection of fluorogenic probes was checked in the presence of TNT, TNB and their taggants 2,4-dinitrotoluene and nitrobenzene.

An experimental design for this part of the work was prepared that was applied to all fluorescent probes. Then, the sensitivity of selected solid supported naphthalimides was studied in the presence of traces of TNT, so the fluorogenic material could be capable of discriminate the presence of the most important explosive, TNT. Having a previous experience in modified materials,[24] additional experiments was performed by supporting a fluorescent probe on polydimethylsiloxane (PDMS), to study a quick positive detection that could be confirmed under careful titration with the test probe in solution. A summary of the experimental procedure to develop these new fluorescent probes is shown in Figure 5.

[23] a) B. Díaz de Greñu, D. Moreno, T. Torroba, A. Berg, J. Gunnars, T. Nilsson, R. Nyman, M. Persson, J. Pettersson, I. Eklind, P. Wästerby, *J. Am. Chem. Soc.,* **2014**, *136*, 4125–4128. b) B. Díaz de Greñu, J. García-Calvo, J. Cuevas, G. García-Herbosa, B. García, N. Busto, S. Ibeas, T. Torroba, B. Torroba, A. Herrera, S. Pons, *Chem. Sci.,* **2015**, *6*, 3757-3764. c) J. García-Calvo, S. Vallejos, F. C. García, J. Rojo, J. M. García, T. Torroba, *Chem. Commun.,* **2016**, *52*, 11915-11918. d) J. García-Calvo, P. Calvo-Gredilla, M. Ibáñez-Llorente, T. Rodríguez, T. Torroba, *Chem. Rec.,* **2016**, *16*, 810-824. e) J. García-Calvo, J. A. Robson, T. Torroba, J. D. E. T. Wilton-Ely, *Chem. Eur. J.,* **2019**, *25*, 14214-14222. f) V. García-Calvo, J. V. Cuevas, H. Barbero, S. Ferrero, C. M. Álvarez, J. A. González, B. Díaz de Greñu, J. García-Calvo, T. Torroba, *Org. Lett.,* **2019**, *21*, 5803–5807. g) N. Busto, P. Calvo, J. Santolaya, J. M. Leal, A. Guédin, G. Barone, T. Torroba, J. L. Mergny, B. García, *Chem. Eur. J.,* **2018**, *24*, 11292-11296. h) J. García-Calvo, T. Torroba, V. Brañas-Fresnillo, G. Perdomo, I. Cózar-Castellano, Y. H. Li, Y. M. Legrand, M. Barboiu, *Chem. Eur. J.,* **2019**, *25*, 9287–9294. i) N. Busto, J. García-Calvo, J. V. Cuevas, A. Herrera; J. L. Mergny, S. Pons, T. Torroba, B. García, *Bioorg. Chem.,* **2021**, *108*, 104660.

[24] a) J. García-Calvo, P. Calvo-Gredilla, S. Vallejos, J. M. García, J. V. Cuevas-Vicario, G. García-Herbosa, M. Avella, T. Torroba, *Green Chem.*, **2018**, *20*, 3875-3883. b) J. García-Calvo, V. García-Calvo, S. Vallejos, F. C. García, M. Avella, J. M. García, T. Torroba, *ACS Appl. Mater. Interfaces,* **2016**, *8*, 24999–25004.

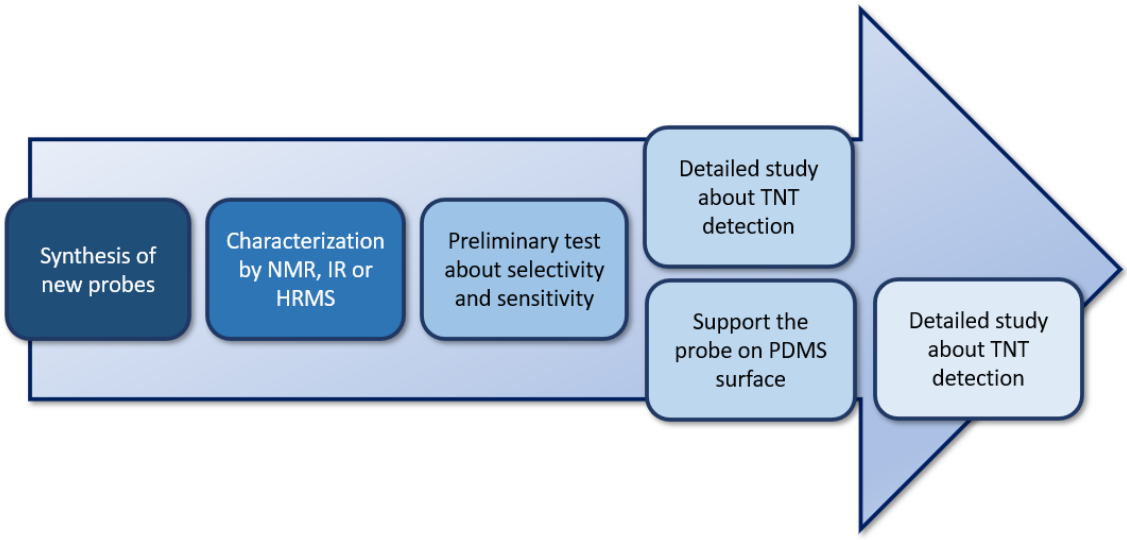

Figure 5. Summary of the experimental procedure followed for the development of new fluorescent sensors sensitive to TNT.

4. DETECTION OF TNT IN DISSOLUTION

This section will detail the synthesis of new fluorescent probes and the optimization of the detection procedure for TNT in solution followed for one of them. So, only the synthesis and the different detection tests carried out for compound AR85 will be detailed in this section, since it was the compound that gave the best results.

4.1. Synthesis. Absorbance and fluorescence interpretation

The synthesis of AR85 was performed by Stille coupling reaction between equimolecular amounts of *N*-(1-Boc-piperidin-4-yl)-4-(tributylstannyl)naphthalene-1,8-dicarboxylmonoimide (AR98) and 2-bromo-1,10-phenantholine, a commercial product, under $Pd(PPh_3)_4$ catalysis in refluxing toluene for 72 hours. Work-up and column chromatography afforded AR85 as a yellowish solid in 85 % yield (Figure 6).

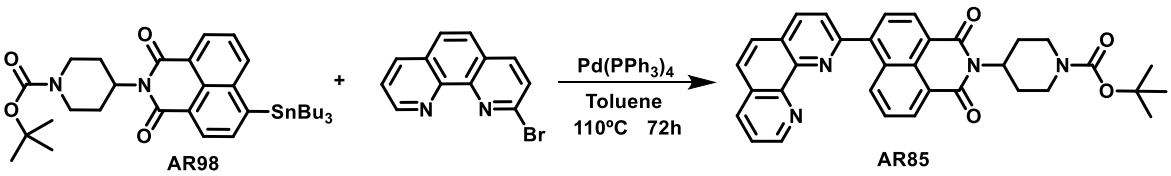

Figure 6. Synthesis of AR85 product.

Comparing the fluorescence quantum yield (Figure 7) of compound AR85 with the other synthesised products, it showed a faint fluorescence but better sensitivity to TNT. The other products had higher fluorescence, but the sensitivity to TATP was lower. Therefore, AR85 was the best choice to be used as a sensor for nitrated aromatic explosives in solution.

	$Ø_F$ (%)
AR51	85.26
AR52	85.28
AR55	91.59
AR67p	84.60
AR85	12.25

Figure 7. Fluorescence quantum yields of the synthesized products.

AR85 was characterized by being very solvatochromic, especially in solvents of higher polarity (Figure 8). Furthermore, the product was insoluble in water and presented a secondary emission band in DMF between 500-600 nm, low but wide. Both the normalized absorbance and emission graphs (Figure 9) showed a bathochromic shift of the maxima corresponding in each case to longer wavelengths as the polarity of the solvent increased.[25] This shift was much more marked for emission, around 55 nm, than for absorption, which was approximately 6 nm.

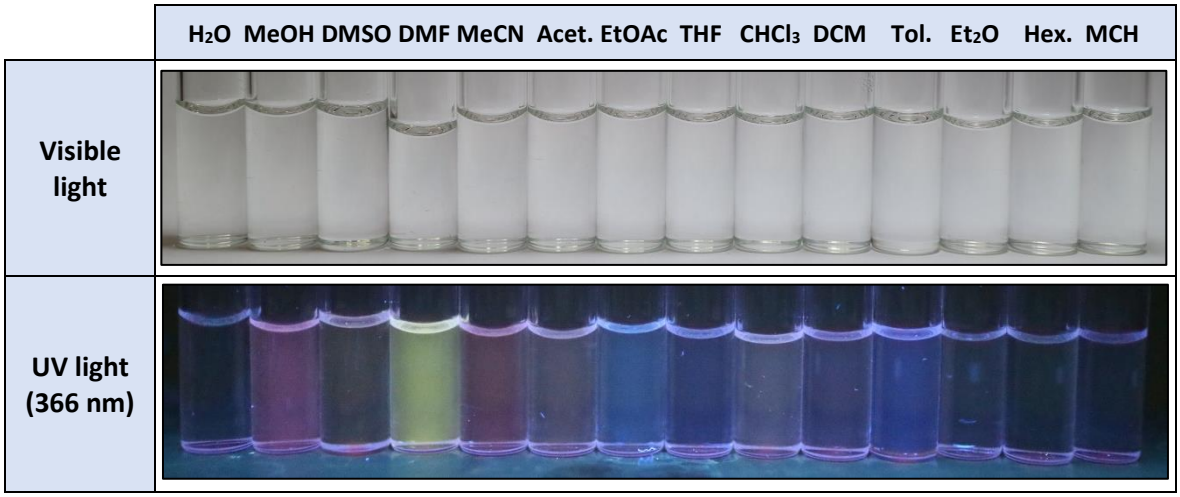

Figure 8. Solvatochromism images. 10 µM solution of AR85 in different solvents under visible and 366 nm light.

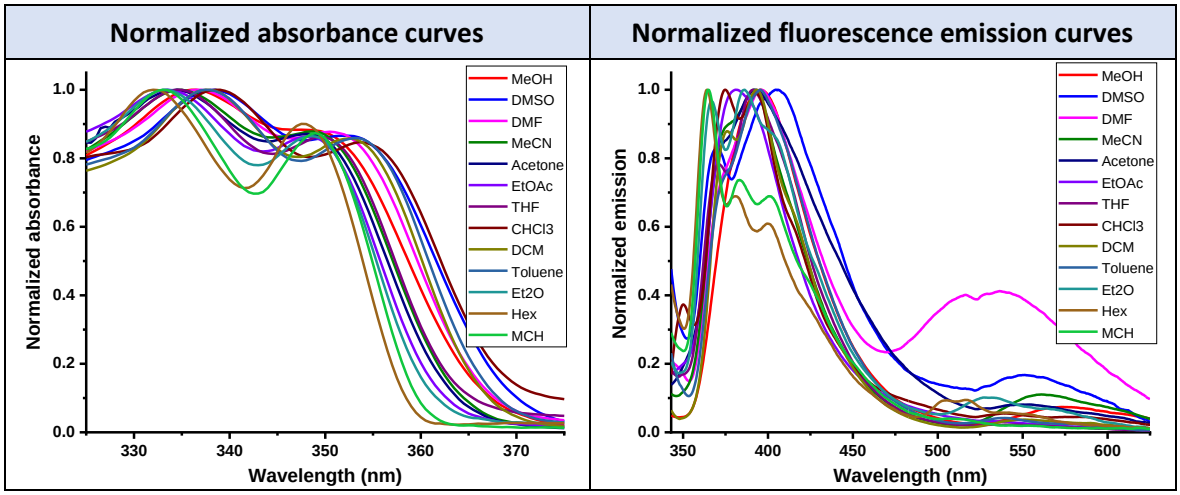

Figure 9. Solvatochromism graphs. Normalized absorbance curves (left) and fluorescence emission curves (right) in several solvents. λ_{exc} = 330 nm.

[25] V. Sharma, F. Chandra, D. Sahoo, A. L. Koner, *Eur. J. Org. Chem.*, **2017**, 6901-6905.

4.2. Preliminary qualitative tests

After the study of the fluorescence of the compounds, qualitative tests were carried out in which the variations of the fluorescence of compound AR85 were studied as a function of the medium in which it was found, that is, increasing the amount of water in a mixture with organic solvent or modifying the pH of the medium. Next, the fluorescence variations of AR85 against different anionic and cationic species were studied. The results are shown in Figure 10.

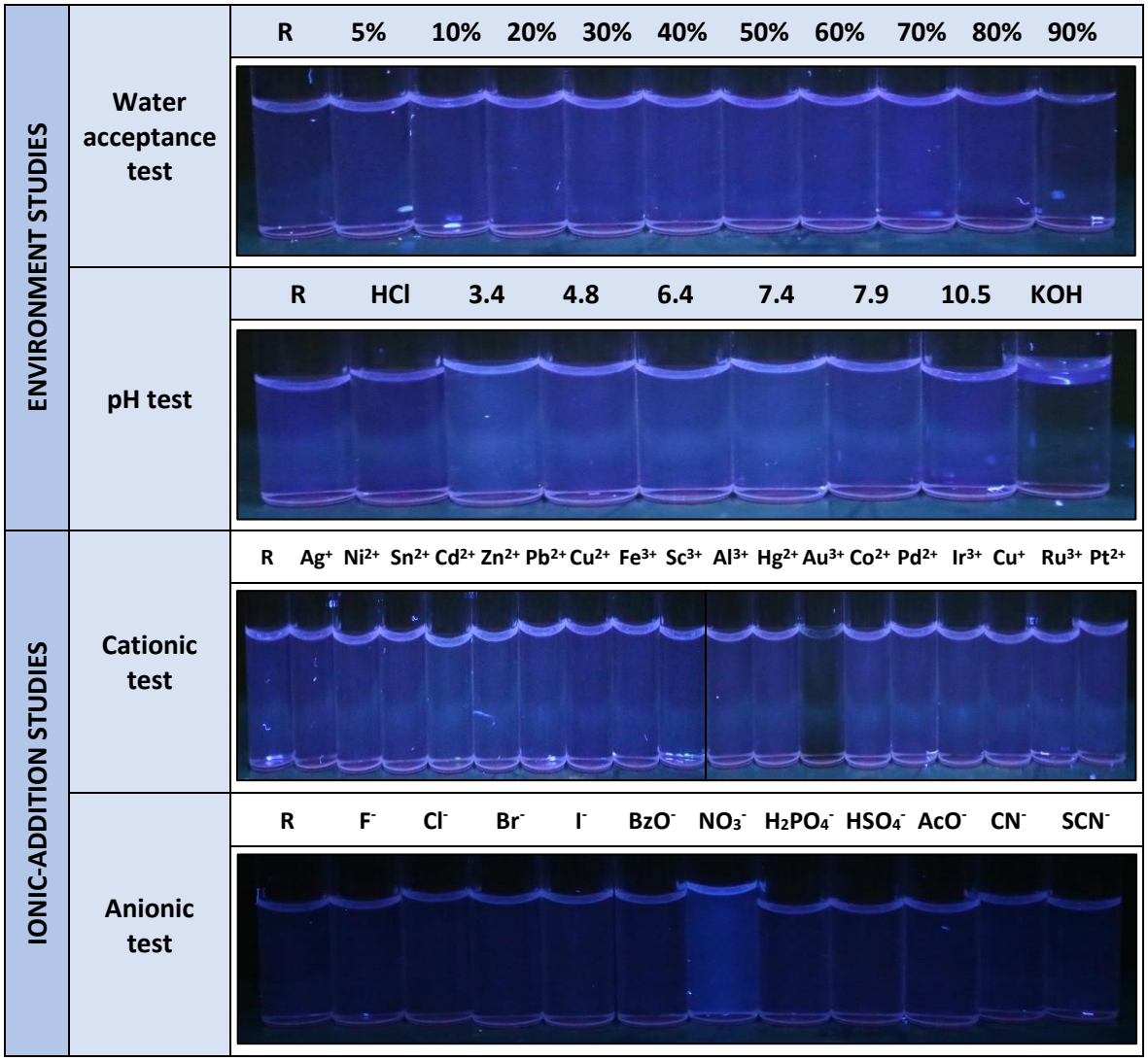

Figure 10. Images of the study of the influence of both the medium and the addition of different species on the fluorescence of AR85 under 366 nm light.

As can be seen, AR85 resulted to be insensitive to the presence of water in mixtures of THF and water, only ACQ was observed at 80-90% water. AR85 proved to be insensitive to pH values between 3 and 10 and also insensitive to almost all common anions and cations.

In tests with common oxidants or reducing agents it showed to be sensitive to the presence of TNB and TNT, with a decrease in the fluorescence emission, while the rest of the synthesised products gave a negative result in this test (Figure 11). Hence, a search for the best solvent for their detection was performed.

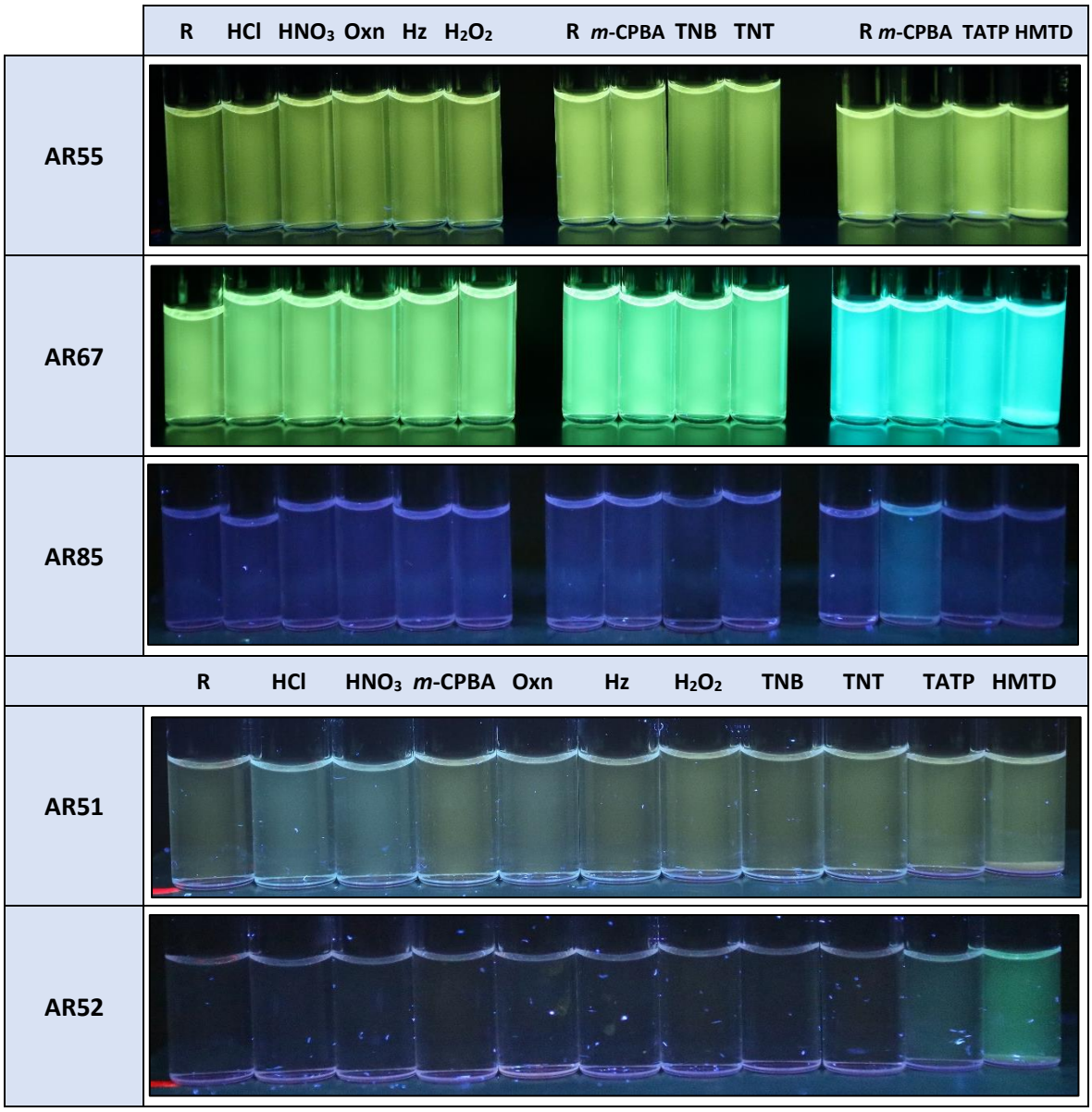

Figure 11. Images of the study of the synthesized products against oxidising and reducing species under 366 nm light.

4.3. Probe in solution: solvent selection

To select the most suitable solvent for more detailed research, a solvent study was performed in which an excess of TNT or TNB was added to a solution of compound AR85. As shown in Figure 12, fluorescence modifications were observed in most solvents, but the most significant changes, in both cases, being in DMF, EtOAc, THF and toluene.

Albeit DMF was a suitable solvent for TNT/TNB titrations, the almost instant interaction of the solvent with the analytes hindered the fluorescent detection process.[26] After several titration experiments (Figure 13), toluene was selected as the solvent showing the highest sensitivity of AR85 to nitroaromatics derivatives. Moreover, toluene was the solvent in which the decrease in fluorescence was stabilised first. It was, therefore, the solvent in which the most detailed titrations were carried out.

[26] C. A. Latendresse, S. C. Fernandes, S. You, H. Q. Zhang, W. B. Euler, *J. Phys. Chem. A.*, **2013**, *117*, 324–332.

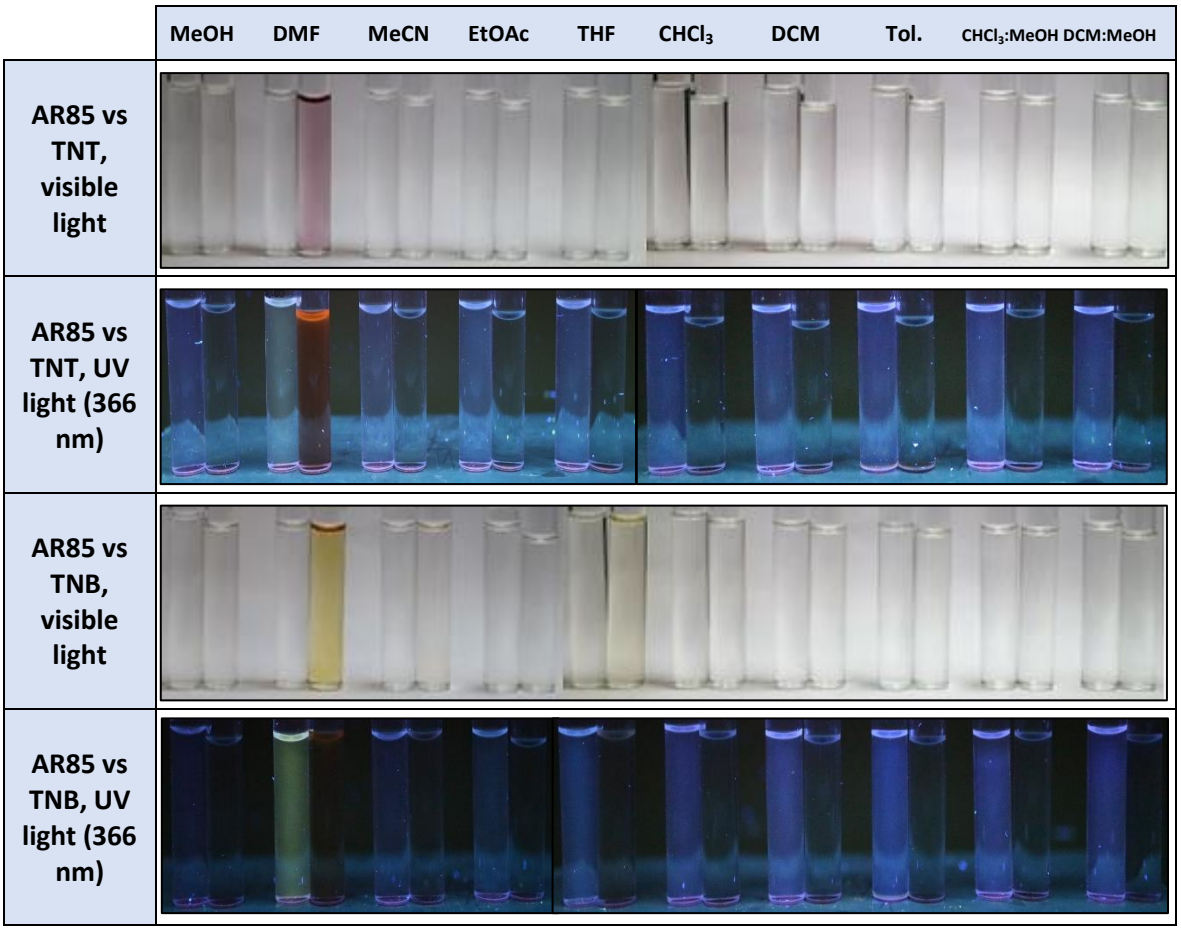

Figure 12. Solvent test. Pairs of 10 µM solutions of AR85 (left vial of each pair) and probe solution with 7 mg of TNT or TNB (right vial of each pair) in different solvents under 366 nm light.

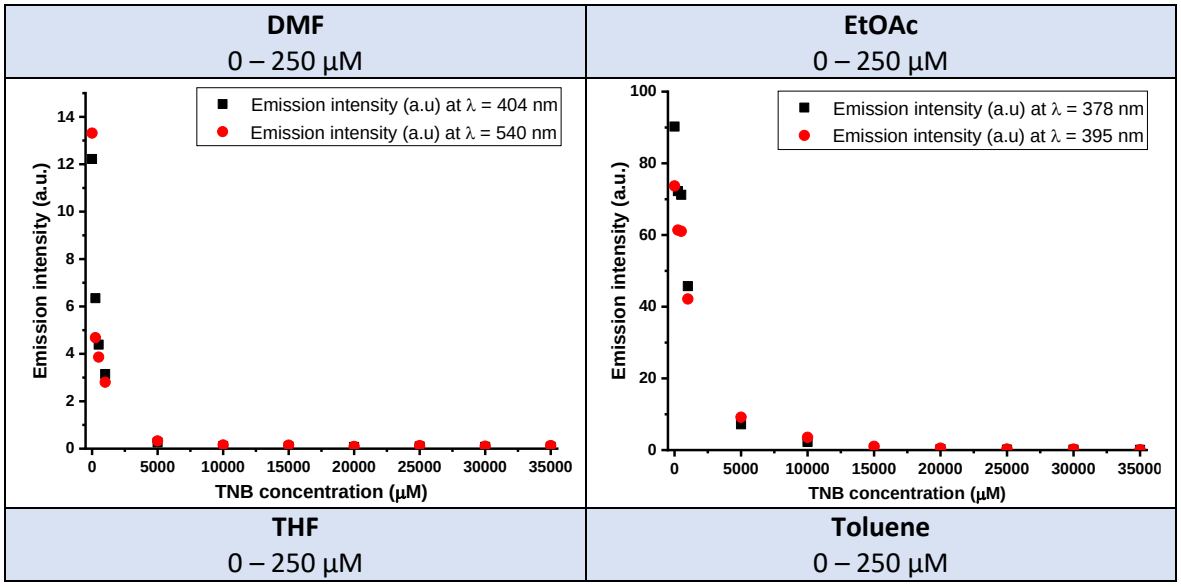

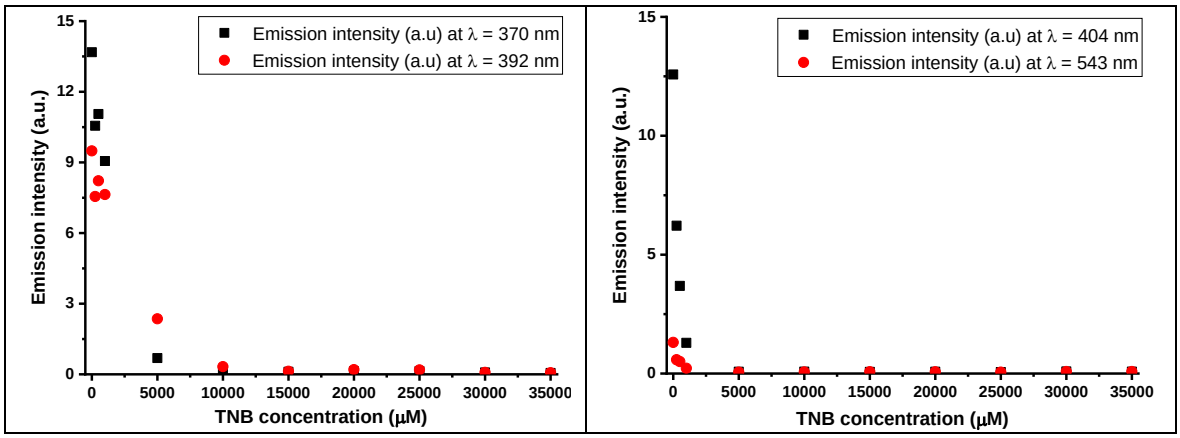

Figure 13. Study of 2.5μM of AR85 with TNB in different solvents. Fluorescence profile at maximum emission wavelength under increasing concentrations of TNB.

4.4. Work concentration

To choose an optimum concentration for the following experiments, the absorbance of the probe was checked to be linear while concentration changes are small (Figure 14). The solvent for this study was DCM.

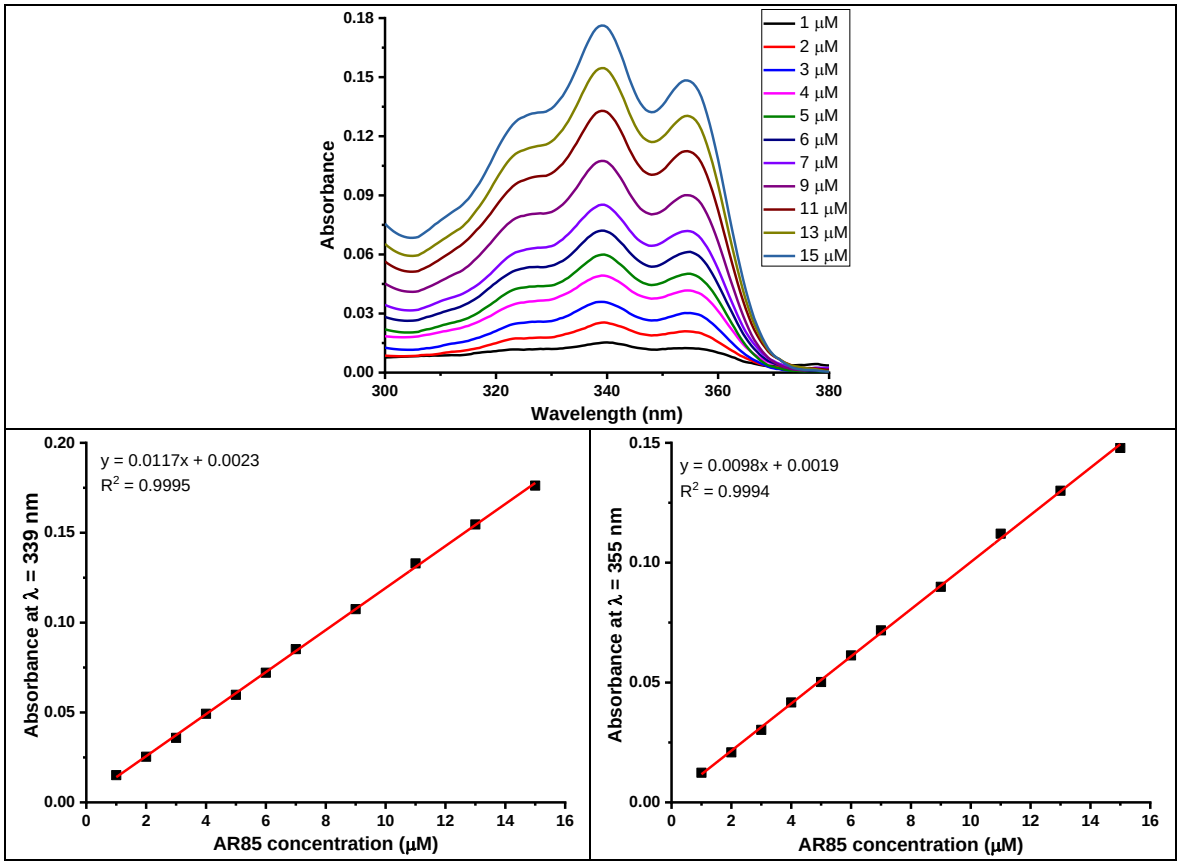

Figure 14. Absorbance spectrum (up), absorbance profile at 339 nm (down left) and absorbance profile at 355 nm (down right) of increasing concentrations of AR85 solution in DCM.

The ideal working concentration should be at 0.1 of absorbance or less, to prevent inner filter effects, possible dynamic quenching or stacking processes. Hence, the chosen concentration was 2.5 μM for all experiments, value around which the Lambert-Beer Law was fulfilled.

4.5. Detailed quantitative studies

Once the most suitable solvent and working concentration had been selected, a kinetic study and titration were carried out to subsequently calculate the LOD, according to the methods described in Chapter 1.

The conditions for carrying out both experiments were the following:

- AR85 solutions (2.5 µM) in toluene was prepared.
- The fluorescence changes were registered at 25ºC.
- λ_{exc} = 330 nm.

4.5.1. TNT/TNB kinetic study:

The kinetic experiments were carried out using an excess of TNT/TNB (20 mM) and recording the fluorescence variations at 5-minute intervals.

In this study, λ_{em} = 404 and 543 nm.

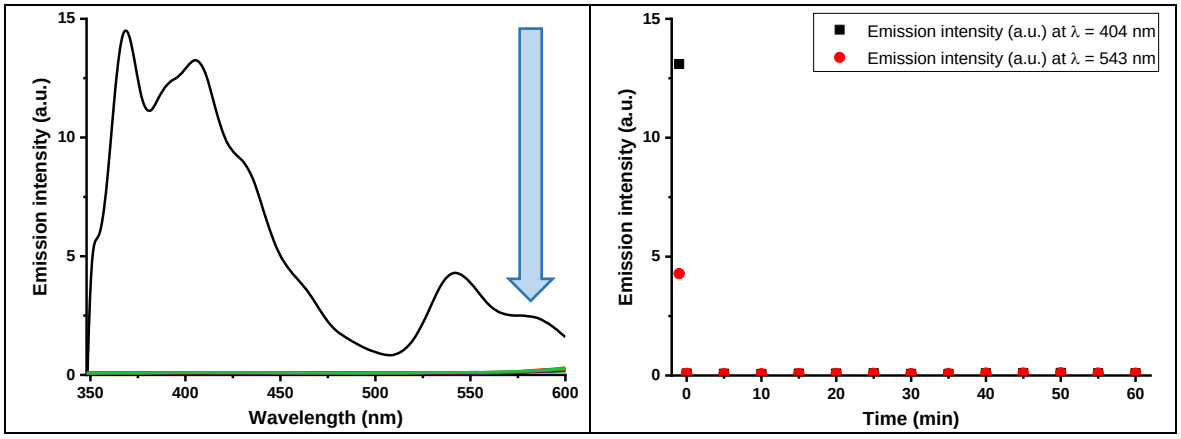

Figure 15. Kinetic study (left) and profile as function as time at 404 nm and 543 nm simultaneously (right) of AR85 in presence of TNT/TNB excess.

As can be observed in Figure 15, kinetic experiments showed that the emission intensity decreased immediately after adding TNT/TNB to AR85 solutions and the decreased intensity was remained stable for long periods of time in this solvent.

4.5.2. TNT titration:

Accurate titrations were performed of a solution of AR85 in toluene with increasing amounts of TNT by successive additions from a concentrated solution in the same solvent. Fluorescent measurements were carried out immediately after the addition of TNT. In addition, the blank (sample only containing probe) was measured three times.

In this titration, λ_{em} = 365 and 391 nm.

The titration curves and titration profile for TNT showed in Figure 16 were obtained.

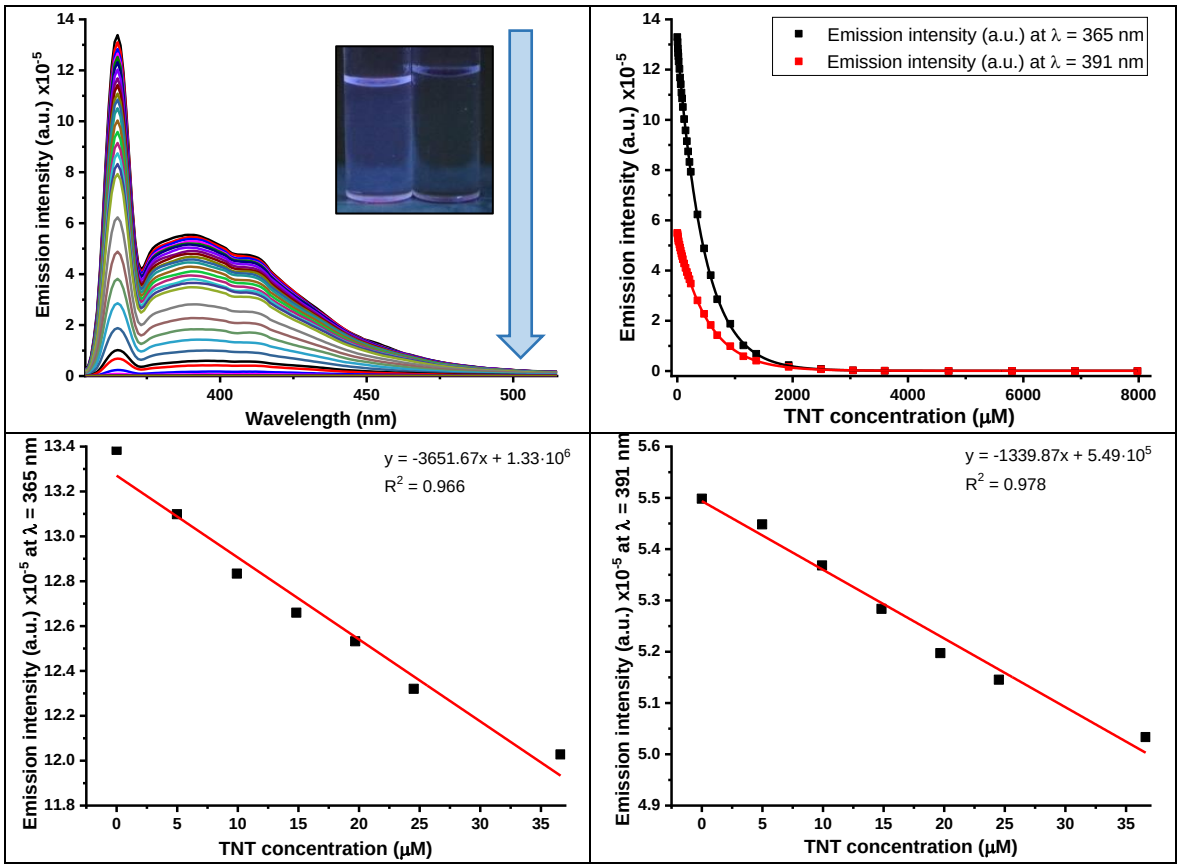

Figure 16. Titration curves (up left) and fluorescent profile at 365 and 391 nm (up right), calibration for the limit of detection using emission values at 365 nm (down left) and calibration for the limit of detection using emission values at 391 nm (down right) of an AR85 solution, 2.5 μM in toluene, under increasing concentrations of TNT. Image of solutions before and after TNT titration (up left).

The limit of detection, LOD, was calculated from the initial titration plot values by IUPAC-consistent methods.[27] The LOD by using emission values at 365 nm was calculated by a linear regression + false positive and negative values,[28] by:

(1) Adjusting to a mean square linear regression.

(2) Removing the "outliers", understanding them as points that are significantly different from the rest, within a 95% of probability.

(3) Adjusting to a linear regression and checking that the slope is significantly different from 0 (95%), P-Value > 0.05.

(4) Calculating the LOD when the probability of false positive (α) and false negative (β) is equal or inferior to 5%.

Taking all this into account, the LOD calculation was performed by the software "R" to provide the fitting and delivering of the results.[29] This method allowed to obtain a **LOD of 1.87 nM or 0.42 ng·mL^{-1} of TNT**. The LOD calculated by using emission values at 391 nm by a linear regression + false positive and negative values and using the R software, as in previous calculation, allowed to obtain a similar result, a **LOD of 1.87 nM**, showing that both wavelength values decrease uniformly in the presence of TNT. For the simplicity of the method, this LOD competes in accuracy with alternative and much more complicate methodologies.[30]

[27] F. Allegrini, A. C. Olivieri, *Anal. Chem.,* **2014**, *86*, 7858–7866.
[28] M. C. Ortiz, L. A. Sarabia, M. S. Sánchez, *Anal. Chim. Acta.,* **2010**, *674*, 123-142.
[29] RStudio, Version 1.4.1103, 2009-2021 RStudio, 250 Northern Ave, Boston, MA 02210.
[30] X. Chen, X. Zhang, H. Wang, L. Zhang, J. Zhu, *Chem. Eur. J.,* **2023**, e202203605.

4.5.3. TNB titration:

Similarly, titrations of AR85 in toluene was carried out with increasing amounts of TNB, adding it from a concentrate solution in the same solvent. Fluorescent measurements were recorded immediately after the addition of TNB.

For this titration, λ_{em} = 365 and 400 nm.

The titration curves and titration profile for TNB showed in Figure 17.

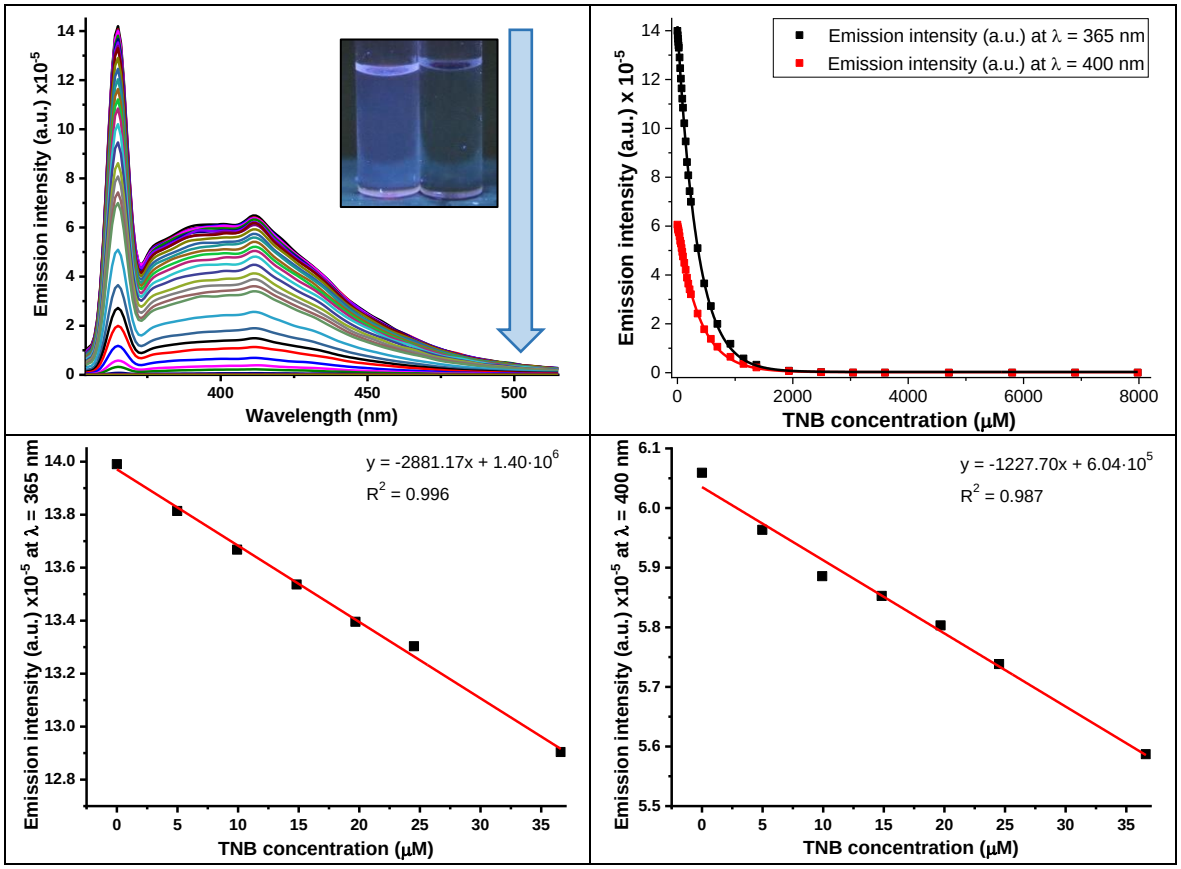

Figure 17. Titration curves (up left) and fluorescent profile at 365 and 400 nm (up right), calibration for the limit of detection using emission values at 365 nm (down left) and calibration for the limit of detection using emission values at 400 nm (down right) of an AR85 solution, 2.5 μM in toluene, under increasing concentrations of TNB. Image of solutions before and after TNB titration (up left).

The LOD was calculated from the plot of two emission profiles values by IUPAC-consistent methods.[27] In this case, we calculated the LOD within the values measured (different than 0) by adjusting the initial values to a mean square linear regression and using the R program.[29] In this way, linear regression at low concentrations of TNB led to a **LOD of 1.88 nM or 0.40 ng·of TNB per millilitre**. Again, the LOD calculated by using emission values at 400 nm through the same methodology gave a similar value, **1.89 nM of TNB**, showing that, for both wavelength, values of fluorescent emission decreased uniformly in the presence of TNB.

4.5.4. Other experiments:

Some naphthalimides have been used for detection of trinitrophenol (TNP), an environmental contaminant and potential explosive,[31] therefore the performance of the fluorescent probe AR85 in the detection of TNP, in comparison to the detection of TNT and TNB, was studied. As in previous

[31] a) H. Ma, C. He, X. Li, O. Ablikim, S. Zhang, M. Zhang, *Sens. Actuators B Chem.*, **2016**, *230*, 746–752. b) X. Jiao, H. Li, X. Cheng, *Mater. Today Chem.*, **2021**, *22*, 100615.

cases, an analysis of the behaviour of AR85 in the presence of excess TNP in different solvents was performed. The result is shown in Figure 18.

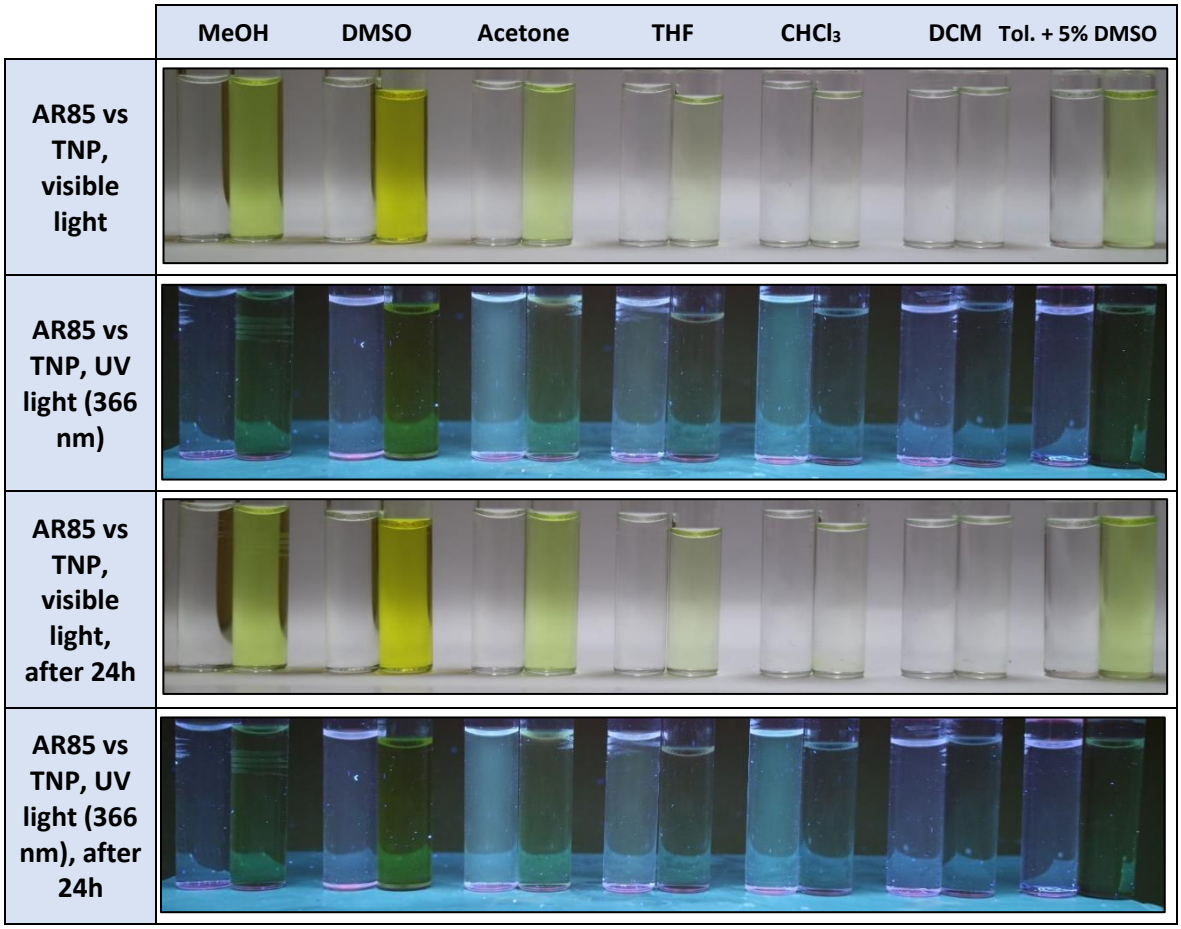

Figure 18. Solvent test. Pairs of 10 µM solutions of AR85 (left vial of each pair) and probe solution with 2 mg of TNP (right vial of each pair) in different solvents under visible light and 366 nm light. There is hardly any variation in the dissolutions at the time and 24 hours later.

TNP was soluble in MeOH, DMSO, acetone and THF but it was not completely soluble in DCM, $CHCl_3$ or toluene, but it was soluble in toluene with 5% v/v of DMSO. To keep the titration conditions as similar as possible to those previously carried out with TNT and TNB, the titration with TNP was performed using a mixture of toluene + 5% DMSO as solvent.

In this way, titrations of AR85 solutions, 2.5 µM in toluene + 5% DMSO, with increasing amounts of TNP, were carried out using experimental conditions analogous to those enunciated above, except λ_{em} = 365 and 397 nm. The titration curves and titration profile for TNP showed in Figure 19.

The LOD from the titration plot values was calculated by IUPAC-consistent methods.[27] In this case, the LOD was estimated within the values measured (different than 0) by adjusting the initial values to a mean square linear regression and using the R program.[29] In this way, linear regression at low concentrations of TNP, by using the emission values at 365 nm, gave a **LOD of 2.16 nM or 0.49 ng of TNP per millilitre**. Again, the LOD calculated by using emission values at 397 nm, determined by the same methodology, gave a similar LOD, **2.19 nM**, showing that both wavelength values decrease uniformly in the presence of TNP, as it happened in previous examples. The obtained LODs compete favourably with those obtained in previously known examples.[31]

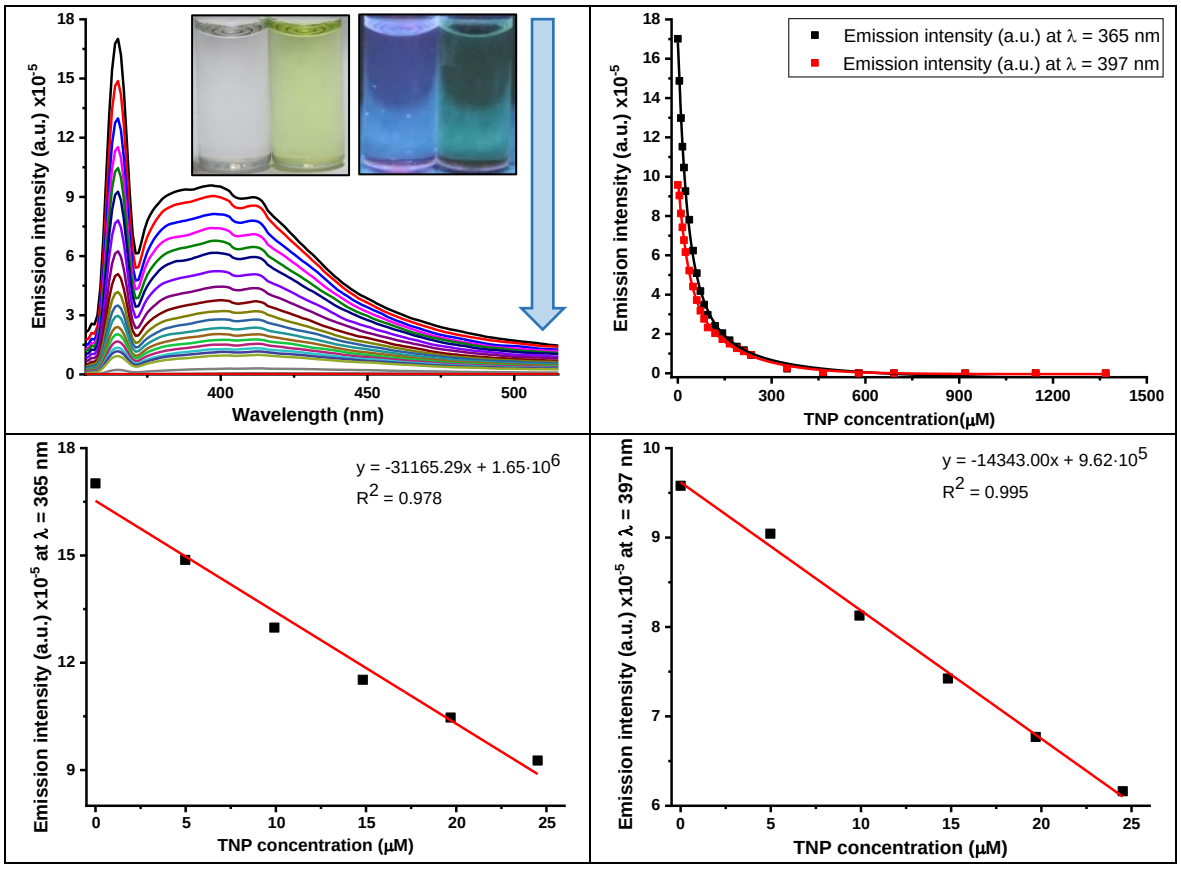

Figure 19. Titration curves (up left) and fluorescent profile at 365 and 397 nm (up right), calibration for the limit of detection using emission values at 365 nm (down left) and calibration for the limit of detection using emission values at 397 nm (down right) of an AR85 solution, 2.5 μM in toluene, under increasing concentrations of TNP. Image of solutions before and after TNP titration under visible light and 366 nm UV light, the yellow-green colour of TNP is clearly visible in both images (up left).

Then, we were curious about the possibility of detecting one explosive taggant, such as 2,4-dinitrotoluene (DNT),[32] or the most common nitrobenzene (NB). In both cases, titration curves and related titration profiles were carried out and some of these graphs are shown in Figure 20.

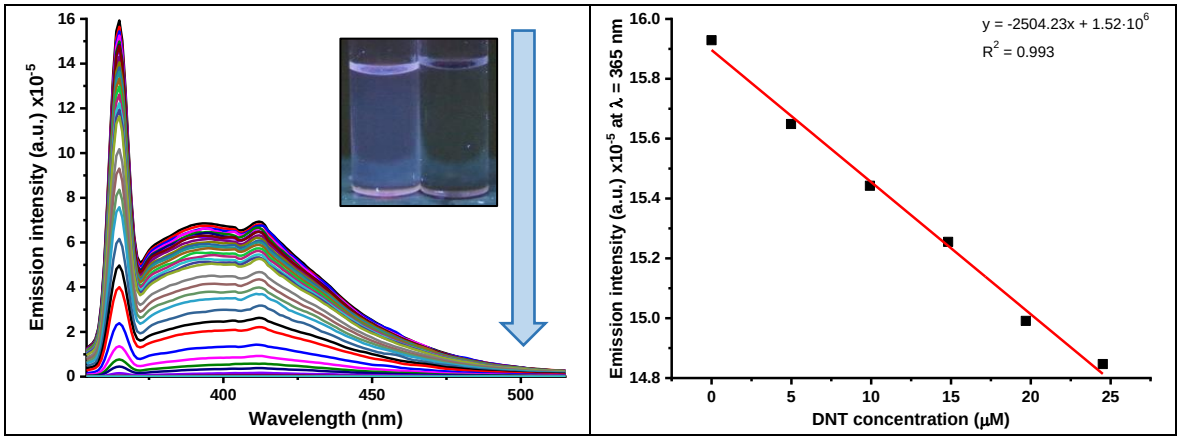

[32] K. L. Hutchinson, D. M. Stoltzfus, P. L. Burn, P. E. Shaw, *Mater. Adv.*, **2020**, *1*, 837-844.

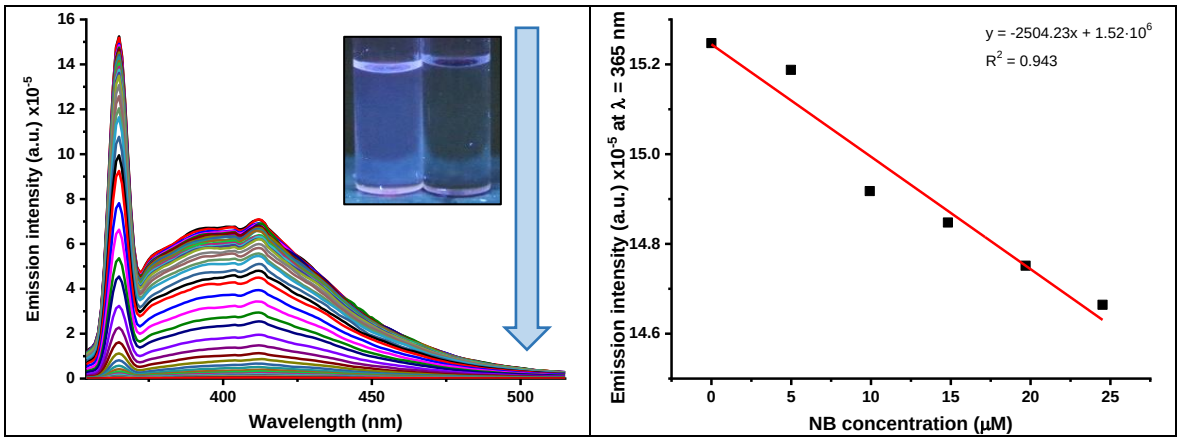

Figure 20. Titration curves (up left) and calibration for the limit of detection using emission values at 365 nm (up right) of an AR85 solution, 2.5 μM in toluene, under increasing concentrations of DNT. Titration curves (down left) and calibration for the limit of detection using emission values at 365 nm (down right) of an AR85 solution, 2.5 μM in toluene, under increasing concentrations of NB.

For both DNT and NB, the form of the titration curves were similar, and also very similar to the previous titrations. DNT presented two emission maxima, one at 365 nm and other at 394 nm, while NB also presented two very similar emission maxima, at 365 nm and at 400 nm. For both emission maxima, the LOD was calculated using measured values (different from 0) by fitting the initial values to a mean square linear regression and using the R program.[29] For both analytes, and for the four emission maxima (although only one of them is shown in Figure 20), a **LOD of 2.16 nM for DNT and NB** was obtained, slightly higher than the LOD obtained for the other analytes analysed.

The simultaneous plotting of the variation of the emission intensity of a solution of AR85 in toluene versus the increasing concentration of the five studied analytes showed a higher selectivity in the response of AR85 to the most nitrated derivatives (Figure 21). That apparently depended on the number of the nitro groups in the molecule and the phenol moiety to exert an increased response of the fluorescent quenching at very low concentrations of the analyte. Albeit the fastest decrease of the fluorescence of AR85 happened in the presence of increasing amounts of TNP, the lowest LOD was found in the presence of TNT.

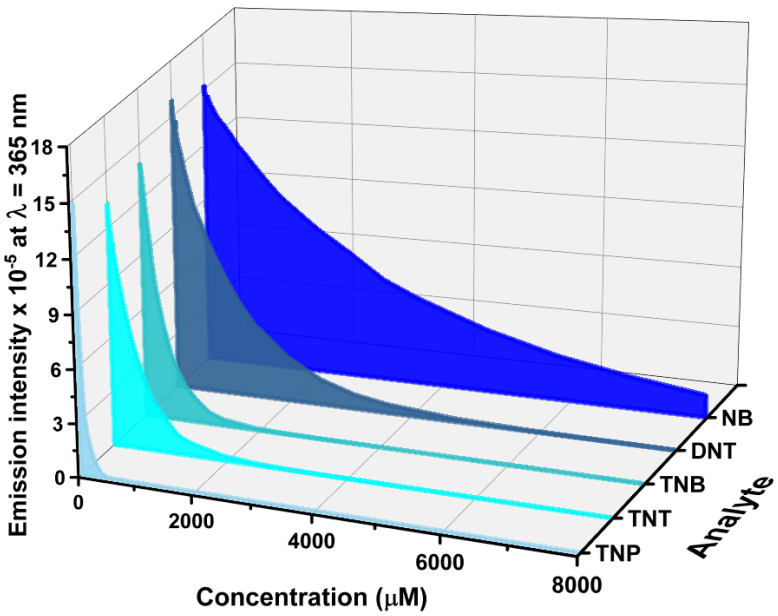

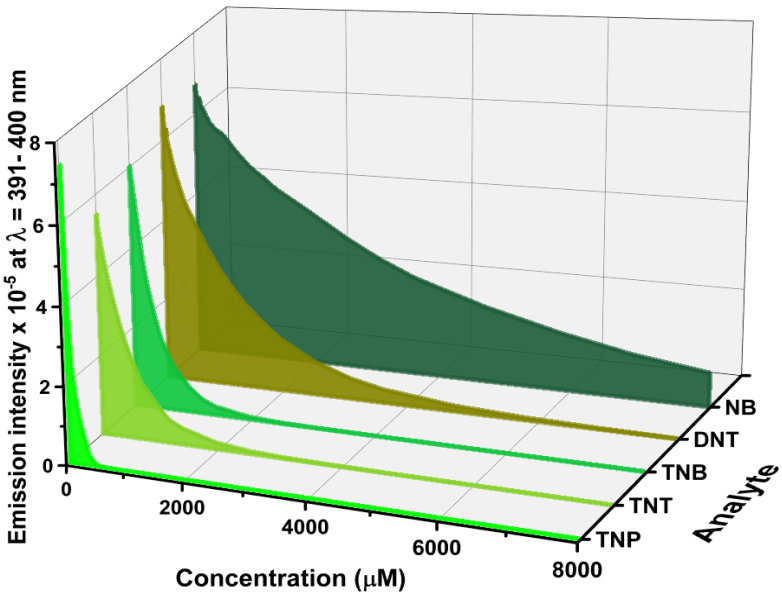

Figure 21. Variation of the emission intensity of a 2.5 µM solution of AR85 in toluene versus increasing concentrations of TNP, TNB, TNT, DNT and NB at the two emission maxima: 365 nm (up) and 391-400 nm (down).

4.5.5. Application under real-life conditions:

The extreme sensitivity of AR85 to the presence of TNT may have several practical applications. One of the most used methods for the detection of TNT traces consists of a swab passed through a surface to get hidden traces of solid TNT which is then subjected to analytical methods to determine its quantity or concentration.

As an alternative to these methodologies, we performed a controlled experiment to test AR85 as a powerful probe for TNT using the procedure followed in the current methods.

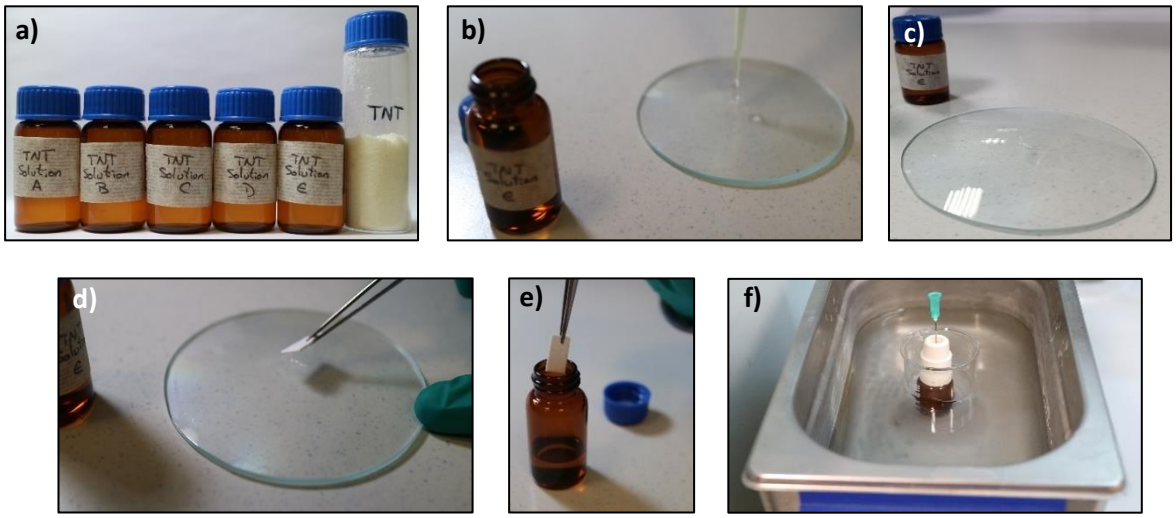

Figure 22. Experimental procedure for its use as cotton swab: TNT solutions used in the experiment (a), TNT deposition process on the watch glass (b), TNT sample after the air-drying process of the solution (c), capture of the TNT with a piece of filter paper (d), insertion of filter paper into a topaz vial (e) and sonication of the sample after removal of the filter paper (f).

Thus, increasing amounts of TNT (everyone calculated to be dissolved in a final volume of 2.5 ml to afford the appropriate concentrations for the titrations) were deposited on a watch glass and left to evaporate to dryness. A fragment (1 cm × 0.5 cm) of filter paper was slid over the watch glass to capture the TNT traces. Each piece of filter paper was then placed in a topaz vial to which 3 ml

of MeOH were added. Next, every vial was placed in an ultrasonic bath for a period of 5 minutes. After this, the filter paper was removed from the vial and the solvent was evaporated until complete dryness. Finally, the probe dissolution and more toluene were added to get a final concentration of AR85, 2.5 µM in a final volume of 2.5 ml The experimental procedure followed is as shown in the images in Figure 22. Afterwards, the fluorescence emission spectra of the different solutions prepared by this procedure were recorded. In addition, the blank (sample only containing probe) was measured three times. In this titration, λ_{em} = 365 and 391 nm.

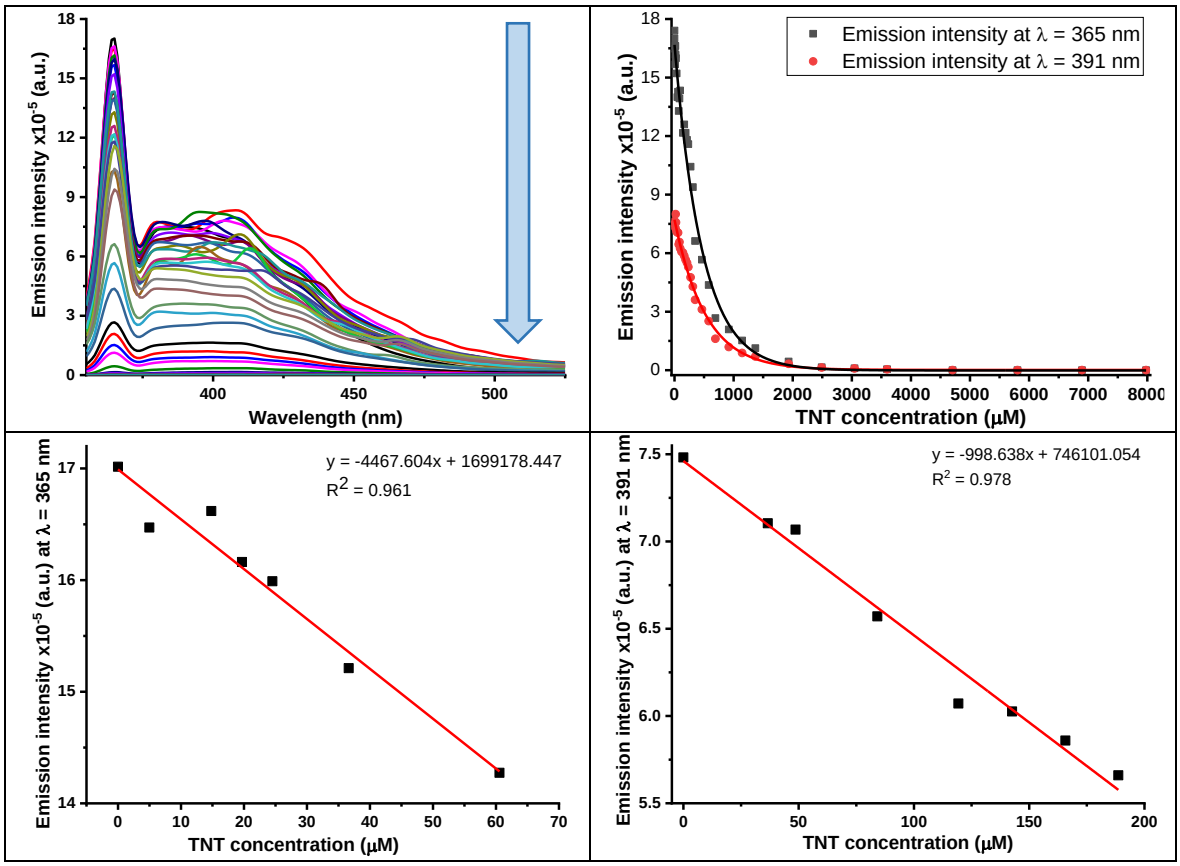

Figure 23. Titration curves (up left), fluorescent profile at 365 and 391 nm (up right), calibration for the LOD using emission values at 365 nm (down left) and calibration for the LOD using emission values at 391 nm (down right) of an AR85 solution, 2.5 µM in toluene, in contact with increasing amounts of TNT collected on a paper filter, dissolved in 2.5 ml toluene, to give progressive TNT concentrations.

The titration profile for TNT showed on Figure 23 was obtained. Again, the LOD within the values measured (different than 0) was calculated by adjusting the initial values to a mean square linear regression and using the R program.[29] Because of the large fluctuations in the spectra, a careful selection of representative values and outliers to be removed was performed with the help of the R program. The values at 365 nm led to **a LOD of 17.31 µM or 3.93 ng of TNT per millilitre** of solvent. Analogously, linear regression at low concentrations of TNT, calculated by using emission values at 391 nm, led to **a LOD of 17.24 nM or 3.91 ng of TNT per millilitre**, showing that the detection of TNT residual on surfaces by using a simple filter paper as swab was performed quantitatively with good reliability and accuracy under real-life conditions. Weighing the filter paper in all steps, we estimated that in the cases of the lowest concentrations (up to around 700 µM), the swap collected almost 100% of TNT, and within the highest concentrations (from 700 µM to the end of the titration) about 90%, thus supporting the feasibility of the detection process. The large fluctuations observed in the titration spectra of Figure 23, with respect to clean spectra observed in Figure 16, could be produced by small impurities acquired during the TNT absorption process, like dust or solvent residuals, therefore a careful study of interferents was performed to understand the implications that should have in the measurements of TNT detection.

4.5.6. Interferents analysis:

The effects that the presence of different cations, anions, redox agents, other explosives, etc may have on the TNT determination of AR85 have been studied and the results are shown in Figure 25 as normalized emission intensity values, by using AR85 maximum emission intensity as the reference. Those tests were performed by dissolving AR85 in THF (2.5 µM) as a general solvent (so the comparison with the tests in toluene is only approximate because many of the interferents are not soluble in toluene), then adding TNT (8 µl 5 mM solution in MeOH, 8 eq.), and then adding to each sample vial the corresponding analyte, which are shown in Figure 24 below.

Cations			Anions		Redox agents and other explosives	
Ag^{+}	Cu^{2+}	Co^{2+}	F^{-}	NO_2^{-}	H_2O_2 (8 µl 5 mM in H_2O, 8 eq)	
Ni^{2+}	Fe^{3+}	Pd^{2+}	Cl^{-}	H_2PO_4-	TNB (8 µl 5 mM in MeOH, 8 eq)	
Sn^{2+}	Sc^{3+}	Ir^{3+}	Br^{-}	HSO_4^{-}	HCl	*m*-CPBA (2mg)
Cd^{2+}	Al^{3+}	Cu^{+}	I^{-}	AcO^{-}	HNO_3	TATP (2 mg)
Zn^{2+}	Hg^{2+}	Ru^{3+}	BzO^{-}	CN^{-}	Oxone	HMTD (2 mg)
Pb^{2+}	Au^{3+}	Pt^{2+}	NO_3^{-}	SCN^{-}	Hydrazine	

Figure 24. Analytes used for the interferent assay.

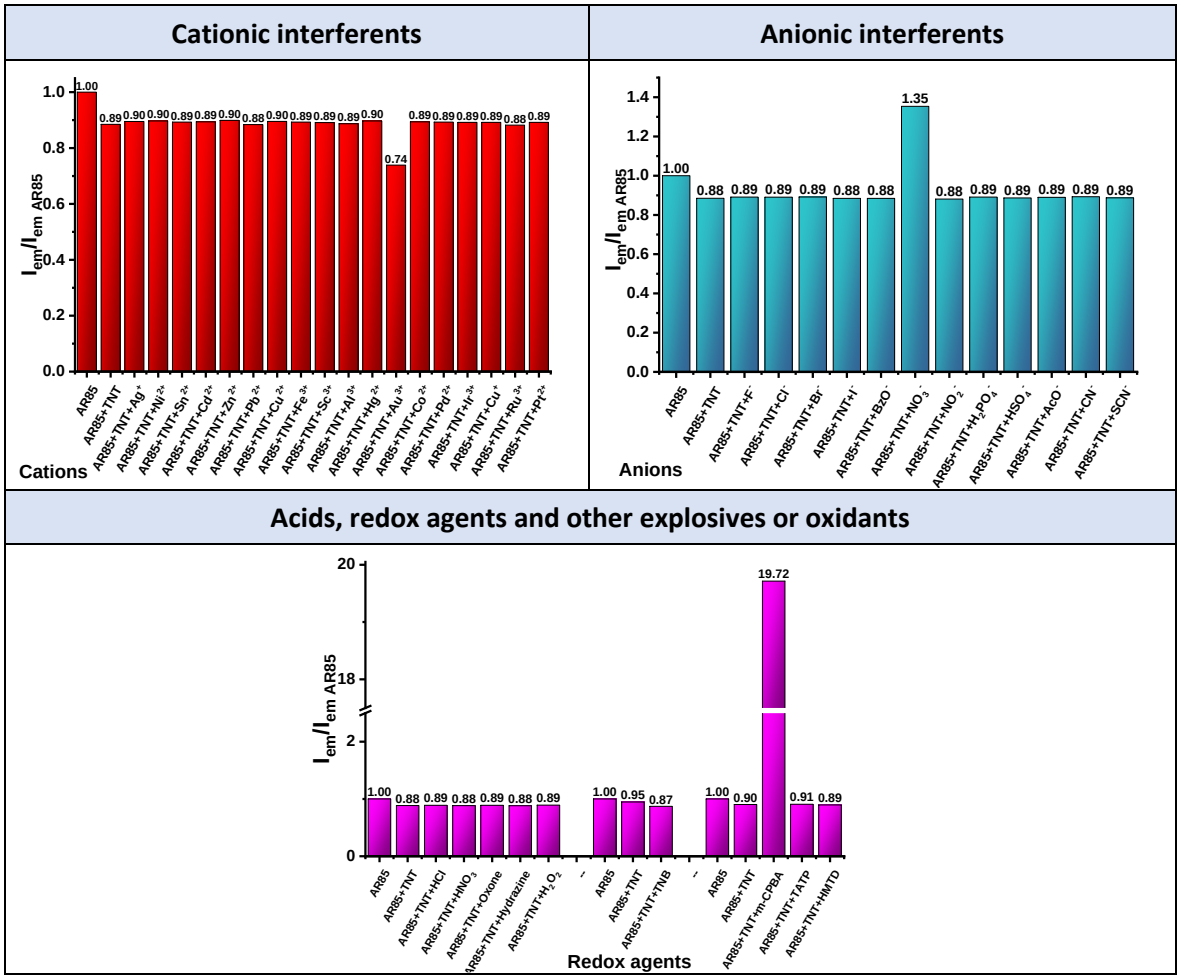

Figure 25. Interference tests between AR85 and common cations (up left), anions (up right), acids, redox agents and other explosives or oxidants (down) in normalized emission intensity graphs, using AR85 measurement as reference.

Every time the mixture of solvents was modified, a reference solution of AR85 was used (experiments with redox agents and other explosives or oxidants). In all cases, a slight decrease in the intensity of the probe emission was observed after the addition of 8 equivalents of TNT. In most of the experiments, the intensity of the fluorescence emission did not change after the addition of 8 equivalents of common cations, anions, redox agents or other explosives in solution, except in three cases:

- In the presence of NO_3^- the fluorescence increased notably, but there was no effect of the presence of NO_2^- in the dissolution.
- There was a drop in fluorescence in the presence of Au^{3+}, albeit it was not considered a common interferent.
- *m*-CPBA produced an enormous increase in fluorescence because of the oxidant nature of the reagent, but there was no effect of the presence of explosive oxidants such as TATP or HMTD.

Nitrate anion can be found in explosive mixtures such as ammonium nitrate; therefore, a full titration analysis of AR85 with ammonium nitrate was accomplished. First, a previous study of solvents for the titration was performed (Figure 26) and concluded that to perform the titration in the closest conditions to previous examples, the mixture of toluene and 5% v/v of DMSO was the most appropriate.

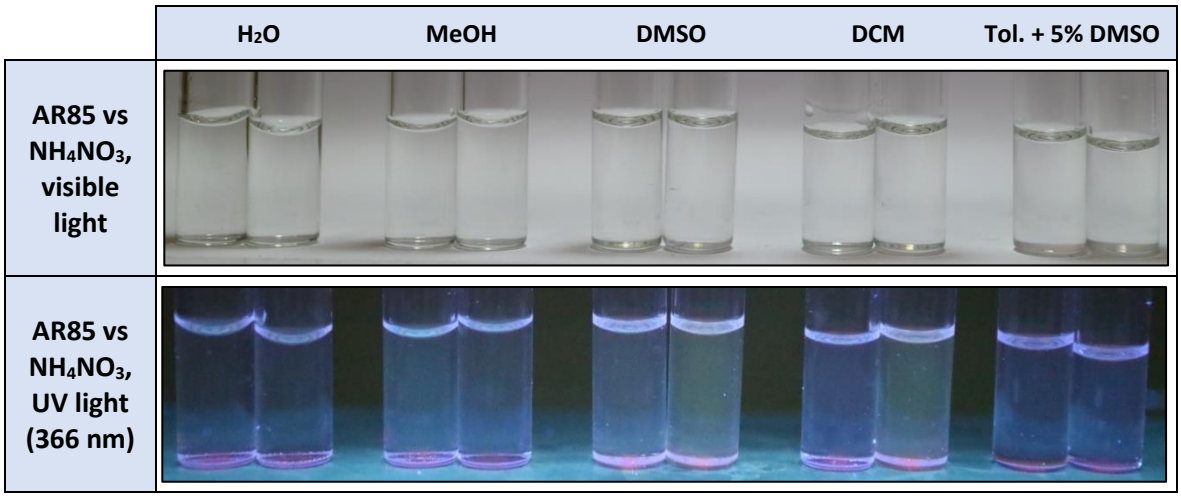

Figure 26. Solvent test. Pairs of 10 µM solutions of AR85 (left vial of each pair) and probe solution with 2 mg of NH_4NO_3 (right vial of each pair) in different solvents under visible light and 366 nm light.

Thus, on a solution of AR85 (2.5 µM) in a mixture of toluene with a 5% DMSO, successive and increasing amounts of NH_4NO_3 from a concentrated solution in the same solvent were added. In this titration, λ_{em} = 365 nm and 397 nm. Measurements were carried out immediately after the addition, resulting in the graphs shown in Figure 27.

The LOD from the titration plot values was calculated by IUPAC-consistent methods.[27] In this case, as before, the LOD was estimated within the values measured (different than 0) by adjusting the initial values to a mean square linear regression and using the R program.[29] In this way, linear regression at low concentrations of TNP, by using the emission values at 365 nm, gave **a LOD of 11.31 µM or 0.90 µg of NH_4NO_3 per millilitre**. Again, the LOD was calculated by using emission values at 397 nm, determined by the same methodology, gave a related **LOD of 9.60 µM**, much higher, in both cases, than in previous examples with nitrated explosives or taggants. Thus, the detection of ammonium nitrate, albeit in much higher amounts than nitrated explosives, complement the usefulness of the fluorescent probe in the detection of traces of explosive substances.

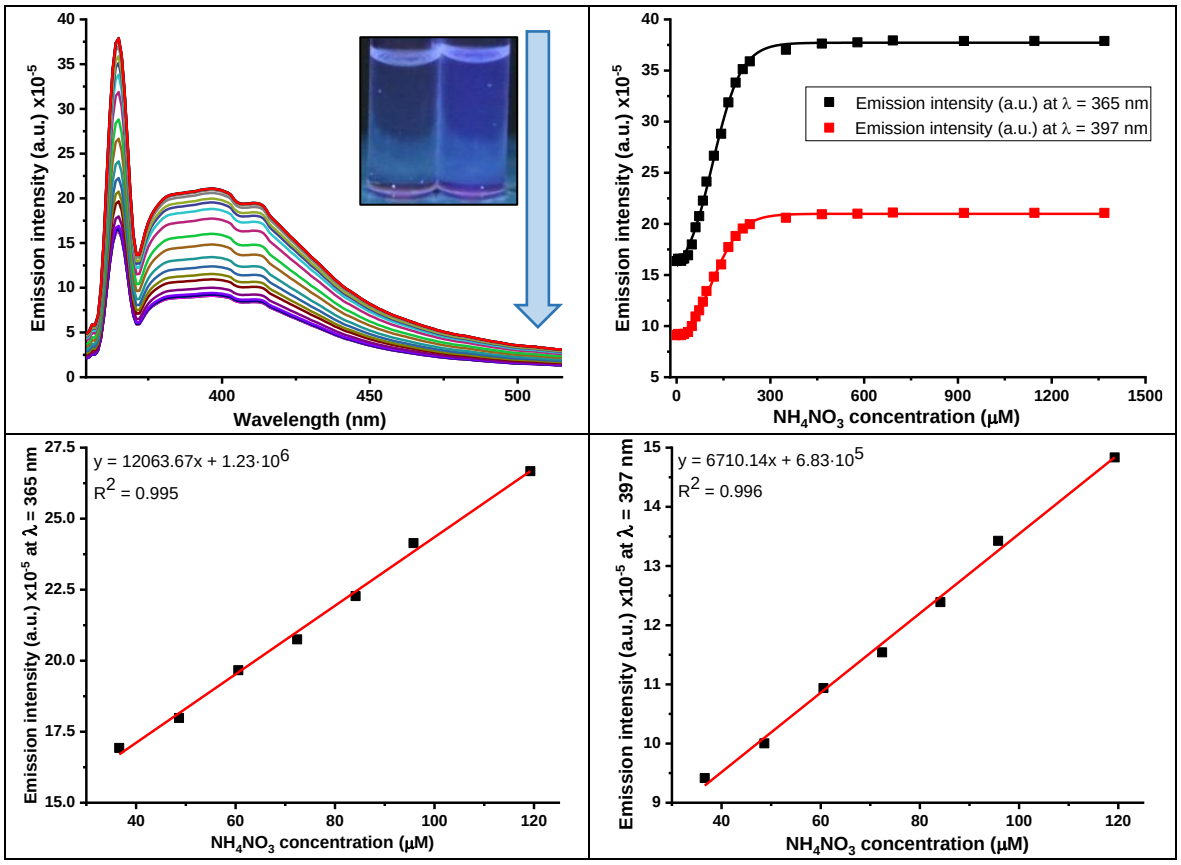

Figure 27. Titration curves (up left), fluorescent profile at 365 and 397 nm (up right), calibration for the LOD using emission values at 365 nm (down left) and calibration for the LOD using emission values at 397 nm (down right) of a 2.5 μM AR85 solution under increasing amounts of NH_4NO_3.

To complement this series, the effect of the other explosives was tested using the swab methodology by performing the experiments in the presence of mixtures of TNT and another explosive in each case. Thus, increasing amounts of equimolecular amounts of TNT and another explosive (TATP, HMTD, TNB, NB, DNT, TNP, NH_4NO_3) were dissolved in 2.5 ml, deposited on a watch glass and then a fragment of filter paper (1×0.5 cm) was slid over everyone, placed in a topaz vial and added of 3 ml of MeOH. Next, the vials were sonicated in an ultrasonic bath for 5 minutes, after that the paper fragments were removed and the solvent was evaporated under nitrogen stream and gentle warming. Finally, 2.5 ml of AR85 in toluene were added and the fluorescence emission spectra were measured. The fluorescence emission intensities corresponding to the measurements at 365 and 391 nm are shown Figure 28.

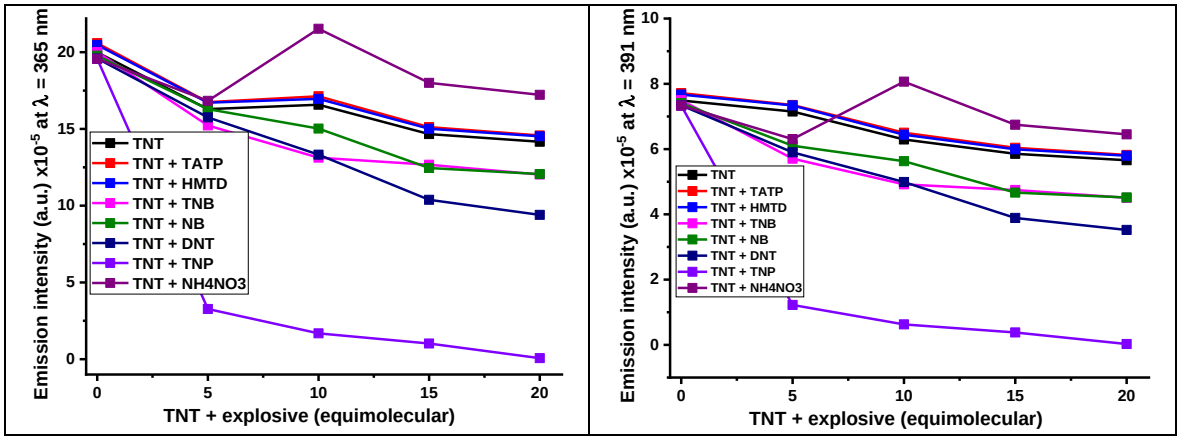

Figure 28. Fluorescence profile at 365 nm (left) and 391 nm (right) of a 2.5 μM AR85 solution in toluene, in the presence of increasing amounts of different explosives collected on a piece of filter paper.

Figure 28 showed that the fluorescence values corresponding to TNT + TATP and TNT + HMTD were similar to the presence of TNT alone, so those explosives do not interfere with the determination of TNT (as observed in Figure 25), as well as the presence of the explosive taggants DNT and NB. The decrease in fluorescence in the case of TNP is remarkable because of the higher sensitivity of AR85 to TNP with respect to TNT. In the case of NH_4NO_3 addiction, the behaviour was anomalous due to the contrary behaviour of each species, a fluorescence emission decrease with TNT from low concentrations, and a fluorescence emission increase with NH_4NO_3 at high concentrations.

Looking for a large scope of the method by extending the procedure to environmental samples, the detection of TNT traces in water and sand were tested. Thus, increasing amounts of TNT, calculated to give 0, 5, 10, 15 and 20 equivalents when dissolved in 2.5 ml, were added to 10 ml of filtered tap water samples, then the mixtures were extracted with toluene and the organic fractions were collected and then evaporated under nitrogen flow and gentle warming. Finally, 2.5 ml of AR85 in toluene, were added and the fluorescence spectra were measured (Figure 29 up). Analogously, increasing amounts of TNT, were added to samples of 1 g sand (grain size approximately 300-350 µm) placed in topaz vials, then 3 ml of MeOH were added and vials were sonicated in an ultrasonic bath for a period of 2 minutes. After that, the content was filtered, the solid was discarded and the solvent was evaporated. Finally, AR85 was added and the fluorescence emission spectra were recorded. (Figure 29 down).

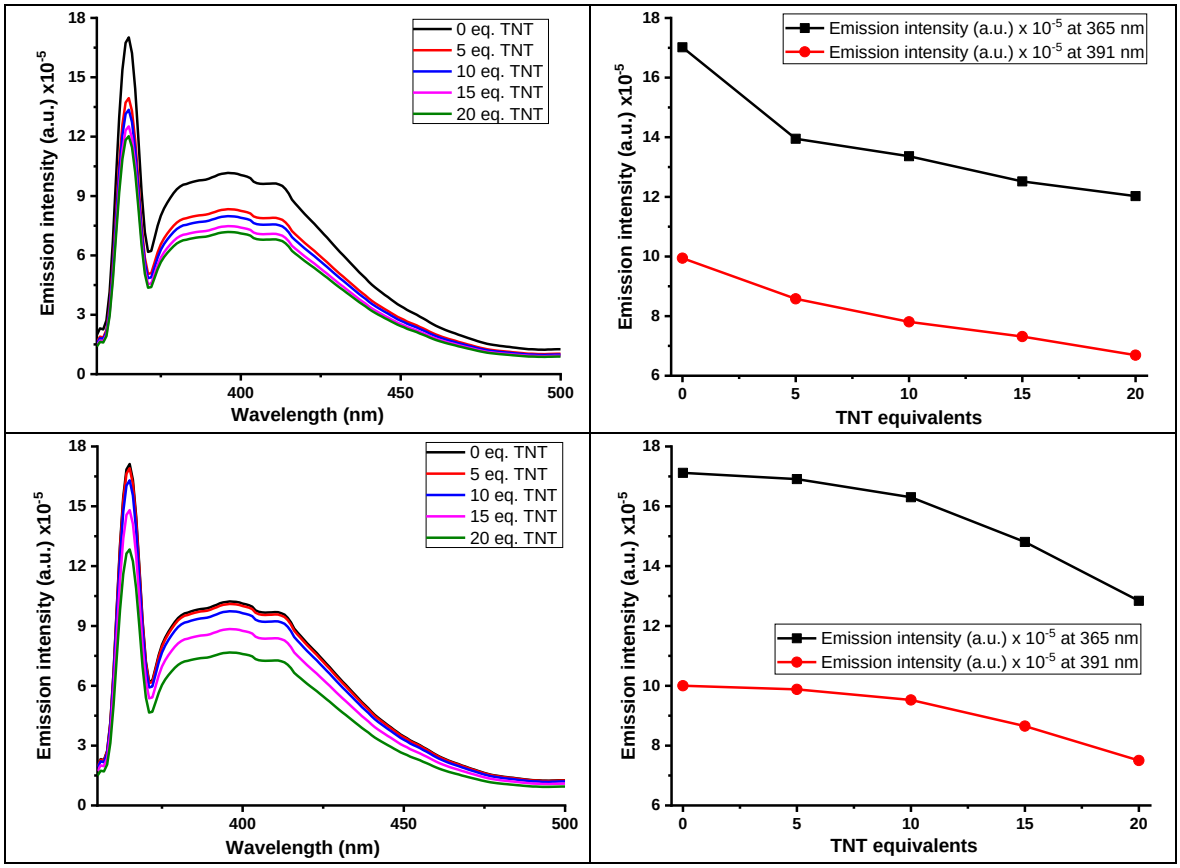

Figure 29. Emission intensity spectra (up left) and fluorescence profiles at 365 and 391 nm (up right) of a 2.5 µM AR85 solution in toluene, in contact with increasing amounts of TNT collected from filtered tap water. Emission intensity spectra (down left) and fluorescence profiles at 365 and 391 nm (down right) of a 2.5 µM AR85 solution in toluene, in contact with increasing amounts of TNT collected from sand.

From the detection tests carried out in water, we concluded that the sensitivity of AR85 probe to TNT in water remained intact, being able to detect the presence of TNT in very low amounts. On the other hand, from the detection assays performed in sand, we noted that the sensitivity of AR85 probe to TNT in sand was significantly affected. The probe was still capable of detecting low

concentrations of TNT, but the fluorescence quenching was much lower than in the previous case, probably because retention of TNT on sand could give to incomplete extraction of TNT from the samples. Therefore, it is possible to perform a fair detection of TATP in water or sand, but sensitivity from water samples was much better than from sand samples.

4.5.7. Detection mechanism:

To understand the interaction between AR85 and TNT, an NMR titration in deuterated benzene was performed. Initially, ^{1}H-NMR spectra of TNT (10 mg in 0.5 ml in C_6D_6) and AR85 (4 mg in 0.5 ml in C_6D_6) were performed as references. After this, increasing amounts of TNT (Figure 30) were added to the NMR tube corresponding to AR85 to carry out the titration (Figure 31).

Addition number	TNT added (µg)	Total TNT added (µg)	Addition number	TNT added (µg)	Total TNT added (µg)
1	0	0	**10**	60	150
2	5	5	**11**	150	300
3	5	10	**12**	200	500
4	5	15	**13**	300	800
5	5	20	**14**	600	1400
6	10	30	**15**	1800	3200
7	10	40	**16**	3600	6800
8	20	60	**17**	3600	10400
9	30	90	**18**	5400	15800

Figure 30. Amounts of TNT used in ^{1}H-NMR titration.

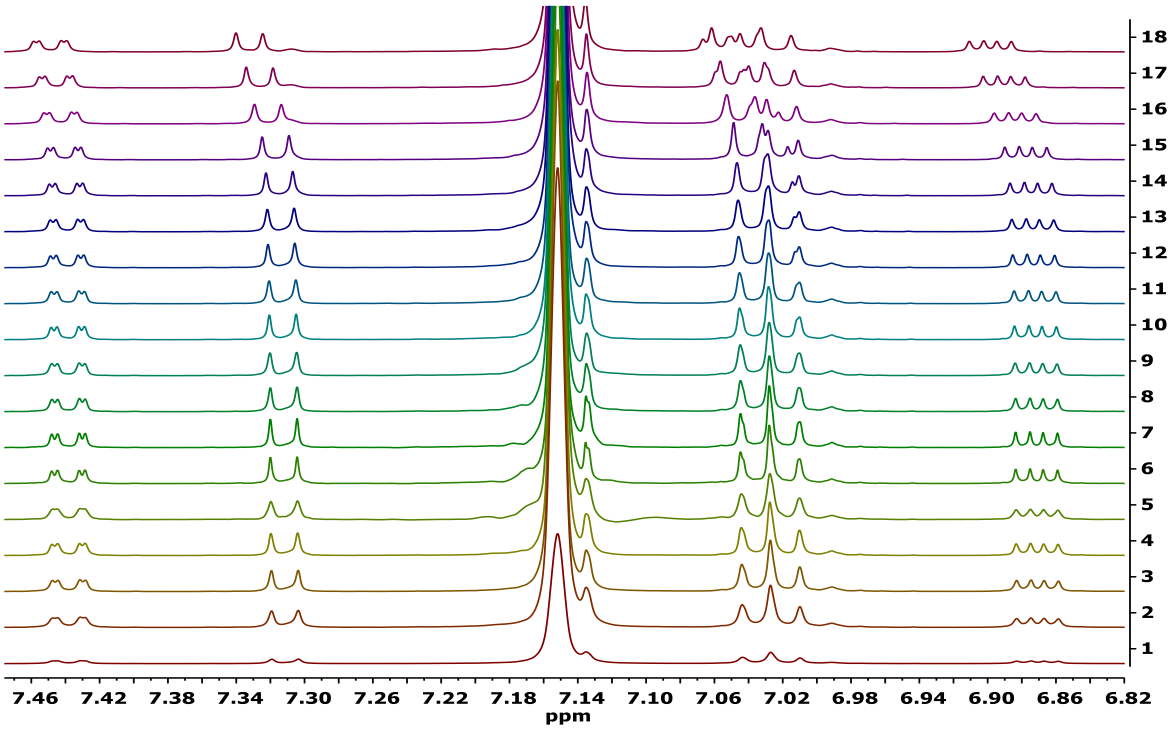

Figure 31. ^{1}H-NMR (C_6D_6, 500 MHz) titration of AR85 (4 mg in 0.5 ml of C_6D_6) with increasing amounts of TNT.

An expanded region between 7.45 and 6.85 ppm (Figure 31) showed the interaction between AR85 and TNT was seen as a complex coupling and simultaneous shift of the triplet at 7.03 ppm and sifting of the signals at 6.88 and 7.33 ppm, by apparent π-π stacking interaction between TNT and the phenanthroline moiety of AR85. The rest of the signals in the aliphatic region as well as the signal at 5.22 ppm remained unchanged, regardless of the amount of TNT added.

5. DETECTION OF TNT ON SURFACES

To complete a real-life alternative to current swab methodologies, a quick TNT fluorescent detection should be required. AR85 was only faintly fluorescent for naked eye clear detection, therefore we searched between the collection of fluorescent probes of Figure 4. AR51, AR52, AR55 and AR67p were extremely fluorescent compounds in common organic solvents of intermediate polarity (Figure 32) but they did not show any characteristic sensitivity to common cations, anions, oxidant o reducing compounds in organic solvents.

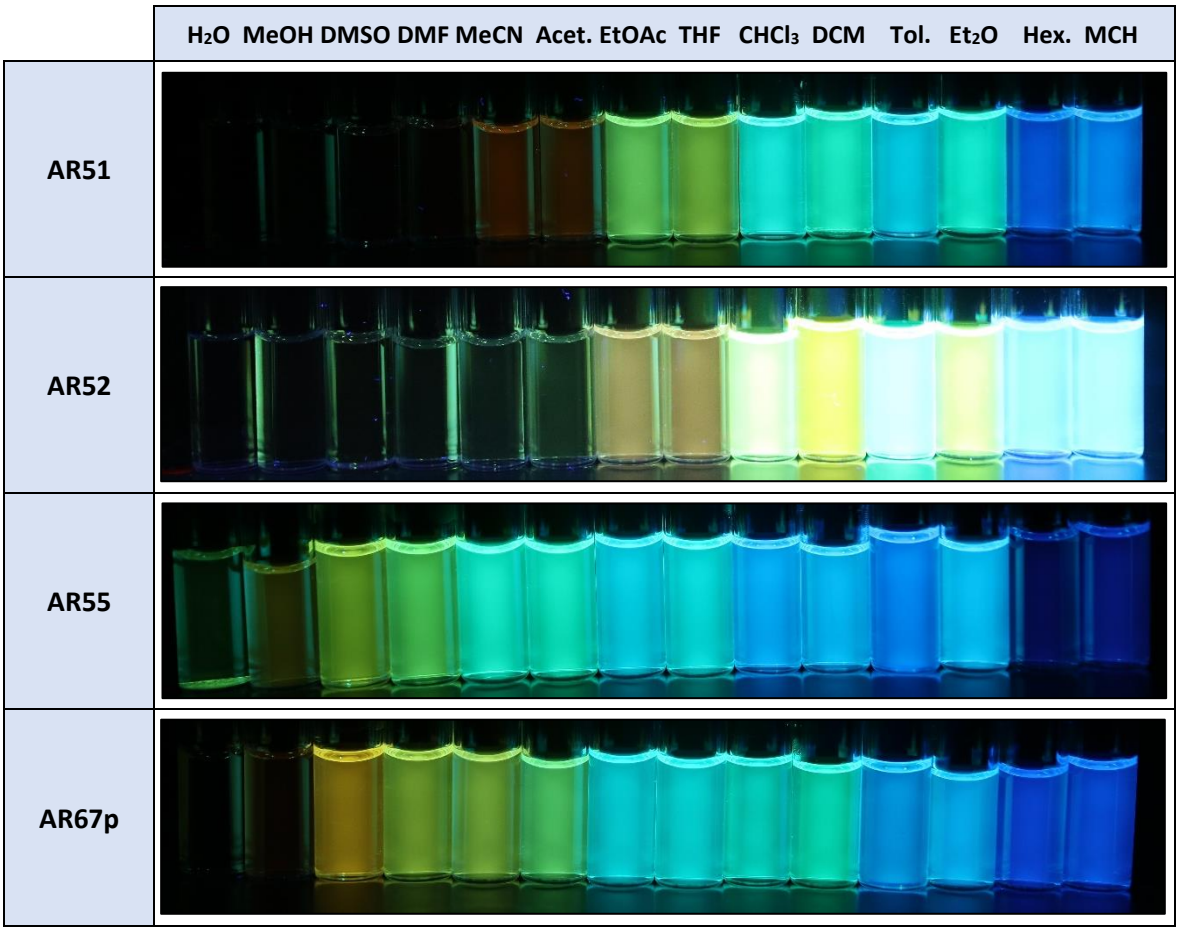

Figure 32. Solvatochromism images of AR51, AR52, AR55 and AR67p under 366 nm light.

Therefore, we selected the most representative of them, AR67p, a very fluorescent compound in all common solvents, except methanol and water. In addition, it was the compound with the lowest fluorescence quantum yield ($Ø_F$ = 84.60%), not considering AR85, so it will allow us to better watch the fluorescence changes occurring.

This compound was therefore used to prepare a solid material for solid TNT detection, based on the ability of TNT of quenching fluorescence.

5.1. Synthesis. Absorbance and fluorescence interpretation

The synthesis of AR67p was performed by Suzuki-Miyaura coupling between equimolecular amounts of *N*-(1-Boc-piperidin-4-yl)-4-bromonaphthalene-1,8-dicarboxylmonoimide (AR43) and 2-(4,4,5,5-tetramethyl-1,3,2-dioxaborolan-2-yl)indolo[3,2,1-jk]carbazole (AR66) under $Pd(PPh_3)_4$ catalysis in refluxing toluene:*n*-butanol:water 4:1:2 v/v for 24 hours. Work-up and column chromatography afforded AR67p as a yellowish solid in 86 % yield. The synthetic process is shown in Figure 33.

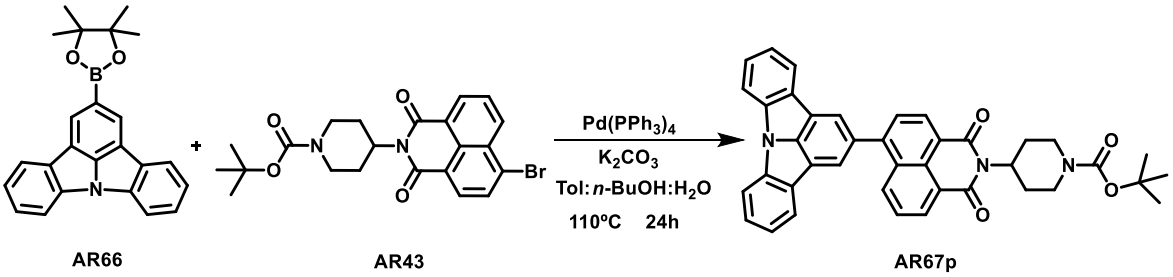

Figure 33. Synthesis of AR67p product.

Deprotection of AR67p by trifluoroacetic acid in chloroform gave quantitatively AR67d (Figure 34), as well a very fluorescent and solvatochromic compound.

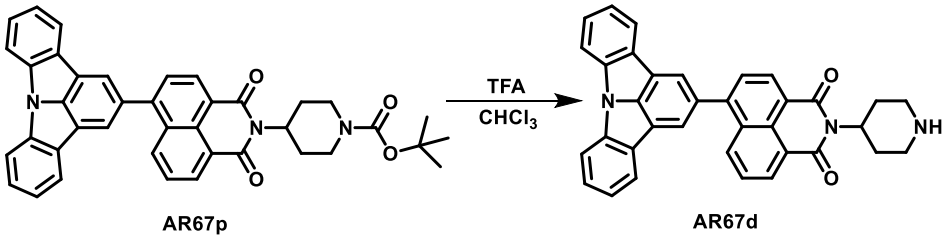

Figure 34. Synthesis of AR67d product.

Both compounds showed very similar optical characteristics. Comparing the fluorescence quantum yields (Figure 35), a slightly decrease for the unprotected compound was observed, which increase the range for appreciating the fluorescence variations that occur.

	$Ø_F$ (%)
AR67p	84.60
AR67d	80.01

Figure 35. Fluorescence quantum yields of the amino-protected and unprotected products.

As can be seen in Figure 36, the form of the absorbance and emission curves were very similar for both compounds, therefore, they had similar optical characteristics. Compound AR67p showed higher fluorescence in less polar solvents, whereas compound AR67d exhibited higher emission in solvents of intermediate polarity, such as EtOAc or $CHCl_3$. Moreover, in the emission plots an evident bathochromic shift was observed.

Both compounds were insoluble in water and showed a low emission intensity in MeOH. The most notable difference between the two was the low emission intensity in hexane and methylcyclohexane when deprotection reaction was performed.

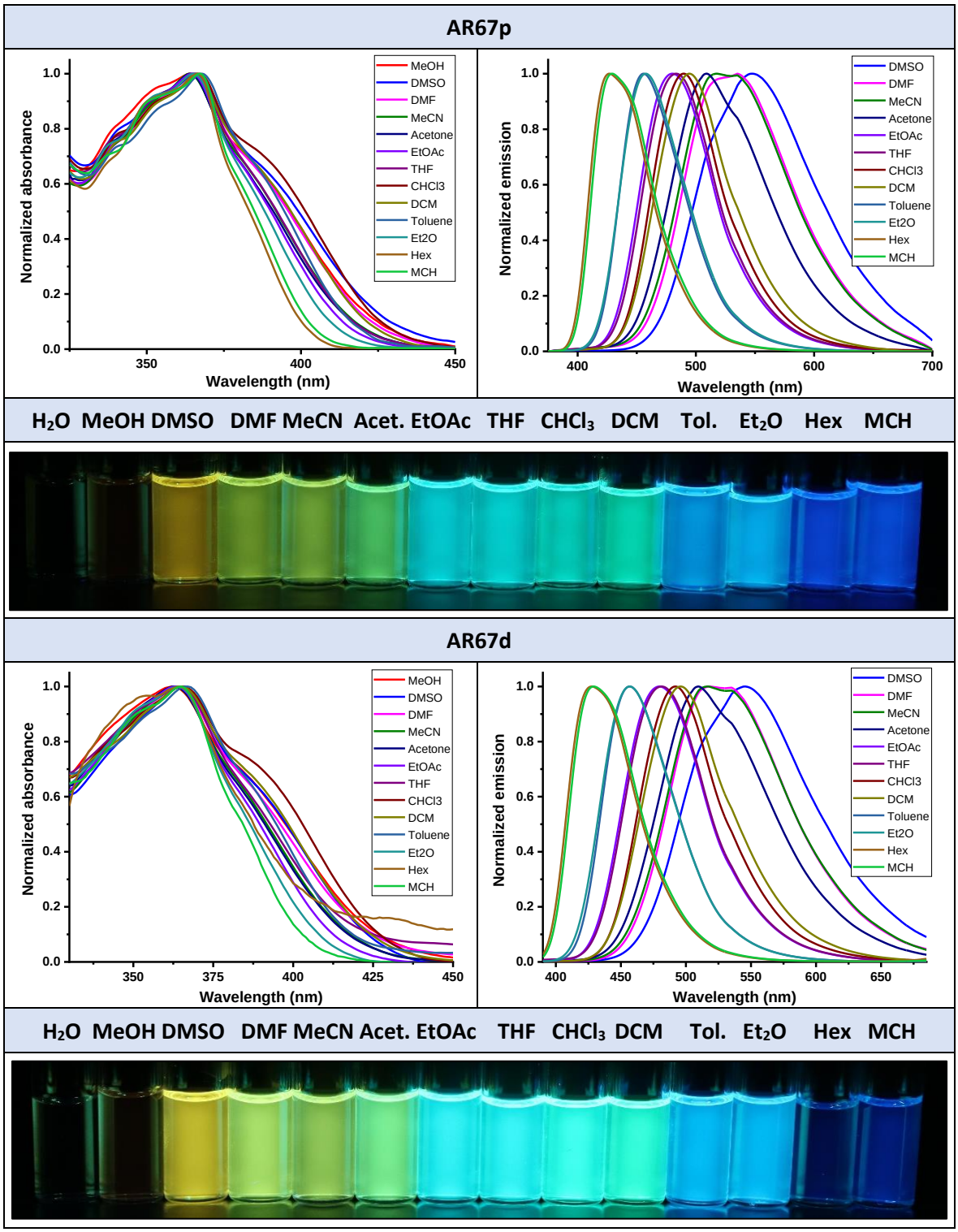

Figure 36. Normalized absorbance curves, normalized emission curves and images of the fluorescence of AR67p and AR67d solutions in different solvents under UV light (366 nm).

5.2. Sylgard synthesis

Sylgard-184 is a commercial variant of polydimethylsiloxane (PDMS) widely used in the energy materials industry due to its simple two-part formulation, ease of mixing and casting and favourable cure times.[33]

Sylgard-184 is made from a base and a curing agent (Dow Corning, commercially available as a kit) which are, generally, mixed in a 10 to 1 proportion. However, it is very common for this ratio to be modified to try to adjust the properties of the material to the requirements of the application. Thus, the amount of curing agent added can be increased to increment its stiffness, the curing time or temperature can be varied[34] and plasticizers can be added to modify its workability.[35]

It was very simple to use. The two components were mixed at a 10:1 resin-to-curative ratio, the gas was removed and, finally, the polymer was cured at 70ºC for 2 hours. Before use, the polymer obtained was washed with hexane and DCM. The transparent fluid obtained can be cured both at room temperature and with heat in a cooker, and the resulting polymer (Figure 37) was characterised by high transparency and good dielectric properties.

Figure 37. Sylgard-184 film.

Besides the Sylgard-184 discussed above, there are other varieties that are usually mixed with Sylgard-184 to try to modify its properties. The most common are:[36]

- Sylgard-182: unlike Sylgard-184, it is translucent and can only be cured by heat, so it has a longer working time.
- Sylgard-170: this is a black polymer with very similar properties to Sylgard-184, the difference being that it is used in medicine, more specifically in the field of prosthetics.
- Sylgard-527: is characterised by a lower viscosity than Sylgard-184. It is widely used to protect small and delicate components in the electronics industry.

5.3. Synthesis of the fluorescent material

Once the probe and the polymer had been obtained, the fluorescent material used in the detection of TNT on surfaces was synthesised.

[33] T. Kosta, T. R. Krawietz, J. O. Mares Jr, *AIP Conf Proc.*, **2020**, *2272*, 040007.
[34] I. D. Johnston, D. K. McCluskey, C. K. L. Tan, M. C. J. Tracey, *Micromech. Microeng.*, **2014**, *24*.
[35] R. N. Palchesko, L. Zhang, Y. Sun, A. W. Feinberg, *PLOS ONE*, **2012**, *7*, 12.
[36] Sylgard 184 Silicone elastomer kit. Obtained from: https://www.dow.com/es-es/pdp.sylgard-184-silicone-elastomer-kit.01064291z.html#overview, accessed: 06/04/2023.

Reaction of AR67d with equimolecular amounts of triethoxy(3-isocyanatopropyl)silane in chloroform at room temperature overnight gave the silylated derivative AR67d-Si. It was immediately subjected to reaction in toluene with Sylgard-184, previously activated with piranha and KOH solutions,[37] to get surface modified AR67d@Sylgard-184. This procedure appeared in the following Figure 38.

The probe attached to the Sylgard-184 polymer surface, AR67d@Sylgard-184, was used to perform contact tests in the presence of traces of solid TNT.

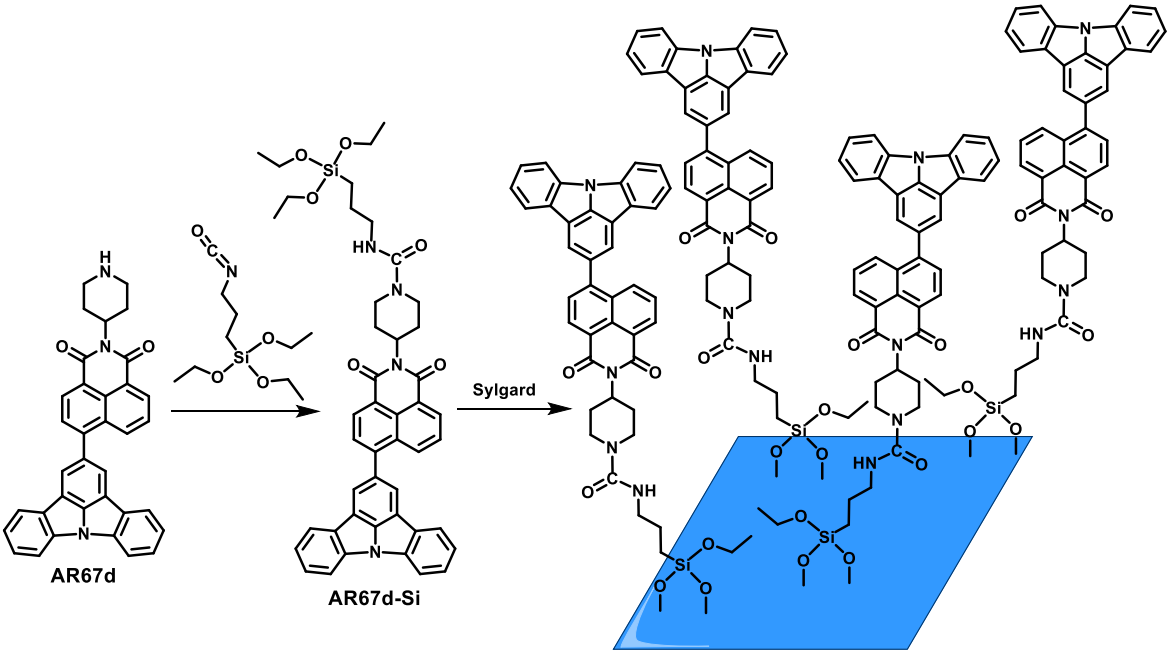

Figure 38. Experimental procedure of bonding to Sylgard.

5.4. Contact test with TNT

Once the fluorescent material was obtained, contact tests were carried out to detect TNT on surfaces. In these tests, 0.5 mg of TNT was deposited and distributed evenly on a clean slide, a fragment of AR67d@Sylgard-184 was picked up and dragged over the TNT covered area of the slide. In addition, 0.5 mg of TNT were diluted in 150 µl of MeOH, from them, 50 µl were taken and deposited on a finger covered with a clean, new glove, the finger was pressed on the surface of AR67d@Sylgard-184. For comparison purposes, several tests in the presence of common solvents of different polarity were also performed by placing 1 ml of solvent in a 12 ml topaz vial, AR67d@Sylgard-184 was fixed to the inside of the vial stopper and the vial was warmed by air until the complete evaporation of the solvent. The result can be observed in Figure 39.

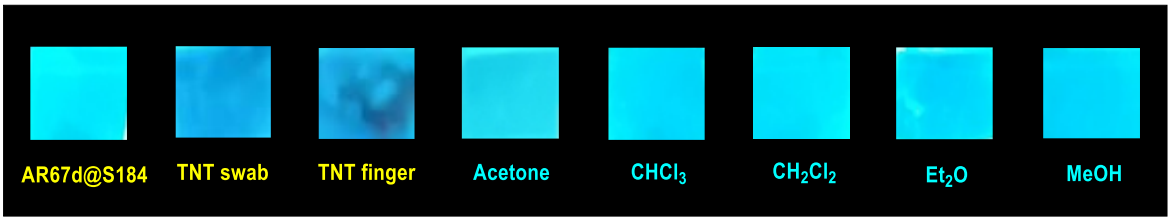

Figure 39. Qualitative studio under 366 nm of pristine AR67@Sylgard-184, after contact with TNT on a surface as the film was used as a swab, TNT on finger after pressed over the film and vapour of different solvents.

[37] D. Maji, S. K. Lahiri, S. Das, *Surf. Interface Anal.*, **2012**, *44*, 62–69.

As can be shown in Figure 39, there was a quenching of fluorescence against TNT, either by dragging or by pressure with the TNT-impregnated finger. Fluorescence variations were measured in both cases, resulting in the graphs shown in Figure 40. This variation was much stronger than in the presence of common solvents, where fluorescence variations were very slight.

For these measurements, λ_{exc} = 360 nm and λ_{em} = 462 (with TNT) and 467 (without TNT) nm.

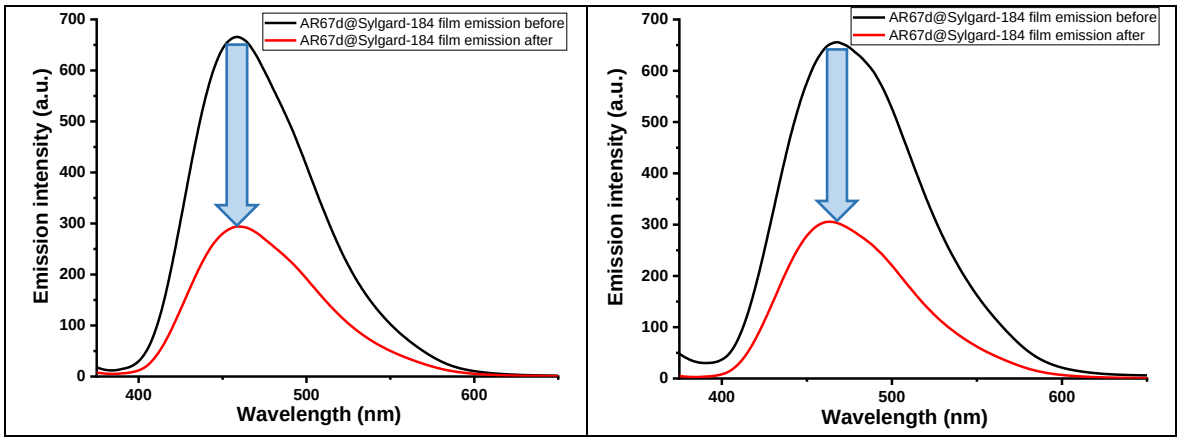

Figure 40. Fluorescence curves of pristine AR67d@Sylgard-184 and after contact with TNT on a surface as the film was used as swab (left) or after TNT of finger applied by pressing on the film (right).

The experiments showed a clear decrease in the fluorescent emission of the AR67d@Sylgard-184 film in the presence of TNT traces from solid surfaces either on glass or finger, with an irregular pattern in the case of TNT on finger, as shown in Figure 40. The quantitative measurements also showed a clear decrease in the initial fluorescence of the film. Therefore, AR67d@Sylgard-184 film is useful under real conditions for a quick qualitative detection of hidden TNT traces and, in combination with the quantitative detection of TNT traces on surfaces by AR85, in toluene solution, constitutes a comprehensive new method for the detection of hidden nitroaromatic explosives in the workplace. The system can be applied with little implementation of laboratory material at control points wherever it could be necessary.

As in the previous case, to extend the methodology to environmental samples, the detection of TNT traces in water and sand was also tested, this time by using AR67d@Sylgard-184. Thus, increasing amounts of TNT (0-0.10-0.20-0.30-0.40 mg) were added to 10 ml of filtered tap water samples. Every mixture was extracted with toluene and the solvent was evaporated under nitrogen stream and gentle warming. Then 0.5 ml of methanol were added on clean slide and dried by using a nitrogen stream. A fragment of AR67d@Sylgard-184 film was dragged over the TNT-coated area for each slide. Fluorescence measurements before and after contacting the polymer with the TNT were performed in all cases analysed. Figure 41 represents the emission variations for every film fragment measured before and after the process.

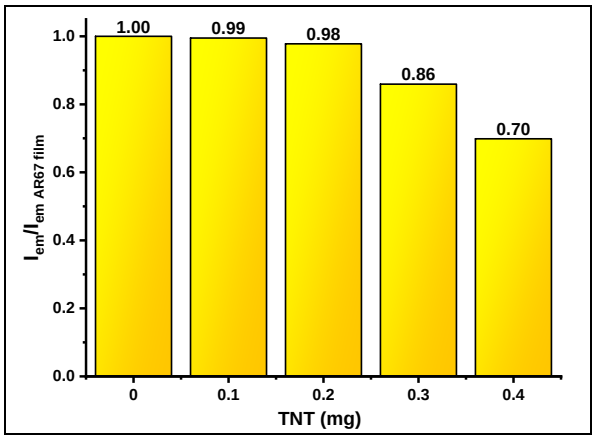

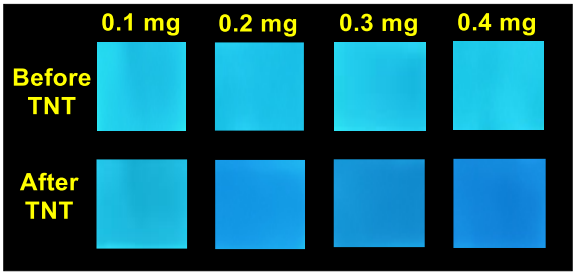

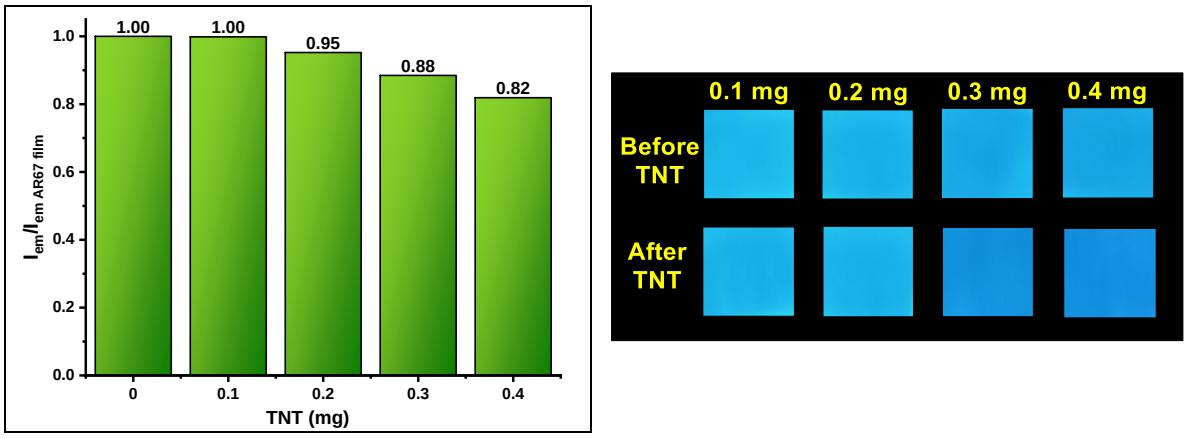

Figure 41. Variation of the fluorescence emission intensity of the AR67d@Sylgard-184 films before and after contact with increasing amounts of TNT (up left) and photographs under 366 nm UV light of AR67d@Sylgard-184 films before and after being in contact with increasing amounts of TNT (up right) collected from filtered tap water samples. Variation of the fluorescence emission intensity of the AR67d@Sylgard-184 films before and after being placed in contact with increasing amounts of TNT (down left) and photographs under 366 nm UV light of AR67d@Sylgard-184 films before and after being in contact with increasing amounts of TNT (down right) collected from sand.

The sensitivity of AR67d@Sylgard-184 to TNT under real conditions in experiments with water and sand was still quite good in both cases, but specially for samples from water in which the sensitivity was excellent for low amounts of TNT and, at higher amounts, the fluorescence quenching was remarkable. The retention of TNT by sand may affect also in this case to the sensitivity of the detection at low amounts of TNT. Therefore, the system is also suitable to perform a fair detection of TATP in water or sand.

6. CONCLUSIONS

In this chapter, we have described the proof of concept of a portable testing setup was for the detection of 2,4,6-trinitrotoluene (TNT), a common component in improvised explosive devices, as well as related explosives such as 1,3,5-trinitrobenzene (TNB), 2,4,6-trinitrophenol (TNP) and explosive taggants such as 2,4-dinitrotoluene (DNT) and nitrobenzene (NB).

As mentioned above, TNT is a secondary explosive for military use, the synthesis of which has evolved considerably over time. Initially, it was obtained from coal tar and now, it is produced from the nitration of DNT. Similarly, detection methods have also developed over time, from analytical methods used in airports or football stadiums (Figure 42)[38] to fluorometric methods such as those described in this chapter. The system developed allows for field-testing and generation of real-time results to test for TNT traces on surfaces by simply passing a piece of paper or of the PDMS-supported sensing material, AR67d@Sylgard-184, on the suspected surface of an ordinary object. In this way, the controlled trapping of the analyte in the paper or chemical sensor gives reliable results for the detection of TNT solid traces under real life conditions. In addition, the LOD obtained for this new system for detecting TNT traces on surfaces competes in accuracy with much more complicated and specialized alternative methodologies.

Figure 42. TrueTraces for explosives detection in football stadiums.

[38] Tecnología TrueTrace. Obtained from: https://www.flir.es/discover/threat-detection/explosives/true-trace/, accessed: 07/04/2023.

The system may have immediate applications in everyday use. Air samples at airports, government buildings, sports arenas or concert halls, should be checked for IED-containing nitroaromatic explosives to prevent terrorist acts, thus avoiding both material and personal damages.

The system provides for a low limit of detection of traces of TNT on surfaces, as it is required to be of practical use and competitive with current detection methods. As a complement, the preparation of a modified Sylgard film that is useful under real conditions for qualitative fluorescent detection of hidden traces of TNT on surfaces or fingers by a swab method was reported. The combination of quantitative and qualitative detection of TNT traces on surfaces constitutes a comprehensive new method for the detection of hidden nitroaromatic explosives in the workplace. TNT detection, as we have shown in this chapter, is a useful and non-invasive method suitable for explosive detection among recent explosive detection technologies to be applied whenever it is necessary for the detection of traces of IEDs before they can cause any harm.

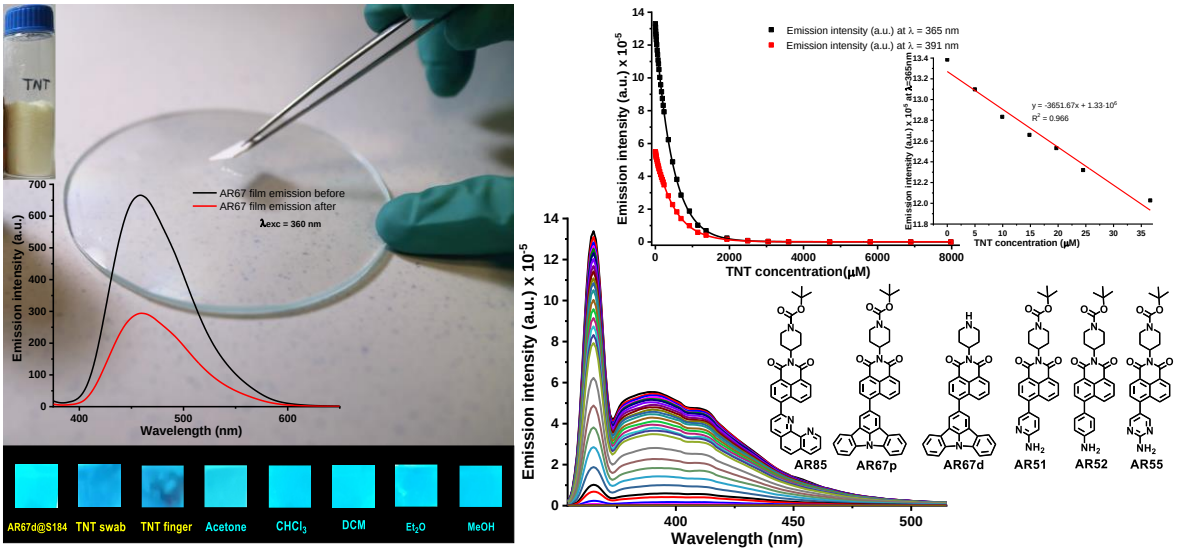

Figure 43. Summary of the experimental procedure performed in this Chapter.

CHAPTER 4

NMI DERIVATIVES: AGGREGATION

This chapter focuses on one of the most important properties of NMIs, the aggregation induced emission (AIE). NMI derivatives of different nature, obtained by different carbon-carbon coupling reactions, formed a variety of nanostructures that were analysed by Scanning Electron Microscopy (SEM), some of them resulting from the AIE phenomenon. For a number of compounds, the elimination of amino-protecting groups and the formation of free amines has led to the possibility of controlling aggregation depending on the protective groups in their structure, which can be useful, for example, in the field of biology.

1. INTRODUCTION

Over the past centuries, a wide range of materials, both natural and synthetic, have been exploited because they exhibit fluorescence, a property that has revolutionised many fields of industry. Although many phenomena associated with fluorescence are studied in dilute solutions, fluorescent materials are often used in aggregate state, for example as thin films for the development of OLEDs or nano-aggregates in aqueous media used for imaging.

One of the predominant characteristics of conventional fluorescent dyes is aggregation-caused quenching (ACQ),[1] which prevents them from achieving the best performance when in solid state or in aggregate state, but which is widely used in areas such as photoacoustic imaging or photodynamic therapy. Diametrically opposed to ACQ is aggregation-induced emission (AIE), a term first introduced in 2001 based on a study of 1-methyl-1,2,3,4,5-pentaphenylsilol,[2] which opened up a new research field for scientists and engineers. Luminogens that are weakly emissive in the molecular state but can be induced to emit efficiently in the aggregate state are called AIEgens, which are characterised by their helix or rotor structures.[3]

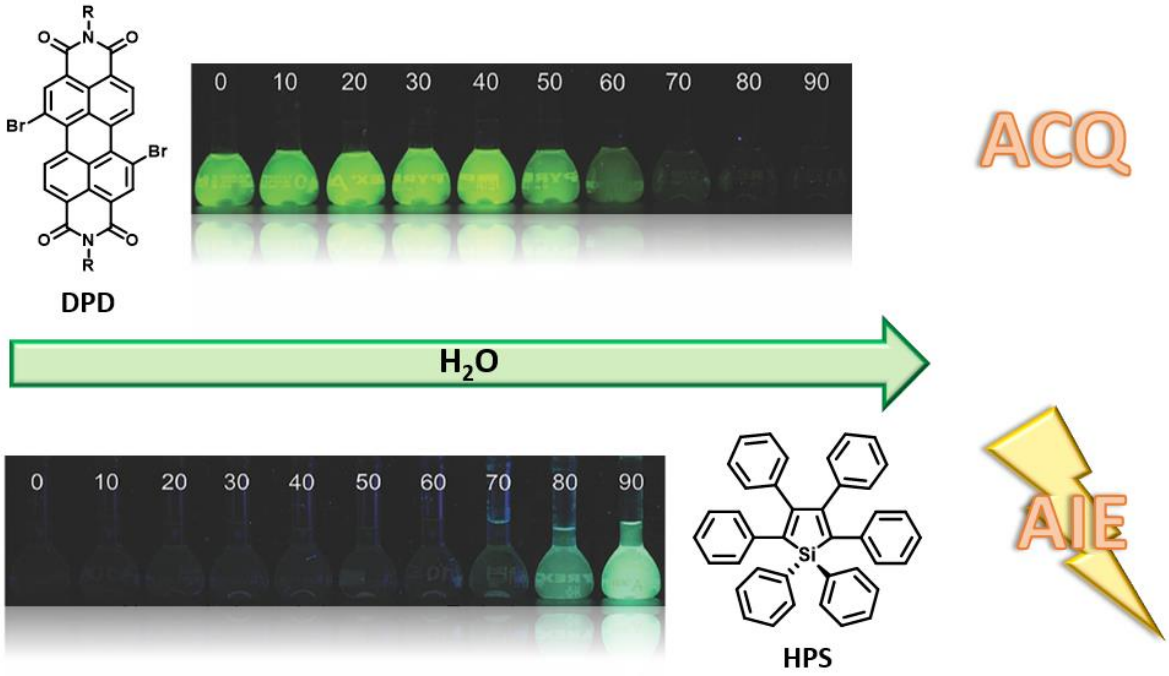

Figure 1. Example of ACQ by DPD (up) and AIE by HPS (down).

[1] a) T. Förster, K. Kasper, *Z. Phys. Chem.*, **1954**, *1*, 275. b) J. B. Birks, Photophysics of aromatic molecules, Wiley, London, **1970**.
[2] J. Luo, Z. Xie, J. W. Y. Lam, L. Cheng, H. Chen, C. Qiu, H. S. Kwok, X. Zhan, Y. Liu, D. Zhu, B. Z. Tang, *Chem. Commun.*, **2001**, 1740.
[3] a) C. Branas, F. J. Azcondo, J. M. Alonso, *IEEE Ind. Electron. Mag.*, **2013**, *7*, 6. b) Y. Gui, K. Chen, Y. Sun, Y. Tan, W. Luo, D. Zhu, Y. Xiong, D. Yan, D. Wang, B. Z. Tang, *Chin. J. Chem.*, **2023**, *41*, 1249—1259.

Figure 1[4] clearly illustrates the difference between the two phenomena. 3,4,9,10-perylentetra-carboxylic diimide (DPD)[5] is a classical ACQ chromophore, characterised by being highly emissive in THF but quenching as water is added, due to the formation of molecular aggregates, because the excited state species generally decay via non-radiative pathways as a result of their rigid and planar structure. In contrast, hexaphenylsilole (HPS)[6] is a representative example of AIEgens because it is non-emissive when molecularly dissolved, for example in THF, but becomes highly emissive when molecules aggregate as the amount of water increases, due to the helix conformation, which prevents deactivation by non-radiative pathways owing to the difficulty in forming π-π interactions.

Theoretical and experimental studies reveal that the mechanism of AIE is based on the restriction of molecular motions (RIM).[7] In a dilute solution, molecules are non-emissive or show weak emission due to free intra- and intermolecular motion. However, in an aggregated state, the active rotation and dynamic vibration of the molecules are hindered, restricting the dissipation of energy from the excited state via non-radiative pathways and emitting more intense fluorescence.

An example of this can be seen in Figure 2,[8] where the aromatic rings of tetraphenylethylene (TPE), in solution, exhibit an active rotation because the bonds that join them to the central olefinic core can rotate freely, releasing all the excess energy in the process of movement, in other words, by a non-radiative decay system. However, the formation of aggregates prevents the rotation of the aromatic rings, so that the excess energy can only be released through an emissive process, thus activating the AIE phenomenon.

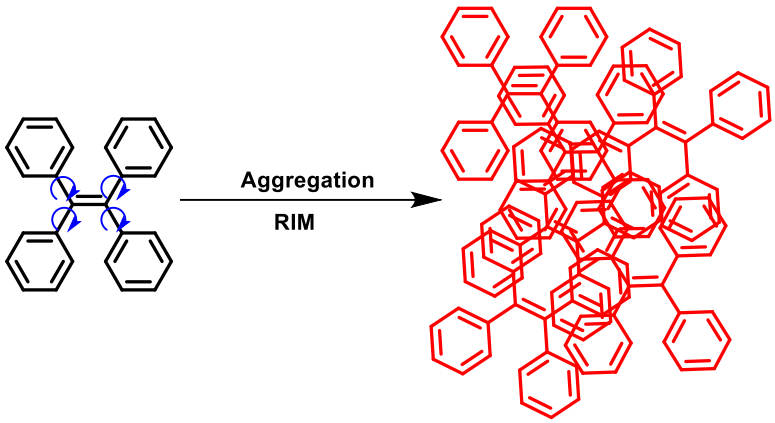

Figure 2. Schematic example of RIM blocking in the aggregated state and emission by AIE.

Most of the AIEgens are characterised by rotor-shaped structures with many common structural features:

- They mainly exhibit structures with highly conjugated aromatic systems, which helps to increase fluorescent emission.
- They feature bonds that allow free rotation between a core and the substituents, which act as moving parts. In the example in Figure 1, the fixed centre corresponds to the heterocycle while the phenyls at the periphery can rotate freely.

[4] a) J. Qi, C. Chen, D. Ding, B. Z. Tang, *Adv. Healthcare Mater.*, **2018**, *7*, 1800477. b) S. Xu, Y. Duan, B. Liu, *Adv. Mater.*, **2019**, 1903530.
[5] H. Tong, Y. Hong, Y. Dong, M. Haussler, J. W. Lam, Z. Li, Z. Guo, Z. Guo, B. Z. Tang, *Chem. Commun.*, **2006**, 3705.
[6] a) M. Jiang, X. Gu, J. W. Y. Lam, Y. Zhang, R. T. K. Kwok, K. S. Wong, B. Z. Tang, *Chem. Sci.*, **2017**, *8*, 5440. b) Y. Chen, W. Zhang, Z. Zhao, Y. Cai, J. Gong, R. T. K. Kwok, J. W. Y. Lam, H. H. Y. Sung, I. D. Williams, B. Z. Tang, *Angew. Chem. Int. Ed.*, **2018**, *57*, 5011. c) W. C. Geng, Y. C. Liu, Z. Zheng, D. Ding, D. S. Guo, *Mater. Chem. Front.*, **2017**, *1*, 2651.
[7] a) J. Mei, Y. Hong, J. W. Y. Lam, A. Qin, Y. Tang, B. Z. Tang, *Adv. Mater.*, **2014**, *26*, 5429–5479. b) Z. Zhao, H. Zhang, J. W. Y. Lam, B. Z. Tang, *Angew. Chem. Int. Ed.*, **2020**, *59*, 9888-9907.
[8] R. D. Martínez-Serrano, Síntesis y caracterización de compuestos con propiedades de emisión inducida por agregación basados en tetrafeniletileno sustituido con grupos tritilo, PhD thesis, National Autonomous University of Mexico, **2016**.

- They usually have radial structures, as for example HPS grows from the central aromatic ring.
- Generally, AIEgens move away from planarity due to bulk and steric interactions of the mobile substituents at the periphery, promoting the formation of aggregates that avoid π-like stacking.

However, these rotor structures lead to broad emission spectra and short absorption wavelengths. The first of these drawbacks can be solved by developing new compounds with FRET systems,[9] while the second can be solved by designing AIEgens with multiphotonic systems or without rotor structures, guided by the theory of the molecular transformation of the excited state.[10] In this new theory, both structures with a twisted double bond and planar or cluster distortion structures can act as central skeletons in the development of AIEgens.

The AIE phenomenon benefits the design of high-performance materials. An example of this is organic AIE nanoparticles that show brighter luminescence with better physical stability than inorganic quantum dots.[11] In addition, it has also been used in emerging research fields such as room temperature fluorescence or triboluminescence (a process in which light emission is produced by the breaking of chemical bonds due to processes of tension, agitation, crushing...).[12] Numerous AIEgens have also been designed and used in optical devices, luminescent sensors, bioimaging (Figure 3)[13] and phototherapy.[14]

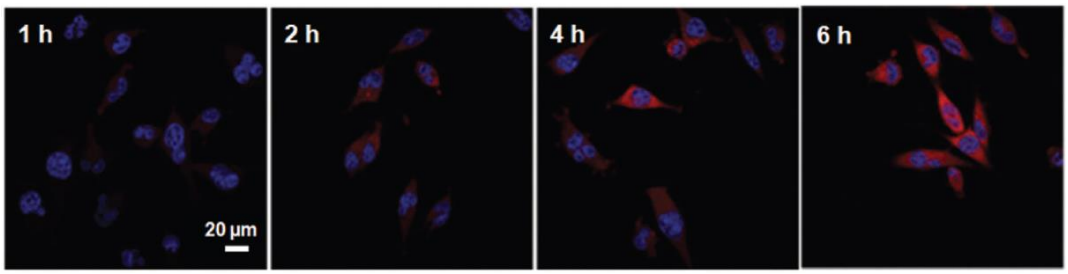

Figure 3. Monitoring of an AIEgen that acts as a transporter of cytotoxic drugs for release into cancer cells over time.

2. OBJECTIVES

As discussed in Chapter 2, one of the most important and typical features of NMIs derivatives is the phenomenon of Aggregation Induced Emission (AIE).[15] The nanostructures formed can be of a very wide variety of nature depending on the substituents on the naphthalene core, which can be studied by different microscopy techniques, including, for example, SEM.

Therefore, the main objective of this chapter is to examine in detail the nanostructures formed when AIE occurs, highlighting the control that can be exerted on this phenomenon according to the amino-protecting groups present in the synthesised compounds. Thanks to the initial water acceptance assay, it was possible to determine the compounds that underwent the AIE phenomenon and its intensity, revealing that it was regulated by the presence of free amines in the

[9] a) Y. Yuan, R. Zhang, X. Cheng, S. Xu, B. Liu, *Chem. Sci.*, **2016**, *7*, 4245. b) C. Li, Y. Zhang, J. Hu, J. Cheng, S. Liu, *Angew. Chem. Int. Ed.*, **2010**, *49*, 5120.
[10] Y. Q. Dong, J. W. Lam, B. Z. Tang, *J. Phys. Chem. Lett.*, **2015**, *6*, 3429.
[11] a) B. Feng, B. Liu, *Acc. Chem. Res.*, **2018**, *51*, 1404. b) K. Li, Z. Zhu, P. Cai, R. Liu, N. Tomczak, D. Ding, J. Liu, W. Qin, Z. Zhao, Y. Hu, X. Chen, B. Z. Tang, B. Liu, *Chem. Mater.*, **2013**, *25*, 4181.
[12] J. C. Zhang, X. Wang, G. Marriott, C. N. Xu, *Prog. Mater. Sci.*, **2019**, *103*, 678-742.
[13] H. Gao, X. Zhang, C. Chen, K. Li, D. Ding, *Adv. Biosys.*, **2018**, *2*, 1800074.
[14] a) D. Ding, K. Li, B. Liu, B. Z. Tang, *Acc. Chem. Res.*, **2013**, *46*, 2441. b) R. T. Kwok, C. W. Leung, J. W. Lam, B. Z. Tang, *Chem. Soc. Rev.*, **2015**, *44*, 4228.
[15] a) S. Sharma, S. Srinivas, S. Rakshit, S. Sengupta, *Org. Biomol. Chem.*, **2022**, *20*, 9422. b) L. He, Q. Li, Y. Zhang, K. Huang, B. Du, L. Liang, *Spectrochim. Acta A Mol. Biomol. Spectrosc.*, **2023**, *296*, 122672.

structures. Subsequently, the nano-aggregates formed were analysed, establishing trends between the different families of compounds studied. This procedure is summarised in Figure 4.

Finally, it is intended to publish the results obtained as a system capable of controlling the aggregation that develops through the AIE phenomenon, allowing to obtain nanostructures on demand to be used in different applications, such as in the field of biology or in photodynamic therapy.

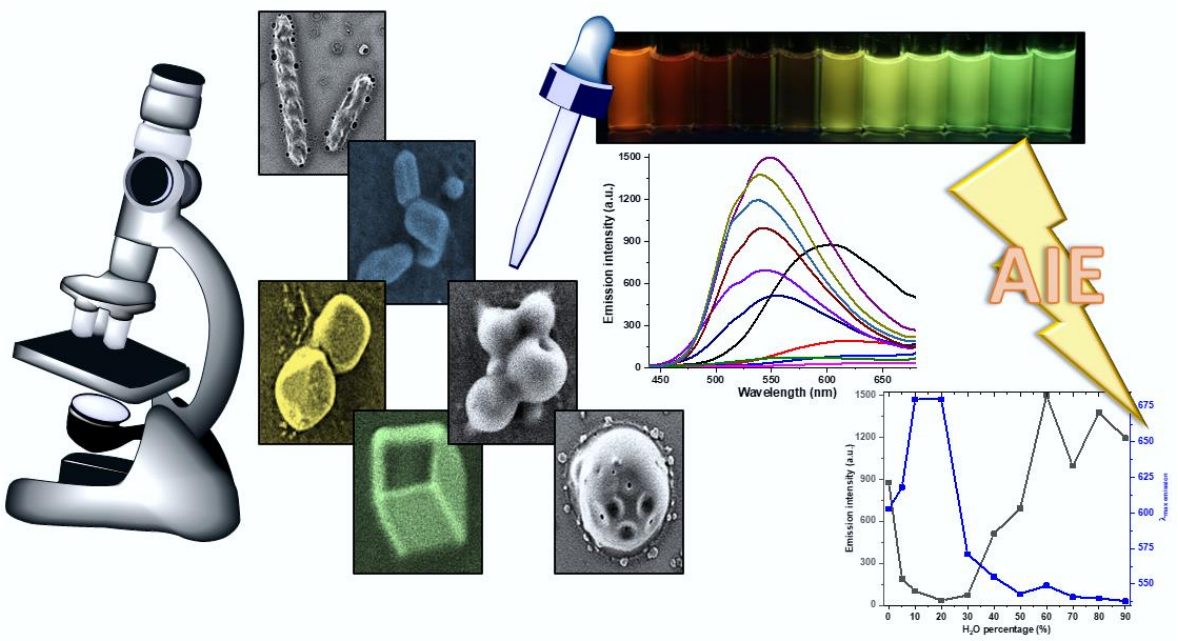

Figure 4. Schematic summary of the procedure followed for the analysis of the nanostructures obtained by the AIE.

3. AGGREGATION ACCORDING TO STRUCTURE

A few NMI derivatives, more specifically those compounds developed in Chapter 3A for the detection of TATP, were synthesised via the Suzuki-Miyaura coupling reaction and analysed in the water acceptance test. In this test, both ACQ and AIE phenomena were observed as a function of the structure of the synthesised derivatives, more specifically as a function of the amino-protecting groups present.

3.1. Synthesis of NMI derivatives

A series of fluorescent compounds based on a naphthalene core were synthesised via the Suzuki-Miyaura carbon-carbon coupling reaction to give rise to the amino-protected products (AR82p and AR83p). The experimental procedure followed is detailed in Section 3 of Chapter 3A, however, a brief reminder is given in Figure 5.

In the same way, the synthesis of the semi-protected products (AR82s and AR83s) was carried out as illustrated in Figure 6. The synthesis of the deprotected compounds (AR82d and AR83d) were finally carried out by stirring the amino-protected products in chloroform with TFA for 3-4 hours at room temperature, as shown in Figure 7 below.

Once the products were obtained, a preliminary fluorescence study was carried out by performing solvatochromism tests, and measurements of fluorescence lifetime (τ) and fluorescence quantum yield ($Ø_F$).

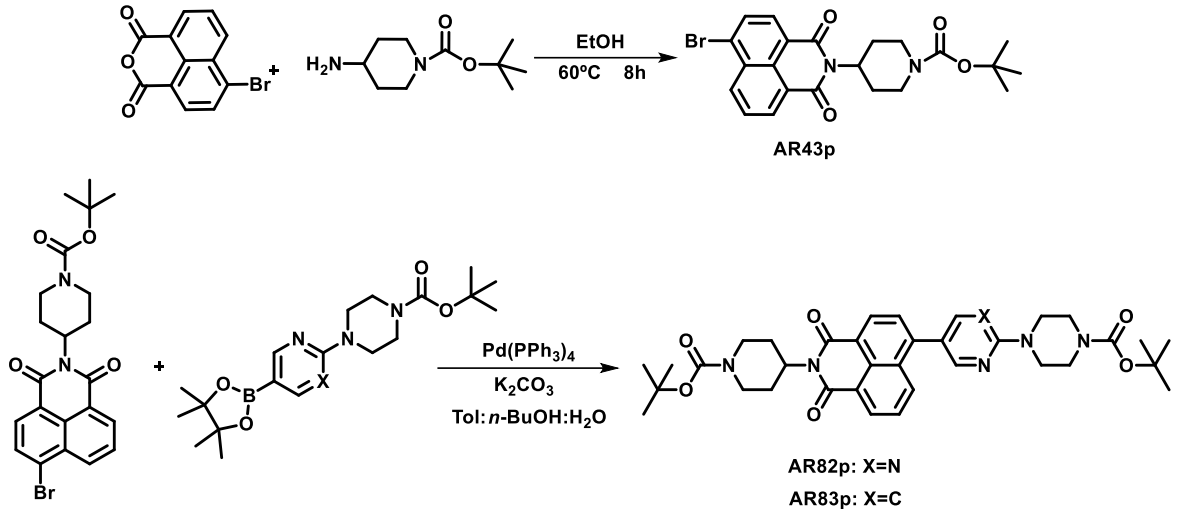

Figure 5. Synthetic scheme of amino-protected products AR82p and AR83p.

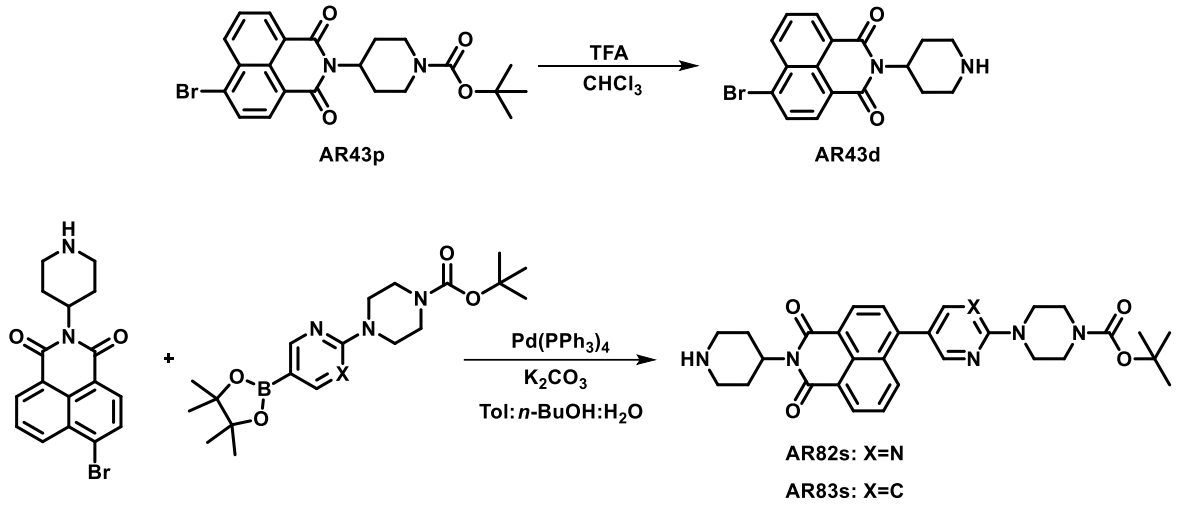

Figure 6. Synthetic scheme of semi-protected products AR82s and AR83s.

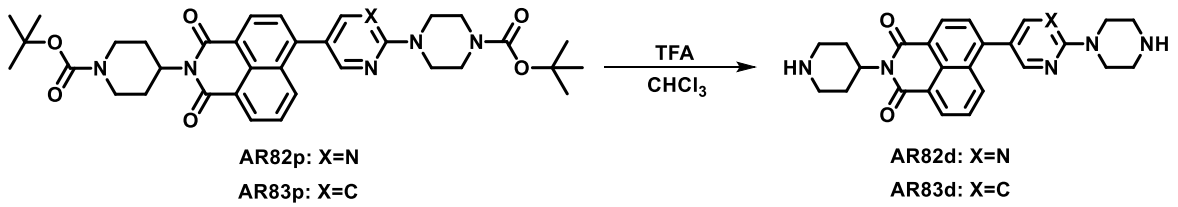

Figure 7. Synthetic scheme of deprotected products AR82d and AR83d.

3.2. Absorbance and fluorescence interpretation

To characterise the fluorescence of these products, the fluorescence lifetime decays and quantum yields were measured. Solvatochromism tests were also performed to establish the most suitable solvent for further studies. Starting with the fluorescence quantum yield, the values obtained are shown in Figure 8 below.

	AR82 (%)	AR83 (%)
Amino-protected (p)	92.87	85.40
Semi-protected (s)	73.00	99.41
Deprotected (d)	67.62	<3

Figure 8. Fluorescence quantum yield of synthesised products.

In general, the highest quantum yields were obtained for the amino-protected products, above 85% in all of them, while the lowest fluorescence was generally observed for the unprotected products. Moreover, for both semi-protected and unprotected products, the fluorescence showed a higher variability. The same comparison was made with the fluorescence lifetime decay of the synthesised products, resulting in Figure 9.

	AR82 (ns)	AR83 (ns)
Amino-protected (p)	2.853	3.199
Semi-protected (s)	3.962	5.291
Deprotected (d)	4.270	4.406/1.991

Figure 9. Fluorescence lifetime decays of synthesized products.

As can be seen in Figure 9, all the values given are of the order of nanoseconds, so regardless of the number of protecting groups present in the compounds, all of them emit fluorescent radiation. In general, as the number of protecting groups decreases, the lifetime decays increase, that is, the lifetime of the excited state becomes longer.

3.2.1. Solvatochromism tests of the AR82 series

The behaviour of each one of the products was studied in solvents of different polarity and the fluorescence images shown in Figure 10 were obtained.

As can be noted, the emission intensity of the AR82p product was higher than the others, while the lowest emission intensity was for the unprotected AR82d compound. These data corroborate the conclusions from the quantum yields. On the other hand, the product AR82p showed more affinity for solvents of lower polarity, being hexane and methylcyclohexane the solvents in which the emission was higher. Compound AR82s presented higher emission in solvents of intermediate polarity and compound AR82d had a higher affinity for solvents of major polarity, being soluble even in water. This shift to solvents of higher polarity as the number of amino-protecting groups decreases was due to the high number of free amines, polar groups that increased the solubility of the product in solvents with these characteristics.

All normalized absorption and emission plots in Figure 11 show a bathochromic shift of both the absorption maximum and the emission maximum, with a much greater shift in the case of emission that moves from the blue region (above 430 nm) to the green region (approximately 510 nm), which can be seen in Figure 10.

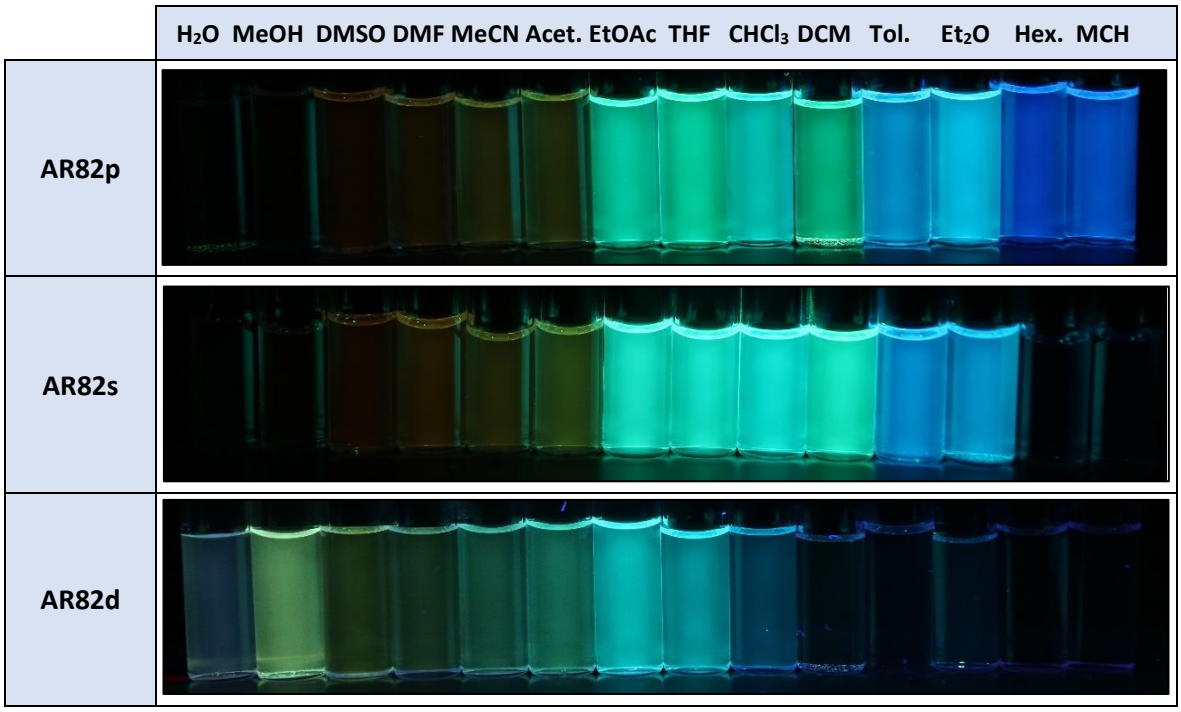

Figure 10. Fluorescent emission of 20 µM solutions of AR82 series in different solvents under 366 nm light.

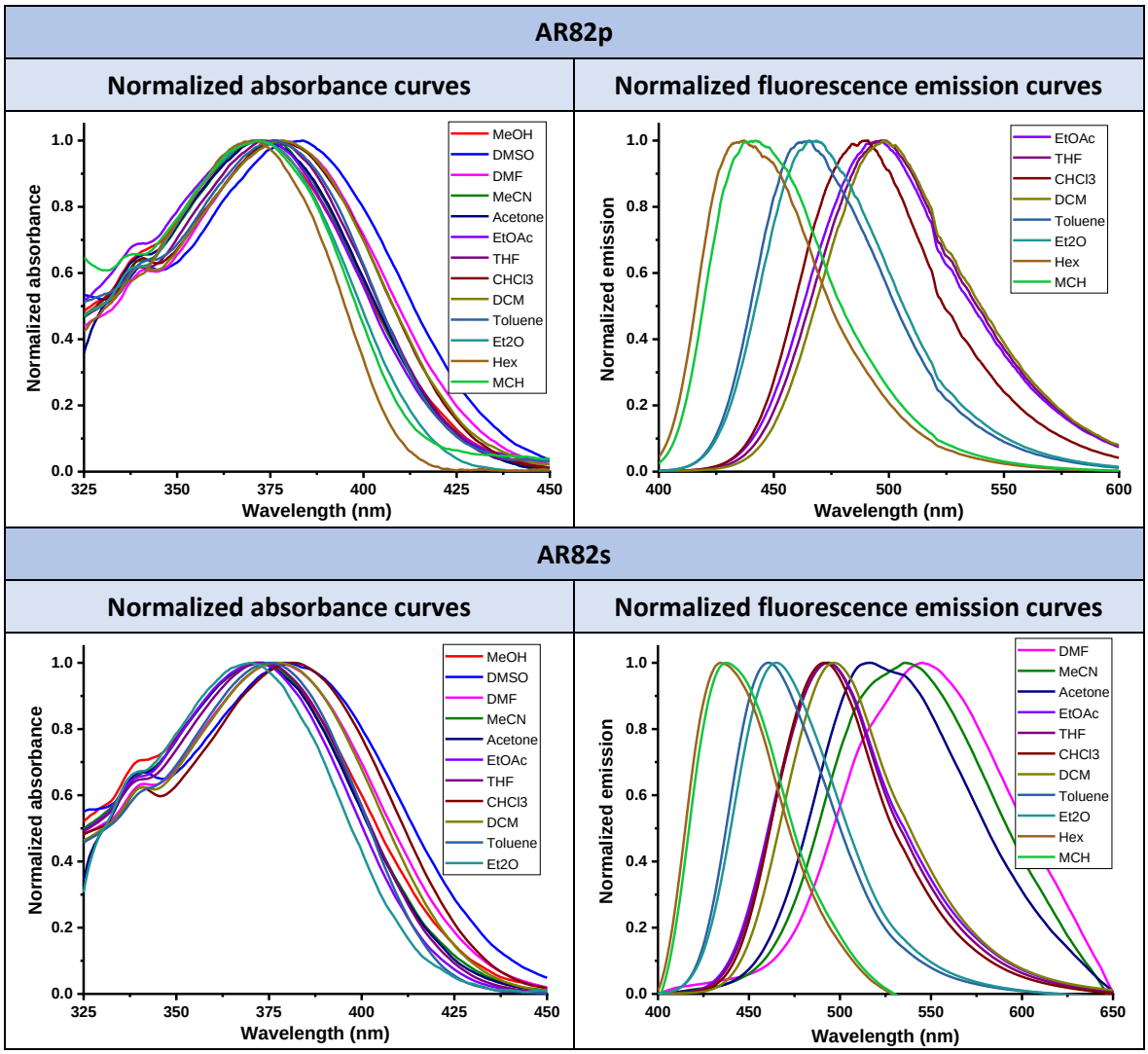

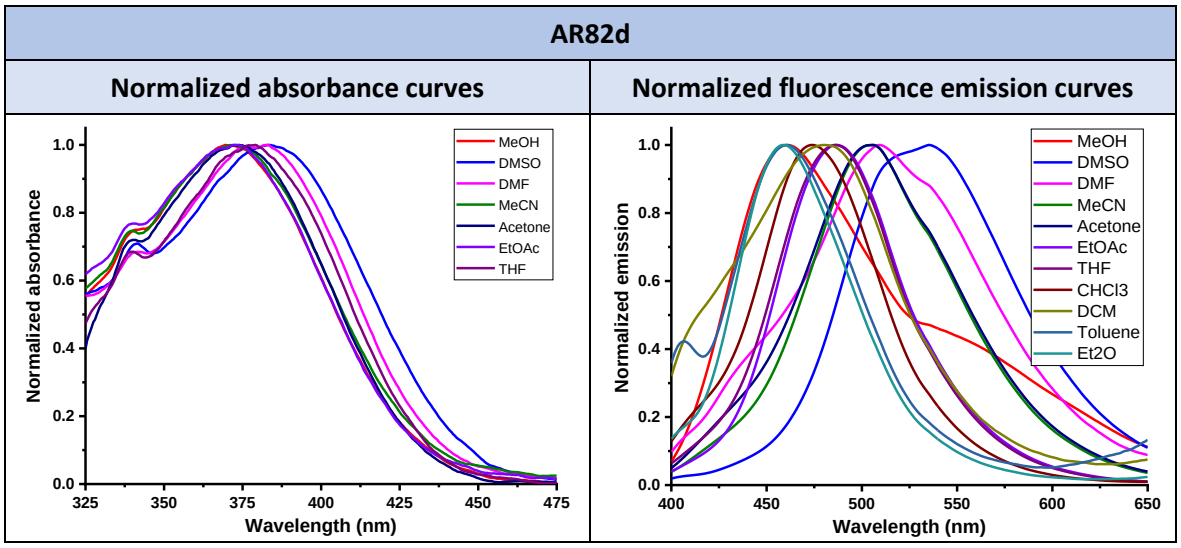

Figure 11. Normalized absorption and emission spectra of 20 µM solutions of the AR82 product series in different solvents.

3.2.2. Solvatochromism tests of the AR83 series

This study was also performed with the AR83 series of compounds (Figure 12 and Figure 13). The results were very similar to those obtained for the AR82 series. In this case, the emission shift for the AR83p and AR83s compounds occurred from the blue to the yellow region (about 550 nm). However, the shift for the protected compound AR83d was much smaller, approximately 60 nm, from the blue to the green region.

Moreover, unlike the previous series, in these compounds, especially in AR83p and AR83s, a shoulder appeared in the emission spectra as the polarity of the solvent increases.

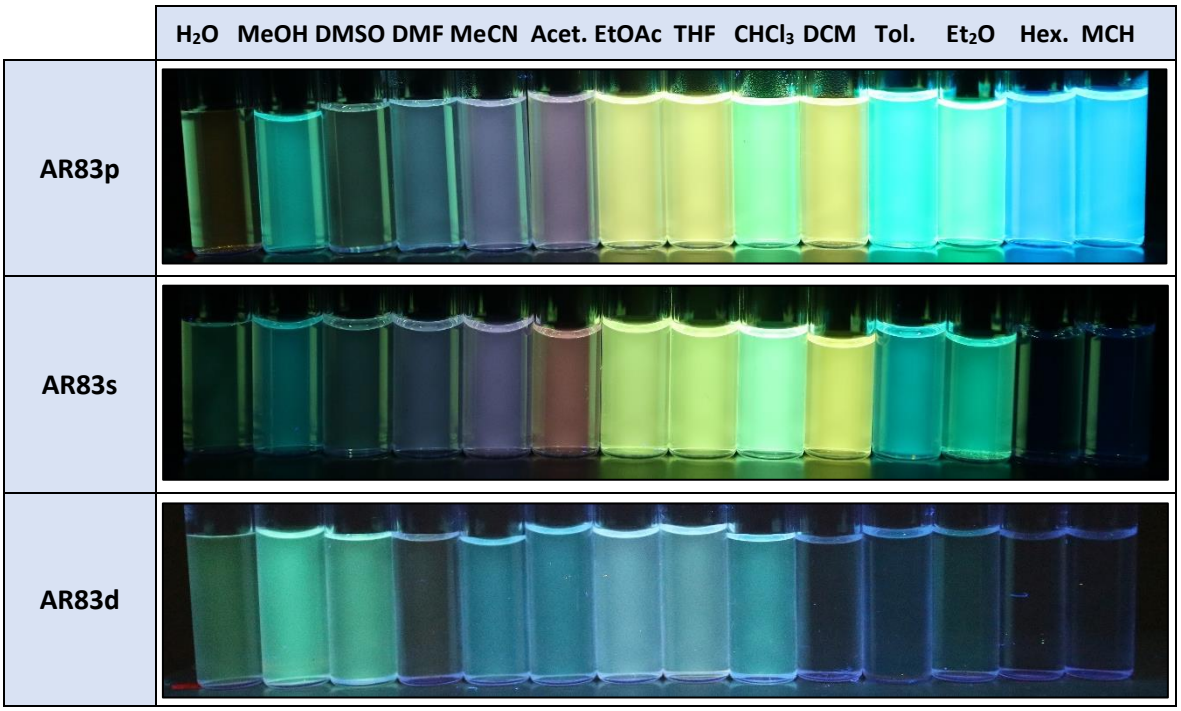

Figure 12. Fluorescent emission of 20 µM solutions of AR83 product series in different solvents under 366 nm light.

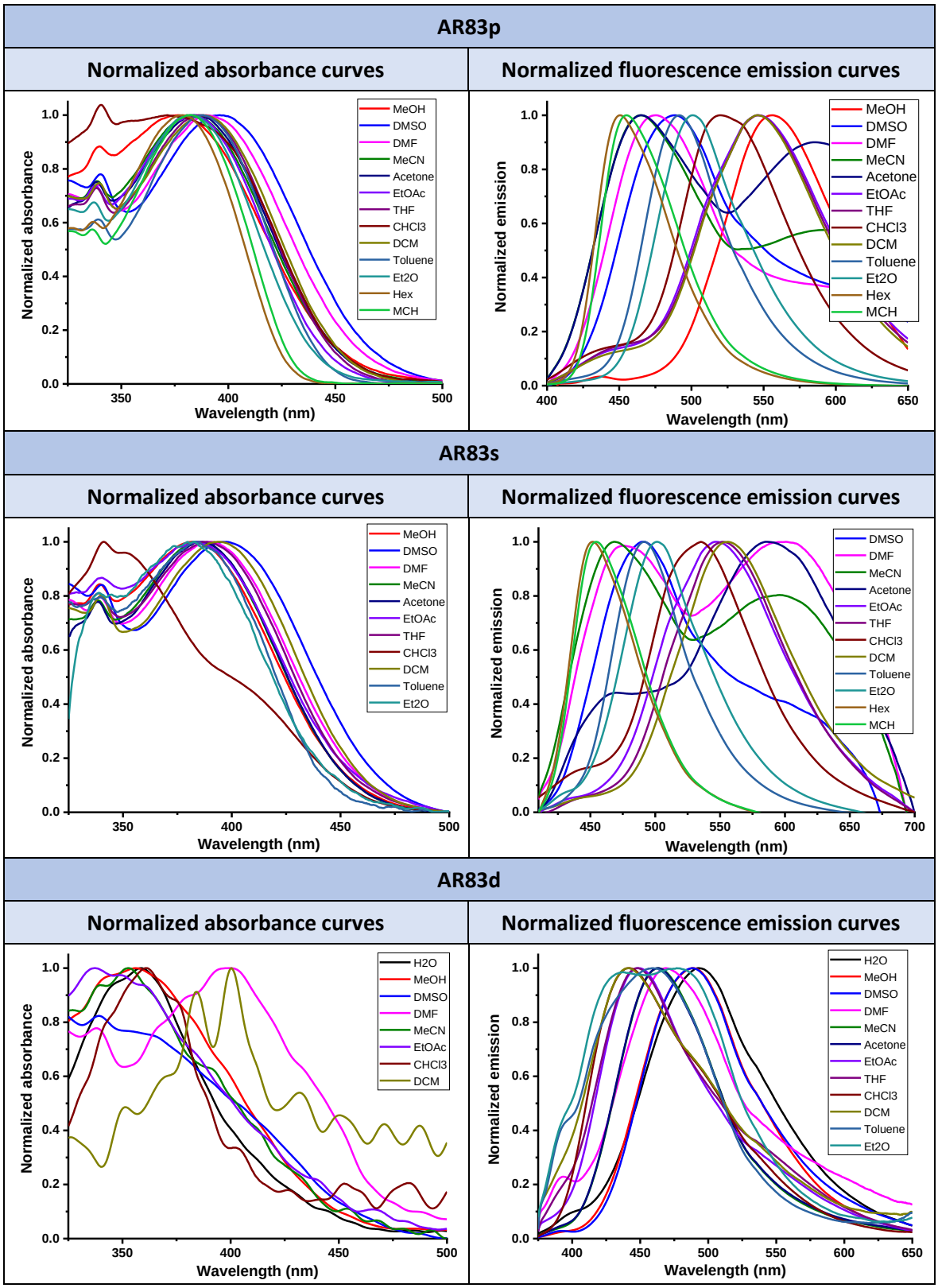

Figure 13. Normalized absorption and emission spectra of 20 µM solutions of the AR83 product series in different solvents.

3.3. Water acceptance test and aggregation analysis

As already detailed in Chapter 1, solvatochromisms are used to select the solvent, miscible with water, in which to perform subsequent assays, such as the water acceptance test. To be comparable, most of them were performed using THF as solvent and in which the amount of water (from 0% to 90%) added was increased. Again, the analysis was performed by families of compounds.

3.3.1. Aggregation analysis of the AR82 series

The solvent used in the water acceptance test of the three products was THF. The result obtained is shown in Figure 14.

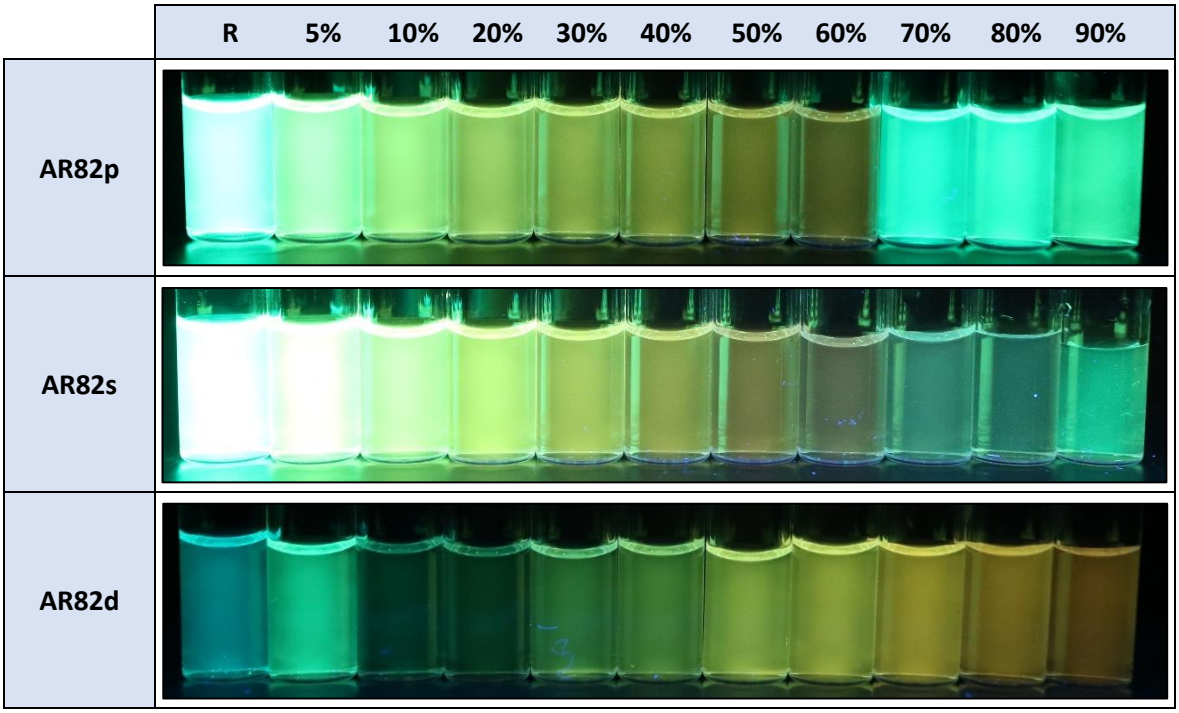

Figure 14. Water acceptance test. 20 µM solutions of the AR82 series of compounds in THF mixtures with increasing amounts of water.

As can be appreciated in Figure 14, the AR82p compound showed a marked AIE phenomenon, since from 70% water there was a slight increase in the emission intensity (Figure 15), as well as a shift of the emission maximum from the yellow region (535-545 nm) to the green region (475 nm).

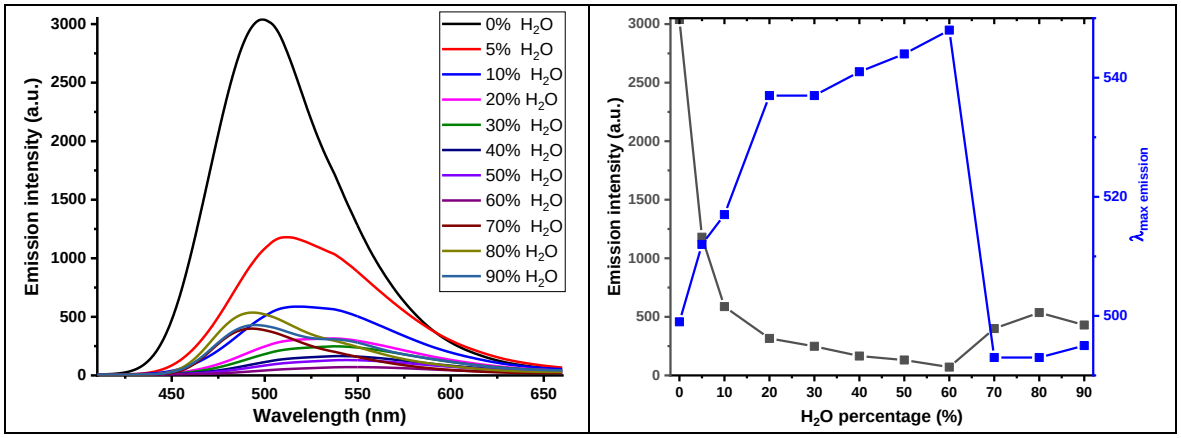

Figure 15. Emission intensity graph (left) and graph of relationship between the emission intensity and the wavelength of the maximum of emission (right) as a function of the amount of water added for AR82p in THF. λ_{exc} = 380 nm.

This THF-H_2O scale was examined in SEM, obtaining the images in Figure 16. At low amounts of water, between 5 and 50%, few nanoparticles were observed, mainly in the form of needles, and it was not until 30% water that the first spherical nanoparticles appeared, with a size of about 366 nm.

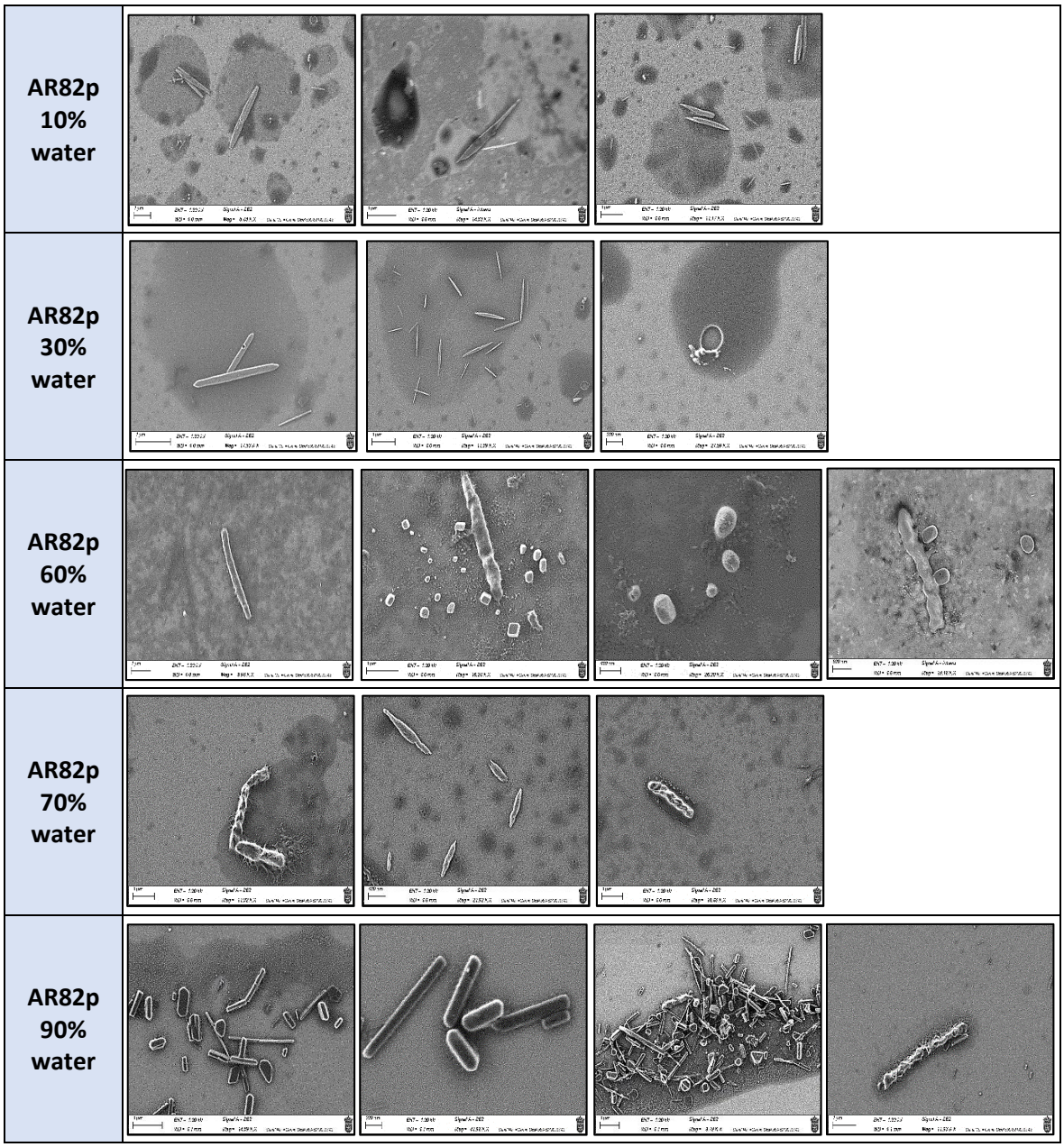

Figure 16. SEM nanoparticles of AR82p in different mixtures of THF-H_2O.

As can be observed in the images of Figure 16, at 60% water, nanofibres, nanosticks and cubic nanoparticles began to appear, with a size of, approximately, 290 nm. Spherical nanoparticles had increased in size to almost 500 nm. In addition, a nanovesicle was observed (the enlarged image is shown in Figure 17). At 70% water, the percentage at which the AIE phenomenon began, both needle-shaped and spherical nanoparticles continued to be observed and helix-shaped fibres appeared, with a length of 2.4 µM and a width of 362 nm. Finally, at 90% water, apart from helix-shaped fibres,

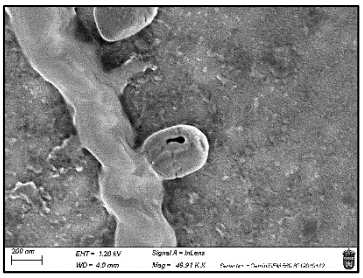

Figure 17. Enlargement of the nanovesicle of compound AR82p in THF with 60% water.

cubic nanoparticles continued to be observed, with a size of around 372 nm, and nanosticks with a length of about 760 nm.

On the other hand, the semi-protected AR82s compound showed a slight increase of the emission intensity when the amount of water was 70-80%, which decays again at 90% water, as shown in Figure 18. Unlike compound AR82p, this only has one amino-protecting group, which makes the observed AIE considerably less intense but, like the previous product, AR82s compound presented a shift of the emission maximum to the green region (above 475 nm).

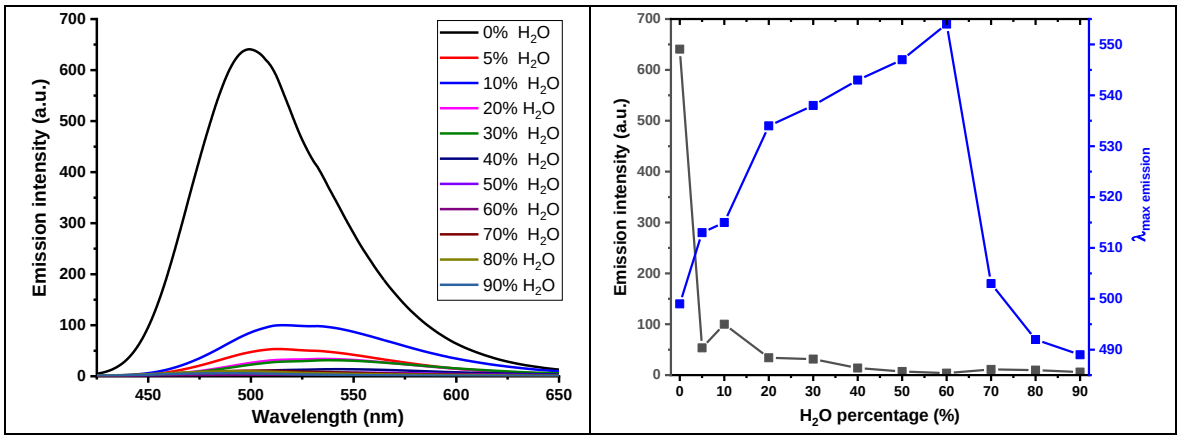

Figure 18. Emission intensity graph (left) and graph of relationship between the emission intensity and the wavelength of the maximum of emission (right) as a function of the amount of water added for AR82s in THF. λ_{exc} = 370 nm.

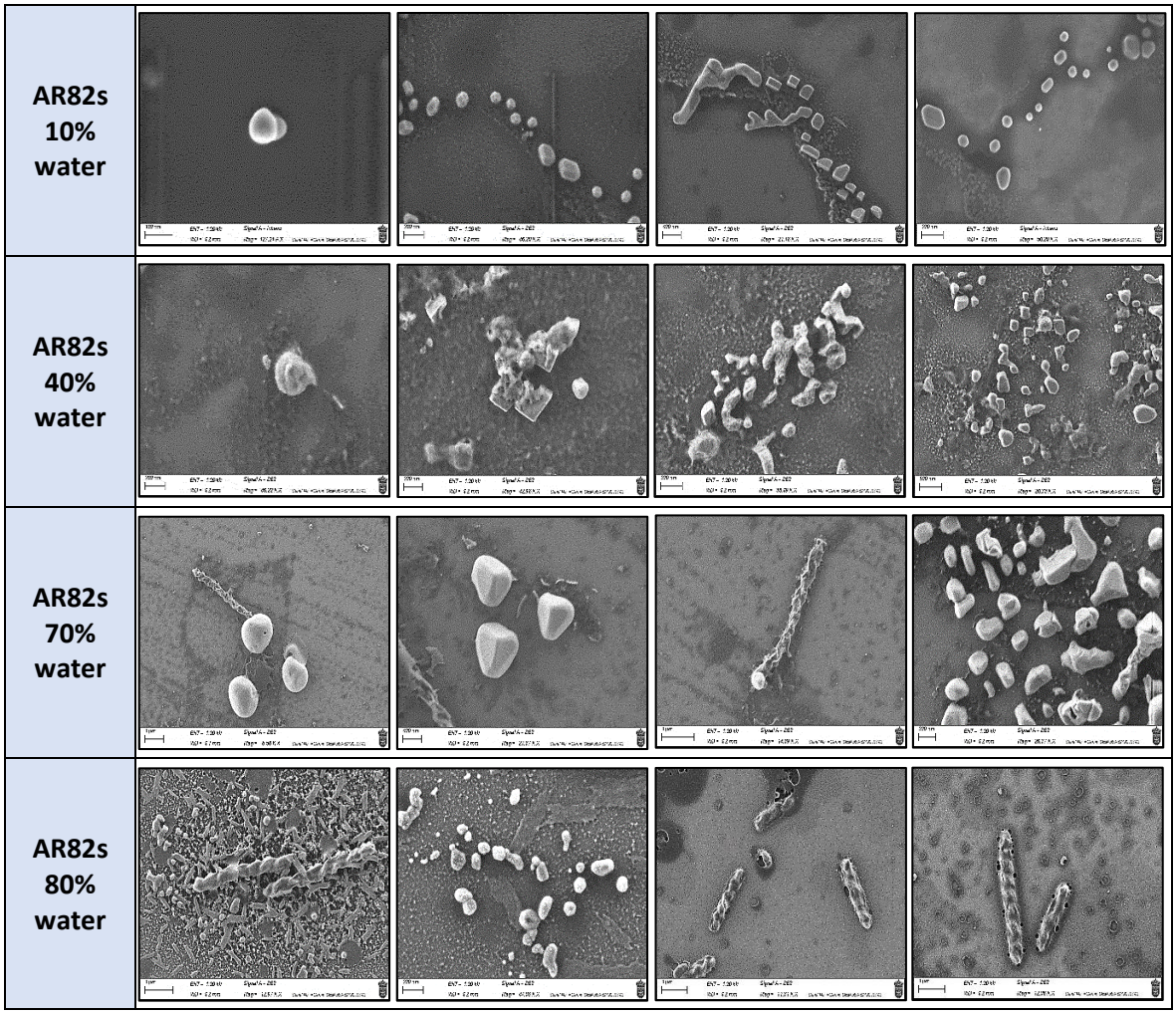

Figure 19. SEM nanoparticles of AR82s in different mixtures of THF-H_2O.

Again, this AIE was analysed in the SEM and the images shown in Figure 19 were obtained. At low percentages of water, spherical nanoparticles, with a diameter of approximately 100 nm, and amorphous nanoparticles, with a size of 90 nm, were observed. As the amount of water in the mixture increases, the polygonal nanoparticles clumped together to form aggregates, which ranged in size from 250-360 nm. In addition, individual spherical nanoparticles and, to a lesser extent, cubic nanoparticles continued to be observed. At 70% water, the formation of helix-shaped nanofibres started. In this case, the spherical nanoparticles had already reached a size of about 1.7 microns while the individual amorphous nanoparticles are 900 nm in size. At 80% water, although the nanoparticles continued to be observed, the most abundant were the helix-shaped nanofibres with dimensions of 500 nm in width and more than 2 microns in length. These nanofibres were very similar to those observed for the previous compound, both in quantity of water and dimensions.

The last compound considered in this series is AR82d, which shows a quenching of fluorescence as the amount of water added increased. Therefore, when there was no amino-protecting group in the structure, the AIE phenomenon did not occur.

3.3.2. Aggregation analysis of the AR83 series

As with the previous compound, firstly, a water acceptance test analysis was performed (Figure 20) in order to determine the phenomena that occurred as the amount of water added to the organic solvent increased. For compounds AR83p and AR83s the organic solvent used was THF while for AR83d MeOH was used.

This test allowed to note the same as in the case of the AR82 series of compounds. The amino-protected compound AR83p showed a marked AIE from 70% water, while in the semi-protected compound AR83s, the AIE phenomenon was also observed from the same amount of water, but the emission intensity was considerably lower, decreasing slightly at 90% water. In total opposition was the unprotected compound AR83d, which presented a low fluorescence emission that faded away as the amount of water increased (ACQ).

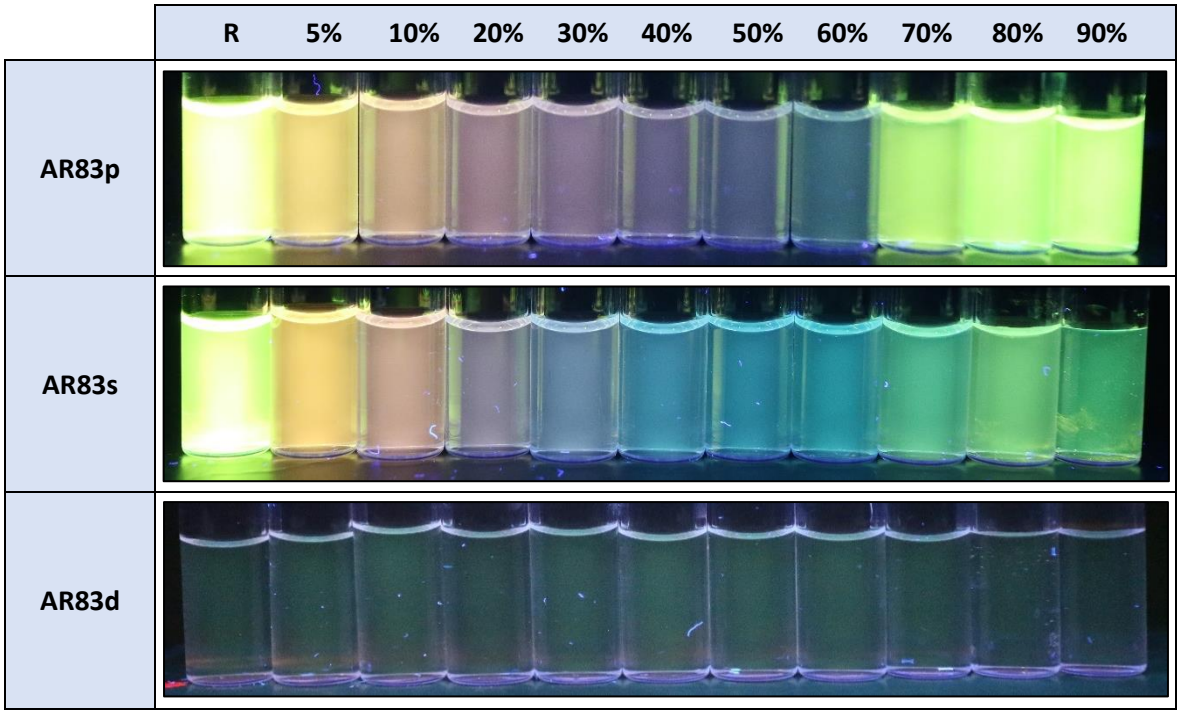

Figure 20. Water acceptance test. 20 µM solutions of the AR83 series of compounds in THF mixtures with increasing amounts of water.

The AIE of compound AR83p was measured and, apart from an increase in emission intensity, a shift of the emission maximum from the orange region (approximately 585-607 nm) to the violet region (above 650 nm) and back to yellow (approximately 550-565 nm) from 70% water was observed.

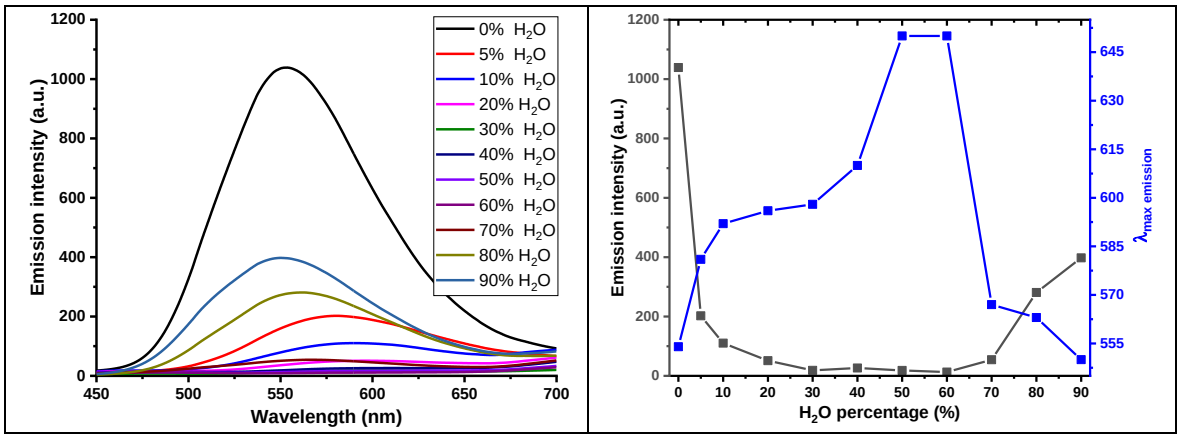

Figure 21. Emission intensity graph (left) and graph of relationship between the emission intensity and the wavelength of the maximum of emission (right) as a function of the amount of water added for AR83p in THF. λ_{exc} = 380 nm.

The nanostructures formed by AIE were studied by SEM, resulting in the images shown in Figure 22.

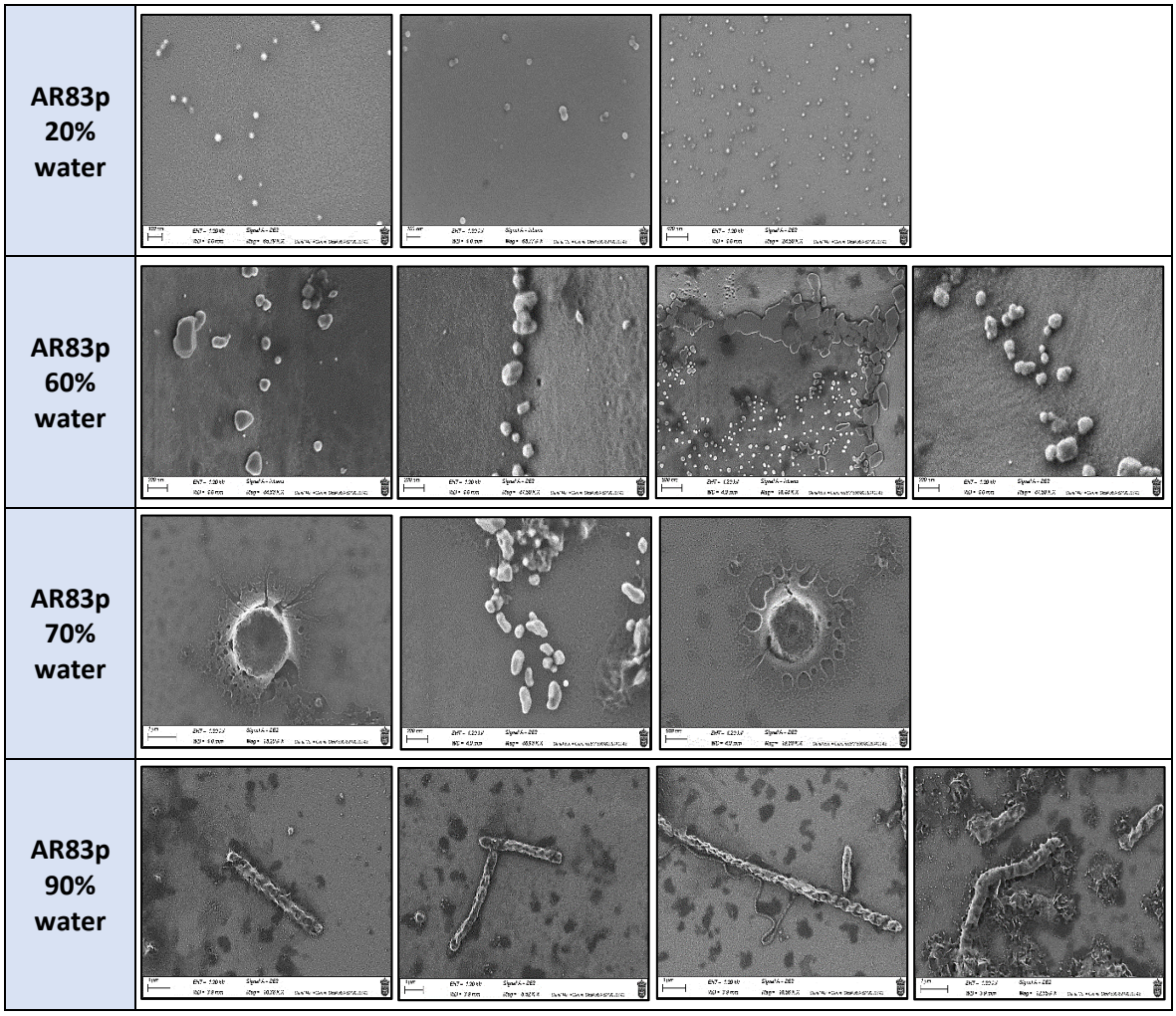

Figure 22. SEM nanoparticles of AR83p in different mixtures of THF-H_2O.

At low water concentrations, only spherical nanoparticles with a size of less than 50 nm were found, either individually or grouped in pairs or trios. As the amount of water increased to 60%, before AIE occurred, polygonal nanoparticles and, to a lesser extent, individual spherical nanoparticles were observed, ranging in size from 100 to 200 nm, the smallest being around 60 nm. At 70% water, the percentage at which the AIE was initiated, amorphous nanoaggregates of cubic nanoparticles and spherical particles with a size of approximately 600 nm were detected. Finally, at 90% water, only helix-shaped nanofibres with an approximate length of 3 µm were observable.

The same analysis was carried out with the AR83s product, confirming the beginning of the AIE from 70% water and also observing a shift of the emission maximum from the orange region (above 580 nm) at low amounts of water to the blue region (around 490 nm) and finally to the green region (between 535-560 nm approximately) from the start of the AIE (Figure 23).

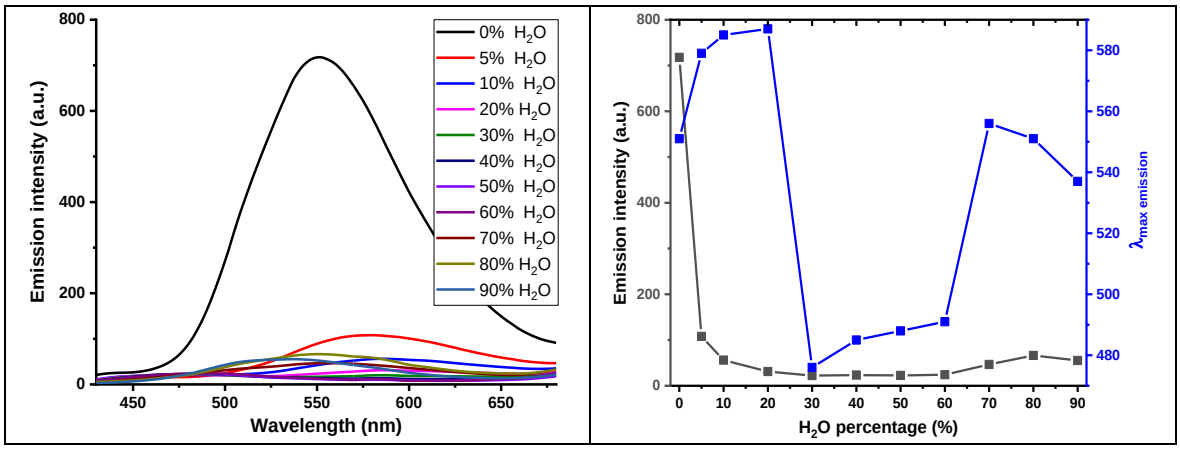

Figure 23. Emission intensity graph (left) and graph of relationship between the emission intensity and the wavelength of the maximum of emission (right) as a function of the amount of water added for AR83s in THF. λ_{exc} = 390 nm.

And newly, the nanostructures formed by the AIE phenomenon were studied by SEM and found to be as shown in the images in Figure 24. At low amounts of water (5%), nanocubes with a size between 150-300 nm were found with amorphous nanoparticles and some larger aggregates.

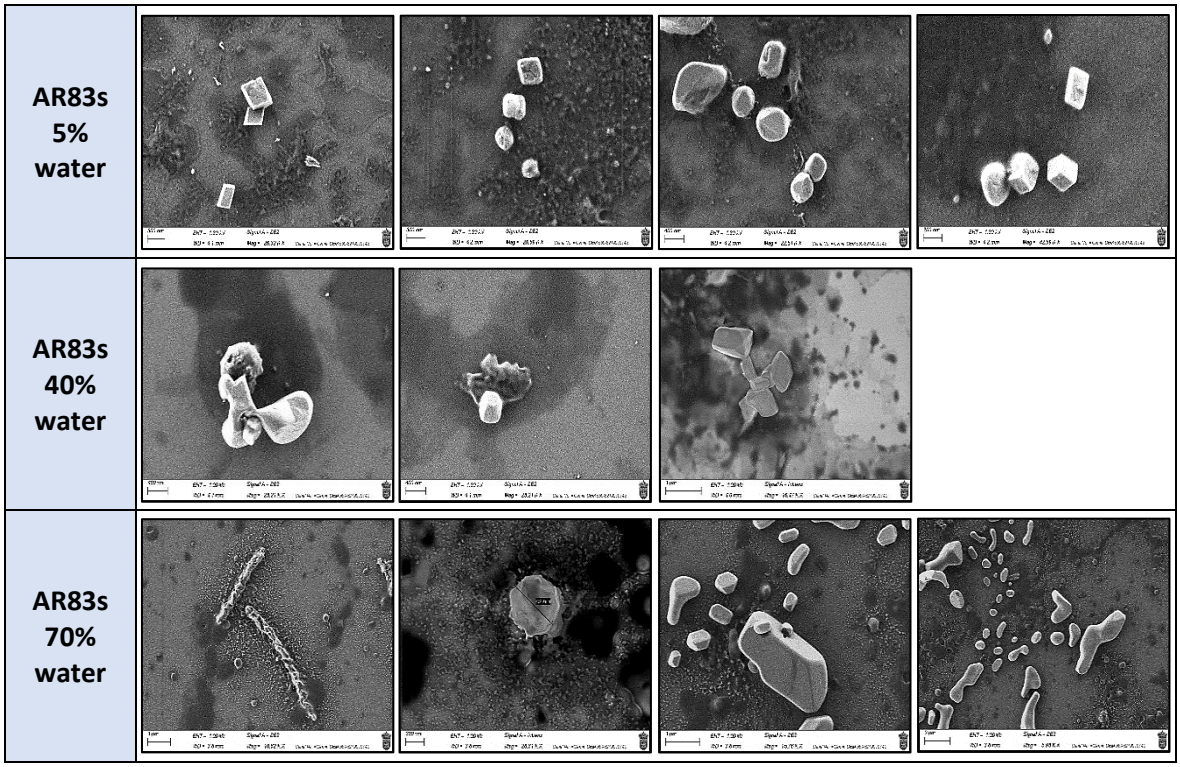

AR83s 90% water	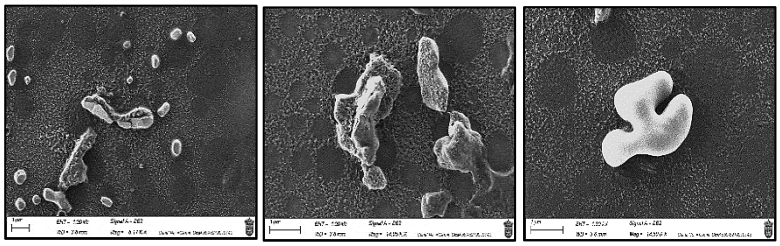

Figure 24. SEM nanoparticles of AR83s in different mixtures of THF-H_2O.

When increasing the amount of water up to 40%, nano-aggregates with sizes larger than 450 nm were observed. At the beginning of the AIE, that is, at 70% water, helix-shaped nanofibres were formed, just like the previous compounds. In addition, at this percentage, spherical nanoparticles were also found, with a size of more than 700 nm, and nanoaggregates with a size of approximately 800 nm. At this amount of water, the formation of a nanovesicle was noticed (Figure 25). Finally, at 90% water, only nanoaggregates larger than one micron were found.

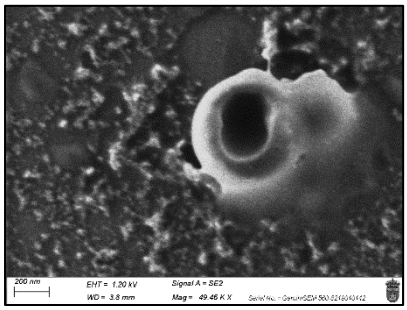

Figure 25. Enlargement of the nanovesicle found for the compound AR83s in THF with 70% water.

The compound AR83d, like the previous AR82d, did not undergo the AIE phenomenon due to the absence of amino-protecting groups in its structure.

4. AGGREGATION OF OTHER NMIs DERIVATIVES

The NMI derivatives that produce the AIE phenomenon are very varied, and some of them will be discussed in this section. On the one hand, the influence of the extent of conjugation on aggregation will be analysed, using NMIs as substituents of pyrene (AR56) and chrysene (AR65) rings. On the other hand, the effect of several substituents on the naphthalene core, such as an indene-carbazole, will also be studied.

4.1. Conjugation extension analysis: AR56

The extension of the conjugation was studied through a derivative formed by a pyrene ring substituted with two NMIs. It was obtained by a Suzuki-Miyaura carbon-carbon coupling reaction, using the previously synthesised diboronate and monobrominated NMI at position 4 as starting materials (Figure 26).

The fluorescence study (Figure 27 and Figure 28) showed that the highest emission occurred in the less polar solvents (hexane and methylcyclohexane) of all the solvents used. In addition, the normalised absorption and emission spectra showed a bathochromic shift of the corresponding maximum, much more pronounced in the case of the emission spectrum, where the maximum shifted towards the red (600-650 nm) as the polarity of the solvent increased.

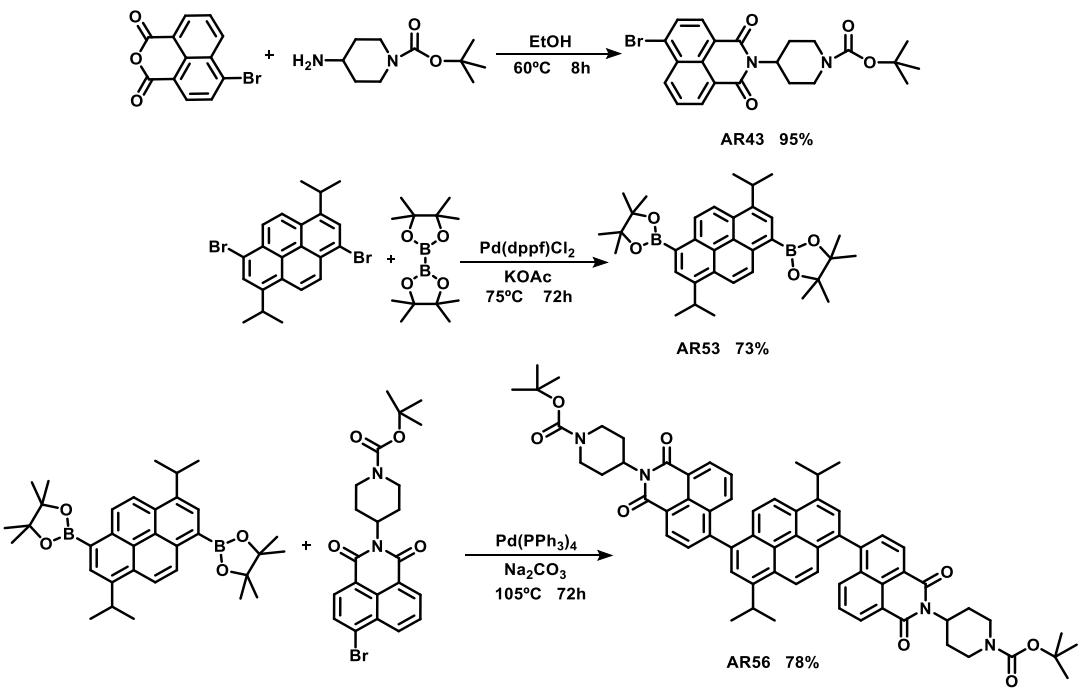

Figure 26. Scheme of the synthetic route followed to obtain the compound AR56.

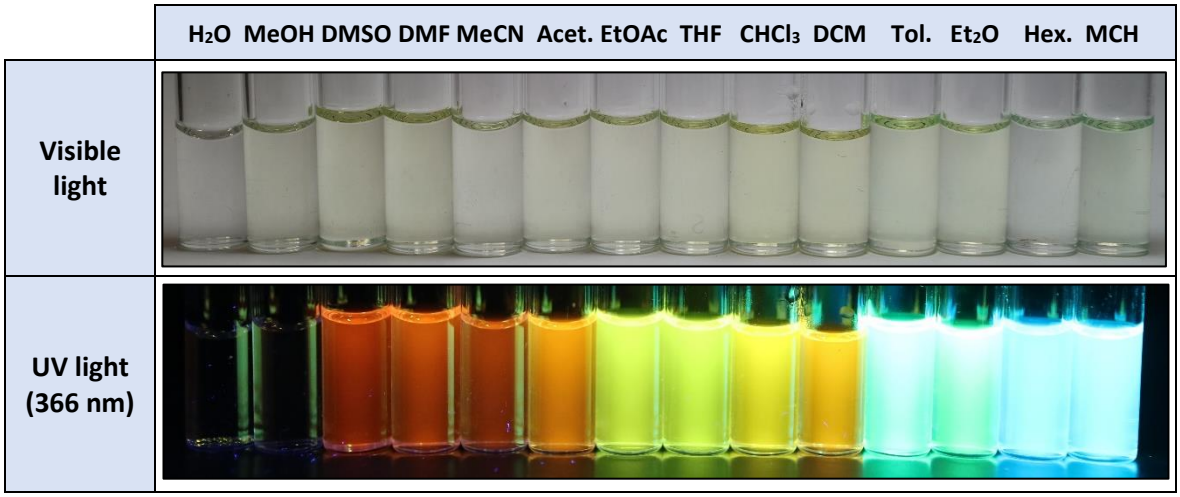

Figure 27. Solvatochromism images. 20 µM solution of AR56 in different solvents under visible and 366 nm light.

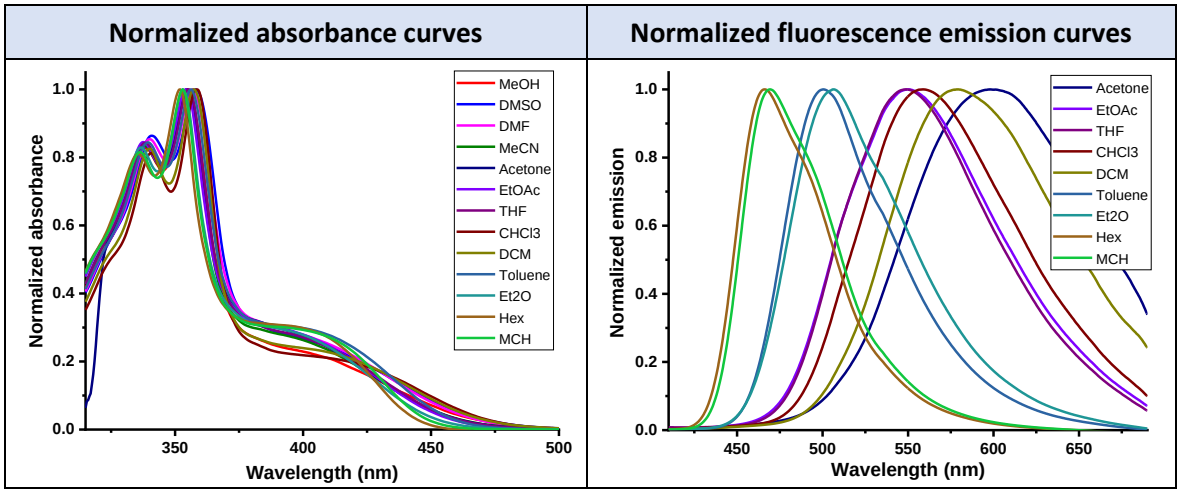

Figure 28. Solvatochromism graphs. Normalized absorbance curves (left) and fluorescence emission curves (right) in several solvents. λ_{exc}=355 nm.

4.1.1. Aggregation analysis using THF as organic solvent

The first aggregation study was carried out using THF as the organic solvent, which lead to AIE from 60% water, as can be observed in Figure 29. This phenomenon was accompanied by a shift of the emission maximum from the orange (600-620 nm) to yellow region (approximately 555-565 nm).

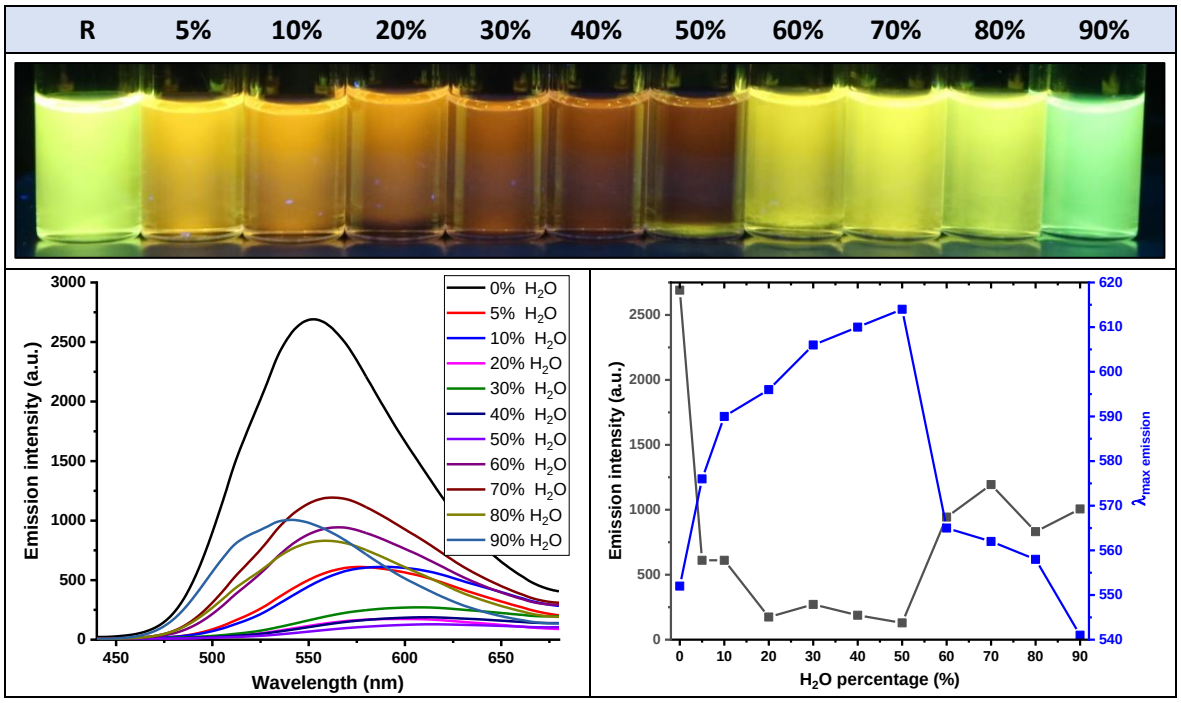

Figure 29. Fluorescence imagen of water acceptance test of a 20 µM solutions of AR56 in THF mixtures with increasing amounts of water (up). Emission intensity graph (down left) and graph of relationship between the emission intensity and the wavelength of the maximum of emission (down right) as a function of the amount of water added for AR56 in THF. λ_{exc} = 355 nm.

The nanostructures formed due to the AIE phenomenon were studied using SEM microscopy (Figure 30). At very low amounts of water, single spherical nanoparticles with a size between approximately 130 nm and 180 nm are observed. In addition, nanocubes were found. By increasing the amount of added water up to 30%, perfect nanocubes and numerous amorphous nanoparticles and aggregates of them were observed, while the individual spherical nanoparticles had disappeared.

Just before the AIE phenomenon occurred, polygonal nanoparticles found were prominent. Aggregates were also present, as in the previous percentage, some of which reach a size of up to one micron, while the smallest ones are about 700 nm. At 60% water, the amount at which the AIE phenomenon starts for this compound, helix-shaped nanofibres were found, with spherical nanoparticles attached to them, which were also observed singly or in pairs, trios or larger aggregates.

Finally, at the highest amount of water considered (90%), nanofibres and aggregates of nanoparticles were again observed, with some of them being vesicles.

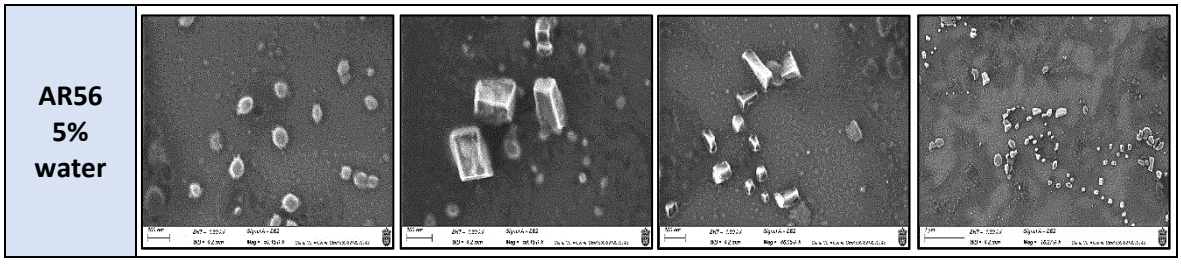

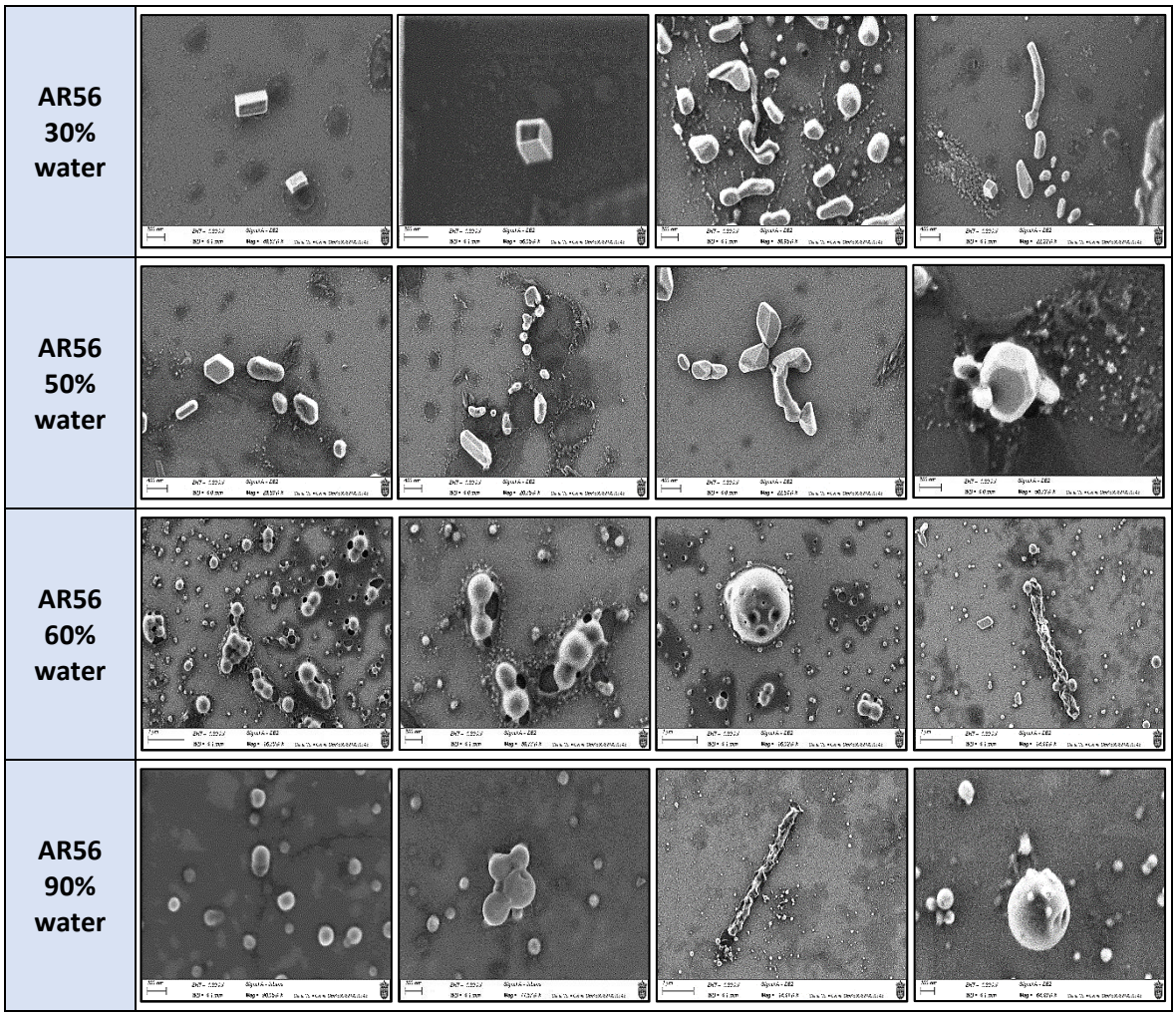

Figure 30. SEM nanoparticles of AR56 in different mixtures of THF-H_2O.

4.1.2. Aggregation analysis using acetone as organic solvent

The aggregation study of this compound was repeated using acetone as solvent, which allows determining the influence of the organic solvent on the AIE phenomenon and on the nanostructures formed. In this case, as shown in Figure 31, the AIE was initiated at 40% water, whereas with THF the amount of water required was higher, at 60%.

The shift of the emission maximum accompanying this phenomenon was more drastic than in THF. While in the previous case the maximum was shifted from orange to yellow region as the polarity of the medium increased, if acetone was used as solvent, the emission maximum moved from red (about 675 nm) to yellow (about 560-575 nm) region. Finally, at higher amounts of water, the emission maximum was in the green region (about 540 nm).

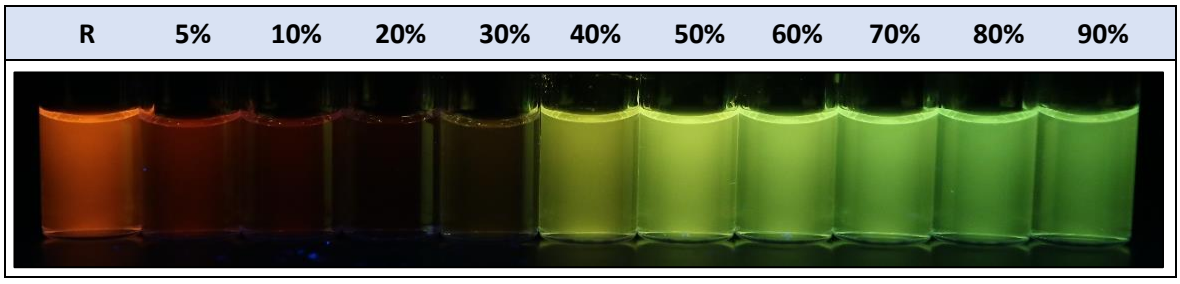

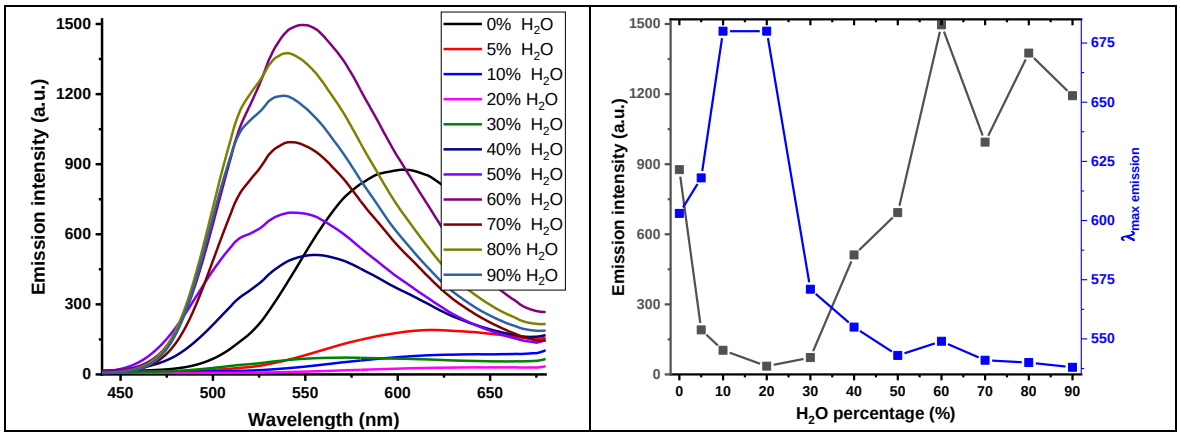

Figure 31. Fluorescence imagen of water acceptance test of a 20 µM solutions of AR56 in acetone mixtures with increasing amounts of water (up). Emission intensity graph (down left) and graph of relationship between the emission intensity and the wavelength of the maximum of emission (down right) as a function of the amount of water added for AR56 in acetone. λ_{exc} = 355 nm.

The formed nanostructures were studied by SEM and the results are shown in Figure 32.

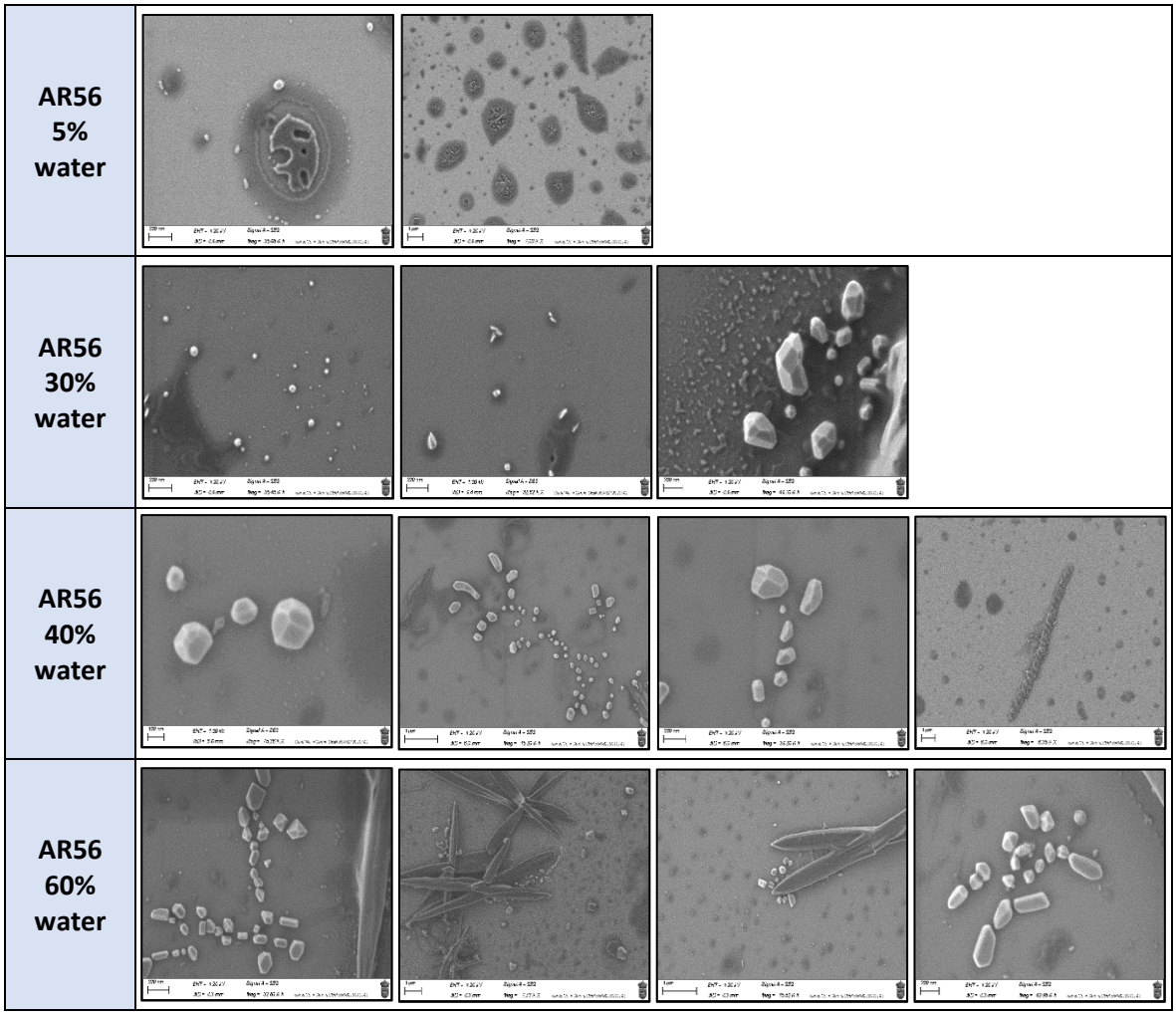

Figure 32. SEM nanoparticles of AR56 in different mixtures of acetone-H_2O.

At 5% water, completely amorphous structures were observed, without any recognisable structure, in contrast to the nanostructures obtained in THF, where nanocubes and spherical nanoparticles were observed. As the amount of water was increased to 30%, individual spherical nanoparticles of less than 100 nm were found, as well as rod-shaped and amorphous

nanoaggregates. At the amount of water at which the AIE phenomenon started, that is at 40%, amorphous aggregates of nanoparticles with a diameter between 250-500 nm were formed. Furthermore, as in THF at 60% water, helix-shaped nanofibres were found. Finally, at 60% water, amorphous nanoparticles of similar size to the previous ones and needle-shaped nanoparticles with a length of more than 5 microns were found. On the other hand, at the highest amounts of water in THF, mainly nanofibres with nanoparticles adhered to them were observed, highlighting the presence of some nanovesicles.

Therefore, although the AIE phenomenon occurred independently of the solvent used, the nanostructures and aggregates formed are completely different, with only the appearance of nanofibres in common with the amount of water in which the AIE was initiated. In fact, the nanostructures formed in THF were more recognisable and interesting, mainly due to the appearance of vesicles, than those obtained in acetone.

4.2. Conjugation extension analysis: AR65

The extension of the conjugation was also studied by replacing the pyrene ring with a chrysene ring. The synthetic route leading to it also involved a Suzuki-Miyaura coupling reaction according to the scheme in Figure 33.

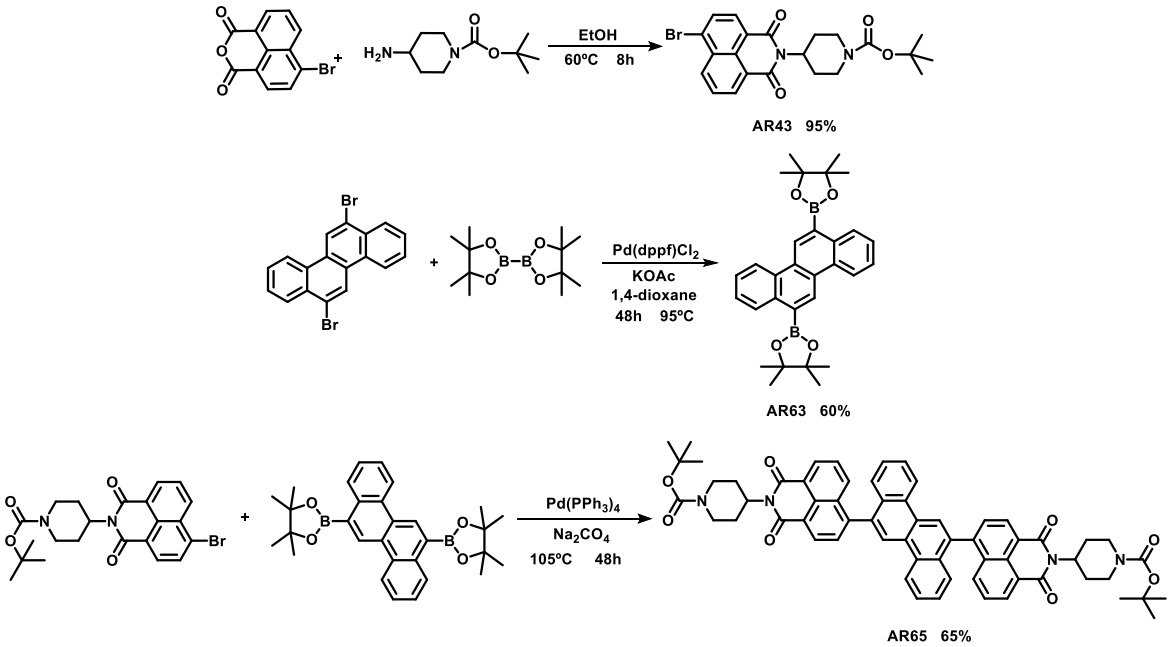

Figure 33. Scheme of the synthetic route followed to obtain the compound AR65.

The fluorescence study (Figure 34 and Figure 35) showed that the highest emission was found in non-polar solvents while in the more polar solvents, such as methanol and water, the emission is zero. In addition, the emission maximum exhibited a marked bathochromic shift from the blue region (above 425 nm), characteristic of NMIs, to the yellow region (over 550 nm).

	H_2O MeOH DMSO DMF MeCN Acet. EtOAc THF $CHCl_3$ DCM Tol. Et_2O Hex. MCH
Visible light	

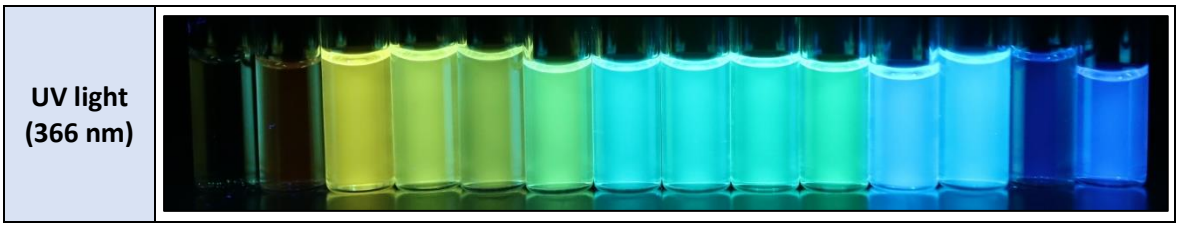

Figure 34. Solvatochromism images. 10 µM solution of AR65 in different solvents under visible and 366 nm light.

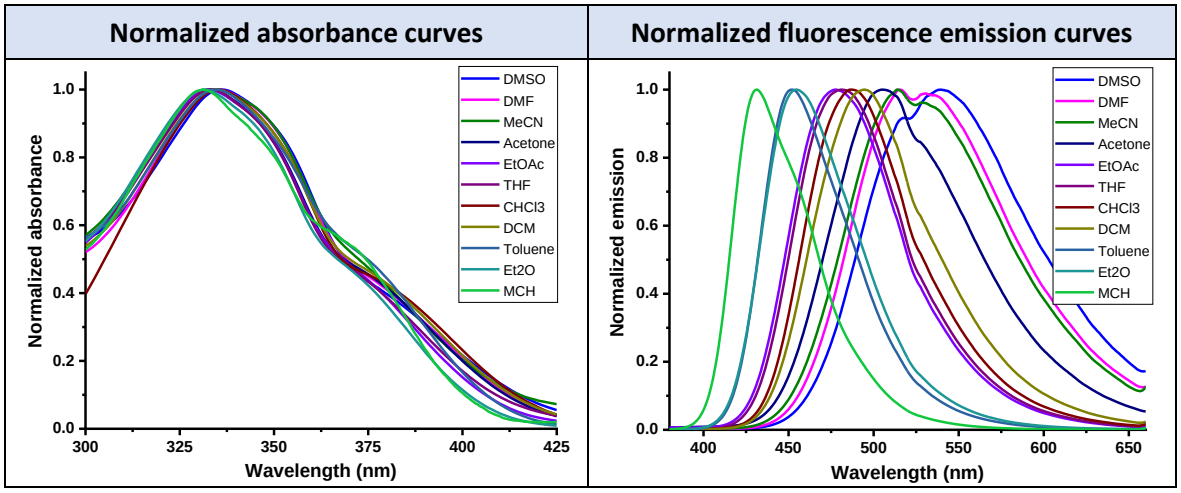

Figure 35. Solvatochromism graphs. Normalized absorbance curves (left) and fluorescence emission curves (right) in several solvents. λ_{exc}=335 nm.

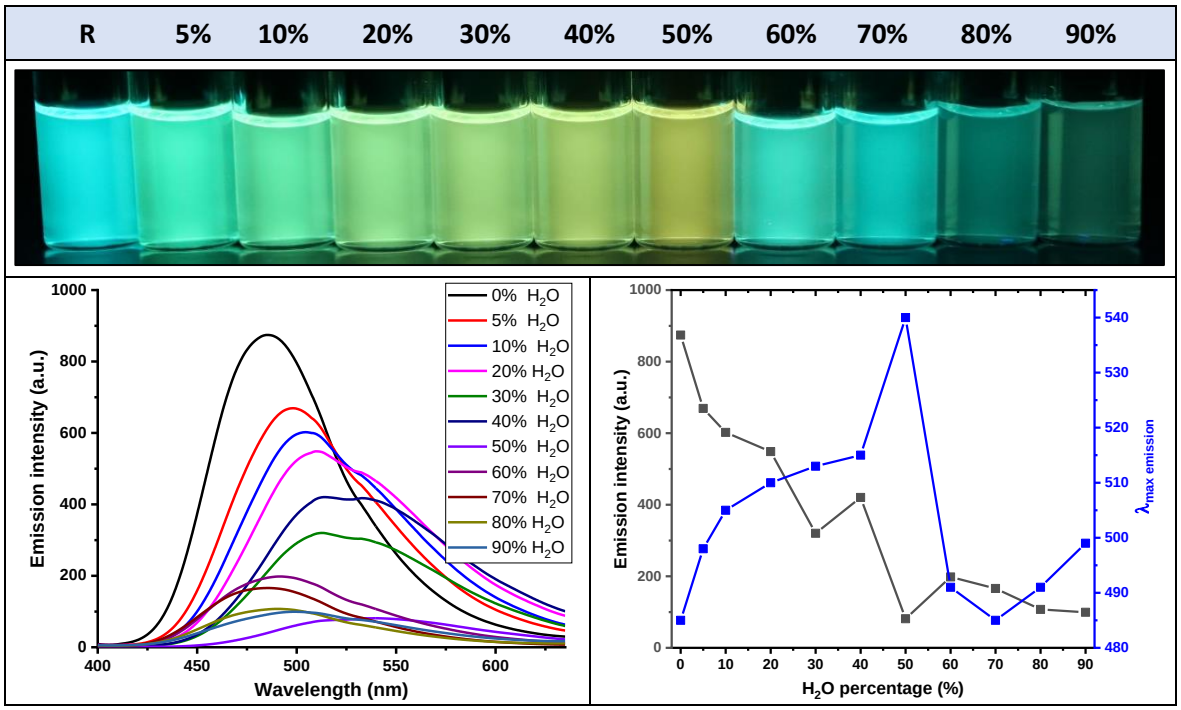

Figure 36. Fluorescence imagen of water acceptance test of a 10 µM solutions of AR65 in THF mixtures with increasing amounts of water (up). Emission intensity graph (down left) and graph of relationship between the emission intensity and the wavelength of the maximum of emission (down right) as a function of the amount of water added for AR65 in THF. λ_{exc} = 335 nm.

The solvent used for the water acceptance test was THF. As can be seen in Figure 36, the emission intensity decreased up to 50% water, after which the emission increased slightly and decreased again after 80% water. This variation of the emission intensity was accompanied by a shift of the emission maximum from the blue-green region (above 485 nm) to the yellow region

(between 520-540 nm) and back to the blue-green region with the highest amounts of water. The nanoestructures formed through this phenomenon were studied by SEM (Figure 37).

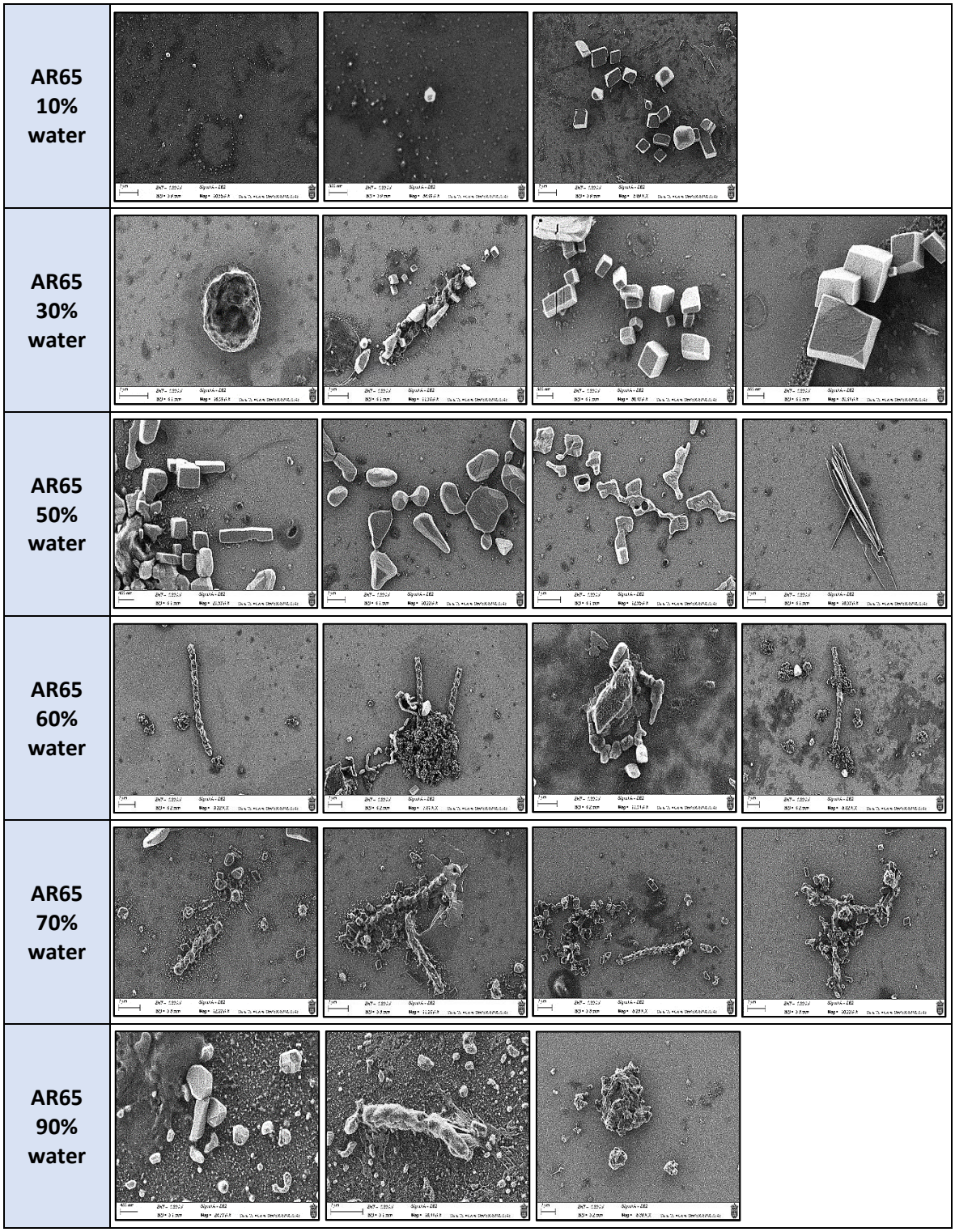

Figure 37. SEM nanoparticles of AR65 in different mixtures of THF-H_2O.

At low amounts of water, when the fluorescence was in the blue-green region, individual spherical nanoparticles with a diameter of approximately 180 nm were found. Nanocubes and amorphous structures of varying width (over 150 nm) were also observed. When increasing the amount of water up to 30%, individual spherical nanoparticles with a diameter of more than 1.5

microns, nanocubes with a side size of more than 250 nm and helix-shaped fibres with attached cubic nanoparticles were encountered.

At 50% water, in the yellow region, nanocubes with a side size of 1.4 microns as well as amorphous nanoparticles and aggregates of them were obtained. Some of these aggregates were needle-shaped. However, the main difference with the previous ratios was the absence of nanofibres. Slightly increasing the amount of water to 60% and returning to the blue-green region, helix-shaped fibres were again found, many of them attached to aggregates of spherical nanoparticles. Nanocubes and amorphous aggregates continued to be observed, as in the previous percentage.

When reaching 70% water, the amount at which the AIE started, the same structures were observed as for the previous percentage: amorphous aggregates and nanofibres with nanocubes attached to them. The same occurred at 90% water.

Comparing the aggregation of the NMI derivatives using a pyrene (AR56) and a chrysene (AR65) as core, the formation of nanocubes at 30% water and nanofibres at 60% water was observed in both cases, as well as the formation of aggregates at relatively low amounts of water. However, the pyrene derivative was much more interesting due to its ability to form vesicles with high amounts of water.

4.3. Analysis of a primary amine- phenyl derivative: AR52

A part of the NMI derivatives analysed had a secondary amine in their structure, such as AR82s and AR83s (Section 4.2). However, the influence of a primary amine on the aggregation of the compound AR52 was studied, also synthesized by a Suzuki-Miyaura carbon-carbon coupling reaction according to the following synthetic route (Figure 38).

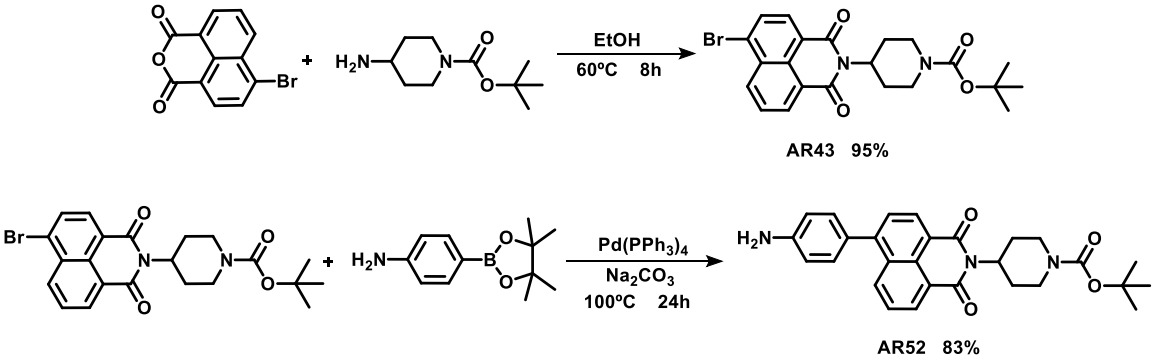

Figure 38. Scheme of the synthetic route followed to obtain the compound AR52.

The fluorescence study (Figure 39 and Figure 40) revealed that the highest emission was found in non-polar solvents, being practically insignificant for the more polar solvents. Again, there was a bathochromic shift of the emission maximum from the blue region (above 450 nm) to the greenish-yellow region (over 590 nm). This shift also occurred for the absorption maximum, being much larger than for all NMI derivatives considered before.

	H_2O MeOH DMSO DMF MeCN Acet. EtOAc THF $CHCl_3$ DCM Tol. Et_2O Hex. MCH
Visible light	

Figure 39. Solvatochromism images. 20 µM solution of AR52 in different solvents under visible and 366 nm light.

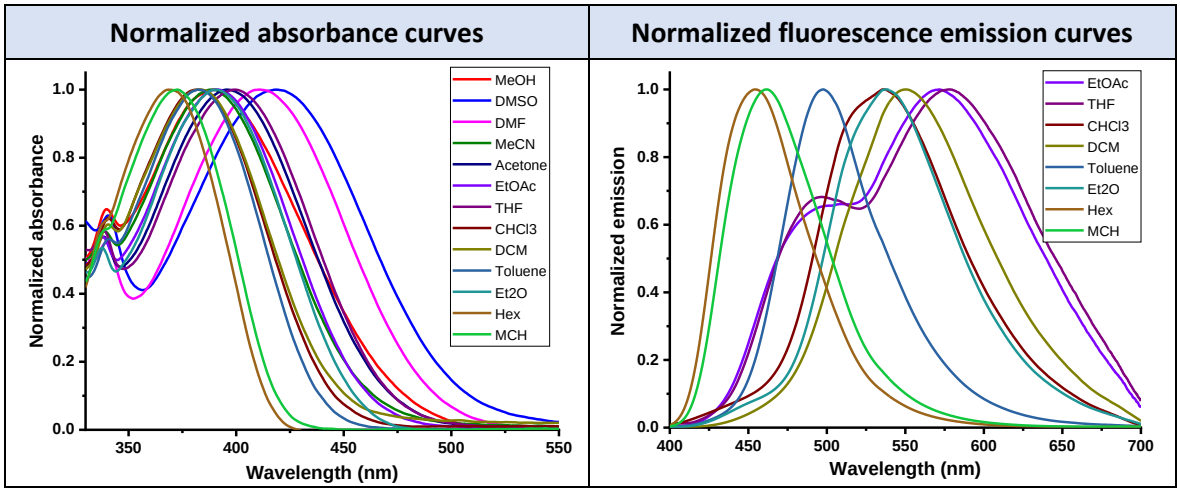

Figure 40. Solvatochromism graphs. Normalized absorbance curves (left) and fluorescence emission curves (right) in several solvents. λ_{exc}=380 nm.

The water acceptance test (Figure 41) was carried out using THF as solvent. In this case, the AIE phenomenon started at 60% water, presenting a very low emission intensity at the previous amounts. This phenomenon was also accompanied by a shift of the emission maximum from the blue region (above 430 nm) to the orange region (around 600 nm) at the same amount of water at which the AIE was initiated.

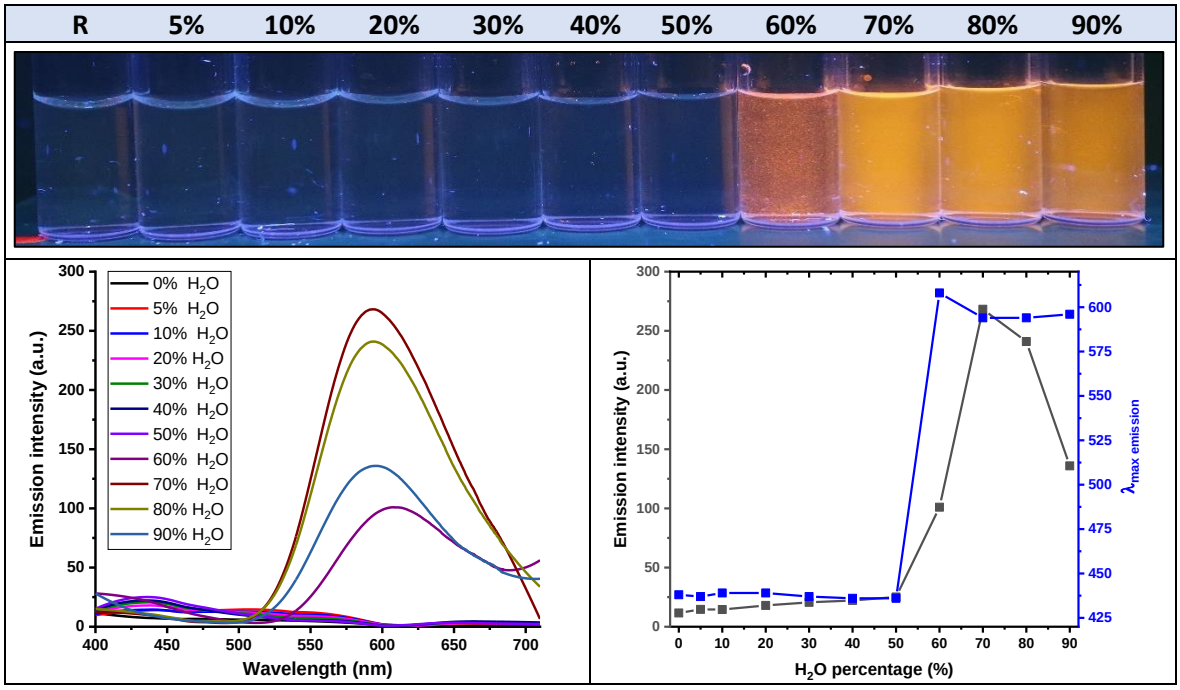

Figure 41. Fluorescence imagen of water acceptance test of a 10 µM solutions of AR52 in THF mixtures with increasing amounts of water (up). Emission intensity graph (down left) and graph of relationship between the emission intensity and the wavelength of the maximum of emission (down right) as a function of the amount of water added for AR65 in THF. λ_{exc} = 380 nm.

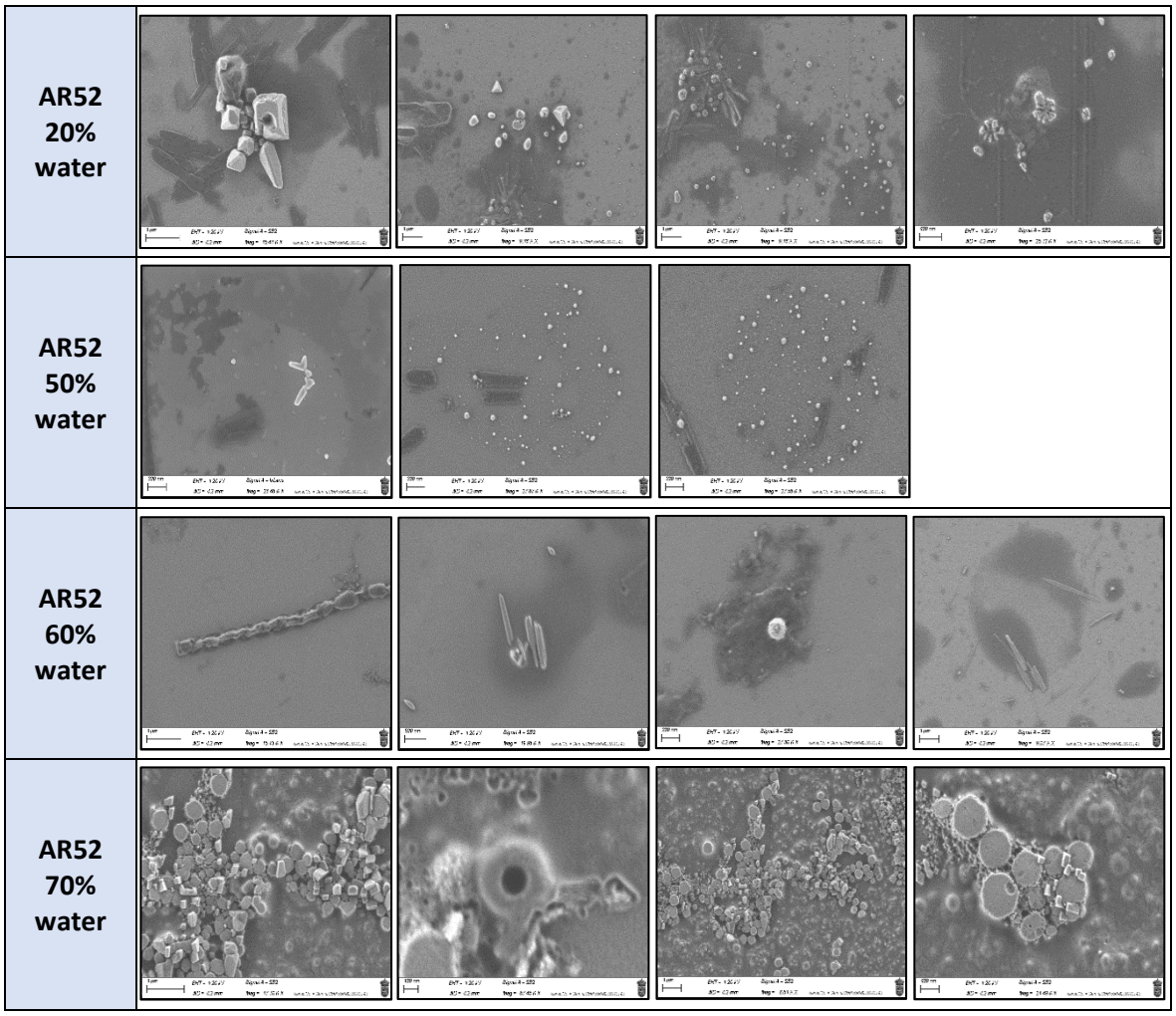

Figure 42. SEM nanoparticles of AR52 in different mixtures of THF-H_2O.

Figure 42 shows the nanostructures formed by this compound. At 20% water, spherical nanoparticles with a diameter of approximately 70-100 nm were encountered, as well as aggregates of these nanoparticles. At 50%, only larger spherical nanoparticles of approximately 125 nm and aggregates were observed. At 60% water, needle-shaped, spherical nanoparticles and aggregates of the latter were found, as in the previous amounts of water. At the percentage at which the AIE started, as with many NMI derivatives, helix-shaped fibres were detected. Finally, at 70% water, mainly aggregates of nanoparticles, both cubic and spherical (around 700 nm in diameter), were observed, and a few vesicles were found in the minority.

This result was reminiscent of compounds AR82p and AR83p, since the AIE that occurred was quite intense and was accompanied by the formation of helix-shaped nanofibres at the amount of water in which this phenomenon was initiated. In contrast to the compounds with secondary amines, vesicles had formed at the highest water content.

4.4. Analysis of a primary amine-pyrimidine derivative: AR55

In this section, the influence of a primary amine attached to a pyrimidine was studied, verifying the influence of the amino-protecting group. For this purpose, compound AR55p was synthesised by a Suzuki-Miyaura carbon-carbon coupling reaction, followed by deprotection of the amino-protecting group to obtain the product AR55d, according to the scheme in Figure 43.

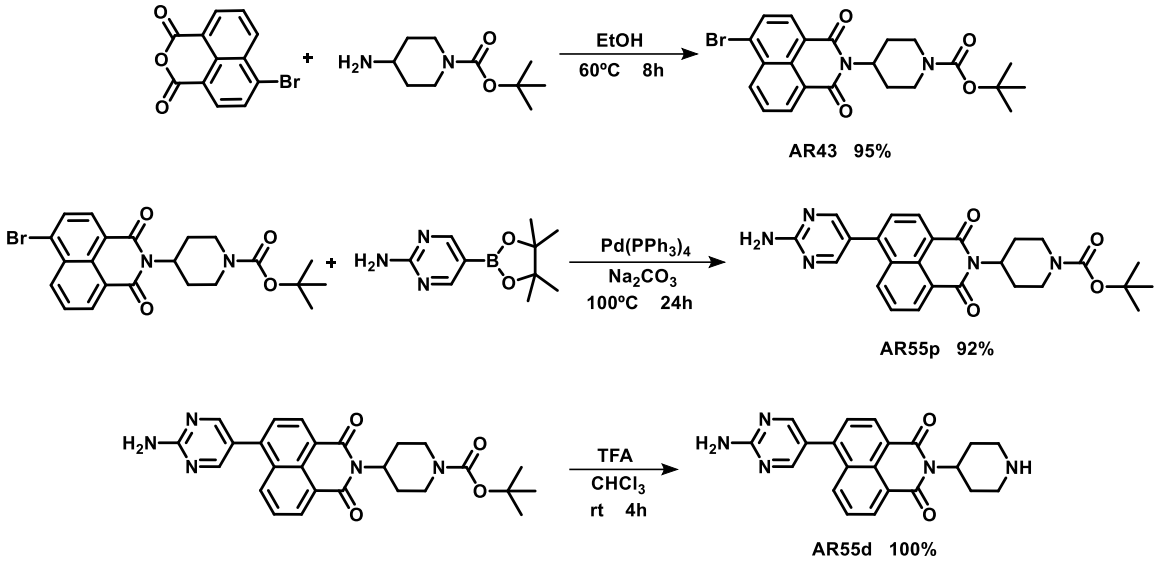

Figure 43. Scheme of the synthetic route followed to obtain AR55 series.

The absorbance and fluorescence study of the amino-protected and unprotected compound (Figure 44 and Figure 45) showed a great similarity between them due to their structural similarity. Both compounds exhibited a bathochromic shift of the emission maximum from the blue region (about 415 nm) to the yellow region (about 550 nm). This shift was also observed, but much smaller, for the absorption maximum. The most striking difference between the two derivatives is the slight emission shown by the amino-protected product AR55p in the most apolar solvents of all those used, which the compound AR55d lacked.

Despite the structural similarities between the AR52 and AR55p compounds, the AR52 showed a strong emission in the intermediate and low polarity solvents, while it was insignificant in the more polar solvents. In contrast, compound AR55p presented emission in all solvents except water. Therefore, in this type of compounds, the presence of a pyrimidine in the structure leads to compounds that are more solvatochromic than those having a phenyl ring.

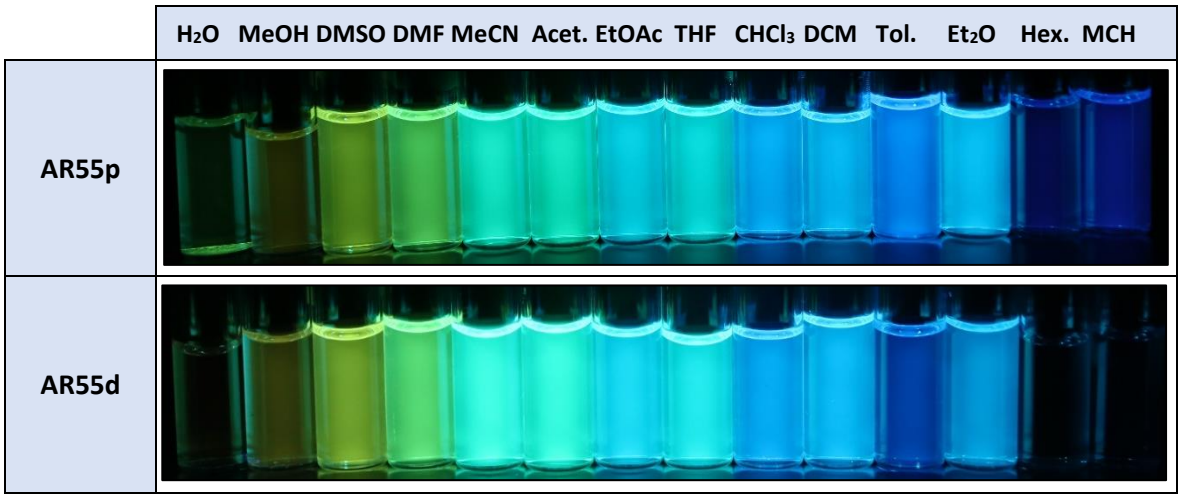

Figure 44. Fluorescent emission of 10 µM solutions of AR55 product series in different solvents under 366 nm light.

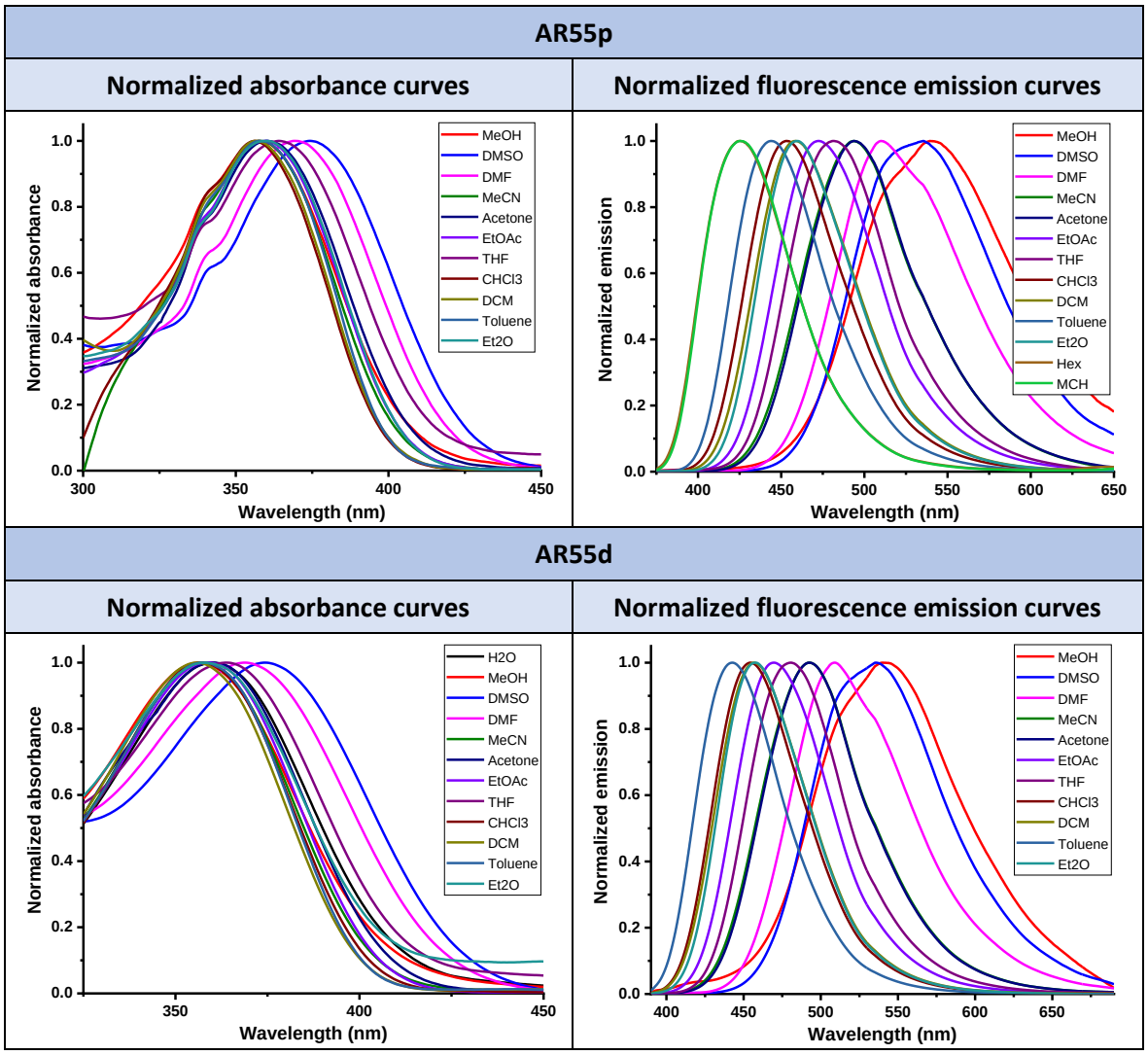

Figure 45. Normalized absorption and emission spectra of 10 µM solutions of the AR55 product series in different solvents.

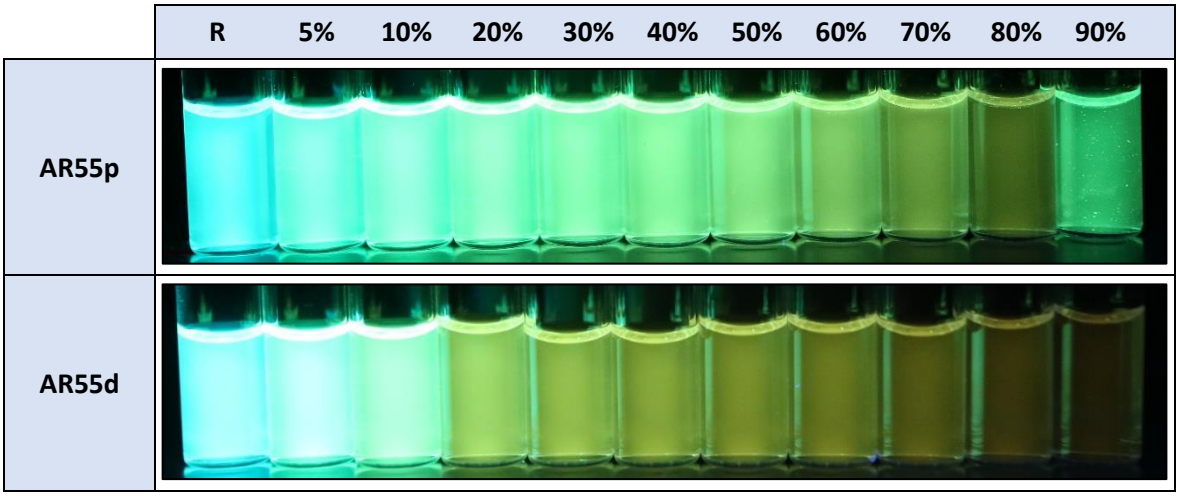

Figure 46. Water acceptance test. 20 µM solutions of the AR55 series of compounds in THF mixtures with increasing amounts of water.

The water acceptance test (Figure 46) was performed using THF as organic solvent for both compounds. AR55p, as expected, showed a decrease in emission intensity as the amount of water was increased up to 90%, when the AIE was initiated. This phenomenon was accompanied by a

slight shift of the emission maximum from the green region (around 507 nm) to the yellow region (around 545 nm) and back to the green region when AIE occurred, this can be noticed in Figure 47. In contrast, the unprotected product AR55d exhibited an ACQ as the amount of water increased, which confirms that, regardless of the substituents at position 4 of the naphthalene core, the AIE disappears.

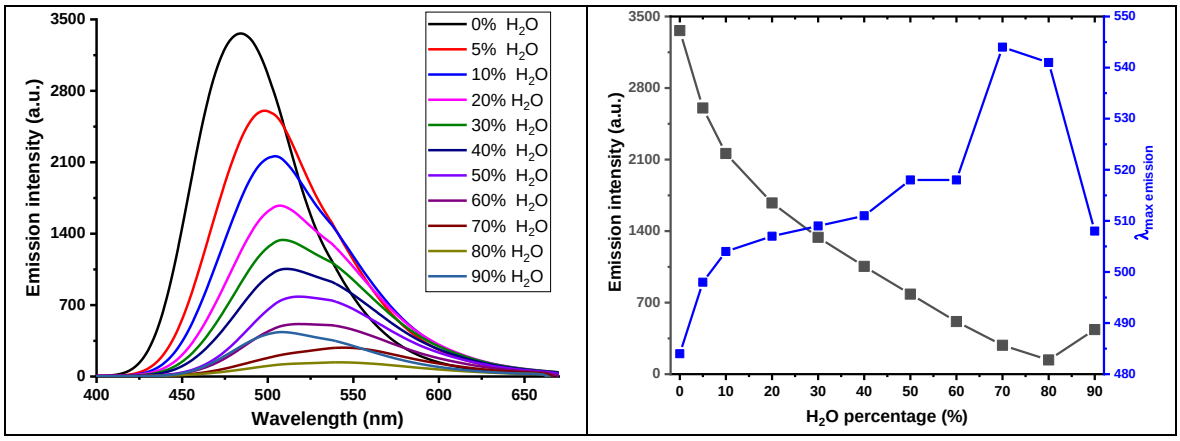

Figure 47. Emission intensity graph (left) and graph of relationship between the emission intensity and the wavelength of the maximum of emission (right) as a function of the amount of water added for AR55p in THF. λ_{exc} = 350 nm.

As in the previous NMI derivatives in the previous sections, the aggregates formed during the AIE phenomenon for the AR55p compound were studied by SEM microscopy, obtaining the results shown in Figure 48 below.

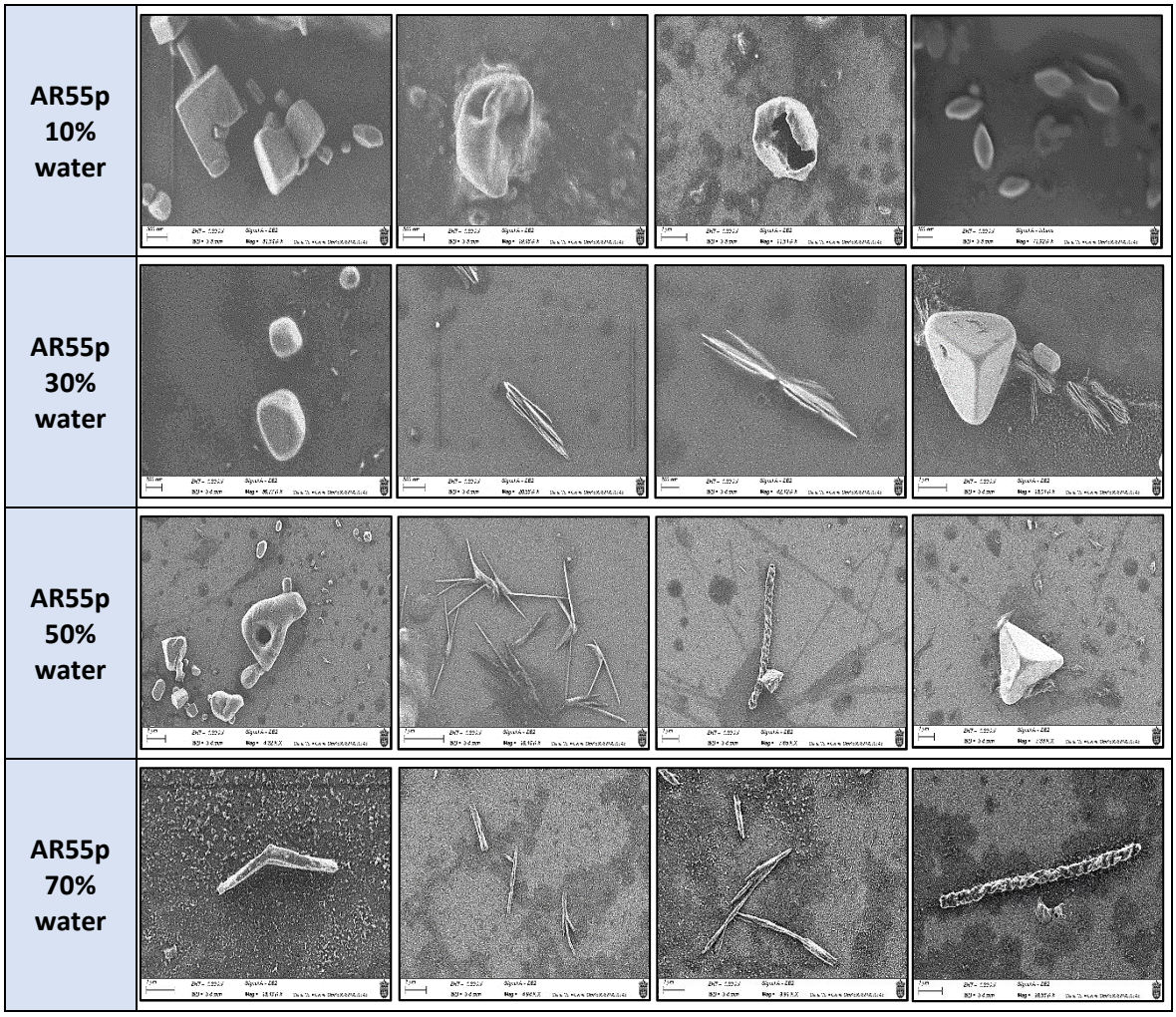

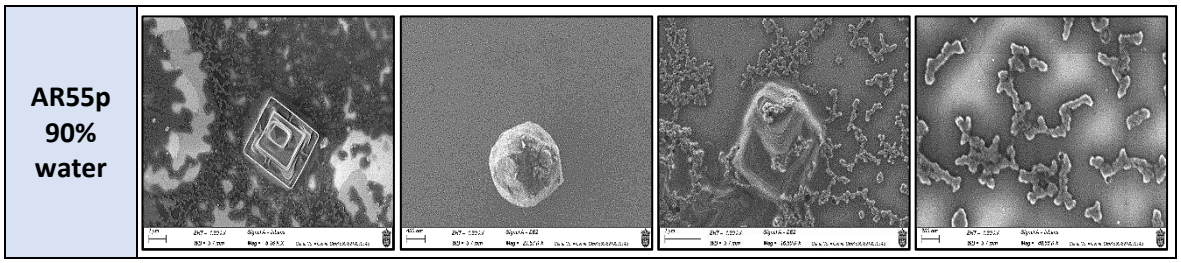

Figure 48. SEM nanoparticles of AR55p in different mixtures of THF-H_2O.

The nanostructures observed for this compound are characterised by being very random. At 10% water, rectangular-shaped nanoparticles were found, with an approximate side size of 430 × 150 nm, as well as amorphous and needle-shaped nanoparticles, with a thickness of around 80-120 nm. When the amount of water was increased to 30%, amorphous nanoparticles with a size ranging from 300-630 nm, aggregates of nanoneedles and, sporadically, some triangular pyramid shaped nanoparticles were detected. At 50% water, needle-shaped nanoparticles and aggregates of them with a thickness between 40-50 nm, aggregates with a size of almost 3 µm and helix-shaped fibres were observed. At this percentage of water, triangular pyramid nanoparticles continued to be observed as well as occasional hollow amorphous particles in the centre. By increasing the amount of water added until 70%, helix-shaped nanoparticles with a thickness of approximately 400 nm continued to be identified, as well as fibres, with a thickness of 250-550 nm, needle-shaped nanoparticles and aggregates of them. Finally, at 90% water, spherical nanoparticles with a diameter of 1.5 µm and aggregates of them were observed, as well as aggregates of cubic nanoparticles.

4.5. Analysis of derivatives with an indole-carbazole substituent: AR67

The analysis of the aggregation of the NMI derivatives concluded with the study of the amino-protected and unprotected compound of the AR67 series. The synthetic route followed to obtain it (Figure 49) involved, as in previous examples, a Suzuki-Miyaura carbon-carbon coupling reaction.

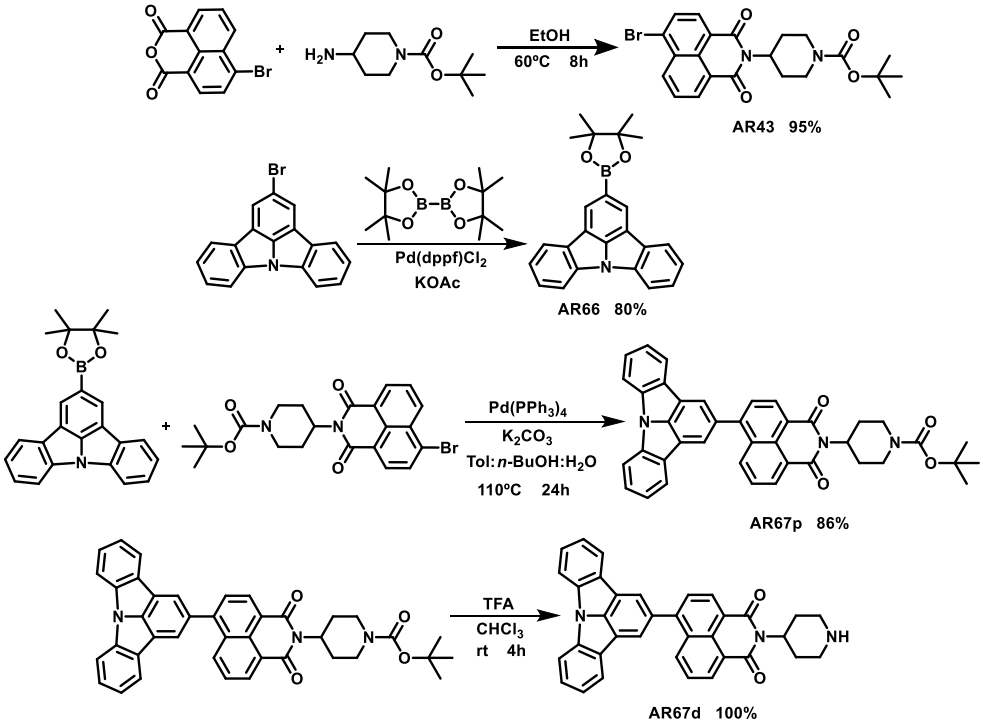

Figure 49. Scheme of the synthetic route followed to obtain the compound AR67.

The fluorescence analysis of the AR67p and AR67d compounds is detailed in Section 5 of Chapter 3B, showing considerable emission in all solvents except the most polar ones, that is, MeOH and water, as well as a bathochromic shift of the emission maximum. The water acceptance test was carried out using THF as the organic solvent, giving the result in Figure 50.

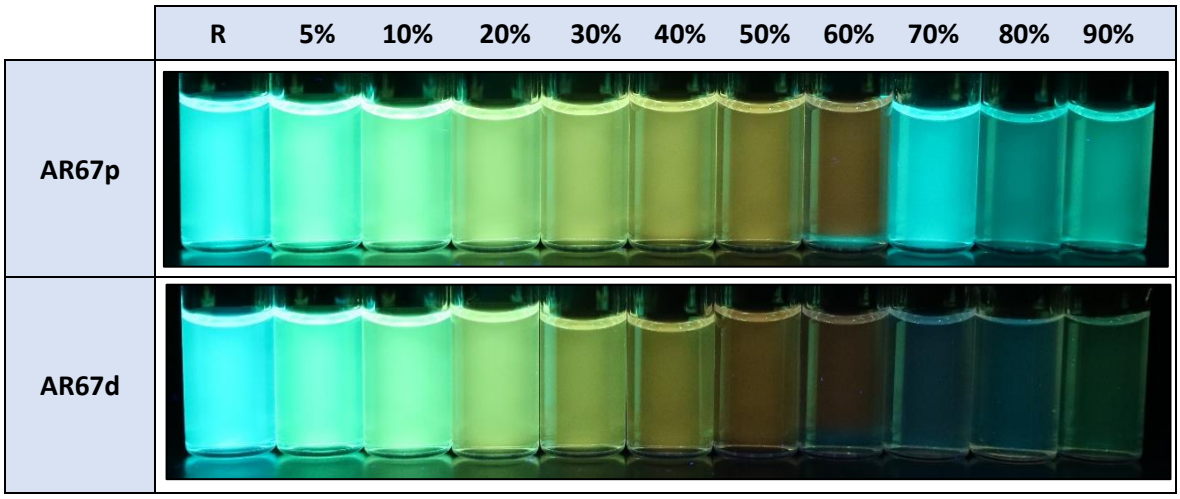

Figure 50. Water acceptance test. 10 µM solutions of the AR67 series of compounds in THF mixtures with increasing amounts of water.

Compound AR67p showed a progressive decrease in emission intensity until 70% water was reached, after which the emission intensity increased (AIE) and then decreased again. This variation in emission intensity was accompanied by a shift of the emission maximum from the blue region (above 490 nm) at 5% of water to the yellow region (approximately 550 nm) when 60% of water was achieved, returning back to the blue region when the AIE started. This can be seen in Figure 51. The compound AR67d, on the other hand, exhibited an ACQ as the amount of water increases, as was the case for all the unprotected compounds considered so far: the absence of the amino-protecting group caused the disappearance of the AIE phenomenon.

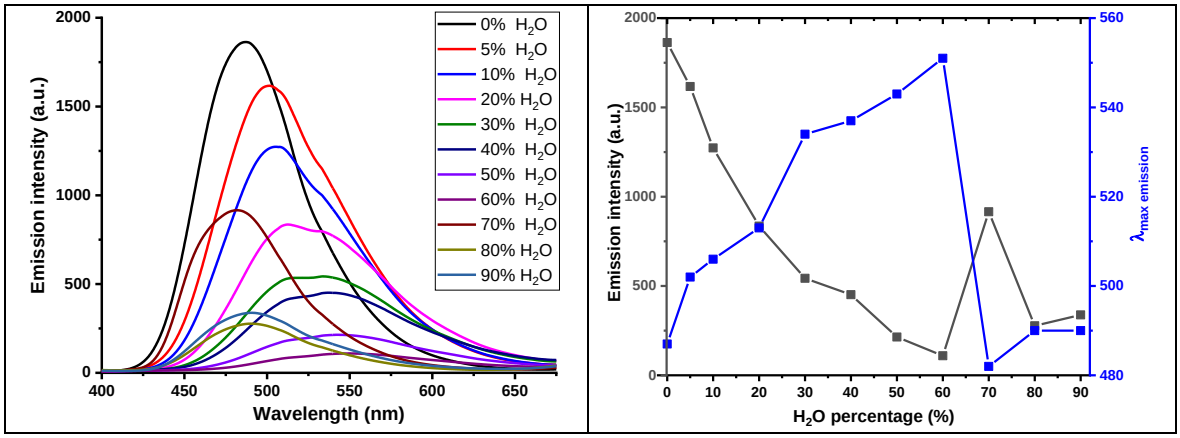

Figure 51. Emission intensity graph (left) and graph of relationship between the emission intensity and the wavelength of the maximum of emission (right) as a function of the amount of water added for AR67p in THF. λ_{exc} = 360 nm.

The formed nanostructures were studied by SEM (Figure 52). At low amounts of water, 10%, individual spherical nanoparticles with a diameter of, approximately, 50 nm were observed, as well as aggregates of the same type of nanoparticles, resulting in structures with a size of around 120 nm. Nanocubes were also observed sporadically. Increasing the amount of water up to 50%, mainly individual spherical nanoparticles of larger diameter than the previous ones (between 80-130 nm) were found, as well as aggregates of them. Some helix-shaped nanofibres were rarely detected. The same structures were also found at 60% water. When the quantity of water raised to 70%, the amount at which the AIE started in this compound, the same was observed as in the previous

percentages: spherical nanoparticles and aggregates of them, but of increasingly larger size. At this percentage, nanosticks were found, which appeared in the form of aggregates when working at 90% water.

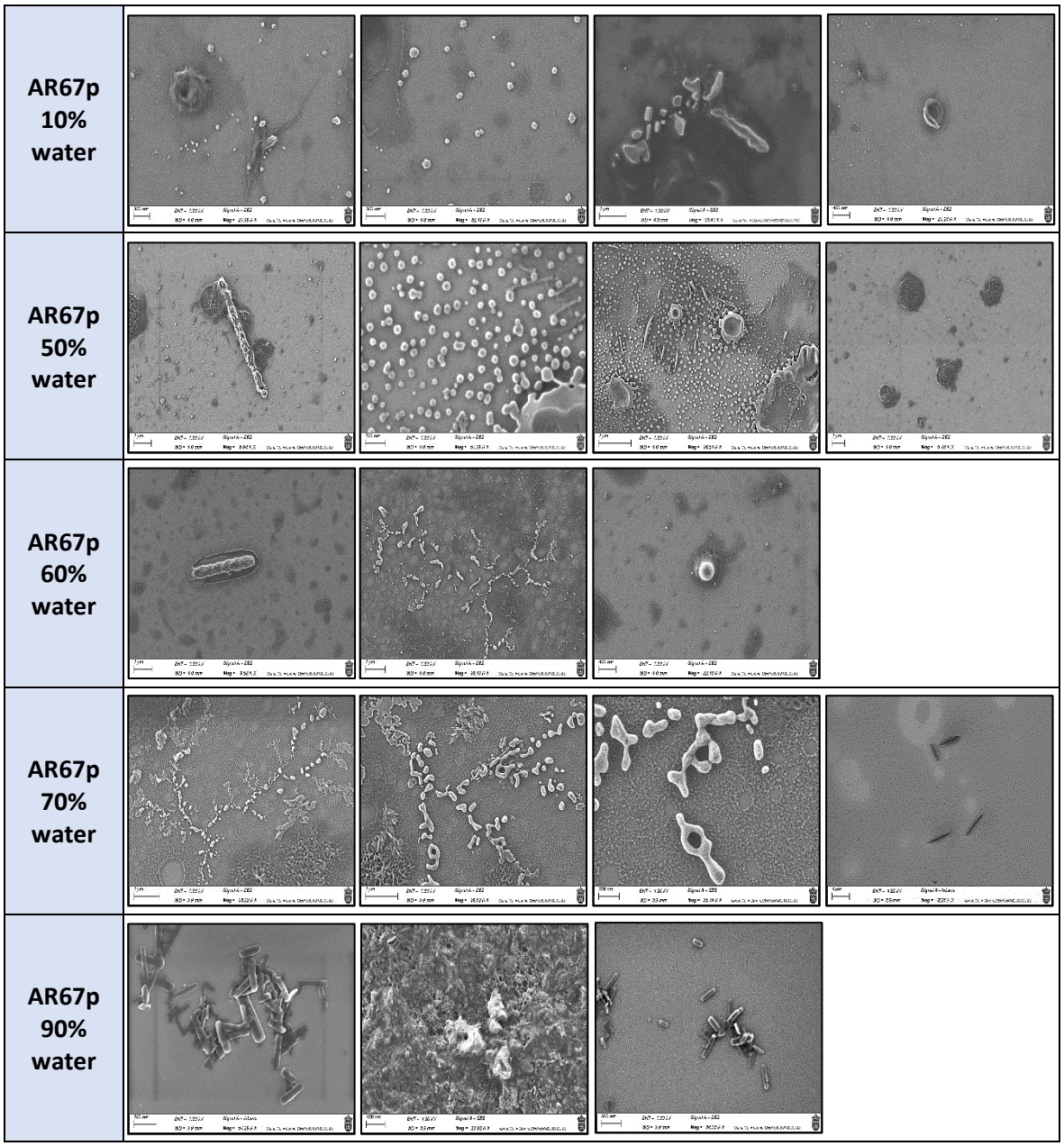

Figure 52. SEM nanoparticles of AR67p in different mixtures of THF-H_2O.

The results obtained for this compound corroborate what has been observed previously: the presence of amino-protecting groups leads to an intense AIE phenomenon, independently of the substituents on the naphthalene core.

5. CONCLUSIONS

A phenomenon that has been studied for the last decades due to its benefits in many fields, such as medicine (bioimaging or phototherapy), the development of luminescent probes or optical devices, is Aggregation Induced Emission (AIE). Many of the NMI derivatives commonly exhibit this phenomenon, which has been studied in depth throughout this chapter.

On the one hand, the influence of the amino-protecting groups in the aggregation process has been analysed, considering amino-protected (AR82p and AR83p), semi-protected (AR82s and AR83s) and unprotected (AR82d and AR83d) compounds. This has allowed to affirm that the amino-protected compounds undergo an intense AIE phenomenon, which is considerably reduced when one of the amino-protecting groups is removed and disappears completely for the unprotected compounds. This has been further corroborated for compounds AR55 and AR67, which show a considerable increase in emission intensity when shielded but this effect disappears when the protecting group is removed (ACQ). Therefore, it is possible to control the intensity of the AIE as a function of the number of free amines present in the compounds, in other words, as a function of the number of protective groups present in the structure.

On the other hand, the influence of the substituents at position 4 of the naphthalene core was studied, maintaining the piperidine protecting group. As shown by compounds AR52, AR55 or AR67, the influence of the amino-protecting group is greater than that of the substituents at position 4, since the removal of the amino-protecting group results in the quenching of the AIE independently of the substituents on the naphthalene core.

It was observed that, most of the compounds considered exhibit helix-shaped fibres at the amount of water at which the AIE was initiated, with nanovesicles forming at the higher water percentages. It has been demonstrated that the solvent has a direct influence on the nanostructures formed by AIE because, in THF, compound AR56 formed nanoparticles of different characteristics and even vesicles, while in acetone the aggregates were observed with lower amounts of water and no vesicles were found.

Thus, once we know how to control the intensity of the AIE by regulating the conditions under which the aggregation is performed (solvent, dye concentration, temperature or amino-protecting groups), the formation of the nanostructures can be controlled, favouring the formation of nanovesicles, which would allow their use, for example, as carriers of substances.

CHAPTER 5

PMI DERIVATIVES: PROPERTIES AND AGGREGATION

Rylenes[1] are a family of polycyclic hydrocarbons consisting of naphthalene rings connected by their peri-positions. The structure of this type of compounds depends on the number of naphthalene rings (n), as shown in Figure 1:

- If n = 0, the compound is called perylene.
- If n = 1, it is terrylene.
- If n = 2, the compound is a quaterrylene.

These three derivatives are the best choice for organic synthesis because of their large absorption coefficient, their strong fluorescence and their high chemical and thermal stability.

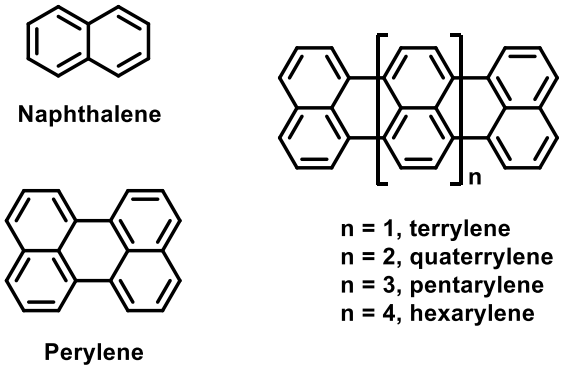

Figure 1. Rylene structures.

Of all the rylenes, the most studied are the perylene derivatives because of their exceptional characteristics. They have a highly conjugated structure which confers them great photoelectronic properties and considerable solubility, a common problem when n > 1. Such compounds can be used in a wide range of applications, for example in the development of luminescent probes,[2] in supramolecular chemistry[3] or in the manufacture of semiconductors.[4]

Perylene is characterised by twelve functionalisable positions known as ortho, peri and bay.[5] Functionalisation with two diimide groups at the end positions of rylene results in rylene diimides (Figure 2).

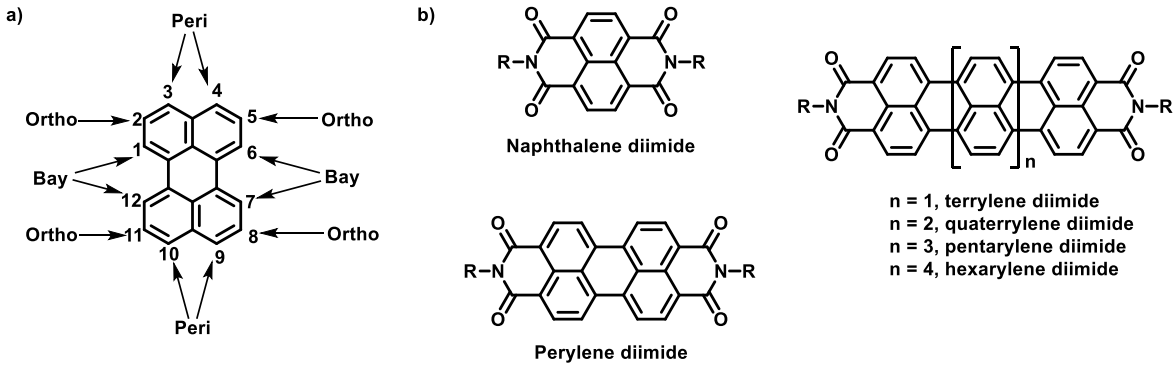

Figure 2. a) Nomenclature and positions of perylene. b) Rylene diimides structures.

Two different derivatives can be obtained by applying this to perylene, depending on the positions at which the functionalisation is performed:

[1] X. Zhao, Y. Xiong, J. Ma, Z. Yuan, *J. Phys. Chem. A.*, **2016**, *120*, 7554–7560.
[2] X. Zhang, S. Rehm, M. M. Safont-Sempere, F. Würthner, *Nat. Chem.,* **2009**, *1*, 623–629.
[3] C. Huang, S. Barlow and S. R. Marder, *J. Org. Chem.*, **2011**, *76*, 2386-2407.
[4] J. Cann, S. Dayneko, J. P. Sun, A. D. Hendsbee, I. G. Hill, G. C. Welch, *J. Mater. Chem. C.*, **2017**, *5*, 2074-2083.
[5] V. Sharma, D. Sahoo, F. Chandra, A. L. Koner, *Chem. Select.*, **2017**, *2*, 11747-11754.

- Perylenemonoimide (PMI): these are obtained by functionalisation of the adjacent peri-positions 3 and 4 with an *N*-imide group.
- Perylenediimide (PDI): these are obtained by functionalisation of the adjacent peri positions with *N*-imide groups (positions 3 and 4 on the one hand and positions 9 and 10 on the other).

However, this chapter will mainly focus on the characteristics and properties of PMI derivatives, with special emphasis on aggregation processes.

1. PMI: STARTING MATERIAL AND APPLICATIONS

PMIs can be obtained from different synthetic routes. The most common, selected by the research group, is the one that uses commercial perylene dianhydride (PDA) as the starting material. The synthetic route for obtaining PDA from acenaphthene (Figure 3) was developed by Kardos in 1913[6] and has now been extensively studied in the literature.

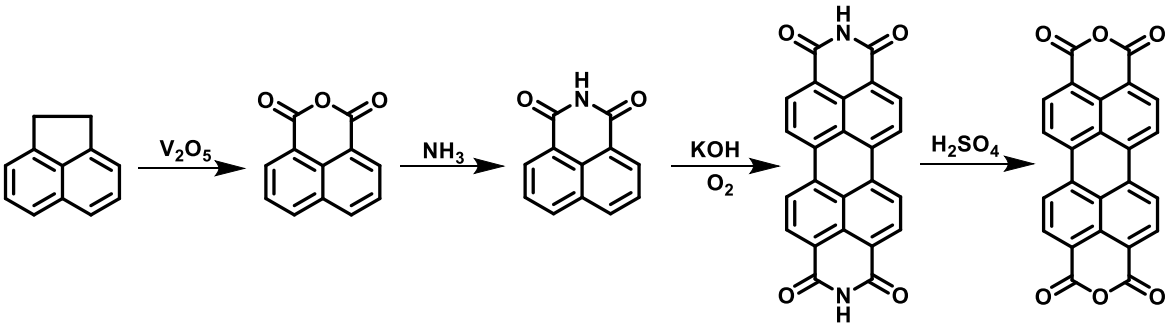

Figure 3. Pathway for the synthesis of the PDA.

PDA can be modified by introducing amines into the anhydride groups or by substituting different positions of the perylene ring, which allows modulation of its characteristics, such as solubility or electronic properties. The most common way to proceed is by introducing *N*-imide groups at the peri-positions of the PDA (Figure 4).[7] Depending on the conditions of introduction of the amine derivatives, two classes can be obtained: perylenomonoimides (PMI) and perylenediimides (PDI).

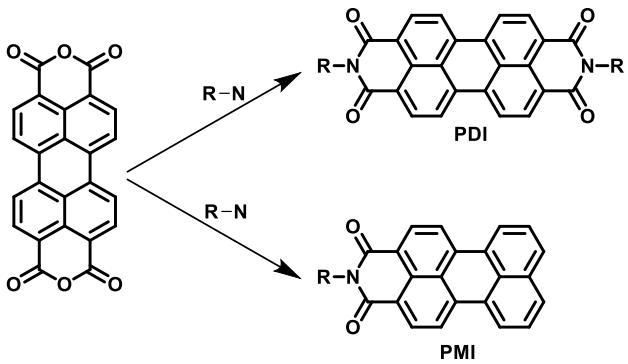

Figure 4. Result of the PDA imidation: PDI and PMI.

[6] M. Kardos, D.R.P. *276357*, **1913**.
[7] a) Y. Nagao, *Prog. Org. Coat.*, **1997**, *31*, 43-49. b) Y. Nagao, N. Ishikawa, Y. Tanabe, T. Misono, *Chem. Lett.*, **1979**, *8*, 151-154.

The properties of PMI depend on its functionalisation. Like perylene, it has several functionalisable positions divided into three groups: ortho, peri and bay (Figure 5). Depending on the position in which the substituents are introduced, the compound will show different properties.

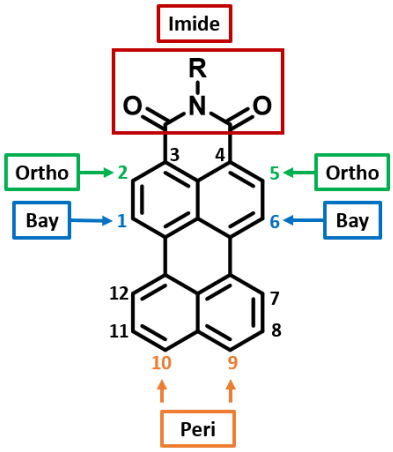

Figure 5. PMI functionalisable positions.

1.1. Applications of PMIs

Initially, perylenes and their derivatives were used as dyes or colourants in the manufacture of industrial paints, used, for example, in the automotive industry, due to their high resistance and quality, or in the textile industry, being used for the dying of synthetic fibres.[8] This was possible because of their high absorptivity, their tunable absorption and emission depending on the substituents in the derivative and the absence of metals. However, their exceptional optical, electrochemical, thermal and luminescent properties have allowed these compounds to be used in more technological applications. Recently, perylene derivatives have had a significant impact on the development of organic electronics,[9] as their excellent photophysical properties make them some of the best n-type semiconductors on the market today. The functionalisation of the *N*-imide position has been the spearhead of this development, allowing the synthesis of electron acceptors of great interest in energy storage or in the research and production of organic field effect transistors (OFETs),[10] organic light emitting diodes (OLEDs)[11] or organic photovoltaic devices (OPVs).[12] In addition, the functionalisation of the different positions of the perylene core of these derivatives has resulted in compounds with high absorption and good capacities as charge carriers that compete with those of fullerenes, allowing their use in the development of solar cells.[13] Another very common application of PMI derivatives is for biological or environmental analysis.[14] For these applications, these compounds must be able to self-assemble in water[15] or have groups

[8] a) E. B. Faulkner, R. J. Schwartz, High Performance Pigments, Wiley-VCH, Weinheim, Germany, **2009**, ISBN: 978-3-527-31405-8. b) H. Zollinger, Color chemistry. Synthesis, properties and applications of organic dyes and pigments, Wiley-VCH, Weinheim, **2003**, ISBN: 3-906390-23-31. c) W. Herbst, K. Hunger, G. Wilker, H. Ohleier, R. Winter, Industrial organic pigments: production, properties, applications, Wiley-VCH, Weinheim, Germany, **2004**, ISBN: 978-3-527-60406-7.
[9] X. Zhan, A. Facchetti, S. Barlow, T. J. Marks, M. A. Ratner, M. R. Wasielewski, S. R. Marder, *Adv. Mater.*, **2011**, *23*, 268-284.
[10] J. T. E. Quinn, J. Zhu, X. Li, J. Wang, Y. Li, *J. Mater. Chem. C.*, **2017**, *5*, 8654-8681.
[11] Y. Qin, G. Li, T. Qi, *Mater. Chem. Front.*, **2020**, *4*, 1554–1568.
[12] N. Liang, D. Meng, Z. Wang, *Acc. Chem. Res.*, **2021**, *54*, 961-975.
[13] a) M. Zhang, Y. Bai, C. Sun, L. Xue, H. Wang, Z. G. Zhang, *Sci. China Chem.*, **2022**, *65*, 462-485. b) V. Sharma, J. D. B. Koenig, G. C. Welch, *J. Mater. Chem. A.*, **2021**, *9*, 6775-6789. c) N. Zink-Lorre, E. Font-Sanchis, A. Sastre-Santos, F. Fernández-Lázaro, *Chem. Commun.*, **2020**, *56*, 3824-3838. d) K. Fujimoto, M. Takahashi, S. Izawa, M. Hiramoto, *Mater.*, **2020**, *13*, 2148.
[14] N. Soh, T. Ueda, *Talanta*, **2011**, *85*, 1233-1237.
[15] D. Görl, X. Zhang, F. Würthner, *Angew. Chem. Int. Ed.*, **2012**, *51*, 6328-6348.

in their structure that allow them to be soluble in water.[16] Water-soluble perylene derivatives are characterised by their biocompatibility, high fluorescence and photostability, which augurs a promising future for these materials in this field. These types of compounds can also be used in bioimaging or as fluorescent markers since the coordination of PMI derivatives with a non-fluorescent biomolecule allows the interaction of this biomolecule with the environment to be detected. An example of the use of PMI derivatives, linked to triphenylphosphine and guanidine, for fluorescence imaging of both cells (Figure 6)[17] and cell organelles, such as mitochondria, allows to understand the differences between the mitochondria of healthy and diseased cells, responsible for tumours and neurodegenerative diseases.

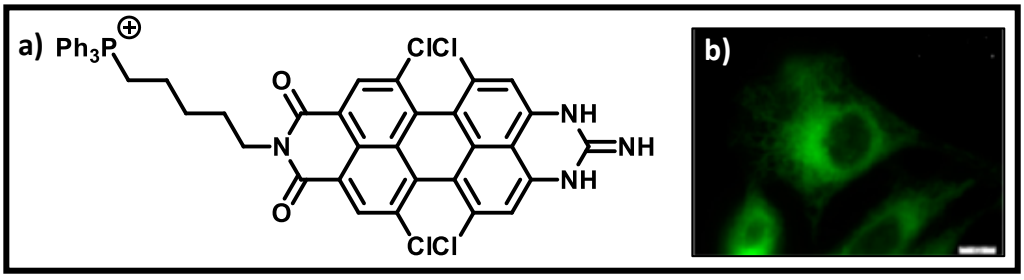

Figure 6. Compound used for fluorescence imaging. a) Structure of the compound. b) Fluorescence image of a cell.

Moreover, PMI derivatives can also be used in the development of fluorescent probes, presenting considerable advantages over the more classical and widely used fluorescent molecules, such as BODIPY compounds, including excitation and emission wavelengths in the visible and NIR regions and high thermal stability. In addition, they also allow the use of silica supports, improving the applicability of this type of compounds as chemosensors.[18]

Finally, the inventiveness of organic chemists to functionalise the perylene ring has allowed the field of application of this type of compounds to be extended even further, as they can be used as building blocks in supramolecular chemistry,[19] in self-assembled nanosystems[20] or in the development of strategies to generate chiral architectures from this initial planar system.[21] Such compounds can also be used in research for the development of new applications linked to a C_{60} fullerene, for the conversion of light energy in photosynthetic systems[22] or in the production of hydrogen.[23]

2. OBJECTIVES

As seen throughout this Chapter, aggregation is one of the most important characteristics of PMI derivatives. Aggregates are of different nature depending on the process followed for their formation.

PMI derivatives are characterised by a shift of the emission maximum, usually from the yellow region (around 575 nm) of the visible spectrum to the red or NIR region (above 700 nm). This shift is produced by increasing the amount of water added to an organic solvent and the aggregates formed depend on this ratio. However, the shift of fluorescence towards the red region is

[16] E. Rostami-Tapeh-Esmail, M. Golshan, M. Salami-Kalajahi, H. Roghani-Mamaqani, *Dyes Pigm.*, **2020**, *180*, 108488.
[17] S. Kaloyanova, Y. Zagranyarski, S. Ritz, M. Hanulova, *J. Am. Chem. Soc.*, **2016**, *138*, 2881-2884.
[18] J. García-Calvo, J. A. Robson, T. Torroba, J. D. E. T. Wilton-Ely, *Chem. Eur. J.*, **2019**, *25*,1 4214-14222.
[19] a) F. Würthner, *Chem. Commun.*, **2004**, *14*, 1564-1579. b) F. Würthner, C. R. Saha-Möller, B. Fimmel, S. Ogi, P. Leowanawat, D. Schmidt, *Chem. Rev.*, **2016**, *116*, 962-1052.
[20] S. Chen, P. Slattum, C. Wang, L. Zang, *Chem. Rev.*, **2015**, *115*, 11967-11998.
[21] J. Li, P. Li, M. Fan, X. Zheng, J. Guan, M. Yin, *Angew. Chem. Int. Ed.*, **2022**, *61*, e202202532.
[22] A. Diacon, O. Krupka, P. Hudhomme, *Molecules*, **2022**, *27*, 6522.
[23] L. Huang, S. W. Tam-Chang, *J. Fluoresc.*, **2011**, *21*, 213–222.

conditioned by other factors, mainly structural, since it occurs when substituents are incorporated that cause an extension of the conjugation in this type of compounds.

On the other hand, both in the literature and in the research carried out during this PhD Thesis, there are innumerable examples of PMI derivatives that undergo the ACQ phenomenon, being very sporadic the cases of AIE for this kind of products. Therefore, along this chapter the aggregates formed by two PMI derivatives that undergo this phenomenon are discussed by increasing the polarity of an organic solvent through the addition of water.

Apart from studying the nanostructures formed by the different derivatives, the aim is also to optimise the conditions to facilitate the obtaining of those that can be used in other applications, such as nanovesicles that can be used in drug delivery. Finally, the intention is to publish the results obtained in high impact journals, demonstrating the influence of the structure on the aggregates obtained. A summary of the procedure followed throughout this chapter is given in Figure 7.

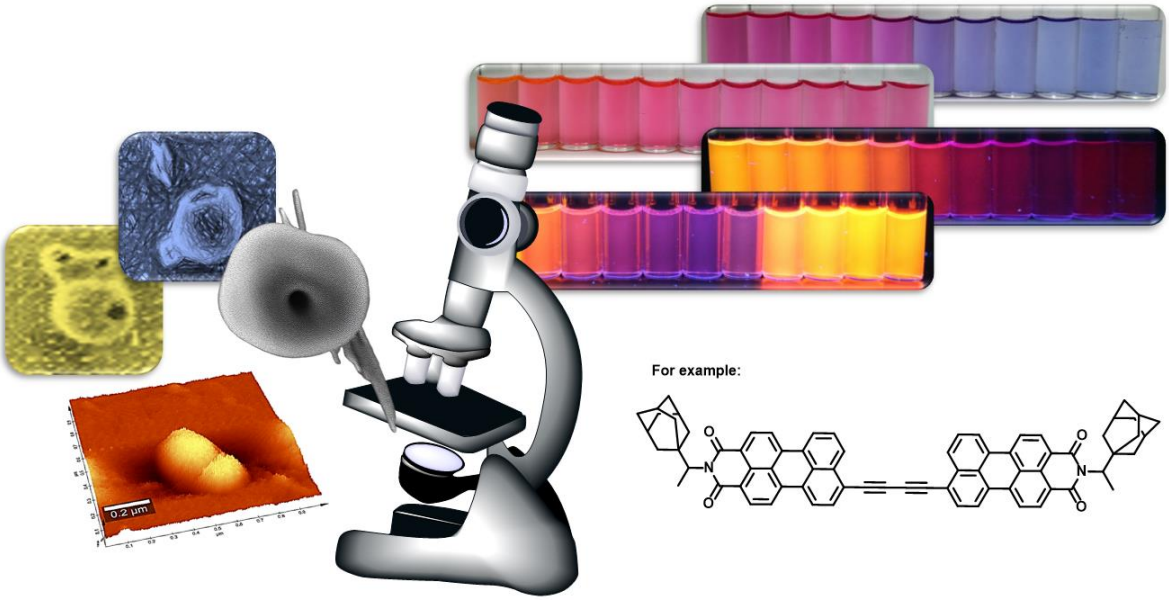

Figure 7. Schematic summary of the procedure followed for the analysis of the nanostructures of the PMI derivatives.

3. π-π STACKING: STUDY OF AGGREGATION IN TERMS OF STRUCTURE

Polycyclic aromatic hydrocarbons (PAHs) are a very versatile class of organic materials built by fusing benzene units, resulting in highly conjugated systems, which makes them intensely coloured, as it is usually the case with most PMI derivatives. In addition, these compounds are characterised by being strongly fluorescent, due to the rigidity provided by the planar aromatic rings of the perylene core, which causes them to exhibit fluorescence quantum yields close to 100%. Normally, these compounds have an absorbance and emission between the visible and near infrared (NIR) region, which can be easily modified by varying the substituents of the PMI,[24] increasing the applicability of these compounds.

These compounds have exceptional optical, electrochemical and thermal properties, which allow them to be used in technological applications.[25] However, perylene derivatives usually have a low solubility in conventional organic solvents, due to the π-π stacking favoured by the planarity of the structure. This problem can be overcome by introducing bulky and branched groups in the

[24] C. Li, H. Wonneberger, *Adv. Mater.*, **2012**, *24*, 613–636.
[25] a) Y. Shi, H. Wu, L. Xue, X. Li, *J. Colloid Interface Sci.*, **2012**, *365*, 172-177. b) K. Kim, G. Kim, S. Kwon, H. Yoon, J. Son, J. Choi, *Dyes Pigm.*, **2018**, *158*, 353-361.

N-imide positions, which has a negligible effect on the optical and electrochemical properties of the chromophores but considerably improves their solubility.

To further understand the properties of PMIs, it is necessary to consider one of their most important properties, the ability of homostacking to occur between molecules.[26] Although aggregates of perylene derivatives have been studied in recent times, it is still very difficult to predict them prior to experimental testing. These aggregates have a direct influence on the energy levels of the molecules, affecting both excitation and emission wavelengths, and on fluorescence quantum yields, since higher aggregation implies a higher probability of deactivation by non-radiative relaxation pathways.

There is a wealth of information and classification forms in the literature on the aggregates formed by PMI or PDI derivatives, which, like NMI derivatives (all of which are included in the rylenes), have the ability to form π-π stacks. Therefore, everything discussed about the aggregation of NMIs in Section 2.1 of Chapter 2 is also attributable to PMIs. As has been done for the derivatives of NMIs, the influence of the different substituents can be analysed as a function of the polarity of the medium for PMI or PDI derivatives:

- Substituents with low polarity (like aliphatic chains): the polarity of the perylene core is higher than the polarity of the substituents. Polar solvents interact with the most polar part of the molecule, that is, the perylene core, leading to a bathochromic shift and the formation of J-aggregates. However, solvents of lower polarity interact with the more non-polar part of the molecule leading to a hypsochromic shift and the formation of H-aggregates. An example of this is the product AR40, shown in Figure 8.[27]

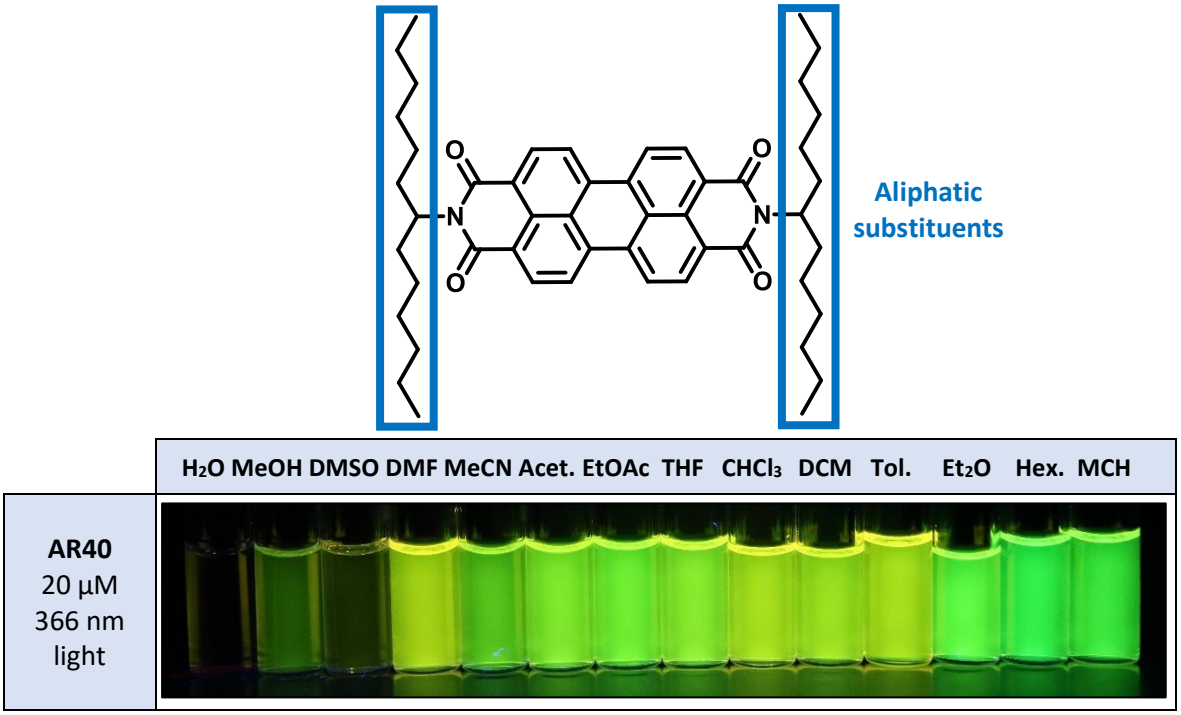

Figure 8. AR40 PMI derivative solvatochromism in different solvents.

[26] X. Cao, L. Meng, Z. Li, Y. Mao, H. Lan, L. Chen, Y. Fan, T. Yi, *J. Am. Chem. Soc.*, **2014**, *30*, 11753-11760.
[27] a) Y. Y. Kim, B. J. Ree, M. Kido, Y. G. Ko, R. Ishige, T. Hirai, D. Wi, J. Kim, W. J. Kim, A. Takahara, M. Ree, *Adv. Electron. Mater.*, **2015**, *1*, 1500197. b) S. Sao, I. Mukherjee, P. De, D. Chaudhuri, *Chem. Commun.*, **2017**, *53*, 3994-3997. c) C. Kaufmann, W. Kim, A. Nowak-Król, Y. Hong, D. Kim, F. Würthner, *J. Am. Chem. Soc.*, **2018**, *140*, 4253−4258. d) M. Wang, Q. Zhang, Z. Li, H. Li, J. M. Lu, *Chem. Asian J.*, **2018**, *13*, 1784-1790.

- Substituents with high polarity: if the polarity of the substituents is high enough, H-aggregates form when the solvent is more polar whereas J-aggregates form in non-polar solvents. An example is compound AR95, shown in Figure 9.

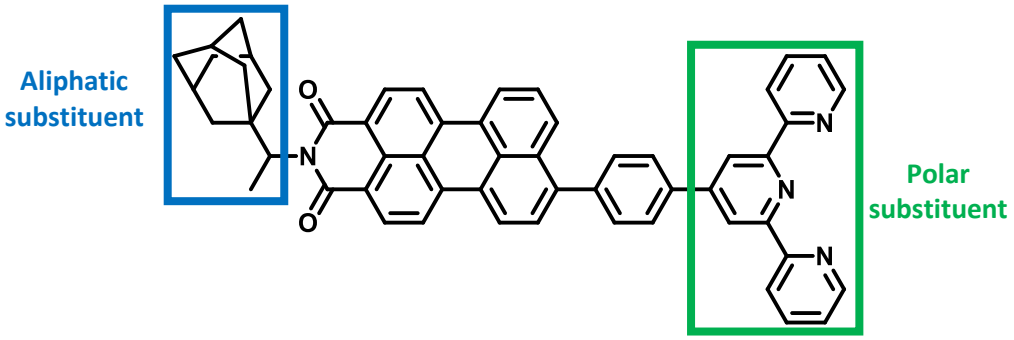

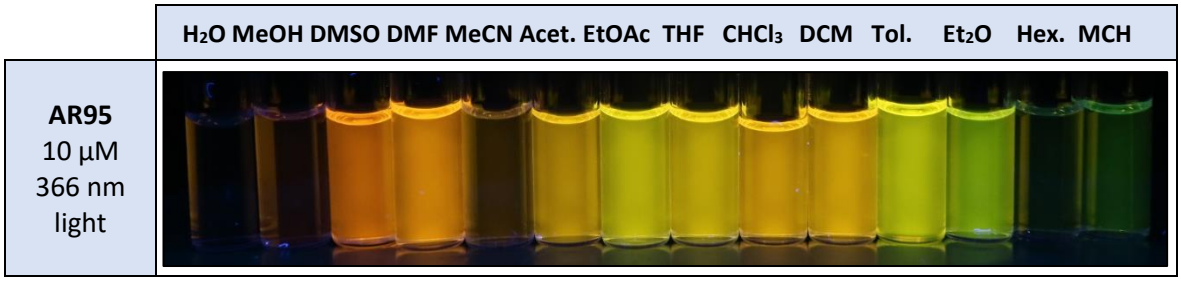

Figure 9. AR95 PMI derivative, solvatochromism in different solvents.

- Conjugation extension: the increase in the number of aromatic rings causes a shift of the emission band and the formation of diverse aggregates. The results show that as the polarity of the solvent increases, the emission shifts to the NIR region. An example is the compound AR34, shown in Figure 10.

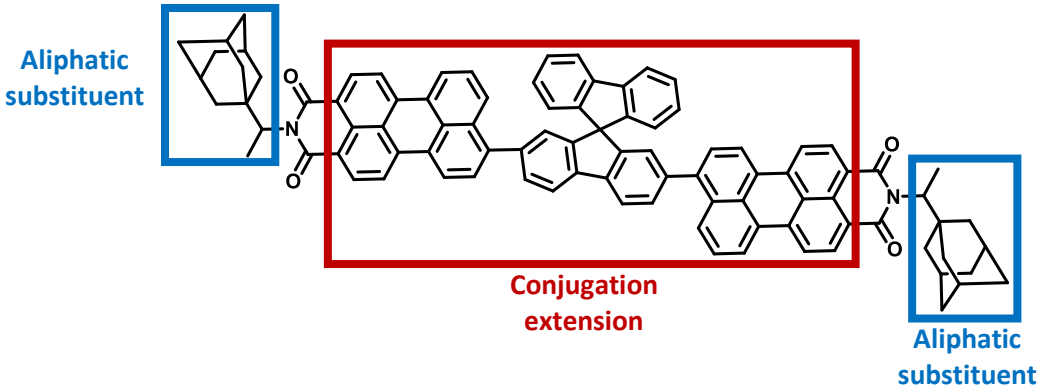

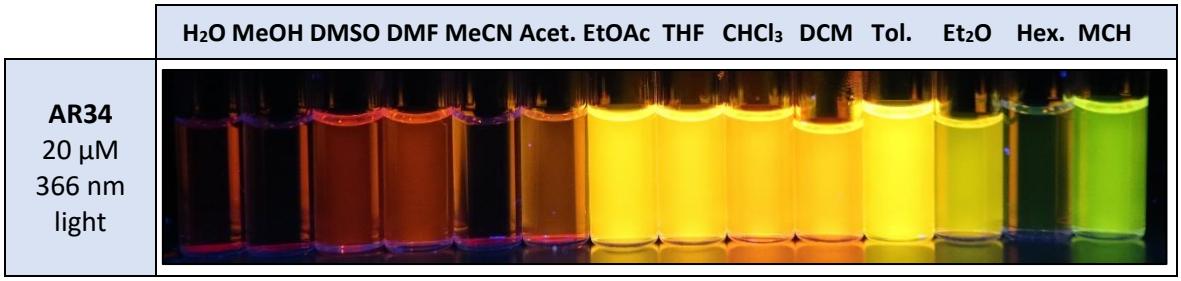

Figure 10. AR34 PMI derivative, solvatochromism in different solvents.

Apart from this, it is important to remark that stacking also depends on other factors such as the position of the substituents or their size.

Another simple model to classify the aggregation of PMIs by considering the three-dimensional distribution of molecules was developed by Hunter and Sanders in 1990.[28] This model is based on electrostatic and Vas der Waals forces and considers independently the σ system and the π system of the aromatic ring, which is formed by three layers: a central one constituted by the σ skeleton with charge +1 and two layers of charge -1/2 constituted by the π systems. A diagram of this system is shown in Figure 11.

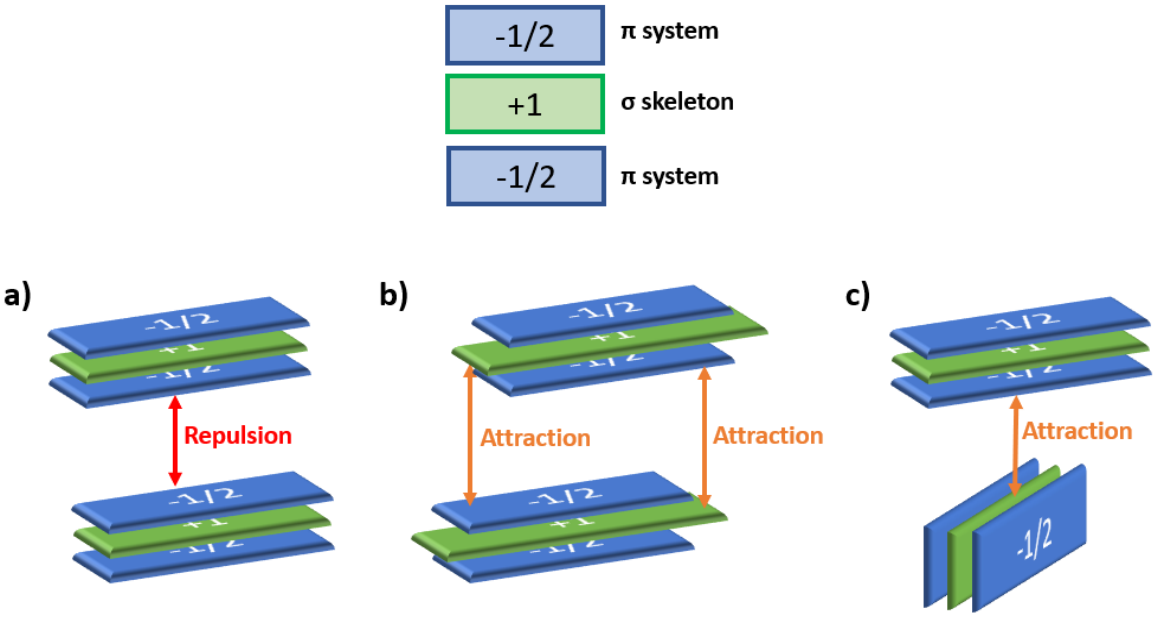

Figure 11. Schematic representation of the Hunter and Sanders model.

Thus, it allows to distinguish two main categories:[29]

- Face-to-face π-π stacking: this is defined as the type of stacking in which the aromatic rings are located parallel. When the rings are perfectly aligned, the π-π repulsion is predominant (Figure 11a), whereas when the aromatic rings are displaced, the predominant interaction is π-σ (Figure 11b). These types of interactions are strongly conditioned by the solvent and are stronger in π-deficient systems, where there is a lower charge density and the repulsion between nearby π clouds is reduced.
- Edge-to-face π-π stacking: this is the stacking in which the aromatic rings are perpendicularly positioned, giving rise to a *T-shaped* geometry. This type of stacking occurs mainly in the solid state. The predominant interaction in this type of system is π-σ (Figure 11c).

A very unusual type of stacking in PMI derivatives is the AIE, which has been discussed in both Section 2.2 of Chapter 2 and Section 1 of Chapter 4 of this thesis. It is much more common for these compounds to undergo ACQ, however, as will be explained below, an example of AIE have been found for PMIs.

[28] a) C. A. Hunter, J. K. M. Sanders, *J. Am. Chem. Soc.*, **1990**, *112*, 5525–5534. b) S. K. Burley, G. A. Petsko, *J. Am. Chem. Soc.*, **1986**, *108*, 7995–8001. c) M. Egli, V. Tereshko, G. N. Mushudov, R. Sanishvili, X. Liu, F. D. Lewis, *J. Am. Chem. Soc.*, **2003**, *125*, 10842-10849.

[29] A. S. Shetty, J. Zhang, J. S. Moore, *J. Am. Chem. Soc.*, **1996**, *118*, 1019-1027.

3.1. Reactivity of PMI derivatives

As it has been analysed, there is a strong dependence between the aggregation of PMI derivatives and their structure. This type of compounds shows several functionalisable positions, however, throughout the present Thesis, only the introduction of substituents in one of the ortho positions has been carried out by means of reactions of different nature, some of which are specified in the Figure 12.[30]

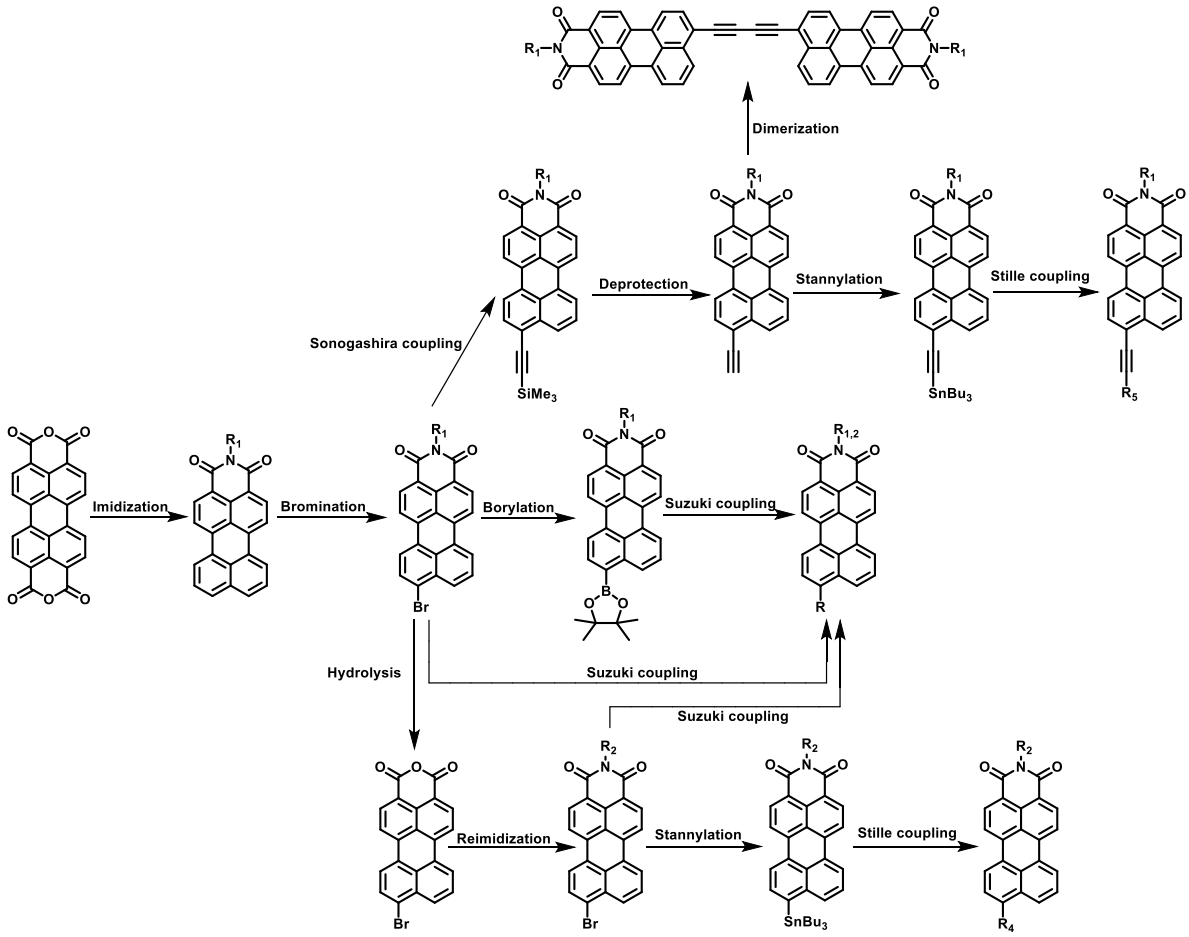

Figure 12. Some synthetic routes for the functionalisation of PMIs.

Many of these reactions have been carried out throughout this Thesis and each of them is exemplified below.

3.1.1. Imidization of PDA to PMI

PMIs are obtained by an imidation-decarboxylation reaction of PDA. There are several different procedures to obtain them. The synthetic route used by the research group[31] consists of a single step (Figure 13) in which the PDA is put in contact with a mild base and the desired amine in a reactor for three days. This procedure has been optimised for the amine 1-(1-adamantyl)ethyl amine hydrochloride.

[30] Y. Hu, S. Chen, L. Zhang, Y. Zhang, Z. Yuan, X. Zhao, Y. Chen, *J. Org. Chem.*, **2017**, *82*, 5926-5931.

[31] a) N. Busto, J. García-Calvo, J. V. Cuevas, A. Herrera, J. L. Mergny, S. Pons, T. Torroba, B. García, *Bioorg. Chem.*, **2021**, *108*, 104660. b) J. García-Calvo, P. Calvo-Gredilla, M. Ibáñez-Llorente, D. C. Romero, J. V. Cuevas, G. García-Herbosa, M. Avella, T. Torroba, *J. Mater. Chem. A.*, **2018**, *6*, 4416–4423. c) L. Pleux, A. L. Smeigh, E. Gibson, Y. Pellegrin, E. Blart, G. Boschloo, A. Hagfeldt, L. Hammarström, F. Odobel, *Energy Environ. Sci.*, **2011**, *4*, 2075-2084.

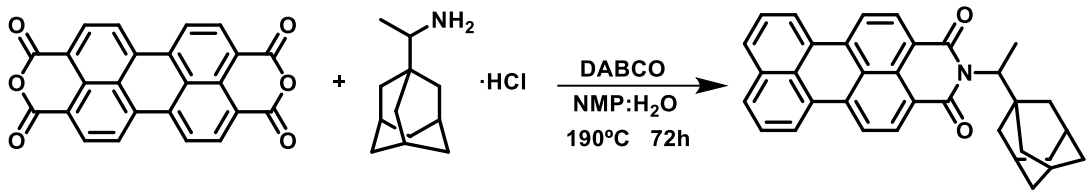

Figure 13. Synthetic scheme for obtaining the starting material for PMIs.

However, this product can also be obtained by a three-step synthetic route, starting with the synthesis of PDI, followed by the formation of the perylene monoanhydride-monoimide and concluded by the decarboxylation of the monoanhydride.[32] Apart from this, there are other synthetic routes to obtain PMI derivatives using the substituted monoanhydride as starting material[33] or other experimental conditions, such as for example imidazole as solvent.[34] This product is employed as a starting material for a large variety of reactions.

3.1.2. Bromination of PMI

A very typical reaction is the bromination of the perylene ring of PMI in order to subsequently perform carbon-carbon coupling reactions. Depending on the conditions under which this reaction proceeds, the positions at which bromination occurs change. If the conditions used in the reaction are mild (Figure 14), the monobrominated product (AR02) at the peri position is obtained selectively.[35]

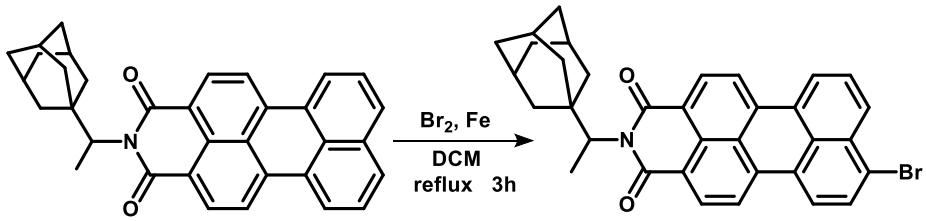

Figure 14. Synthetic scheme of PMI monobromination to obtain AR02.

In contrast, if the conditions under which the reaction is carried out are "stronger", such as high temperature and excess bromine, a mixture of the two tri-brominated products together with a small amount of the tetra-brominated product is usually obtained.[36]

3.1.3. Borylation of PMI

To carry out the Suzuki-Miyaura reaction, the borylation of PMI at the peri position is performed (AR01, Figure 15) following the conditions found in the literature.[37] For this purpose, monobrominated PMI, bis(pinacolyl)boronate and a mild base were dissolved in 1,4-dioxane under inert atmosphere, using palladium(II) as catalyst ([1,1'-bis(diphenylphosphino)ferrocene]dichloro-palladium(II), Pd(dppf)Cl_2 5% mol). The resulting mixture was stirred at 75ºC for 12-24 hours and finally was purified on a chromatographic column using DCM as eluent.

[32] a) Y. Geerts, H. Quante, H. Platz, R. Mahrt, M. Hopmeier, A. Böhm, K. Müllen; *J. Mater. Chem.*, **1998**, *8*, 2357–2369. b) Y. Hu, S. Chen, L. Zhang, Y. Zhang, Z. Yuan, X. Zhao, Y. Chen, *J. Org. Chem.*, **2017**, *82*, 5926-5931.
[33] O. Krupka, P. Hudhomme, *Int. J. Mol. Sci.*, **2023**, *24*, 6308.
[34] A. M. Philip, E. Sebastian, G. Gopan, R. Ramakrishnan, M. Hariharan, *J. Chem. Sci.*, **2018**, *130*, 137.
[35] K. Pal, V. Sharma, A. Lal-Koner, *Chem. Commun.*, **2017**, *53*, 7909-7912.
[36] D. Sahoo, V. Sharma, R. Roy, N. Varghese, K. Mohanta, A. Lal-Koner, *Chem. Commun.*, **2019**, *55*, 103-106.
[37] W. L. Gong, Z. J. Xiong, B. Xin, H. Yin, J. S. Duan, J. Yan, T. Chen, Q. X. Hua, B. Hu, Z. L. Huang, M. Q. Zhu, *J. Mater. Chem. C.*, **2016**, *4*, 2498-2505.

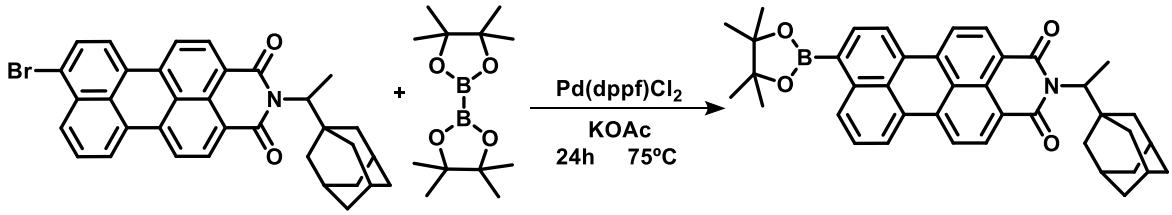

Figure 15. Borylation scheme of PMI to obtain AR01.

3.1.4. Carbon-carbon coupling reactions of PMI

The carbon-carbon coupling reactions that can be developed with PMI are very numerous. Throughout this thesis, all of them have been used to introduce substituents at the peri position. The most commonly used was the Suzuki-Miyaura coupling reaction (Figure 16), with many of them using the boronic ester from the previous section.

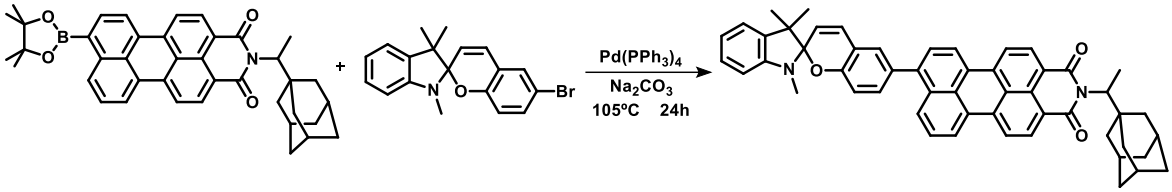

Figure 16. Reaction example for a Suzuki-Miyaura coupling reaction for PMIs to obtain AR19.

The general procedure used in this type of reaction, arylboronate derivative, brominated derivative, the base (Na_2CO_4, 4 equivalents) and palladium(0) catalyst were dissolved in a mixture of solvents under inert atmosphere until a concentration 1-5 mM and stirred under reflux for 16-48 hours. The product was purified by column chromatography (by using DCM:MeOH from 0 to 5% as eluent) to obtain products from orange to red. There are multiple solvent mixtures available for use in this reaction[38] but the most general has been a mixture of toluene:*n*-BuOH:H_2O (4:1:0.3).[39]

Another coupling that has been carried out is the Sonogashira reaction, for which the conditions described in the literature have been followed (Figure 17).[40] This reaction can be performed in a wide variety of solvents (DMF, THF…). However, it was developed by the research group using toluene with 20% triethylamine as solvent. Subsequently, the deprotection of the trimethylsilyl group has been carried out according to the conditions previously described (Figure 18).[41]

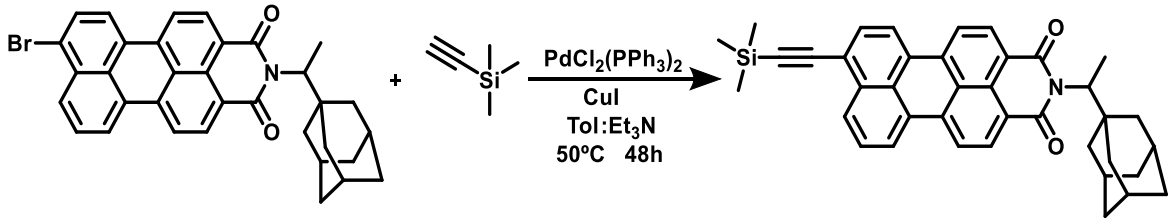

Figure 17. Reaction example for a Sonogashira coupling for PMIs to obtain AR22p.

[38] a) R. Arunchai, T. Sudyoadsuk, N. Prachumrak, S. Namuangruk, V. Promarak, M. Sukwattanasinitta, P. Rashatasakhon, *New J. Chem.*, **2015**, *39*, 2807. b) X. Luo, Y. Qu, Y. Zhang, Y. Wu, W. Yuan, L. Wuan, *J. Chem. Eng.*, **2021**, *415*, 129095.

[39] a) B. Díaz de Greñu, D. Moreno, T. Torroba, A. Berg, J. Gunnars, T. Nilsson, R. Nyman, M. Persson, J. Pettersson, I. Eklind, P. Wästerby, *J. Am. Chem. Soc.*, **2014**, *136*, 4125–4128. b) J. García-Calvo, P. Calvo-Gredilla, M. Ibáñez-Llorente, T. Rodríguez, T. Torroba, *Chem. Rec.*, **2016**, *16*, 810-824.

[40] a) H. Kang, W. Jiang, Z. Wang, *Dyes Pigm.*, **2013**, *97*, 244-249. b) L. Turunen, F. Pan, N. K. Beyeh, J. F. Trant, R. H. A. Ras, K. Rissanen, *Cryst. Growth Des.*, **2018**, *18*, 513−520.

[41] L. Turunen, N. K. Beyeh, F. Pan, A. Valkonen, K. Rissanen, *Chem. Commun.*, **2014**, *50*, 15920-15923.

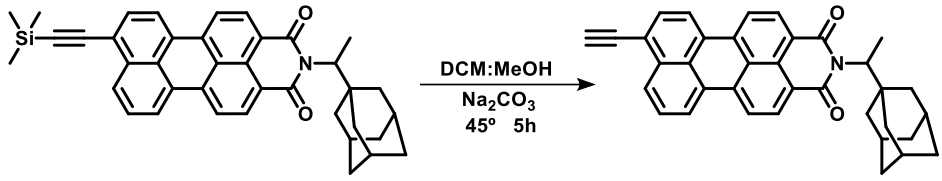

Figure 18. Reaction example for a deprotection of trimethylsilyl group for PMIs to obtain AR22d.

Some of the PMI derivatives obtained through the carbon-carbon couplings discussed so far will be studied in more detail in the following sections 4 and 5.

Finally, the last carbon-carbon coupling reaction developed was the Stille coupling reaction for those products for which the previous reactions did not work (Figure 19).

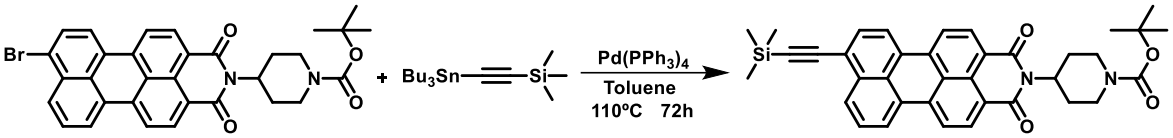

Figure 19. Reaction example for a Stille coupling for PMIs to obtain AR96.

According to the general procedure, the monobrominated compound, the organostannic derivative and the palladium catalyst were dissolved in toluene under inert atmosphere until a concentration between 0-2 mM and stirred for three days at 110ºC. After work-up, the obtained product was purified by column chromatography (DCM:MeOH from 0 to 5% as eluent) and the product was, usually, obtained as a red solid.

3.1.5. Reimidization of PMI

The substituents present on the *N*-imide group are capable of varying certain properties of PMI derivatives, such as preventing π-π stacking if the amines are sufficiently bulky, making them soluble in common solvents. Substitution may also be desired because certain amines do not withstand the conditions of monoimide formation from PDA, such as amines protected with a BOC, which have to be introduced at a later stage. Therefore, the reasons for replacing the *N*-imide group in the PMI can be very diverse.

The reimidization process involves the formation of a monoanhydride (AR30), by a saponification treatment, followed by the introduction of a primary amine (AR31), as can be seen in the example in Figure 20.

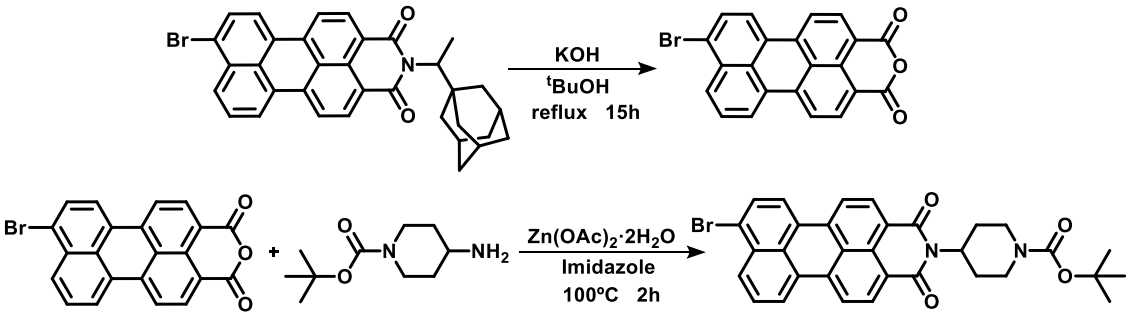

Figure 20. Reaction example for a reimidization for PMIs.

The conditions for conducting this reimidization process depend on the amine to be introduced, as larger and bulkier amines require more drastic conditions while smaller amines can use the conditions indicated in Figure 20.[42]

[42] A. Bolag, N. Sakai, S. Matile, *Chem. Eur. J.*, **2016**, *22*, 9006-9014.

3.2. Aggregation as a function of concentration

Aggregation can be analysed not only by changes in the luminescence of the compounds, but also by the effect of concentration. Applying this to PMI derivatives, the effect of different concentrations (27, 54 and 81 mM) was studied in the signals of the ^{1}H-NMR spectra. In general, the aliphatic signals are concentration independent whereas the aromatic signals corresponding to the perylene core undergo a shift to lower ppm with increasing concentration. This is exemplified in Figure 21.

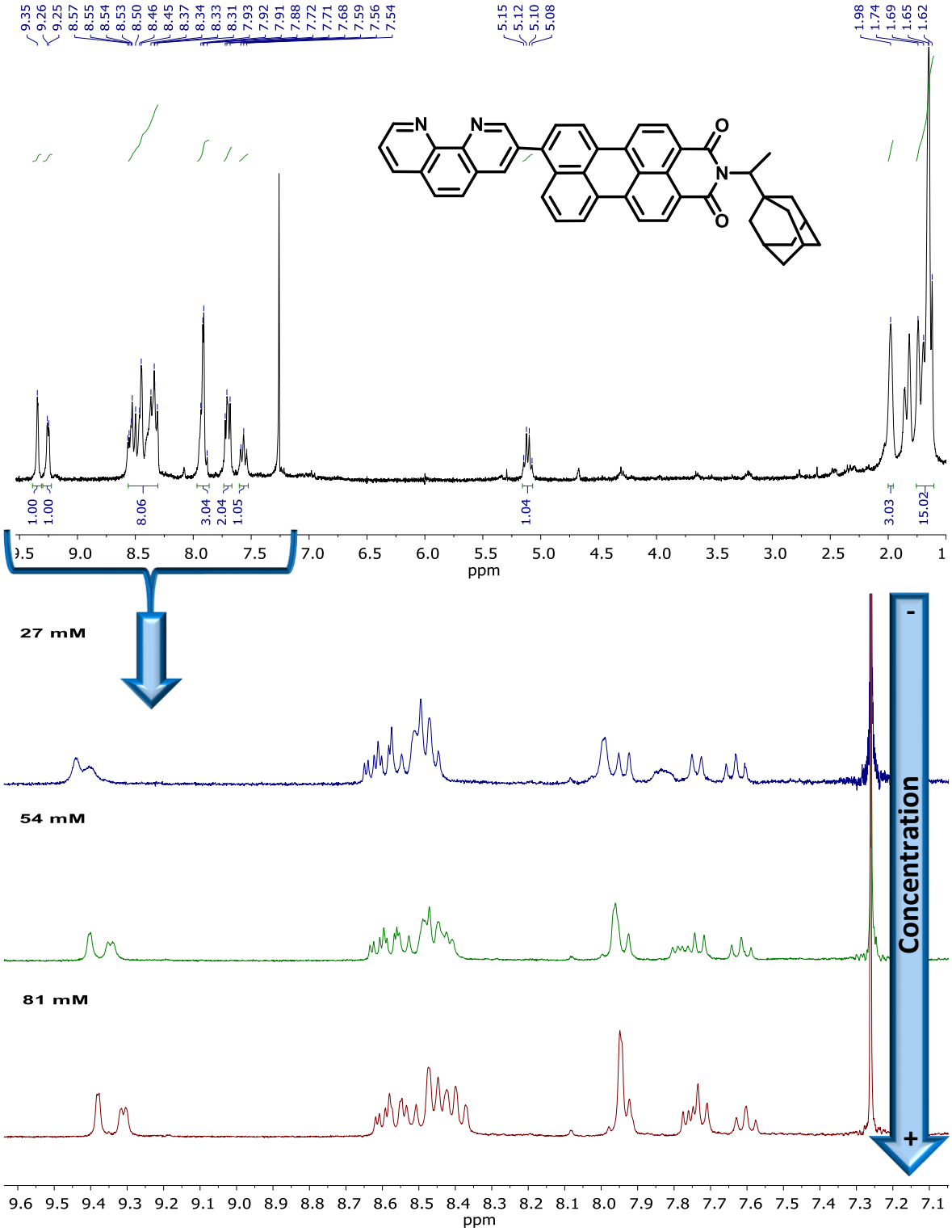

Figure 21. PMI AR05, effect of concentration on aggregation.

4. FLUORESCENCE REDSHIFT: AGGREGATION ANALYSIS

Typically, PMI derivatives tend to undergo fluorescence quenching (ACQ) as the amount of water added to an organic solvent, usually THF, is increased. However, certain PMIs have been found in which the fluorescence shifts towards the red region as the content of water rises, and these are the ones discussed in this section.

4.1. Derivatives with triple bonds: AR20

Firstly, a PMI derivative will be analysed in which an extension of the conjugation has been carried out by introducing a triple bond in the peri position of the perylene ring and then a dimerization has been carried out. The synthetic route followed to obtain this product is shown in Figure 22.

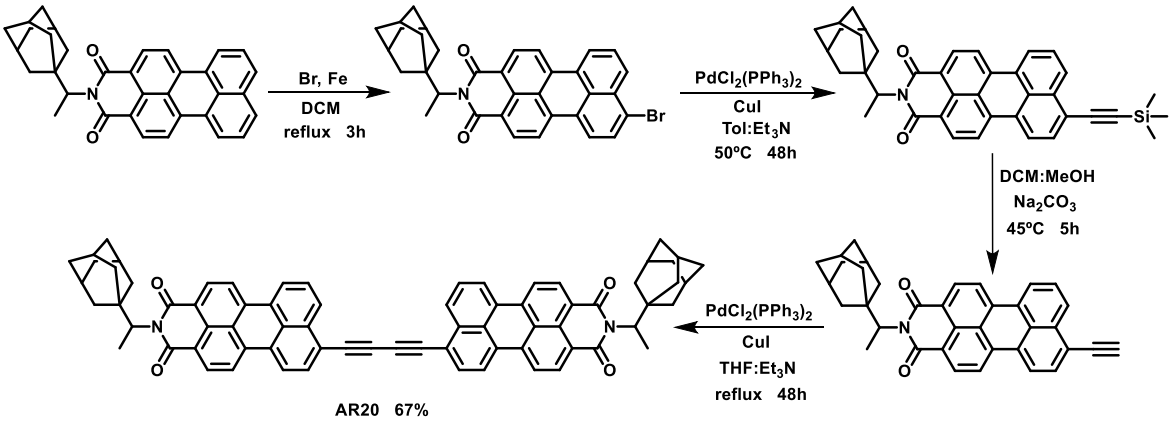

Figure 22. Synthetic route followed to obtain the AR20 PMI derivative.

The fluorescence study (Figure 23 and Figure 24) showed that the highest fluorescence emission was produced in solvents of intermediate polarity, being insoluble in both higher and lower polarity solvents. In fact, the fluorescence quantum yield of this product in chloroform was 38.99%, much lower than the values to which PMI derivatives typically exhibit. The emission maximum experienced a slight bathochromic shift as the polarity of the solvent increases, while the absorption maximum underwent a hypsochromic shift, where the absorption maximum shifted to longer wavelengths as the polarity of the solvent decreases.

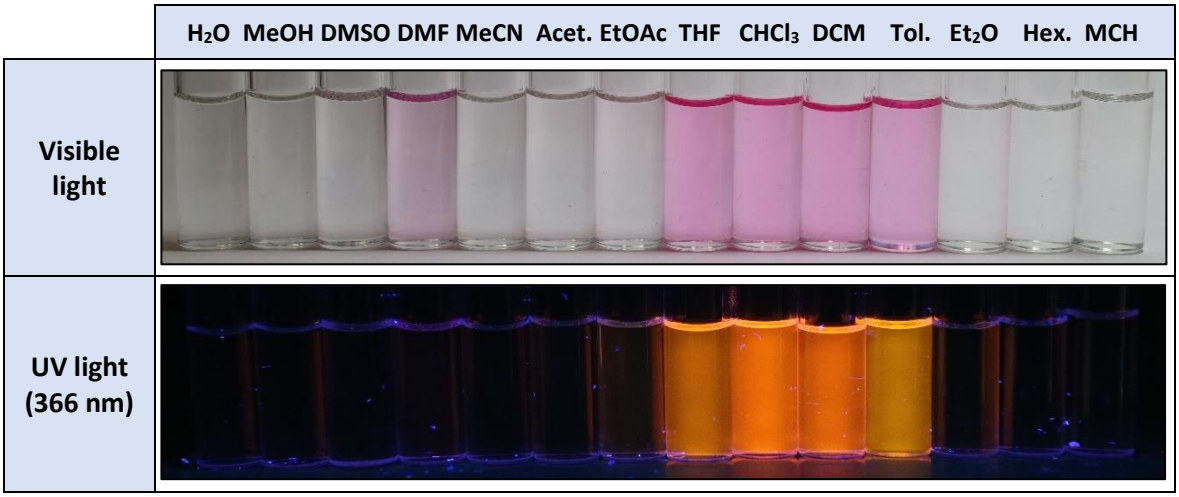

Figure 23. Solvatochromism images, 20 µM solution of AR20 in different solvents under visible and 366 nm light.

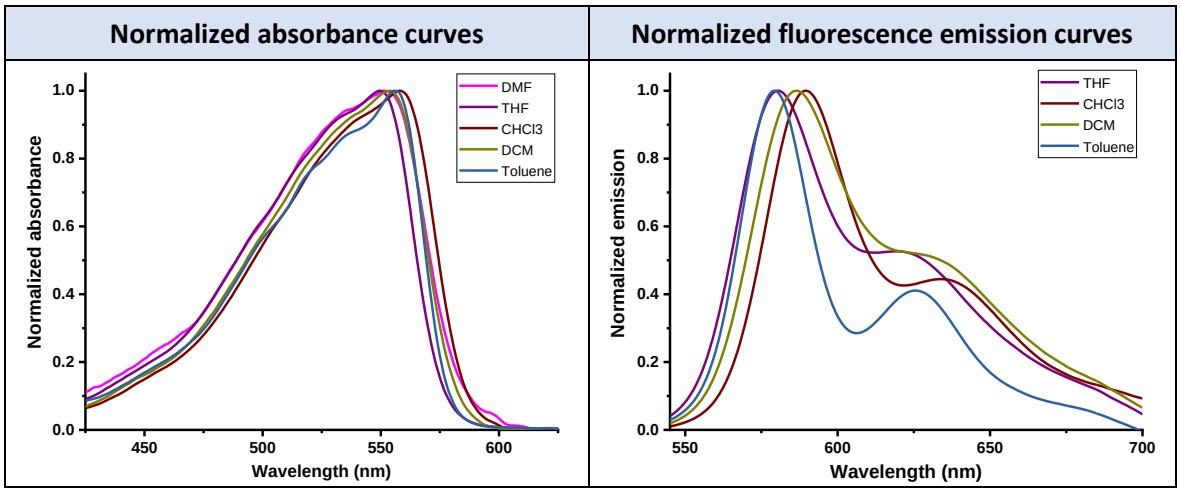

Figure 24. Solvatochromism graphs. Normalized absorbance curves (left) and fluorescence emission curves (right) in some solvents. λ_{exc}=530 nm.

To carry out the study of the aggregation of the AR20 compound, a water acceptance test was performed (Figure 25) using THF as organic solvent. A shift of the emission maximum towards the red region (between approximately 630-710 nm) was observed from 40% water. This was accompanied by a continuous decrease in the emission intensity as the amount of water added increased. On the other hand, the absorption spectrum showed the growth of a second band about 610 nm as the amount of water increases.

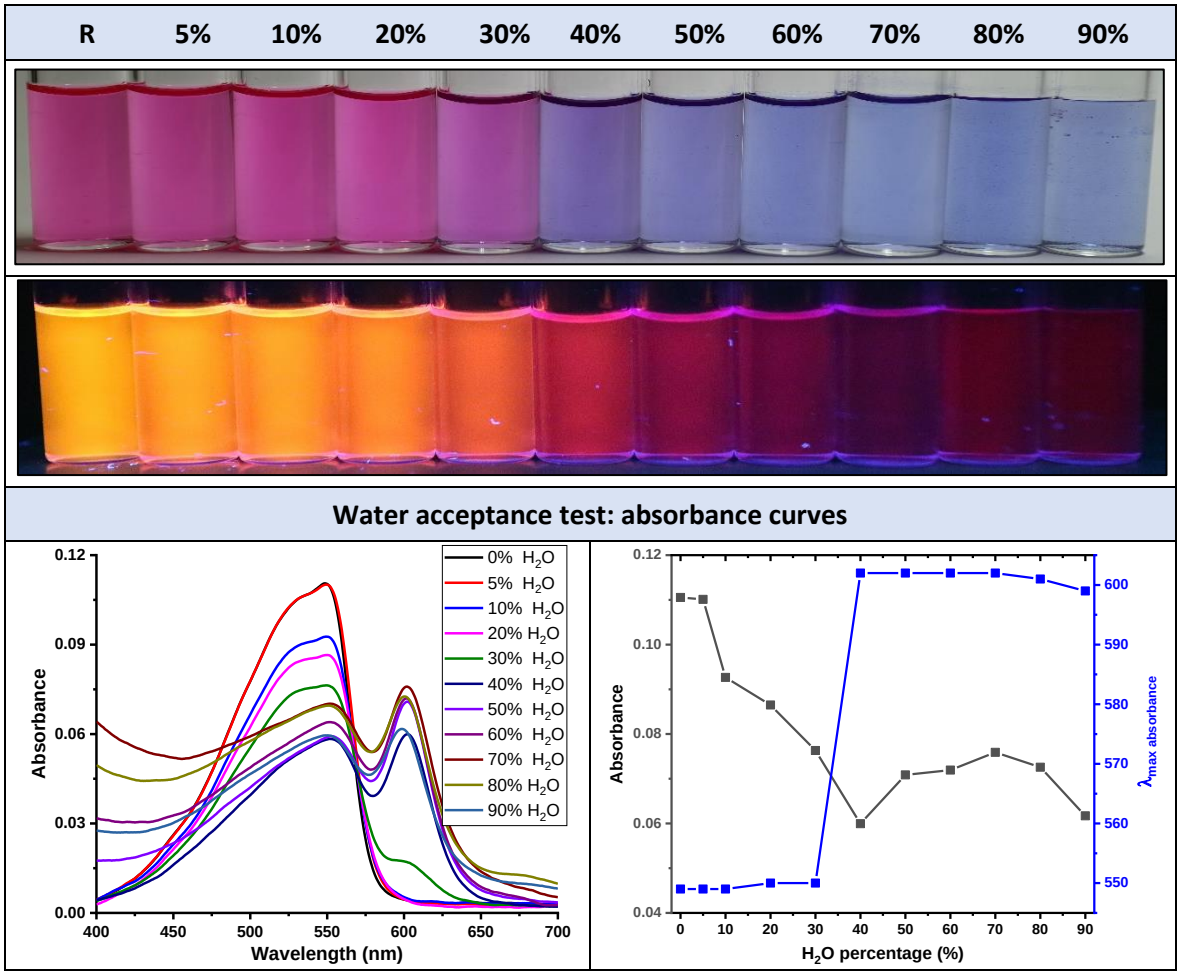

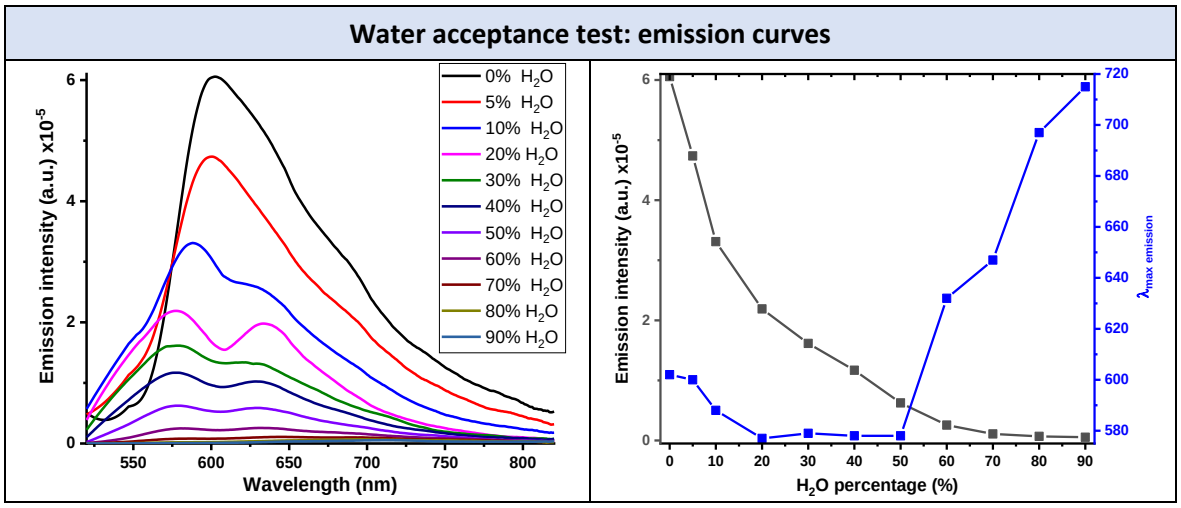

Figure 25. Visible and fluorescence images of water acceptance test of a 20 µM solutions of AR20 in THF mixtures with increasing amounts of water (up). Absorbance graph (middle left) and graph of relationship between the absorbance and the wavelength of the maximum of absorbance (middle right) as a function of the amount of water added for AR20 in THF. Emission intensity graph (down left) and graph of relationship between the emission intensity and the wavelength of the maximum of emission (down right) as a function of the amount of water added for AR20 in THF. λ_{exc} = 510 nm.

The nanostructures formed during the red shift of the emission band were studied by SEM microscopy (Figure 26). For this compound, as the amount of water added to the THF-H_2O mixture increases, a growth of the formed nanoparticles was observed.

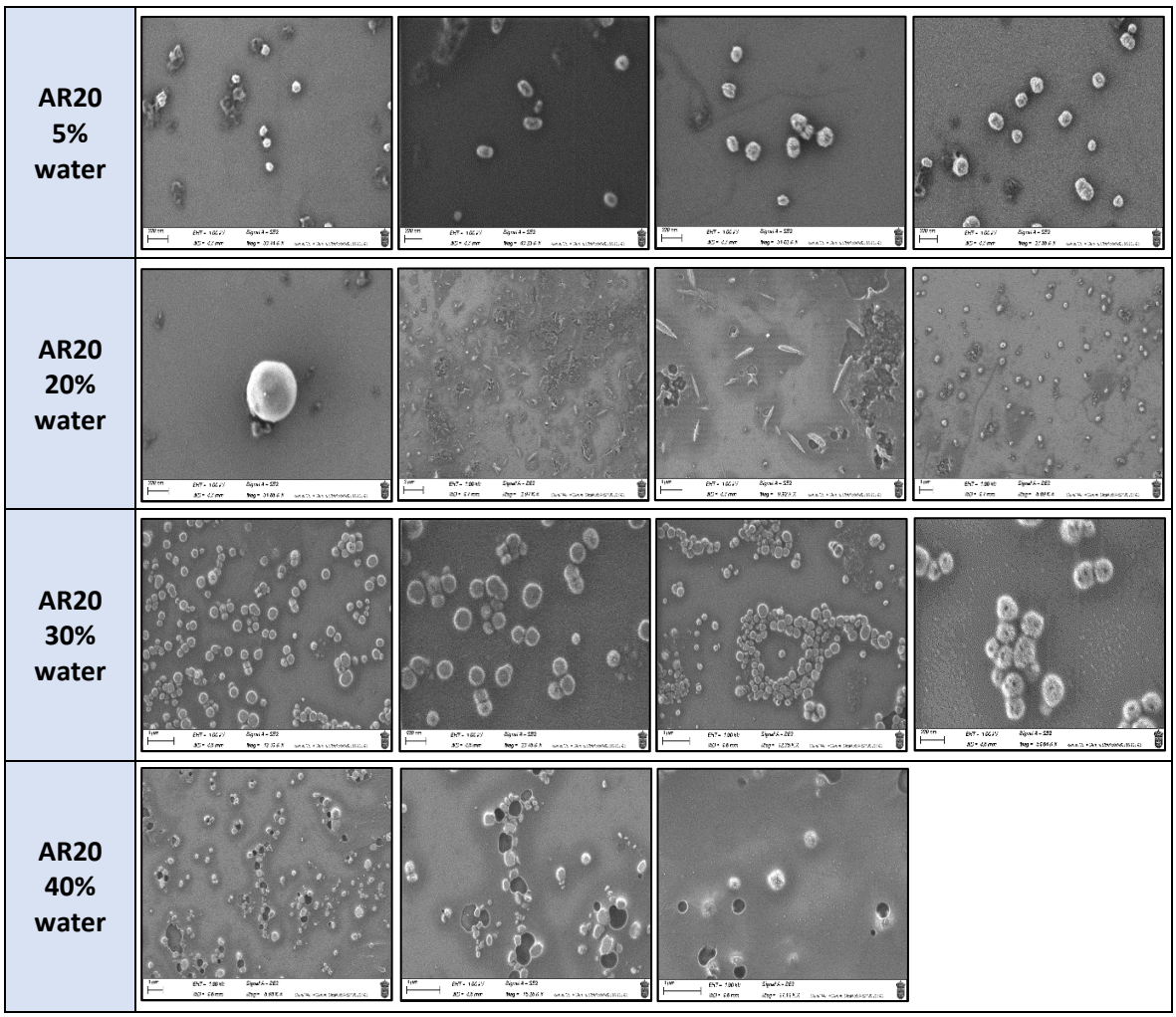

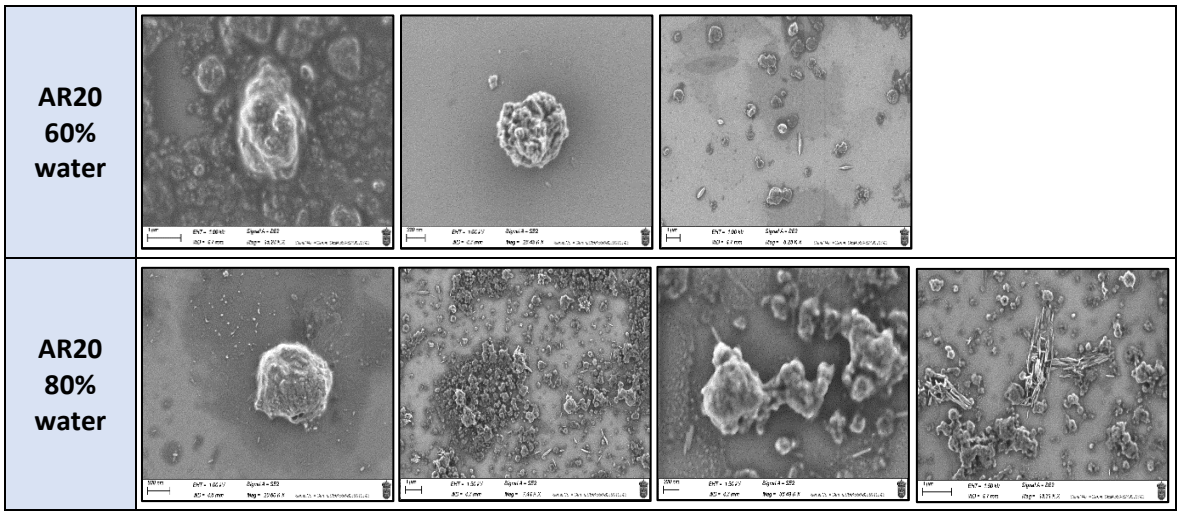

Figure 26. SEM nanoparticles of AR20 in different mixtures of THF-H_2O.

At low amounts of water (5%), individual spherical nanoparticles were found to be less than 100 nm in size, some of them in pairs. At 20% water, these nanoparticles had grown to approximately 100 nm and needle-shaped nanoparticles were also observed. At 30% water, spherical nanoparticles, ranging in size from 270-300 nm, were formed into aggregates, while at 40% water, these nanoparticles had grown to sizes between 300-400 nm. At 60% water, the nanoparticles were no longer sphere-shaped, but were now amorphous, with a size of approximately 600 nm. Finally, at 80% water, the amorphous nanoparticles clumped together to form aggregates larger than 1.5 microns in size as well as needle-shaped nanoparticles and aggregates of them.

4.2. Spiro derivatives: AR34 and AR35

Secondly, a study of two PMI derivatives was carried out in which the extension of the conjugation was carried out by the introduction of a 9,9'-spirobi[9H-fluorene] in one of the peri positions of the perylene ring. The synthetic route followed to obtain them is shown in Figure 27.

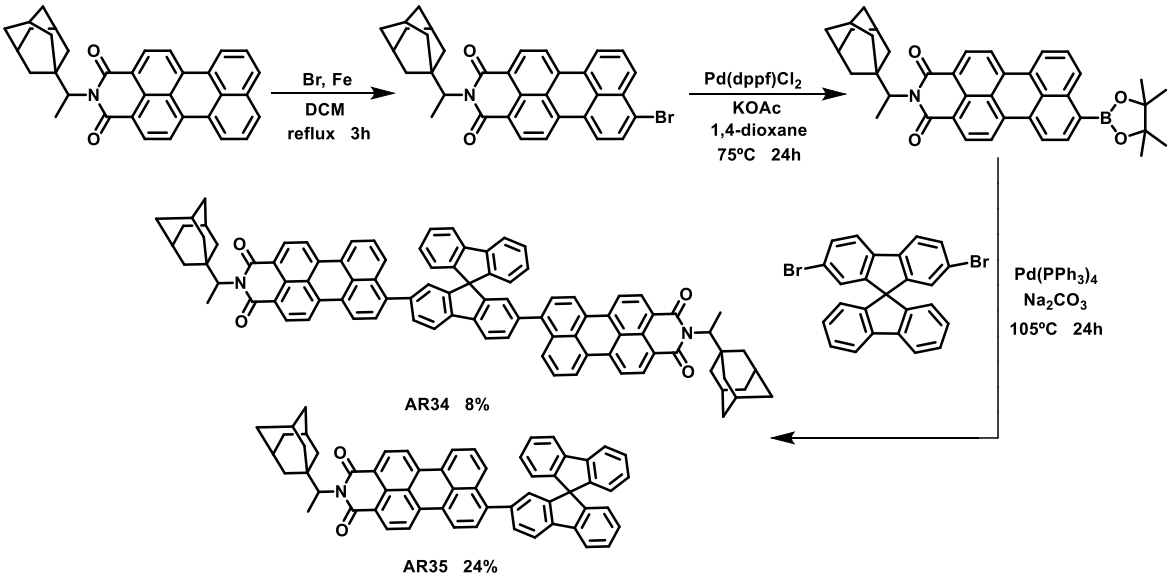

Figure 27. Synthetic route followed to obtain the AR34 and AR35 PMI derivatives.

The fluorescence analysis of both compounds (Figure 28 and Figure 29) shows that there were several resemblances between them due to their structural similarity. Both compounds showed the highest emission in non-polar solvents, decreasing it with increasing polarity (the fluorescence

quantum yields of AR34 and AR35 in MCH are 80% and 94% respectively). In all the plots in Figure 29, a bathochromic shift was also observed, much more noticeable for the emission spectra.

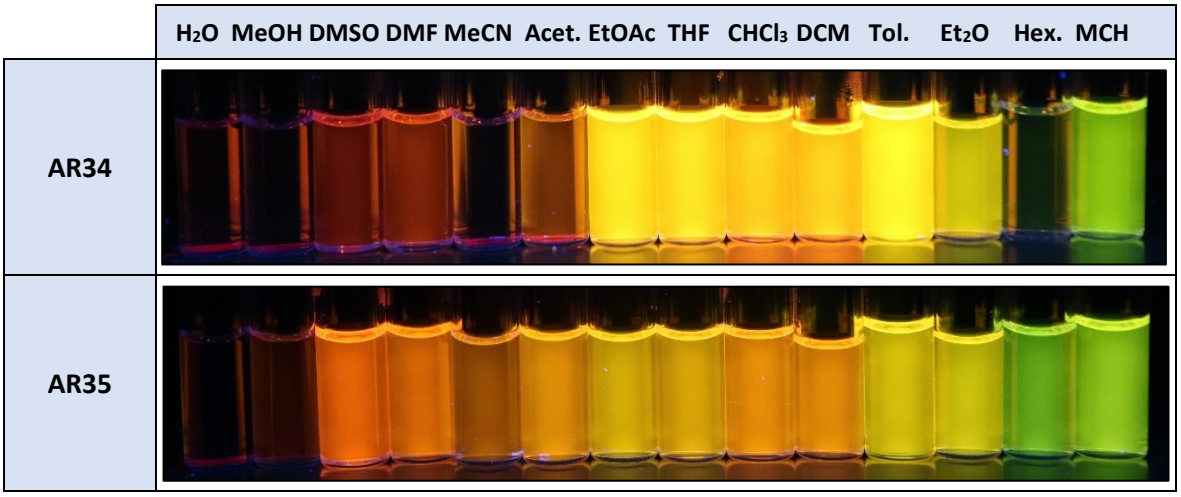

Figure 28. Fluorescent emission of 20 µM solutions of AR34 and AR35 in different solvents under 366 nm light.

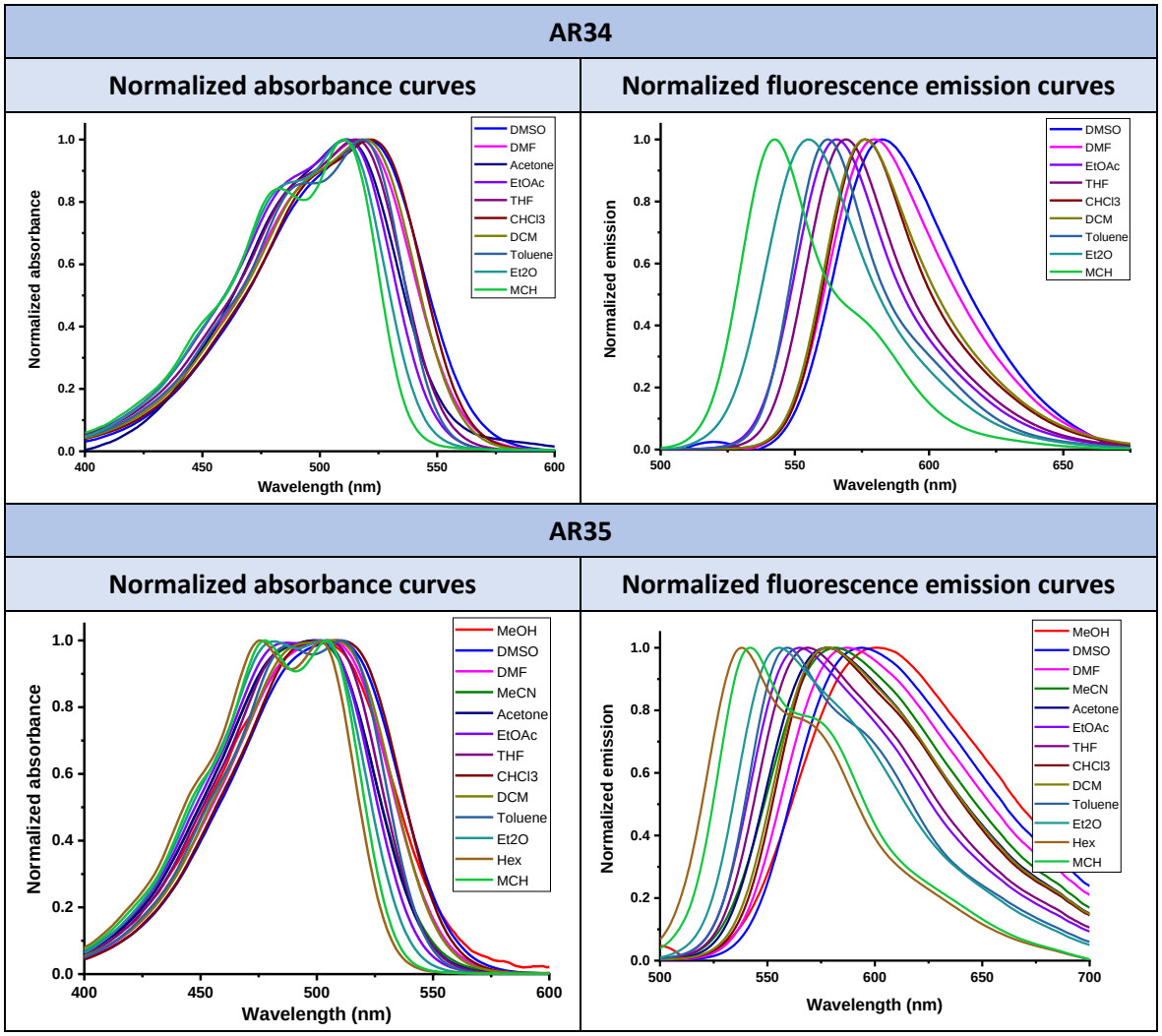

Figure 29. Normalized absorption and emission spectra of 20 µM solutions of the AR34 and AR35 products in different solvents.

Next, the water acceptance test (Figure 30) was performed using THF as organic solvent. For both products, a red shift was observed from 40% water.

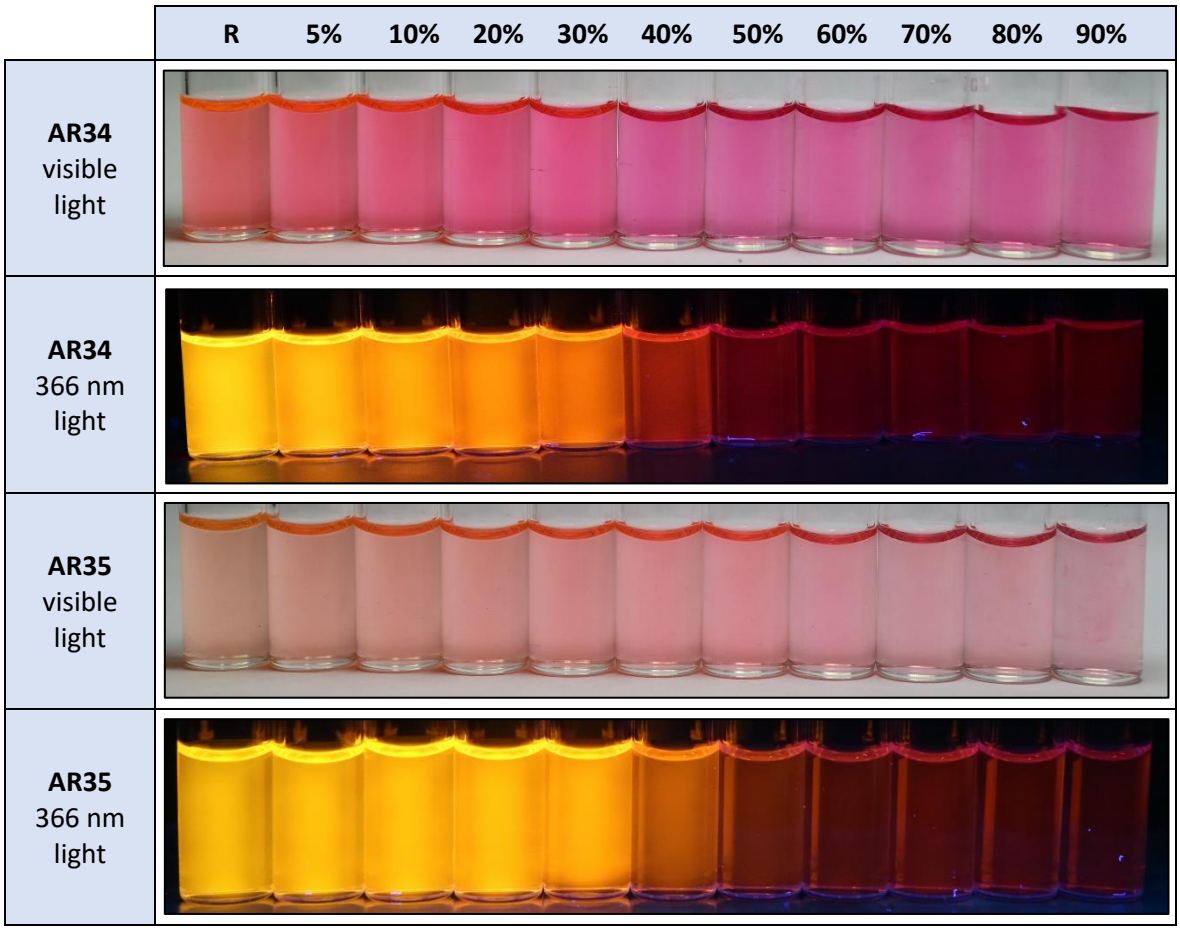

Figure 30. Water acceptance test. 20 µM solutions of the AR34 and AR35 compounds in THF mixtures with increasing amounts of water.

Each of these compounds was then studied individually. In the case of AR34 (Figure 31), the emission intensity decreased as the amount of water increased until it reached 40%, after which it was stabilised near 0. This decrease in emission intensity was accompanied by a shift of the emission maximum from the yellow region (around 570-585 nm) to the red region (between approximately 620-630 nm). In the visible, from 40% water, the appearance of a new maximum at 525 nm and the disappearance of the maximum at 517 nm was observed, that is, although very slight, there was also a shift towards the red region in the visible.

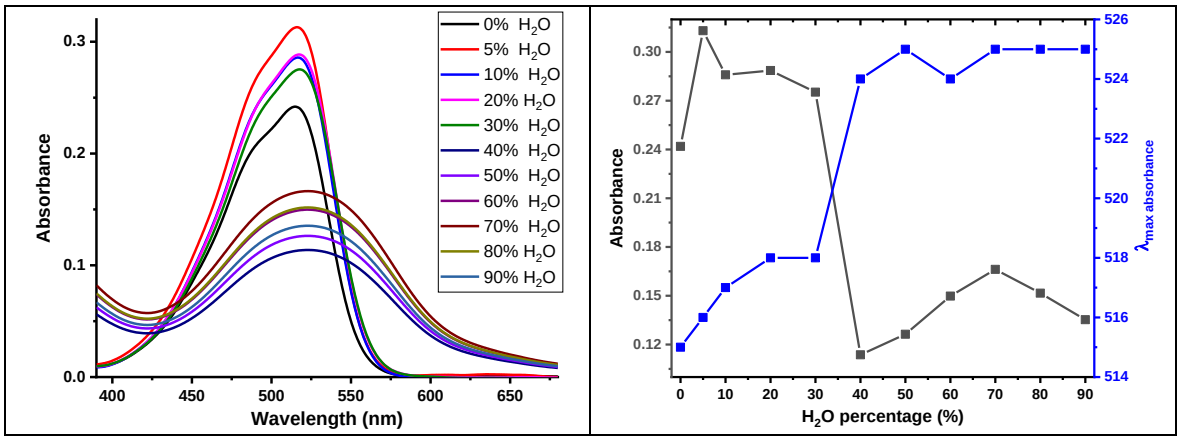

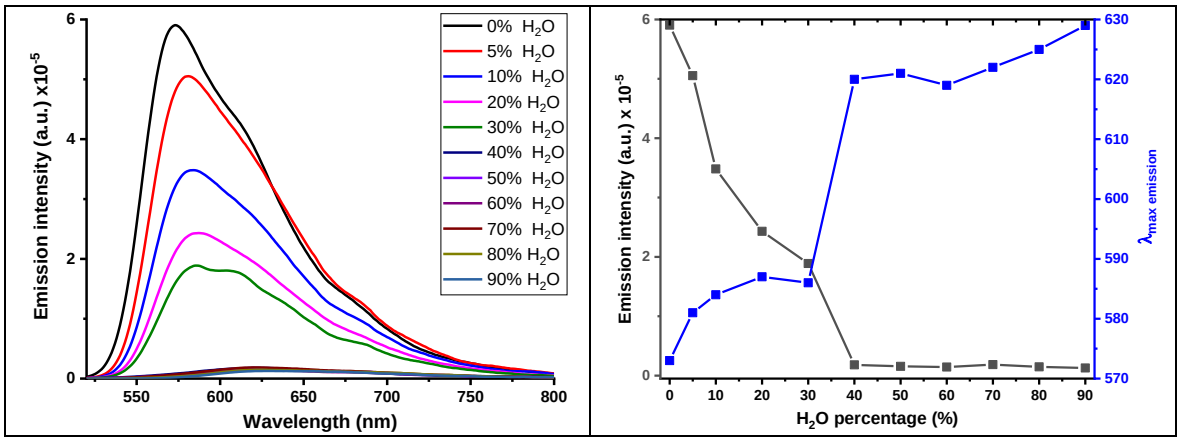

Figure 31. Absorbance graph (up left) and graph of relationship between the absorbance and the wavelength of the maximum of absorbance (up right) as a function of the amount of water added for AR34 in THF. Emission intensity graph (down left) and graph of relationship between the emission intensity and the wavelength of the maximum of emission (down right) as a function of the amount of water added for AR34 in THF. λ_{exc} = 510 nm.

The nanostructures formed as the amount of water increased were studied by SEM (Figure 32), Figure 3, showing how the size of the nanoparticles and aggregates increased as the amount of water increased. At 5% water, spherical nanoparticles with a size between 40-125 nm were found, and smaller ones were observed. By increasing the amount of water to 20%, the size of the nanoparticles increased to 150-250 nm, and aggregates of nanoparticles were found. In addition, at this percentage of water, the first needle-shaped nanoparticles with a length of around 380 nm were detected.

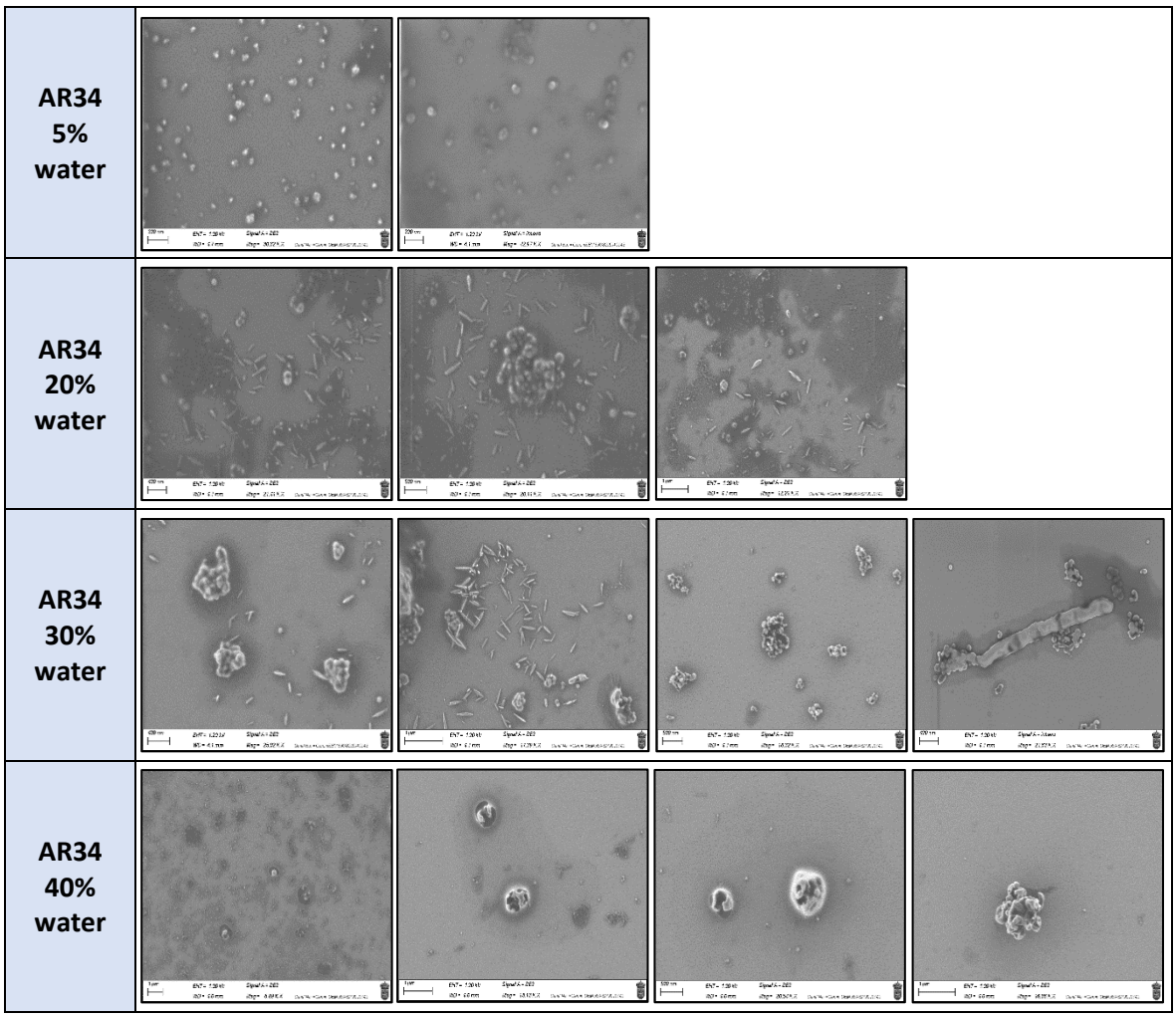

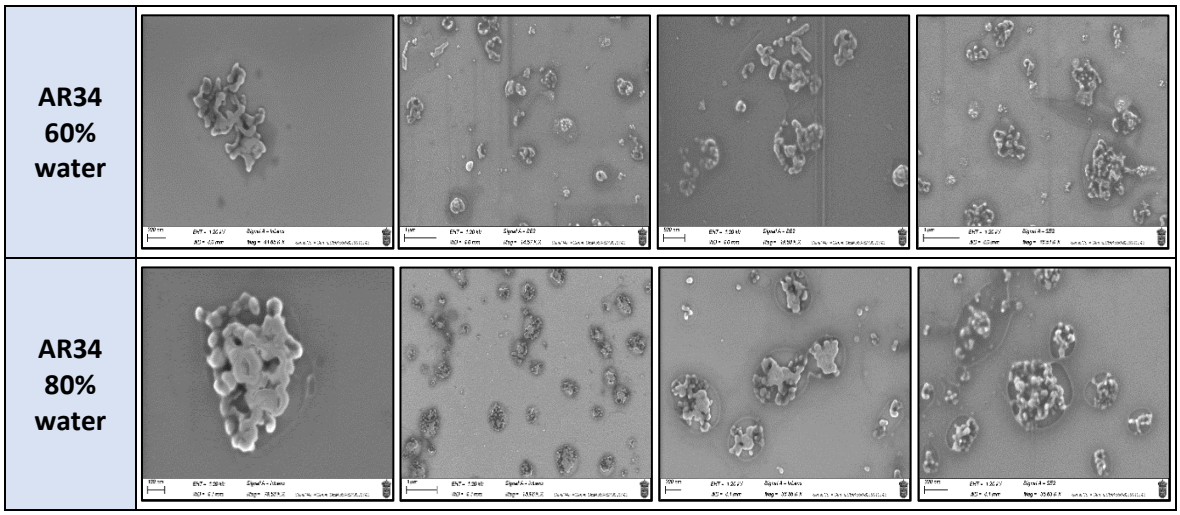

Figure 32. SEM nanoparticles of AR34 in different mixtures of THF-H_2O.

At 30% water, aggregates of nanoparticles up to 600 nm in size were encountered, as well as needle-shaped nanoparticles. As the amount of water added to the organic solvent increased, the size of the aggregates formed enlarged. Thus, at 40% water, the size of the aggregates was approximately 400-700 nm while at 60% water the aggregates had grown to 900 nm-1.1 µm and continued to increase in size at 80%. At 60% water, nano-needle aggregates were also observed.

The AR35 compound showed the same behaviour as the previous PMI derivative, as can be seen in Figure 33.

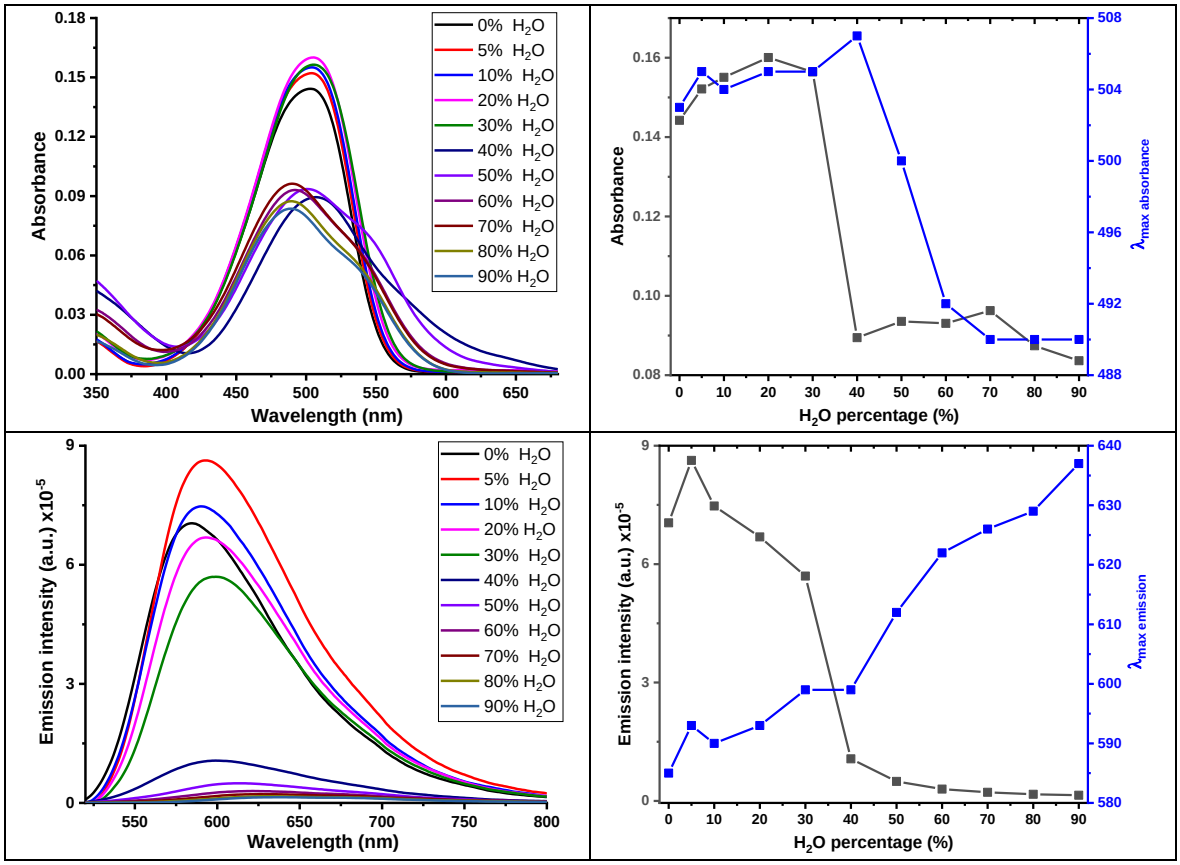

Figure 33. Absorbance graph (up left) and graph of relationship between the absorbance and the wavelength of the maximum of absorbance (up right) as a function of the amount of water added for AR35 in THF. Emission intensity graph (down left) and graph of relationship between the emission intensity and the wavelength of the maximum of emission (down right) as a function of the amount of water added for AR35 in THF. λ_{exc} = 500 nm.

As the percentage of water increased, the emission maximum shifted from the yellow to the red region, all accompanied by a decrease in emission intensity until it stabilised at a value close to 0. In the visible, the same trend was also observed. The formed nanostructures were studied by SEM microscopy, resulting in the images shown in Figure 34.

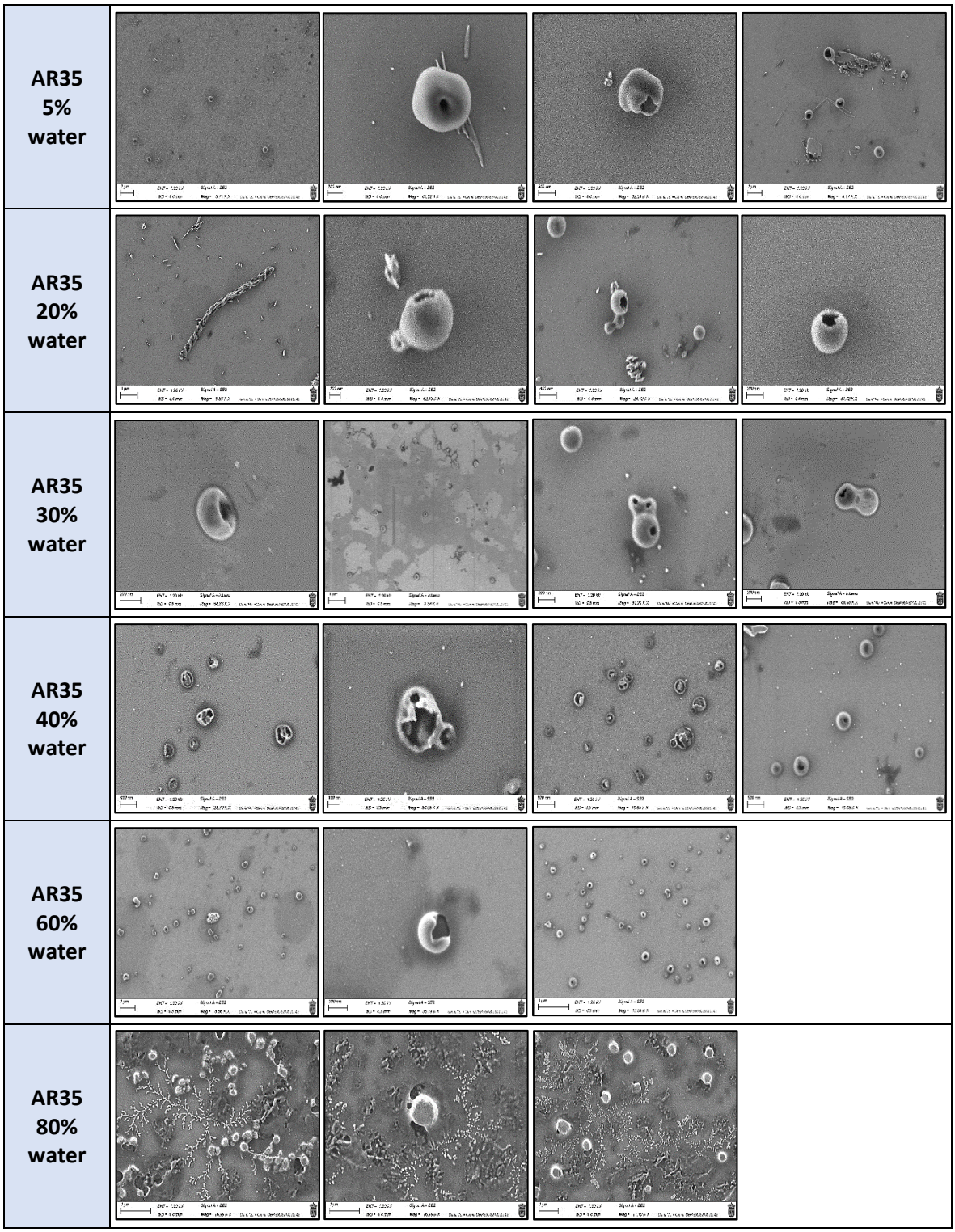

Figure 34. SEM nanoparticles of AR35 in different mixtures of THF-H_2O.

At 5% water, spherical nanoparticles with a diameter of approximately 60 nm and nanovesicles with a size between 400-500 nm were observed, some of which have not finished forming correctly. As the amount of water was increased to 20%, needle-shaped nanoparticles, helix-shaped fibres

and vesicles were found with a similar size to those of the previous percentage of water, although some of them were observed grouped in pairs. As the amount of water increased, nanovesicles continued to be detected, but at 40% and 60% water, some of them were broken or more amorphous. Finally, at 80% water, aggregates of amorphous particles and some individual spherical particles between 850-900 nm in size were found, but no vesicles.

These vesicles were studied using AFM microscopy, where the samples were deposited on a mica surface. The most interesting structures are shown in Figure 35.

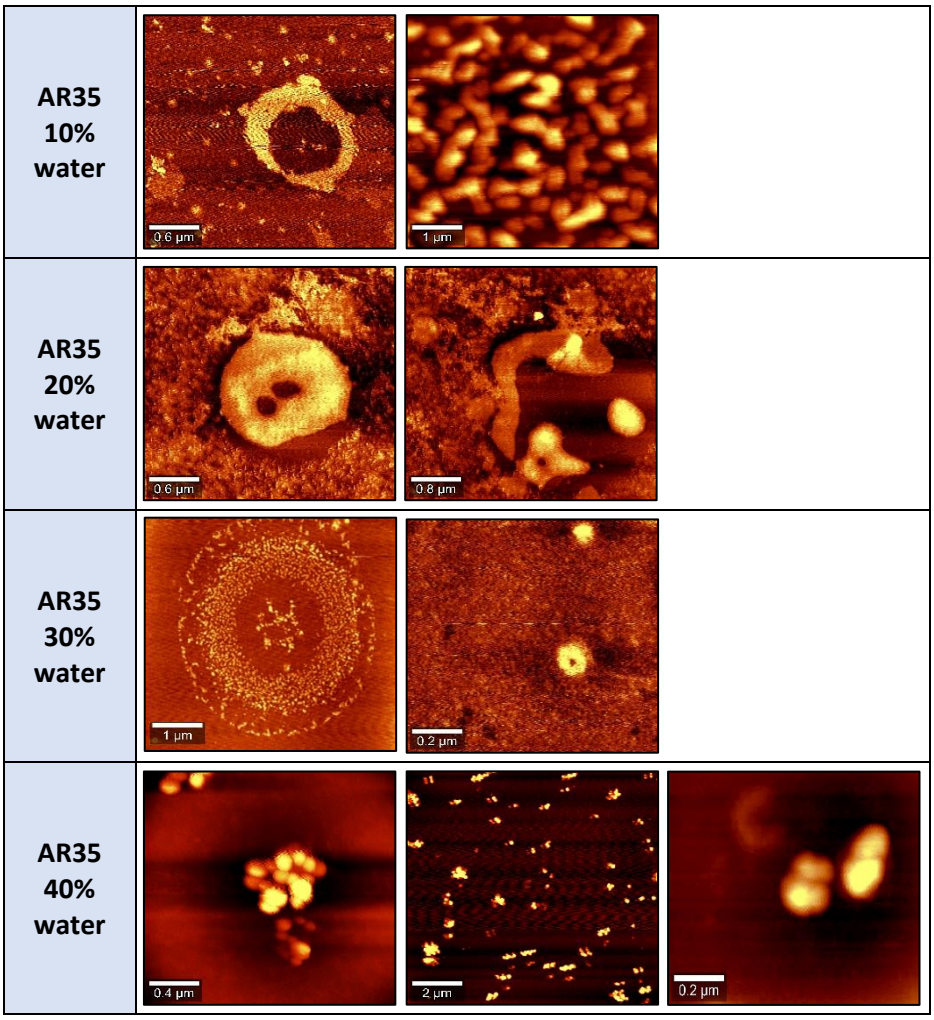

Figure 35. AFM nanoparticles of AR35 in different mixtures of THF-H_2O.

By means of this microscopy technique, nanovesicles were only found, in a very isolated and sporadic way, at 20% and 30% of water. Therefore, the formation of nanovesicles was conditioned by the surface on which the samples were deposited, since a silicon disc was used for the SEM measurements, while a mica plate was chosen for the AFM measurements.

Basically, during the AFM measurements, spherical nanoparticles were observed to form aggregates as the amount of water in the mixture increased. At 10% water, a ring-shaped nanostructure was discovered.

5. AIE IN PMI DERIVATIVES

As already mentioned, AIE is a very common phenomenon in NMI derivatives. However, in PMI derivatives the most common phenomenon is ACQ as the amount of water added to the mixture with the organic solvent increases. The synthetic route of the AR19 compound and the water acceptance test (in Figure 36) clearly show this phenomenon.

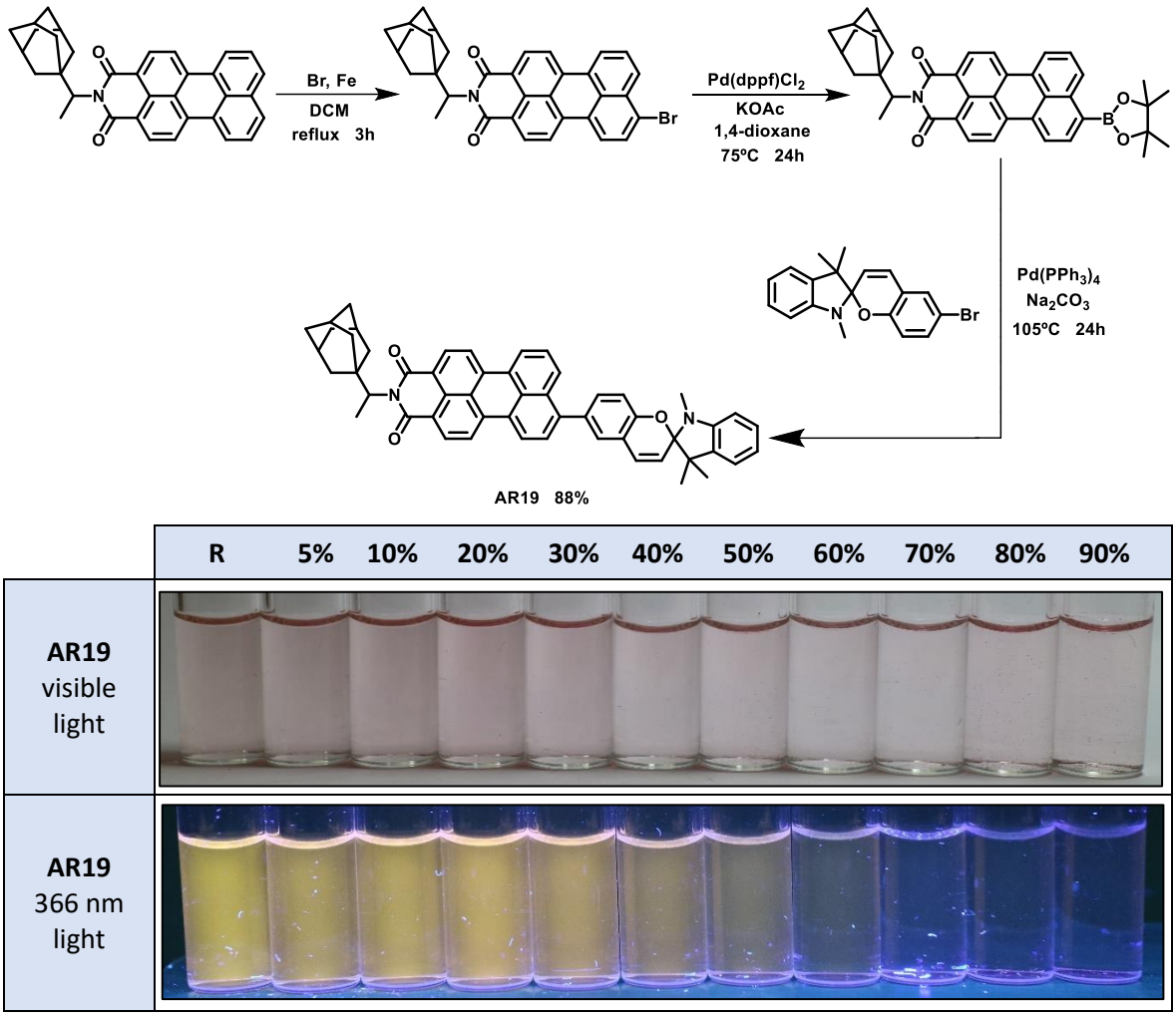

Figure 36. Synthetic route to obtain AR19 (up) and water acceptance test (down) of a 20 µM solutions of AR19 compound in MeCN mixtures with increasing amounts of water.

Therefore, the fact that the AIE is produced in this type of derivatives is a remarkable phenomenon. The synthetic route leading to the compounds with this property is shown below in Figure 37. Like most of the products detailed in this Chapter, they were obtained by a Suzuki-Miyaura carbon-carbon coupling reaction between the boronate of PMI and a dibrominated-pyrene.

Fluorescence analysis of the compounds showed remarkable similarities due to the structural resemblances between them (Figure 38 and Figure 39). For both compounds, the highest emission intensity was achieved in the most apolar of the solvents used. The biggest difference between the two compounds was observed in hexane, being green with compound AR48 and yellow with AR49. In addition, both derivatives showed a bathochromic shift of both the absorption and emission maxima, being more marked in the latter case. The fluorescence quantum yields increased as the conjugation of the products increased, with AR48 showing 94% compared to AR49, with 85%.

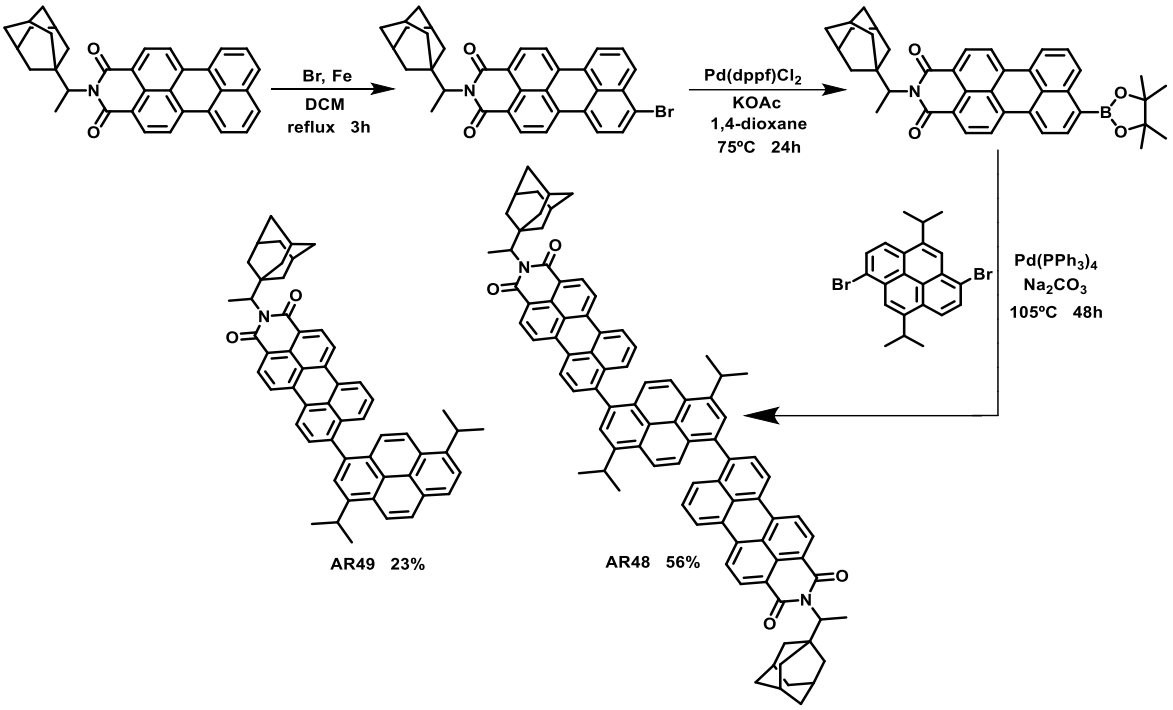

Figure 37. Synthetic route followed to obtain the AR48 and AR49 PMI derivatives.

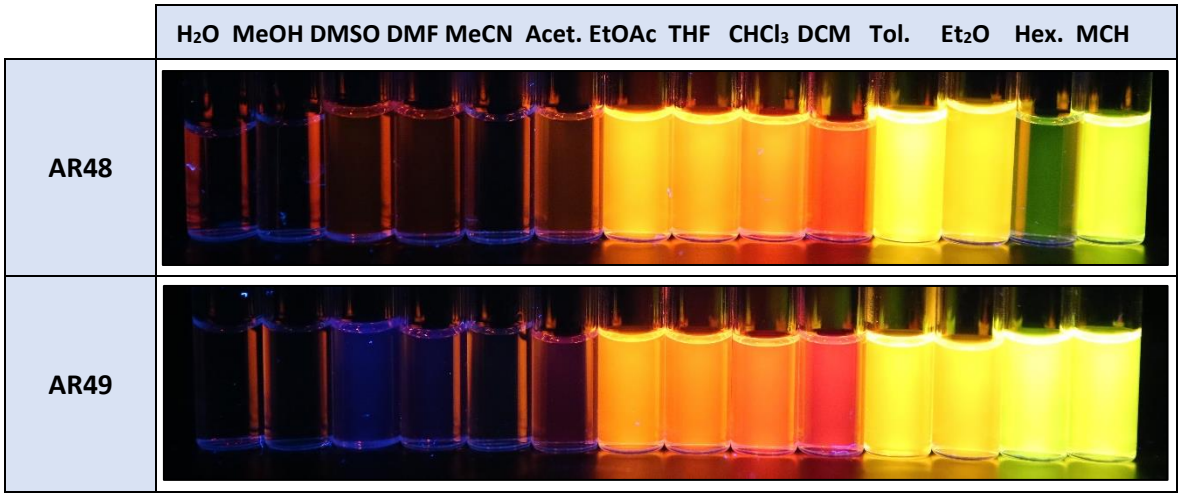

Figure 38. Fluorescent emission of 20 µM solutions of AR48 and AR49 in different solvents under 366 nm light.

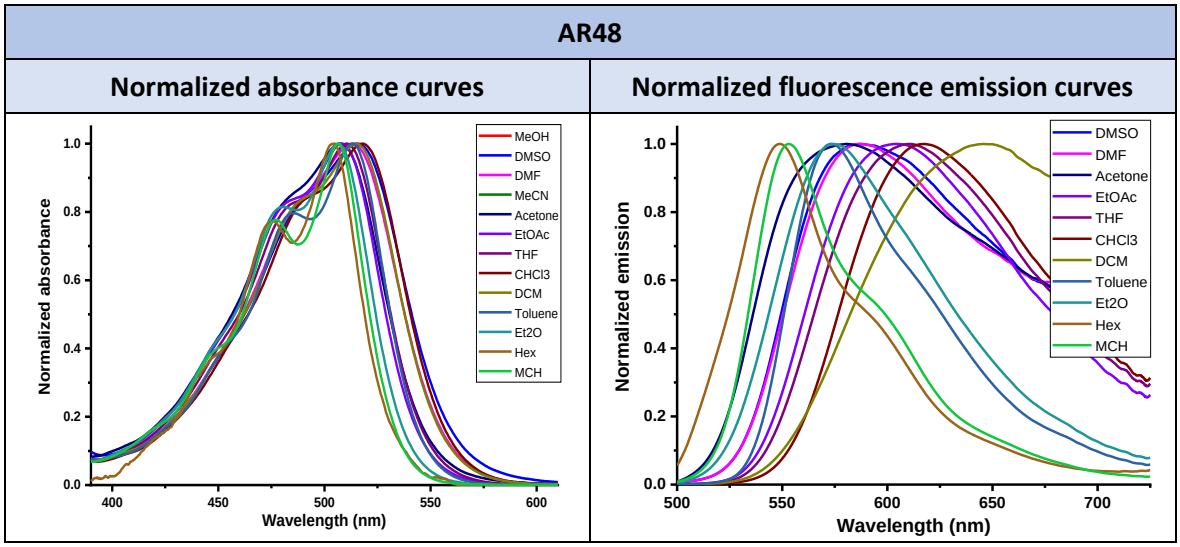

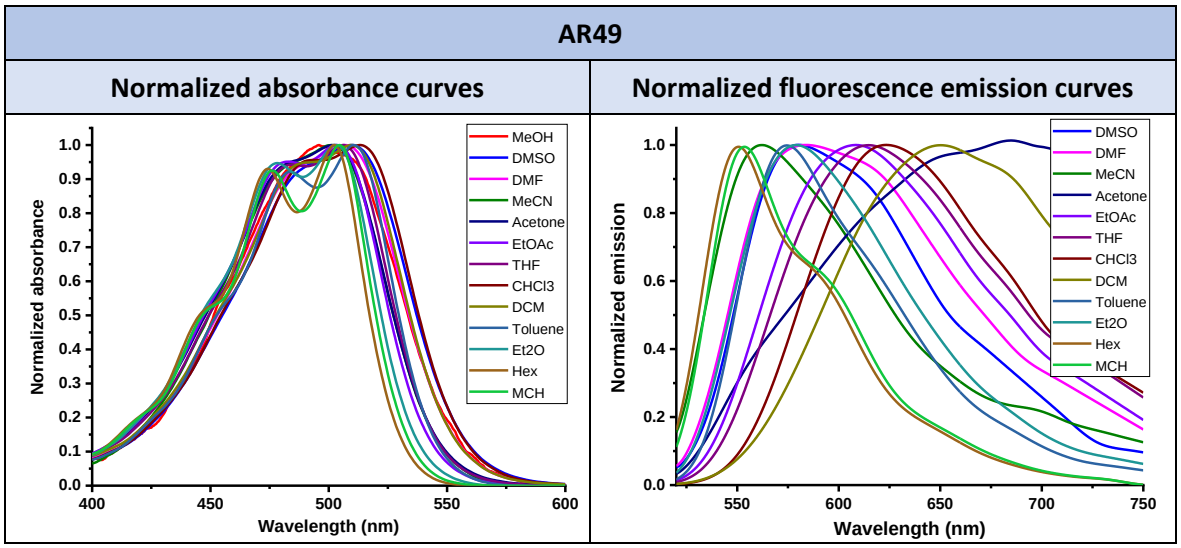

Figure 39. Normalized absorption and emission spectra of 20 µM solutions of AR48 and AR49 in different solvents.

The water acceptance test performed for both compounds, using THF as organic solvent (Figure 40), showed a marked increase in the emission intensity for compound AR49 from 60% water, while for compound AR48 this increase was much lighter at higher amounts of water, highlighting the shift of the emission band towards the red as the amount of water increases.

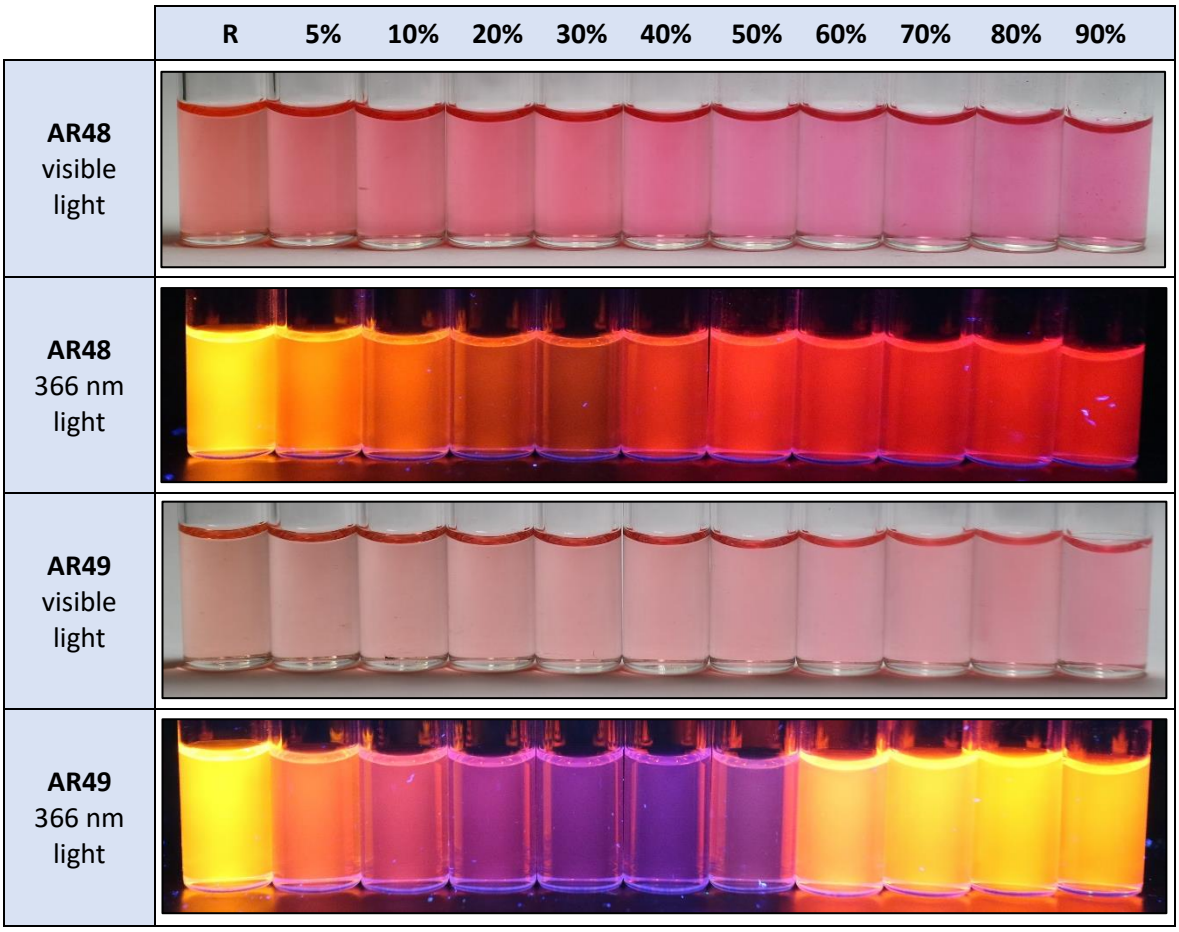

Figure 40. Water acceptance test. 20 µM solutions of the AR48 and AR49 compounds in THF mixtures with increasing amounts of water.

Each of these compounds was then studied individually. Compound AR48 showed a shift from orange region (approximately 613 nm) to the red region (about 640 nm) of the emission maximum as the amount of water increased, accompanied by a slight increase in emission intensity from 70% onwards. This can be showed in Figure 41.

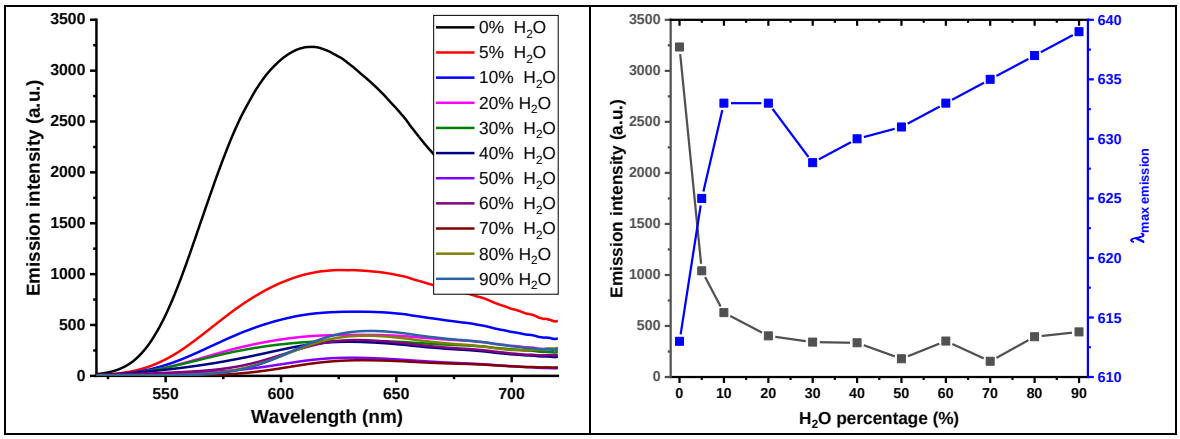

Figure 41. Emission intensity graph (left) and graph of relationship between the emission intensity and the wavelength of the maximum of emission (right) as a function of the amount of water added for AR48 in THF. λ_{exc} = 480 nm.

The nanostructures formed with the different amounts of water were studied by SEM. This product was characterised by the presence of nanovesicles up to 70% water, at which point the AIE started and the vesicles disappeared. The different structures formed can be visualised in Figure 42 below.

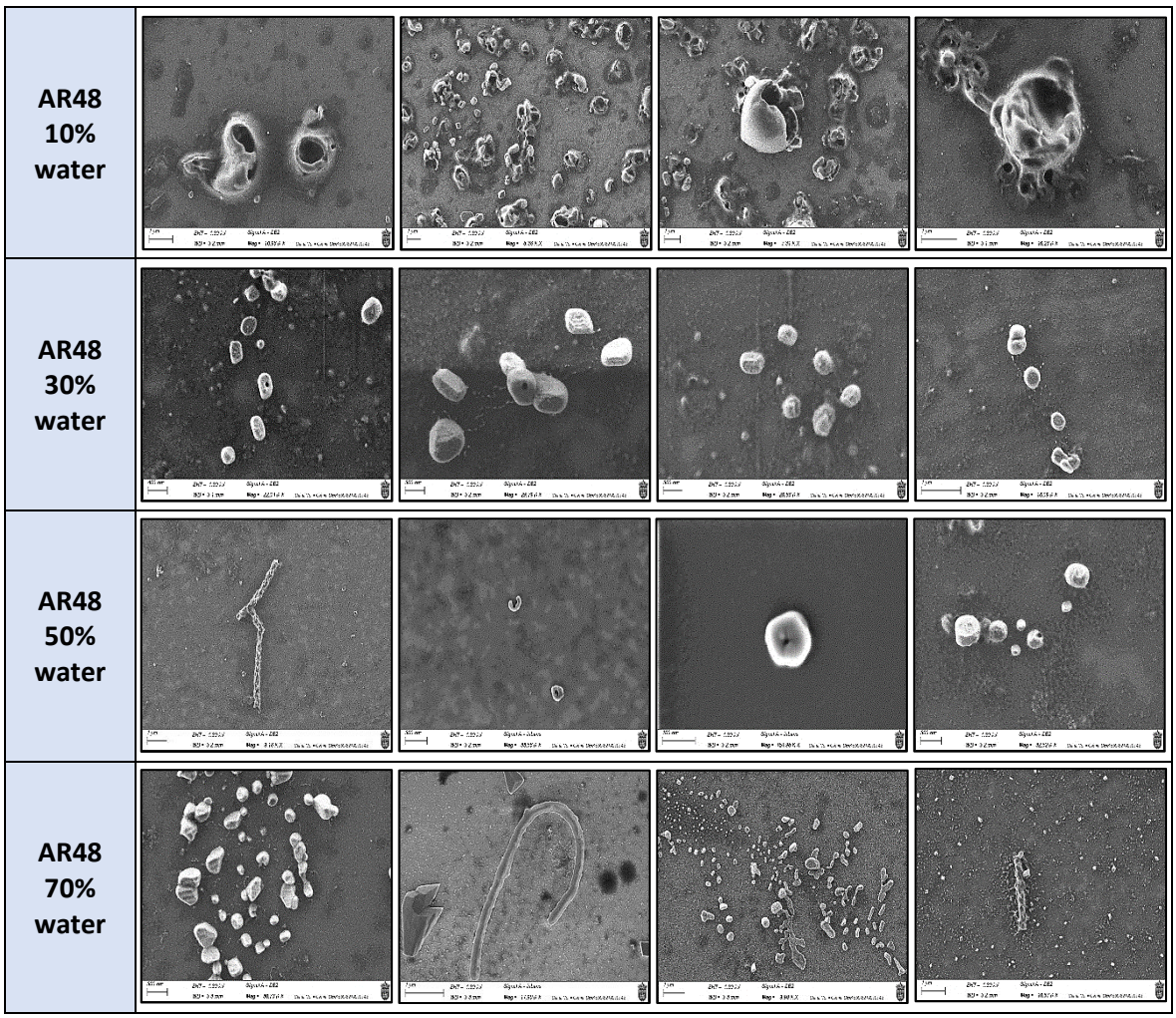

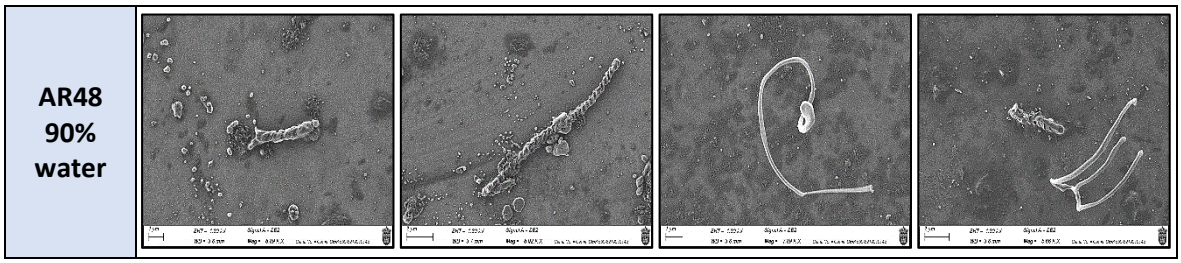

Figure 42. SEM nanoparticles of AR48 in different mixtures of THF-H_2O.

At 10% water, numerous nanovesicles were observed at an intermediate point in the formation process. The most voluminous ones were approximately 2.5 µm in diameter, with a cavity of 1.2 µm. Spherical nanoparticles with a diameter of around 250 nm were also found. By increasing the amount of water up to 30%, better formed and defined vesicles appeared, but much less abundant, as well as nanoparticles with a diameter between 360-550 nm. At 50% water, both single and paired nanoparticles and aggregates of them were detected. At this amount of water, helix-shaped nanofibres and sporadic nanovesicles were found. As the water continued to increase up to the amount at which the AIE phenomenon began (70%), aggregates of nanoparticles with a size of approximately 700 nm were found, as well as fibres and nanosticks, with a thickness of 220 nm. As in the next percentage, the absence of nanovesicles was noteworthy. Finally, at 90%, aggregates were present, with a size of more than 800 nm, and fibres, some of which were helix-shaped and approximately 500 nm thick.

These nanovesicles were attempted to be studied by AFM (Figure 43), however, only the growth of the nanoparticles was observed as the amount of water in the mixture increased.

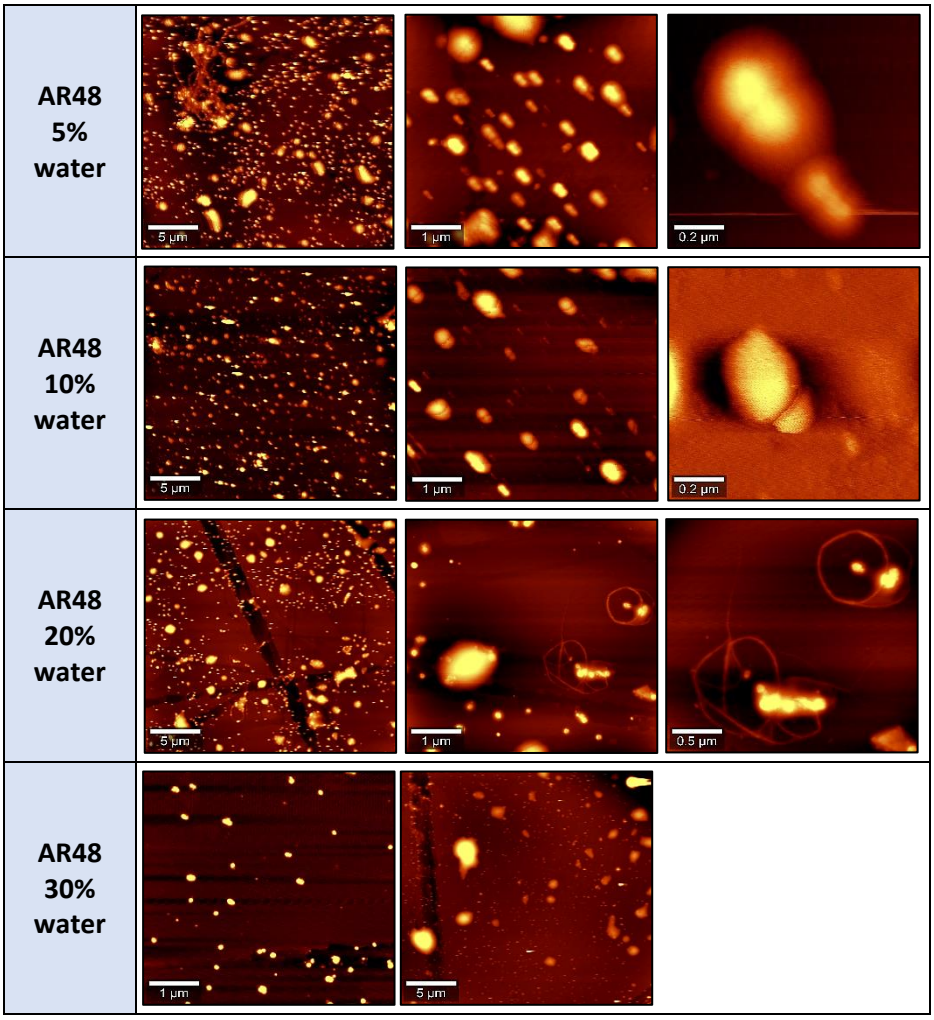

AR48 40% water	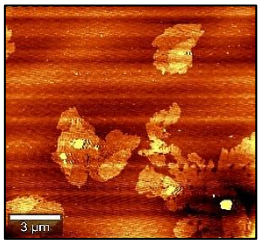

Figure 43. AFM nanoparticles of AR48 in different mixtures of THF-H_2O.

Thus, with 5% water, the nanoparticles had a diameter of approximately 15 nm. They were in pairs and, in turn, grouped in pairs. At 10% water, the nanoparticles continue to be grouped in pairs, which can be clearly shown in the 3D image in Figure 44, with a diameter of about 20 nm. When 20% water was reached, the nanoparticles began to form aggregates with a size of around 120 nm, while individually they were 40 nm in size. At this amount of water, the first fibres were formed. At 30% water, the individual nanoparticles reached a size of 50 nm, and continue to grow at 40% water until they achieved up to 70 nm, while the aggregates were closer to 355 nm in size.

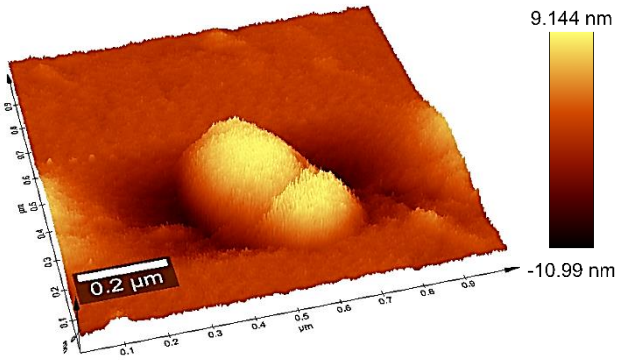

Figure 44. Three-dimensional AFM image of a pair of AR48 nanoparticles in a 10% H_2O mixture.

Comparing the nanostructures obtained by the two microscopy techniques, the strong influence of the deposition surface on the structures formed, and subsequently observed, is again evident.

Performing the same analysis for the pyrene derivative with a single substituent (AR49), a marked increase in emission intensity was observed from 60% water (Figure 45), which is accompanied by a shift of the emission maximum from the violet region (above 655 nm) to the yellow region (627 nm).

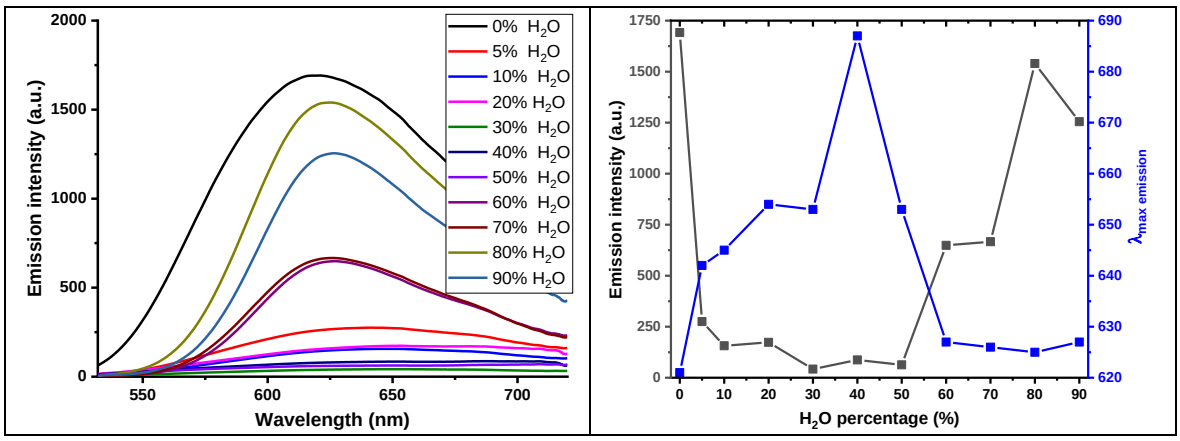

Figure 45. Emission intensity graph (left) and graph of relationship between the emission intensity and the wavelength of the maximum of emission (right) as a function of the amount of water added for AR49 in THF. λ_{exc} = 500 nm.

This AIE phenomenon was studied by SEM microscopy and the structures shown in Figure 46 were obtained. For this compound, as the amount of water increased, the size of the spherical nanoparticles and the aggregates they form grew.

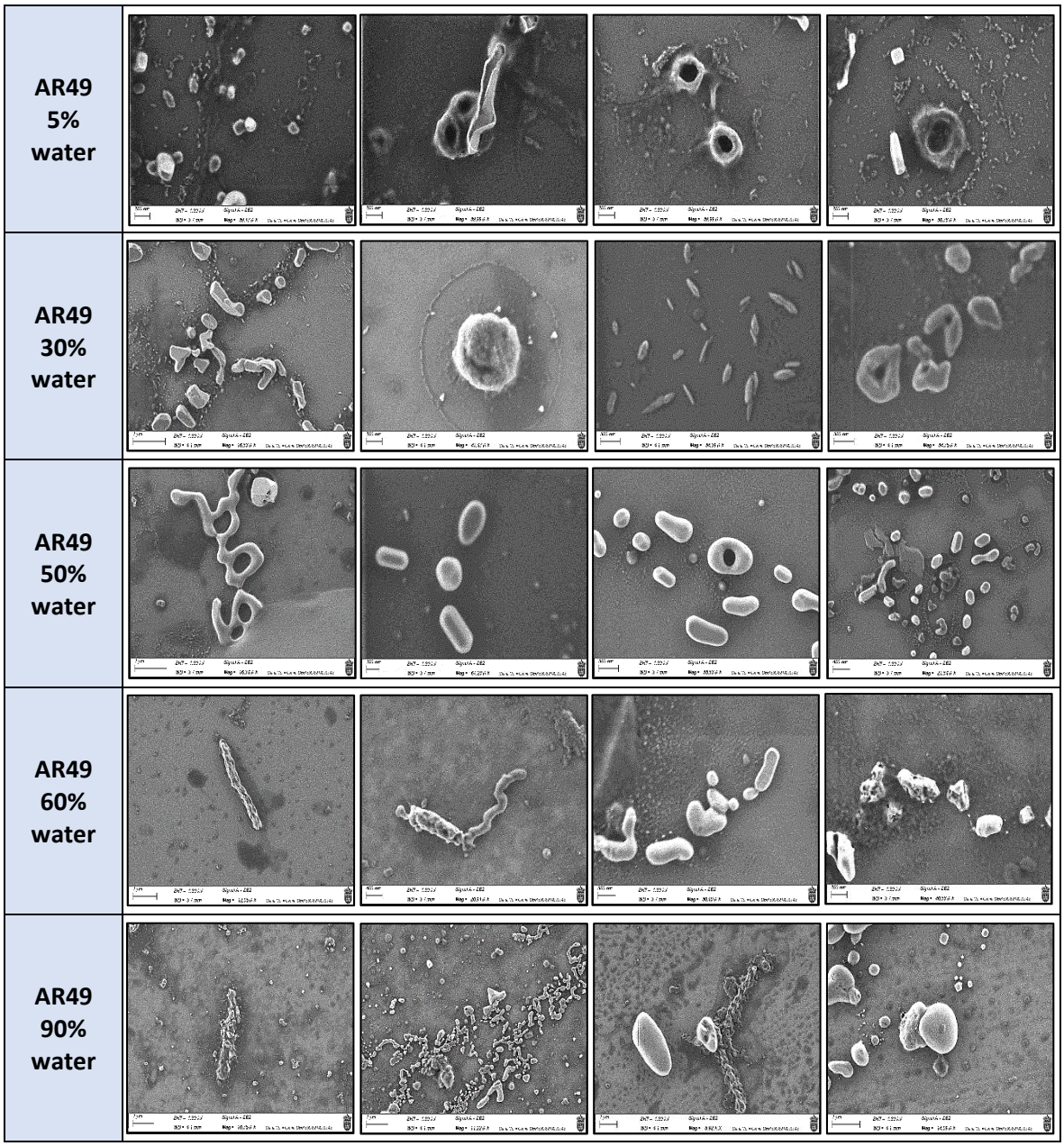

Figure 46. SEM nanoparticles of AR49 in different mixtures of THF-H_2O.

Thus, at 5% water, nanoparticles with a diameter of approximately 150 nm were found, as well as the occasional aggregate of nanoparticles and the sporadic presence of rod-shaped nanoparticles. When the amount of water raised to 30%, individual nanoparticles and larger aggregates were observed in contrast to the previous amount of water. At this percentage of water, nanoneedles and aggregates of them were found to be approximately 200 nm long and 60 nm wide. Increasing the amount of water until it was equivalent to that of THF, spherical nanoparticles, with a diameter slightly exceeding 200 nm, and elongated nanoparticles, as well as aggregates of them, were encountered. At 60% water, the amount at which the AIE phenomenon started for this PMI derivative, helix-shaped nanofibres were found, as with the NMI derivatives, with a thickness ranging between 250-350 nm. Aggregates larger than 750 nm were also detected. Finally, at 90%

water, nanofibres continued to be obtained, with a thickness between 400-500 nm, with particles adhering to their surface, and aggregates of very different sizes, from 500 nm to 1.4 µm.

6. CONCLUSIONS

The functionalisation of perylene rings can be carried out in different positions. The most common of them, performed throughout this doctoral thesis, is the functionalisation of the peri-positions. The functionalisation of two adjacent peri-positions by means of an *N*-imide group regulates the aggregation and solubility of the derivatives, while the extension of the conjugation by introducing different groups in one of the peri-positions generally causes a shift of the emission maximum towards the red region of the electromagnetic spectrum as the amount of water added to an organic solvent increase.

The nanostructures formed by the different derivatives under these conditions are tremendously varied, ranging from simple spherical or needle-shaped nanoparticles to vesicles, opening the possibility that these types of compounds can be used in the transport of analytes.

The most common phenomenon that PMI derivatives can undergo is ACQ, and there are countless examples of this in the literature.[43] However, it has been shown that, using certain substituents and under certain conditions, PMI derivatives can give rise to the AIE phenomenon, characteristic, for example, of NMI derivatives. Those compounds which, in addition to exhibiting this phenomenon, are accompanied by a shift of the emission maximum towards the red region also have the option of giving rise to the formation of nanovesicles.

However, the structures formed, both when there is a shift of the emission maximum and when the AIE phenomenon occurs, are strongly conditioned by the surface on which the deposition is carried out. It has been verified how the same sample forms different nanostructures on a silicon surface and on a mica surface. In fact, it has been demonstrated that the formation of nanovesicles is highly favoured on the silicon surface, being found very sporadically on the mica surface.

Therefore, once the optimal conditions for the formation of nanovesicles from PMI derivatives have been established, it will be possible to study their use in, for example, the carrier transport of drugs.

[43] a) S. Xu, Y. Duan, B. Liu, *Adv. Mater.*, **2019**, 1903530. b) H. Gao, X. Zhang, C. Chen, K. Li, D. Ding, *Adv. Biosys.*, **2018**, *2*, 1800074. c) J. Qi, C. Chen, D. Ding, B. Z. Tang, *Adv. Healthcare Mater.*, **2018**, *7*, 1800477. d) P. Chena, P. Lva, C. S. Guoa, R. P. Wanga, X. Sua, H. T. Fenga, B. Z. Tang, *Chin. Chem. Lett.*, **2023**, *34*, 108041.

FINAL CONCLUSIONS AND FUTURE RESEARCH LINES

The final part of each of the chapters included in this Doctoral Thesis has its own conclusions, due to the autonomous character of all of them. However, in this final section, the aim is to compile all the aspects studied, establishing some general conclusions. In addition, future lines of research are suggested that will allow this Doctoral Thesis to be used as starting material for future projects.

1. CONCLUSIONS

The general conclusions derived from the overview of the different chapters that constituted this Doctoral Thesis are presented below. Each of the conclusions drawn are linked to one or more of the objectives set out in the Introduction to this Thesis, which allows us to clearly answer the questions posed at the beginning of this research work.

1. The design and establishment of an action protocol to study the characteristics and properties of the synthesised products, regardless of their nature. This procedure is aimed at evaluating the detection capacity of the compounds against different anionic, cationic, oxidising and reducing species. Furthermore, this protocol also takes into consideration the state in which the detection of the analyte is carried out: in solution, in the gas phase or in the solid state. Therefore, regardless of the type of probe that is developed, the method of action is standardised. In addition, this protocol also allows the analysis of other fluorescence properties of the compounds, such as the AIE phenomenon.

2. The versatility of NMI derivatives, since the same compound has a wide range of applications, being used either for the detection of different analytes (TNT, TATP, Hg^{2+}) or in the formation of nanostructures.

3. TATP is an explosive that is currently widely used in the development of IEDs and is characterised by its low vapour pressure, which is the basis for the development of current methods for the detection of peroxide derivatives. However, although current methods have low LODs, they are very bulky, require specialised personnel, do not allow *in situ* analysis and the costs, both energetic and economic, are very high. To solve this problem, a system based on the absorption of a probe on silica nanoparticles (AR82s·SiO_2) has been developed that detects TATP in the gas phase both in laboratory conditions and in conditions close to reality, enabling the presence or absence of TATP in a matter of seconds and with a detection limit of 13.03 ng of TATP, which is sufficiently low to compete with existing methods. Therefore, this detection system could be used in public buildings, sports stadiums or concert halls to prevent terrorist attacks.

4. The validation of the TATP detection system has been carried out in solution, in the gas phase at laboratory scale and in the gas phase in an office under real-life conditions. In all three cases, the LODs obtained are sufficiently low to compete with, and even improve on, current detection systems. In addition, to facilitate the detection of TATP, an APP has been developed that establishes, only through a photograph of the AR82s·SiO_2 probe, the presence or absence of explosive as well as the approximate amount in the environment. This telephone application has been validated both on a laboratory scale and in conditions close to reality, allowing us to know, practically immediately and without specialised equipment, the presence of TATP.

5. Within the nitrated explosives, TNT has had a long history, being its applications mainly military. Therefore, in this Doctoral Thesis, a probe (AR85) has been developed capable of discriminating, in solution, between the existing nitrated explosives, presenting a low detection limit for TNT (1.87 nM).

6. TNT can be detected in solid form by means of an NMI derivative attached to the PDMS surface (AR67d@Sylgard-184), which allows controlled trapping of the analyte, resulting in

a decrease of the emission intensity. Furthermore, it has been shown that the detection system is hardly affected by the presence of interferents such as sand or water.

7. In NMI derivatives, the aggregation and AIE phenomenon can be controlled by the number of amino-protecting groups, or free amines, present in the structure. If the compounds have two amino-protecting groups, they show an intense AIE, while the absence of them results in an ACQ. On the other hand, if they only have one amino-protecting group in their structure, the AIE produced is of an intermediate intensity.
8. The AIE phenomenon for NMI derivatives depends more on the presence of amino-protecting groups than on the substituents on the naphthalene ring at position 4. The AIE phenomenon disappears as soon as the compounds are deprotected, irrespective of their substituents.
9. PMI derivatives in which an extension of conjugation occurs, such as by the introduction of a spiro moiety, experience a shift of the emission maximum towards the red region of the visible or NIR spectrum as the amount of water added to an organic solvent, usually THF, is increased. Such compounds are more likely to lead to vesicle formation.
10. Although infrequent, PMI derivatives can also experience the AIE phenomenon when an extension of the conjugation occurs, being conditioned by the degree of conjugation of the compound under study. In addition, it has been shown that the AIE for PMI derivatives is more intense when the shift of the emission maximum does not reach the red region of the electromagnetic spectrum.
11. The formed nanostructures have a strong dependence on the surface on which the deposition is performed, because the same is not observed on a silicon disc as on a mica plate, regardless of the nature of the synthesised compound.

2. FUTURE RESEARCH LINES

This PhD Thesis deals with very diverse aspects related to the detection of analytes that are dangerous for current society and with the aggregation and fluorescence properties that NMI and PMI derivatives produce. However, there are still many aspects that can be explored to improve the systems developed or to better understand the properties studied. Thus, some lines of research that allow us to continue with the work of this Doctoral Thesis are:

1. Automatising the system developed for the detection of TATP, which will increase the safety of operators, without the need for sample pre-treatment and providing immediate and *in situ* results. In addition, to improve the sensitivity of the detection system and reduce the LOD, a pre-concentrator could be provided to operate semi-continuously and maintain the sensor's ability to provide real-time results.
2. Developing another support for the AR82s·SiO_2 system that is more versatile and resistant than the glass support used so far, such as attaching the probe to polymeric fibres, which may even improve detection capability by increasing the contact surface area exposed to TATP vapours.
3. Establishing the most favourable conditions for the formation of nanovesicles, both PMI and NMI derivatives, by modifying variables such as temperature, deposition surface or the substituents attached to the perylene and naphthalene rings or the *N*-imide position. In this way, once we have perfect control over their production, we will be able to study their behaviour in the transport of substances and drugs.
4. Studying the AIE control phenomenon in amino-protected, semi-protected and unprotected NMI derivatives through the introduction of other substituents in the *N*-imide

positions. Thus, in the amino-protected compounds, a symmetric or asymmetric substitution can be carried out, which will allow to explore the influence of these groups on the AIE. Moreover, it has been demonstrated that these NMI derivatives sporadically generate nanovesicles, so that, in parallel, it is possible to work on improving the conditions for obtaining them.

5. To increase the conjugation of PMI derivatives, which induce the AIE phenomenon or a shift of the emission maximum towards the red region, via cyclisation reactions to analyse their effect on the fluorescence properties.

SCIENTIFIC PRODUCTIVITY DURING THE PhD THESIS

1. SCIENTIFIC RESEARCH ARTICLES

1. **Title:** Microwave detection of wet triacetone triperoxide (TATP): non-covalent forces and water dynamics.
   Authors: Susana Blanco, Alberto Macario, José García-Calvo, **Andrea Revilla-Cuesta**, Tomás Torroba, Juan Carlos López.
   Journal: Chemistry: A European Journal.
   Year: 2021.
   Volume: 27.
   Issue: 5.
   Pages: 1680-1687.
   DOI: 10.1002/chem.202003499.
   Journal classification (2021 JCR ranking data): 64/179 (Chemistry Multicisciplinary, SCIE). Second quartile (Q2). Journal Impact Factor: 5.02.

2. **Title:** Self-assembly hydrosoluble coronenes: a rich source of supramolecular turn-on fluorogenic sensing materials in aqueous media.
   Authors: Daisy Carolina Romero, Patricia Calvo-Gredilla, José García-Calvo, Alberto Díez-Varga, José Vicente Cuevas, **Andrea Revilla-Cuesta**, Natalia Busto, Irene Abajo-Cuadrado, Gabriel Aullón, Tomás Torroba.
   Journal: Organic Letters.
   Year: 2021.
   Volume: 23.
   Issue: 22.
   Pages: 8727-8732.
   DOI: 10.1021/acs.orglett.1c03175.
   Journal classification (2021 JCR ranking data): 4/56 (Chemistry Organic, SCIE). First quartile (Q1). Journal Impact Factor: 6.072.

3. **Title:** Dye-modified silica-anatase nanoparticles for the ultrasensitive fluorogenic detection of the improvised explosive TATP in an air microfluidic device.
   Authors: Sindija Lapcinska, **Andrea Revilla-Cuesta**, Irene Abajo-Cuadrado, José Vicente Cuevas, Manuel Avella, Pavel Arsenyan, Tomás Torroba.
   Journal: Materials Chemistry Frontiers.
   Year: 2021.
   Volume: 5.
   Pages: 8097-8107.
   DOI: 10.1039/d1qm01041g.
   Journal classification (2021 JCR ranking data): 33/179 (Chemistry Multidisciplinary, SCIE). First quartile (Q1). Journal Impact Factor: 8.683.

4. **Title:** Synthesis of water-soluble hemicoronenediimides by photocyclization of perylenediimides: turn-on fluorescent probes in water by complexation with cucurbit[7]uril or binding to G-quadruplex motifs.
   Authors: Natalia Busto, Daisy Carolina Romero, **Andrea Revilla-Cuesta**, Irene Abajo-Cuadrado, José Vicente Cuevas, Teresa Rodríguez, Begoña García, Tomás Torroba.
   Journal: Dyes and Pigments.
   Year: 2022.
   Volume: 205.
   Pages: 110557.

DOI: 10.1016/j.dyepig.2022.110557.
Journal classification (2021 JCR ranking data): 16/73 (Chemistry Applied, SCIE). First quartile (Q1). Journal Impact Factor: 5.122.

5. **Title:** New fluorescent reporters capable of ultra-sensitively detecting trinitrotoluene on surfaces: A proof-of-concept for finding hidden nitroaromatics in the workroom.
Authors: **Andrea Revilla-Cuesta**, Irene Abajo-Cuadrado, María Medrano, Mateo M. Salgado, Giuditta Pecori, Teresa Rodríguez, Carla Hernando-Muñoz, José García-Calvo, Julia Arcos and Tomás Torroba.
Journal: Journal of Photochemistry and Photobiology, A: Chemistry.
Year: 2023.
Volume: 444.
Pages: 114911.
DOI: 10.1016/j.jphotochem.2023.114911.
Journal classification (2021 JCR ranking data): 64/165 (Chemistry Physical, SCIE). Second quartile (Q2). Journal Impact Factor: 5.141.

6. **Title:** Silica nanoparticle/fluorescent dye assembly capable of ultrasensitively detecting airborne triacetone triperoxide: proof-of-concept Detection of improvised explosive devices in the workroom.
Authors: **Andrea Revilla-Cuesta**, Irene Abajo-Cuadrado, María Medrano, Mateo M. Salgado, Manuel Avella, Teresa Rodríguez, José García-Calvo, Tomás Torroba.
Journal: ACS Applied Materials and Interfaces.
Year: 2023.
Status: Accepted.
Journal classification (2021 JCR ranking data): 49/345 (Material Science SCIE). First quartile (Q1). Journal Impact Factor: 10.383.

2. BOOK CHAPTERS

1. **Title:** Explosive detection: sensors, electronic system and data processing.
Authors: Tomás Torroba, Israel Schechter, José García-Calvo, **Andrea Revilla-Cuesta**.
Book: Development of new chemical sensor and optical technologies for fast and sensitive detection of improvised explosives.
Year of publication: 2019.
Book ISBN: 978-94-024-1729-6.
DOI: 10.1007/978-94-024-1729-6.
Editorial: Springer.

3. SCIENTIFIC PRESENTATIONS AT NATIONAL AND INTERNATIONAL CONGRESSES AND CONFERENCES

1. **Title:** Host-guest chemistry of water-soluble coronenediimide nanoaggregates.
Authors: Daisy Carolina Romero, Patricia Calvo-Gredilla, José García-Calvo, José Vicente Cuevas, **Andrea Revilla-Cuesta**, Tomás Torroba.
Congress/conference: XXXVII Reunión Bienal de la Real Sociedad Española de Química.
Place/date: Donostia-San Sebastián (Spain), May 26-30, 2019.
Abstract book: page 454.

2. **Title:** Supported nanoparticles for catalysis.
   Authors: José García-Calvo, **Andrea Revilla-Cuesta**, Tomás Torroba.
   Congress/conference: XXXVII Reunión Bienal de la Real Sociedad Española de Química.
   Place/date: Donostia-San Sebastián (Spain), May 26-30, 2019.
   Abstract book: page 502.

3. **Title:** Wetting triacetone triperoxide allows its detection by microwave spectroscopy.
   Authors: Susana Blanco, Alberto Macario, José Garcia-Calvo, **Andrea Revilla-Cuesta**, Tomás Torroba, Juan Carlos López.
   Congress/conference: 2020 International-Symposium on Molecular Spectroscopy.
   Place/date: Illinois (USA), June 24, 2020.
   Abstract book: http://hdl.handle.net/2142/107682.

4. **Title:** A supramolecular reflection in gold: templated formation of gold nanodendrites from self-assembled organic nanoparticles.
   Authors: Tomás Torroba, Mateo M. Salgado, **Andrea Revilla-Cuesta**, Patricia Calvo-Gredilla, Javier Gutiérrez.
   Congress/conference: XXVIII RSEQ Biennial Meeting in Organic Chemistry.
   Place/date: Santa Cruz de Tenerife (Spain), June 10-12, 2020.
   Abstract book: OC, page 73.

5. **Title:** Surface functionalized silica nanoparticles for the off–on fluorogenic detection of an improvised explosive, TATP, in a vapour flow.
   Authors: Patricia Calvo-Gredilla, José García-Calvo, Mateo M. Salgado, **Andrea Revilla-Cuesta**, Tomás Torroba.
   Congress/conference: XXVIII RSEQ Biennial Meeting in Organic Chemistry.
   Place/date: Santa Cruz de Tenerife (Spain), June 10-12, 2020.
   Abstract book: FP15, page 91.

6. **Title:** New naphthalenemonoimides with applications for the detection of peroxide species.
   Authors: Mateo M. Salgado, **Andrea Revilla-Cuesta**, Patricia Calvo-Gredilla, Tomás Torroba.
   Congress/conference: XXVIII RSEQ Biennial Meeting in Organic Chemistry.
   Place/date: Santa Cruz de Tenerife (Spain), June 10-12, 2020.
   Abstract book: FP88, page 164.

7. **Title:** Pyrene derivatives that form organic nanoparticles in mixtures of organic-aqueous mixtures of solvents.
   Authors: **Andrea Revilla-Cuesta**, Mateo M. Salgado, Patricia Calvo-Gredilla, Tomás Torroba.
   Congress/conference: XXVIII RSEQ Biennial Meeting in Organic Chemistry.
   Place/date: Santa Cruz de Tenerife (Spain), June 10-12, 2020.
   Abstract book: FP79, page 155.

8. **Title:** Derivados del pireno para la obtención de nanopartículas orgánicas en mezclas de agua y disolventes orgánicos.
   Authors: **Andrea Revilla-Cuesta**, Irene Abajo-Cuadrado, Tomás Torroba.
   Congress/conference: VII Jornadas de doctorandos de la Universidad de Burgos.

Place/date: Burgos (Spain), March 09-10, 2021.
Abstract book: page 299-312. ISBN: 978-84-18465-03-1.

9. **Title:** Organic nanoparticles of pyrene derivative.
   Authors: **Andrea Revilla-Cuesta**, Irene Abajo-Cuadrado, Mateo M. Salgado, Ángel Sáez, María Medrano, Carla Hernando, Tomás Torroba.
   Congress/conference: RSEQ Symposium.
   Place/date: online, September 27-30, 2021.
   Abstract book: P141.

10. **Title:** New naphtalenemonoimides with applications for the detection of oxidative species and cations.
    Authors: Mateo M. Salgado, Irene Abajo-Cuadrado, Ángel Sáez, Carla Hernando, María Medrano, **Andrea Revilla-Cuesta**, Tomás Torroba.
    Congress/conference: RSEQ Symposium.
    Place/date: online, September 27-30, 2021.
    Abstract book: P230.

11. **Title:** New derivatives of perylenemonoimide and ruthenium(II) complexes of interest a fluorescent markers in bioconjugation.
    Authors: Ángel. Sáez, Carla Hernando, Mateo M. Salgado, María Medrano, Irene Abajo-Cuadrado, **Andrea Revilla-Cuesta**, Tomás Torroba.
    Congress/conference: RSEQ Symposium.
    Place/date: online, September 27-30, 2021.
    Abstract book: P076.

12. **Title:** A supramolecular reflection in gold: templated formation of gold nanodendrites from self-assembled organic nanoparticles.
    Authors: Tomás Torroba, Mateo M. Salgado, **Andrea Revilla-Cuesta**, María Medrano, Irene Abajo-Cuadrado, Carla Hernando, Ángel Sáez, Javier Gutiérrez.
    Congress/conference: RSEQ Symposium.
    Place/date: online, September 27-30, 2021.
    Abstract book: P184.

13. **Title:** Nanopartículas de sílice-anatasa modificadas con colorante para la detección fluorescente ultrasensible del explosivo improvisado TATP en un dispositivo microfluídico de aire.
    Authors: **Andrea Revilla-Cuesta**, Irene Abajo-Cuadrado, Tomás Torroba.
    Congress/conference: VIII Jornadas de doctorandos de la Universidad de Burgos.
    Place/date: Burgos (Spain), April 25-26, 2022.
    Abstract book: pages 223-234. ISBN: 978-84-18465-23-9.

14. **Title:** Dye-modified silica-anatase nanoparticles for the detection of the improvised explosive TATP in an air microfluidic device.
    Authors: **Andrea Revilla-Cuesta**, Sindija. Lapcinska, Irene Abajo-Cuadrado, José Vicente Cuevas, Manuel Avella, Pavel Arsenyan, Tomás Torroba.
    Congress/conference: XXXVIII Reunión Bienal RSEQ.
    Place/date: Granada (Spain), June 27-30, 2022.
    Abstract book: PP719, page 1253. ISBN: 978-84-09-42159-6.

15. **Title:** From fluorescent biomarkers to soft nanotransporters.
    Authors: Tomás Torroba, Carla Hernando, Mateo M. Salgado, **Andrea Revilla-Cuesta**, Irene Abajo-Cuadrado, Natalia Busto, Javier Gutiérrez.
    Congress/conference: XXXVIII Reunión Bienal RSEQ.
    Place/date: Granada (Spain), June 27-30, 2022.
    Abstract book: S13-OC06, page 451. ISBN: 978-84-09-42159-6.

16. **Title:** Self-assembly hydrosoluble coronenes: a rich source of supramolecular turn-on fluorogenic sensing materials in aqueous media.
    Authors: Irene Abajo-Cuadrado, Daisy Carolina Romero, Patricia Calvo-Gredilla, José García-Calvo, Alberto Díez, José Vicente Cuevas, **Andrea Revilla-Cuesta**, Natalia Busto, Gabriel Aullón.
    Congress/conference: XXXVIII Reunión Bienal RSEQ.
    Place/date: Granada (Spain), June 27-30, 2022.
    Abstract book: PP754, page 1285. ISBN: 978-84-09-42159-6.

17. **Title:** Silica nanoparticle/fluorescent dye assembly capable of ultrasensitively detecting airbone triacetone triperoxide: proof-of-concept detection of improvised explosive devices in the workroom.
    Authors: **Andrea Revilla-Cuesta**, Irene Abajo-Cuadrado, María. Medrano, Mateo M. Salgado, Manuel Avella, Teresa Rodríguez, José García-Calvo, Tomás Torroba.
    Congress/conference: XXXIX Reunión Bienal RSEQ.
    Place/date: Zaragoza (Spain), June 25-30, 2023.

18. **Title:** New fluorescent reporters capable of ultrasensitively detecting trinitrotoluene on surfaces: proof-of-concept detection of hidden nitroaromatics in the woorkroom.
    Authors: Irene Abajo-Cuadrado, **Andrea Revilla-Cuesta**, Mateo M. Salgado, Giuditta Pecori, Carla Hernando, Tomás Torroba.
    Congress/conference: XXXIX Reunión Bienal RSEQ.
    Place/date: Zaragoza (Spain), June 25-30, 2023.

19. **Title:** Self-assembling depsipeptides on aggregation-induced emission luminogens as a new way to create programmable nanovesicles, soft nanocarriers and Trojan horses of drug-peptide conjugates.
    Authors: Carla Hernando, Mateo M. Salgado, **Andrea Revilla-Cuesta**, Irene Abajo-Cuadrado, Natalia Busto, Javier Gutiérrez, Giampaolo Barone, Angelo Spinello, Tomás Torroba.
    Congress/conference: The International Symposium on Macrocyclic and Supramolecular Chemistry.
    Place/date: Reykjavik (Iceland), June 25-29, 2023.

20. **Title:** From hidden explosive sensors to environmental plastic degradation: opportunities of the locally directed oxidation events on surfaces.
    Authors: **Andrea Revilla-Cuesta**, Irene Abajo-Cuadrado, Carla Hernando, Federica Betocchini, Tomás Torroba.
    Congress/conference: 19th International Conference on Thin Films.
    Place/date: Burgos (Spain), September 26-29, 2023.

4. PATENTS

1. **Patent number:** P202330107.
   Title: Compuesto naftaleno-1,8-dicarboxilmonoimida, procedimiento de preparación, y su uso como detector de explosivos oxidantes.
   Authors: **Andrea Revilla-Cuesta**, Irene Abajo-Cuadrado, María Medrano, Mateo M. Salgado, Tomás Torroba.
   Country: Spain.
   Application date: 13/02/2023.
   Holder: University of Burgos.

5. PARTICIPATION IN PROJECTS

1. **Project code:** G5536-COORDINADOR 2.
   Title: Development of new chemical sensors and optical technologies for fast and sensitive detection of improvised explosives.
   Funding entity: OTAN-North Atlantic Treaty Organisation.
   Duration: 41 months. From 01/09/2018 to 01/02/2022.
   Principal investigator: Tomás Torroba.

2. **Title:** Nuevas estrategias en el tratamiento de la obesidad y diabetes mellitus empleando el factor de preimplantación (PIF) en modelos preclínicos murinos. (DIABO-PIF).
   Funding entity: Fundación Bancaria Caixa D. Estalvis I Pensions de Barcelona, La Caixa.
   Duration: 27 months. From 01/06/2019 to 31/08/2021.
   Principal investigator: Tomás Torroba and Germán Manuel Perdomo Hernandez.

3. **Project code:** PID2019-111215RB-I00.
   Title: Desarrollo de nuevos sensores químicos para la detección rápida y selectiva de dispositivos explosivos improvisados.
   Funding entity: Agencia Estatal de Investigación.
   Duration: 36 months. From 01/06/2020 to 31/05/2023.
   Principal investigator: Tomás Torroba.

4. **Project code:** UBU20-04.
   Title: El factor de preimplantación (PIF) en el tratamiento de la diabetes mellitus tipo 2 (PIF-T2DM).
   Funding entity: Fundación Bancaria Caixa D. Estalvis I Pensions de Barcelona, La Caixa.
   Duration: 25 months. From 01/12/2020 to 31/12/2022.
   Principal investigator: Tomás Torroba.

5. **Project code:** PDC2022-133955-I00.
   Title: Sistema de colorante AIE en nanopartículas de sílice para la detección ultrasensible de TATP en aire: un prototipo de nariz química para detectar IEDs en almacenes de equipaje.
   Funding entity: Ministerio de Ciencia e Innovación.
   Duration: 24 months. From 01/12/2022 to 30/11/2024.
   Principal investigator: Tomás Torroba.

6. PhD THESIS FUNDING

1. **Reference:** FPU18/03225.
   Call: Convocatoria 2018 de las Ayudas para la Formación de Profesorado Universitario (FPU).
   Funding entities: Ministerio de Ciencia, Innovación y Universidades.
   Duration: from 30/09/2019 to 29/09/2023.

2. **Reference:** EST22/00518.
   Call: Convocatoria 2022 de las Ayudas a la movilidad para estancias breves y traslados temporales para beneficiarios del programa de Formación del Profesorado Universitario (FPU).
   Funding entities: Ministerio de Universidades.
   Duration: from 05/09/2022 to 04/12/2022.

ANNEX I: APPARATUS, REAGENTS AND SOLVENTS

This section details the characteristics of the apparatus used in the different measurements carried out throughout this Doctoral Thesis, as well as the reagents and solvents used in the synthetic routes or experiments done.

1. APPARATUS

1. **Atomic force microscopy (AFM):** images obtained using a Confocal Raman Microscope - Atomic Force Microscope model Alpha300 R - Alpha300A AFM WITec, with a motorised x-y-sample scanning platform. For the samples analysed, a He-Ne laser of 532 nm and magnifications of 10x (Na 0.25), 20x (NA 0.5 and 0.4) and 50x (NA 0.55 and 0.8) were used. The images are processed with WITec's Project FOUR software.
2. **Elemental analysis:** a Thermo Scientific organic elemental microanalyser model FLASH 2000 was utilised.
3. **Excitation spectra:** these spectra are recorded using an Edimburgh Instruments FLS980 fluorometer with a 350W continuous emission power Xenon lamp. Measurements are made using a 3.5 ml HELLMAN 110-QS cuvette, with a 1 cm optical path, at a temperature of 25°C.
4. **Fluorescence decay lifetimes (τ):** this parameter was measured with a time-correlated single photon counting instrument (Edimburgh Instruments FLS980) with a picosecond pulsed laser light source, adapted to the excitation wavelength of the compounds to be measured. The measurements were carried out in a HELLMAN 110-QS cuvette of 3.5 ml volume, at a temperature of 25°C.
5. **Fluorescence measurements:** fluorescence measurements of the compounds were carried out using a Hitachi F-7000 fluorometer or an Edimburgh Instruments FLS980 fluorometer, both equipped with 350W Xenon lamps of continuous emission power. All samples were measured in HELLMAN 110-QS cuvettes of 3.5 ml volume, with an optical path length of 1 cm, at a temperature of 25°C.
6. **Fluorescence quantum yields ($Ø_F$):** the measurements were carried out using an Edimburgh Instruments FLS980 fluorometer, with picosecond pulsed diode lasers with a wavelength matched to the excitation wavelength of the sample, equipped with an integrating sphere of the Edimburgh Instruments brand. Measurements were also carried out with a HELLMAN 110-QS cuvette of 3.5 ml volume.
7. **High resolution mass spectra (HRMS):** spectra were acquired using a Bruker Autoflex matrix-assisted laser desorption ionisation-assisted time-of-flight (MALDI-TOF) mass spectrometer, using dithranol (DIT) or trans-2-[3-(4-(4-tert-butylphenyl)-2-methyl-2-propenylidene]malononitrile (DCTB) as matrixes, in modes positive or negative. Routine mass spectra were carried out using an Agilent 6545 Q-TOF time-of-flight mass spectrometer, coupled to a liquid chromatograph.
8. **Infrared spectra (IR):** the spectrophotometer used was a model JASCO FT/IR-4200 equipped with an ATR accessory model JASCO ATR PRO ONE. The spectra were recorded with a resolution of 4 cm^{-1}.
9. **Scanning electron microscopy (SEM):** the different images have been recorded using a JEOL JSM-6460LV Scanning Electron Microscope, with backscattered electron, secondary electron and energy dispersive X-ray detectors. The instrument is equipped with a high vacuum system as well as an Au metallisation system. Although the samples measured in this equipment were of an organic nature, it was not necessary to subject them to a metallisation process, but the application of a voltage of 1.2 kV was sufficient.

10. **Transmision electron microscopy (TEM):** the images were obtained using a Talos F200X STEM transmission electron microscope with an energy dispersive spectrometry (EDS) chemical analysis system and a CMOS digital camera for image acquisition with a maximum resolution of 4×4 k.
11. **Melting point (m.p.):** a 50W Gallenkamp device is employed.
12. **NMR spectra:** proton, carbon and dept spectra were performed either by Varian Mercury - 300 Nuclear Magnetic Resonance Spectrometer or by BRUKER High Resolution Nuclear Magnetic Resonance Spectrometer, model ADVANCE NEO 4500 500 MHz. In all the spectra performed, the chemical shifts are reported in ppm with respect to the residual solvent signals, while the coupling constants (*J*) are reported in Hz. NMR spectra were analyzed using MestReNova software.
13. **Ultrasonic bath:** an Elmasonic model ELMA S 30H has been used, with the possibility of regulating the bath temperature as well as the sonication time.
14. **Ultraviolet-visible (UV-Vis) absorption spectra:** a Hitachi spectrophotometer model U-3900 has been used throughout this Doctoral Thesis. The samples were measured using a cuvette HELLMA 110-QS of 3.5 ml volume with 1 cm of optical path, at a temperature of 25°C.

2. REAGENTS AND SOLVENTS

All the materials and solvents used throughout this Doctoral Thesis are available through various commercial brands such as TCI, Sigma-Aldrich, Fluorochem, Activate Scientific or BLD Pharmatech among others.

Thin layer chromatography (TLC) was performed using aluminium plates coated with SiO_2 F-254 from Silicycle and revealed under UV light of 366 nm. On the other hand, column chromatography was performed using silica gel with a particle size of 40-63 µm, VWR BDH Chemicals.

The silica nanoparticles used for the development of the AR82s·SiO_2 sensor had a particle size of 10-20 nm, from Aldrich Chemistry. The stripper used in this system for the detection of TATP vapours is of the BOSCH brand, model QHG 660 LCD Professional, while the compressor is of the Dürr Technik brand, model Sicolab 062MFA/0626 1220.

ANNEX II:
NMI
DERIVATIVES

INDEX OF ANNEX II COMPOUNDS

Synthesis of **AR43p** 245
Synthesis of **AR43d** 248
Synthesis of **AR51** 251
Synthesis of **AR52** 259
Synthesis of **AR55p** 267
Synthesis of **AR55d** 275
Synthesis of **AR82p** 282
Synthesis of **AR82s** 291
Synthesis of **AR82d** 341
Synthesis of **AR83p** 369
Synthesis of **AR83s** 377
Synthesis of **AR83d** 385
Synthesis of **AR90p** 399
Synthesis of **AR90s** 407
Synthesis of **AR90d** 422
Synthesis of **AR66** 434
Synthesis of **AR67p** 437
Synthesis of **AR67d** 445
Synthesis of **AR53** 452
Synthesis of **AR56** 455
Synthesis of **AR63** 464
Synthesis of **AR65** 467
Synthesis of **AR98** 475
Synthesis of **AR85** 476
Synthesis of **AR94p** 517
Synthesis of **AR94d** 525
Synthesis of **AR08p** 528
Synthesis of **AR08d** 530
Synthesis of **AR09** 533
Synthesis of **AR80** 535

Synthesis of *N*-(*N*-Boc-piperidin-4-yl)-4-bromonaphthalene-1,8-dicarboxylmonoimide (AR43p)

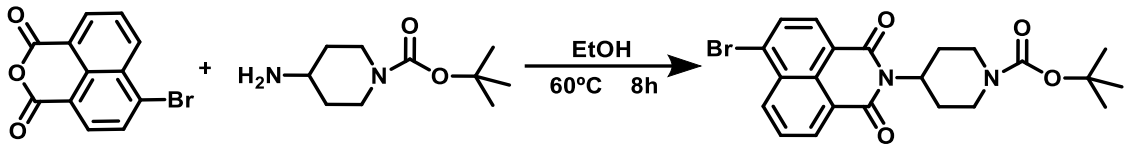

In a 100 ml flask, provided with a magnetic stirrer, 2 g of 4-bromo-1,8-naphthalic anhydride (7.22 mmol) and 2.9 g of 4-amino-1-Boc-piperidine (14.44 mmol) were dissolved in 40 ml of ethanol and the mixture was stirred 8 hours at 60ºC. After that, the mixture was filtered, cooling to room temperature and the solvent was evaporated under reduce pressure. The organic solid was purified by column chromatography (SiO_2, DCM), getting 3.15 g of a white solid, 95% yield.

m.p.: 144-150ºC.

IR (ATR, cm^{-1}): 2977-2849, 1689 (C=O), 1649 (C=O), 1419 (C-O), 1359, 1344, 1244, 1173 (C-N), 1143 (-CH_3), 1101, 1032 (C-Br), 981, 894, 774, 747, 424.

^{1}H-NMR (300 MHz, $CDCl_3$) δ (ppm): 8.48 (d, *J* = 7.1 Hz, 1H, $\mathbf{H_{Ar}}$), 8.35 (d, *J* = 8.4 Hz, 1H, $\mathbf{H_{Ar}}$), 8.23 (d, *J* = 7.9 Hz, 1H, $\mathbf{H_{Ar}}$), 7.86 (d, *J* = 7.9 Hz, 1H, $\mathbf{H_{Ar}}$), 7.70 (t, *J* = 7.9 Hz, 1H, $\mathbf{H_{Ar}}$), 5.17 – 5.02 (m, 1H, C**H**), 4.42 – 4.10 (m, 2H, C$\mathbf{H}_2$), 2.69 (m, 4H, 2×C$\mathbf{H}_2$), 1.64 (m, 2H, C$\mathbf{H}_2$), 1.45 (s, 9H, 3×C$\mathbf{H}_3$).

^{13}C-NMR (75MHz, $CDCl_3$) δ (ppm): 163.3 (**C**=O), 163.2 (**C**=O), 154.3 (**C**=O), 132.4 ($\mathbf{C}_{Ar}$H), 131.5 ($\mathbf{C}_{Ar}$H), 130.7 ($\mathbf{C}_{Ar}$H), 130.6 ($\mathbf{C}_{Ar}$H), 129.8 ($\mathbf{C}_{Ar}$), 129.5 ($\mathbf{C}_{Ar}$), 128.3 ($\mathbf{C}_{Ar}$), 127.6 ($\mathbf{C}_{Ar}$H), 122.9 ($\mathbf{C}_{Ar}$), 122.0 ($\mathbf{C}_{Ar}$), 79.2 (**Cq**), 51.6 (**C**H), 43.8 (**C**H_2), 28.2 (**C**H_3), 27.9 (**C**H_2).

HRMS (MALDI, DCTB-) m/z: calculated for $C_{22}H_{23}BrN_2O_4$: 458.0836 (M^-); found 458.0802.

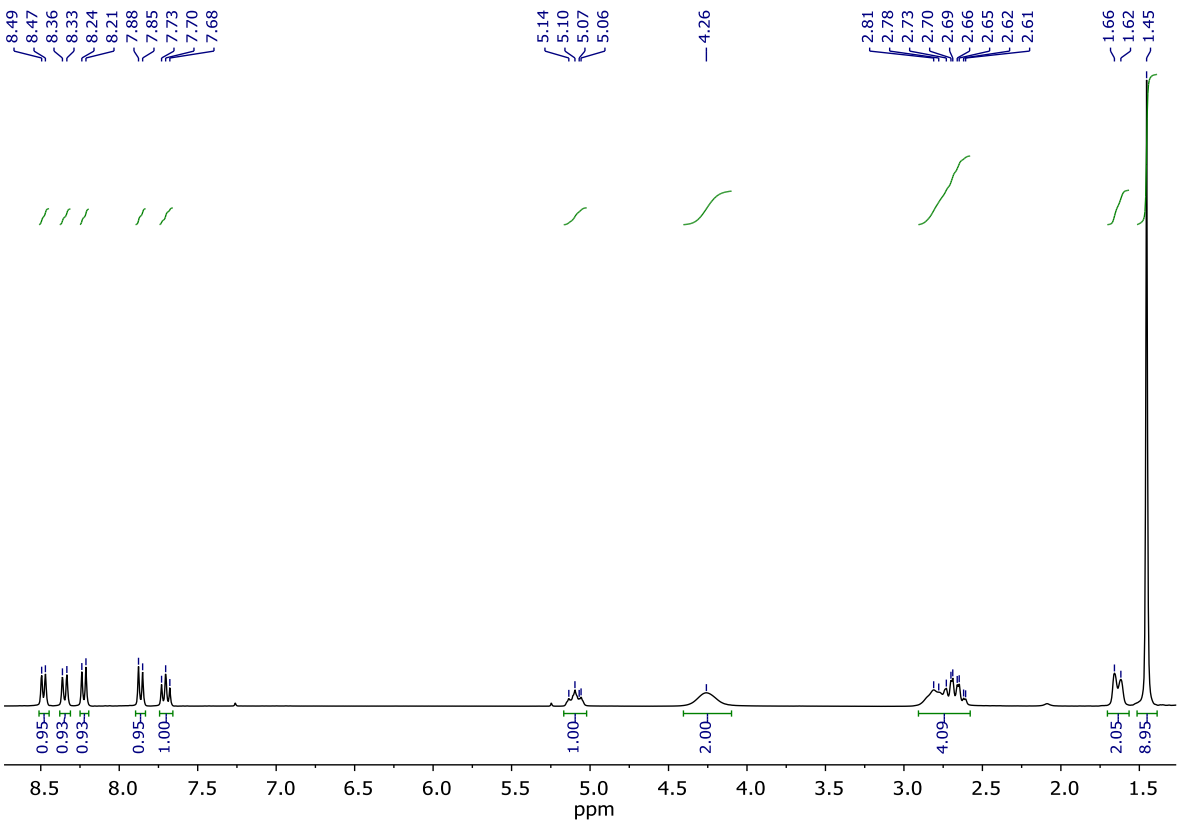

Figure 1. ^{1}H-NMR ($CDCl_3$, 300 MHz) of AR43p.

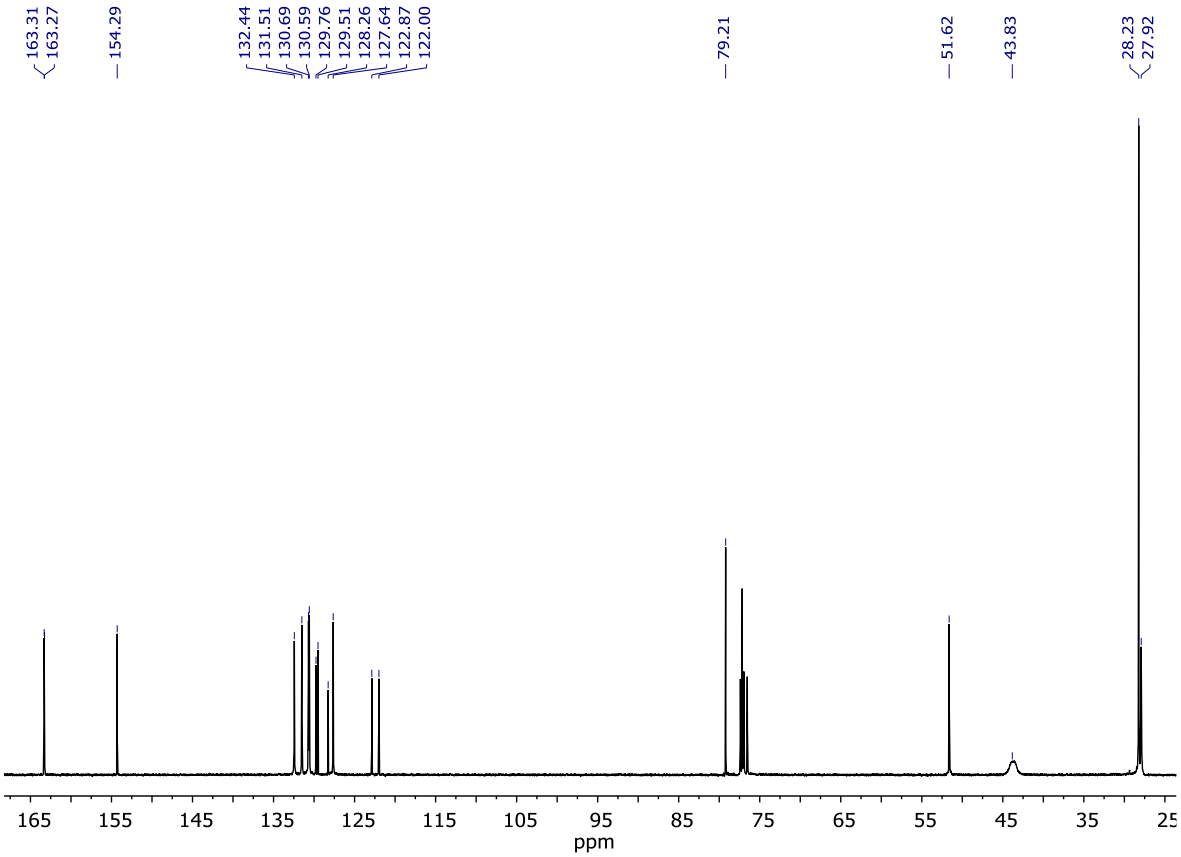

Figure 2. ^{13}C-NMR ($CDCl_3$, 75 MHz) of AR43p.

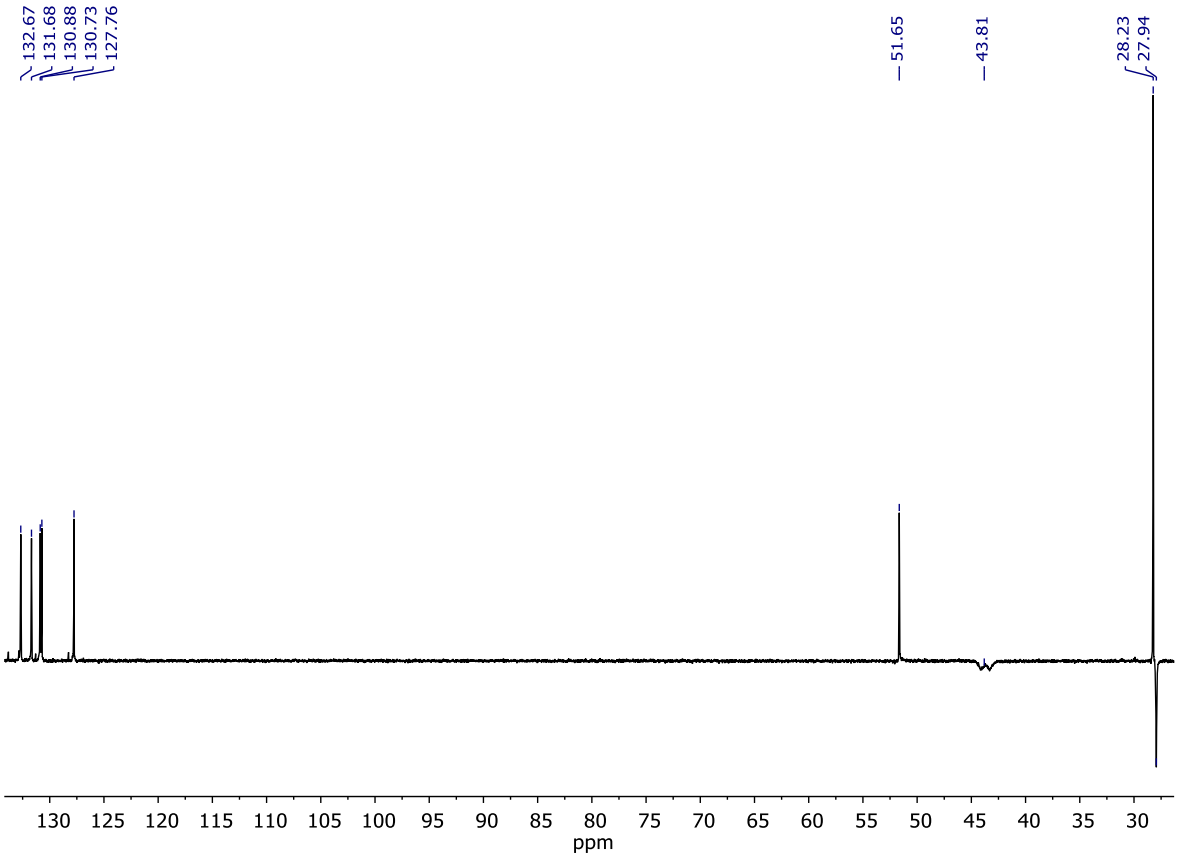

Figure 3. DEPT NMR ($CDCl_3$, 75 MHz) of AR43p.

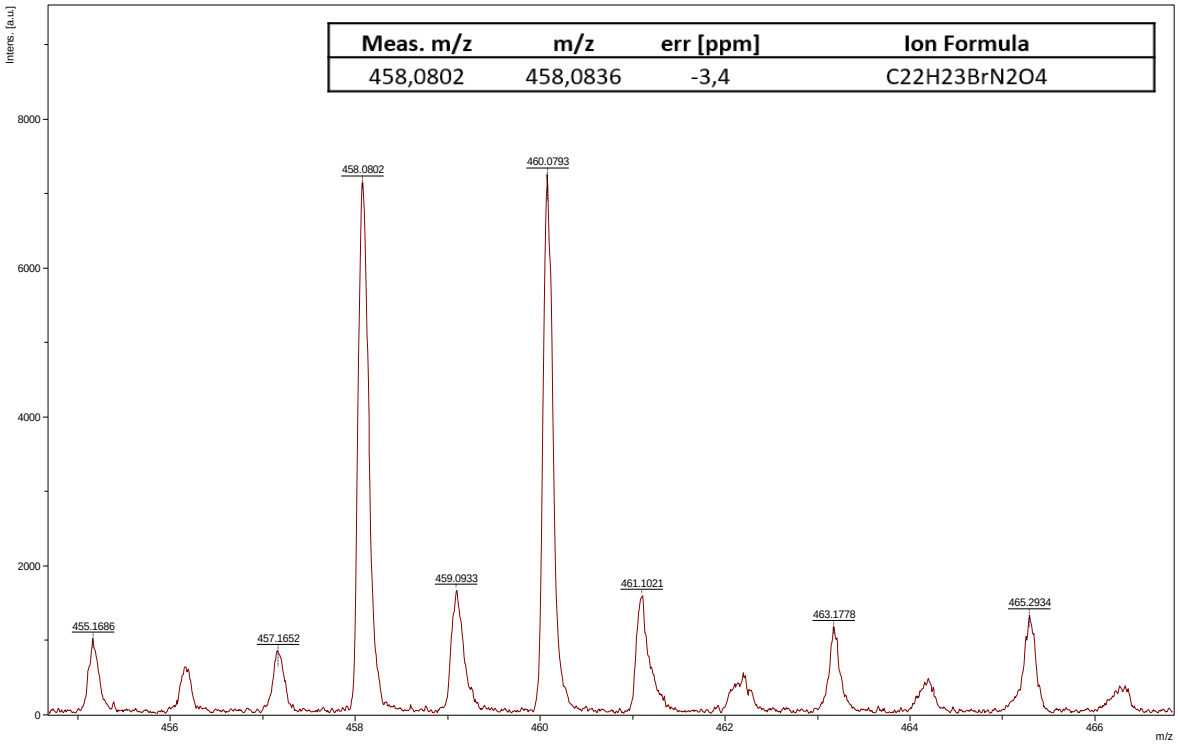

Figure 4. HRMS (MALDI, DCTB-) of AR43p.

Synthesis of *N*-(piperidin-4-yl)-4-bromonaphthalene-1,8-dicarboxylmonoimide (AR43d)

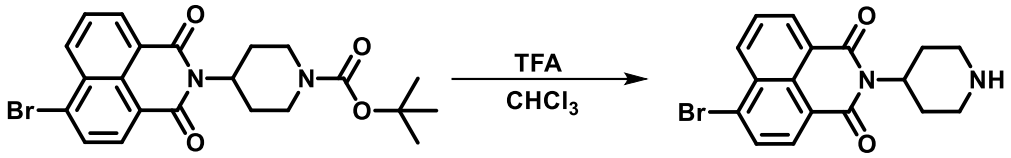

In a 50 ml flask with a magnetic stirrer, 150 mg of *N*-(Boc-piperidine)-4-bromonaphthalene-1,8-dicarboxylmonoimide (AR43p, 0.33 mmol) were dissolved in 15 ml of chloroform and, then, 2 ml of trifluoroacetic acid (26 mmol) and the mixture was stirred 4 hours at room temperature. Afterwards, 10 ml of water were poured into the flask and the mixture was neutralized employing a 40% sodium hydroxide solution until it reached a neutral pH. Then, 20 ml of water was added and the mixture was extracted three times with cloroform (3×30 ml). The organic extracts were combined, dried over anhydrous Na_2SO_4 and the solvent was evaporated under reduce pressure. The product is a white solid obtained with a 100% yield (117 mg).

m.p.: 88-89°C.

IR (ATR, cm^{-1}): 3359 (N-H), 2973 – 2830, 1686 (C=O), 1579, 1477, 1417, 1390, 1357, 1238, 1162 (C-N), 1121, 1097, 1076, 1049 (C-Br), 998, 932, 861, 807, 761, 642, 543, 511, 462, 408.

^{1}H-NMR (300 MHz, CD_3OD) δ (ppm): 8.61 – 8.55 (m, 2H, 2×**H_{Ar}**), 8.36 (d, *J* = 7.9 Hz, 1H, **H_{Ar}**), 8.10 (d, *J* = 7.9 Hz, 1H, **H_{Ar}**), 7.90 (dd, *J* = 8.5, 7.3 Hz, 1H, **H_{Ar}**), 5.31 (m, 1H, C**H**), 3.60 – 3.52 (m, 2H, N**H** y ½C**H_2**), 3.27 – 2.93 (m, 5H, 2×C**H_2** y ½C**H_2**), 2.04 – 1.95 (m, 2H, C**H_2**).

^{13}C-NMR (75MHz, $CDCl_3$) δ (ppm): 163.7 (C=O), 133.1 (**C_{Ar}**H), 132.1 (**C_{Ar}**H), 131.3 (**C_{Ar}**H), 131.1 (**C_{Ar}**H), 128.9 (**C_{Ar}**), 128.1 (**C_{Ar}**H), 123.3 (**C_{Ar}**), 122.4 (**C_{Ar}**), 53.4 (**Cq**), 50.6 (**C**H), 45.5 (**C**H_2), 27.7 (**C**H_2).

HRMS (MALDI, DCTB+) m/z: calculated for $C_{17}H_{15}BrN_2O_2$: 359.0390 (M^+ + H); found 359.0391.

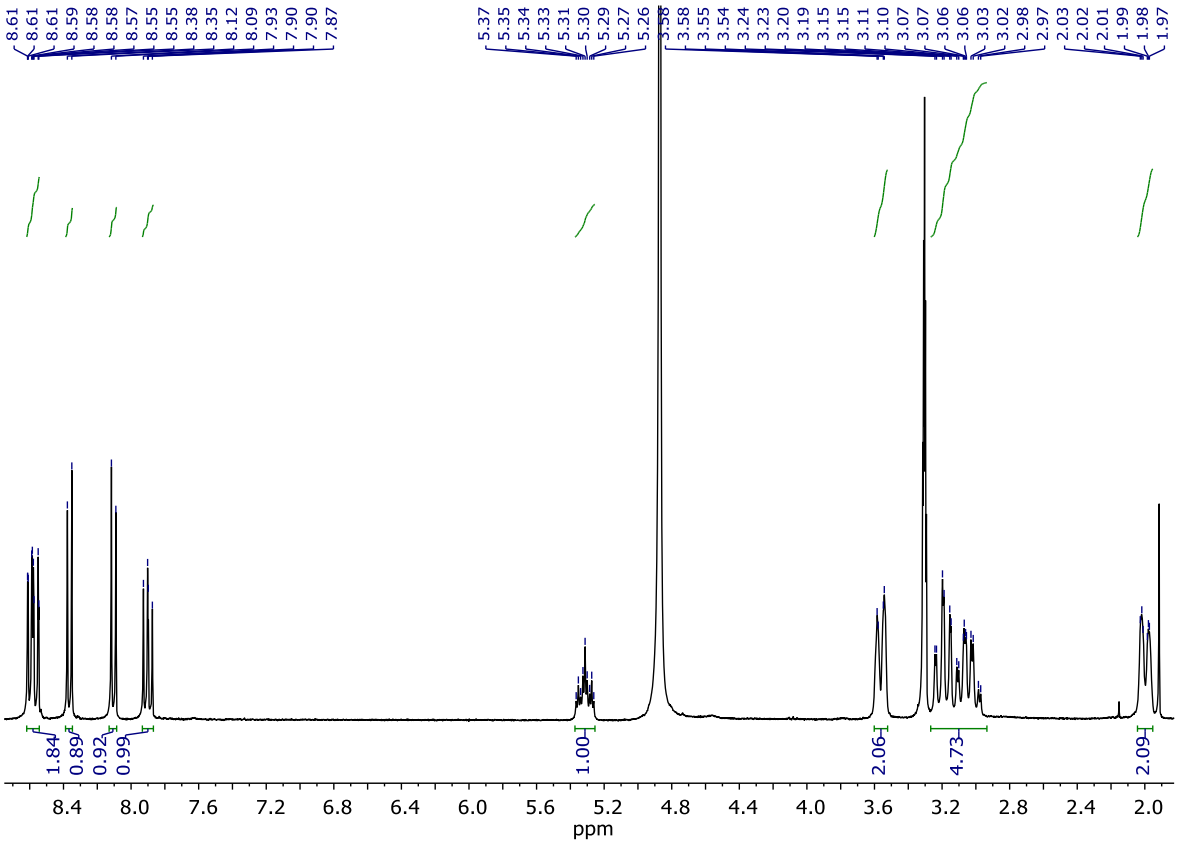

Figure 5. ^{1}H-NMR (CD_3OD, 300 MHz) of AR43d.

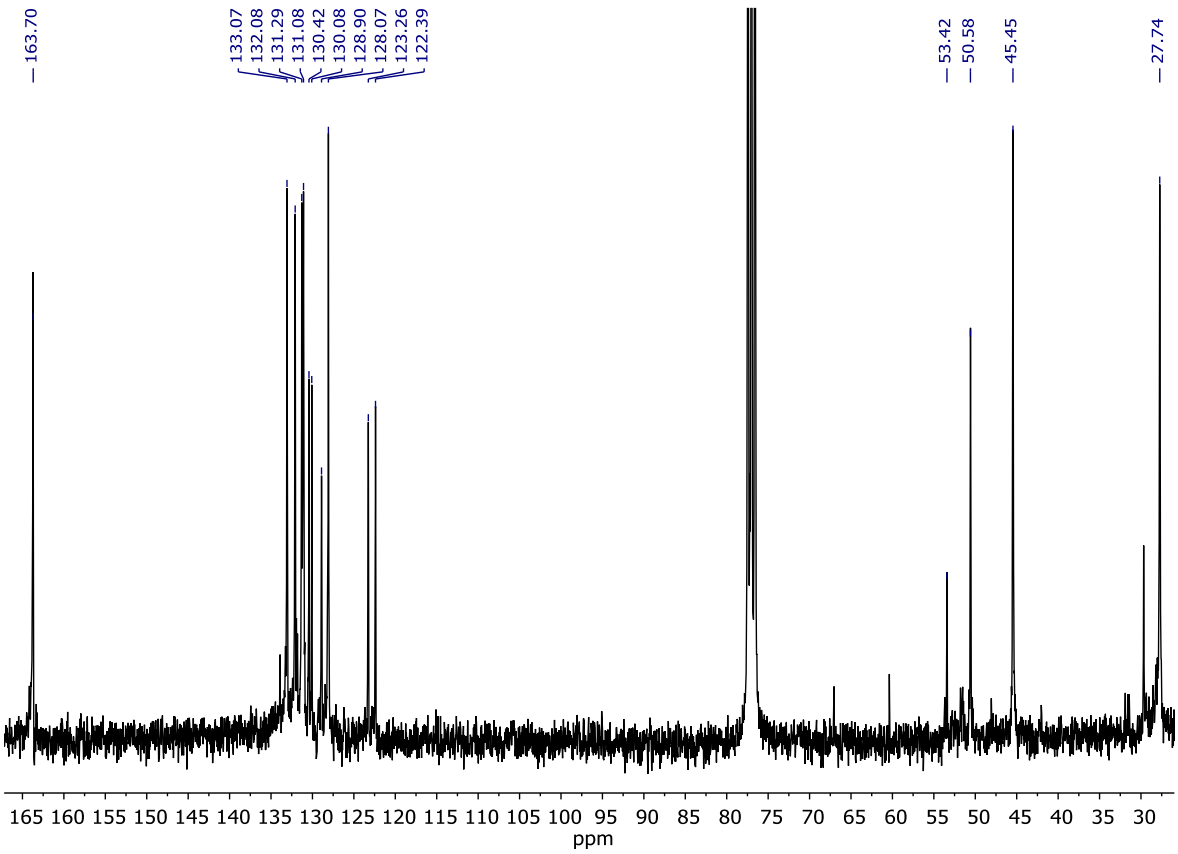

Figure 6. ^{13}C-NMR ($CDCl_3$, 75 MHz) of AR43d.

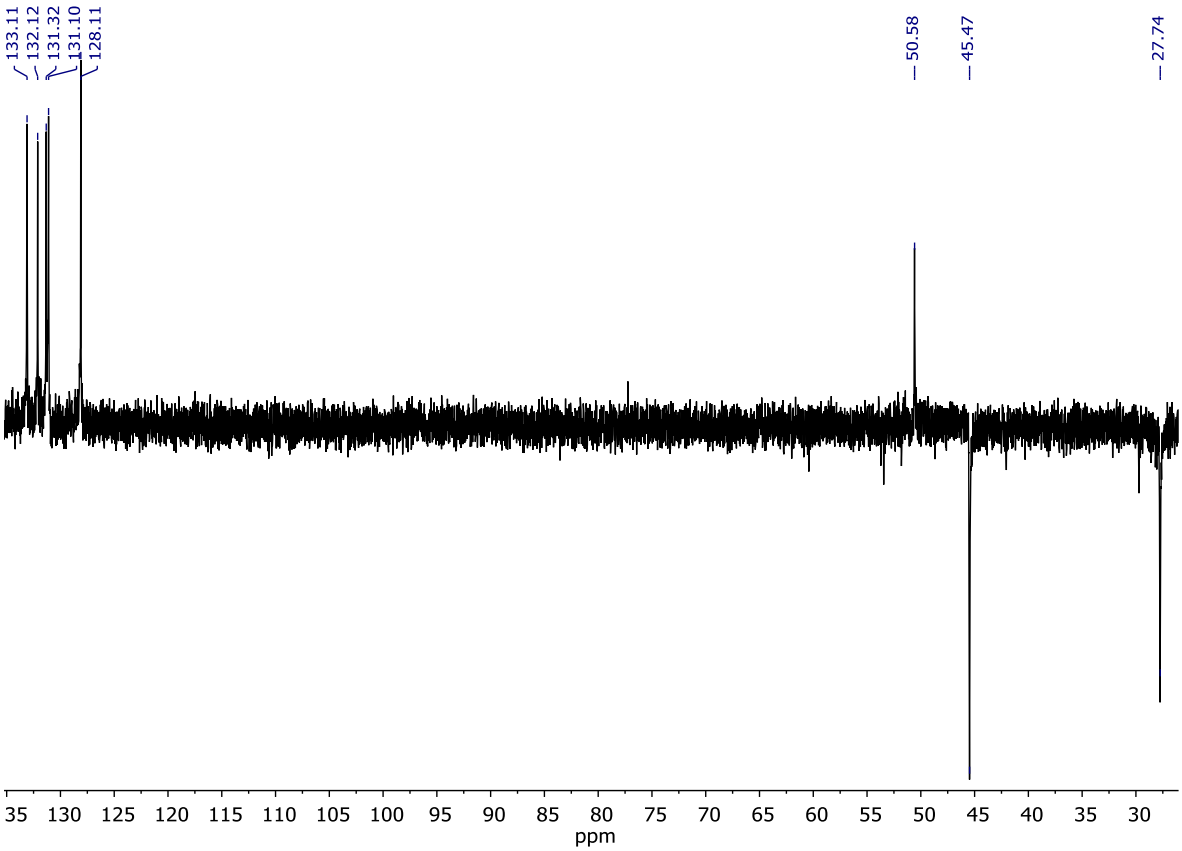

Figure 7. DEPT NMR ($CDCl_3$, 75 MHz) of AR43d.

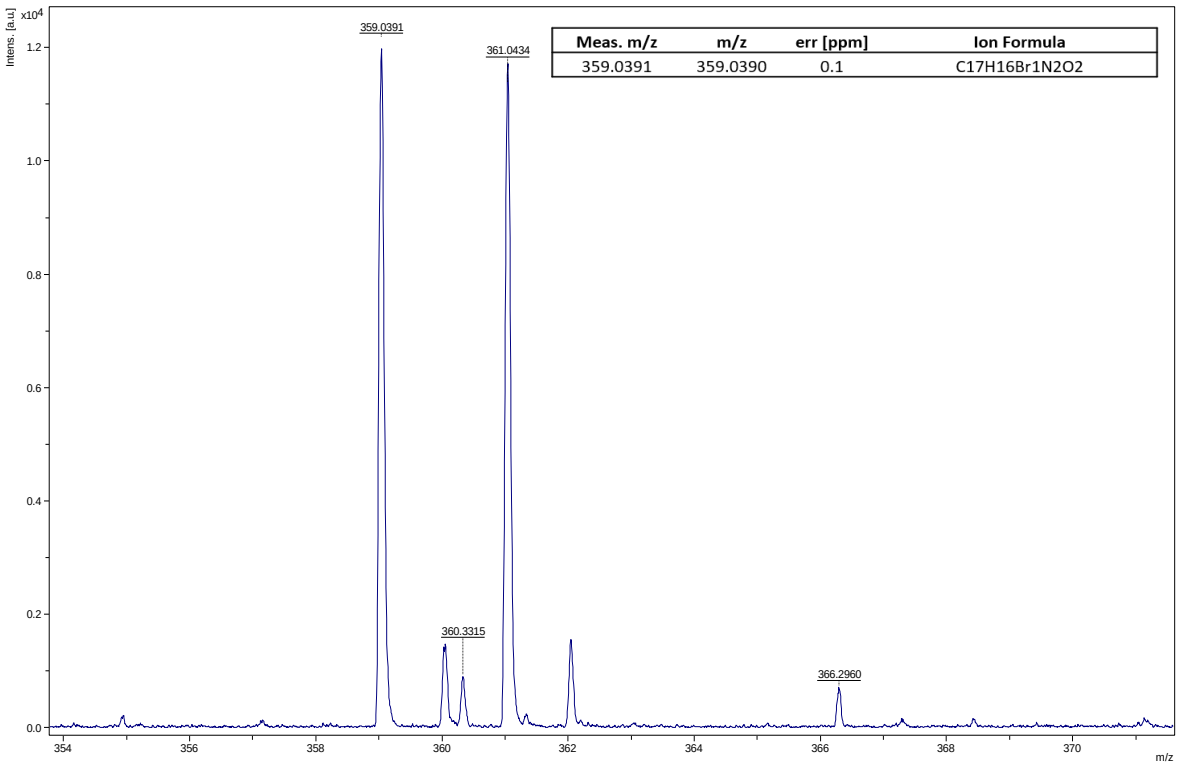

Figure 8. HRMS (MALDI, DCTB+) of AR43d.

Synthesis of *N*-(*N'*-Boc-piperidin-4-yl)-4-(6-aminopyridin-3-yl)naphthalene-1,8-dicarboxylmonoimide (AR51)

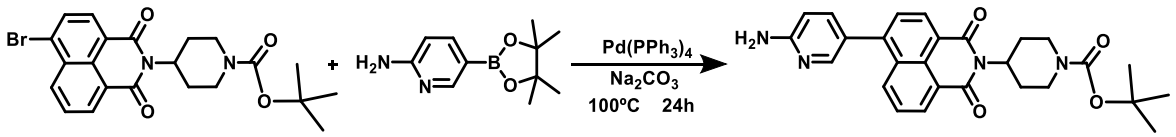

In a 100 ml Schlenk with a magnetic stirrer, 105 mg of *N*-(Boc-piperidine)-4-bromonaphthalene-1,8-dicarboxylmonoimide (AR43p, 0.29 mmol), 67 mg of 5-(4,4,5,5-tetramethyl-1,2,3-dioxaborolan-2-yl)pyridin-2-amine (0.30 mmol) and 105 mg of sodium carbonate (0.99 mmol) were dissolved in toluene:*n*-butanol:water (20:5:5 ml) under nitrogen atmosphere. The catalyst, 12 mg of $Pd(PPh_3)_4$ (0.01 mmol) was added and the resulting solution was stirred at 100ºC for 24 hours. Later, the solvent was evaporated under reduce pressure, DCM was added and washed three times with water (3×100 ml). The organic layer was dried over Na_2SO_4 and the solvent was evaporated under reduce pressure. The organic solid was purified by column chromatographic (SiO_2, DCM:MeOH) to obtain 94 mg of a yellow solid, 89% yield.

m.p.: 133-135ºC.

IR (ATR, cm^{-1}): 3343 (N-H), 2923-2852 (C-H), 1692 (C=O), 1649 (C=O), 1581, 1503, 1428, 1401, 1349, 1239, 1146 (C-N), 1106, 1032, 978, 943, 897, 864, 781, 754, 451.

^{1}H-NMR (300 MHz, $CDCl_3$) δ (ppm): 8.59 (d, *J* = 7.5 Hz, 2H, 2×**H$_{Ar}$**), 8.26 (m, 2H, 2×**H$_{Ar}$**), 7.70 (dd, *J* = 8.5, 7.3 Hz, 1H, **H$_{Ar}$**), 7.65 (d, *J* = 7.5 Hz, 1H, **H$_{Ar}$**), 7.61 (dd, *J* = 8.5, 2.4 Hz, 1H, **H$_{Ar}$**), 6.69 (d, *J* = 8.5 Hz, 1H, **H$_{Ar}$**), 5.25 – 5.11 (m, 1H, C**H**), 4.79 (s, 2H, N**H**$_2$), 4.30 (s, 2H, C**H**$_2$), 2.95 – 2.67 (m, 4H, 2×C**H**$_2$), 1.69 (m, 2H, C**H**$_2$), 1.49 (s, 9H, 3×C**H**$_3$).

^{13}C-NMR (75MHz, $CDCl_3$) δ (ppm): 164.7 (**C**=O), 164.5 (**C**=O), 158.5 (**C**$_{Ar}$), 154.8 (**C**=O), 148.7 (**C**$_{Ar}$H), 143.8 (**C**$_{Ar}$), 139.3 (**C**$_{Ar}$H), 132.2 (**C**$_{Ar}$H), 131.4 (**C**$_{Ar}$H), 131.1 (**C**$_{Ar}$H), 130.1 (**C**$_{Ar}$), 128.9 (**C**$_{Ar}$), 127.8 (**C**$_{Ar}$H), 127.0 (**C**$_{Ar}$H), 124.7 (**C**$_{Ar}$), 123.4 (**C**$_{Ar}$), 122.0 (**C**$_{Ar}$), 108.5 (**C**$_{Ar}$H), 79.7 (**Cq**), 51.9 (**C**H), 44.1 (**C**H$_2$), 28.6 (**C**H$_3$), 28.4 (**C**H$_2$).

HRMS (MALDI, DCTB+) m/z: calculated for $C_{27}H_{28}N_4O_4$: 473.2183 (M^++H); found 473.2184.

UV-Vis ($CHCl_3$), λ_{max} nm (log ε): 365 (4.1).

Ø (MCH, %): 85.26.

τ (375 nm, MCH, ns): 1.415/3.836 (χ^2: 1.068).

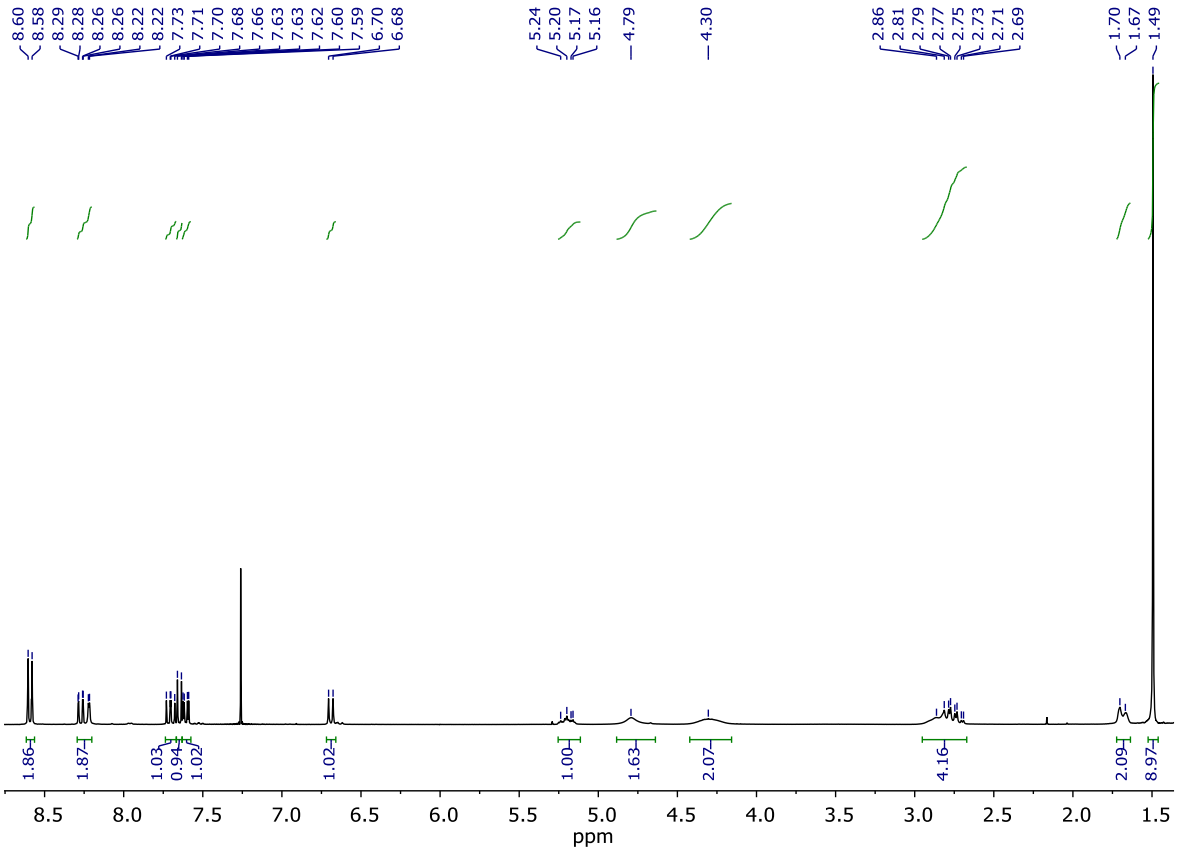

Figure 9. ^{1}H-NMR ($CDCl_3$, 300 MHz) of AR51.

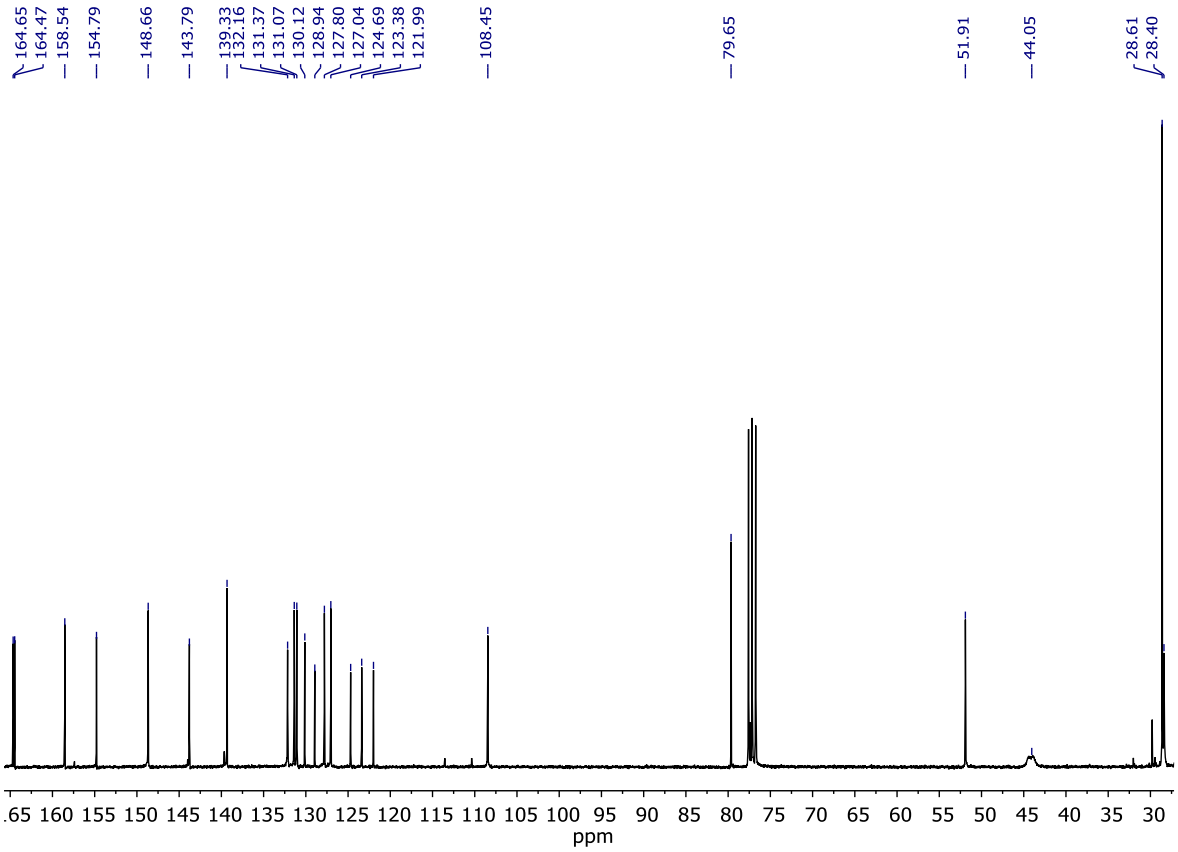

Figure 10. ^{13}C-NMR ($CDCl_3$, 75 MHz) of AR51.

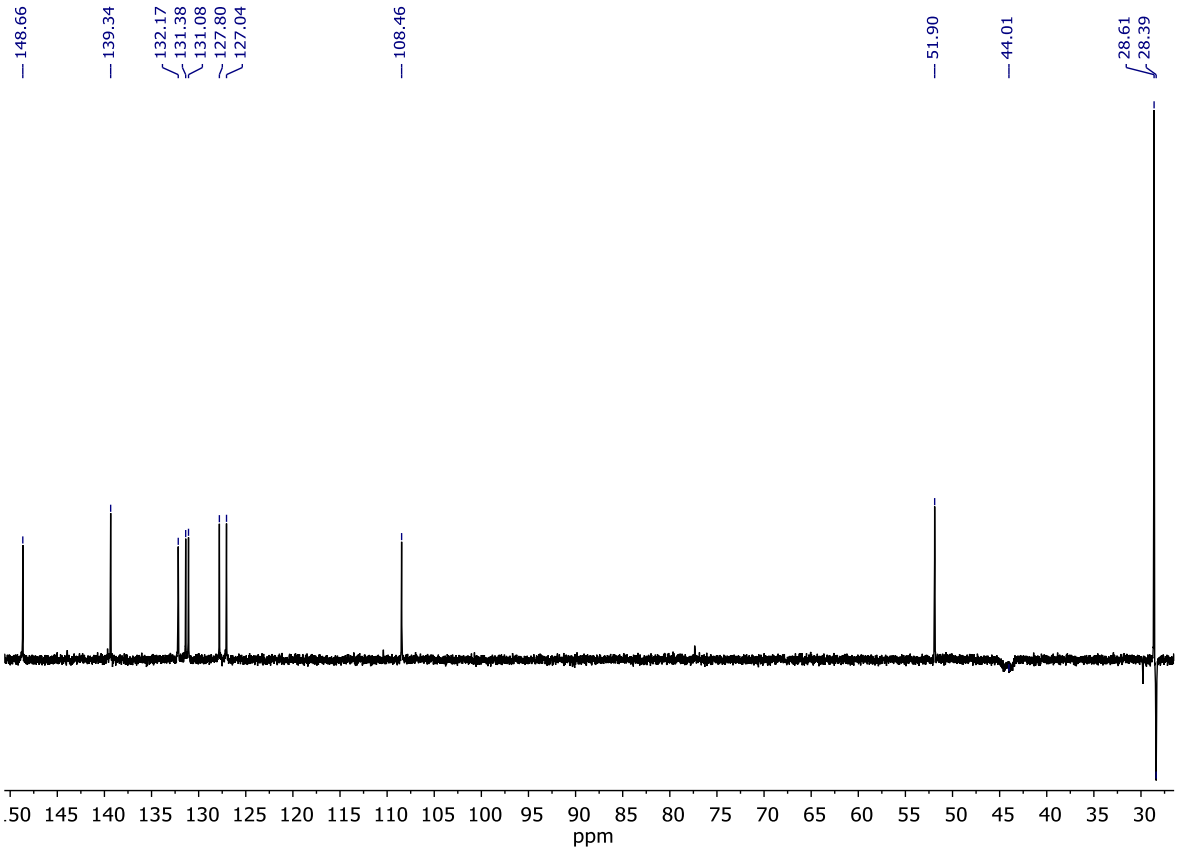

Figure 11. DEPT NMR ($CDCl_3$, 75 MHz) of AR51.

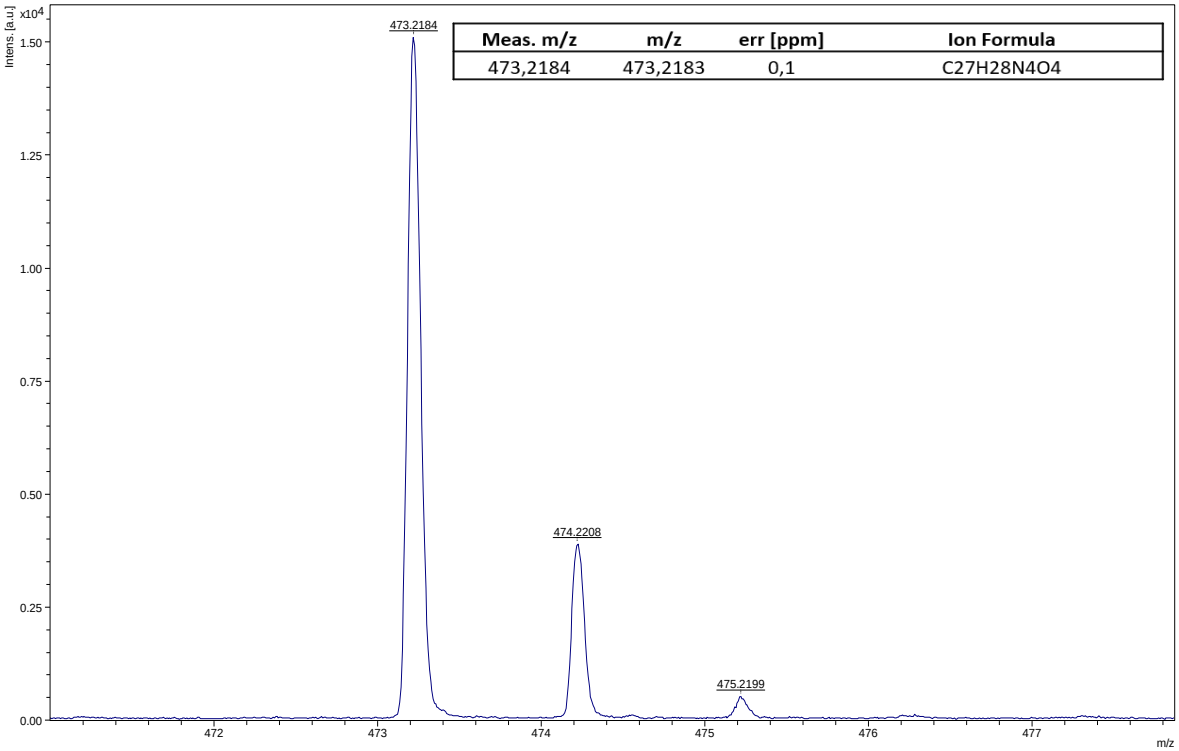

Meas. m/z	m/z	err [ppm]	Ion Formula
473,2184	473,2183	0,1	C27H28N4O4

Figure 12. HRMS (MALDI, DCTB+) of AR51.

Solvatochromism:

The concentration of the compound was 20 µM and the excitation wavelength was 360 nm.

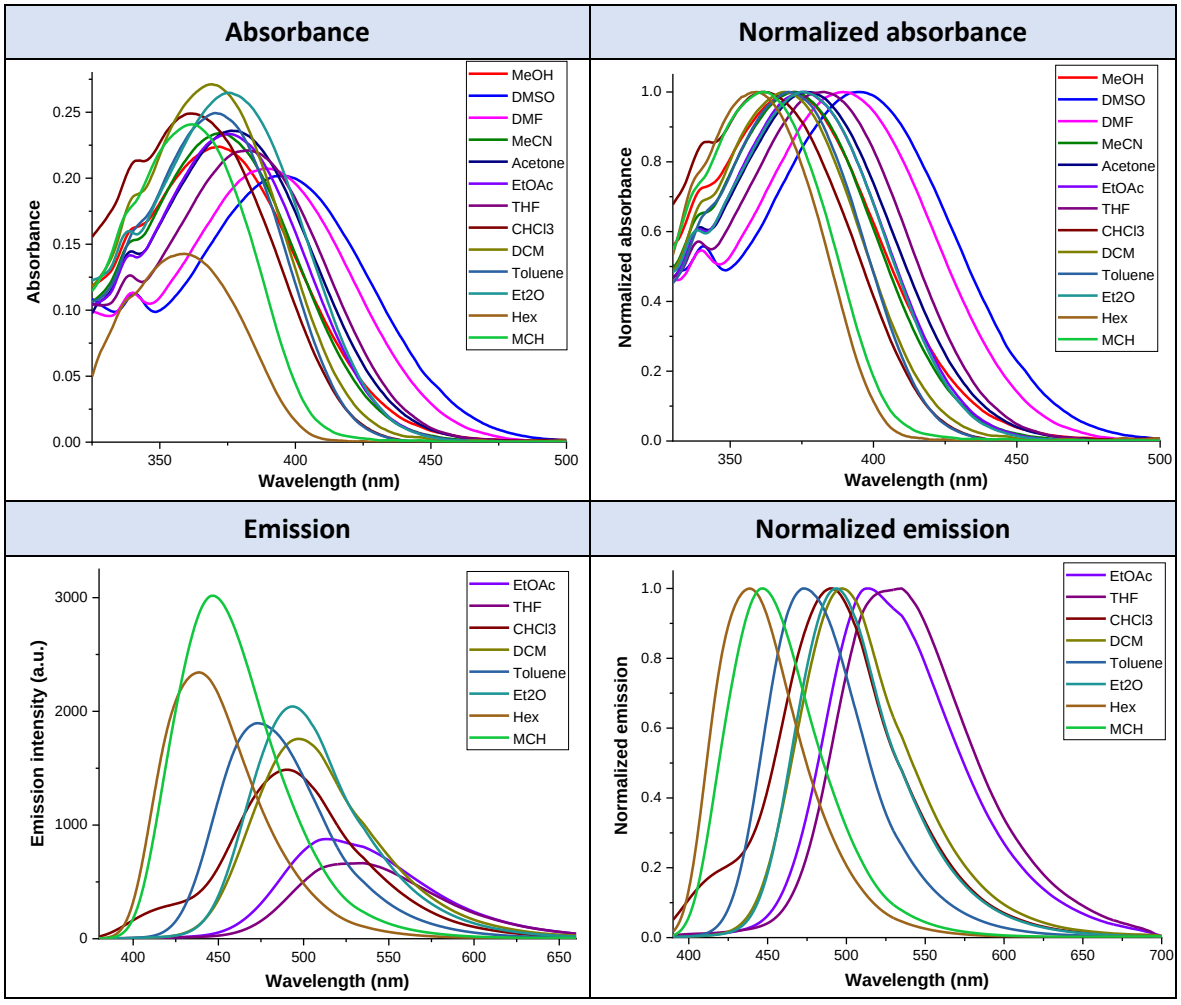

Figure 13. Solvatochromism of AR51.

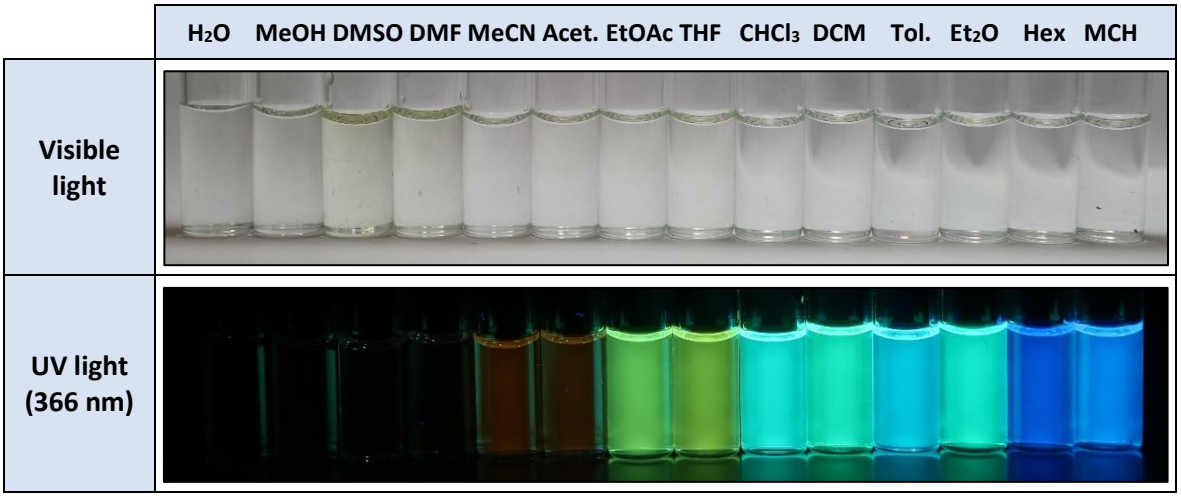

Figure 14. Solvatochromism of AR51 under visible (up) and UV (down) light.

Fluorescence decay lifetime (τ):

The solvent used was methylcyclohexane. The concentration of the compound was 20 µM.

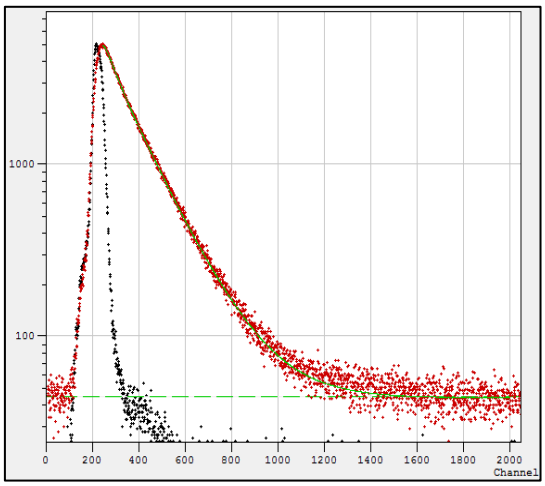

Figure 15. Fluorescence decay lifetime of AR51.

Water acceptance test:

The solvent used was MeOH and the concentration of the compound was 20 µM.

	R	5%	10%	20%	30%	40%	50%	60%	70%	80%	90%
Visible light	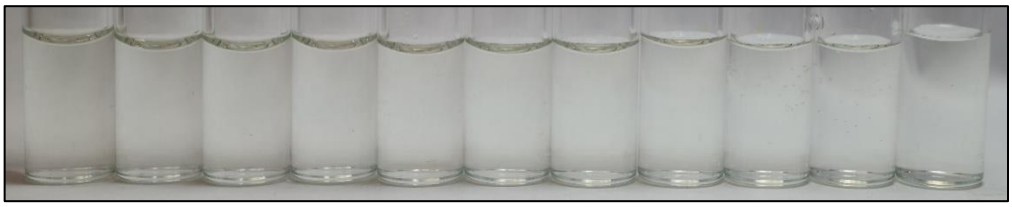										
UV light (366 nm)	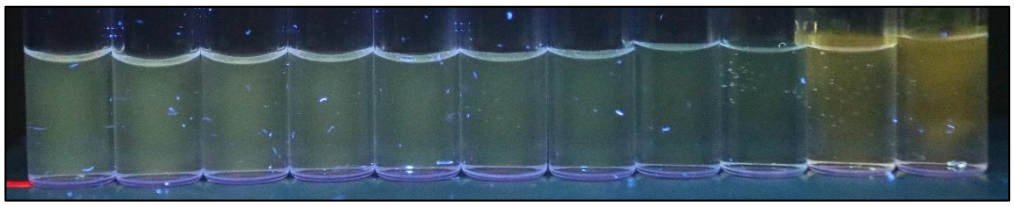										

Figure 16. Water acceptance test of AR51 in MeOH under visible (up) and UV (down) light.

	R	5%	10%	20%	30%	40%	50%	60%	70%	80%	90%
Visible light											
UV light (366 nm)	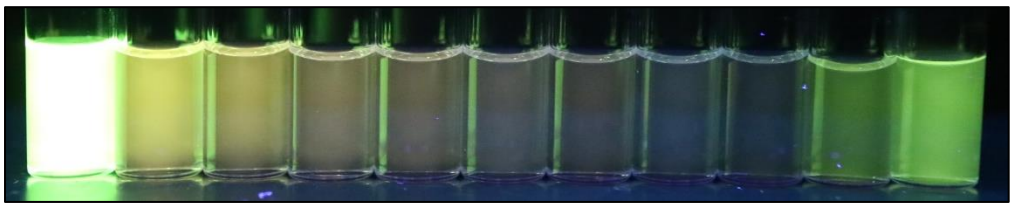										

Figure 17. Water acceptance test of AR51 in THF under visible (up) and UV (down) light.

The maximum aumount of water that was admitted by the product in THF was 40%. The yellow fluorescence at 80% and 90% of water was due to the formation of nanoparticules, giving rise to the AIE phenomenon.

The change of solvent to THF was allowed us to study the AIE phenomenon more clearly. In that solvent, the shift of the emission maximum was clearly observed: with a low water amount, it was in the yellow region (550-570 nm), between 40-70% of water it was moved to the blue region (above 465 nm) and, finally, with high water content (80-90%) the emission maximum was shifted to the green region (535-540 nm). As for the intensity of fluorescent emission, a slight increase was observed at higher water percentages (AIE).

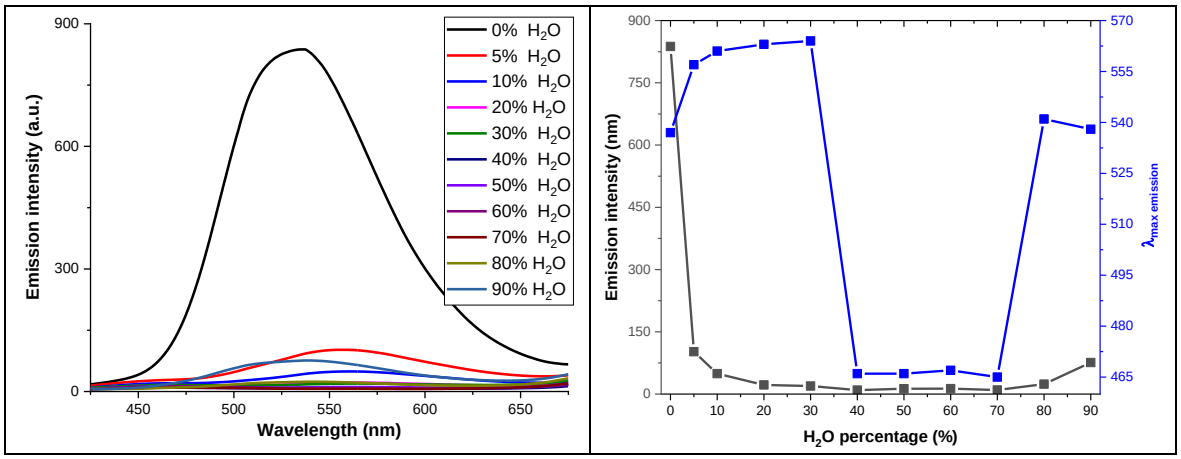

Figure 18. Emission intensity graph (left) and graph of relationship between the emission intensity and the wavelength of the maximum of emission (right) as a function of the amount of water added for AR51. λ_{exc} = 360 nm.

pH test:

For this test, the proportion of water that the compound could accept in MeOH was 40%. The concentration of the compound was 20 µM and the solvent used was MeOH.

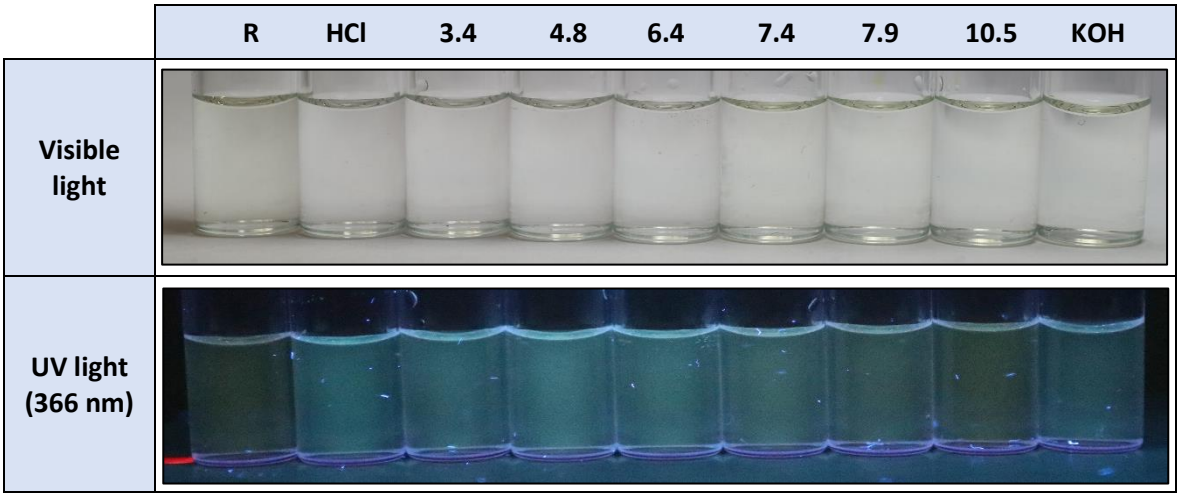

Figure 19. pH test of AR51 under visible (up) and UV (down) light.

The fluorescent emmision was become slightly bluelish at acidic pH. As the pH was basified, the fluorescence turned green.

Cations and anions test:

The concentration of the compound was 20 µM and the solvent used was MeOH.

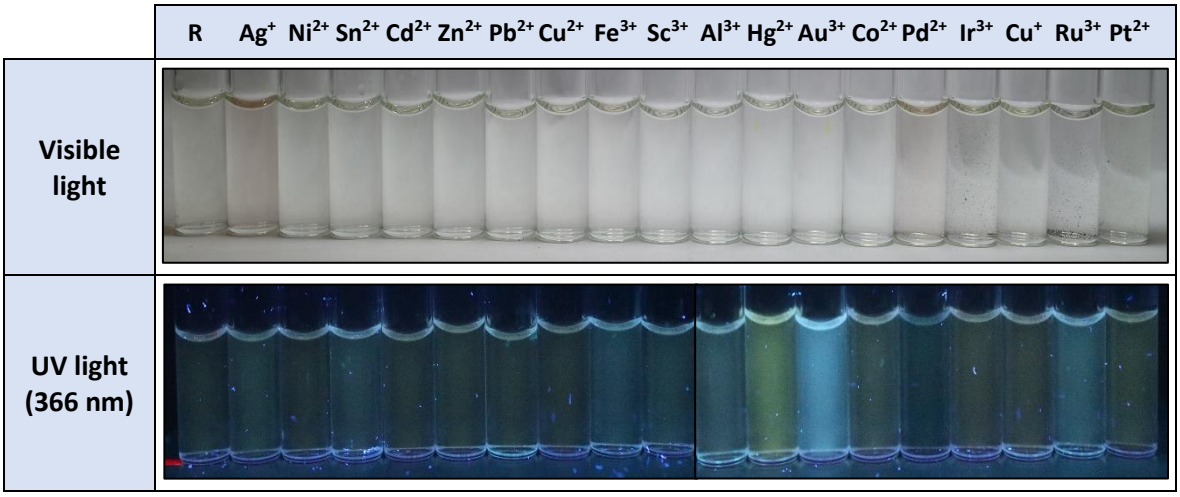

Figure 20. Cations test of AR51 under visible (up) and UV (down) light.

The most evident changes were observed with respect to Hg^{2+} (yellow fluorescence) and Au^{3+} (blue fluorescence).

The concentration of the compound was 20 µM and the solvent used was MeOH.

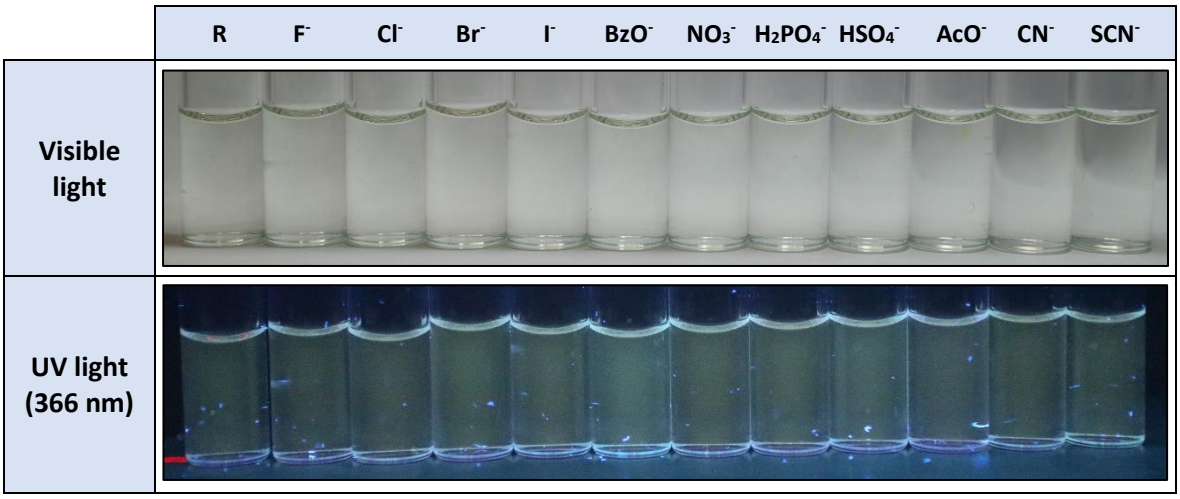

Figure 21. Anions test of AR51 under visible (up) and UV (down) light.

No significant changes were observed.

Oxidant and reductant reagents test:

The solvent used was MeOH and concentration of the compound was 20 µM.

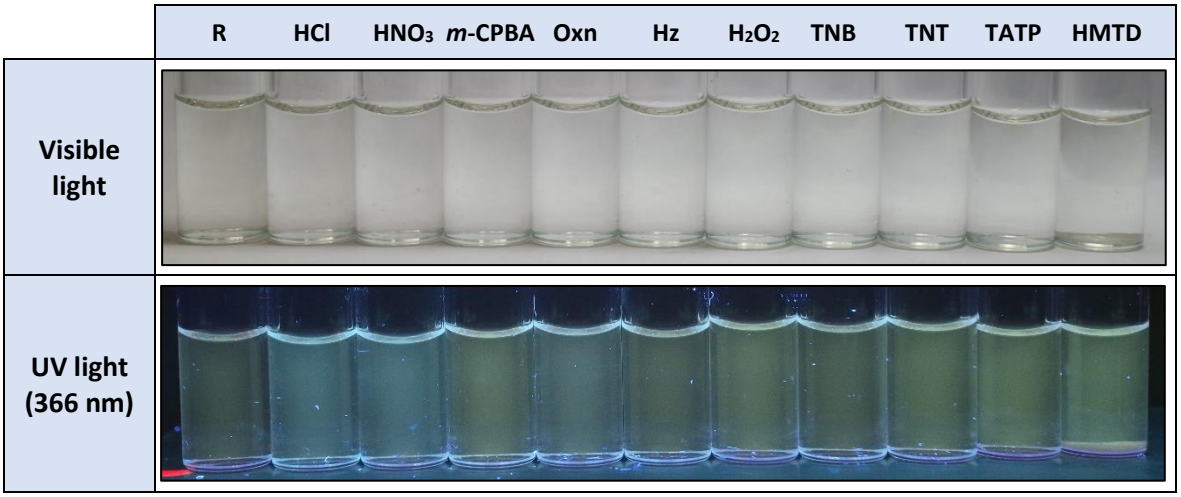

Figure 22. Oxidant and reductant reagents test of AR51 under visible (up) and UV (down) light.

The most significant changes were observed respect *m*-CPBA, hidrazine, H_2O_2, TNB, TNT, TATP and HMTD, in which the fluorescence was turned greenish due to the amount of water added. With respect to the bluelish fluorescence with HCl and HNO_3, was due to the acidity of the medium.

Synthesis of *N*-(*N'*-Boc-piperidin-4-yl)-4-(4-aminophenyl)naphthalene-1,8-dicarboxylmonoimide (AR52)

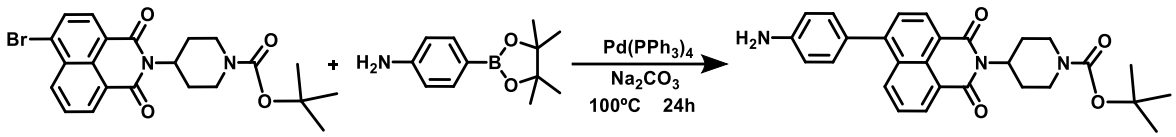

In a 100 ml Schlenk with a magnetic stirrer, 105 mg of *N*-(Boc-piperidine)-4-bromonaphthalene-1,8-dicarboxylmonoimide (AR43p, 0.29 mmol), 66 mg of 4-(4,4,5,5-tetramethyl-1,2,3-dioxaborolan-2-yl)aniline (0.30 mmol) and 105 mg of sodium carbonate (0.99 mmol) were dissolved in toluene:*n*-butanol:water under (20:5:5 ml) under nitrogen atmosphere. Then, 12 mg ofthe catalyst $Pd(PPh_3)_4$ (0.01 mmol)was added and the mixture was stirred at 100ºC for 24 hours. Afterwards, the solvent was evaporated under reduce pressure, the solid was dissolved in 50 ml of DCM and washed three times with water (3×100 ml).The organic extracts were combined, dried over Na_2SO_4 and the solvent was evaporated under reduce pressure. The organic solid was purified by column chromatographic (SiO_2, DCM:MeOH) getting 88 mg of a yellow solid (83% yield).

m.p.: 186-188ºC.

IR (ATR, cm^{-1}): 3457-3352 (N-H), 2977-2855 (C-H), 1689 (C=O), 1649 (C=O), 1581, 1506, 1425 (C-O), 1395, 1349, 1275, 1241, 1160 (C-N), 1146, 1104, 1032, 981, 943, 897, 828, 781, 754, 451.

^{1}H-NMR (300 MHz, $CDCl_3$) δ (ppm): 8.56 (d, *J* = 7.4 Hz, 2H, 2×$\mathbf{H_{Ar}}$), 8.34 (d, *J* = 8.5 Hz, 1H, $\mathbf{H_{Ar}}$), 7.66 (m, 2H, 2×$\mathbf{H_{Ar}}$), 7.31 (d, *J* = 8.4 Hz, 2H, 2×$\mathbf{H_{Ar}}$), 6.85 (d, *J* = 8.4 Hz, 2H, 2×$\mathbf{H_{Ar}}$), 5.21 (m, 1H, C**H**), 4.11 (m, 4H, N$\mathbf{H_2}$ y C$\mathbf{H_2}$), 2.81 (m, 4H, 2×C$\mathbf{H_2}$), 1.68 (m, 2H, C$\mathbf{H_2}$), 1.50 (s, 9H, 3×C$\mathbf{H_3}$).

^{13}C-NMR (75MHz, $CDCl_3$) δ (ppm): 164.9 (**C**=O), 164.7 (**C**=O), 154.8 (**C**=O), 147.3 ($\mathbf{C}_{Ar}$), 147.1 ($\mathbf{C}_{Ar}$), 133.0 ($\mathbf{C}_{Ar}$H), 131.2 ($\mathbf{C}_{Ar}$H), 131.1 ($\mathbf{C}_{Ar}$H), 130.1 ($\mathbf{C}_{Ar}$), 129.0 ($\mathbf{C}_{Ar}$), 128.8 ($\mathbf{C}_{Ar}$), 127.7 ($\mathbf{C}_{Ar}$H), 126.7 ($\mathbf{C}_{Ar}$H), 123.3 ($\mathbf{C}_{Ar}$), 121.3 ($\mathbf{C}_{Ar}$), 115.1 ($\mathbf{C}_{Ar}$H), 79.6 (**Cq**), 51.9 (**C**H), 44.2 (**C**H_2), 28.6 (**C**H_3), 28.4 (**C**H_2).

HRMS (MALDI, DCTB+) m/z: calculated for $C_{28}H_{29}N_3O_4$: 470.2074 (M^+-H); found 470.2105.

UV-Vis ($CHCl_3$), λ_{max} nm (log ε): 382 (4.1).

Ø (Hex, %): 85.28.

τ (375 nm, Hex, ns): 0.708/4.446 (χ^2: 1.062).

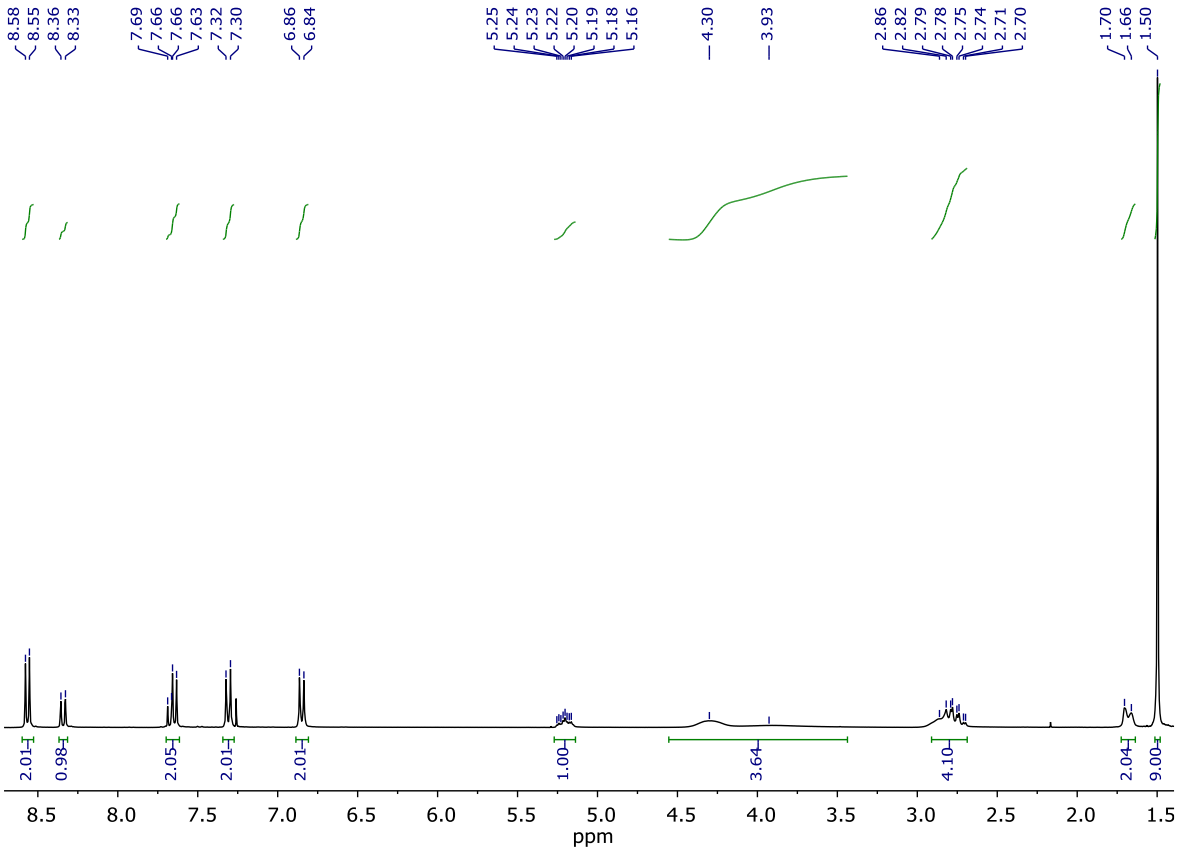

Figure 23. ^{1}H-NMR ($CDCl_3$, 300 MHz) of AR52.

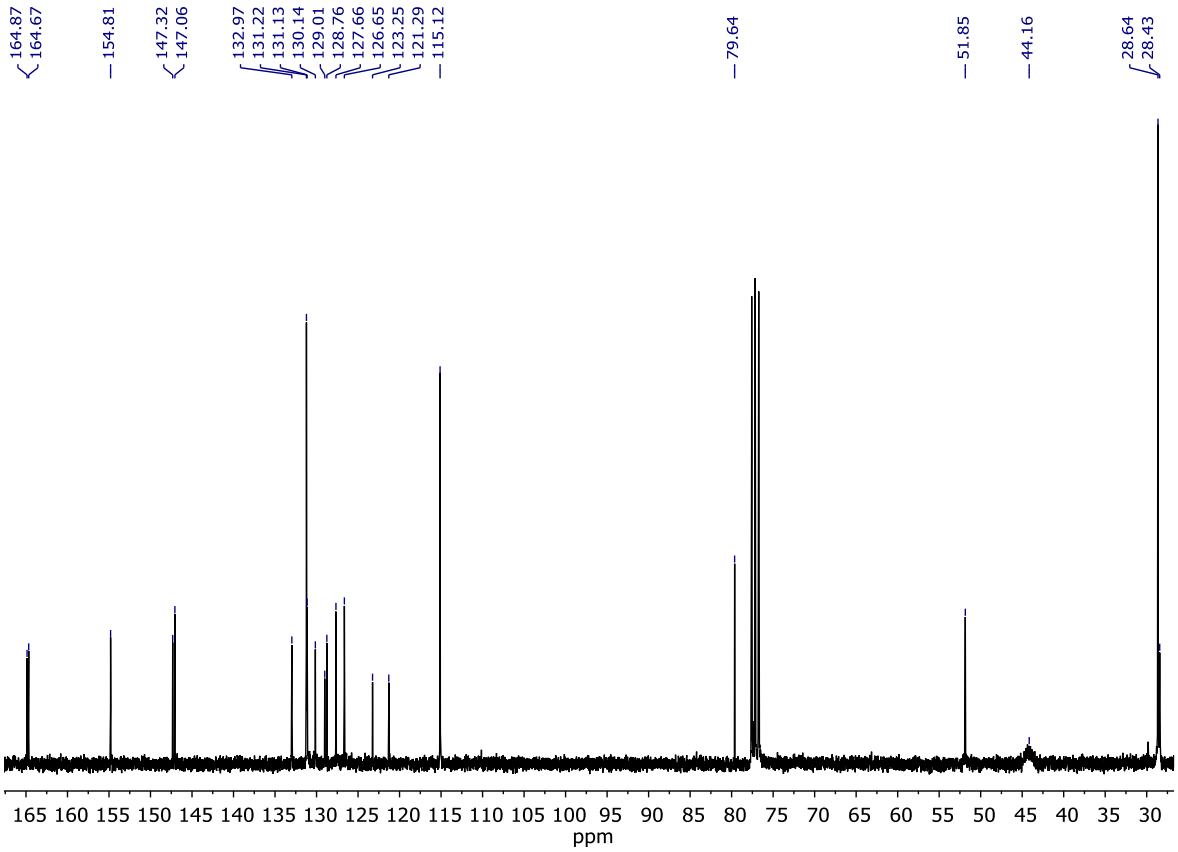

Figure 24. ^{13}C-NMR ($CDCl_3$, 75 MHz) of AR52.

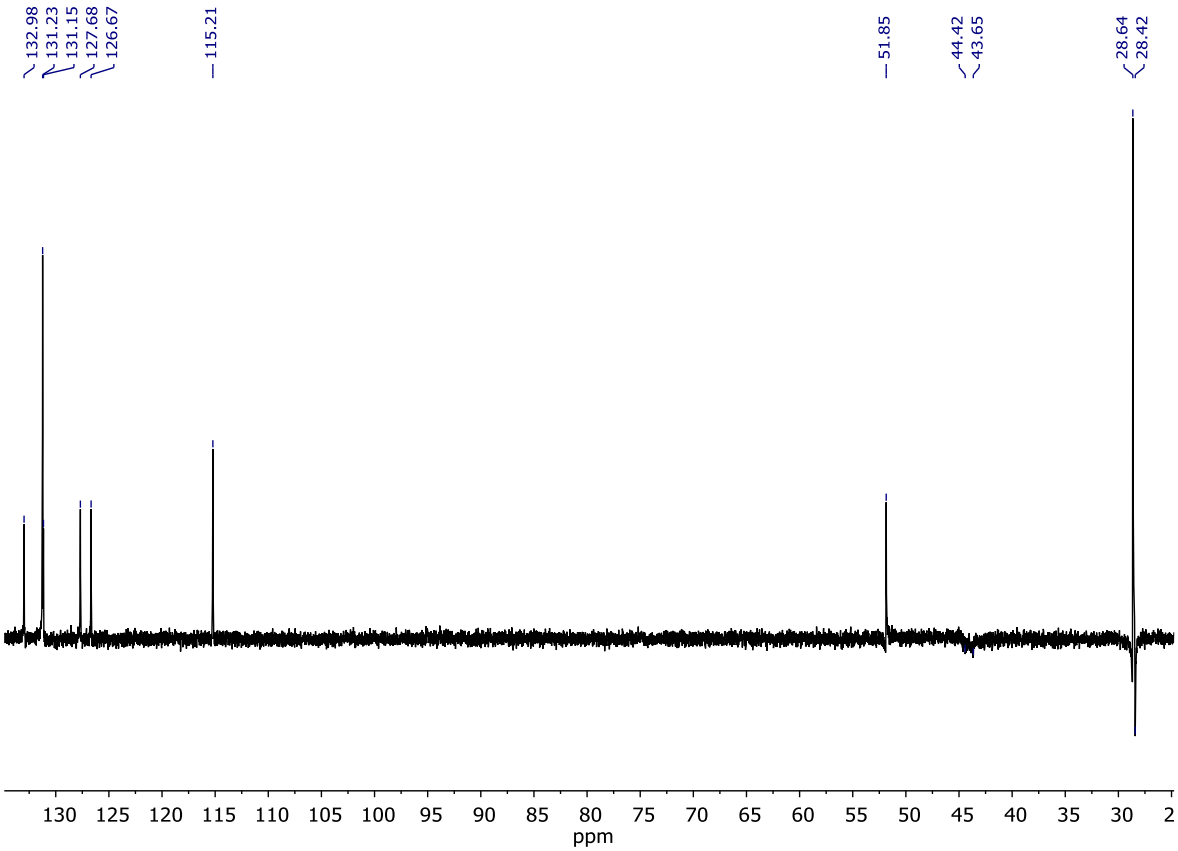

Figure 25. DEPT NMR ($CDCl_3$, 75 MHz) of AR52.

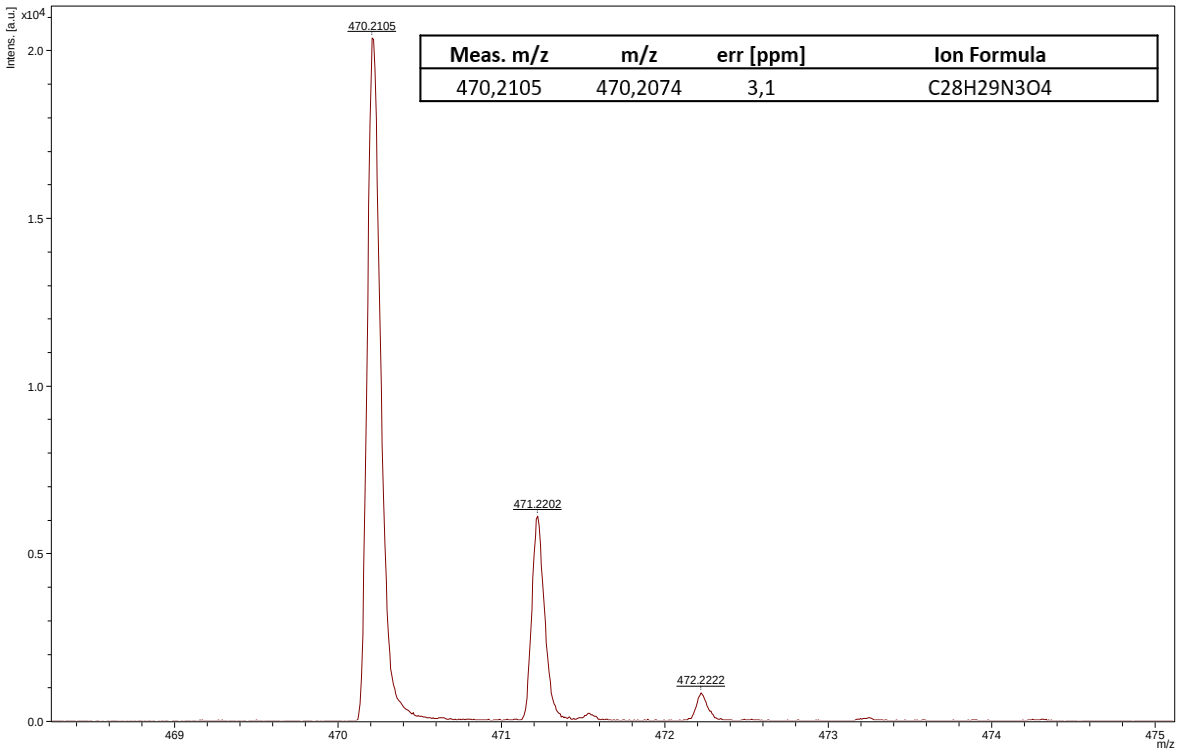

Meas. m/z	m/z	err [ppm]	Ion Formula
470,2105	470,2074	3,1	C28H29N3O4

Figure 26. HRMS (MALDI, DCTB+) of AR52.

Solvatochromism:

The concentration of the compound was 20 µM and the excitation wavelength was 380 nm.

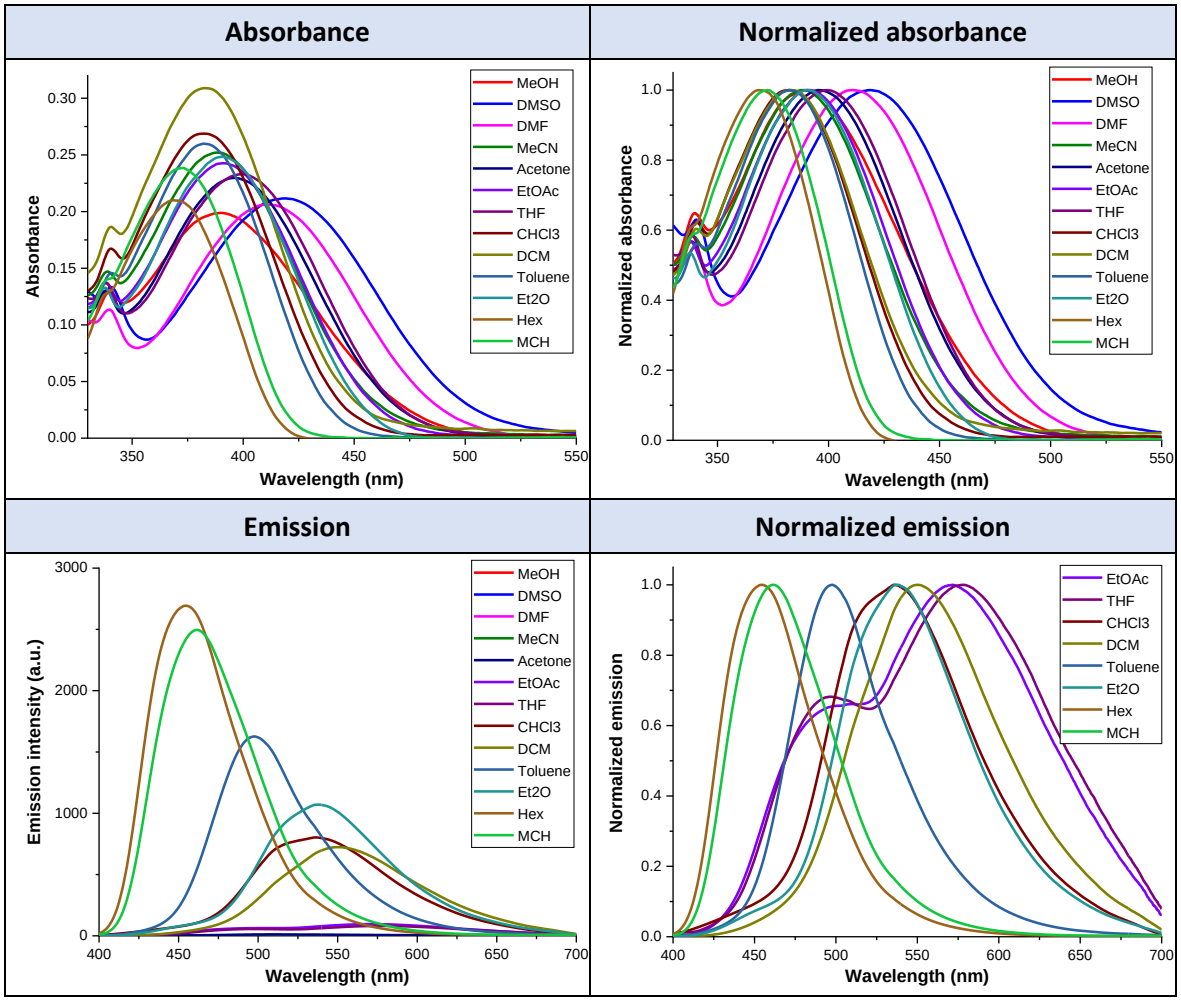

Figure 27. Solvatochromism of AR52.

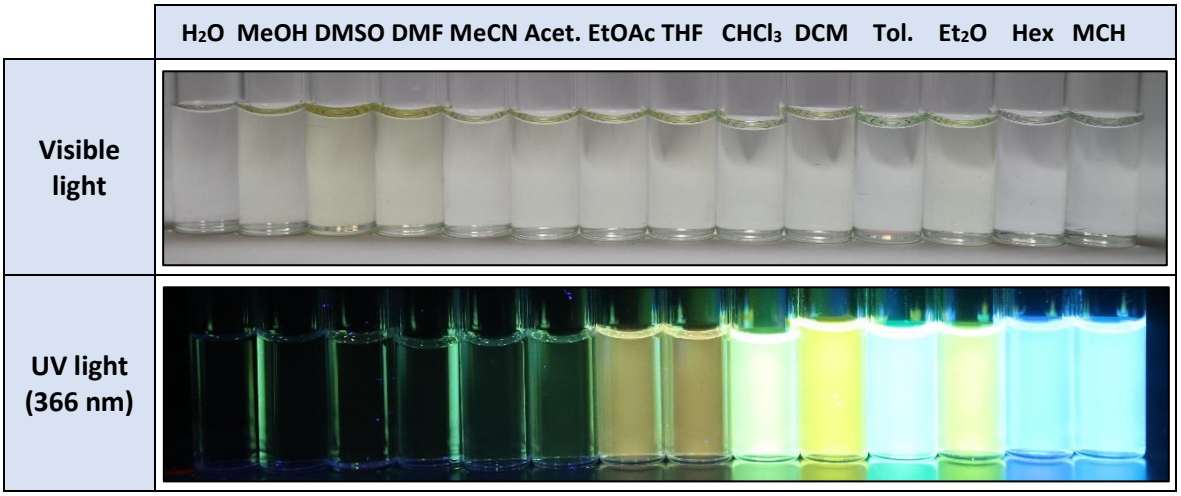

Figure 28. Solvatochromism of AR52 under visible and 366 nm light.

Fluorescence decay lifetime (τ):

The solvent used was hexane. The concentration of the compound was 20 µM.

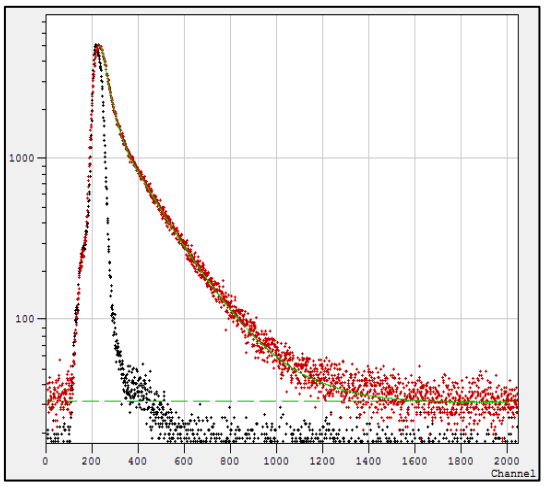

Figure 29. Fluorescence decay lifetime of AR52.

Water acceptance test:

The solvent used was MeOH and the concentration of the compound was 20 µM.

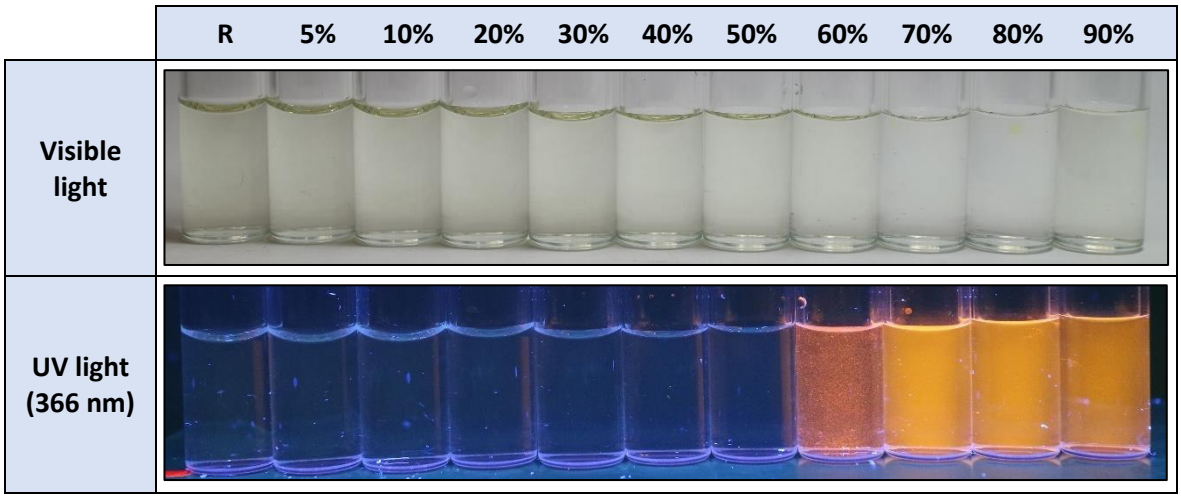

Figure 30. Water acceptance test of AR52 under visible (up) and UV (down) light.

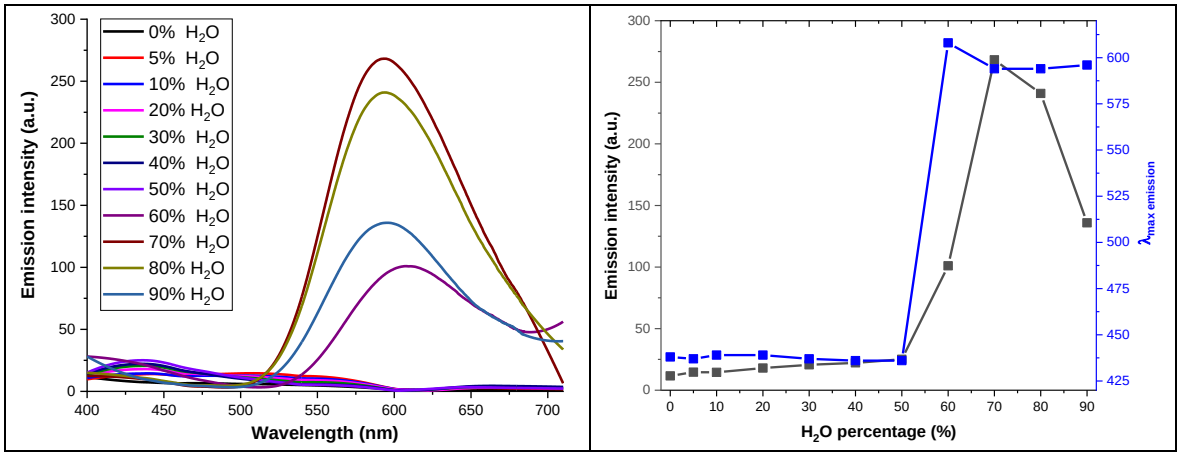

Figure 31. Emission intensity graph (left) and graph of relationship between the emission intensity and the wavelength of the maximum of emission (right) as a function of the amount of water added for AR52. λ_{exc} = 380 nm.

The maximum aumount of water that was admitted by the product was 50%. There was a marked shift of the emission maximum from blue to orange region, accompanied by a high increase in the intensity of the fluorescent emission, from 60% water due to the formation of nanoparticles (AIE).

SEM nanoparticles:

AR52 20% of water	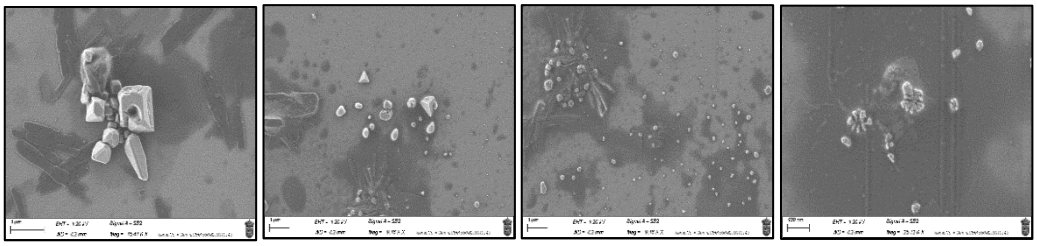
AR52 50% of water	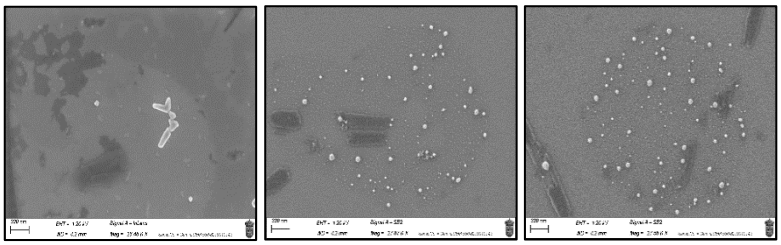
AR52 60% of water	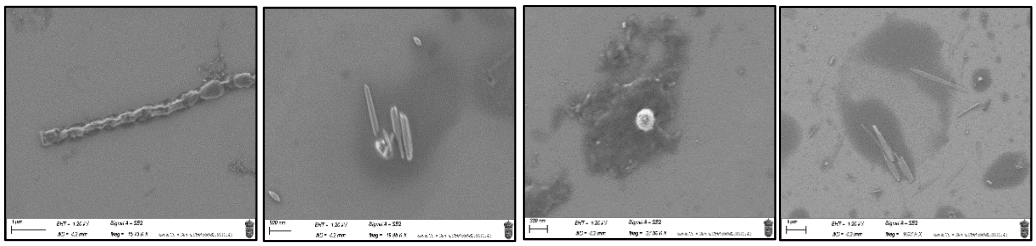
AR52 70% of water	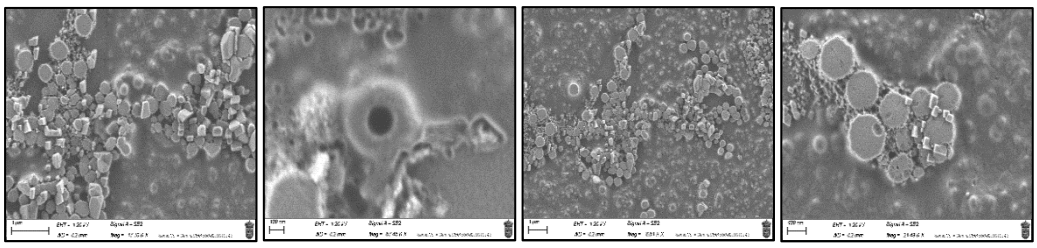

Figure 32. SEM nanoparticles of AR52 in different mixtures of water and MeOH.

pH test:

The prortion of water that the compound could accept was 40%. The concentration of the compound was 20 µM and the solvent used was MeOH.

	R	HCl	3.4	4.8	6.4	7.4	7.9	10.5	KOH
Visible light	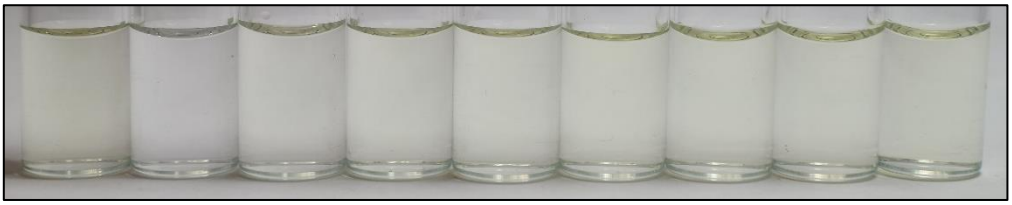								
UV light (366 nm)	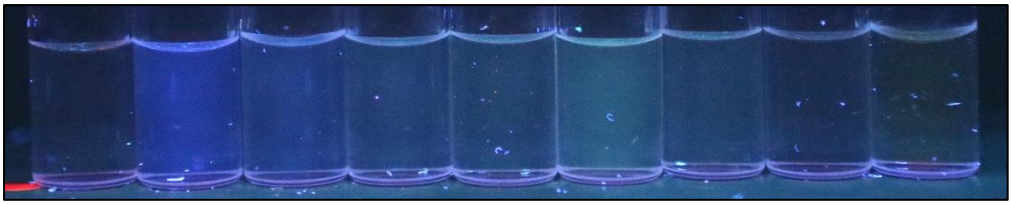								

Figure 33. pH test of AR52 under visible (up) and UV (down) light.

The fluorescent emmision was blue at very acidic pH and slightly greenish at physiological pH.

Cations and anions test:

The concentration of the compound was 20 µM and the solvent used was MeOH.

	R	Ag^{+}	Ni^{2+}	Sn^{2+}	Cd^{2+}	Zn^{2+}	Pb^{2+}	Cu^{2+}	Fe^{3+}	Sc^{3+}	Al^{3+}	Hg^{2+}	Au^{3+}	Co^{2+}	Pd^{2+}	Ir^{3+}	Cu^{+}	Ru^{3+}	Pt^{2+}
Visible light	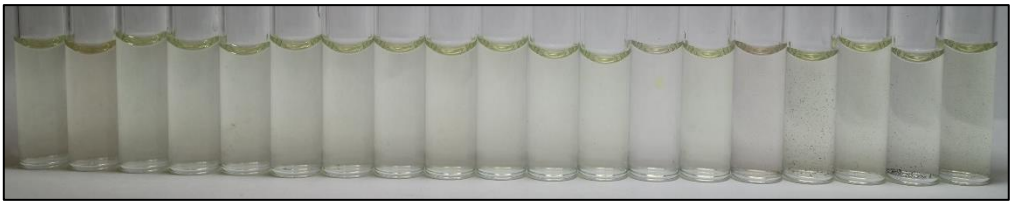																		
UV light (366 nm)	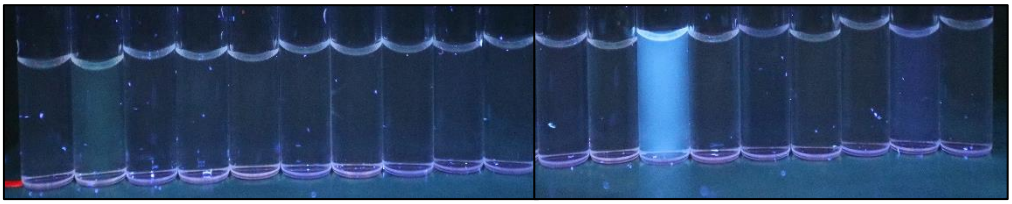																		

Figure 34. Cations test of AR52 under visible (up) and UV (down) light.

The most evident change was observed with respect to Au^{3+} and, with the Ag+, the fluorescence was turned slightly greenish.

The concentration of the compound was 20 µM and the solvent used was MeOH.

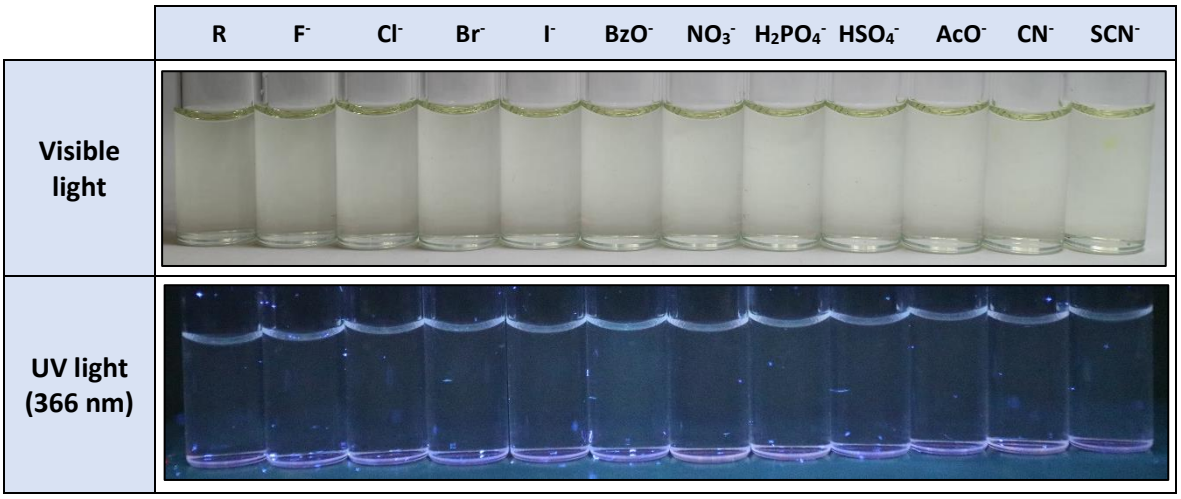

Figure 35. Anions test of AR52 under visible (up) and UV (down) light.

No significant changes were observed.

Oxidant and reductant reagents test:

The solvent used was MeOH and concentration of the compound was 20 µM.

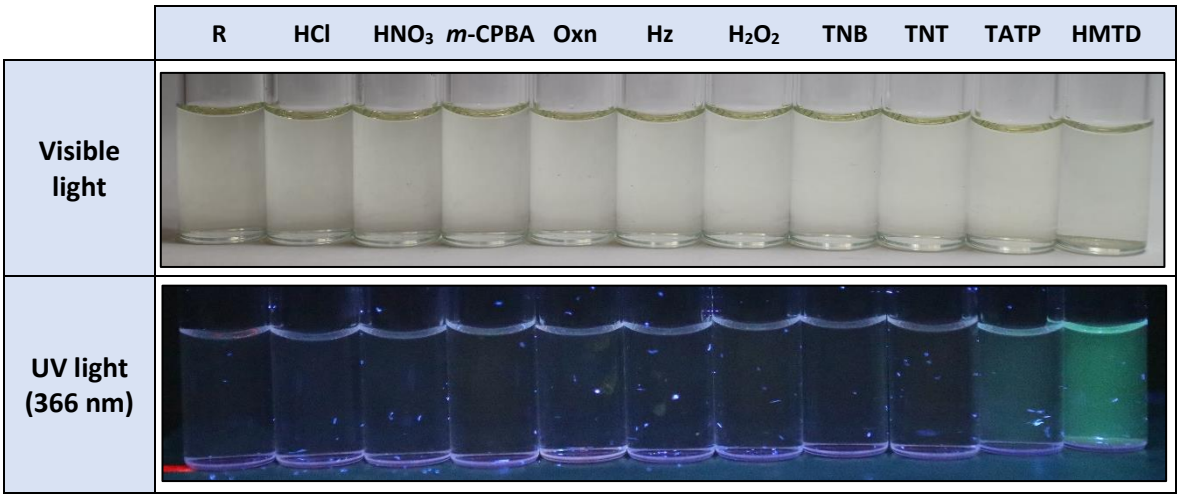

Figure 36. Oxidant and reductant reagents test of AR52 under visible (up) and UV (down) light.

The only changes were observed respect TATP and HMTD, in which the fluorescence was turned greenish.

Synthesis of *N*-(*N'*-Boc-piperidin-4-yl)-4-(2-aminopyrimidin-5-yl)naphthalene-1,8-dicarboxyl-monoimide (AR55p).

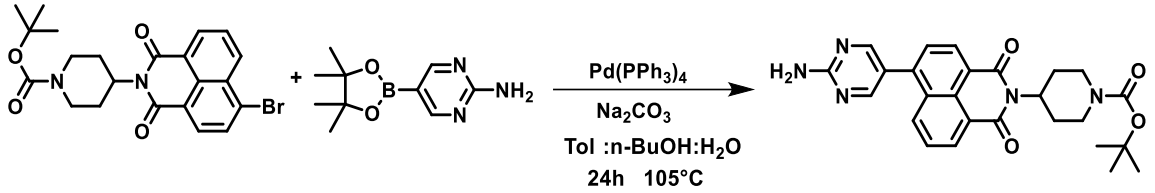

200 mg of *N*-(*N'*-Boc-piperidin-4-yl)-4-bromonaphthalen-1,8-dicarboxylmonoimide (AR43, 0.44 mmol), 101 mg of 2-amino-5-pyrimidin-5-yl pinacol ester (0.46 mmol) and 461 mg of sodium carbonate (4.35 mmol) were dissolved in a mixture of tolune:*n*-butanol:H_2O (20:5:10 ml) under nitrogen atmsphere. Then, 25 mg of $Pd(PPh_3)_4$ (0.05 eq) were added and the mixture was stirred overnight at 105°C. Afterwards, the solvent was evaporated under reduced pressure and the solid was dissolved in 50 ml of DCM and washed three times with water (3×50 ml). The organic layer was dried over anhidrous Na_2SO_4 and the solvent was evaporated under reduced pressure. The organic solid was purified by column chromatogaphic (SiO_2, DCM:MeOH) getting 190 mg of a pale yellow solid, 92 % yield.

m.p.: 233-235°C.

IR (ATR, cm^{-1}): 3299-3140 (N-H), 2980-2867, 1689 (C=O), 1653 (C=O), 1581, 1497, 1464, 1414, 1350, 1272, 1242, 1168 (C-N), 1111, 1030, 982, 901, 868, 781, 757, 454, 430.

^{1}H-NMR (300 MHz, $CDCl_3$) δ (ppm): 8.65 – 8.60 (m, 2H, **H_{Ar}**), 8.47 (s, 2H, **H_{Ar}**), 8.22 (dd, *J* = 8.5, 1.1 Hz, 1H, **H_{Ar}**), 7.75 (dd, *J* = 8.5, 7.3 Hz, 1H, **H_{Ar}**), 7.65 (d, *J* = 7.5 Hz, 1H, **H_{Ar}**), 5.43 (s, 2H, C**H_2**), 5.20 (m, 1H, C**H**), 4.30 (s, 2H, N**H_2**), 2.90 – 2.69 (m, 4H, 2xC**H_2**), 1.73 – 1.64 (m, 2H, C**H_2**), 1.50 (s, 9H, 3xC**H_3**).

^{13}C-NMR (75 MHz, $CDCl_3$) δ (ppm): 164.5 (**C**=O), 164.3 (**C**=O), 162.5 (**C**=O), 158.6 (**C_{Ar}**H), 154.8 (**C_{Ar}**), 140.0 (**C_{Ar}**), 131.7 (**C_{Ar}**H), 131.4 (**C_{Ar}**H), 131.1 (**C_{Ar}**H),128.9 (**C_q**), 128.0 (**C_{Ar}**H), 127.6 (**C_{Ar}**H), 123.6 (**C_{Ar}**), 122.8 (**C_{Ar}**), 79.7 (**C_q**), 52.1 (**C**H), 44.3 (**C**H_2), 28.6 (**C**H_3), 28.4 (**C**H_2).

HRMS (MALDI, DCTB+) m/z: calculated for $C_{26}H_{27}N_5O_4$: 474.2136 (M^+); found: 474.2157.

UV-Vis ($CHCl_3$), λ_{max} nm (log ε): 364 (4.3).

Ø ($CHCl_3$, %): 91.59.

τ (375 nm, $CHCl_3$, ns): 3.608 ns (χ^2: 1.067).

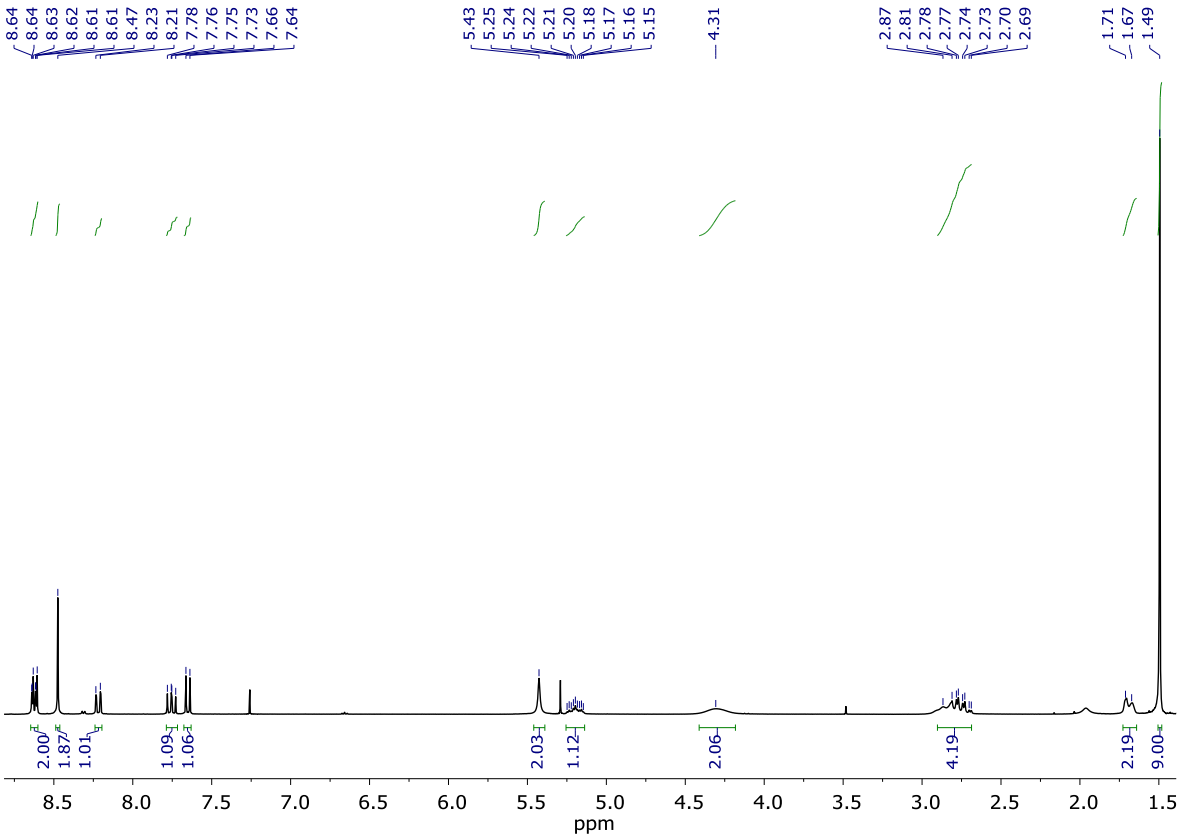

Figure 37. ^{1}H-NMR ($CDCl_3$, 300 MHz) of AR55p.

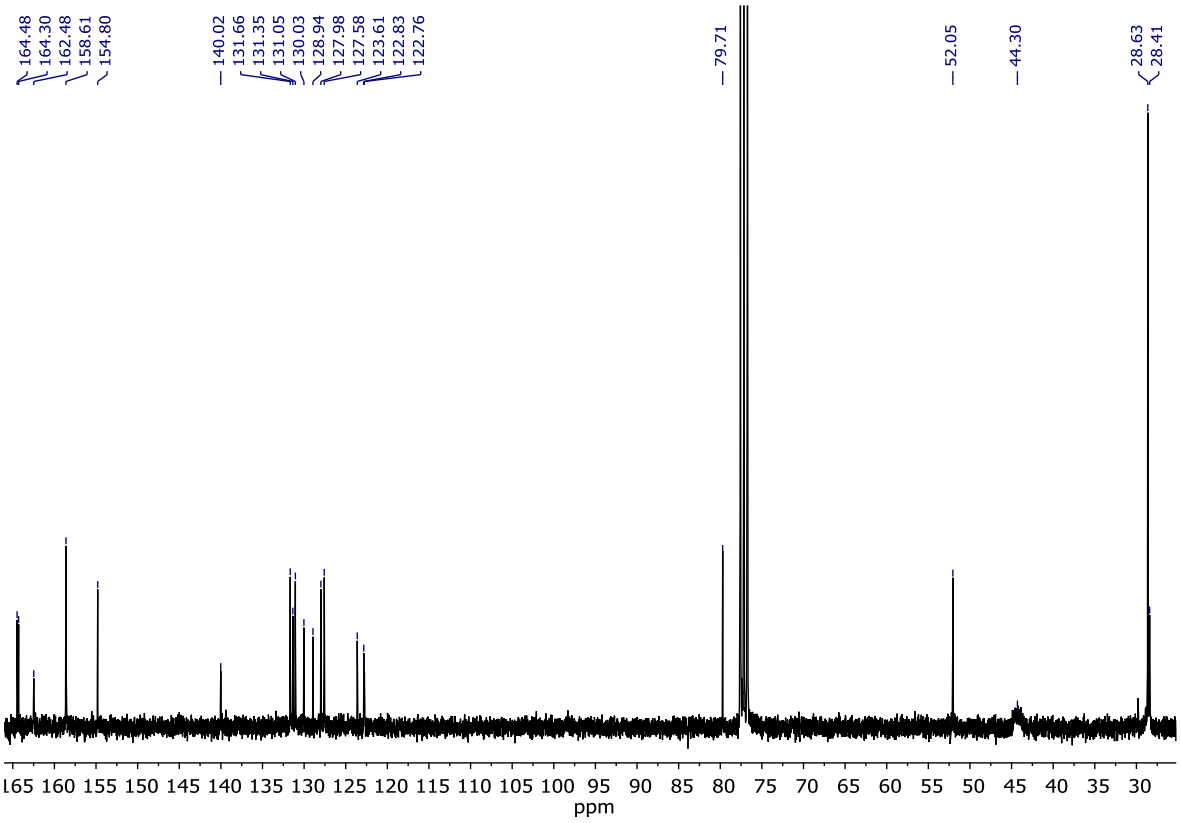

Figure 38. ^{13}C-NMR ($CDCl_3$, 75 MHz) of AR55p.

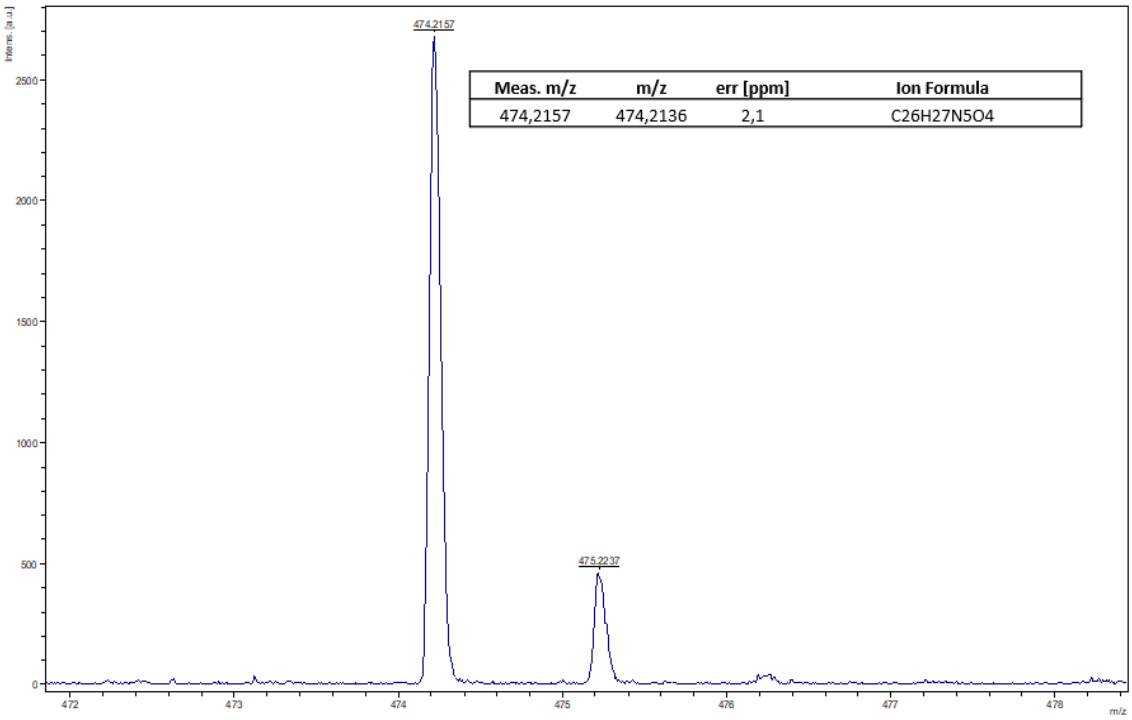

Figure 39. HRMS (MALDI, DCTB+) of AR55p.

Fluorescence decay lifetime (τ):

The solvent used was $CHCl_3$. The concentration of the compound was 10 µM.

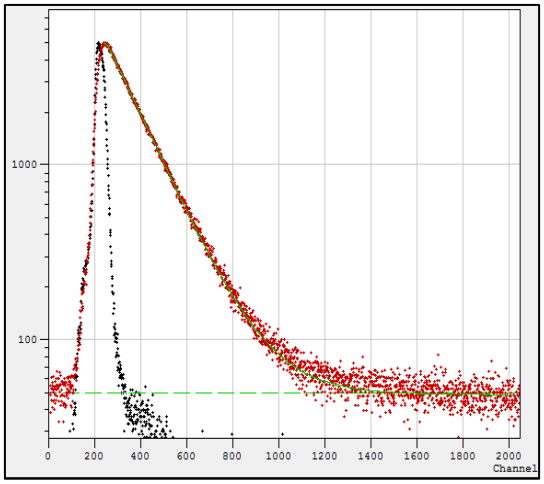

Figure 40. Fluorescence decay lifetime of AR55p.

Solvatochromism:

The concentration of the compound was 20 µM and the excitation wavelength was 350 nm.

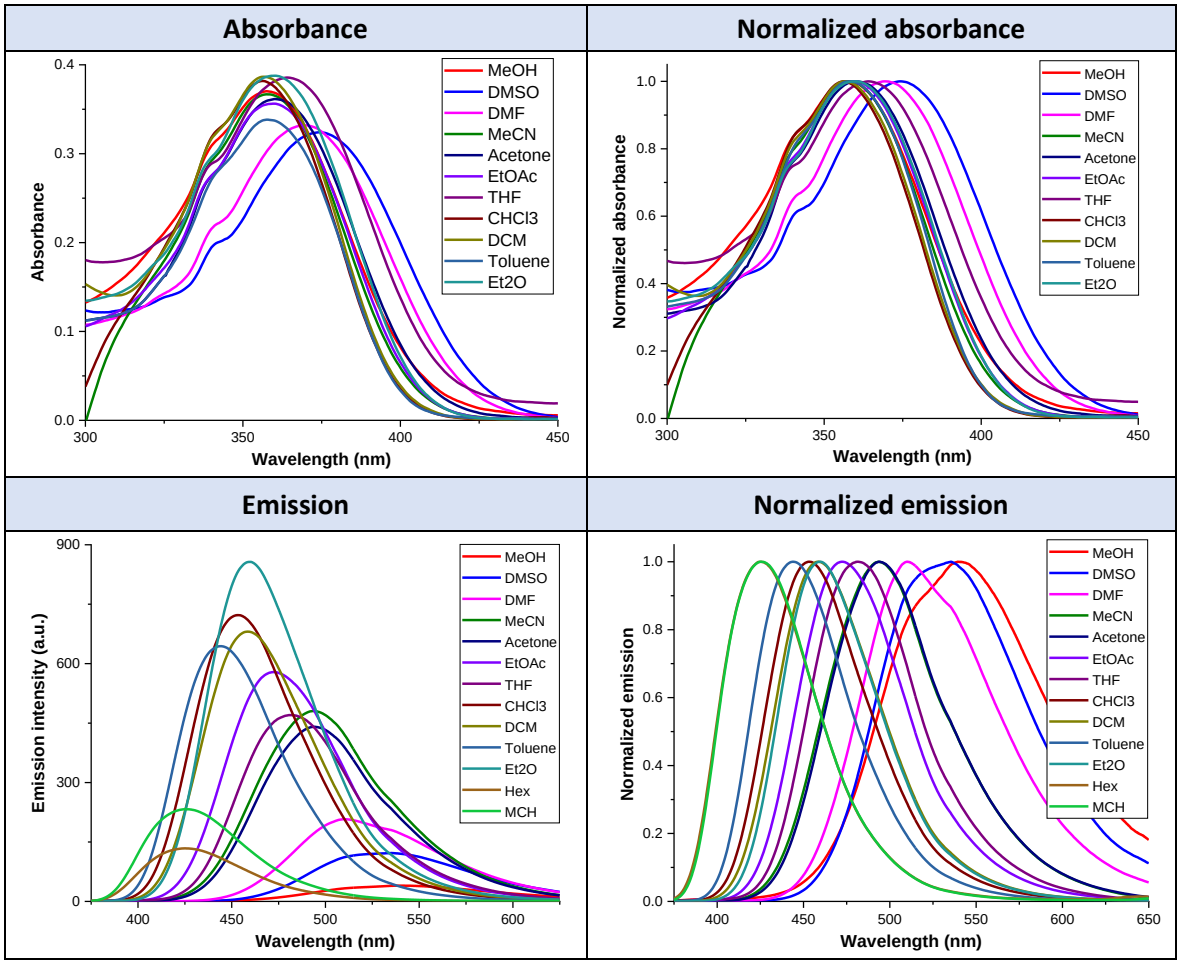

Figure 41. Solvatochromism of AR55p.

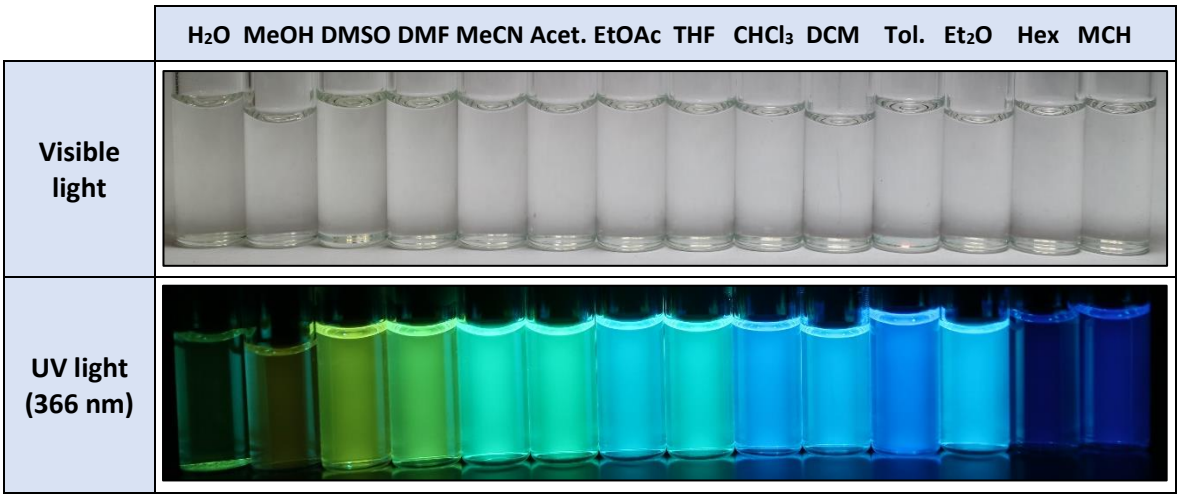

Figure 42. Solvatochromism of AR55p under visible and 366 nm light.

Water acceptance test:

The solvents were THF and MeOH and the concentration was 20 µM.

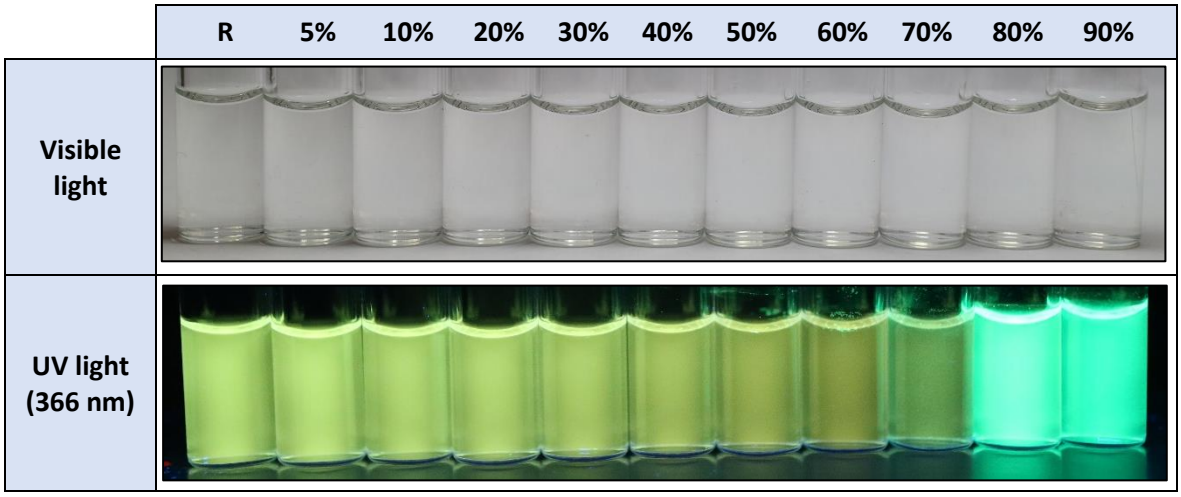

Figure 43. Water acceptance test of AR55p in MeOH under visible (up) and UV (down) light.

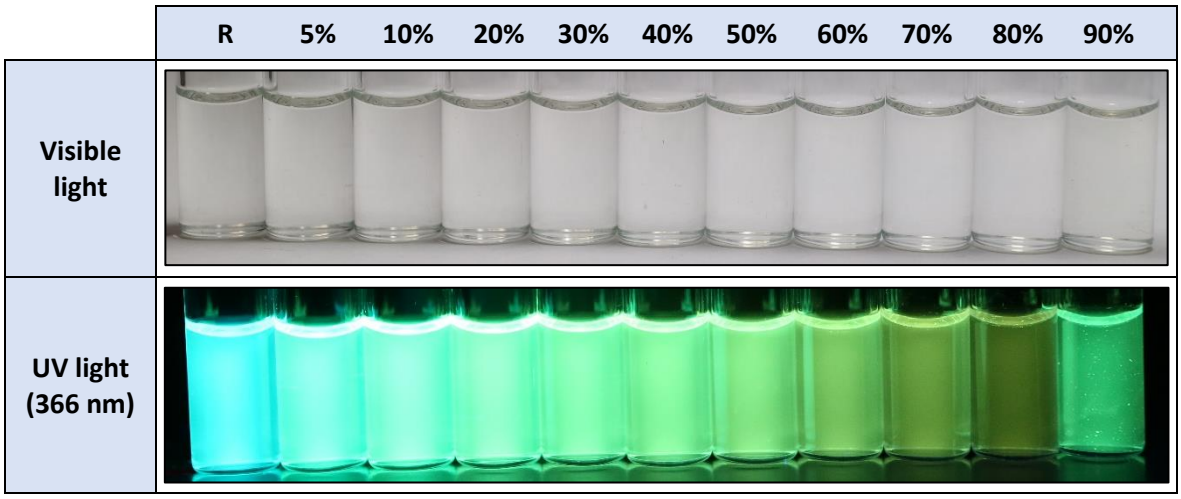

Figure 44. Water acceptance test of AR55p in THF under visible (up) and UV (down) light.

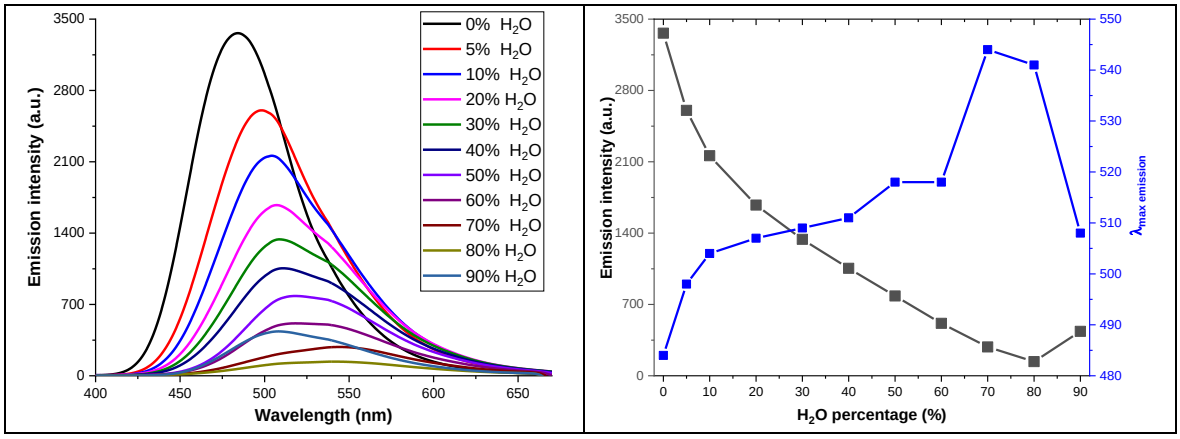

Figure 45. Emission intensity graph (left) and graph of relationship between the emission intensity and the wavelength of the maximum of emission (right) as a function of the amount of water added for AR55p in THF. λexc = 350 nm.

The maximum amount of water that was admitted by the product was 60%. There was a marked shift of the emission maximum from yellow to green region, accompanied by a high increase in the intensity of the fluorescent emission, from 80% water, due to aggregation-induced-emission (AIE). In THF, the same phenomenon was observed but with less intensity.

SEM nanoparticles:

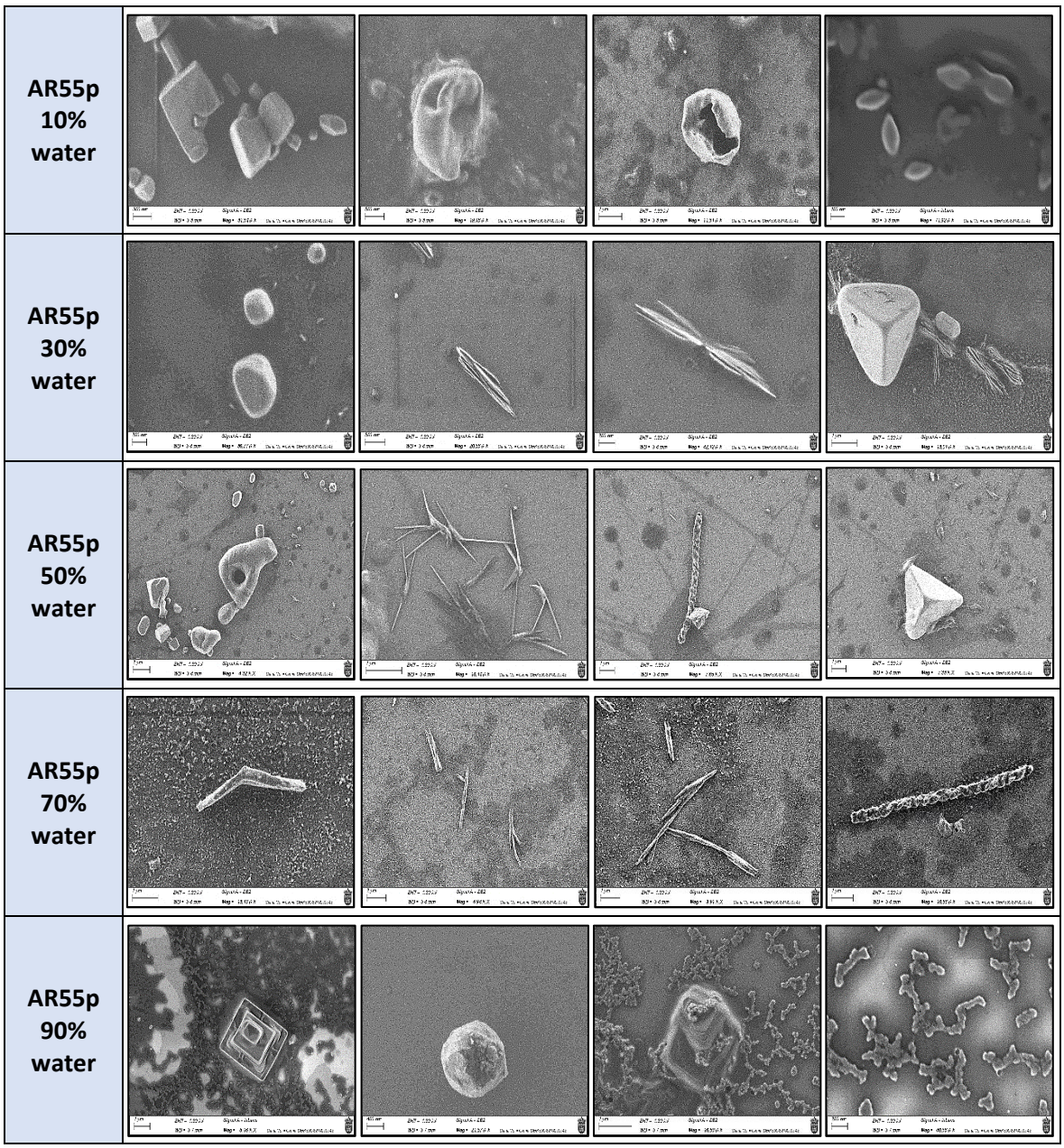

Figure 46. SEM nanoparticles of AR55p in different mixtures of THF-H_2O.

pH test:

The proportion of water that the compound could accept was 50%. The concentration of the compound was 20 µM and the solvent used was MeOH.

	R	HCl	3.4	4.8	6.4	7.4	7.9	10.5	KOH
Visible light	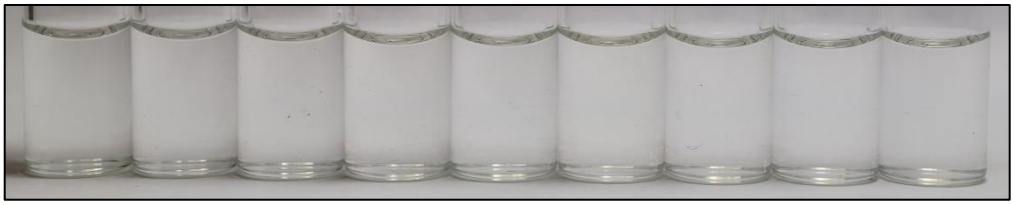								
UV light (366 nm)	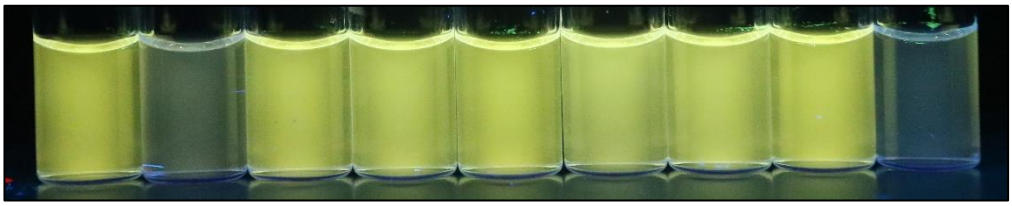								

Figure 47. pH test of AR55p under visible (up) and UV (down) light.

The fluorescent emission was quenched at very acidic and basic pH.

Cations and anions test:

The concentration of the compound was 20 µM and the solvent used was MeOH.

	R	Ag^{+}	Ni^{2+}	Sn^{2+}	Cd^{2+}	Zn^{2+}	Pb^{2+}	Cu^{2+}	Fe^{3+}	Sc^{3+}	Al^{3+}	Hg^{2+}	Au^{3+}	Co^{2+}	Pd^{2+}	Ir^{3+}	Cu^{+}	Ru^{3+}	Pt^{2+}
Visible light	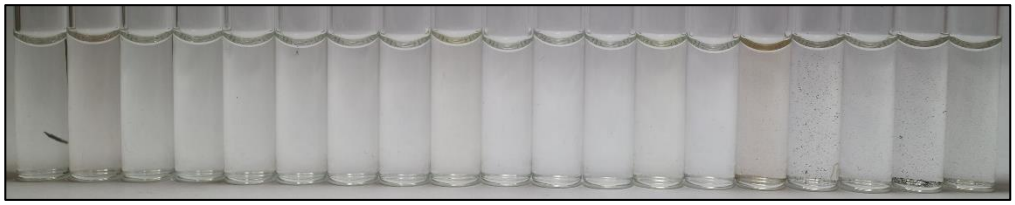																		
UV light (366 nm)	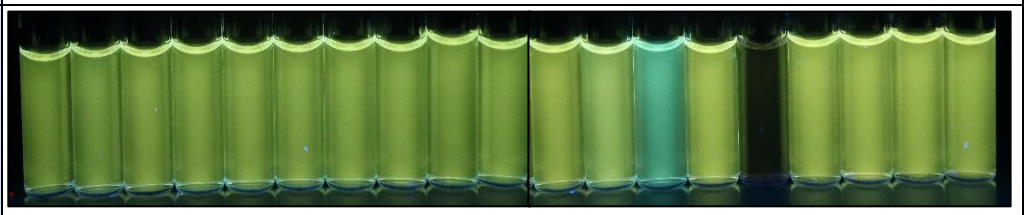																		

Figure 48. Cations test of AR55p under visible (up) and UV (down) light.

Changes were observed with Au^{3+}, with greenish fluorescence, and Pd^{2+} with fluorescence quenching.

The concentration of the compound was 20 µM and the solvent used was MeOH.

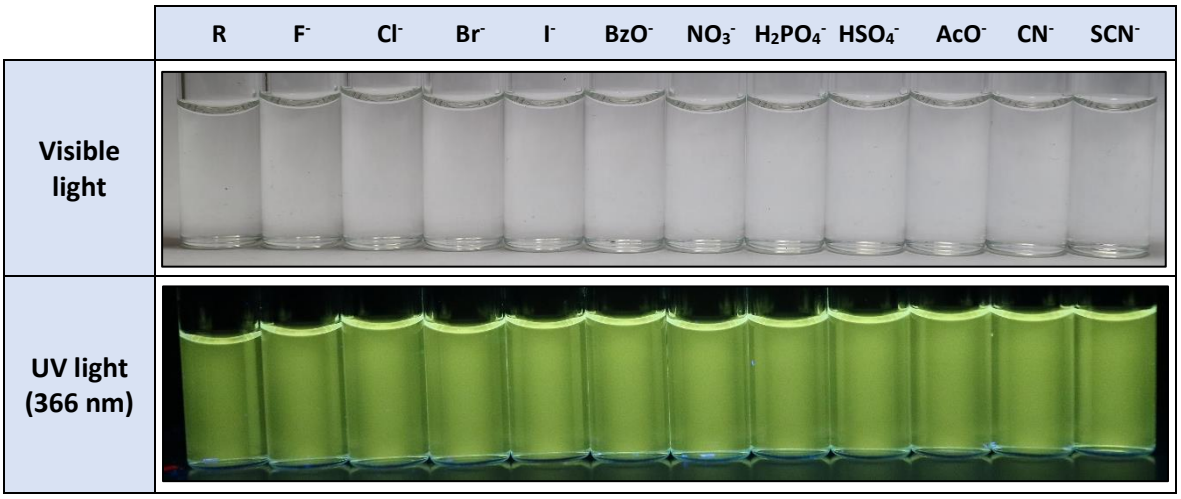

Figure 49. Anions test of AR55p under visible (up) and UV (down) light.

No significant changes were observed.

Oxidant and reductant reagents test:

The solvent was MeOH and concentration of compound was 20 µM.

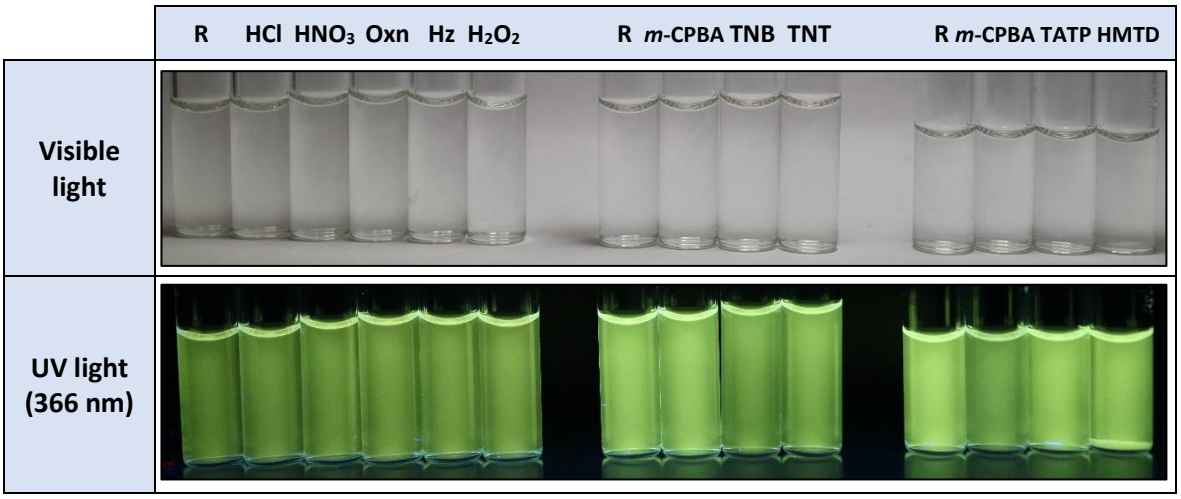

Figure 50. Oxidants and reductant reagents tests of AR55p under visible (up) and UV (down) light.

No significant changes were observed.

Synthesis of *N*-(piperidin-4-yl)-4-(2-aminopyrimid-5-yl)naphthalene-1,8-dicarboxylmonoimide (AR55d).

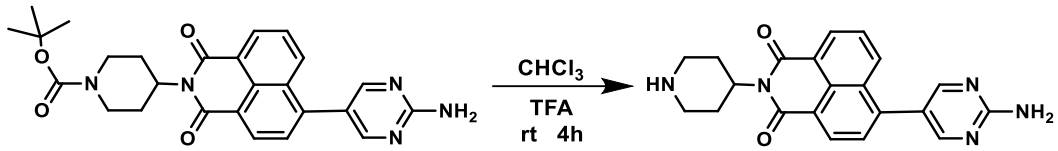

In a 50 ml flask, 25 mg of *N*-[(*N'*-Boc)piperidin-4-yl]-4-(2-aminopyrimid-5-yl)naphthalene-1,8-dicarboxylmonoimide (AR55p, 50.7 mmol) were dissolved in 25 ml of $CHCl_3$ and 2 ml of TFA were added and the resultingbmixture was stirred 4 hours at room temperature. Once the reaction had finalized, the mixture was neutralized with a 40% NaOH solution until it reached a neutral pH. Then, the product was extracted six times with 30 ml of DCM (6×30 ml). Then, the organic layers were combined and dried over anhidrous Na_2SO_4. The solvent was removed under reduced pressure, getting 18 mg of yellow solid, 95 % yield.

m.p.: 268-270°C (decomposition).

IR (ATR, cm^{-1}): 3180 (N-H), 3066-2949, 1647 (C=O), 1576, 1501, 1458, 1354, 1235, 1127 (C-N), 1046, 986, 956, 896, 851, 834, 782, 753, 720.

^{1}H-NMR (300 MHz, CD_3OD) δ (ppm): 8.65 (dd, *J* = 7.5, 1.3 Hz, 2H, **H_{Ar}**), 8.51 (s, 2H, **H_{Ar}**), 8.37 (dd, *J* = 8.5, 1.1 Hz, 1H, **H_{Ar}**), 7.91-7.79 (m, 2H, **H_{Ar}**), 5.45-5.29 (m, 1H, C**H**), 4.60 (s, 2H, N**H_2**), 3.58-3.49 (m, 2H, C**H_2**), 3.24-2.97 (m, 5H, 1xN**H** + 2xC**H_2**), 2.04-1.97 (m, 2H, C**H_2**).

^{13}C-NMR (125 MHz, CD_3OD) δ (ppm): 165.8 (**C**=O), 165.6 (**C**=O), 164.9 (**C_{Ar}**), 164.5 (**C_{Ar}**), 159.9 (**C_{Ar}**H), 142.1 (**C_{Ar}**), 132.9 (**C_{Ar}**), 132.4 (**C_{Ar}**), 132.0 (**C_{Ar}**H), 131.3 (**C_{Ar}**H), 130.1 (**C_{Ar}**H), 129.9 (**C_{Ar}**), 129.1 (**C_{Ar}**), 128.6 (**C_{Ar}**H), 127.6 (**C_{Ar}**H), 124.5 (**C_{Ar}**), 123.5 (**C_{Ar}**), 122.9 (**C_{Ar}**), 46.2 (**C**H_2), 30.8 (**C**H_2), 27.7 (**C**H_2).

HRMS (TOF, ESI-) m/z: calculated for $C_{21}H_{20}N_5O_2$: 374.1612 ($M+H^+$); found: 374.1619.

UV-Vis ($CHCl_3$), λ_{max} nm (log ε): 357 (4.2).

Ø ($CHCl_3$, %): 92.56.

τ (375 nm, $CHCl_3$, ns): 3.741 ns (χ^2: 1.084).

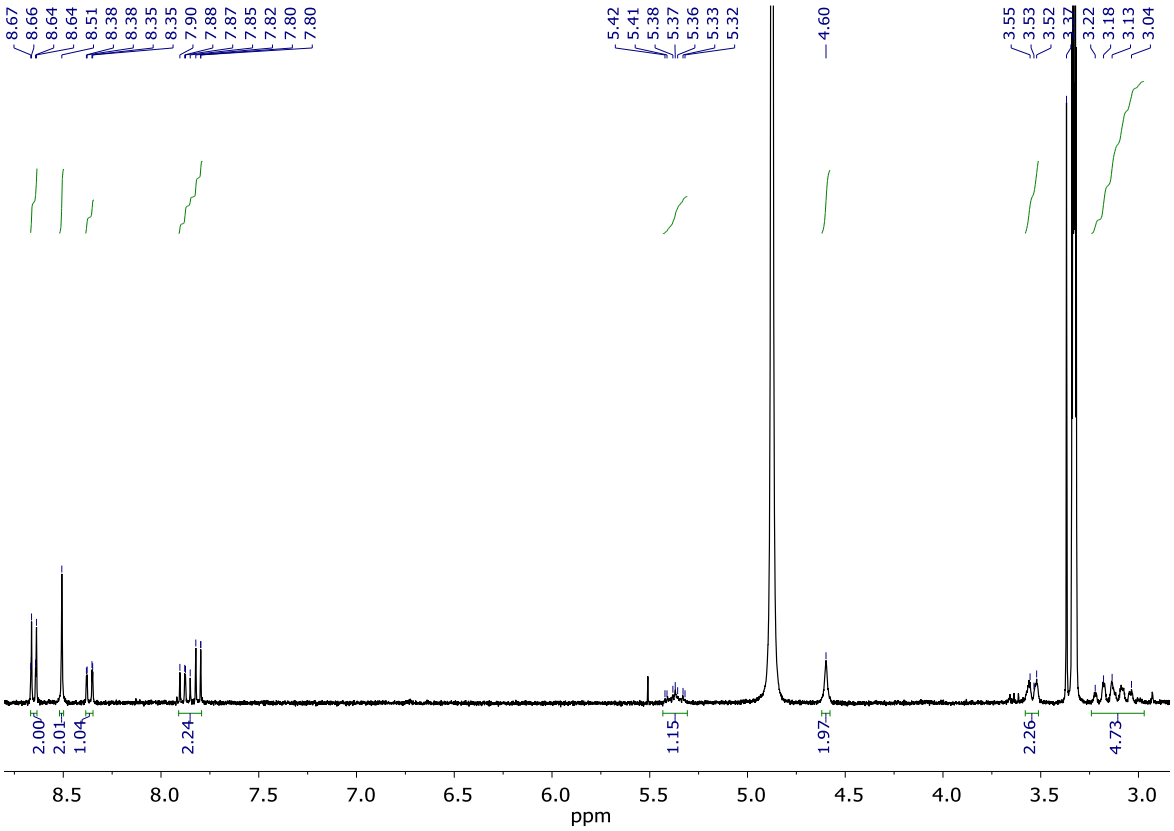

Figure 51. ^{1}H-NMR (CD_3OD, 300 MHz) of AR55d.

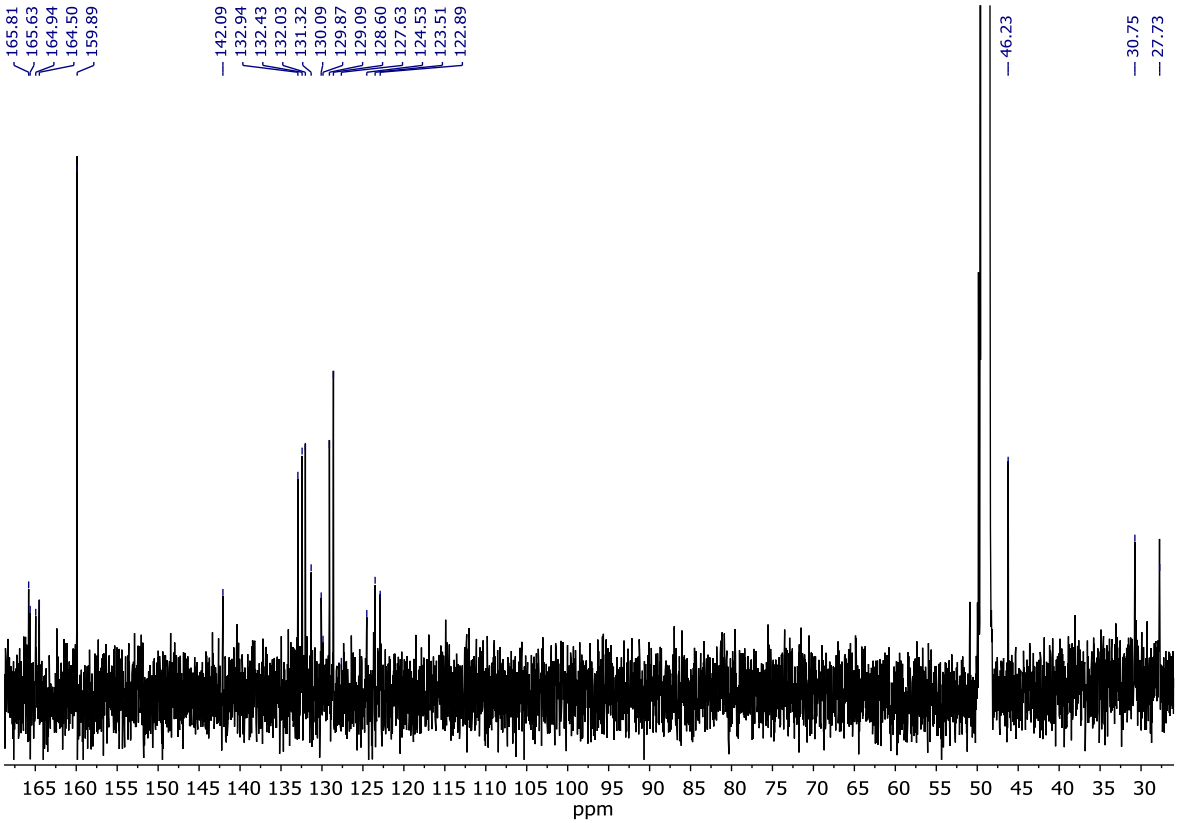

Figure 52. ^{13}C-NMR (CD_3OD, 150 MHz) of AR55d.

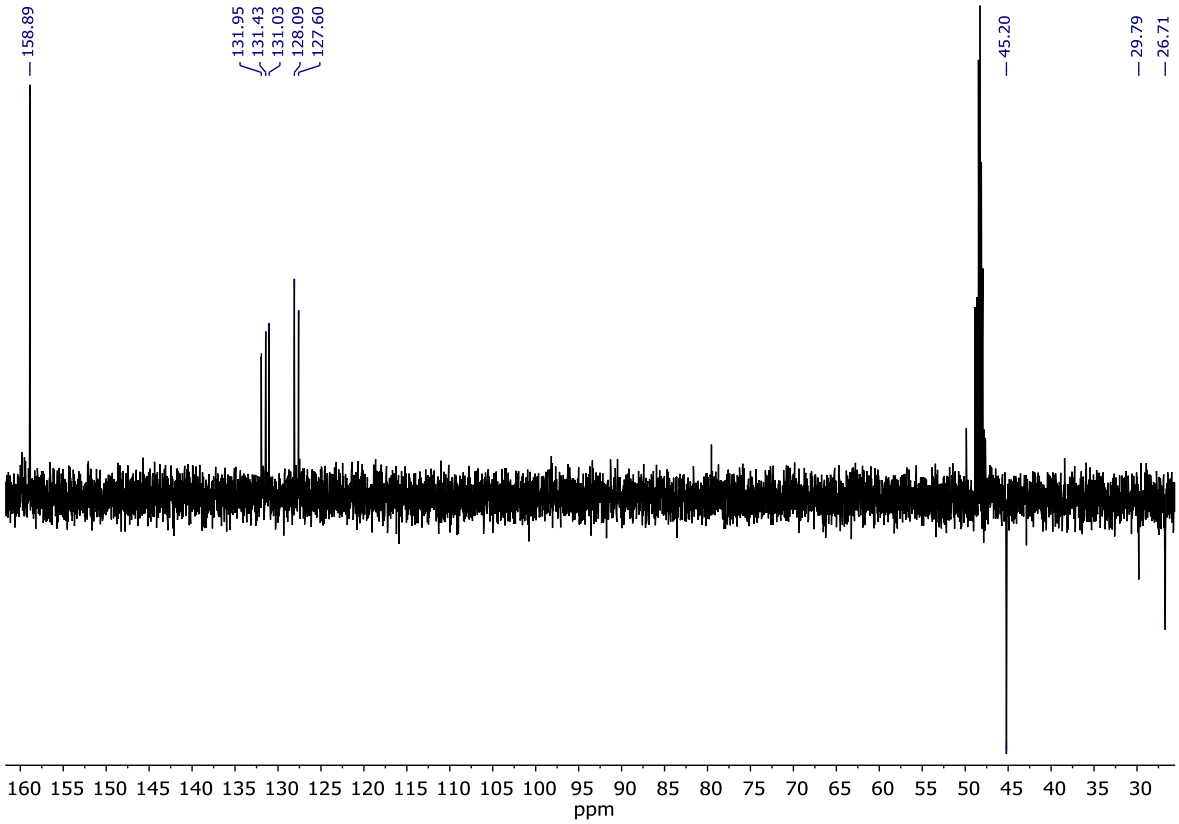

Figure 53. DEPT NMR (CD_3OD, 150 MHz) of AR55d.

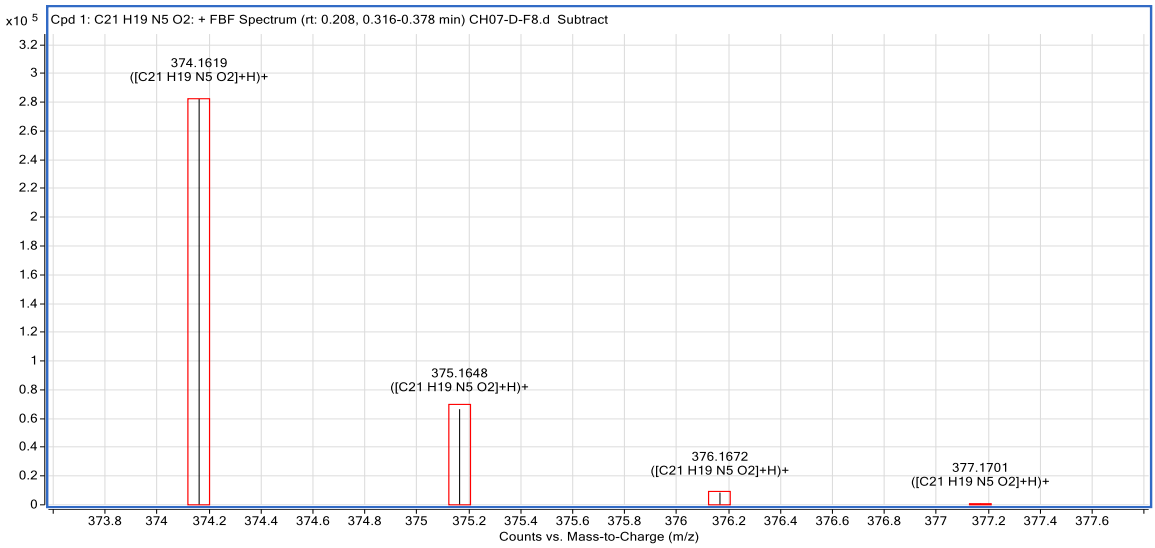

Figure 54. HRMS (TOF, ESI-) of AR55d.

Solvatochromism:

The concentration of the compound was 10 µM and the excitation wavelength was 370 nm.

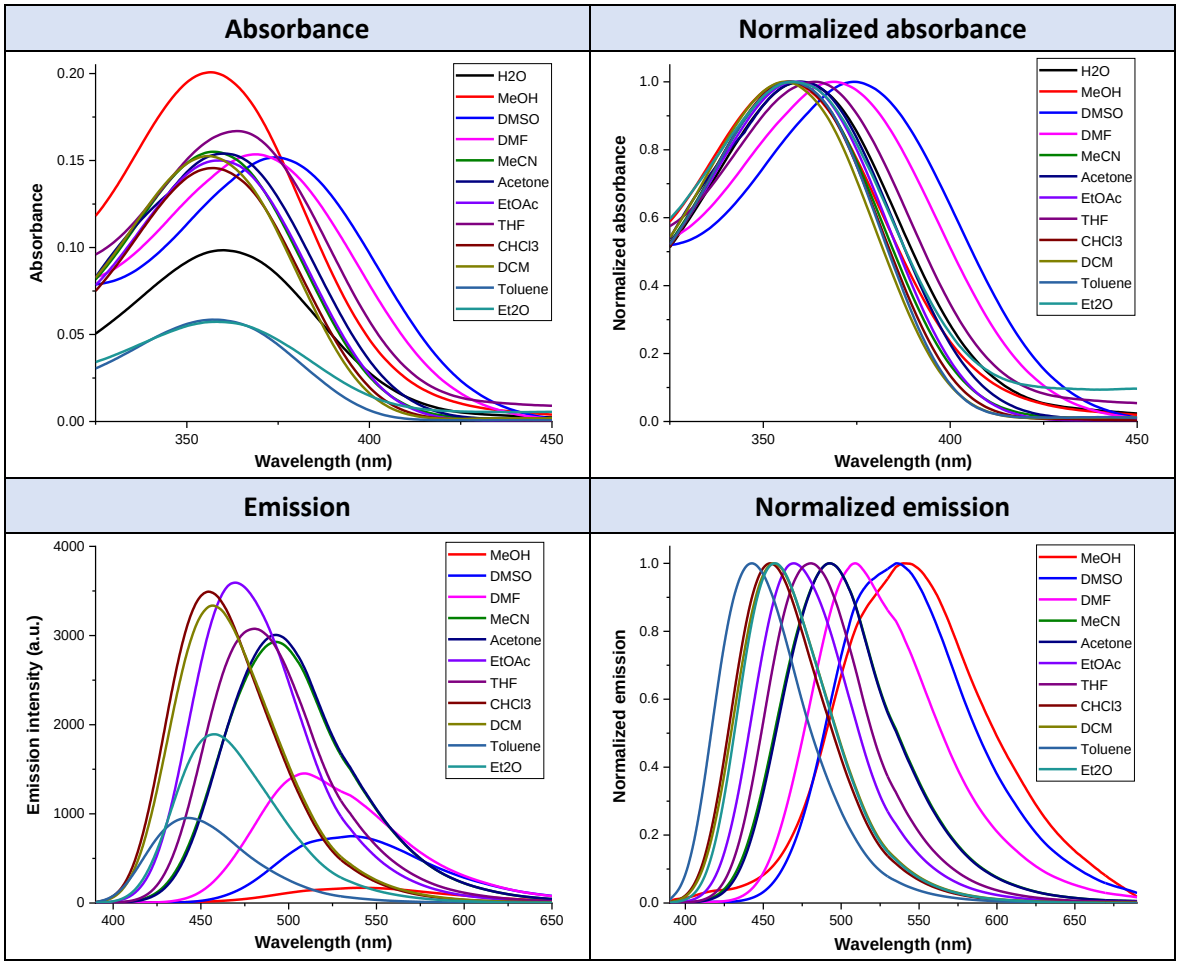

Figure 55. Solvatochromism of AR55d.

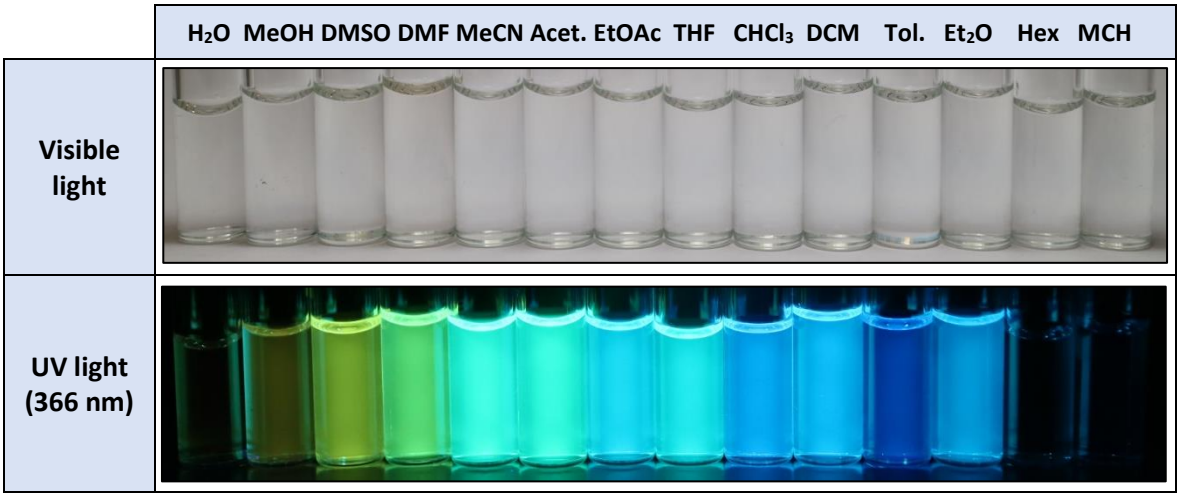

Figure 56. Solvatochromism of AR55d under visible and 366 nm light.

Fluorescence decay lifetime (τ):

The solvent used was $CHCl_3$. The concentration of the compound was 10 µM.

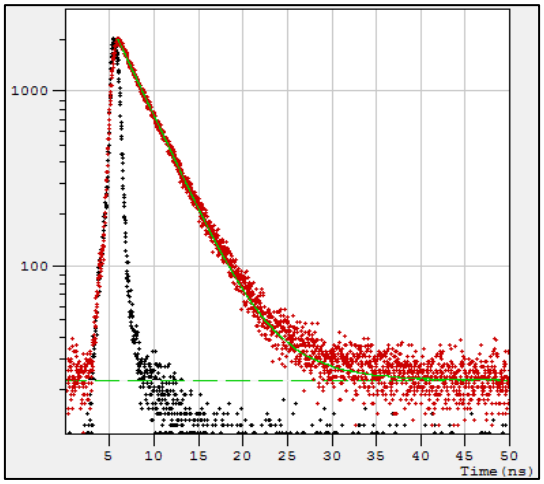

Figure 57. Fluorescence decay lifetime of AR55d.

Water acceptance test:

The solvents were THF and MeOH and the concentration was 10 µM.

	R	5%	10%	20%	30%	40%	50%	60%	70%	80%	90%
Visible light											
UV light (366 nm)	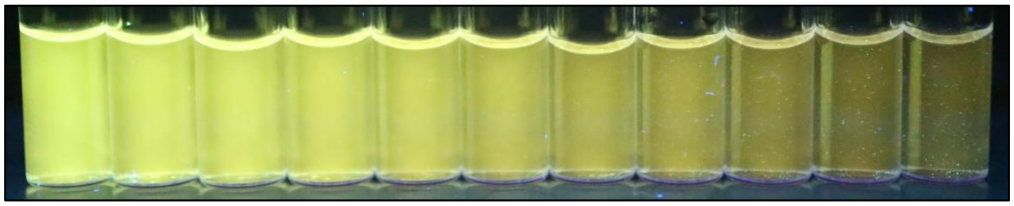										

Figure 58. Water acceptance test of AR55d in MeOH under visible (up) and UV (down) light.

	R	5%	10%	20%	30%	40%	50%	60%	70%	80%	90%
Visible light											
UV light (366 nm)	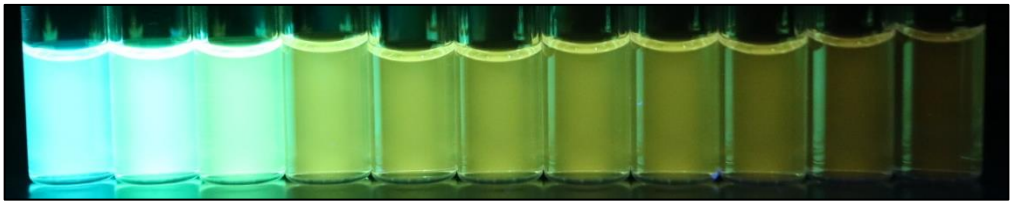										

Figure 59. Water acceptance test of AR55d in THF under visible (up) and UV (down) light.

Regardless of the solvent used, an ACQ was observed as the amount of water in the solution was increased.

pH test:

The proportion of water that the compound could accept was 60%. The concentration of the compound was 10 µM and the solvent used was MeOH.

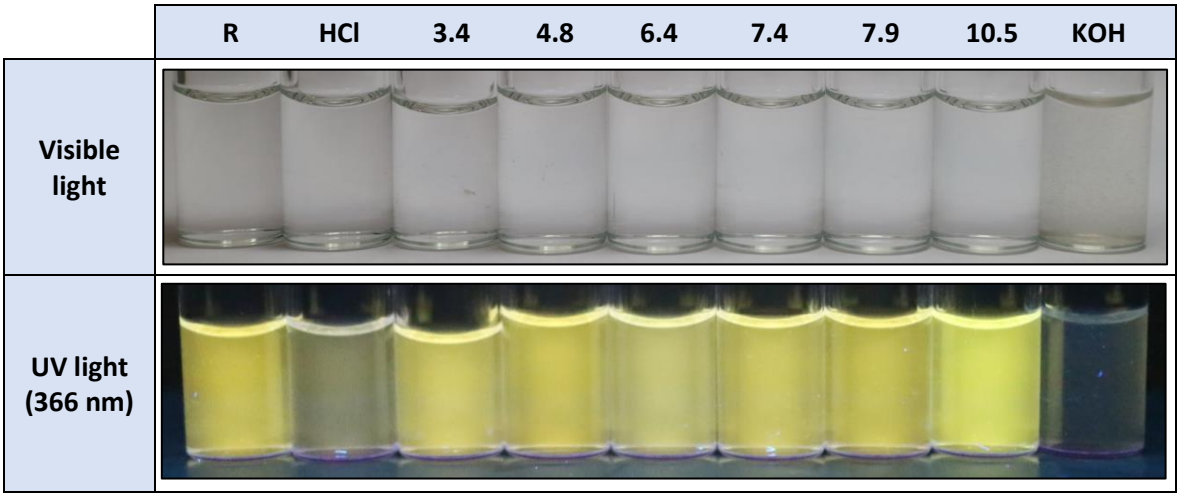

Figure 60. pH test of AR55d under visible (up) and UV (down) light.

The fluorescent emission was quenched at very acidic and basic pH.

Cations and anions test:

The concentration of the compound was 10 µM and the solvent used was MeOH.

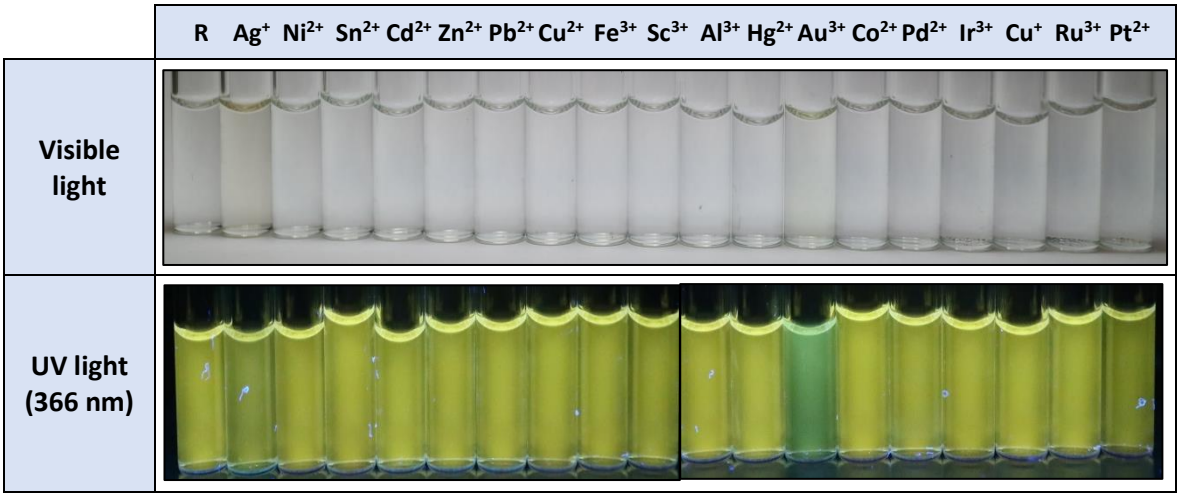

Figure 61. Cations test of AR55d under visible (up) and UV (down) light.

Fluorescence was quenched slightly in the presence of Ag^{+} while it turns green in the presence of Au^{3+}.

The concentration of the compound was 10 µM and the solvent used was MeOH.

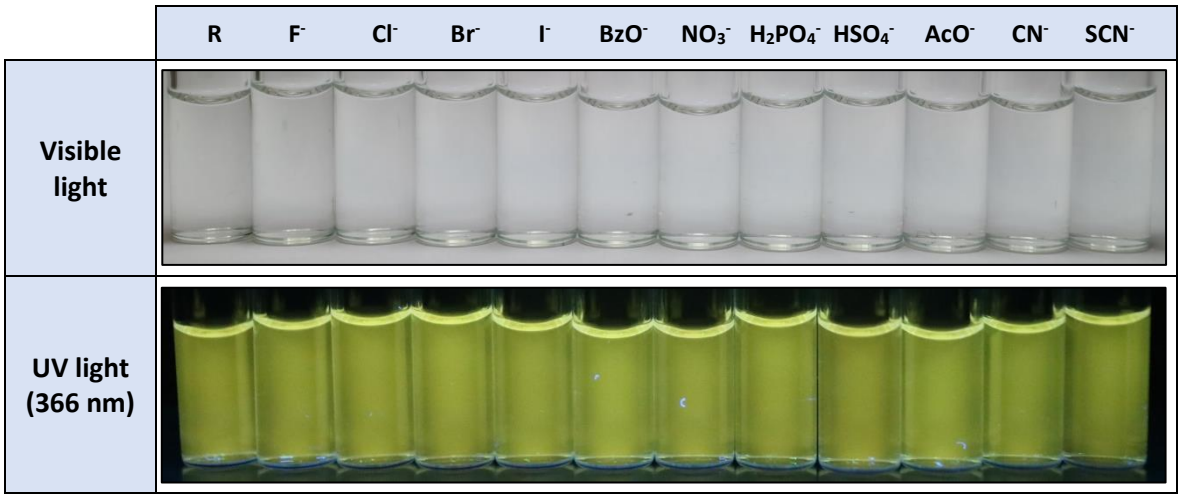

Figure 62. Anions test of AR55d under visible (up) and UV (down) light.

No significant changes were observed.

Oxidant and reductant reagents test:

The solvent was MeOH and concentration of compound was 10 µM.

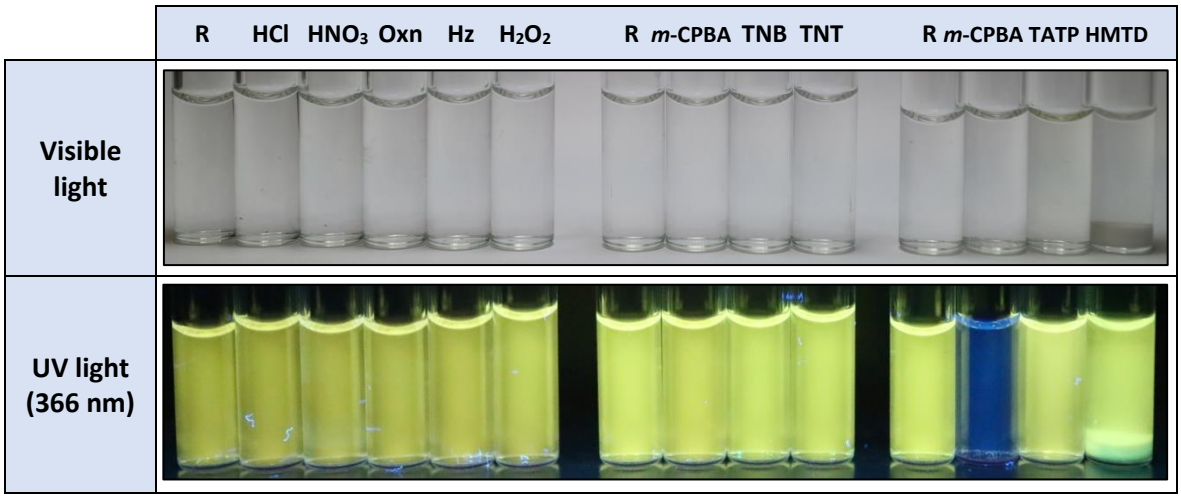

Figure 63. Oxidants and reductant reagents tests of AR55d under visible (up) and UV (down) light.

No significant changes were observed.

Synthesis of *N*-(N-Boc-piperidin-4-yl)-4-[2-(4-Boc-piperazin-1-yl)pyrimidin-5-yl]naphthalene-1,8-dicarboxylmonoimide (AR82p)

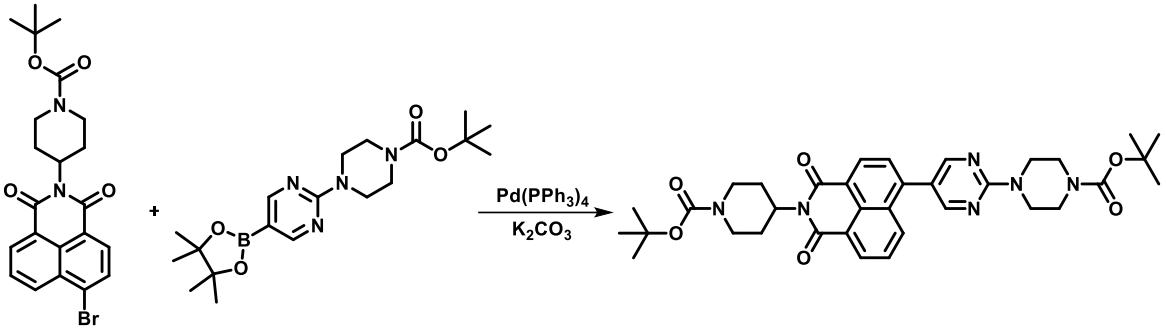

250 mg of *N*-(*N*-Boc-piperidin-4-yl)-4-bromonaphthalene-1,8-dicarboxylmonoimide (AR43, 0.54 mmol), 223 mg of 2-(4-Boc-piperazine)pyrimidine-5-boronic acid pinacol ester (0.57 mmol) and 752 mg of potassium carbonate (5.44 mmol) were dissolved in a mixture of toluene:butanol:water (4:1:2 ml) under nitrogen atmosphere and the catalyst, $Pd(PPh_3)_4$ was added. The resulting mixture was stirred overnight at 110°C. After that, the solvent was evaporated under reduce pressure , the solid was dissolved in DCM and washed with water (3×100 ml). The organic extracts were combined, dried over anhidrous Na_2SO_4 and the solvent was evaporated under reduce pressure. The organic solid was purified by column chromatography (SiO_2, DCM:MeOH) to obtain 280 mg of a yellow solid, 80% yield.

m.p.: 226-229°C (decomposition).

IR (ATR, cm^{-1}): 3437 (N-H), 2977 – 2860 (C-H), 1699 (C=O), 1657 (C=O), 1585, 1513, 1450,1420, 1352, 1244, 1169 (C-N), 1106, 999, 948, 780, 759.

^{1}H-NMR (300 MHz, $CDCl_3$) δ (ppm): 8.57 (d, *J* = 7.6 Hz, 2H, 2×**H$_{Ar}$**), 8.44 (m, 2H, 2×**H$_{Ar}$**), 8.21 (d, *J* = 8.4 Hz, 1H, **H$_{Ar}$**), 7.70 (dd, *J* = 8.4, 7.3 Hz, 1H, **H$_{Ar}$**), 7.60 (d, *J* = 7.6 Hz, 1H, **H$_{Ar}$**), 5.16 (m, 1H, C**H**), 4.26 (s, 2H, C**H**$_2$), 3.89 (m, 4H, 2×C**H**$_2$), 3.53 (m, 4H, 2×C**H**$_2$), 2.72 (m, 4H, 2×C**H**$_2$), 1.65 (m, 2H, C**H**$_2$), 1.47 (m, 18H, 6×C**H**$_3$).

^{13}C-NMR (75MHz, $CDCl_3$) δ (ppm): 164.5 (**C**=O), 164.3 (**C**=O), 161.2 (**C**=O), 158.2 (**C**$_{Ar}$H), 140.7 (**C**$_{Ar}$), 132.3 (**C**$_{Ar}$), 132.2 (**C**$_{Ar}$), 132.1 (**C**$_{Ar}$), 131.6 (**C**$_{Ar}$H), 131.1 (**C**$_{Ar}$H), 130.1 (**C**$_{Ar}$), 128.7 (**C**$_{Ar}$H), 128.5 (**C**$_{Ar}$H), 127.7 (**C**$_{Ar}$H), 127.3 (**C**$_{Ar}$H), 123.6 (**C**$_{Ar}$), 121.0 (**C**$_{Ar}$), 80.3 (**Cq**), 79.6 (**Cq**), 52.0 (**C**H), 43.9 (**C**H$_2$), 28.6 (**C**H$_3$), 28.5 (**C**H$_3$), 28.4 (**C**H$_2$) .

HRMS (MALDI, DIT-) m/z: calculated for $C_{35}H_{42}N_6O_6$: 642.3160 (M^-); found 642.3181.

UV-Vis ($CHCl_3$), λ_{max} nm (log ε): 380 (4.3).

Ø (MCH, %): 92.87.

τ (375 nm, MCH, ns): 2.853 (χ^2: 1.080).

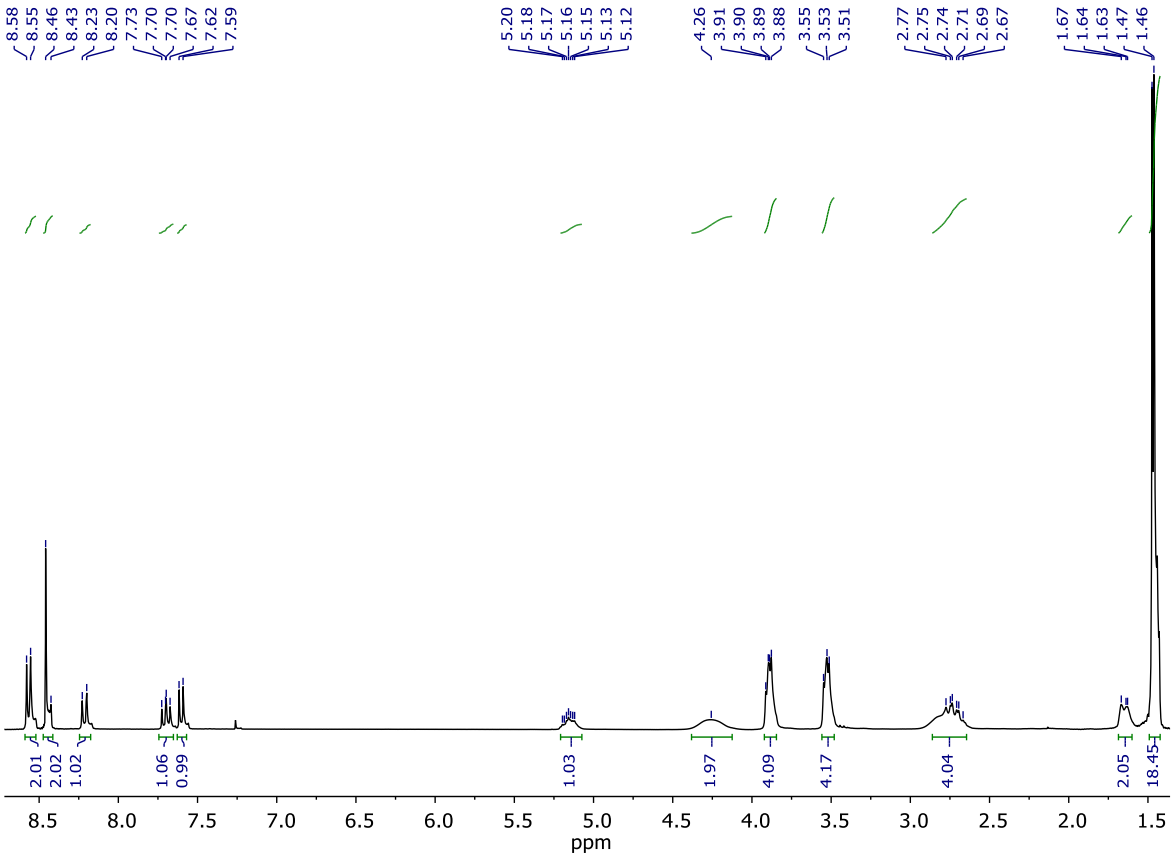

Figure 64. ^{1}H-NMR ($CDCl_3$, 300 MHz) of AR82p.

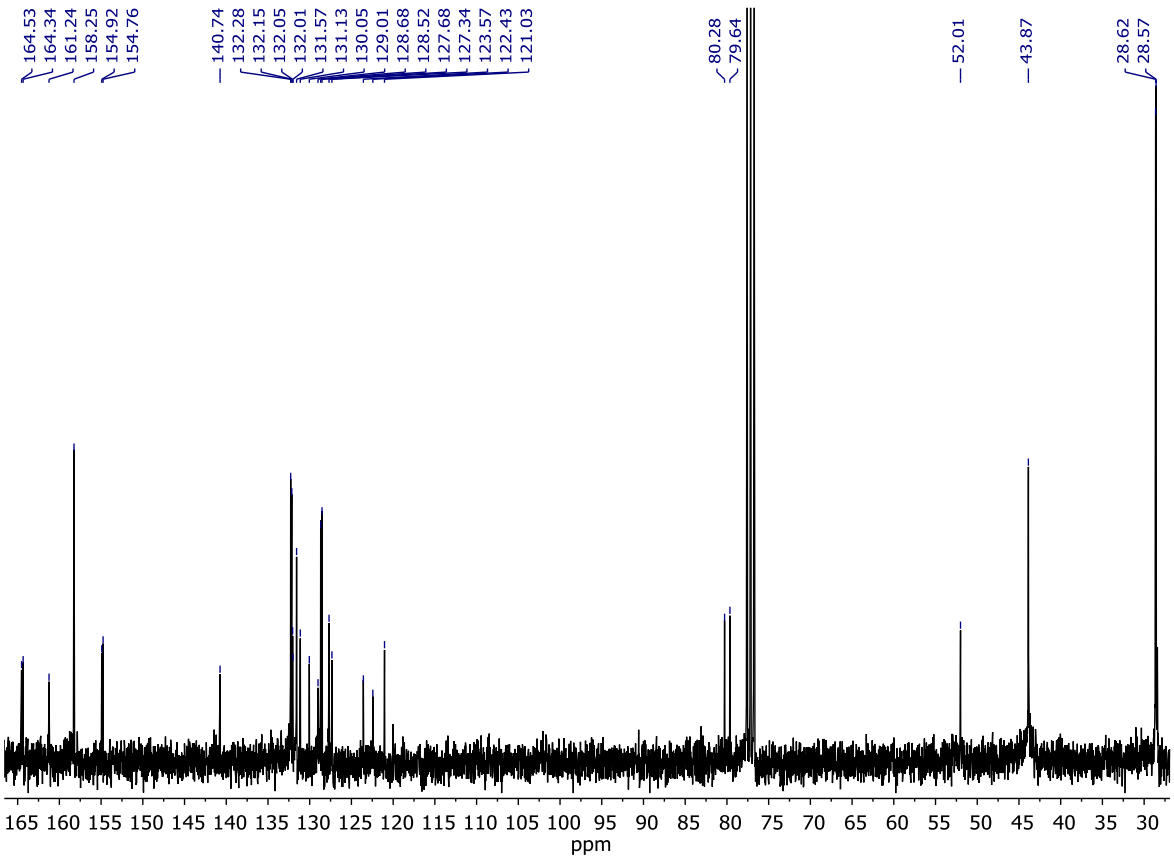

Figure 65. ^{13}C-NMR ($CDCl_3$, 75 MHz) of AR82p.

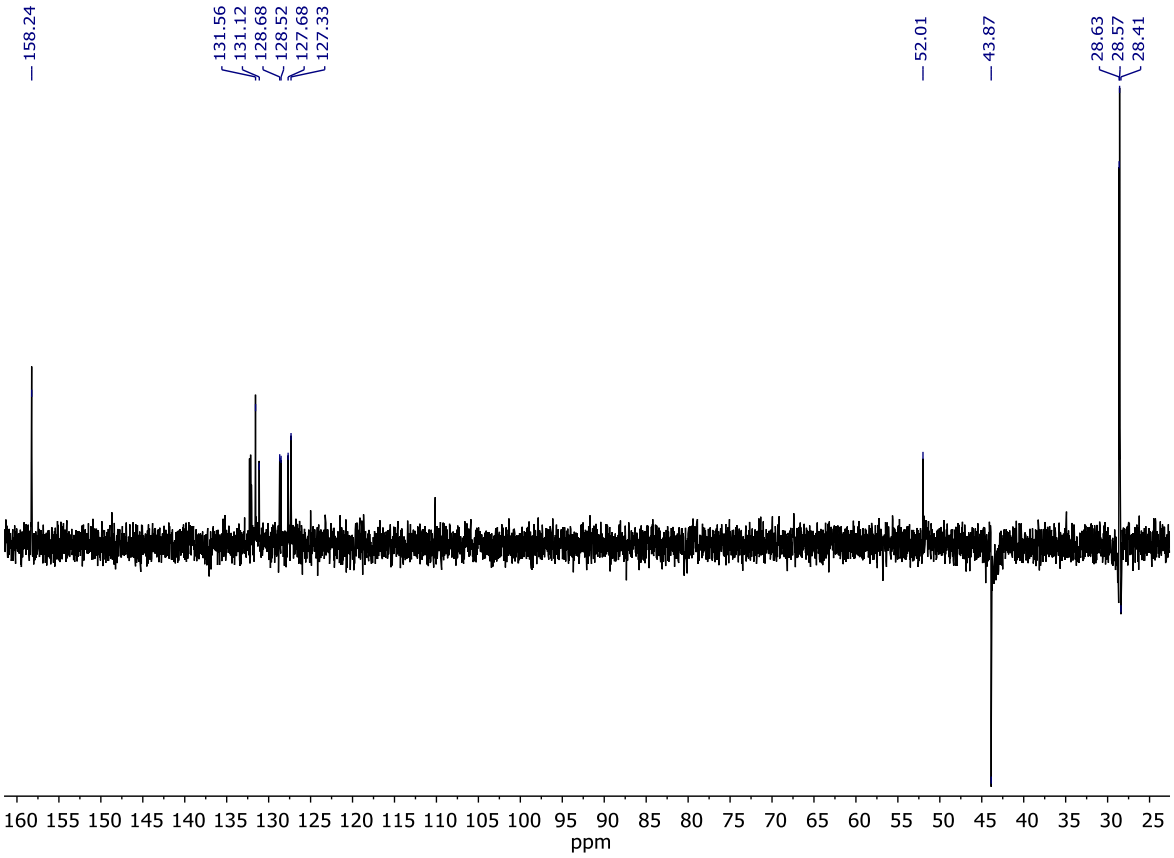

Figure 66. DEPT NMR ($CDCl_3$, 75 MHz) of AR82p.

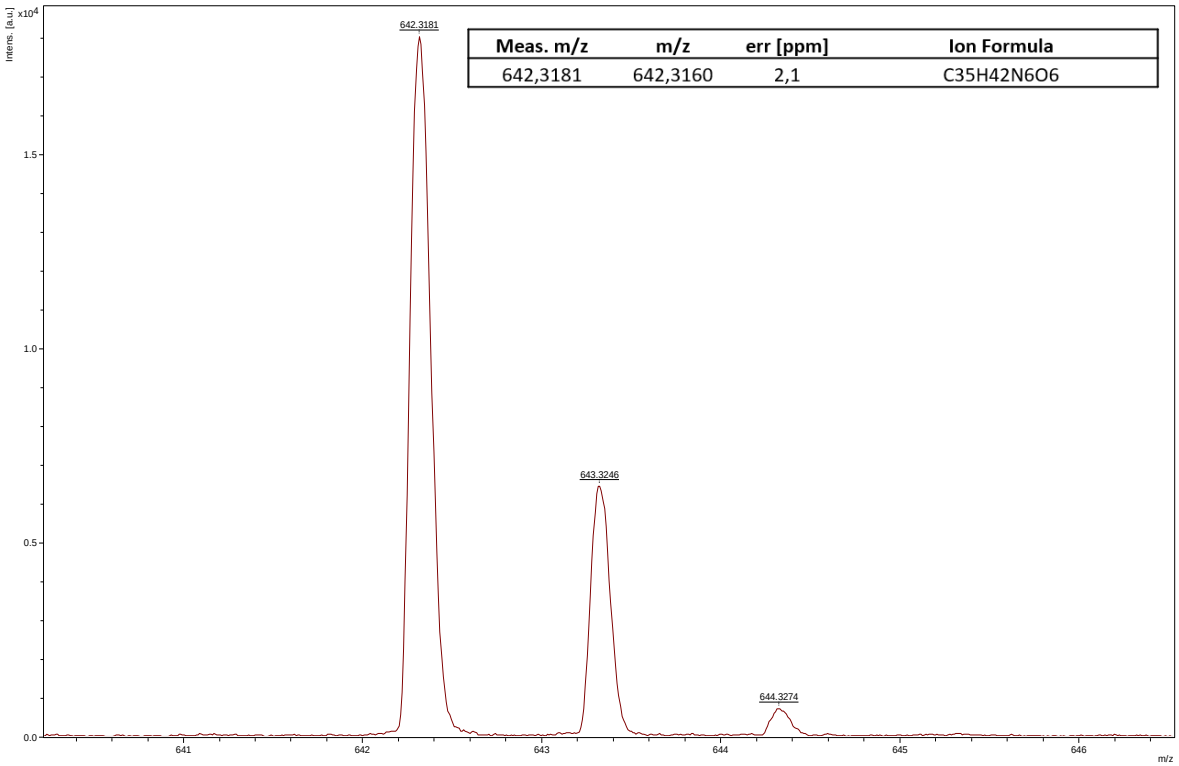

Figure 67. HRMS (MALDI, DIT-) of AR82p.

Solvatochromism:

The concentration of the compound was 20 µM and the excitation wavelength was 380 nm.

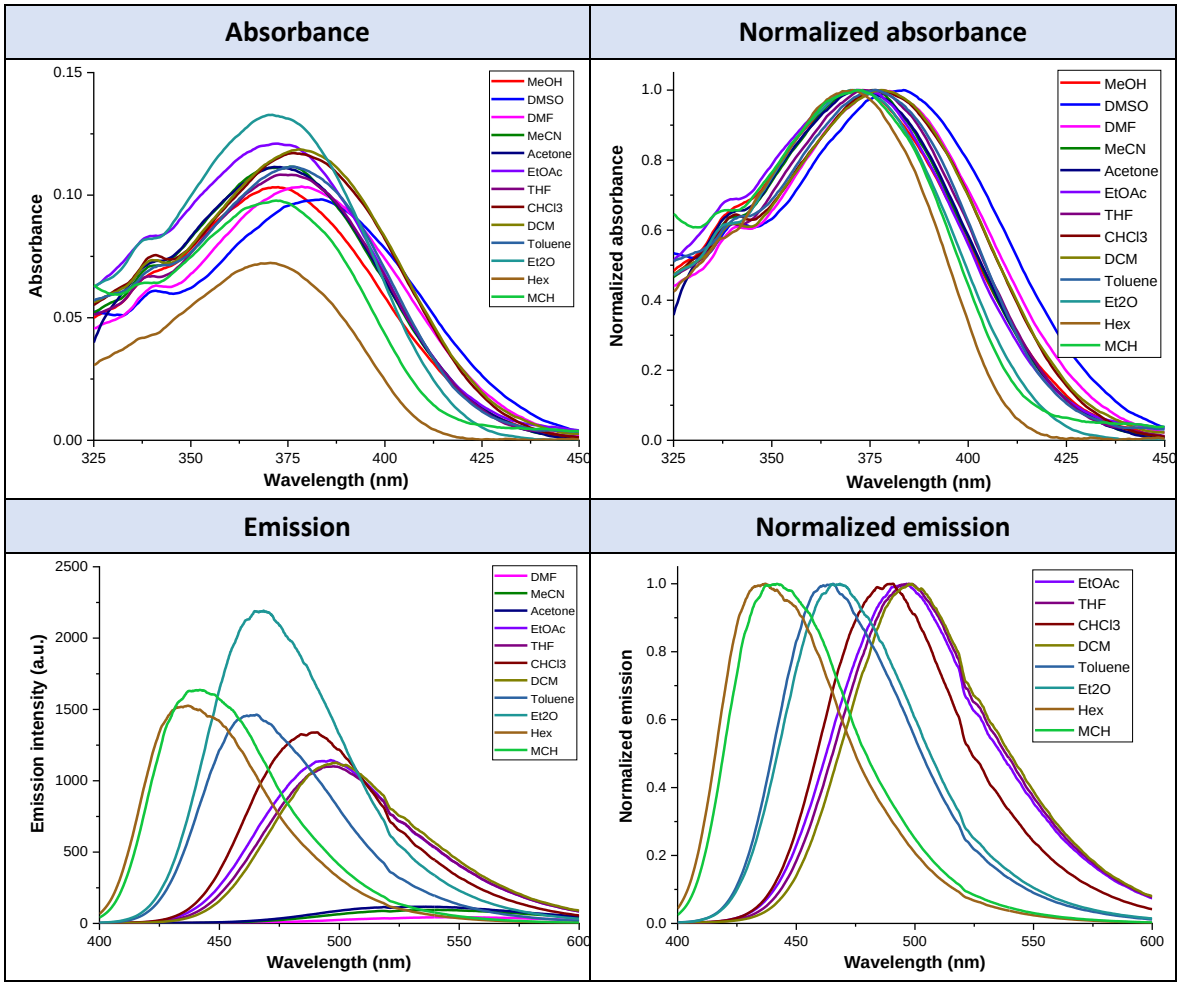

Figure 68. Solvatochromism of AR82p.

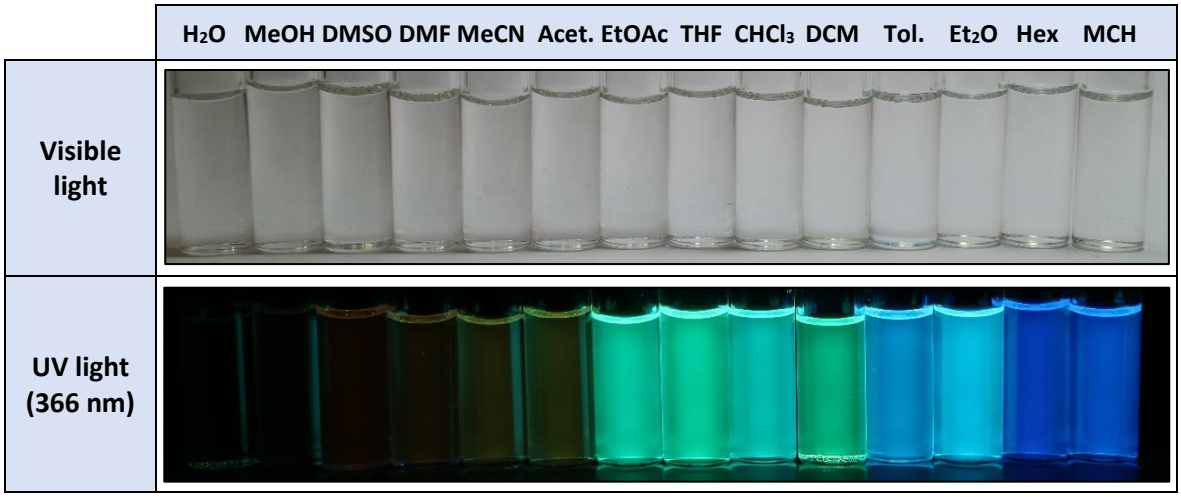

Figure 69. Solvatochromism of AR82p under visible and 366 nm light.

Fluorescence decay lifetime (τ):

The solvent used was MCH and the concentration of the compound was 20 µM.

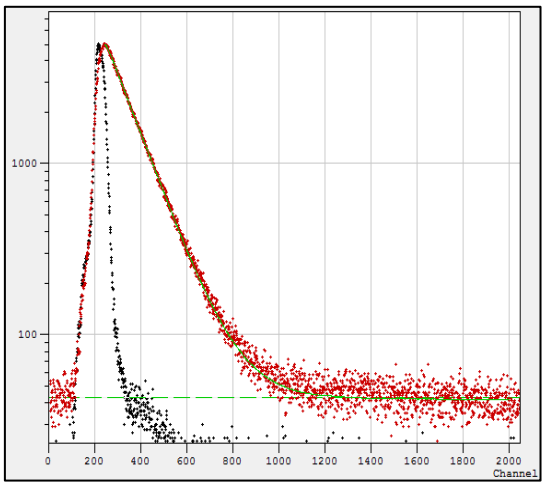

Figure 70. Fluorescence decay lifetime of AR82p.

Water acceptance test:

The solvent used was MeCN and THF and the concentration of the compound was 20 µM.

	R	5%	10%	20%	30%	40%	50%	60%	70%	80%	90%
Visible light	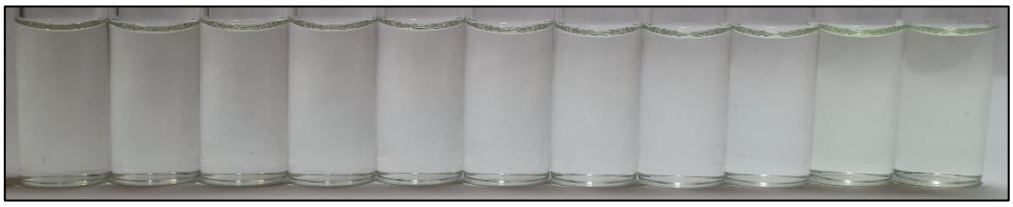										
UV light (366 nm)	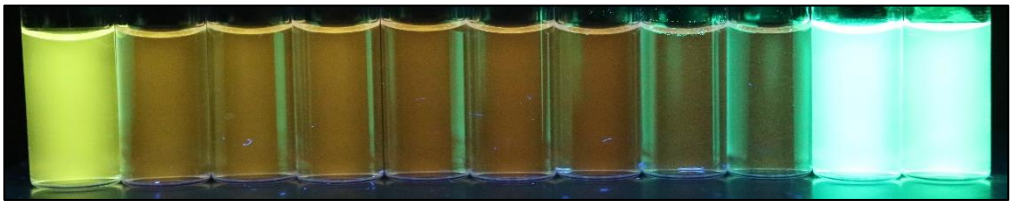										

Figure 71. Water acceptance test of AR82p in MeCN under visible (up) and UV (down) light.

	R	5%	10%	20%	30%	40%	50%	60%	70%	80%	90%
Visible light	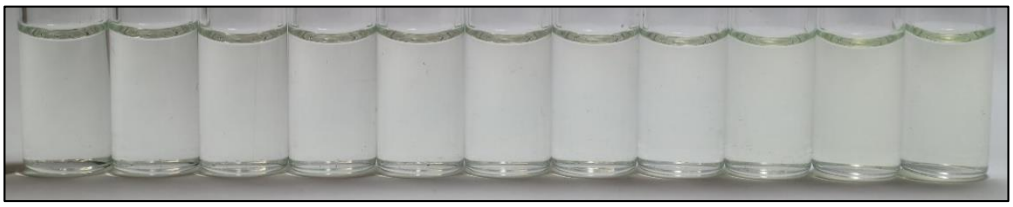										
UV light (366 nm)	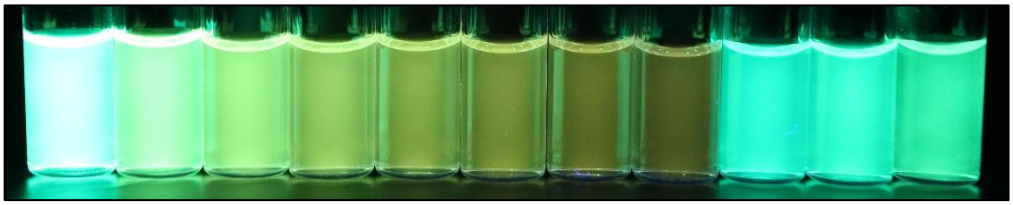										

Figure 72. Water acceptance test of AR82p in THF under visible (up) and UV (down) light.

There was a marked increase in emission intensity from 80% water (AIE). This phenomenon was also studied using THF as solvent and the same amounts of water. In this solvent, a slight increase in the intensity of fluorescent emission was observed from 70% water. In both cases, there was a shift of the emission maximum from brown-yellow (535 – 545 nm) to green region (about 475 nm).

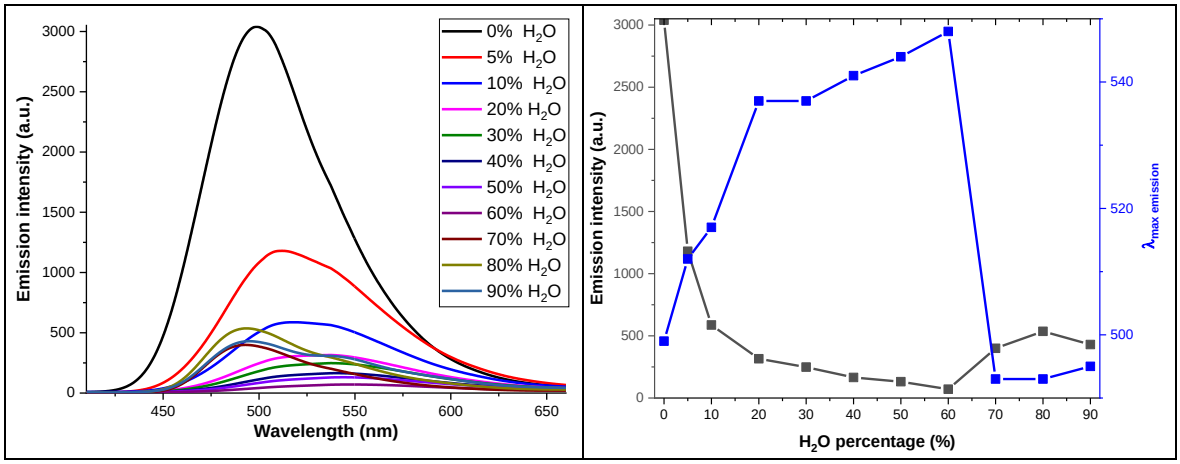

Figure 73. Emission intensity graph (left) and graph of relationship between the emission intensity and the wavelength of the maximum of emission (right) as a function of the amount of water added for AR82p in THF.

pH test:

The prortion of water that the compound could accept was 40%. The concentration of the compound was 20 µM and the solvent used was MeCN.

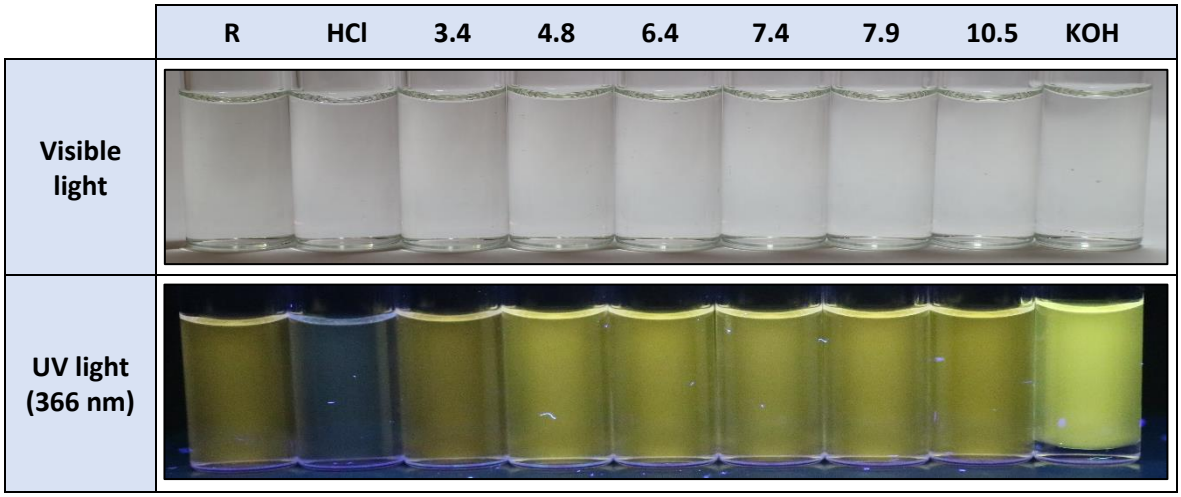

Figure 74. pH test of AR82p under visible (up) and UV (down) light.

The most significative change was the quenching of the emission at very acidic pH and the fluorescence colour change to yellow at very basic pH.

Cations and anions test:

The concentration of the compound was 20 µM and the solvent used was MeCN.

	R	Ag^{+}	Ni^{2+}	Sn^{2+}	Cd^{2+}	Zn^{2+}	Pb^{2+}	Cu^{2+}	Fe^{3+}	Sc^{3+}	Al^{3+}	Hg^{2+}	Au^{3+}	Co^{2+}	Pd^{2+}	Ir^{3+}	Cu^{+}	Ru^{3+}	Pt^{2+}
Visible light																			
UV light (366 nm)	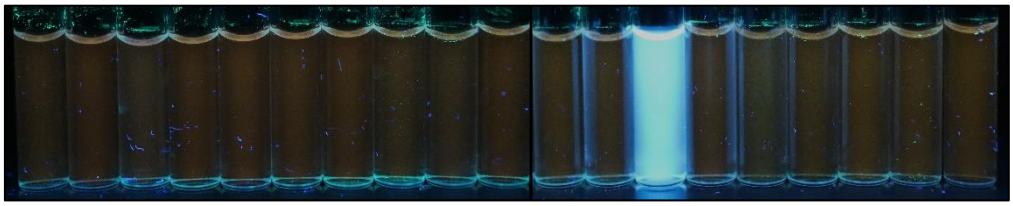																		

Figure 75. Cations test of AR82p under visible (up) and UV (down) light.

Under visible light, a response to Pd^{2+} was observed, while under UV light, a fluorescence change to blue was taken place to Au^{3+}.

The concentration of the compound was 20 µM and the solvent used was MeCN.

	R	F^{-}	Cl^{-}	Br^{-}	I^{-}	BzO^{-}	NO_3^{-}	$H_2PO_4^{-}$	HSO_4^{-}	AcO^{-}	CN^{-}	SCN^{-}
Visible light	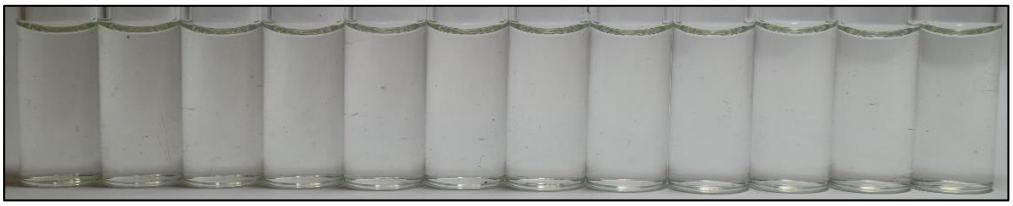											
UV light (366 nm)	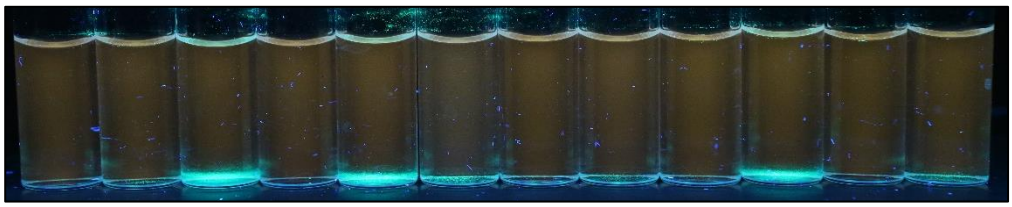											

Figure 76. Anions test of AR82p under visible (up) and UV (down) light.

No significant changes were observed.

Oxidant and reductant reagents test:

The solvent used was MeCN and concentration of the compound was 20 µM.

	R	HCl	HNO_3	*m*-CPBA	Oxn	Hz	H_2O_2	TNB	TNT	TATP
Visible light	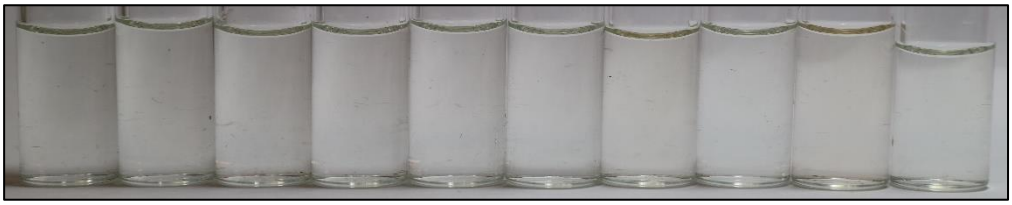									
UV light (366 nm)	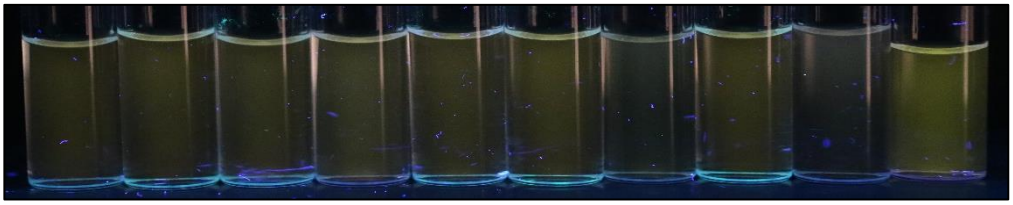									

Figure 77. Oxidant and reductant reagents test of AR82p under visible (up) and UV (down) light.

No significant changes were observed.

SEM nanoparticles:

AR82p 10% of water	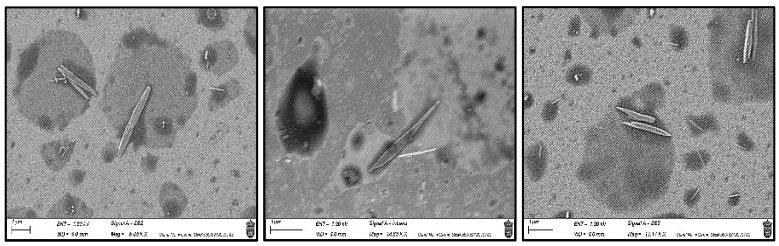
AR82p 30% of water	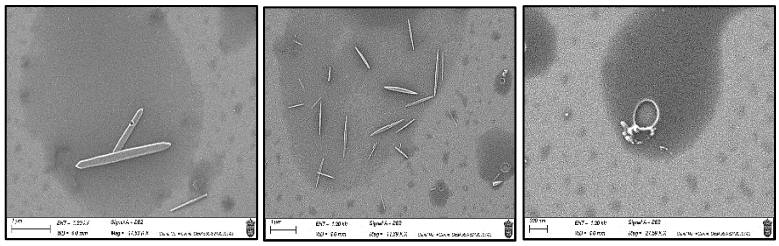
AR82p 60% of water	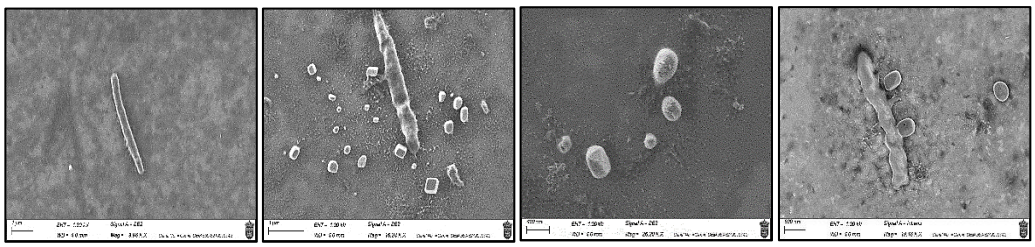
AR82p 70% of water	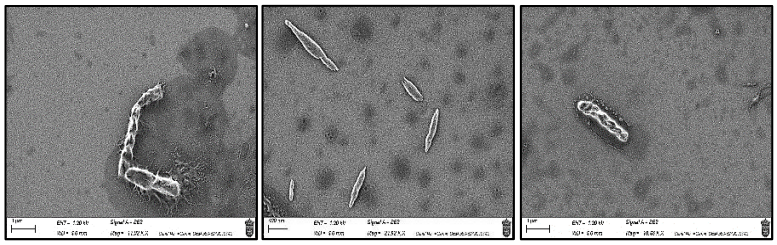
AR82p 90% of water	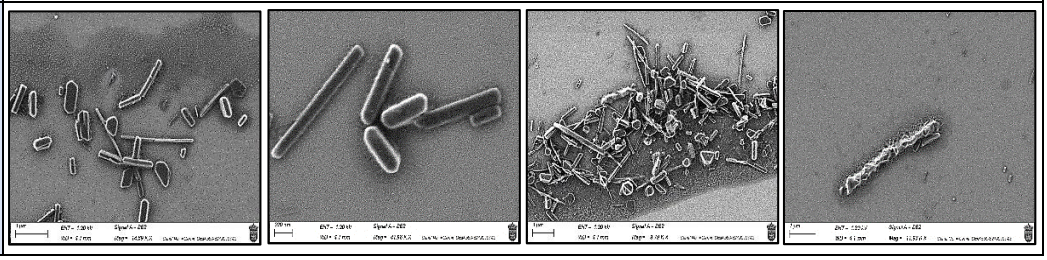

Figure 78. SEM nanoparticles of AR82p in different mixtures of water and THF.

Synthesis of *N*-(piperidin-4-yl)-4-[2-(4-Boc-piperazin-1-yl)pyrimidin-5-yl]naphthalene-1,8-dicarboxylmonoimide (AR82s)

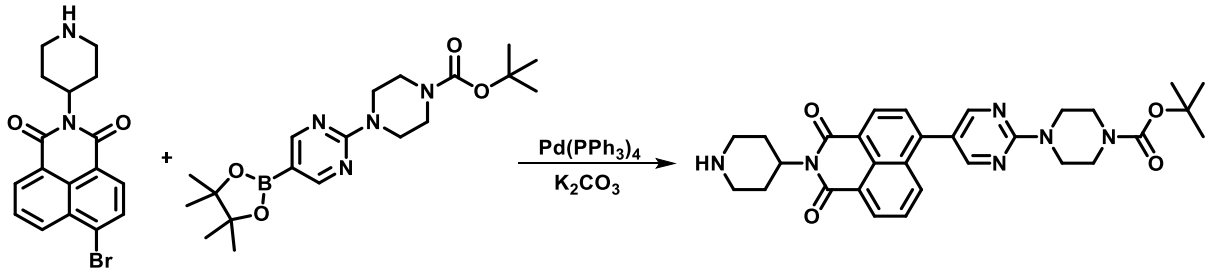

150 mg of *N*-(piperidin-4-yl)-4-bromonaphthalene-1,8-dicarboxylmonoimide (AR43d, 0.42 mmol), 172 mg of 2-(4-Boc-piperazine)pyrimidine-5-boronic acid pinacol ester (0.44 mmol) and 451 mg of potassium carbonate (3.26 mmol) were dissolved in a mixture of toluene:*n*-butanol:water (4:1:2 ml) under nitrogen atmosphere and, then, the $Pd(PPh_3)_4$ was added. The resulting mixture was stirred overnight at 110°C, the solvent was evaporated under reduce pressure. The solid was dissolved in DCM and washed with water (3×100 ml). The organic extracts were combined, dried over anhidrous Na_2SO_4 and the solvent was evaporated under reduce pressure. The organic solid was purified by column chromatography (SiO_2, DCM:MeOH) getting 87 mg of a yellow solid, 38% yield.

m.p.: 302-304°C (decomposition).

IR (ATR, cm^{-1}): 3440 (N-H), 2922 – 2480, 1693 (C=O), 1650 (C=O), 1585, 1509, 1450 (C-O), 1402, 1351, 1238, 1162 (C-N), 1121, 998, 947, 780, 753, 687, 642, 508.

^{1}H-NMR (300 MHz, $CDCl_3$) δ (ppm): 8.62 (dd, *J* = 7.4, 1.7 Hz, 2H, 2×**H$_{Ar}$**), 8.50 (s, 2H, 2×**H$_{Ar}$**), 8.25 (dd, *J* = 8.5, 1.1 Hz, 1H, **H$_{Ar}$**), 7.73 (dd, *J* = 8.5, 7.4 Hz, 1H, **H$_{Ar}$**), 7.64 (d, *J* = 7.4 Hz, 1H, **H$_{Ar}$**), 5.26 – 5.13 (m, 1H, C**H**), 3.93 (m, 4H, 2×C**H**$_2$), 3.56 (m, 4H, 2×C**H**$_2$), 3.29 (m, 2H, C**H**$_2$), 2.89 – 2.65 (m, 4H, 2×C**H**$_2$), 2.13 (s, 1H, N**H**), 1.73 (m, 2H, C**H**$_2$), 1.51 (s, 9H, 3×C**H**$_3$).

^{13}C-NMR (75MHz, $CDCl_3$) δ (ppm): 164.5 (**C**=O), 164.3 (**C**=O), 164.1 (**C**=O), 158.2 (**C**$_{Ar}$H), 154.9 (**C**$_{Ar}$), 140.7 (**C**$_{Ar}$), 132.1 (**C**$_{Ar}$), 131.9 (**C**$_{Ar}$H), 131.8 (**C**$_{Ar}$), 131.7 (**C**$_{Ar}$), 131.5 (**C**$_{Ar}$), 131.4 (**C**$_{Ar}$), 130.1 (**C**$_{Ar}$), 129.0 (**C**$_{Ar}$), 127.8 (**C**$_{Ar}$H), 127.5 (**C**$_{Ar}$H), 123.3 (**C**$_{Ar}$), 122.2 (**C**$_{Ar}$), 121.0 (**C**$_{Ar}$), 80.4 (**Cq**), 44.1 (**C**H$_2$), 28.6 (**C**H$_3$), 25.8 (**C**H$_2$).

HRMS (MALDI, DCTB+) m/z: calculated for $C_{30}H_{34}N_6O_4$: 543.2714 (M^+ + H); found 543.2689.

UV-Vis ($CHCl_3$), λ_{max} nm (log ε): 385 (4.9).

Ø ($CHCl_3$, %): 73.00.

τ (375 nm, $CHCl_3$, ns): 3.962 (χ^2: 1.072).

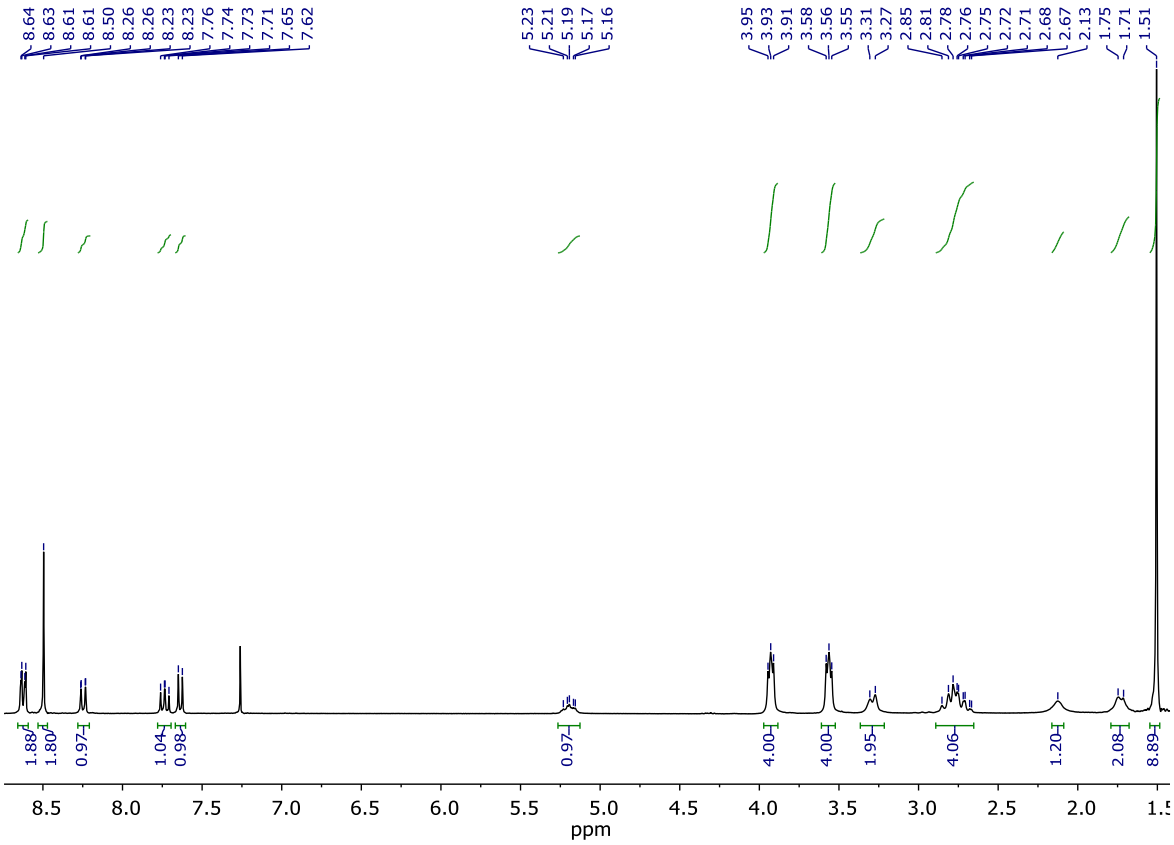

Figure 79. ^{1}H-NMR ($CDCl_3$, 300 MHz) of AR82s.

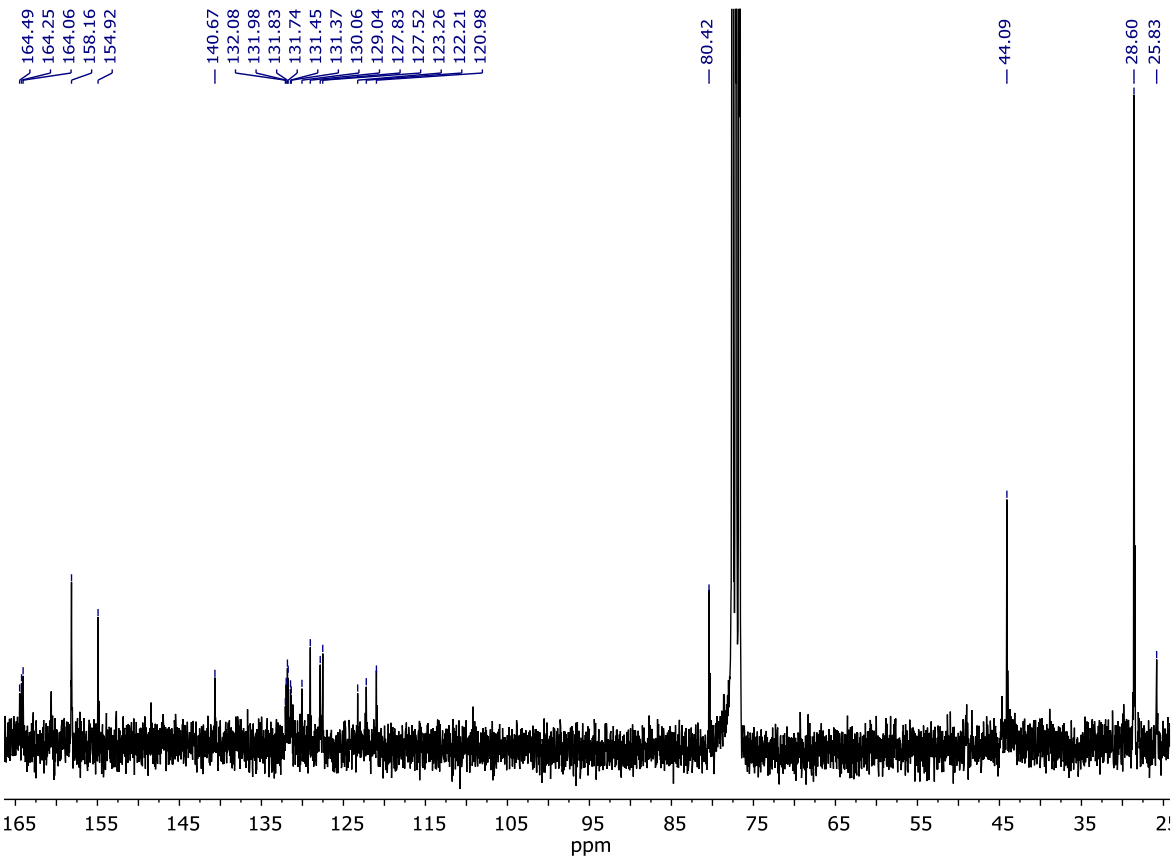

Figure 80. ^{13}C-NMR ($CDCl_3$, 75 MHz) of AR82s.

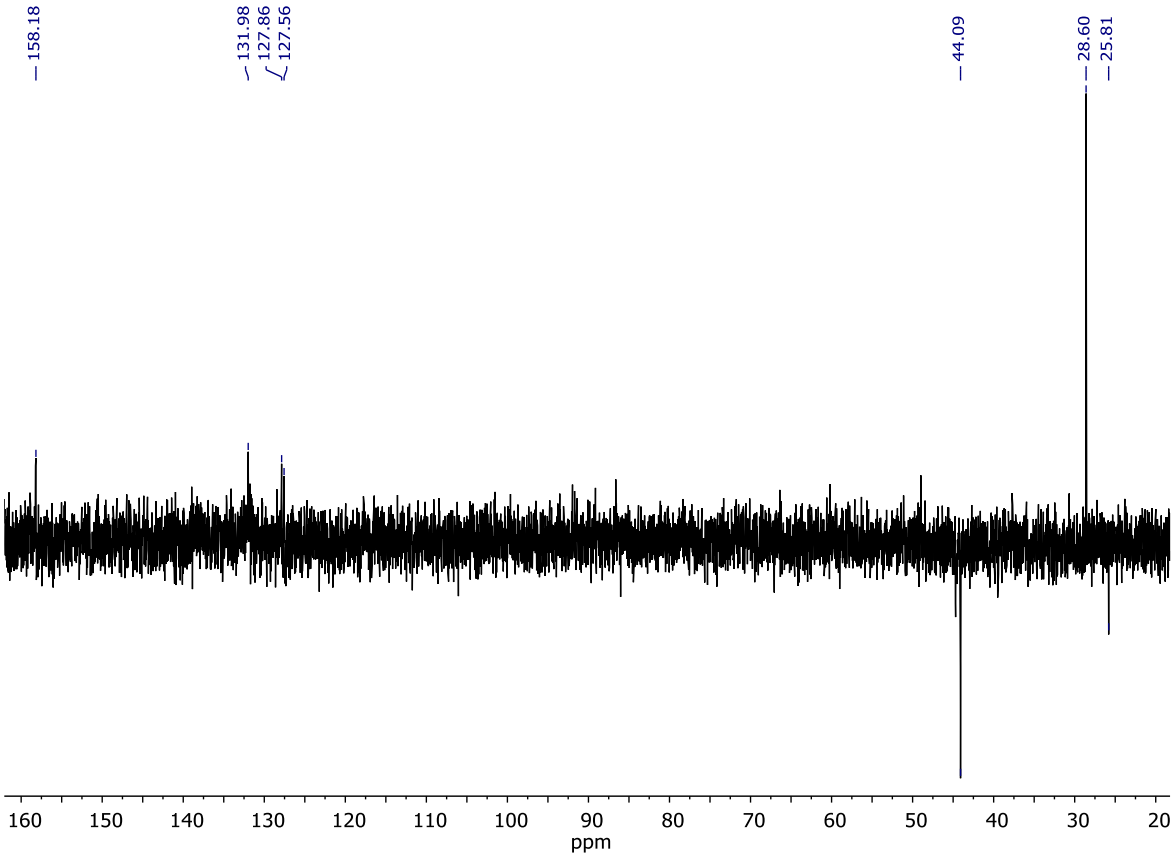

Figure 81. DEPT NMR ($CDCl_3$, 75 MHz) of AR82s.

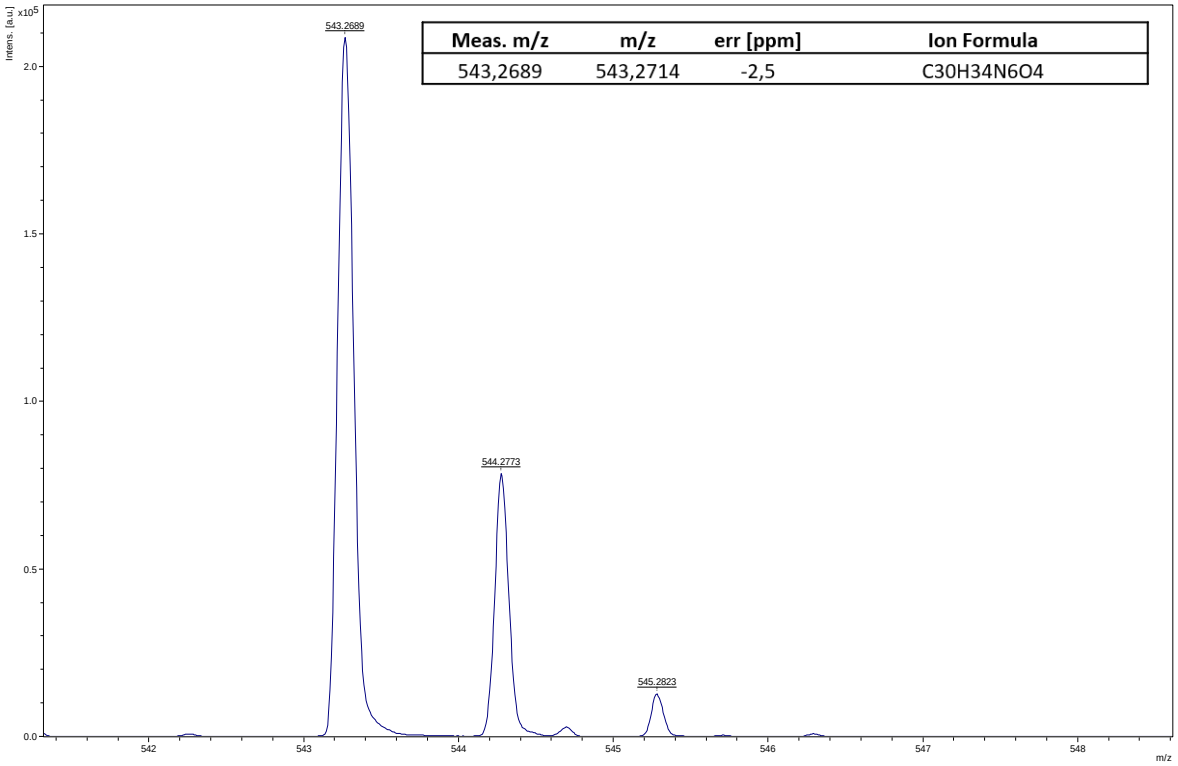

Meas. m/z	m/z	err [ppm]	Ion Formula
543,2689	543,2714	-2,5	C30H34N6O4

Figure 82. HRMS (MALDI, DCTB+) of AR82s.

Solvatochromism:

The concentration of the compound was 20 µM and the excitation wavelength was 370 nm.

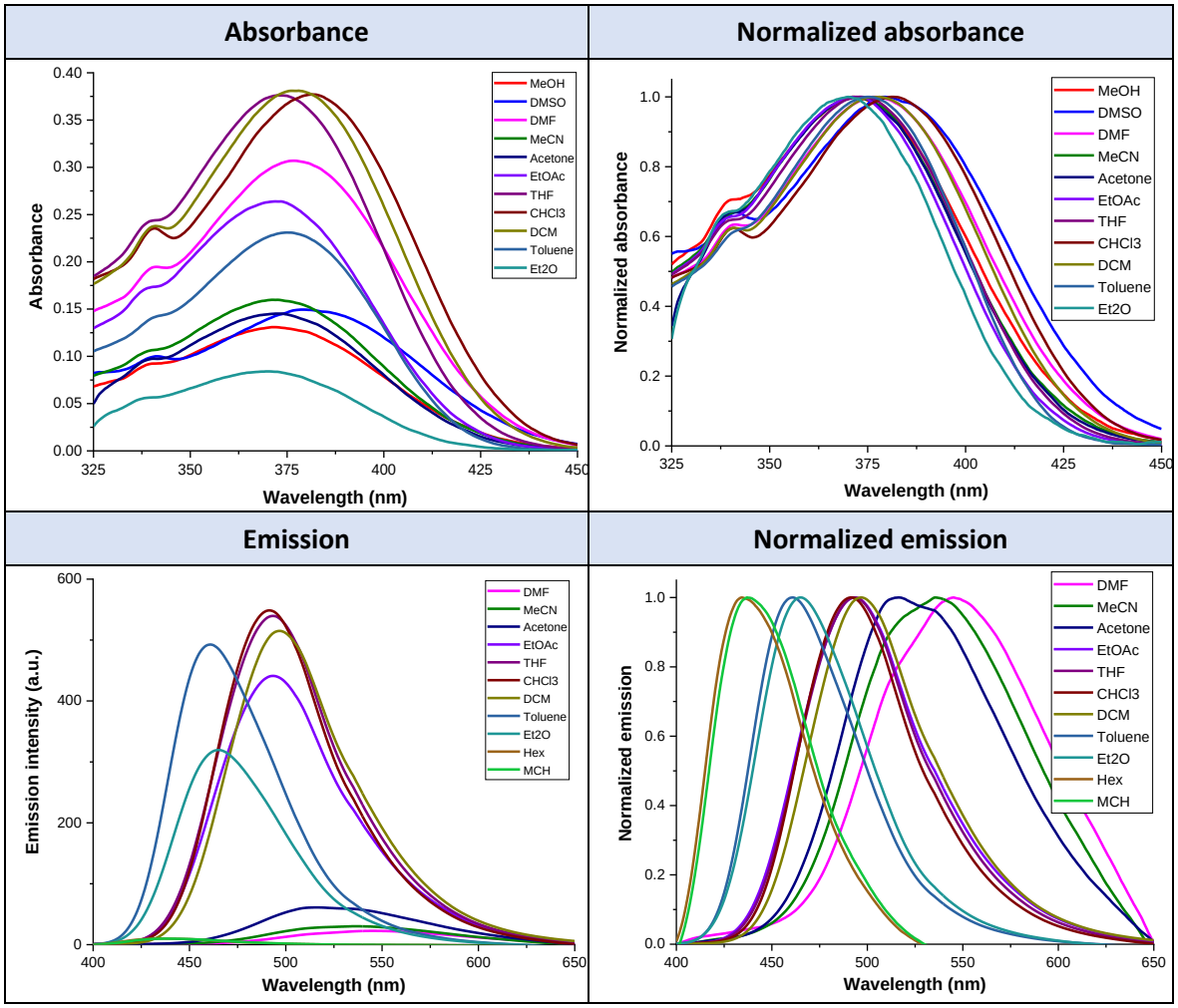

Figure 83. Solvatochromism of AR82s.

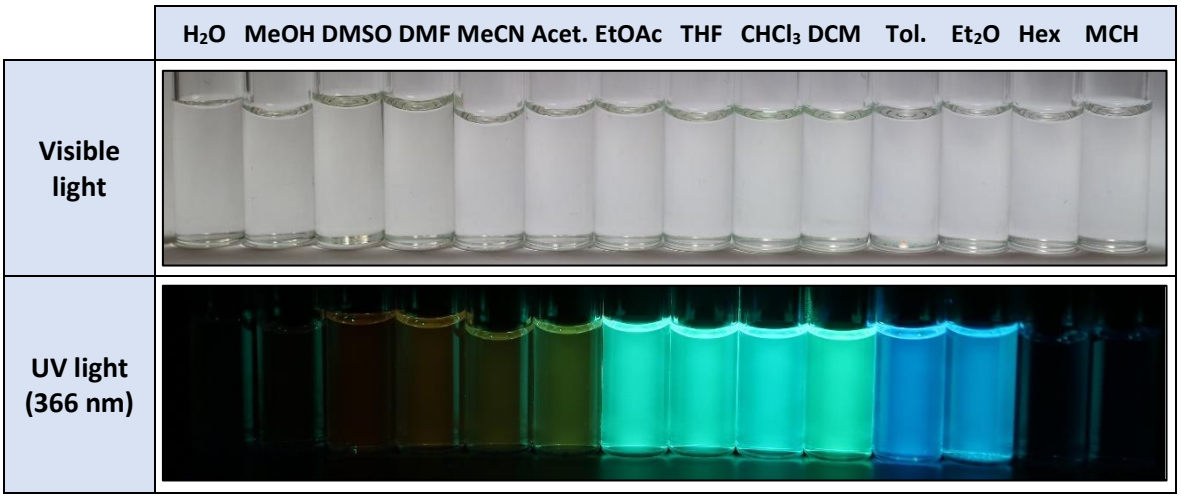

Figure 84. Solvatochromism of AR82s under visible and 366 nm light.

Fluorescence decay lifetime (τ):

The solvent used was $CHCl_3$. The concentration of the compound was 20 µM.

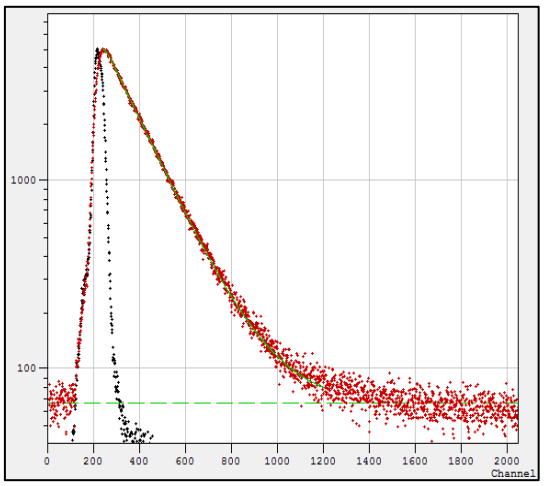

Figure 85. Fluorescence decay lifetime of AR82s.

Water acceptance test:

The solvent used was acetone and the concentration of the compound was 20 µM.

	R	5%	10%	20%	30%	40%	50%	60%	70%	80%	90%
Visible light											
UV light (366 nm)	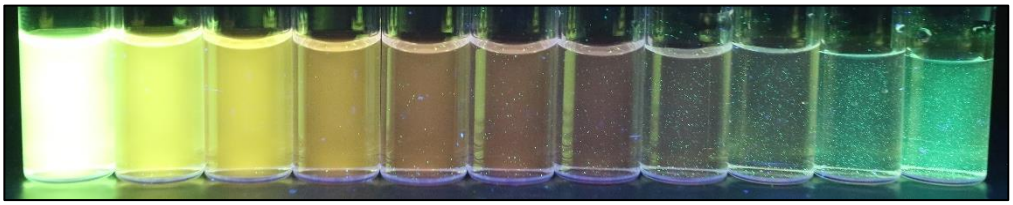										

Figure 86. Water acceptance test of AR82s in acetone under visible (up) and UV (down) light.

	R	5%	10%	20%	30%	40%	50%	60%	70%	80%	90%
Visible light	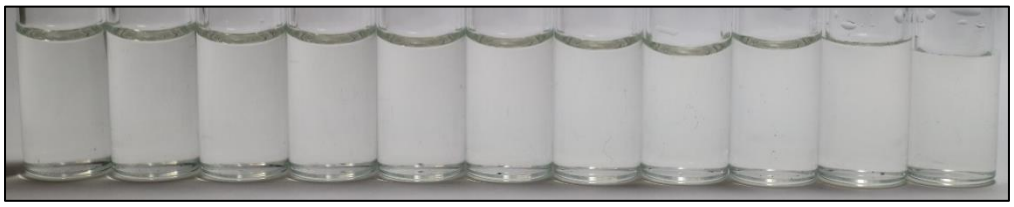										
UV light (366 nm)	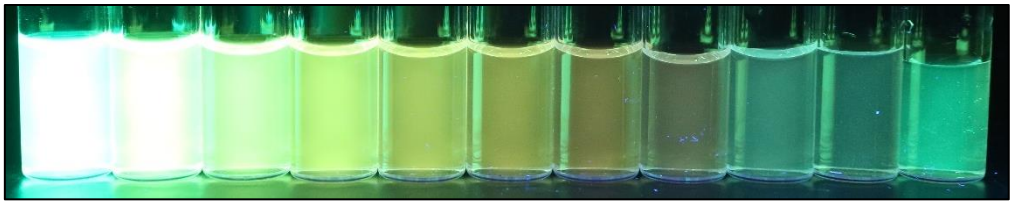										

Figure 87. Water acceptance test of AR82s in THF under visible (up) and UV (down) light.

There was a very slight increase in emission intensity at 80% and 90% of water (AIE) and the result using THF as a solvent was very similar. The emission maximum was shifted from yellow region (530-555 nm), with intermediate amounts of water, to the green region (490 – 505 nm), with high water content.

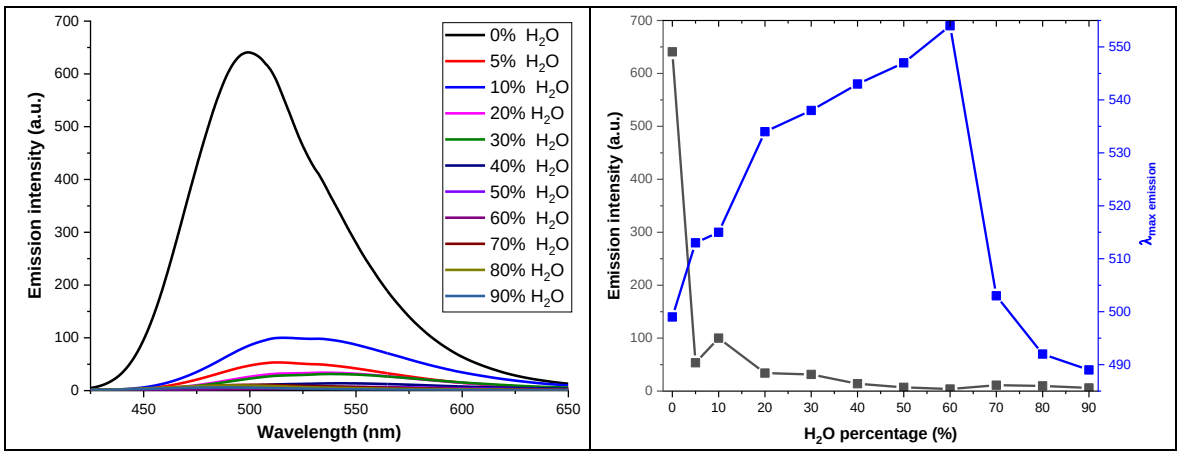

Figure 88. Emission intensity graph (left) and graph of relationship between the emission intensity and the wavelength of the maximum of emission (right) as a function of the amount of water added for AR82s using THF as a solvent.

SEM nanoparticles:

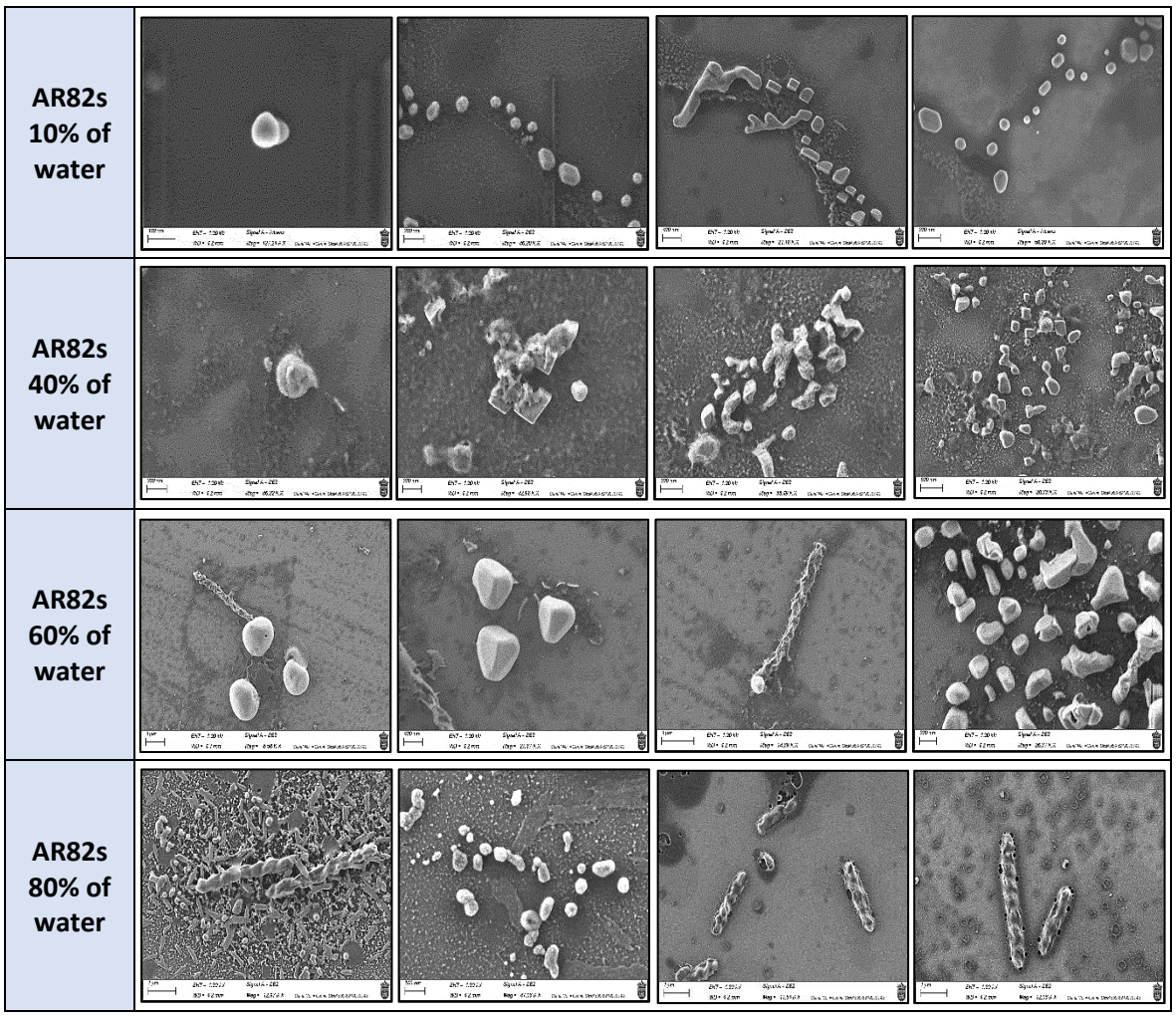

Figure 89. SEM nanoparticles of AR82s in different mixtures of water and THF.

pH test:

The amount of water that the compound could accept was 20%. The concentration of the compound was 20 µM and the solvent used was acetone.

	R	HCl	3.4	4.8	6.4	7.4	7.9	10.5	KOH
Visible light	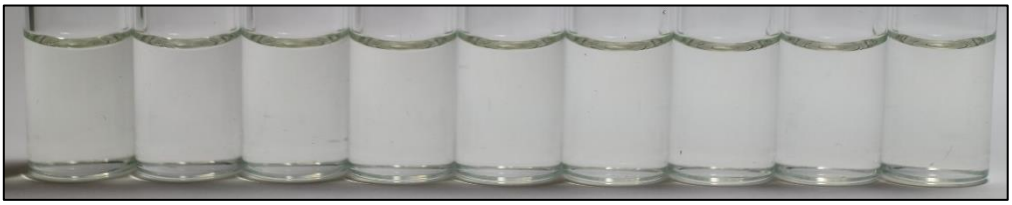								
UV light (366 nm)	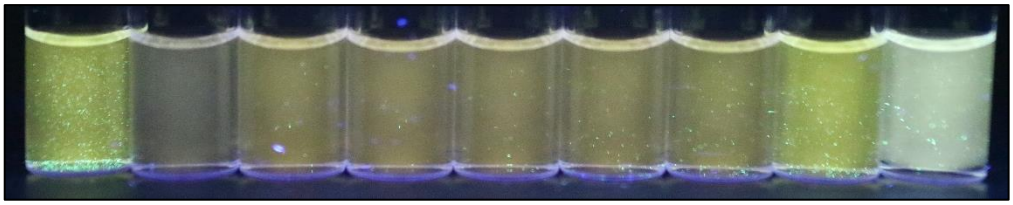								

Figure 90. pH test of AR82s under visible (up) and UV (down) light.

The most significative change was the quenching of the emission at very acidic pH and the fluorescence colour change to white at very basic pH. For intermediate pH, the fluorescence was turned brownish.

Cations and anions test:

The concentration of the compound was 20 µM and the solvent used was acetone.

	R	Ag^{+}	Ni^{2+}	Sn^{2+}	Cd^{2+}	Zn^{2+}	Pb^{2+}	Cu^{2+}	Fe^{3+}	Sc^{3+}	Al^{3+}	Hg^{2+}	Au^{3+}	Co^{2+}	Pd^{2+}	Ir^{3+}	Cu^{+}	Ru^{3+}	Pt^{2+}
Visible light																			
UV light (366 nm)	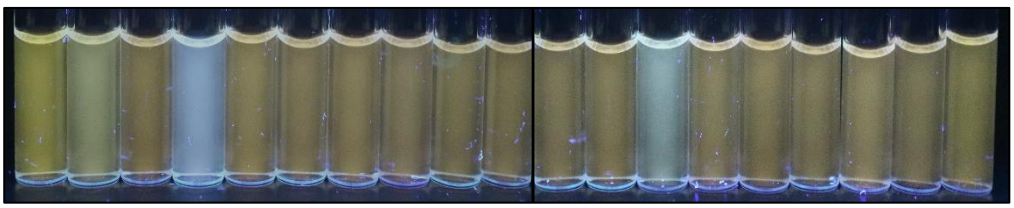																		

Figure 91. Cations test of AR82s under visible (up) and UV (down) light.

The most significant changes under UV light were the turn of the fluorescence to white against Sn^{2+} and Au^{3+}.

The concentration of the compound was 20 µM and the solvent used was acetone.

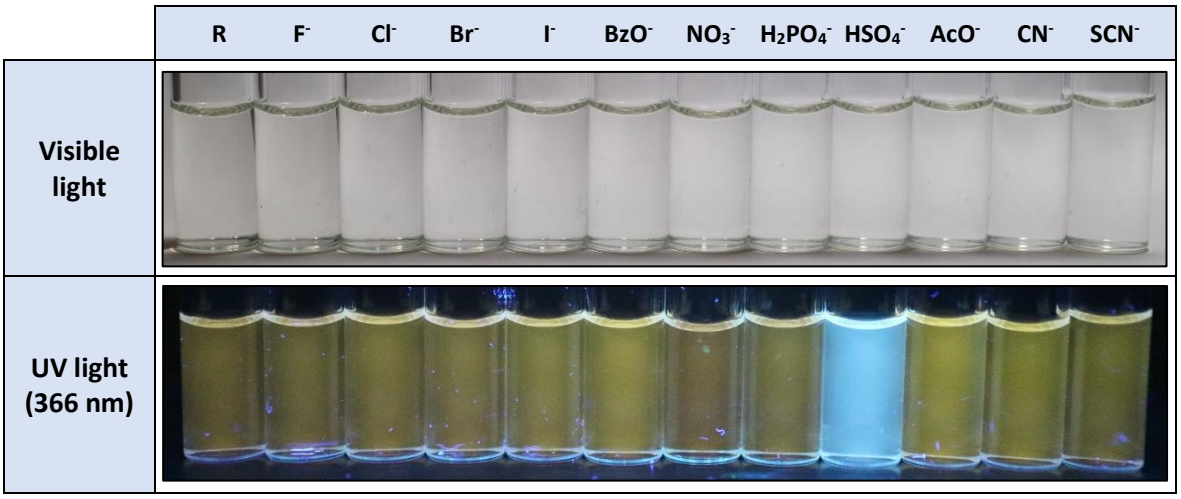

Figure 92. Anions test of AR82s under visible (up) and UV (down) light.

The only response of the probe to the different anionic analytes was against HSO_4^-.

Oxidant and reductant reagents test:

The solvent used was acetone and concentration of the compound was 20 µM.

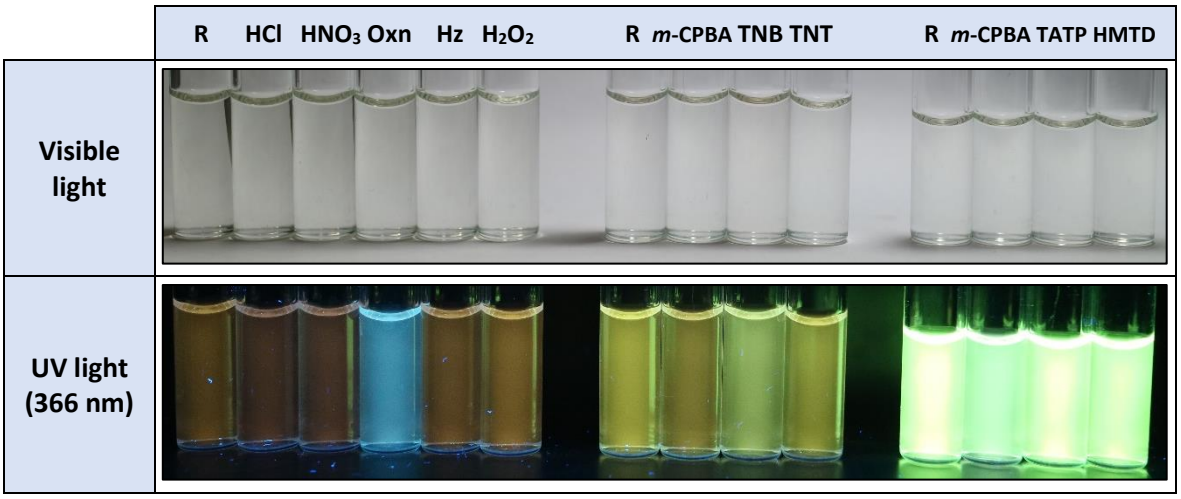

Figure 93. Oxidant and reductant reagents test of AR82s under visible (up) and UV (down) light.

The most significant change was the turn of the fluorescence to blue against oxone.

Previous solvents test:

In order to determine the fluorescence variation of the compound under study in the presence of TATP, some test were carried out for the probe in 9 different solvents. The AR82s concentration was 20 µM and the TATP was added in excess (7 mg in each vial). All the test were performed at room temperature and the photographs were taken immediately after the addition of TATP and again after 24 hours.

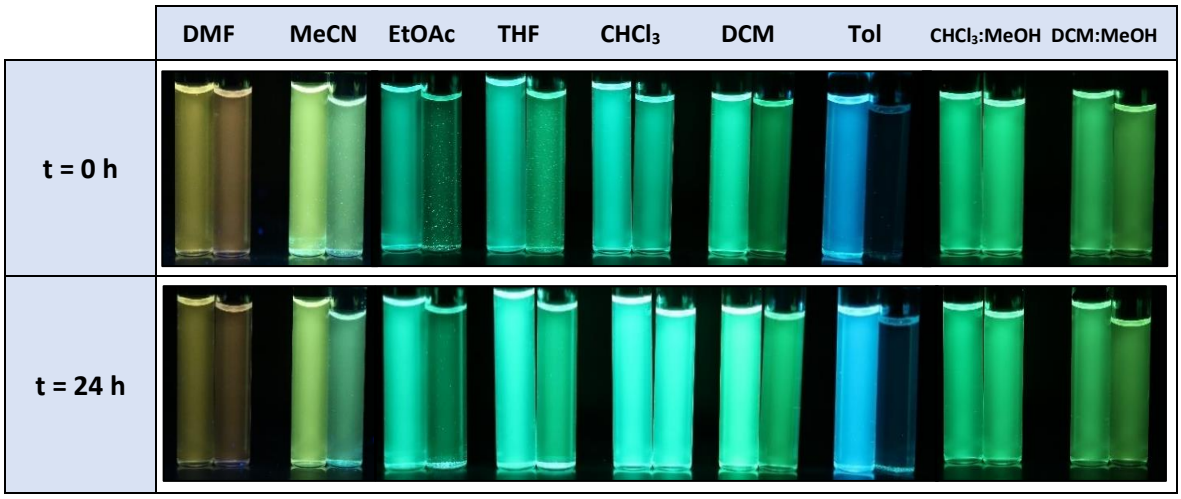

Figure 94. Pairs of AR82s (left) and AR82s with excess of TATP (right) in different solvents at time 0 h (up) and 24 h (down).

The biggest changes were seen in DMF and MeCN with a fluorescence colour change and in toluene and DCM with a decrease in the emission intensity.

Work concentration test:

In order to choose an optimum concentration for the next quantitative studio, the absorbance and fluorescence of the probe was checked to be linear while concentration changes was small, even when working with an excess of *m*-CPBA (7000 µM). The solvent used for this test was DCM and the excitation wavelength was 370 nm for all measurements.

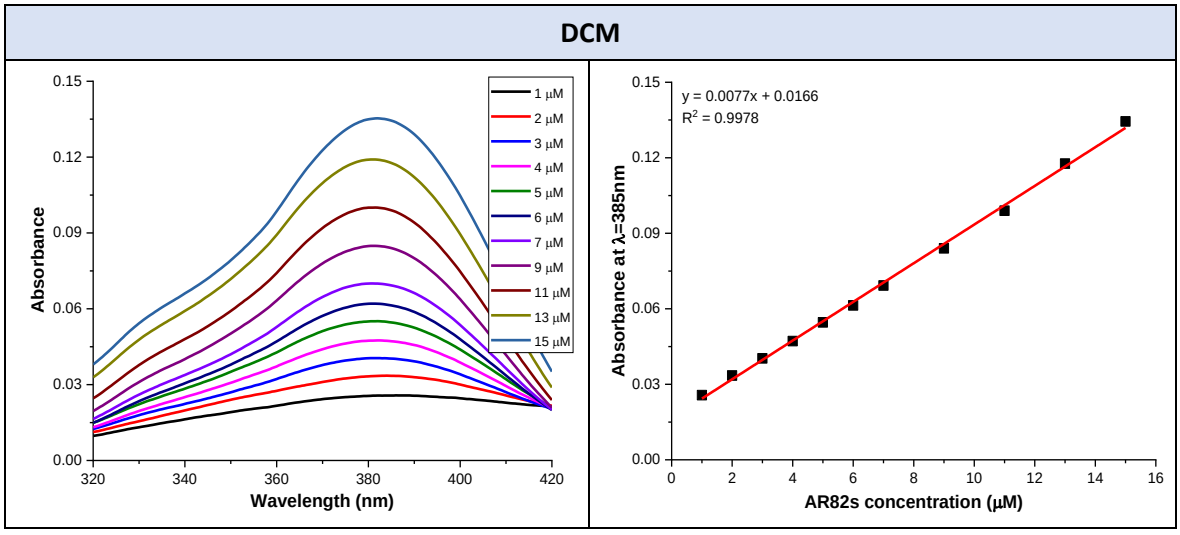

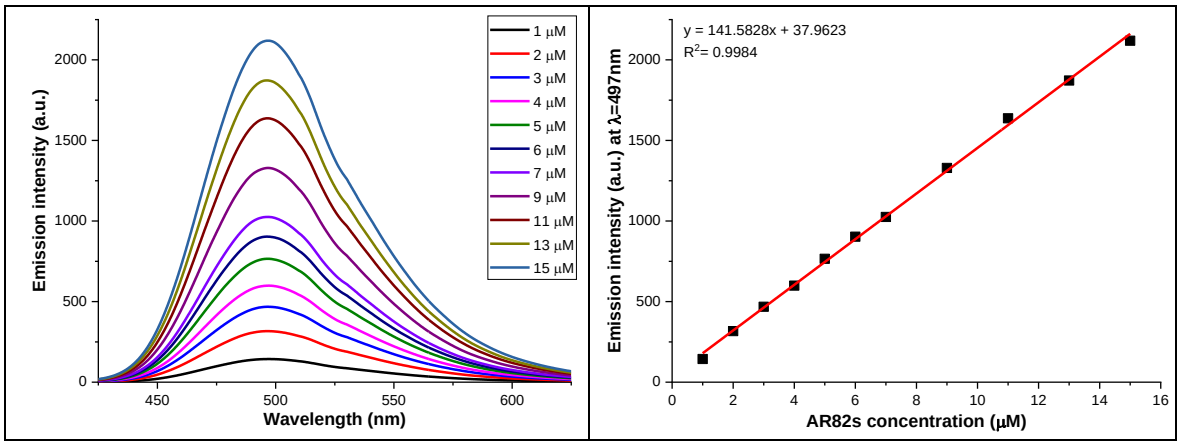

Figure 95. Absorbance spectrum (up left), absorbance profile at 385 nm (up right), fluorescence spectrum (down left) and fluorescence profile at 497 nm (down right) of increasing concentrations of AR82s solution in DCM.

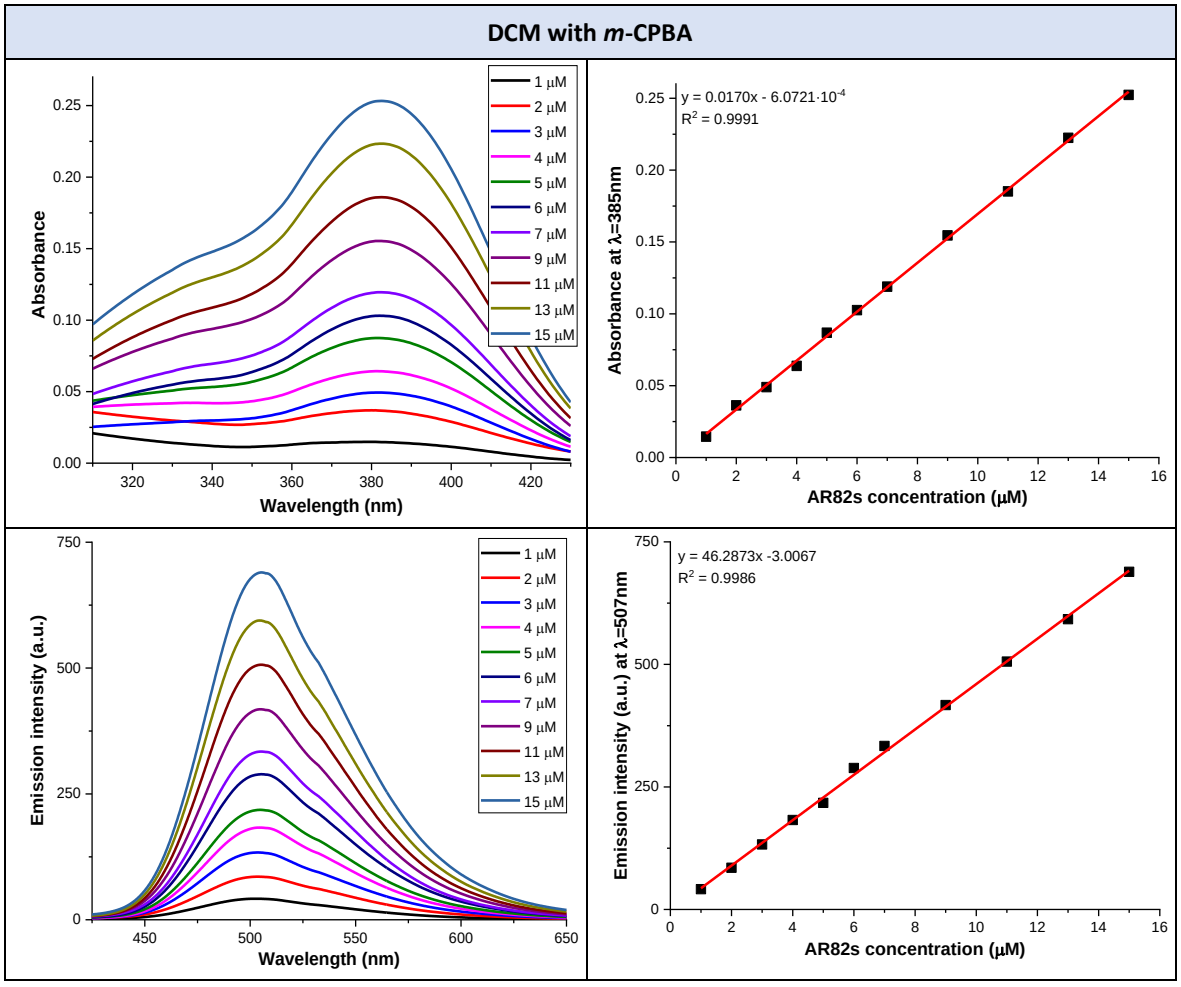

Figure 96. Absorbance spectrum (up left), absorbance profile at 385 nm (up right), fluorescence spectrum (down left) and fluorescence profile at 507 nm (down right) of increasing concentrations of AR82s with a excess of m-CPBA solution in DCM.

The ideal working concentration should stay at 0.1 of absorbance or less, to avoid inner filter effects, possible dynamic quenching or stacking processes. It was implied a concentration below 11 µM. Taking the results into account, the chosen concentration was 2.5 µM, value around which the Lambert-Beer Law (or pseudo-Lambert-Beer linear behaviour for fluorescence) was fulfilled.

Solvents test with TATP:

For all solvents, the working concentration of AR82s was 2.5 µM, the excitation wavelength was 370 nm and the temperature for all test was 25ºC.

In the kinetic studies, TATP was in excess (20 mM) and the fluorescence emission measurements were made during 25 minutes in the case of DMF and 60 minutes in MeCN, toluene and DCM at 5 minutes time intervals. In the titration, the TATP concentration was between 0 and 35000 µM and it was added directly as solid. The measurements were carried out inmediately after the adittion of the probe.

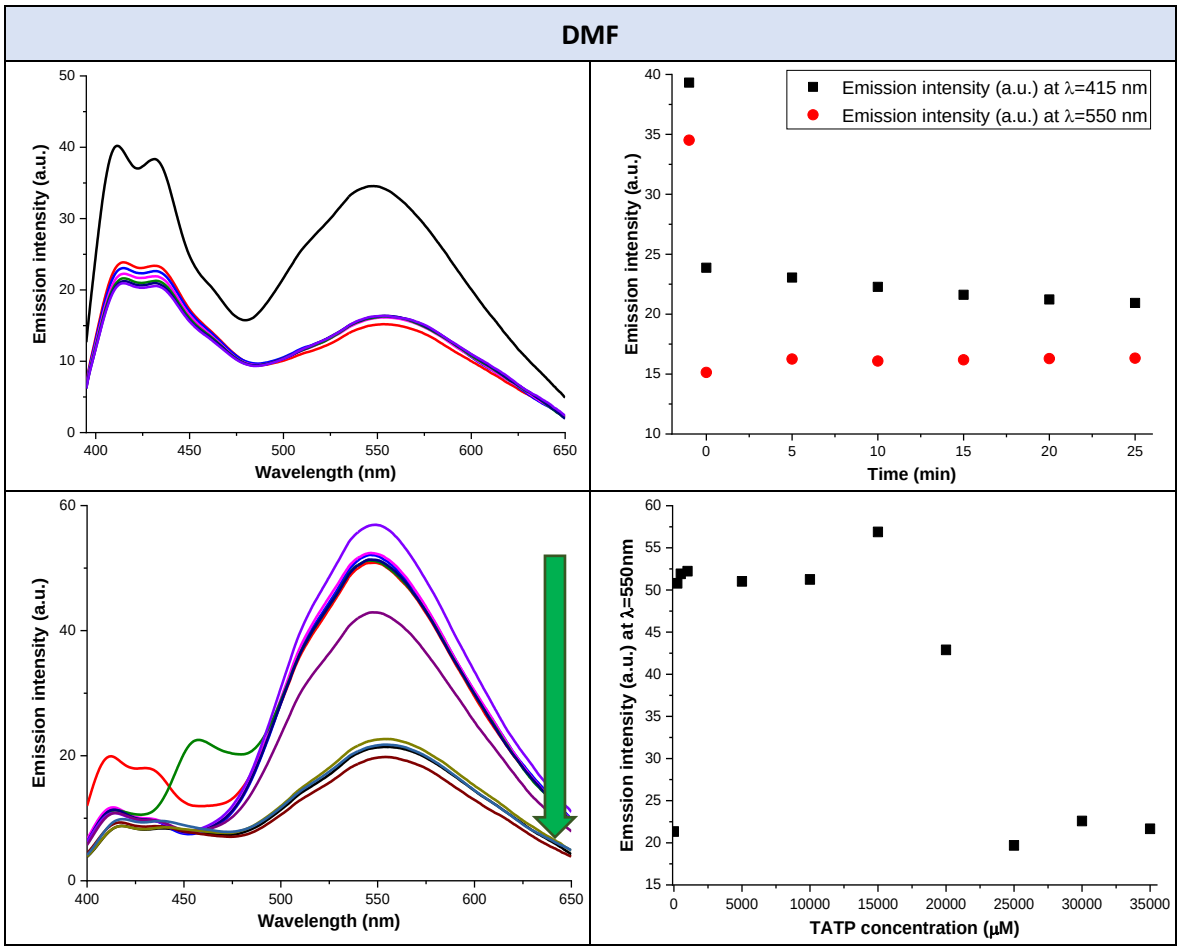

Figure 97. Study of AR82s with TATP in DMF. Kinetic study (up left) and profile as function as time at 415 nm and 550 nm simultaneously (up right) in presence of TATP excess. Titration (down left) and fluorescence profile at 550 nm (down right) under increasing concentrations of TATP.

There was a drop in the emission intensity band immediately after adding TATP. According to the fluorescence spectra, the LOD of TATP was somewhere between 15000 and 20000 µM, too high for a good probe.

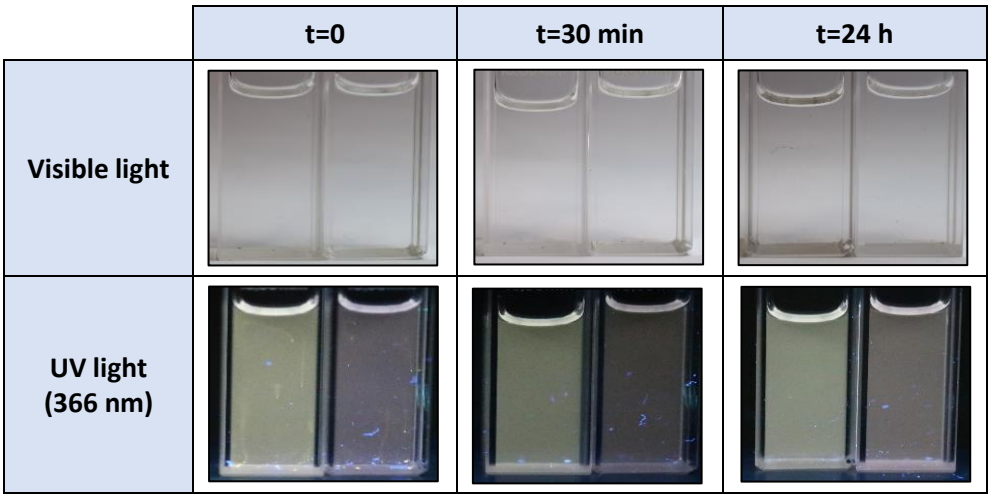

Figure 98. Kinetic study at different times under visible (up) and UV (down) light in DMF. In each photo, left vial was contained the probe and right vial was contained the probe and an excess of TATP.

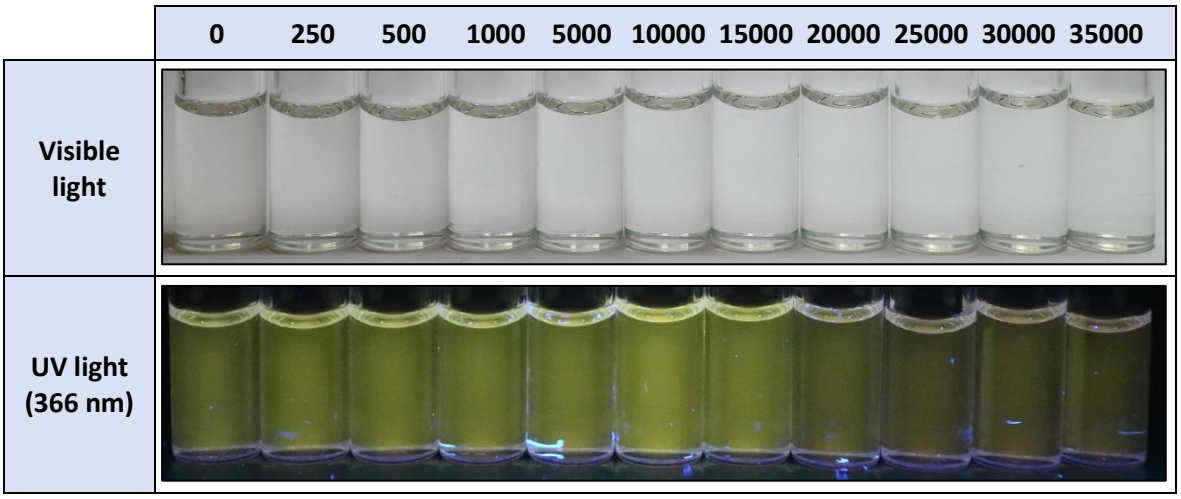

Figure 99. Titration of AR82s with an excess of TATP under visible (up) and UV (down) light in DMF.

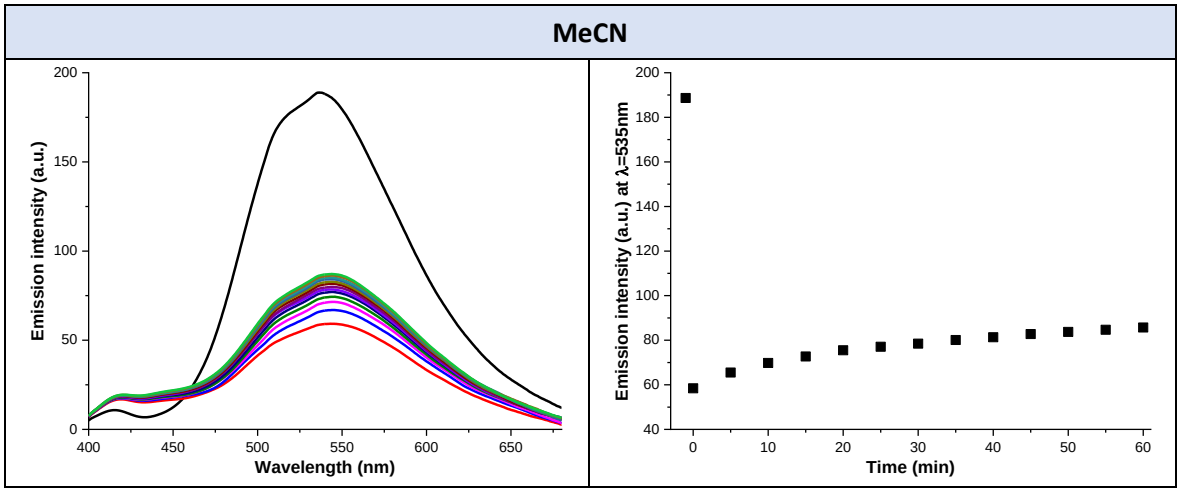

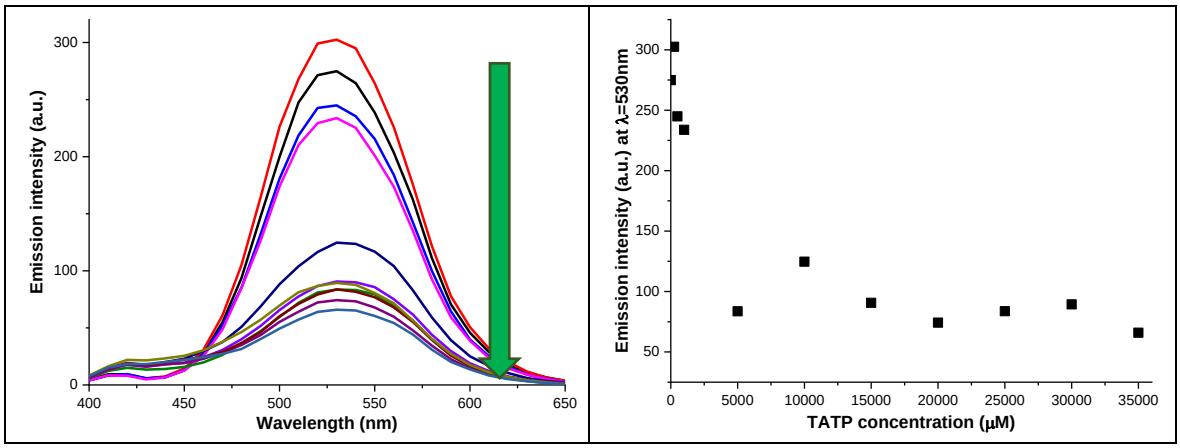

Figure 100. Study of AR82s with TATP in MeCN. Kinetic study (up left) and profile as function as time at 535 nm (up right) in presence of TATP excess. Titration (down left) and fluorescence profile at 530 nm (down right) under increasing concentrations of TATP.

There was a drop in the emission intensity band immediately after adding TATP which was stabilized after 40 minutes. According to the fluorescence spectra, the LOD of TATP was somewhere between 1000 and 5000 μM, a little high for a good probe.

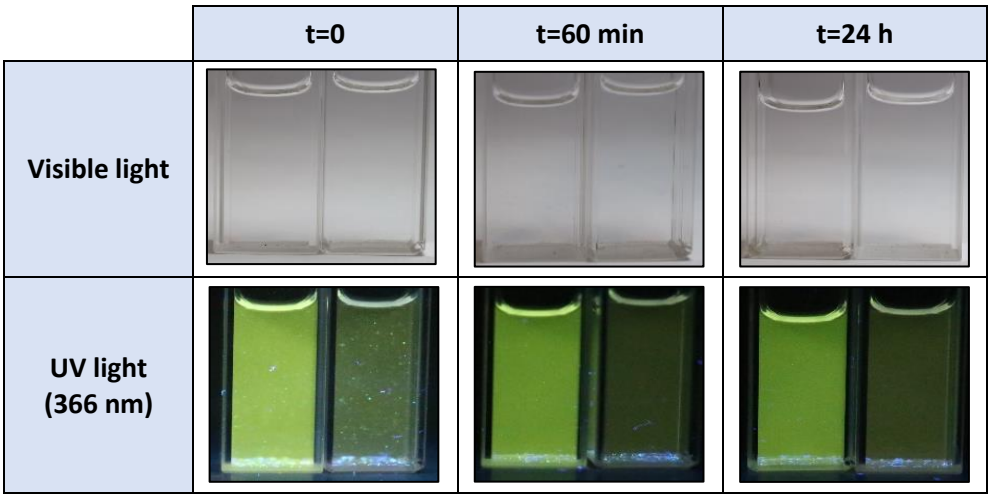

Figure 101. Kinetic study at different times under visible (up) and UV (down) light in MeCN. In each photo, left vial was contained the probe and right vial was contained the probe and an excess of TATP.

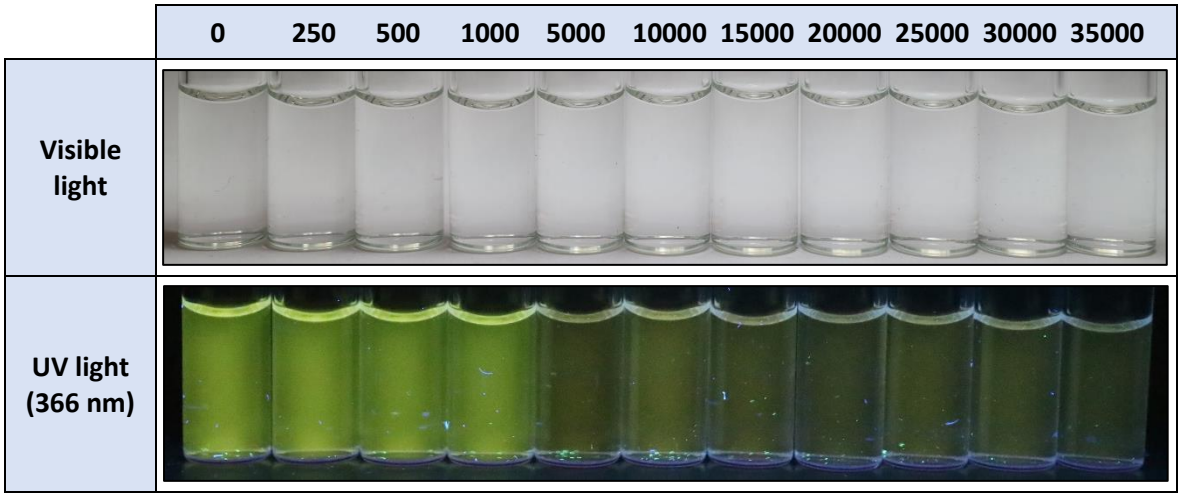

Figure 102. Titration of AR82s with an excess of TATP under visible (up) and UV (down) light in MeCN.

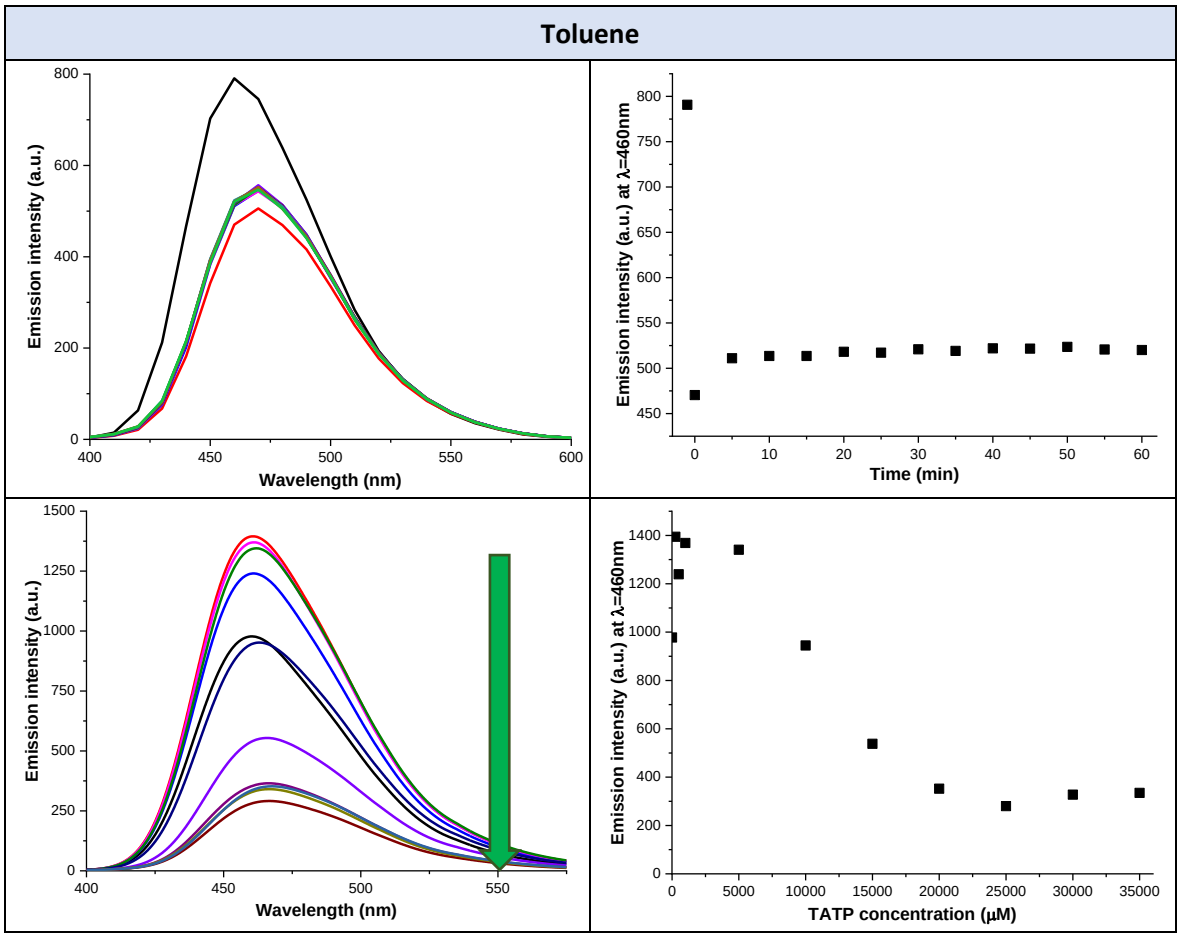

Figure 103. Study of AR82s with TATP in toluene. Kinetic study (up left) and profile as function as time at 460 nm (up right) in presence of TATP excess. Titration (down left) and fluorescence profile at 460 nm (down right) under increasing concentrations of TATP.

There was a decrease in the emission intensity band immediately after adding TATP which was stabilized after 5 minutes. According to the fluorescence spectra, the LOD of TATP was somewhere between 5000 and 10000 µM with a small initial increase and then a considerable decrease in emission intensity.

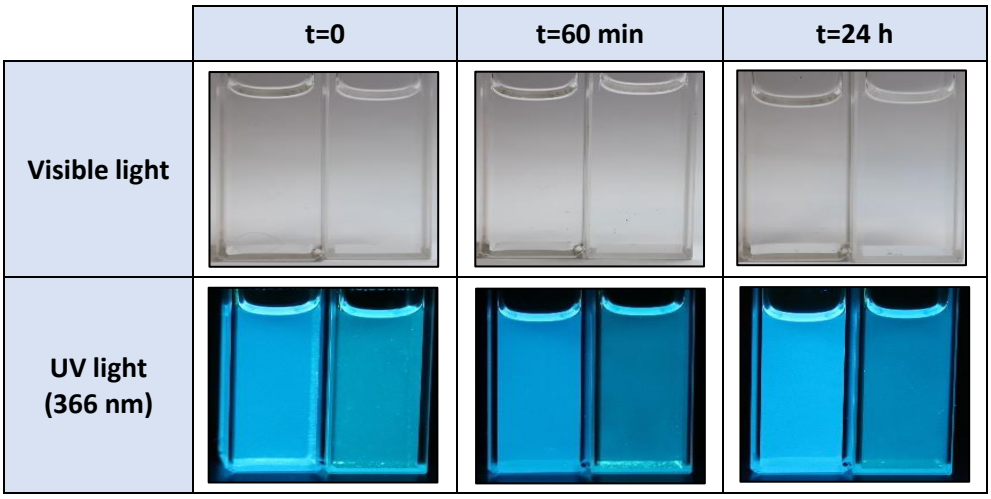

Figure 104. Kinetic study at different times under visible (up) and UV (down) light in toluene. In each photo, left vial was contained the probe and right vial was contained the probe and an excess of TATP.

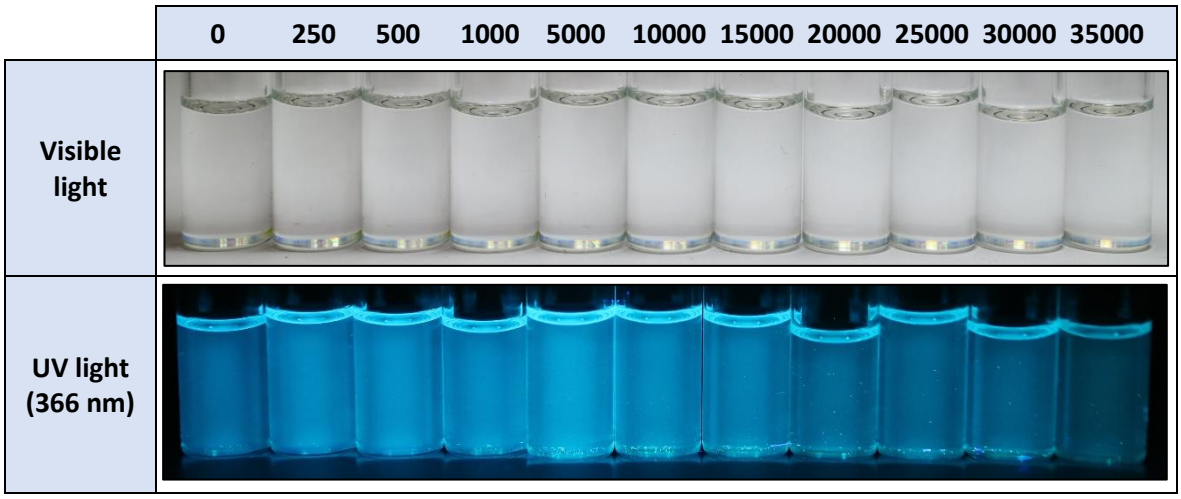

Figure 105. Titration of AR82s with an excess of TATP under visible (up) and UV (down) light in toluene.

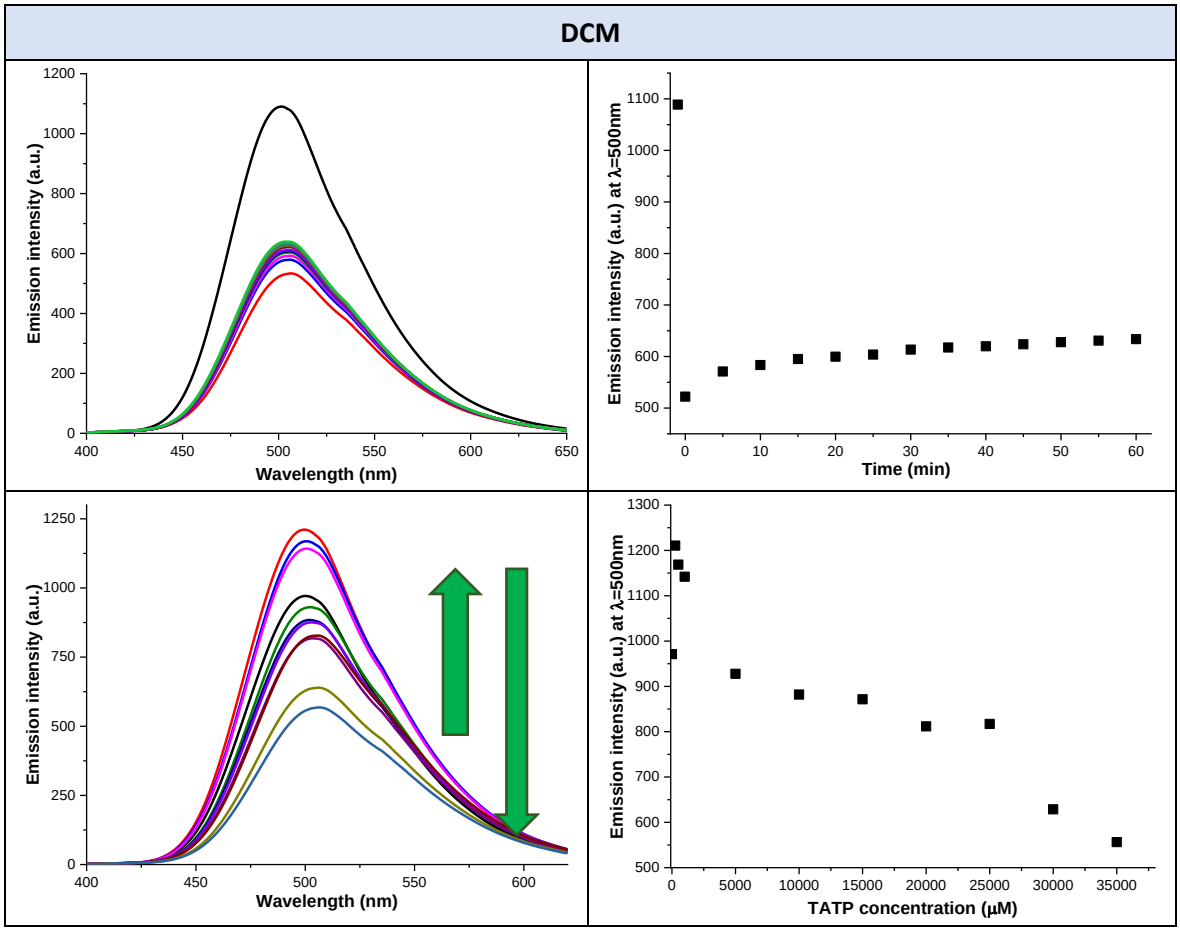

Figure 106. Study of AR82s with TATP in DCM. Kinetic study (up left) and profile as function as time at 500 nm (up right) in presence of TATP excess. Titration (down left) and fluorescence profile at 500 nm (down right) under increasing concentrations of TATP.

There was a decrease in the emission intensity band immediately after adding TATP which was stabilized after 30 minutes. According to the fluorescence spectra, the LOD of TATP was somewhere between 0 and 250 µM, it was the solvent that gave the lowest detection limit.

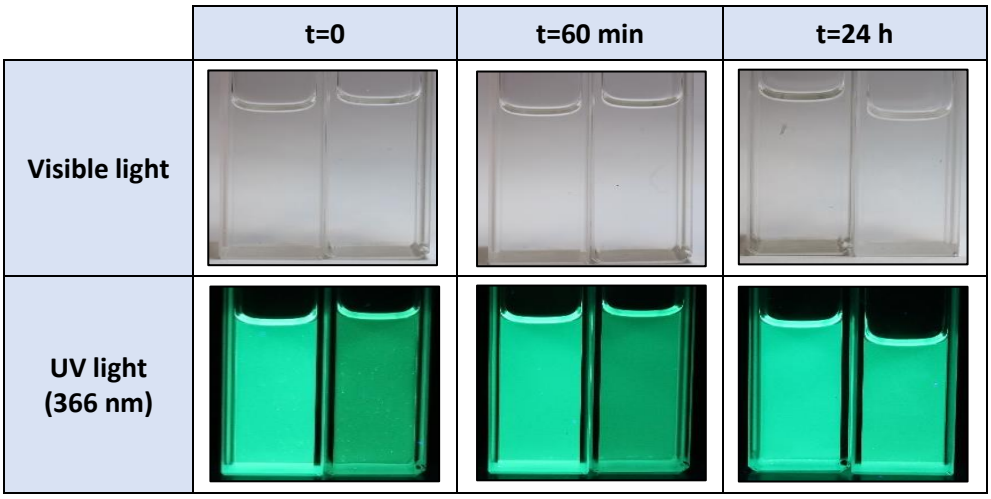

Figure 107. Kinetic study at different times under visible (up) and UV (down) light in DCM. In each photo, left vial was contained the probe and right vial was contained the probe and an excess of TATP.

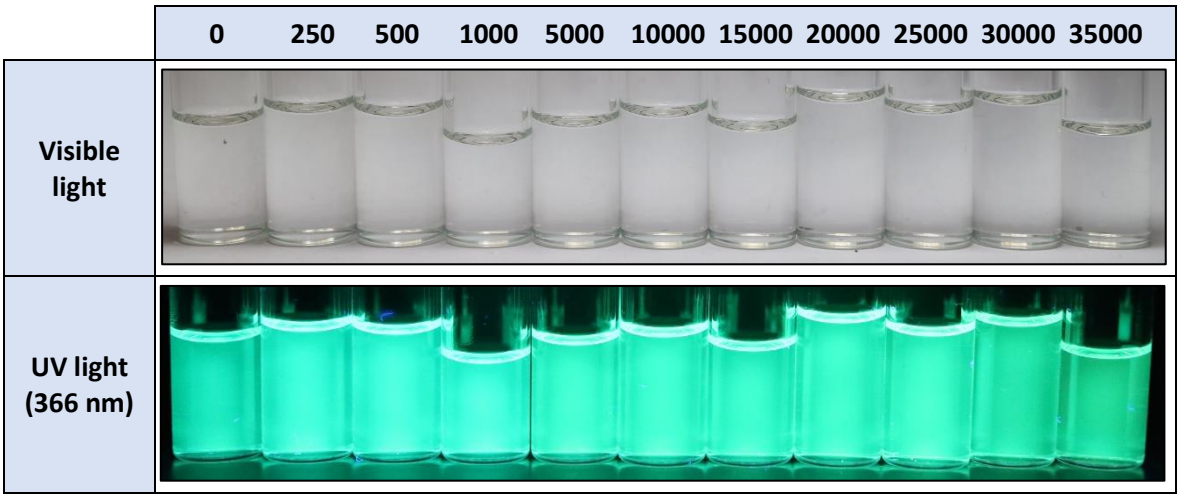

Figure 108. Titration of AR82s with an excess of TATP under visible (up) and UV (down) light in DCM.

Titration with TATP in DCM and LOD calculations:

The working concentration of AR82s was 2.5 µM, the TATP was directly as a solid and its concentration was between 0 and 25 mM. The measurements were carried out inmediately after the addition of TATP. The excitation wavelength was 370 nm and the fluorescence changes were registred at 25ºC.

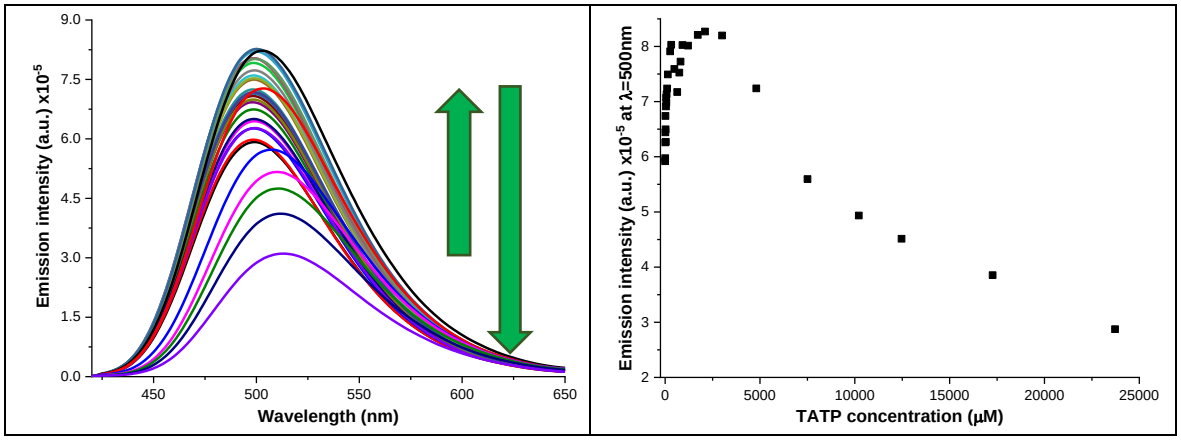

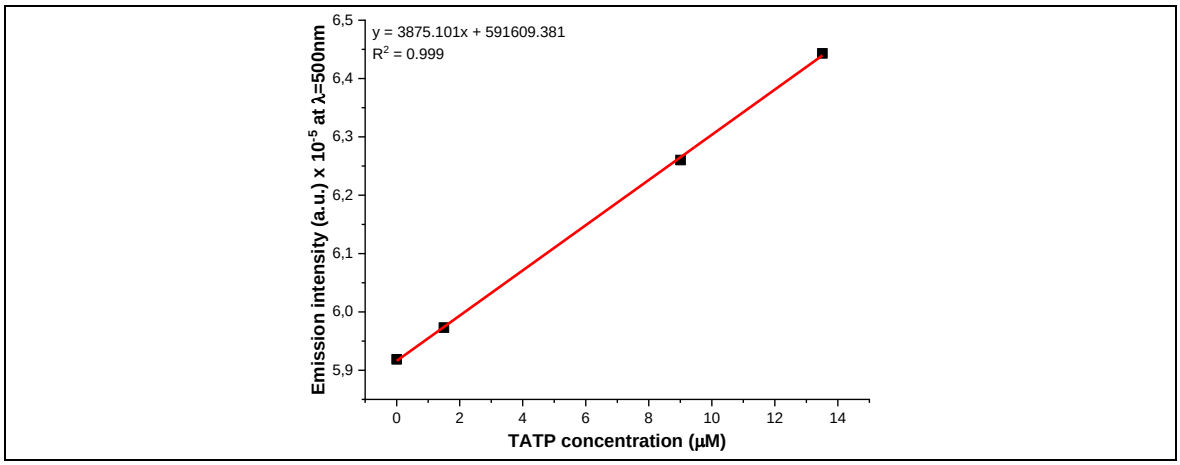

Figure 109. Titration (up left), fluorescence profile at 500 nm (up right) and calibration for the LOD calculation using emission values at 500 nm (down) of a 2.5 µM of AR82s solution in DCM under increasing concentrations of TATP.

A initial increase in the emission intensity was observed, followed by a significat decrease in emission. The LOD of AR82s with TATP was calculated by linear regression + false positive and negative at 500 nm.

For this method, the R software was used and the value of the LOD was 0.87 µM.

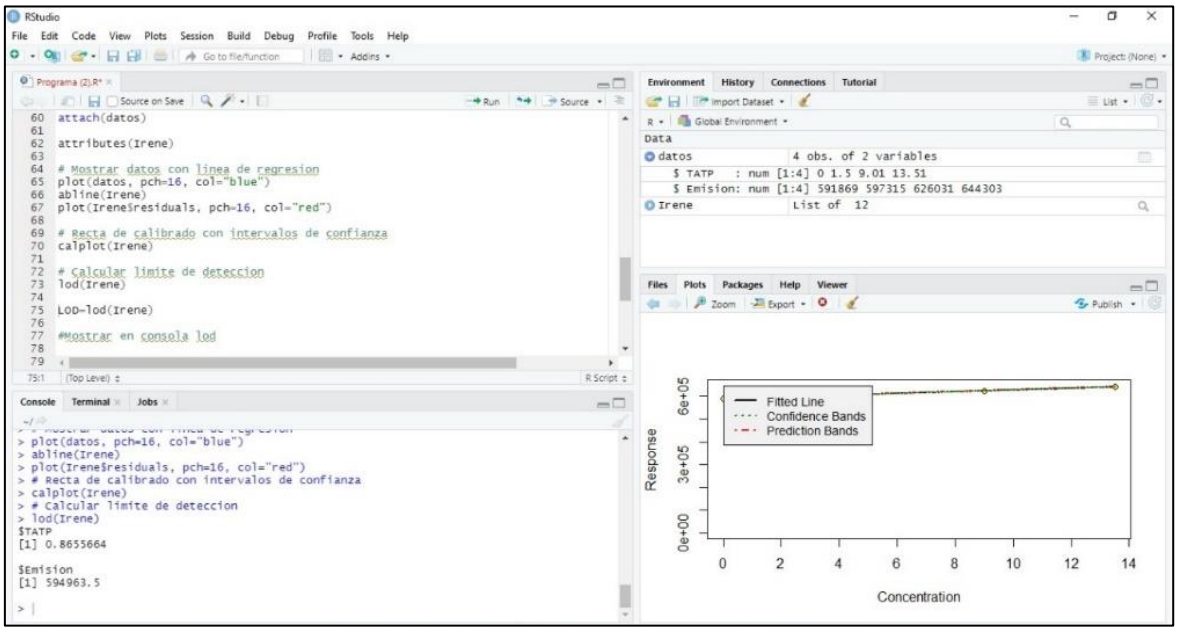

Figure 110. Calculation of LOD by the R software.

Titration with *m*-CPBA in DCM and LOD calculations:

To compare the results and the possibility of having different processes, not only the response to TATP was evaluated. The changes with *m*-CPBA, other strong oxidant, were also measeured, determining their optical changes and the LOD.

The working concentration of AR82s was 2.5 µM, the excitation wavelength was 370 nm and the fluorescence changes were registred at 25ºC. In the kinetic study, the *m*-CPBA was in excess (7 mM) and the fluorescence emission measurements were made during the subsequent 2 hours, at the increasing time intervals. In the titration, the concentration of the *m*-CPBA was between 0 and 20 mM, measuring the variation of the fluorescence after each addition.

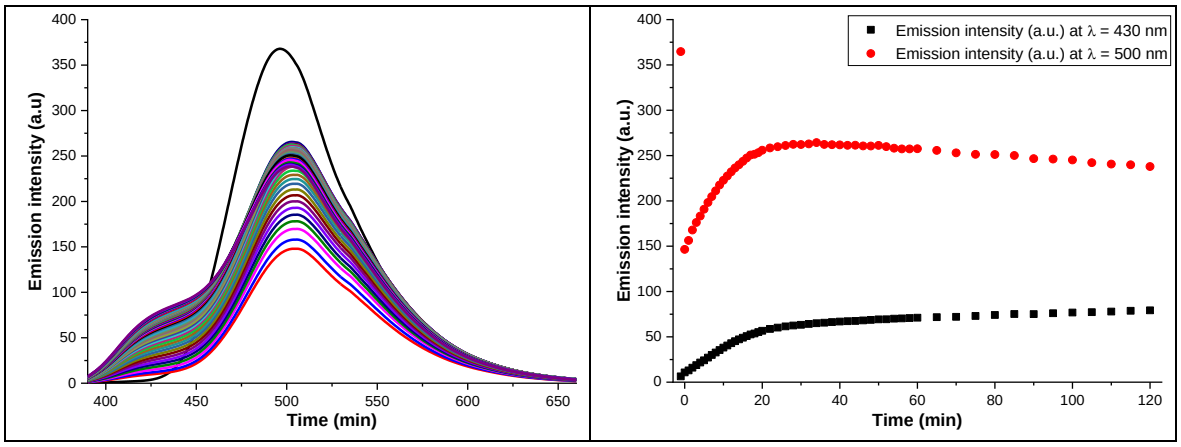

Figure 111. Kinetic study (left) and fluorescence profile at 430 nm and 500 nm simultaneously (right) of a 2.5 µM of AR82s solution in DCM under increasing concentrations of m-CPBA.

The fluorescence profile was showed that the emission intensity in the band with a maximum of 500 nm was falled drastically just after the addition of *m*-CPBA, at which point it was begun to increase again, reaching a certain stability after 30 minutes. Initially, there was no band in the area of 430 nm but it was begun to appear after the addition of *m*-CPBA and it was increased gradually. It was reached some stability after 30 minutes.

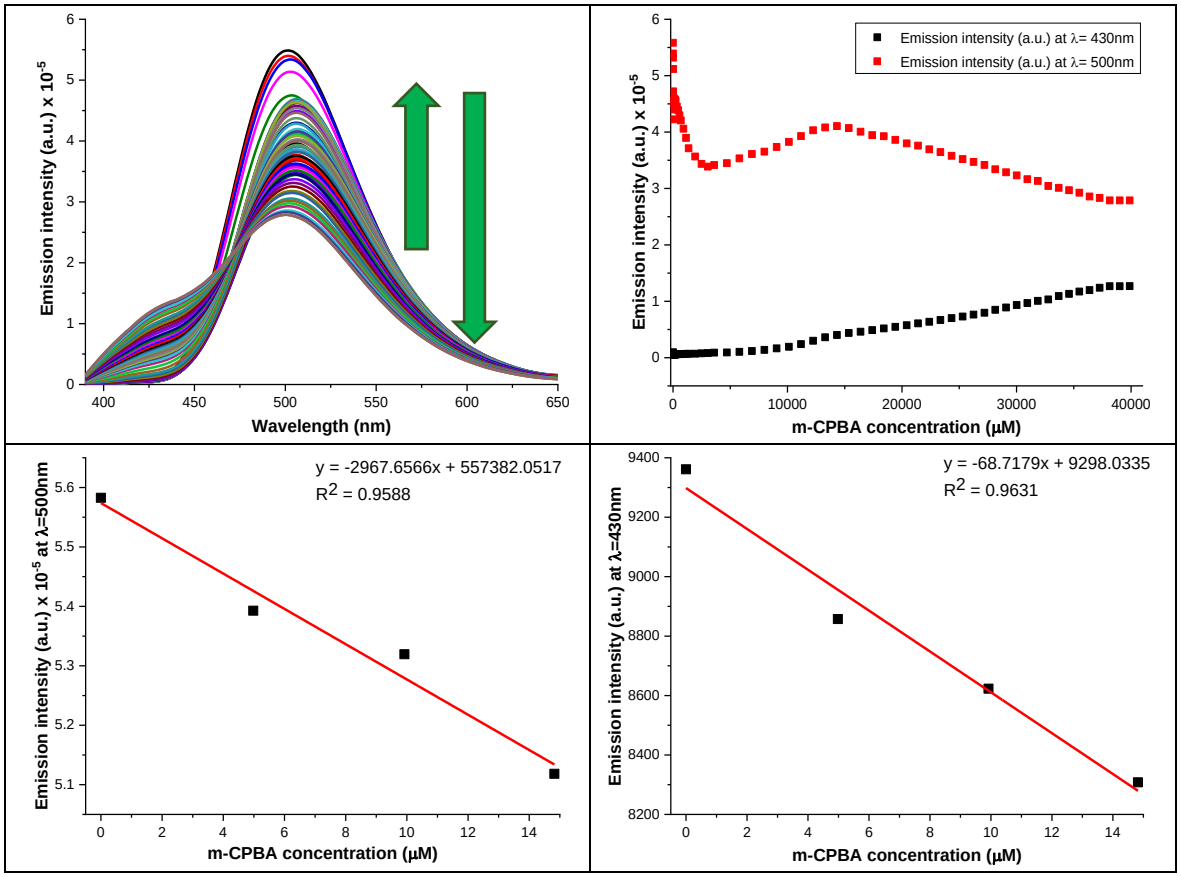

Figure 112. Titration (up left), fluorescence profile at 430 nm and 500 nm simultaneously (up right) and calibration for the LOD calculation using emission values at 430 nm (down right) and 500 nm (down left) of a 2.5 µM of AR82s solution in DCM under increasing concentrations of m-CPBA.

The LOD of AR82s with TATP was calculated by linear regression + false positive and negative at 500 nm. For this method, the R software was used and the value of the LOD was 2.1 nM.

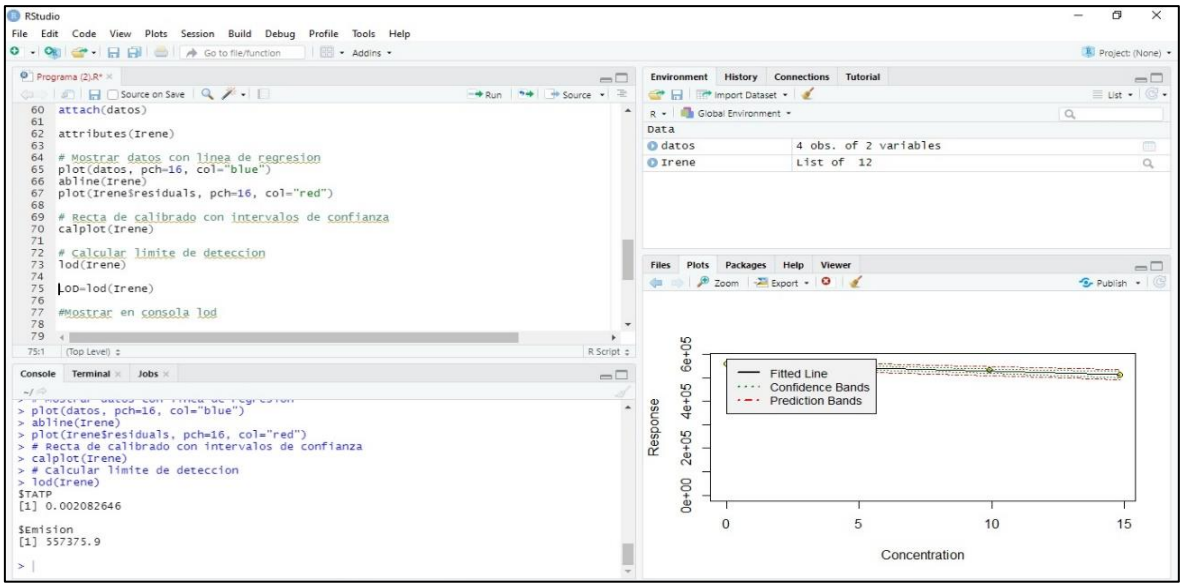

Figure 113. Calculation of LOD by the R software at 500 nm.

At 430 nm, the LOD was estimeed by linear regression + false positive and negative. The R software was used and the value of the LOD was 2.1 nM.

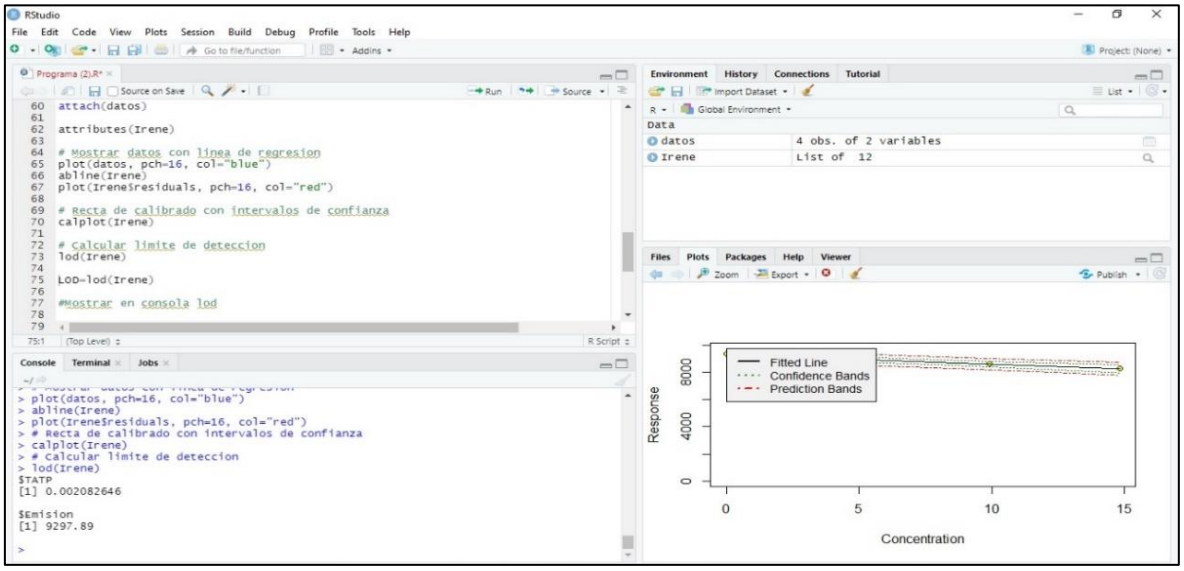

Figure 114. Calculation of LOD by the R software at 430 nm.

TATP gas detection in modified nanoparticles:

Several nanoparticles samples were modified by adsorption of the probe and tested as potential TATP sensors. In all three cases, 100 mg of the SiO_2 nanoparticles (5-15 µm particle size, 99.5% trace metal basis, Aldrich Chemistry) and 1 mg of the probe were added to a 5 ml of $CHCl_3$ and thin foil was used to cover the vial to avoid degradation of the nanoparticles by the action of light. The resulting suspension was stirred at 60°Cunder a stream of nitrogen until complete evaporation of solvent (approximately 30 minutes). After that, nanoparticles with the adsorbed compound (AR82s·SiO_2) were washed mith hexane (3×3 ml) and the solvent residues were dried with a stream of nitrogen, working in the dark throughout the all process.

The supported probe was evaluated by several methods that was given complementary information about the influence of different analytes. In a first instance, the colour variationof the

nanoparticles before and after exposure to TATP was tested. Afterwards, the detection capacity was evaluated by a more quantitative approach by registering changes in fluorescence intensity (by comparing the fluorescence quantum yield for higer precision and in the position of the maximum of emission. Finally, a quantitative study for the specific detection of TATP vapours was also performed.

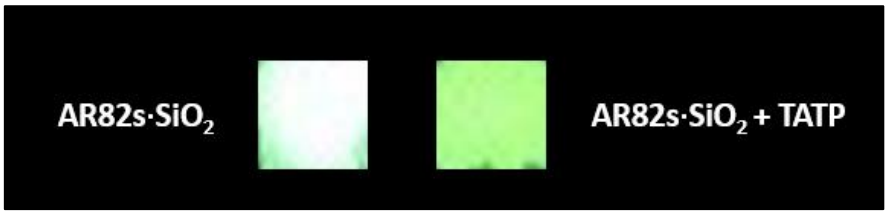

Figure 115. Colour comparation between the nanoparticules with the probe over glass plates before and after the exposure to TATP.

The increase in fluorescence of solid was recorded by measuring the solids and determining the increase in fluorescence quantum yield (ØF). The most straightforward way to detect the presence of the analyte was the increase in fluorescence of the modified material. However, the measurements were sometimes reliant on the position of the solid in the fluorometer (especially in powder samples) and these factors were difficult to control without designing a specific device for doing so. As a consequence, fluorescence quantum yields were the most trustworthy way to measure it quantitatively.

The initial evaluation of the AR82s adsorbed on SiO_2 nanoparticles against TATP in vapor was carried out by placing, at the bottom of an Eppendorf, 30 mg of the corresponding nanoparticles and 4 mg of TATP in the upper part of the Eppendorff, which was placed horizontally. The Eppendorf was covered with tin foil to prevent the degradation of the nanoparticles by action of light and was heated, at a temperature not higher than 60ºC, until the complete evaporation of TATP. Once evaporated, the probe and the TATP were kept in contact for ten minutes more before proceeding to measure the emission and the excitation spectrums and the quantum yield of the nanoparticles, both exposed to the TATP and before said exposure, with a Edimburg Instrument FLS – 980 fluorimeter at an excitation wavelength of 370 nm an at 25ºC.

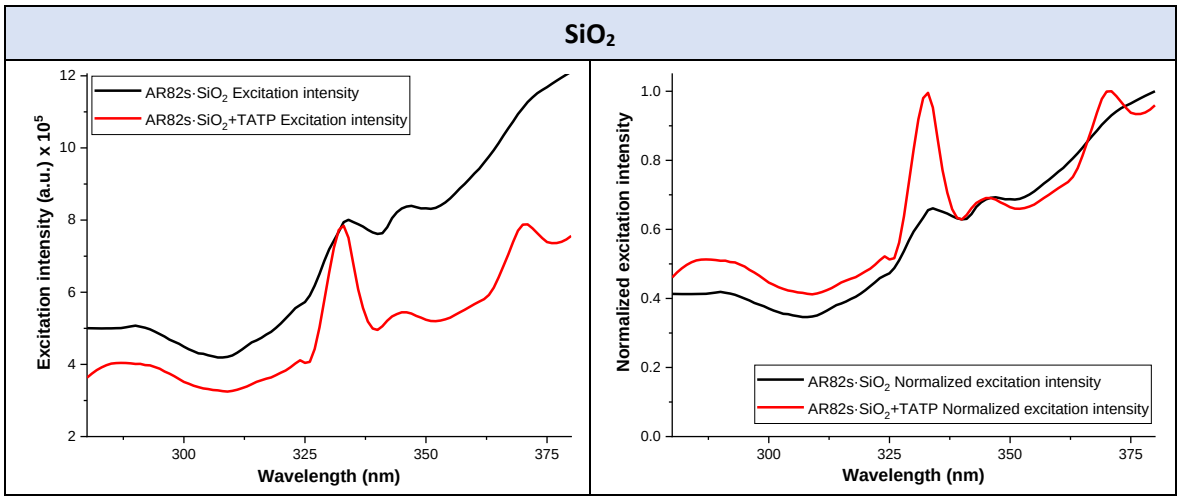

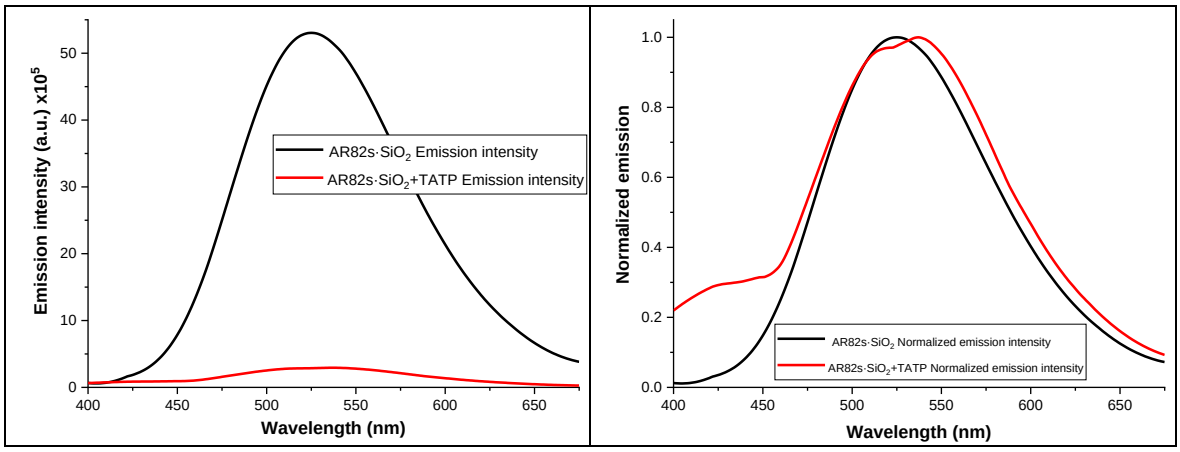

Figure 116. Response of fluorescence (down) and excitation (up) of AR82s adsorbed in SiO_2 nanoparticles.

The variation of quantum yields between the probe and the probe after the exposure to TATP was a parameter that provides lower errors, less than 2%.

$$\frac{\emptyset_{probe+TATP}}{\emptyset_{probe}} = 0.081$$

Fluorescence intensity with the probe was around 12 times lower after the exposure to TATP vapour.

Titration with TATP in vapour phase:

The titration of AR82s adsorbed onto SiO_2 nanoparticles was carried out by placing 15 mg of nanoparticles in an Eppendorf, covered with tin foil to avoid degradation of the nanoparticles by the action of light, and increasing amounts of TATP (from 0.025 to 2 mg) in another Eppendorf. Both were connected to each other and to an air stream provided by a compressor. Working in the absence of light, TATP was heated, to a temperature no higher than 60ºC, until its complete evaporation, keeping probe and TATP in contact in the system for 10 additional minutes after the complete TATP evaporation. After this time, the emission measurements of the nanoparticles exposed to TATP was carried out in an Edimburg Instrument FLS-980 fluorimeter at an excitation wavelength of 370 nm at 25ºC.

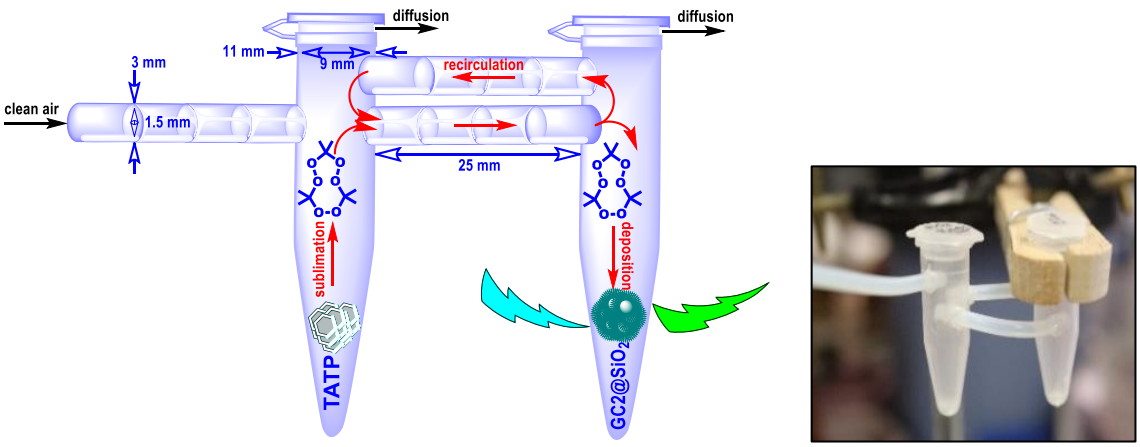

Figure 117. Microfluidic device used for titrations in vapour phase (left) and the actual aspect of the system (right).

The microfluidic device dimensions were: Eppendorf: outer top diameter 11mm, inner top diameter 9 mm, outer bottom diameter 5 mm, inner bottom diameter 3 mm, volume 1.5 ml, height (with lid)

40 mm, height (without lid) 38 mm. Tubing: outer diameter 3 mm, inner diameter 1.5 mm, length (flow tube) 25 mm, length (return tube) 35 mm.

TATP (mg)	Time required for complete evaporation
0.032	1’41”
0.048	1’45”
0.083	2’14”
0.114	2’42”
0.158	3’10”
0.203	3’21”
0.247	3’57”
0.333	4’26”
0.483	5’03”
0.800	7’45”
1.000	11’23”
1.400	13’13”
2.100	19’37”

Figure 118. Time required for total evaporation of the different amounts of TATP used in the experiment.

The calibration was performed in steady state, fixed quantities of TATP were vaporized in the presence of a sample containing 15 mg of AR82s·SiO_2 nanoparticles and the fluorescence increase was measured 10 minutes after the complete vaporization of each TATP sample.

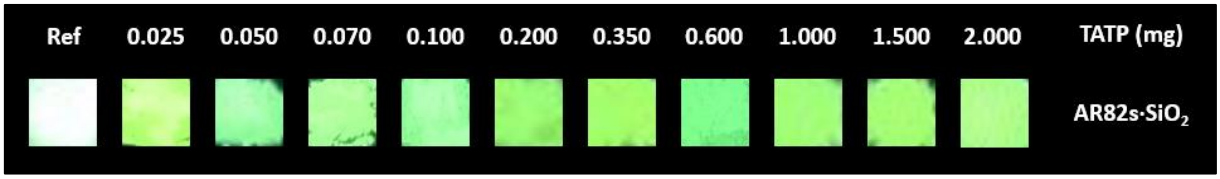

Figure 119. Response of AR82s·SiO_2 exposed to different quantities of TATP.

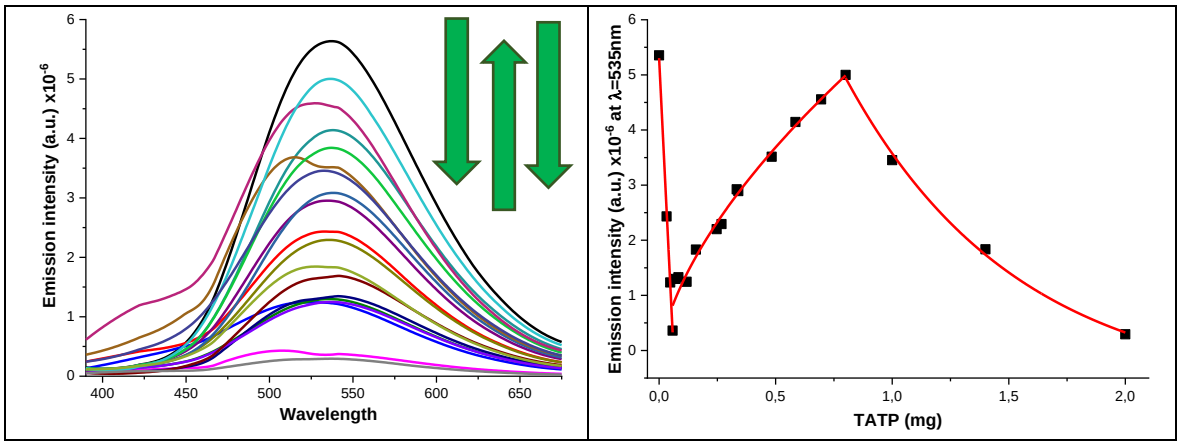

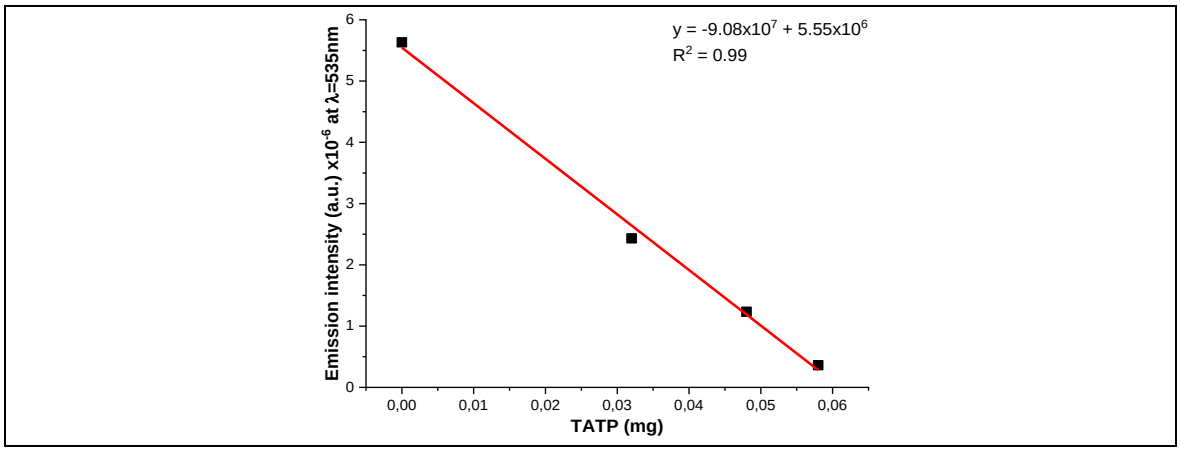

Figure 120. Titration (up left), fluorescence profile at 535 nm (up right) and calibration for the LOD calculation using emission values at 535 nm (down) of AR82s·SiO_2 under increasing concentrations of TATP in vapour phase.

The LOD was calculated by linear regression + false positive and negative at 535 nm. For this method, the R software was used and the value of the LOD was 1.30 µg.

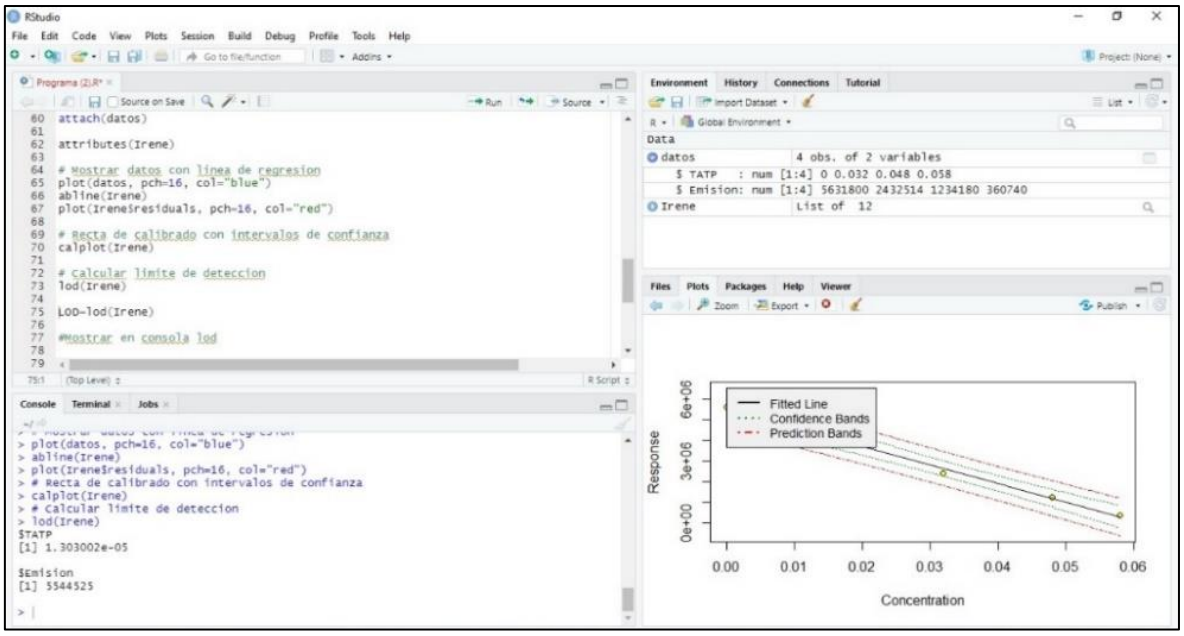

Figure 121. Calculation of LOD by the R software.

Mobile phone application:

In this case an OPPO Find X3 Pro 5G (dedicated to the application) was used to detect the presence of TATP in a vapour flow. The application was developed in collaboration with J. Rafael Santana Tejada.

The purpouse of the application was to detect the amount of TATP from an imagen of AR82s·SiO_2 sample exposed to TATP vapours. The user had to configure the system correctly in order to obtain a suitable result. The application has two systems for determining the amount of TATP by RGB:

- Interval search: each sample exposed to a known amount of TATP was configured with several colours, in which the target could be included. To detect the amount of TATP to which the nanoparticles were exposed, a colour was selected and an interval search was carried out.

Example: suppose we have a target colour 50, 240, 70 and we have the following intervals [40, 130, 60], [10,250, 60] and [55, 244, 71]. The comparison algorithm will detect that the target 50, 240, 70 is in the interval [40, 230, 60] 50, 240, 70 [55, 244, 71].

- Radio search: suppose we have a target colour 50, 240, 70 and we work with a radious of 10. The intervals we have are [40, 230, 60], [10, 250, 60] and [85, 244, 41]. When the compare algorithm will detect that the target 50, 240, 70 is in the radius of the interval [40, 230, 60] since if we add the radius ±10 we would have this radious [40, 230, 60] or [60, 250, 80].

The system of the application was composed of the following components:

- Mobile application: it was developed with IONIC technology with which we have the possibility of generating an APK for Android or IPA for IOS.
- *Laravel api*: communication with the backend where queries were made from the mobile application to the database.
- Database: system of tables designed to be able to store colours dynamically and to meet the needs of the application.

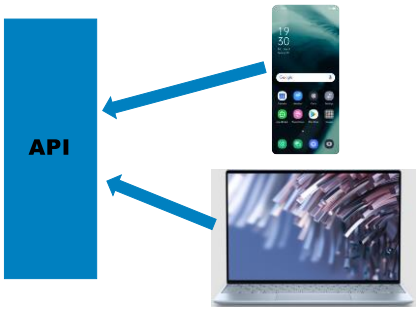

Figure 122. System structure of the mobile application

System configuration: the application is made up of different configurable sections:

- Login: to be able to enter the system, access credentials are required.
- Menu: allows us to view and access to the different options of the application.
- Users: the list of users authorised to access the application is displayed, as well as the option to delete them.
- User settings: personal data (name, email, password…) can be changed from this screen.
- New user: allows you to create new users by filling in the required information. The data will be verified before granting access to the application.
- Colour list: list of the different nanoparticle colours for each amount of TATP in vapour phase, accessed from "menu" and then "my colours". In this screen, colours can be delete and update the data at any time as well as watch the rest of the stored colours.
- New colour: to add a new colour to a TATP measurement, we click on "add colour" and select the TATP quantity and add an RGB colour, manually or by selecting it on an image. The latter is the fastest method as it allows you to save and continue adding colours.
- Colour detection: once the system is configured with the different TATP measurements, in the "analysis" screen you can take a picture or select an image from the gallery and choose the point where you want to detect how much TATP it has been exposed to. The images are very important because the higher the quality, the higher the accuracy in detecting RGB colour.

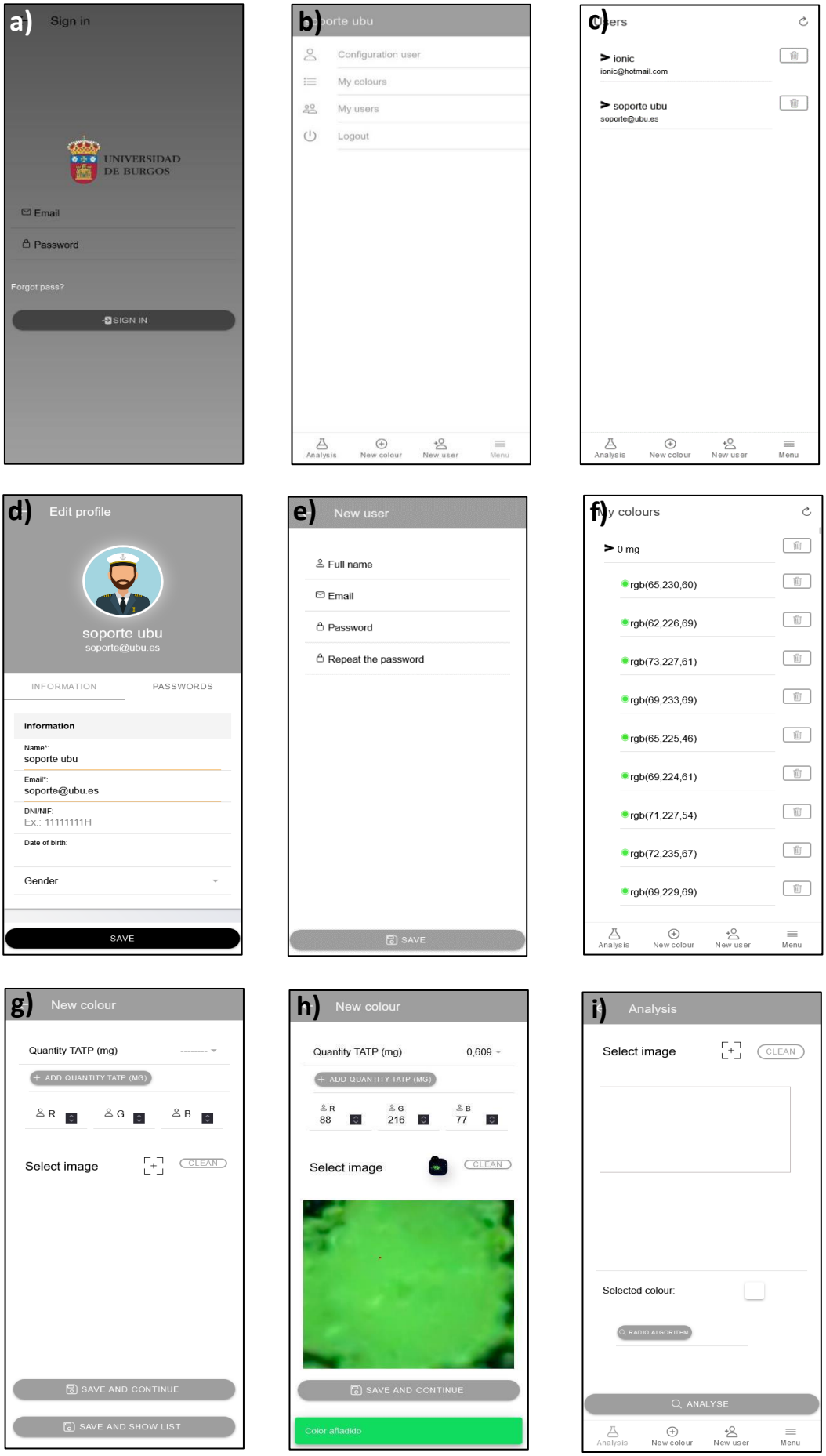
a)
Sign in
UNIVERSIDAD DE BURGOS
Email
Password
Forgot pass?
SIGN IN
b)
Configuration user
My colours
My users
Logout
Analysis
New colour
New user
Menu
c)
ionic
ionic@hotmail.com
soporte ubu
soporte@ubu.es
Analysis
New colour
New user
Menu
d)
Edit profile
soporte ubu
soporte@ubu.es
INFORMATION
PASSWORDS
Information
Name*:
soporte ubu
Email*:
soporte@ubu.es
DNI/NIF:
Ex.: 11111111H
Date of birth:
Gender
SAVE
e)
New user
Full name
Email
Password
Repeat the password
SAVE
f)
0 mg
rgb(65,230,60)
rgb(62,226,69)
rgb(73,227,61)
rgb(69,233,69)
rgb(65,225,46)
rgb(69,224,61)
rgb(71,227,54)
rgb(72,235,67)
rgb(69,229,69)
Analysis
New colour
New user
Menu
g)
New colour
Quantity TATP (mg)
ADD QUANTITY TATP (MG)
R
G
B
Select image
CLEAN
SAVE AND CONTINUE
SAVE AND SHOW LIST
h)
New colour
Quantity TATP (mg)
0,609
ADD QUANTITY TATP (MG)
R
88
G
216
B
77
Select image
CLEAN
SAVE AND CONTINUE
Color añadido
i)
Analysis
Select image
CLEAN
Selected colour:
RADIO ALGORITHM
ANALYSE
Analysis
New colour
New user
Menu

Figure 123. Screenshots of the mobile application.
a) login.
b) menu.
c) list of users.
d) edit profile of an user.
e) new user.
f) list of colours.
g) and h) new colour.
i) and j) colour detection

The figures showed an example for a 2 mg image obtained by the device from previous section and the system with the color configuration should detect it. As we can see, the system is correct since the range of colors is in the correct range. In the lower part we have the option to change the radio search algorithm that is named in the introduction section.

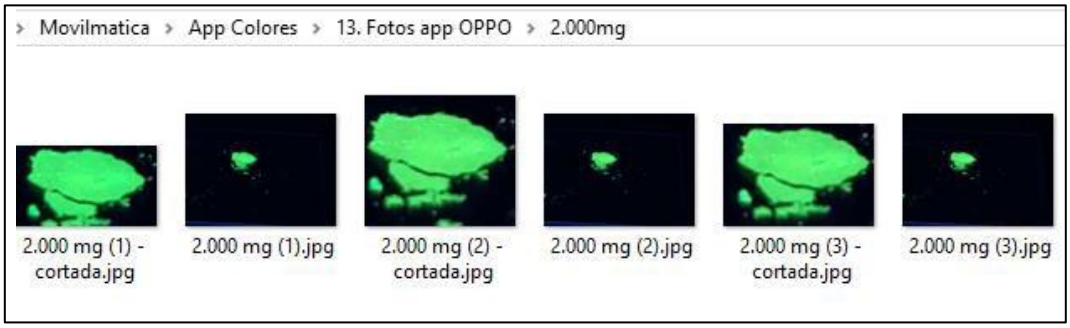

Figure 124. Images of the data base.

The application was part of an autonomous system for capturing and quantitative evaluation of fluorescent probe images based on mobile telephony composed of: (1) customised display box (2) 360º metal bracket (3) customised APP and (4) OPPO Find X3 Pro5G.

Figure 125. The dark box (left) with a metal support (right).

The system allows photographs to be taken with a mobile camera from very short distances of a sensor material previously exposed to an explosive atmosphere. For this, the sensing material was placed in a dark box with a metal holder and a UV lamp (366 nm) to illuminate the material. The application to compare the photo with a database of images of the material exposed to different

amounts of TATP in vapour phase is loaded on the mobile phone so, that from the comparison and the calculated calibration curve, the amount of the explosive that has come into contact with the AR82s·SiO_2 can be extracted.

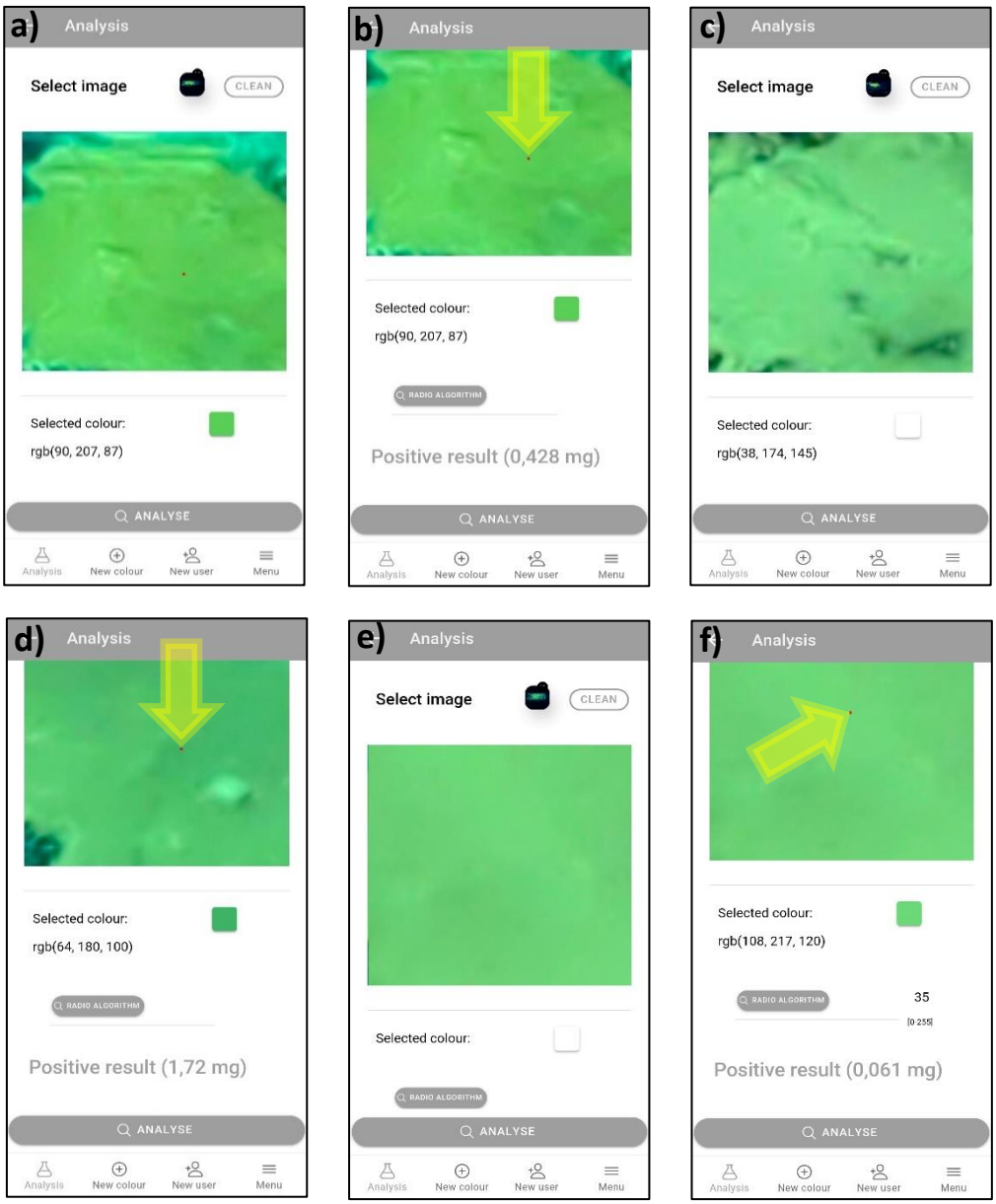

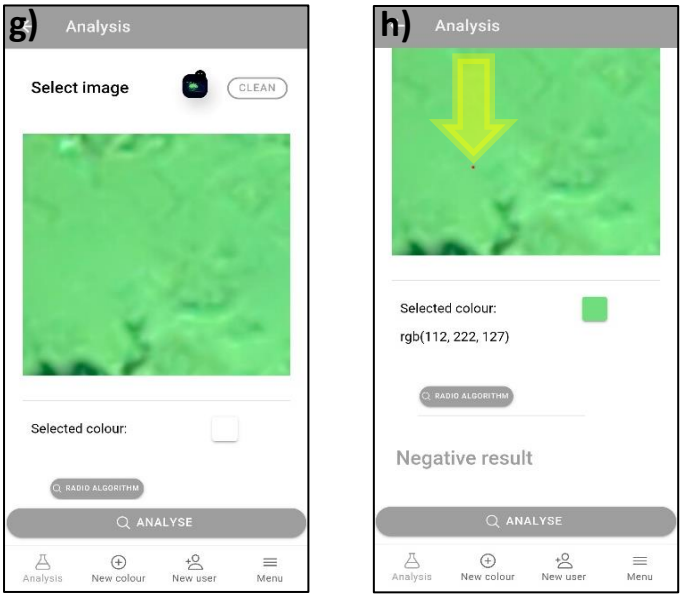

Figure 126. Images of the data base used for search and compare selected samples:
a) selected image (0.428 mg of TATP).
b) a positive result.
c) selected image (1.720 mg of TATP).
d) a positive result.
e) selected image (0.061 mg of TATP).
f) a positive result.
g) selected image (no TATP).
h) a negative result.
The yellow arrows indicate the point where the selected color is measured.

Validation of fluorescent device in real life scenarios:

The experiments were carried out in an office with dimensions 3.07×3.54×2.15 m (height×length× width). An air compressor was placed inside it, which was generated a continous stream of clean air, that was passed through the TATP in the direction of the point where the particles were arranged, and three heaters that help regulate the temperature inside the room.

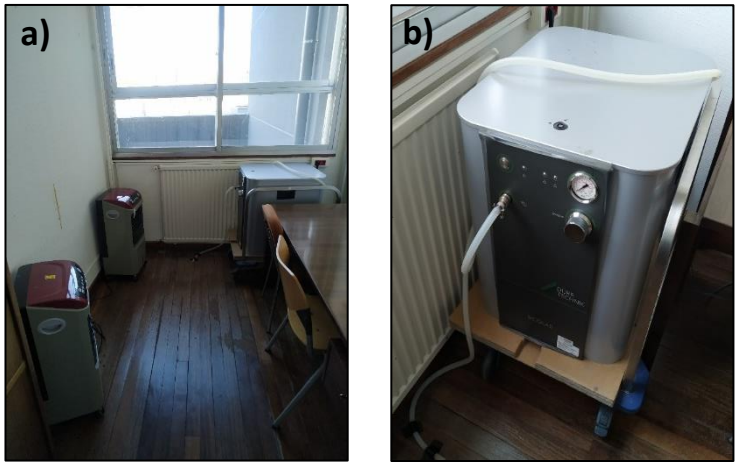

Figure 127. Office experiments with AR82s·SiO_2 with TATP in vapour phase.
a) shows the dimensions and the arrangement of the elements inside the office.
b) shows the compressor used in the experiments.

Varying amounts of TATP (specified in each experiment) were placed 30 cm from the source of the airflow. Approximately 0.75 mg of AR82s·SiO_2 were placed on the surface of a cover glass, adhered to it with the help of a small amounto of adhesive tape. This process was repeated 6 times and the cover glasses were placed at increasing distances from the point where the TATP was located (10-25-50-100-150-200 cm).

Figure 128. Office experiments with AR82s·SiO_2 with TATP in vapour phase.
a) arrangement of the TATP in front of yhe airflow outlet.
b) distribution of the sensing nanoparticles in the room.
c) and d) assembly for measurement of the particles.

To carry out the measurements in the fluorimeter, they were covered with a quartz sheet that ensured the nanoparticles were remained in a fixed position. This sheet had then to be removed to leave the particles were exposed to TATP vapors during the experiment. A measurement of the particles without being subjected to TATP was also made before and after remaining the same time as the particles that were subjected to TATP vapours to use as a reference.

Fluorescence measurements were made for each group of particles before and after the exposure to TATP vapours using a excitation wavelength of 370 nm. Photos of the particles were taken under identical conditions. Two representative experiments are detailed.

Experiment 4. 250 mg of TATP at 26°C during 30 minutes.

Of the 252.3 mg of TATP initially weighed, only 38.6 mg were evaporated under the temperature and time conditions used in this experiment, remaining 216.7 mg of TATP as solid. The experimental procedure was similar to the previous ones.

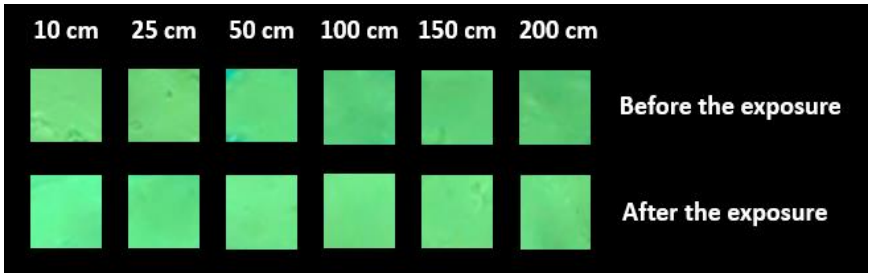

Figure 129. Comparative photograph taken under 366 nm light before and after exposure to TATP vapours at 26°C during 30 minutes.

Experiment 5. 250 mg of TATP at 28ºC during 30 minutes.

Of the 252.3 mg of TATP initially weighed, only 97.3 mg were evaporated under the temperature and time conditions used in this experiment, remaining 155 mg of TATP as solid. The experimental procedure for this measurements was similar to the previous ones.

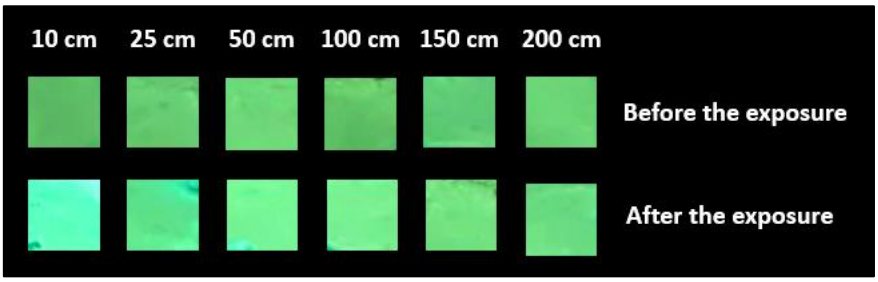

Figure 130. Comparative photograph taken under 366 nm light before and after exposure to TATP vapours at 28ºC during 30 minutes.

For an easier visualization of the whole data, the following Figures have been made, representing the normalized emision intensity variation before and after exposure to TATP vapours versus distance to the TATP source.

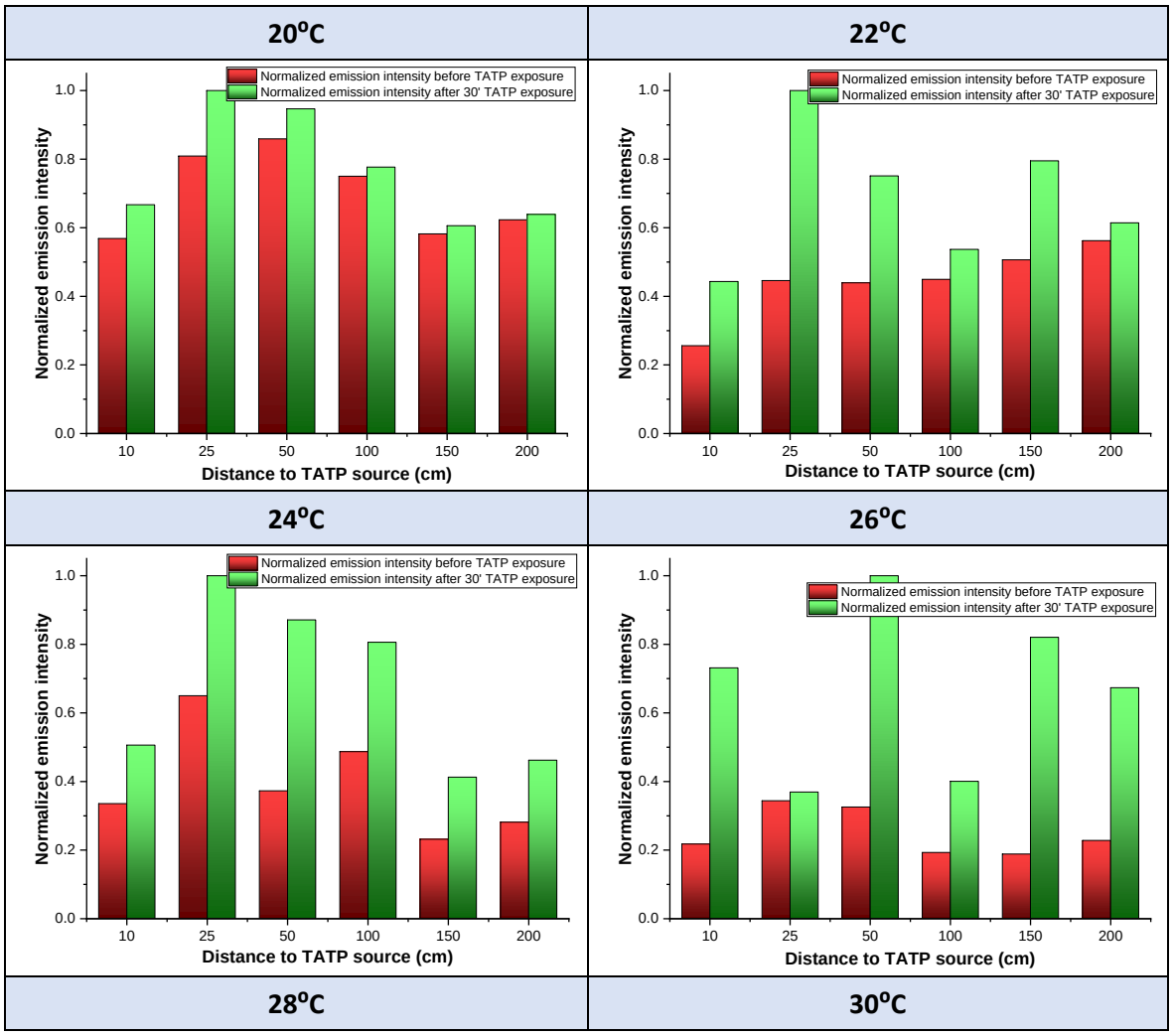

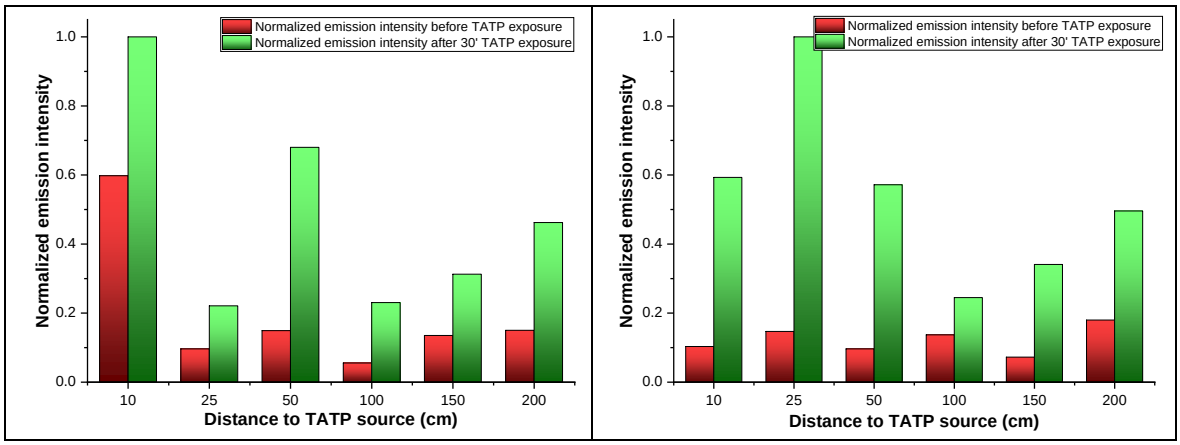

Figure 131. Summary of experiments at different temperatures. Normalized emission intensity variation before and after exposure to TATP vapour versus distance to the TATP source in both cases.

The following graphs show all the data together to facilitate comparison.

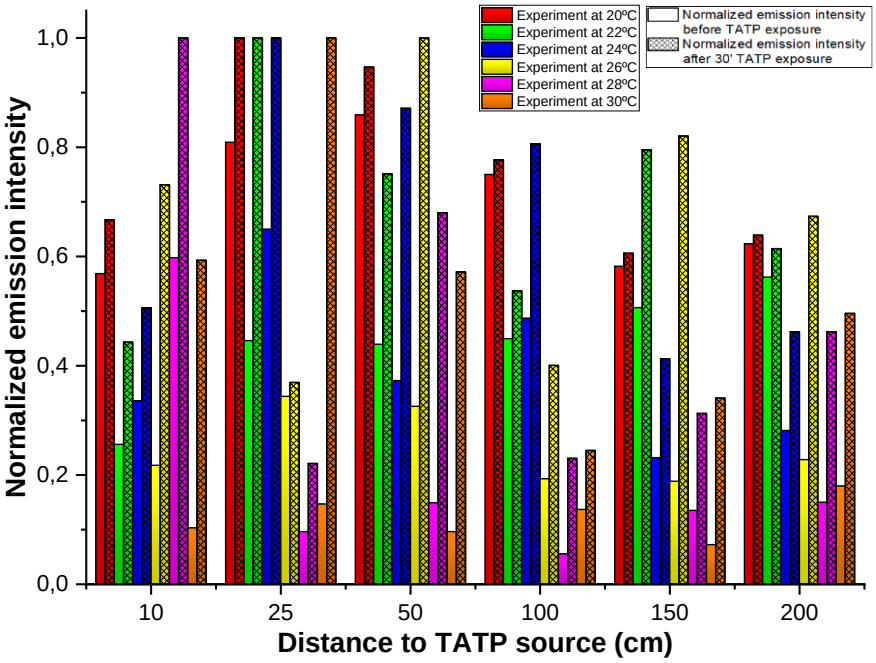

Figure 132. Summary of experiments at different temperatures. Normalized emission intensity variation before and after exposure to TATP versus distance to the TATP source.

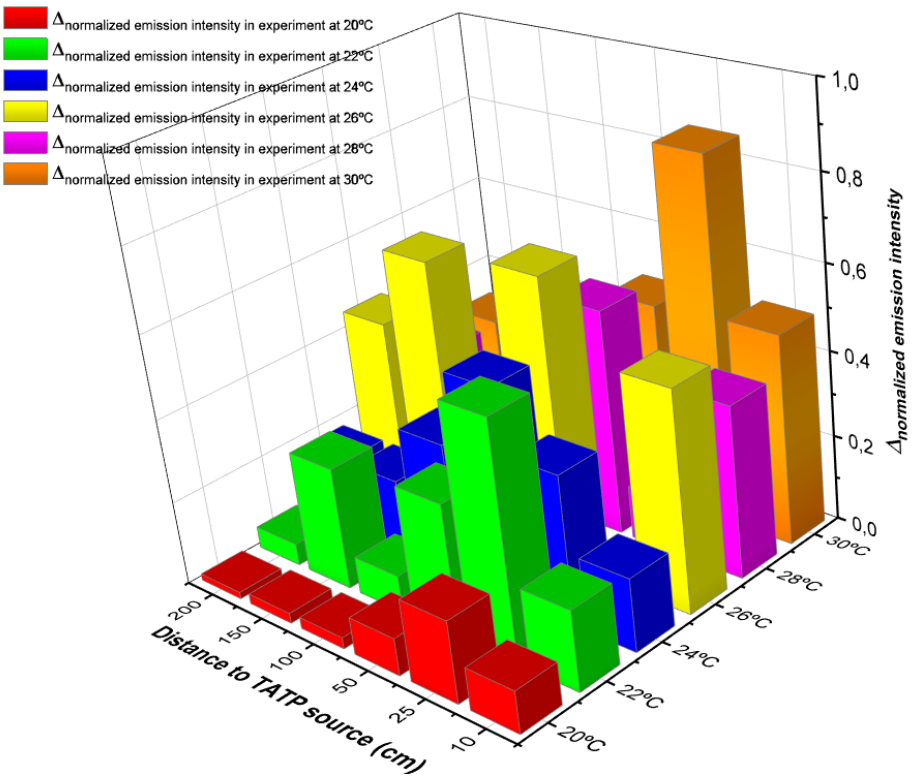

Figure 133. Summary 3D graph of experiments at different temperatures. Increase in normalized emission intensity variation before and after exposure to TATP versus distance to the TATP source. λ_{exc} = 370 nm.

Following the results of the previous series of experiments, it was observed that the best temperature conditions to perform the experiment was around 26ºC. Therefore, a series of 6 additional experiments were performedin which room temperature was raised up to 30ºC thanks to the use of a heater. Once this temperature was reached, the heater was turned off and the room temperature was left to regulate itself, with the temperature oscillating between 30 and 26ºC. The experiments had a duration of 30 minutes.

The experiments were carried out in an office with dimensions 3.07×3.54×2.15 m (hiegth×length× width). The following figures ilustrate both the dimensions and the arrangement of the differen elements in the room when proceeding with the experiments.

Figure 134. Images of the dimensions and arrangement of the elements inside the office.

Inside it, an air compressor was placed, which generated a continuous stream of clean air that passed through the TATP the direction of the points where the particles were arranged, and a

heater that helped regulate the temperature inside the room. Once the temperature of 30ºC was reached, the heater was turned off and the temperature was left to regulate itself.

For all experiments, 250 mg of TATP were placed 30 cm from the source of the airflow. Approximately,0.75 mg of AR82s·SiO_2 nanoparticles were placed on the surface of a cover glass, adhered to it with the help of a small amount of adhesive tape, as the previous experiments. This process was repeatedsix times and the cover glasses were placed at increasing distances from the point where the TATP was located (10, 25, 50, 100, 150 and 200 cm).

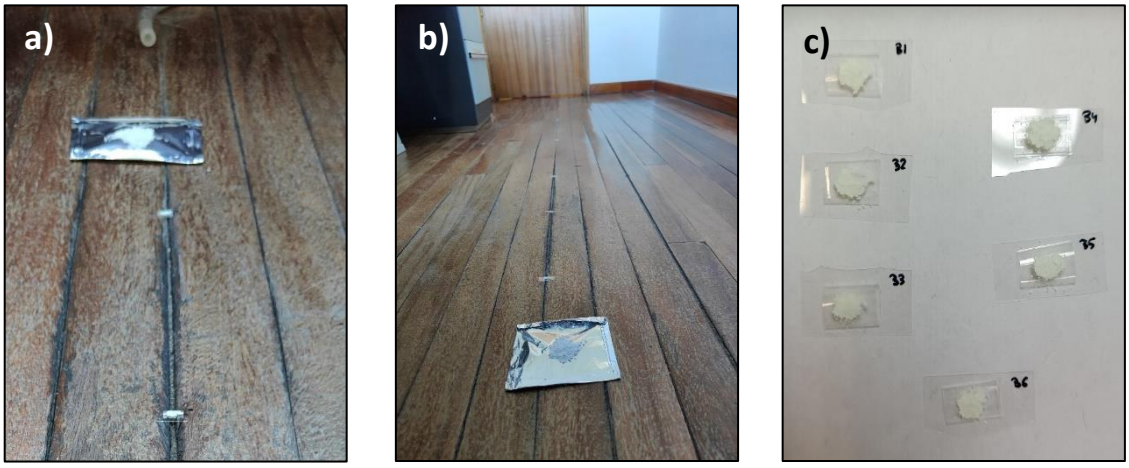

Figure 135. Arrangement the AR82·SiO_2 nanoparticles in the office.
a) Arrangement of the TATP in front of the airflow outlet.
b) distribution of sensing nanoparticles in the room.
c) assembly for measurement of the nanoparticles.

Once TATP and particles were placed, these were left in the presence of TATP vapours for a period of 30 minutes. To carry out the measurements in the fluorimeter, they were covered with a quartz sheet that ensured the particles remained in a fixed position. This sheet was removed to leave the particles exposed to TATP vapours during the experiment. A measurement of the particles without being subjected to TATP was also made before and after remaining the same time as the particles that were subjected to TATP vapours to use as a reference.

Fluorescence measurements were made for each group of particles before and after the exposure to TATP vapours. Photos of the particles were taken under identical conditions and the excitation wavelength was 370 nm.

Experiment 7: at 26ºC during 30 minutes.

Of the 256 mg of TATP initially weighed, only 23 mg were evaporated under the temperature and time conditions used in this experiment, remaining 233 mg of TATP as solid.

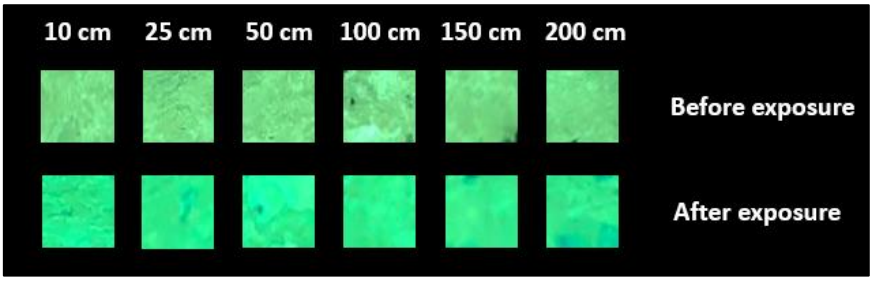

Figure 136. Comparative photograph taken under 366 nm light before and after exposure to TATP vapours at 26ºC during 30 minutes.

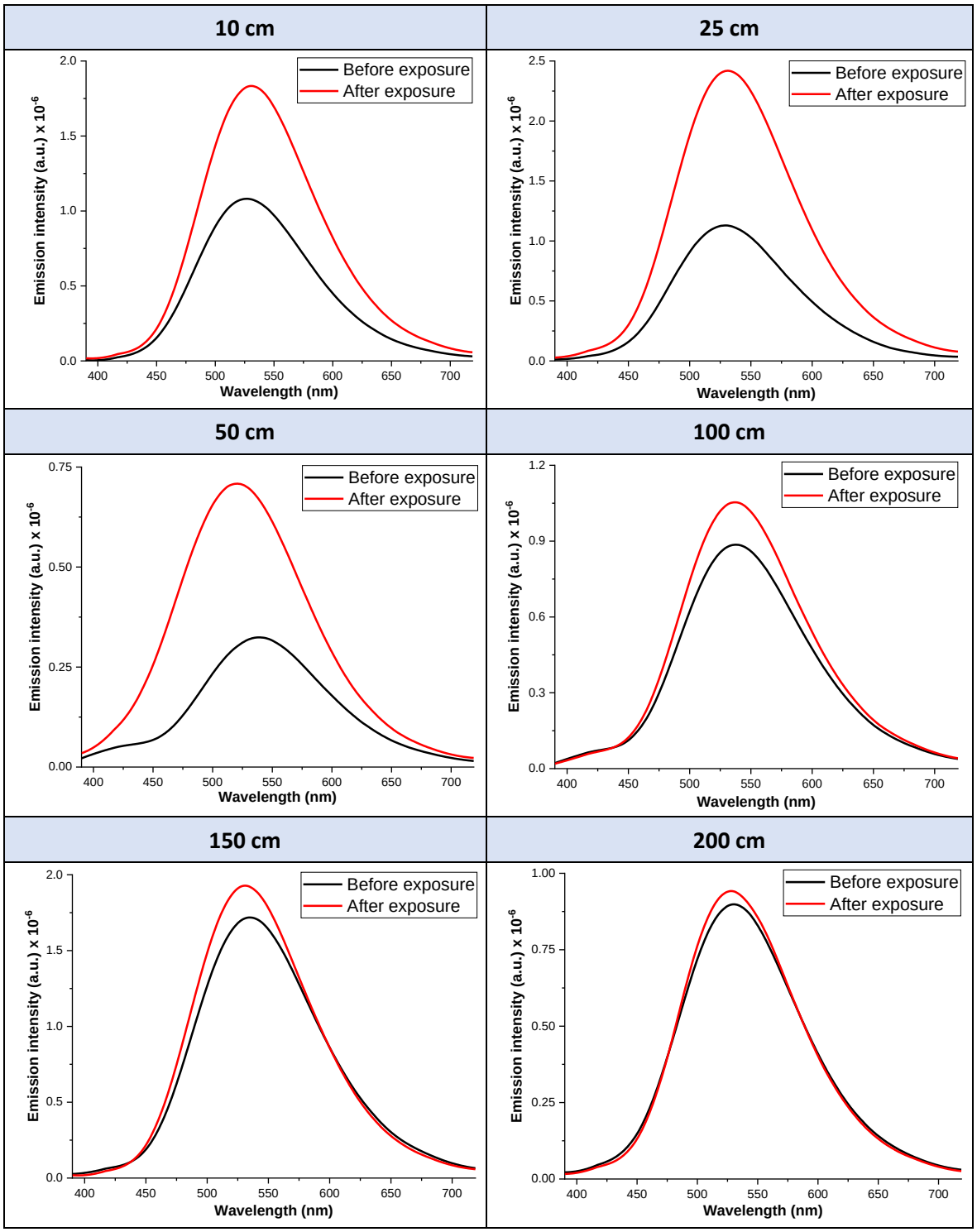

Figure 137. Emission spectra of the nanoparticles before and after exposure to TATP vapours at 26ºC during 30 minutes.

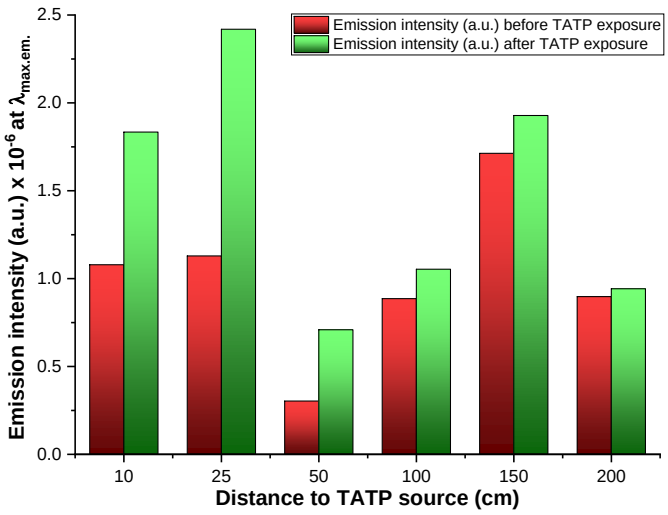

Figure 138. Histogram plotting the peak emission before and after exposure to TATP vapours at 26ºC during 30 minutes.

The average increase in the emision intensity for particles were located 50 cm or less from the TATP source was 206%, while the increase for the emission intensity for nanoparticles were located one meter or more was only 112%.

Sensing AR82s·SiO_2 particles position	Increase in emission intensity
10 cm	170%
25 cm	214%
50 cm	234%
100 cm	119%
150 cm	113%
200 cm	105%

Figure 139. Increment in fluorescence emission intensity of sensing nanoparticles as a function of their distance from the TATP source.

Experiment 8: at 26ºC during 30 minutes.

Of the 256 mg of TATP initially weighed, only 23 mg were evaporated under the temperature and time conditions used in this experiment, remaining 233 mg of TATP as solid in this case too.

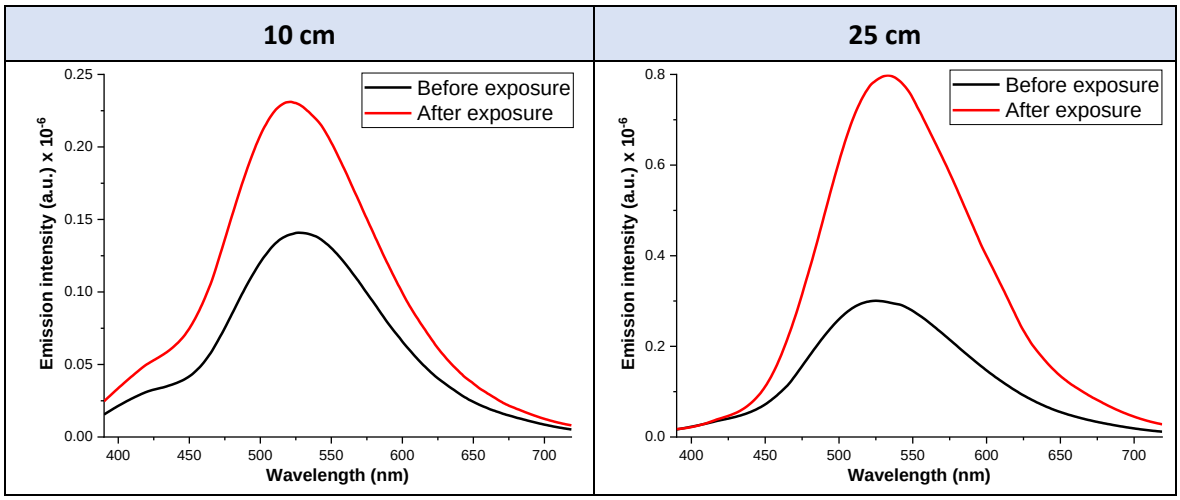

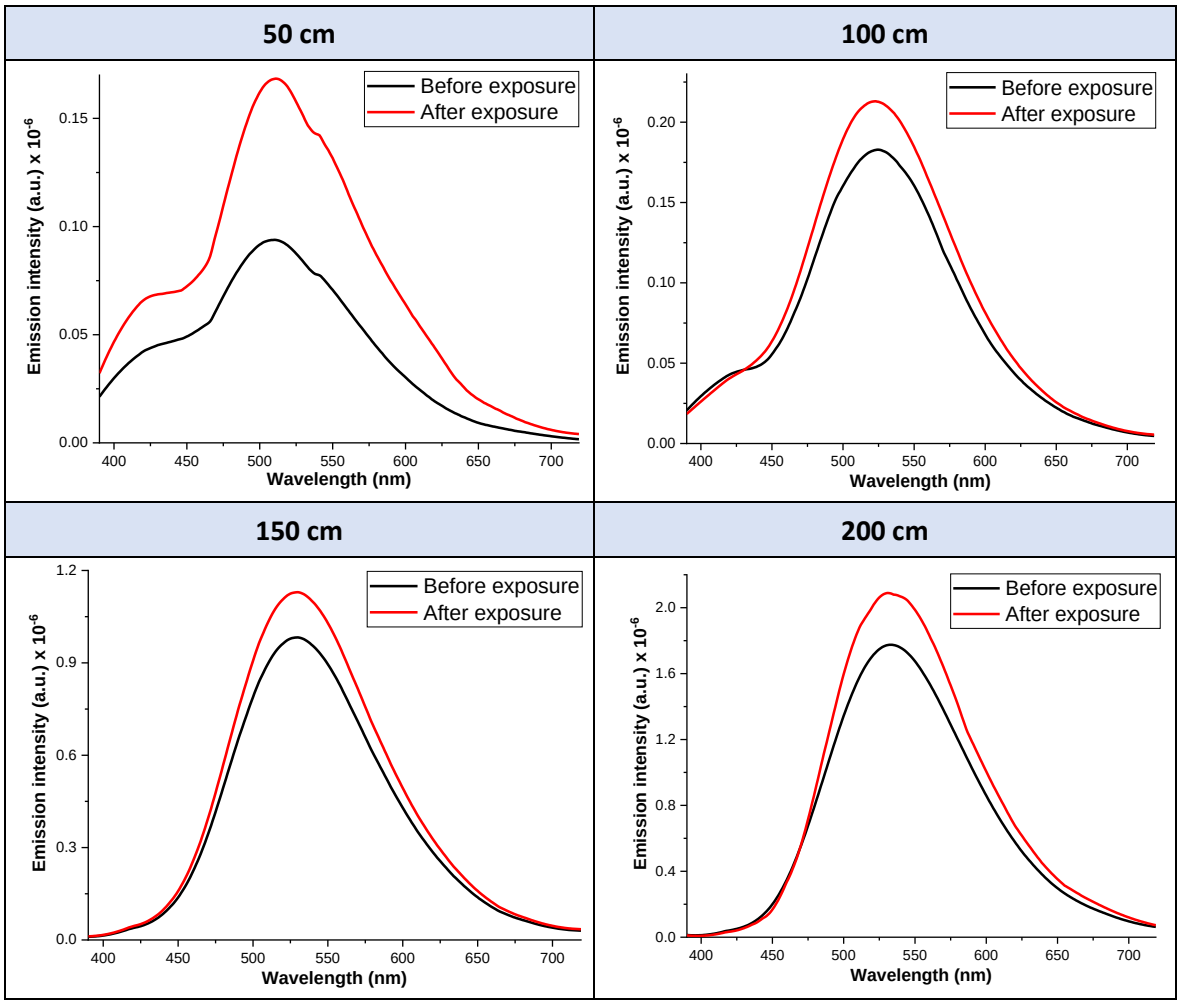

Figure 140. Emission spectra of the nanoparticles before and after exposure to TATP vapours at 26ºC during 30 minutes.

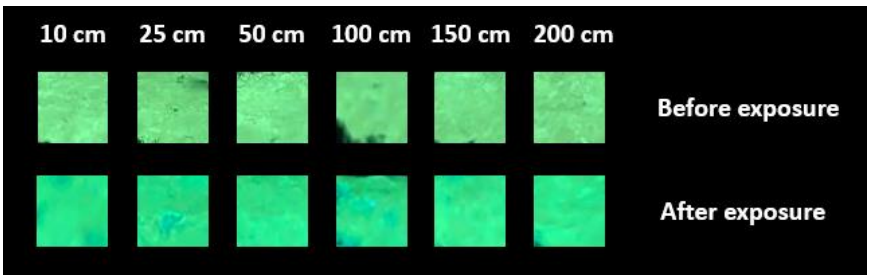

Figure 141. Comparative photograph taken under 366 nm light before and after exposure to TATP vapours at 26ºC during 30 minutes.

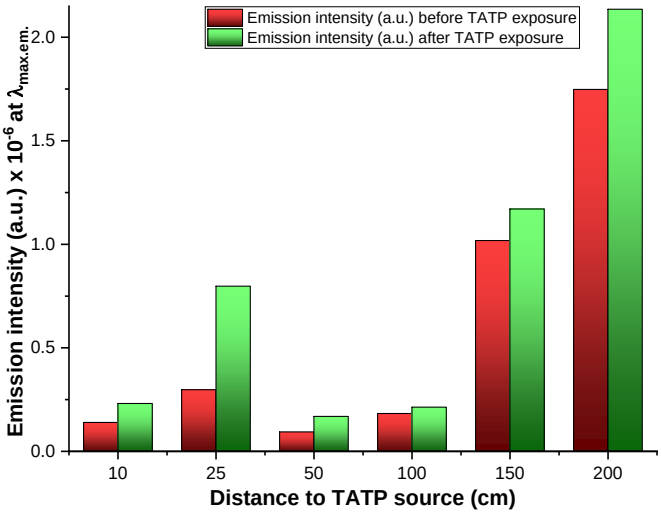

Figure 142. Histogram plotting the peak emission before and after exposure to TATP vapours at 26ºC during 30 minutes.

The average increase in the emision intensity for particles were located 50 cm or less from the TATP source was 205%, while the increase for the emission intensity for nanoparticles were located one meter or more was only 118%.

Sensing AR82s·SiO_2 particles position	Increase in emission intensity
10 cm	166%
25 cm	268%
50 cm	180%
100 cm	117%
150 cm	115%
200 cm	122%

Figure 143. Increment in fluorescence emission intensity of sensing nanoparticles as a function of their distance from the TATP source.

Experiment 9: at 26ºC during 30 minutes.

Of the 251 mg of TATP initially weighed, only 36 mg were evaporated under the temperature and time conditions used in this experiment, remaining 215 mg of TATP as solid.

10 cm	25 cm
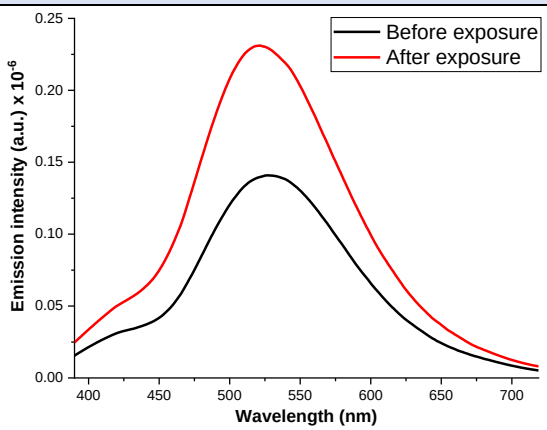	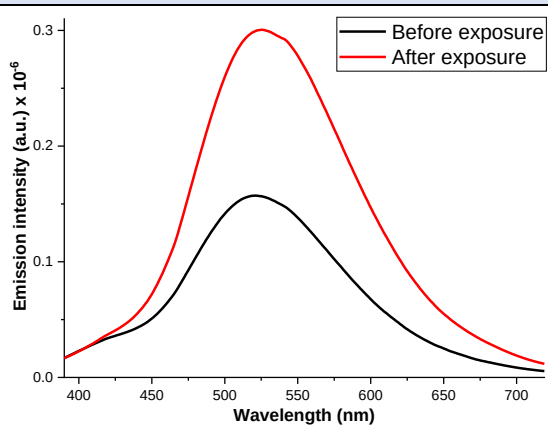

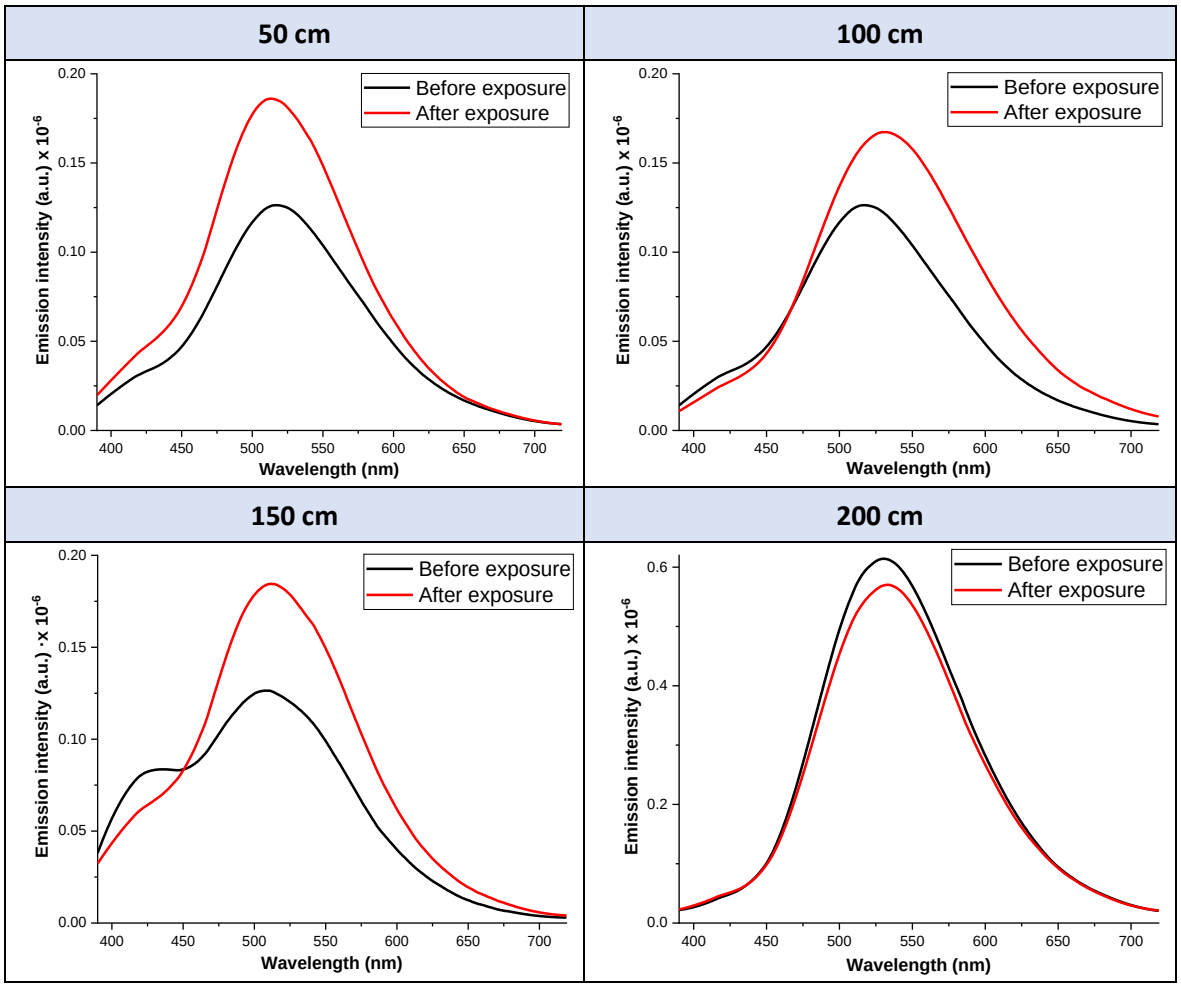

Figure 144. Emission spectra of the nanoparticles before and after exposure to TATP vapours at 26ºC during 30 minutes.

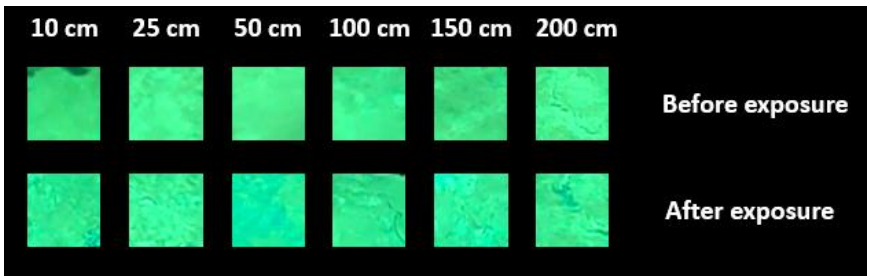

Figure 145. Comparative photograph taken under 366 nm light before and after exposure to TATP vapours at 26ºC during 30 minutes.

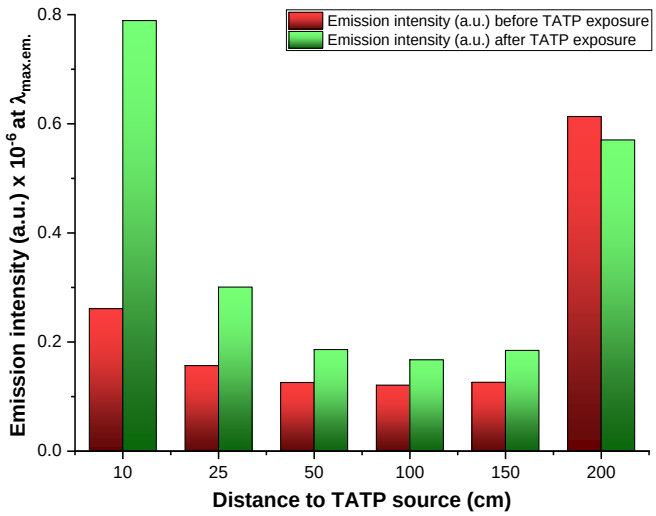

Figure 146. Histogram plotting the peak emission before and after exposure to TATP vapours at 26ºC during 30 minutes.

The average increase in the emision intensity for particles were located 50 cm or less from the TATP source was 214%, while the increase for the emission intensity for nanoparticles were located one meter or more was only 126%.

Sensing AR82s·SiO_2 particles position	Increase in emission intensity
10 cm	302%
25 cm	192%
50 cm	148%
100 cm	138%
150 cm	146%
200 cm	93%

Figure 147. Increment in fluorescence emission intensity of sensing nanoparticles as a function of their distance from the TATP source.

Experiment 10: at 26ºC during 30 minutes.

Of the 250 mg of TATP initially weighed, only 36 mg were evaporated under the temperature and time conditions used in this experiment, remaining 214 mg of TATP as solid.

10 cm	25 cm
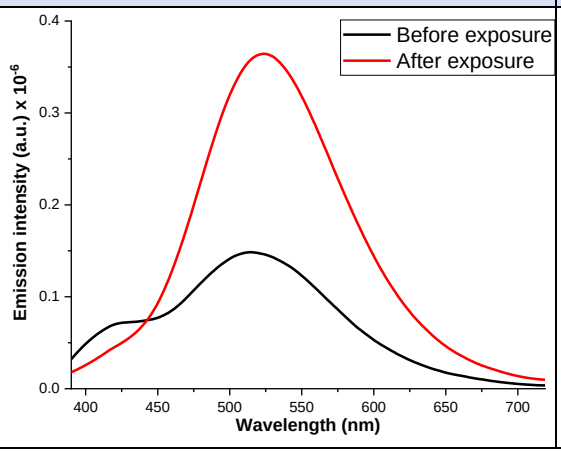	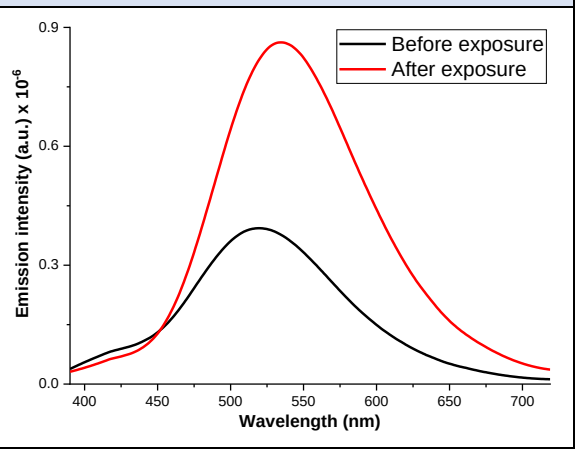

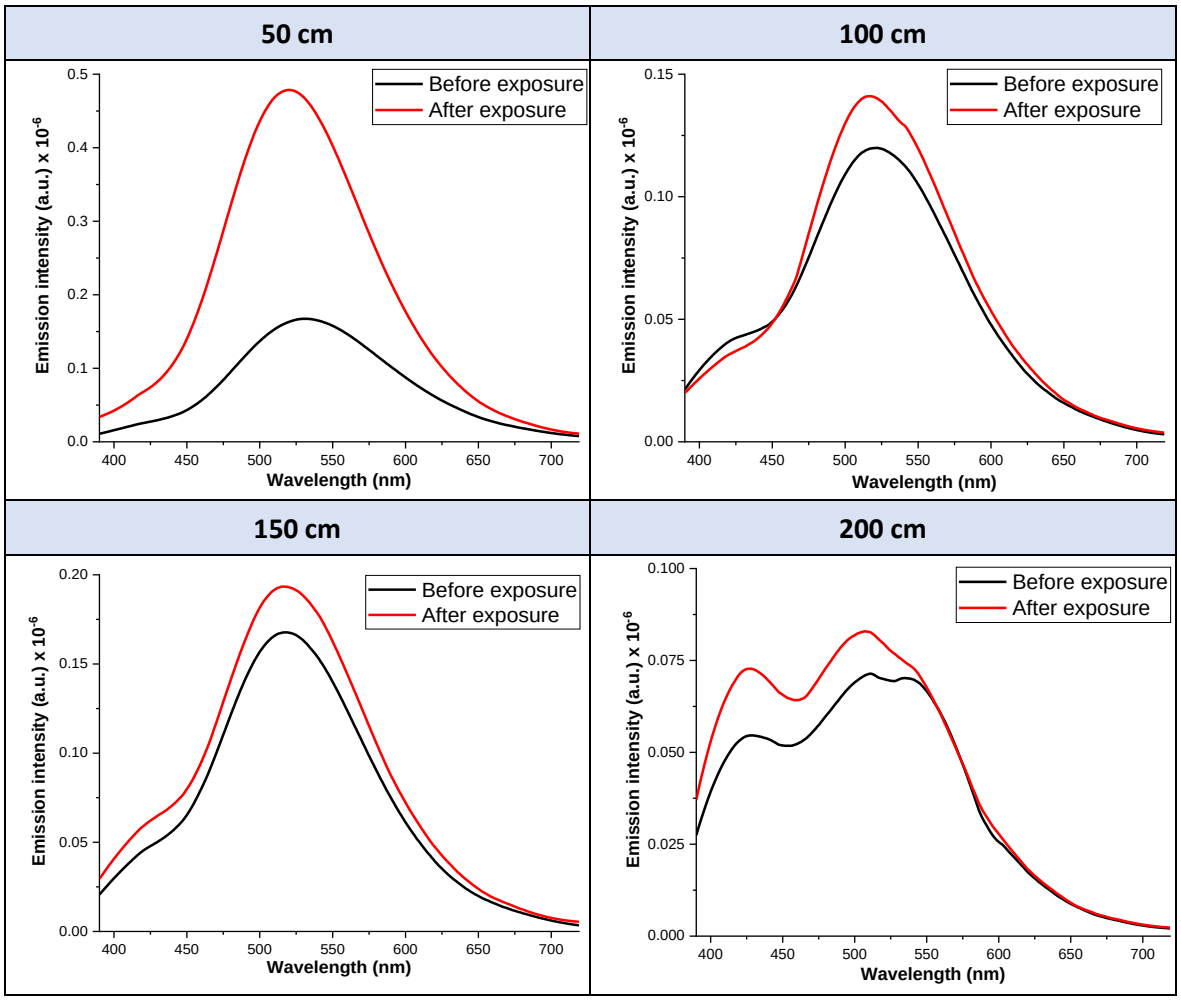

Figure 148. Emission spectra of the nanoparticles before and after exposure to TATP vapours at 26ºC during 30 minutes.

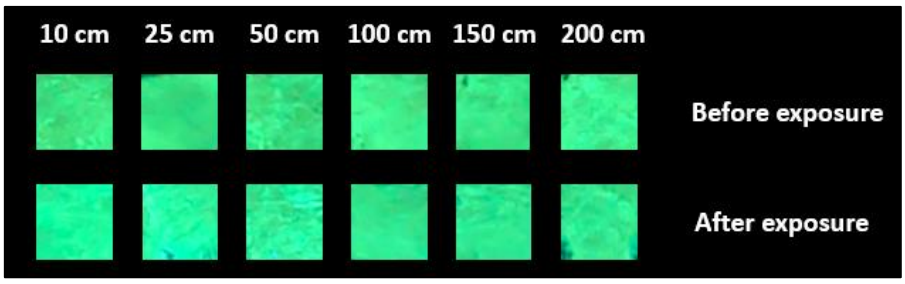

Figure 149. Comparative photograph taken under 366 nm light before and after exposure to TATP vapours at 26ºC during 30 minutes.

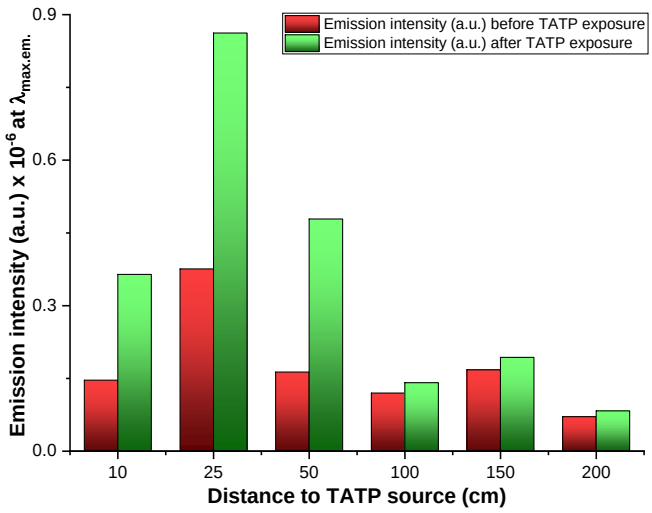

Figure 150. Histogram plotting the peak emission before and after exposure to TATP vapours at 26ºC during 30 minutes.

The average increase in the emision intensity for particles were located 50 cm or less from the TATP source was 257%, while the increase for the emission intensity for nanoparticles were located one meter or more was only 117%.

Sensing AR82s·SiO_2 particles position	Increase in emission intensity
10 cm	249%
25 cm	229%
50 cm	293%
100 cm	118%
150 cm	115%
200 cm	117%

Figure 151. Increment in fluorescence emission intensity of sensing nanoparticles as a function of their distance from the TATP source.

Experiment 11: at 26ºC during 30 minutes.

Of the 254 mg of TATP initially weighed, only 32 mg were evaporated under the temperature and time conditions used in this experiment, remaining 222 mg of TATP as solid.

10 cm	25 cm
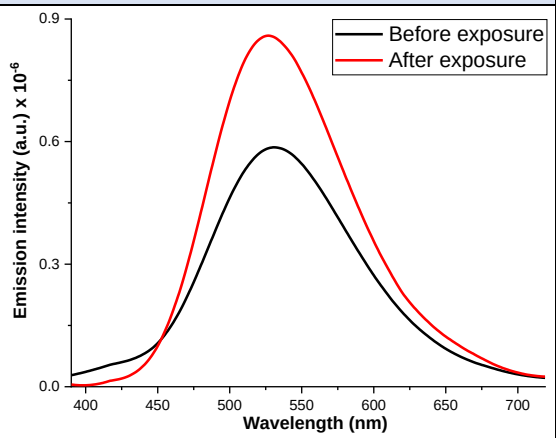	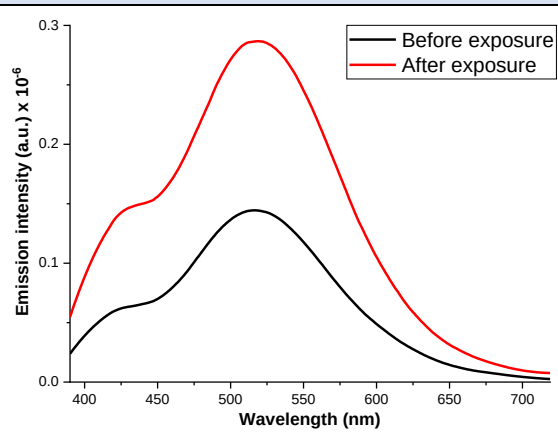

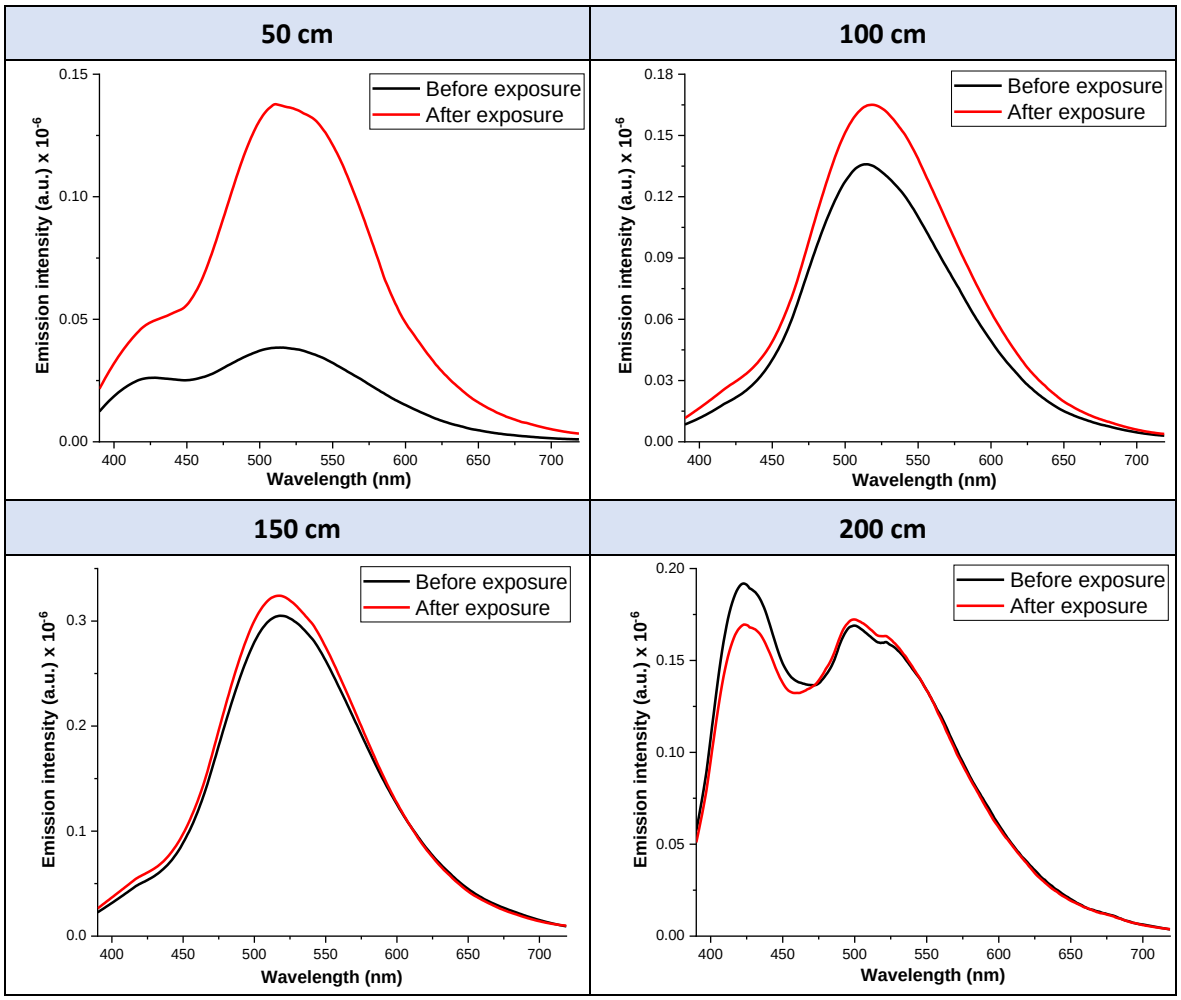

Figure 152. Emission spectra of the nanoparticles before and after exposure to TATP vapours at 26ºC during 30 minutes.

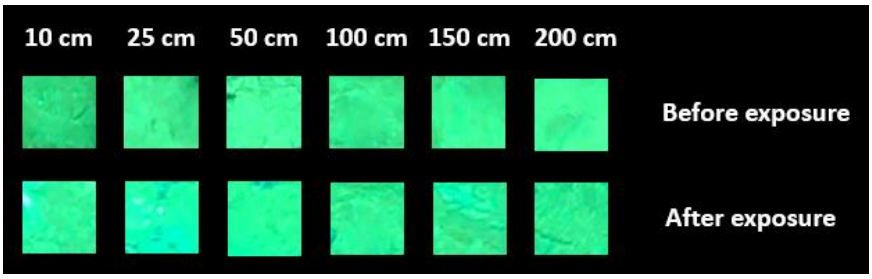

Figure 153. Comparative photograph taken under 366 nm light before and after exposure to TATP vapours at 26ºC during 30 minutes.

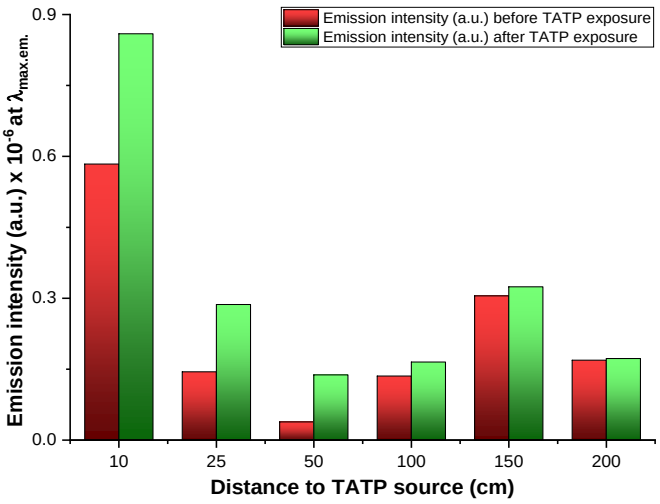

Figure 154. Histogram plotting the peak emission before and after exposure to TATP vapours at 26ºC during 30 minutes.

The average increase in the emision intensity for particles were located 50 cm or less from the TATP source was 235%, while the increase for the emission intensity for nanoparticles were located one meter or more was only 110%.

Sensing AR82s·SiO_2 particles position	Increase in emission intensity
10 cm	147%
25 cm	199%
50 cm	359%
100 cm	122%
150 cm	106%
200 cm	102%

Figure 155. Increment in fluorescence emission intensity of sensing nanoparticles as a function of their distance from the TATP source.

Experiment 12: at 26ºC during 30 minutes.

Of the 254 mg of TATP initially weighed, only 32 mg were evaporated under the temperature and time conditions used in this experiment, remaining 222 mg of TATP as solid.

10 cm	25 cm
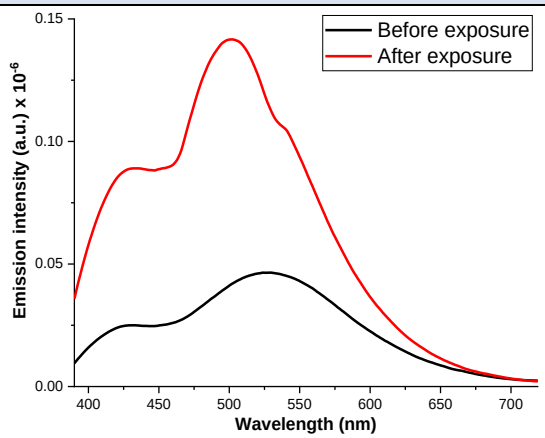	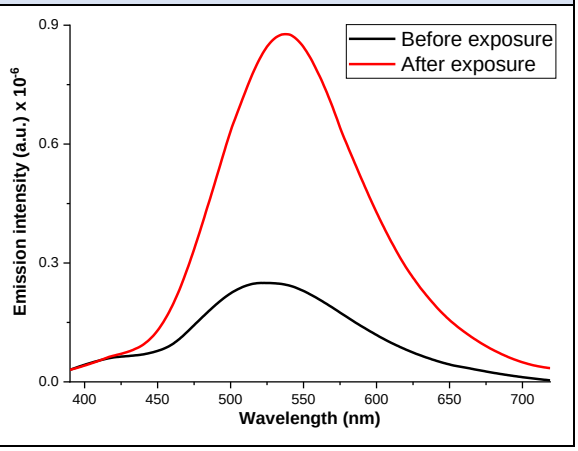

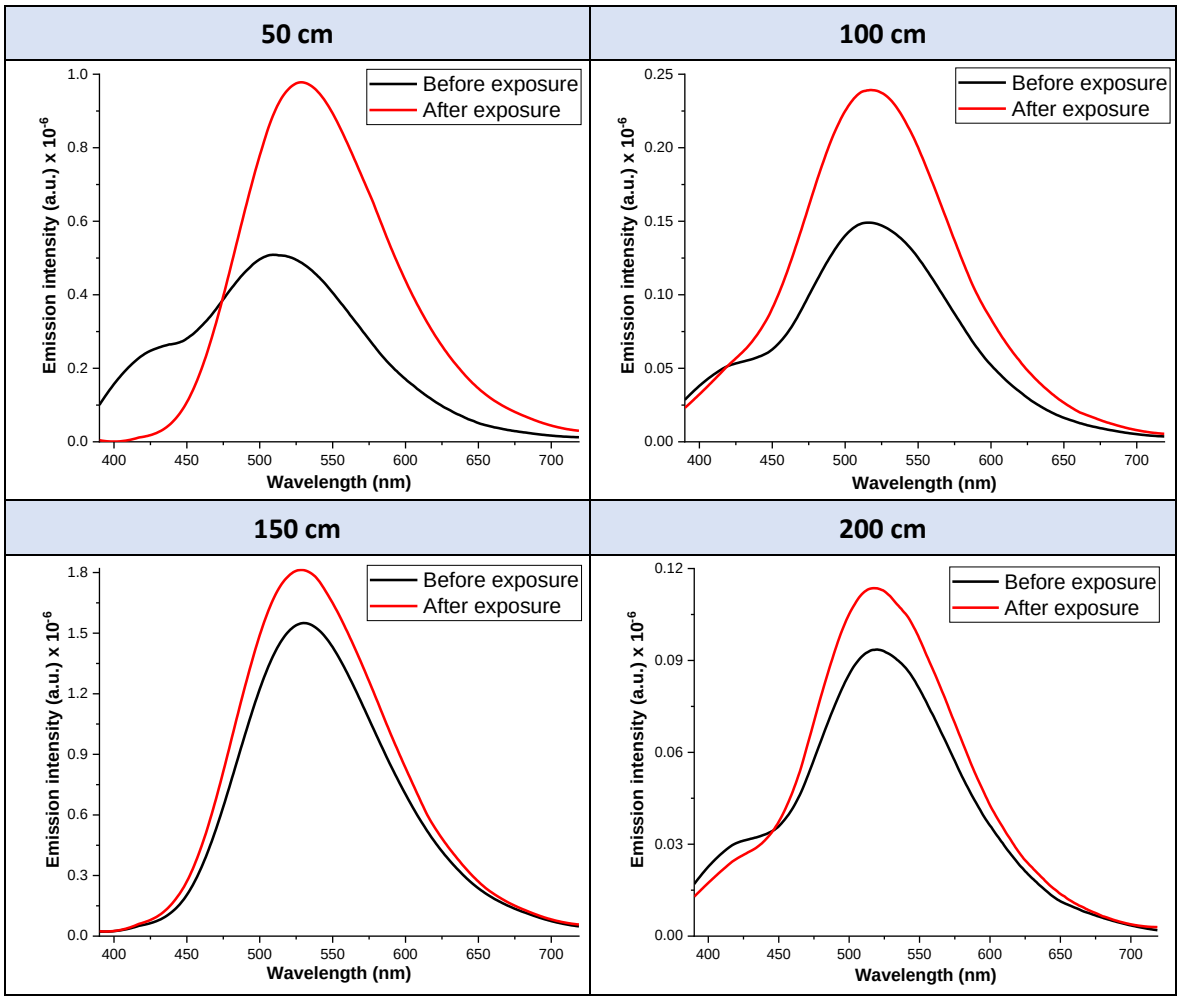

Figure 156. Emission spectra of the nanoparticles before and after exposure to TATP vapours at 26ºC during 30 minutes.

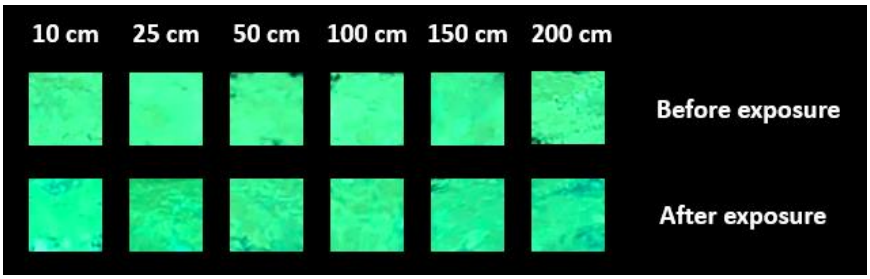

Figure 157. Comparative photograph taken under 366 nm light before and after exposure to TATP vapours at 26ºC during 30 minutes.

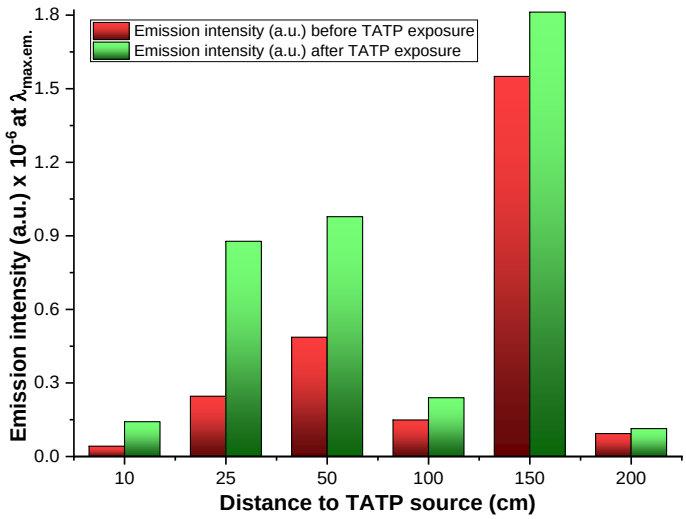

Figure 158. Histogram plotting the peak emission before and after exposure to TATP vapours at 26ºC during 30 minutes.

The average increase in the emision intensity for particles were located 50 cm or less from the TATP source was 299%, while the increase for the emission intensity for nanoparticles were located one meter or more was only 133%.

Sensing AR82s·SiO_2 particles position	Increase in emission intensity
10 cm	338%
25 cm	357%
50 cm	201%
100 cm	161%
150 cm	117%
200 cm	122%

Figure 159. Increment in fluorescence emission intensity of sensing nanoparticles as a function of their distance from the TATP source.

For an easier visualization of the whole data, the following graphs have been made, representing the normalized emision intensity variation before and after exposure to TATP vapours versus distance to the TATP source.

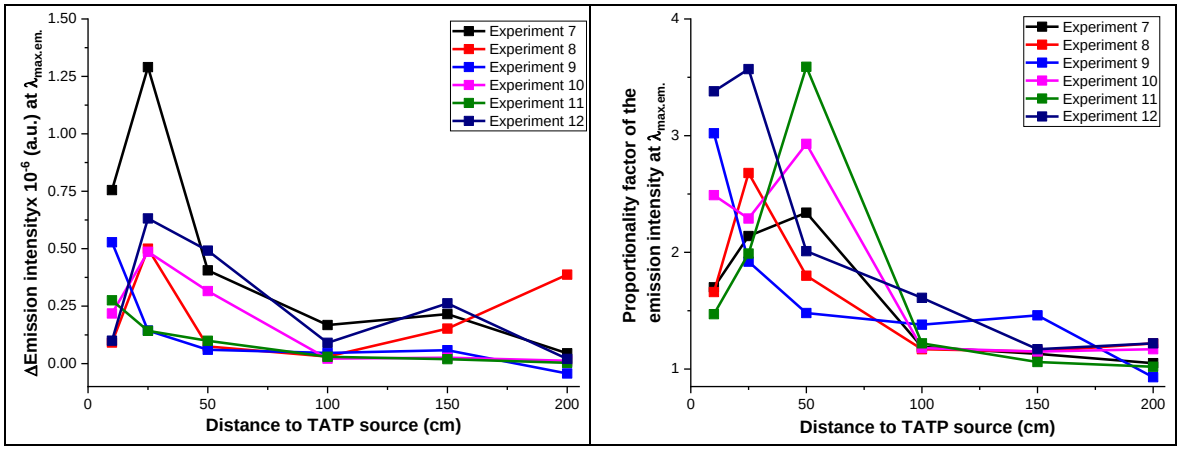

Figure 160. Summary of experiments 7-12 against TATP vapour at. Emission intensity variation before and after exposure to TATP (left) and emission intensity proportionality factor (divided between the target, right) versus distance to the TATP source in both cases.

Maximum emission intensity data from previous experiments were organized according to the distance to the TATP source, representing, on the one hand, emission before contact with TATP vapours and, on the other hand, emission after contact with said vapours. This data were also normalized with respect to the maximum of emission from each experiment.

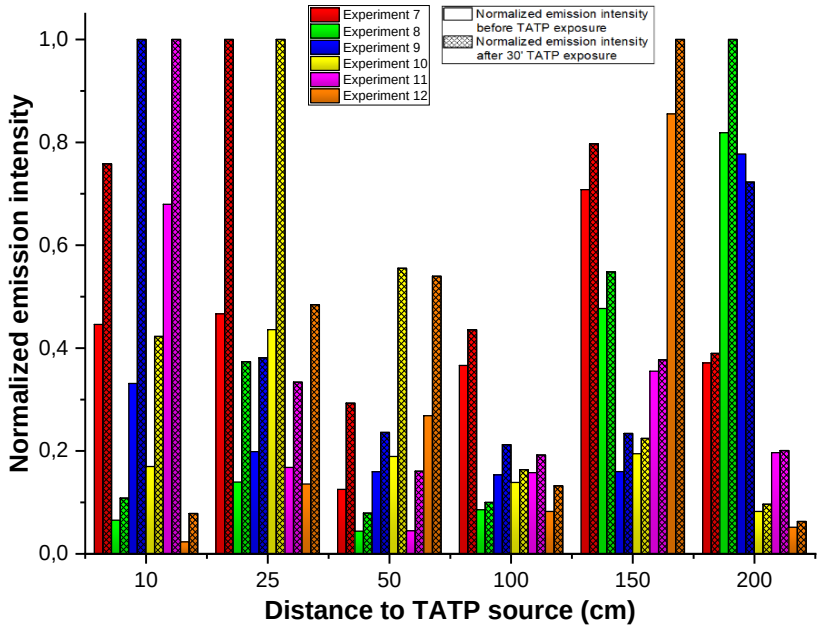

Figure 161. Summary of experiments 7-12. Normalized emission intensity variation before and after exposure to TATP versus distance to the TATP source.

After this, a common initial emission level was established using the lowest value measured for the nanoparticles prior to the exposure to TATP vapours. And finally, the substraction was made between the final and initial emission.

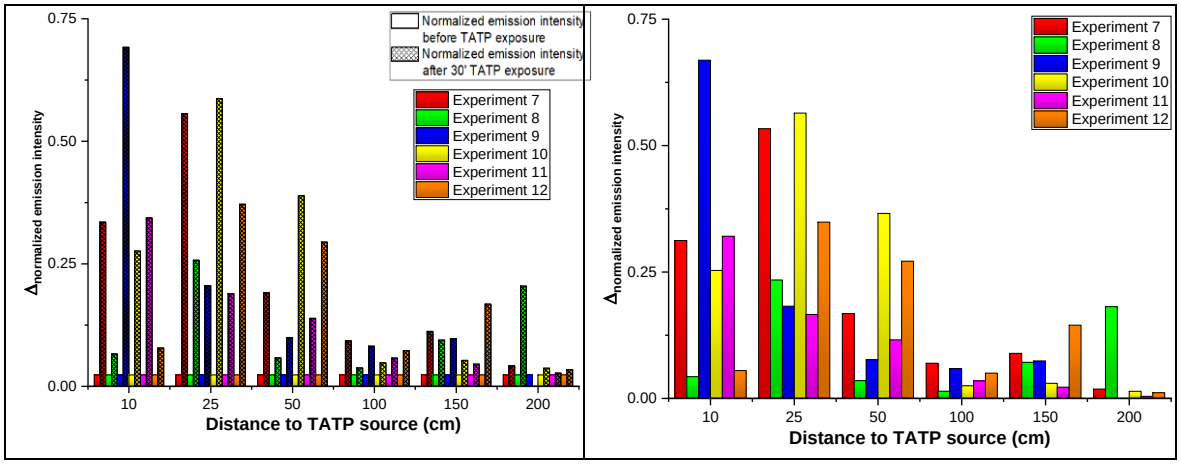

Figure 162. Summary of experiments 7-12. Normalized emission intensity setting a common initial particulate emission level before and after exposure to TATP vapours (left) and variation of the normalized emission intensity (right) as a function of the distance to the TATP source in both cases.

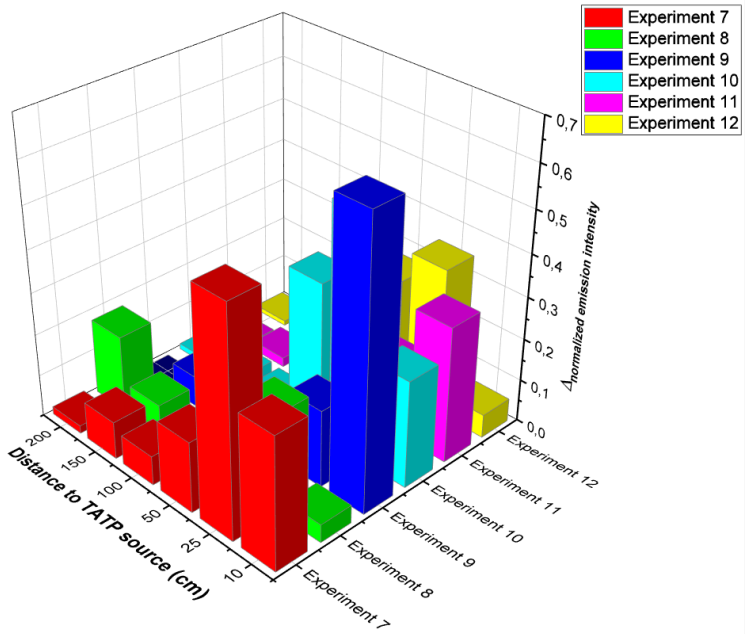

Figure 163. Summary of experiments 7-12. 3D representation of the variation of the normalized emission intensity as a function of the distance to the TATP source.

A selection of the measurements was made, discarding outliers and choosing only 3 measurements for each of the distances to the TATP source. Using these measurements, the average and standard deviation of the normalized variation of the emission intensity for each point were calculated and represented.

Distance (cm)	Experiment					
	7	8	9	10	11	12
10	**0.312**	0.043	**0.669**	0.252	**0.321**	0.055
25	0.533	0.234	**0.182**	**0.564**	**0.166**	0.349
50	**0.168**	0.035	0.076	0.366	**0.116**	**0.271**
100	**0.069**	0.014	**0.059**	0.025	0.035	**0.050**
150	0.089	0.071	**0.074**	**0.029**	**0.022**	0.145
200	**0.018**	0.181	-0.054	**0.014**	0.004	**0.011**

Figure 164. Values of variation of normalized the emission intensity as a function of the distance to the TATP source.

Distance (cm)	Average normalized emission variation	Standard deviation
10	0.434	0.203
25	0.304	0.225
50	0.185	0.079
100	0.059	0.011
150	0.042	0.028
200	0.014	0.004

Figure 165. Values of the average and standard deviation of normalized emission variation as a function of the distance to the TATP source.

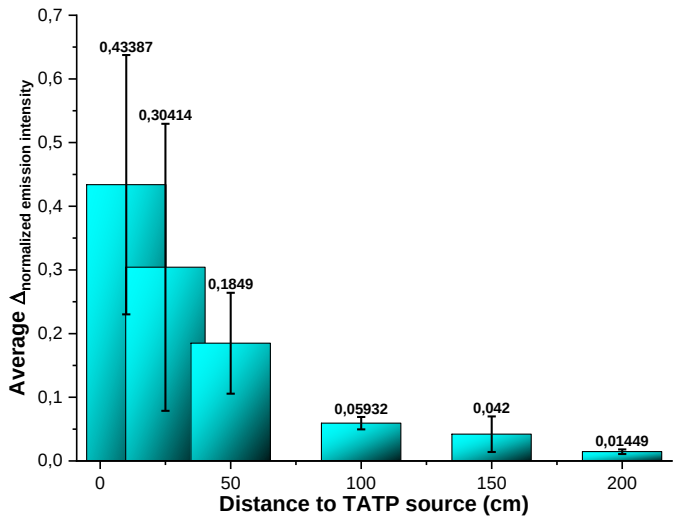

Figure 166. Average and standard deviation of normalized emission variation as a function of the distance to the TATP source.

^{1}H-NMR titration of AR82s against TATP with Amberlite:

An NMT titration was performed. Initially, ^{1}H-NMR of TATP (5 mg in 0.5 ml in $CDCl_3$), AR82s (3 mg in 0.5 ml in $CDCl_3$) and Amberlite (spatula tip) were performed as a reference. After this, the following amounts of TATP to the NMR tube corresponding to AR82s to carry out the titration.

Addition number	TATP mass added (µg)	Total mass of TATP added (µg)	Addition number	TATP mass added (µg)	Total mass of TATP added (µg)
1	0	0	**10**	60	150
2	5	5	**11**	150	300
3	5	10	**12**	200	500
4	5	15	**13**	300	800
5	5	20	**14**	600	1400
6	10	30	**15**	1800	3200
7	10	40	**16**	3600	6800
8	20	60	**17**	3600	10400
9	30	90	**18**	5400	15800

Figure 167. Additions of TATP to the ^{1}H-NMR titration fo AR82s.

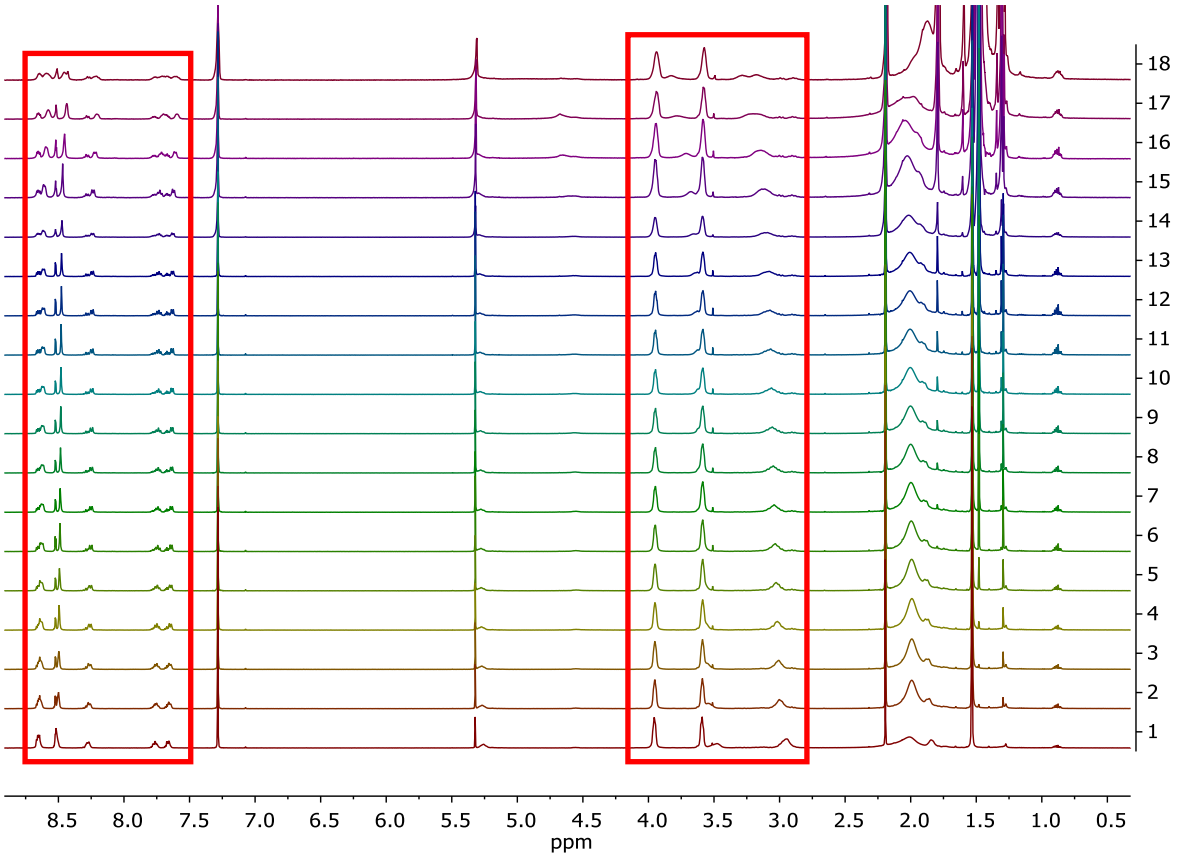

Figure 168. ^{1}H-NMR ($CDCl_3$, 500 MHz) titration of AR82s with increasing amounts of TATP in the presence of amberlite.

pH of TATP solution was approximately 5, pH of AR82s solution was 7 an the pH of AR82s solution with Amberlite was approximately 7 but the final pH of the titration was 2 (all of the was measured using litmus paper).

^{1}H-NMR titration of AR82s with *m*-CPBA:

The mechanism of oxidation of AR82s in the presence of increasing amounts of peroxide was studied by NMR titration by using *m*-CPBA.

Addition number	*m*-CPBA mass added (µg)	Total mass of *m*-CPBA added (µg)	Addition number	*m*-CPBA mass added (µg)	Total mass of *m*-CPBA added (µg)
1	0	0	**9**	30	90
2	5	5	**10**	60	150
3	5	10	**11**	1500	300
4	5	15	**12**	200	500
5	5	20	**13**	300	800
6	10	30	**14**	600	1400
7	10	40	**15**	1800	3200
8	20	60			

Figure 169. Amounts of m-CPBA used in NMR titration.

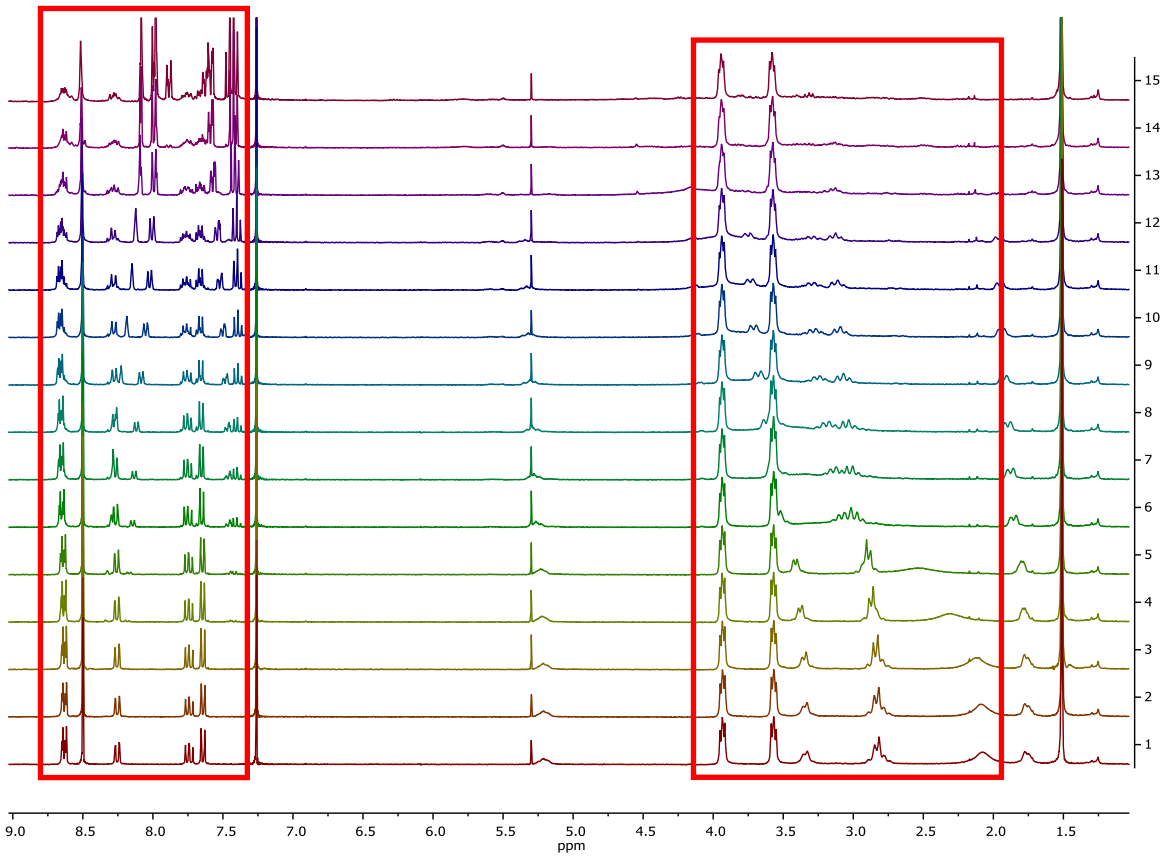

Figure 170. ^{1}H NMR titration of 10 mg AR82s in 0.5 ml of $CDCl_3$ with increasing amounts of m-CPBA.

The titration showed oxidation of the unprotected secondary amino group with progressive disappearance of the proton signal of the amine group and chemical shift of the methylene groups of the oxidized piperidine group (the signals between 1.8 and 3.7 ppm).

Synthesis of *N*-(piperidin-4-yl)-4-[2-(piperazin-1-yl)pyrimidin-5-yl]naphthalene-1,8-dicarboxyl-monoimide (AR82d)

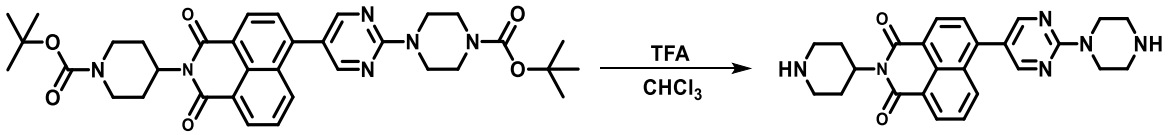

In a 50 ml flask, 150 mg of *N*-(*N*-Boc-piperidin-4-yl)-4-[2-(4-Boc-piperazin-1-yl)pyrimidin-5-yl]naphthalene-1,8-dicarboxylmonoimide (AR82p, 0.23 mmol) were dissolved in 15 ml of chloroform and, then, 2 ml of TFA (26 mmol) was added. After 4 hours under stirring at room temperature, 10 ml of water were poured into the flask and the resulting mixture was neutralized employing a 40% sodium hidroxide solution until it reached a neutral pH. Then, 20 ml of water were added into the flask and the mixture was extracted three times with chloroform (3×30 ml). The organic extracts were combined, dried over anhidrous Na_2SO_4 and the solvent was evaporated under reduce pressure, to obtain 100 mg of a yellow solid, 98% yield.

m.p.: 230-233°C.

IR (ATR, cm^{-1}): 3448 (N-H), 3007 – 2501, 1655 (C=O), 1584, 1506, 1449, 1349, 1271, 1236, 1197, 1173 (C-N), 1116, 1041, 948, 828, 781, 720, 535, 505, 432.

^{1}H-NMR (300 MHz, TFA) δ (ppm): 8.72 (m, 2H, 2×**H$_{Ar}$**), 8.63 (m, 2H, 2×**H$_{Ar}$**), 8.04 (m, 1H, **H$_{Ar}$**), 7.74 (m, 2H, 2×**H$_{Ar}$**), 5.57-5.39 (m, 1H, C**H**), 4.37 (s, 4H, 2×C**H**$_2$), 3.64 (s, 6H, 3×C**H**$_2$), 3.36-3.09 (m, 4H, 2×C**H**$_2$), 2.05 (m, 2H, C**H**$_2$).

^{13}C-NMR (75MHz, TFA) δ (ppm): 169.9 (**C**=O), 169.5 (**C**=O), 169.2 (**C**=O), 168.9 (**C**=O), 160.0 (**C**$_{Ar}$H), 159.3 (**C**$_{Ar}$H), 155.6 (**C**$_{Ar}$), 154.9 (**C**$_{Ar}$), 139.8 (**C**$_{Ar}$), 139.2 (**C**$_{Ar}$), 137.2 (**C**$_{Ar}$H), 136.5 (**C**$_{Ar}$H), 135.7 (**C**$_{Ar}$H), 135.1 (**C**$_{Ar}$H), 134.5 (**C**$_{Ar}$H), 133.1 (**C**$_{Ar}$), 132.4 (**C**$_{Ar}$H), 132.3 (**C**$_{Ar}$H), 132.0 (**C**$_{Ar}$), 131.9 (**C**$_{Ar}$H), 131.6 (**C**$_{Ar}$H), 131.4 (**C**$_{Ar}$), 126.3 (**C**$_{Ar}$), 126.2 (**C**$_{Ar}$), 125.6 (**C**$_{Ar}$), 125.5 (**C**$_{Ar}$), 125.3 (**C**$_{Ar}$), 124.7 (**C**$_{Ar}$), 52.6 (**C**H), 51.9 (**C**H), 49.2 (**C**H$_2$), 48.6 (**C**H$_2$), 46.9 (**C**H$_2$), 46.3 (**C**H$_2$), 45.4 (**C**H$_2$), 44.7 (**C**H$_2$), 44.2 (**Cq**), 28.0 (**C**H$_2$), 27.3 (**C**H$_2$).

HRMS (MALDI, DCTB+) m/z: calculated for $C_{25}H_{26}N_6O_2$: 443.2190 (M^+ + H); found 443.2193.

UV-Vis ($CHCl_3$), λ_{max} nm (log ε): 380 (3.3).

Ø (EtOAc, %): 67.62.

τ (375 nm, EtOAc, ns): 4.270 (χ^2: 1.015).

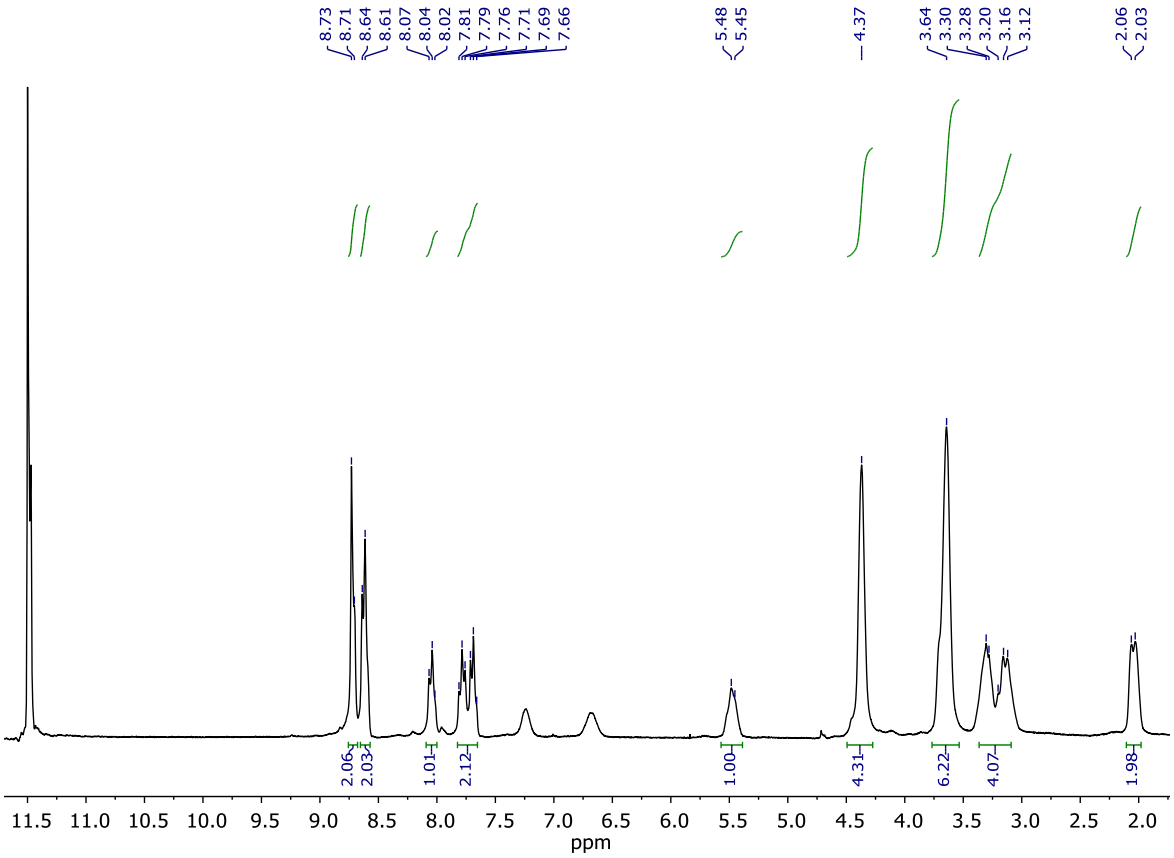

Figure 171. ¹H-NMR (TFA, 300 MHz) of AR82d.

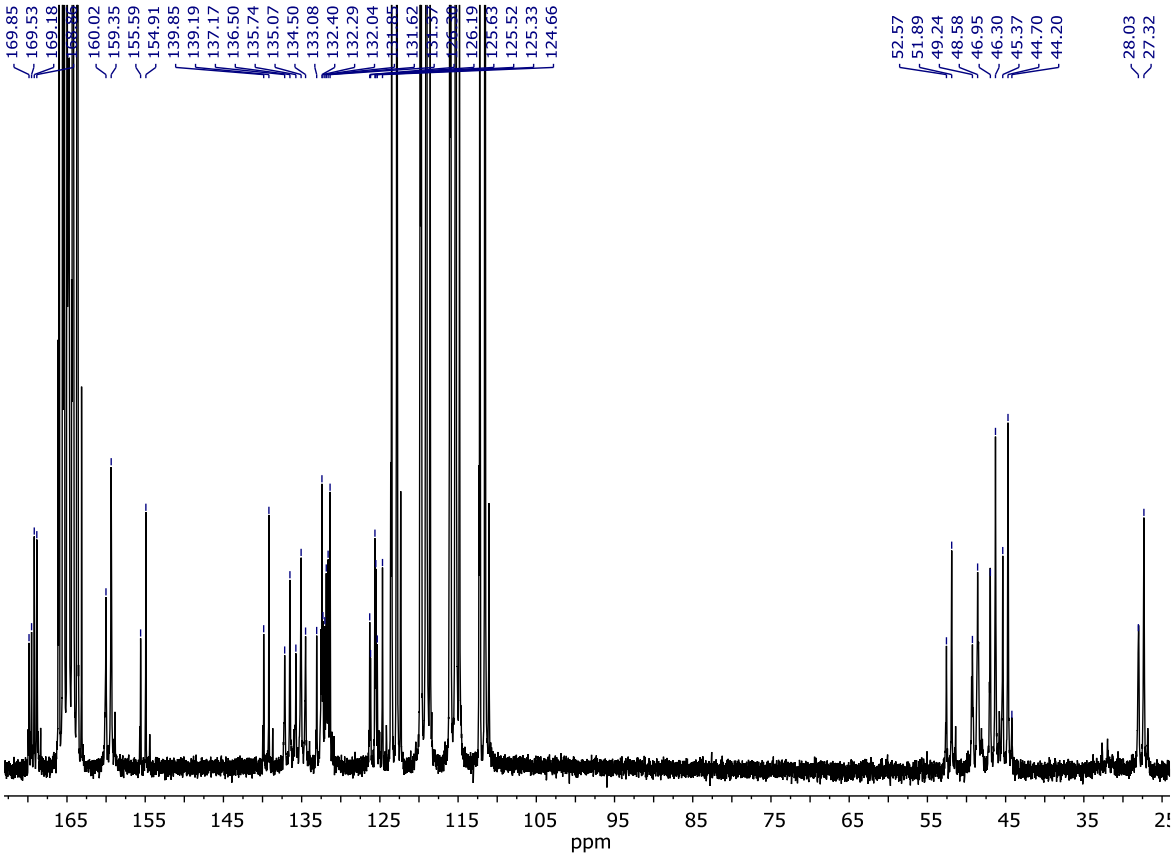

Figure 172. ¹³C-NMR (TFA, 75 MHz) of AR82d.

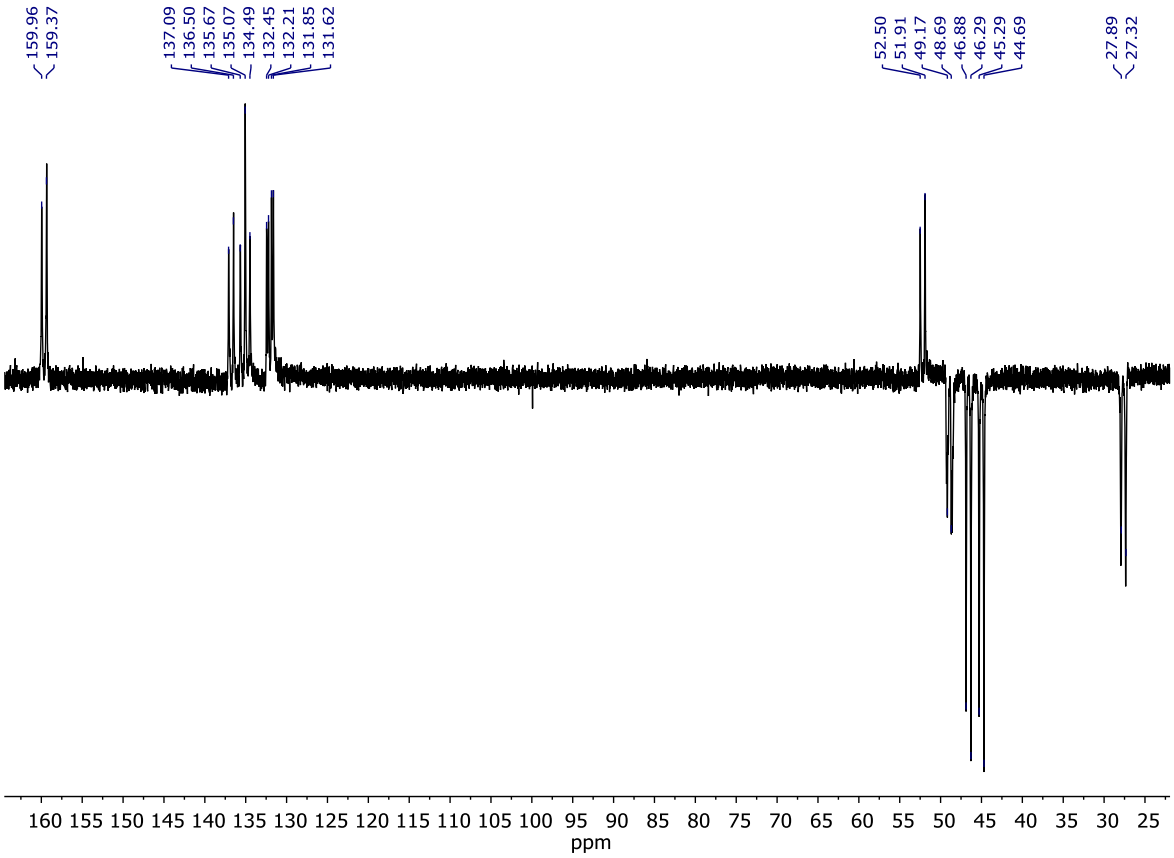

Figure 173. DEPT NMR (TFA, 75 MHz) of AR82d.

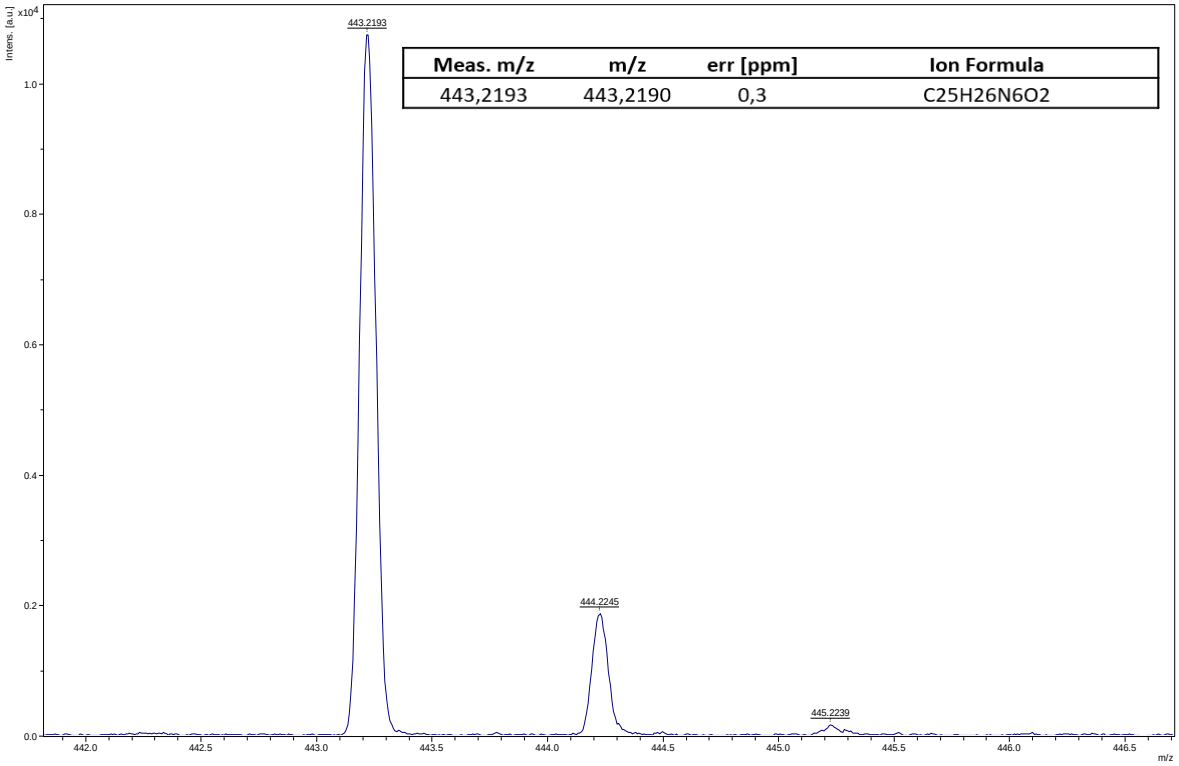

Meas. m/z	m/z	err [ppm]	Ion Formula
443,2193	443,2190	0,3	C25H26N6O2

Figure 174. HRMS (MALDI, DCTB+) of AR82d.

Solvatochromism:

The concentration of the compound was 20 µM and the excitation wavelength was 360 nm.

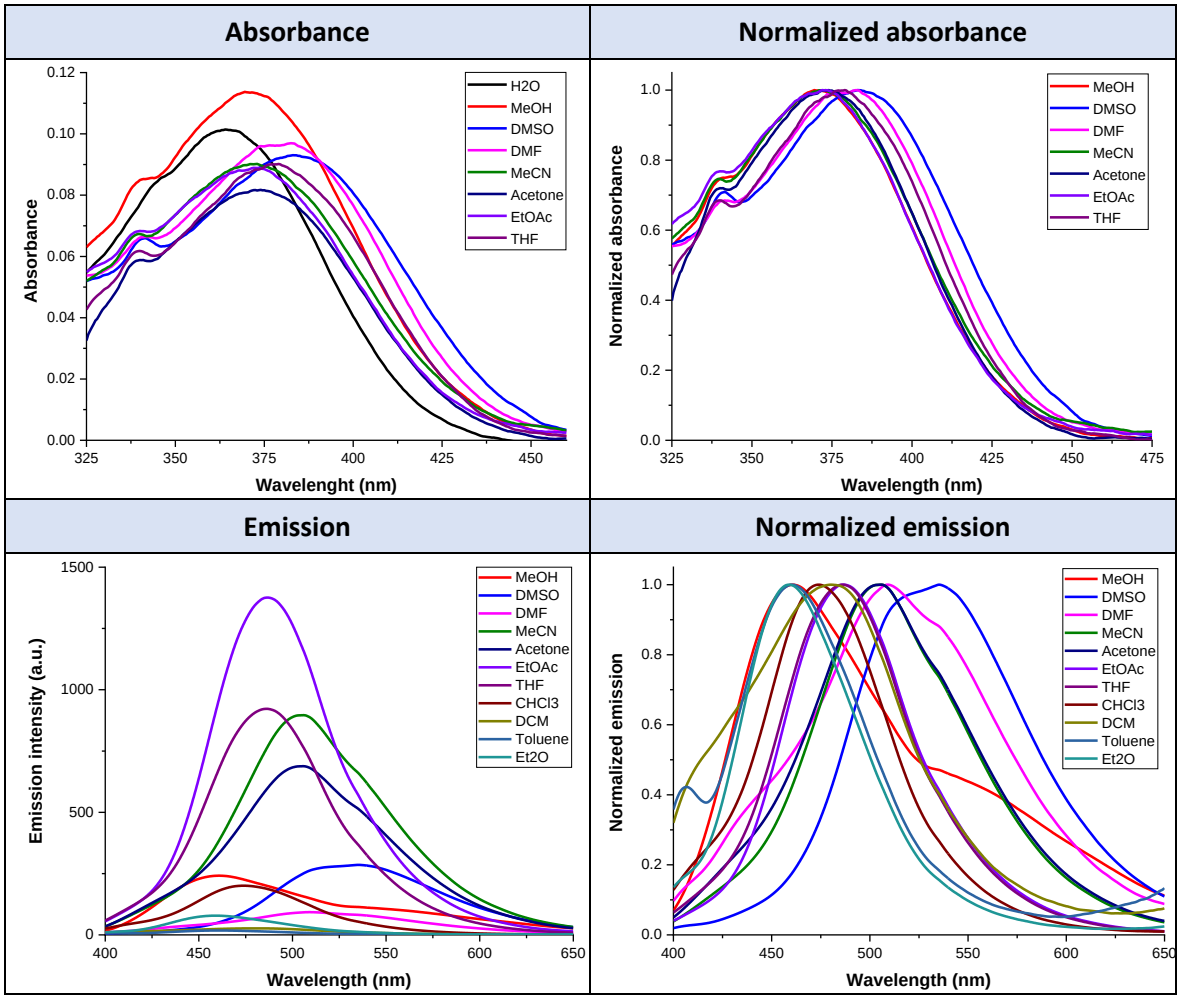

Figure 175. Solvatochromism of AR82d.

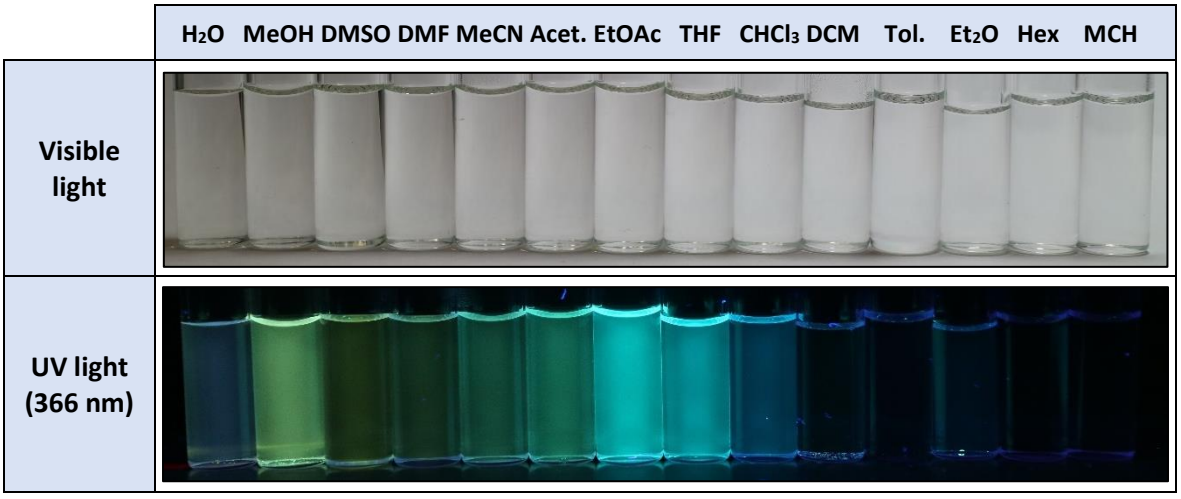

Figure 176. Solvatochromism of AR82d under visible and 366 nm light.

Fluorescence decay lifetime (τ):

The solvent used was ethyl acetate. The concentration of the compound was 20 µM.

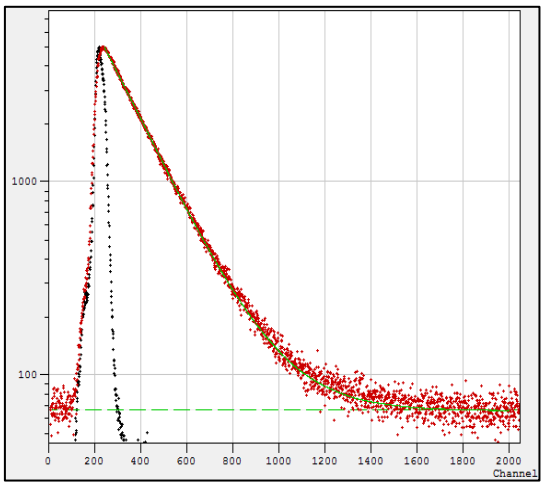

Figure 177. Fluorescence decay lifetime of AR82d.

Water acceptance test:

The solvent used was MeOH and the concentration of the compound was 20 µM.

	R	5%	10%	20%	30%	40%	50%	60%	70%	80%	90%
Visible light											
UV light (366 nm)	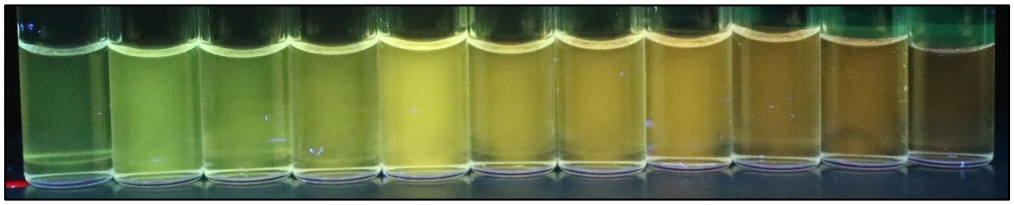										

Figure 178. Water acceptance test of AR82d under visible (up) and UV (down) light.

There was a quenching in the fluorescent emission as the amount of water was increased (ACQ).

pH test:

The amount of water that the compound could accept was 30%. The concentration of the compound was 20 µM and the solvent used was MeOH.

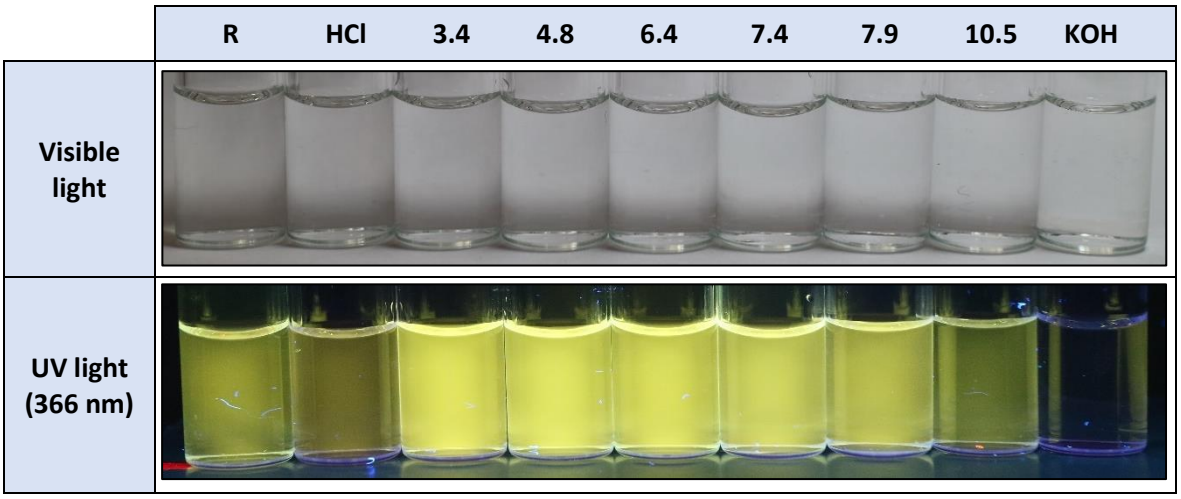

Figure 179. pH test of AR82d under visible (up) and UV (down) light.

There was a quenching in the emission at very basic pH. At intermediate pH, the colour of the fluorescence was changed from green to yellow (3.4 – 7.9).

Cations and anions test:

The concentration of the compound was 20 µM and the solvent used was MeOH.

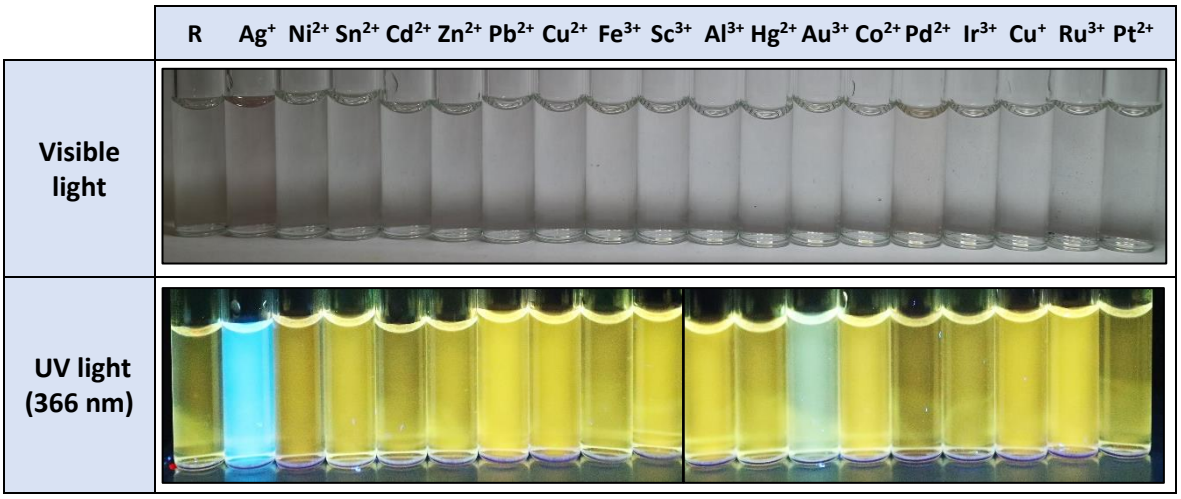

Figure 180. Cations test of AR82d under visible (up) and UV (down) light.

The most significant changes under UV light were the turn of the fluorescence to blue against Ag^{+} and Au^{3+}.

The concentration of the compound was 20 µM and the solvent used was MeOH.

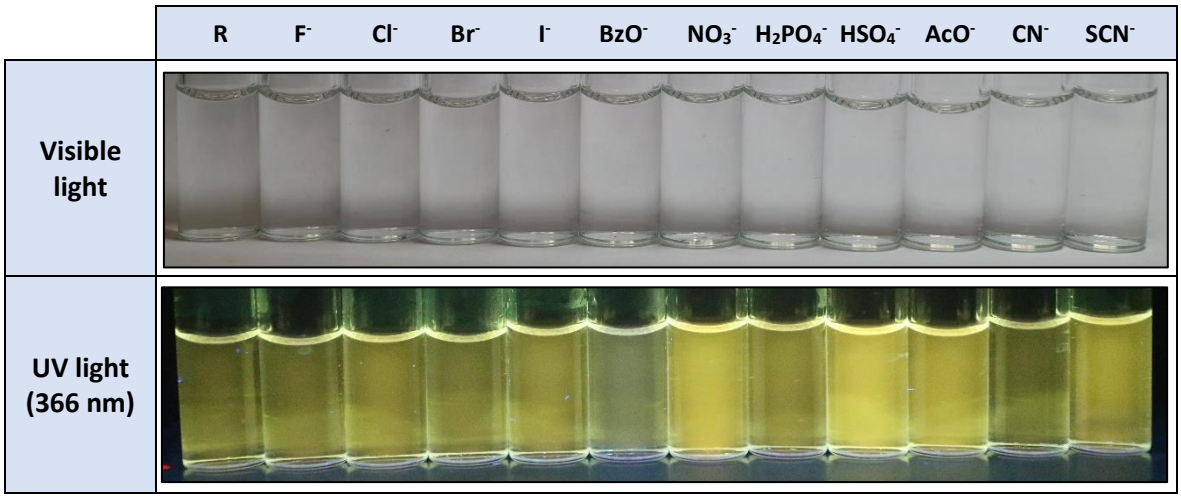

Figure 181. Anions test of AR82d under visible (up) and UV (down) light.

No significant changes were observed.

Oxidant and reductant reagents test:

The solvent used was MeOH and concentration of the compound was 20 µM.

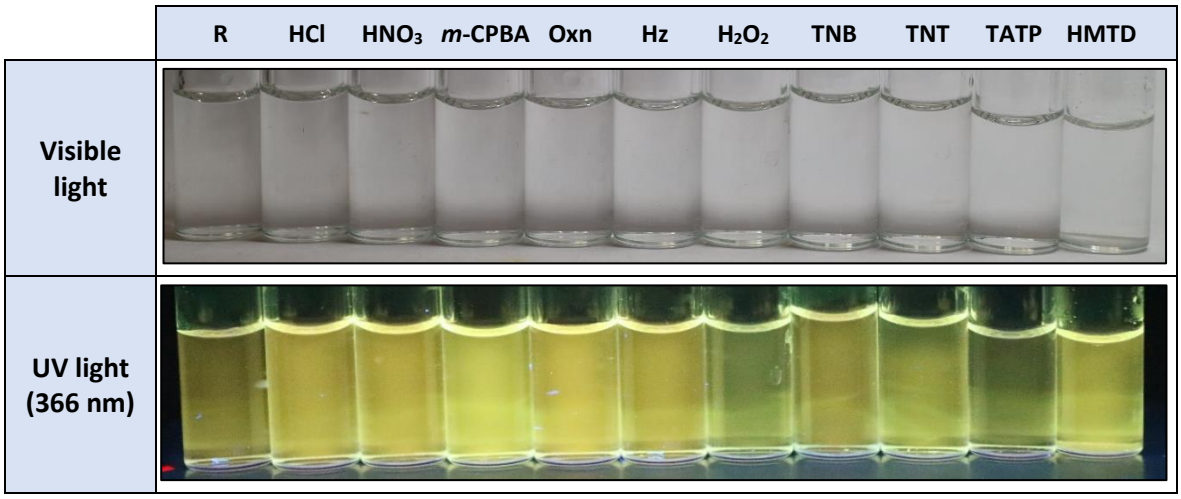

Figure 182. Oxidant and reductant reagents test of AR82d under visible (up) and UV (down) light.

There was a slight change against the TATP, it was changed from yellow to green.

Previous solvents test:

In order to determine the fluorescence variation of the compound under study in the presence of TATP, some test were carried out for the probe in 9 different solvents. The AR82d concentration was 20 µM and the TATP was added in excess (7 mg in each vial). All the test were performed at room temperature and the photographs were taken immediately after the addition of TATP and again after 24 hours.

The biggest fluorescence changes were seen in DMF, MeCN and DCM:MeOH (9:1) with a emission intensity increase and in toluene a fluorescence colour change was observed. The studies were also performed in $CHCl_3$, THF, EtOAc and DCM with a colour change and in $CHCl_3$:MeOH (9:1) with a increase in the emission intensity, but less than the previous ones.

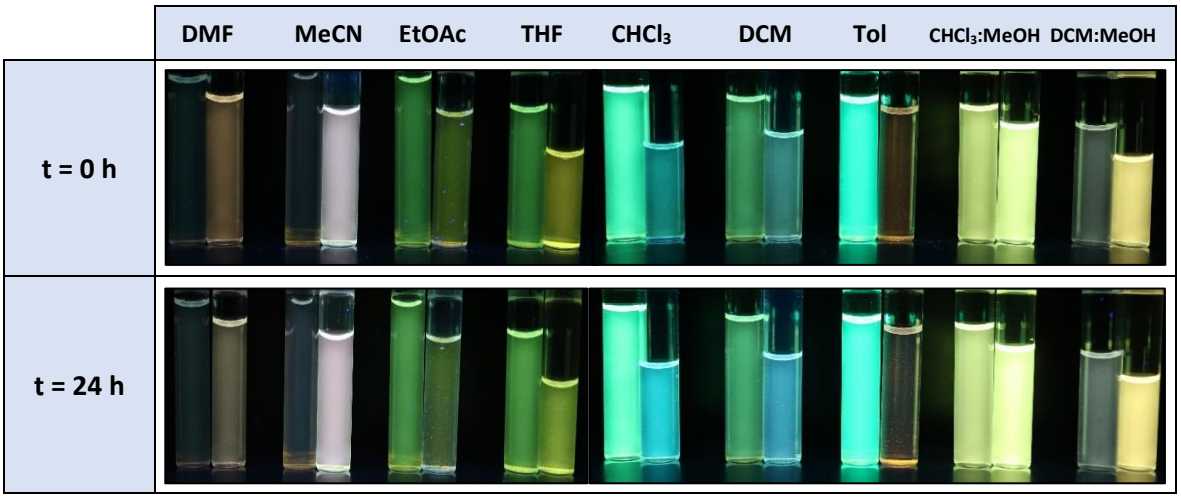

Figure 183. Pairs of AR82d (left) and AR82d with excess of TATP (right) in different solvents at time 0 h (up) and 24 h (down).

Work concentration test:

In order to choose an optimum concentration for the next quantitative studio, the absorbance and fluorescence of the probe was checked to be linear while concentration changes was small. The solvents used for this test were toluene, EtOAc and DCM. The excitation wavelength for all measurements was 360 nm.

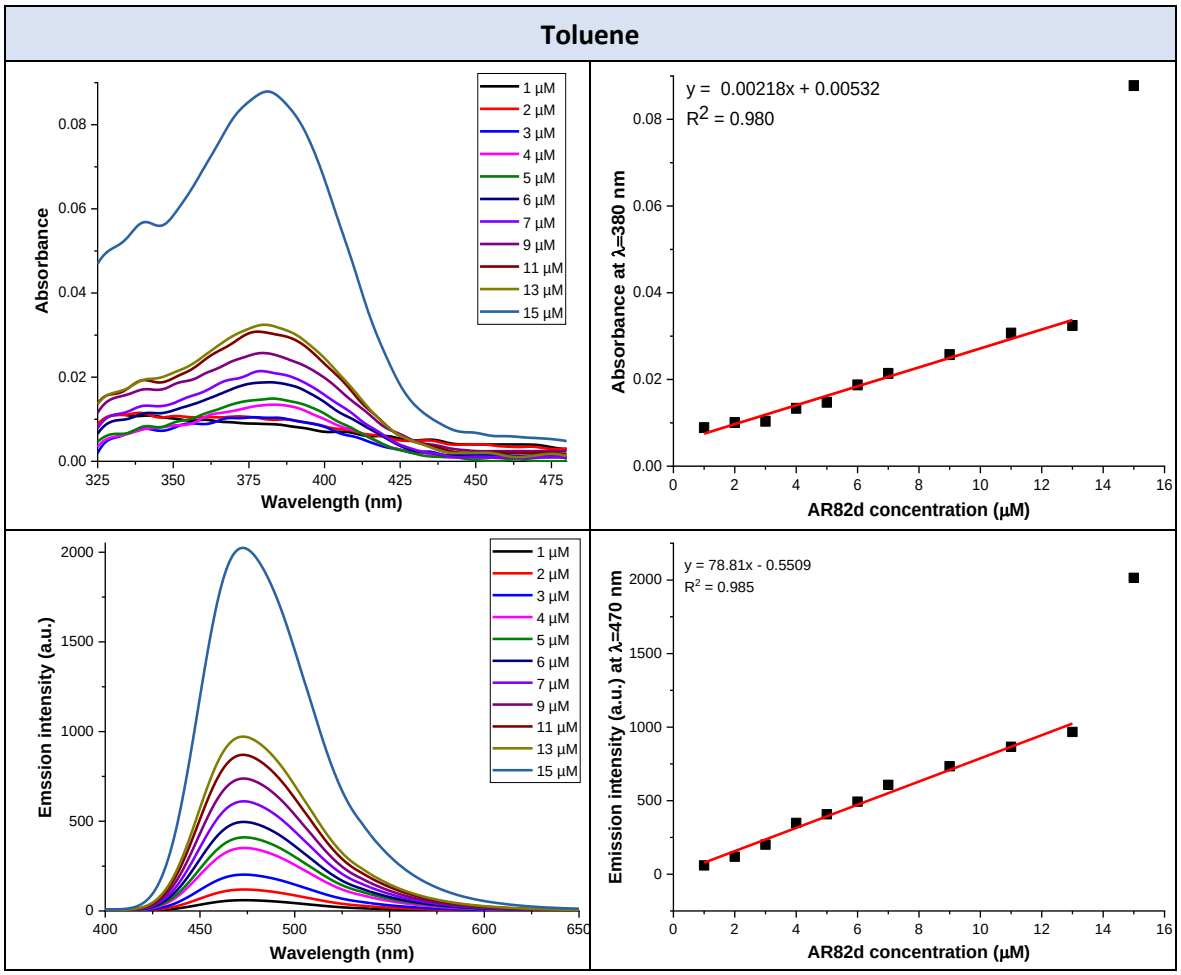

Figure 184. Absorbance spectrum (up left), absorbance profile at 380 nm (up right), fluorescence spectrum (down left) and fluorescence profile at 470 nm (down right) of increasing concentrations of AR82d solution in toluene.

The ideal working concentration should stay at 0.1 of absorbance or less, to avoid inner filter effects, possible dynamic quenching or stacking processes. It was implied a concentration below 13 µM. Taking the results into account, the chosen concentration was 1 µM, value around which the Lambert-Beer Law (or pseudo-Lambert-Beer linear behaviour for fluorescence) was fulfilled.

With *m*-CPBA the obtained result was the same: the concentration of the probe had to be less than 7 µM, so a concentration of 1 µM was adequate.

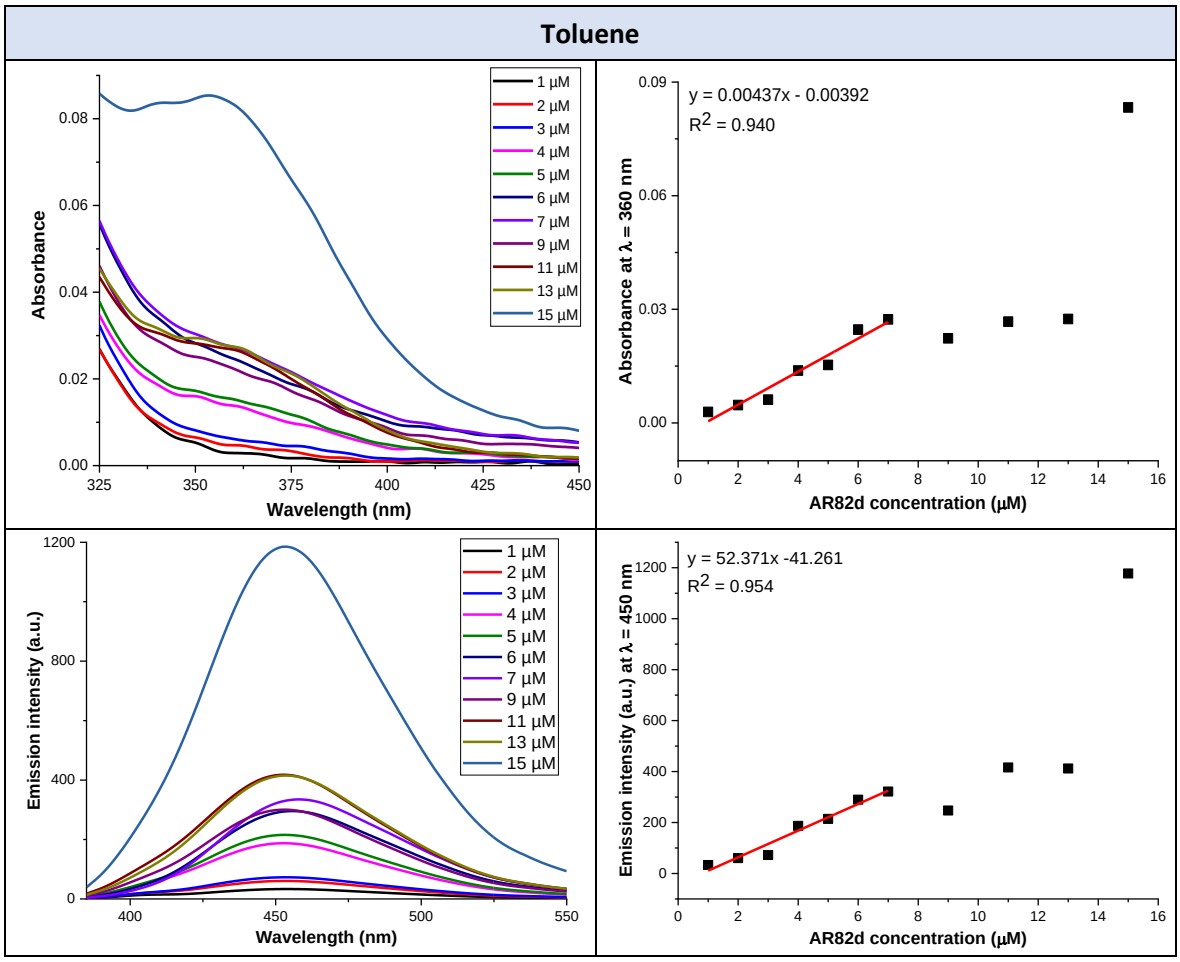

Figure 185. Absorbance spectrum (up left), absorbance profile at 360 nm (up right), fluorescence spectrum (down left) and fluorescence profile at 450 nm (down right) of increasing concentrations of AR82d solution with a m-CPBA excess (7000 µM) in toluene.

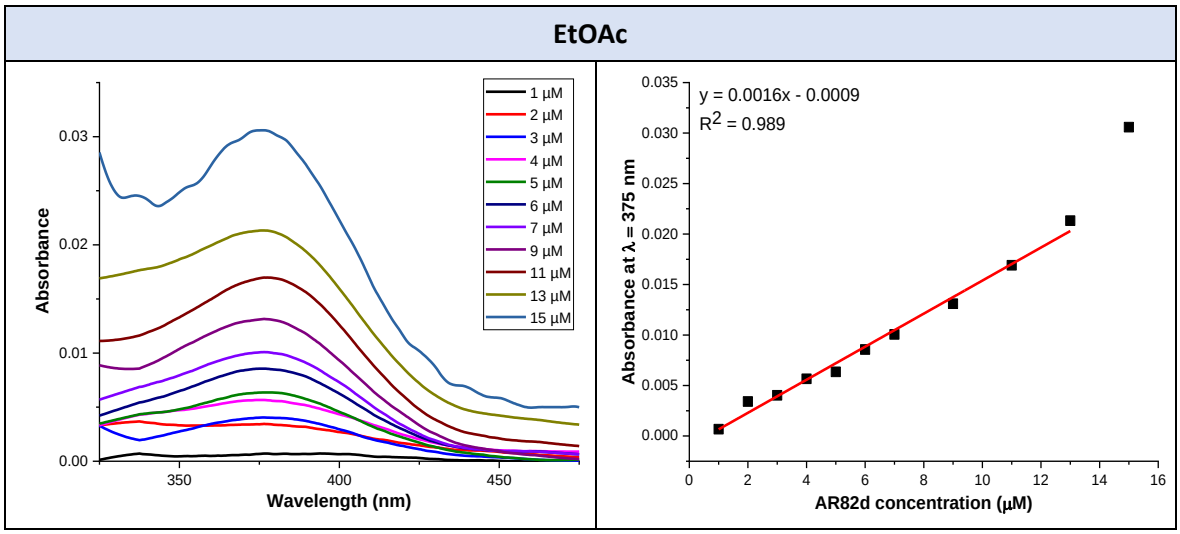

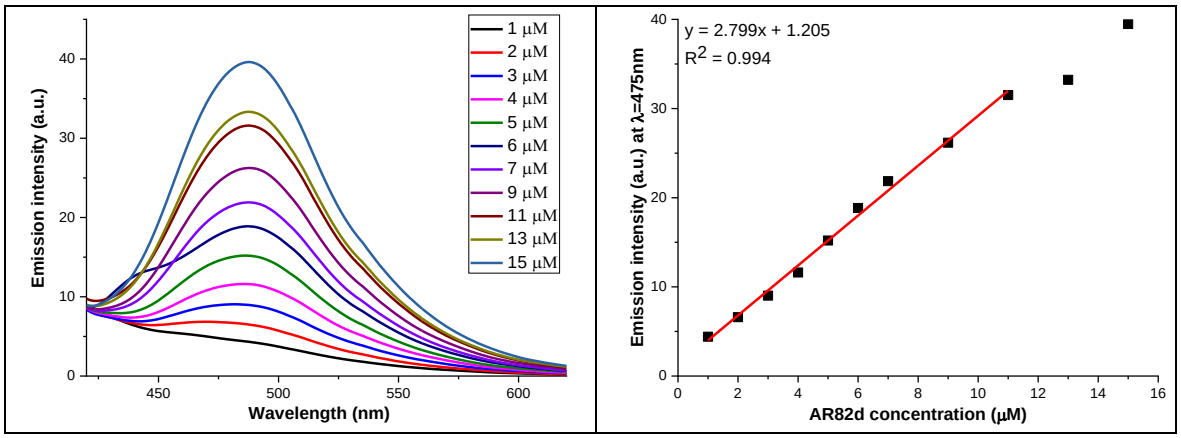

Figure 186. Absorbance spectrum (up left), absorbance profile at 375 nm (up right), fluorescence spectrum (down left) and fluorescence profile at 475 nm (down right) of increasing concentrations of AR82d solution in EtOAc.

The obtained result was similar to the previous one. To work at an absorbance of less than 0.1, the probe concentration had to be below 12 µM, so a good working concentration was 2.5 µM, while with *m*-CPBA, the concentration should be below 6 µM so, 1 µM was also suitable. It was a concentration around which the Lambert-Beer Law (or pseudo-Lambert-Beer) was fulfilled.

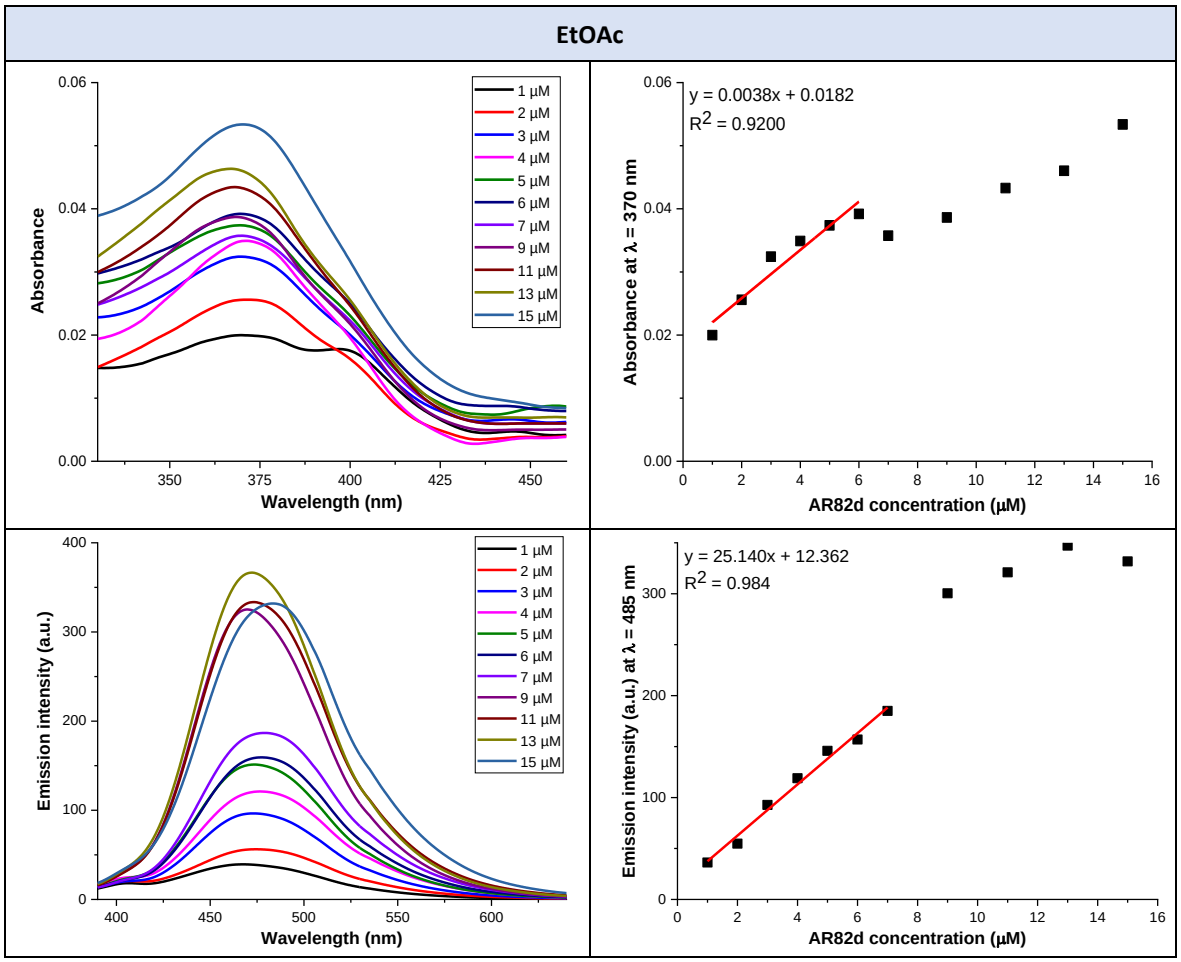

Figure 187. Absorbance spectrum (up left), absorbance profile at 370 nm (up right), fluorescence spectrum (down left) and fluorescence profile at 485 nm (down right) of increasing concentrations of AR82d solution with a m-CPBA excess (7000 µM) in EtOAc.

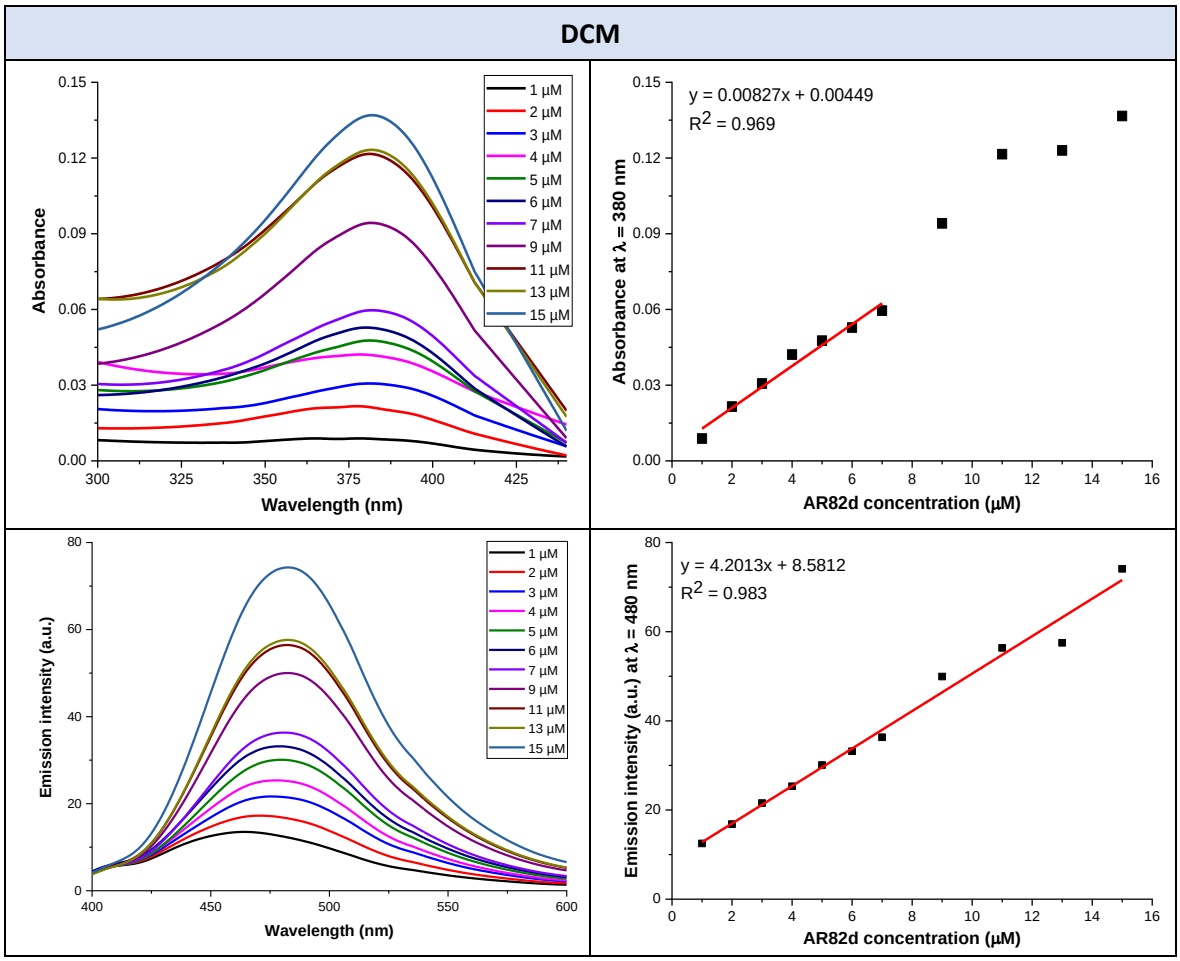

Figure 188. Absorbance spectrum (up left), absorbance profile at 380 nm (up right), fluorescence spectrum (down left) and fluorescence profile at 480 nm (down right) of increasing concentrations of AR82d solution in DCM.

The result obtained with this solvent was similar to that obtained with the two previous ones.

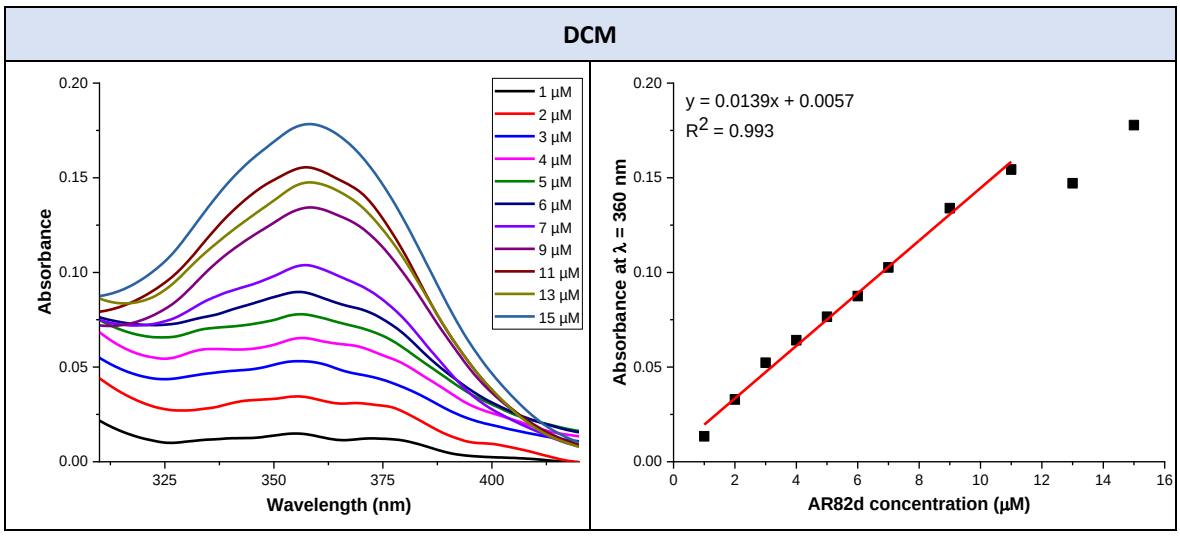

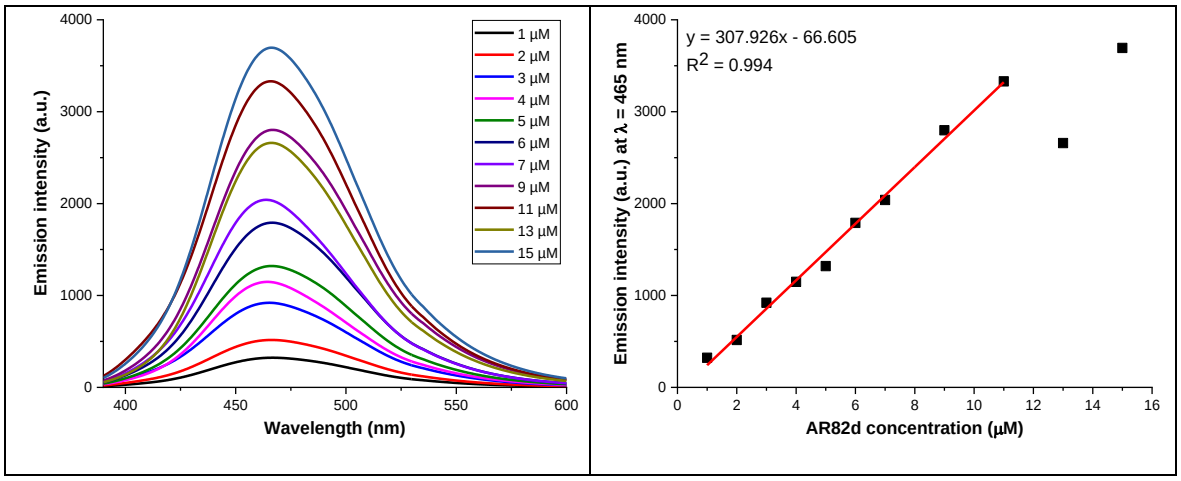

Figure 189. Absorbance spectrum (up left), absorbance profile at 360 nm (up right), fluorescence spectrum (down left) and fluorescence profile at 465 nm (down right) of increasing concentrations of AR82d solution with a m-CPBA excess (7000 µM) in DCM.

Solvents test with TATP:

For all solvents, the working concentration of AR82d was 2.5 µM, the excitation wavelength was 360 nm and the temperature for all test was 25ºC. In the kinetic studies, TATP was in excess (20 mM) and the fluorescence emission measurements were made during 30 minutes in the case of DMF, 150 minutes in MeCN, 120 minutes in DCM, 45 minutes in the mixture DCM:MeOH (9:1) and 60 minutes for all other solvents, at 5 or 10 minutes time intervals. In the titration, the TATP concentration was between 0 and 35000 µM and it was added directly as solid. The measurements were carried out inmediately after the adittion of the probe.

DMF

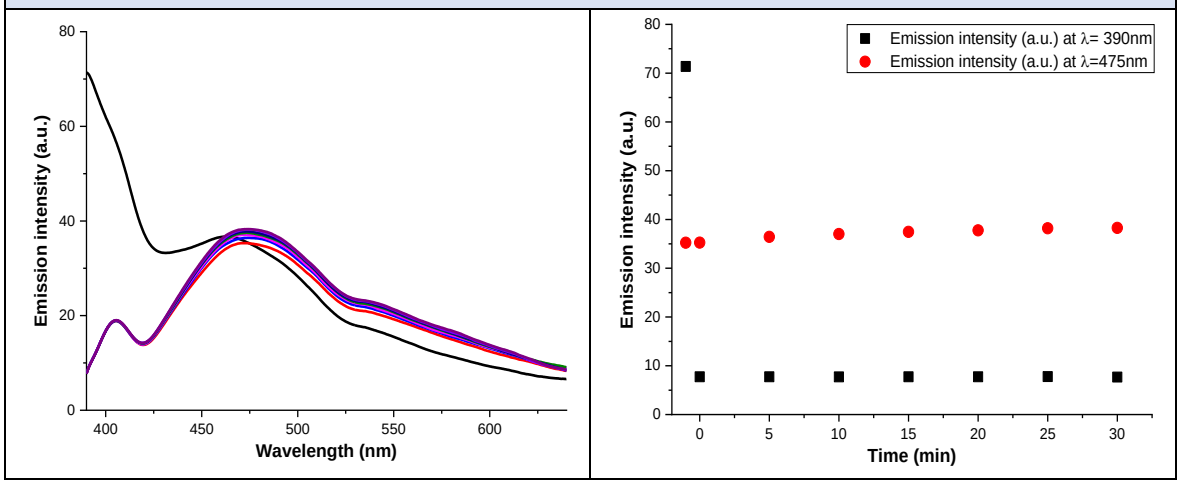

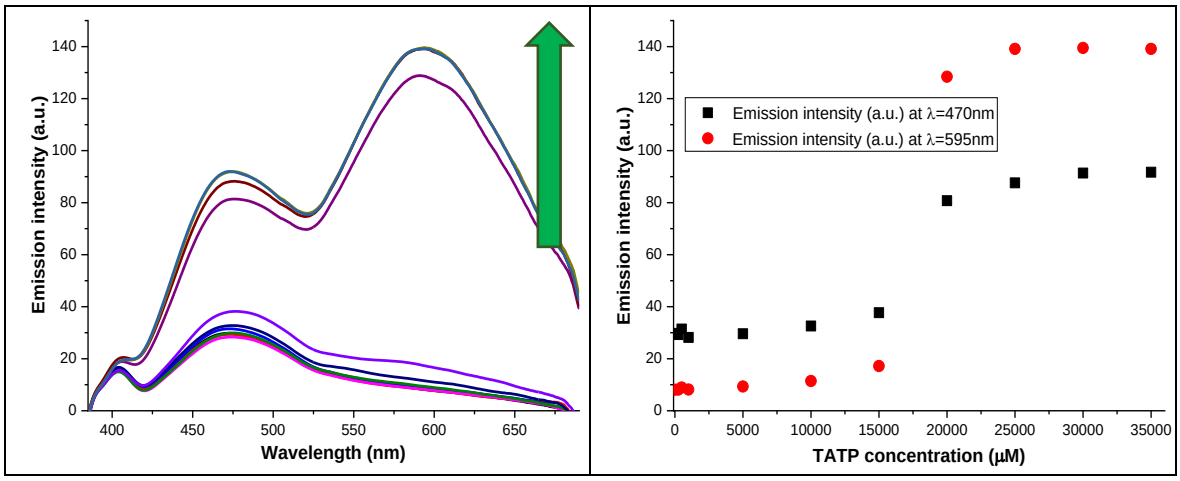

Figure 190. Study of AR82d with TATP in DMF. Kinetic study (up left) and profile as function as time at 390 nm and 475 nm simultaneously (up right) in presence of TATP excess. Titration (down left) and fluorescence profile at 470 nm and 595 nm simultaneously (down right) under increasing concentrations of TATP.

There was a change in the emission intensity band immediately after adding TATP. According to the fluorescence spectra, the LOD of TATP was somewhere between 15000 and 20000 µM with a increase of the emission intensity.

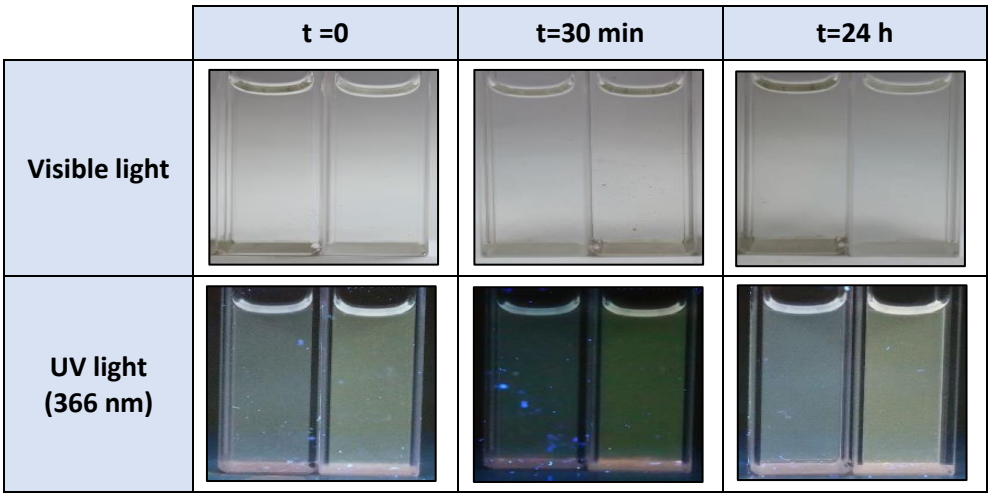

Figure 191. Kinetic study at different times under visible (up) and UV (down) light in DMF. In each photo, left vial was contained the probe and right vial was contained the probe and an excess of TATP.

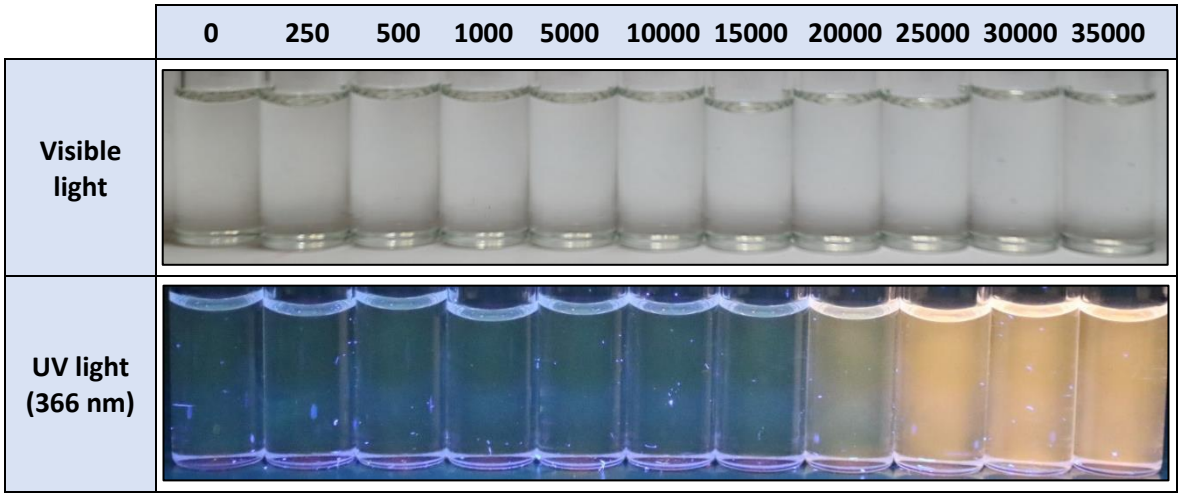

Figure 192. Titration of AR82d with an excess of TATP under visible (up) and UV (down) light in DMF.

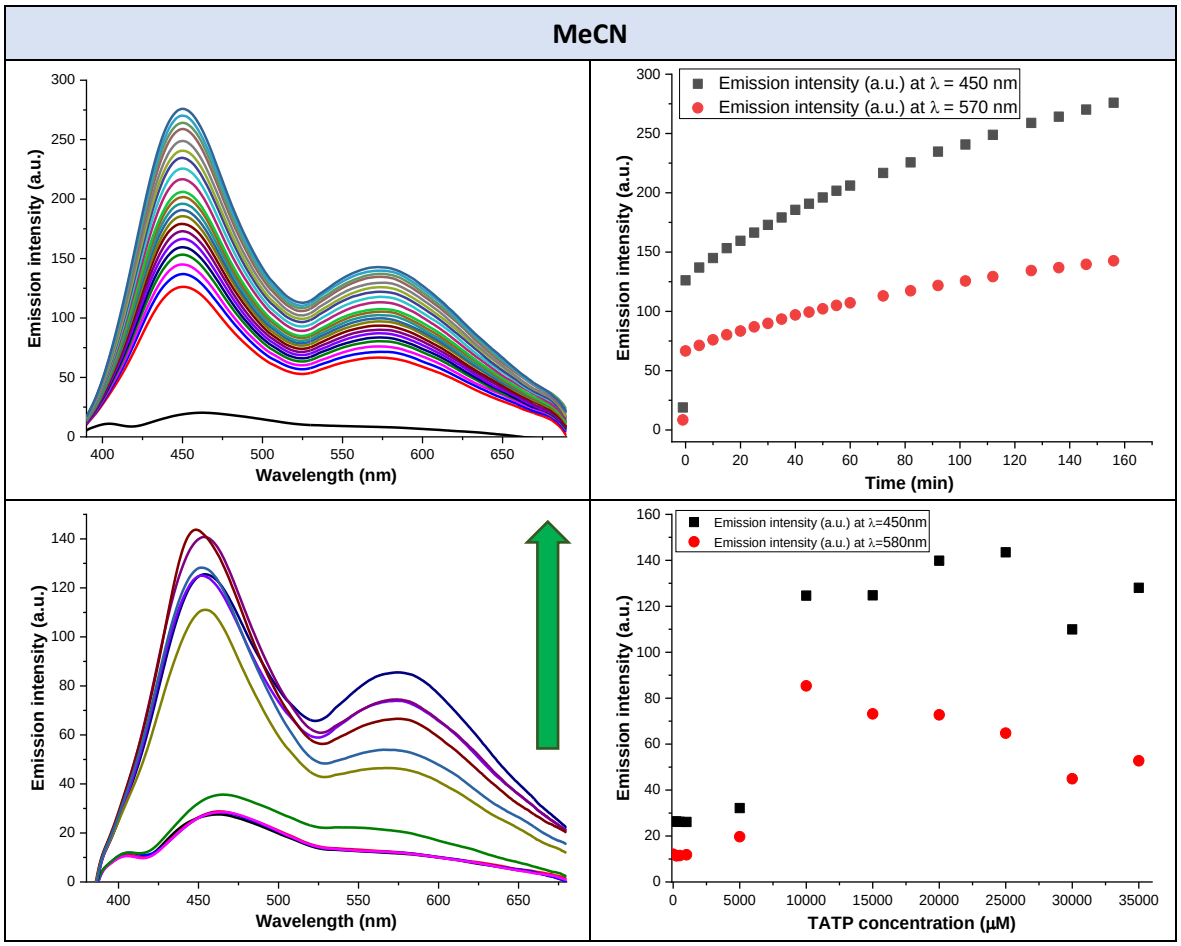

Figure 193. Study of AR82d with TATP in MeCN. Kinetic study (up left) and profile as function as time at 450 nm and 570 nm simultaneously (up right) in presence of TATP excess. Titration (down left) and fluorescence profile at 450 nm and 580 nm simultaneusly (down right) under increasing concentrations of TATP.

There was an increase in the emission intensity band immediately after adding TATP and it was stabilized after 140-160 minutes. According to the fluorescence spectra, the LOD was somewhere between 5000 and 10000 µM with a increase of the emission intensity.

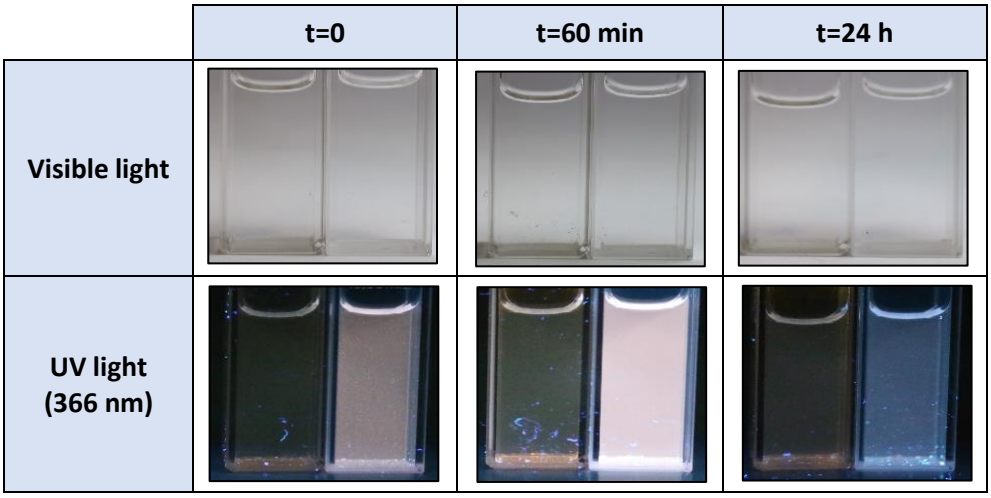

Figure 194. Kinetic study at different times under visible (up) and UV (down) light in MeCN. In each photo, left vial was contained the probe and right vial was contained the probe and an excess of TATP.

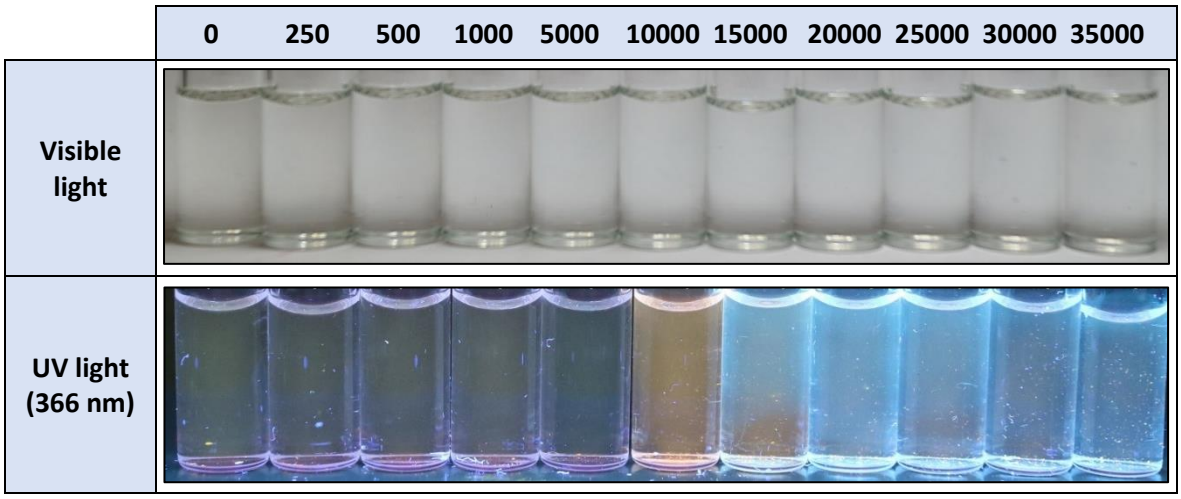

Figure 195. Titration of AR82d with an excess of TATP under visible (up) and UV (down) light in MeCN.

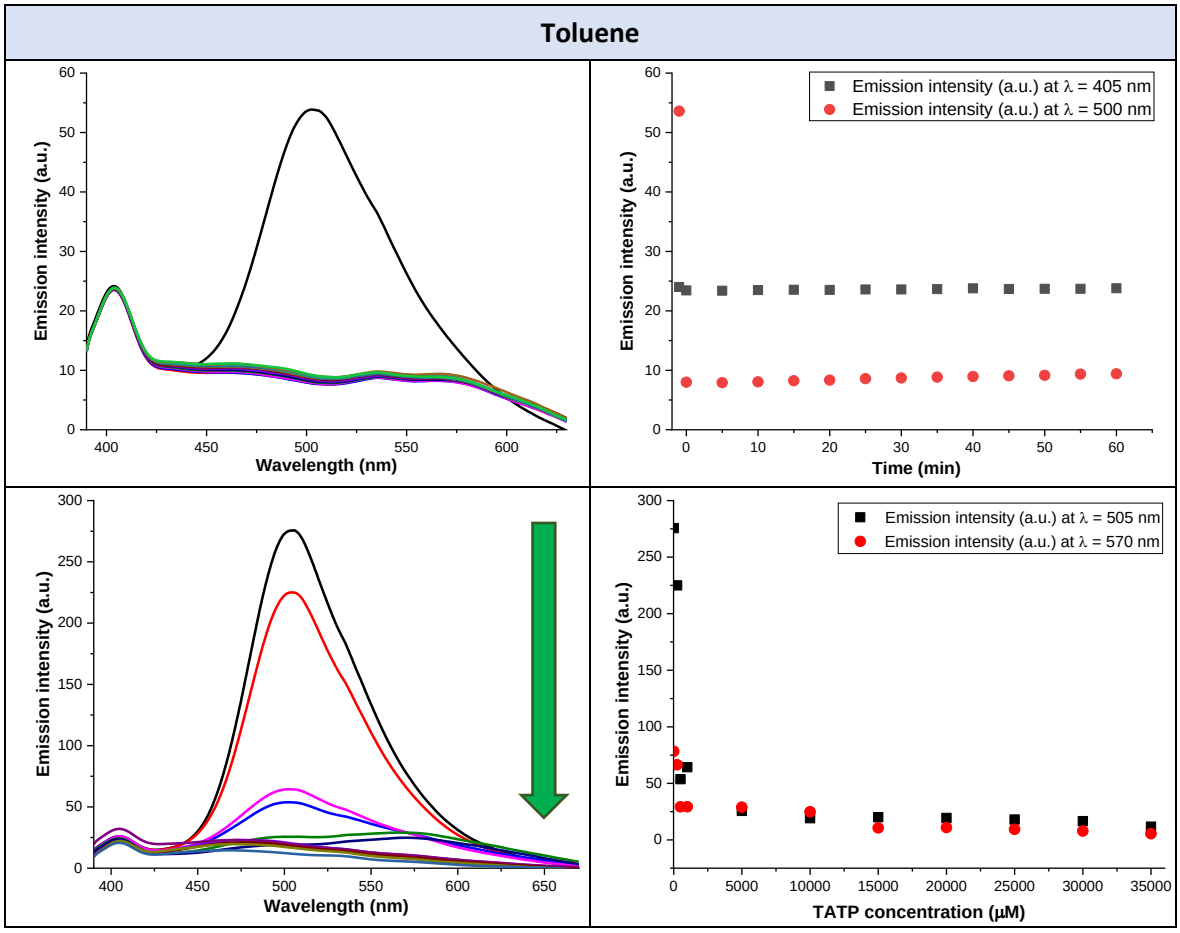

Figure 196. Study of AR82d with TATP in toluene. Kinetic study (up left) and profile as function as time at 450 nm and 570 nm simultaneously (up right) in presence of TATP excess. Titration (down left) and fluorescence profile at 505 nm and 570 nm simultaneusly (down right) under increasing concentrations of TATP.

There was a drop in the emission intensity band immediately after adding TATP. According to the fluorescence spectra, the LOD was somewhere between 0 and 250 µM.

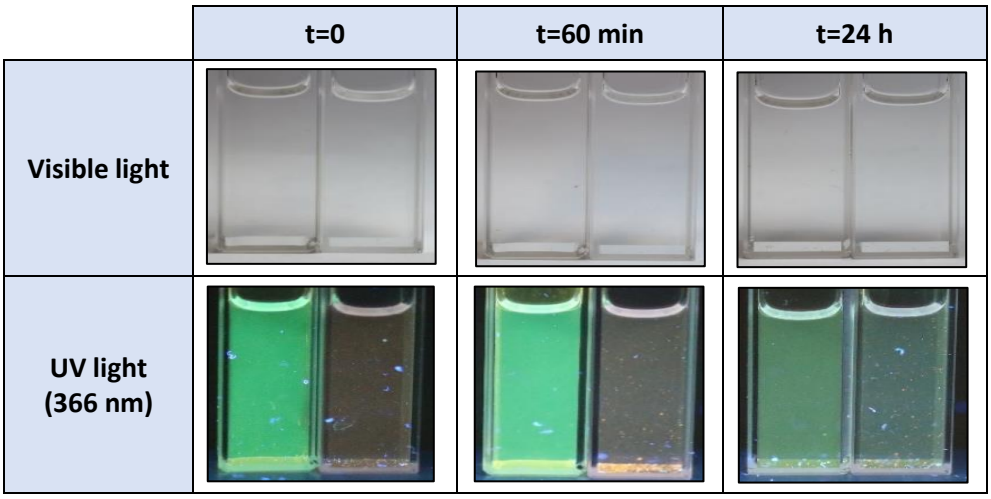

Figure 197. Kinetic study at different times under visible (up) and UV (down) light in toluene. In each photo, left vial was contained the probe and right vial was contained the probe and an excess of TATP.

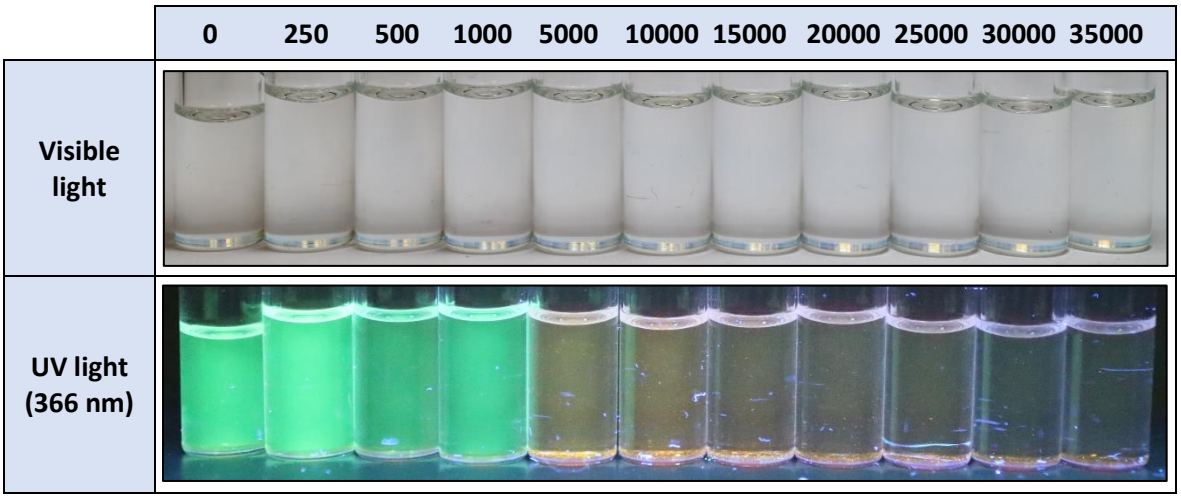

Figure 198. Titration of AR82d with an excess of TATP under visible (up) and UV (down) light in toluene.

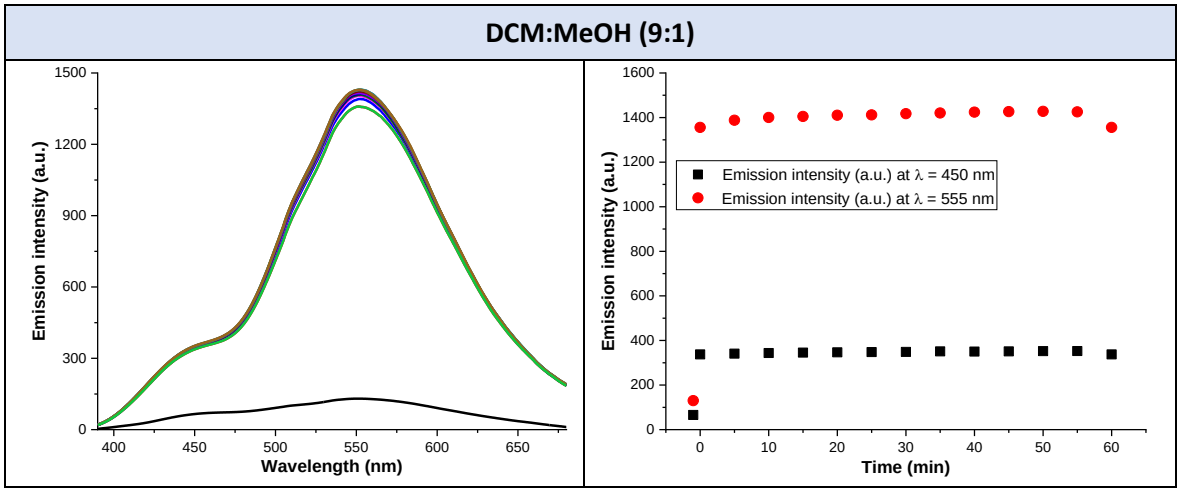

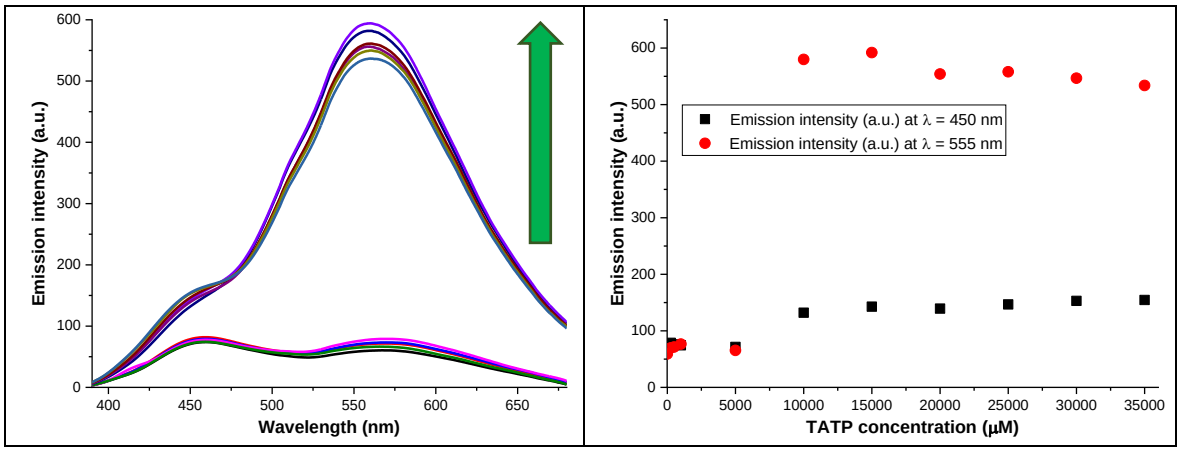

Figure 199. Study of AR82d with TATP in DCM:MeOH (9:1). Kinetic study (up left) and profile as function as time at 450 nm and 555 nm simultaneously (up right) in presence of TATP excess. Titration (down left) and fluorescence profile at 450 nm and 555 nm simultaneously (down right) under increasing concentrations of TATP.

There was an increase in the emission intensity band immediately after adding TATP. According to the fluorescence spectra, the LOD was somewhere between 5000 and 10000 μM.

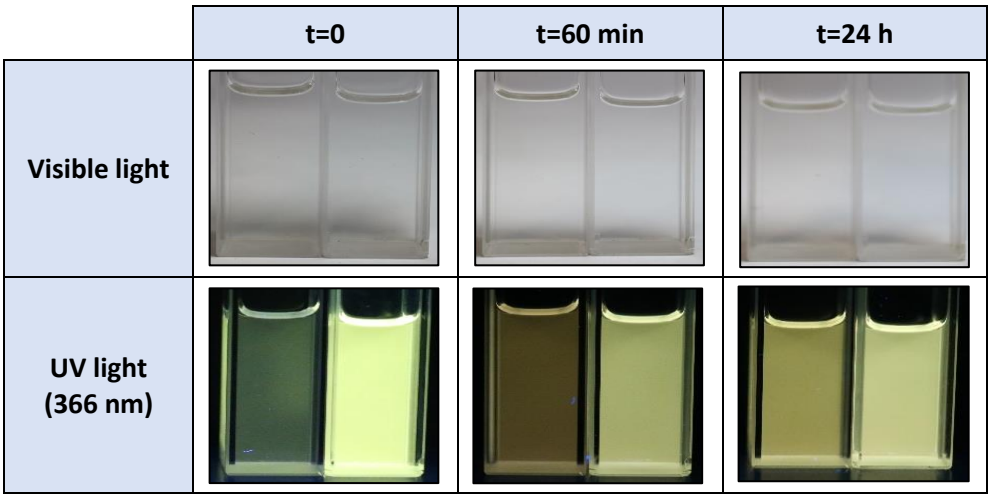

Figure 200. Kinetic study at different times under visible (up) and UV (down) light in DCM:MeOH (9:1). In each photo, left vial was contained the probe and right vial was contained the probe and an excess of TATP.

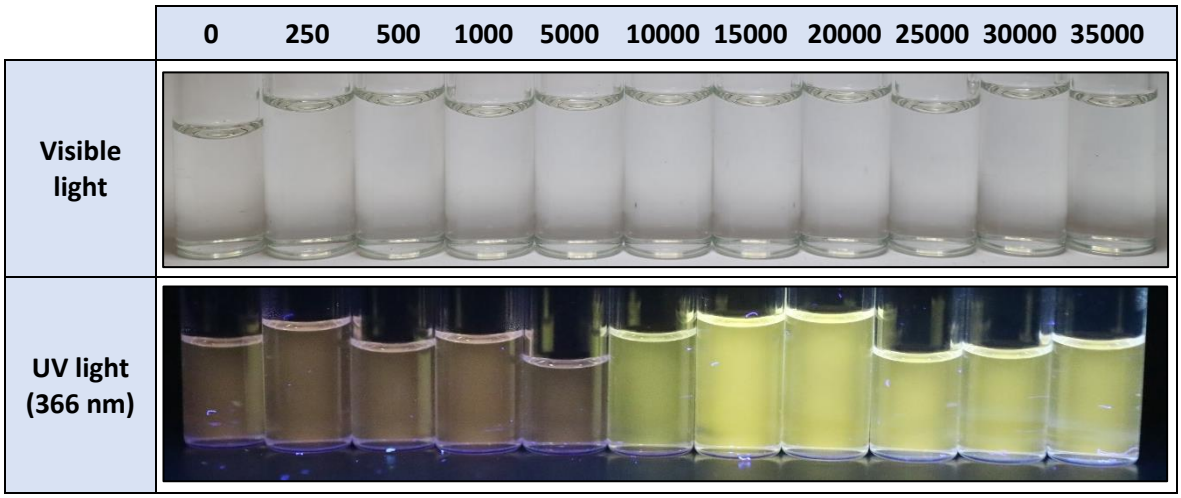

Figure 201. Titration of AR82d with an excess of TATP under visible (up) and UV (down) light in DCM:MeOH (9:1).

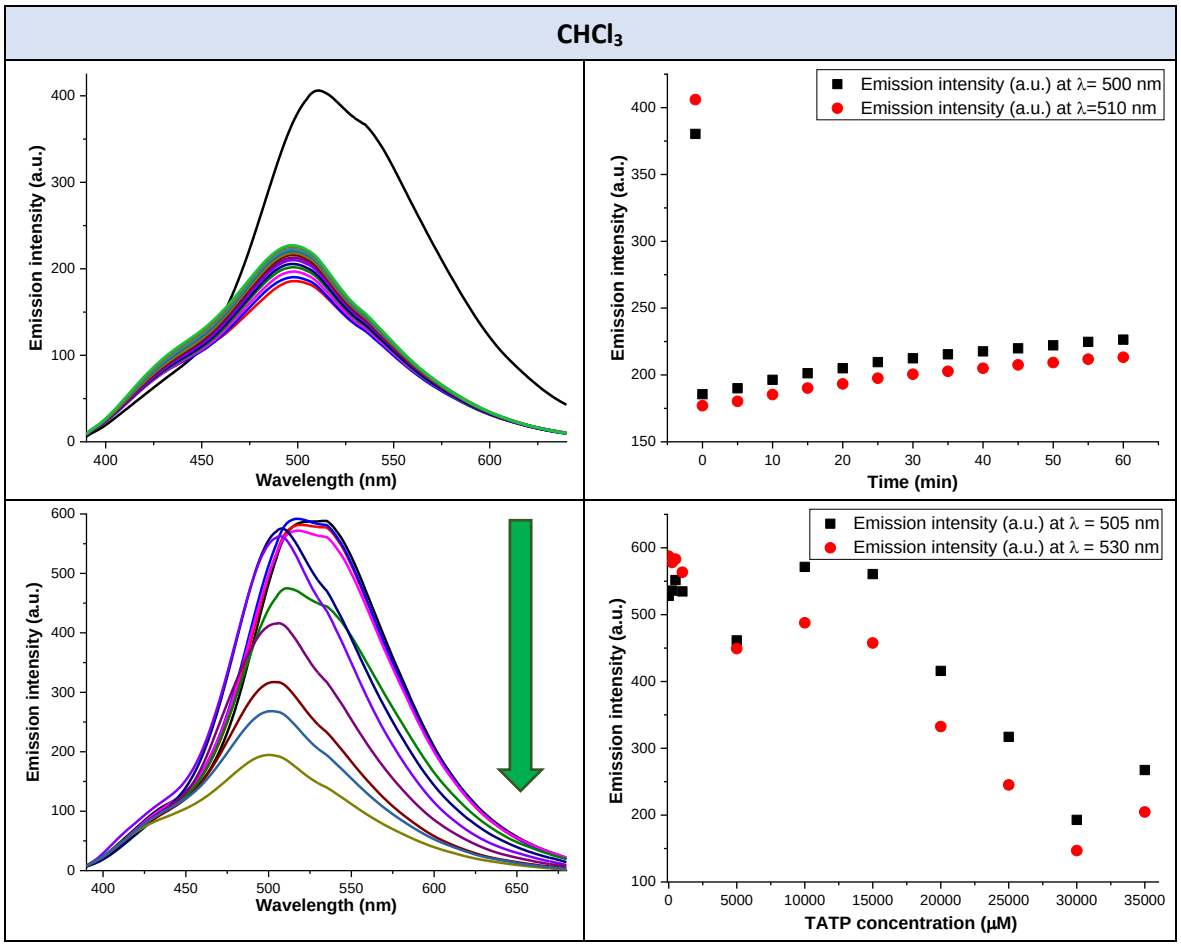

Figure 202. Study of AR82d with TATP in $CHCl_3$. Kinetic study (up left) and profile as function as time at 500 nm and 510 nm simultaneously (up right) in presence of TATP excess. Titration (down left) and fluorescence profile at 505 nm and 530 nm simultaneously (down right) under increasing concentrations of TATP.

There was a decrease in the emission intensity band immediately after adding TATP. According to the fluorescence spectra, the LOD was somewhere between 1000 and 5000 µM, a bit high limit.

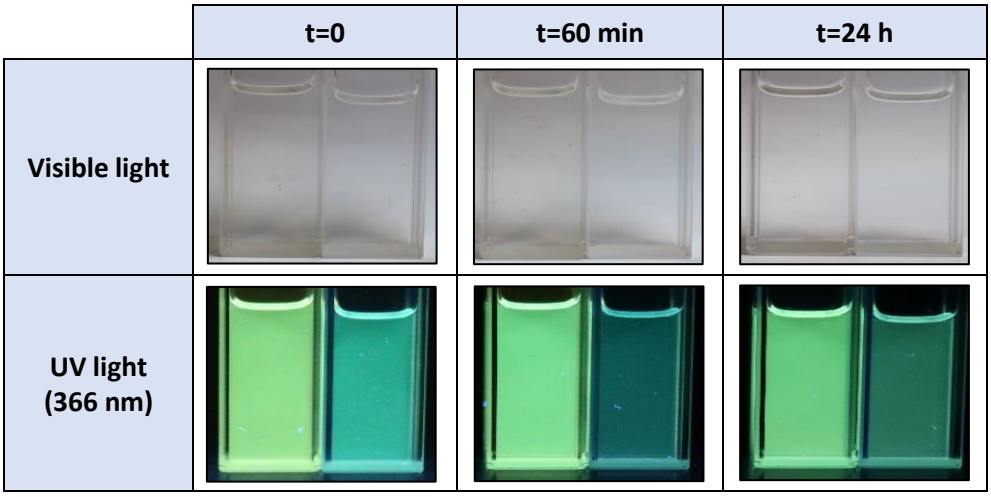

Figure 203. Kinetic study at different times under visible (up) and UV (down) light in $CHCl_3$. In each photo, left vial was contained the probe and right vial was contained the probe and an excess of TATP.

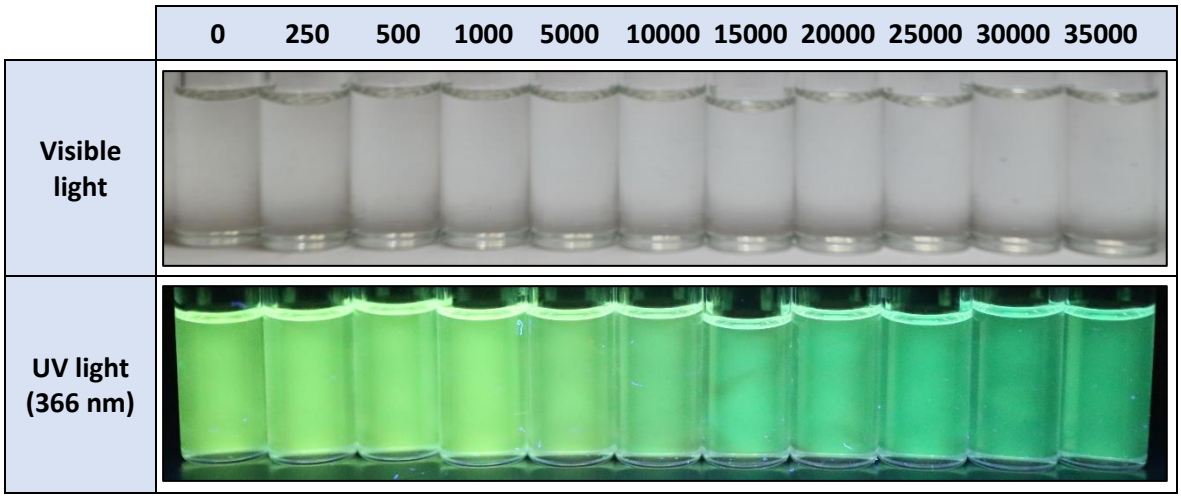

Figure 204. Titration of AR82d with an excess of TATP under visible (up) and UV (down) light in $CHCl_3$.

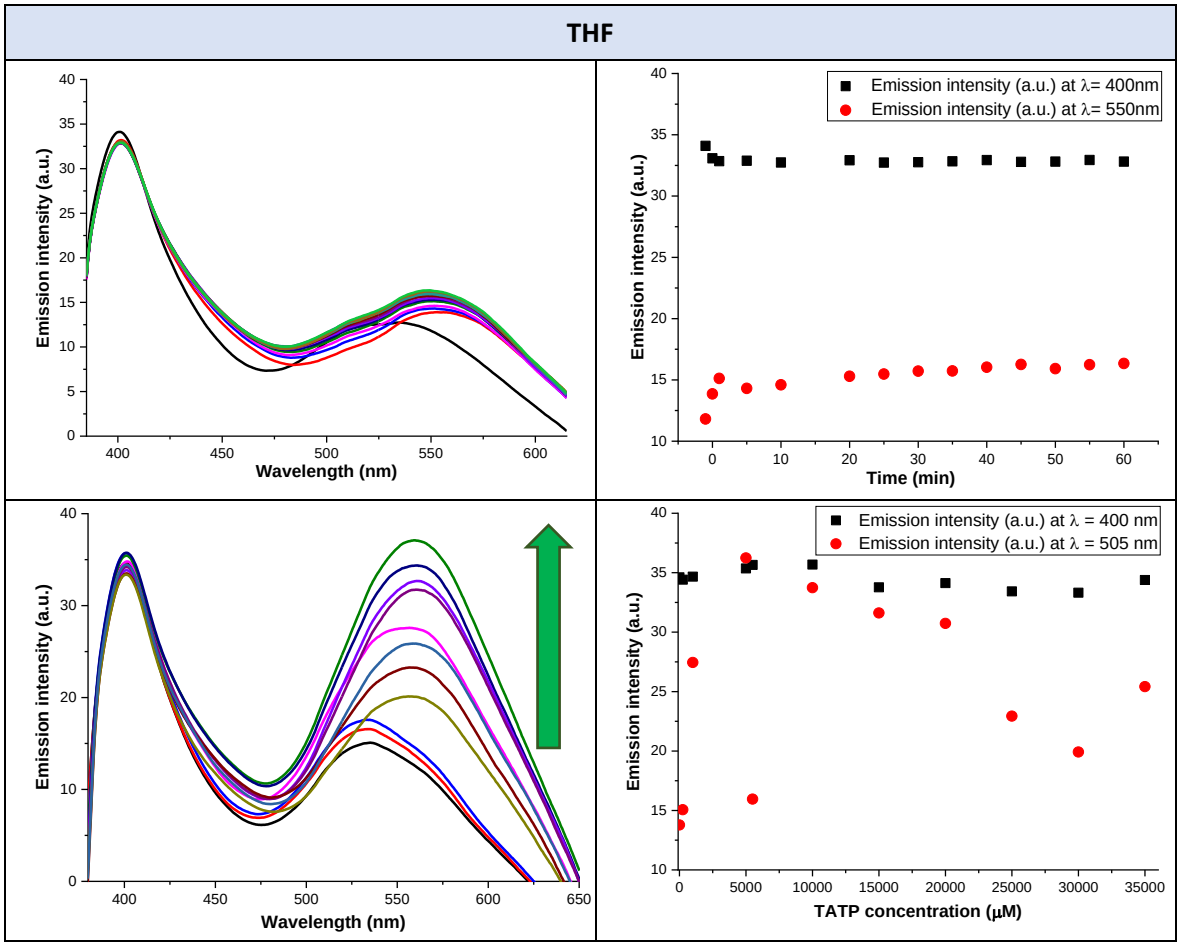

Figure 205. Study of AR82d with TATP in THF. Kinetic study (up left) and profile as function as time at 400 nm and 550 nm simultaneously (up right) in presence of TATP excess. Titration (down left) and fluorescence profile at 400 nm and 550 nm simultaneusly (down right) under increasing concentrations of TATP.

Related to the 550 nm band, there was a low increase in the emission intensity and a shifted to higher wavelengths immediately after adding TATP. According to the fluorescence spectra, the LOD was somewhere between 1000 and 5000 µM, a bit high limit.

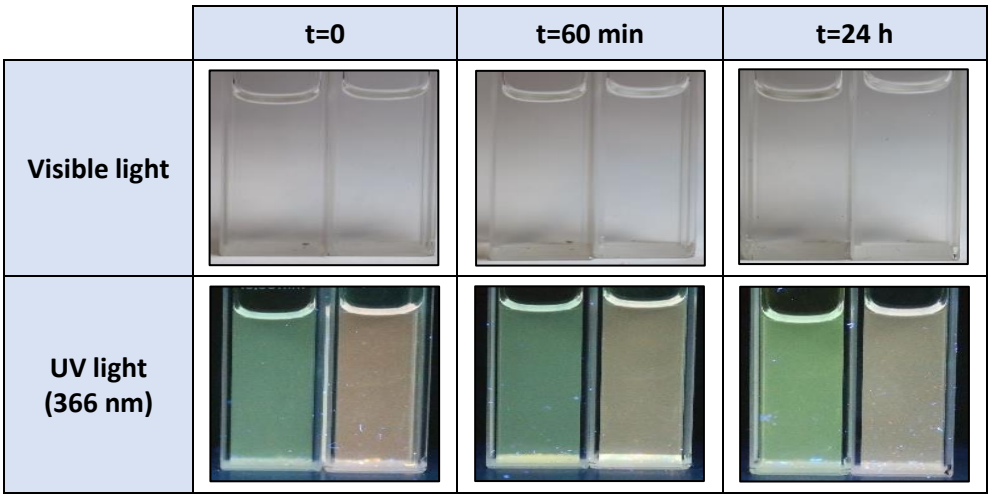

Figure 206. Kinetic study at different times under visible (up) and UV (down) light in THF. In each photo, left vial was contained the probe and right vial was contained the probe and an excess of TATP.

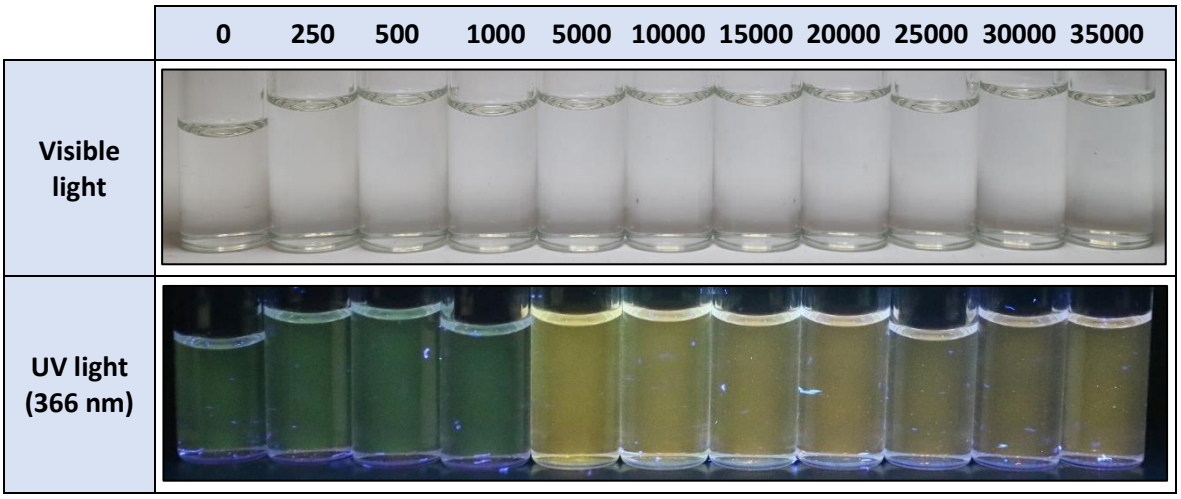

Figure 207. Titration of AR82d with an excess of TATP under visible (up) and UV (down) light in THF.

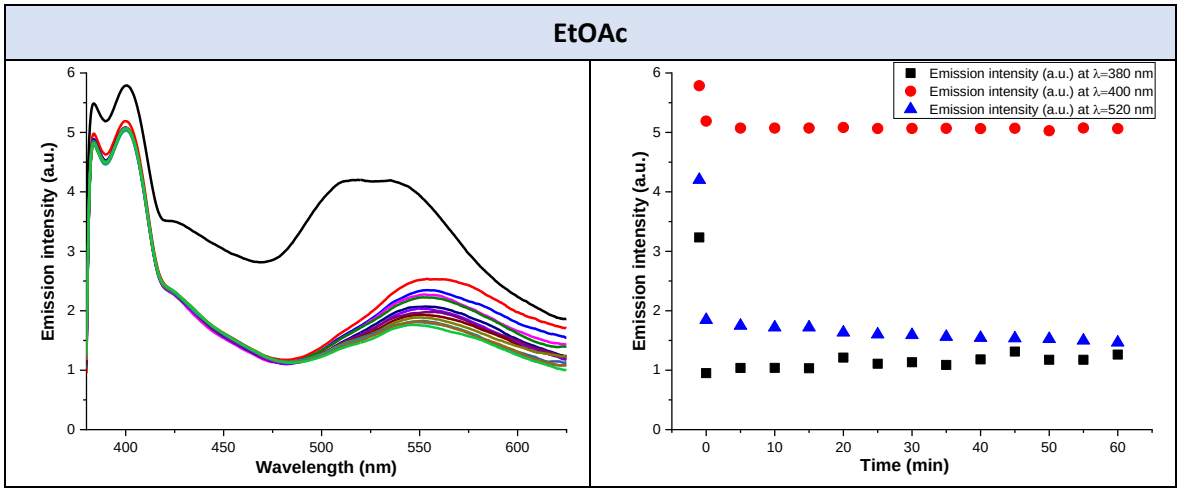

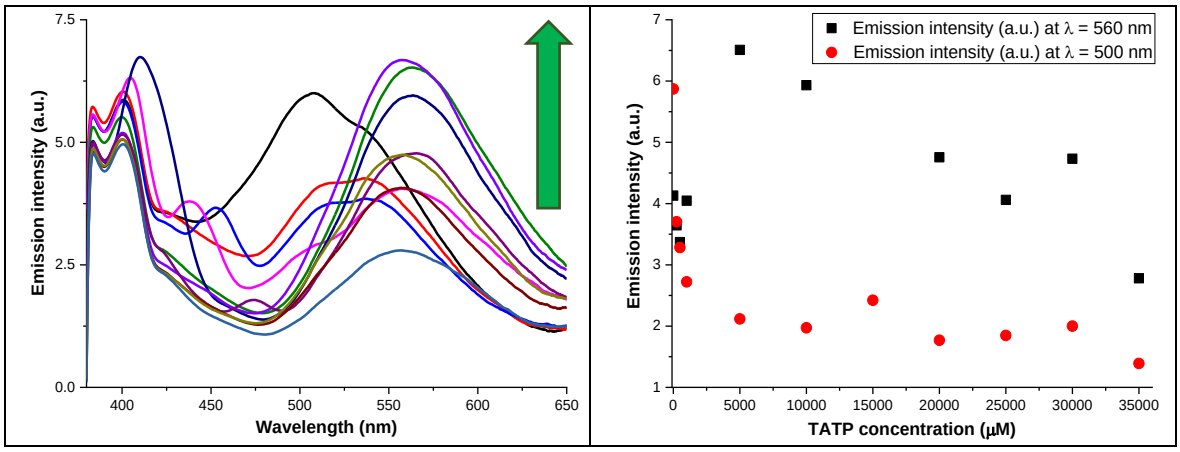

Figure 208. Study of AR82d with TATP in EtOAc. Kinetic study (up left) and profile as function as time at 380 nm, 400 nm and 520 nm simultaneously (up right) in presence of TATP excess. Titration (down left) and fluorescence profile at 500 nm and 560 nm simultaneously (down right) under increasing concentrations of TATP.

There was a drop in the emission intensity and a shifted to higher wavelengths immediately after adding TATP. According to the fluorescence spectra, the LOD was somewhere between 1000 and 5000 µM, with a displacement of the maximum emission.

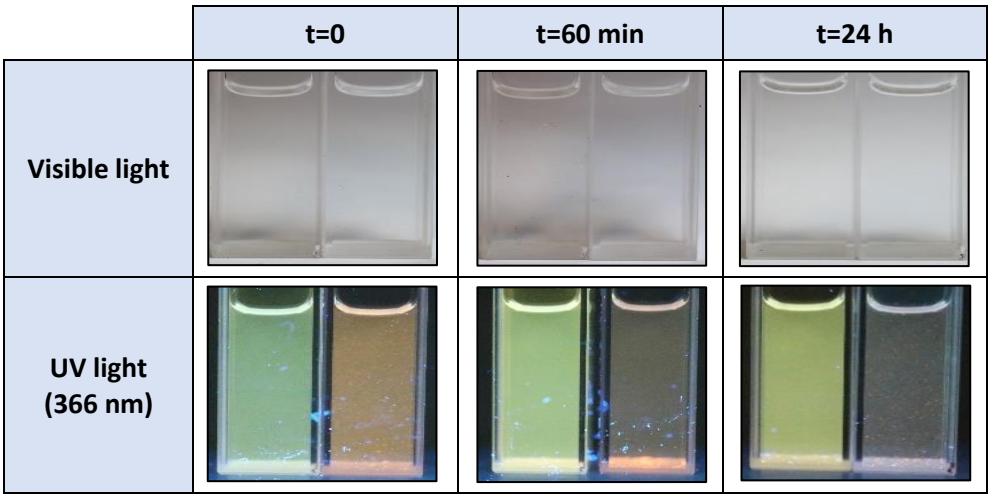

Figure 209. Kinetic study at different times under visible (up) and UV (down) light in EtOAc. In each photo, left vial was contained the probe and right vial was contained the probe and an excess of TATP.

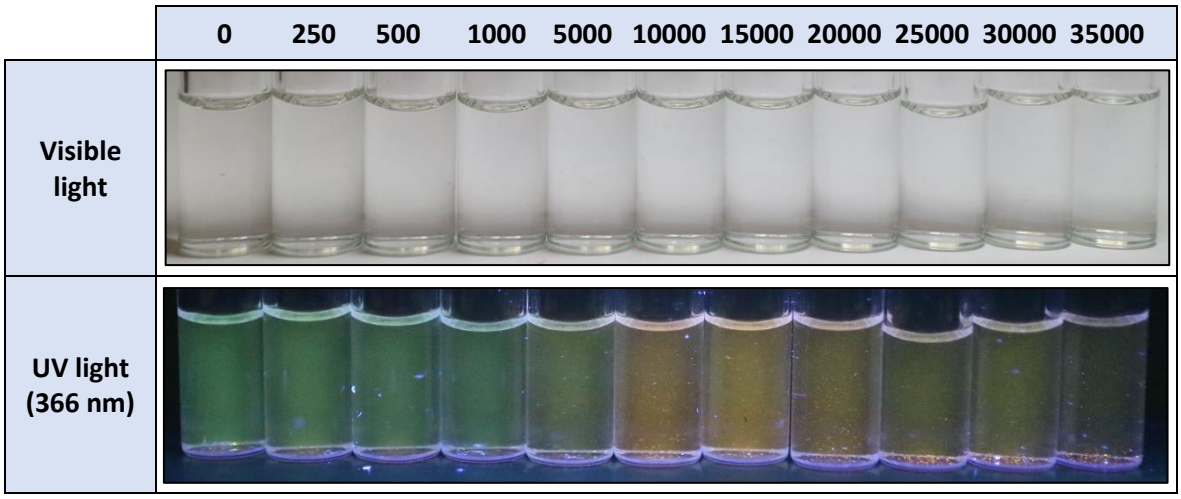

Figure 210. Titration of AR82d with an excess of TATP under visible (up) and UV (down) light in EtOAc.

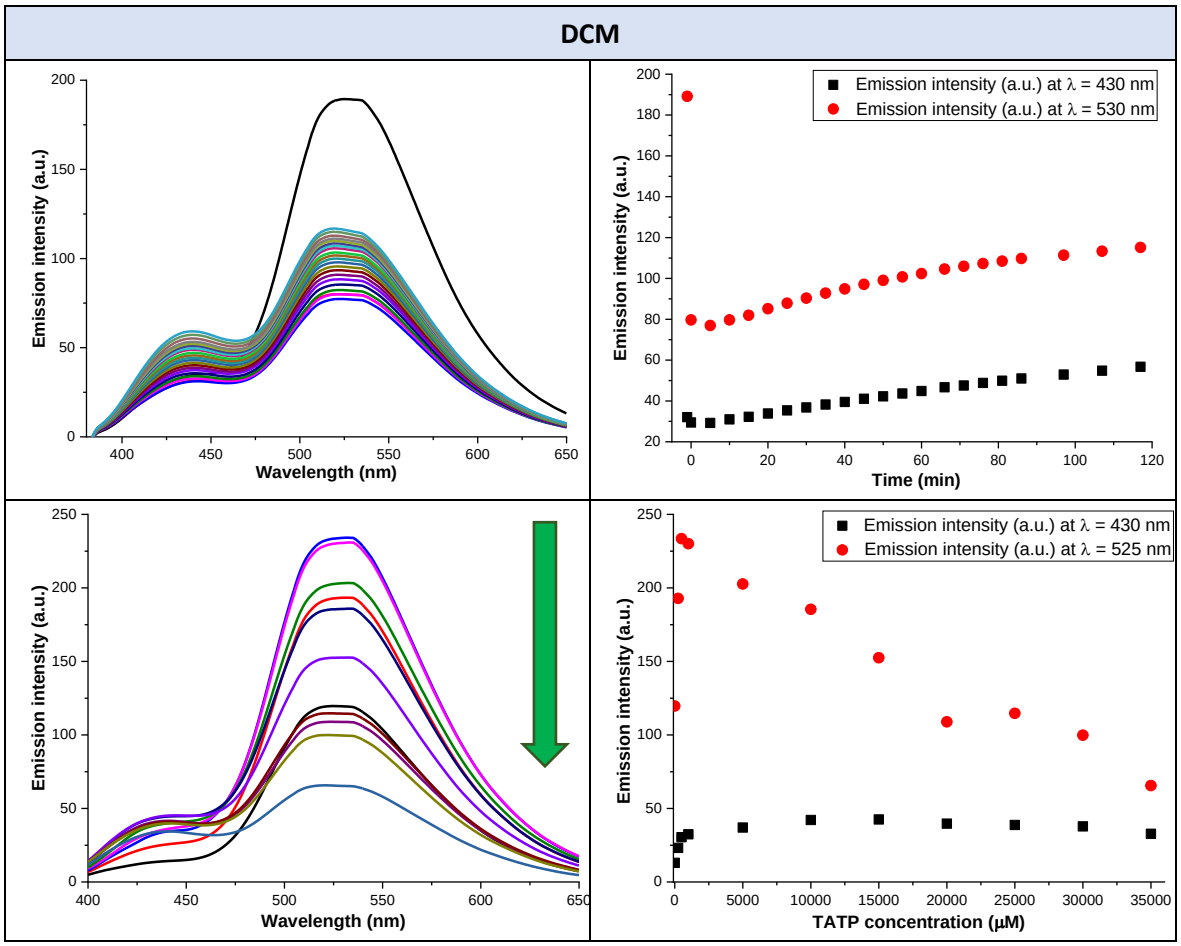

Figure 211. Study of AR82d with TATP in DCM. Kinetic study (up left) and profile as function as time at 430 nm and 530 nm simultaneously (up right) in presence of TATP excess. Titration (down left) and fluorescence profile at 430 nm and 525 nm simultaneously (down right) under increasing concentrations of TATP.

There was a change in the emission intensity immediately after adding TATP. The LOD was somewhere between 0 and 250 µM, with an increase of the intensity.

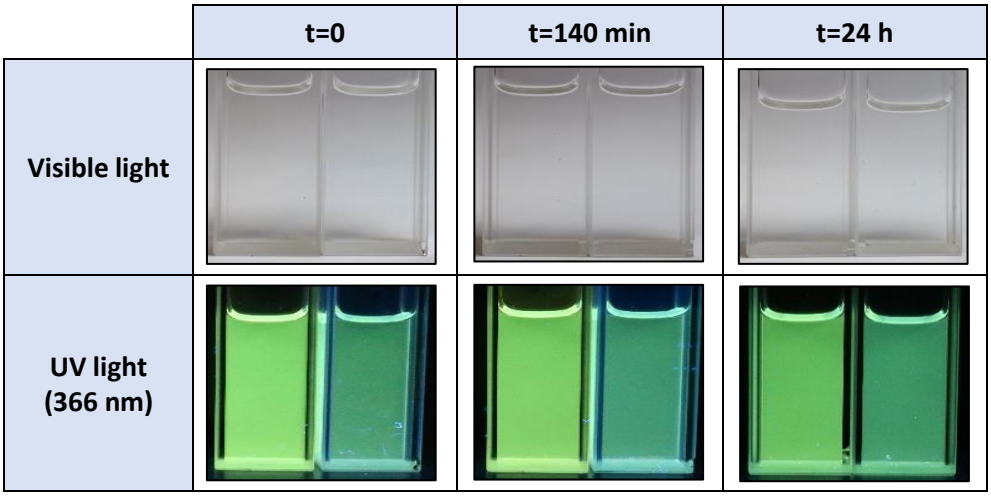

Figure 212. Kinetic study at different times under visible (up) and UV (down) light in DCM. In each photo, left vial was contained the probe and right vial was contained the probe and an excess of TATP.

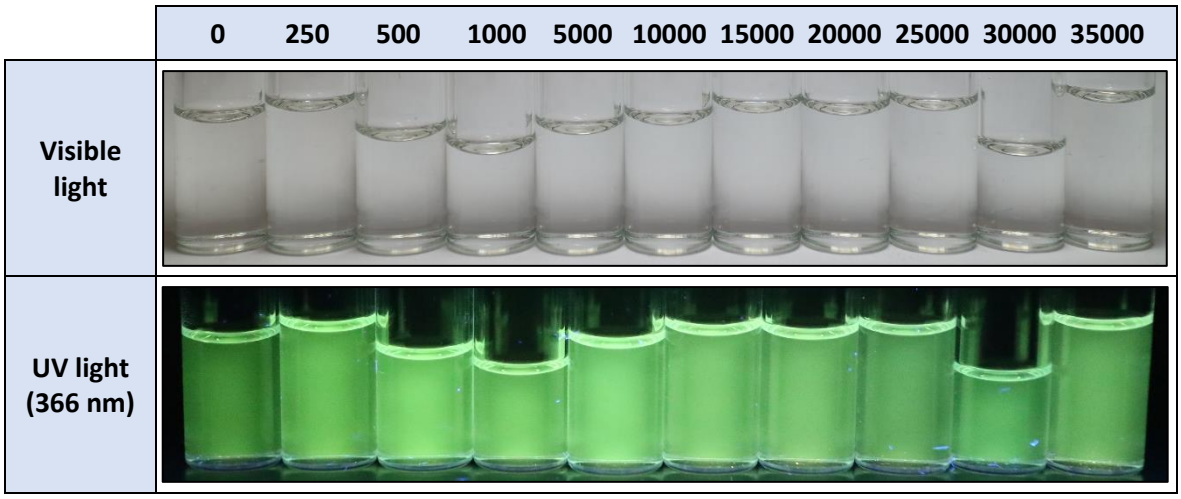

Figure 213. Titration of AR82d with an excess of TATP under visible (up) and UV (down) light in DCM.

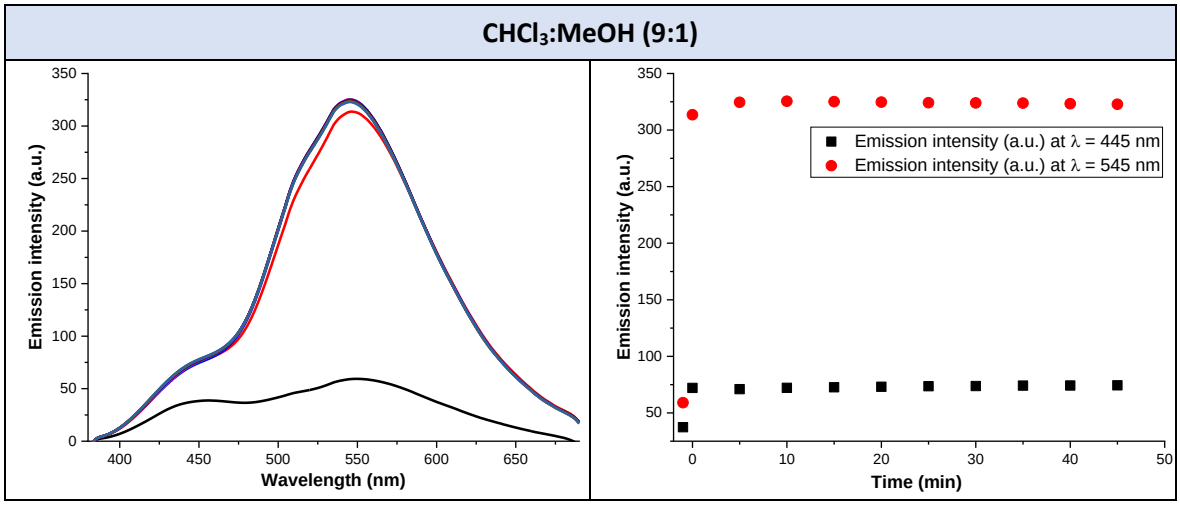

Figure 214. Kinetic study (up left) and profile as function as time at 445 nm and 545 nm simultaneously (up right) in presence of TATP excess in $CHCl_3$:MeOH (9:1).

There was an increase in the emission intensity immediately after adding TATP. It was seemed thet the probe itself was increased its emission in this solvent.

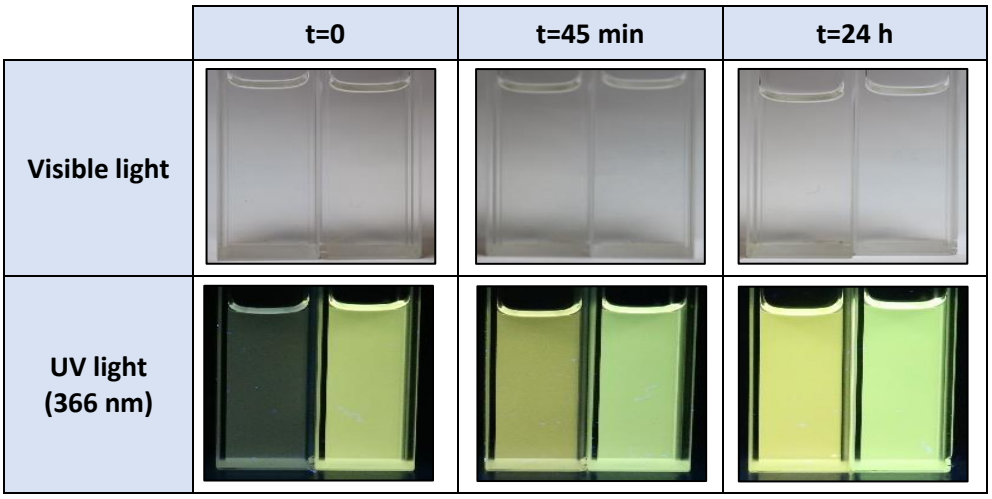

Figure 215. Kinetic study at different times under visible (up) and UV (down) light in CHCl3:MeOH (9:1). In each photo, left vial was contained the probe and right vial was contained the probe and an excess of TATP.

Titrations in toluene and LOD calculations:

Titration of AR82d with TATP in toluene.

The working concentration of AR82d was 1 µM and the TATP was directly added as a solid because when it was added in solution a strange and inconsistent behaviour was observed. Its concentration was between 0 and 25 mM.

The measurements were carried out inmediately after the addition of TATP. The excitation wavelength was 370 nm and the fluorescence changes were registred at 25ºC.

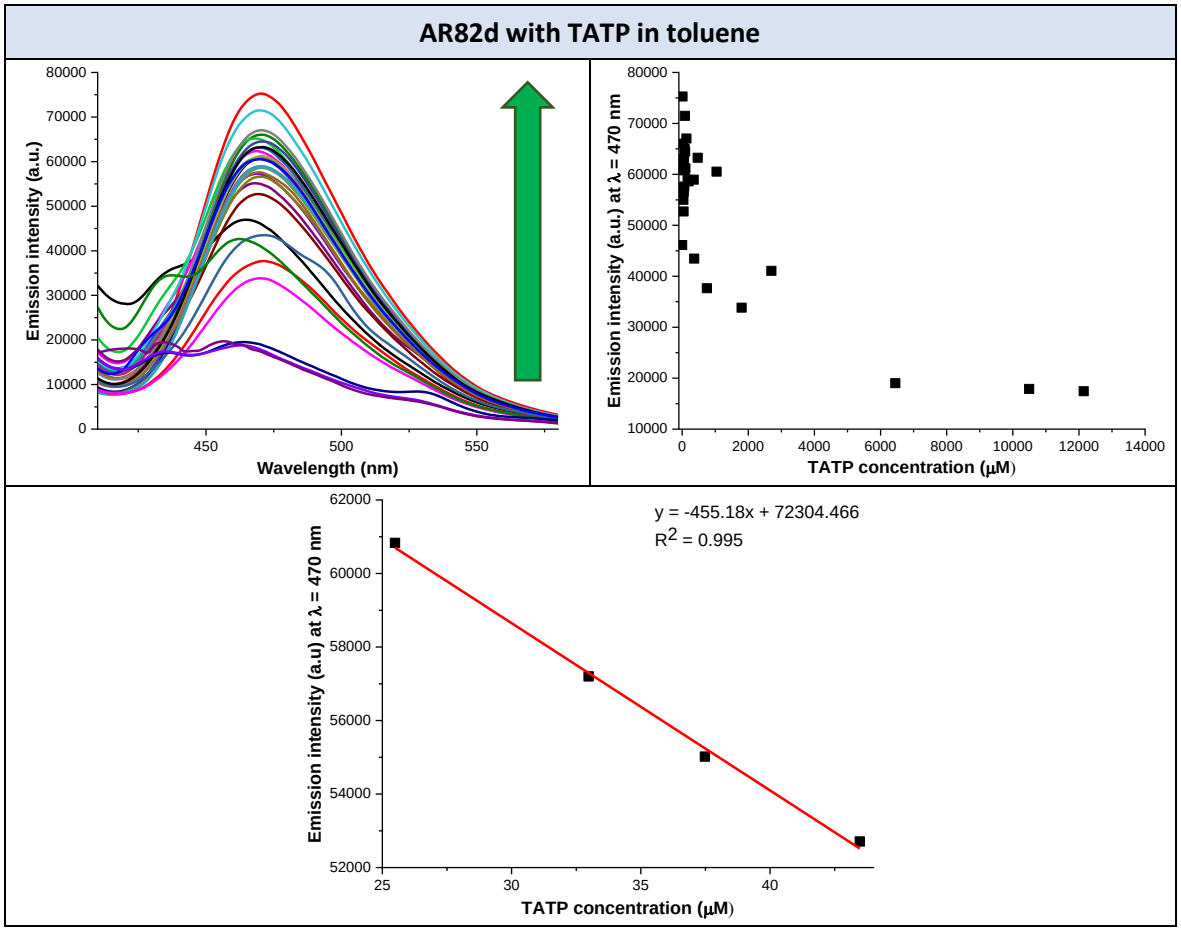

Figure 216. Titration (up left), fluorescence profile at 470 nm (up right) and calibration for the LOD calculation using emission values at 470 nm (down) of a 1 µM of AR82d solution in toluene under increasing concentrations of TATP.

A decrease in the emission intensity was observed until it was stabilized around 6000 µM TATP. The LOD of AR82d with TATP was calculated using a linear regression + false positive and negative at 470 nm. For this method, the R software was used and the value of the LOD was 9.3 nM.

Finally, titration of 1 µM AR82d was performed with increasing amounts of *m*-CPBA in toluene. In this case, the oxidant was added in solution and the excitation wavelength was 360 nm. The measurements was also registered at 25ºC.

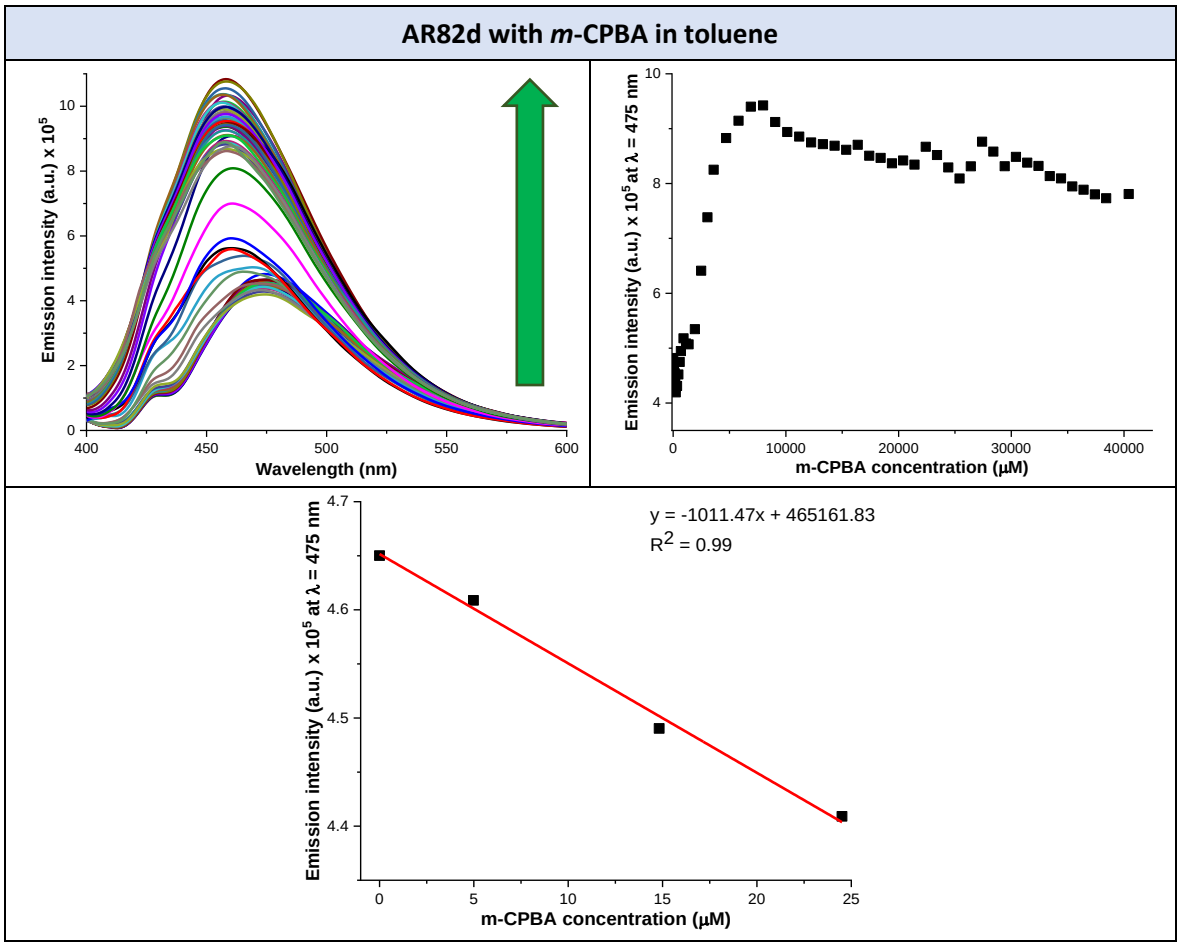

Figure 217. Titration (up left), fluorescence profile at 475 nm (up right) and calibration for the LOD calculation using emission values at 470 nm (down) of a 1 μM of AR82d solution in toluene under increasing concentrations of m-CPBA.

An increase in the emission intensity was observed until it was stabilized around 10000 μM *m*-CPBA. The LOD of AR82d with *m*-CPBA was calculated by linear regression + false positive and negative at 475 nm. The R software was used and the value of the LOD was 2.16 nM.

TATP gas detection in modified nanoparticles:

Several nanoparticles samples were modified by adsorption of the probe and tested as potential TATP sensors. In all three cases, 100 mg of the corresponding nanoparticles and 1 mg of the probe were used to adsorption using the method described above:

- Modified silica nanoparticles (AR82d·SiO_2).
- Modified titanium (IV) oxide nanoparticles (AR82d·TiO_2).
- Modified titanium silicon oxide nanoparticles (AR82d·$SiTiO_4$).

The supported probe was evaluated by several methods. In a first instance, the colour variationof the nanoparticles before and after exposure to TATP was tested. Afterwards, the detection capacity was evaluated by a more quantitative approach by registering changes in fluorescence intensity (by comparing the fluorescence quantum yield for higer precision and in the position of the maximum of emission. Finally, a quantitative study for the specific detection of TATP vapours was also performed.

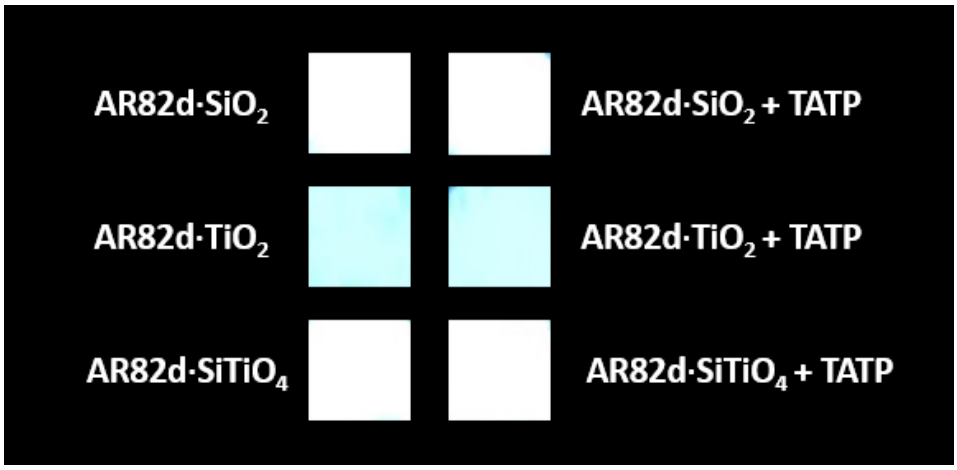

Figure 218. Colour comparation between the nanoparticules with the probe over glass plates before and after the exposure to TATP.

The increase in fluorescence of solid was recorded by measuring the solids and determining the increase in fluorescence quantum yield ($Ø_F$). The most straightforward way to detect the presence of the analyte was the increase in fluorescence of the modified material.

The excitation wavelength for all experiments was 360 nm and the temperature for all test was 25ºC.

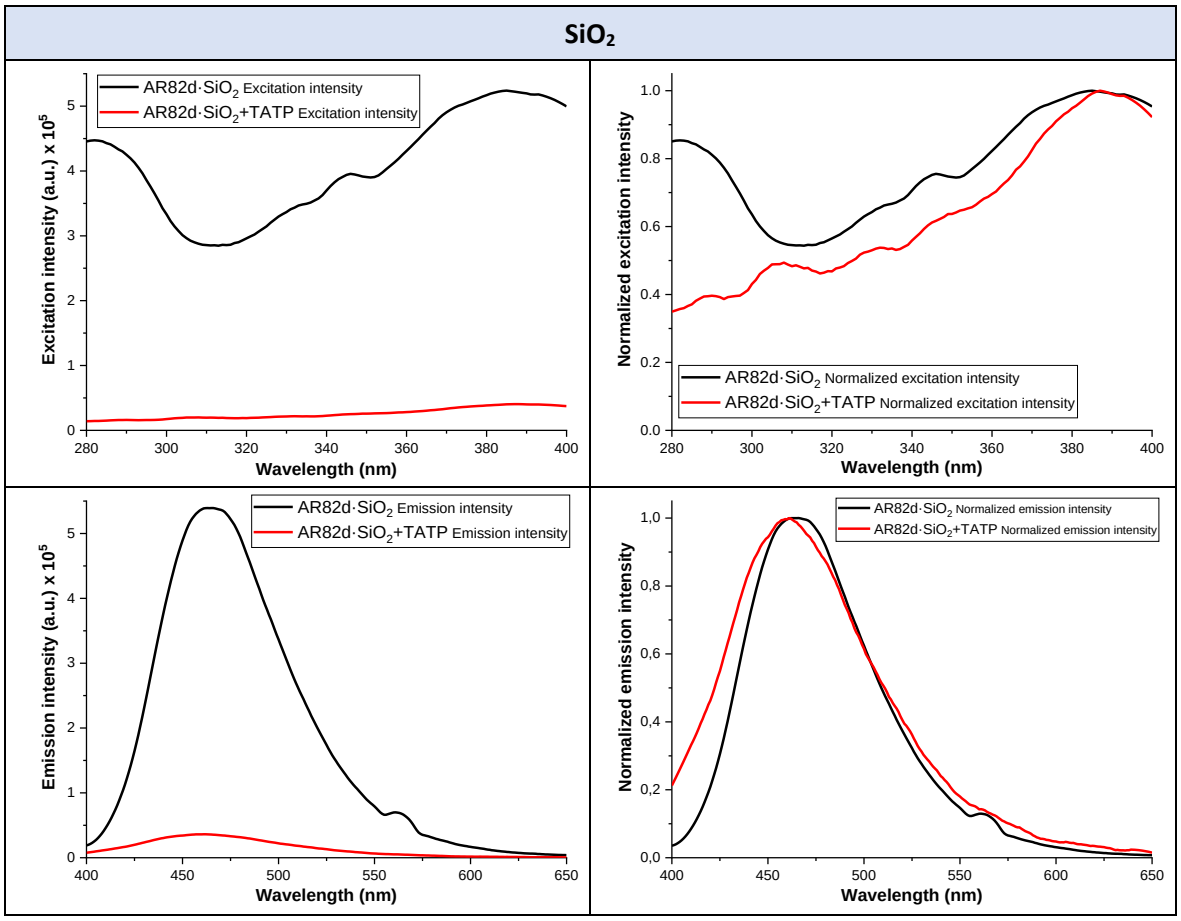

Figure 219. Response of fluorescence (down) and excitation (up) of AR82d adsorbed in SiO_2 nanoparticles.

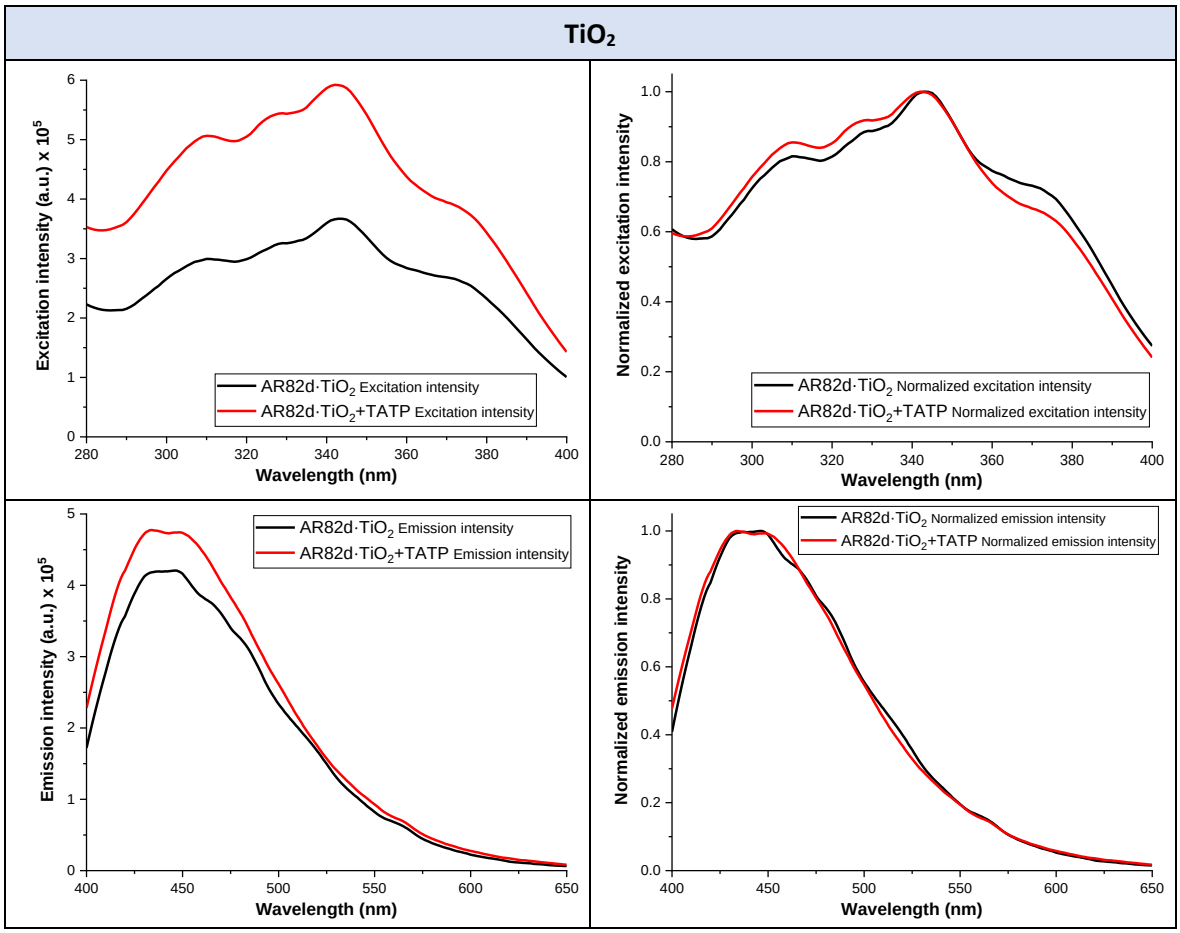

Figure 220. Response of fluorescence (down) and excitation (up) of AR82d adsorbed in TiO_2 nanoparticles.

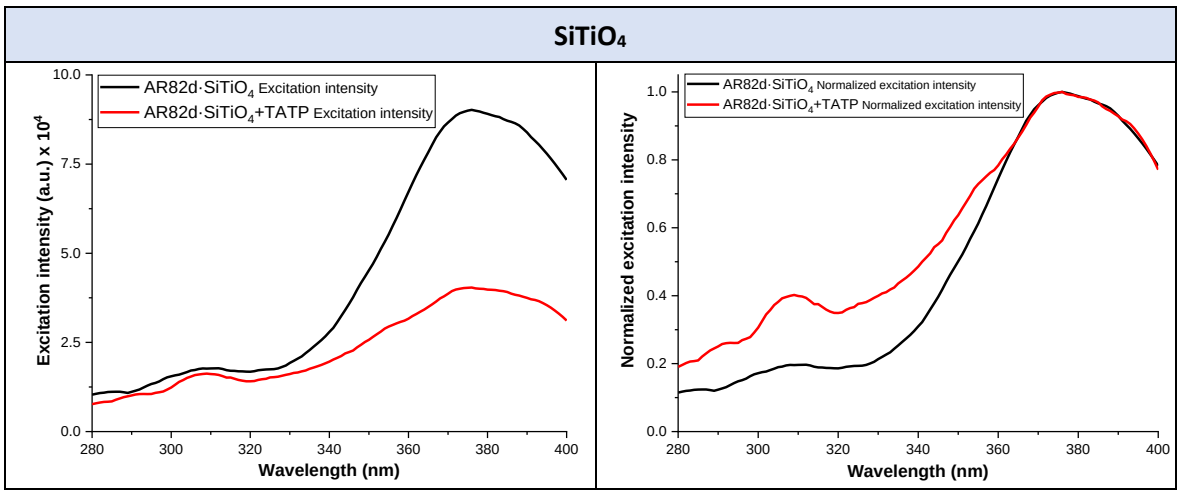

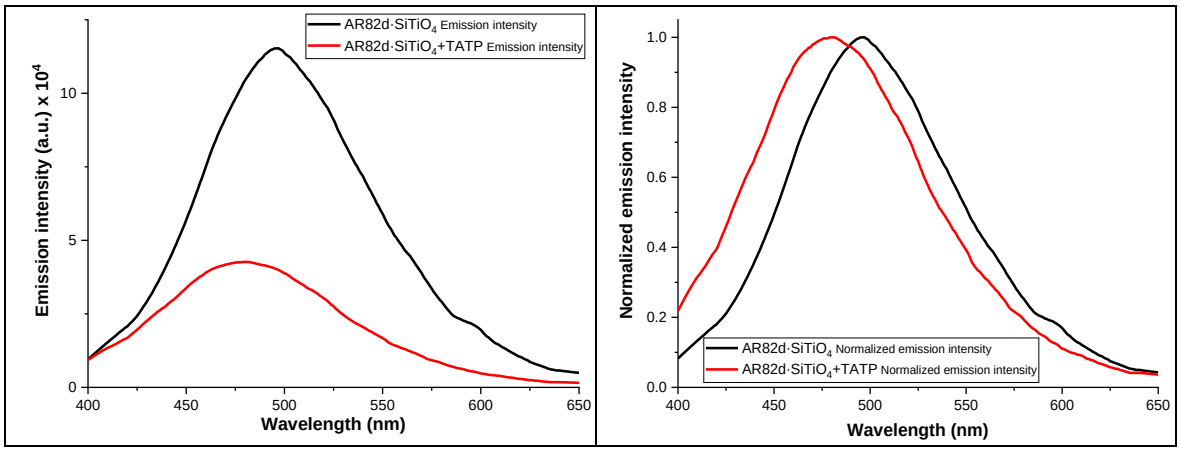

Figure 221. Response of fluorescence (down) and excitation (up) of AR82d adsorbed in $SiTiO_4$ nanoparticles.

As it could be seen in the excitation spectra, the maximum for AR82d·TiO_2 (342 nm) was differed respecting the maximum for AR82d·SiO_2 and AR82d·$SiTiO_4$ (380 nm) and the one previously obtained for the compound in solution (360 nm). Emission measurements were made at the aforementioned wavelengths with similar results.

In doing so, it was necessary to have a fluorometer provided with an integration sphere. The accurach of this method was checked by measuring several replicas, obtaining errors of less than 2%.

	$Ø_{Probe+TATP}$	$Ø_{Probe}$	$Ø_{Probe+TATP}/Ø_{Probe}$
AR82d·SiO_2	<2%	18.6%	0.11
AR82d·TiO_2	2.75%	2.72%	1.01
AR82d·$SiTiO_4$	3.15%	11.1%	0.27

Figure 222. Variation in fluorescence between the initial and after being under excess of TATP.

In general, we could conclude that quantum yields were followed the pattern seen in the previously shown emission intensity spectra. In the case of AR82d·SiO2 and AR82d·SiTiO4, it was decreased after exposure to TATP while in the case of AR82d TiO2, it was ncreased very slightly. However, vapor phase detection tests were not continued due to problems of solubility, and therefore adsorption to the nanoparticles, of the compound AR82d.

Synthesis of *N*-(*N*-Boc-piperidin-4-yl)-4-[2-(4-Boc-piperazin-1-yl)pyridin-5-yl]naphthalene-1,8-dicarboxylmonoimide (AR83p)

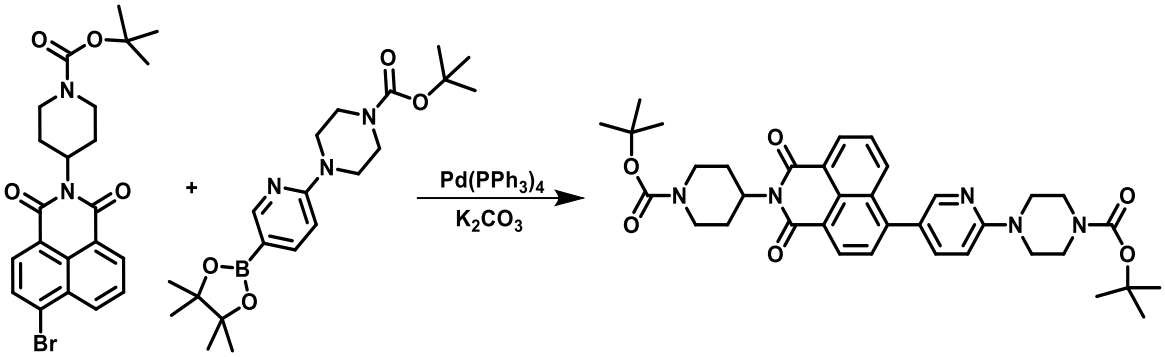

250 mg of *N*-(*N*-Boc-piperidin-4-yl)-4-bromonaphthalene-1,8-dicarboxylmonoimide (AR43p, 0.54 mmol), 221 mg of 2-(4-Boc-piperazine)pyridine-5-boronic acid pinacol ester (0.57 mmol) and 752 mg of potassium carbonate (5.44 mmol) were dissolved in a mixture of toluene:butanol:water (4:1:2 ml) under nitrogen atmosphere and the catalyst, $Pd(PPh_3)_4$ was added. The resulting mixture was stirred overnight at 110°C. Afterwards, the solvent was evaporated under reduce pressure and the solid was dissolved in DCM and washed with water (3×100 ml). The organic extracts were combined, dried over anhidrous Na_2SO_4 and the solvent was evaporated under reduce pressure. The organic solid was purified by column chromatography (SiO_2, DCM:MeOH) getting 256 mg of a yellow solid, 74% yield.

m.p.: 244-247°C.

IR (ATR, cm^{-1}): 2973 – 2841, 1693 (C=O), 1677 (C=O), 1650 (C=O), 1585, 1495, 1453 (C-O), 1408, 1348, 1235, 1159 (C-N), 1103, 1034, 995, 932, 899, 861, 777, 755, 630, 454.

^{1}H-NMR (300 MHz, $CDCl_3$) δ (ppm): 8.49 (d, *J* = 7.6 Hz, 2H, 2×$\mathbf{H_{Ar}}$), 8.31 – 8.19 (m, 2H, 2×$\mathbf{H_{Ar}}$), 7.67 – 7.52 (m, 3H, 3×$\mathbf{H_{Ar}}$), 6.76 (d, *J* = 8.8 Hz, 1H, $\mathbf{H_{Ar}}$), 5.11 (m, 1H, C**H**), 4.24 (s, 2H, C$\mathbf{H_2}$), 3.58 (m, 8H, 4×C$\mathbf{H_2}$), 2.87 – 2.61 (m, 4H, 2×C$\mathbf{H_2}$), 1.61 (m, 2H, C$\mathbf{H_2}$), 1.44 (d, *J* = 2.4 Hz, 18H, 6×C$\mathbf{H_3}$).

^{13}C-NMR (75MHz, $CDCl_3$) δ (ppm): 164.4 (**C**=O), 164.2 (**C**=O), 158.7 ($\mathbf{C}_{Ar}$), 154.7 ($\mathbf{C}_{Ar}$), 148.6 ($\mathbf{C}_{Ar}$H), 143.6 ($\mathbf{C}_{Ar}$), 138.9 ($\mathbf{C}_{Ar}$H), 132.0 ($\mathbf{C}_{Ar}$H), 131.2 ($\mathbf{C}_{Ar}$H), 130.9 ($\mathbf{C}_{Ar}$H), 129.8 ($\mathbf{C}_{Ar}$), 128.8 ($\mathbf{C}_{Ar}$), 127.5 ($\mathbf{C}_{Ar}$H), 126.8 ($\mathbf{C}_{Ar}$H), 123.7 ($\mathbf{C}_{Ar}$), 123.2 ($\mathbf{C}_{Ar}$), 121.6 ($\mathbf{C}_{Ar}$), 106.5 ($\mathbf{C}_{Ar}$H), 80.0 (**Cq**), 79.4 (**Cq**), 51.7 (**C**H), 44.8 (**C**H_2), 43.6 (**C**H_2), 28.5 (**C**H_3), 28.4 (**C**H_3), 28.2 (**C**H_2).

HRMS (MALDI, DIT-) m/z: calculated for $C_{36}H_{43}N_5O_6$: 641.3208 (M^-); found 641.3232.

UV-Vis ($CHCl_3$), λ_{max} nm (log ε): 390 (3.9).

Ø (Hex, %): 85.40.

τ (375 nm, Hex, ns): 3.199 (χ^2: 1.153).

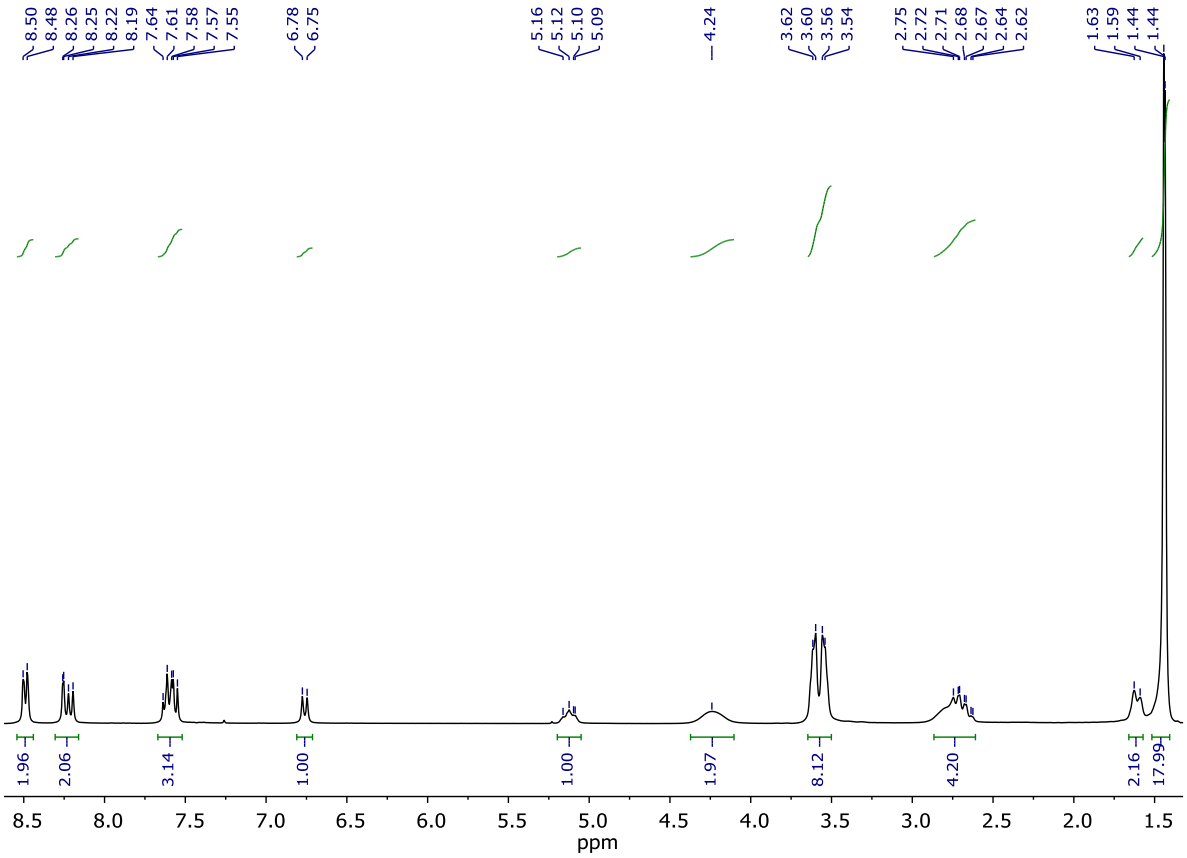

Figure 223. ^{1}H-NMR ($CDCl_3$, 300 MHz) of AR83p.

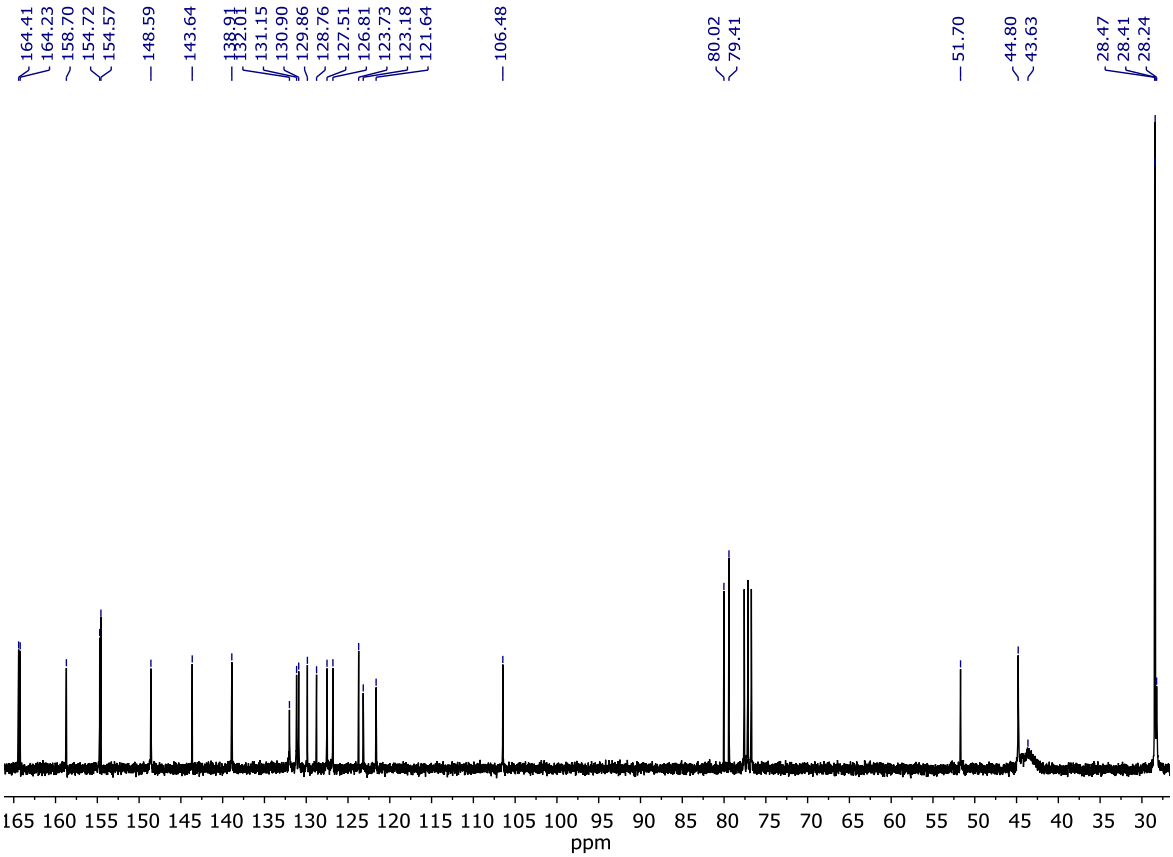

Figure 224. ^{13}C-NMR ($CDCl_3$, 75 MHz) of AR83p.

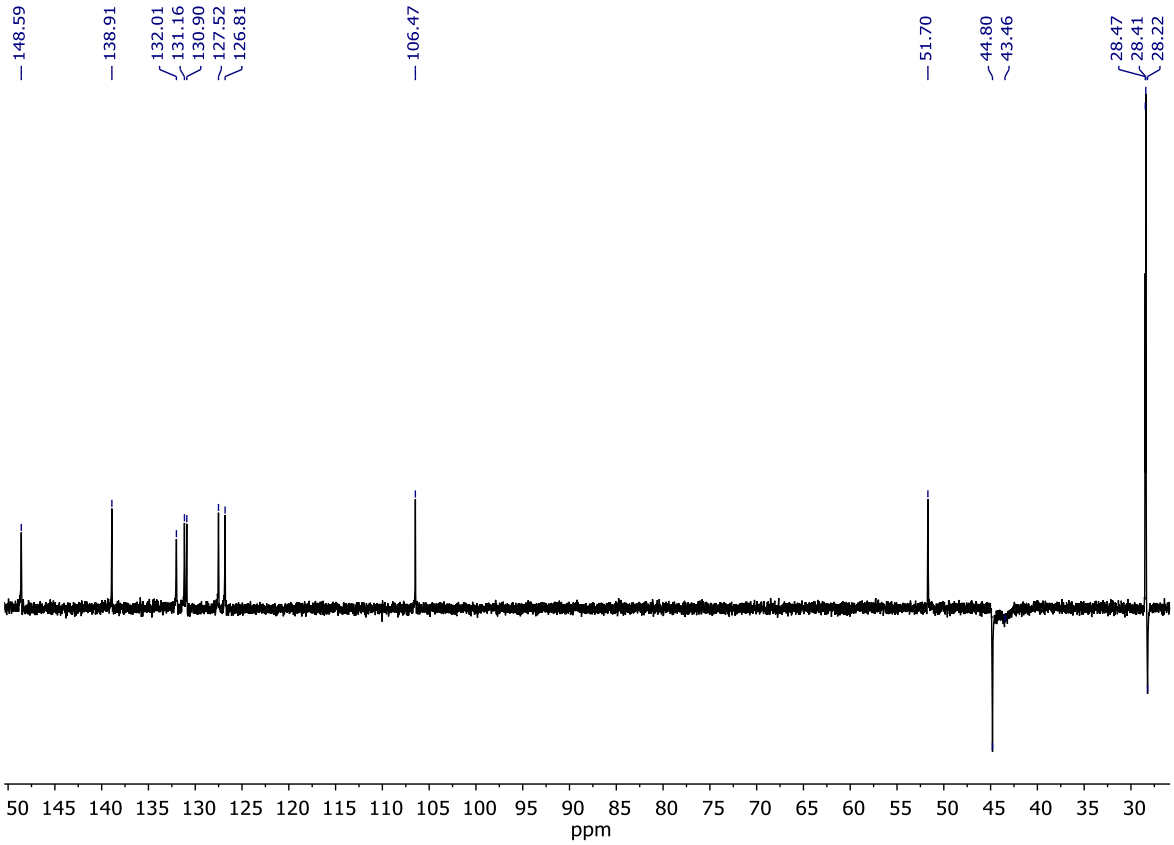

Figure 225. DEPT NMR ($CDCl_3$, 75 MHz) of AR83p.

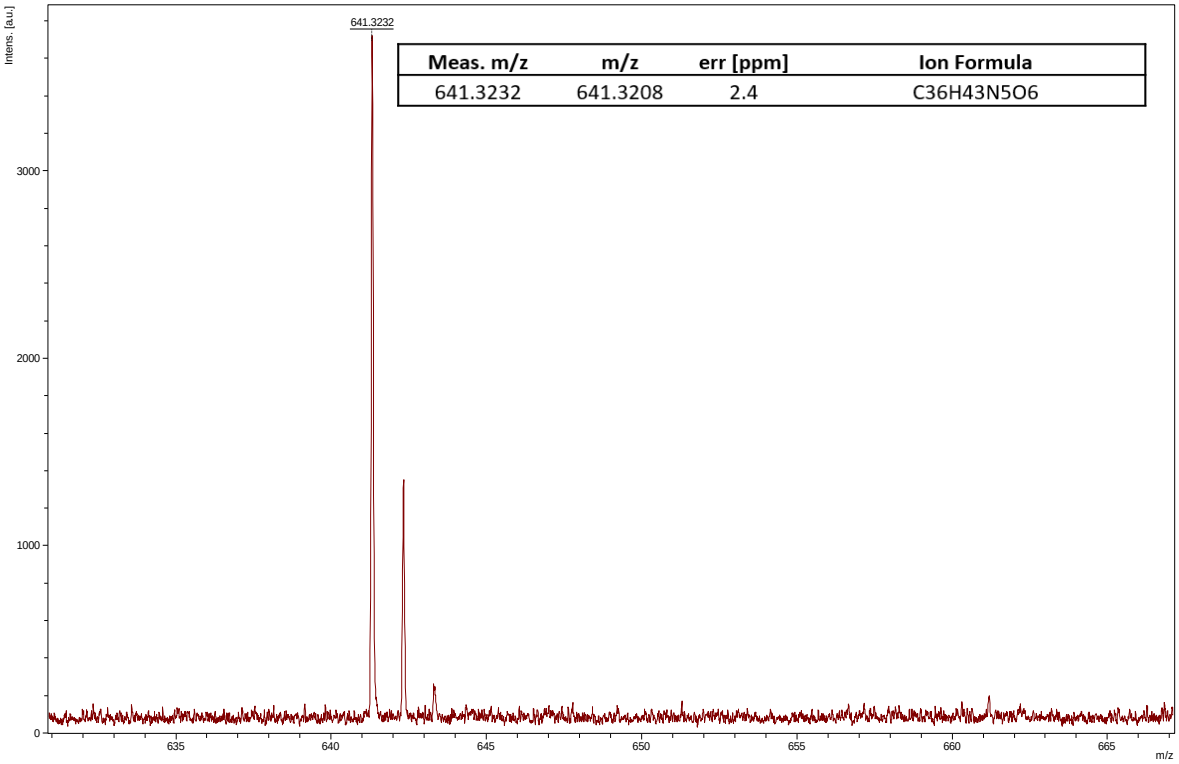

Figure 226. HRMS (MALDI, DIT-) of AR83p

Solvatochromism:

The concentration of the compound was 20 µM and the excitation wavelength was 380 nm.

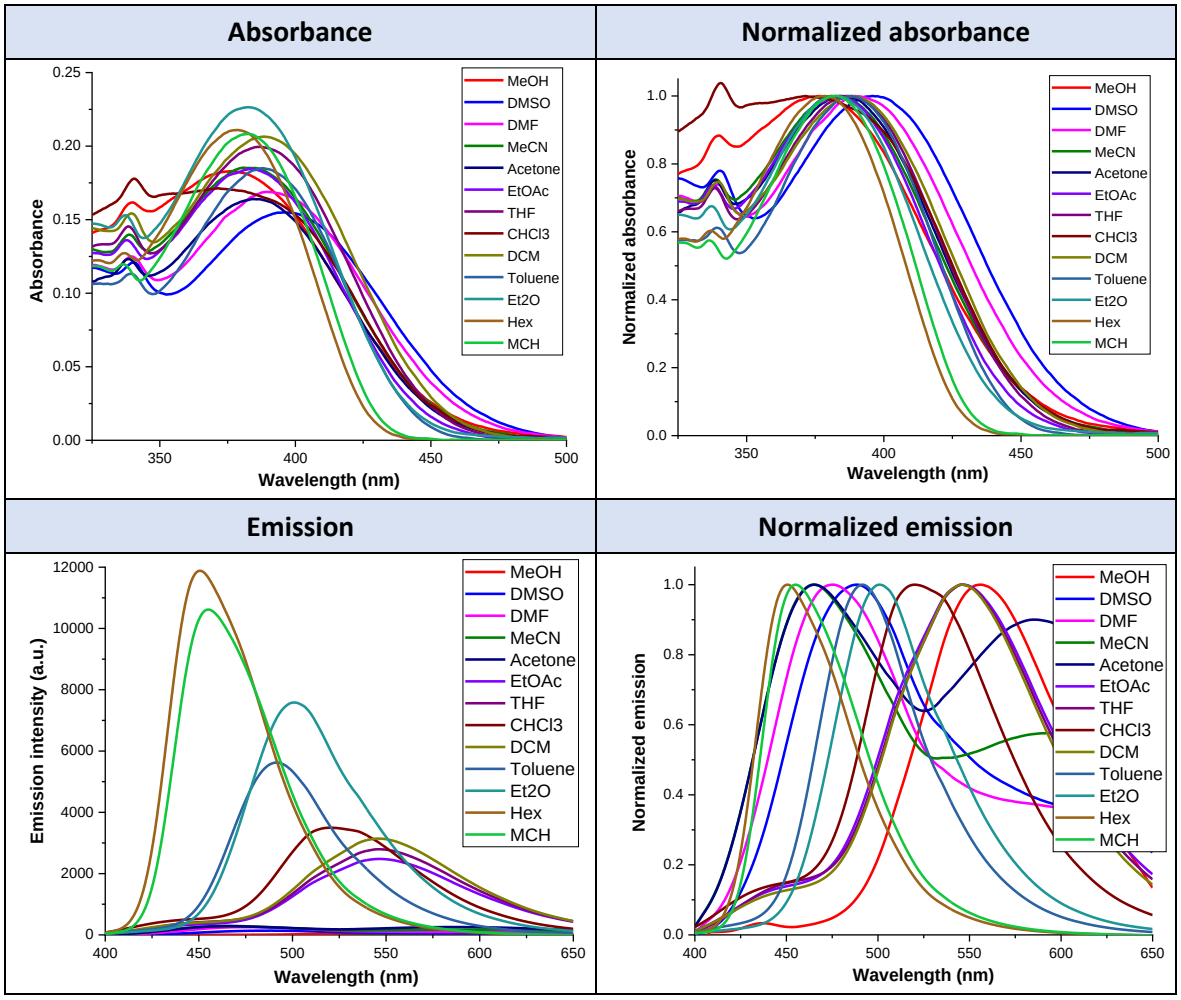

Figure 227. Solvatochromism of AR83p.

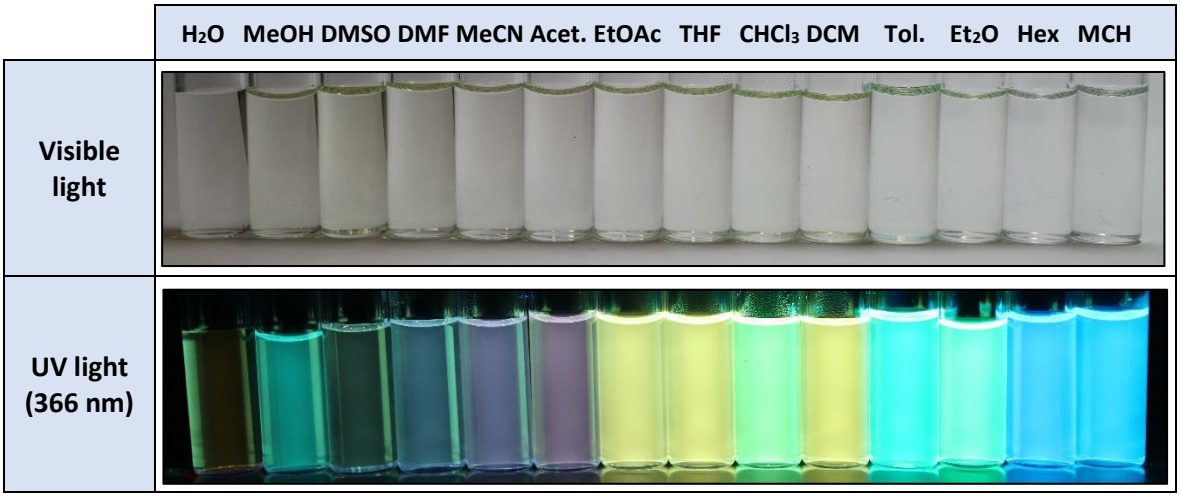

Figure 228. Solvatochromism of AR83p under visible and 366 nm light.

Fluorescence decay lifetime (τ):

The solvent used was hexane. The concentration of the compound was 20 µM.

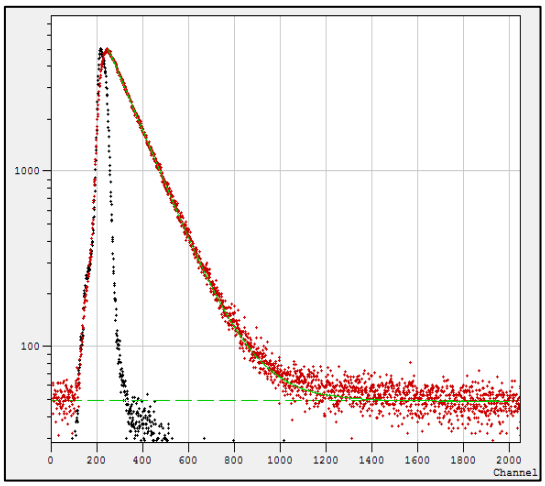

Figure 229. Fluorescence decay lifetime of AR83p.

Water acceptance test:

The solvent used was MeOH and THF and the concentration of the compound was 20 µM.

	R	5%	10%	20%	30%	40%	50%	60%	70%	80%	90%
Visible light	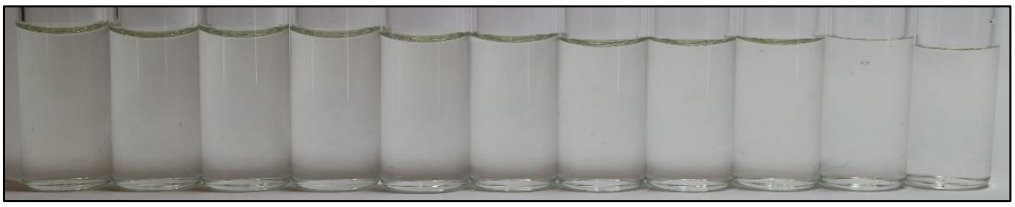										
UV light (366 nm)	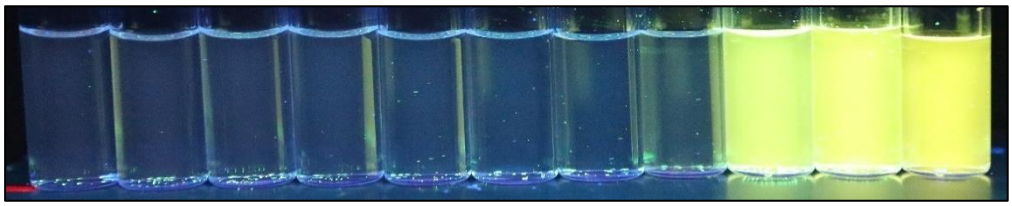										

Figure 230. Water acceptance test of AR83p in MeOH under visible (up) and UV (down) light.

	R	5%	10%	20%	30%	40%	50%	60%	70%	80%	90%
Visible light											
UV light (366 nm)	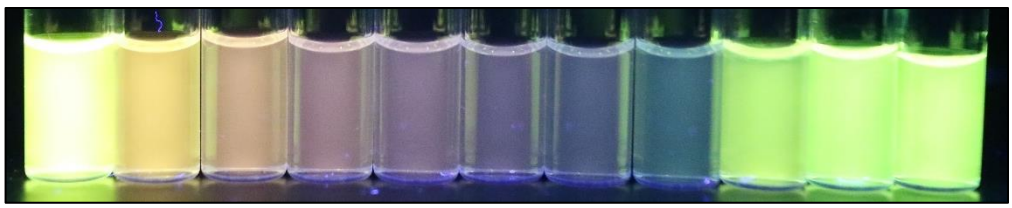										

Figure 231. Water acceptance test of AR83p in THF under visible (up) and UV (down) light.

In both solvents, there was a strong increase in emission intensity from 70% water (AIE), which also coincided with what was observed using THF as solvent. In addition, using THF, there was a shift of the emission maximum from the red-purple region (580-650 nm) to the yellow-greenish region (550-570 nm).

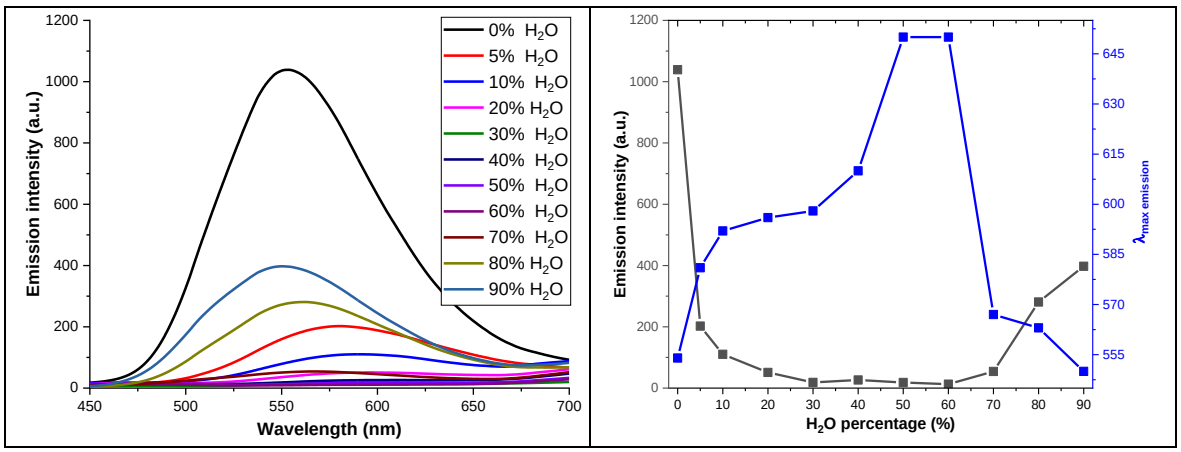

Figure 232. Emission intensity graph (left) and graph of relationship between the emission intensity and the wavelength of the maximum of emission (right) as a function of the amount of water added for AR83p using THF as a solvent.

SEM nanoparticles:

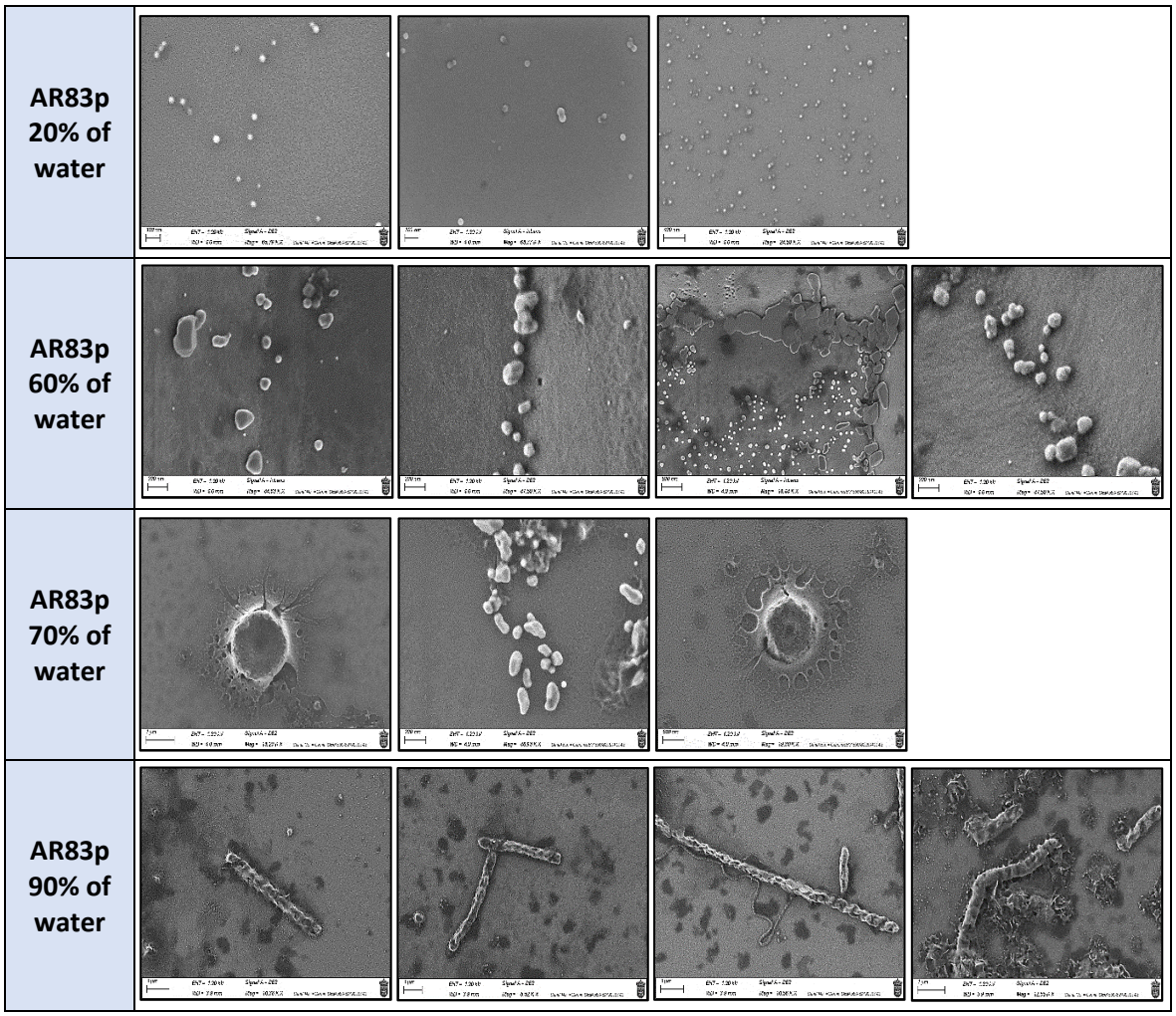

Figure 233. SEM nanoparticles of AR83p in different mixtures of water and THF.

pH test:

The amount of water that the compound could accept was 90%. The concentration of the compound was 20 µM and the solvent used was MeOH.

	R	HCl	3.4	4.8	6.4	7.4	7.9	10.5	KOH
Visible light	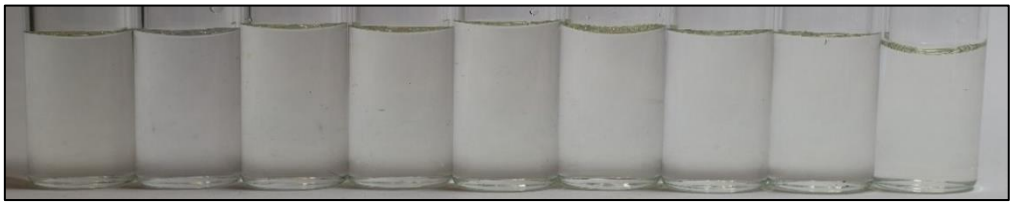								
UV light (366 nm)	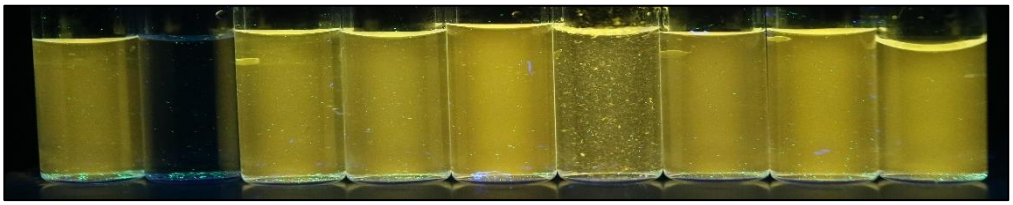								

Figure 234. pH test of AR83p under visible (up) and UV (down) light.

There was a quenching in the emission at very acidic pH while, at physiological pH, the compound was precipitated.

Cations and anions test:

The concentration of the compound was 20 µM and the solvent used was a mixture of MeOH and water (90%).

	R	Ag^{+}	Ni^{2+}	Sn^{2+}	Cd^{2+}	Zn^{2+}	Pb^{2+}	Cu^{2+}	Fe^{3+}	Sc^{3+}	Al^{3+}	Hg^{2+}	Au^{3+}	Co^{2+}	Pd^{2+}	Ir^{3+}	Cu^{+}	Ru^{3+}	Pt^{2+}
Visible light	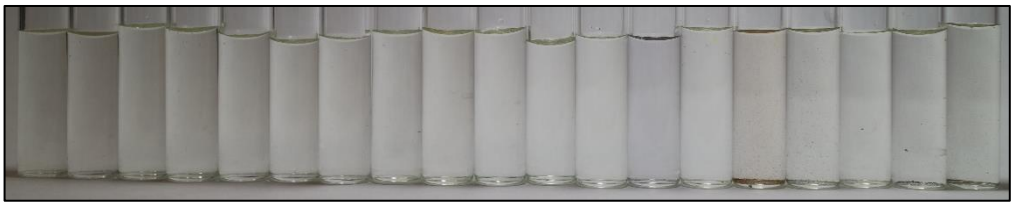																		
UV light (366 nm)	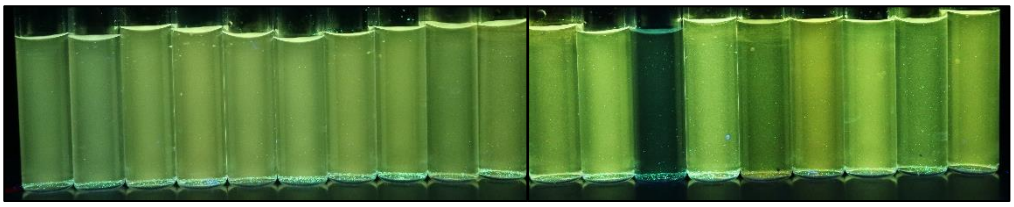																		

Figure 235. Cations test of AR83p under visible (up) and UV (down) light.

The most significant change under UV light was the quenching of the fluorescence against the Au^{3+}.

The concentration of the compound was 20 µM and the solvent used was a mixture of MeOH and water (90%).

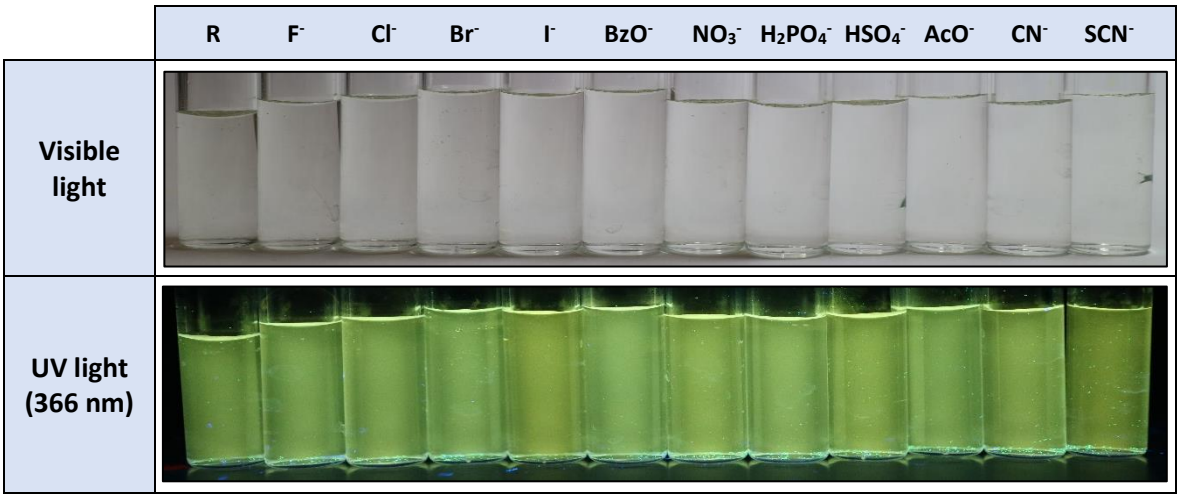

Figure 236. Anions test of AR83p under visible (up) and UV (down) light.

No significant changes were observed.

Oxidant and reductant reagents test:

The solvent used was a mixture of MeOH and water (90%) and concentration of the compound was 20 µM.

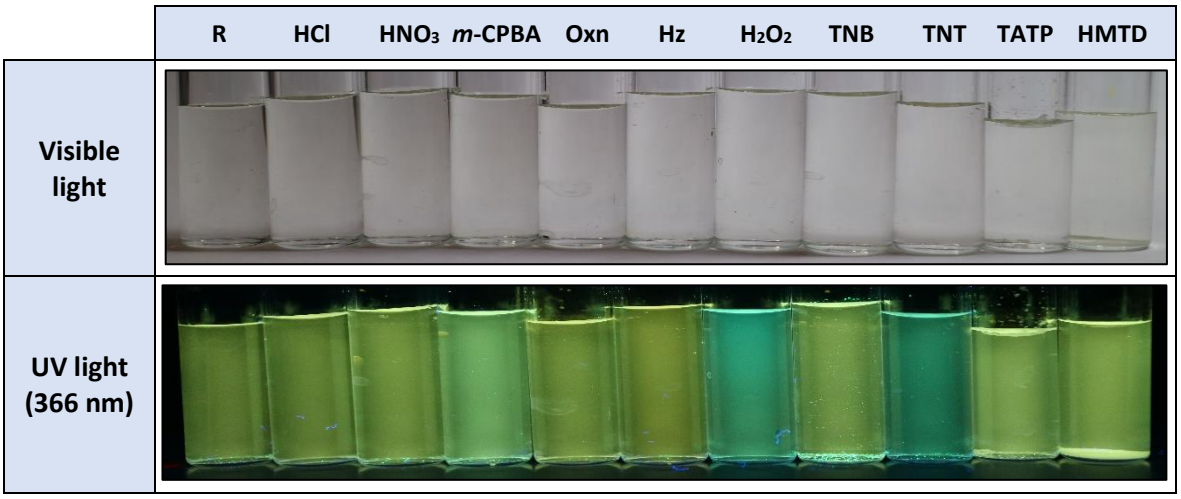

Figure 237. Oxidant and reductant reagents test of AR83p under visible (up) and UV (down) light.

No significant changes were observed.

Synthesis of *N*-(piperidin-4-yl)-4-[2-(4-Boc-piperazin-1-yl)pyridin-5-yl]naphthalene-1,8-dicarboxylmonoimide (AR83s)

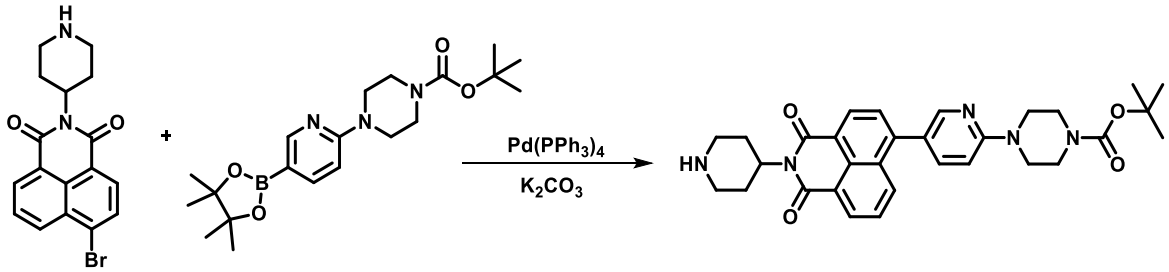

150 mg of *N*-(piperidin-4-yl)-4-bromonaphthalene-1,8-dicarboxylmonoimide (AR43d, 0.42 mmol), 171 mg of 2-(4-Boc-piperazine)pyridine-5-boronic acid pinacol ester (0.44 mmol) and 451 mg of potassium carbonate (3.26 mmol) were dissolved in a mixture of toluene:butanol:water (4:1:2 ml) under nitrogen atmosphere and the catalyst, $Pd(PPh_3)_4$ was added. After it was stirred overnight at 110°C, the solvent was evaporated under reduce pressure, the solid was dissolved in DCM and washed with water (3×100 ml). The organic extracts were combined, dried over anhidrous Na_2SO_4 and the solvent was evaporated under reduce pressure. The organic solid was purified by column chromatography (SiO_2, DCM:MeOH) getting 113 mg of a brown solid, 50% yield.

m.p.: 216-218°C (decomposition).

IR (ATR, cm^{-1}): 3425 (N-H), 2970 – 2851, 1689 (C=O), 1585, 1405 (C-O), 1351, 1238, 1118 (C-N), 992, 929, 753, 717, 693, 535.

^{1}H-NMR (300 MHz, $CDCl_3$) δ (ppm): 8.60 (d, *J* = 7.5 Hz, 2H, 2×**H$_{Ar}$**), 8.30 (m, 2H, 2×**H$_{Ar}$**), 7.72 – 7.61 (m, 3H, 3×**H$_{Ar}$**), 6.80 (d, *J* = 9.0 Hz, 1H, **H$_{Ar}$**), 5.40 – 5.25 (m, 1H, C**H**), 3.83 (s, 2H, C**H**$_2$), 3.69 – 3.57 (m, 8H, 4×C**H**$_2$), 3.41 – 3.09 (m, 5H, 2×C**H**$_2$ y N**H**), 1.97 (d, *J* = 11.1 Hz, 2H, C**H**$_2$), 1.50 (s, 9H, 3×C**H**$_3$).

^{13}C-NMR (75MHz, $CDCl_3$) δ (ppm): 164.4 (**C**=O), 164.2 (**C**=O), 158.9 (**C**$_{Ar}$), 154.9 (**C**$_{Ar}$), 148.7 (**C**$_{Ar}$H), 144.1 (**C**$_{Ar}$), 139.1 (**C**$_{Ar}$H), 132.4 (**C**$_{Ar}$H), 131.7 (**C**$_{Ar}$H), 131.4 (**C**$_{Ar}$H), 130.1 (**C**$_{Ar}$), 128.9 (**C**$_{Ar}$), 127.8 (**C**$_{Ar}$H), 127.0 (**C**$_{Ar}$H), 123.8 (**C**$_{Ar}$), 123.0 (**C**$_{Ar}$), 121.5 (**C**$_{Ar}$), 106.6 (**C**$_{Ar}$H), 80.3 (**Cq**), 48.9 (**C**H), 44.9 (**C**H$_2$), 43.3 (**C**H$_2$), 28.5 (**C**H$_3$), 25.8 (**C**H$_2$).

HRMS (MALDI, DIT+) m/z: calculated for $C_{31}H_{35}N_5O_4$: 543.2714 (M^+ + 2); found 543.2748.

UV-Vis ($CHCl_3$), λ_{max} nm (log ε): 415 (3.9).

Ø ($CHCl_3$, %): 99.41.

τ (375 nm, $CHCl_3$, ns): 5.291 (χ^2: 1.040).

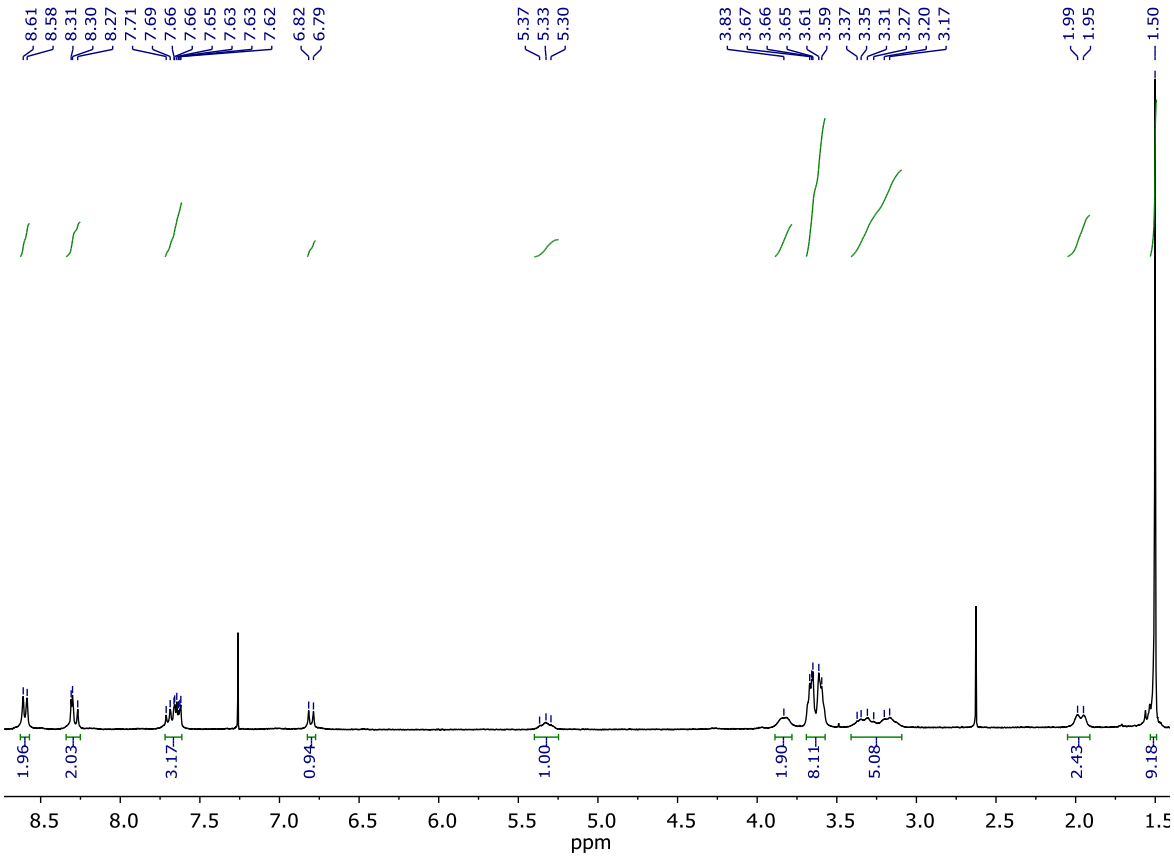

Figure 238. ^{1}H-NMR ($CDCl_3$, 300 MHz) of AR83s.

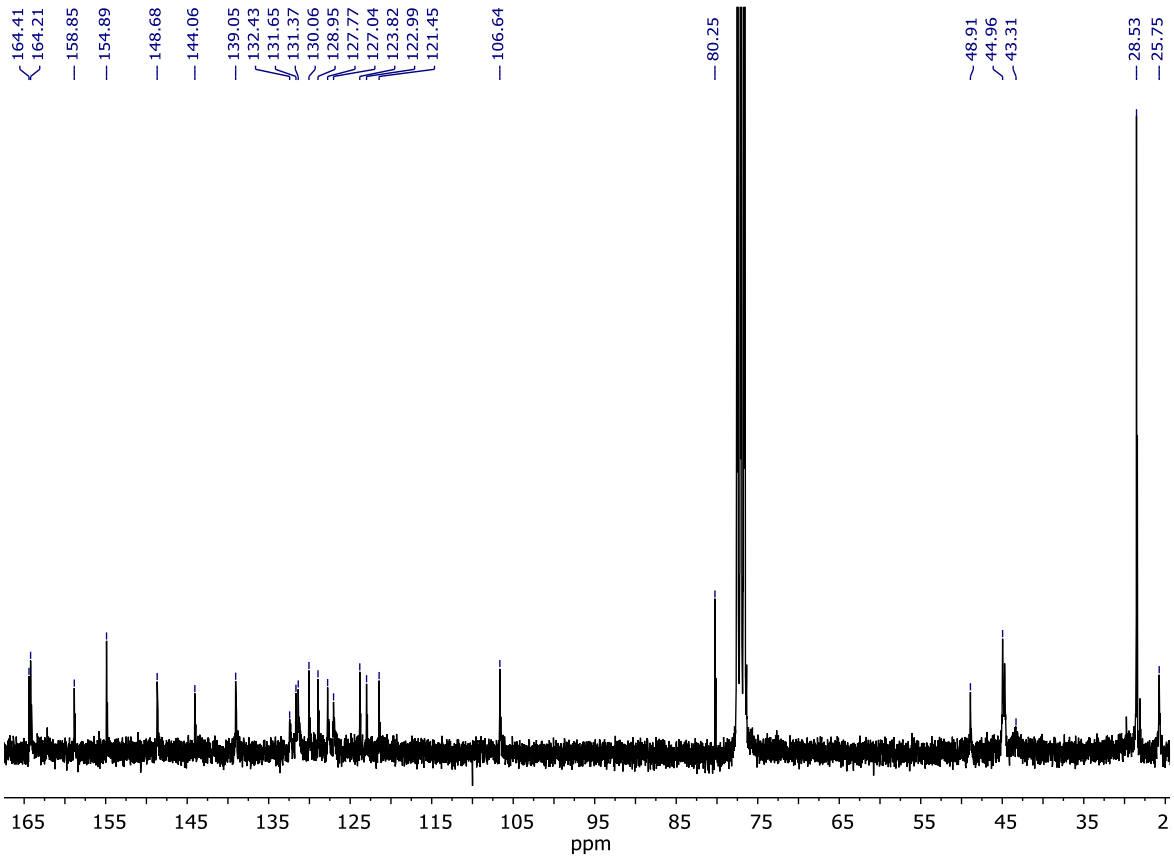

Figure 239. ^{13}C-NMR ($CDCl_3$, 75 MHz) of AR83s.

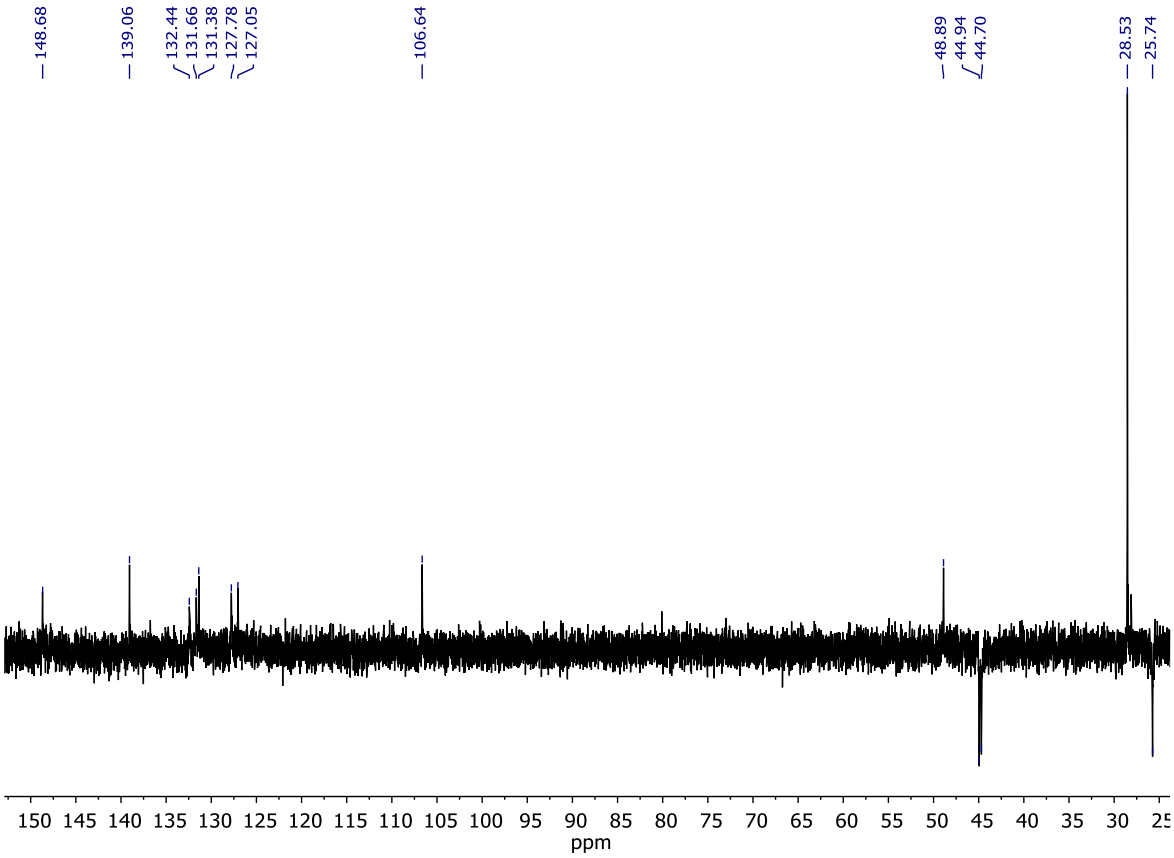

Figure 240. DEPT NMR ($CDCl_3$, 75 MHz) of AR83s.

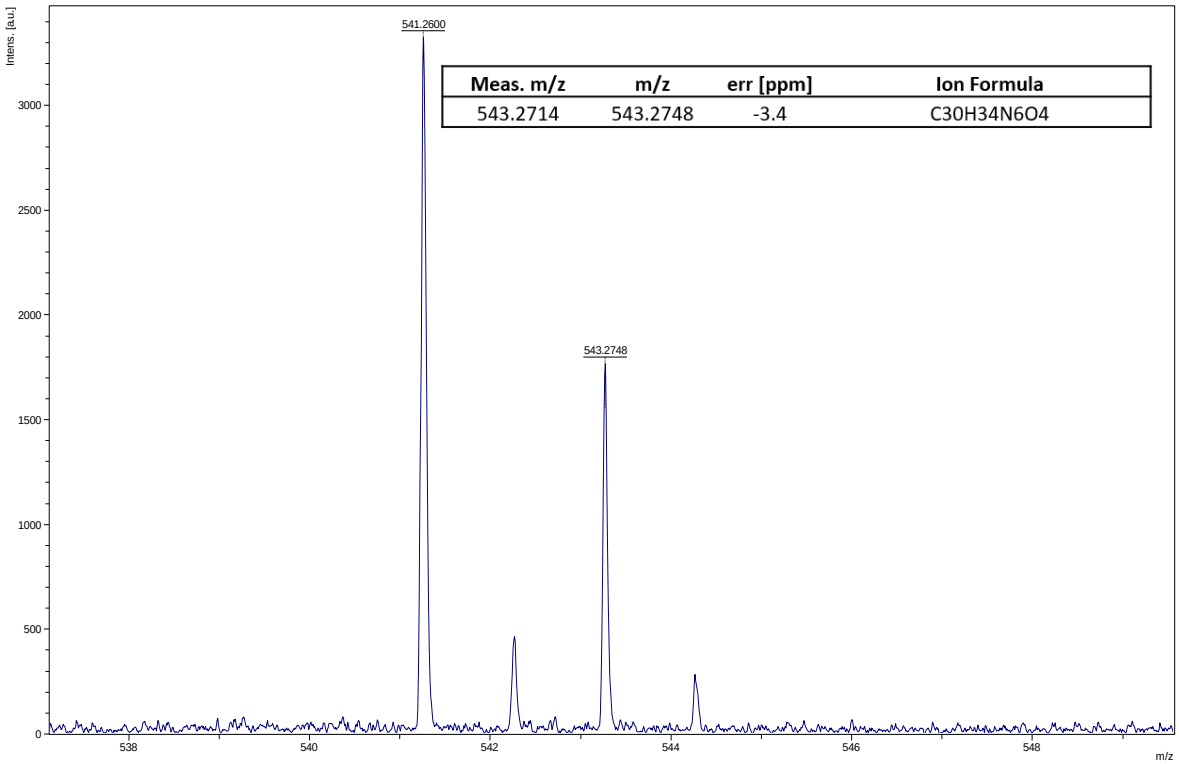

Meas. m/z	m/z	err [ppm]	Ion Formula
543.2714	543.2748	-3.4	C30H34N6O4

Figure 241. HRMS (MALDI, DIT+) of AR83s.

Solvatochromism:

The concentration of the compound was 20 µM and the excitation wavelength was 390 nm.

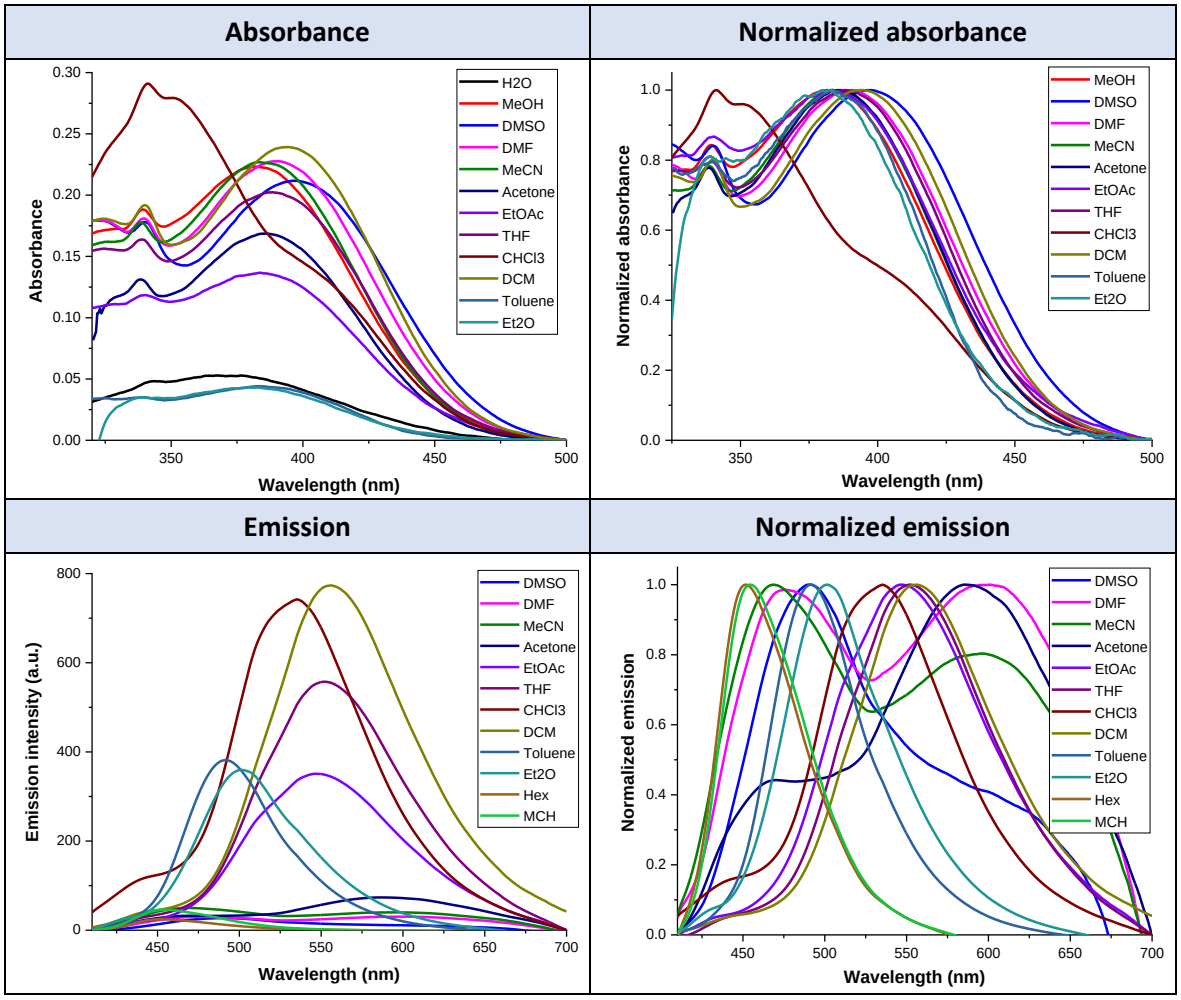

Figure 242. Solvatochromism of AR83s.

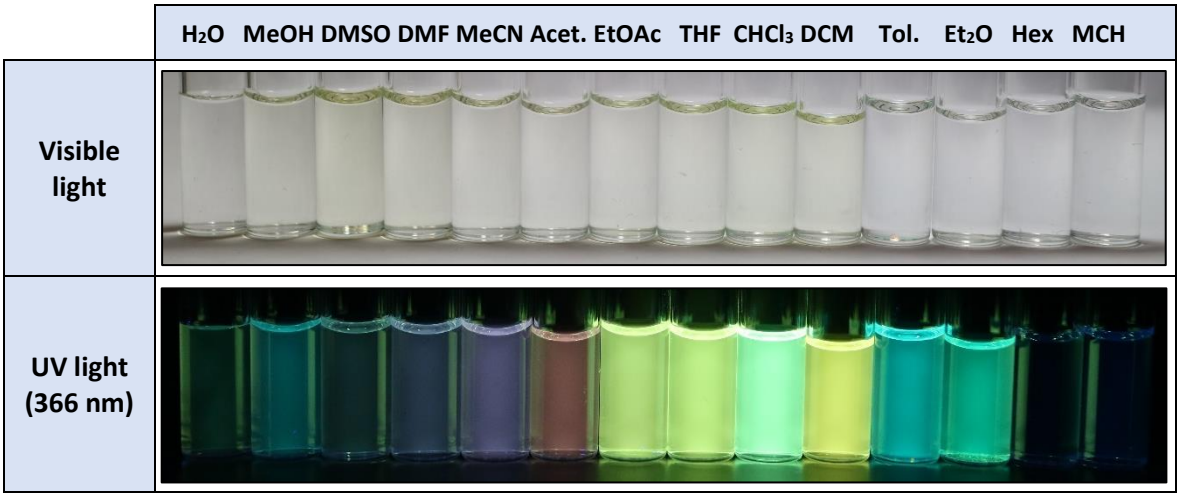

Figure 243. Solvatochromism of AR83s under visible and 366 nm light.

Fluorescence decay lifetime (τ):

The solvent used was chloroform. The concentration of the compound was 20 µM.

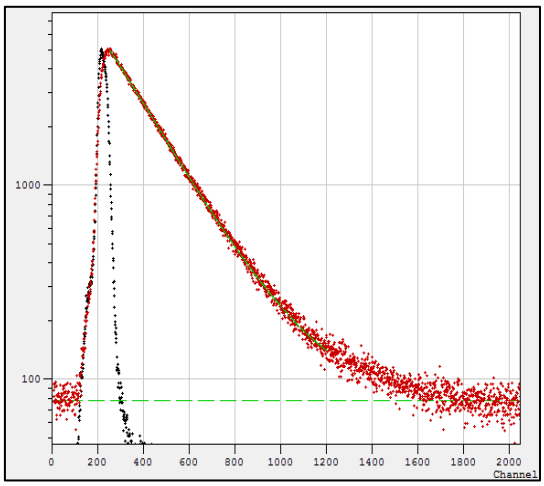

Figure 244. Fluorescence decay lifetime of AR83s.

Water acceptance test:

The solvent used was acetone and THF and the concentration of the compound was 20 µM.

	R	5%	10%	20%	30%	40%	50%	60%	70%	80%	90%
Visible light											
UV light (366 nm)	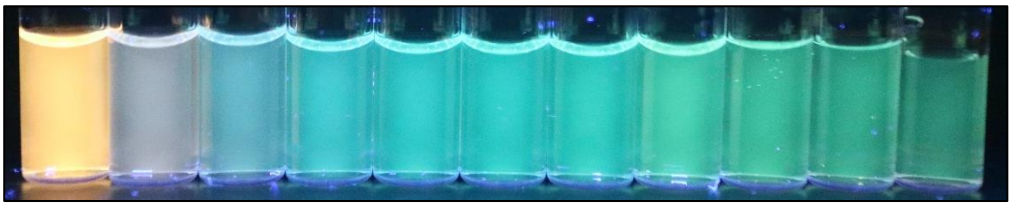										

Figure 245. Water acceptance test of AR83s in acetone under visible (up) and UV (down) light.

	R	5%	10%	20%	30%	40%	50%	60%	70%	80%	90%
Visible light											
UV light (366 nm)	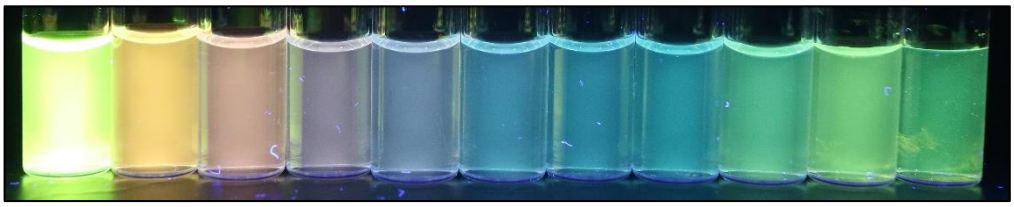										

Figure 246. Water acceptance test of AR83s in THF under visible (up) and UV (down) light.

There was a slight increase in emission intensity from 70% water (AIE) using both acetone and THF as solvent. At low amounts of water, the emission maximum was in the red region (about 580 nm) while, between 30% and 60% water, it was shifted to the bluo region (485 nm). At high percentages of water, from 70%, the emission maximum was shifted to the green region (530-560 nm).

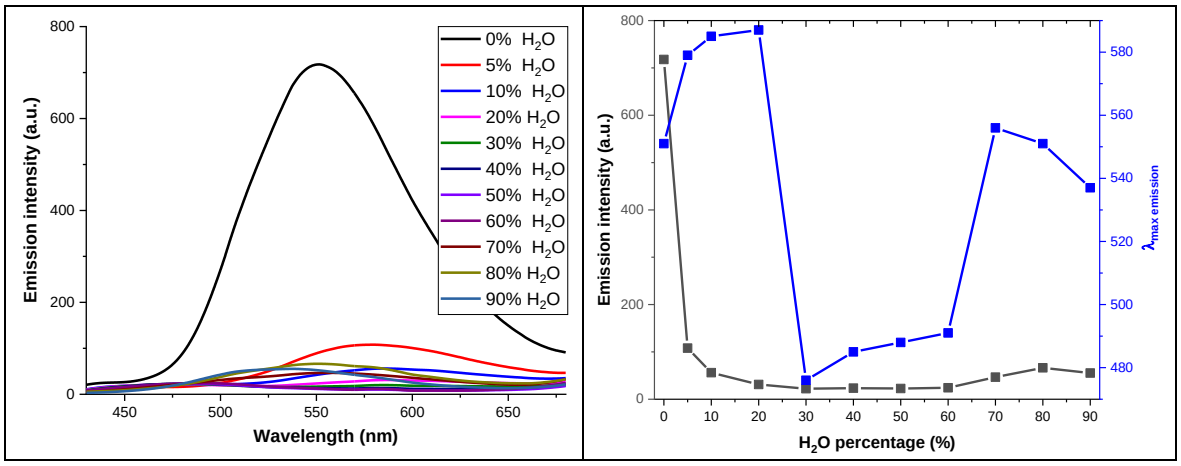

Figure 247. Emission intensity graph (left) and graph of relationship between the emission intensity and the wavelength of the maximum of emission (right) as a function of the amount of water added for AR83s using THF as a solvent.

SEM nanoparticles:

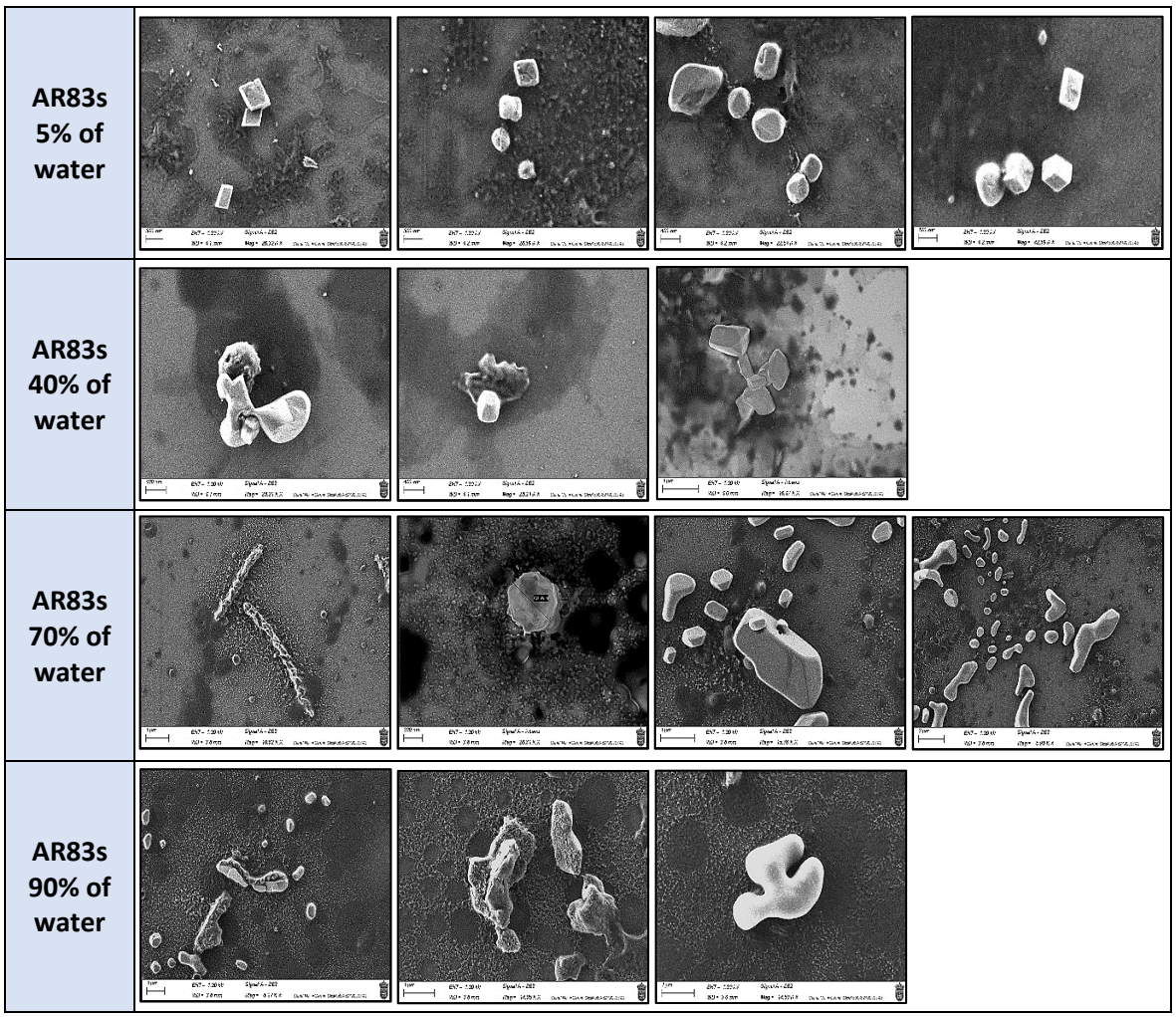

Figure 248. SEM nanoparticles of AR83p in different mixtures of water and THF.

pH test:

The amount of water that the compound could accept was 20%. The concentration of the compound was 20 µM and the solvent used was acetone.

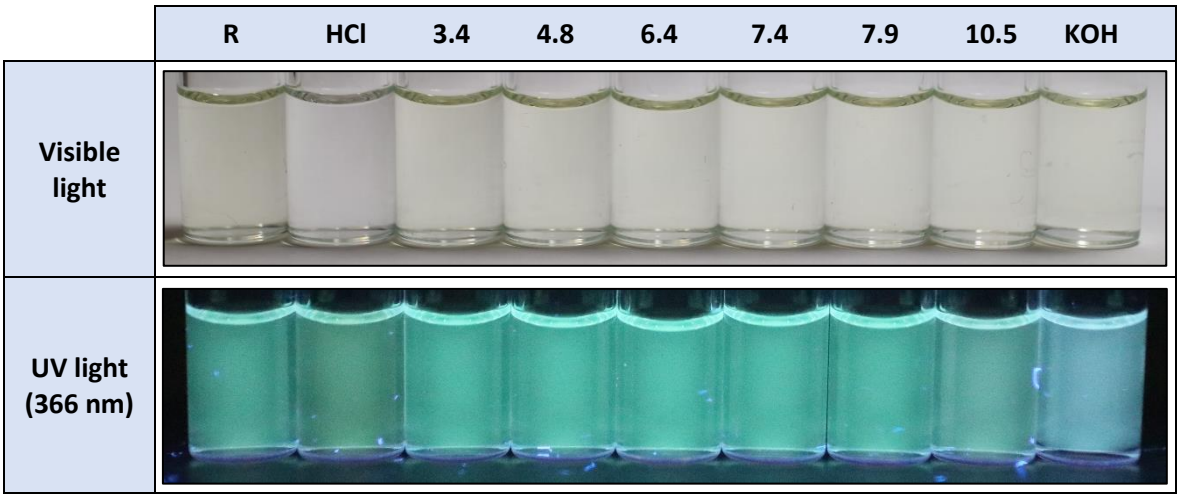

Figure 249. pH test of AR83s under visible (up) and UV (down) light.

No significant changes were observed.

Cations and anions test:

The concentration of the compound was 20 µM and the solvent used was acetone.

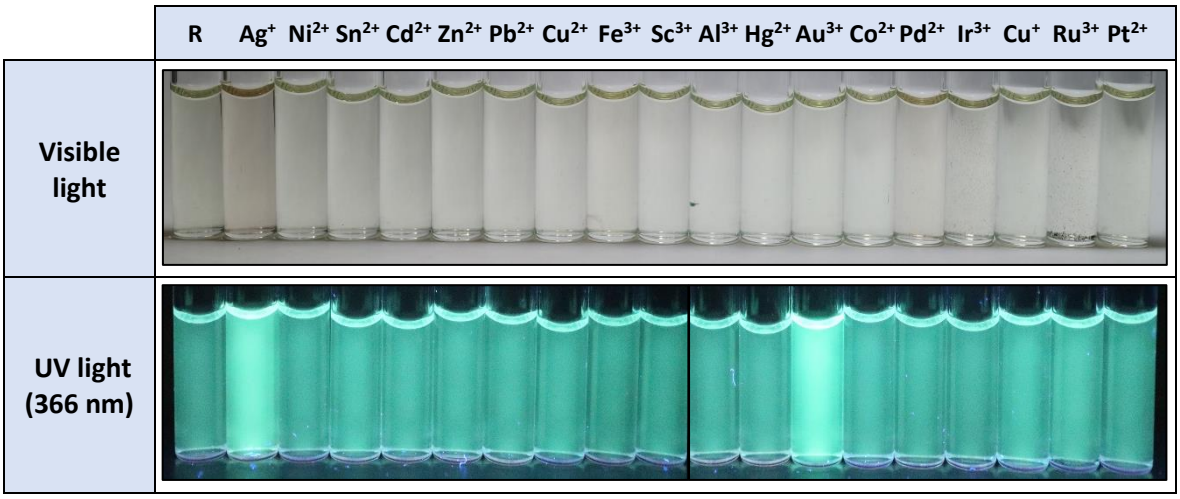

Figure 250. Cations test of AR83s under visible (up) and UV (down) light.

The fluorescence was become brighter when the probe was exposed to Ag^{+} and Au^{3+}.

The concentration of the compound was 20 µM and the solvent used was acetone.

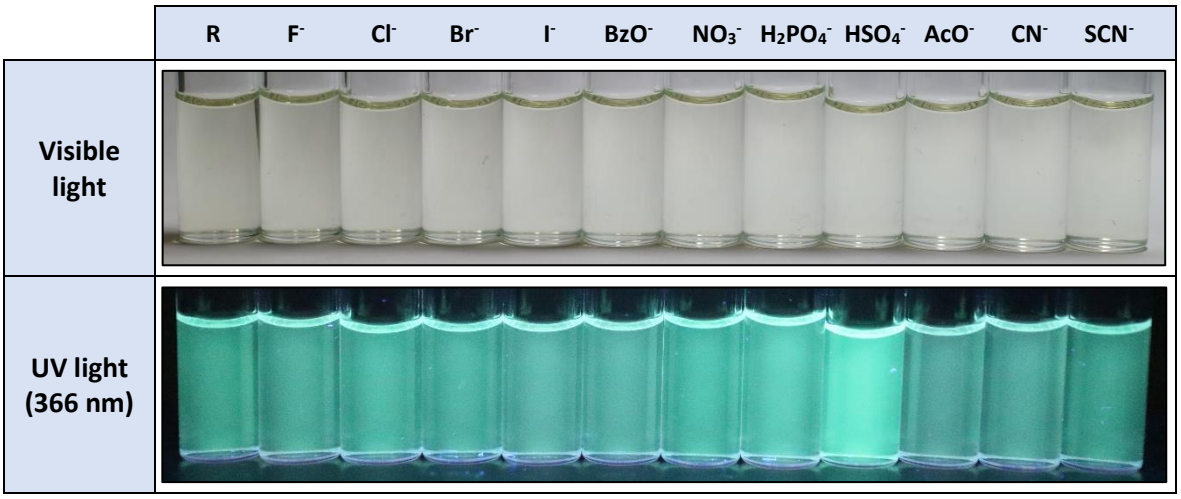

Figure 251. Anions test of AR83s under visible (up) and UV (down) light.

No significant changes were observed.

Oxidant and reductant reagents test:

The solvent used was a mixture of MeOH and water and concentration of the compound was 20 µM.

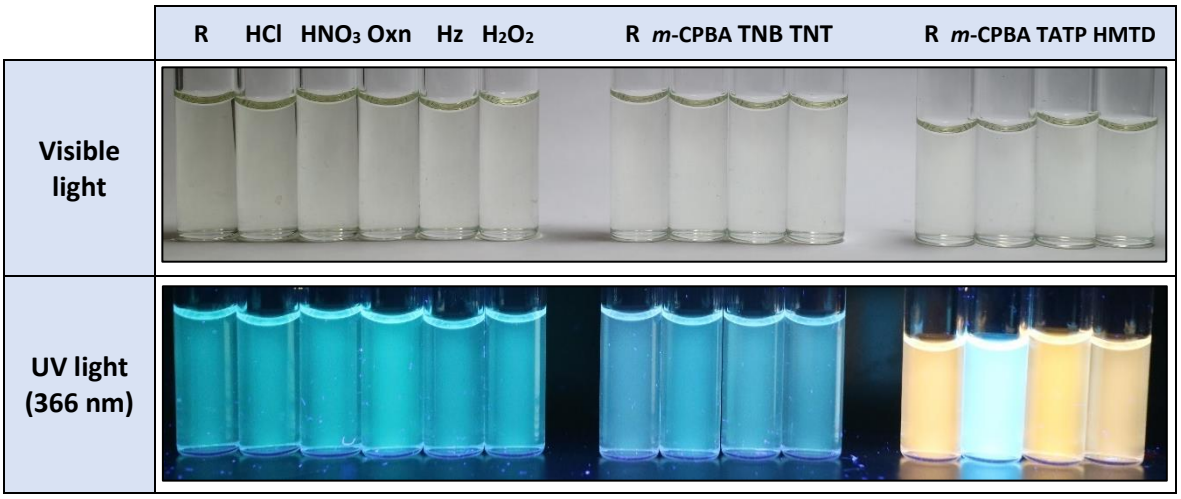

Figure 252. Oxidant and reductant reagents test of AR83p under visible (up) and UV (down) light.

The most important change was the change in fluorescence colour from orange to blue against *m*-CPBA.

Synthesis of *N*-(piperidin-4-yl)-4-[2(4-piperazin-1-yl)pyridin-5-yl]naphthalene-1,8-dicarboxyl-monoimide (AR83d)

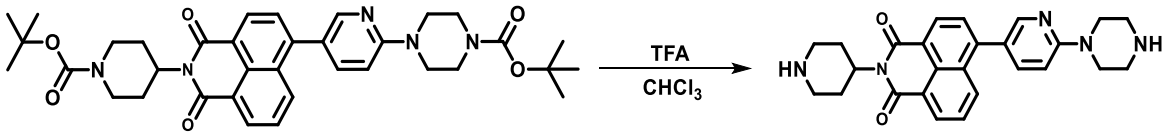

150 mg of *N*-(*N*-Boc-piperidin-4-yl)-4-[2-(4-Boc-piperazin-1-yl)pyridin-5-yl]naphthalene-1,8-dicarbo xylmonoimide (AR83p, 0.23 mmol) were dissolved in 15 ml of chloroform and, then, 2 ml of trifluoroacetic acid (26 mmol) was added. The mixture was stirred 4 hours at room temperature. Afterwards, 10 ml of water were poured into the flask and the mixture was neutralized employing a 40% sodium hidroxide solution until it reached a neutral pH. Then, 20 ml of water were added into the flask and the mixture was extracted three times with chloroform (3×30 ml). The organic extracts were combined, dried over anhidrous Na_2SO_4 and the solvent was evaporated under reduce pressure, to obtain 100 mg of a yellow solid, 99% yield.

m.p.: 274-277°C.

IR (ATR, cm^{-1}): 3236 (N-H), 2925 – 2737, 1693 (C=O), 1650 (C=O), 1579, 1495, 1348, 1235, 1151 (C-N), 1105, 782, 755, 459.

^{1}H-NMR (300 MHz, $CDCl_3$) δ (ppm): 8.60 (d, *J* = 7.6 Hz, 2H, 2×**H$_{Ar}$**), 8.34 – 8.29 (m, 2H, 2×**H$_{Ar}$**), 7.73 – 7.63 (m, 3H, 3×**H$_{Ar}$**), 6.81 (d, *J* = 8.8 Hz, 1H, **H$_{Ar}$**), 5.25 – 5.16 (m, 1H, C**H**), 3.65 (m, 4H, 2×C**H**$_2$), 3.27 (m, 2H, C**H**$_2$), 3.04 (m, 4H, 2×C**H**$_2$), 2.86 – 2.65 (m, 4H, 2×C**H**$_2$), 2.01 (s, 2H, 2×N**H**), 1.72 (m, 2H, C**H**$_2$).

^{13}C-NMR (75MHz, $CDCl_3$) δ (ppm): 164.7 (**C**=O), 164.6 (**C**=O), 159.4 (**C**$_{Ar}$), 148.8 (**C**$_{Ar}$H), 143.9 (**C**$_{Ar}$), 138.9 (**C**$_{Ar}$H), 132.2 (**C**$_{Ar}$H), 131.3 (**C**$_{Ar}$H), 131.1 (**C**$_{Ar}$H), 130.1 (**C**$_{Ar}$), 129.0 (**C**$_{Ar}$), 127.7 (**C**$_{Ar}$H), 126.9 (**C**$_{Ar}$H), 123.6 (**C**$_{Ar}$), 123.5 (**C**$_{Ar}$), 121.9 (**C**$_{Ar}$), 106.5 (**C**$_{Ar}$H), 52.1 (**C**H), 47.0 (**C**H$_2$), 46.3 (**C**H$_2$), 46.1 (**C**H$_2$), 30.2 (**C**H$_2$).

HRMS (MALDI, DCTB+) m/z: calculated for $C_{26}H_{27}N_5O_2$: 442.2238 (M^+ + H); found 442.2233.

UV-Vis ($CHCl_3$), λ_{max} nm (log ε): 350 (3.3).

Ø (MeOH, %): <3.

τ (350 nm, MeOH, ns): 1.991/4.406 (χ^2: 1.116).

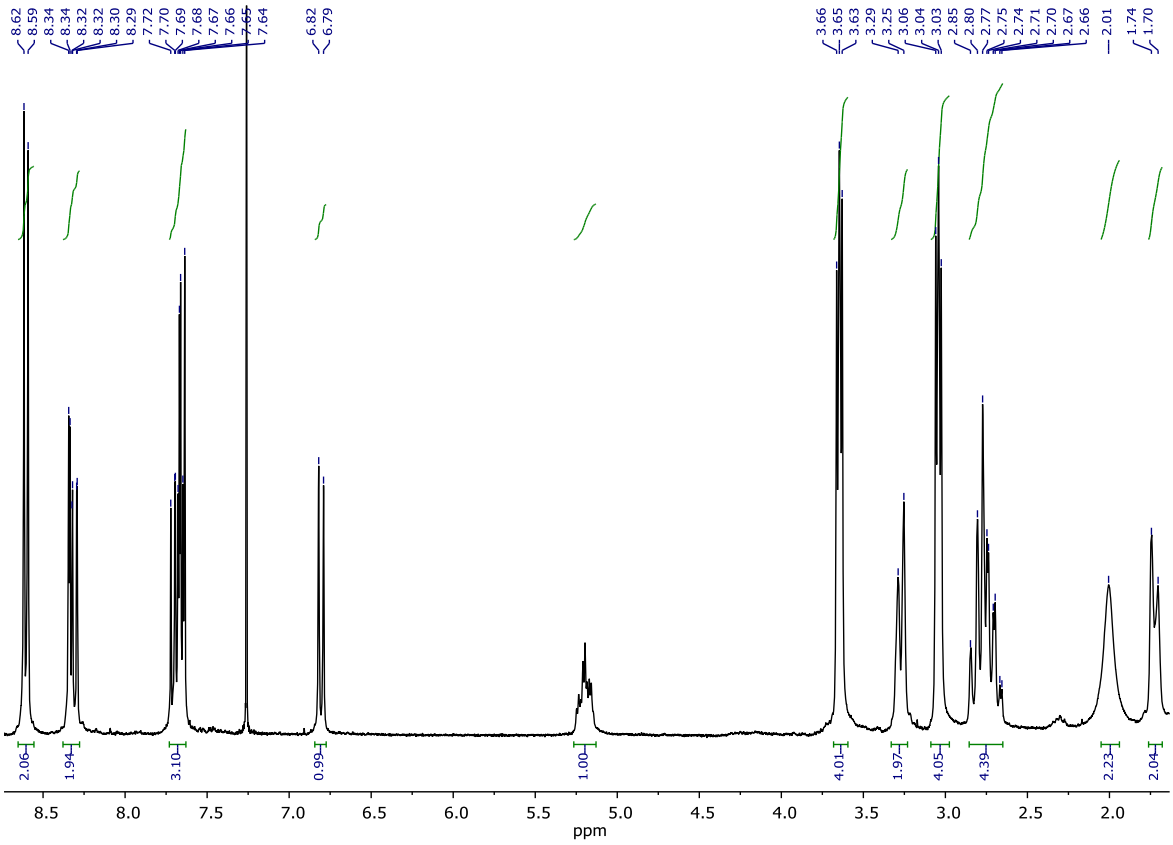

Figure 253. ^{1}H-NMR ($CDCl_3$, 300 MHz) of AR83d.

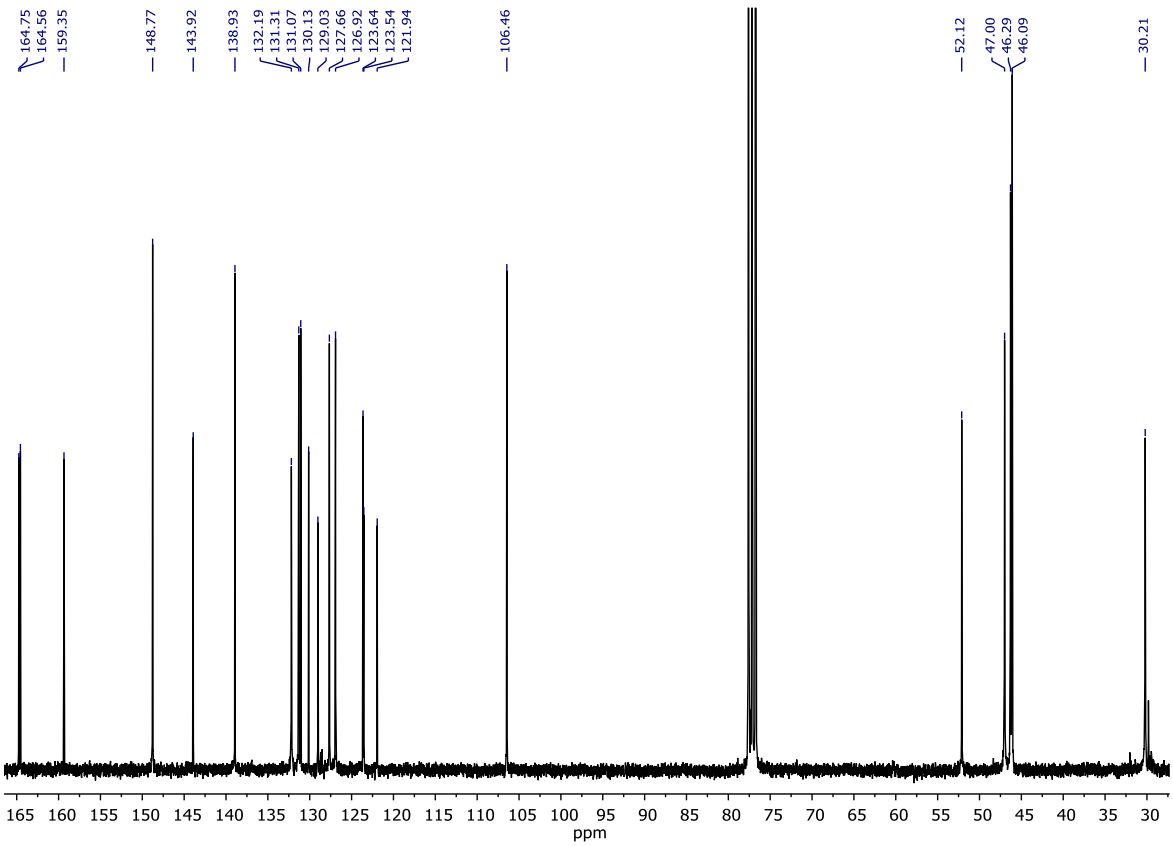

Figure 254. ^{13}C-NMR ($CDCl_3$, 75 MHz) of AR83d.

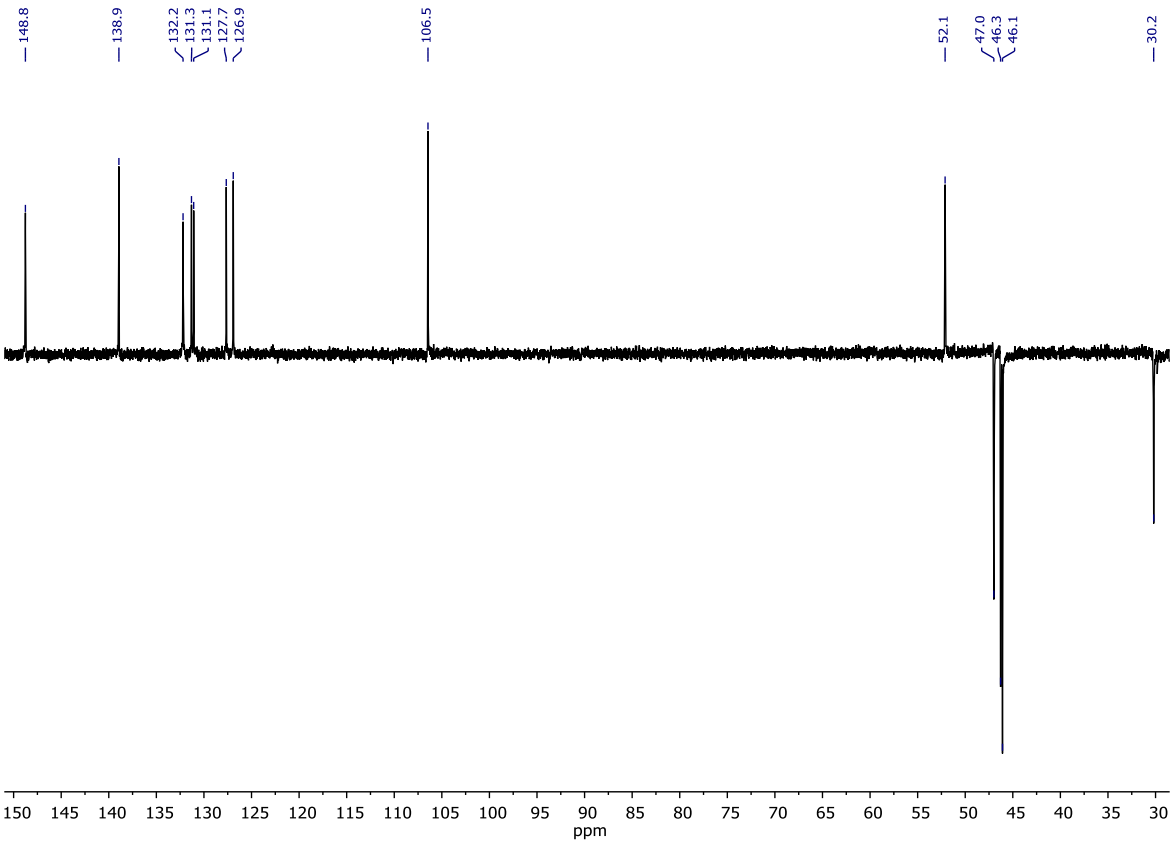

Figure 255. DEPT NMR ($CDCl_3$, 75 MHz) of AR83d.

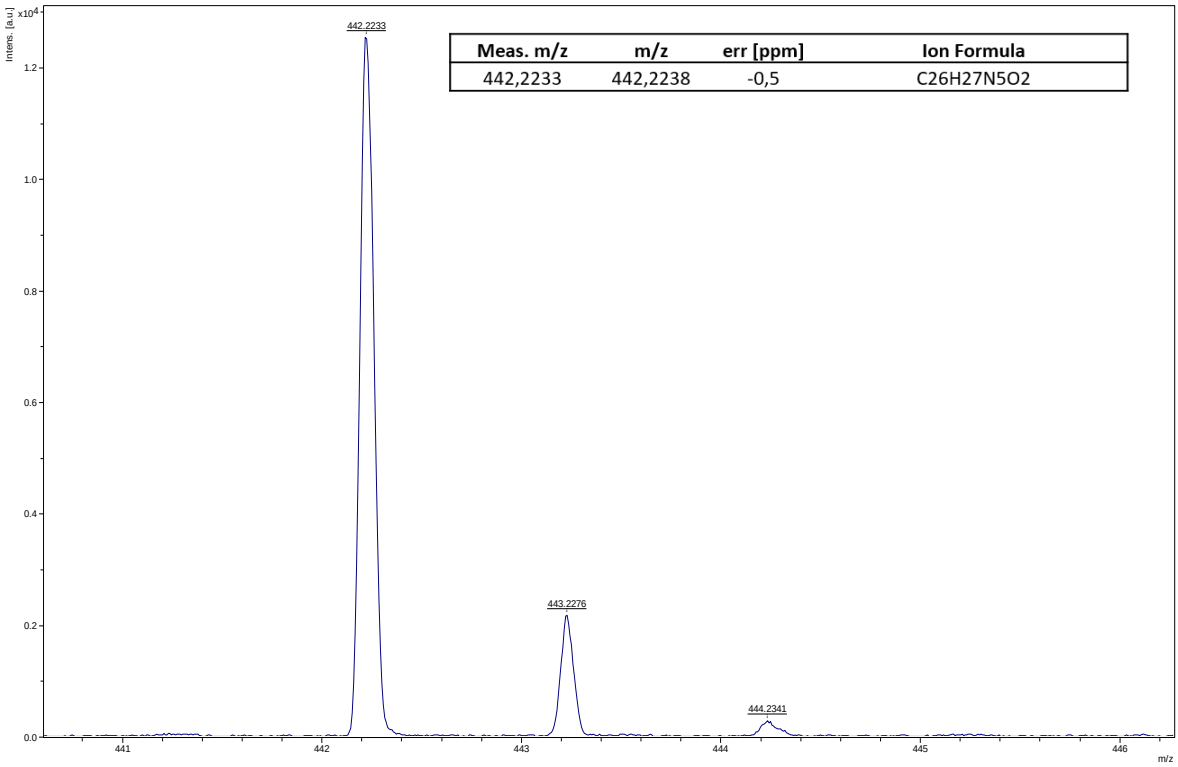

Meas. m/z	m/z	err [ppm]	Ion Formula
442,2233	442,2238	-0,5	C26H27N5O2

Figure 256. HRMS (MALDI, DCTB+) of AR83d.

Solvatochromism:

The concentration of the compound was 20 µM and the excitation wavelength was 350 nm.

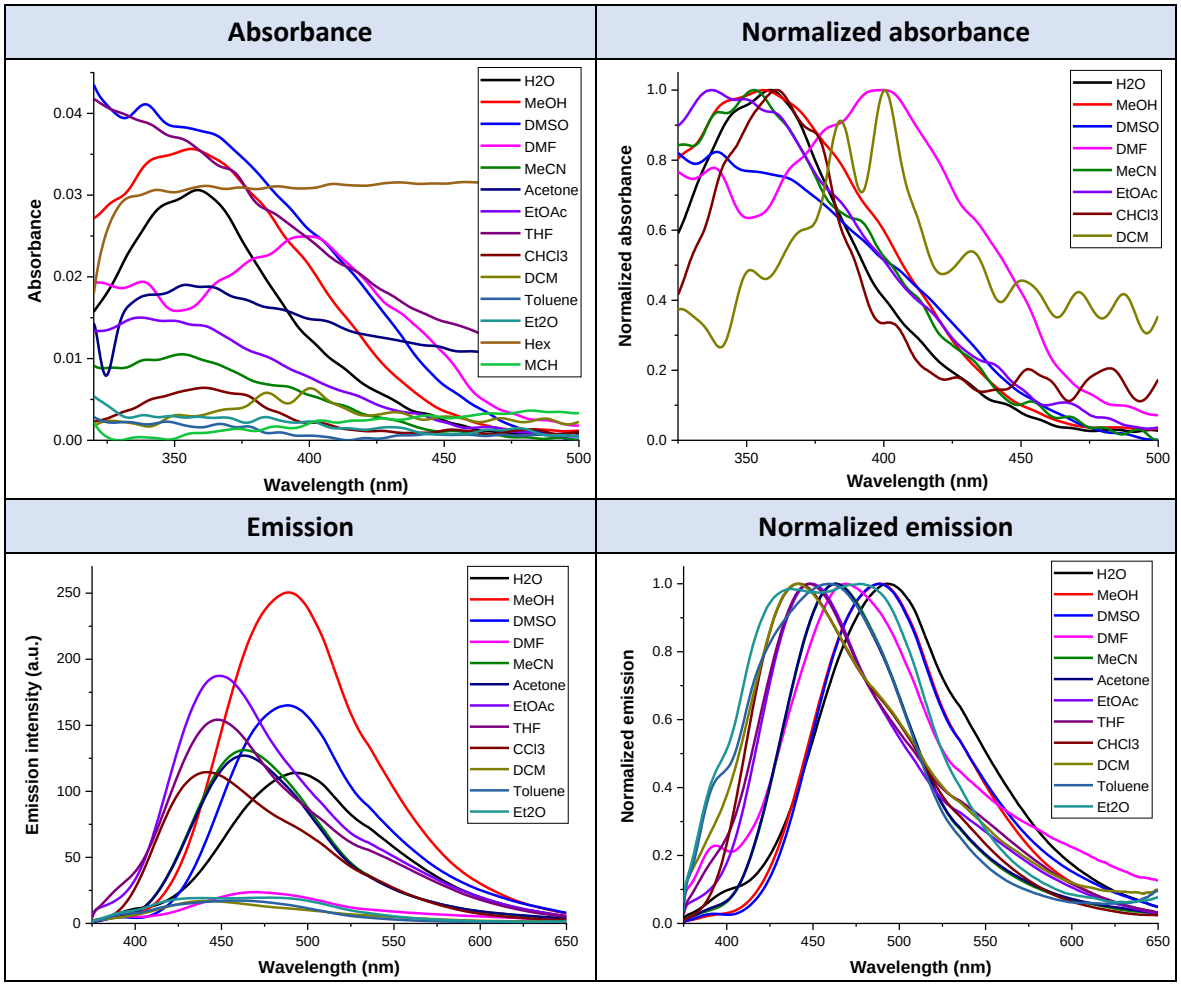

Figure 257. Solvatochromism of AR83d.

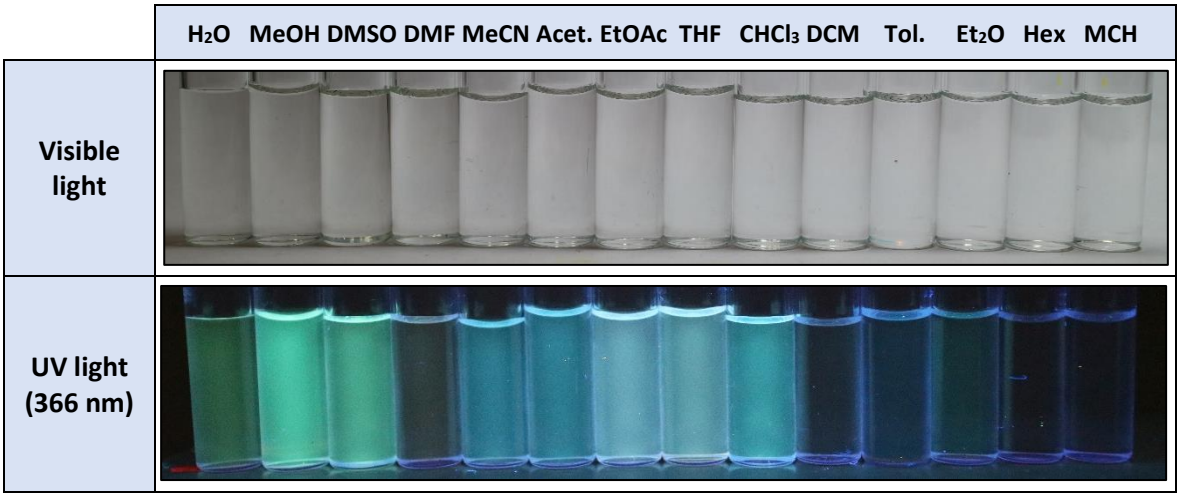

Figure 258. Solvatochromism of AR83d under visible and 366 nm light.

Fluorescence decay lifetime (τ):

The solvent used was MeOH and the concentration of the compound was 20 µM.

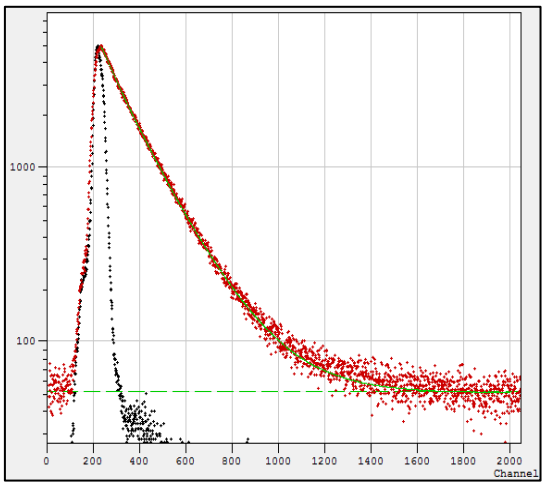

Figure 259. Fluorescence decay lifetime of AR83d.

Water acceptance test:

The solvent used was MeOH and the concentration of the compound was 20 µM.

	R	5%	10%	20%	30%	40%	50%	60%	70%	80%	90%
Visible light											
UV light (366 nm)	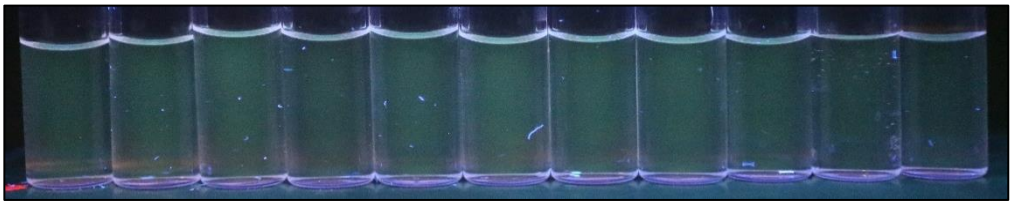										

Figure 260. Water acceptance test of AR83d under visible (up) and UV (down) light.

The fluorescent emission was quenched as the amount of water was increased (ACQ).

pH test:

The amount of water for the performance of this test was 90%. The concentration of the compound was 20 µM and the solvent used was MeOH.

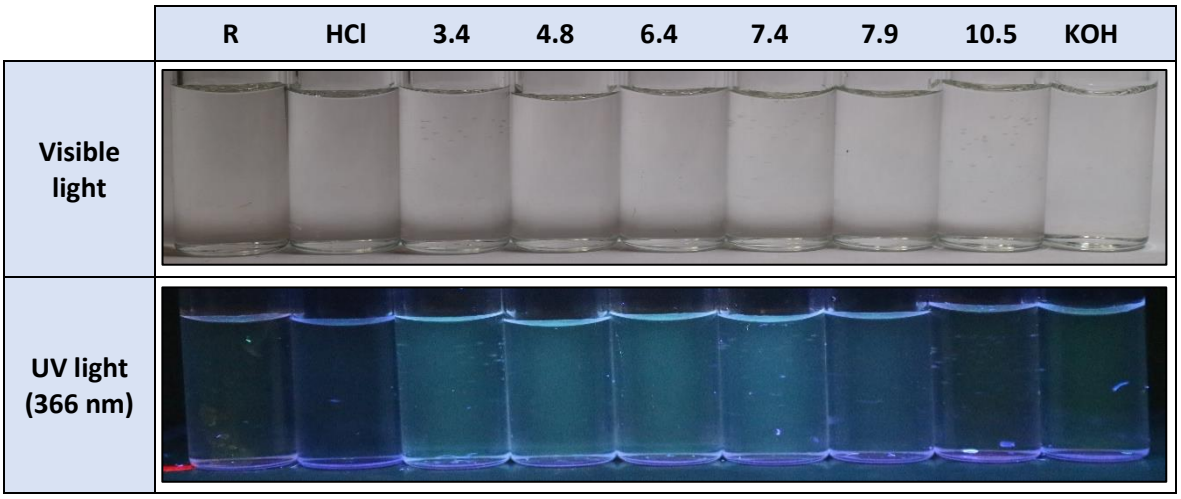

Figure 261. pH test of AR83d under visible (up) and UV (down) light.

There was a slight increase in the fluorescence intensity at intermediate pHs.

Cations and anions test:

The concentration of the compound was 20 µM and the solvent used was a mixture of MeOH and water (90%).

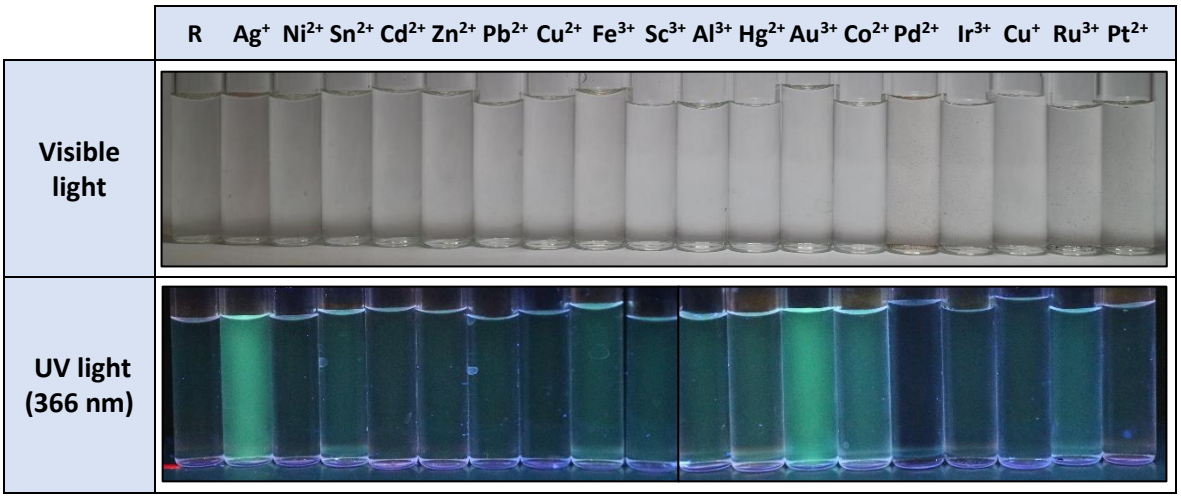

Figure 262. Cations test of AR83d under visible (up) and UV (down) light.

The most significant changes under UV light were the increase in the fluorescence emission when the probe was exposed to Ag^{+} and Au^{3+}.

The concentration of the compound was 20 µM and the solvent used was a mixture of MeOH and water (90%).

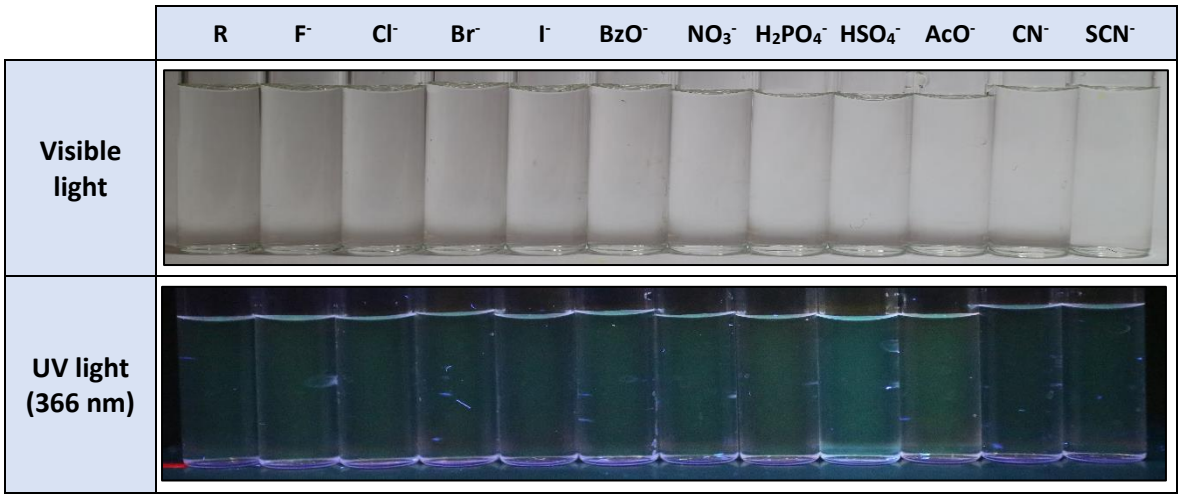

Figure 263. Anions test of AR83d under visible (up) and UV (down) light.

No significant changes were observed.

Oxidant and reductant reagents test:

The solvent used was a mixture of MeOH and water (90%) and concentration of the compound was 20 µM.

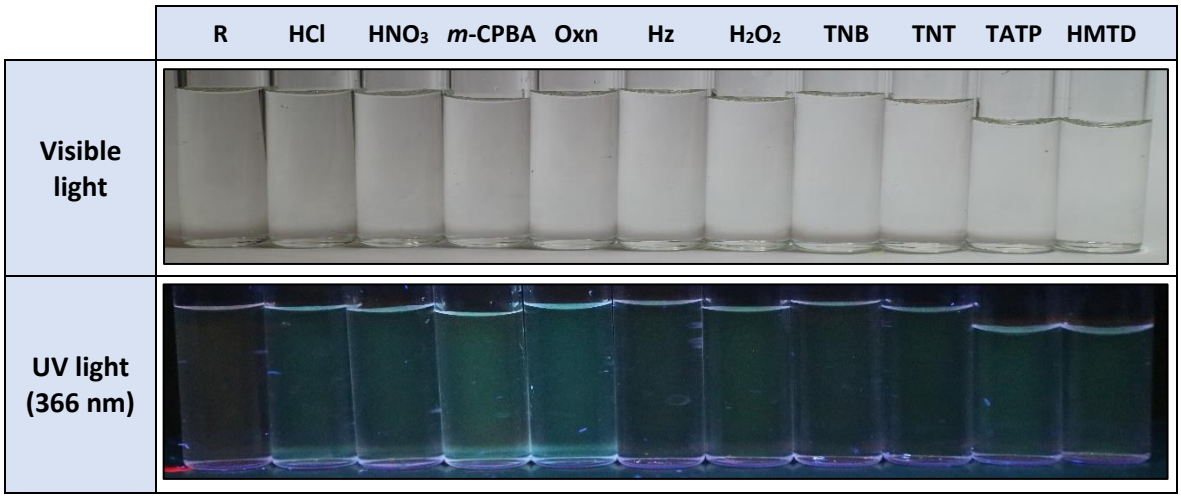

Figure 264. Oxidant and reductant reagents test of AR83d under visible (up) and UV (down) light.

No significant changes was observed.

Previous solvents test:

In order to determine the fluorescence variation of the compound under study in the presence of TATP, some test were carried out for the probe in 9 different solvents. The AR83d concentration was 25 µM and the TATP was added in excess (7 mg in each vial). All the test were performed at room temperature and the photographs were taken immediately after the addition of TATP and again after 24 hours.

The biggest fluorescence changes were seen in DMF, MeCN, $CHCl_3$:MeOH (9:1) and DCM:MeOH (9:1).

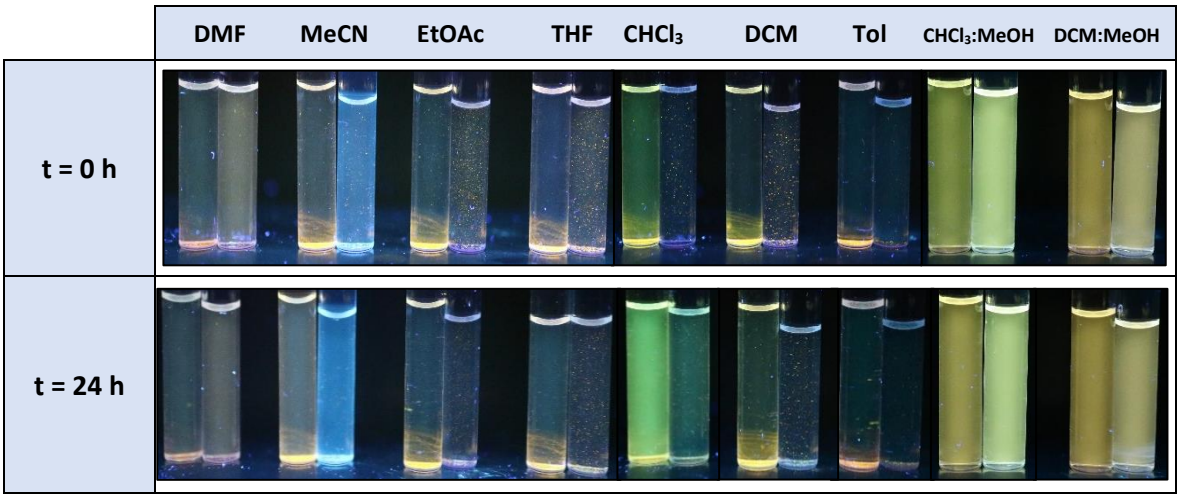

Figure 265. Pairs of AR83d (left) and AR83d with excess of TATP (right) in different solvents at time 0 h (up) and 24 h (down).

Solvents test with TATP:

For all solvents, the working concentration of AR83d was 2.5 µM, the excitation wavelength was 350 nm and the temperature for all test was 25ºC. In the kinetic studies, TATP was in excess (20 mM) and the fluorescence emission measurements were made during 40 minutes, at 5 minutes time intervals. In the titration, the TATP concentration was between 0 and 35000 µM and it was added directly as solid. The measurements were recorded after the adittion of the probe.

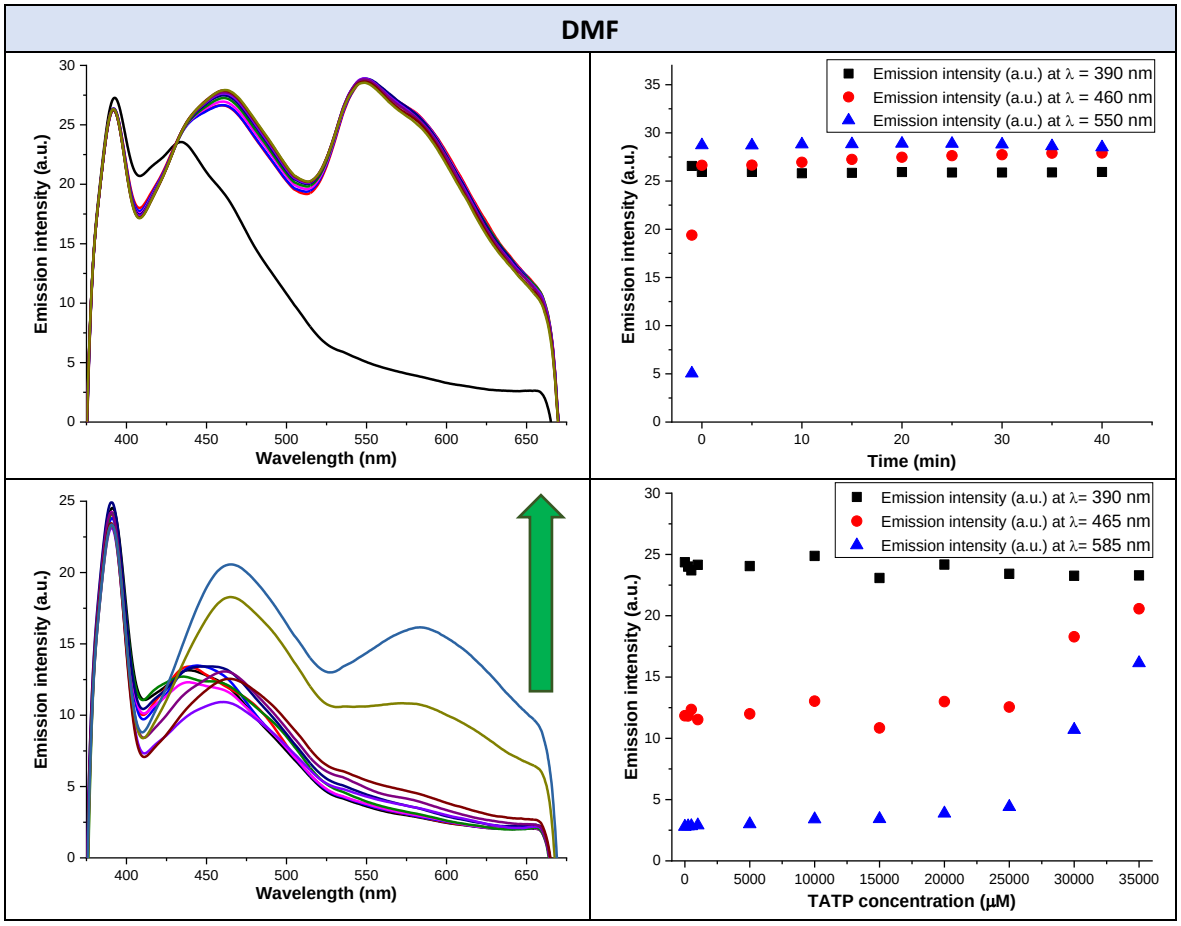

Figure 266. Study of AR83d with TATP in DMF. Kinetic study (up left) and profile as function as time at 390 nm, 460 nm and 550 nm simultaneously (up right) in presence of TATP excess. Titration (down left) and fluorescence profile at 390 nm, 465 nm and 585 nm simultaneusly (down right) under increasing concentrations of TATP.

There was a increase change in the emission intensity band immediately after adding TATP. The LOD of TATP was somewhere between 25000 and 30000 µM with the emergence of a new maximum peak.

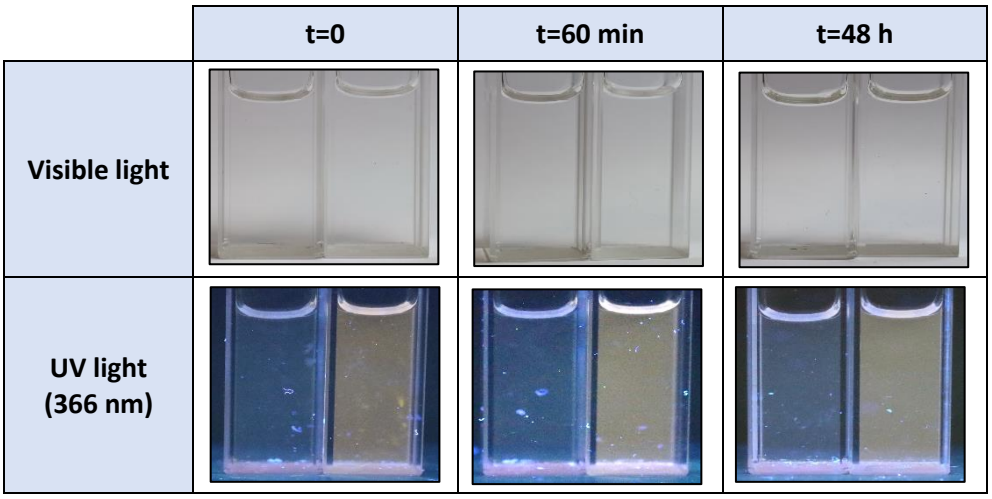

Figure 267. Kinetic study at different times under visible (up) and UV (down) light in DMF. In each photo, left vial was contained the probe and right vial was contained the probe and an excess of TATP.

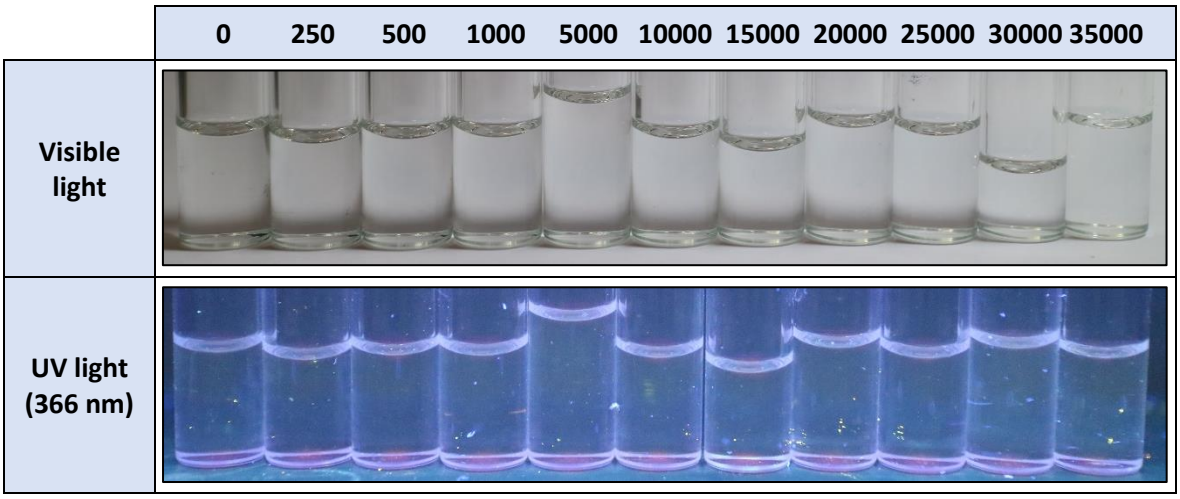

Figure 268. Titration of AR83d with an excess of TATP under visible (up) and UV (down) light in DCM.

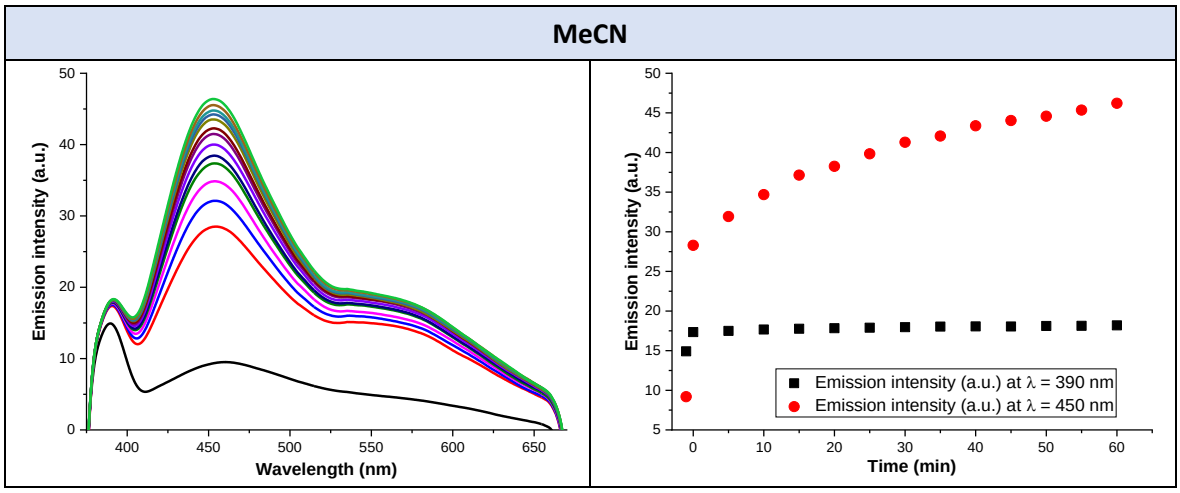

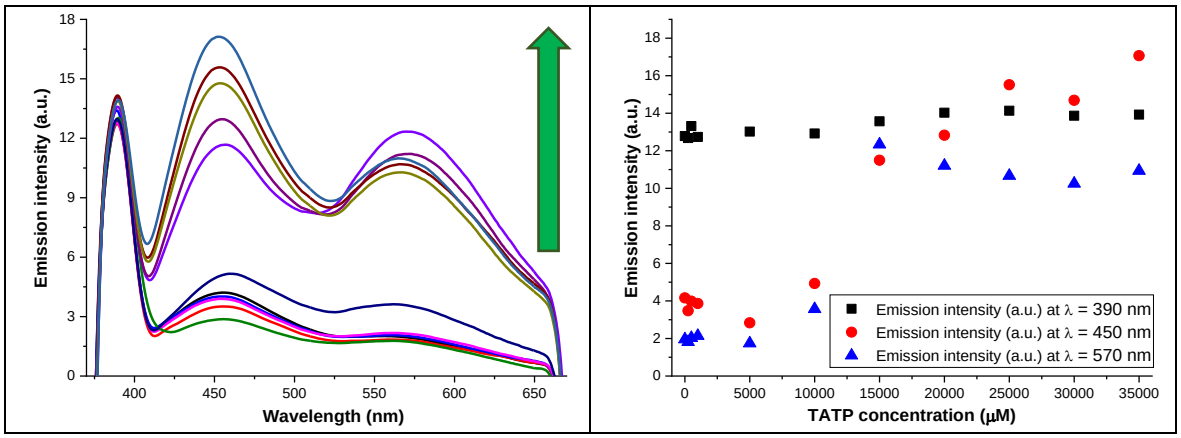

Figure 269. Study of AR83d with TATP in MeCN. Kinetic study (up left) and profile as function as time at 390 nm and 450 nm simultaneously (up right) in presence of TATP excess. Titration (down left) and fluorescence profile at 390 nm, 450 nm and 570 nm simultaneusly (down right) under increasing concentrations of TATP.

There was a increase change in the emission intensity band immediately after adding TATP. According to the spectra, the LOD of TATP was somewhere between 10000 and 15000 µM, a fairly high limit, with the appearance of a new emission peak.

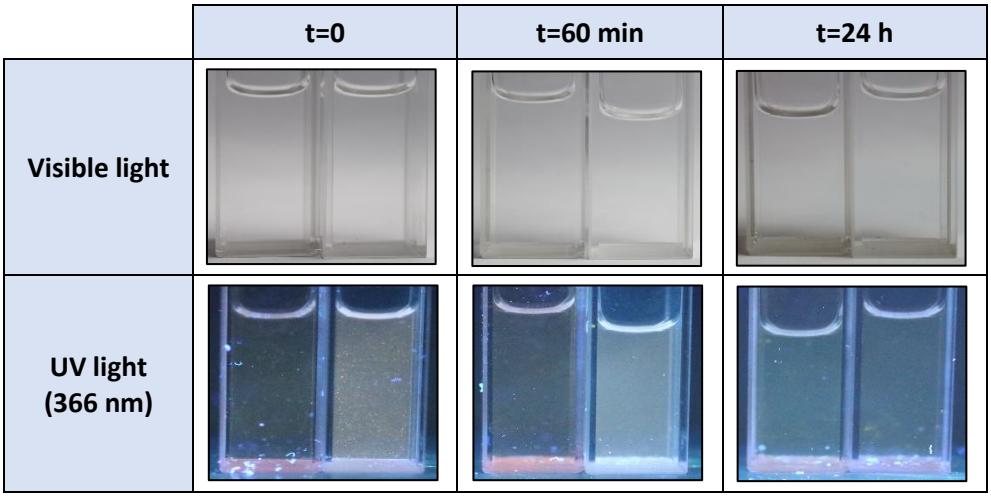

Figure 270. Kinetic study at different times under visible (up) and UV (down) light in MeCN. In each photo, left vial was contained the probe and right vial was contained the probe and an excess of TATP.

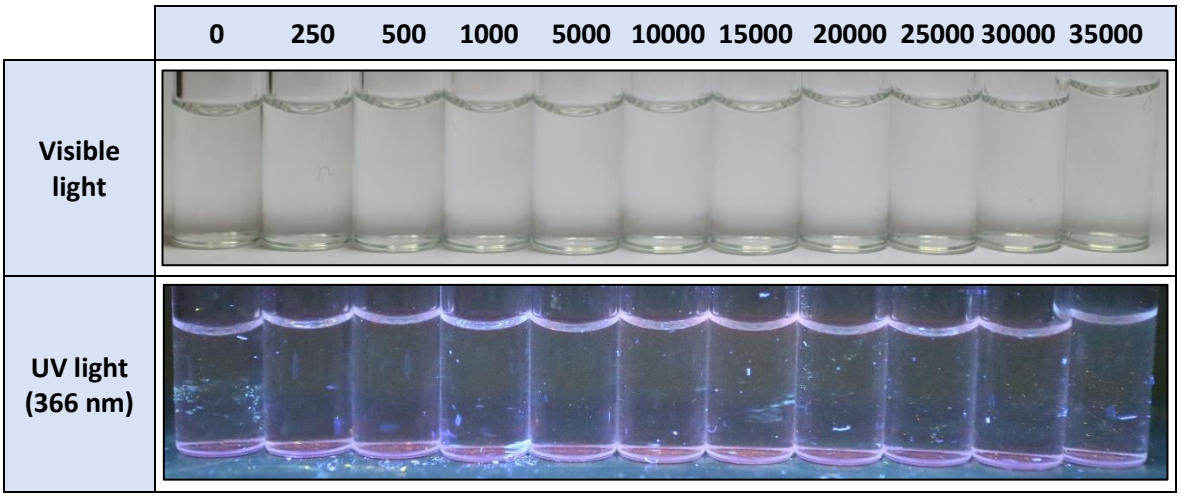

Figure 271. Titration of AR83d with an excess of TATP under visible (up) and UV (down) light in MeCN.

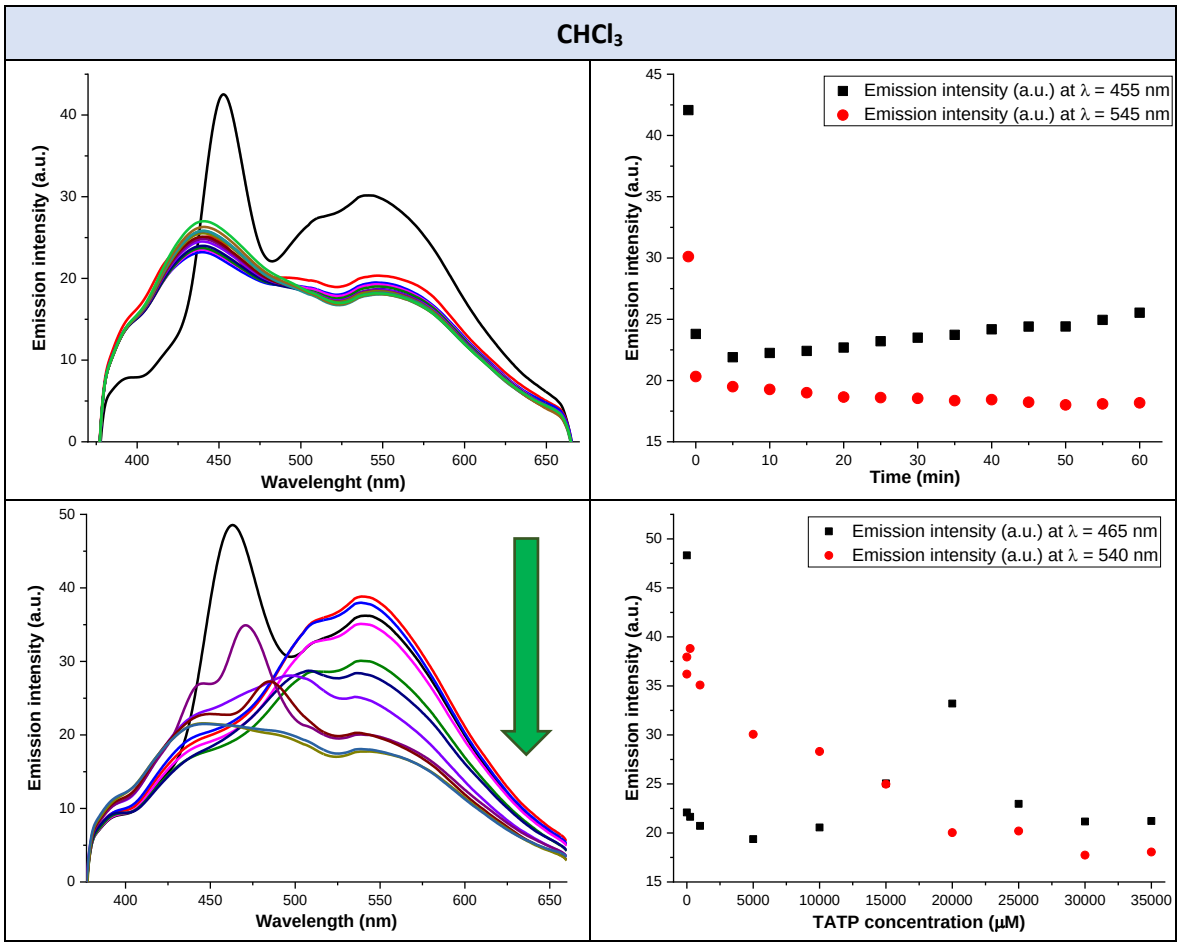

Figure 272. Study of AR83d with TATP in $CHCl_3$. Kinetic study (up left) and profile as function as time at 455 nm and 545 nm simultaneously (up right) in presence of TATP excess. Titration (down left) and fluorescence profile at 465 nm and 540 nm simultaneusly (down right) under increasing concentrations of TATP.

There was a decrease change in the emission intensity band immediately after adding TATP. The LOD of TATP was somewhere between 1000 and 5000 µM with the dissappearance of a maximum emission.

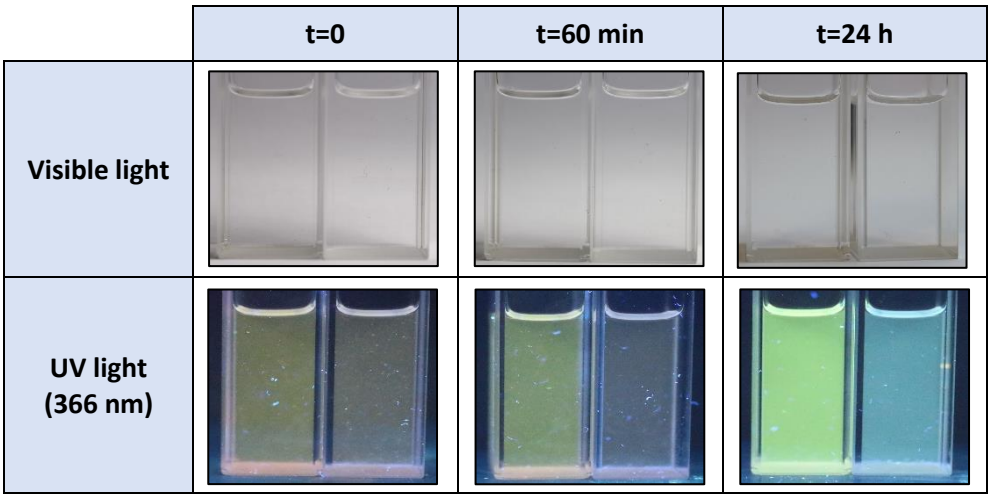

Figure 273. Kinetic study at different times under visible (up) and UV (down) light in $CHCl_3$. In each photo, left vial was contained the probe and right vial was contained the probe and an excess of TATP.

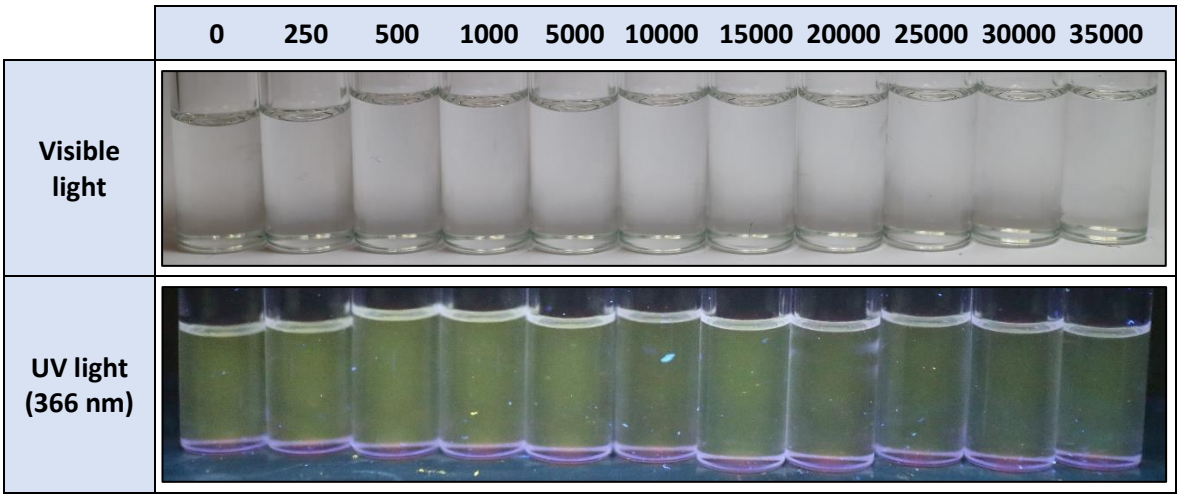

Figure 274. Titration of AR83d with an excess of TATP under visible (up) and UV (down) light in $CHCl_3$.

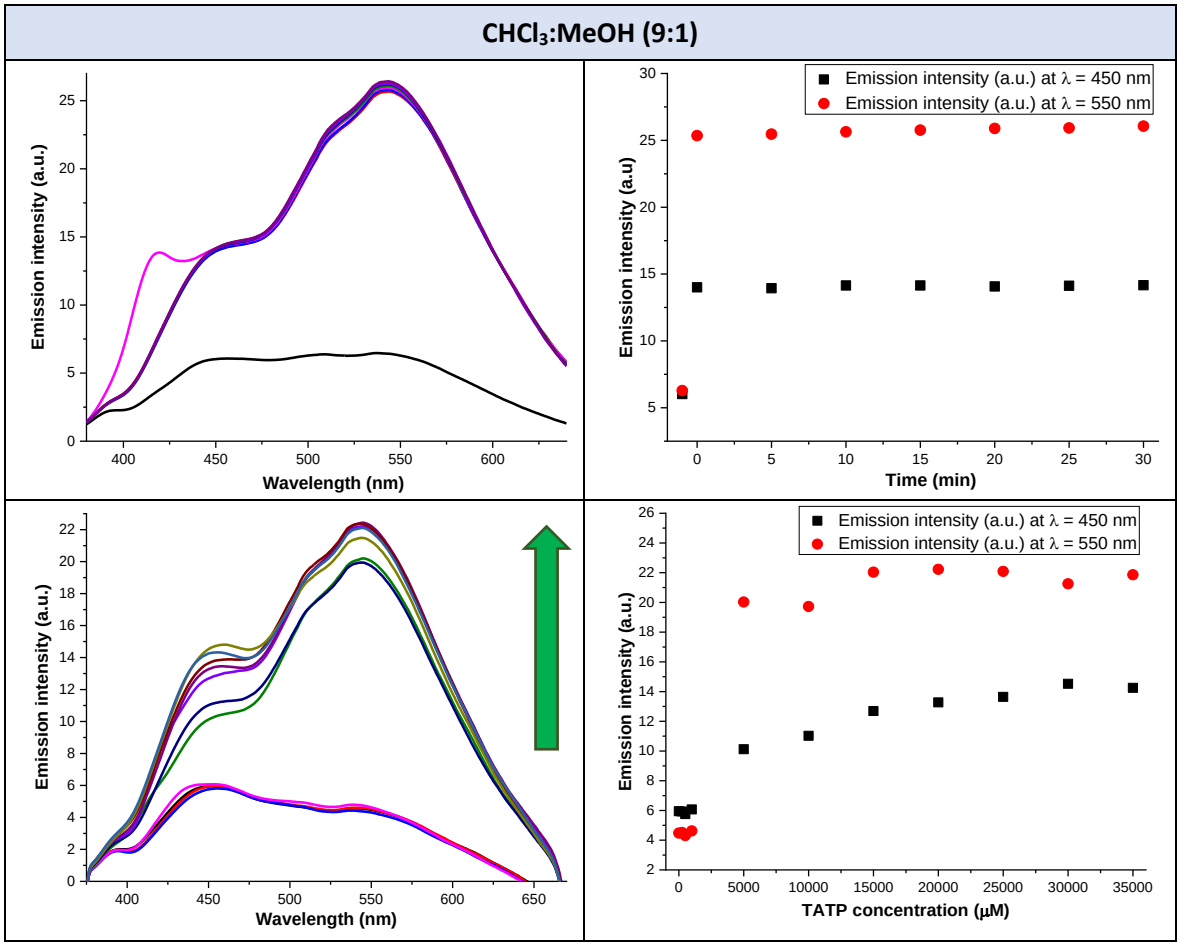

Figure 275. Study of AR83d with TATP in $CHCl_3$:MeOH (9:1). Kinetic study (up left) and profile as function as time at 450 nm and 550 nm simultaneously (up right) in presence of TATP excess. Titration (down left) and fluorescence profile at 450 nm and 550 nm simultaneusly (down right) under increasing concentrations of TATP.

There was a increase change in the emission intensity band immediately after adding TATP. According to the spectra, the LOD of TATP was somewhere between 5000 and 10000 μM.

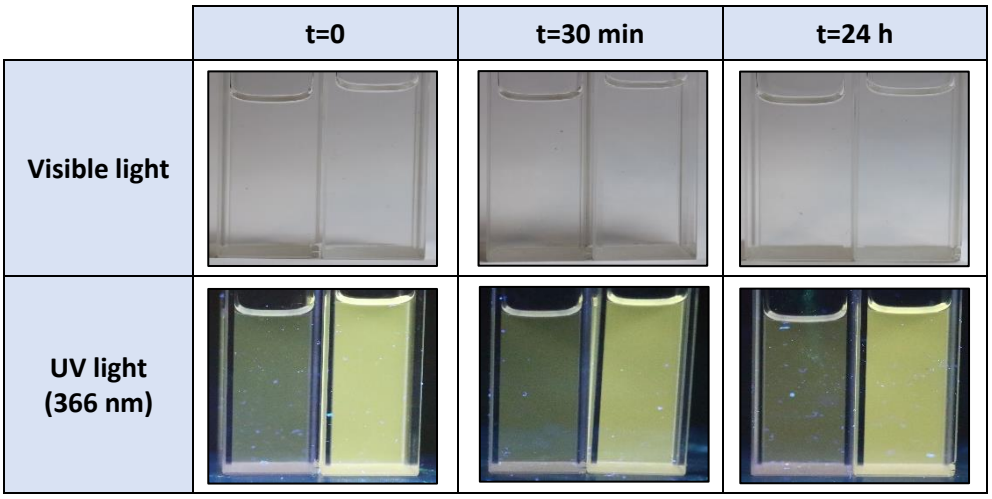

Figure 276. Kinetic study at different times under visible (up) and UV (down) light in $CHCl_3$:MeOH (9:1). In each photo, left vial was contained the probe and right vial was contained the probe and an excess of TATP.

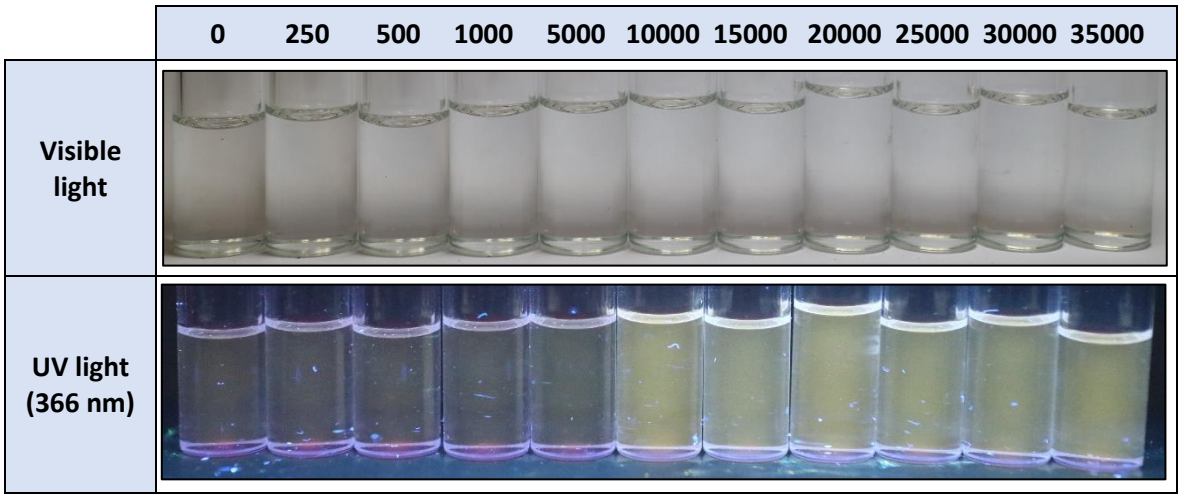

Figure 277. Titration of AR83s with an excess of TATP under visible (up) and UV (down) light in CHCl3:MeOH (9:1).

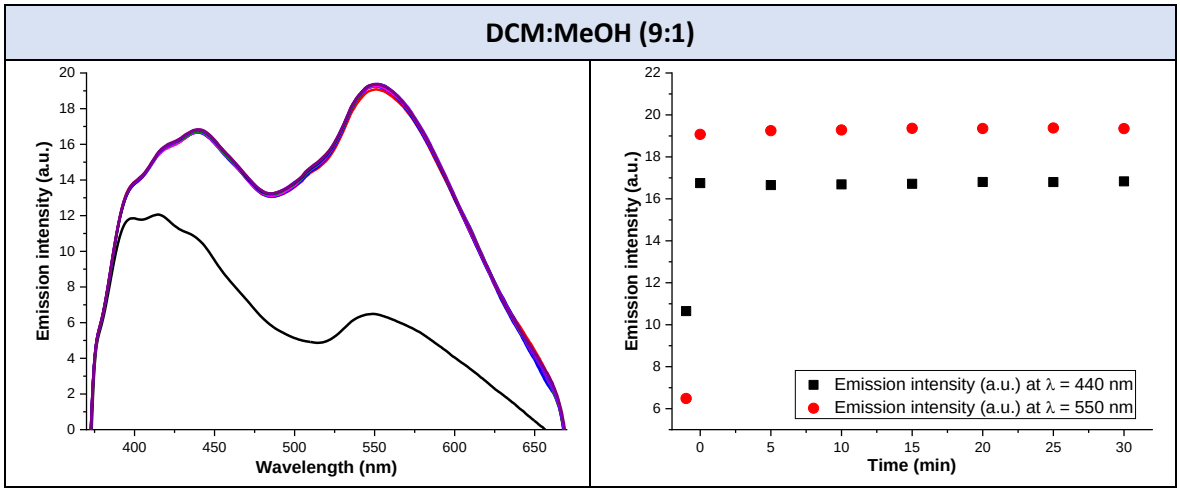

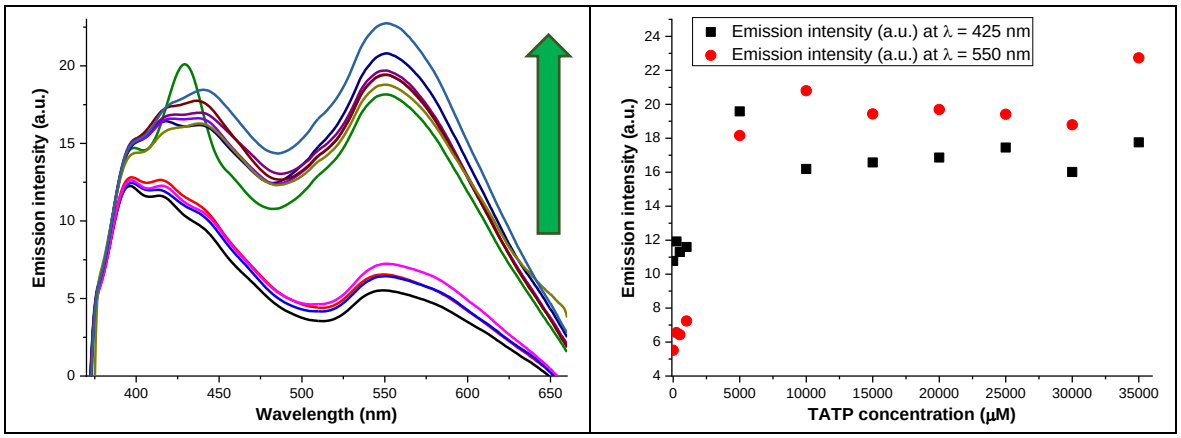

Figure 278. Study of AR83d with TATP in DCM:MeOH (9:1). Kinetic study (up left) and profile as function as time at 450 nm and 550 nm simultaneously (up right) in presence of TATP excess. Titration (down left) and fluorescence profile at 415 nm and 560 nm simultaneusly (down right) under increasing concentrations of TATP.

There was a increase change in the emission intensity band immediately after adding TATP. According to the fluorescence spectra, the LOD of TATP was somewhere between 1000 and 5000 μM.

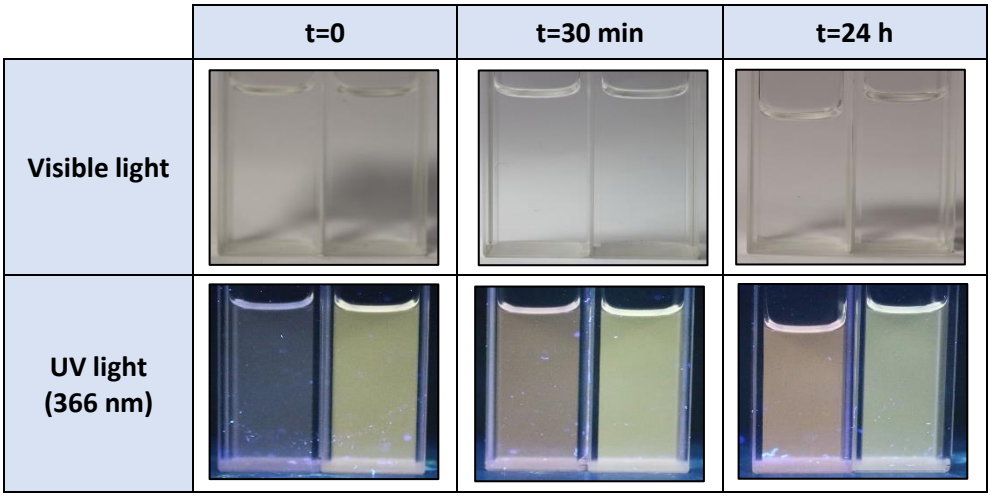

Figure 279. Kinetic study at different times under visible (up) and UV (down) light in DCM:MeOH (9:1). In each photo, left vial was contained the probe and right vial was contained the probe and an excess of TATP.

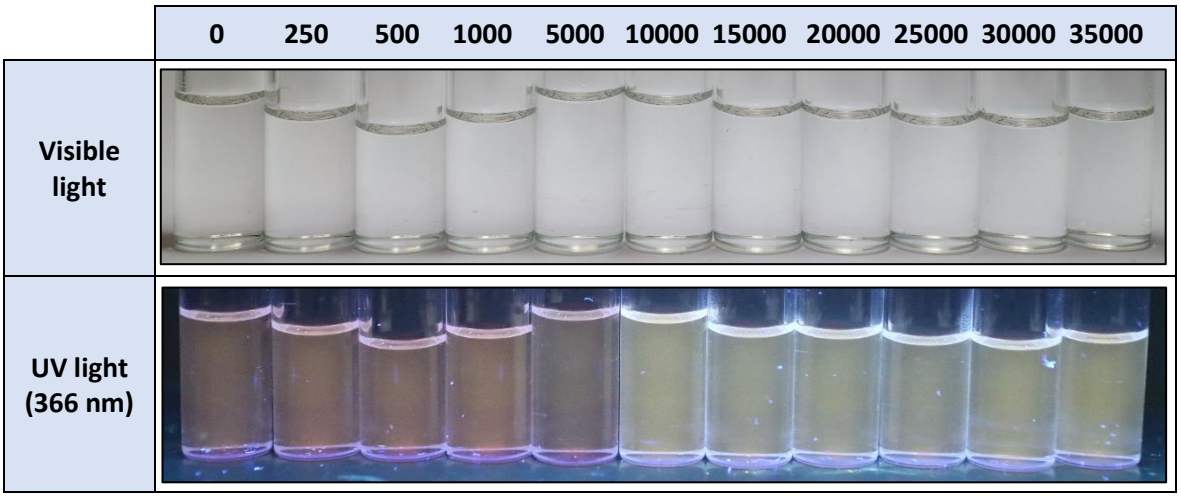

Figure 280. Titration of AR83d with an excess of TATP under visible (up) and UV (down) light in DCM:MeOH (9:1).

Because of the low sensitivity the study was discontinued.

Synthesis of *N*-(*N*-Boc-piperidin-4-yl)-4-[(4-Boc-piperazin-1-yl)phenyl]naphthalene-1,8-dicarboxylmonoimide (AR90p)

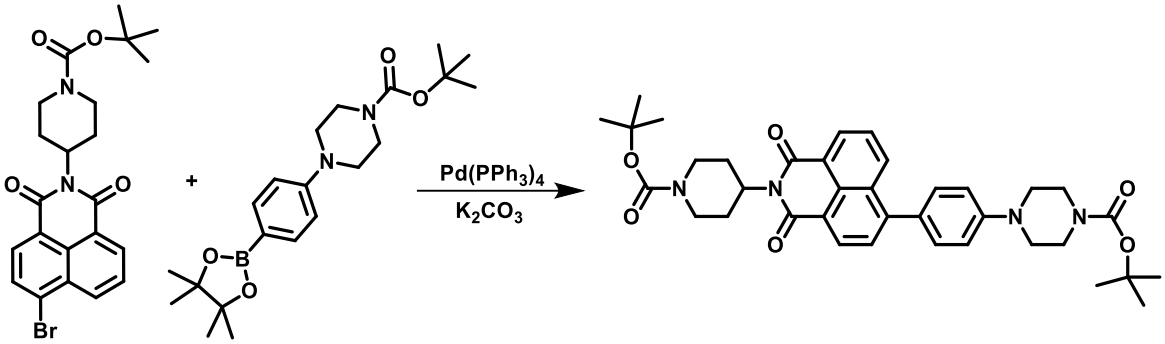

250 mg of *N*-(Boc-piperidine)-4-bromonaphthalene-1,8-dicarboxylmonoimide (AR43p, 0.54 mmol), 220 mg of 2-(4-Boc-piperazine)phenyl-5-boronic acid pinacol ester (0.57 mmol) and 752 mg of potassium carbonate (5.44 mmol) were dissolved in a mixture of toluene:butanol:water (4:1:2 ml) under nitrogen atmosphere and, then, the catalyst, $Pd(PPh_3)_4$ was added. The mixture was stirred overnight at 110°C. Afterwards, the solvent was evaporated under reduce pressure and the solid was dissolved in DCM and washed with water (3×100 ml). The organic extracts were combined, dried over anhidrous Na_2SO_4 and the solvent was evaporated under reduce pressure. The organic solid was purified by column chromatography (SiO_2, DCM:MeOH) getting 242 mg of a yellow solid, 70% yield.

m.p.: 250-252°C.

IR (ATR, cm^{-1}): 3006-2832, 1686 (C=O), 1650 (C=O), 1582, 1507, 1420 (C-O), 1351, 1232, 1159 (C-N), 1124, 1097, 1037, 977, 915, 902, 861, 812, 780, 755, 663, 639, 531, 457.

^{1}H-NMR (300 MHz, $CDCl_3$) δ (ppm): 8.58 (d, *J* = 7.7 Hz, 2H, 2×**H_{Ar}**), 8.32 (d, *J* = 8.5 Hz, 1H, **H_{Ar}**), 7.67 (t, *J* = 8.0 Hz, 2H, 2×**H_{Ar}**), 7.42 (d, *J* = 8.5 Hz, 2H, 2×**H_{Ar}**), 7.07 (d, *J* = 8.5 Hz, 2H, 2×**H_{Ar}**), 5.20 (m, 1H, C**H**), 4.30 (s, 2H, C**H_2**), 3.64 (m, 4H, 2×C**H_2**), 3.27 (m, 4H, 2×C**H_2**), 2.94 – 2.69 (m, 4H, 2×C**H_2**), 1.68 (m, 2H, C**H_2**), 1.49 (s, 18H, 6×C**H_3**).

^{13}C-NMR (75MHz, $CDCl_3$) δ (ppm): 164.8 (**C**=O) , 164.6 (**C**=O), 154.8 (**C**=O), 154.7 (**C**=O), 151.2 (**C_{Ar}**), 146.8 (**C_{Ar}**), 132.8 (**C_{Ar}**H), 131.2 (**C_{Ar}**), 131.1 (**C_{Ar}**), 131.0 (**C_{Ar}**H), 130.1 (**C_{Ar}**), 129.0 (**C_{Ar}**), 127.7 (**C_{Ar}**H), 126.8 (**C_{Ar}**H), 123.3 (**C_{Ar}**), 121.5 (**C_{Ar}**), 116.1 (**C_{Ar}**H), 80.2 (**Cq**), 79.6 (**Cq**), 51.9 (**C**H), 48.9 (**C**H_2), 43.8 (**C**H_2), 28.6 (**C**H_3), 28.5 (**C**H_3), 28.4 (**C**H_2).

HRMS (MALDI, DIT-) m/z: calculated for $C_{37}H_{44}N_4O_6$: 640.3255 (M^-); found 640.3261.

Ø (MCH, %): 93.19.

τ (375 nm, MCH, ns): 3.542 (χ^2: 0.975).

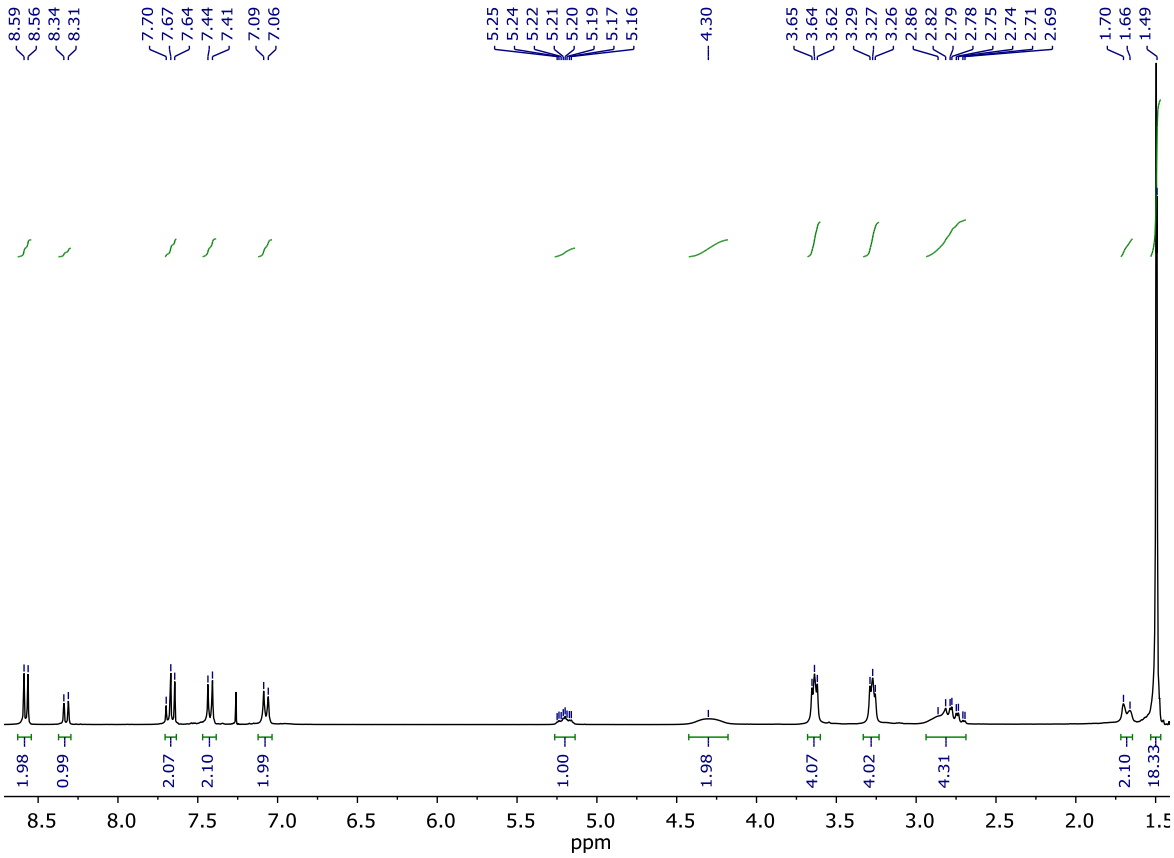

Figure 281. ^{1}H-NMR ($CDCl_3$, 300 MHz) of AR90p.

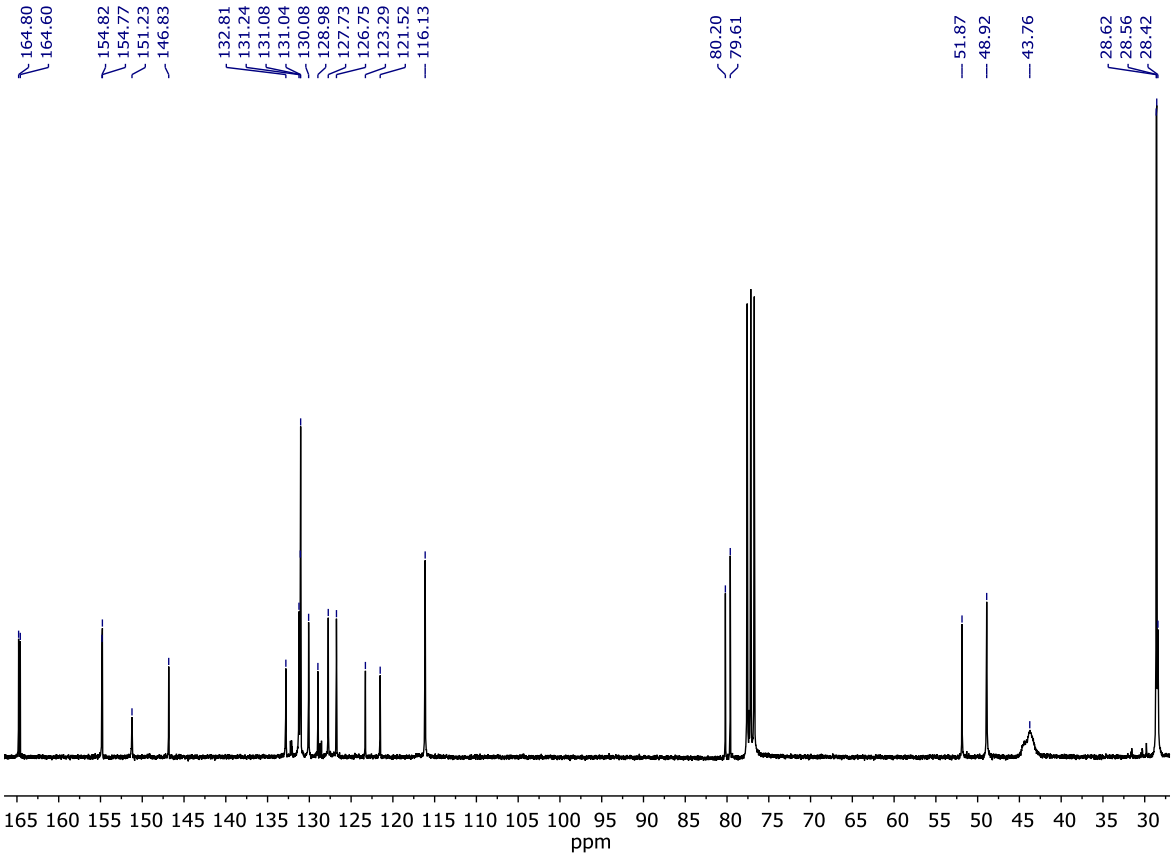

Figure 282. ^{13}C-NMR ($CDCl_3$, 75 MHz) of AR90p.

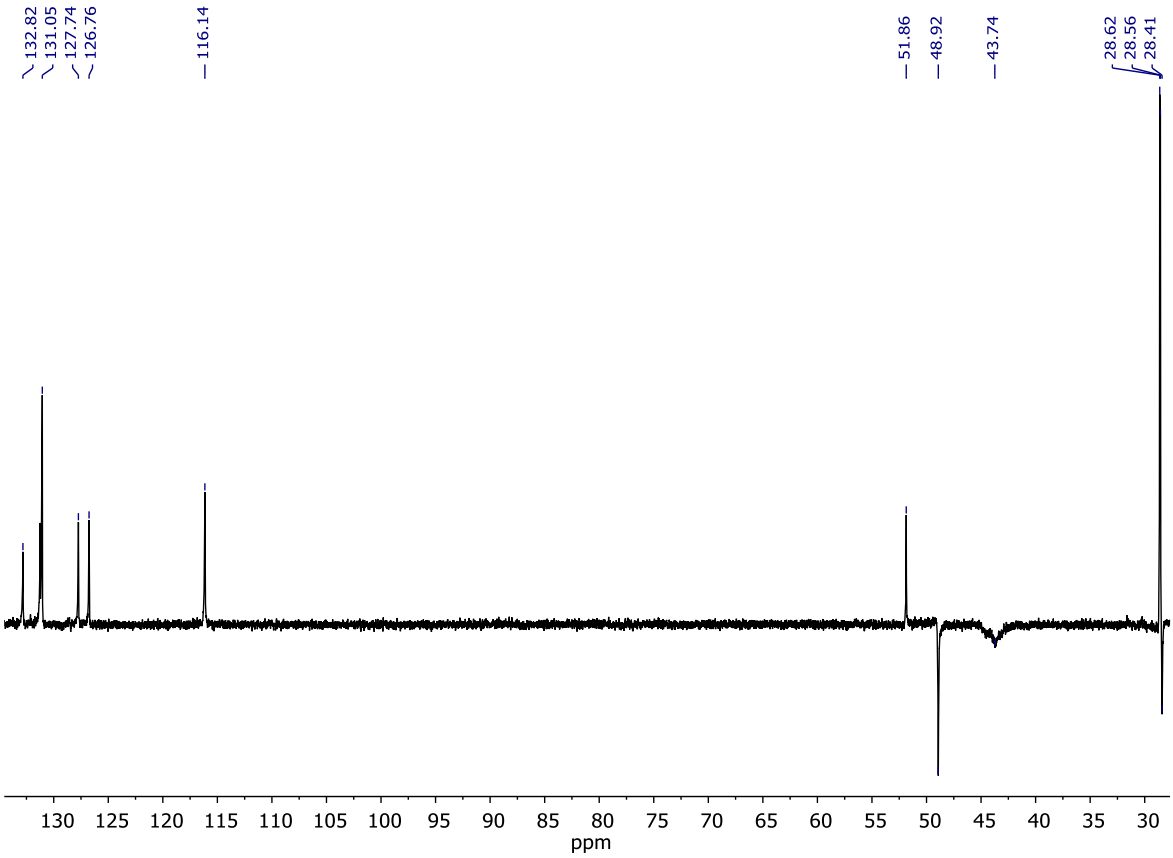

Figure 283. DEPT NMR ($CDCl_3$, 75 MHz) of AR90p.

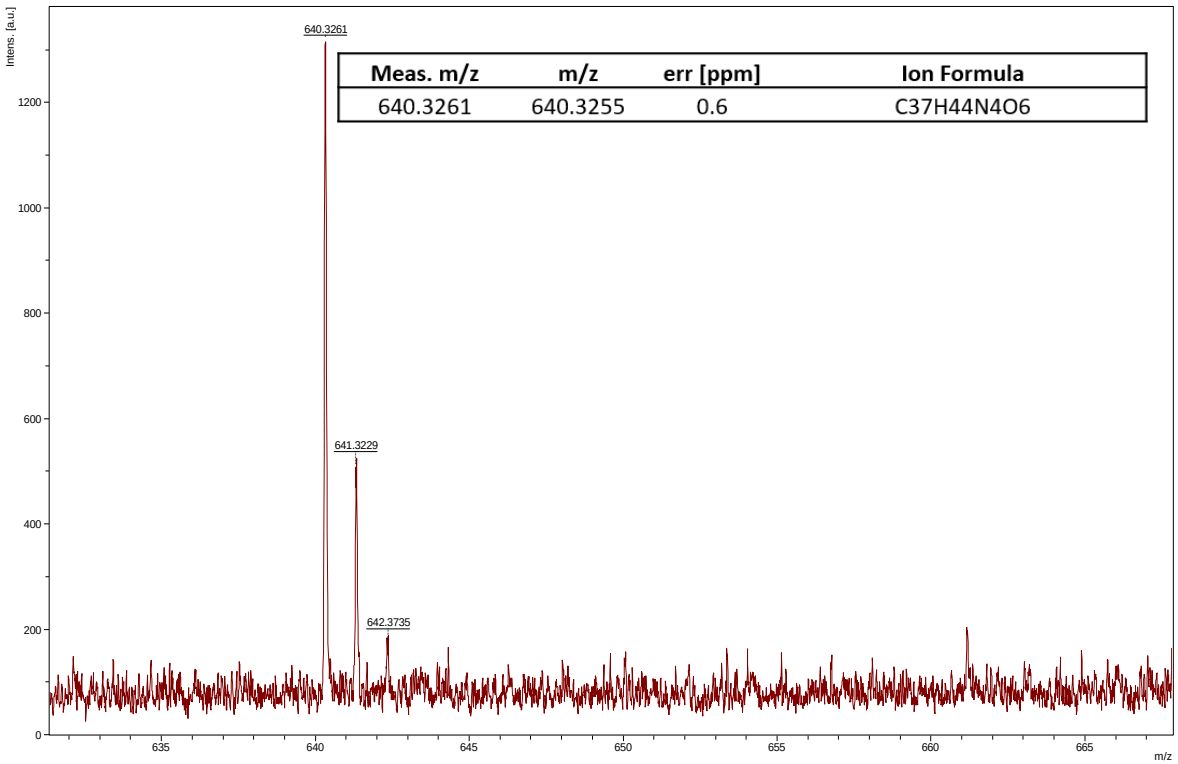

Meas. m/z	m/z	err [ppm]	Ion Formula
640.3261	640.3255	0.6	C37H44N4O6

Figure 285. HRMS (MALDI, DIT-) of AR90p.

Solvatochromism:

The concentration of the compound was 20 µM and the excitation wavelength was 380 nm.

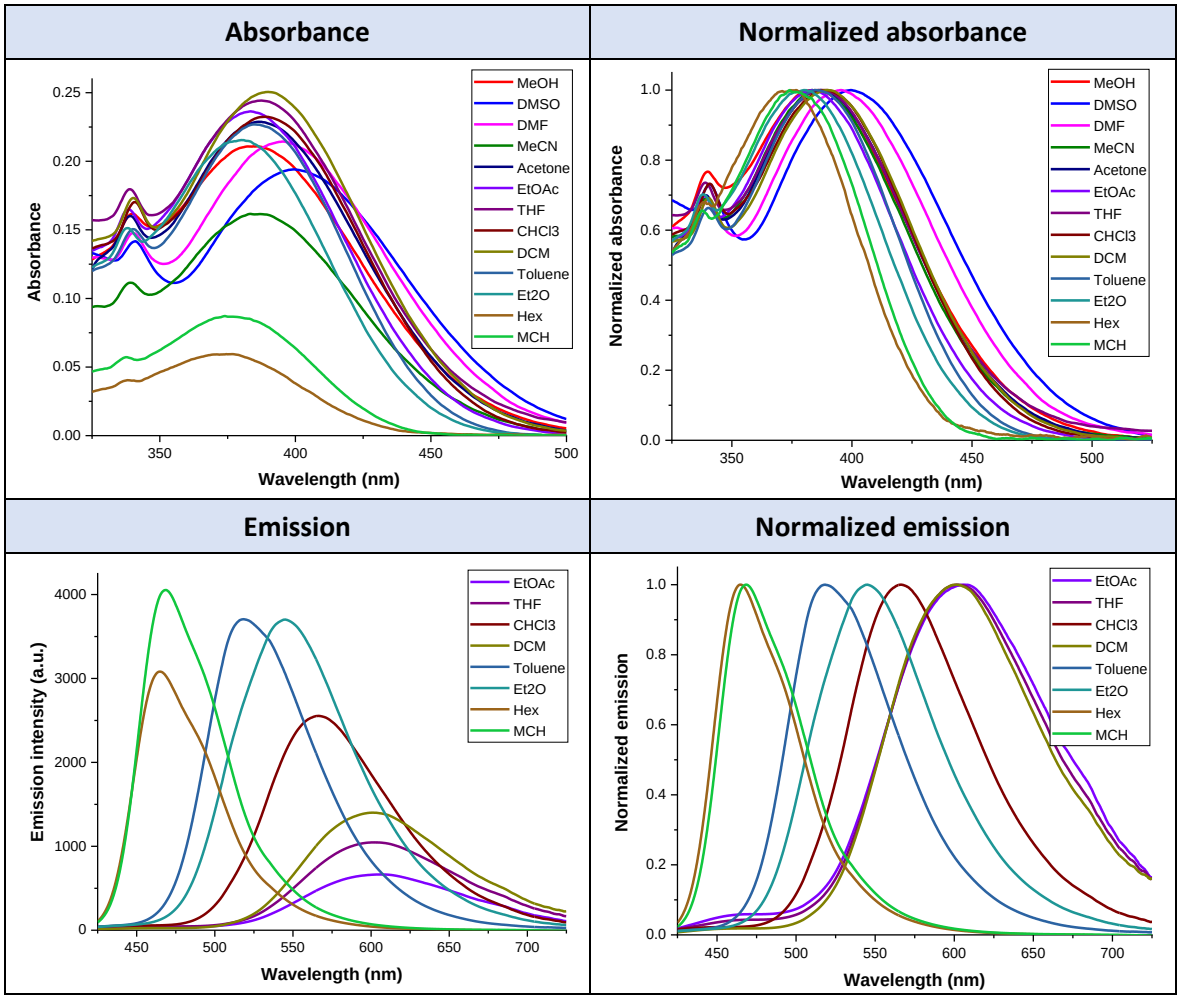

Figure 286. Solvatochromism of AR90p.

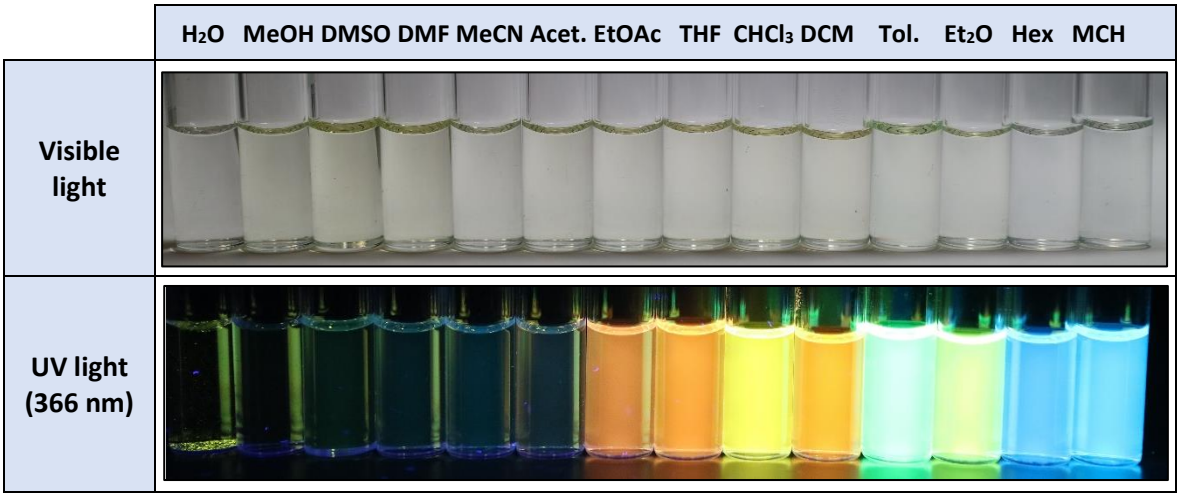

Figure 287. Solvatochromism of AR90p under visible and 366 nm light.

Fluorescence decay lifetime (τ):

The solvent used was MCH. The concentration of the compound was 20 µM.

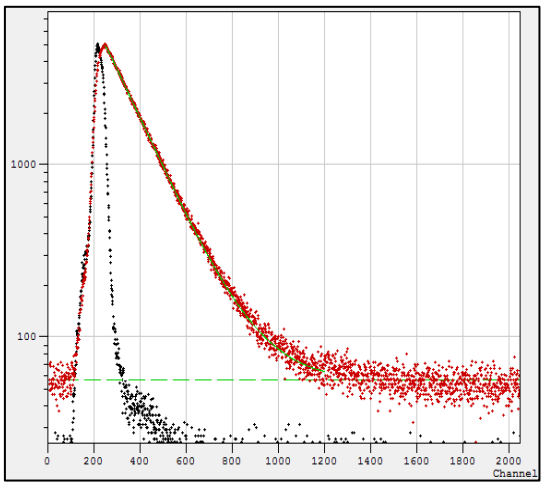

Figure 288. Fluorescence decay lifetime of AR90p.

Water acceptance test:

The solvent used was THF and the concentration of the compound was 20 µM.

	R	5%	10%	20%	30%	40%	50%	60%	70%	80%	90%
Visible light											
UV light (366 nm)	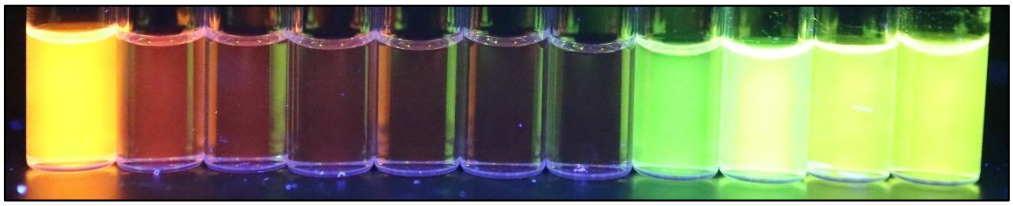										

Figure 289. Water acceptance test of AR90p under visible (up) and UV (down) light.

There was a increase in emission intensity from 60% water (AIE). At low amount of water, the maximum emission was shifted from red region to yellow greenish region.

pH test:

The amount of water for the performance of this test were 10% and 60%. The concentration of the compound was 20 µM and the solvent used was THF.

	R	HCl	3.4	4.8	6.4	7.4	7.9	10.5	KOH
Visible light									
UV light (366 nm)									

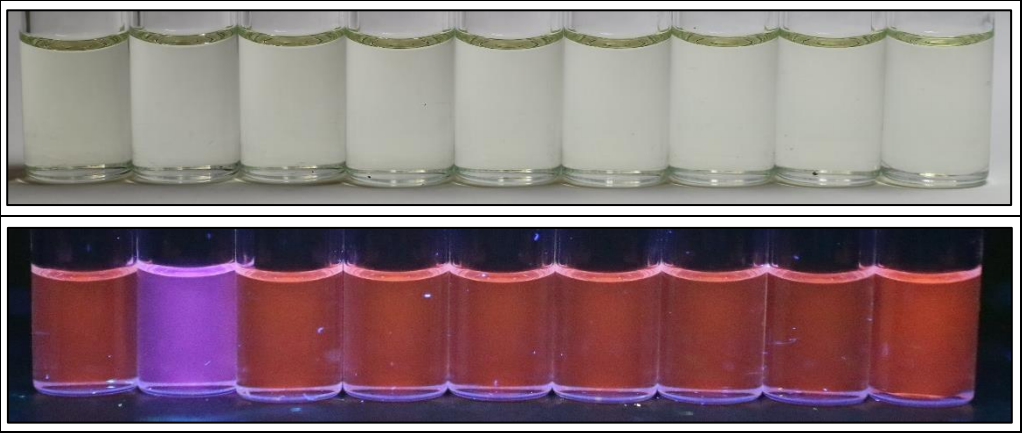

Figure 290. pH test of AR90p at 10% of water under visible (up) and UV (down) light.

	R	HCl	3.4	4.8	6.4	7.4	7.9	10.5	KOH
Visible light									
UV light (366 nm)									

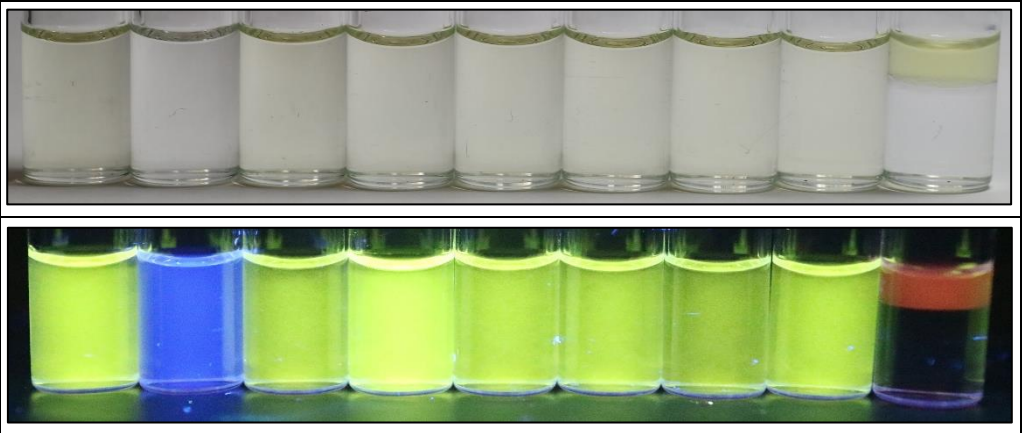

Figure 291. pH test of AR90p at 60% of water under visible (up) and UV (down) light.

The most important change was the response to highly acidic media in both amounts of water.

Cations and anions test:

The concentration of the compound was 20 µM and the solvent used was THF.

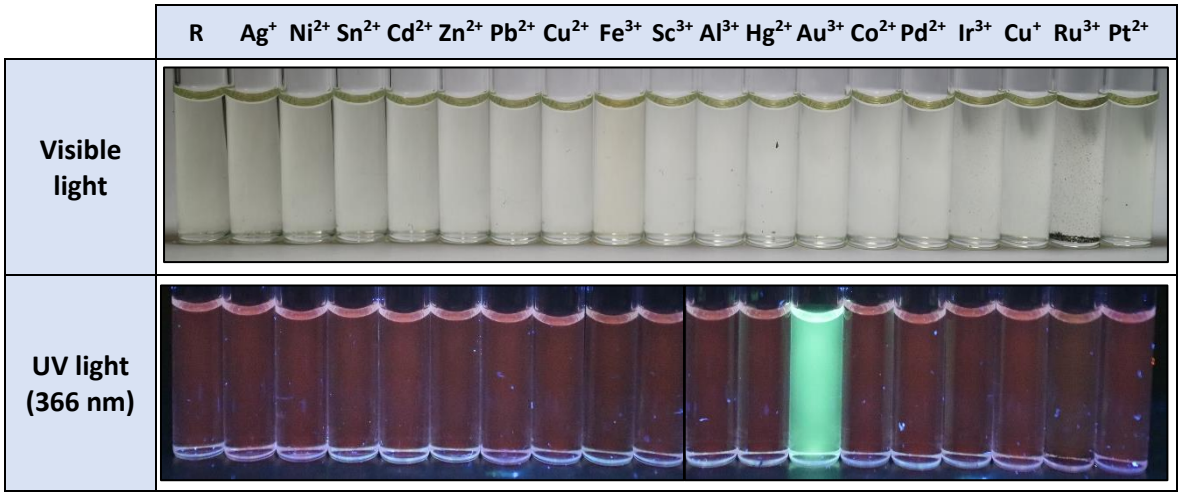

Figure 292. Cations test of AR90p under visible (up) and UV (down) light.

The only change observed was the change in fluorescence from red to green in the presence of Au^{3+}.

The concentration of the compound was 20 µM and the solvent used was THF.

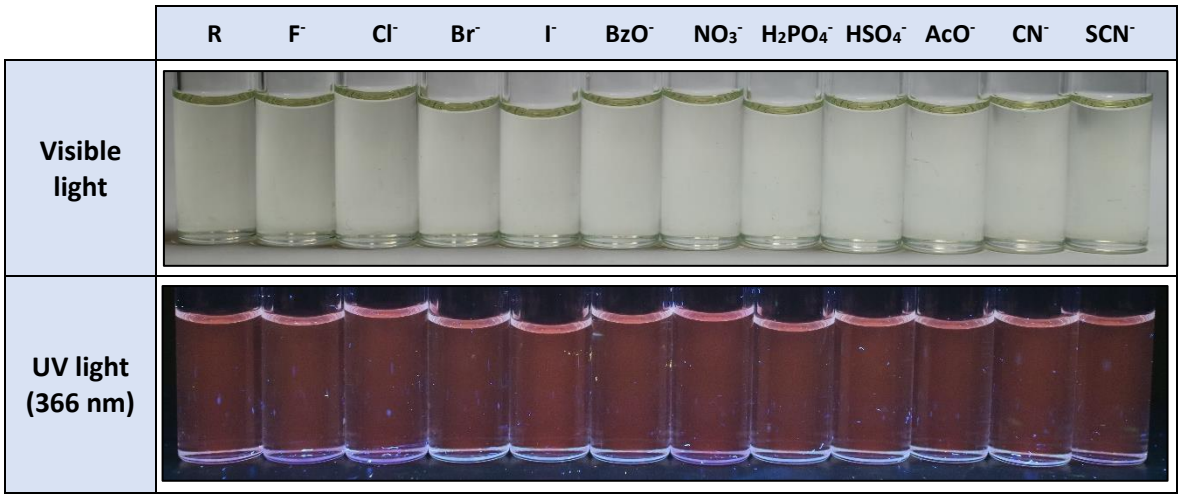

Figure 293. Anions test of AR90p under visible (up) and UV (down) light.

No significant changes were observed.

Oxidant and reductant reagents test:

The solvent used was THF and concentration of the compound was 20 µM.

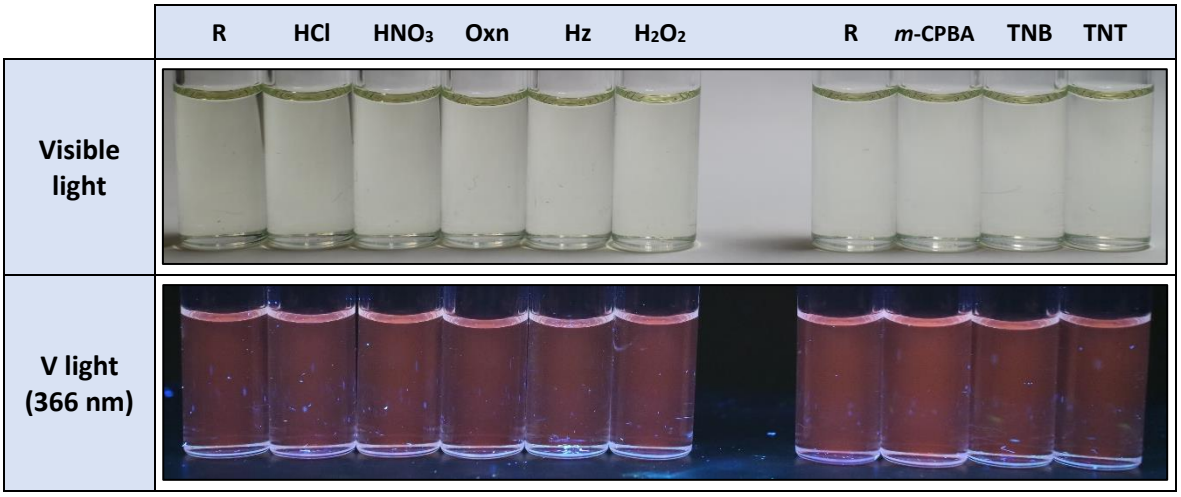

Figure 294. Oxidant and reductant reagents test of AR90p under visible (up) and UV (down) light.

No significant changes were observed.

Synthesis of *N*-(piperidin-4-yl)-4-[(4-Boc-piperazin-1-yl)phenyl]naphthalene-1,8-dicarboxyl-monoimide (AR90s)

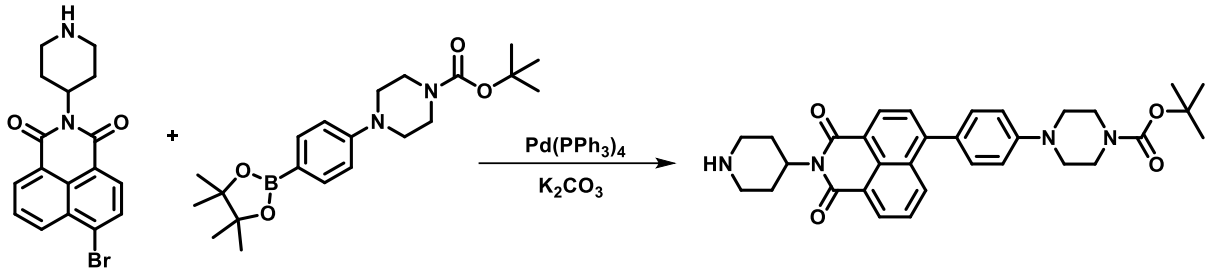

150 mg of *N*-piperidine-4-bromonaphthalene-1,8-dicarboxylmonoimide (AR43d, 0.42 mmol), 179 mg of 2-(4-Boc-piperazine)pyridine-5-boronic acid pinacol ester (0.44 mmol) and 451 mg of potassium carbonate (3.26 mmol) were dissolved in a mixture of toluene:*n*-butanol:water (4:1:2 ml) under nitrogen atmosphere and, then, the catalyst, $Pd(PPh_3)_4$ was added and the resulting mixture was stirred overnight at 110°C. Afterwards, the solvent was evaporated under reduce pressure, the solid was dissolved in DCM and washed with water (3×100 ml). The organic extracts were combined, dried over anhidrous Na_2SO_4 and the solvent was evaporated under reduce pressure. The organic solid was purified by column chromatography (SiO_2, DCM:MeOH) getting 190 mg of a brown solid, 84% yield.

m.p.: 188-190°C.

IR (ATR, cm^{-1}): 3407 (N-H), 3054-2851, 1689 (C=O), 1590, 1489, 1399, 1363, 1235, 1159 (C-N), 1118, 992, 929, 809, 750, 717, 693, 540.

^{1}H-NMR (300 MHz, $CDCl_3$) δ (ppm): 8.59 (d, *J* = 7.5 Hz, 2H, 2×**H$_{Ar}$**), 8.33 (dd, *J* = 8.5, 0.9 Hz, 1H, **H$_{Ar}$**), 7.68 (t, *J* = 8.0 Hz, 2H, 2×**H$_{Ar}$**), 7.43 (d, *J* = 8.6 Hz, 2H, 2×**H$_{Ar}$**), 7.07 (d, *J* = 8.7 Hz, 2H, 2×**H$_{Ar}$**), 5.21 (m, 1H, C**H**), 3.64 (m, 4H, 2×C**H**$_2$), 3.27 (m, 6H, 3×C**H**$_2$), 2.86-2.68 (m, 4H, 2×C**H**$_2$), 2.14 (s, 1H, N**H**), 1.73 (m, 2H, C**H**$_2$), 1.50 (s, 9H, 3×C**H**$_3$).

^{13}C-NMR (75MHz, $CDCl_3$) δ (ppm): 164.6 (**C**=O), 164.4 (**C**=O), 154.8 (**C**$_{Ar}$), 151.3 (**C**$_{Ar}$), 147.1 (**C**$_{Ar}$), 133.1 (**C**$_{Ar}$H), 131.5 (**C**$_{Ar}$H) , 131.4 (**C**$_{Ar}$H), 131.0 (**C**$_{Ar}$H), 130.1 (**C**$_{Ar}$), 129.9 (**C**$_{Ar}$), 129.0 (**C**$_{Ar}$), 127.8 (**C**$_{Ar}$H), 126.8 (**C**$_{Ar}$H), 122.9 (**C**$_{Ar}$), 121.1 (**C**$_{Ar}$), 116.1 (**C**$_{Ar}$), 80.2 (**Cq**), 48.8 (**C**H$_2$), 44.7 (**C**H$_2$), 43.6 (**C**H$_2$), 28.6 (**C**H$_3$), 25.8 (**C**H$_2$).

HRMS (MALDI, DIT+) m/z: calculated for $C_{32}H_{36}N_4O_4$+H: 541.2815 (M^++H); found 541.2807.

UV-Vis ($CHCl_3$), λ_{max} nm (log ε): 310 (4.0).

Ø (THF, %): 3.07.

τ (280 nm, THF, ns): 1.786/6.278 (χ^2: 1.114).

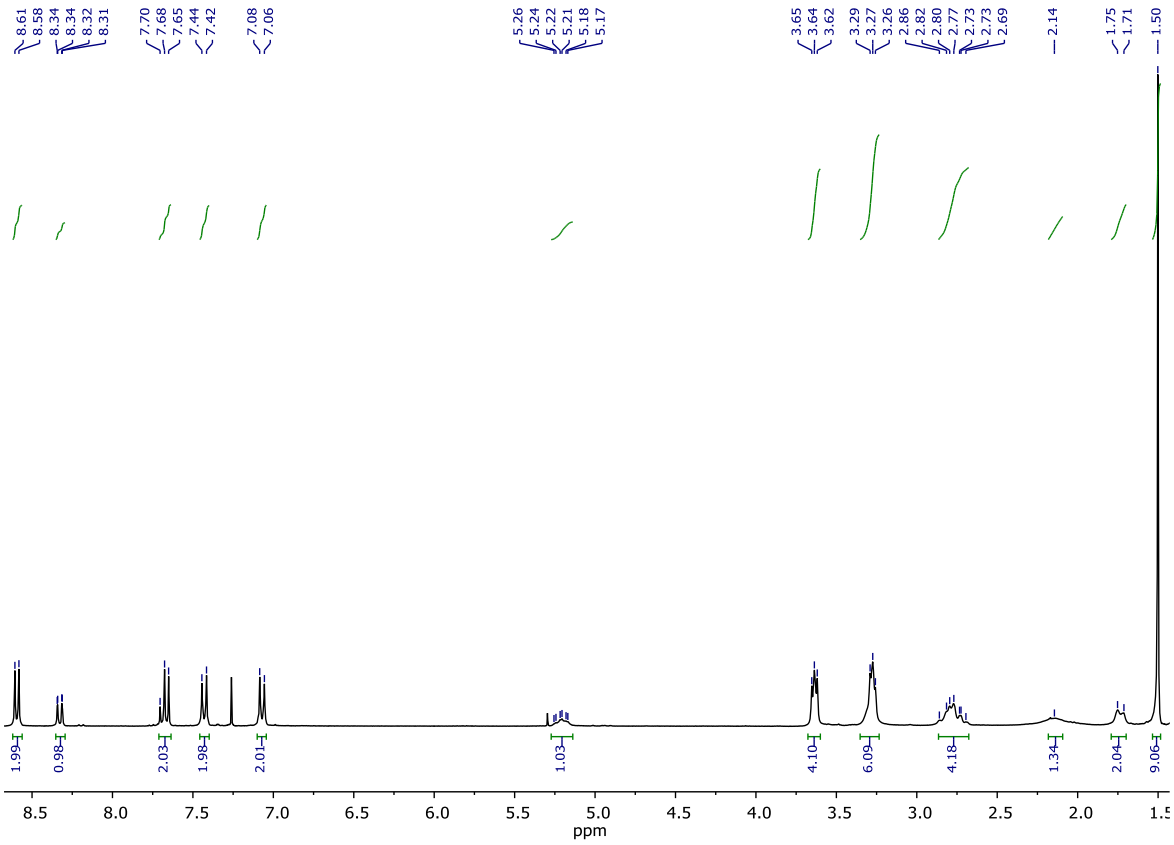

Figure 295. ^{1}H-NMR ($CDCl_3$, 300 MHz) of AR90s.

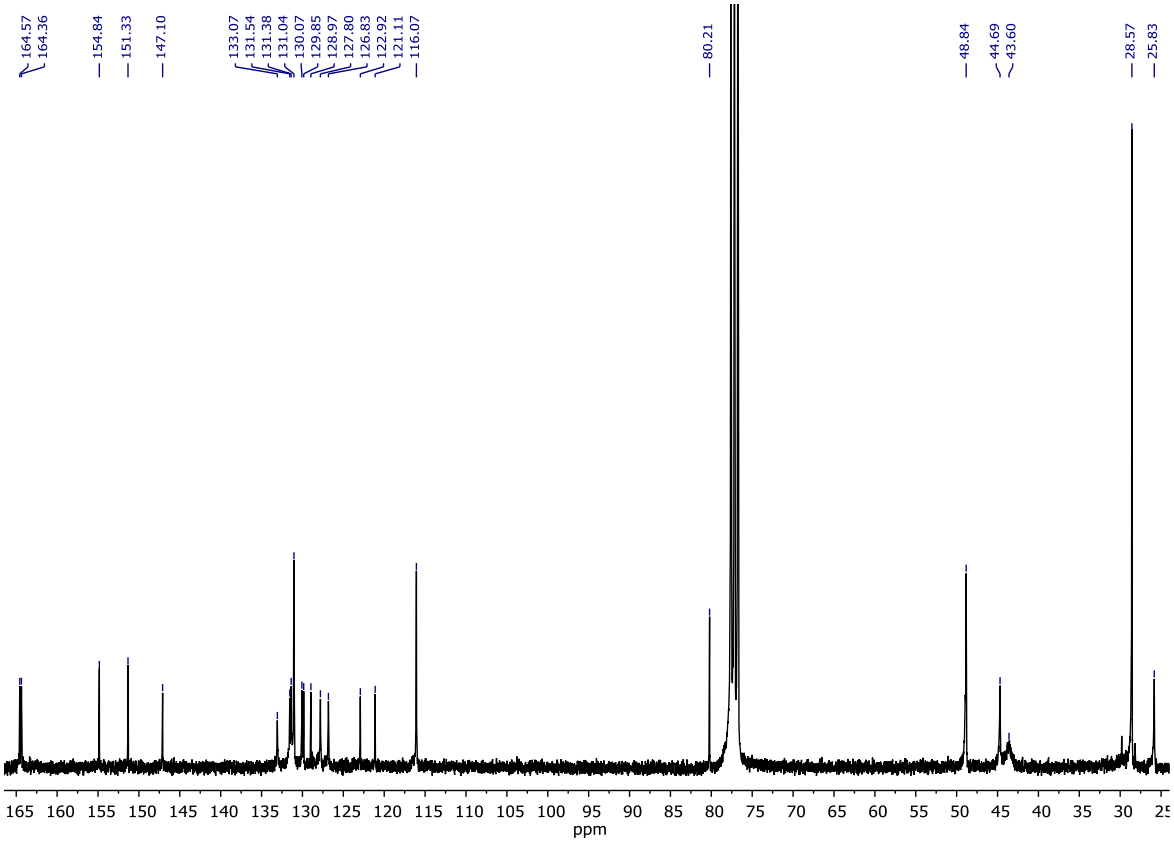

Figure 296. ^{13}C-NMR ($CDCl_3$, 75 MHz) of AR90s.

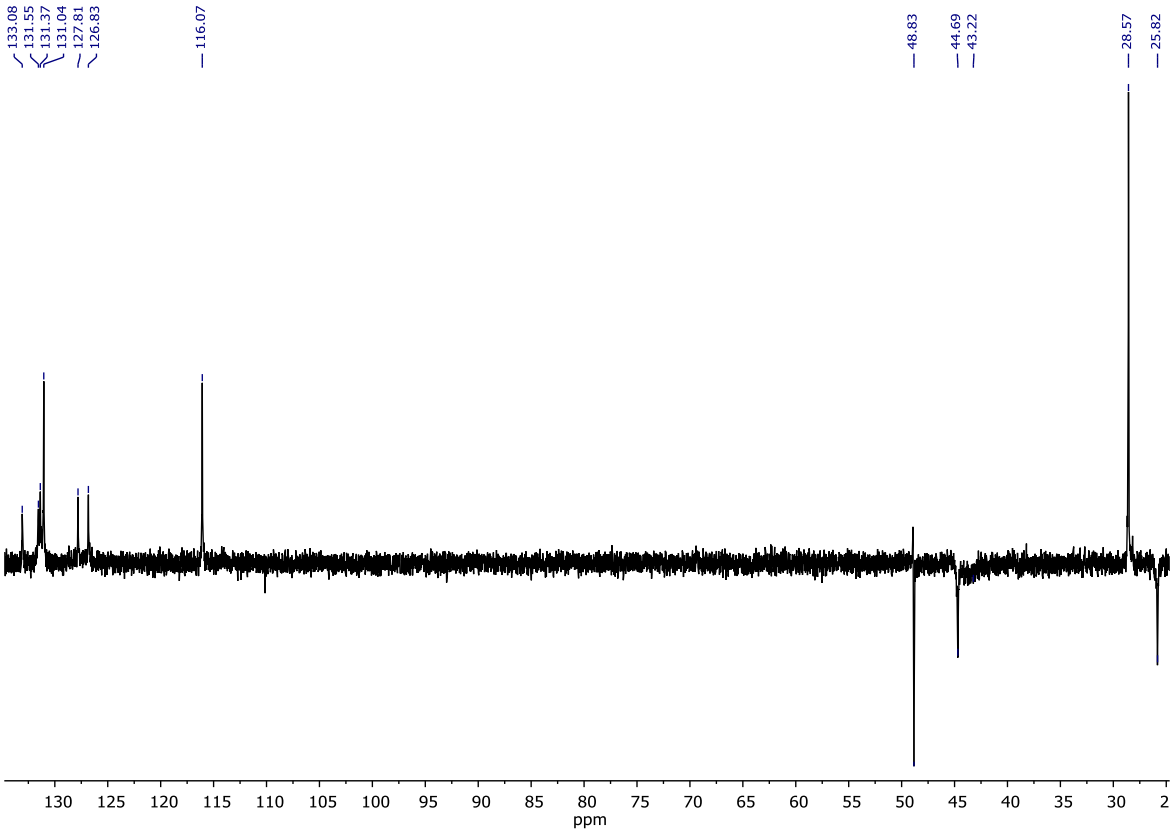

Figure 297. DEPT NMR ($CDCl_3$, 75 MHz) of AR90s.

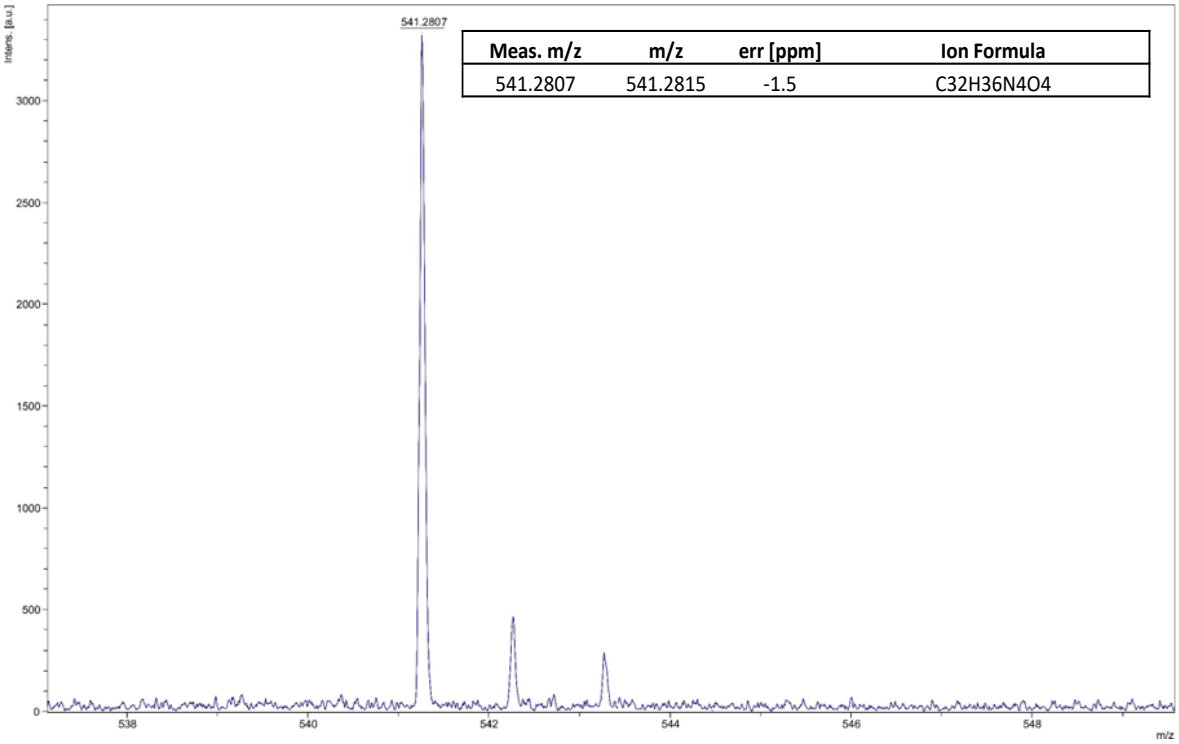

Meas. m/z	m/z	err [ppm]	Ion Formula
541.2807	541.2815	-1.5	C32H36N4O4

Figure 298. HRMS (MALDI, DIT+) of AR90s.

Solvatochromism:

The concentration of the compound was 20 µM and the excitation wavelength was 310 nm.

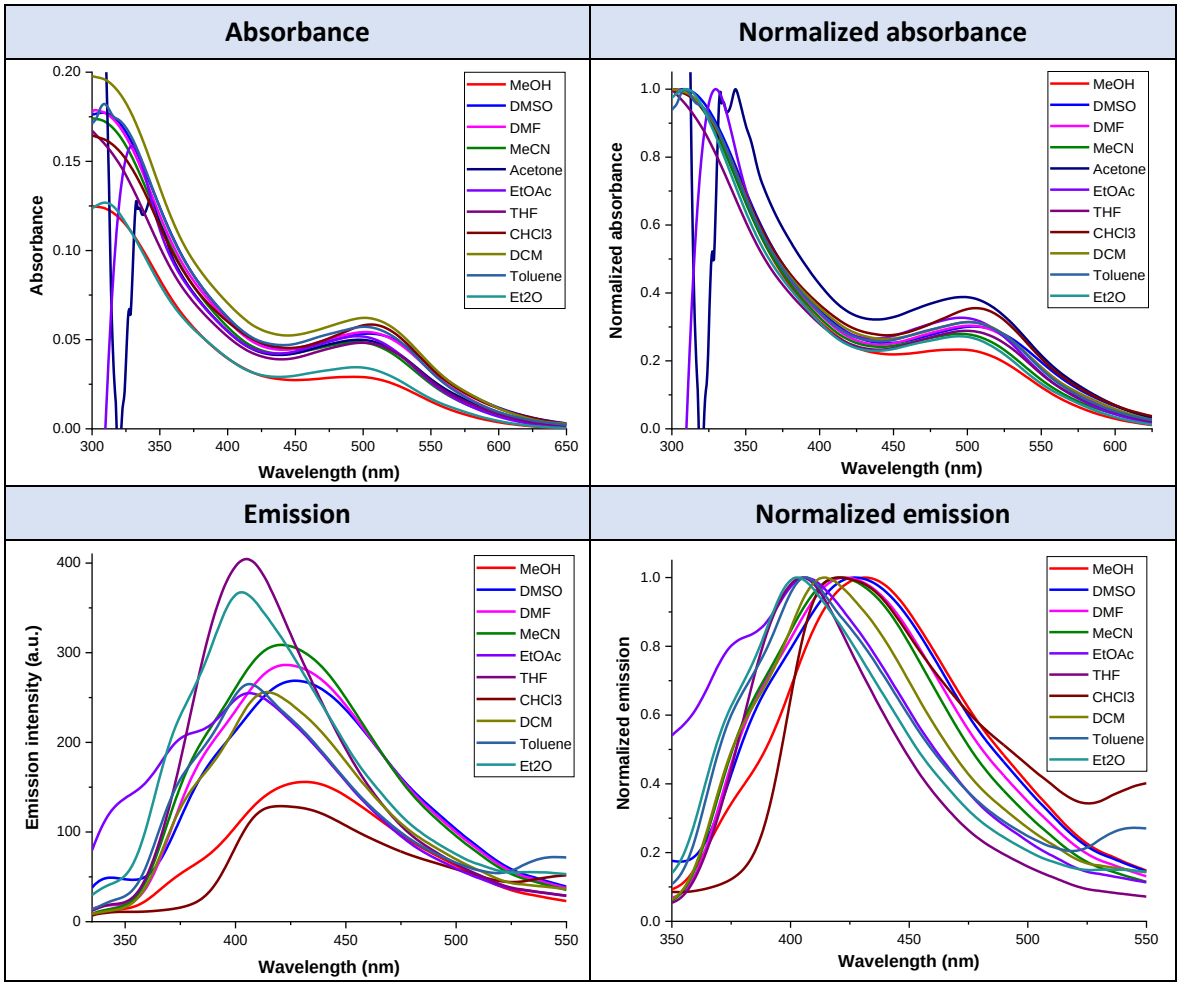

Figure 299. Solvatochromism of AR90s.

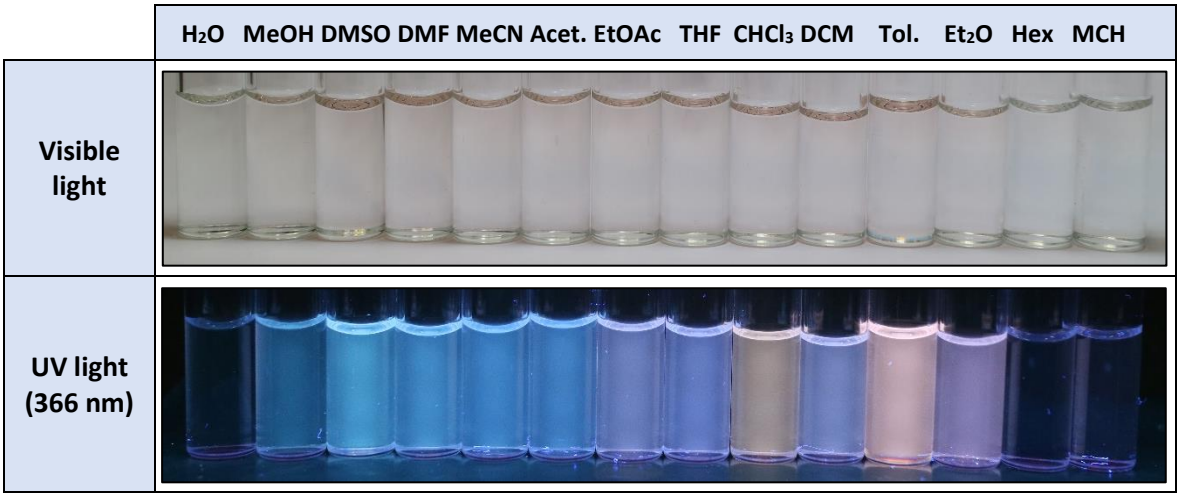

Figure 300. Solvatochromism of AR90s under visible and 366 nm light.

Fluorescence decay lifetime (τ):

The solvent used was THF. The concentration of the compound was 20 µM.

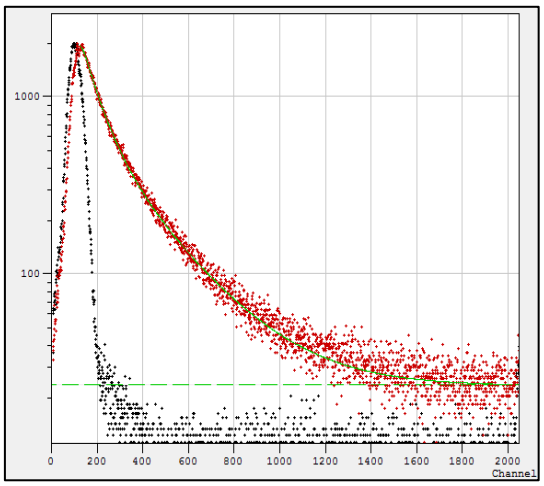

Figure 301. Fluorescence decay lifetime of AR90s.

Water acceptance test:

The solvent used was MeOH and the concentration of the compound was 20 µM.

	R	5%	10%	20%	30%	40%	50%	60%	70%	80%	90%
Visible light	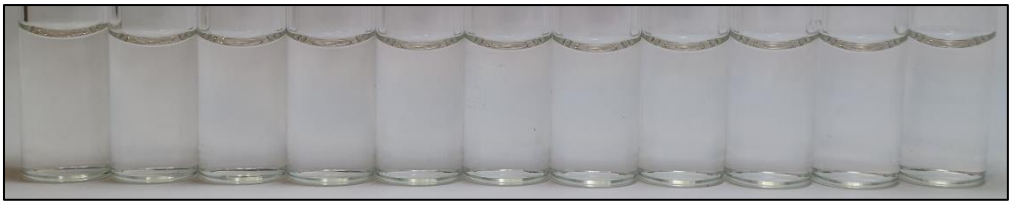										
UV light (366 nm)	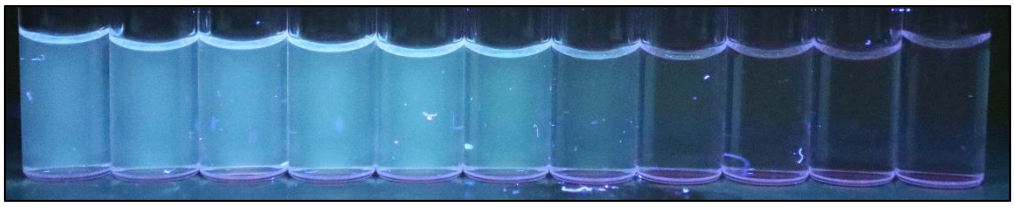										

Figure 302. Water acceptance test of AR90s under visible (up) and UV (down) light.

The maximum amount of water that was admitted by the product was 40%. From 60% water, the fluorescence was quenched (ACQ).

pH test:

The amount of water for the performance of this test was 40%. The concentration of the compound was 20 µM and the solvent used was MeOH.

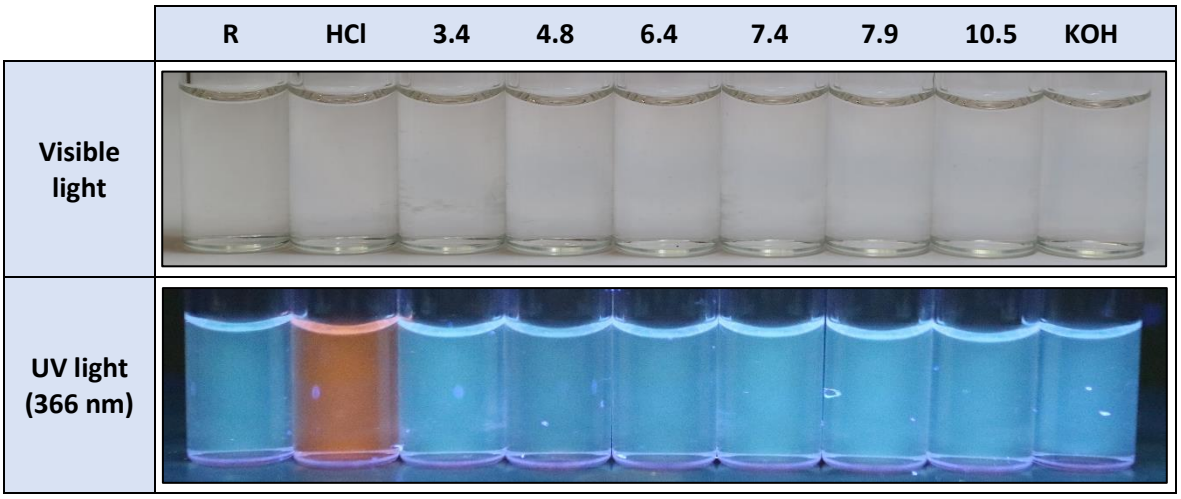

Figure 303. pH test of AR90s under visible (up) and UV (down) light.

The most important change in fluorescence was the response to highly acidic media.

Cations and anions test:

The concentration of the compound was 20 µM and the solvent used was MeOH.

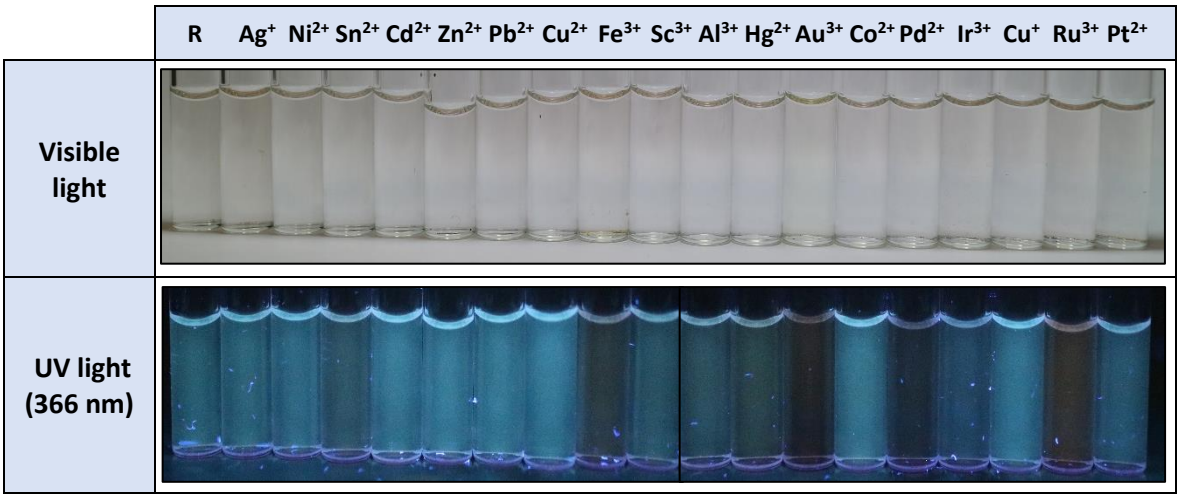

Figure 304. Cations test of AR90s under visible (up) and UV (down) light.

The most significant changes were the fluorescence quenching when was confronted with Fe^{3+}, Au^{3+}, Pd^{2+} and Ru^{3+}.

The concentration of the compound was 20 µM and the solvent used was MeOH.

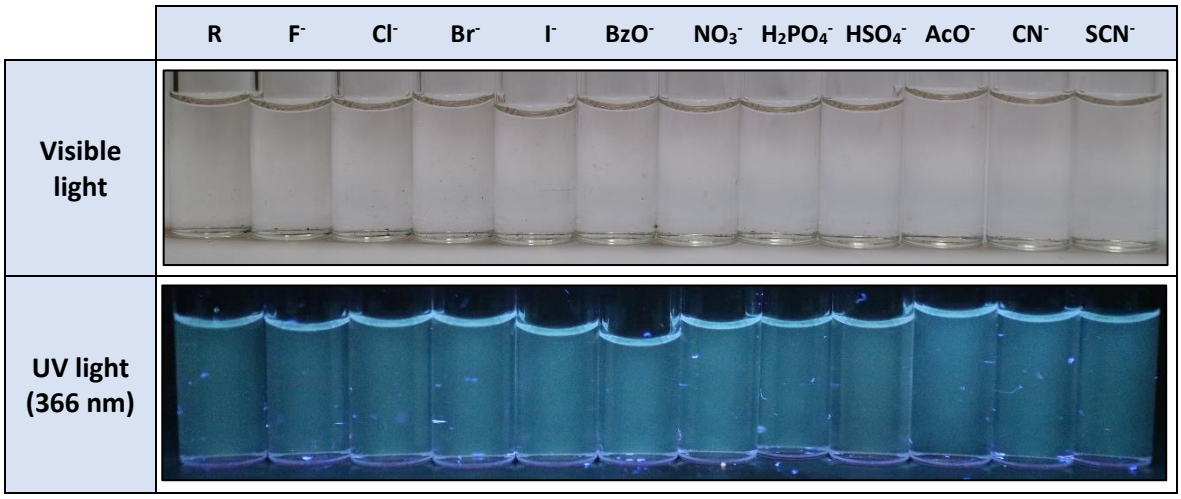

Figure 305. Anions test of AR90s under visible (up) and UV (down) light.

No significant changes were observed.

Oxidant and reductant reagents test:

The solvent used was THF and concentration of the compound was 20 µM.

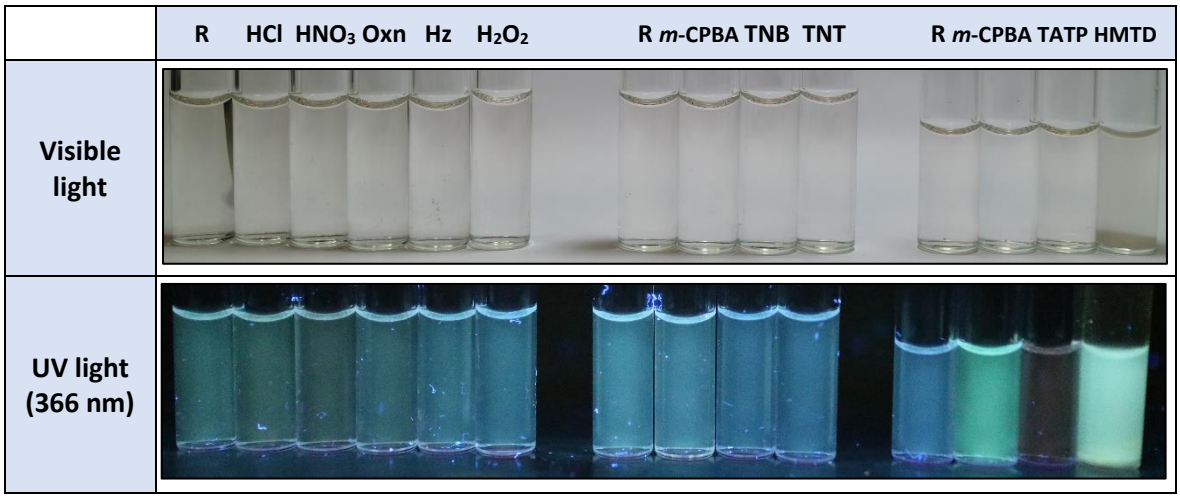

Figure 306. Oxidant and reductant reagents test of AR90s under visible (up) and UV (down) light.

The most significat change was the fluorescence quenching whan exposed to TATP. In addition, in front of HMTD the colour of the fluorescence was become turquoise blue.

Previous solvents test:

In order to determine the fluorescence variation of the compound under study in the presence of TATP, some test were carried out for the probe in 9 different solvents. The AR90s concentration was 20 µM and the TATP was added in excess (7 mg in each vial). All the test were performed at room temperature and the photographs were taken immediately after the addition of TATP and again after 72 hours.

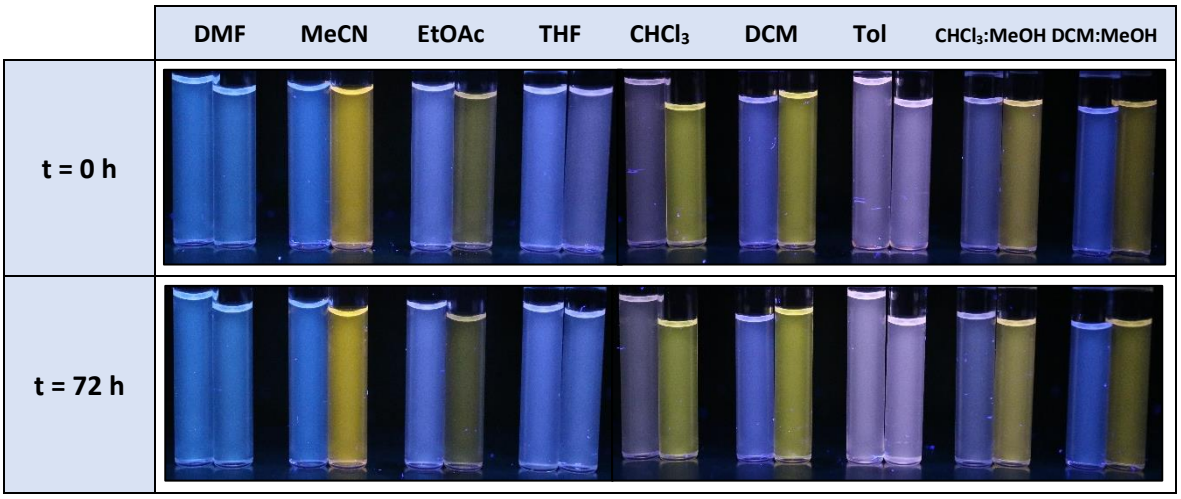

Figure 307. Pairs of AR90s (left) and AR90s with excess of TATP (right) in different solvents at time 0 h (up) and 72 h (down).

The biggest fluorescence changes were seen in EtOAc, MeCN, $CHCl_3$, DCM, $CHCl_3$:MeOH (9:1) and DCM:MeOH (9:1) so kinetic studies and TATP titrations were carried out in these solvents.

Solvents test with TATP:

For all solvents, the working concentration of AR90s was 2.5 µM, the excitation wavelength was 310 nm and the temperature for all test was 25ºC.

In the kinetic studies, TATP was in excess (20 mM) and the fluorescence emission measurements were made during the subsequent minutes at 5 min, 10 min and 30 min time intervals. In the titration, the TATP concentration was between 0 and 35000 µM and it was added directly as solid. The measurements were carried out inmediately after the adittion of the probe.

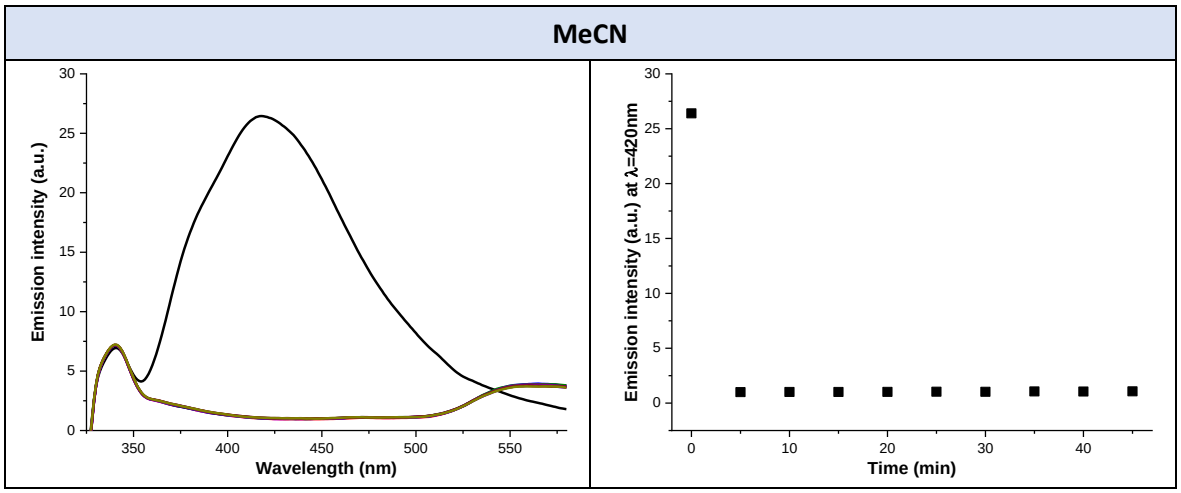

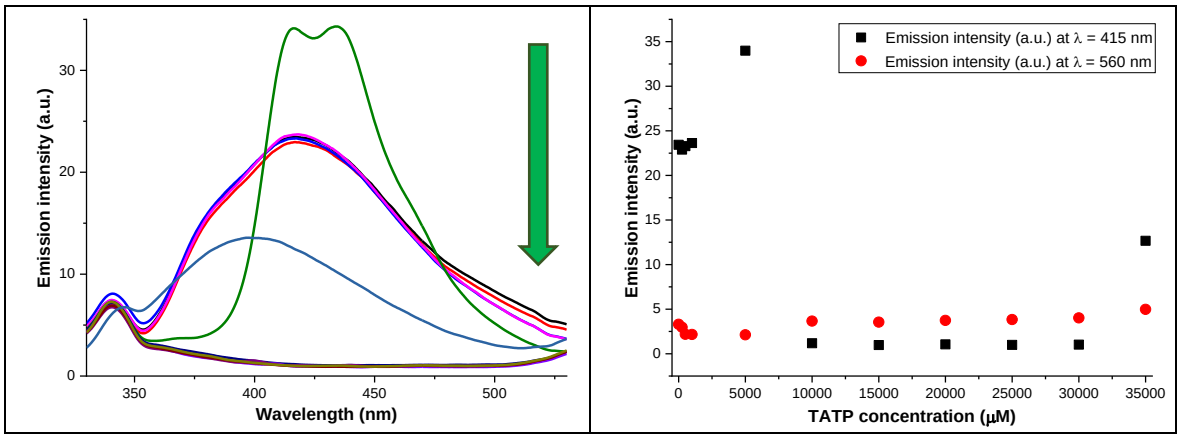

Figure 308. Study of AR90s with TATP in MeCN. Kinetic study (up left) and profile as function as time at 420 nm (up right) in presence of TATP excess. Titration (down left) and fluorescence profile at 415 nm and 560 nm simultaneusly (down right) under increasing concentrations of TATP.

There was a decrease change in the emission intensity band immediately after adding TATP. The LOD of TATP was somewhere between 5000 and 10000 μM, a fairly high limit, with a decrease in emission intensity.

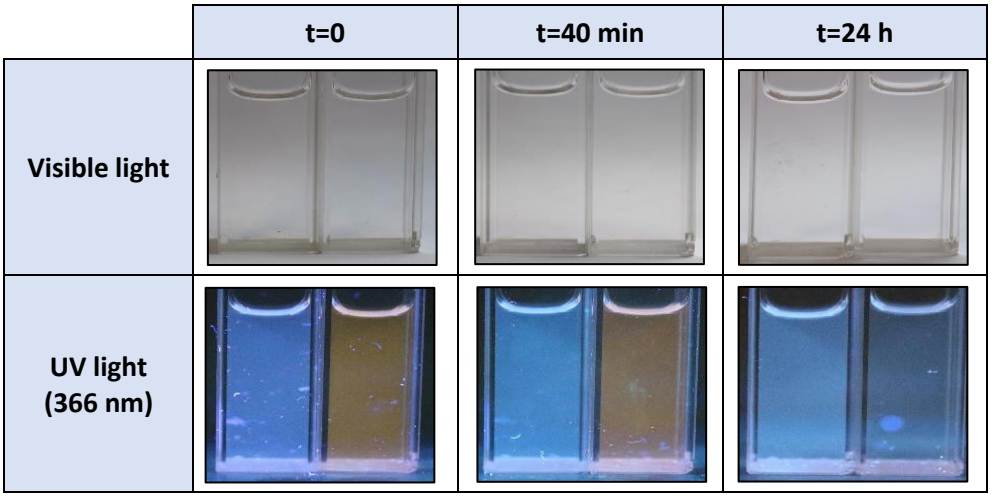

Figure 309. Kinetic study at different times under visible (up) and UV (down) light in MeCN. In each photo, left vial was contained the probe and right vial was contained the probe and an excess of TATP.

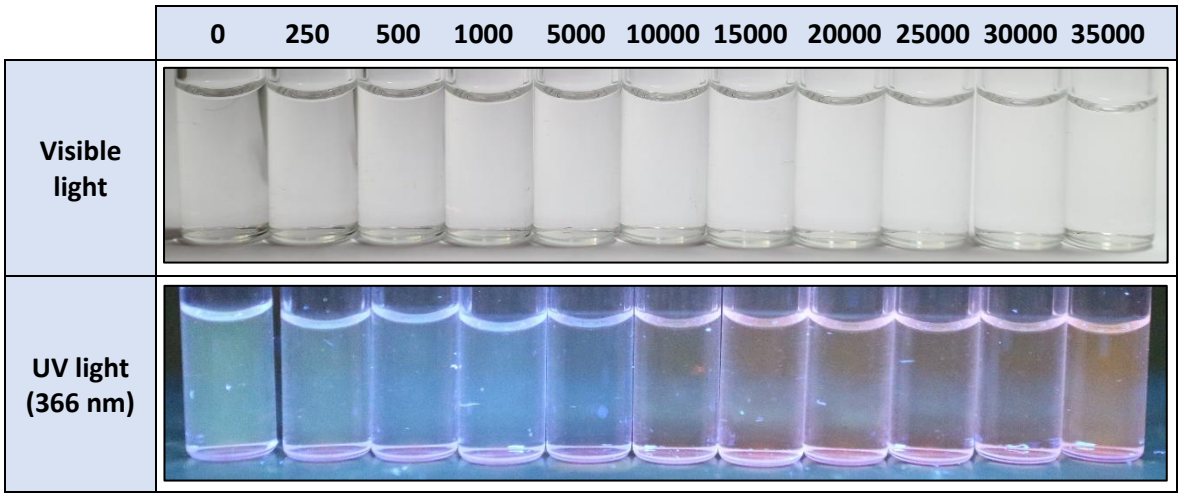

Figure 310. Titration of AR90s with an excess of TATP under visible (up) and UV (down) light in MeCN.

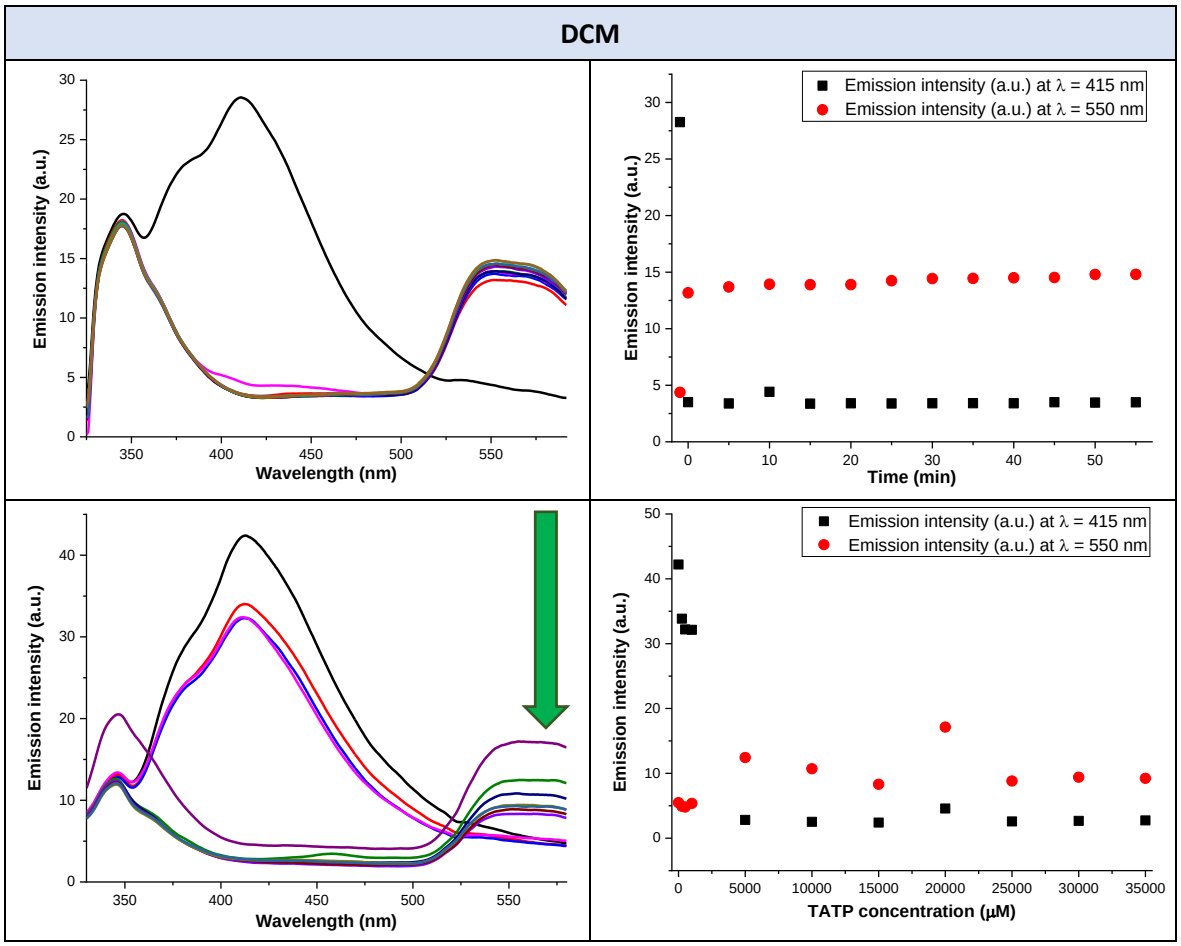

Figure 311. Study of AR90s with TATP in DCM. Kinetic study (up left) and profile as function as time at 415 nm and 550 nm simultaneusly (up right) in presence of TATP excess. Titration (down left) and fluorescence profile at 415 nm and 560 nm simultaneusly (down right) under increasing concentrations of TATP.

There was a decrease in the emission intensity band immediately after adding TATP. The LOD of TATP was somewhere between 1000 and 5000 µM, slightly less than in the previous solvent, but still too high a range, with a decrease in emission intensity.

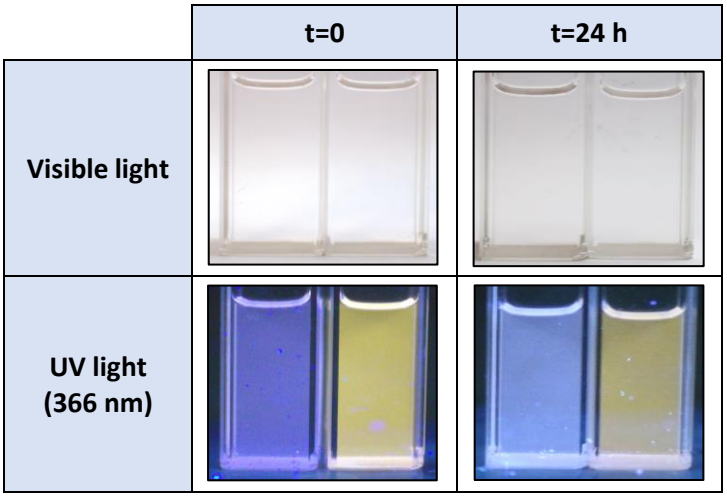

Figure 312. Kinetic study at different times under visible (up) and UV (down) light in DCM. In each photo, left vial was contained the probe and right vial was contained the probe and an excess of TATP.

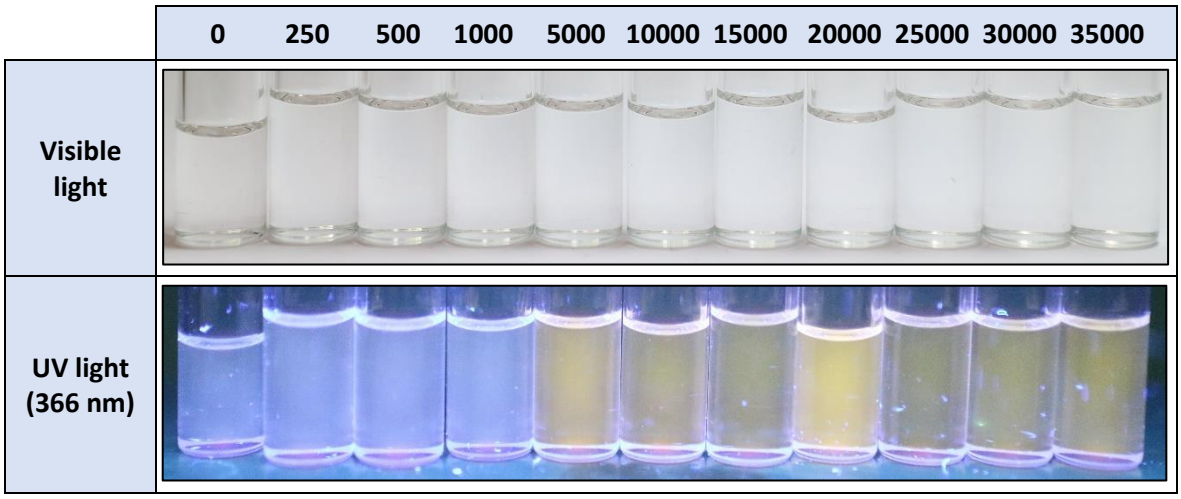

Figure 313. Titration of AR90s with an excess of TATP under visible (up) and UV (down) light in DCM.

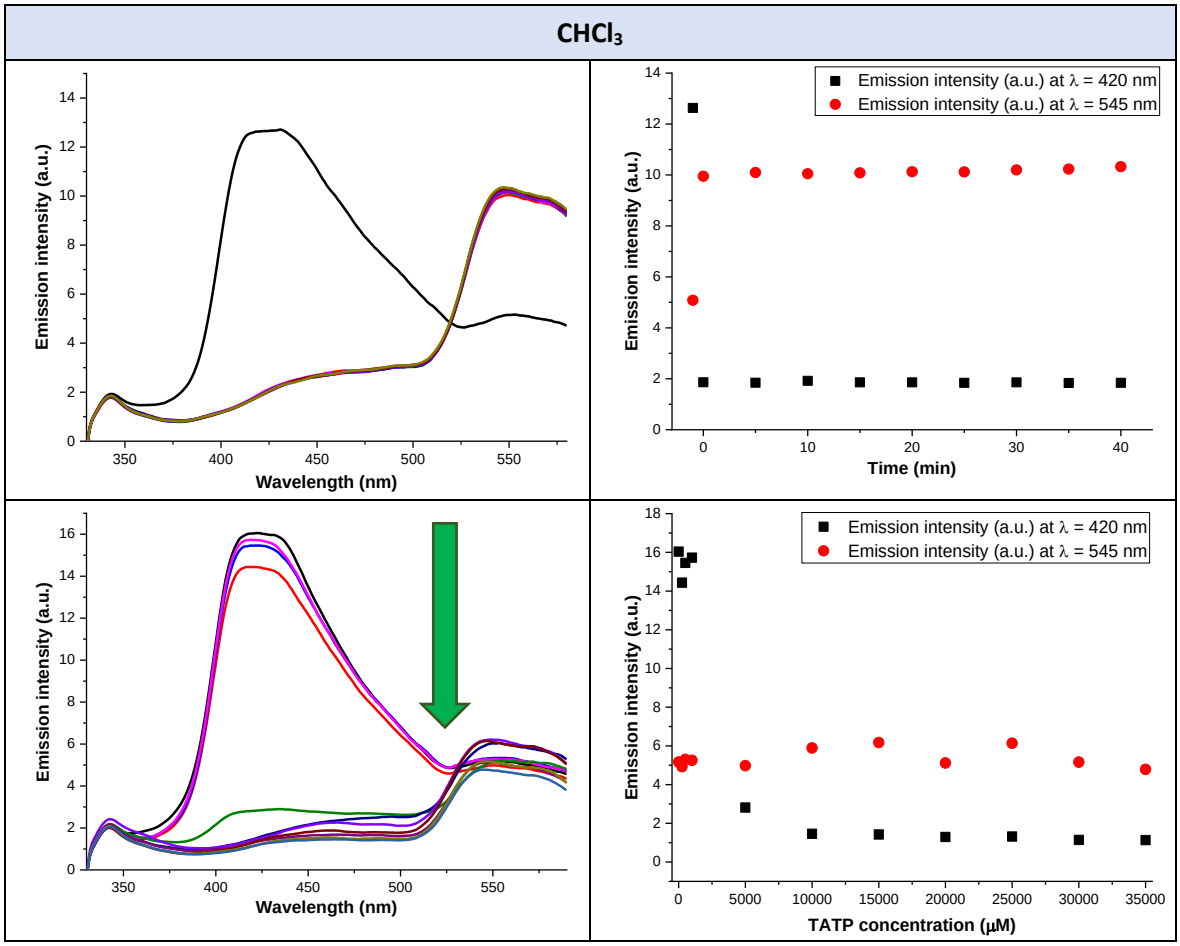

Figure 314. Study of AR90s with TATP in $CHCl_3$. Kinetic study (up left) and profile as function as time at 420 nm and 545 nm simultaneously (up right) in presence of TATP excess. Titration (down left) and fluorescence profile at 420 nm and 545 nm simultaneusly (down right) under increasing concentrations of TATP.

There was a decrease in the emission intensity band immediately after adding TATP. According to the fluorescence spectra, the LOD of TATP was somewhere between 1000 and 5000 µM, as in the previous solvent, with a strong decrease in emission intensity.

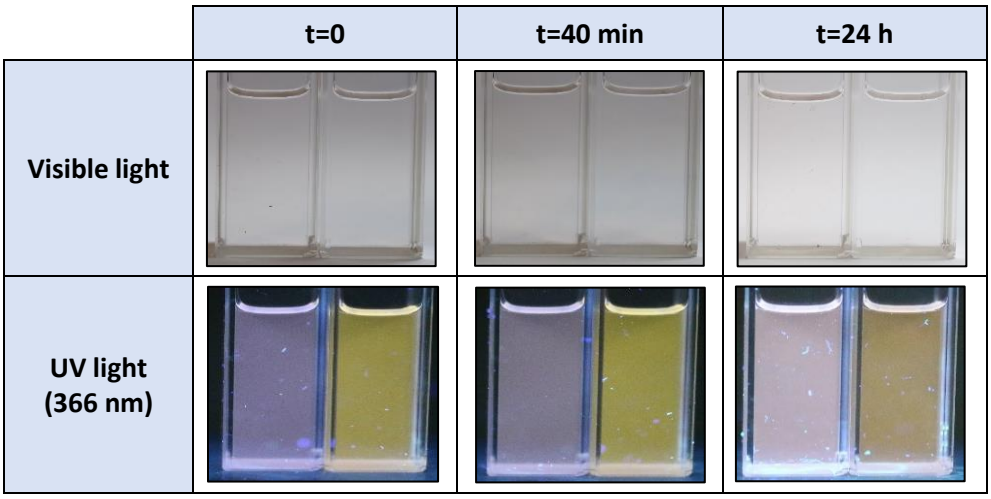

Figure 315. Kinetic study at different times under visible (up) and UV (down) light in $CHCl_3$. In each photo, left vial was contained the probe and right vial was contained the probe and an excess of TATP.

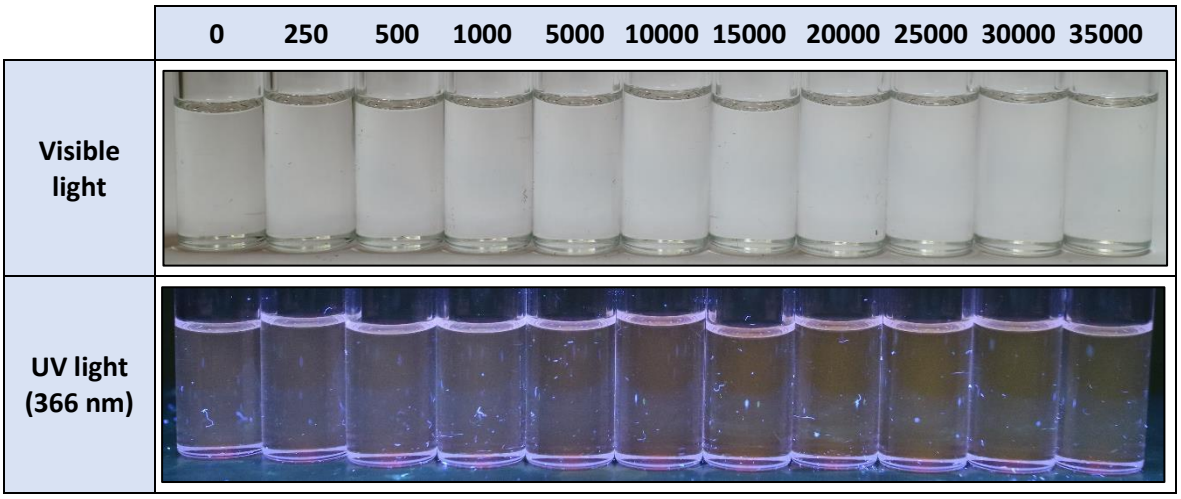

Figure 316. Titration of AR90s with an excess of TATP under visible (up) and UV (down) light in $CHCl_3$.

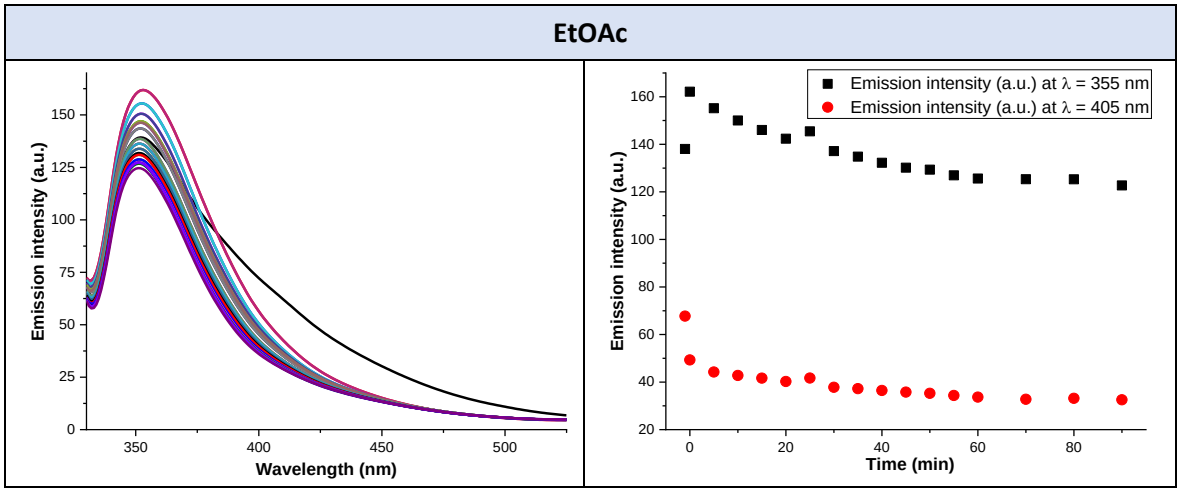

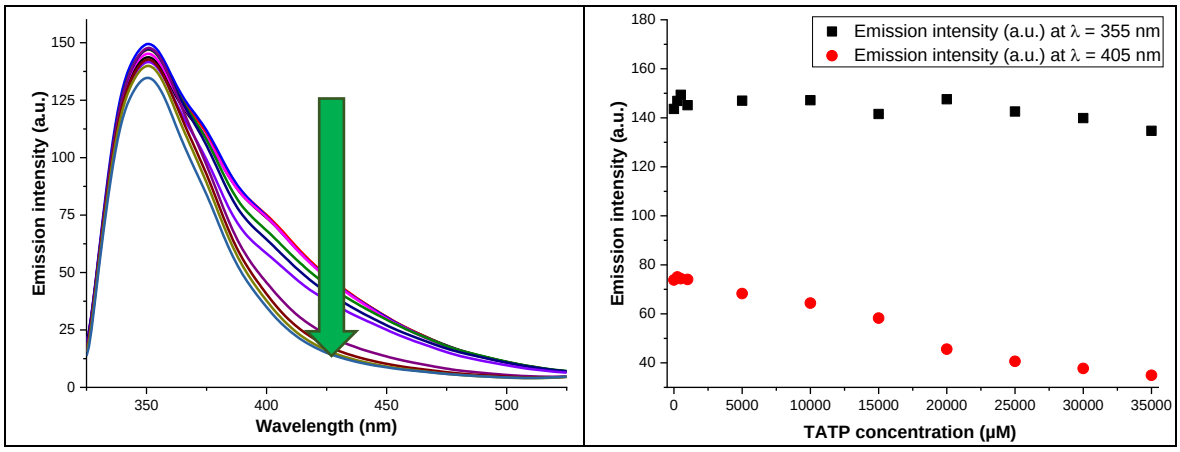

Figure 317. Study of AR90s with TATP in EtOAc. Kinetic study (up left) and profile as function as time at 355 nm and 405 nm simultaneously (up right) in presence of TATP excess. Titration (down left) and fluorescence profile at 355 nm and 405 nm simultaneously (down right) under increasing concentrations of TATP.

There was a decrease in emission intensity as time elapsed until stabilization was reached at around 60 minutes. According to the fluorescence spectra, the LOD was somewhere between 1000 and 5000 µM with a small decrease in emission intensity.

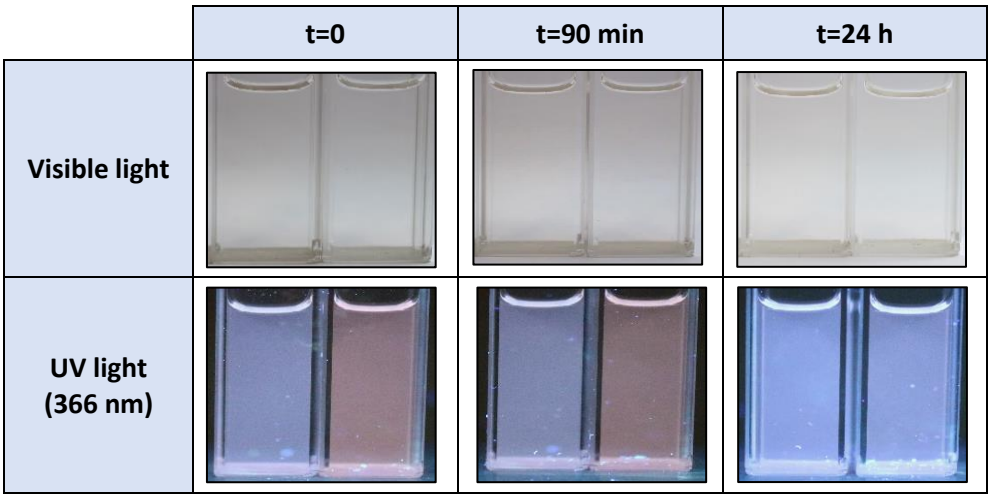

Figure 318. Kinetic study at different times under visible (up) and UV (down) light in EtOAc. In each photo, left vial was contained the probe and right vial was contained the probe and an excess of TATP.

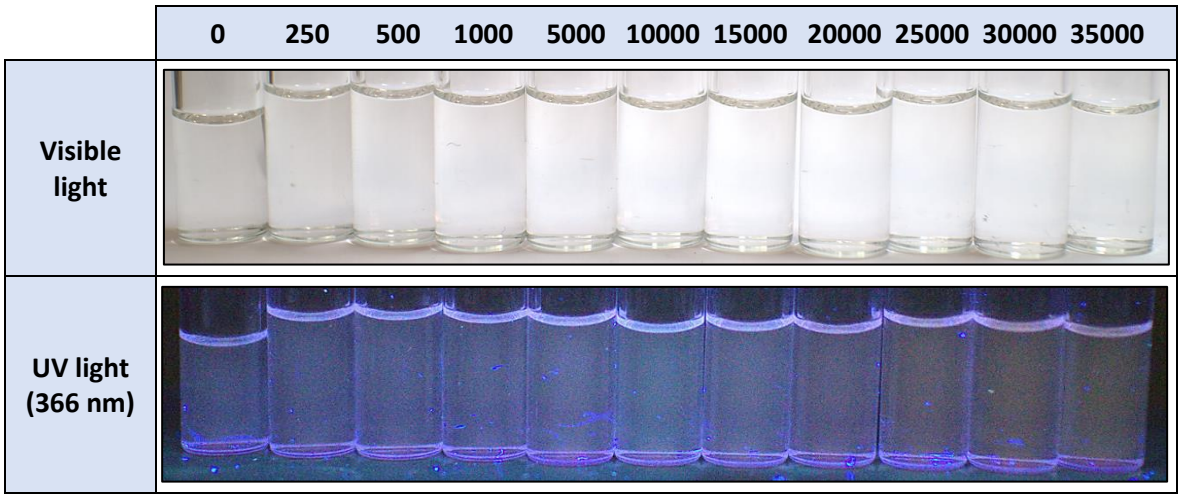

Figure 319. Titration of AR90s with an excess of TATP under visible (up) and UV (down) light in EtOAc.

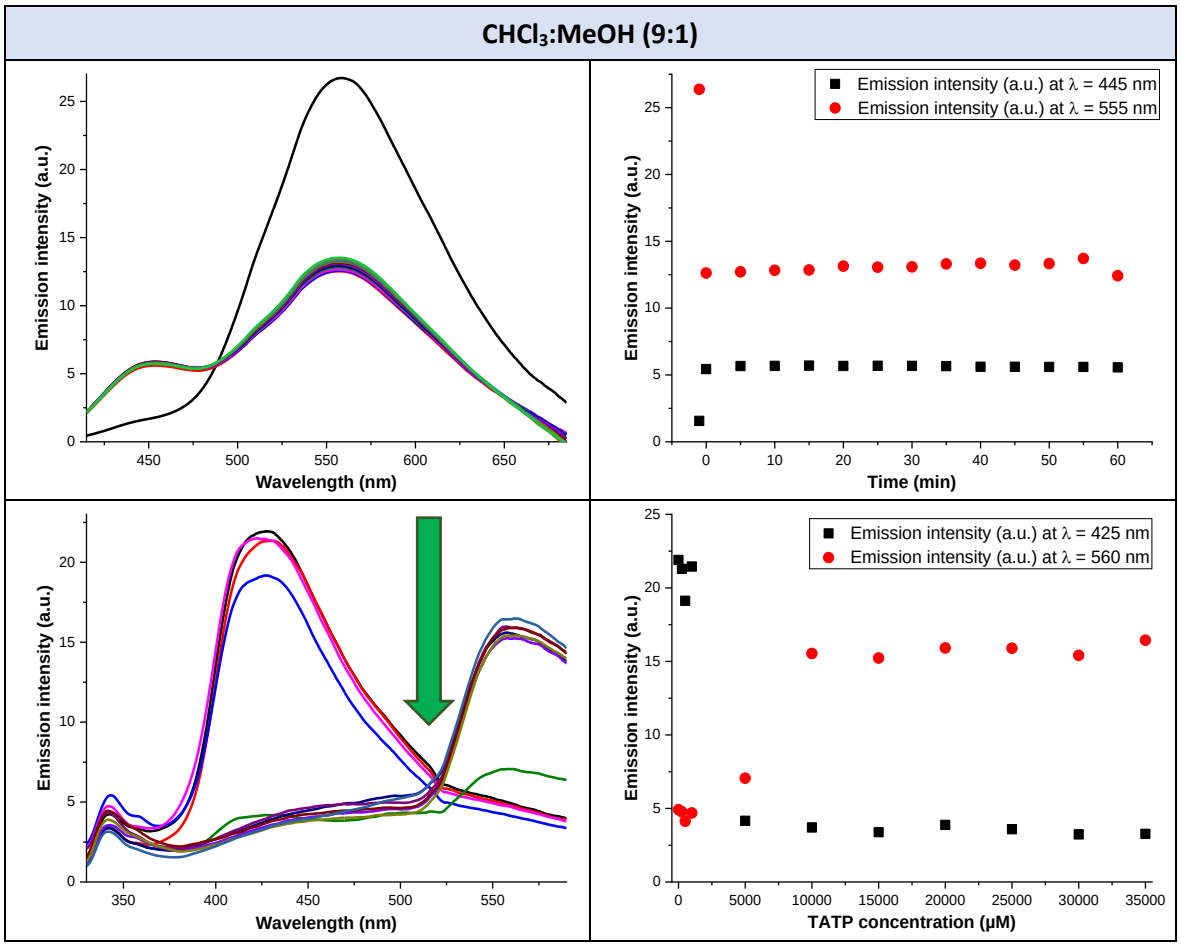

Figure 320. Study of AR90s with TATP in $CHCl_3$:MeOH (9:1). Kinetic study (up left) and profile as function as time at 445 nm and 555 nm simultaneously (up right) in presence of TATP excess. Titration (down left) and fluorescence profile at 425 nm and 560 nm simultaneusly (down right) under increasing concentrations of TATP.

There was a decrease in the emission intensity band immediately after adding TATP but, in the 445 nm band, an increase in the intensity was observed. According to the fluorescence spectra, the LOD of TATP was somewhere between 1000 and 5000 µM with an increase in emission intensity in the 560 nm band stronger than the decrease in the 425 nm band.

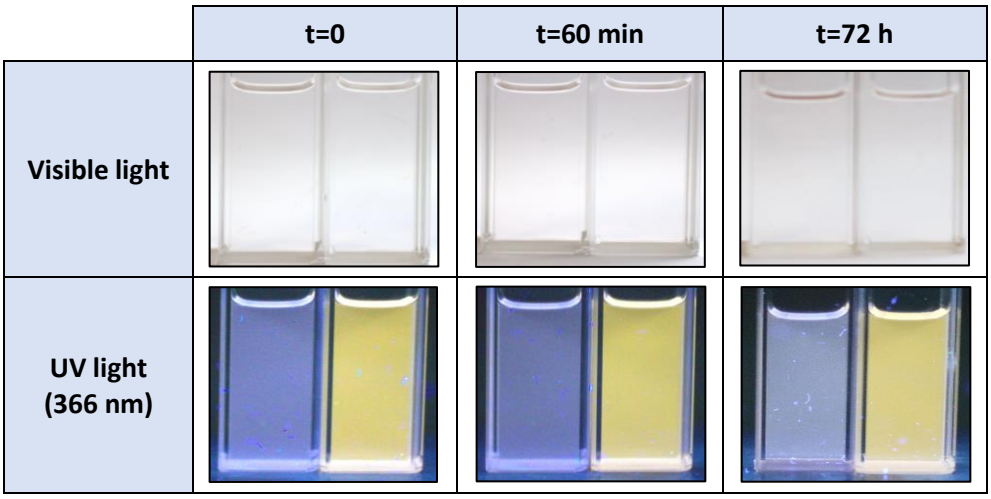

Figure 321. Kinetic study at different times under visible (up) and UV (down) light in $CHCl_3$:MeOH (9:1). In each photo, left vial was contained the probe and right vial was contained the probe and an excess of TATP.

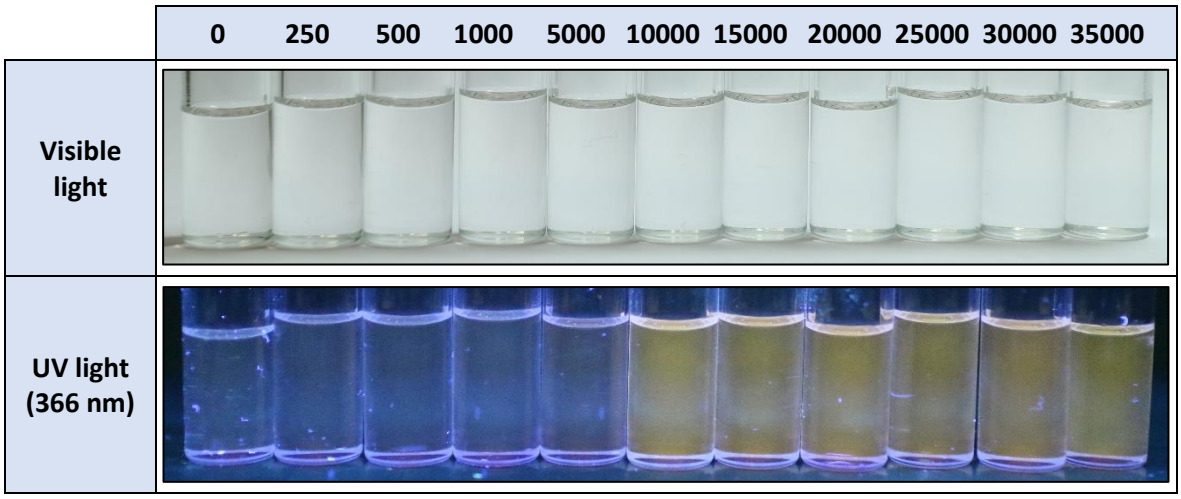

Figure 322. Titration of AR90s with an excess of TATP under visible (up) and UV (down) light in $CHCl_3$:MeOH (9:1).

Because of the low sensitivity the study was discontinued.

Synthesis of *N*-(piperidin-4-yl)-4-[(4-piperazin-1-yl)phenyl]naphthalene-1,8-dicarboxylmonoimide (AR90d)

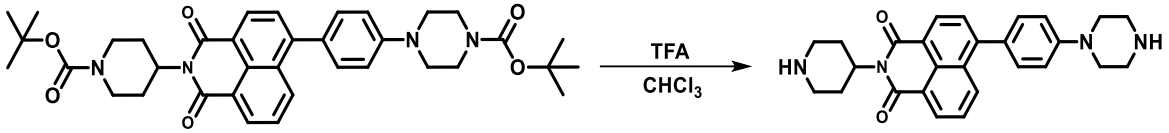

150 mg of *N*-(Boc-piperidine)-4-[(4-Boc-piperazine)phenyl]naphthalene-1,8-dicarboxylmonoimide (AR90p, 0.34 mmol) were dissolved in 15 ml of chloroform and, then, 2 ml of trifluoroacetic acid (26 mmol) was added. The mixture was stirred about 3 hours at room temperature. Afterwards, 10 ml of water were poured into the flask and the mixture was neutralized employing a 40% sodium hidroxide solution until it reached a neutral pH. Then, 20 ml of water were added into the flask and the mixture was extracted three times with chloroform (3×30 ml). The organic extracts were combined, dried over anhidrous Na_2SO_4 and the solvent was evaporated under reduce pressure, to obtain 148 mg of a yellow solid, 99% yield.

m.p.: 285-288°C.

IR (ATR, cm^{-1}): 3422 (N-H), 2940-2827, 1696 (C=O), 1650 (C=O), 1585, 1507, 1396, 1351, 1232, 1154 (C-N), 1115, 912, 777, 755, 583.

^{1}H-NMR (300 MHz, $CDCl_3$) δ (ppm): 8.59 (d, *J* = 7.5 Hz, 2H, 2×**H$_{Ar}$**), 8.34 (dd, *J* = 8.5, 1.1 Hz, 1H, **H$_{Ar}$**), 7.66 (m, 2H, 2×**H$_{Ar}$**), 7.42 (d, *J* = 8.8 Hz, 2H, 2×**H$_{Ar}$**), 7.07 (d, *J* = 8.8 Hz, 2H, 2×**H$_{Ar}$**), 5.20 (m, 1H, C**H**), 3.32-3.22 (m, 6H, 2×C**H**$_2$ + 2×N**H**), 3.07-3.10 (m, 4H, 2×C**H**$_2$), 2.81-2.68 (m, 4H, 2×C**H**$_2$), 1.72 (m, 4H, 2×C**H**$_2$).

^{13}C-NMR (75MHz, $CDCl_3$) δ (ppm): 164.9 (**C**=O), 164.7 (**C**=O), 151.9 (**C**$_{Ar}$), 146.9 (**C**$_{Ar}$), 132.8 (**C**$_{Ar}$H), 131.2 (**C**$_{Ar}$H), 131.1 (**C**$_{Ar}$H), 131.0 (**C**$_{Ar}$H), 130.1 (**C**$_{Ar}$), 129.5 (**C**$_{Ar}$), 129.0 (**C**$_{Ar}$), 127.7 (**C**$_{Ar}$H), 126.7 (**C**$_{Ar}$H), 123.4 (**C**$_{Ar}$), 121.5 (**C**$_{Ar}$), 115.6 (**C**$_{Ar}$H), 52.1 (**C**H), 49.9 (**C**H$_2$), 47.1 (**C**H$_2$), 46.2 (**C**H$_2$), 30.3 (**C**H$_2$).

HRMS (MALDI, DIT+) m/z: calculated for $C_{27}H_{28}N_4O_2$+H: 441.2285 (M^++H); found 441.2306.

UV-Vis ($CHCl_3$), λ_{max} nm (log ε): 390 (3.6).

Ø (Toluene, %): 96.12.

τ (375 nm, Toluene, ns): 5.278 (χ^2: 1.025).

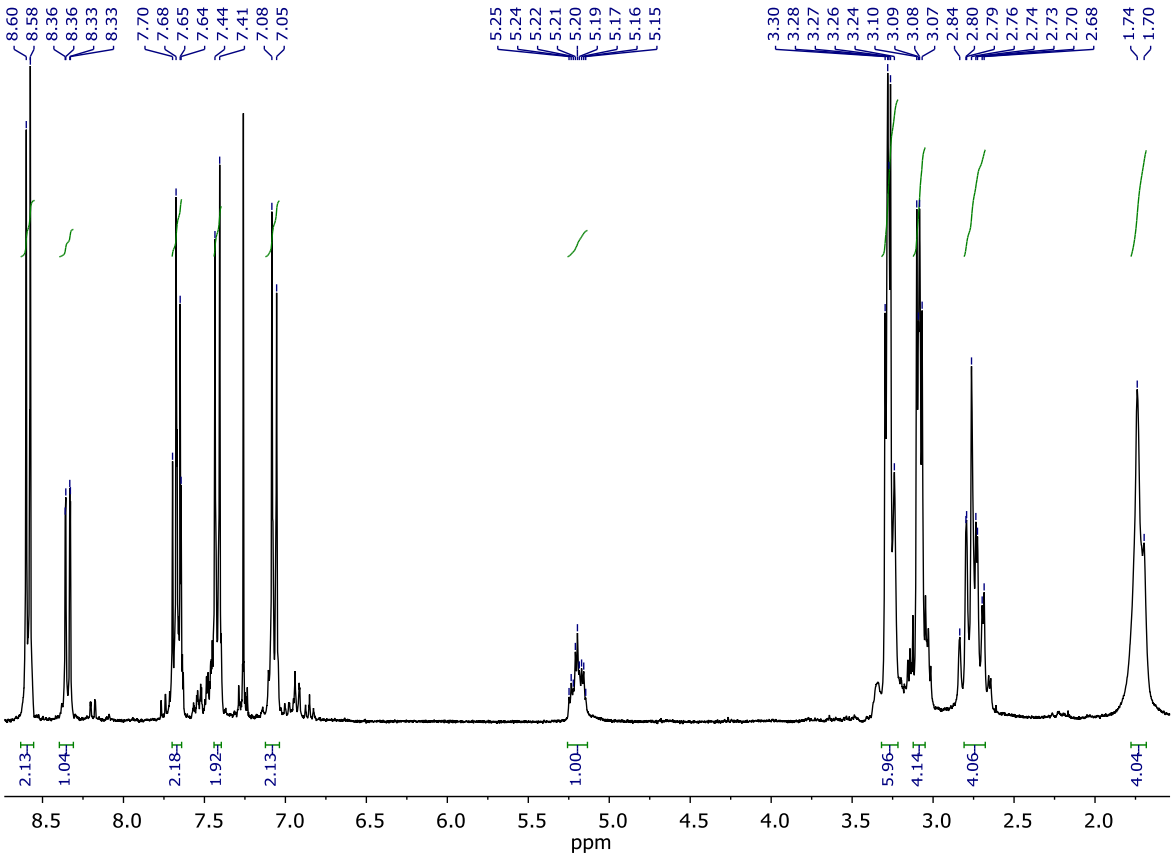

Figure 323. ^{1}H-NMR ($CDCl_3$, 300 MHz) of AR90d.

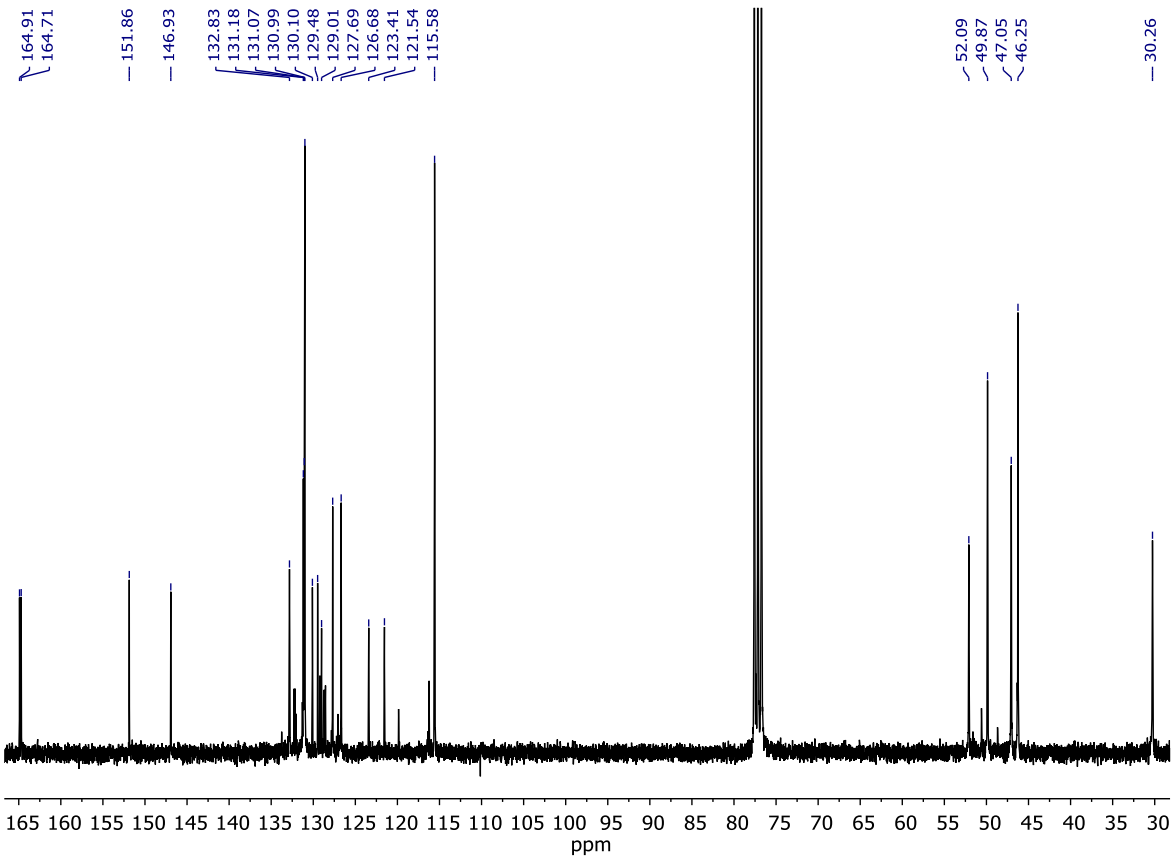

Figure 324. ^{13}C-NMR ($CDCl_3$, 75 MHz) of AR90d.

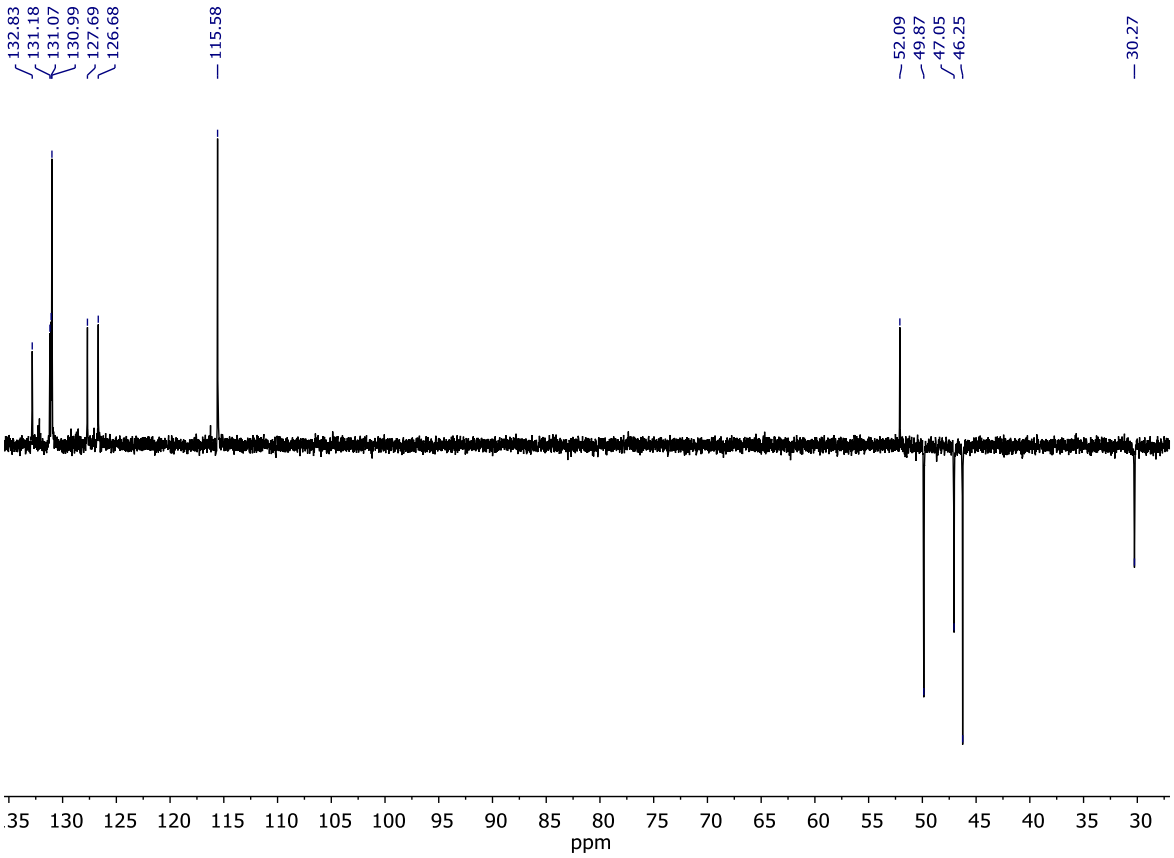

Figure 325. DEPT NMR ($CDCl_3$, 75 MHz) of AR90d.

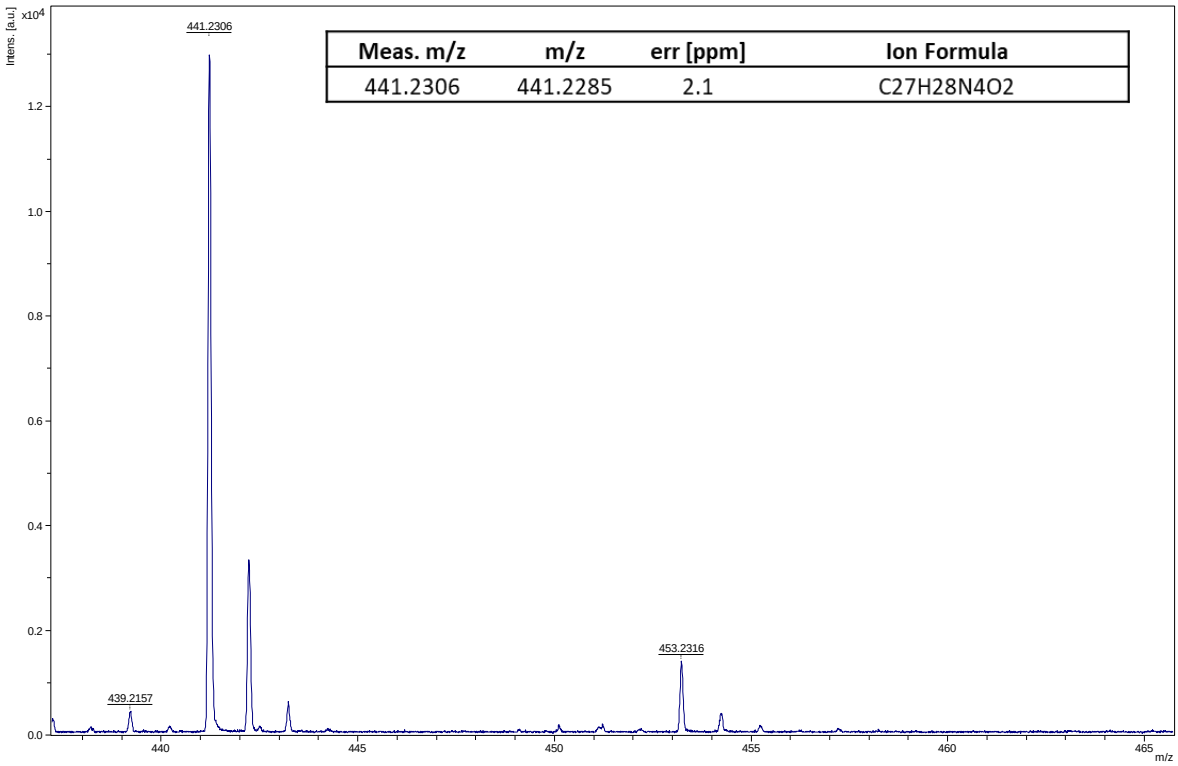

Meas. m/z	m/z	err [ppm]	Ion Formula
441.2306	441.2285	2.1	C27H28N4O2

Figure 326. HRMS (MALDI, DIT+) of AR90d.

Solvatochromism:

The concentration of the compound was 20 µM and the excitation wavelength was 385 nm.

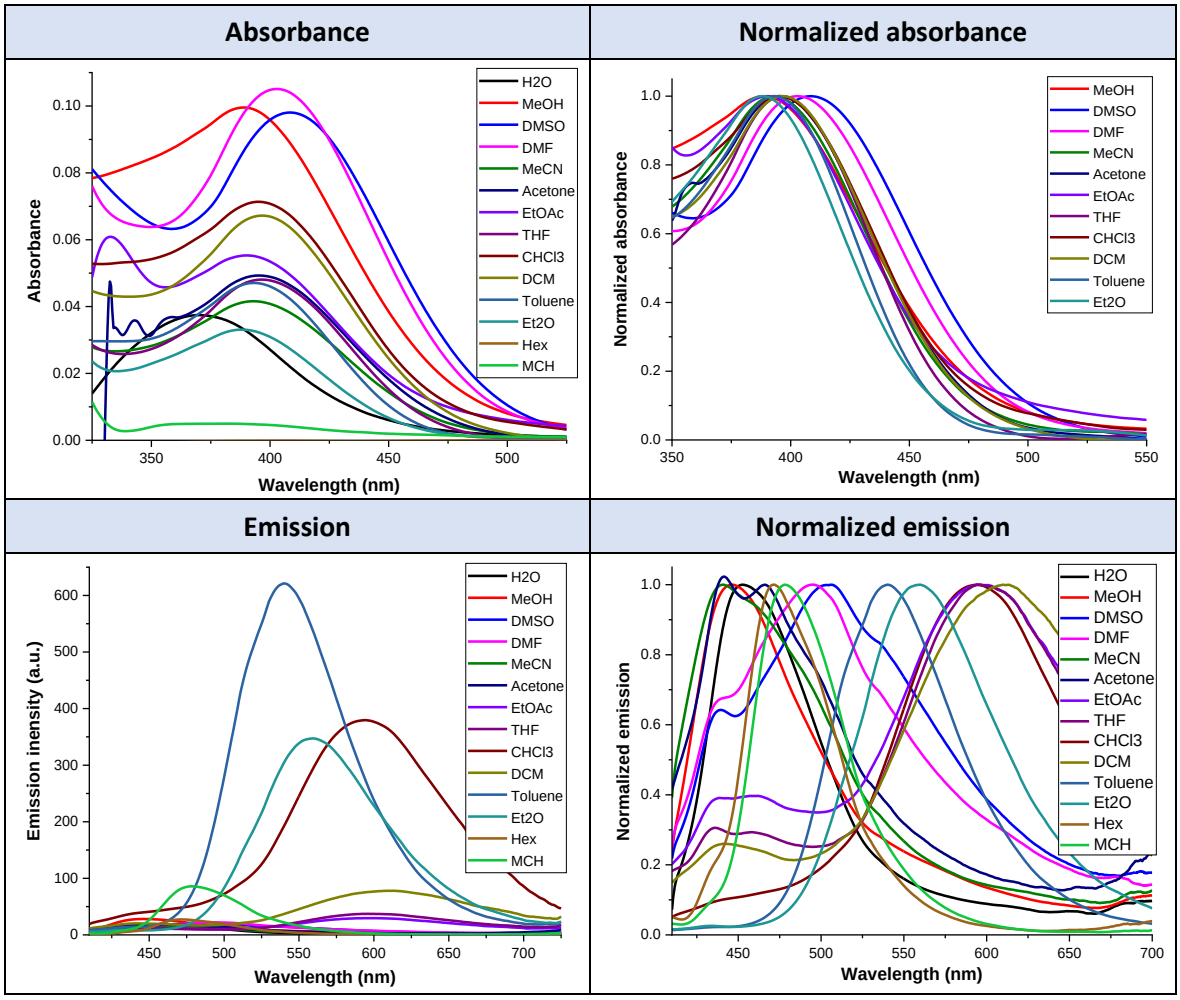

Figure 327. Solvatochromism of AR90d.

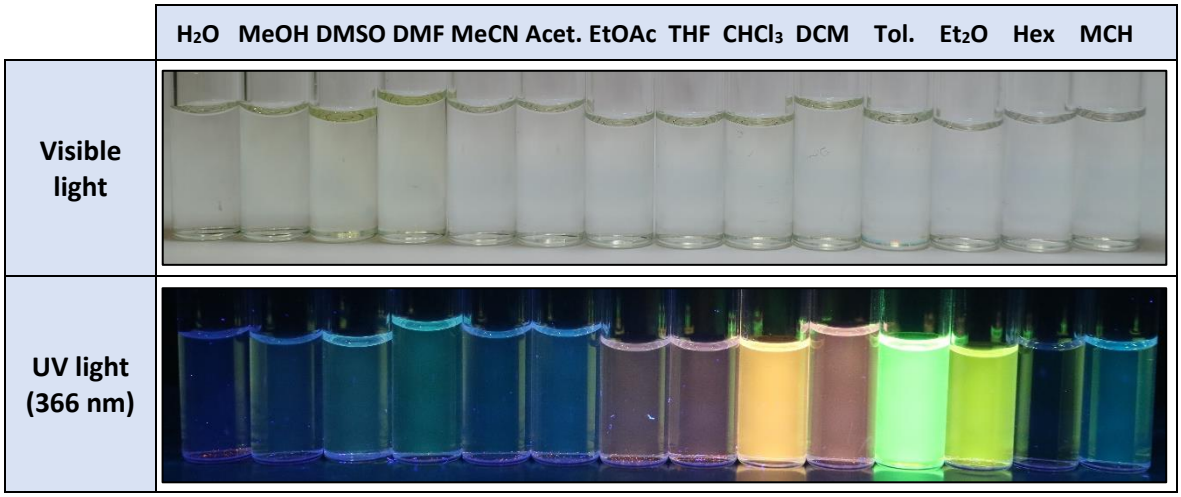

Figure 328. Solvatochromism of AR90d under visible and 366 nm light.

Fluorescence decay lifetime (τ):

The solvent used was toluene. The concentration of the compound was 20 µM.

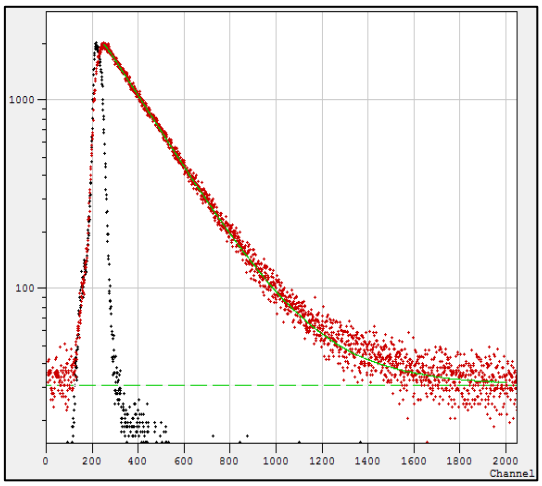

Figure 329. Fluorescence decay lifetime of AR90d.

Water acceptance test:

The solvent used was MeOH and the concentration of the compound was 20 µM.

	R	5%	10%	20%	30%	40%	50%	60%	70%	80%	90%
Visible light	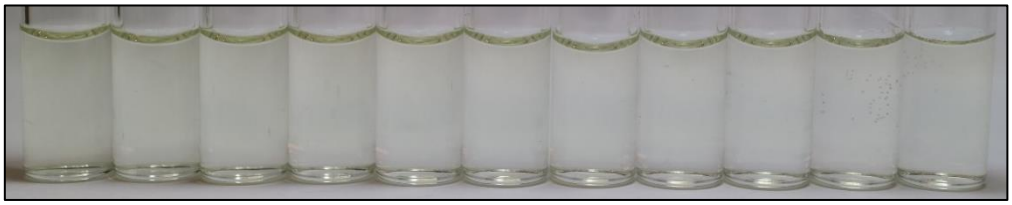										
UV light (366 nm)	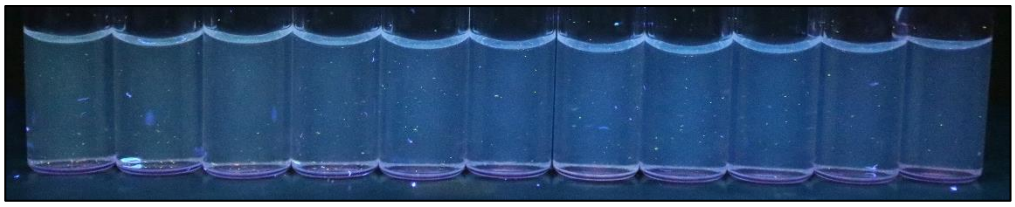										

Figure 330. Water acceptance test of AR90d under visible (up) and UV (down) light.

From 20% water, there was a slight increase in emission intensity.

pH test:

The amount of water for the performance of this test was 20%. The concentration of the compound was 20 µM and the solvent used was MeOH.

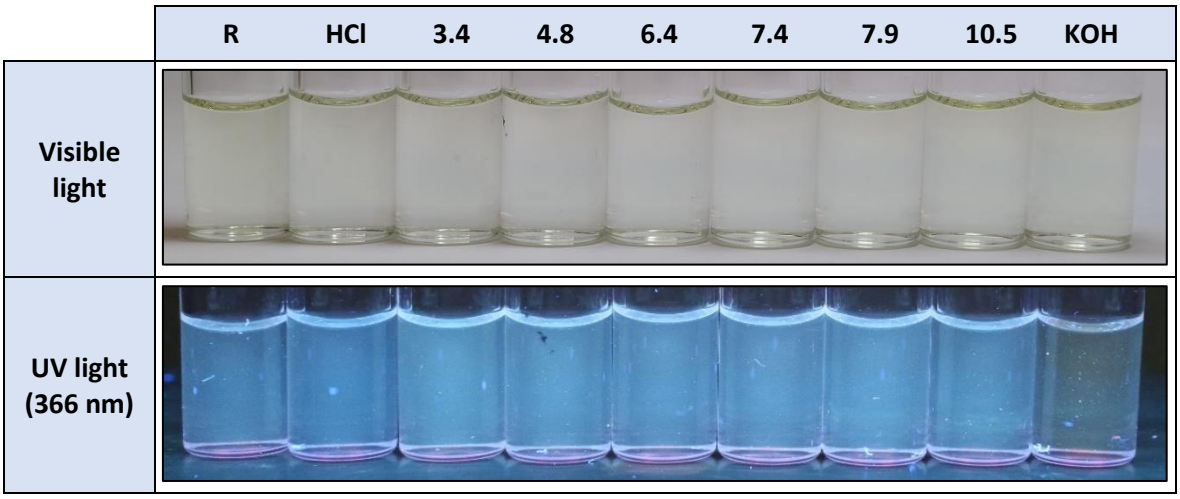

Figure 331. pH test of AR90d under visible (up) and UV (down) light.

The most important change was the fluorescence quenched at very basic pH.

Cations and anions test:

The concentration of the compound was 20 µM and the solvent used was MeOH.

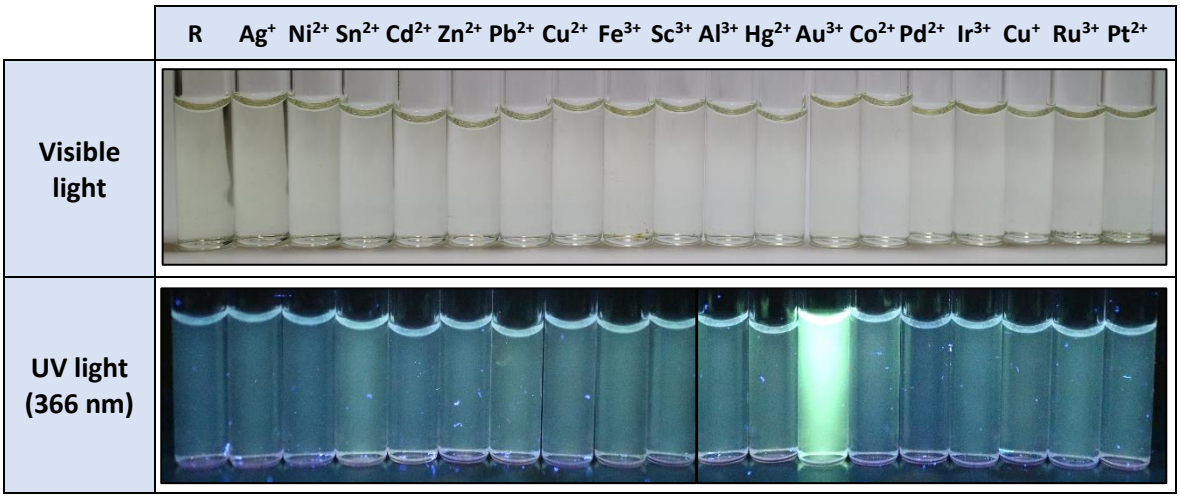

Figure 332. Cations test of AR90d under visible (up) and UV (down) light.

The most significant change was the green color acquired by the fluorescence when was confronted with Au^{3+}.

The concentration of the compound was 20 µM and the solvent used was MeOH.

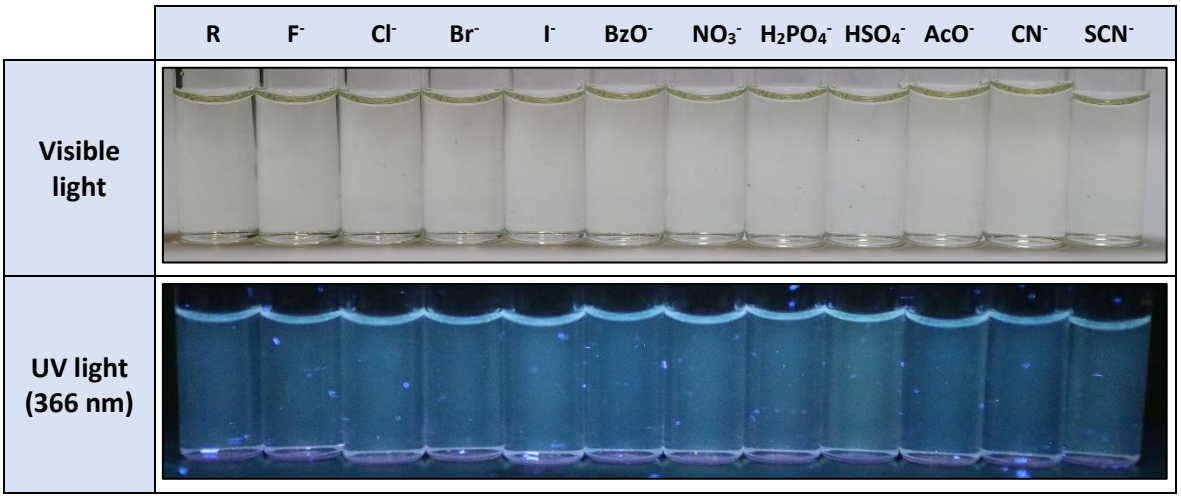

Figure 333. Anions test of AR90d under visible (up) and UV (down) light.

No significant changes were observed.

Oxidant and reductant reagents test:

The solvent used was THF and concentration of the compound was 20 µM.

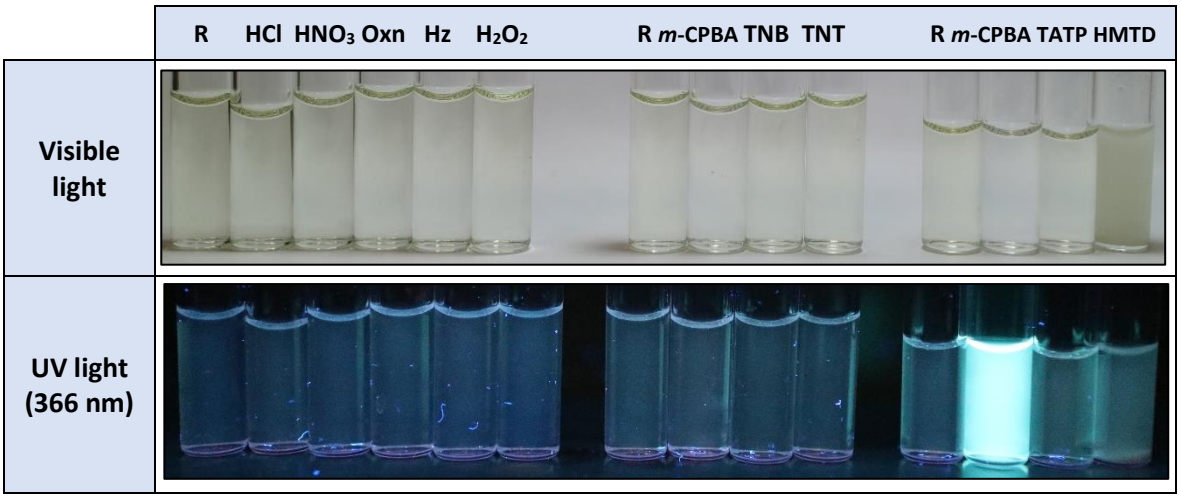

Figure 334. Oxidant and reductant reagents test of AR90d under visible (up) and UV (down) light.

No significant changes were observed except for a strong increase in fluorescence against *m*-CPBA.

Previous solvents test:

In order to determine the fluorescence variation of the compound under study in the presence of TATP, some test were carried out for the probe in 9 different solvents. The AR90d concentration was 20 µM and the TATP was added in excess (7 mg in each vial). All the test were performed at room temperature and the photographs were taken immediately after the addition of TATP and again after 72 hours.

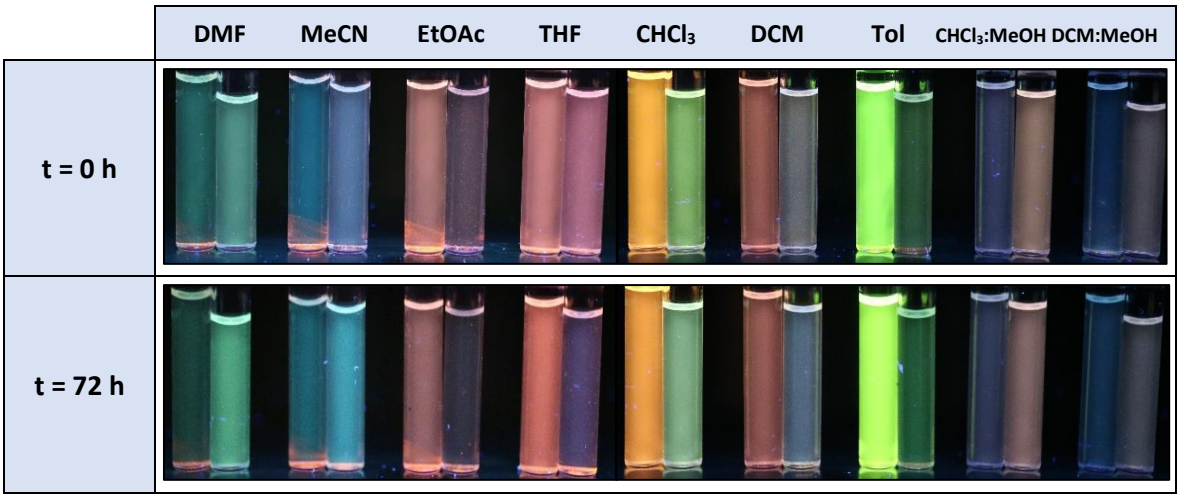

Figure 335. Pairs of AR90d (left) and AR90d with excess of TATP (right) in different solvents at time 0 h (up) and 72 h (down).

The biggest fluorescence changes were seen in $CHCl_3$, toluene and $CHCl_3$:MeOH (9:1) so these were the chosen solvents to perform the kinetic studies and TATP titrations experiments.

Solvents test with TATP:

For all solvents, the working concentration of AR90d was 2.5 µM, the excitation wavelength was 385 nm and the temperature for all test was 25ºC.

In the kinetic studies, TATP was in excess (20 mM) and the fluorescence emission measurements were made during the subsequent minutes at 5 min, 10 min and 30 min time intervals. In the titration, the TATP concentration was between 0 and 35000 µM and it was added directly as solid. The measurements were carried out inmediately after the adittion of the probe.

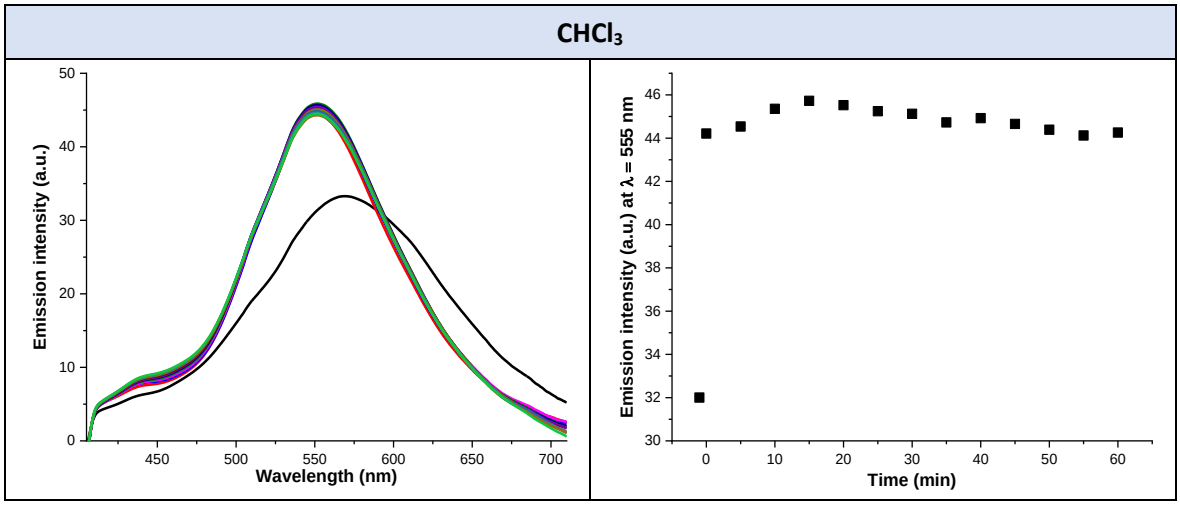

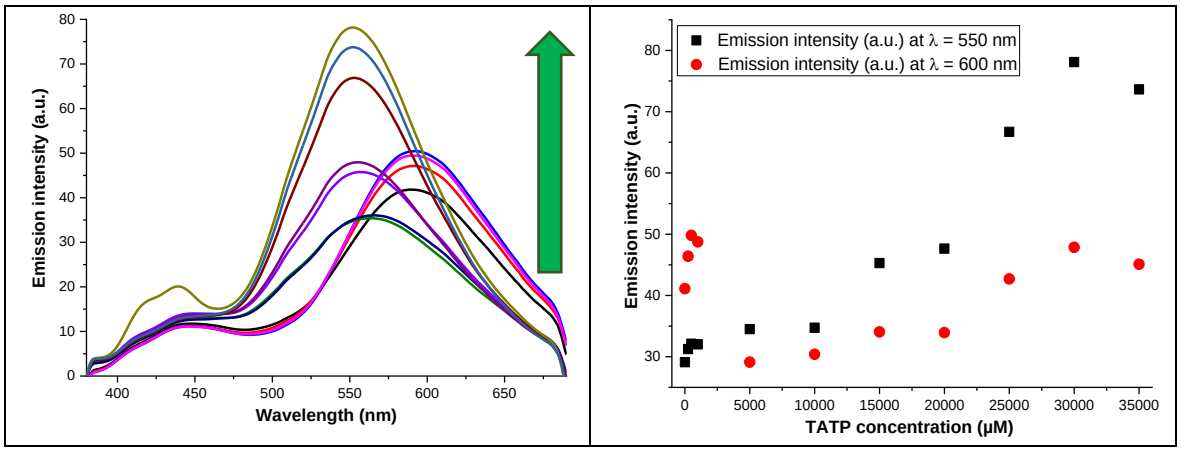

Figure 336. Study of AR90d with TATP in $CHCl_3$. Kinetic study (up left) and profile as function as time at 555 nm (up right) in presence of TATP excess. Titration (down left) and fluorescence profile at 550 nm and 600 nm simultaneusly (down right) under increasing concentrations of TATP.

There was a change in the emission intensity band immediately after adding TATP. According to the fluorescence spectra, the LOD was somewhere between 1000 and 5000 µM.

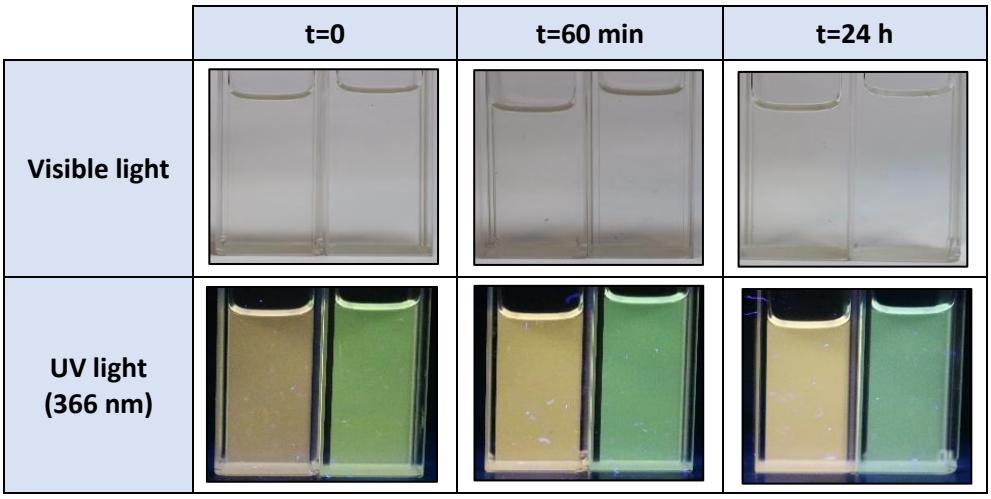

Figure 337. Kinetic study at different times under visible (up) and UV (down) light in CHCl3. In each photo, left vial was contained the probe and right vial was contained the probe and an excess of TATP.

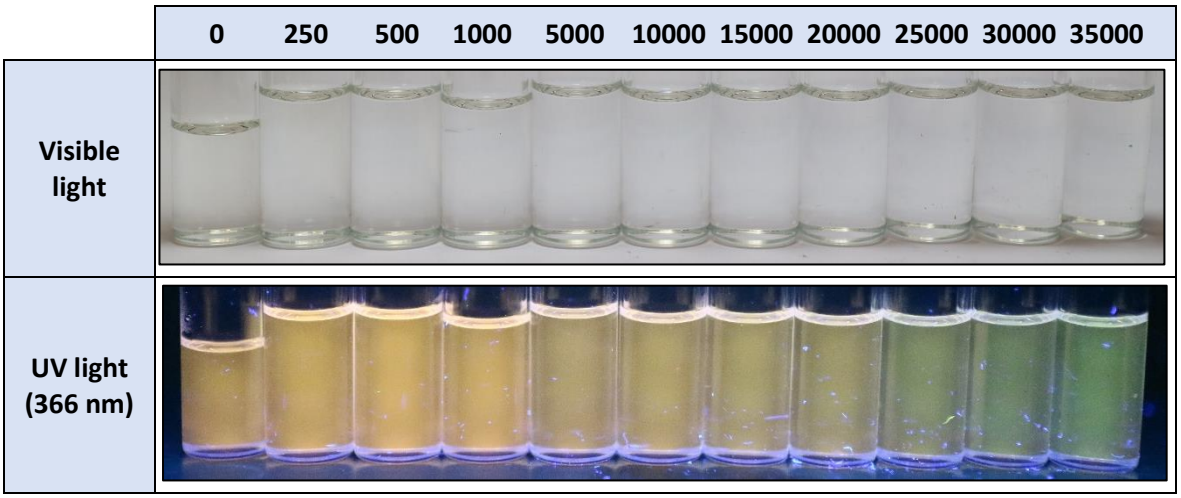

Figure 338. Titration of AR90d with an excess of TATP under visible (up) and UV (down) light in CHCl3.

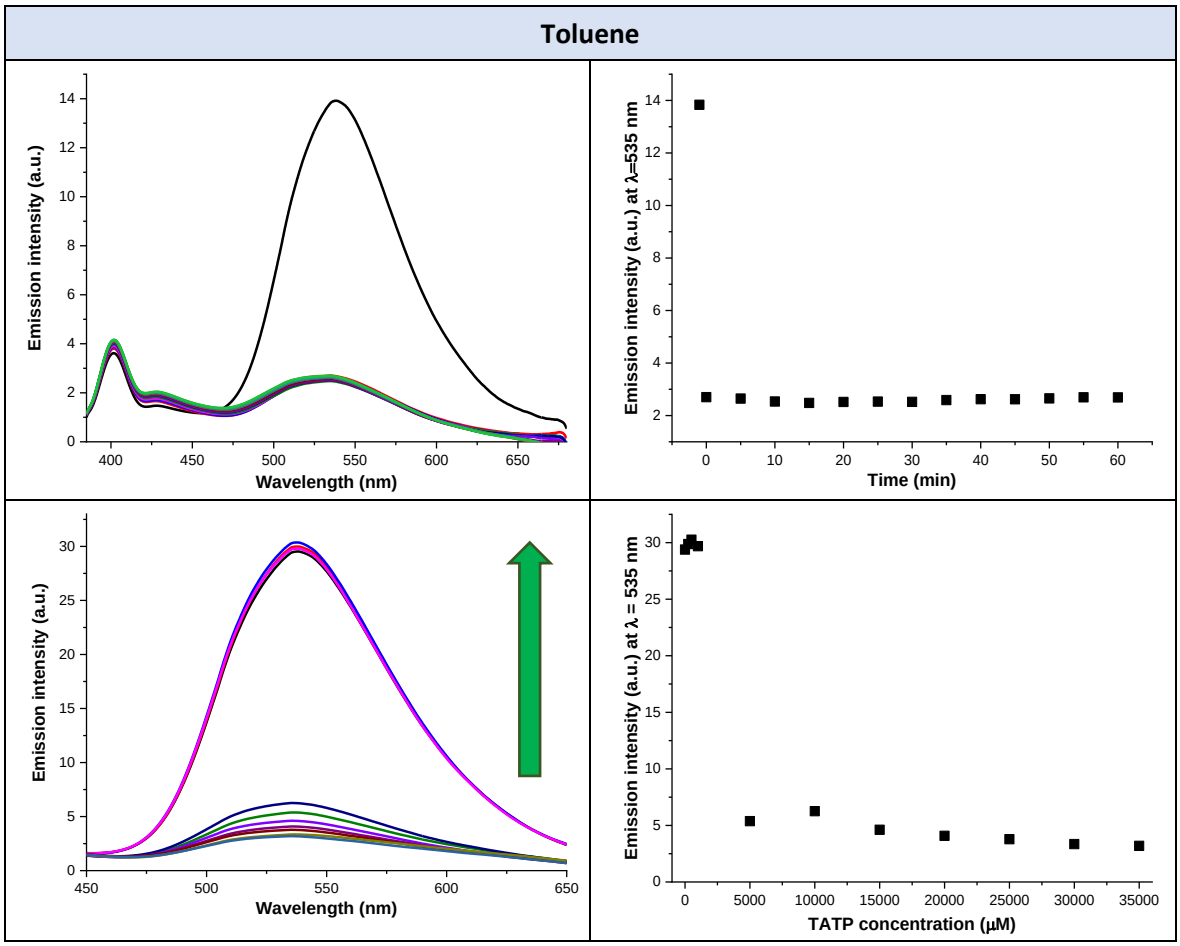

Figure 339. Study of AR90d with TATP in toluene. Kinetic study (up left) and profile as function as time at 555 nm (up right) in presence of TATP excess. Titration (down left) and fluorescence profile at 535 nm (down right) under increasing concentrations of TATP.

There was a marked decrease change in the emission intensity band immediately after adding TATP. According to the fluorescence spectra, the LOD was somewhere between 1000 and 5000 µM with a decrease of the intensity.

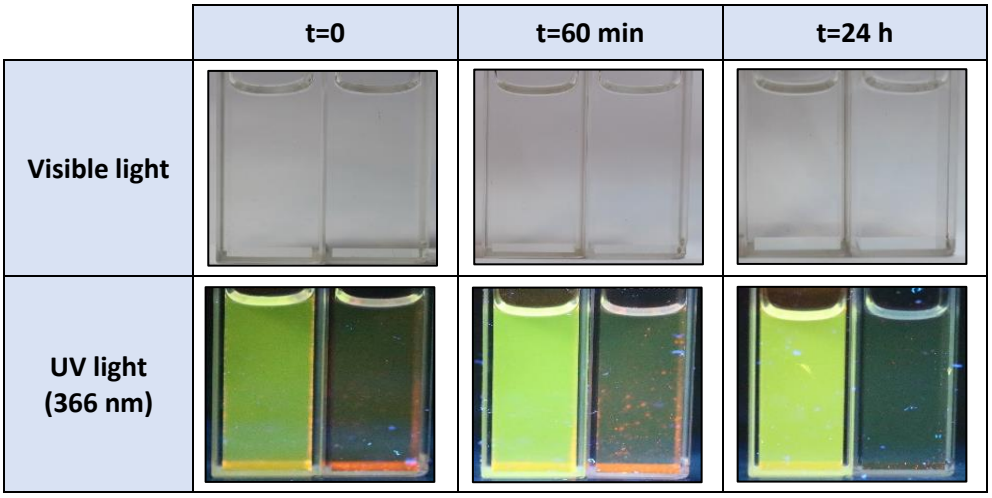

Figure 340. Kinetic study at different times under visible (up) and UV (down) light in toluene. In each photo, left vial was contained the probe and right vial was contained the probe and an excess of TATP.

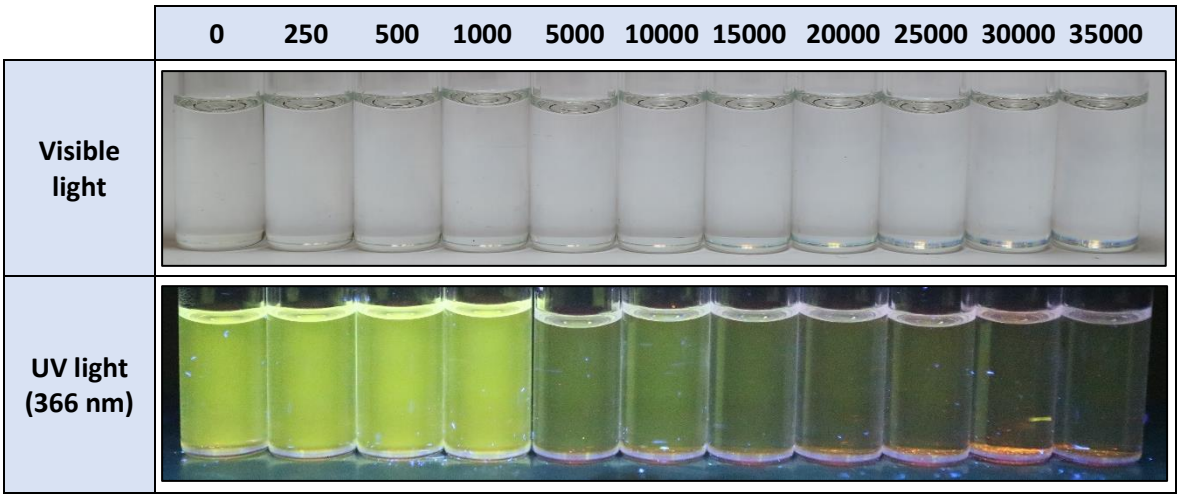

Figure 341. Titration of AR90d with an excess of TATP under visible (up) and UV (down) light in toluene.

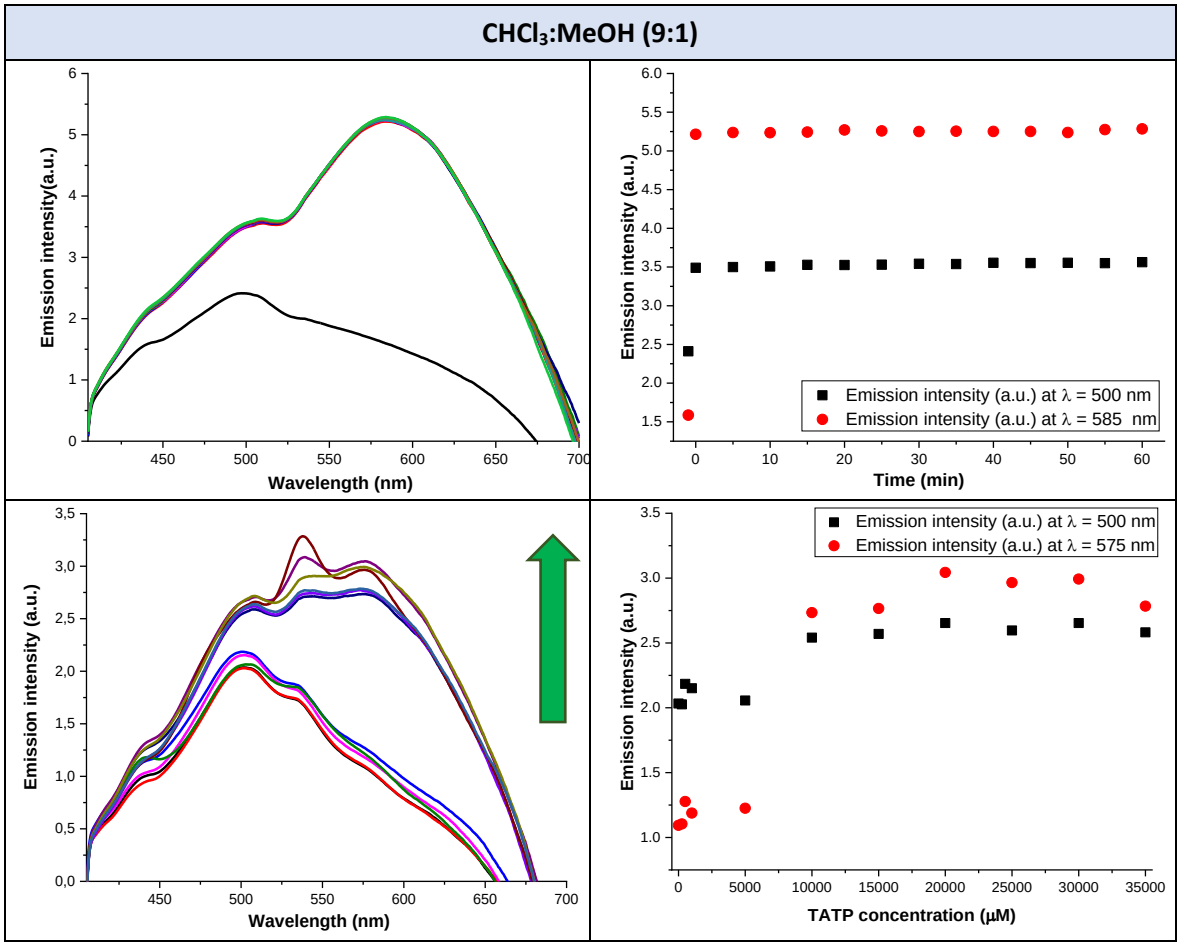

Figure 342. Study of AR90d with TATP in $CHCl_3$:MeOH (9:1). Kinetic study (up left) and profile as function as time at 500 nm and 585 nm simultaneusly (up right) in presence of TATP excess. Titration (down left) and fluorescence profile at 500 nm and 575 nm simultaneously (down right) under increasing concentrations of TATP.

There was a increase in the emission intensity band immediately after adding TATP but emission intensity was remained stable. According to the fluorescence spectra, the LOD was somewhere between 1000 and 5000 µM with a increase of the intensity.

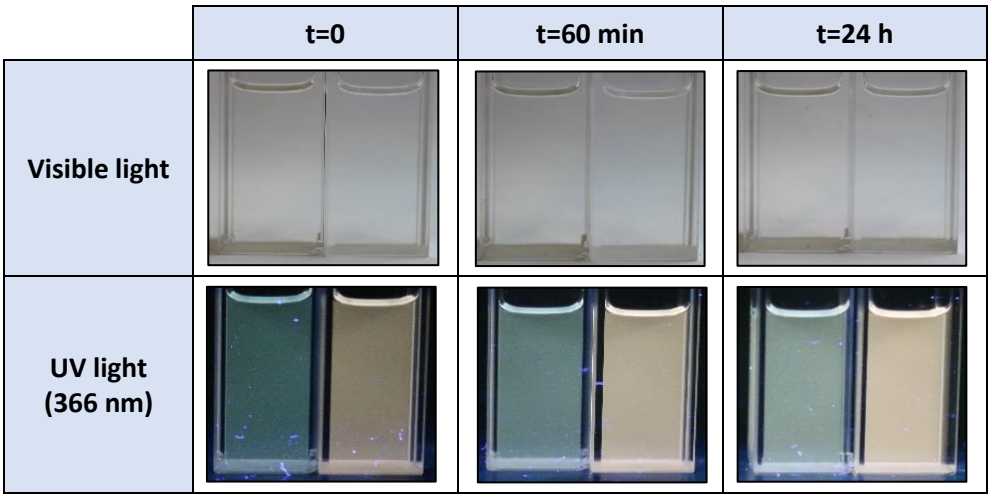

Figure 343. Kinetic study at different times under visible (up) and UV (down) light in $CHCl_3$:MeOH (9:1). In each photo, left vial was contained the probe and right vial was contained the probe and an excess of TATP.

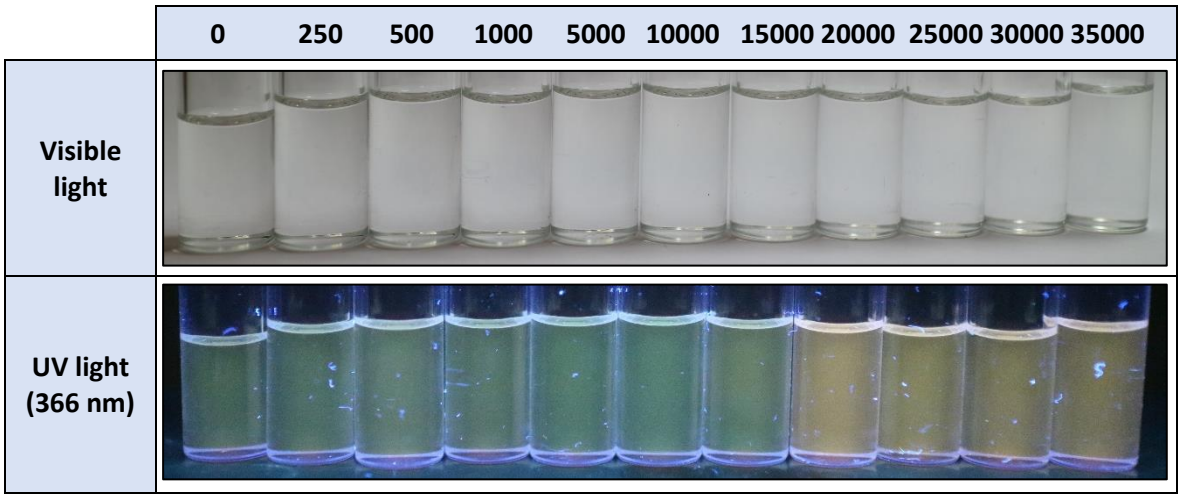

Figure 344. Titration of AR90d with an excess of TATP under visible (up) and UV (down) light in $CHCl_3$:MeOH (9:1).

Because of the low sensitivity the study was discontinued.

Synthesis of 2-(pinacolylboronate)indolo[3,2,1-jk]carbazole (AR66)

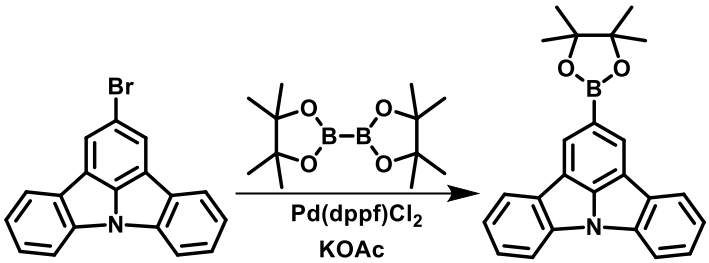

100 mg of 2-bromoindolo[3,2,1-jk]carbazole (0.31 mmol), 131 mg of potassium acetate (1.34 mmol) and 96 mg of bis(pinacolyl)boronate (0.38 mmol) were dissolved in 5 ml of dry 1,4-dioxane under nitrogen atmosphere. Then, 18 mg fo $Pd(dppf)Cl_2$ (0.005 mmol) were added and the obtained solution was stirred at 75°C for 24 hours. Afterwards, the solvent was evaporated under reduce pressure and 50 ml of water were added. The mixture was extracted three times with DCM (3×100 ml). Organic extracts were combined, dried over anhidrous Na_2SO_4 and the solvent was evaporated under reduced pressure. The organic solid obtained was purified by column chromatographic (SiO_2, DCM:Hx 50% v/v), getting 91 mg of a pale yellow solid, 80% yield.

m.p.: 227-231°C.

IR (ATR, cm^{-1}): 3051, 2976-2851 (C-H), 1602, 1585, 1447 (C-O), 1399, 1375, 1330 (C-B), 1309, 1262, 1216, 1135 (C-N), 1037, 959, 866, 780, 741, 684, 660, 552, 421.

^{1}H-NMR (300 MHz, $CDCl_3$) δ (ppm): 8.59 (s, 2H, 2×$\mathbf{H_{Ar}}$), 8.14 (ddd, *J* = 7.8, 1.1, 0.7 Hz, 2H, 2×$\mathbf{H_{Ar}}$), 7.86 (dt, *J* = 7.8, 0.7 Hz, 2H, 2×$\mathbf{H_{Ar}}$), 7.55 (m, 2H, 2×$\mathbf{H_{Ar}}$), 7.36 (td, *J* = 7.8, 1.0 Hz, 2H), 1.48 (s, 12H, 4×C$\mathbf{H}_3$).

^{13}C-NMR (75MHz, $CDCl_3$) δ (ppm): 145.9 ($\mathbf{C}_{Ar}$), 138.8 ($\mathbf{C}_{Ar}$), 130.0 ($\mathbf{C}_{Ar}$), 126.7 ($\mathbf{C}_{Ar}$H), 126.3 ($\mathbf{C}_{Ar}$H), 123.2 ($\mathbf{C}_{Ar}$H), 121.9 ($\mathbf{C}_{Ar}$H), 118.3 ($\mathbf{C}_{Ar}$), 112.2 ($\mathbf{C}_{Ar}$H), 83.9 (**Cq**), 25.0 ($\mathbf{C}H_3$).

HRMS (MALDI, DIT+) m/z: calculated for $C_{24}H_{22}BNO_2$: 367.1725 (M^+); found 367.1742.

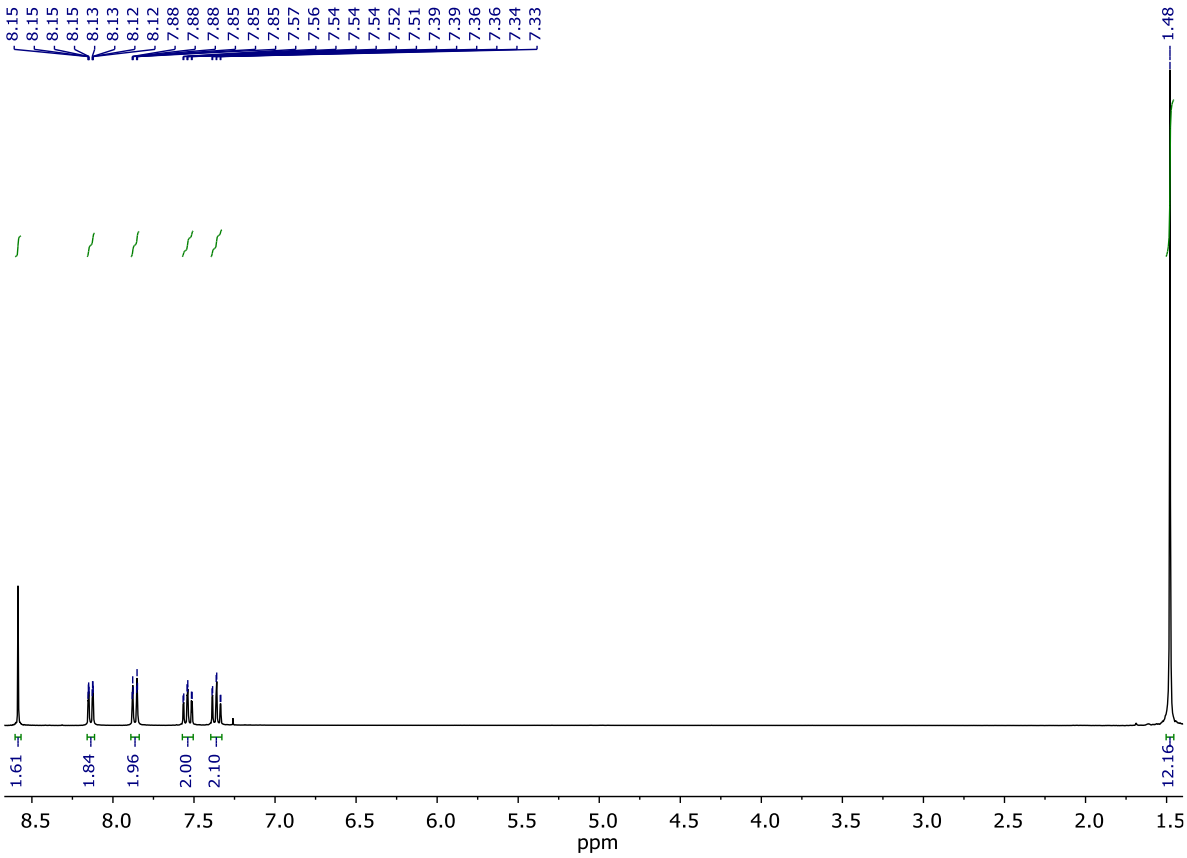

Figure 345. ^{1}H-NMR ($CDCl_3$, 300 MHz) of AR66.

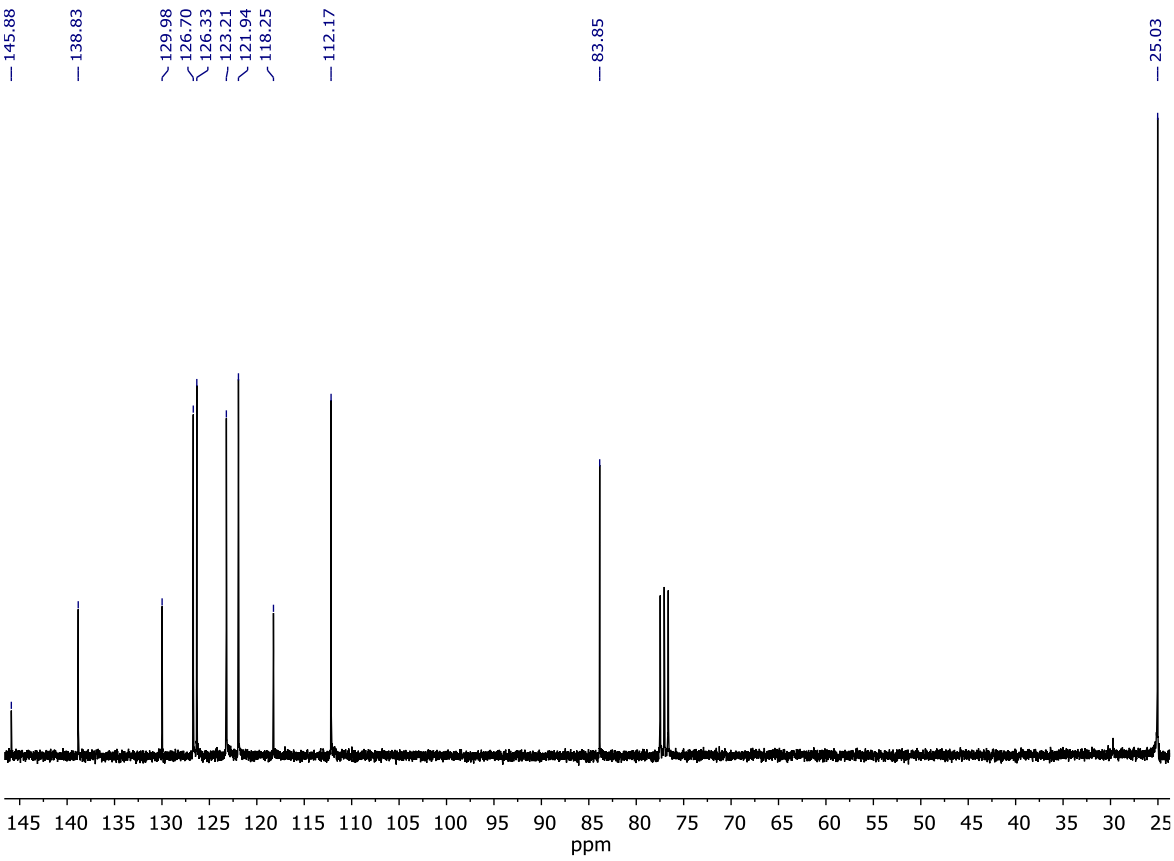

Figure 346. ^{13}C-NMR ($CDCl_3$, 75 MHz) of AR66.

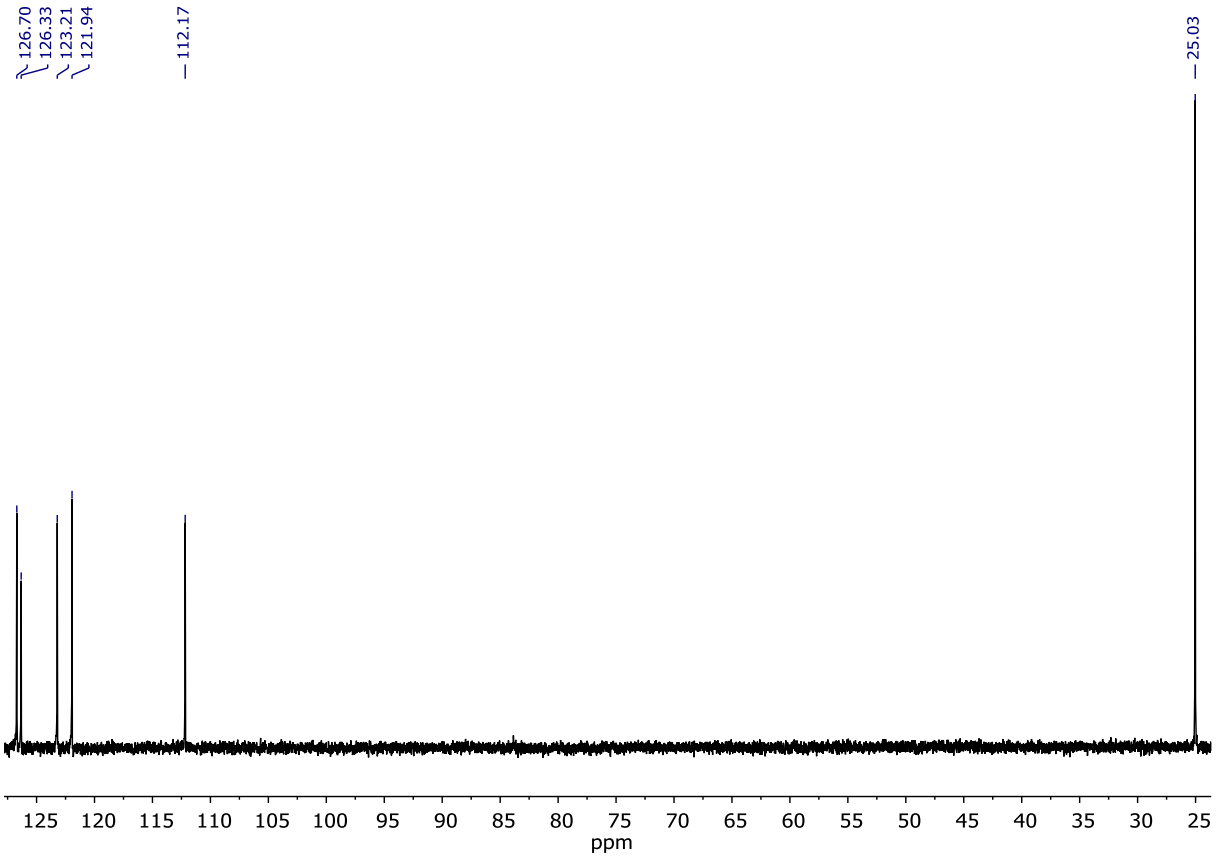

Figure 347. DEPT NMR ($CDCl_3$, 75 MHz) of AR66.

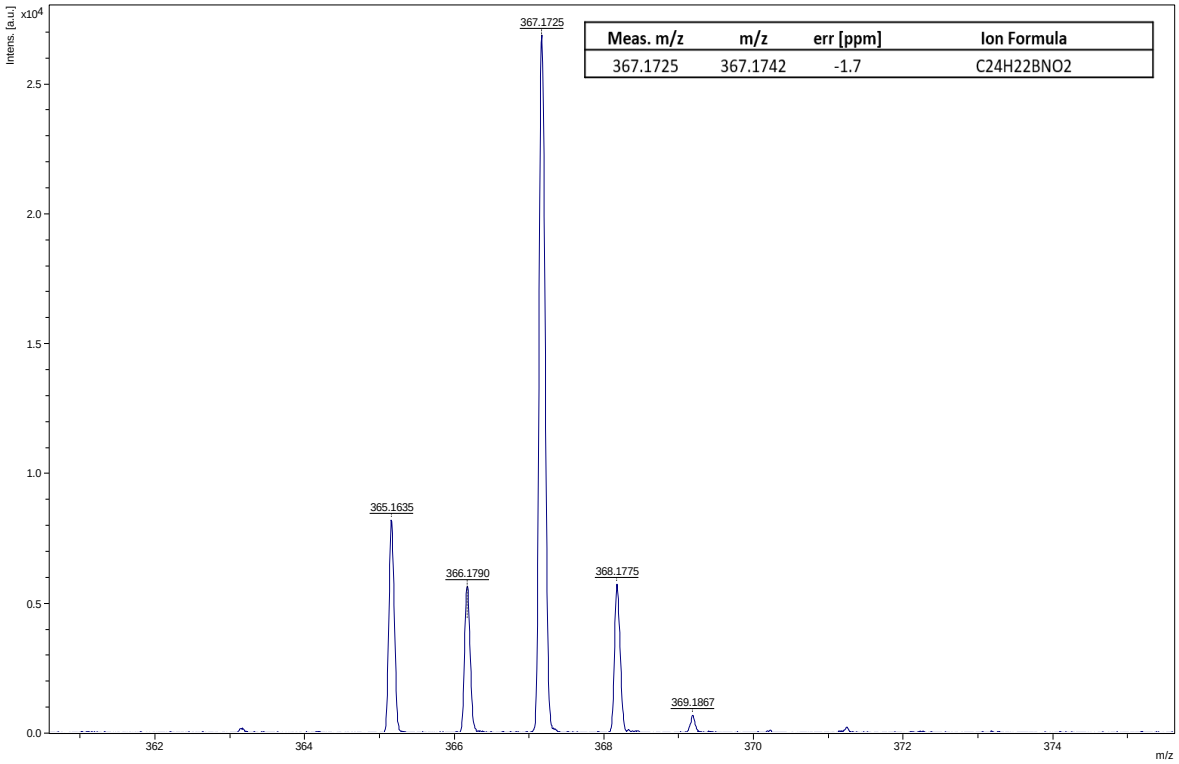

Meas. m/z	m/z	err [ppm]	Ion Formula
367.1725	367.1742	-1.7	C24H22BNO2

Figure 348. HRMS (MALDI, DIT-) of AR66.

Synthesis of *N*-(*N'*-Boc-piperidin-4-yl)-4-(indolo[3,2,1-jk]carbazol-2-yl)naphthalene-1,8-dicarboxylmonoimide (AR67p)

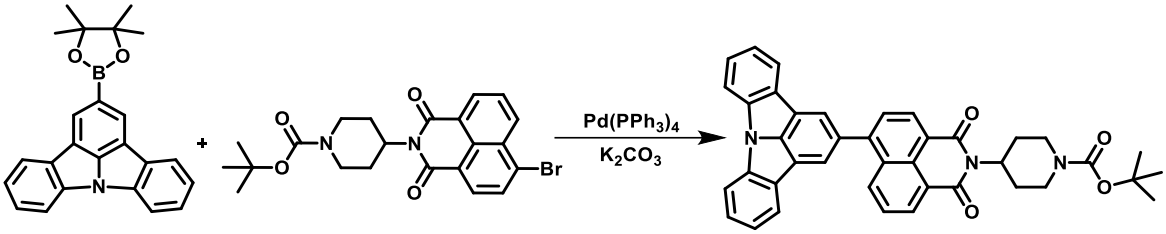

100 mg of 2-(pinacolylboronate)indolo[3,2,1-jk]carbazole (AR66, 0.27 mmol), 131 mg of *N*-(Boc-piperidin-4-yl)-4-bromonaphthalene-1,8-dicarboxylmonoimide (AR43p, 0.29 mmol), 105 mg of potassium carbonate (0.99 mmol) and 12 mg of $Pd(PPh_3)_4$ (0.01 mmol) were dissolved in a mixture of toluene:*n*-butanol:water (4:1:2 ml) under nitrogen atmosphere. The mixture was stirred 105°C for 24 hours and, afterwards, 50 ml of water were added and the resulting mixture was extracted three times with DCM (3×100 ml). The organic extracts were combined, dried over anhidrous Na_2SO_4 and the solvent was evaporated under reduced pressure. As a result, the product was obtained and purified by column chromatographic (SiO_2, DCM:MeOH 0.3% v/v), obtaining 144 mg of orange solid, 86% yield.

m.p.: 249-251°C.

IR (ATR, cm^{-1}): 3057-2848, 1696 (C=O), 1656 (C=O), 1582, 1450 (C-O), 1423, 1351, 1336, 1240, 1162 (C-N), 1145, 1103, 1031, 977, 885, 777, 734, 681, 666, 535, 457, 421.

^{1}H-NMR (300 MHz, $CDCl_3$) δ (ppm): 8.66 – 8.53 (m, 2H, 2×**H$_{Ar}$**), 8.26 (dd, *J* = 8.5, 1.1 Hz, 1H, **H$_{Ar}$**), 8.19 – 8.07 (m, 4H, 4×**H$_{Ar}$**), 7.94 (d, *J* = 8.1 Hz, 2H, 2×**H$_{Ar}$**), 7.82 (d, *J* = 7.5 Hz, 1H, **H$_{Ar}$**), 7.64 – 7.58 (m, 3H, 3×**H$_{Ar}$**), 7.38 (td, *J* = 7.7, 1.1 Hz, 2H, 2×**H$_{Ar}$**), 5.31-5.21 (m, 1H, C**H**), 4.34 (s, 2H, C**H$_2$**), 2.96-2.75 (m, 4H, 2×C**H$_2$**), 1.77-1.68 (m, 2H, C**H$_2$**), 1.52 (s, 9H, 3×C**H$_3$**).

^{13}C-NMR (75MHz, $CDCl_3$) δ (ppm): 164.7 (C=O), 164.5 (C=O), 154.7 (**C$_{Ar}$**), 148.5 (**C$_{Ar}$**), 143.6 (**C$_{Ar}$**), 139.2 (**C$_{Ar}$**), 133.9 (**C$_{Ar}$**), 133.0 (**C$_{Ar}$**H), 131.1 (**C$_{Ar}$**H), 130.8 (**C$_{Ar}$**H), 129.6 (**C$_{Ar}$**), 128.8 (**C$_{Ar}$**H), 127.4 (**C$_{Ar}$**H), 126.8 (**C$_{Ar}$**H), 123.4 (**C$_{Ar}$**H), 122.7 (**C$_{Ar}$**H), 121.4 (**C$_{Ar}$**H), 118.5 (**C$_{Ar}$**), 112.4 (**C$_{Ar}$**H), 79.5 (**Cq**), 51.82 (**C**H), 43.8 (**C**H$_2$), 28.52 (**C**H$_3$), 28.35 (**C**H$_2$).

HRMS (MALDI, DIT-) m/z: calculated for $C_{40}H_{33}N_3O_4$: 619.2466 (M^-); found 619.2429.

UV-Vis ($CHCl_3$), λ_{max} nm (log ε): 368 (4.3).

Ø (Toluene, %): 84.60.

τ (375 nm, MCH, ns): 2.622 (χ^2: 1.058).

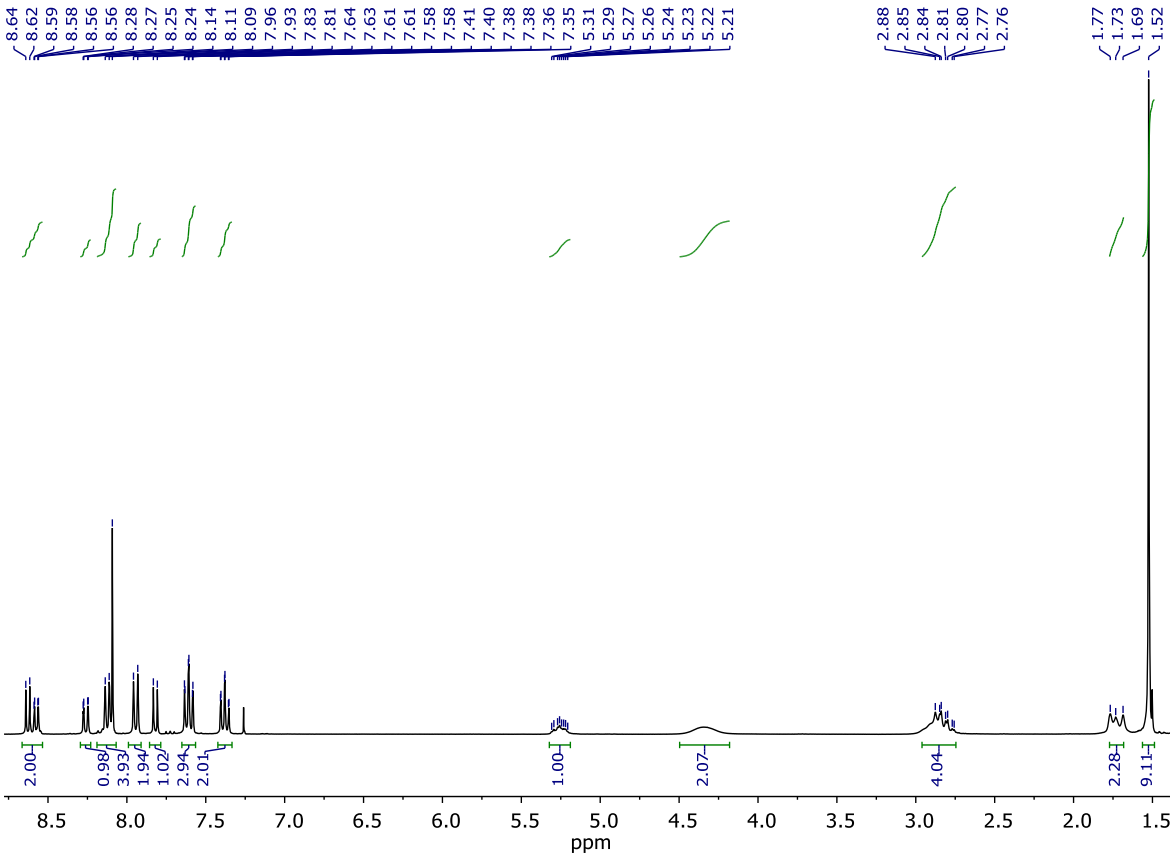

Figure 349. ^{1}H-NMR ($CDCl_3$, 300 MHz) of AR67p.

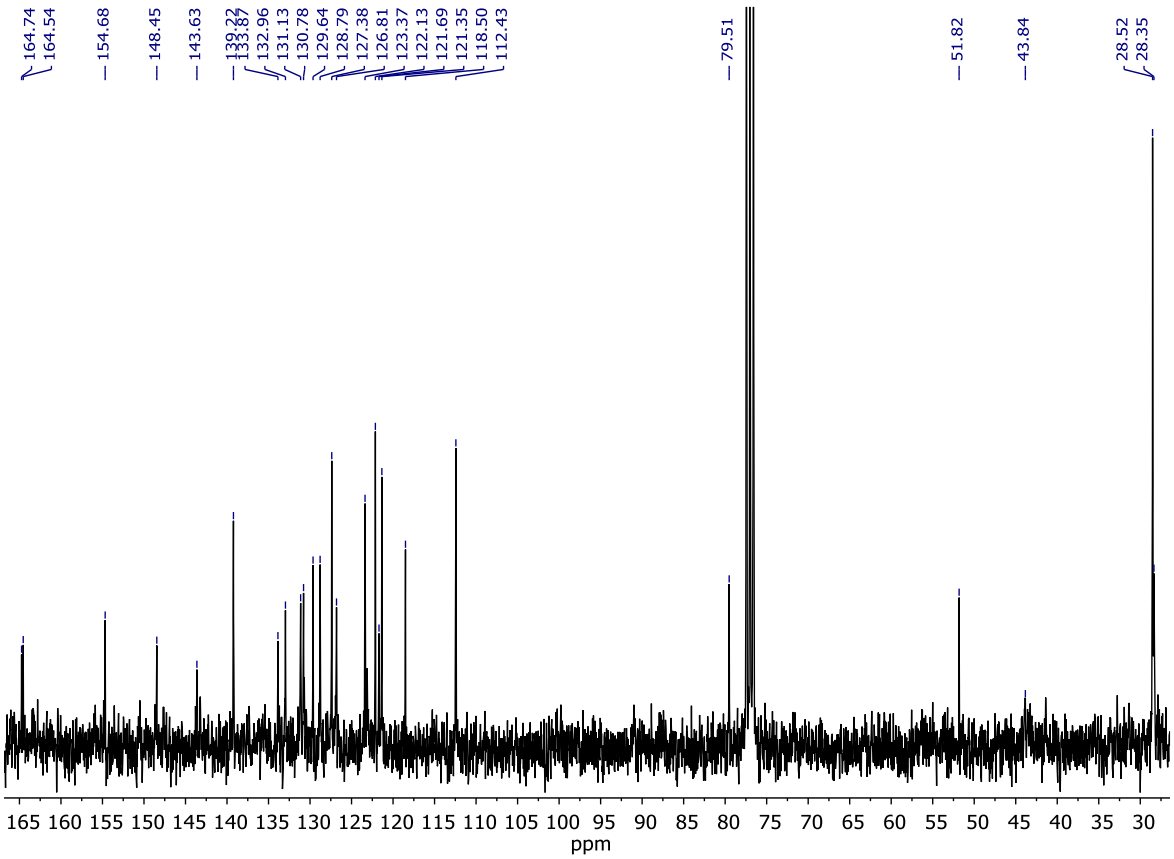

Figure 350. ^{13}C-NMR ($CDCl_3$, 75 MHz) of AR67p.

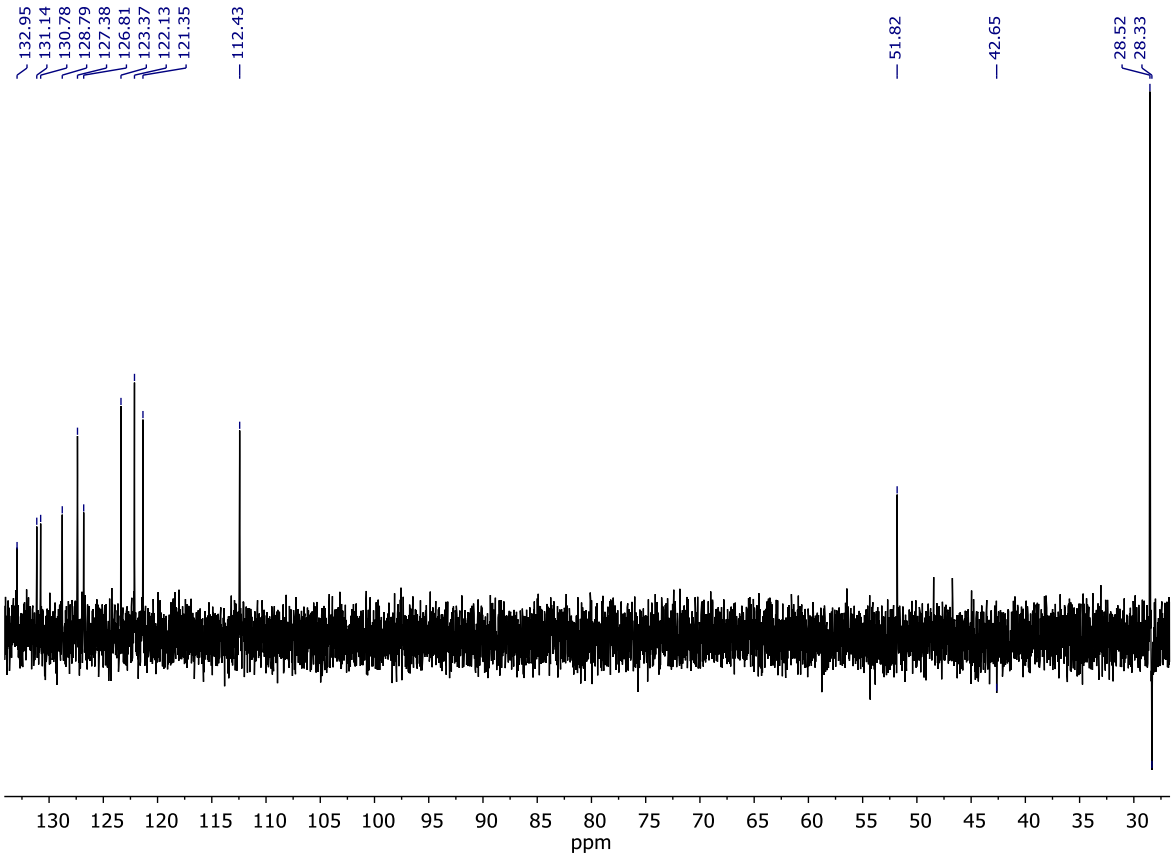

Figure 351. DEPT NMR ($CDCl_3$, 75 MHz) of AR67p.

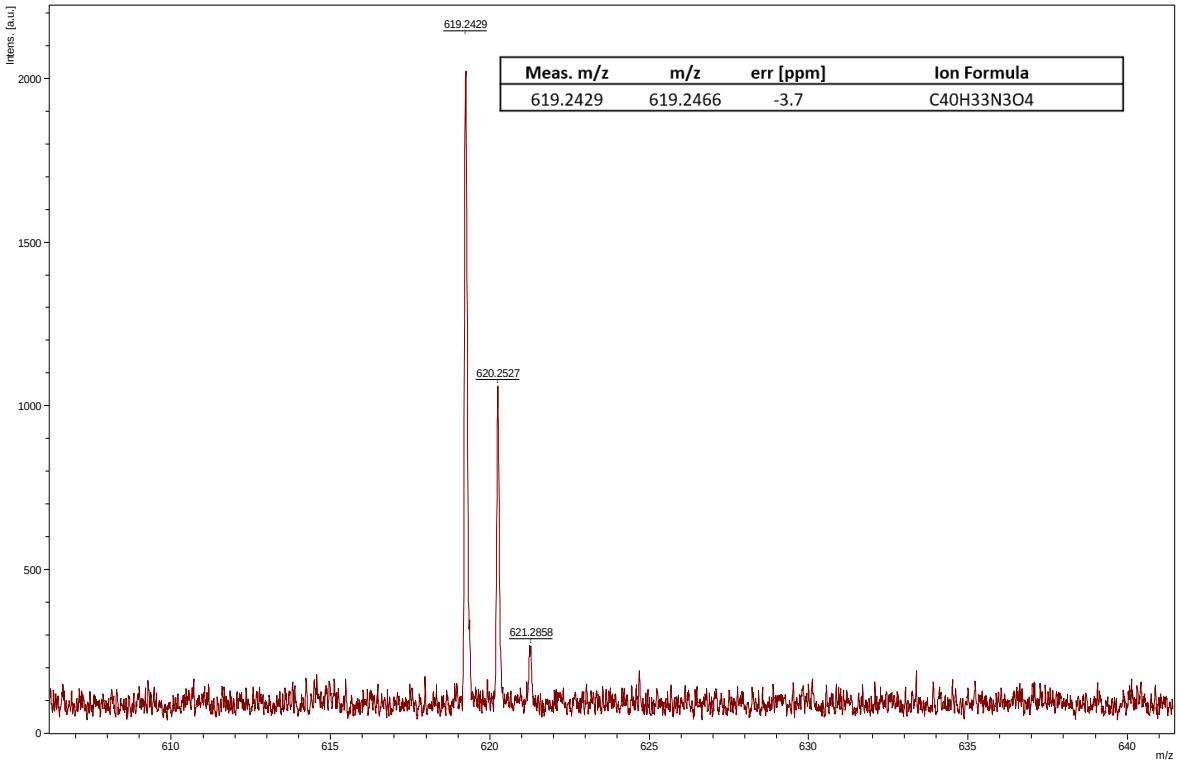

Figure 352. HRMS (MALDI, DIT-) of AR67p.

Solvatochromism:

The concentration of the compound was 10 µM and the excitation wavelength was 360 nm.

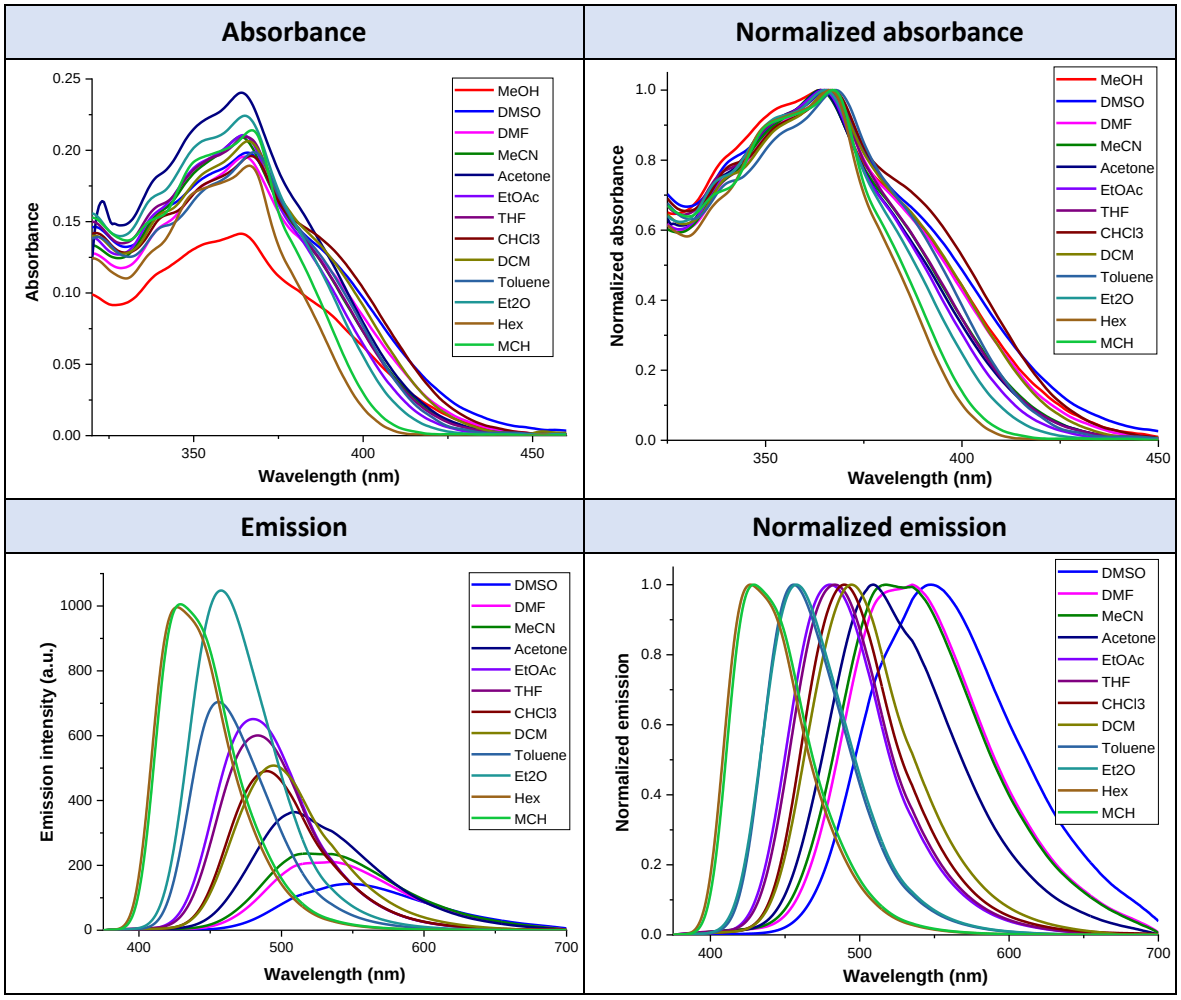

Figure 353. Solvatochromism of AR67p.

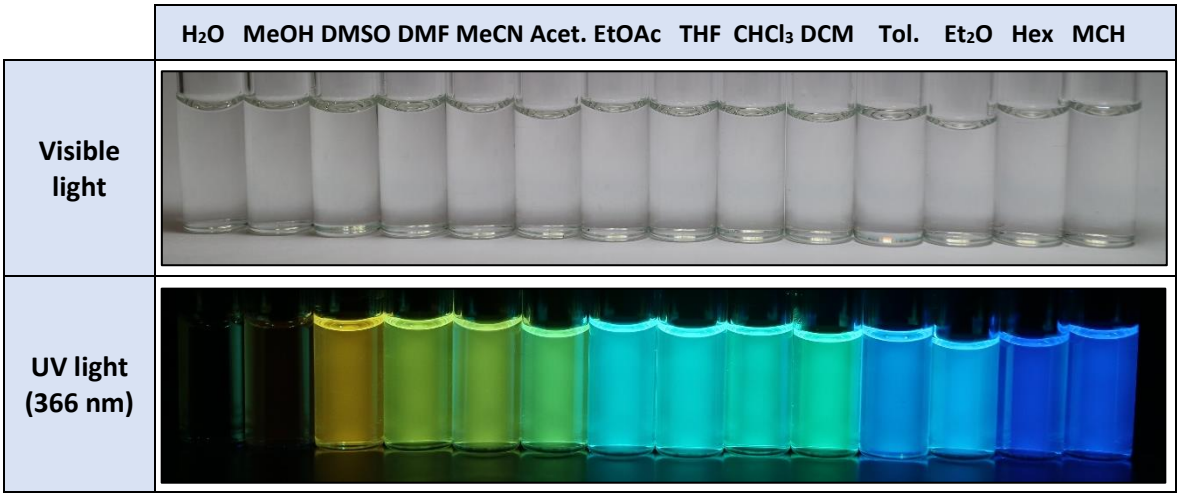

Figure 354. Solvatochromism of AR67p under visible and 366 nm light

Fluorescence decay lifetime (τ):

The solvent used was MCH. The concentration of the compound was 10 µM.

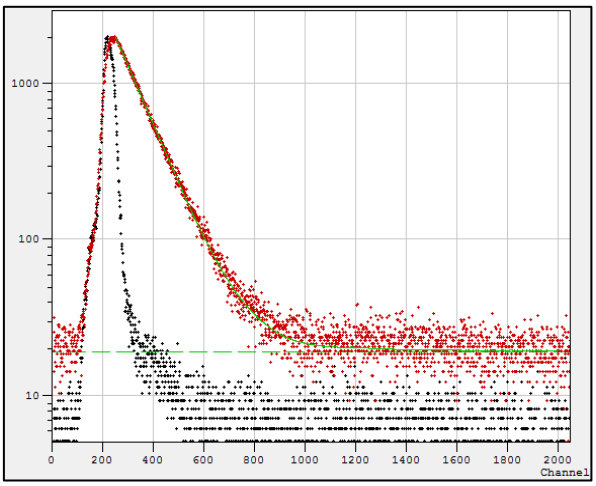

Figure 355. Fluorescence decay lifetime of AR67p.

Water acceptance test:

The solvent used was THF and the concentration of the compound was 10 µM.

	R	5%	10%	20%	30%	40%	50%	60%	70%	80%	90%
Visible light	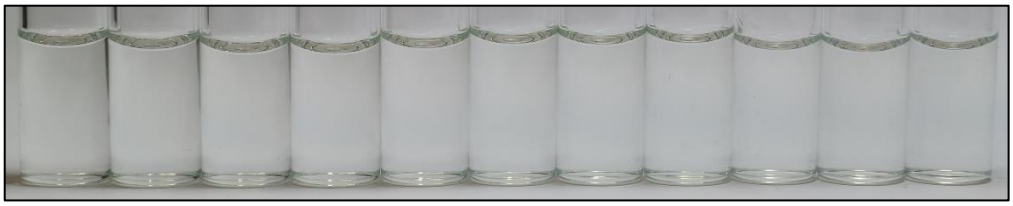										
UV light (366 nm)	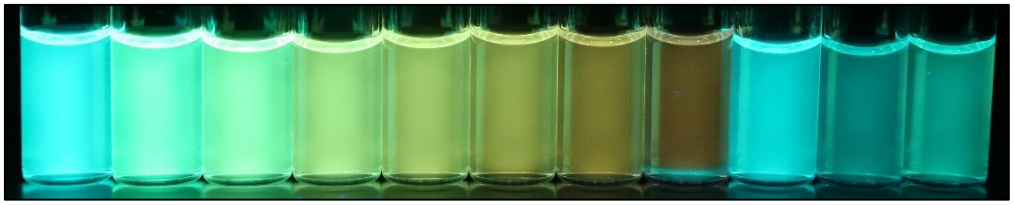										

Figure 356. Water acceptance test of AR67p under visible (up) and UV (down) light.

At 60% water, there was a significant increase in the emission intensity and, at 70% of water, it was decreased again. On the other hand, between 30% and 60% water, the emission maximum was shifted to the yellow region (above 540 nm).

SEM nanoparticles:

AR67p 10% of water	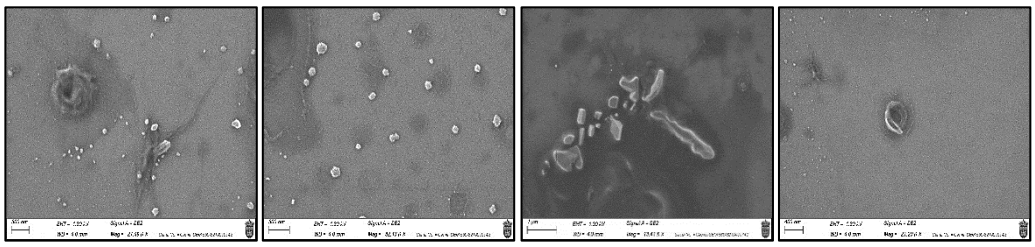

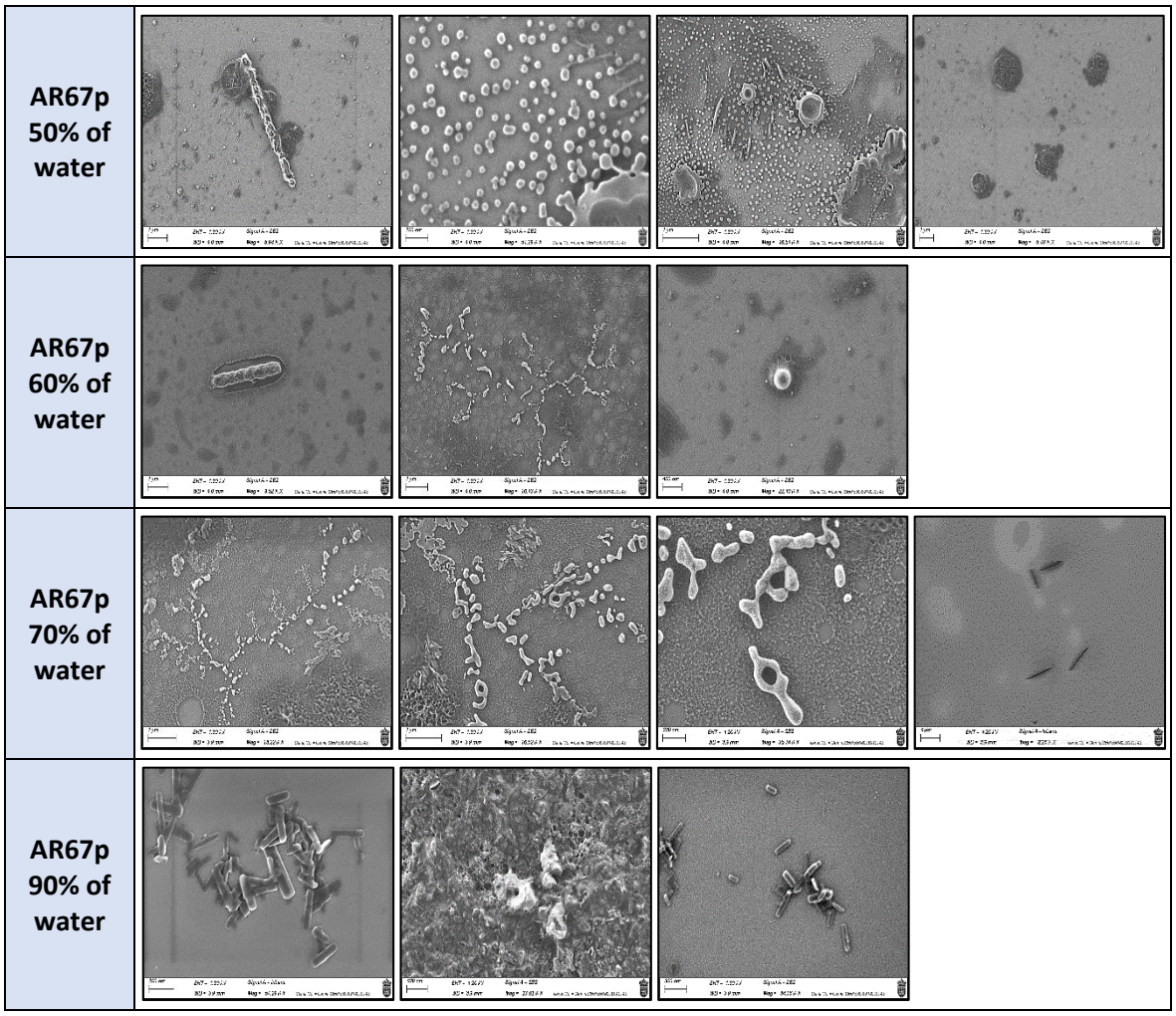

Figure 357. SEM nanoparticles of AR67p in different mixtures of water and THF.

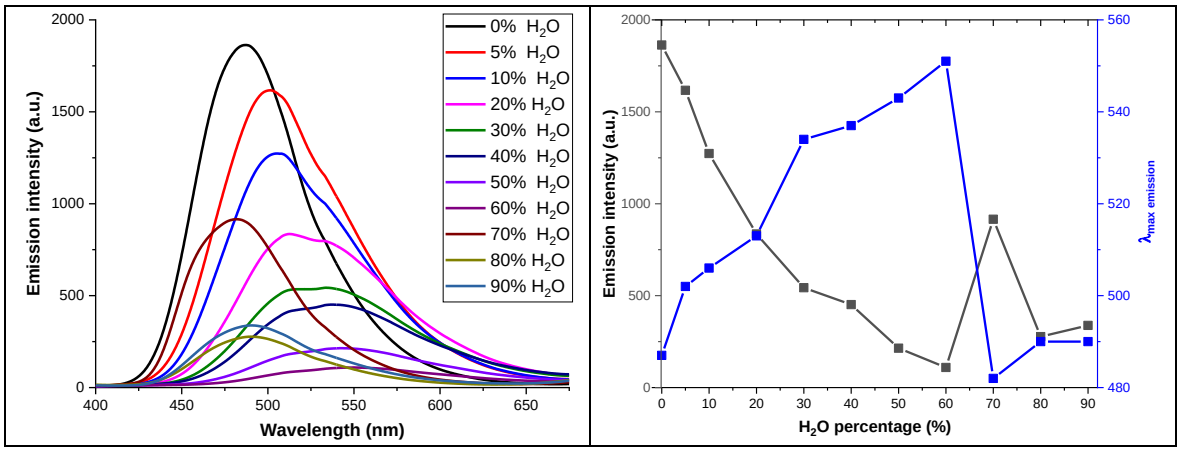

Figure 358. Emission intensity graph (left) and graph of relationship between the emission intensity and the wavelength of the maximum of emission (right) as a function of the amount of water added for AR67p using THF as a solvent.

pH test:

The amount of water for the performance of this test was 50%. The concentration of the compound was 10 µM and the solvent used was THF.

	R	HCl	3.4	4.8	6.4	7.4	7.9	10.5	KOH
Visible light	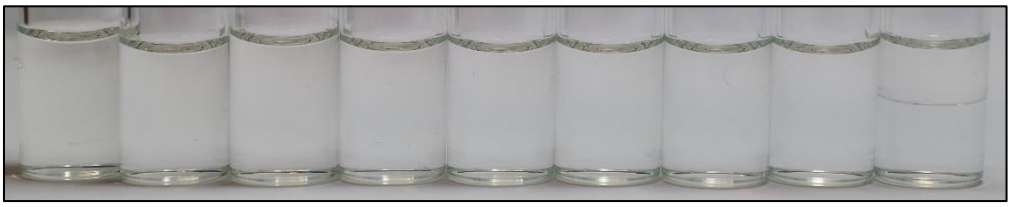								
UV light (366 nm)	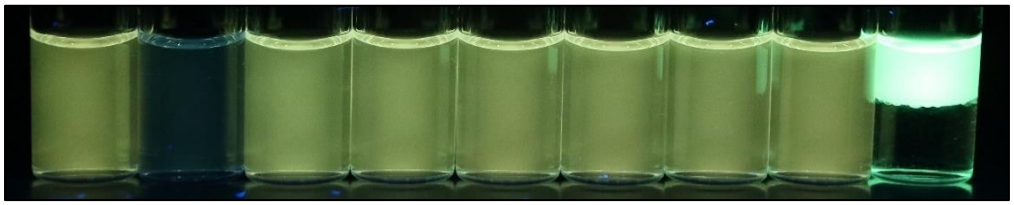								

Figure 359. pH test of AR67p under visible (up) and UV (down) light.

The most important change was the fluorescence quenched at very acidic pH.

Cations and anions test:

The concentration of the compound was 10 µM and the solvent used was THF.

	R	Ag^{+}	Ni^{2+}	Sn^{2+}	Cd^{2+}	Zn^{2+}	Pb^{2+}	Cu^{2+}	Fe^{3+}	Sc^{3+}	Al^{3+}	Hg^{2+}	Au^{3+}	Co^{2+}	Pd^{2+}	Ir^{3+}	Cu^{+}	Ru^{3+}	Pt^{2+}
Visible light	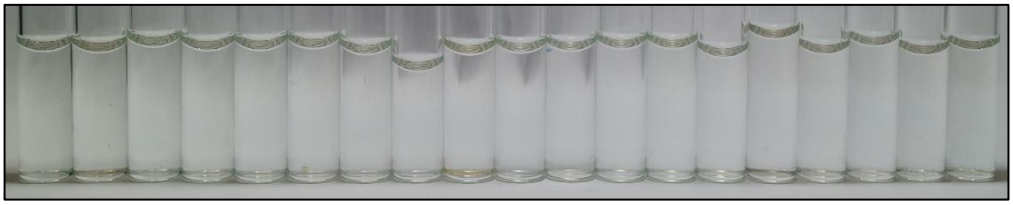																		
UV light (366 nm)	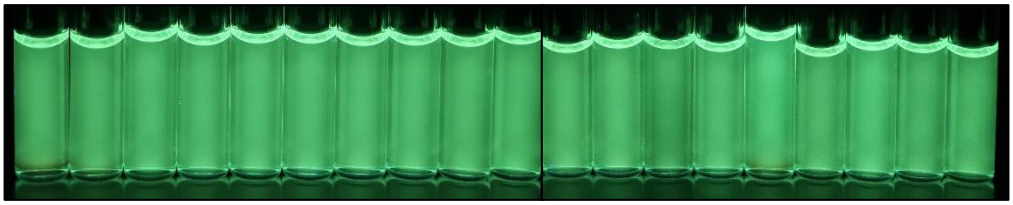																		

Figure 360. Cations test of AR67p under visible (up) and UV (down) light.

No significant changes were observed.

The concentration of the compound was 10 µM and the solvent used was THF.

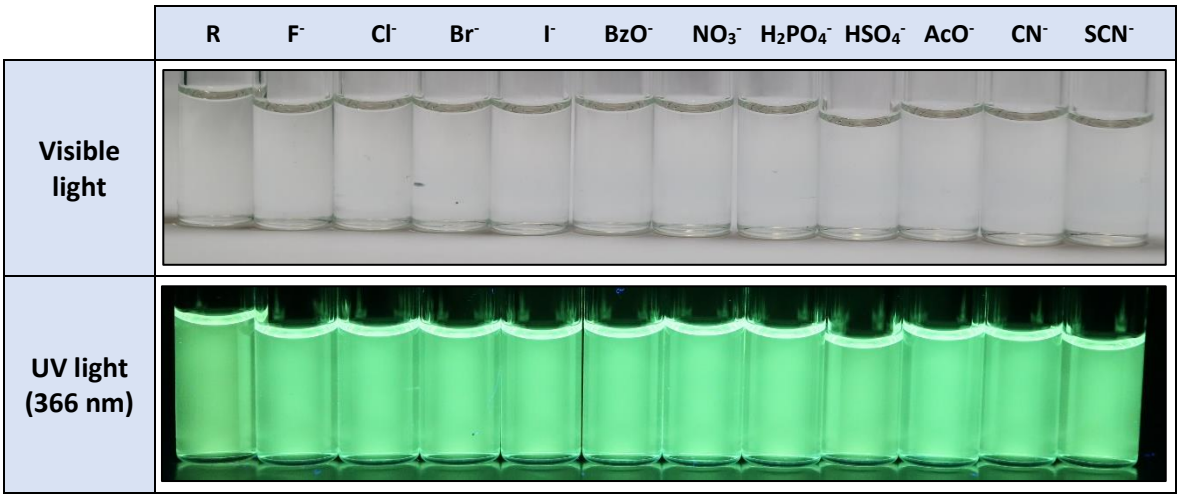

Figure 361. Anions test of AR67p under visible (up) and UV (down) light.

No significant changes were observed.

Oxidant and reductant reagents test:

The solvent used was THF and concentration of the compound was 10 µM.

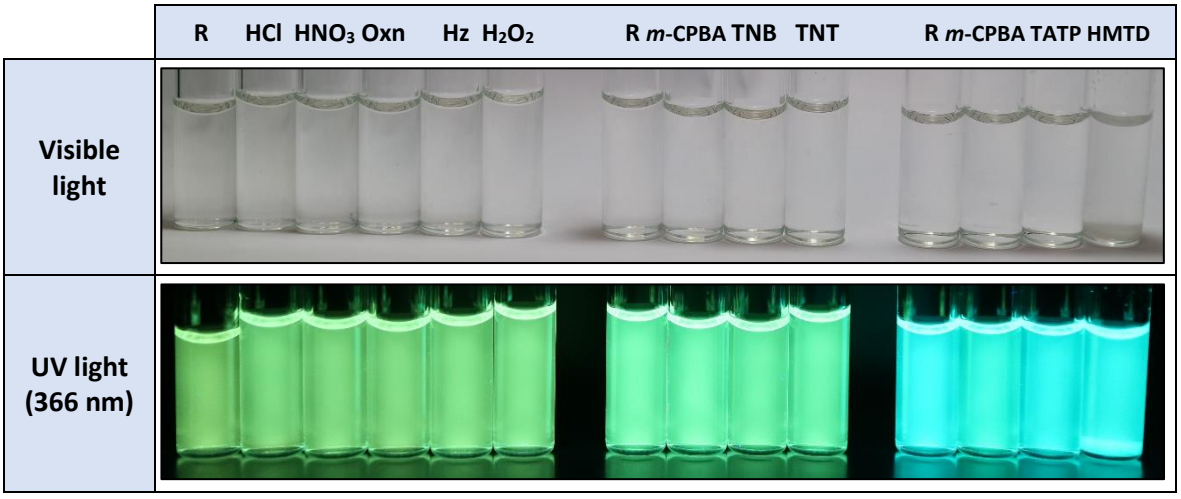

Figure 362. Oxidant and reductant reagents test of AR67p under visible (up) and UV (down) light.

No significant changes were observed.

Synthesis of *N*-(piperidin-4yl)-4-(indolo[3,2,1-jk]carbazol-2-yl)naphthalene-1,8-dicarboxylmonoimide (AR67d)

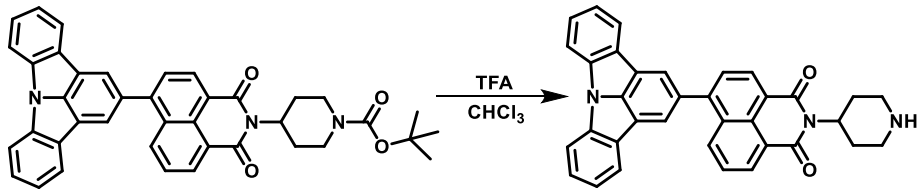

150 mg of *N*-(Boc-piperidine)-4-(indolo[3,2,1-jk]carbazole)naphthalene-1,8-dicarboxylmonoimide (AR67d, 0.24 mmol) were dissolved in 15 ml of chloroform and, then, 2 ml of trifluoroacetic acid (26 mmol) was added. The mixture was stirred about 3 hours at room temperature. Afterwards, 10 ml of water were poured into the flask and the mixture was neutralized employing a 40% sodium hidroxide solution until it reached a neutral pH. Then, 20 ml of water were added into the flask and the mixture was extracted three times with chloroform (3×30 ml). The organic extracts were combined, dried over anhidrous Na_2SO_4 and the solvent was evaporated under reduce pressure, to obtain 126 mg of a yellow solid, 100% yield.

m.p.: 282-283°C.

IR (ATR, cm^{-1}): 3558 (N-H), 3313-2855, 1689 (C=O), 1652 (C=O), 1581, 1449, 1352, 1263, 1236, 1137 (C-N), 879, 778, 735, 457.

^{1}H-NMR (300 MHz, $CDCl_3$) δ (ppm): 8.58 (dd, *J* = 15.6, 7.3 Hz, 2H, 2×**H$_{Ar}$**), 8.21 (d, *J* = 8.4 Hz, 1H, **H$_{Ar}$**), 8.09 (m, 4H, 4×**H$_{Ar}$**), 7.92 (d, *J* = 8.1 Hz, 2H, 2×**H$_{Ar}$**), 7.78 (d, *J* = 7.5 Hz, 1H, **H$_{Ar}$**), 7.58 (q, *J* = 8.4 Hz, 3H, 3×**H$_{Ar}$**), 7.36 (t, *J* = 7.5 Hz, 2H, 2×**H$_{Ar}$**), 5.25 (t, *J* = 9.0 Hz, 1H C**H**), 3.30 (m, 2H, C**H**$_2$), 2.79 (m, 4H, 2×C**H**$_2$), 2.04 (s, 1H, N**H**), 1.78 (m, 2H, C**H**$_2$).

^{13}C-NMR (75MHz, $CDCl_3$) δ (ppm): 164.9 (**C**=O), 164.7 (**C**=O), 148.3 (**C**$_{Ar}$), 143.7 (**C**$_{Ar}$), 139.3 (**C**$_{Ar}$), 133.9 (**C**$_{Ar}$), 132.8 (**C**$_{Ar}$H), 131.1 (**C**$_{Ar}$H), 130.8 (**C**$_{Ar}$H), 130.7 (**C**$_{Ar}$), 129.7 (**C**$_{Ar}$), 128.8 (**C**$_{Ar}$H), 127.5 (**C**$_{Ar}$H), 126.8 (**C**$_{Ar}$H), 123.4 (**C**$_{Ar}$H), 123.3 (**C**$_{Ar}$), 122.2 (**C**$_{Ar}$H), 121.9 (**C**$_{Ar}$), 121.5 (**C**$_{Ar}$H), 118.5 (**C**$_{Ar}$), 112.5 (**C**$_{Ar}$H), 52.1 (**C**H), 47.0 (**C**H$_2$), 30.2 (**C**H$_2$).

UV-Vis ($CHCl_3$), λ_{max} nm (log ε): 369 (4.3).

Ø (Toluene, %): 99.01.

τ (375 nm, Toluene, ns): 3.065 (χ^2: 1.080).

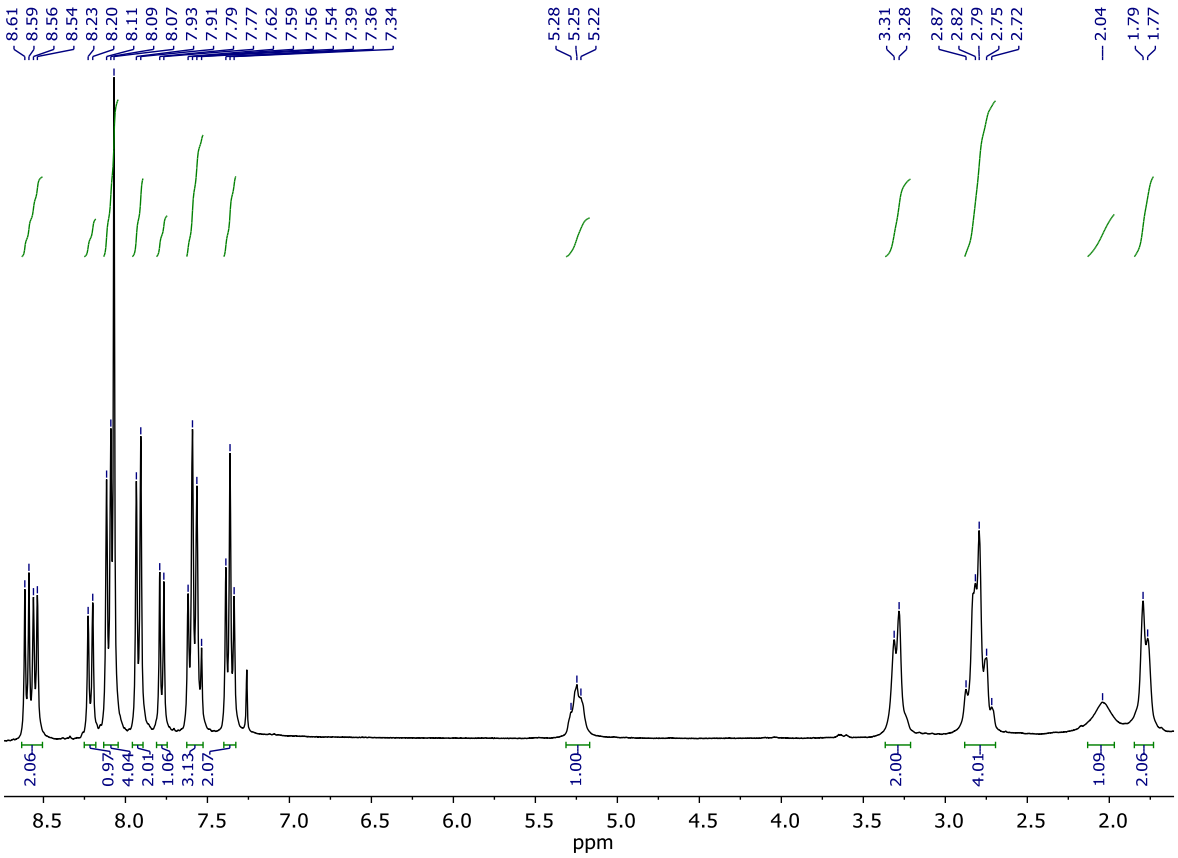

Figure 363. ^{1}H-NMR ($CDCl_3$, 300 MHz) of AR67d.

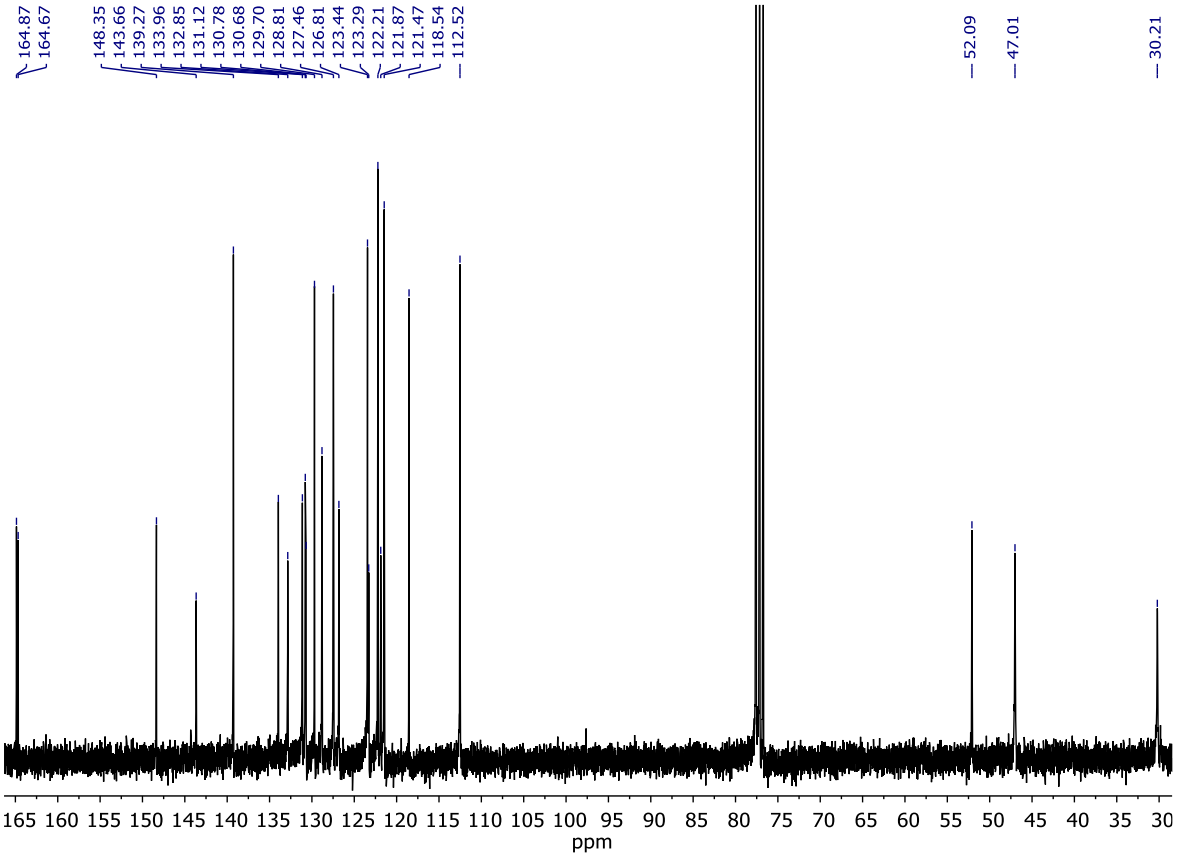

Figure 364. ^{13}C-NMR ($CDCl_3$, 75 MHz) of AR67d.

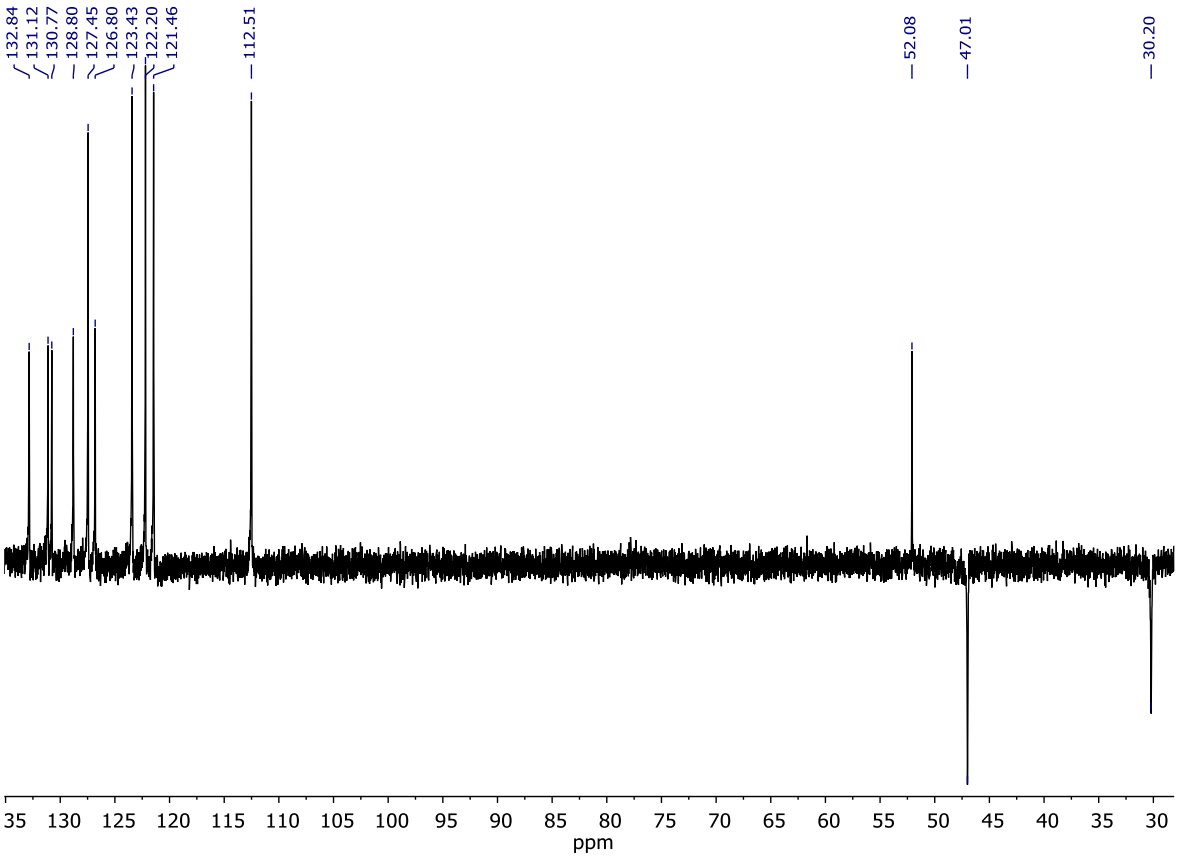

Figure 365. DEPT NMR ($CDCl_3$, 75 MHz) of AR67d.

Fluorescence decay lifetime (τ):

The solvent used was toluene. The concentration of the compound was 10 µM.

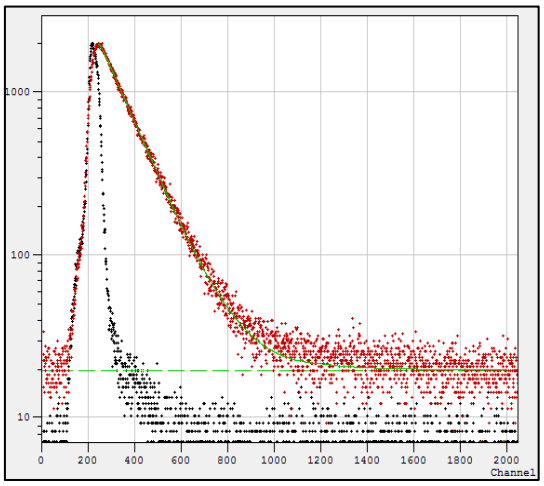

Figure 366. Fluorescence decay lifetime of AR67d.

Solvatochromism:

The concentration of the compound was 10 µM and the excitation wavelength was 360 nm.

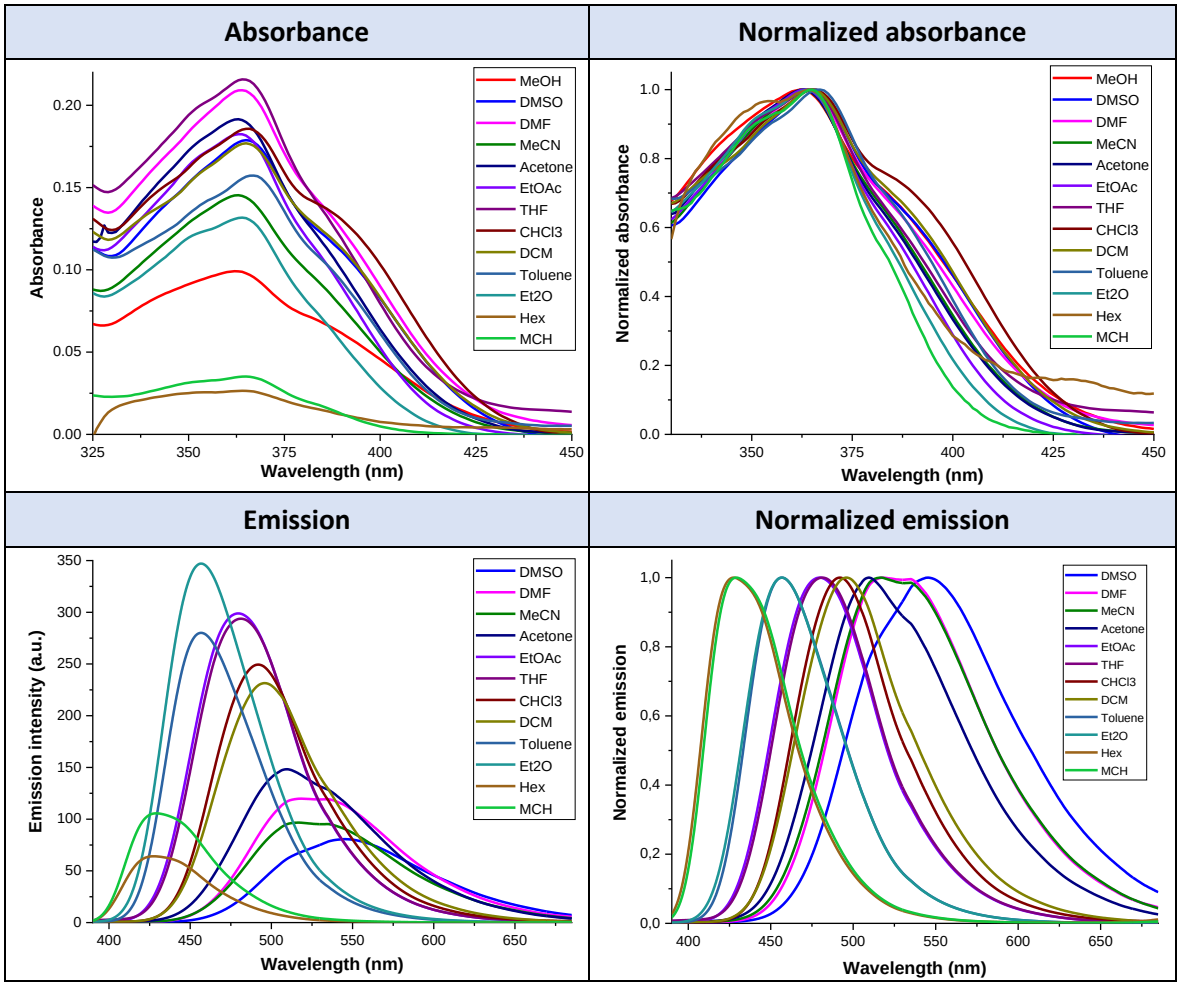

Figure 367. Solvatochromism of AR67d.

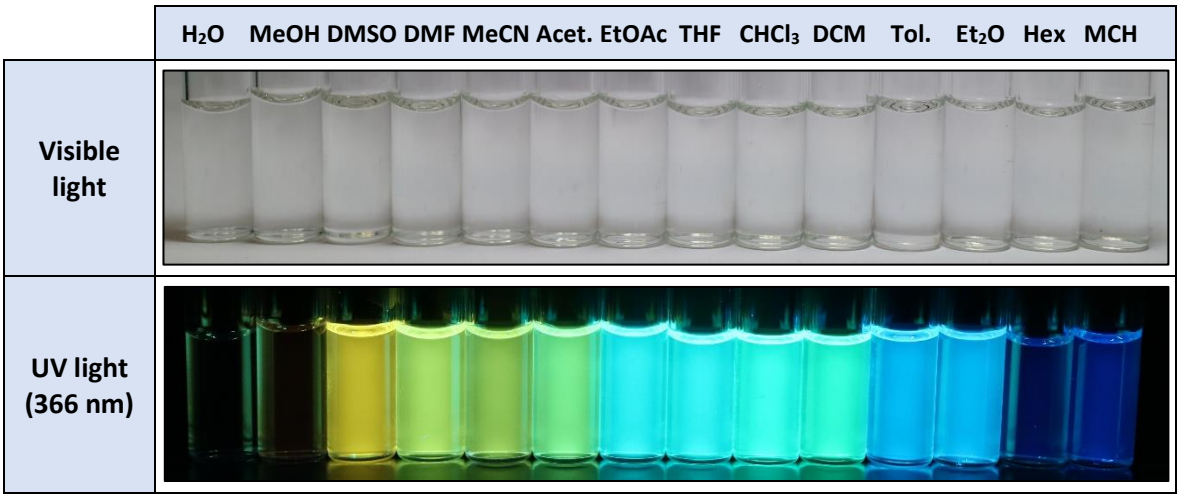

Figure 368. Solvatochromism of AR67d under visible and 366 nm light.

Water acceptance test:

The solvent used was THF and the concentration of the compound was 10 µM.

	R	5%	10%	20%	30%	40%	50%	60%	70%	80%	90%
Visible light											
UV light (366 nm)	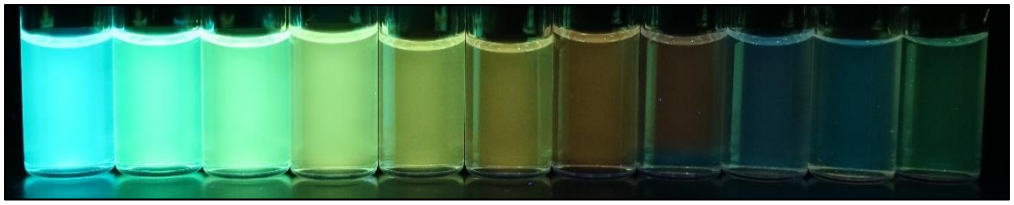										

Figure 369. Water acceptance test of AR67d under visible (up) and UV (down) light.

Fluorescence quenching was occurred as the amount of water added was increased.

pH test:

The amount of water for the performance of this test was 40%. The concentration of the compound was 10 µM and the solvent used was THF.

	R	HCl	3.4	4.8	6.4	7.4	7.9	10.5	KOH
Visible light	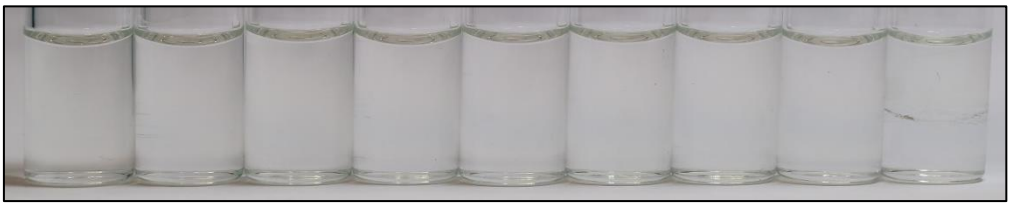								
UV light (366 nm)	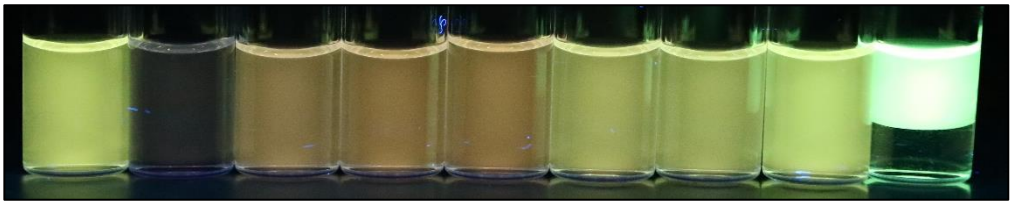								

Figure 370. pH test of AR67d under visible (up) and UV (down) light.

The most important change was the fluorescence quenched at very acidic pH.

Cations and anions test:

The concentration of the compound was 10 µM and the solvent used was THF.

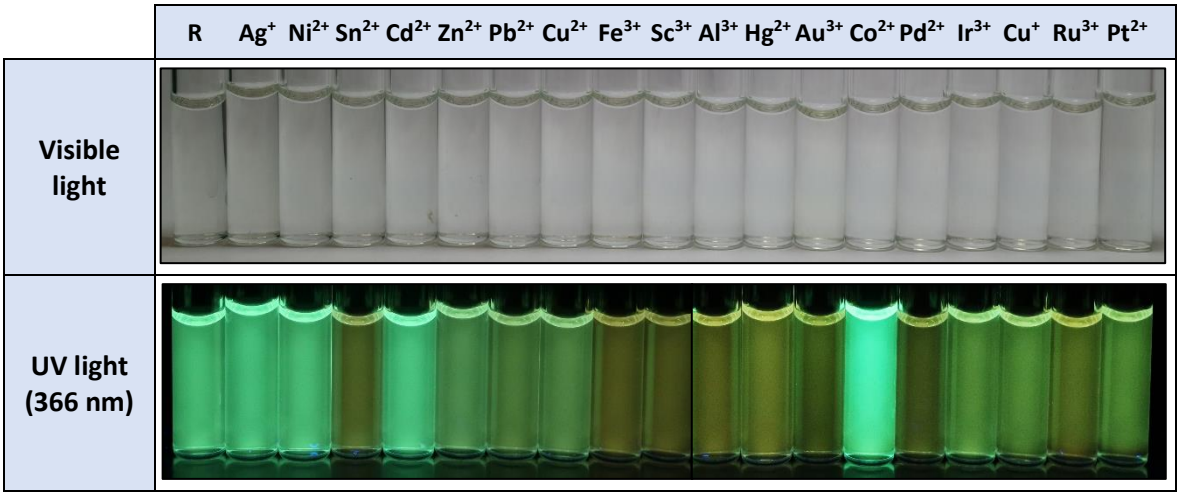

Figure 371. Cations test of AR67d under visible (up) and UV (down) light.

No significant changes were observed.

The concentration of the compound was 10 µM and the solvent used was THF.

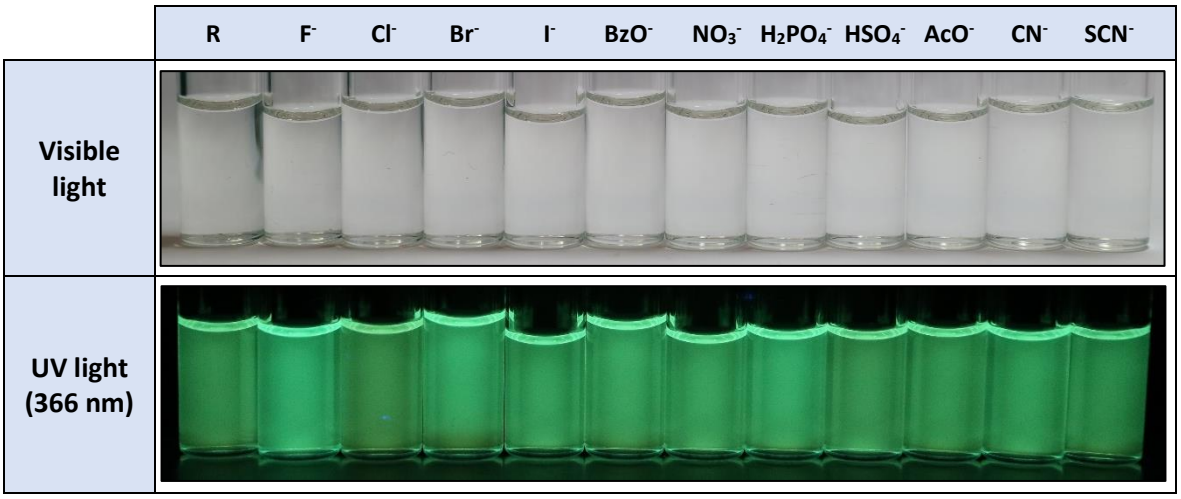

Figure 372. Anions test of AR67d under visible (up) and UV (down) light.

No significant changes were observed.

Oxidant and reductant reagents test:

The solvent used was THF and concentration of the compound was 10 µM.

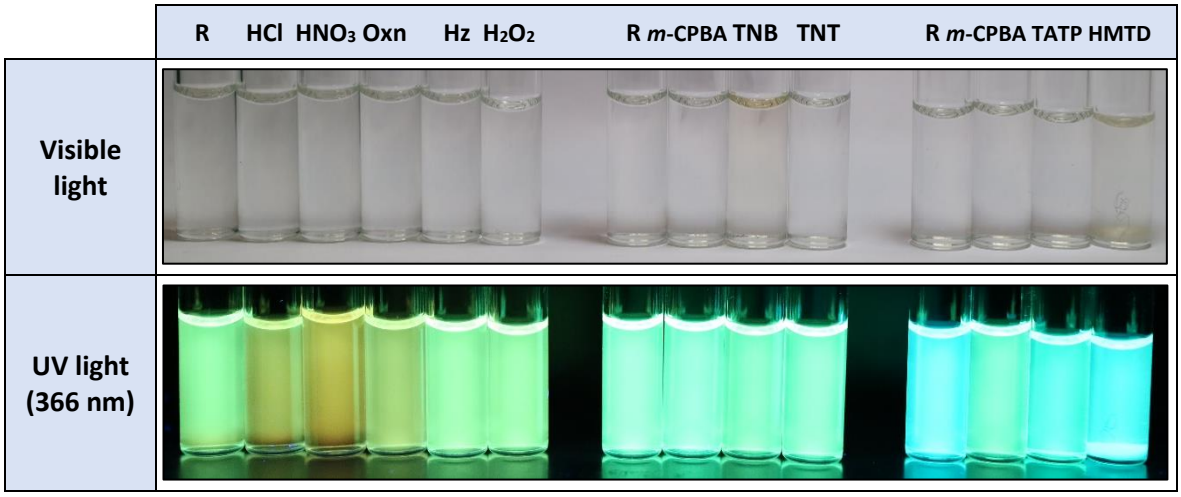

Figure 373. Oxidant and reductant reagents test of AR67d under visible (up) and UV (down) light.

There was a slight change in fluorescence color when the probe was exposed to TNB.

Synthesis of 1,6-bis(pinacolylboronate)-3,8-diisopropylpyrene (AR53)

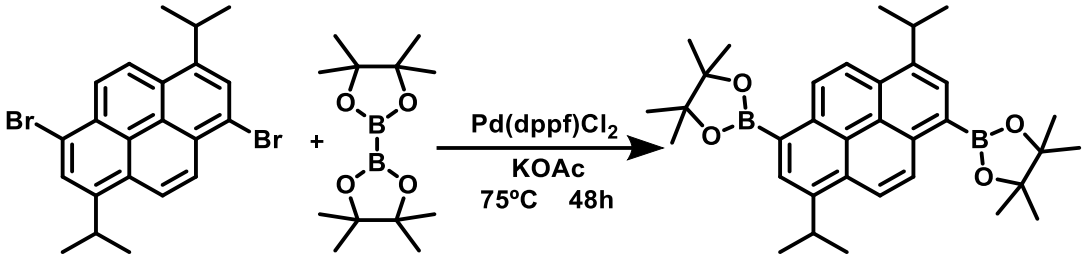

100 mg of 1,6-dibromo-3,8-diisopropylpyrene (0.23 mmol), 123 mg of bis(pinacolyl)boronate (0.48 mmol), 131 mg of potassium acetate (1.34 mmol) and 18 mg of $Pd(dppf)Cl_2$ (0.005 mmol) were dissolved, in a 50 ml Schlenck, in 15 ml of 1,4-dioxane under nitrogen atmosphere and the solution was stirred 48 hours at 75ºC. Afterwards, the solvent was evaporated under reduce pressure, 50 ml of water were added and the mixture was extracted three times with DCM (3×100 ml). The organic layer was dried over Na_2SO_4 and the solvent was evaporated under reduce pressure. The organic solid was purified by a column chromatographic (SiO_2, DCM:Hx 1:1), getting 90 mg of a solid, 73% yield.

m.p.: 207-209ºC.

IR (ATR, cm^{-1}): 2961-2865, 1606, 1558, 1507, 1462 (C-O), 1330 (B-O), 1265, 1132, 1064, 1019, 962, 858, 812, 753, 731, 663, 573.

^{1}H-NMR (300 MHz, $CDCl_3$) δ (ppm): 9.13 (d, *J* = 9.6 Hz, 2H, 2×**H_{Ar}**), 8.52-8.39 (m, 4H, 4×**H_{Ar}**), 4.10 (hept, *J* = 7.1 Hz, 2H, 2×C**H**), 1.61-1.46 (m, 36H, 12×C**H_3**).

^{13}C-NMR (75MHz, $CDCl_3$) δ (ppm): 141.5 (**C_{Ar}**H), 134.4 (**C_{Ar}**), 130.4 (**C_{Ar}**), 130.3 (**C_{Ar}**), 129.0 (**C_{Ar}**H), 125.4 (**C_{Ar}**), 122.5 (**C_{Ar}**H), 83.9 (**C**$(CH_3)_2$), 29.3 (**C**H$(CH_3)_2$), 25.2 (**C**H_3), 24.2 (**C**H_3).

HRMS (MALDI, DCTB+) m/z: calculated for $C_{34}H_{44}B_2O_2$: 538.3432 (M^+); found 538.3400.

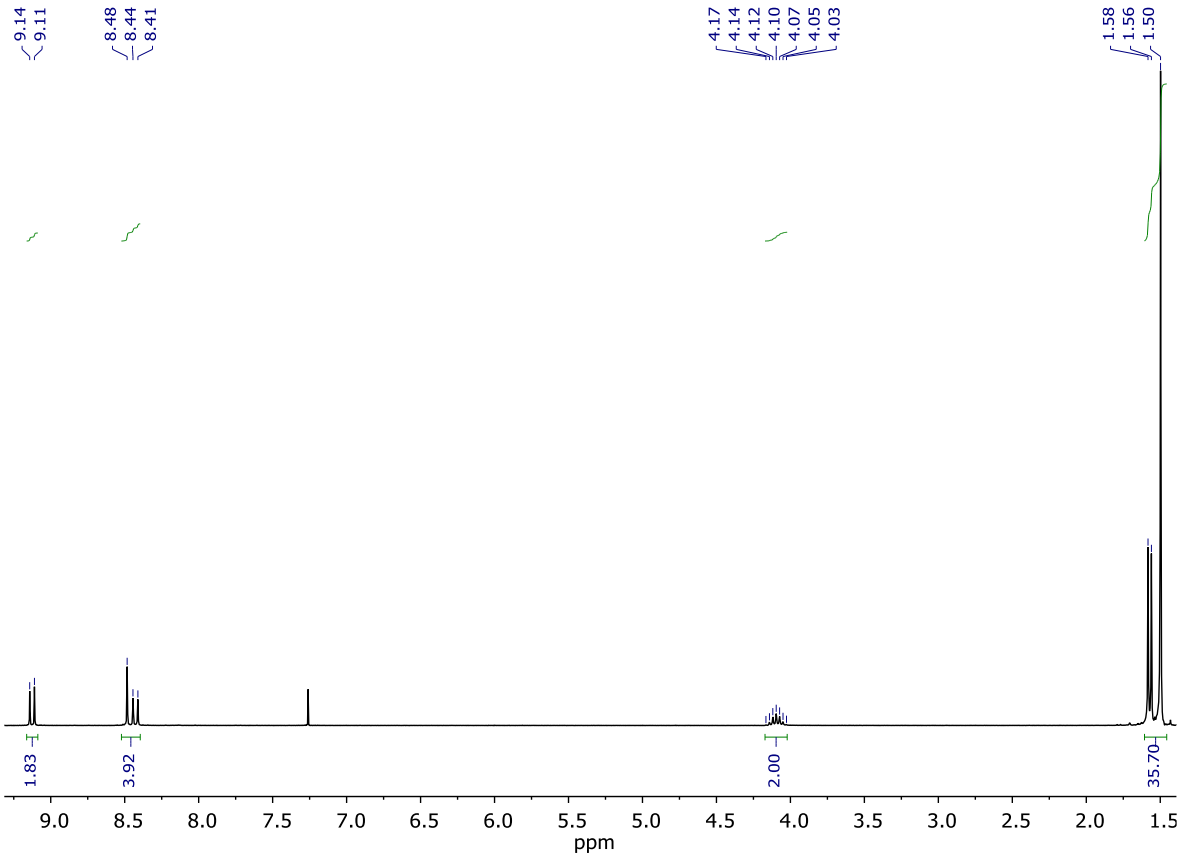

Figure 374. ^{1}H-NMR ($CDCl_3$, 300 MHz) of AR53.

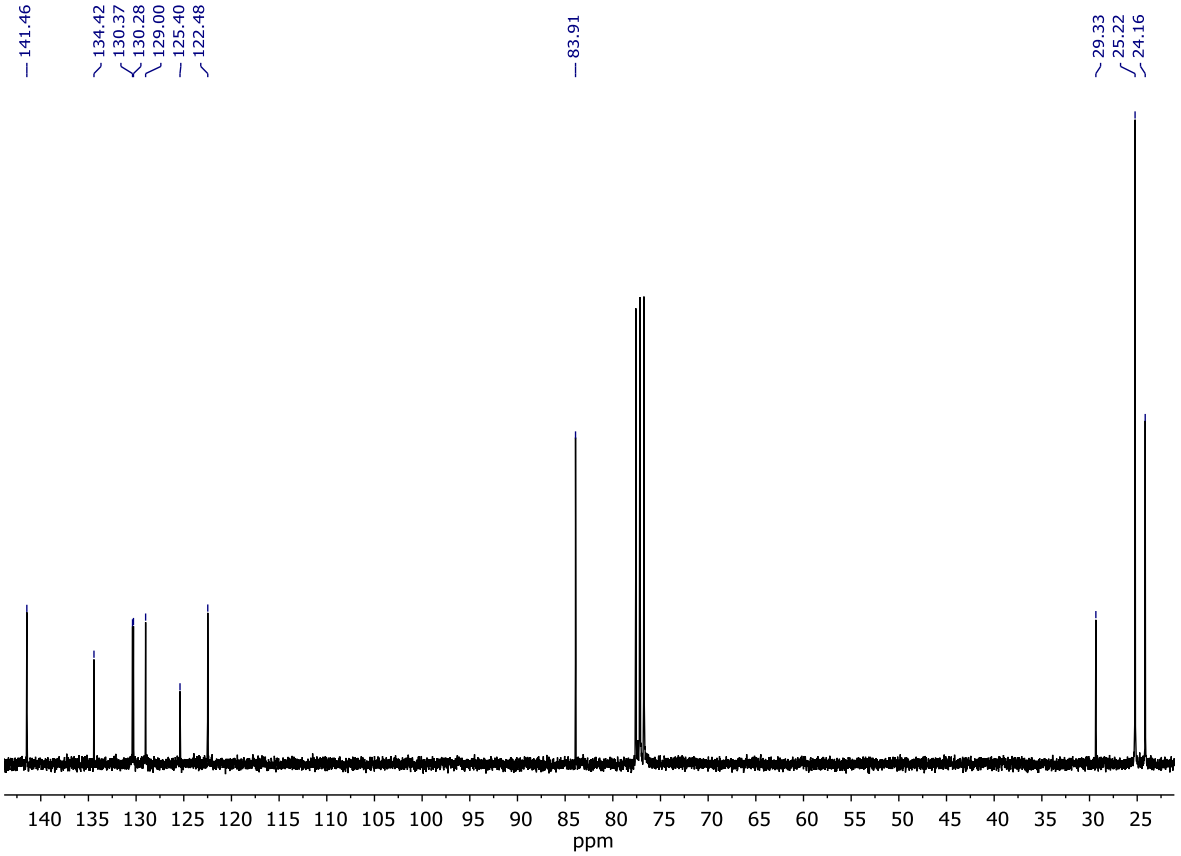

Figure 375. ^{13}C-NMR ($CDCl_3$, 75 MHz) of AR53.

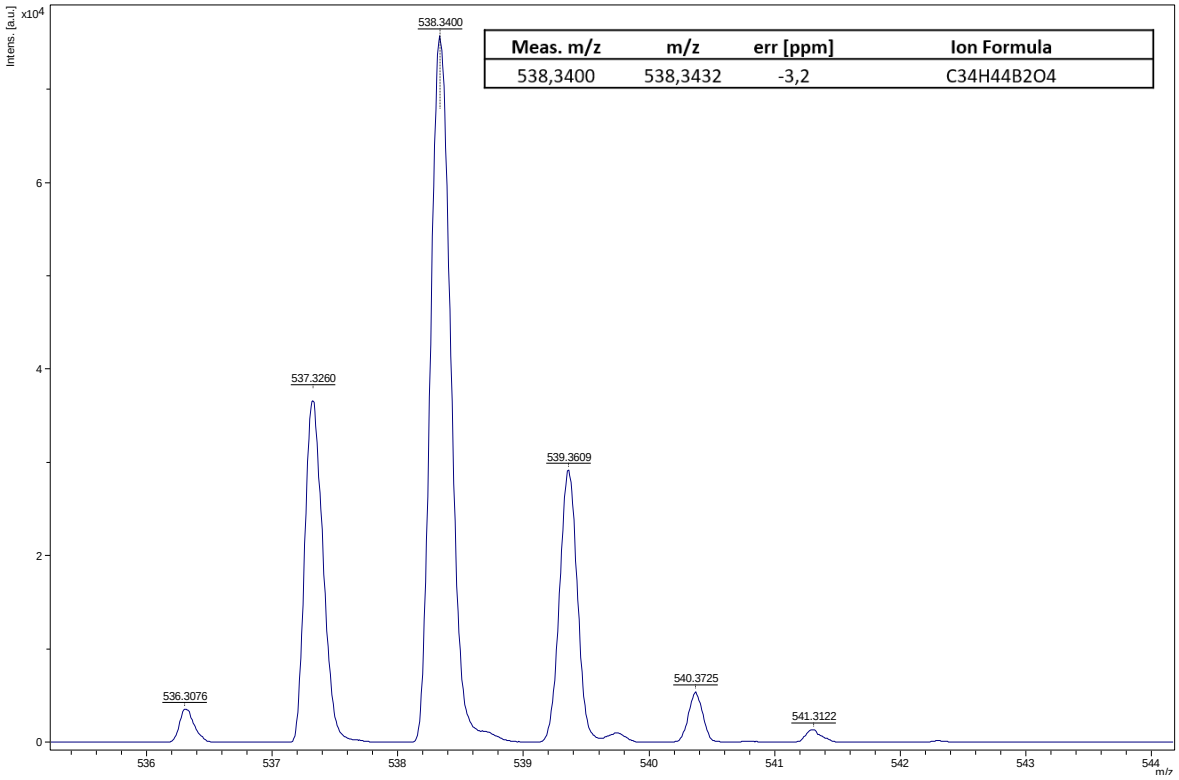

Meas. m/z	m/z	err [ppm]	Ion Formula
538,3400	538,3432	-3,2	C34H44B2O4

Figure 376. HRMS (MALDI, DCTB+) of AR53.

Synthesis of 1,6-bis(*N*-(*N*-Boc-piperidin-4-yl)naphthalene-1,8-dicarboxylmonoimide)-3,8-diiso-propylpyrene (AR56)

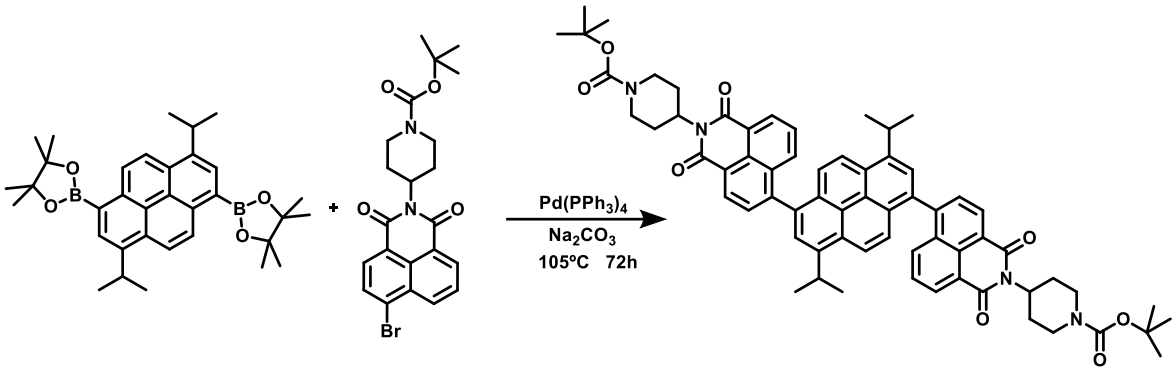

In a 100 ml Schlenk with a magnetic stirrer, 100 mg of 1,6-bis(pinacolylboronate)-3,8-diisopropyl pyrene (AR53, 0.19 mmol), 270 mg of *N*-(Boc-piperidine)-4-bromonaphthalene-1,8-dicarboxyl monoimide (0.59 mmol) and 105 mg of sodium carbonate (0.99 mmol) were dissolved in a mixture of toluene:butanol:water (30.2:7.5:2.6 ml) under nitrogen atmosphere. The catalyst, 12 mg of $Pd(PPh_3)_4$ (0.01 mmol), was added and the resulting solution was stirred at 105ºC for 48 hours. Afterwards, the solvent was evaporated under reduce pressure, the solid was dissolved in DCM and washed three times with water (3×100 ml), and, the last, the water was extracted three times with DCM (3×100 ml). The organic extracts were combined, dried over Na_2SO_4 and the solvent was evaporated under reduce pressure. The organic solid was purified by column chromatography (SiO_2, pentane:DCM) to obtain 151 mg of a yellow solid, 78% yield.

m.p.: 240-242ºC (decomposition).

IR (ATR, cm^{-1}): 2963-2866, 1695 (C=O), 1662 (C=O), 1584, 1452 (C-O), 1398, 1344, 1244, 1158 (C-N), 1140 (-CH_3), 1104, 1032, 975, 897, 862, 825, 781, 759, 457.

^{1}H-NMR (300 MHz, $CDCl_3$) δ (ppm): 8.80 (d, *J* = 7.5 Hz, 2H, 2×**H$_{Ar}$**), 8.64 (d, *J* = 7.5 Hz, 2H, 2×**H$_{Ar}$**), 8.27 (m, 3H, 3×**H$_{Ar}$**), 7.96 (d, *J* = 6.1 Hz, 3H, 3×**H$_{Ar}$**), 7.78 (d, *J* = 8.4 Hz, 2H, 2×**H$_{Ar}$**), 7.66 (d, *J* = 8.4 Hz, 2H, 2×**H$_{Ar}$**), 7.58 (m, 2H, 2×**H$_{Ar}$**), 5.31 (m, 2H, 2×C**H**), 4.37 (m, 4H, 2×C**H**$_2$), 4.07 (m, 2H, 2×C**H**), 2.88 (m, 8H, 4×C**H**$_2$), 1.78 (m, 4H, 2×C**H**$_2$), 1.57-1.48 (m, 30H, 10×C**H**$_3$).

^{13}C-NMR (75MHz, $CDCl_3$) δ (ppm): 164.8 (**C**=O), 164.6 (**C**=O), 154.8 (**C**=O), 146.4 (**C**$_{Ar}$), 142.8 (**C**$_{Ar}$), 133.9 (**C**$_{Ar}$), 133.1 (**C**$_{Ar}$H), 131.6 (**C**$_{Ar}$), 131.5 (**C**$_{Ar}$H), 130.9 (**C**$_{Ar}$H), 129.6 (**C**$_{Ar}$H), 128.7 (**C**$_{Ar}$), 128.5 (**C**$_{Ar}$), 127.9 (**C**$_{Ar}$), 127.3 (**C**$_{Ar}$H), 127.2 (**C**$_{Ar}$H), 125.7 (**C**$_{Ar}$), 125.5 (**C**$_{Ar}$H), 125.3 (**C**$_{Ar}$H), 123.4 (**C**$_{Ar}$), 122.8 (**C**$_{Ar}$H), 122.7 (**C**$_{Ar}$), 79.7 (**Cq**), 52.0 (**C**H), 44.2 (**C**H$_2$), 29.2 (**C**H), 28.6 (**C**H$_3$), 28.5 (**C**H$_2$), 24.2 (**C**H$_3$).

HRMS (MALDI, DCTB-) m/z: calculated for $C_{66}H_{66}N_4O_8$: 1042.4875 (M^-); found 1042.4839.

UV-Vis ($CHCl_3$), λ_{max} nm (log ε): 360 (4.8).

Ø (Hex, %): 92.58.

τ (375 nm, Hex, ns): 2.991 (χ^2: 1.004).

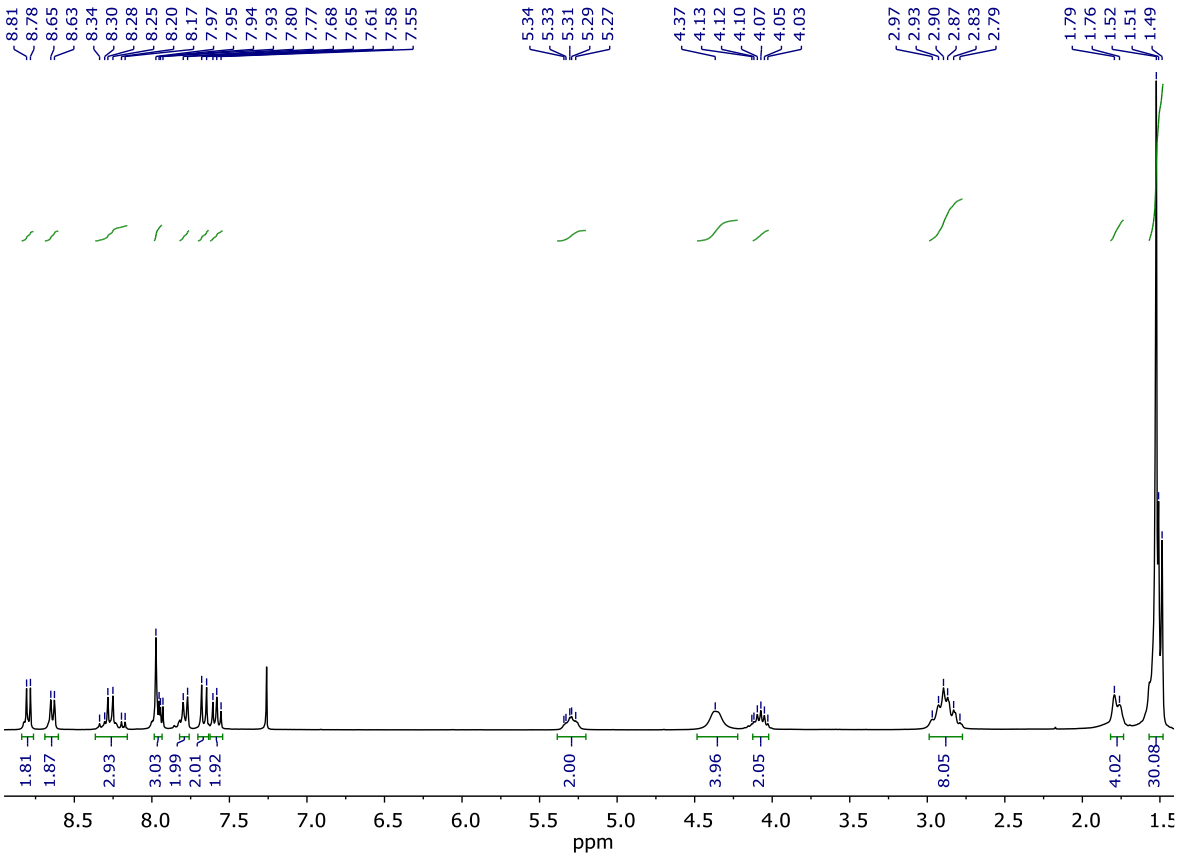

Figure 377. ^{1}H-NMR ($CDCl_3$, 300 MHz) of AR56.

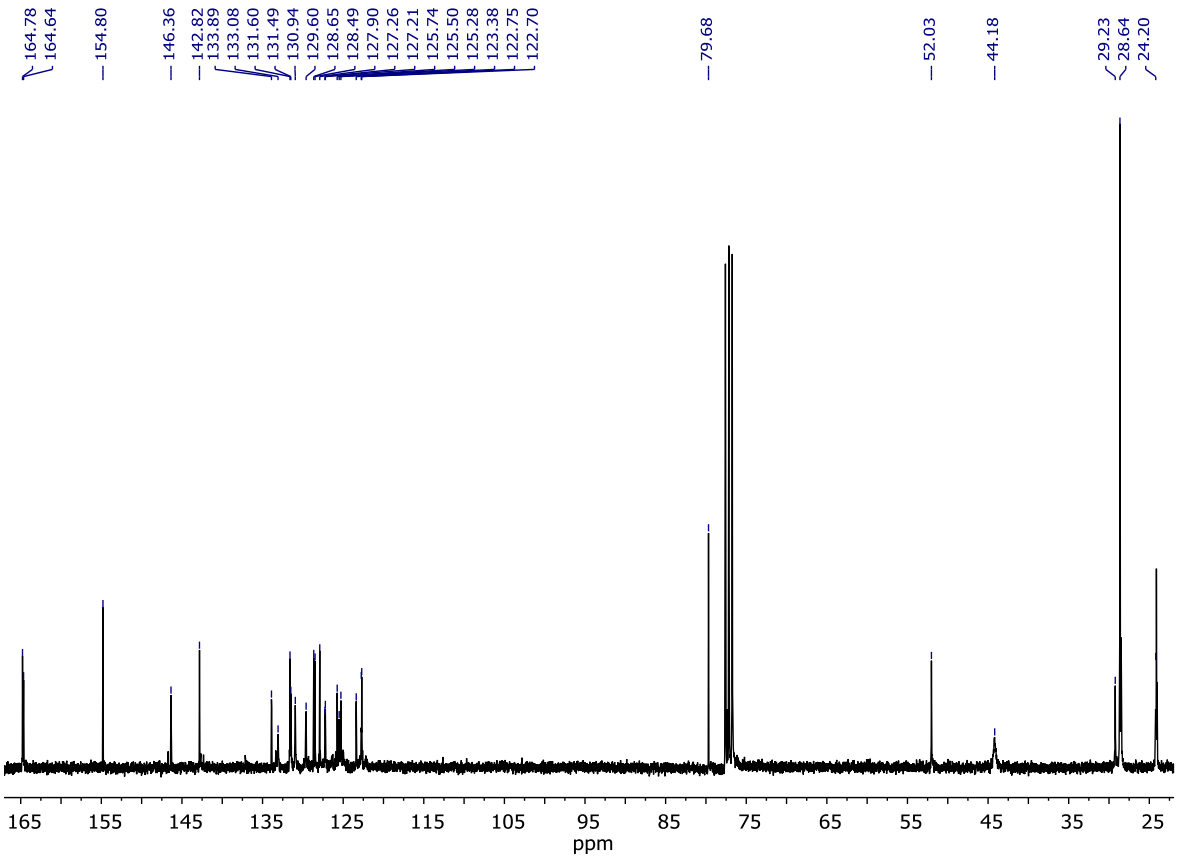

Figure 378. ^{13}C-NMR ($CDCl_3$, 75 MHz) of AR56.

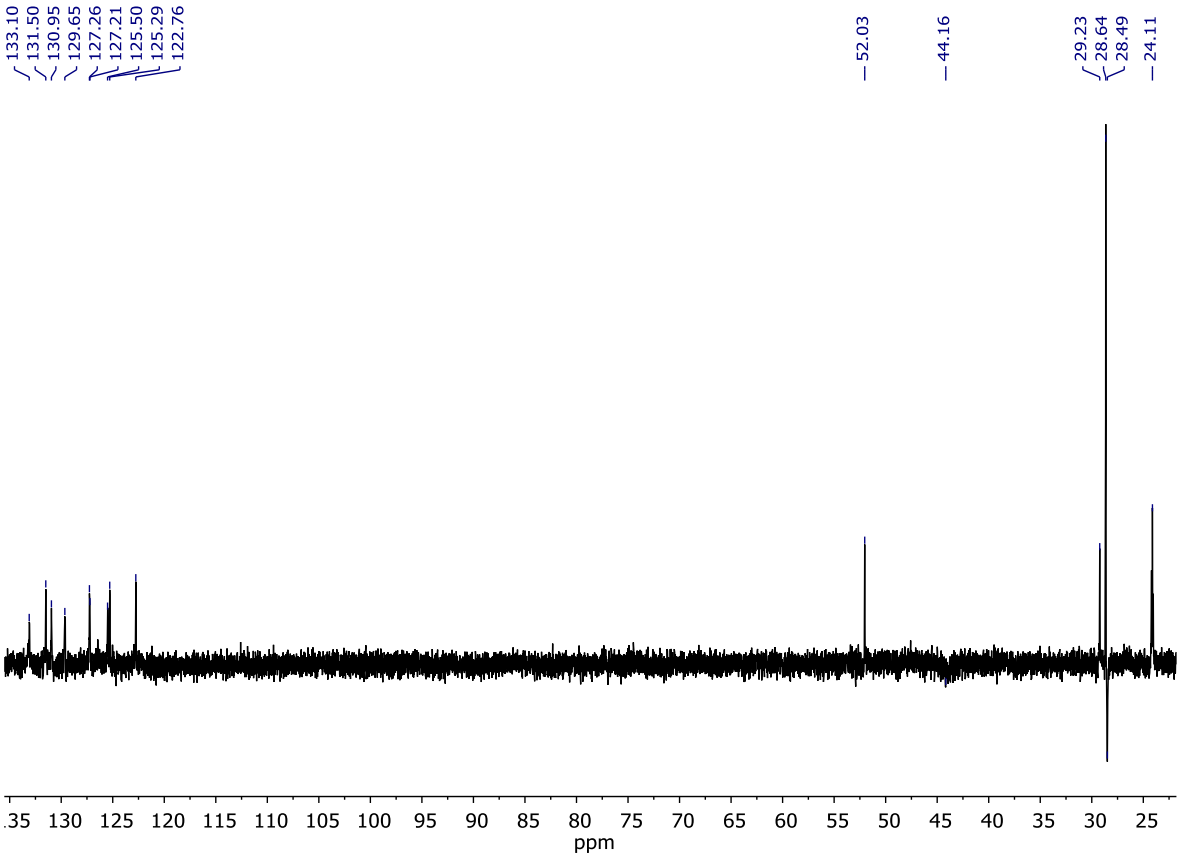

Figure 379. DEPT NMR ($CDCl_3$, 75 MHz) of AR56.

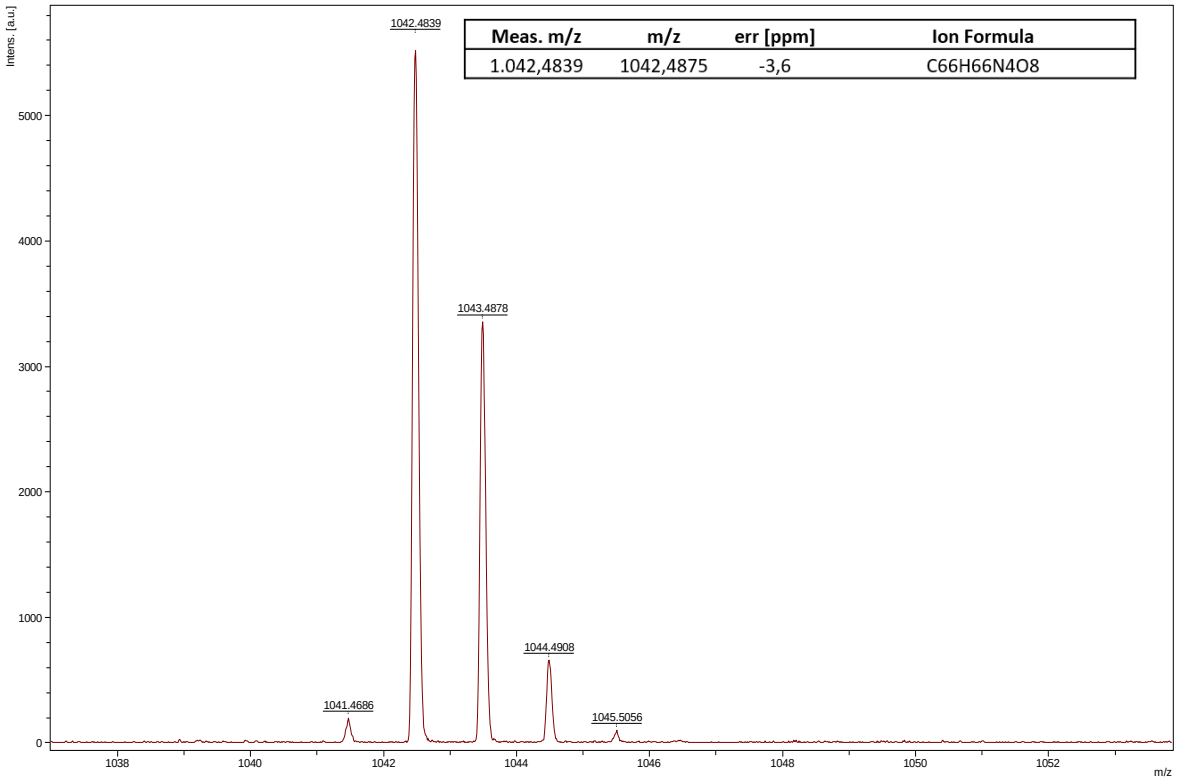

Meas. m/z	m/z	err [ppm]	Ion Formula
1.042,4839	1042,4875	-3,6	C66H66N4O8

Figure 380.HRMS (MALDI, DCTB-) of AR56.

Solvatochromism:

The concentration of the compound was 20 µM and the excitation wavelength was 355 nm.

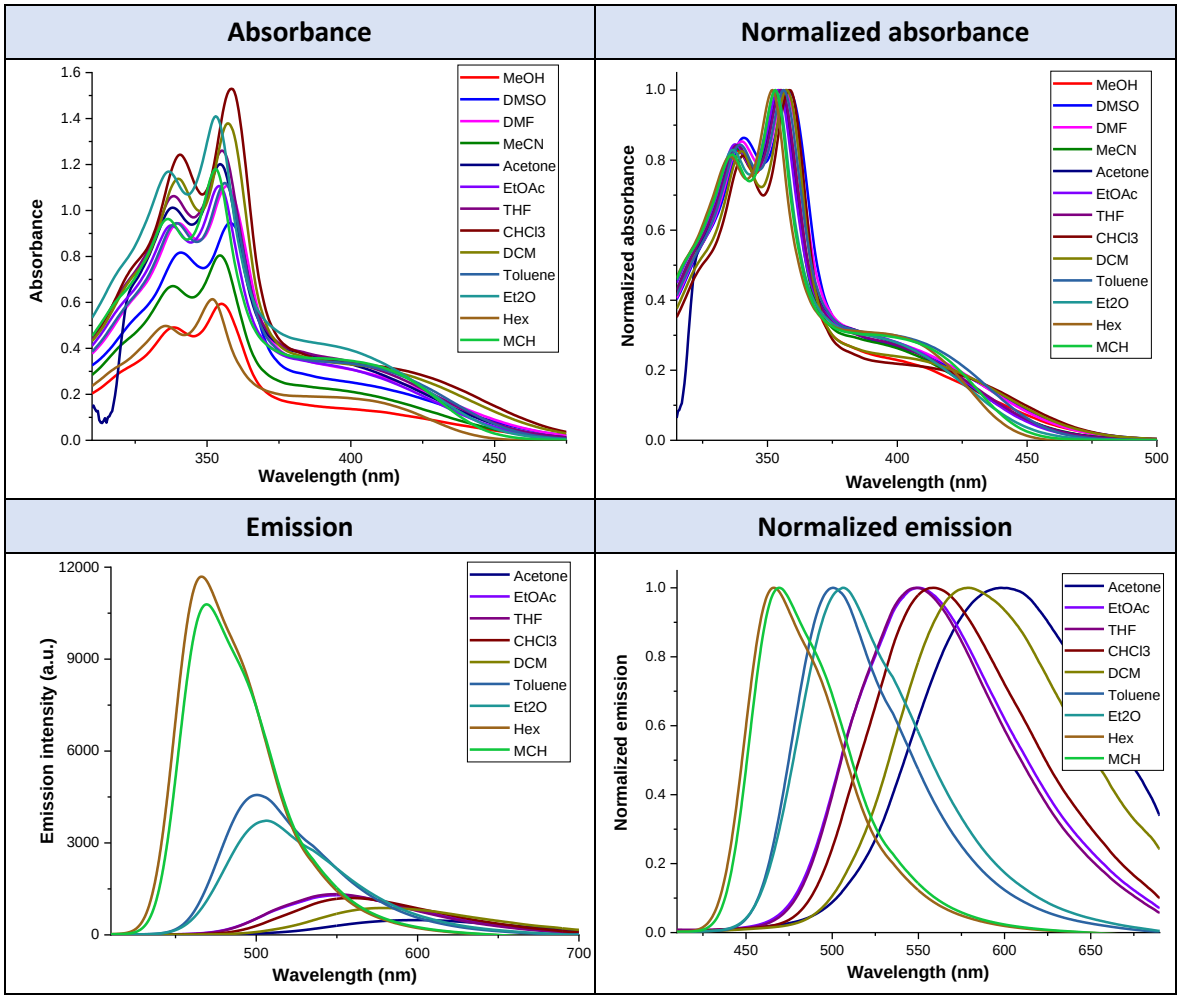

Figure 381. Solvatochromism of AR56.

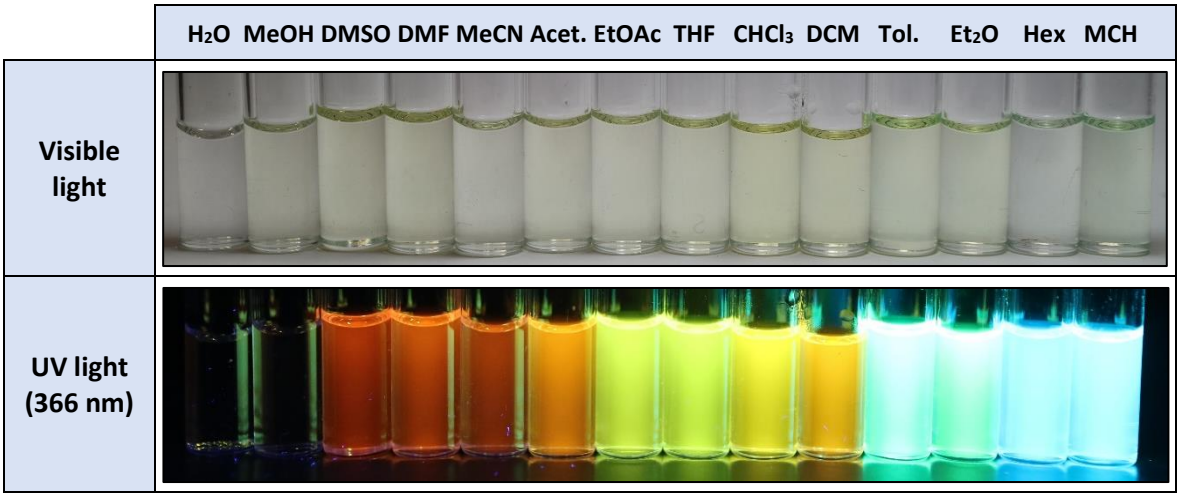

Figure 382. Solvatochromism of AR56 under visible and 366 nm light.

Fluorescence decay lifetime (τ):

The solvent used was hexane. The concentration of the compound was 20 µM.

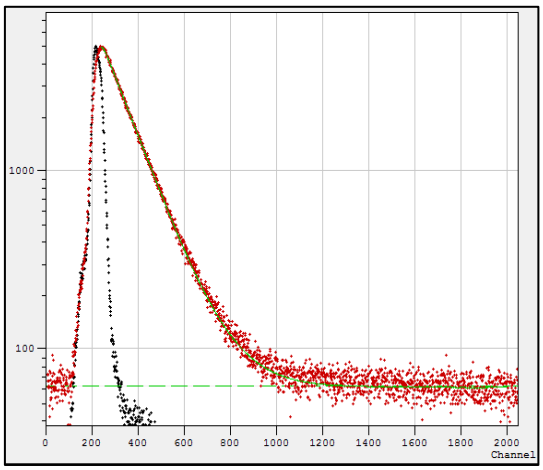

Figure 383. Fluorescence decay lifetime of AR56.

Water acceptance test:

The solvent used was acetone and the concentration of the compound was 20 µM.

	R	5%	10%	20%	30%	40%	50%	60%	70%	80%	90%
Visible light	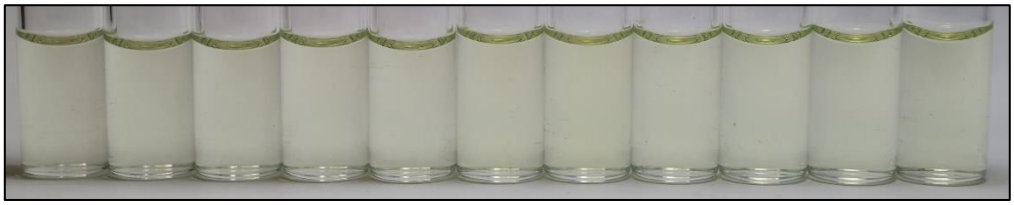										
UV light (366 nm)											

Figure 384. Water acceptance test of AR56 in acetone under visible (up) and UV (down) light.

	R	5%	10%	20%	30%	40%	50%	60%	70%	80%	90%
Visible light											
UV light (366 nm)	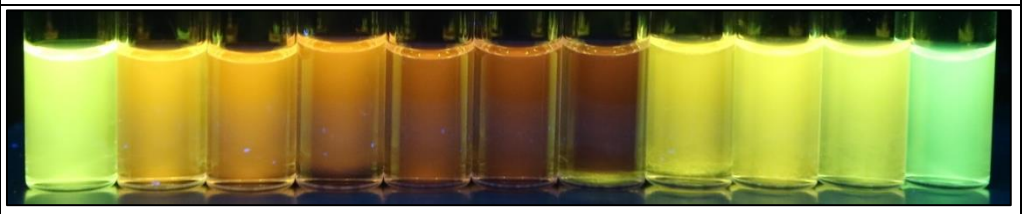										

Figure 385. Water acceptance test of AR56 in THF under visible (up) and UV (down) light.

There was a quenching of fluorescence up to 40% of water. The shift of the emission maximum from the red to the greenish-yellow region was observed with increasing water content due to the formation of organic nanoparticles (AIE). In addition, the emission intensity was increased considerably at 40% and above.

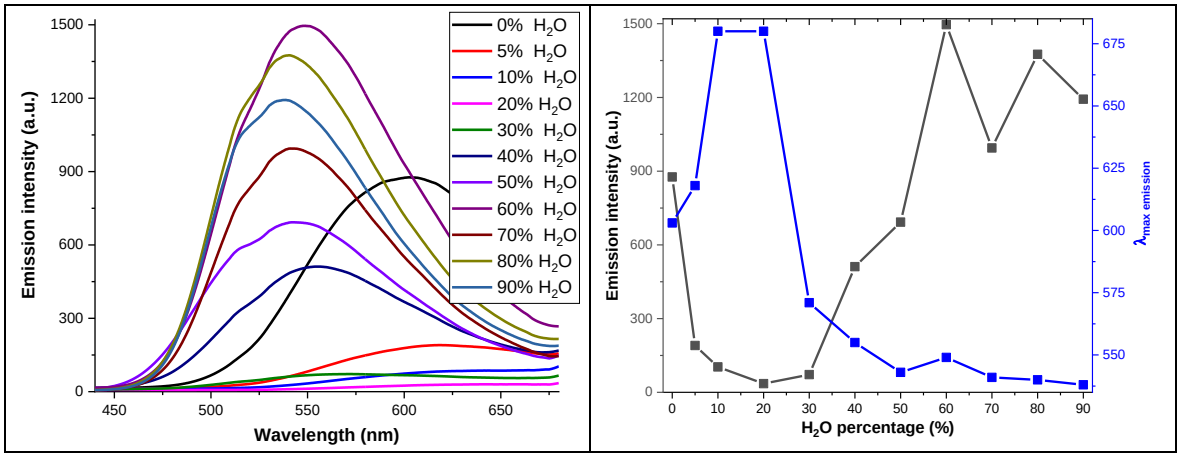

Figure 386. Emission intensity graph (left) and graph of relationship between the emission intensity and the wavelength of the maximum of emission (right) as a function of the amount of water added for AR56 in acetone.

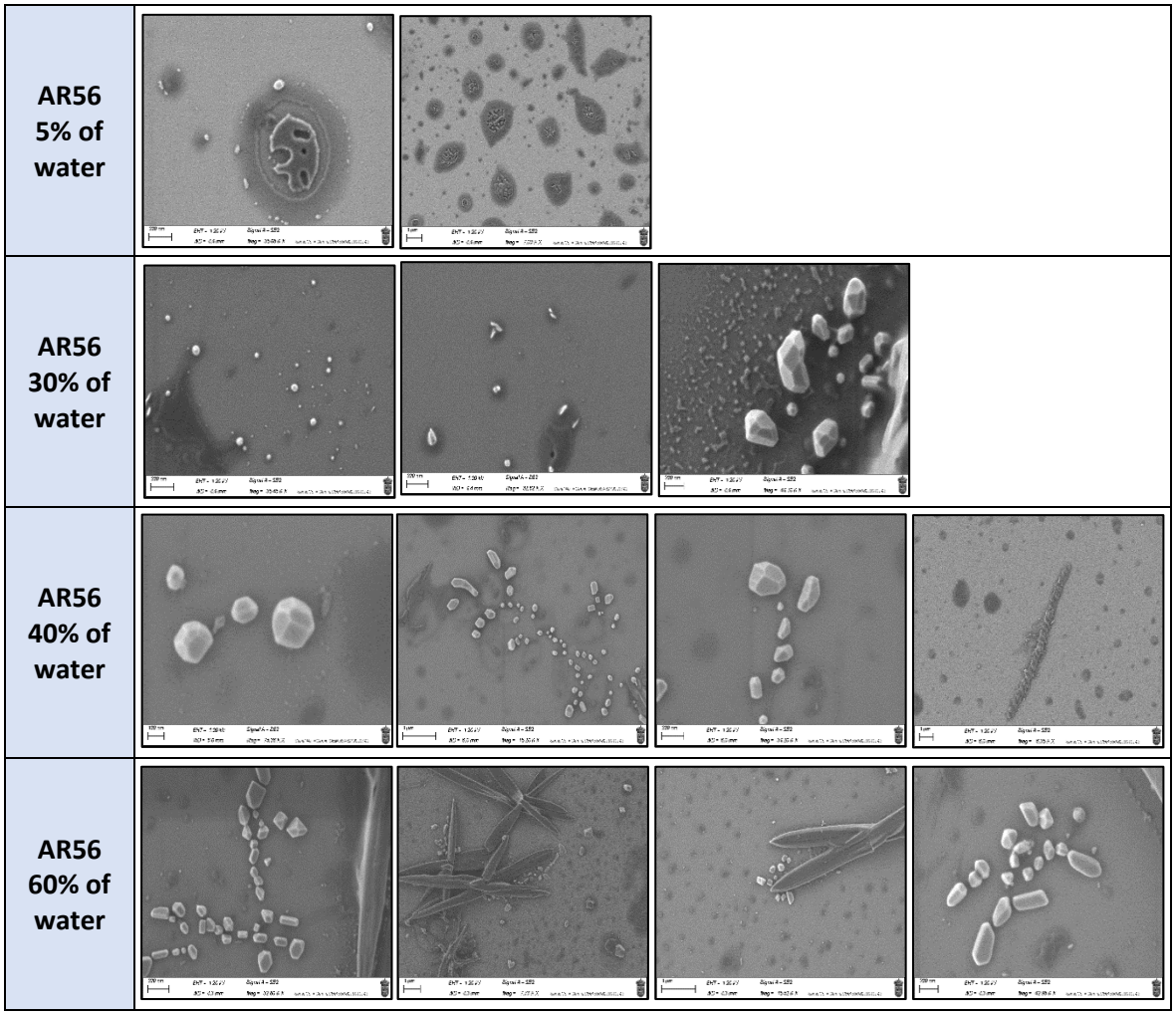

Figure 387. SEM nanoparticles of AR56 in different mixtures of water and acetone.

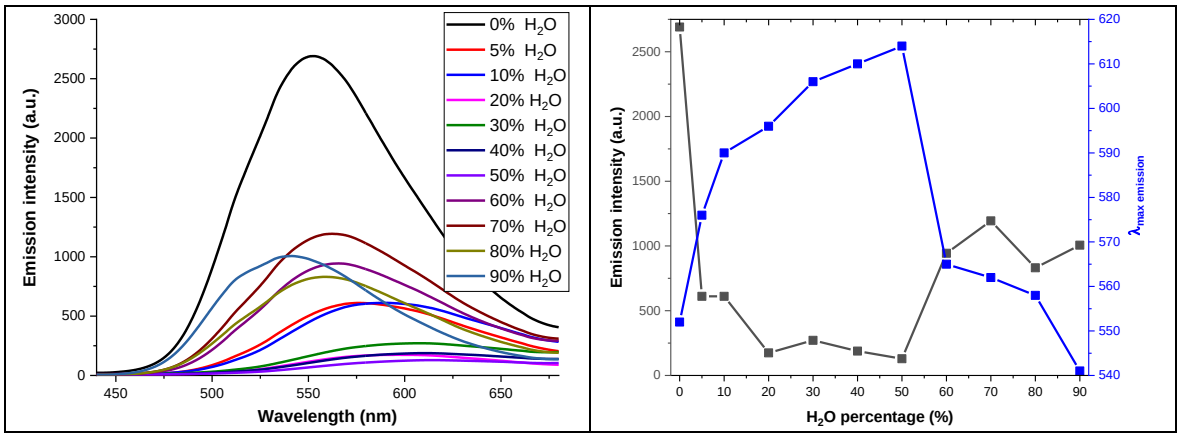

Figure 388. Emission intensity graph (left) and graph of relationship between the emission intensity and the wavelength of the maximum of emission (right) as a function of the amount of water added for AR56 in THF.

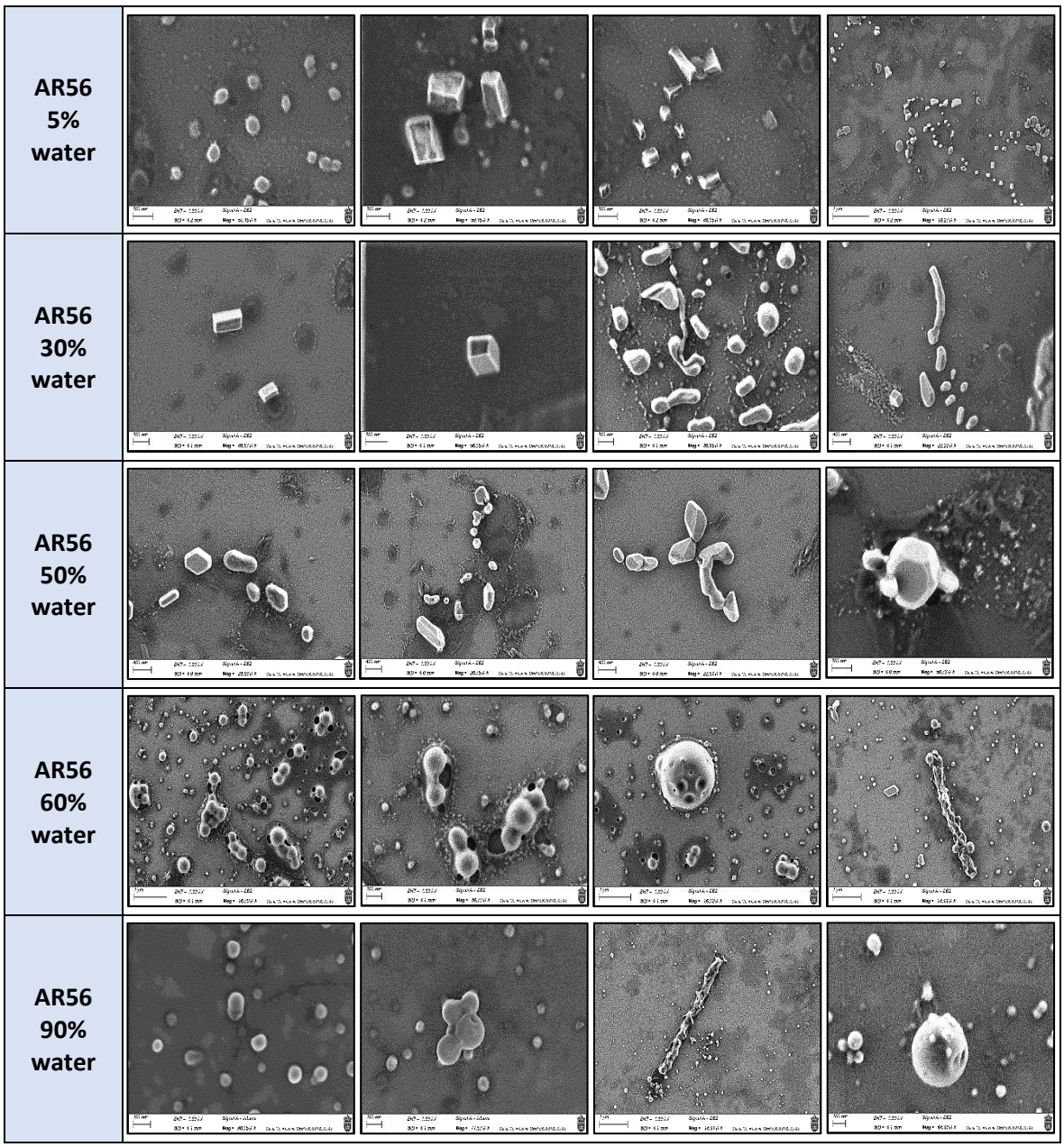

Figure 389. SEM nanoparticles of AR56 in different mixtures of water and THF.

pH test:

The proportion of water that the compound could accept was 40%. The concentration of the compound was 20 µM and the solvent used was acetone.

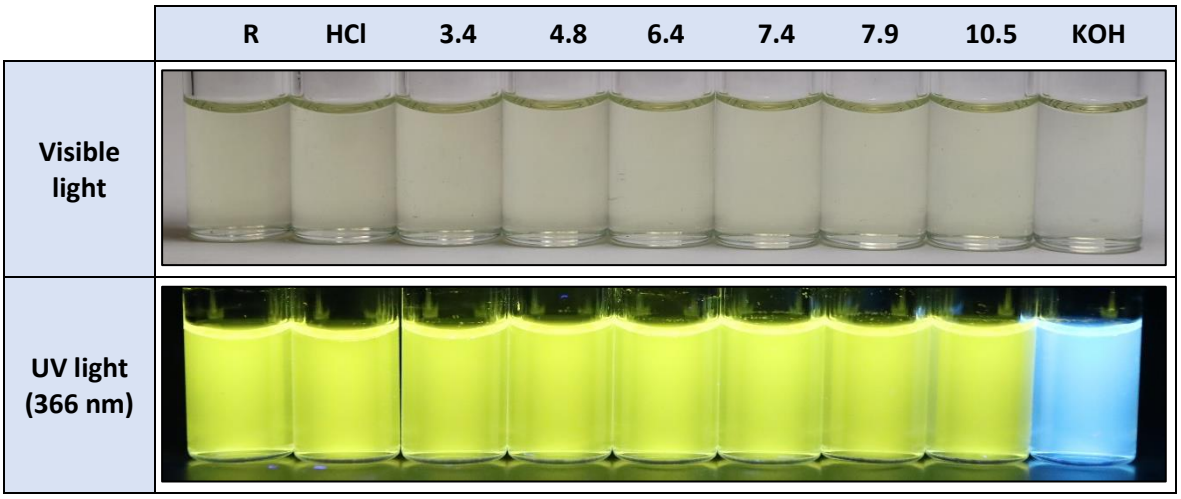

Figure 390. pH test of AR56 under visible (up) and UV (down) light.

No significant changes were observed with exception of very basic pH solution, in which the fluorescence was turned blue.

Cations and anions test:

The concentration of the compound was 20 µM and the solvent used was acetone.

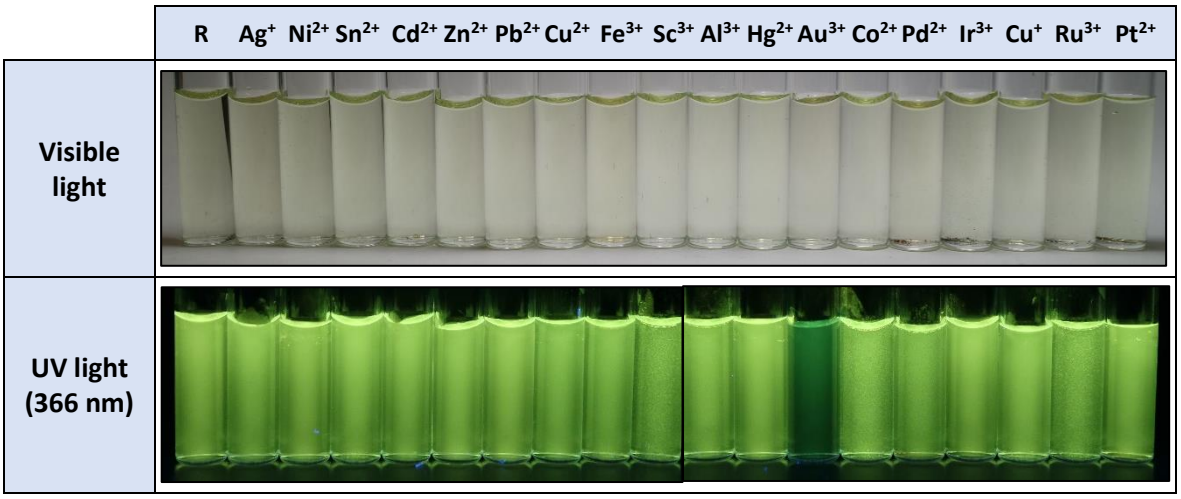

Figure 391. Cations test of AR56 under visible (up) and UV (down) light.

The fluorescence was quenched in presence of Au^{3+}.

The concentration of the compound was 20 µM and the solvent used was acetone.

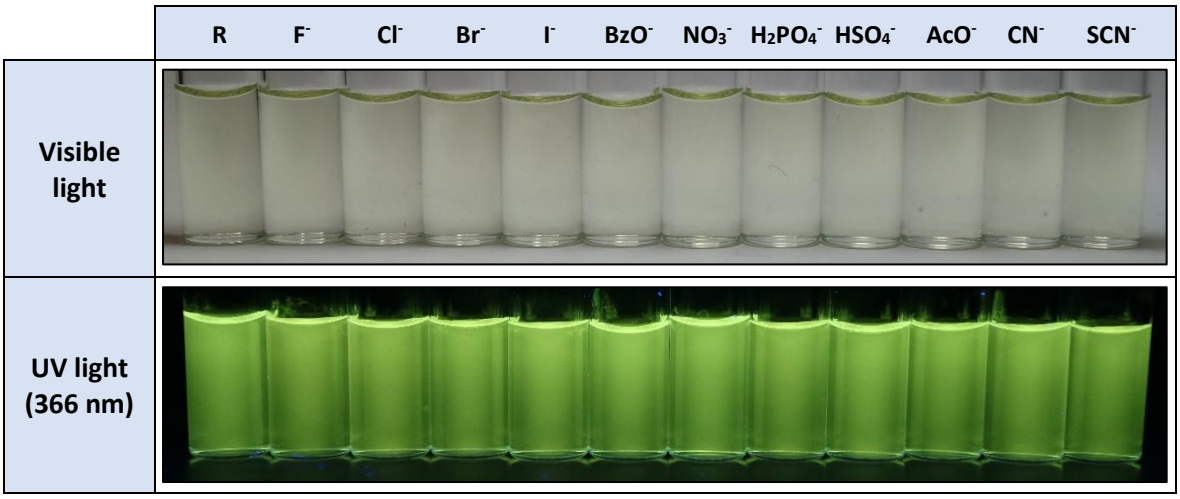

Figure 392. Anions test of AR56 under visible (up) and UV (down) light.

No significant changes were observed.

Oxidant and reductant reagents test:

The solvent used was acetone and concentration of the compound was 20 µM.

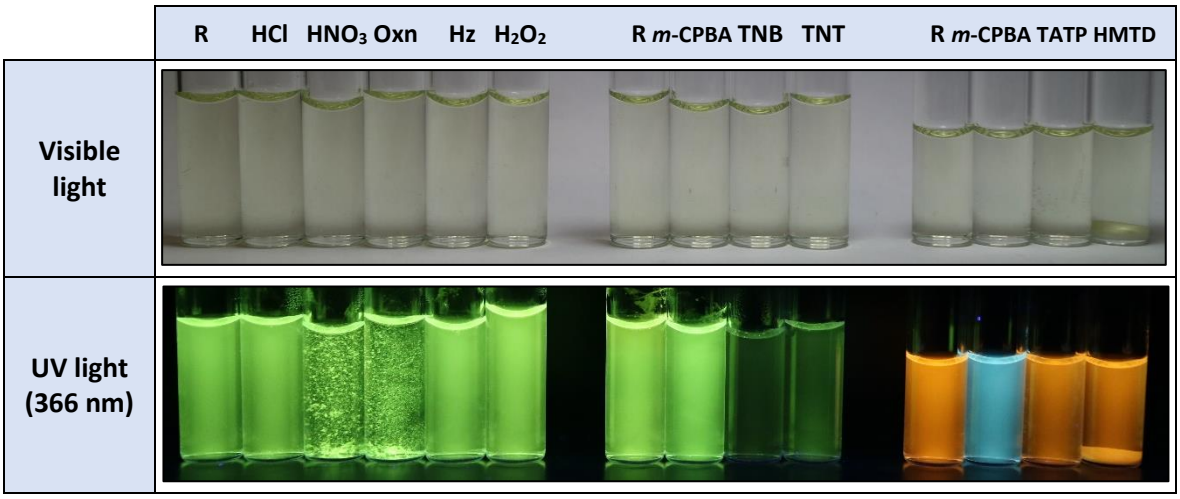

Figure 393. Oxidant and reductant reagents test of AR56 under visible (up) and UV (down) light.

In one hand, the fluorescence was quenched with the nitro derivatives TNT and TNB. In the other hand, the fluorescence was turned blue in presence of *m*-CPBA.

Synthesis of 6,12-bis(pinacolylboronate)chrysene (AR63)

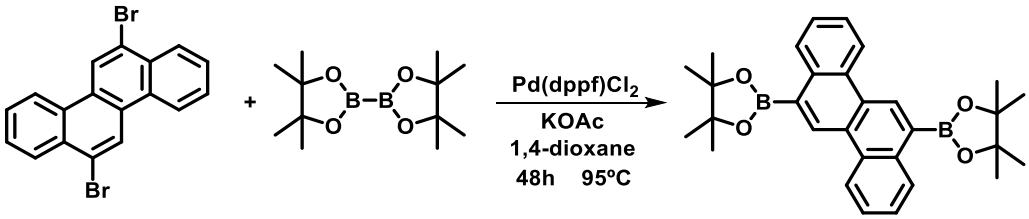

107 mg of 6,12-dibromochrysene (0.28 mmol), 155 mg of bis(pinacolyl)boronate (0.61 mmol) and 136 mg of potassium acetate (1.40 mmol) were dissolved in 5 ml of dry 1,4-dioxane under nitrogen atmosphere. Then, 18 mg of the catalyst Pd(dppf)Cl_2 (0.005 mmol) was added and the resulting solution was stirred at 95ºC for 48 hours. Afterwards, the solvent was evaporated under reduce pressure and the solid was dissolved in 50 ml of DCM and washed three times with water (3×50 ml). The organic extracts were combined, dried over Na_2SO_4 anhidrous and the solvent was evaporated under reduce pressure. The solid obtained was purified by column chromatographic (SiO_2, DCM:Hx), getting 80 mg of a red solid, 60% yield.

m.p.: 241-243ºC (decomposition).

IR (ATR, cm^{-1}): 3085-3052, 1592, 1511, 1482 (C-O), 1433, 1298 (C-B), 1263, 1029, 943, 876, 816, 783, 754, 700, 681, 565, 505, 478, 430.

^{1}H-NMR (300 MHz, $CDCl_3$) δ (ppm): 9.37 (s, 2H, 2×$\mathbf{H_{Ar}}$), 9.00-8.90 (m, 4H, 4×$\mathbf{H_{Ar}}$), 7.75-7.65 (m, 4H, 4×$\mathbf{H_{Ar}}$), 1.50 (s, 24H, 8×C$\mathbf{H_3}$).

^{13}C-NMR (75MHz, $CDCl_3$) δ (ppm): 135.0 ($\mathbf{C}_{Ar}$), 131.7 ($\mathbf{C}_{Ar}$H), 130.5 ($\mathbf{C}_{Ar}$), 129.1 ($\mathbf{C}_{Ar}$H), 129.0 ($\mathbf{C}_{Ar}$), 126.6 ($\mathbf{C}_{Ar}$H), 126.4 ($\mathbf{C}_{Ar}$H), 123.6 ($\mathbf{C}_{Ar}$H), 84.1 (**Cq**), 25.2 (**C**H_3).

HRMS (MALDI, DIT+) m/z: calculated for $C_{30}H_{34}B_2O_4$: 480.2648 (M^+); found 480.2650.

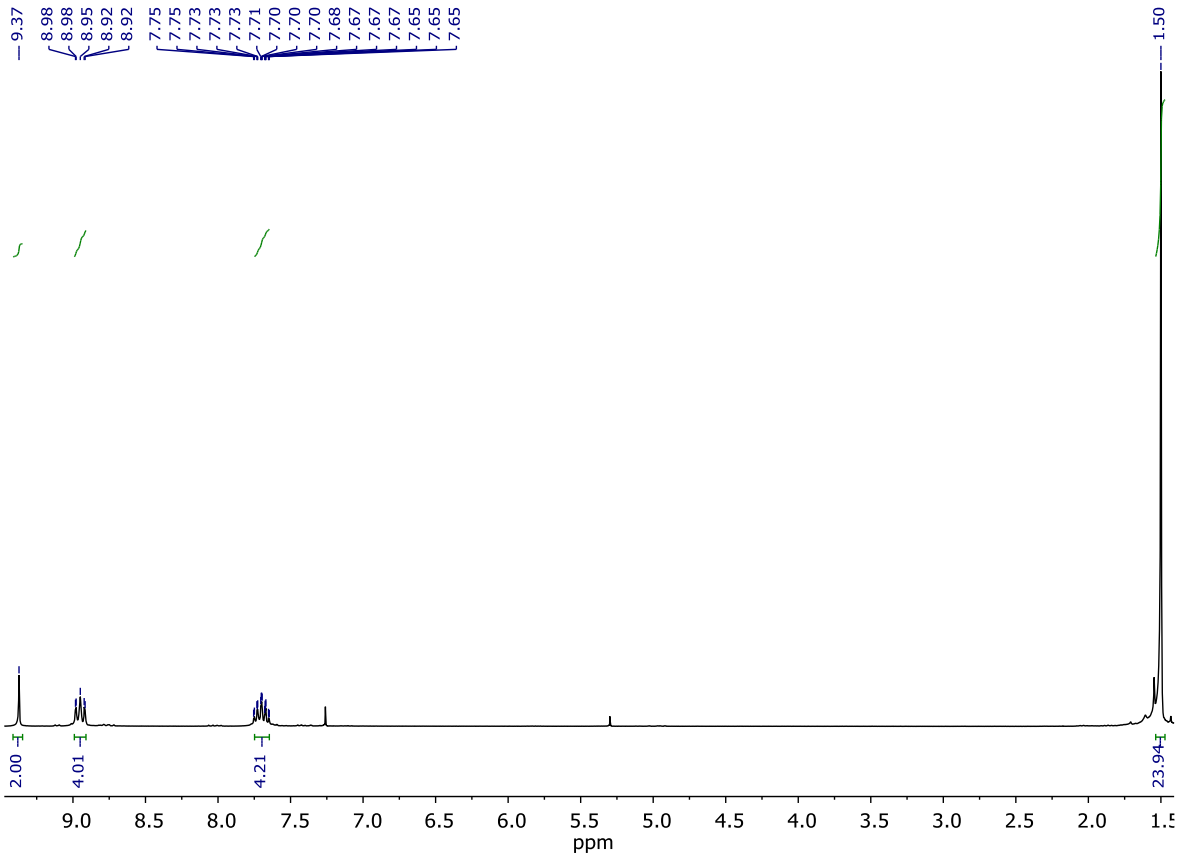

Figure 394. ^{1}H-NMR ($CDCl_3$, 300 MHz) of AR63.

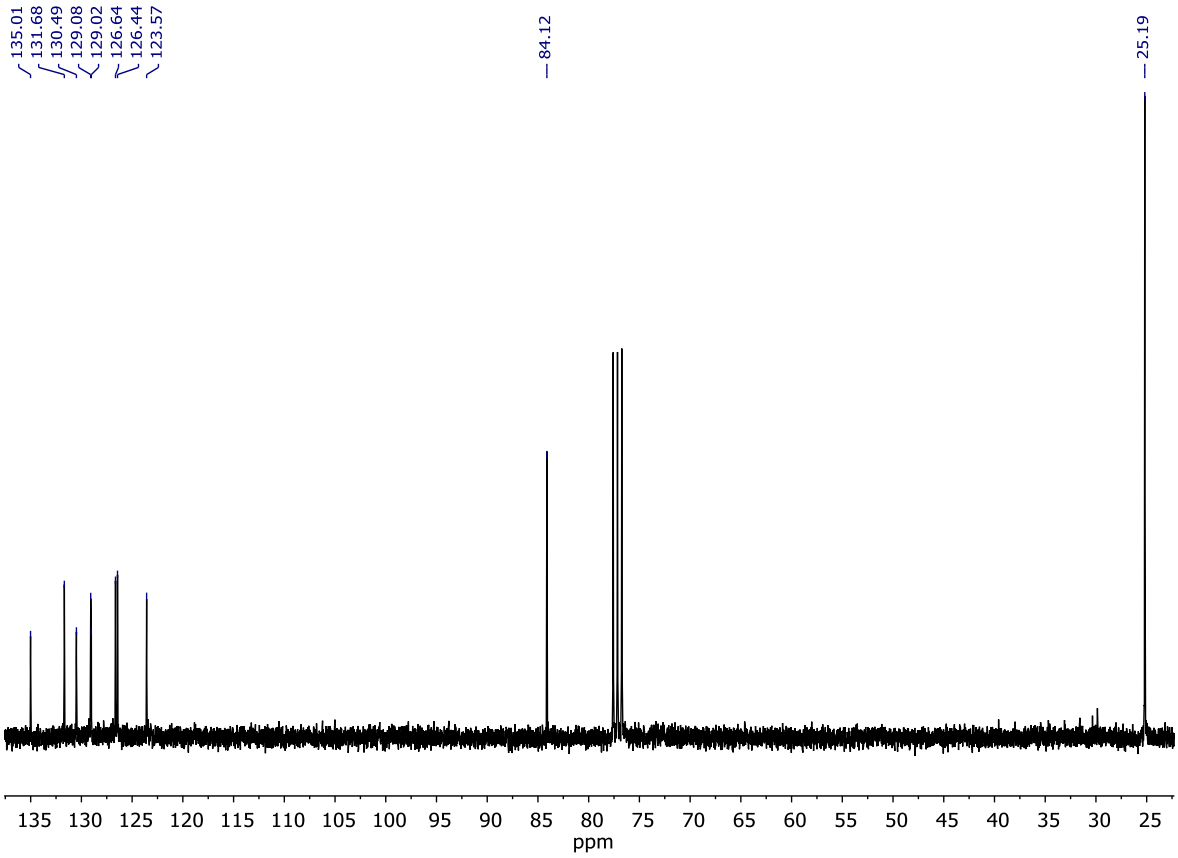

Figure 395. ^{13}C-NMR ($CDCl_3$, 75 MHz) of AR63.

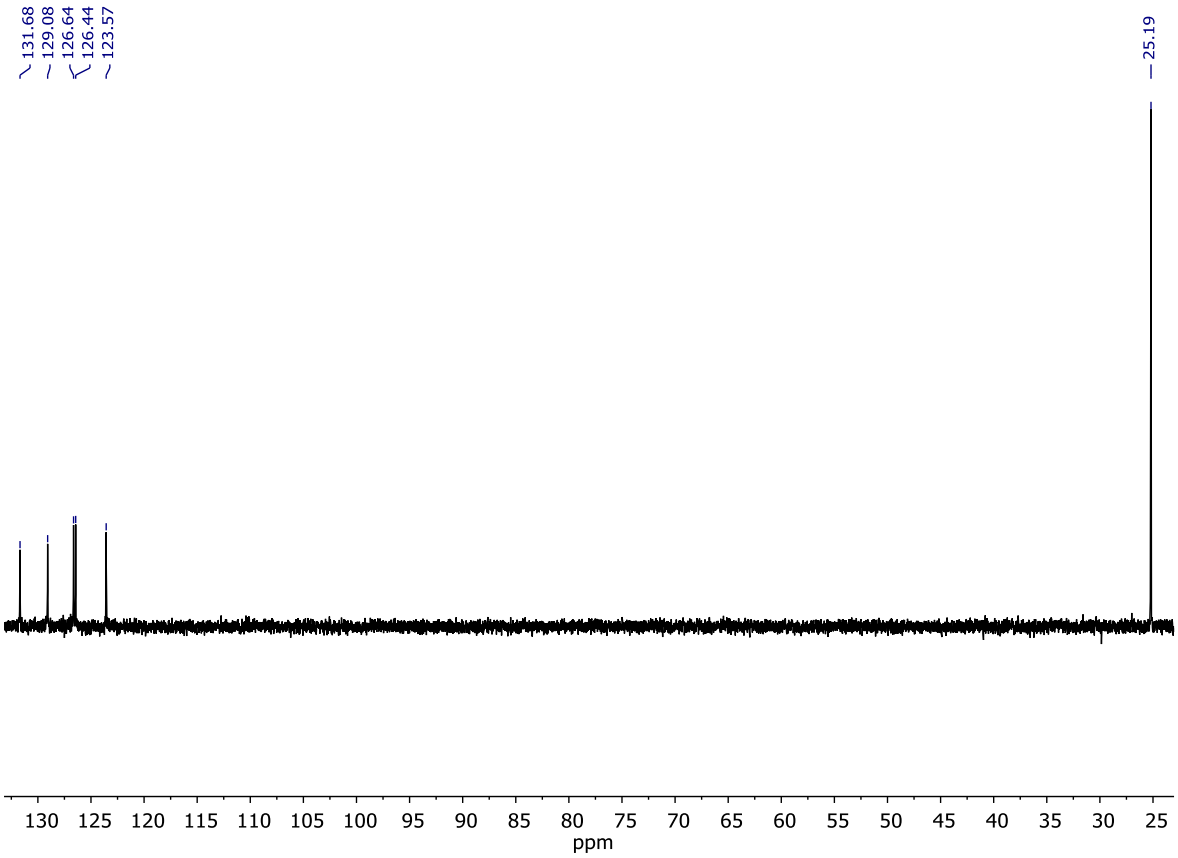

Figure 396. DEPT NMR ($CDCl_3$, 75 MHz) of AR63.

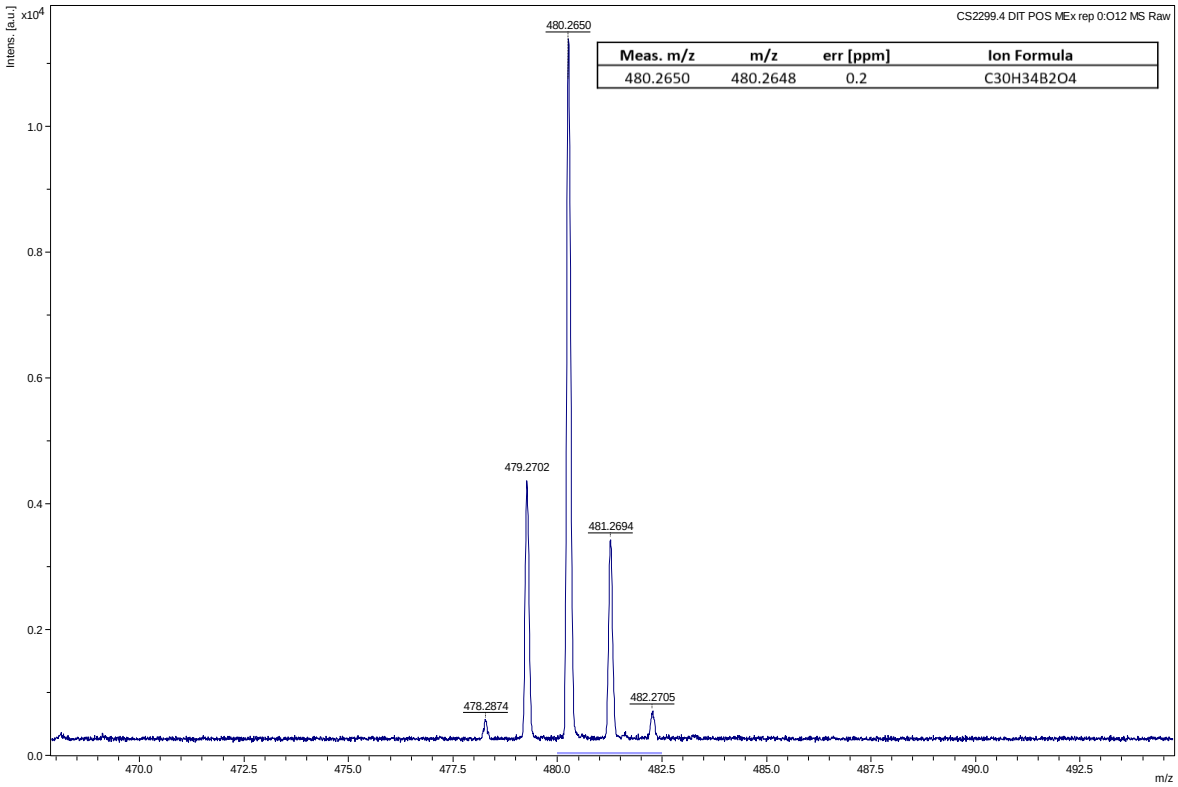

Figure 397. HRMS (MALDI, DIT+) of AR63.

Synthesis of 6,12-bis(*N*-(*N*-Boc-piperidin-4-yl)naphthalene-1,8-dicarboxylmonoimide)chrysene (AR65)

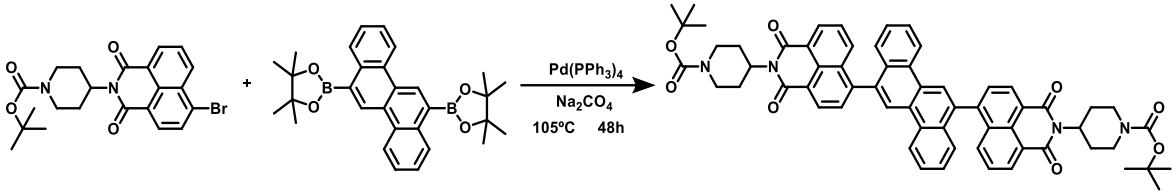

100 mg of 6,12-bis(pinacolylboronate)chrysene (AR63, 0.21 mmol), 200 mg of *N*-(Boc-piperidine)-4-bromonaphthalene-1,8-dicarboxylmonoimide (AR43p, 0.44 mmol) and 105 mg of sodium carbonate (0.99 mmol) were dissolved in a mixture of toluene:*n*-butanol:water (4:1:2 ml) under argon atmosphere and 12 mg of the catalyst $Pd(PPh_3)Cl_2$ (0.005 mmol) was added and the resulting solution was stirred at 110ºC for 48 hours. Then, the solvent was evaporated under reduce pressure and the solid was dissolved in 50 ml of DCM and washed three times with water (3×50 ml). The organic extracts were combined, dried over anhidrous Na_2SO_4 and the solvent was evaporated under reduce pressure. The solid obtained was purified by column chromatographic (SiO_2, DCM:MeOH 1%), getting 281 mg of a yellow solid, 65% yield.

m.p.: 277-279ºC (decomposition).

IR (ATR, cm^{-1}): 2973-2851, 1696 (C=O), 1656 (C=O), 1588, 1420 (C-O), 1399, 1346, 1276, 1243, 1165 (C-N), 1145, 1103, 1034, 1007, 962, 893, 863, 809, 780, 761, 701, 546, 454.

^{1}H-NMR (300 MHz, $CDCl_3$) δ (ppm): 8.90 – 8.76 (m, 6H, 6×**H$_{Ar}$**), 8.63 (d, *J* = 7.2 Hz, 2H, 2×**H$_{Ar}$**), 7.97 (dd, *J* = 7.2, 3.6 Hz, 2H, 2×**H$_{Ar}$**), 7.89 (d, *J* = 8.4 Hz, 2H, 2×**H$_{Ar}$**), 7.75 – 7.66 (m, 2H, 2×**H$_{Ar}$**), 7.63 – 7.55 (m, 2H, 2×**H$_{Ar}$**), 7.52 – 7.44 (m, 4H, 4×**H$_{Ar}$**), 5.38 – 5.21 (m, 2H, 2×C**H**), 4.51 – 4.21 (m, 4H, 2×C**H**$_2$), 3.07 – 2.73 (m, 8H, 4×C**H**$_2$), 1.81 – 1.71 (m, 4H, 2×C**H**$_2$), 1.52 (s, 18H, 6×C**H**$_3$).

^{13}C-NMR (75MHz, $CDCl_3$) δ (ppm): 164.7 (**C**=O), 164.6 (**C**=O), 154.8 (**C**=O), 145.6 (**C**$_{Ar}$), 136.5 (**C**$_{Ar}$),132.9 (**C**$_{Ar}$H), 131.7 (**C**$_{Ar}$), 131.6 (**C**$_{Ar}$H), 131.6 (**C**$_{Ar}$), 131.5 (**C**$_{Ar}$), 131.1 (**C**$_{Ar}$H), 131.0 (**C**$_{Ar}$), 130.6 (**C**$_{Ar}$), 129.3 (**C**$_{Ar}$H), 129.2 (**C**$_{Ar}$H), 128.6 (**C**$_{Ar}$), 127.9 (**C**$_{Ar}$), 127.5 (**C**$_{Ar}$H), 127.3 (**C**$_{Ar}$H), 127.1 (**C**$_{Ar}$H), 123.6 (**C**$_{Ar}$H), 123.5 (**C**$_{Ar}$), 123.2 (**C**$_{Ar}$H), 123.1 (**C**$_{Ar}$), 79.7 (**Cq**), 52.1 (**C**H), 44.5 (**C**H$_2$), 43.9 (**C**H$_2$), 29.8 (**C**H$_2$), 28.7 (**C**H$_3$), 28.5 (**C**H$_2$).

HRMS (MALDI, DIT-) m/z: calculated for $C_{62}H_{56}N_4O_8$: 984.4093 (M^--H); found 984.4083.

UV-Vis ($CHCl_3$), λ_{max} nm (log ε): 490 (8.0).

Ø (Tol, %): 62.38.

τ (280 nm, Tol, ns): 2.228 (χ^2: 1.101).

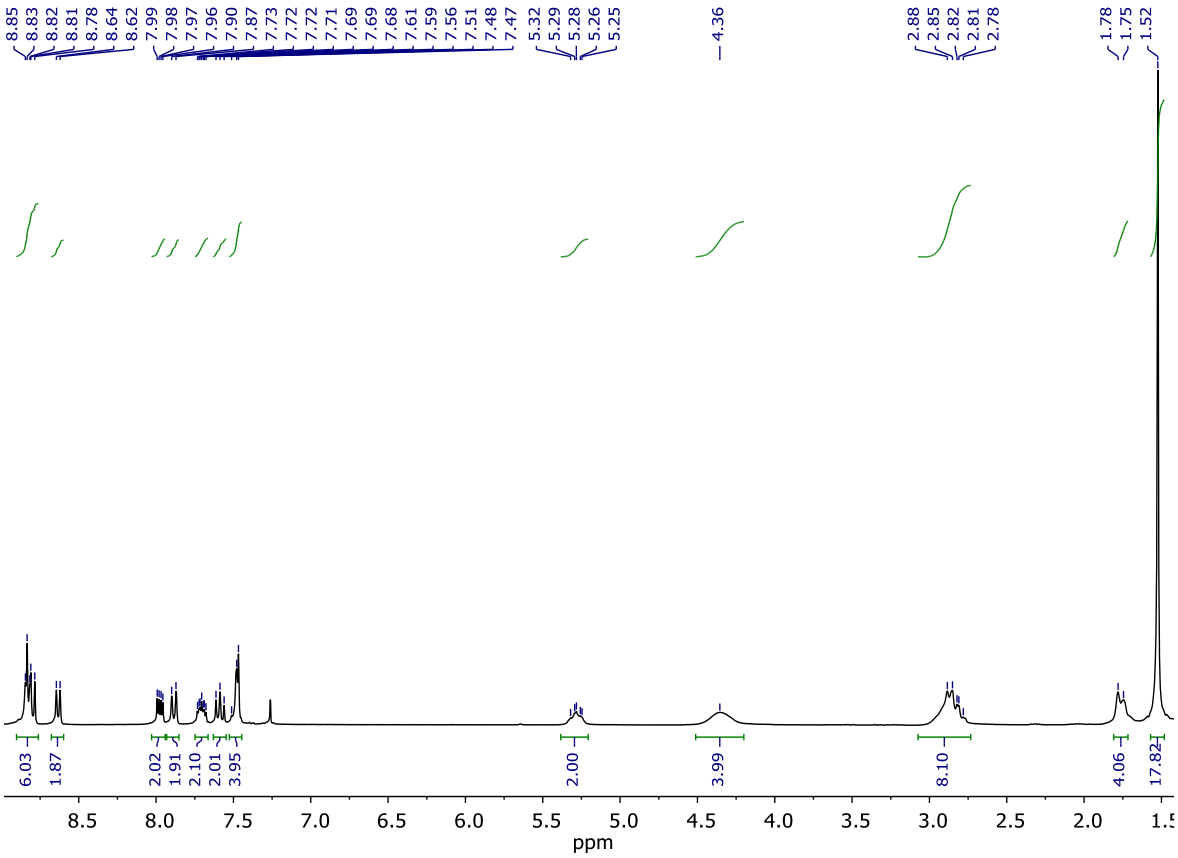

Figure 398. ^{1}H-NMR ($CDCl_3$, 300 MHz) of AR65.

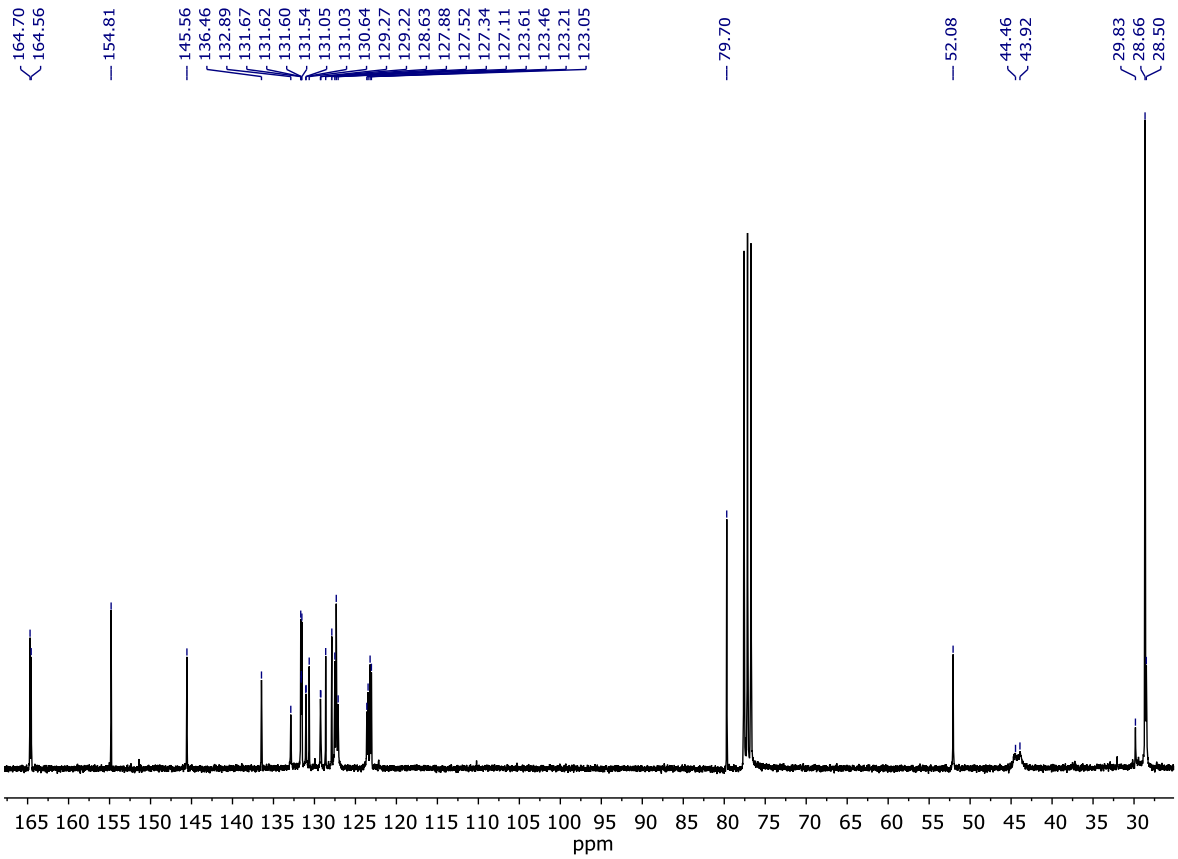

Figure 399. ^{13}C-NMR ($CDCl_3$, 75 MHz) of AR65.

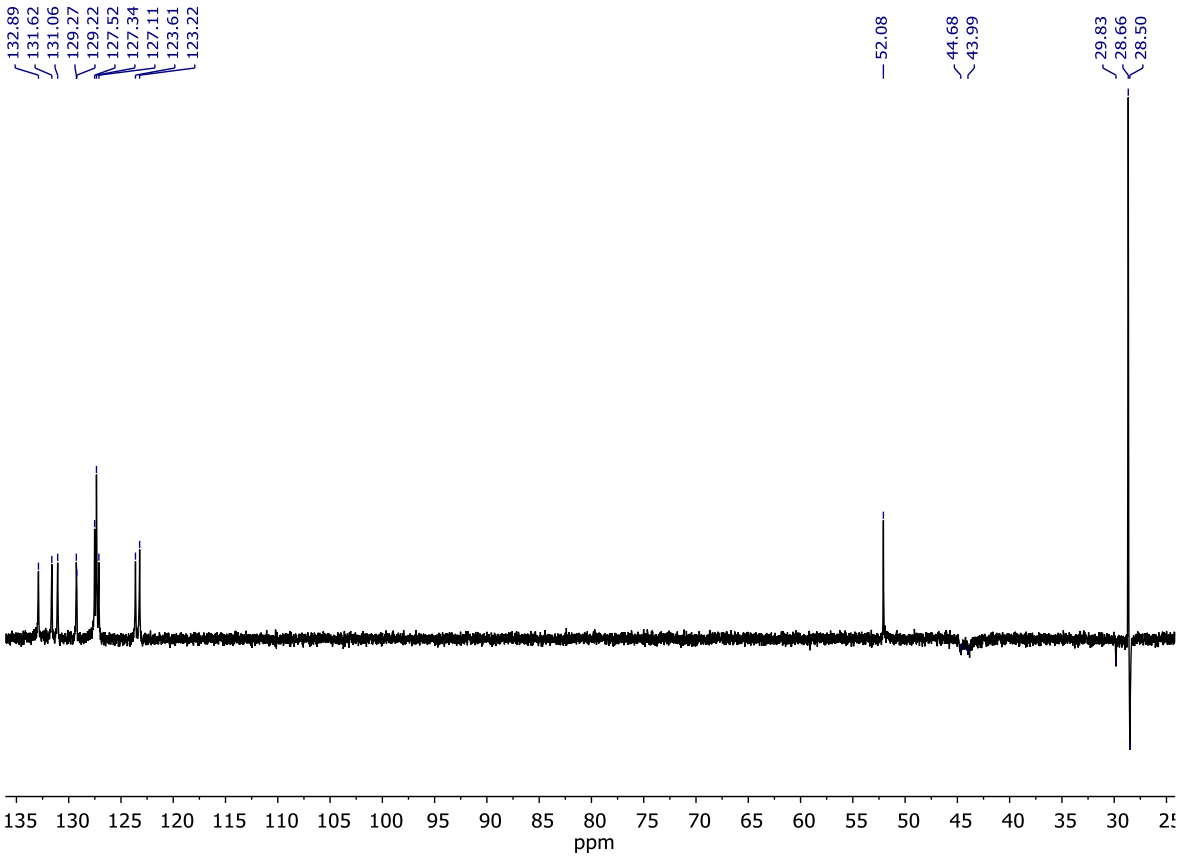

Figure 400. DEPT NMR ($CDCl_3$, 75 MHz) of AR65.

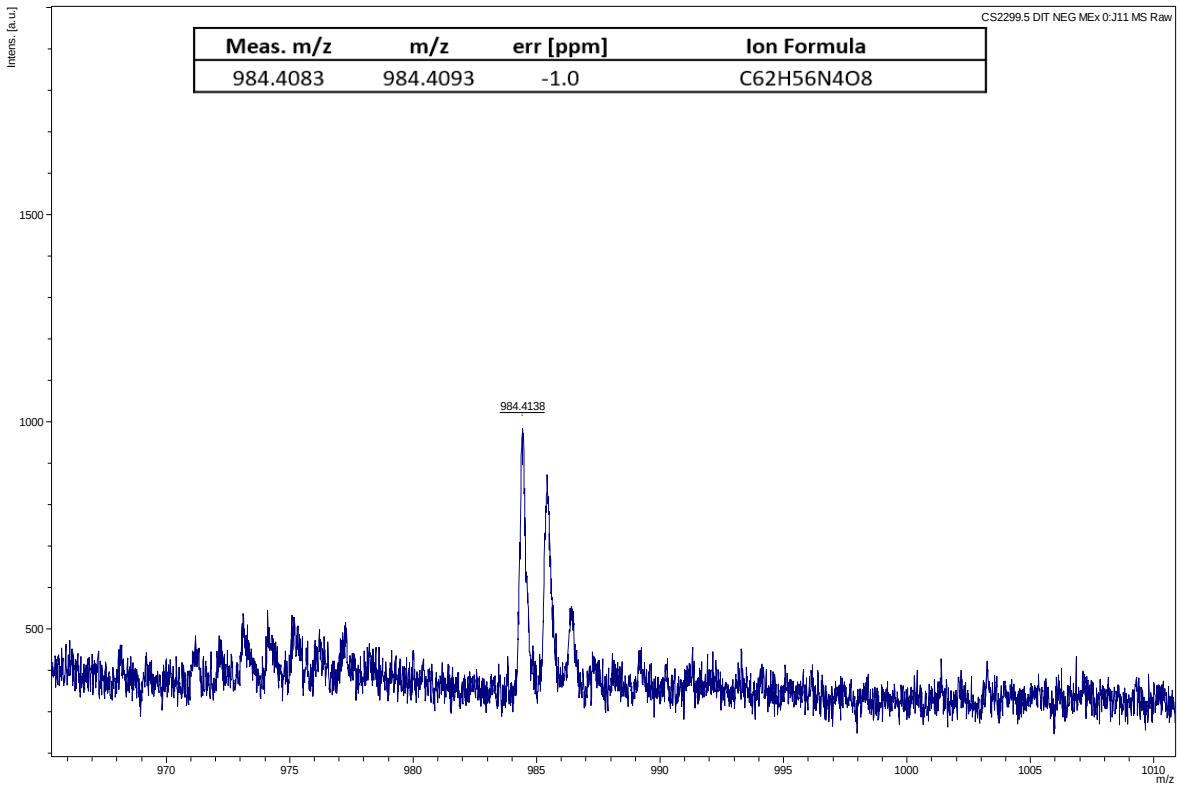

Meas. m/z	m/z	err [ppm]	Ion Formula
984.4083	984.4093	-1.0	C62H56N4O8

Figure 401. HRMS (MALDI, DIT-) of AR65.

Solvatochromism:

The concentration of the compound was 10 µM and the excitation wavelength was 335 nm.

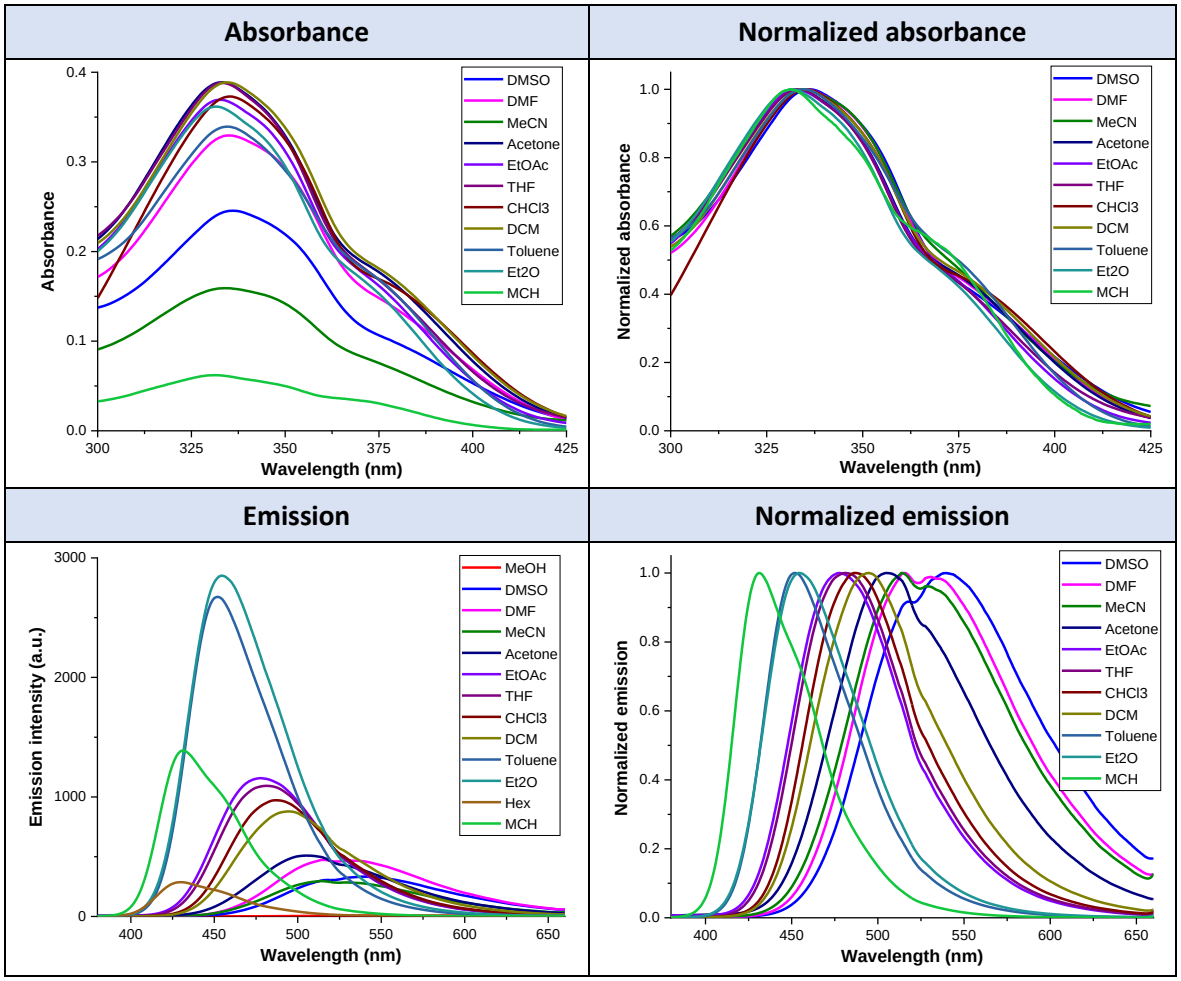

Figure 402. Solvatochromism of AR65.

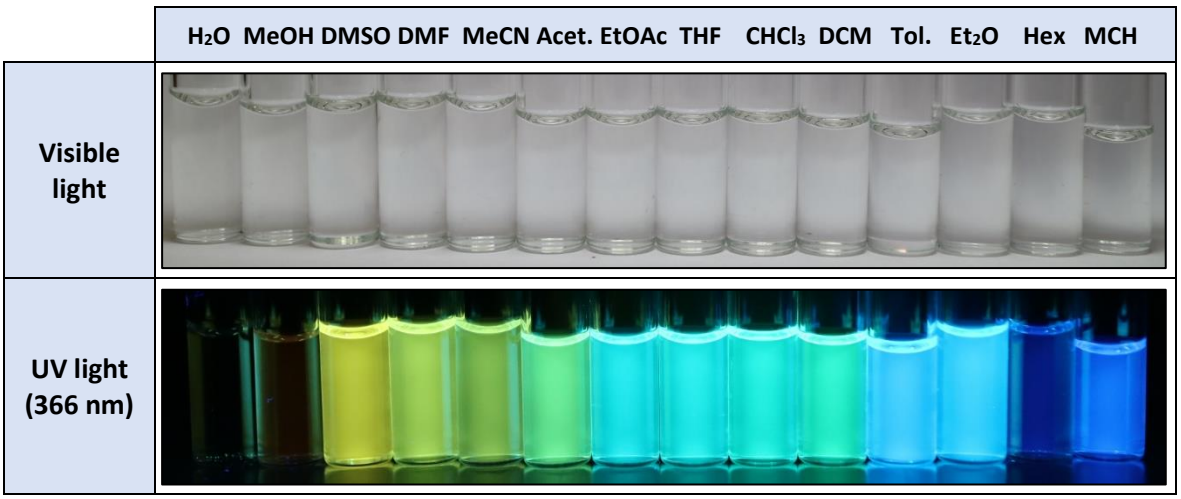

Figure 403. Solvatochromism of AR65 under visible and 366 nm light.

Fluorescence decay lifetime (τ):

The solvent used was toluene. The concentration of the compound was 10 µM.

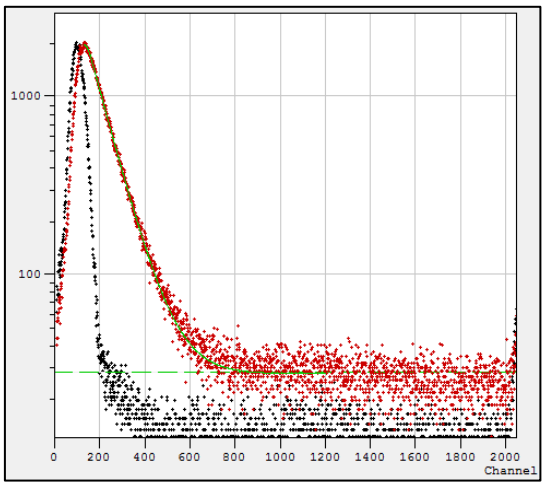

Figure 404. Fluorescence decay lifetime of AR65.

Water acceptance test:

The solvent used was THF and the concentration of the compound was 10 µM.

	R	5%	10%	20%	30%	40%	50%	60%	70%	80%	90%
Visible light	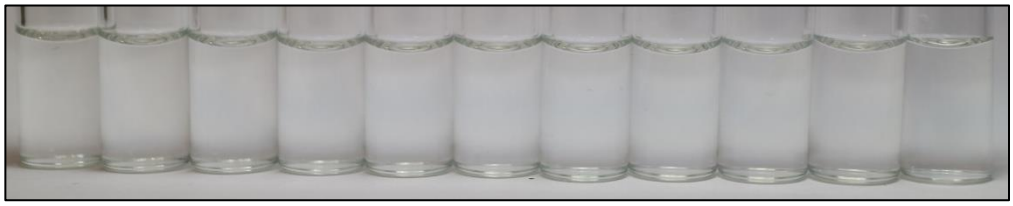										
UV light (366 nm)	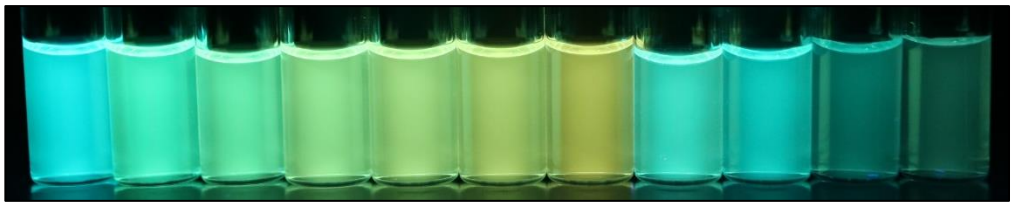										

Figure 405. Water acceptance test of AR65 under visible (up) and UV (down) light.

There was a noticeable fluorescence quenching up to 50% of water, at 60 – 70% of water, there was a slight increase in fluorescent intensity. The emission maximum was also shifted from green to yellow region when the amount of water was ranged from 5 to 50%, while it was returned to blue region when AIE ocurrs.

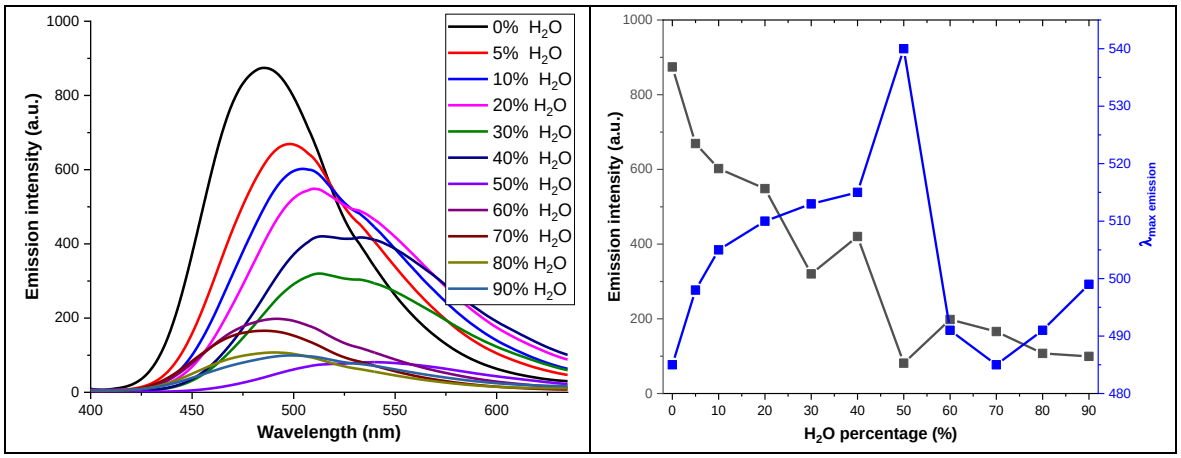

Figure 406. Emission intensity graph (left) and graph of relationship between the emission intensity and the wavelength of the maximum of emission (right) as a function of the amount of water added for AR65.

AR65 10% water	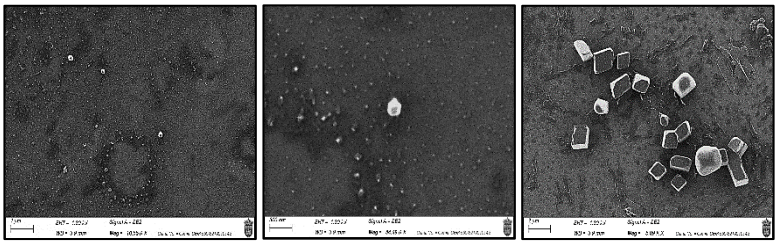
AR65 30% water	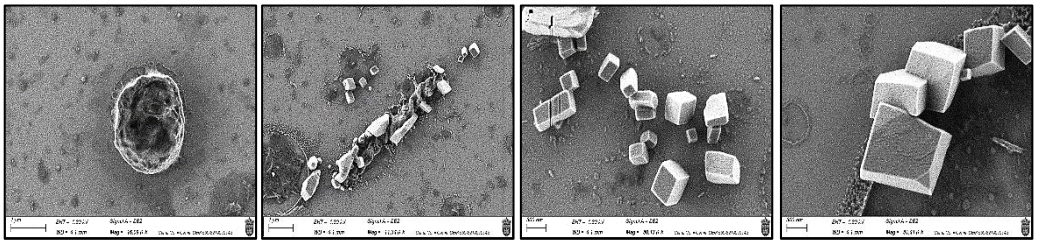
AR65 50% water	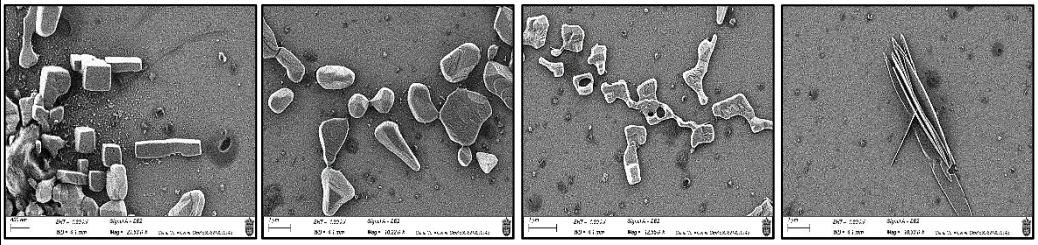
AR65 60% water	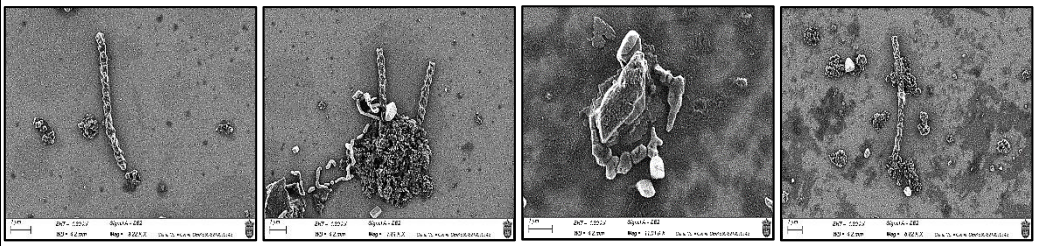
AR65 70% water	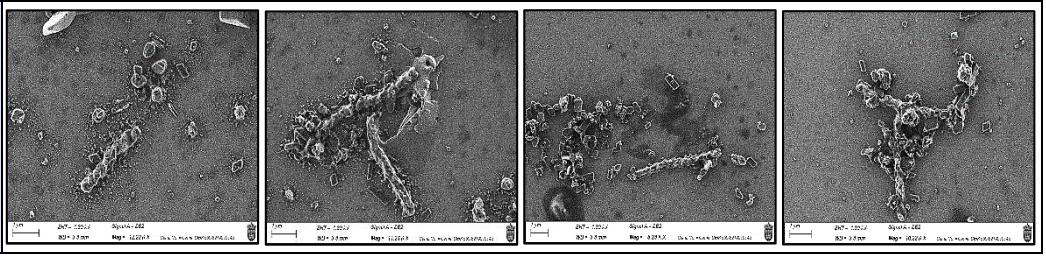

AR65 90% water	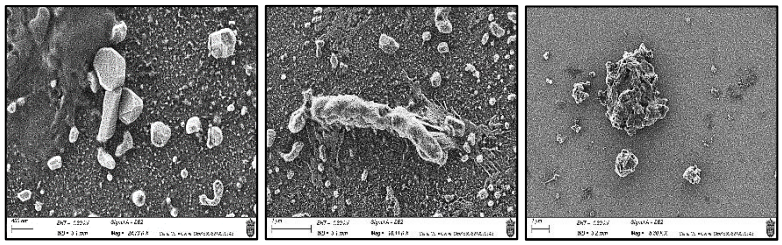

Figure 407. SEM nanoparticles of AR65 in different mixtures of THF-H_2O.

pH test:

The proportion of water used to do this test was 50%. The concentration of the compound was 10 µM and the solvent used was THF.

	R	HCl	3.4	4.8	6.4	7.4	7.9	10.5	KOH
Visible light	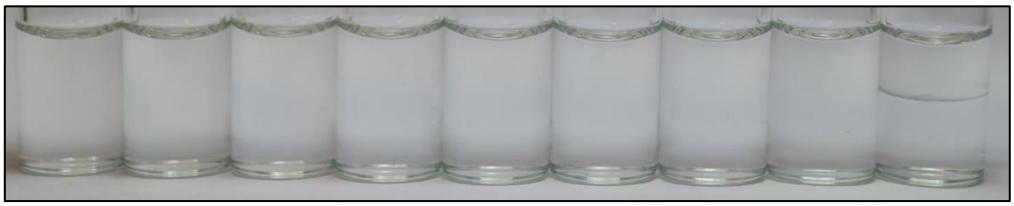								
UV light (366 nm)	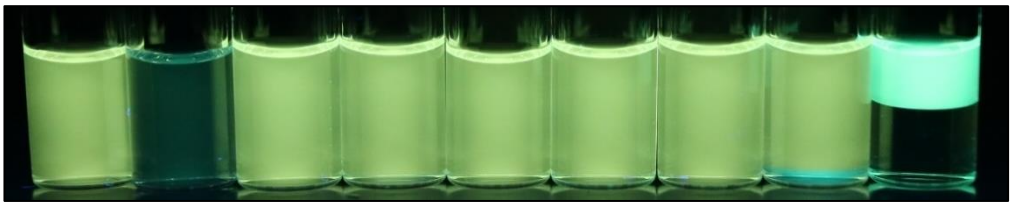								

Figure 408. pH test of AR65 under visible (up) and UV (down) light.

The fluorescence was quenched at very acid pH but the fluorescence intensity was increased at very basic pH.

Cations and anions test:

The concentration of the compound was 10 µM and the solvent used was THF.

	R	Ag^{+}	Ni^{2+}	Sn^{2+}	Cd^{2+}	Zn^{2+}	Pb^{2+}	Cu^{2+}	Fe^{3+}	Sc^{3+}	Al^{3+}	Hg^{2+}	Au^{3+}	Co^{2+}	Pd^{2+}	Ir^{3+}	Cu^{+}	Ru^{3+}	Pt^{2+}
Visible light																			
UV light (366 nm)	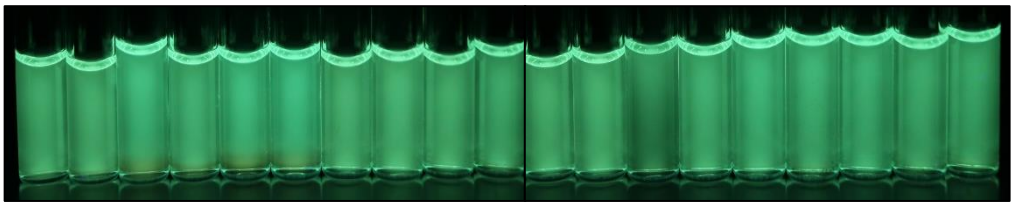																		

Figure 409. Cations test of AR56 under visible (up) and UV (down) light.

No significat changes was observed.

The concentration of the compound was 10 µM and the solvent used was THF.

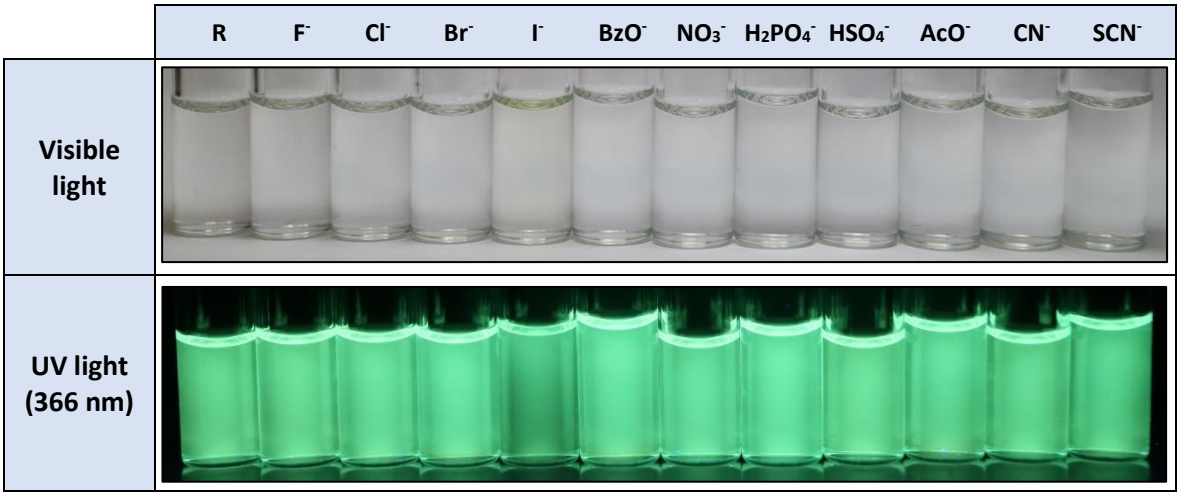

Figure 410. Anions test of AR65 under visible (up) and UV (down) light.

No significant changes were observed.

Oxidant and reductant reagents test:

The solvent used was aTHF and concentration of the compound was 10 µM.

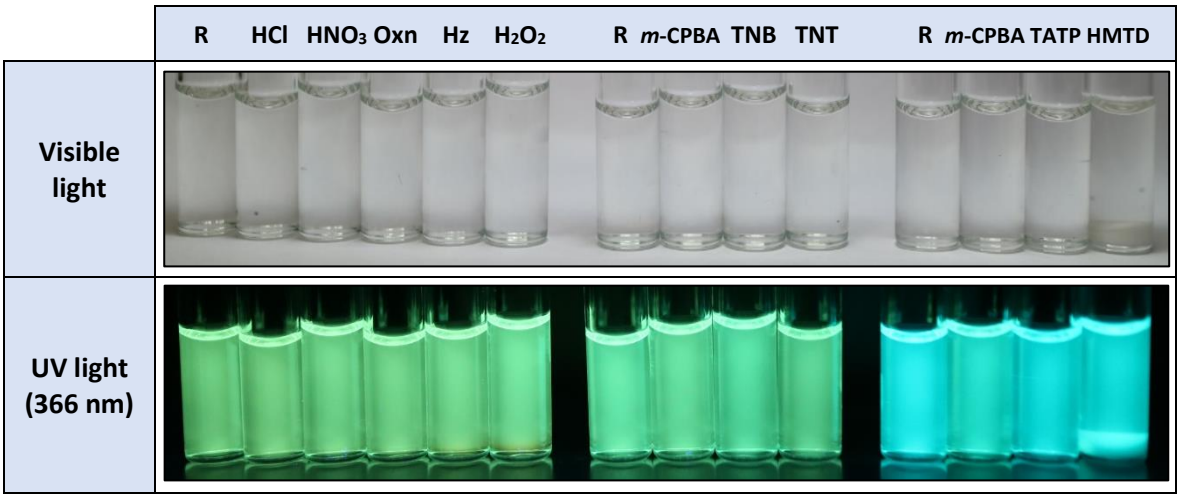

Figure 411. Oxidant and reductant reagents test of AR65 under visible (up) and UV (down) light.

No significat changes was observed.

Synthesis of *N*-(*N*-Boc-piperidin-4-yl)-4-(tributylstannyl)naphthalene-1,8-dicarboxylmonoimide (AR98)

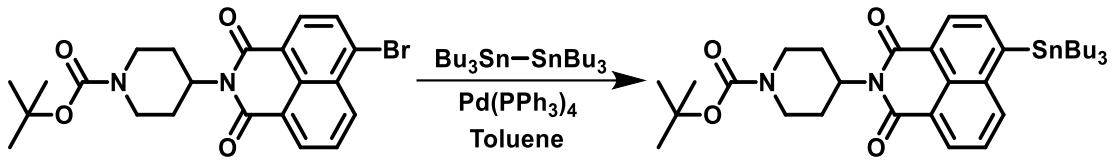

200 mg of *N*-(*N*-Boc-piperidin-4-yl)-4-bromonaphthalene-1,8-dicarboxylmonoimide (AR43, 0.43 mmol) and 265 mg of bis(tributyltin) (0.46 mmol) were dissolved in 5 ml of toluene under argon atmosphere and 12 mg of the catalyst, $Pd(PPh_3)_4$, (0.01 mmol) was added and the resulting solution was stirred at 110°C for 72 hours. Then, the solvent was evaporated under reduce pressure and the solid was dissolved in 50 ml of DCM and washed three times with water (3×50 ml). The organic extracts were combined, dried over anhidrous Na_2SO_4 and the solvent was evaporated under reduce pressure, getting 291 mg of a yellow solid with a quantitative yield. This compound is used without further purification in the following reaction

Synthesis of *N*-(*N*-Boc-piperidin-4-yl)-4-(1,10-phenanthrolin-2-yl)naphthalene-1,8-dicarboxyl-monoimide (AR85)

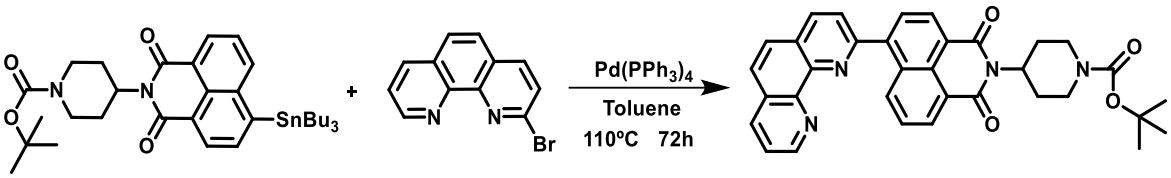

100 mg of *N*-(*N*-Boc-piperidin-4-yl)-4-(tributylstannyl)naphthalene-1,8-dicarboxylmonoimide (AR98, 0.15 mmol) and 41 mg of 2-bromo-1,10-phenanthroline (0.16 mmol) were dissolved in 5 ml of toluene under nitrogen atmosphere. 12 mg of the catalyst, $Pd(PPh_3)_4$ (0.01 mmol), were added and the resulting mixture was stirred at 110ºC for 72 hours. Afterwards, the solvent was evaporated under reduce pressure, the obtained solid was dissolved in 50 ml of DCM and washed three times with a solution of potassium fluoride 1M (3×50 ml), washed another three times with sodium hydroxide 1M solution (3×50 ml), three times with water (3×50 ml) and one more time with brine (1×50 ml). The organic layer was dried over anhidrous Na_2SO_4 and the solvent was evaporated under reduce pressure. The organic solid was purified by column chromatography (SiO_2, DCM:MeOH 1%) to obtain 71 mg of orange solid, 85% yield.

m.p.: 106-108ºC.

IR (ATR, cm^{-1}): 2971 – 2857, 1685 (C=O), 1655 (C=O), 1578, 1487 (C-O), 1443, 1401, 1338, 1244, 1164 (C-N), 1143, 1116, 1065, 1032, 981, 894, 846, 810, 778, 729, 619, 592, 570, 417.

^{1}H-NMR (300 MHz, $CDCl_3$) δ (ppm): 9.25 (d, *J* = 3.5 Hz, 1H, 3×**H$_{Ar}$**), 8.57 (m, 2H, 2×**H$_{Ar}$**), 8.33 (m, 2H, 2×**H$_{Ar}$**), 8.04 (m, 2H, 2×**H$_{Ar}$**), 7.80 (m, 4H, 4×**H$_{Ar}$**), 7.68 (m, 1H, **H$_{Ar}$**), 5.15 (m, 1H, C**H**), 4.29 (s, 2H, C**H**$_2$), 2.92 – 2.69 (m, 4H, 2×C**H**$_2$), 1.67 (m, 2H, C**H**$_2$), 1.49 (s, 9H, 3×C**H**$_3$).

^{13}C-NMR (75MHz, $CDCl_3$) δ (ppm): 164.0 (**C**=O), 154.8 (**C**$_{Ar}$), 150.7 (**C**$_{Ar}$H), 142.8 (**C**$_{Ar}$), 138.3 (**C**$_{Ar}$H), 136.7 (**C**$_{Ar}$), 136.4 (**C**$_{Ar}$H), 133.2 (**C**$_{Ar}$H), 132.2 (**C**$_{Ar}$H), 131.4 (**C**$_{Ar}$H), 131.2 (**C**$_{Ar}$H), 130.6 (**C**$_{Ar}$), 130.2 (**C**$_{Ar}$), 129.1 (**C**$_{Ar}$), 128.2 (**C**$_{Ar}$H),127.7 (**C**$_{Ar}$), 127.2 (**C**$_{Ar}$H), 126.2 (**C**$_{Ar}$), 126.1 (**C**$_{Ar}$H), 123.7 (**C**$_{Ar}$H), 123.5 (**C**$_{Ar}$), 122.6 (**C**$_{Ar}$), 79.7 (**Cq**), 52.1 (**C**H) ,43.2 (**C**H$_2$), 28.6 (**C**H$_3$), 28.4 (**C**H$_2$).

HRMS (MALDI, DCTB+) m/z: calculated for $C_{34}H_{30}N_4O_4$+Na: 581.2165 (M+Na$^+$); found 581.2192.

UV-Vis ($CHCl_3$), λ_{max} nm (log ε): 339 (4.1).

Ø (MeOH, %): 22.25.

τ (280 nm, MeOH, ns): 0.540/2.819 (χ^2: 1.036).

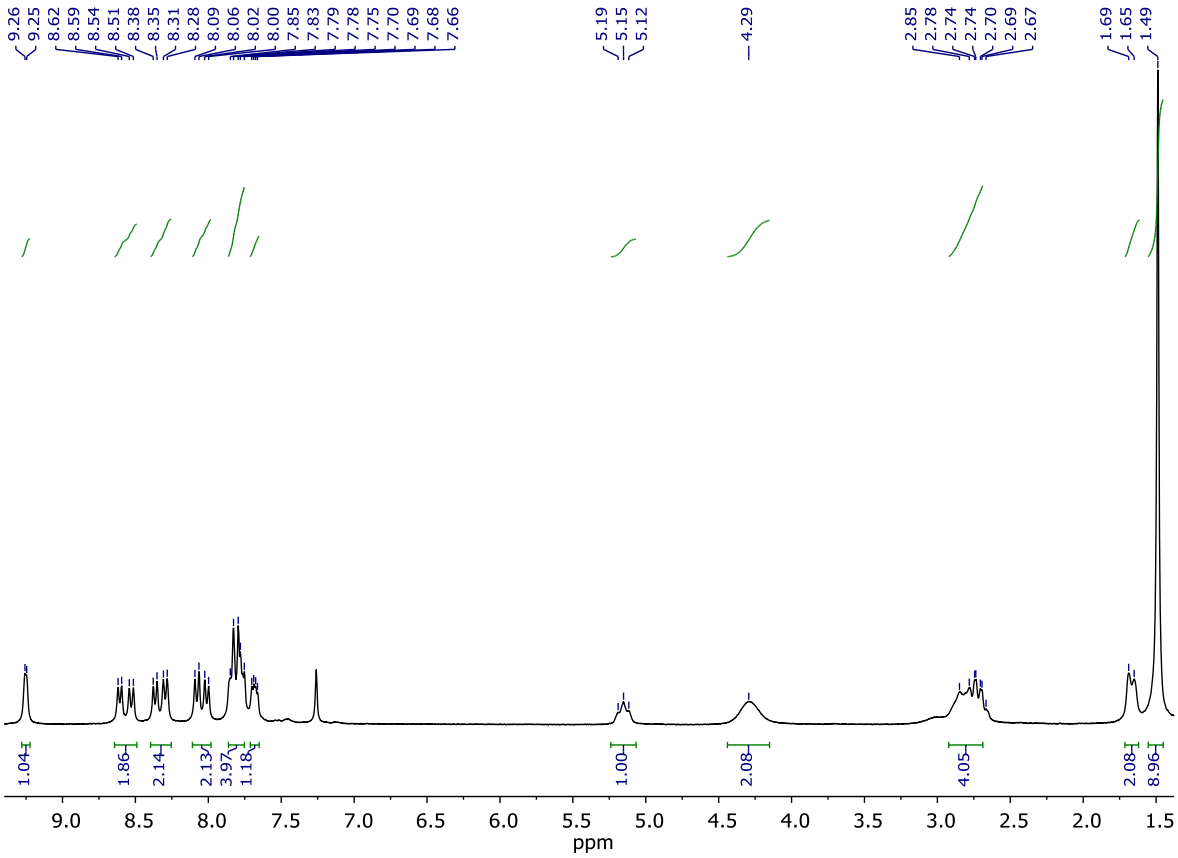

Figure 412. ^{1}H-NMR ($CDCl_3$, 300 MHz) of AR85.

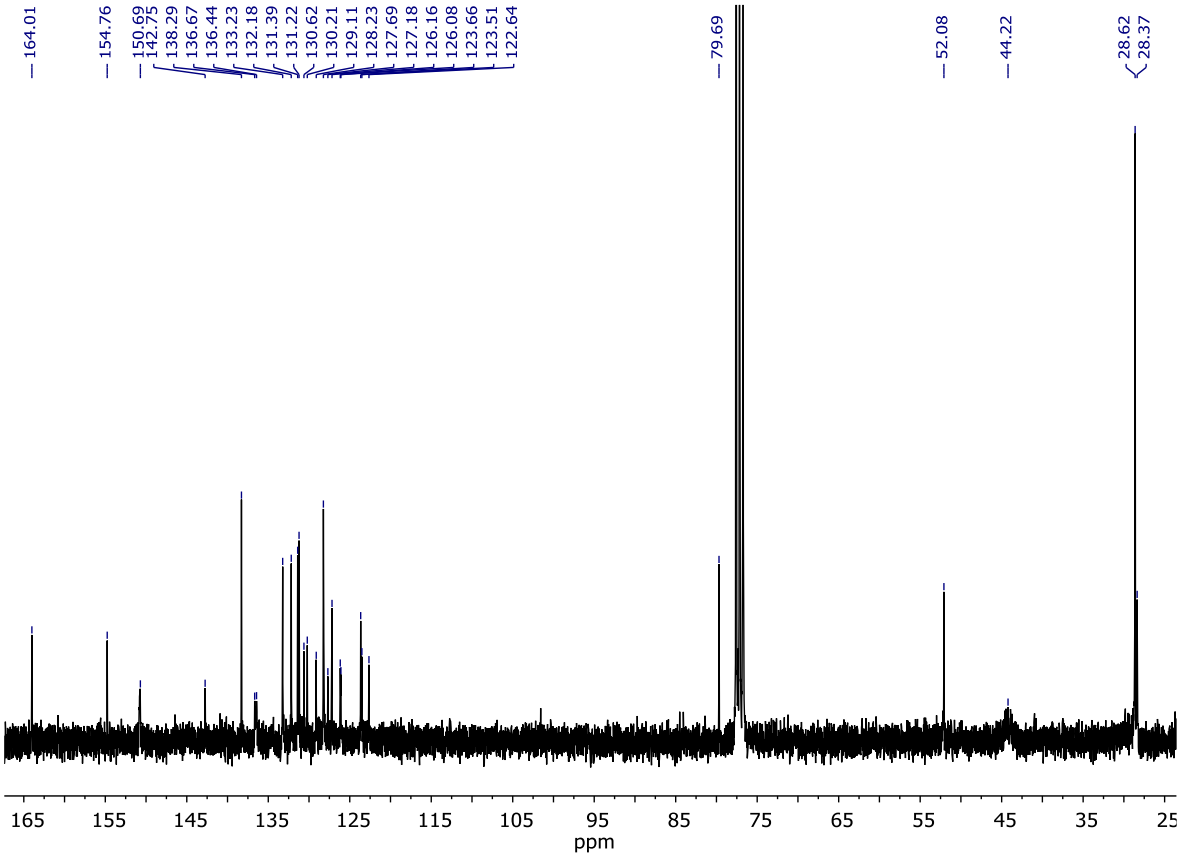

Figure 413. ^{13}C-NMR ($CDCl_3$, 75 MHz) of AR85.

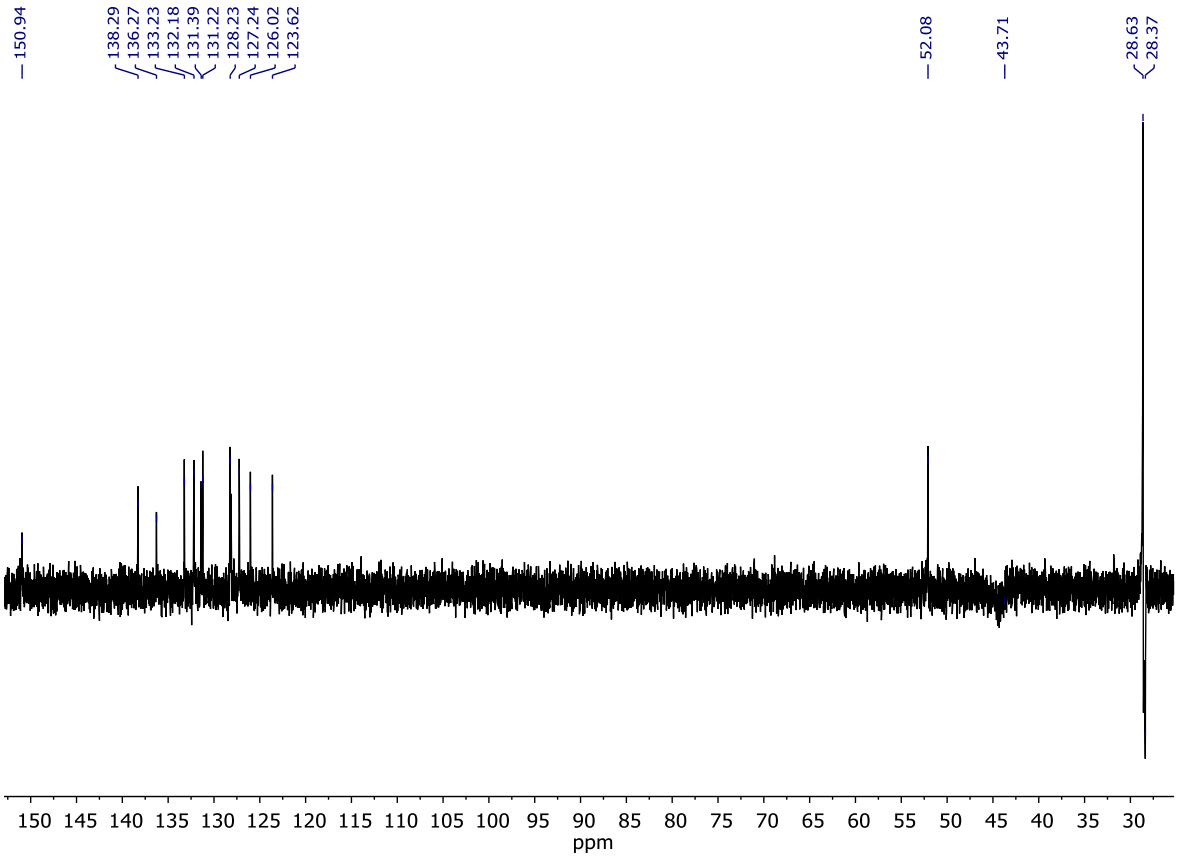

Figure 414. DEPT NMR ($CDCl_3$, 75 MHz) of AR85.

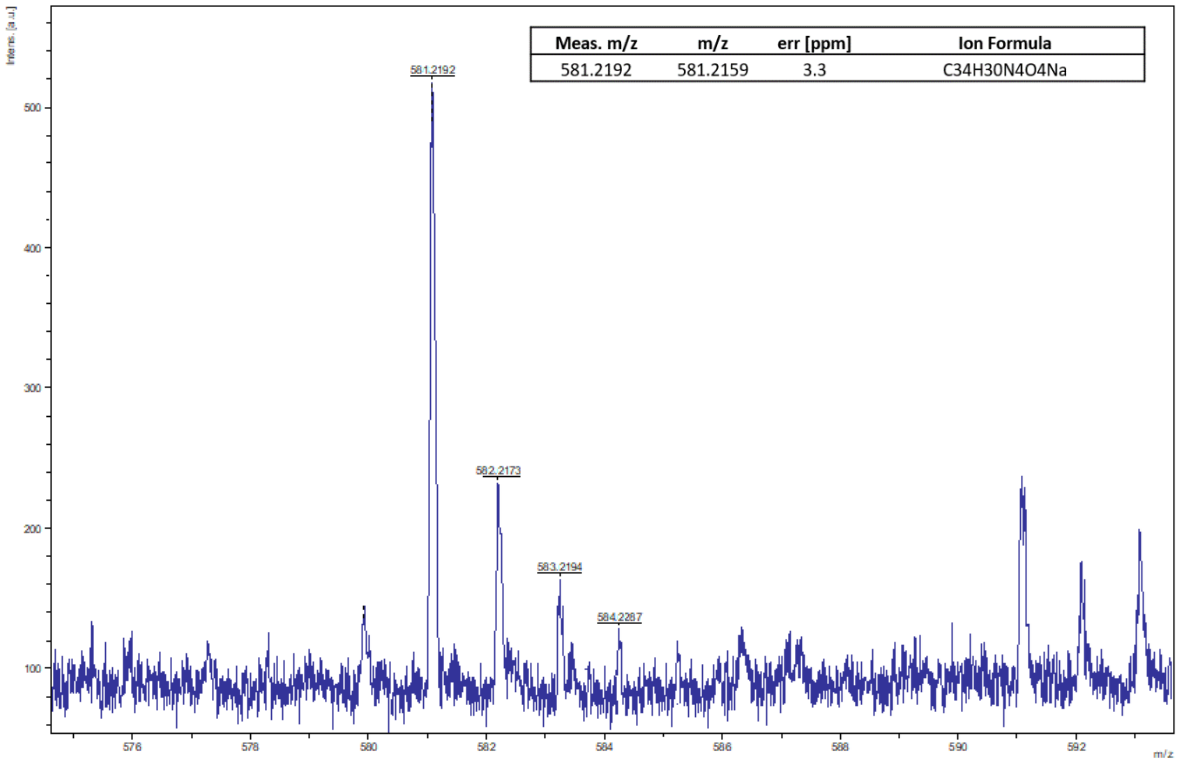

Figure 415. HRMS (MALDI, DCTB+) of AR85.

Solvatochromism:

The concentration of the compound was 10 µM and the excitation wavelength was 330 nm.

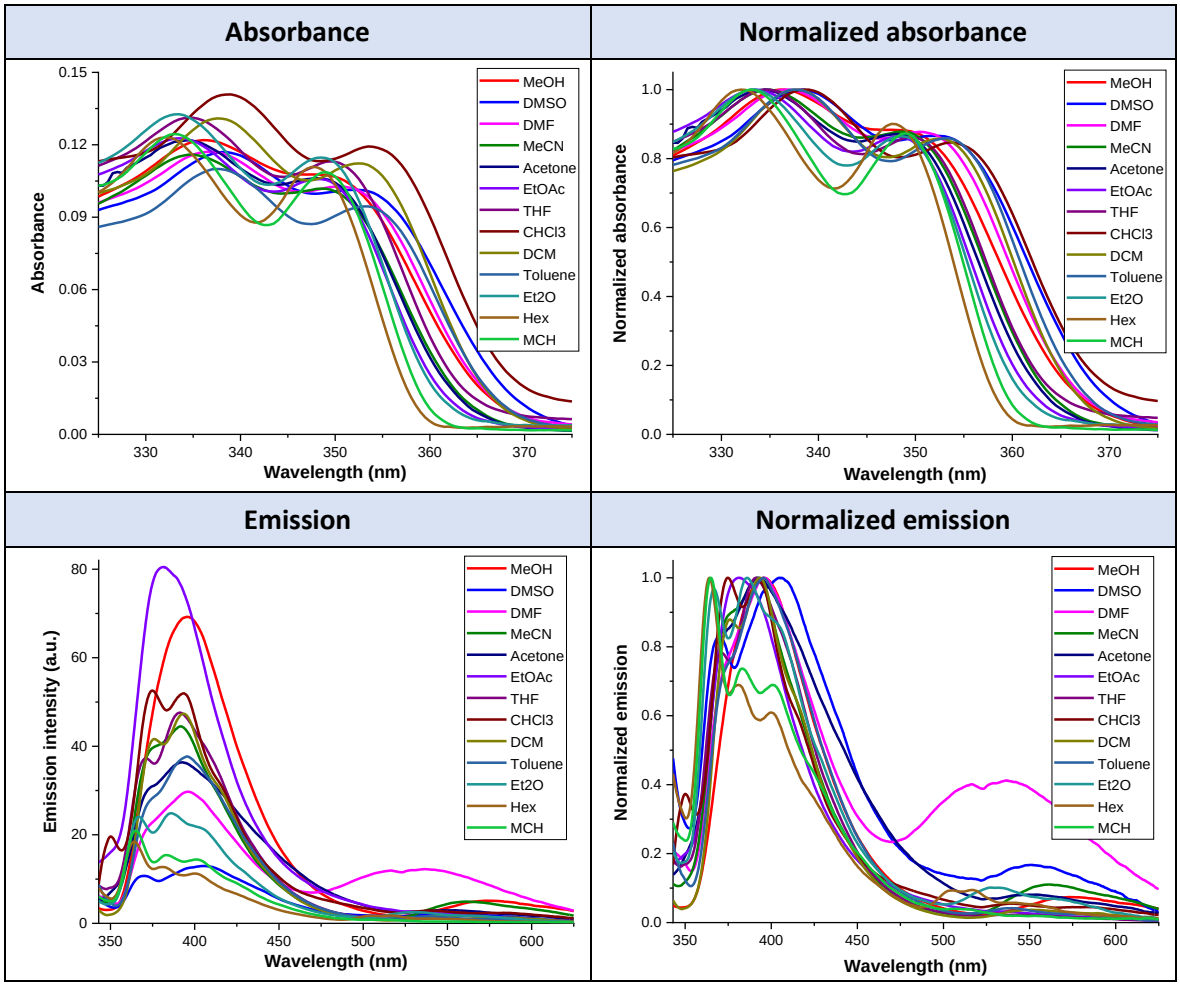

Figure 416. Solvatochromism of AR85.

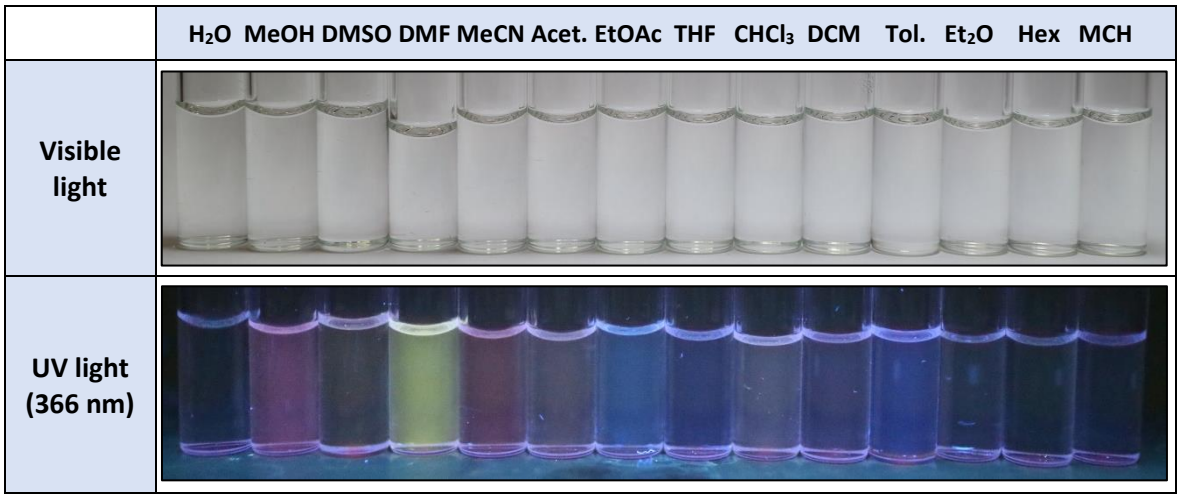

Figure 417. Solvatochromism of AR85 under visible and 366 nm light.

Fluorescence decay lifetime (τ):

The solvent used was MeOH. The concentration of the compound was 10 µM.

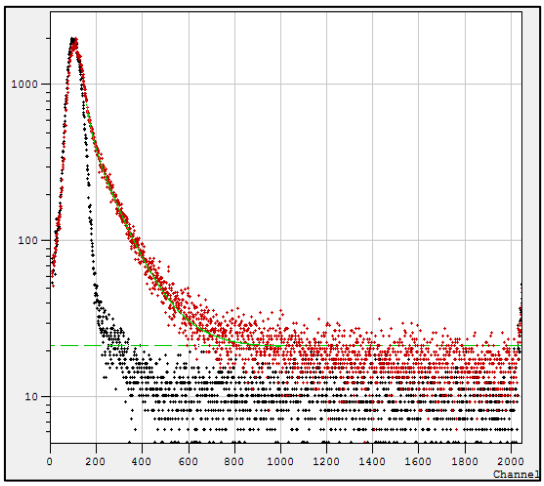

Figure 418. Fluorescence decay lifetime of AR85.

Water acceptance test:

The solvent used was THF and the concentration of the compound was 10 µM.

	R	5%	10%	20%	30%	40%	50%	60%	70%	80%	90%
Visible light											
UV light (366 nm)	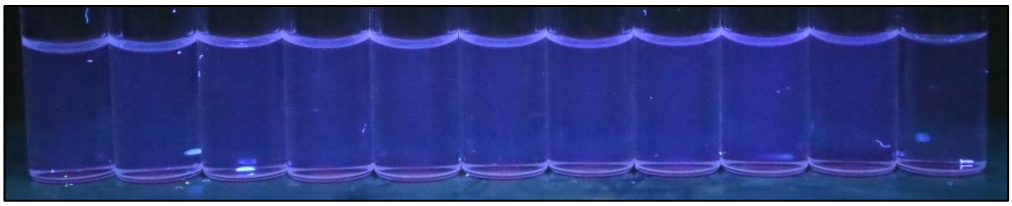										

Figure 419. Water acceptance test of AR85 under visible (up) and UV (down) light.

There was a quenching of fluorescence with high amounts of water (80 – 90%).

pH test:

The prortion of water that the compound could accept was 70%. The concentration of the compound was 10 µM and the solvent used was THF.

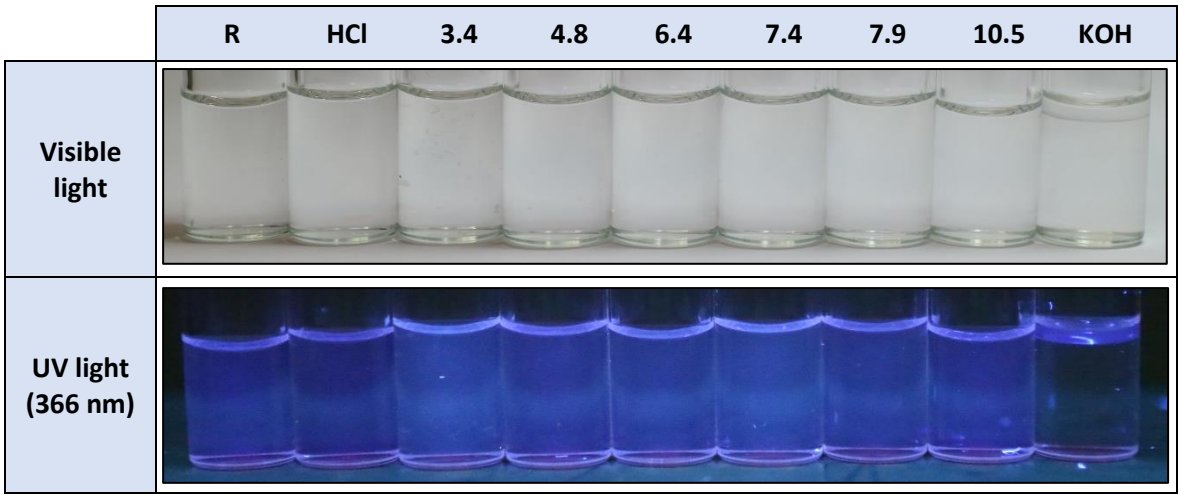

Figure 420. pH test of AR85 under visible (up) and UV (down) light.

No significant changes was observed.

Cations and anions test:

The concentration of the compound was 10 µM and the solvent used was THF.

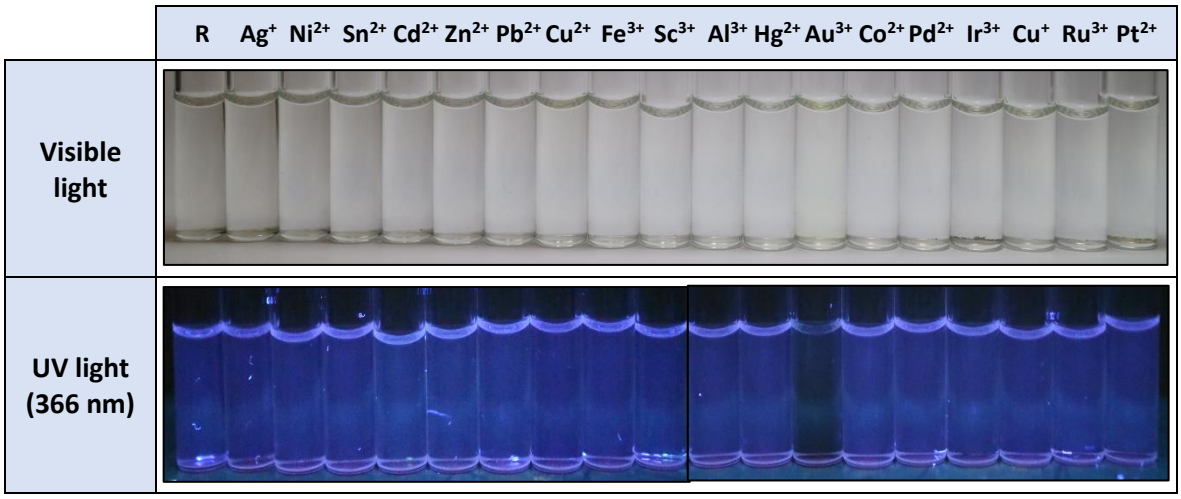

Figure 421. Cations test of AR85 under visible (up) and UV (down) light.

Under visible light, the change of the colour to pale yellow was observed. Under UV light, the fluorescence was quenched.

The concentration of the compound was 10 µM and the solvent used was THF.

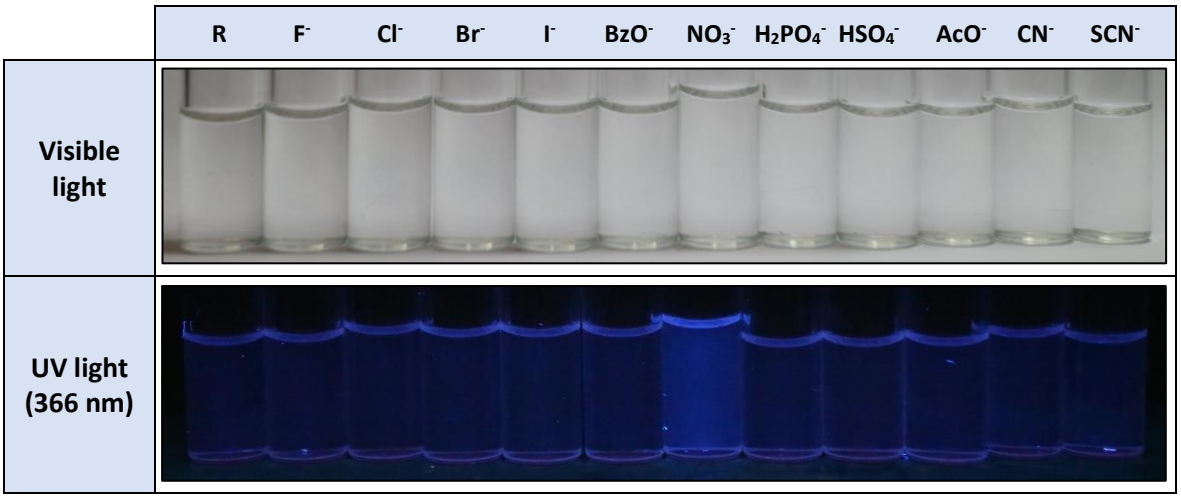

Figure 422. Anions test of AR85 under visible (up) and UV (down) light.

The only change observed was an increase in fluorescence against the nitrate (NO_3^-).

Oxidant and reductant reagents test:

The solvent used was THF and concentration of the compound was 10 µM.

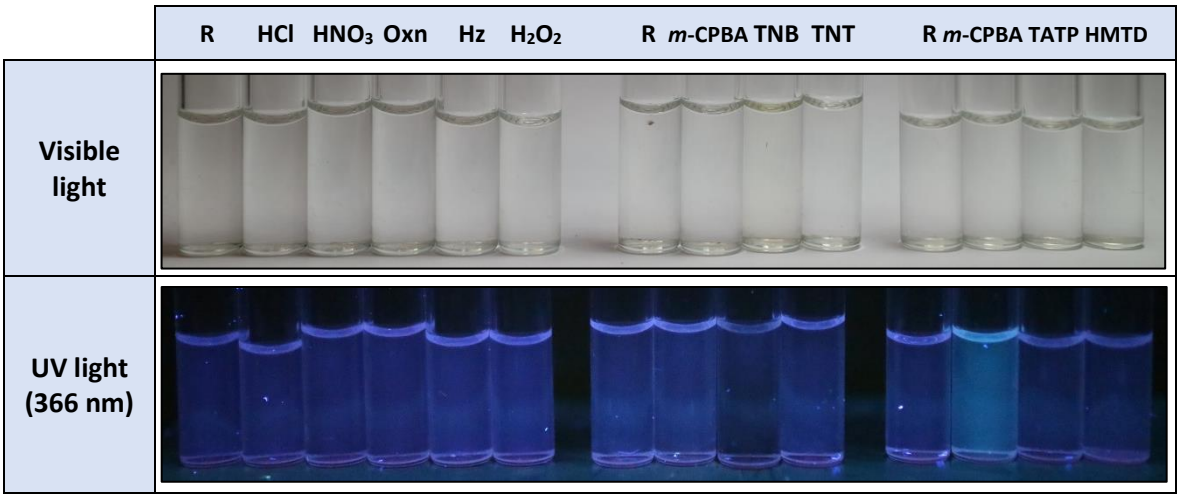

Figure 423. Oxidant and reductant reagents test of AR85 under visible (up) and UV (down) light.

The most important change observed was the quenching of fluorescence against TNB. Under UV light, the solution was appeared pale yellow.

In order to determine the fluorescence variation of the compound under study in the presence of HMTD, some test were carrier out for each probe in 9 different solvents. The probe concentration was 10 µM and the HMTD was added in excess (7 mg in each vial) to ensure complete reaction with the probe. All the test were performed at room temperature and the photographs were taken immediately after the addition of HMTD and again after 24 hours under 366 nm light.

The changes observed in some solvents were very small and were due to the fact that the HMTD was remained in suspension generating these changes due to the opacity of the solution. No further testing was done.

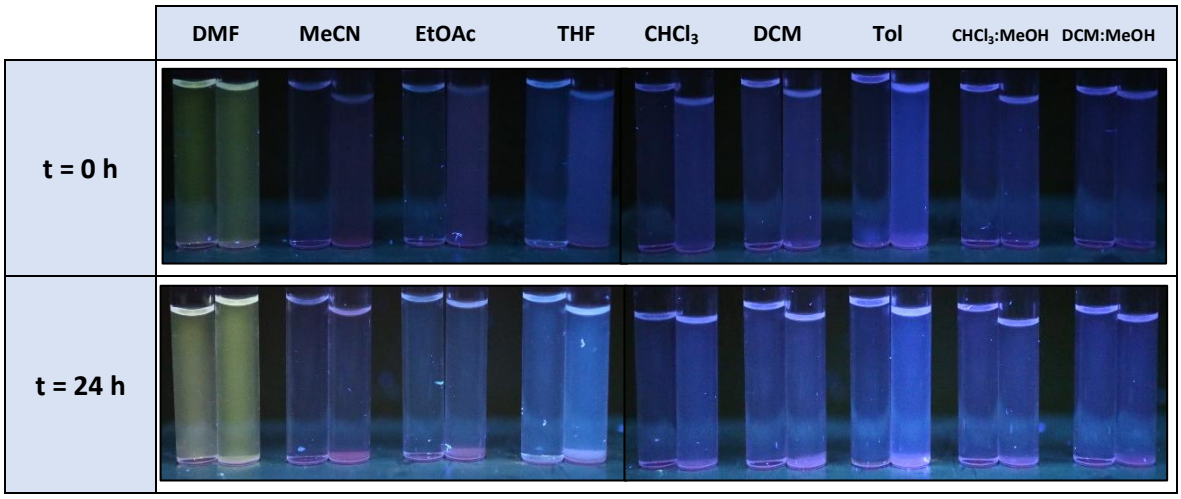

Figure 424. Pairs of AR85 (left) and AR85 with excess of HMTD (right) in different solvents at time 0 h and 24 h under 366 nm light.

Previous solvents test:

In order to determine the fluorescence variation of the compound under study in the presence of TNB and TNT, some test were carried out for the probe in 10 different solvents. The AR85 concentration was 10 µM and the TNB or TNT was added in excess (7 mg in each vial). All the test were performed at room temperature and the photographs were taken immediately after the addition of the analyte and again after 24 hours for TNB.

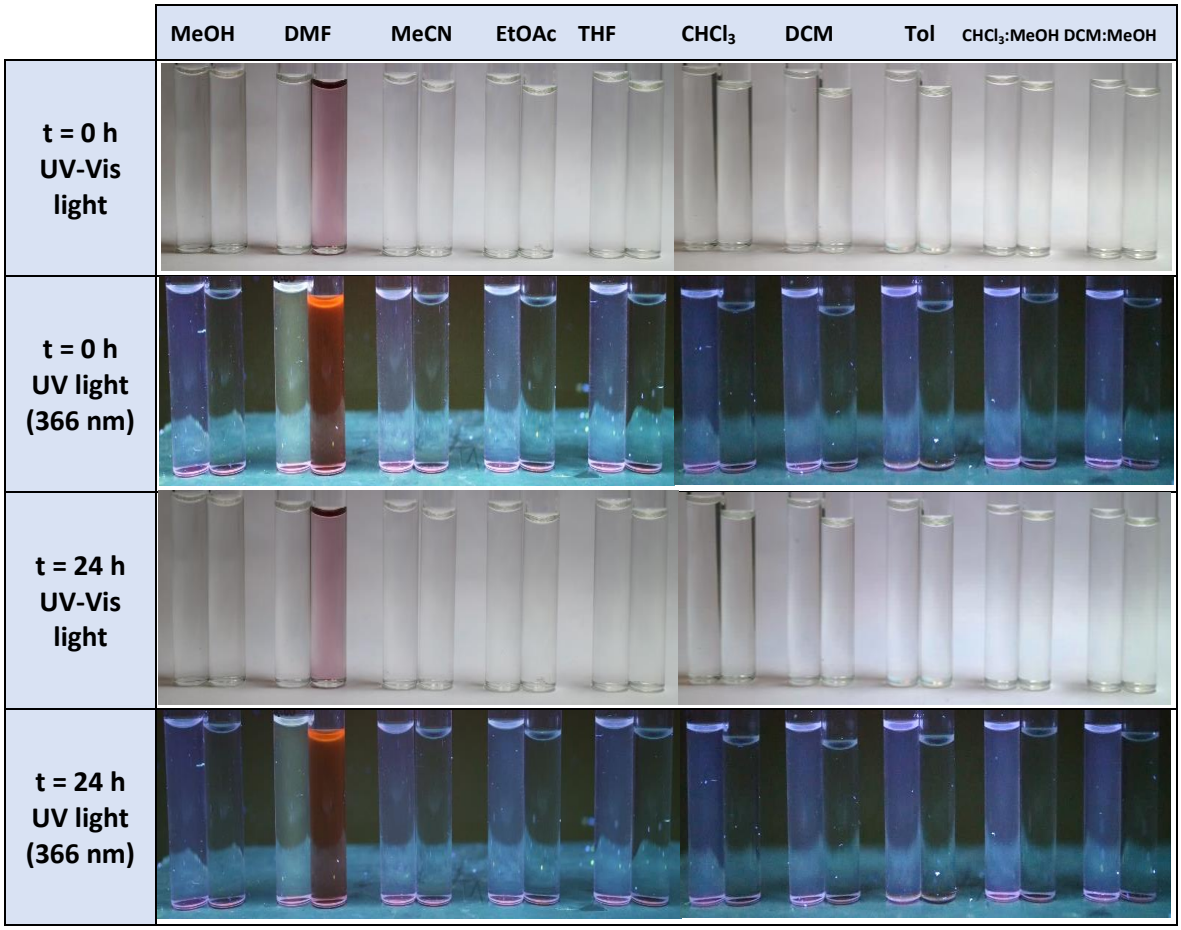

Figure 425. Pairs of AR85 (left) and AR85 with excess of TNT (right) in different solvents at time 0 h.

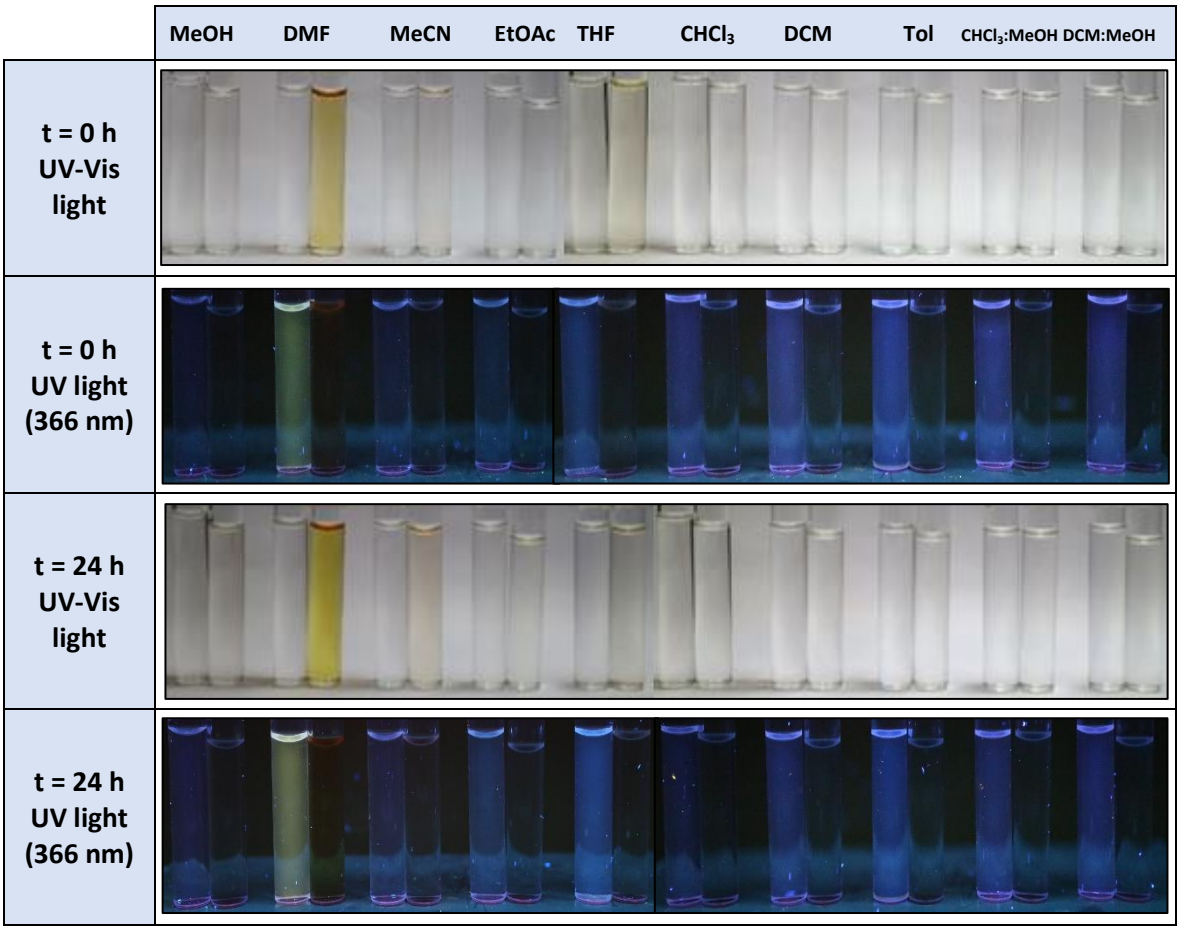

Figure 426. Pairs of AR85 (left) and AR85 with excess of TNB (right) in different solvents at time 0 h and 24 h.

The result obtained in both cases was the same: the most significant changes were observed in DMF, EtOAc, THF and toluene but present in all the solvents.

Work concentration test:

In order to choose an optimum concentration for the next quantitative studio, the absorbance and fluorescence of the probe was checked to be linear while concentration changes was small. The solvent used for this test was DCM.

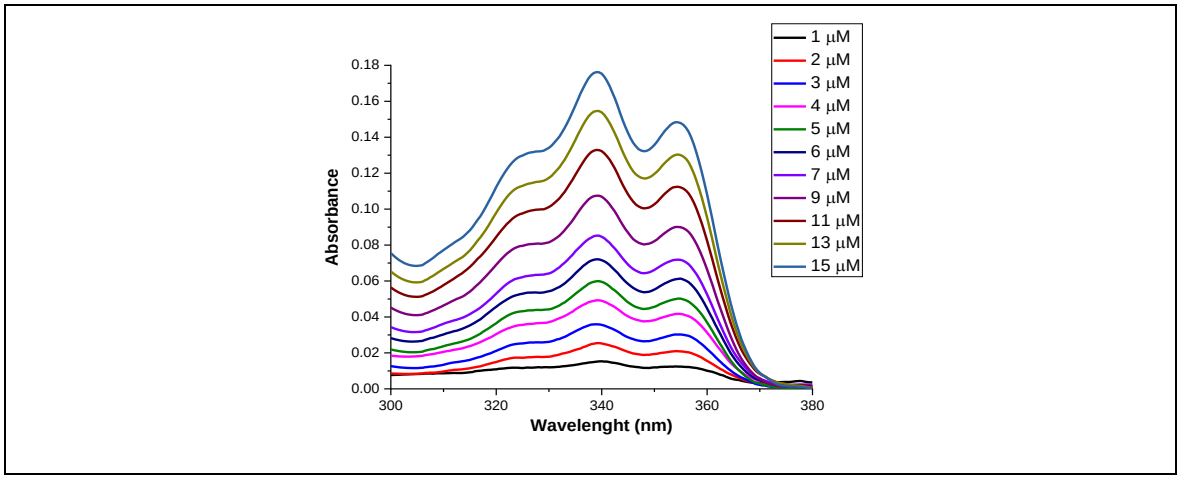

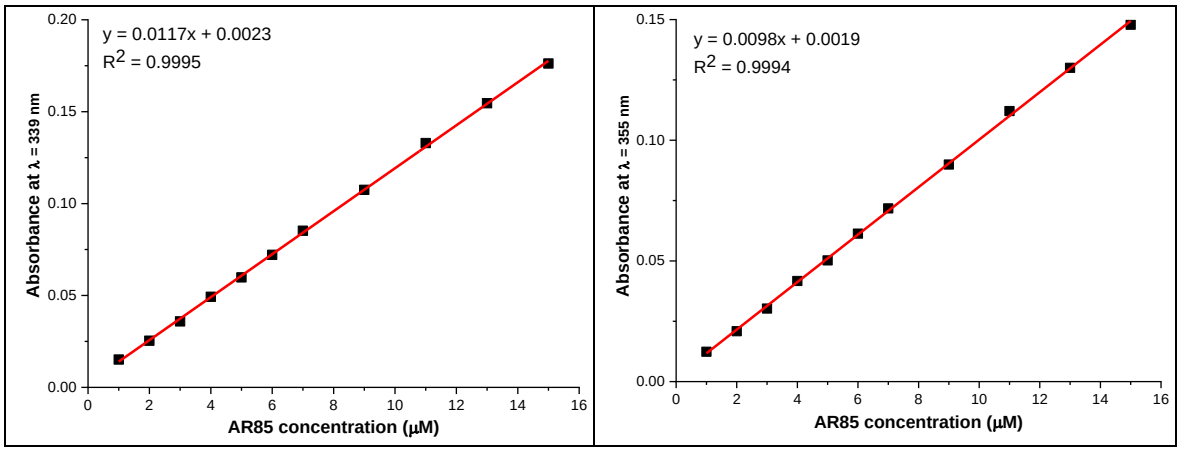

Figure 427. Absorbance spectrum (up) and absorbance profile at 339 nm (down left) and 355 nm (down right) of increasing concentrations of AR85 solution in DCM

The ideal working concentration should be at 0.1 of absorbance or less, to prevent inner filter effects, possible dynamic quenching or stacking processes. It was implied a concentration below 11 µM. Taking the results into account, the chosen concentration was 2.5 µM, value around which the Lambert-Beer Law was fulfilled.

Solvents test with TNB:

For all solvents, the working concentration of AR85 was 2.5 µM. In the kinetic studies, TNB was in excess but, in the titration, the TNB concentration was between 0 and 35000 µM. The excitation wavelength was 330 nm for all experiments and the temperature for all test was 25ºC.

Measurements were carried out immediately after the addition of TNB and the graphs were plotted at all emission maxima that were found.

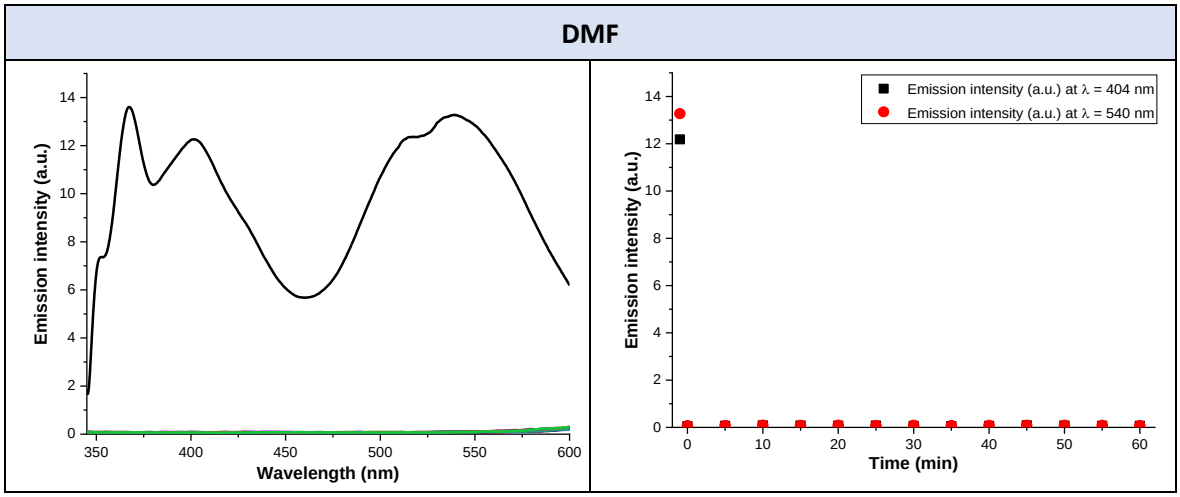

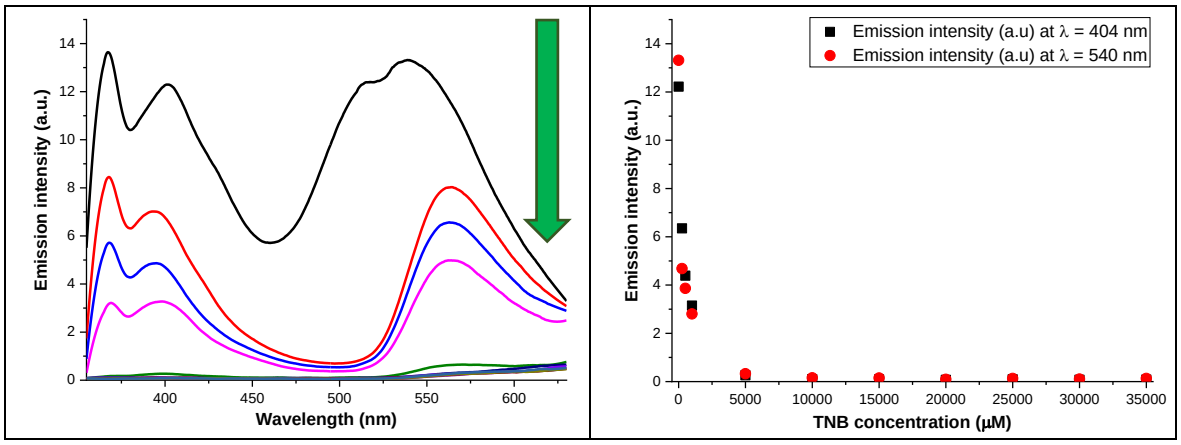

Figure 428. Study of AR85 with TNB in DMF. Kinetic study (up left) and profile as function as time at 404 nm and 540 nm simultaneusly (up right) in presence of TNB excess. Titration (down left) and fluorescence profile at 404 nm and 540 nm simultaneusly (down right) under increasing concentrations of TNB.

Without taking into account the difficulties of this solvent, there was a drop in the emission intensity immediately after adding TNB, followed by its stabilization at once. The LOD of TNB was somewhere between 0 and 250 µM with a decrease in emission intensity.

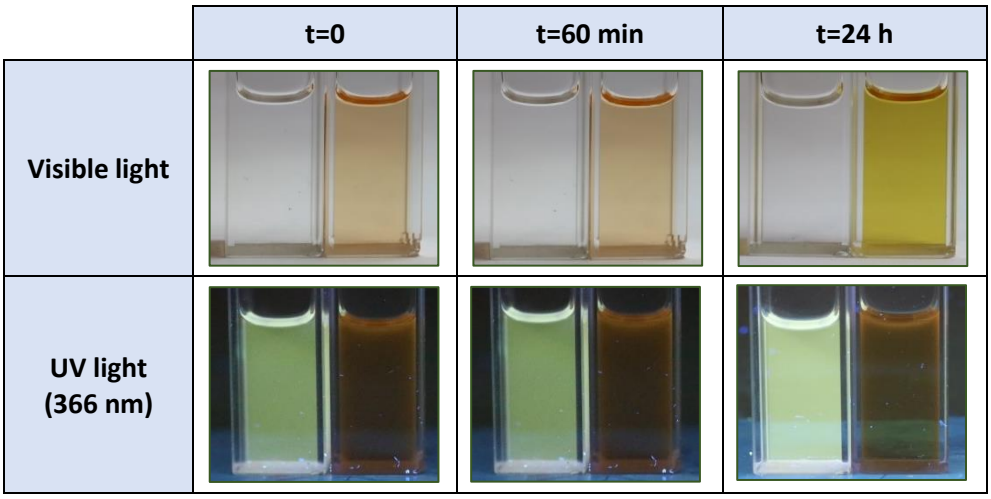

Figure 429. Kinetic study at different times under visible (up) and UV (down) light in DMF. In each photo, left vial was contained the probe and right vial was contained the probe and an excess of TNB.

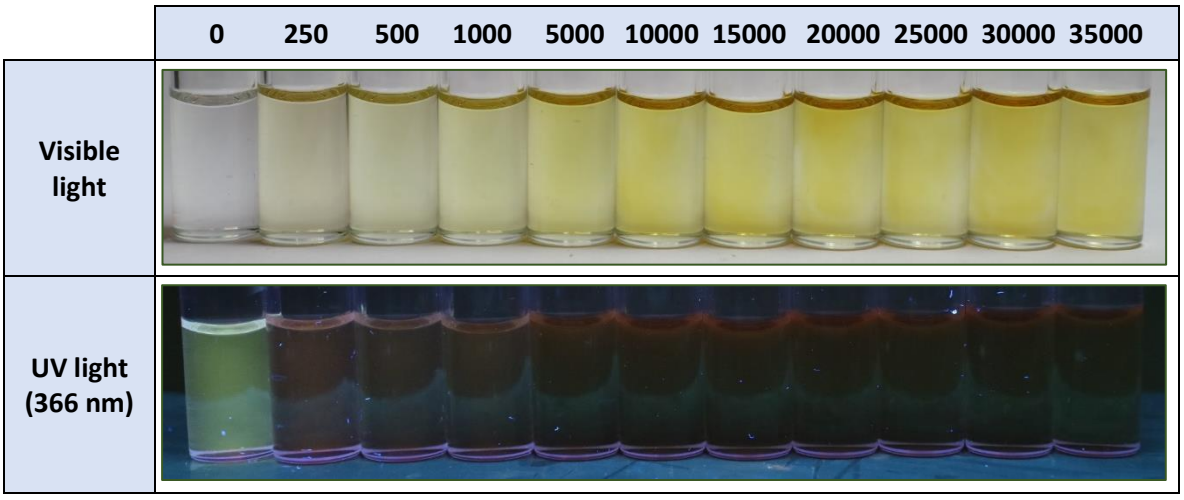

Figure 430. Titration of AR85 with an excess of TNB under visible (up) and UV (down) light in DMF.

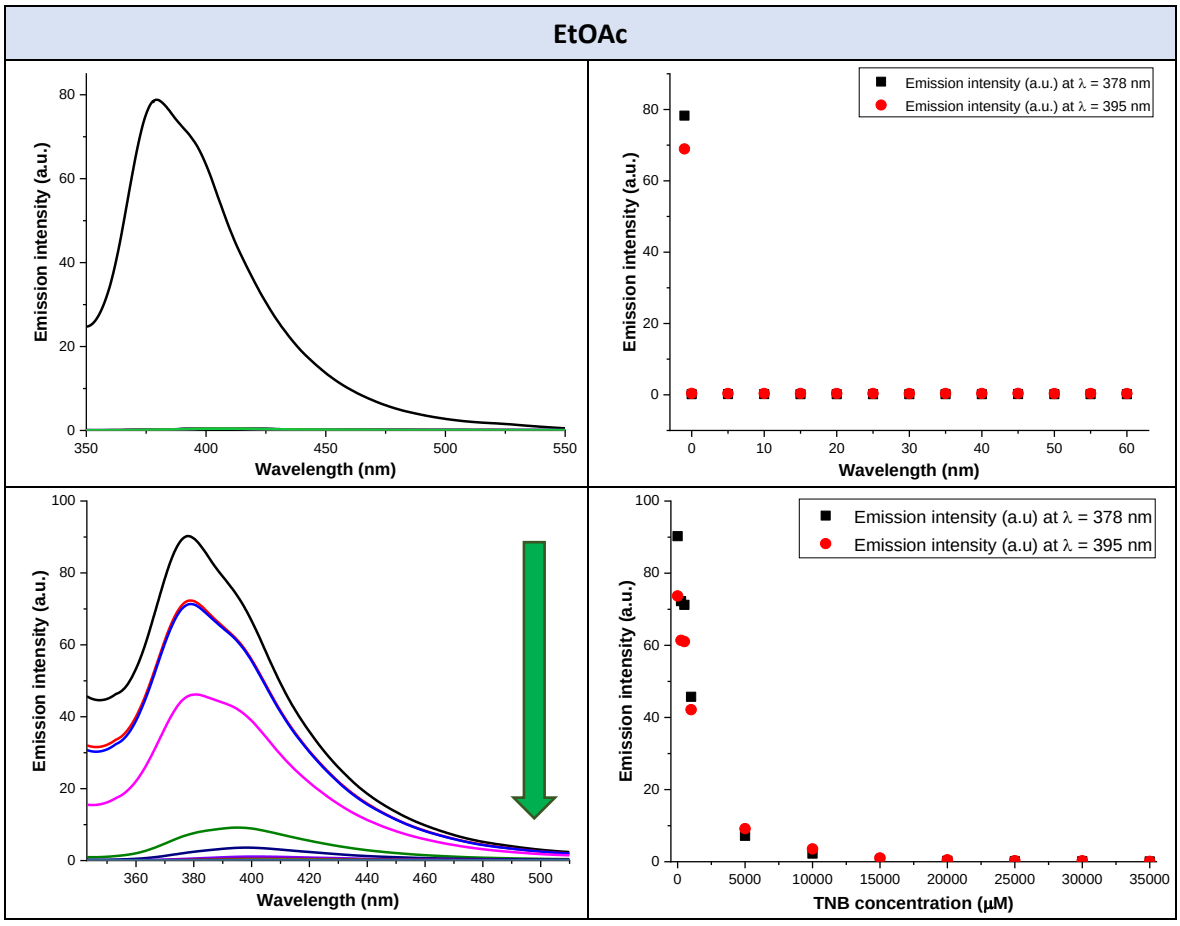

Figure 431. Study of AR85 with TNB in EtOAc. Kinetic study (up left) and profile as function as time at 378 nm and 395 nm simultaneusly (up right) in presence of TNB excess. Titration (down left) and fluorescence profile at 378 nm and 395 nm simultaneusly (down right) under increasing concentrations of TNB.

A decrease in emission intensity was occurred immediately after the addition of TNB, followed by its rapid stabilization. The lower detection limit of TNB was somewhere between 0 and 250 µM with a decrease in emission intensity.

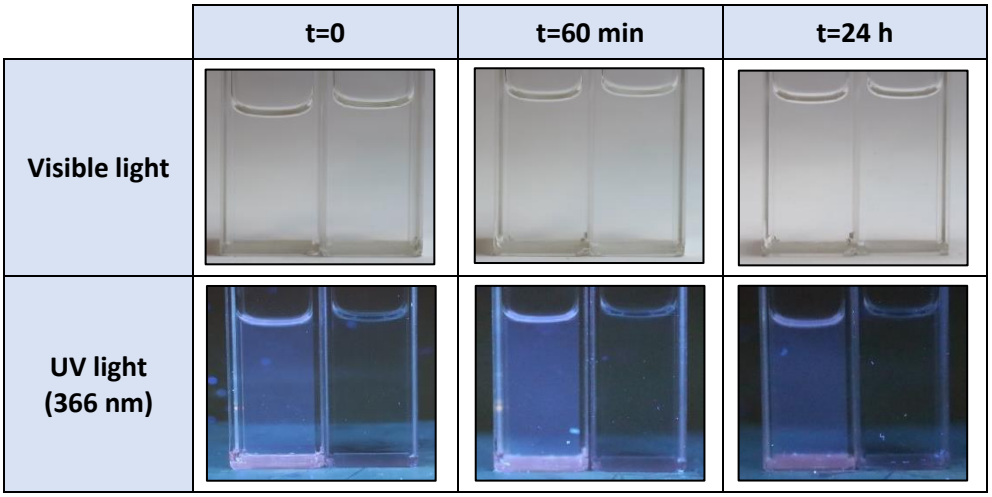

Figure 432. Kinetic study at different times under visible (up) and UV (down) light in EtOAc. In each photo, left vial was contained the probe and right vial was contained the probe and an excess of TNB.

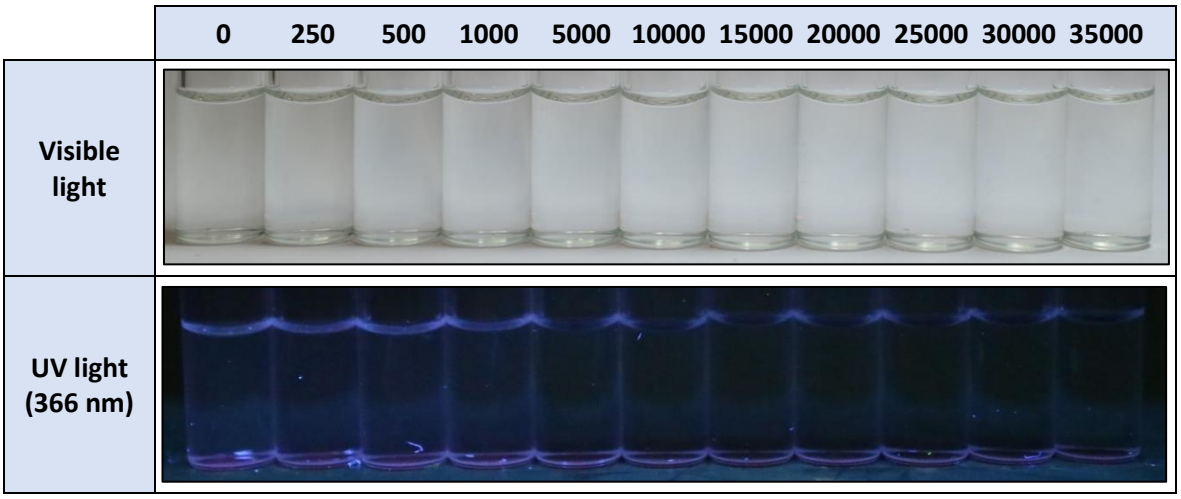

Figure 433. Titration of AR85 with an excess of TNB under visible (up) and UV (down) light in EtOAc.

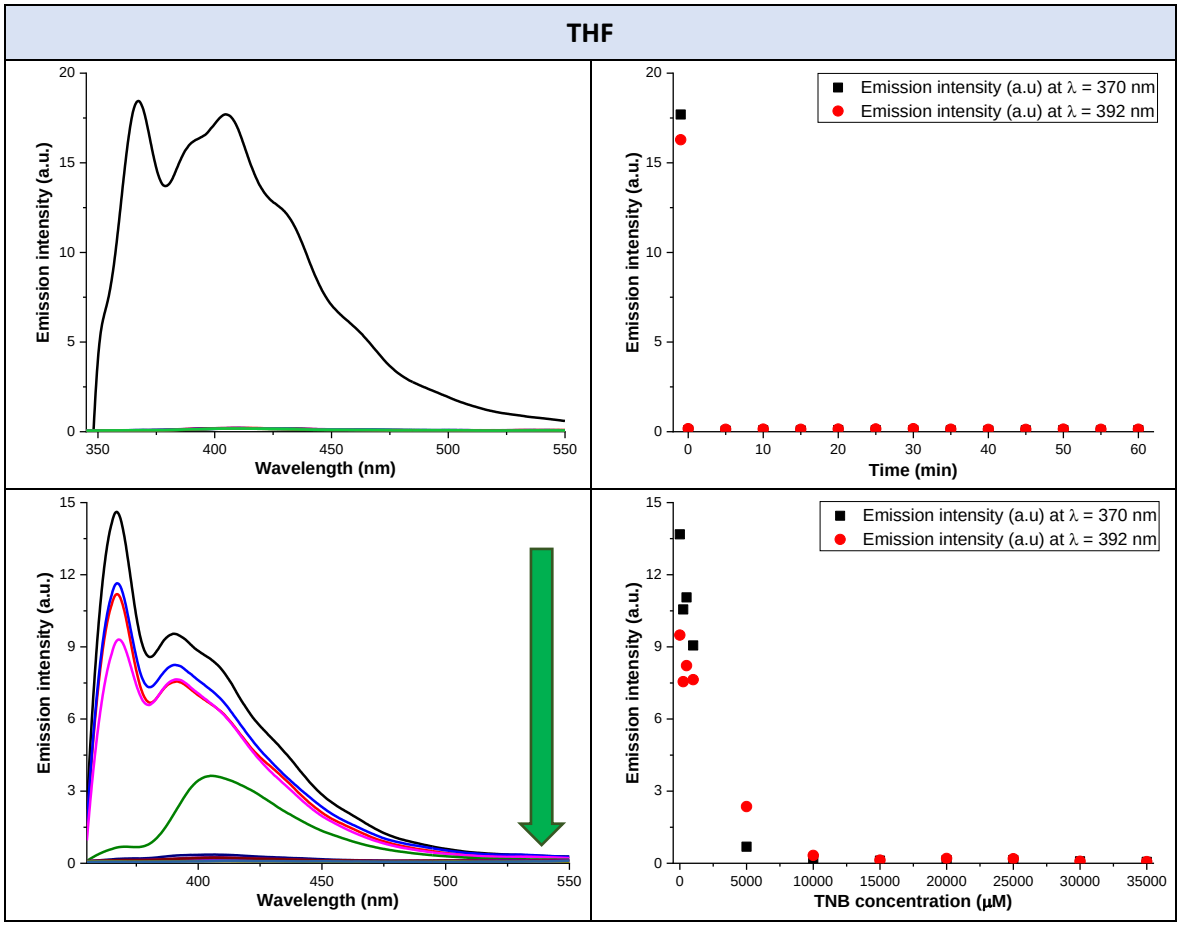

Figure 434. Study of AR85 with TNB in THF. Kinetic study (up left) and profile as function as time at 370 nm and 392 nm simultaneusly (up right) in presence of TNB excess. Titration (down left) and fluorescence profile at 378 nm and 395 nm simultaneusly (down right) under increasing concentrations of TNB.

A decrease in emission intensity was occurred immediately after the addition of TNB, followed by its rapid stabilization. The LOD of TNB was somewhere between 0 and 250 µM with a decrease in emission intensity.

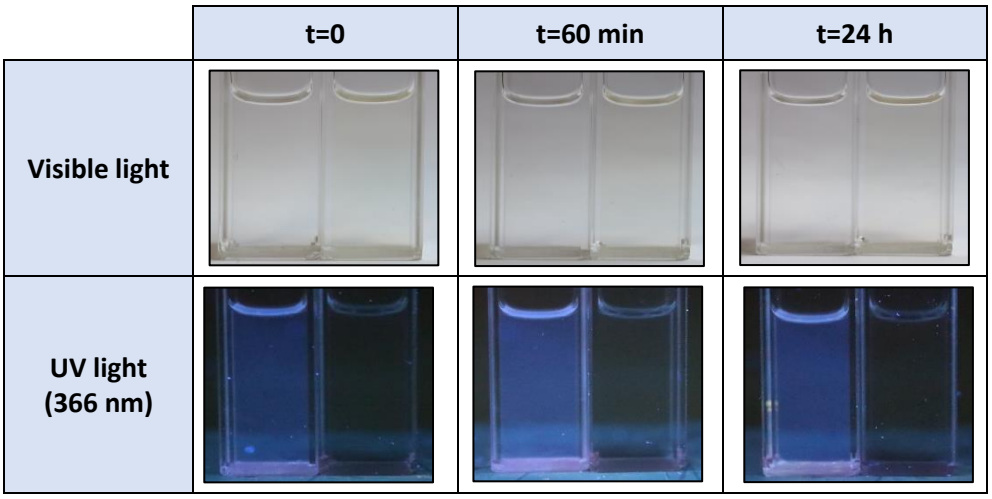

Figure 435. Kinetic study at different times under visible (up) and UV (down) light in THF. In each photo, left vial was contained the probe and right vial was contained the probe and an excess of TNB.

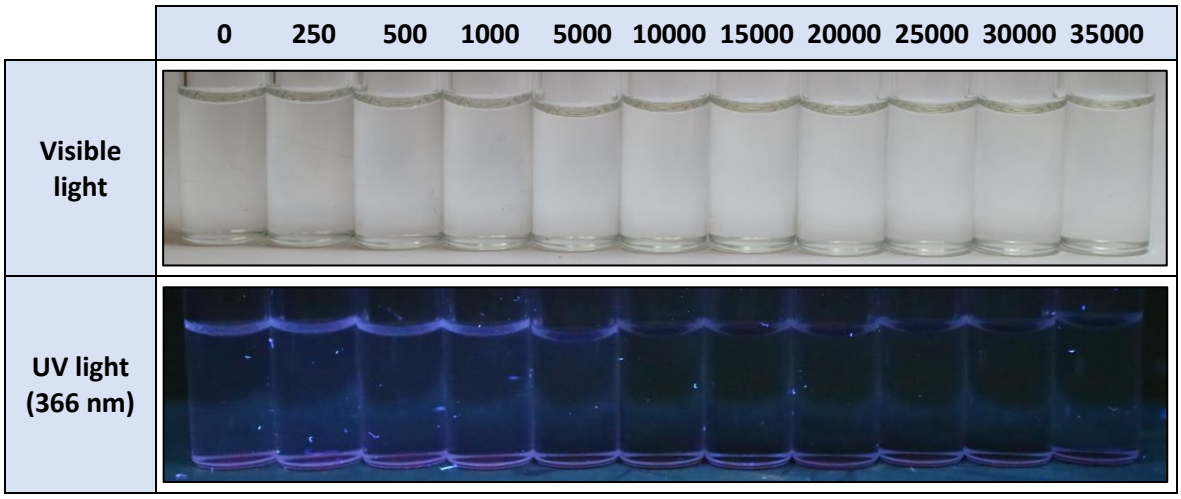

Figure 436. Titration of AR85 with an excess of TNB under visible (up) and UV (down) light in THF.

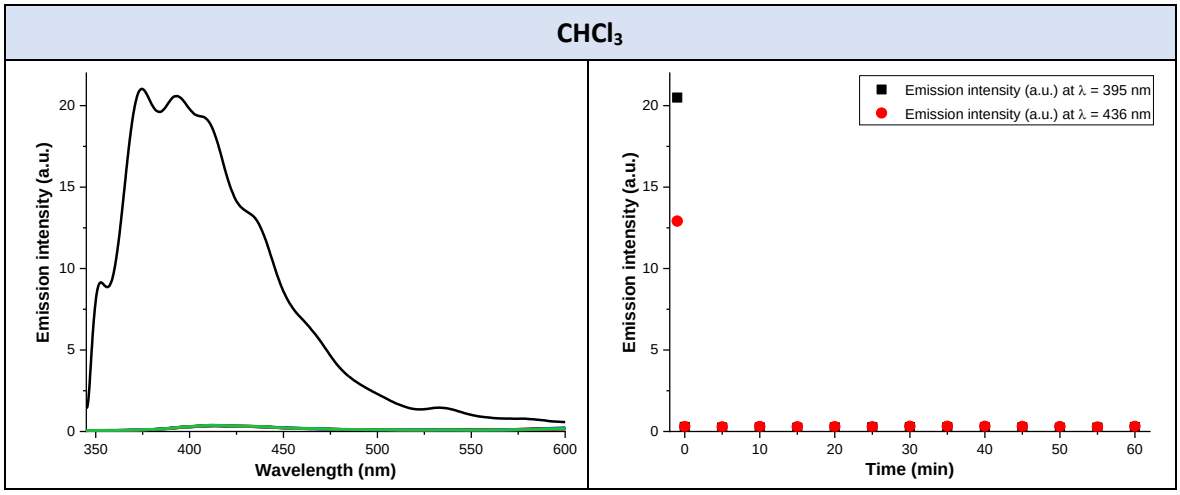

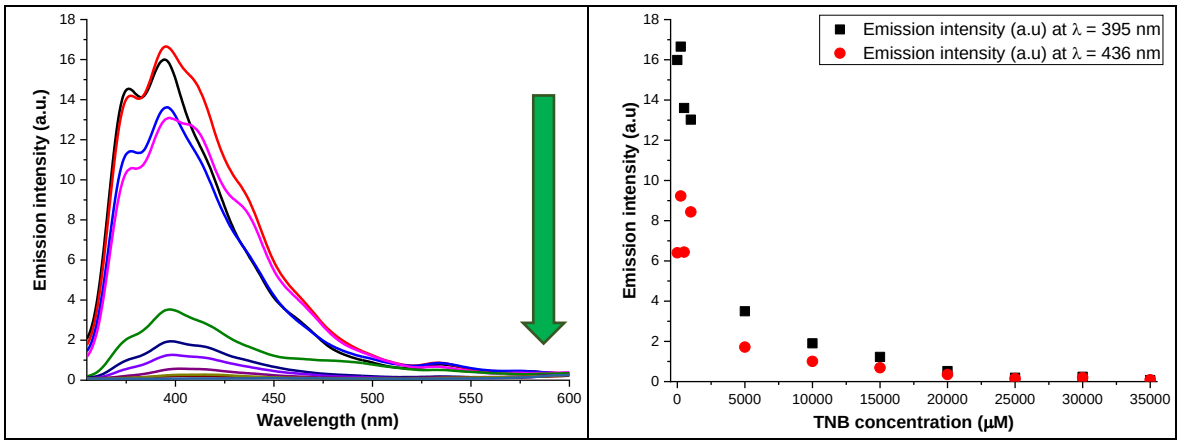

Figure 437. Study of AR85 with TNB in $CHCl_3$. Kinetic study (up left) and profile as function as time at 395 nm and 436 nm simultaneusly (up right) in presence of TNB excess. Titration (down left) and fluorescence profile at 395 nm and 436 nm simultaneusly (down right) under increasing concentrations of TNB.

There was a drop in the emission intensity immediately after adding TNB, followed by its stabilization at once. The mathematical calculation of the LOD had not been carried out yet, but according to the fluorescence spectra, it was somewhere between 0 and 250 µM.

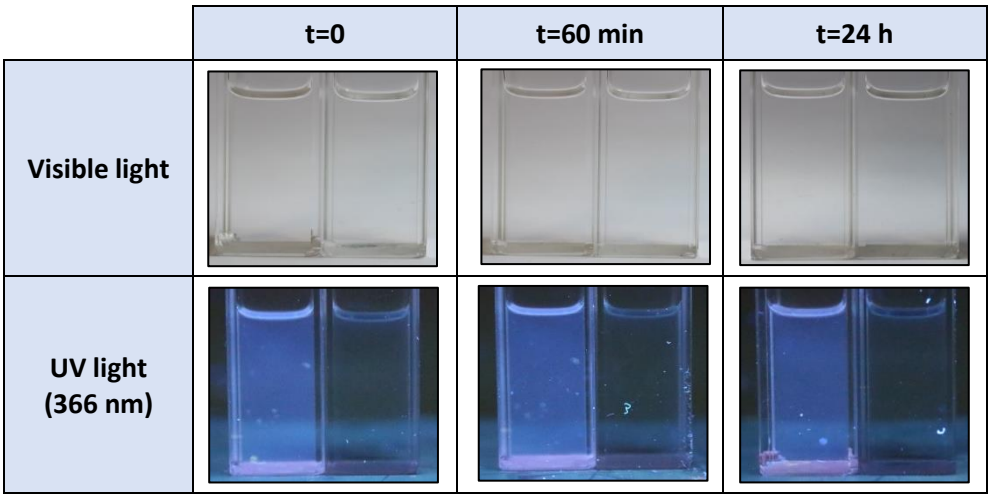

Figure 438. Kinetic study at different times under visible (up) and UV (down) light in $CHCl_3$. In each photo, left vial was contained the probe and right vial was contained the probe and an excess of TNB.

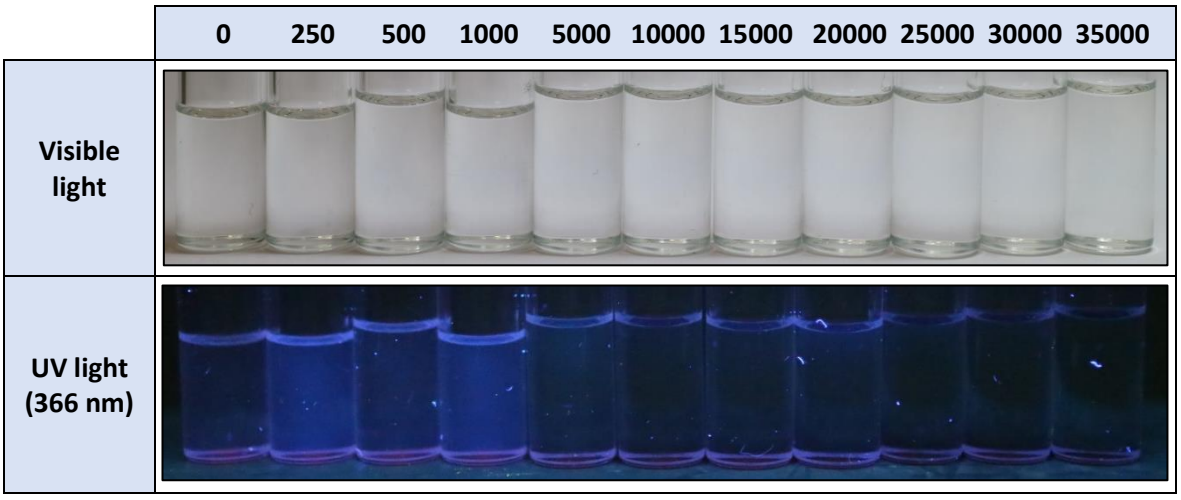

Figure 439. Titration of AR85 with an excess of TNB under visible (up) and UV (down) light in $CHCl_3$.

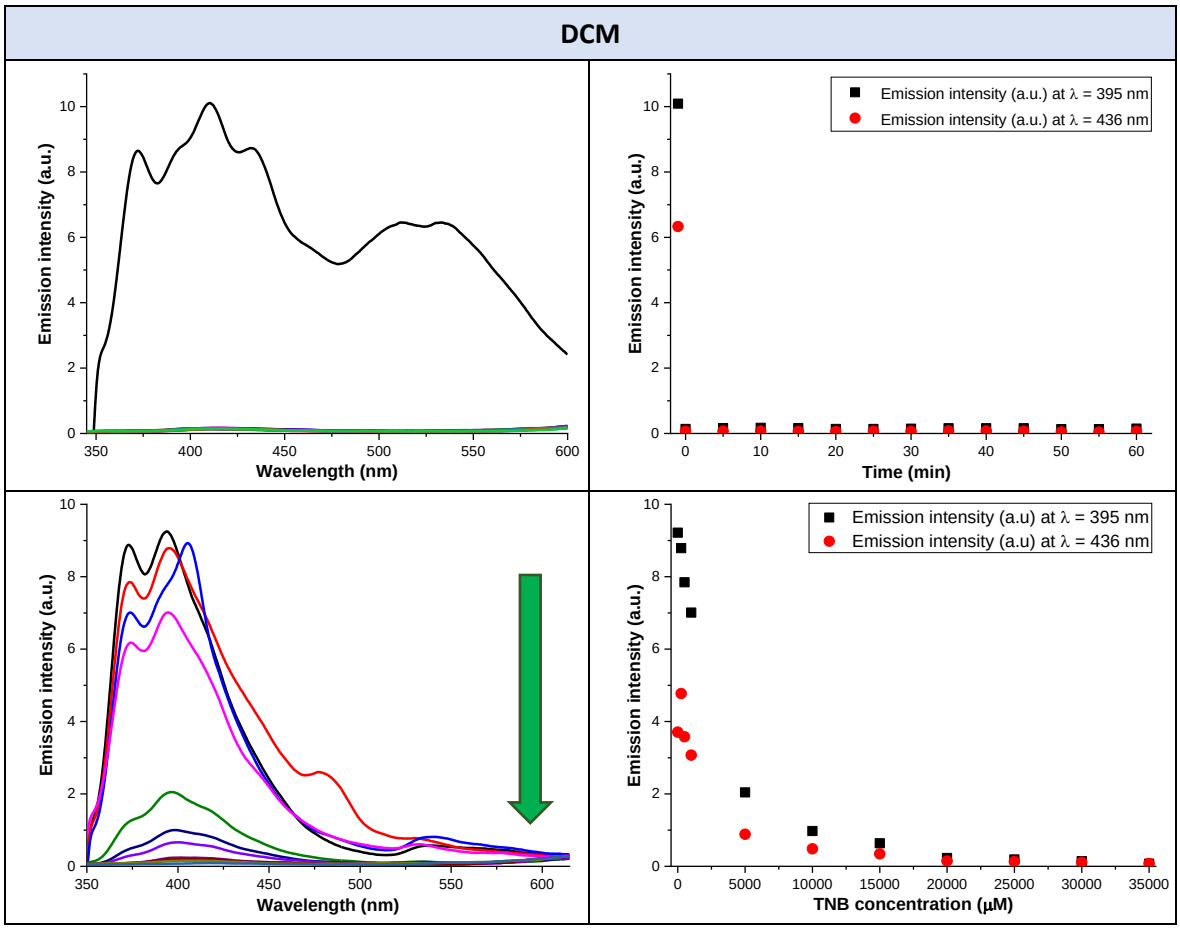

Figure 440. Study of AR85 with TNB in DCM. Kinetic study (up left) and profile as function as time at 395 nm and 436 nm simultaneusly (up right) in presence of TNB excess. Titration (down left) and fluorescence profile at 395 nm and 436 nm simultaneusly (down right) under increasing concentrations of TNB.

There was a drop in the emission intensity immediately after adding TNB, followed by its stabilization at once. According to the fluorescence spectra, the LOD was somewhere between 0 and 250 µM by a decrease in fluorescence.

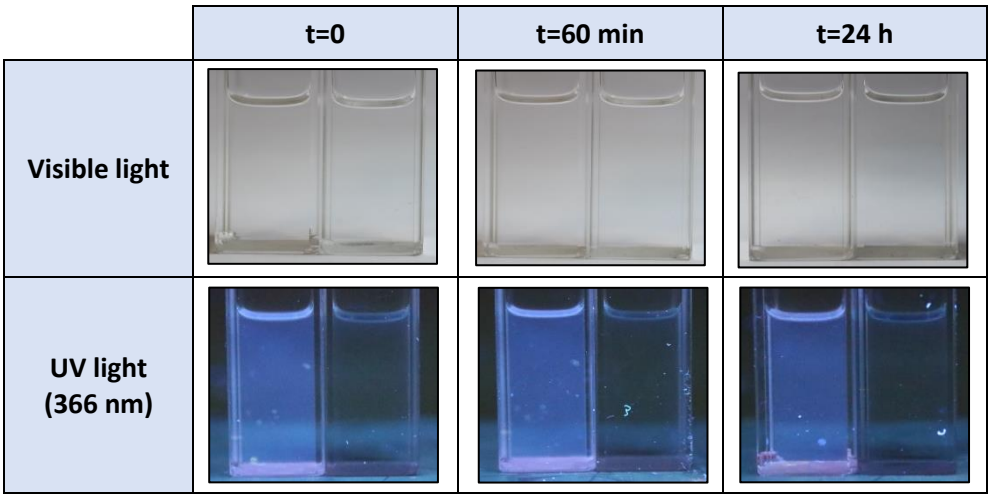

Figure 441. Kinetic study at different times under visible (up) and UV (down) light in DCM. In each photo, left vial was contained the probe and right vial was contained the probe and an excess of TNB.

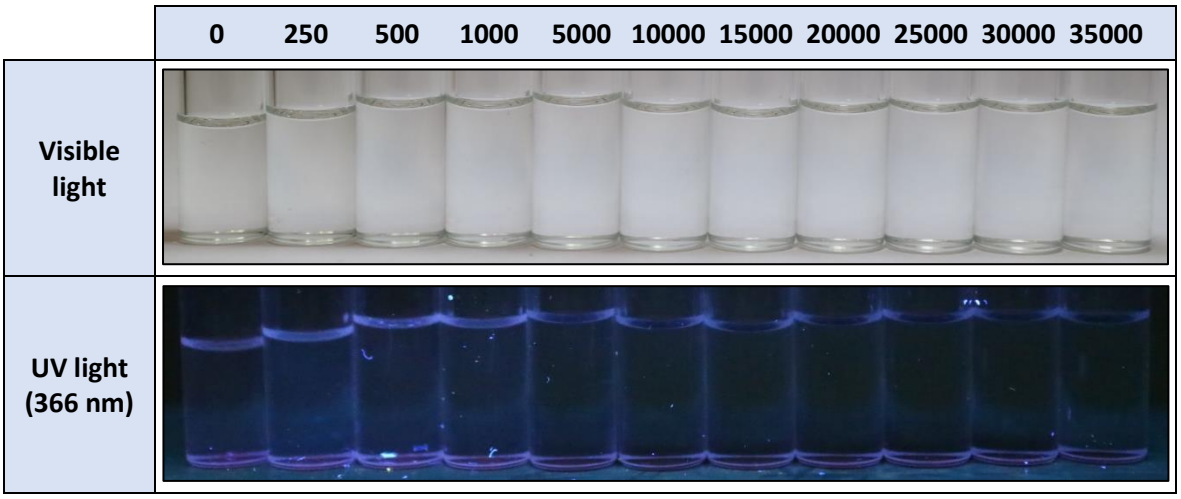

Figure 442. Titration of AR85 with an excess of TNB under visible (up) and UV (down) light in DCM.

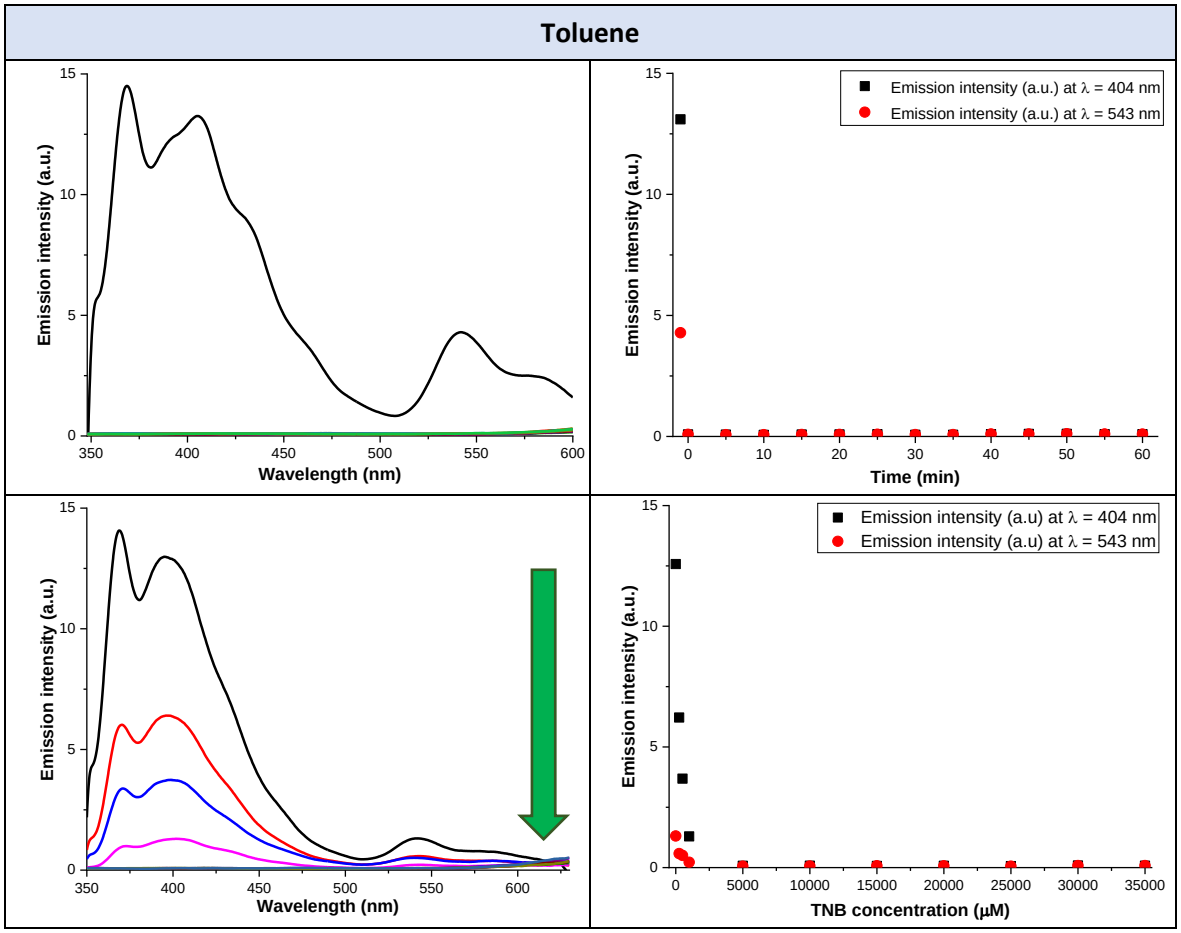

Figure 443. Study of AR85 with TNB in toluene. Kinetic study (up left) and profile as function as time at 404 nm and 543 nm simultaneusly (up right) in presence of TNB excess. Titration (down left) and fluorescence profile at 404 nm and 543 nm simultaneusly (down right) under increasing concentrations of TNB.

There was a decrease in the emission intensity immediately after adding TNB, followed by its stabilization at once. According to the fluorescence spectra, the LOD was somewhere between 0 and 250 µM. In this solvent, the most stable decrease and the highest stabilization was achieved.

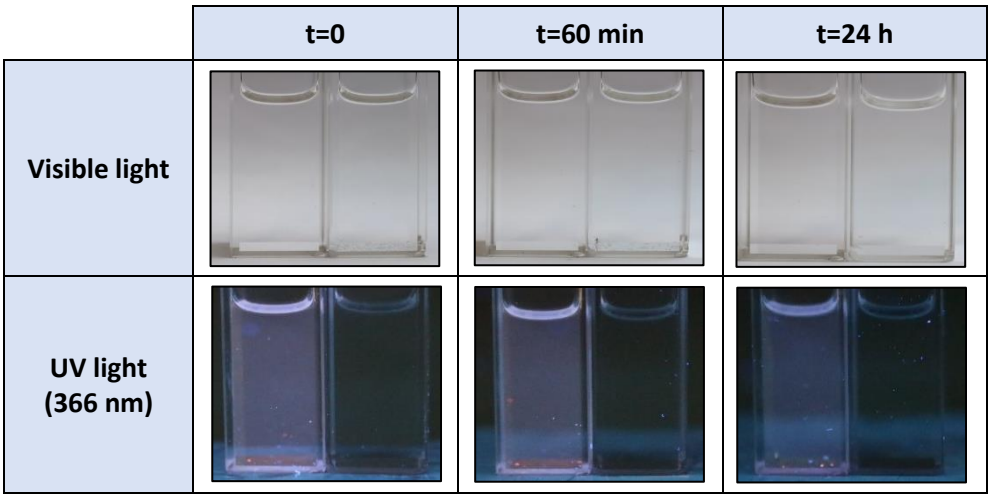

Figure 444. Kinetic study at different times under visible (up) and UV (down) light in toluene. In each photo, left vial was contained the probe and right vial was contained the probe and an excess of TNB.

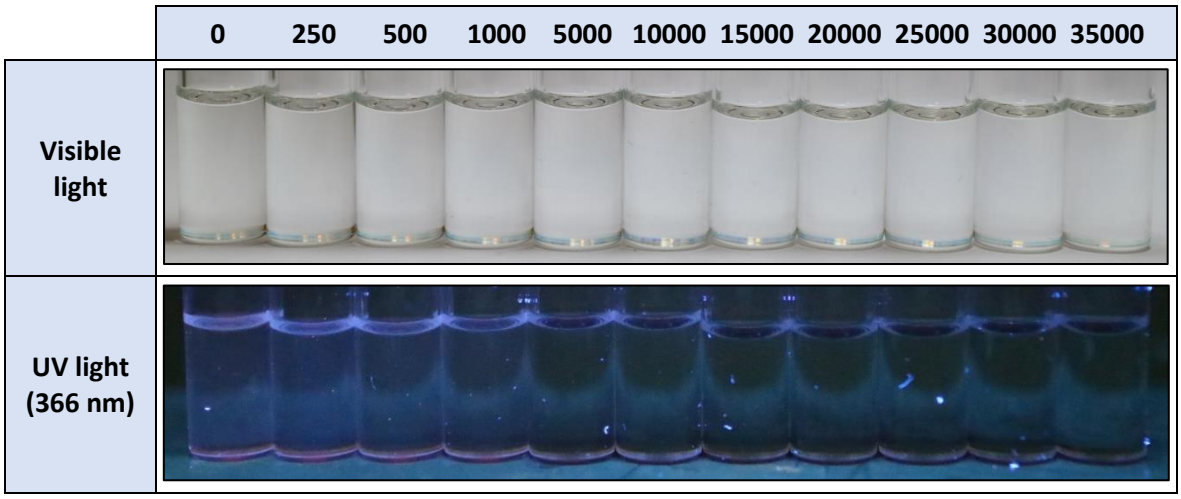

Figure 445. Titration of AR85 with an excess of TNB under visible (up) and UV (down) light in toluene.

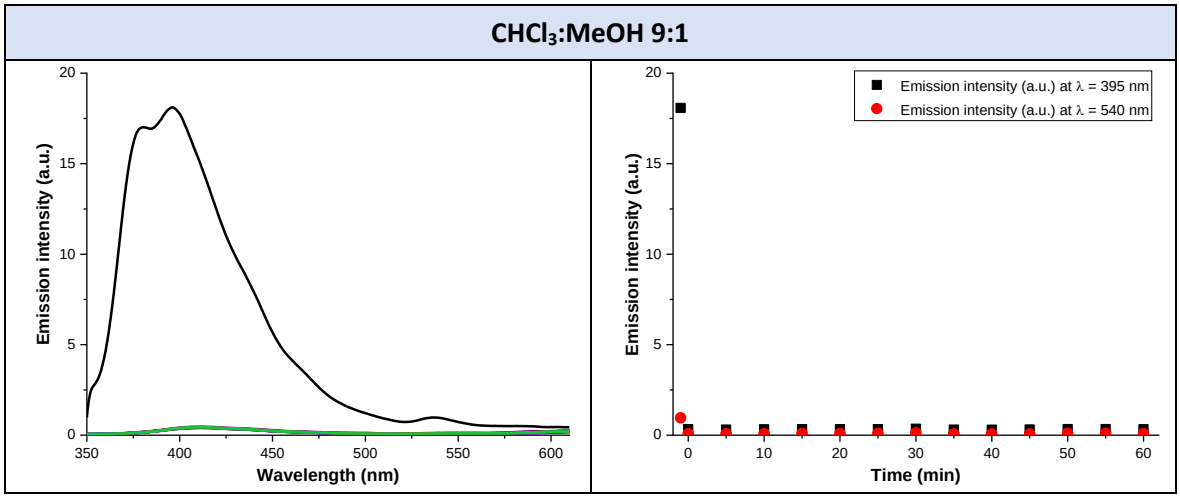

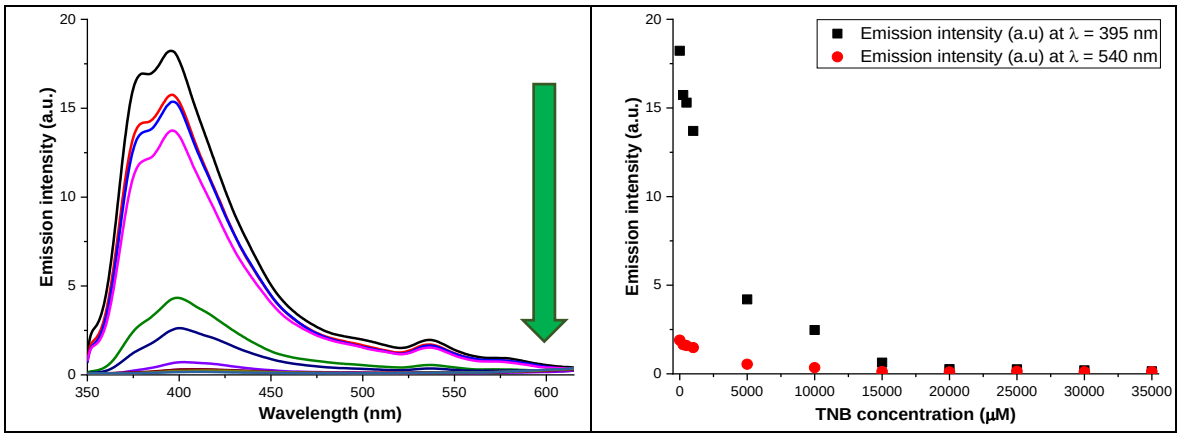

Figure 446. Study of AR85 with TNB in $CHCl_3$:MeOH 9:1. Kinetic study (up left) and profile as function as time at 395 nm and 540 nm simultaneusly (up right) in presence of TNB excess. Titration (down left) and fluorescence profile at 395 nm and 540 nm simultaneusly (down right) under increasing concentrations of TNB.

There was a decrease in the emission intensity immediately after adding TNB, followed by its stabilization at once. According to the fluorescence spectra, the LOD was somewhere between 0 and 250 μM.

	t=0	t=60 min	t=24 h
Visible light			
UV light (366 nm)	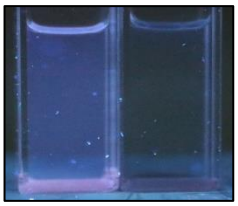	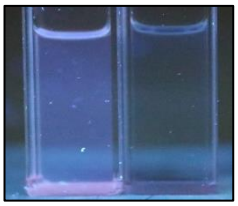	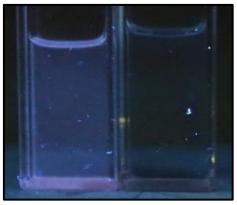

Figure 447. Kinetic study at different times under visible (up) and UV (down) light in $CHCl_3$:MeOH 9:1. In each photo, left vial was contained the probe and right vial was contained the probe and an excess of TNB.

	0	250	500	1000	5000	10000	15000	20000	25000	30000	35000
Visible light	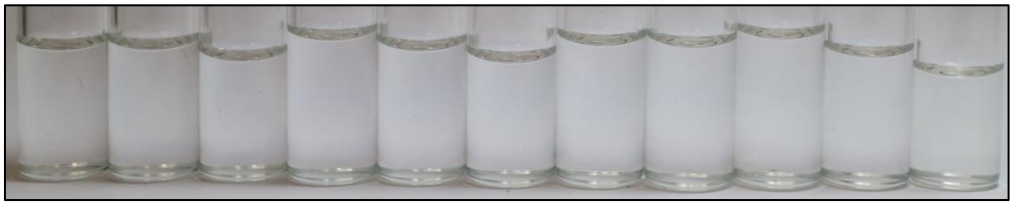										
UV light (366 nm)	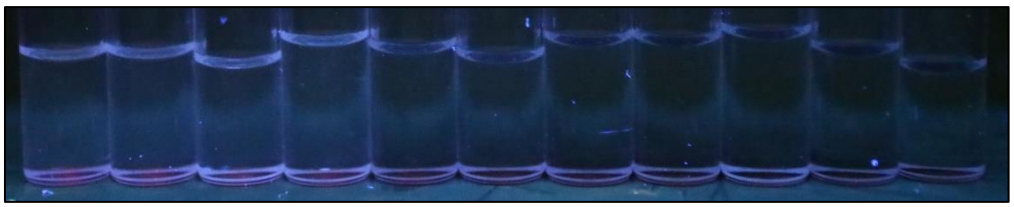										

Figure 448. Titration of AR85 with an excess of TNB under visible (up) and UV (down) light in $CHCl_3$:MeOH 9:1.

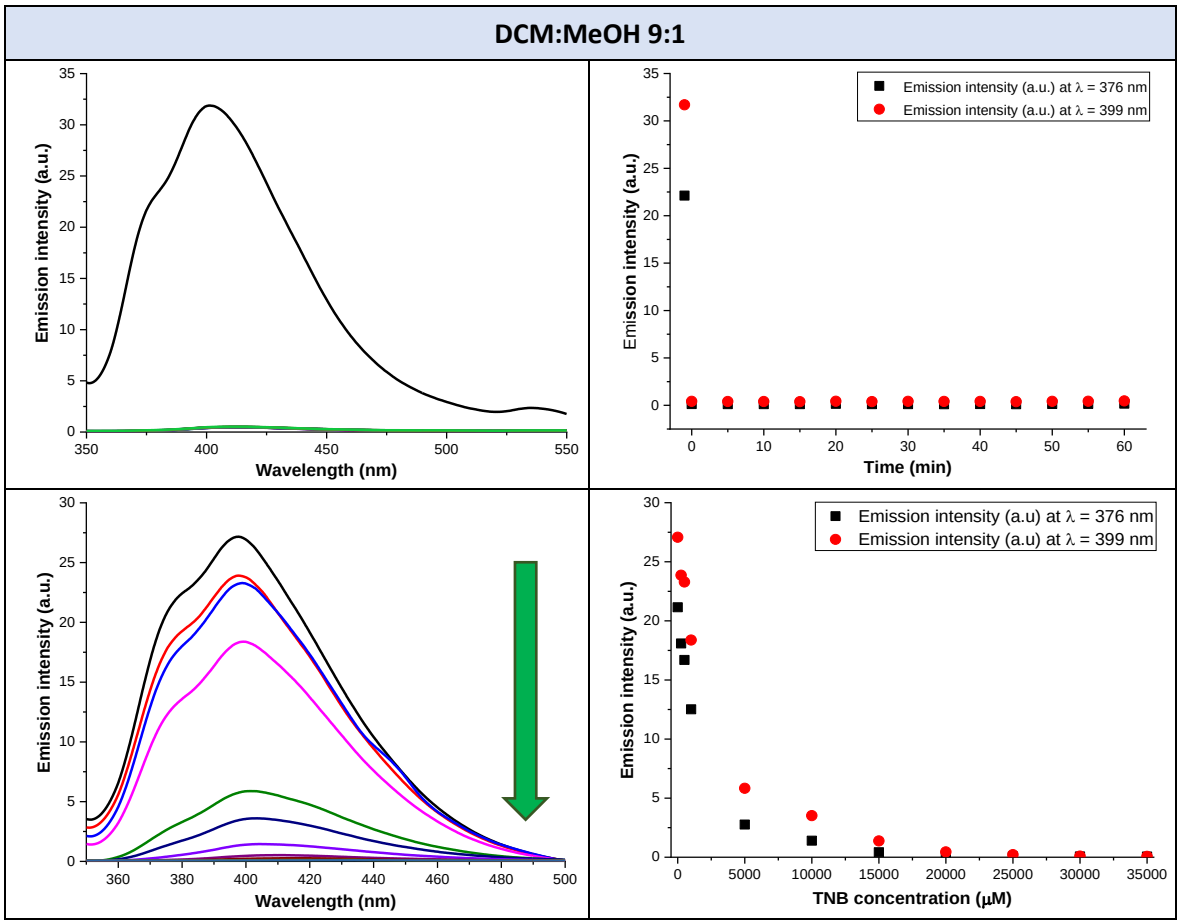

Figure 449. Study of AR85 with TNB in DCM:MeOH 9:1. Kinetic study (up left) and profile as function as time at 376 nm and 399 nm simultaneusly (up right) in presence of TNB excess. Titration (down left) and fluorescence profile at 376 nm and 399 nm simultaneusly (down right) under increasing concentrations of TNB.

There was a drop in the emission intensity immediately after adding TNB, followed by its stabilization. According to the fluorescence spectra, the LOD was somewhere between 0 and 250 µM.

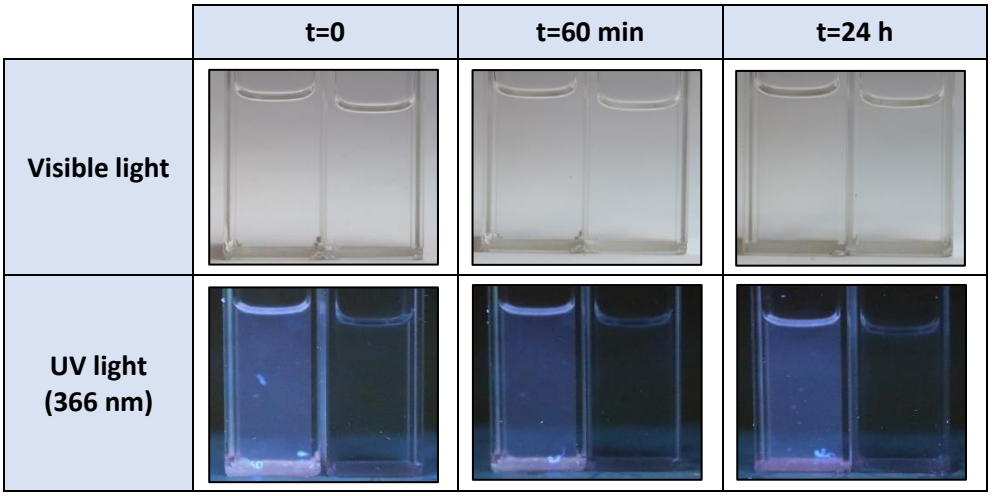

Figure 450. Kinetic study at different times under visible (up) and UV (down) light in DCM:MeOH 9:1. In each photo, left vial was contained the probe and right vial was contained the probe and an excess of TNB.

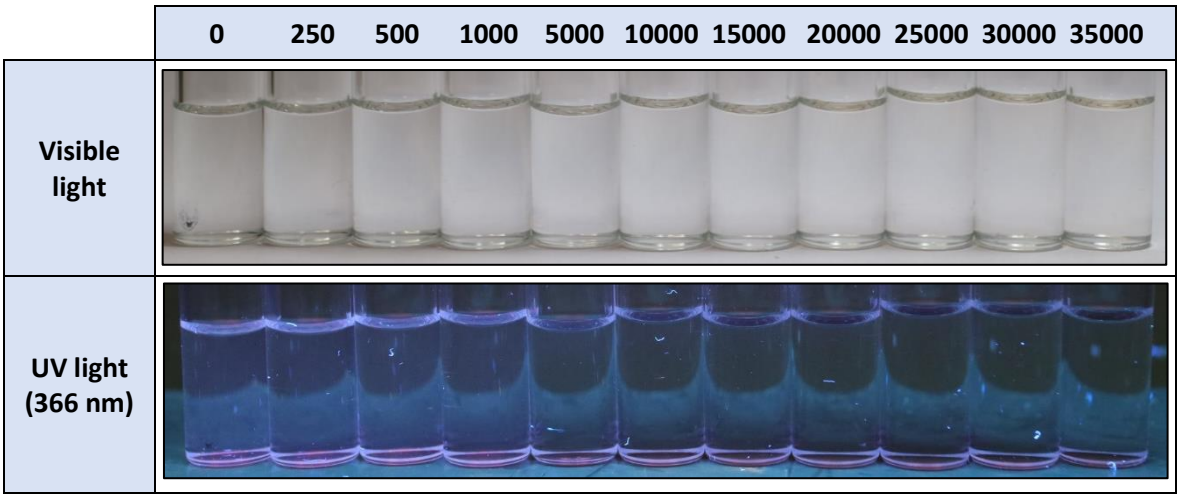

Figure 451. Titration of AR85 with an excess of TNB under visible (up) and UV (down) light in DCM:MeOH 9:1.

Titration of AR85 with TNT in toluene and LOD calculations.

The working concentration of AR85 was 2.5 µM and the concentration of TNT was increased by adding from a concentrated solution in the same solvent. The measurements were carried out inmediately after the addition of TNT. The excitation wavelength was 330 nm and the fluorescence changes were registred at 25ºC.

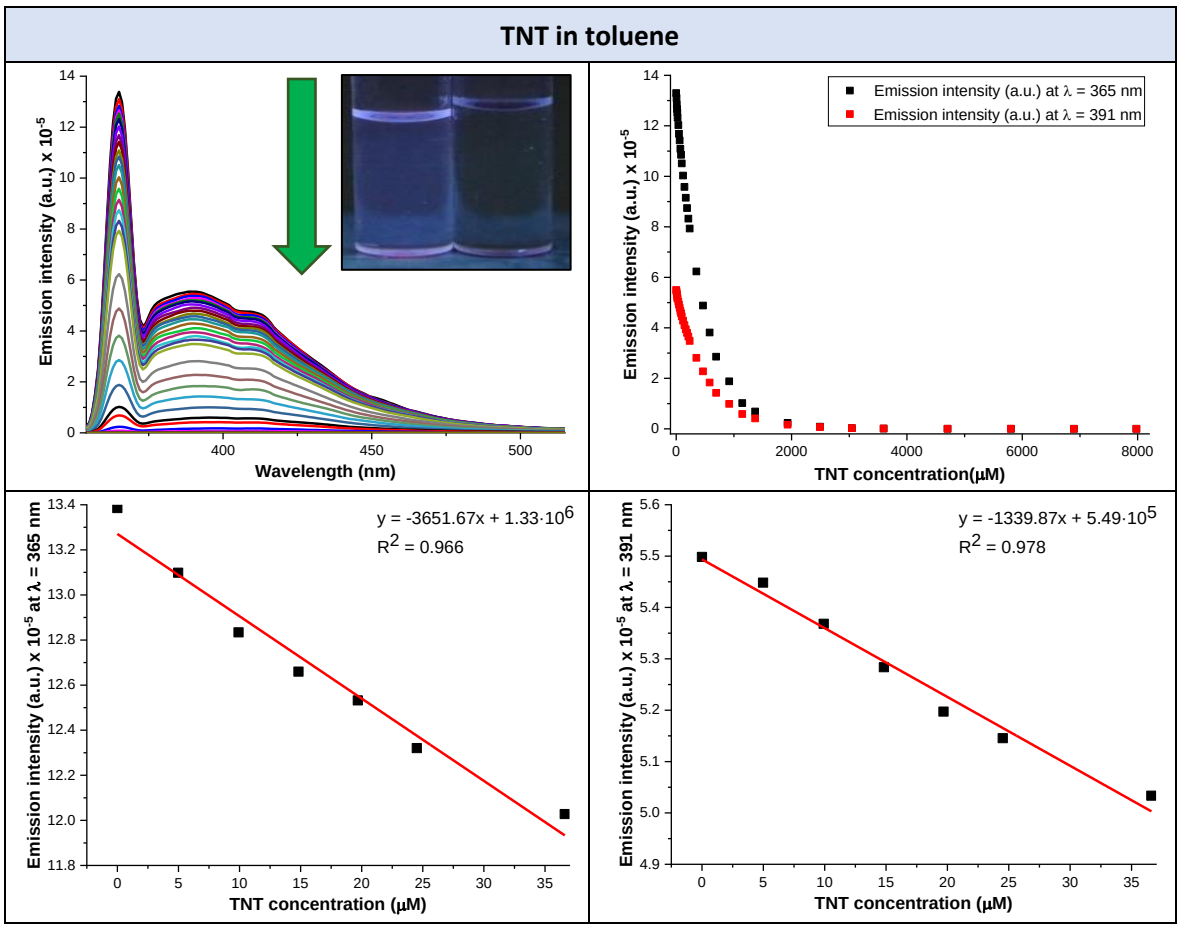

Figure 452. Titration (up left), fluorescence profile at 365 nm and 400 nm (up right), calibration for the LOD calculation using emission values at 365 nm (down left) and calibration for the LOD calculation using emission values at 391 nm (down right) of a AR85 solution in toluene under increasing concentrations of TNT.

A decrease in emission intensity was observed as the amount of TNT added was increased until stabilization was reached. The LOD of AR85 with TNT was calculated by linear regression + false positive and negative at 365 nm and 391 nm.

Based on the results of several authors, there are many factors that must be considered when calculating the limit of detection:

- Adjusting to a mean square linear regression.
- Removing the "outliers". Understanding them as points that are significantly different from the rest, within a 95 % of probability. If it is not possible to fulfil this part, the measurements should be repeated.
- Adjusting to a linear regression and checking that the slope is significantly different from 0 (95%). P-Value >0.05.
- Calculation of the LOD when the probability of false positive (α) and false negative (β) is equal or inferior to 5 %; or the value that the author is looking for. To do so, some software such as "R" could provide the fitting and give the results.

LOD was calculated using emission values at 365 nm. For this method, the R software was used and the value of the LOD was 1.87 nM.

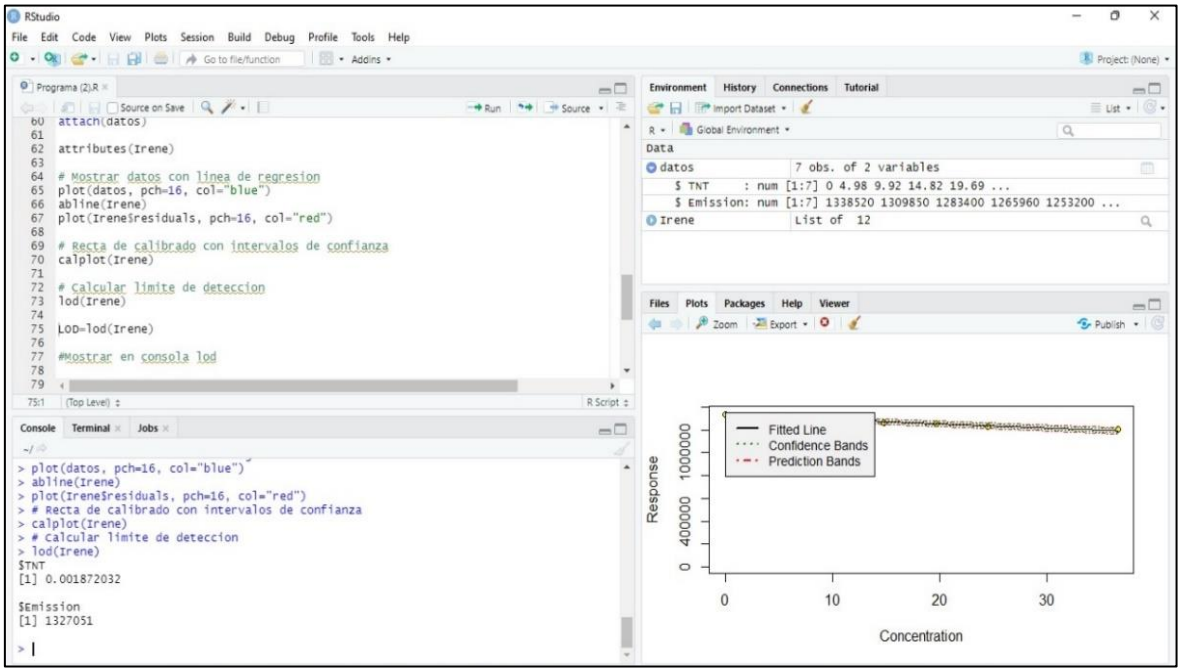

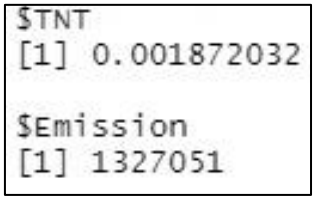

Figure 453. Calculation of the TNT limit of detection using the R software program and the emission values at 365 nm.

LOD was calculated using emission values at 391 nm. For this method, the R software was used and the value of the LOD was 1.87 nM.

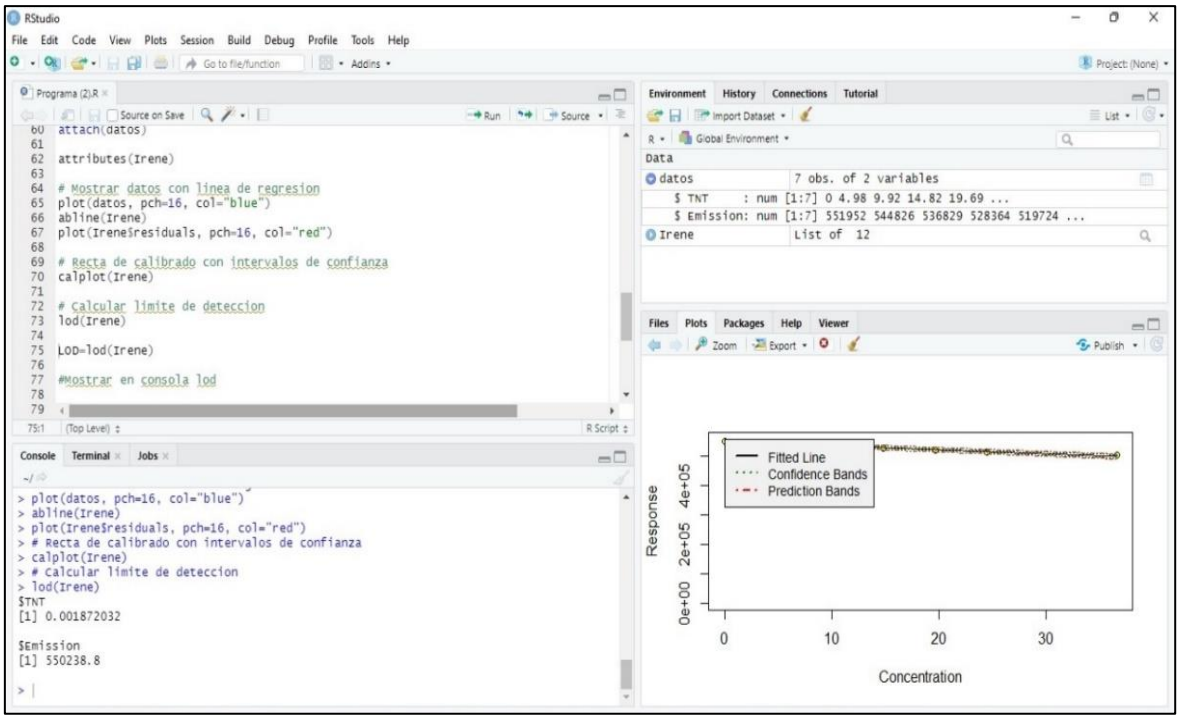

Figure 454. Calculation of the TNT limit of detection using the R software program and the emission values at 391 nm.

To confirm that the work concentration was correct, we performed some additional experiments at different concentrations. 5 solutions of AR85 (2.5-6.0-9.0-12.0-15.0 µM) in toluene were prepared. Conditions were: [TNT] was increased by adding from a concentrated solution in the same solvent. Measurements were carried out immediately after the addition of TNT. λ_{exc} = 330 nm, λ_{em} = 365 nm/391 nm. Fluorescence changes were registered at 25ºC.

AR85 2.5 µM vs TNT

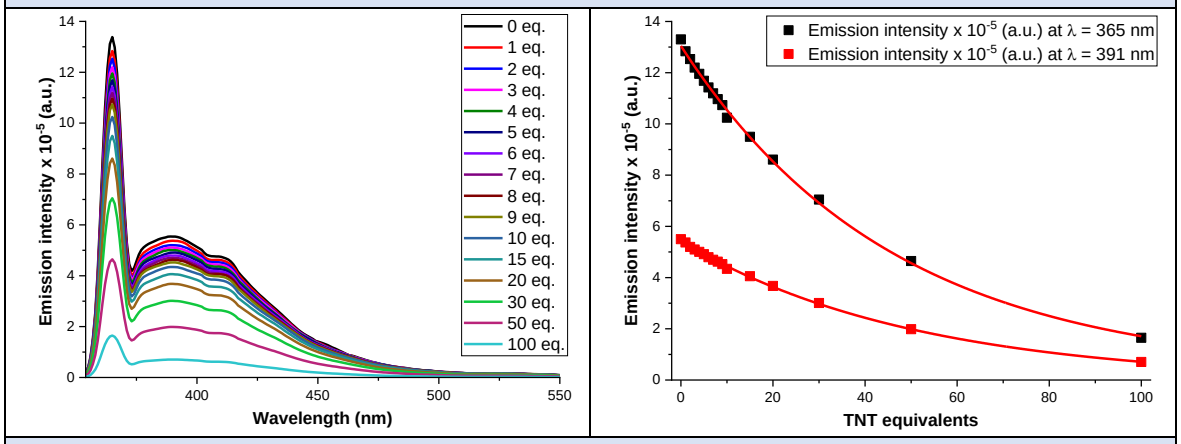

AR85 6.0 µM vs TNT

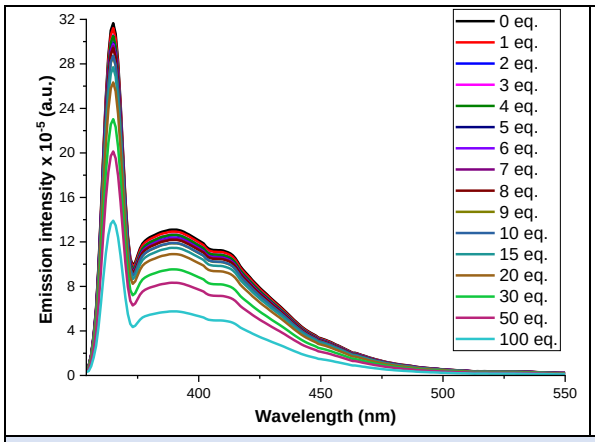

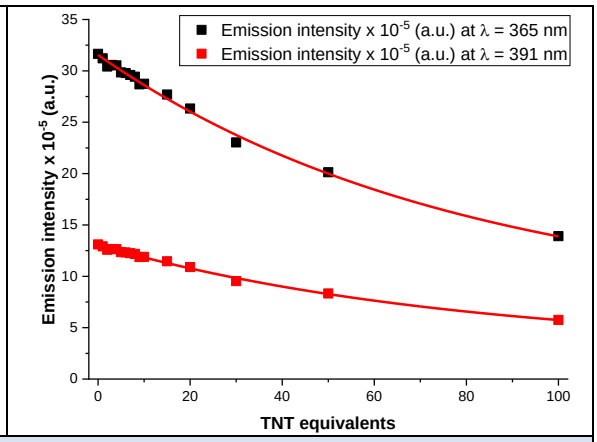

AR85 9.0 µM vs TNT

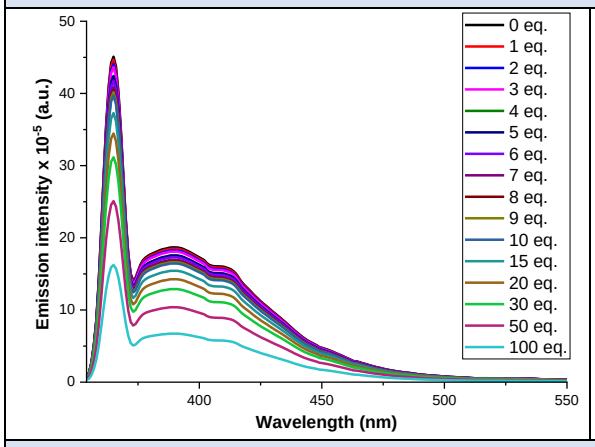

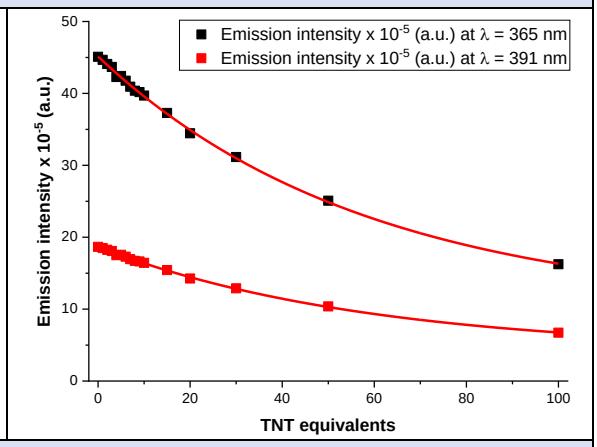

AR85 12.5 µM vs TNT

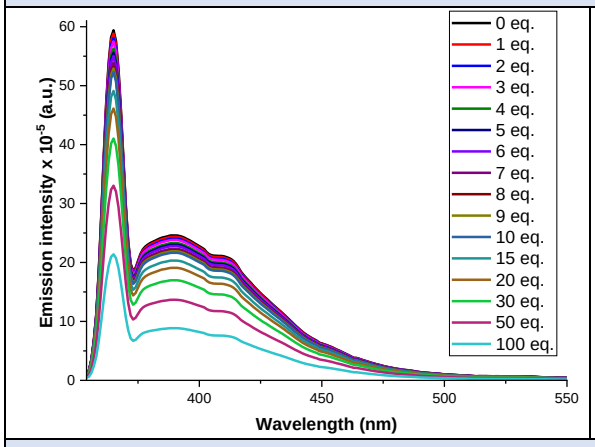

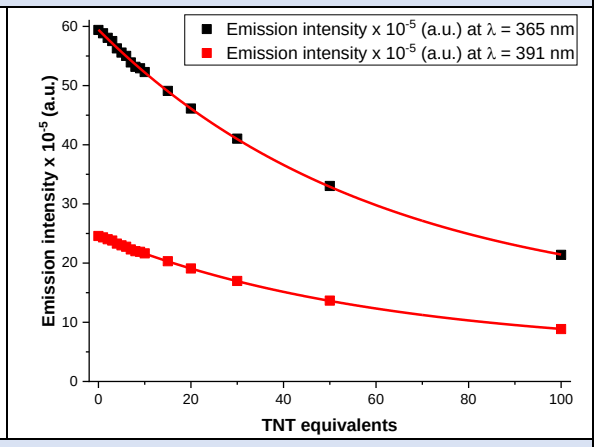

AR85 15.0 µM vs TNT

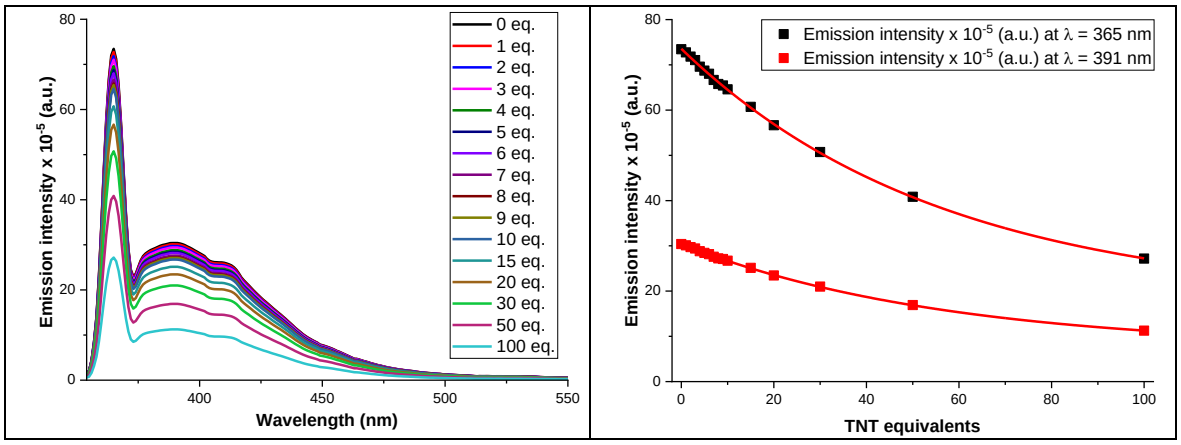

Figure 455. Titrations (left side) and fluorescence profiles at 365nm and 391nm simultaneously (right side) of 2.5-6.0-9.0-12.0-15.0 µM AR85 solutions in toluene under increasing concentrations (1-100 eq.) of TNT.

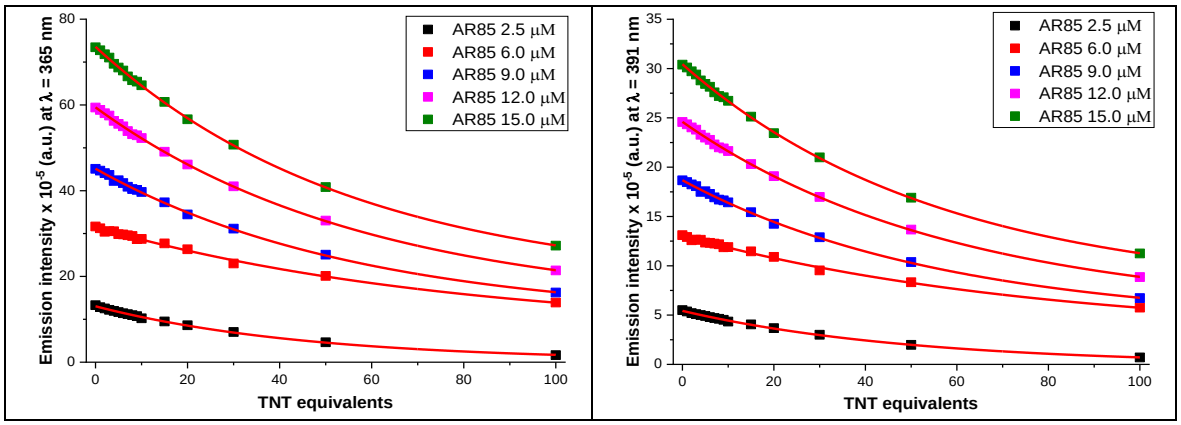

Figure 456. Comparison of emission intensity profiles at 365 nm (left) and 391 nm (right) of 2.5-6.0-9.0-12.0-15.0 µM AR85 solutions in toluene under increasing concentrations (1-100 eq.) of TNT.

Therefore, the best behavior was seen at the lowest concentration used for the measurements.

Titration of AR85 with TNB in toluene and LOD calculations.

The working concentration of AR85 was 2.5 µM and the concentration of TNB was increased by adding from a concentrated solution in the same solvent. The measurements were carried out inmediately after the addition of TNB. The excitation wavelength was 330 nm and the fluorescence changes were registred at 25ºC.

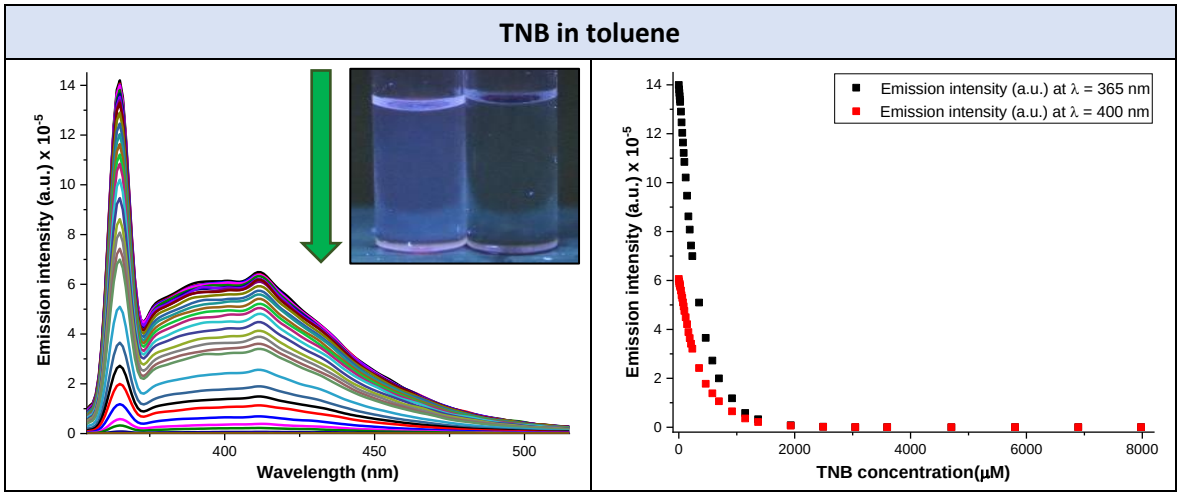

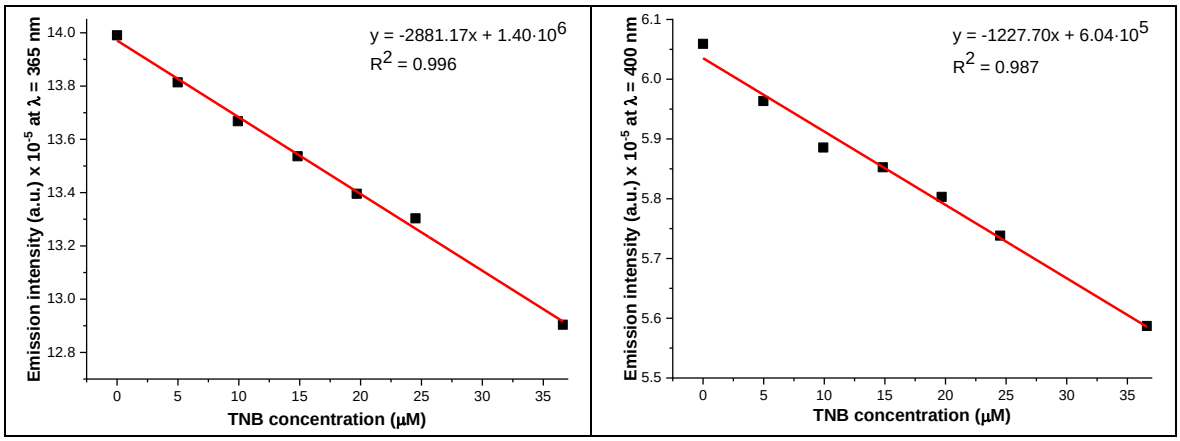

Figure 457. Titration (up left), fluorescence profile at 365 nm and 391 nm (up right), calibration for the LOD calculation using emission values at 365 nm (down left) and calibration for the LOD calculation using emission values at 391 nm (down right) of a AR85 solution in toluene under increasing concentrations of TNB.

A decrease in emission intensity was observed with the increase of the amount of TNT until stabilization was reached. The LOD of AR85 with TNB was calculated by linear regression + false positive and negative at 365 nm and 391 nm.

At 365 nm, the R software was used and the value of the LOD was 1.88 nM.

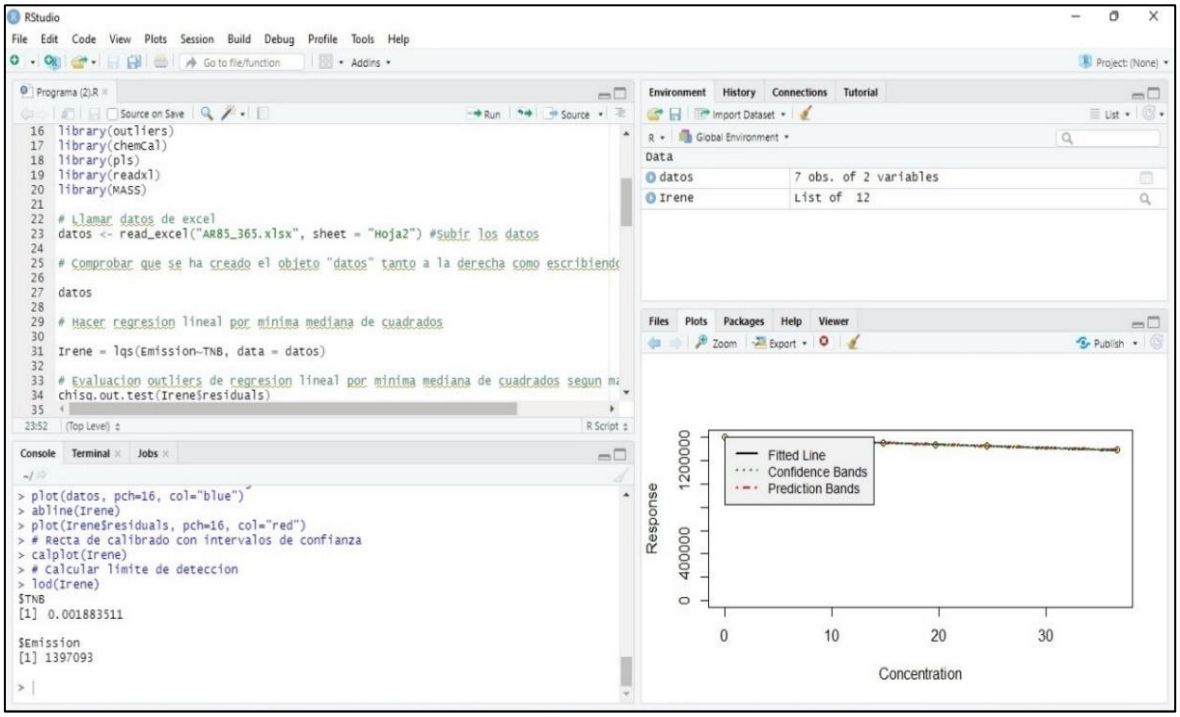

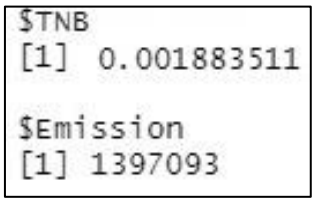

Figure 458. Calculation of the TNB limit of detection using the R software program and the emission values at 365 nm.

LOD was calculated using emission values at 400 nm. The R software was used and the value of the LOD was 1.89 nM.

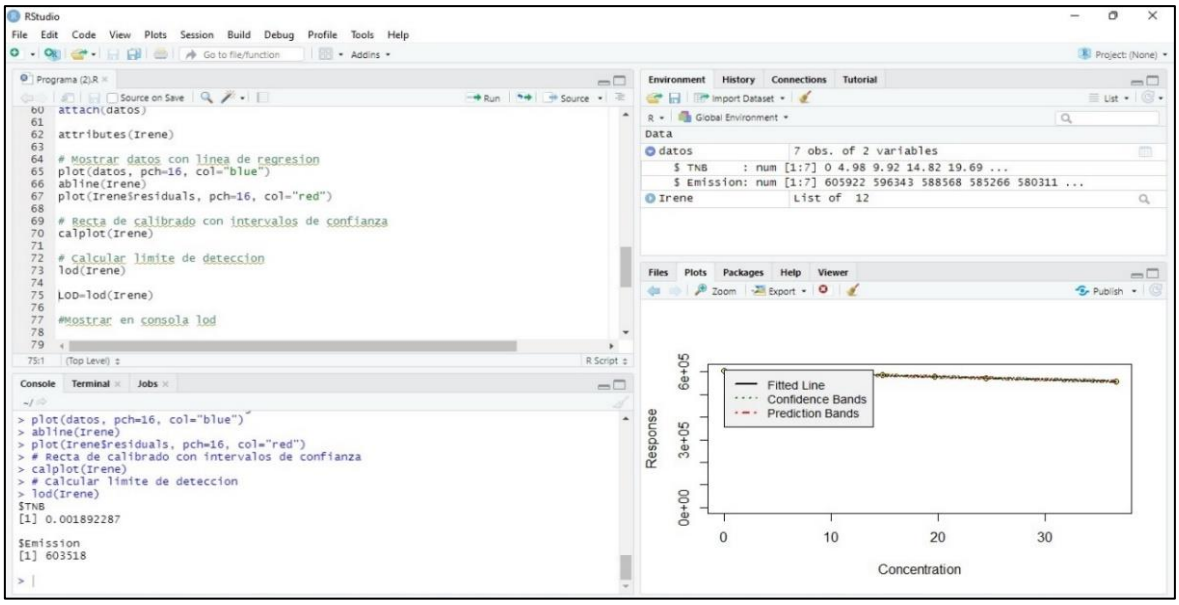

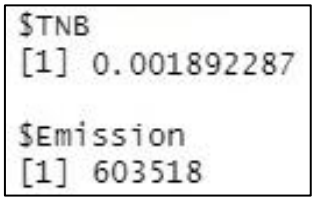

Figure 459. Calculation of the TNB limit of detection using the R software program and the emission values at 400 nm.

Titration of AR85 with nitrobenzene in toluene and LOD calculations.

The working concentration of AR85 was 2.5 µM and the concentration of nitrobenzene was increased by adding from a concentrated solution in the same solvent. The measurements were carried out inmediately after the addition of nitrobenzene. The excitation wavelength was 330 nm and the fluorescence changes were registred at 25ºC.

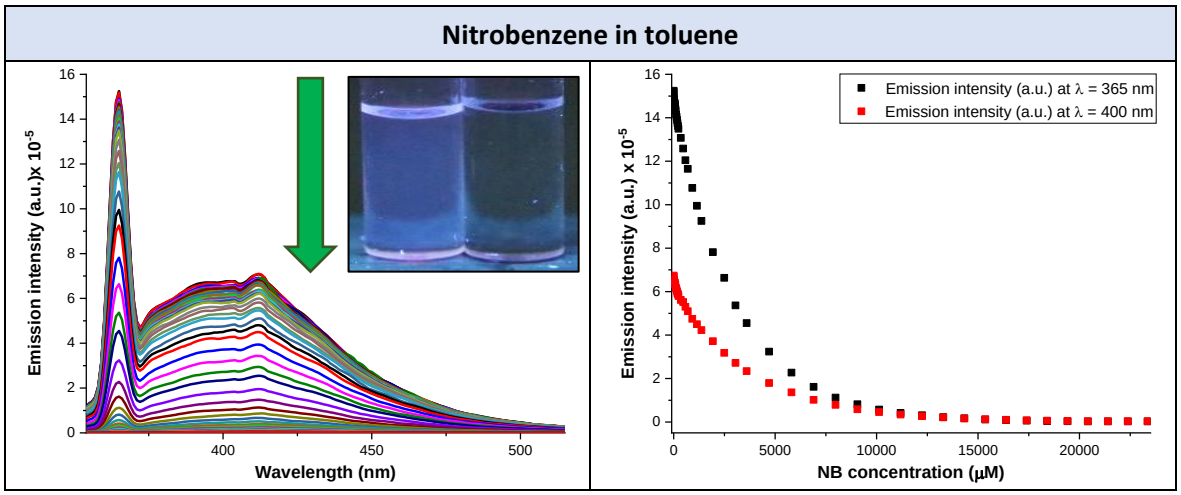

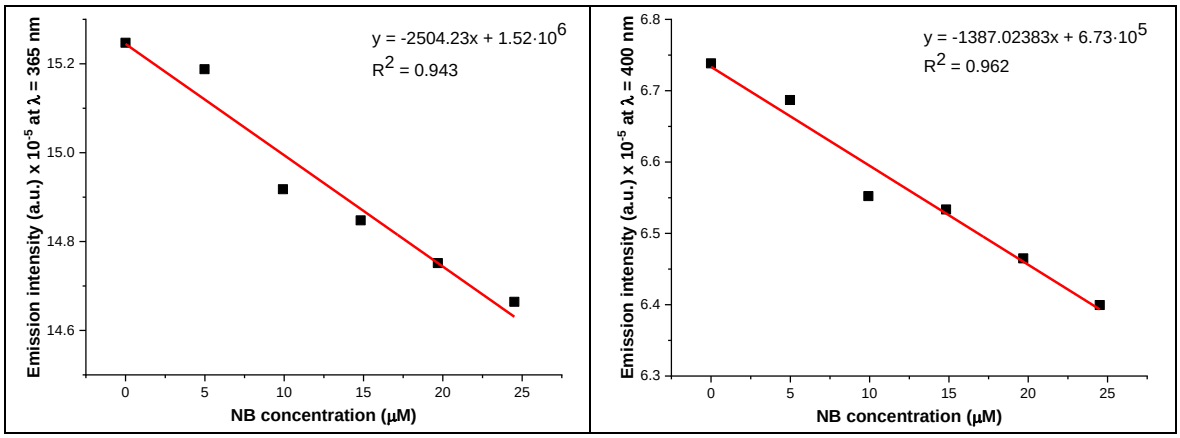

Figure 460. Titration (up left), fluorescence profile at 365 nm and 400 nm (up right), calibration for the LOD calculation using emission values at 365 nm (down left) and calibration for the LOD calculation using emission values at 400 nm (down right) of a AR85 solution in toluene under increasing concentrations of NB.

A decrease in emission intensity was observed with the increase of the amount of nitrobenzene until stabilization was reached. The calculation of the LOD by linear regression + false positive and negative at 365 nm. With this method, the R software was used and the value of the LOD was 2.16 nM.

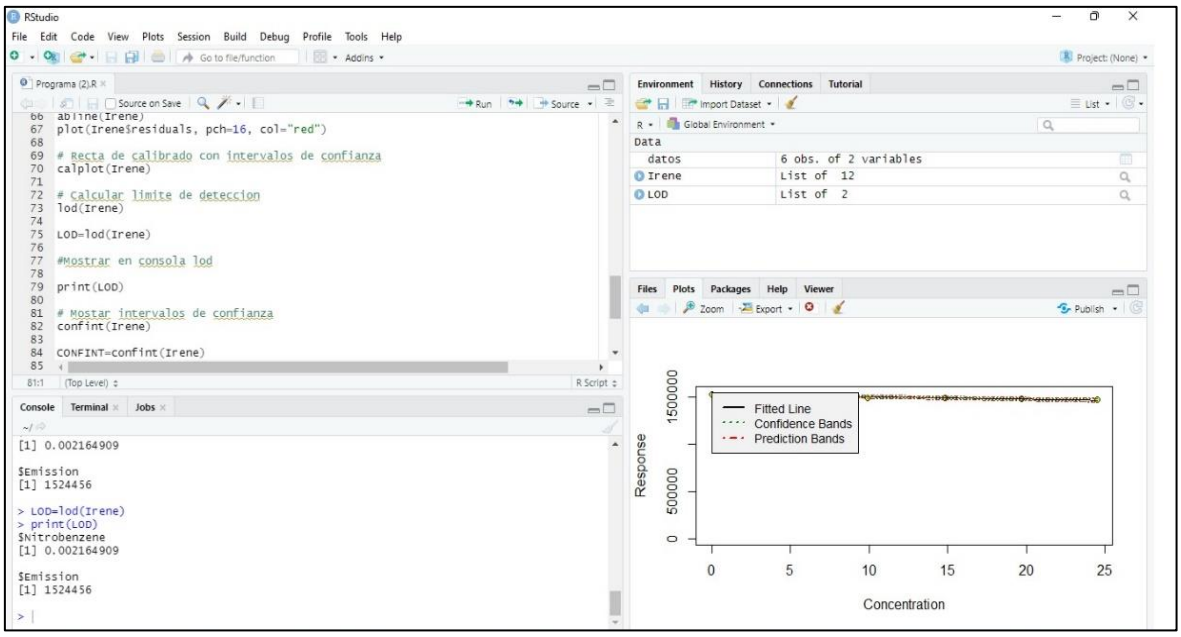

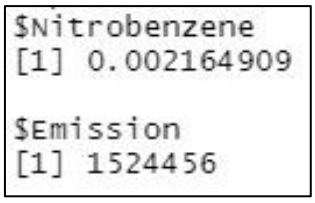

Figure 461. Calculation of the NB limit of detection using the R software program and the emission values at 365 nm.

Calculation of the LOD by linear regression + false positive and negative at 400 nm. With this method, the R software was used and the value of the LOD was 2.16 nM.

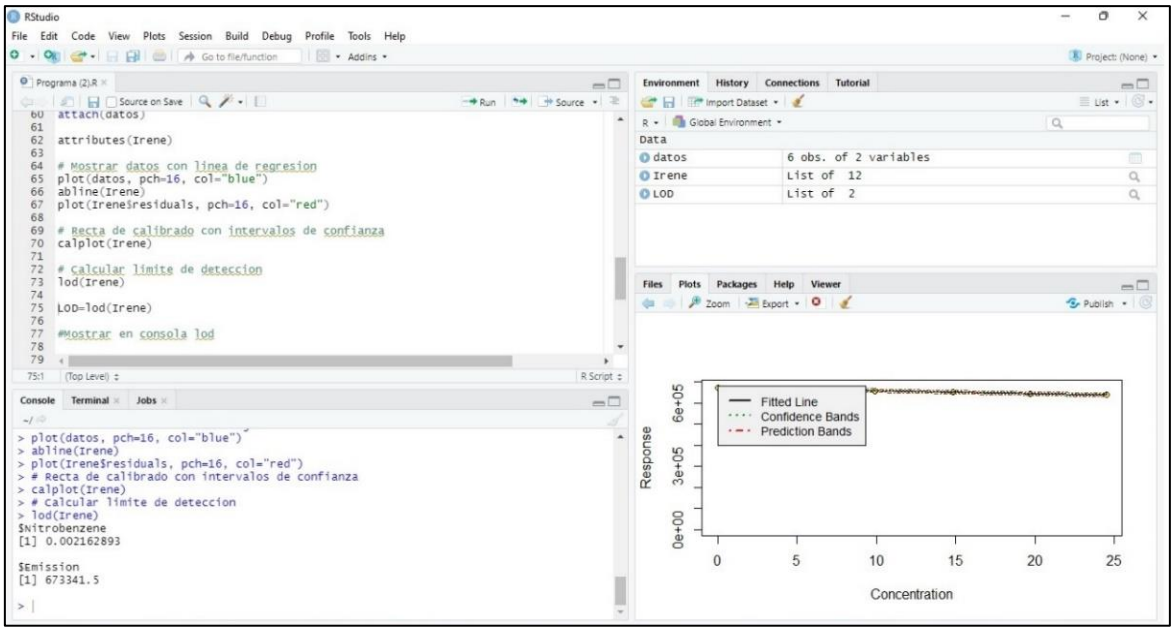

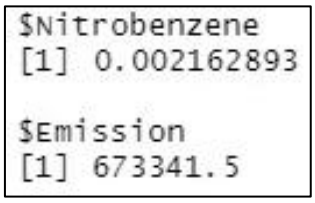

Figure 462. Calculation of the NB limit of detection using the R software program and the emission values at 400 nm.

Titration of AR85 with 2,4-dinitrotoluene in toluene and LOD calculations.

The working concentration of AR85 was 2.5 µM and the concentration of 2,4-dinitrotoluene was increased by adding from a concentrated solution in the same solvent. The measurements were carried out inmediately after the addition of DNT. The excitation wavelength was 330 nm and the fluorescence changes were registred at 25ºC.

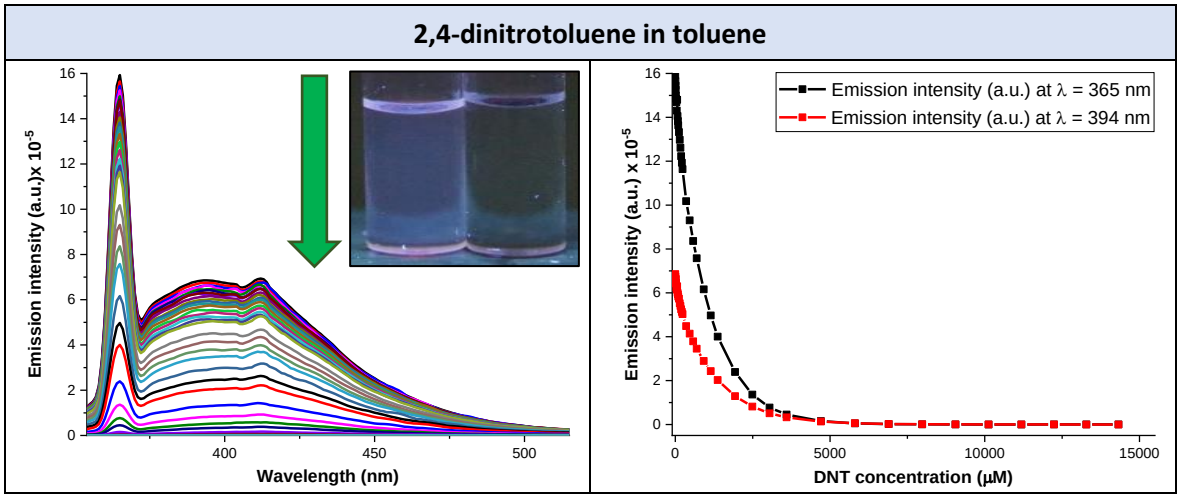

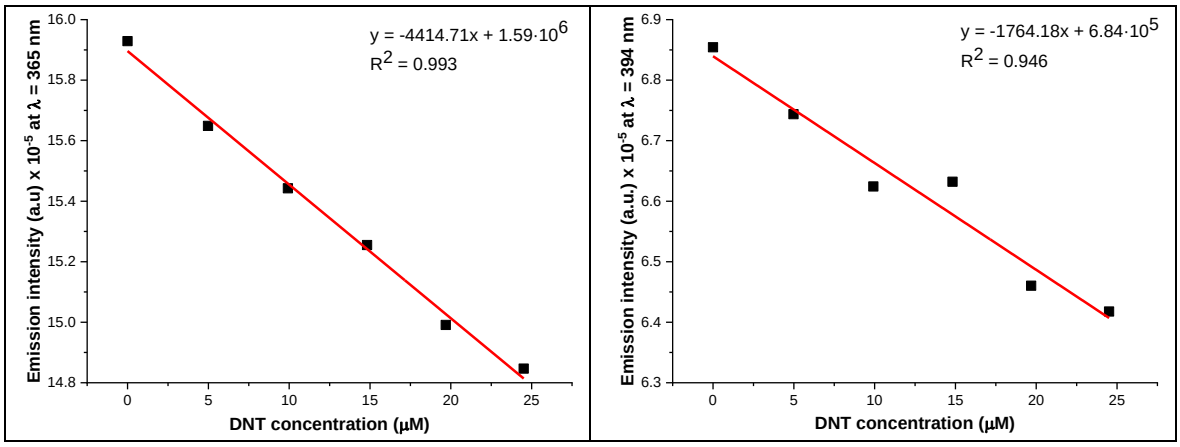

Figure 463. Titration (up left), fluorescence profile at 365 nm and 400 nm (up right), calibration for the LOD calculation using emission values at 365 nm (down left) and calibration for the LOD calculation using emission values at 394 nm (down right) of a AR85 solution in toluene under increasing concentrations of DNT.

A drop in emission intensity was observed as the amount of 2,4-dinitrotoluene added was increased until stabilization was reached. The LOD of AR85 in the two maximum of emission with 2,4-dinitrotoluene was calculated using three different method.

Calculation of the LOD by linear regression + false positive and negative at 365 nm. With this method, the R software was used and the value of the LOD was 2.16 nM.

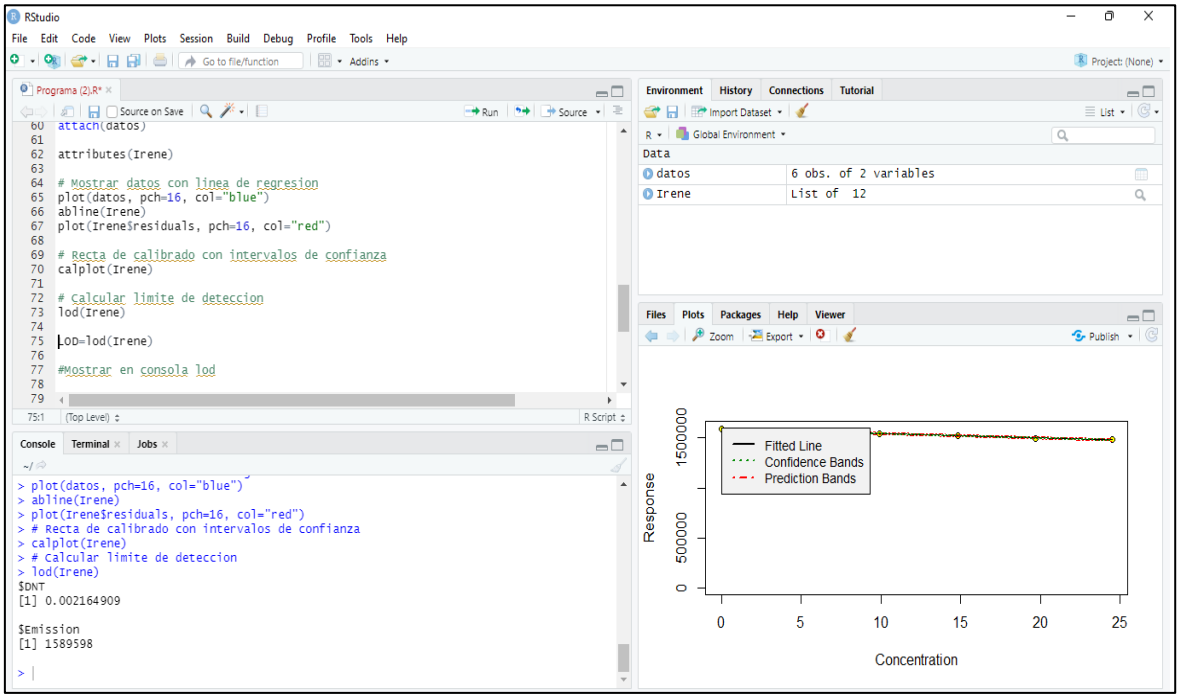

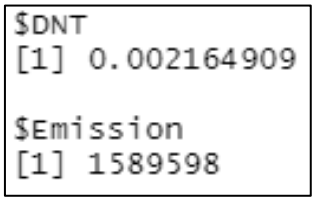

Figure 464. Calculation of the DNB limit of detection using the R software program and the emission values at 365 nm.

Calculation of the LOD by linear regression + false positive and negative at 394 nm. With this method, the R software was used and the value of the LOD was 2.16 nM.

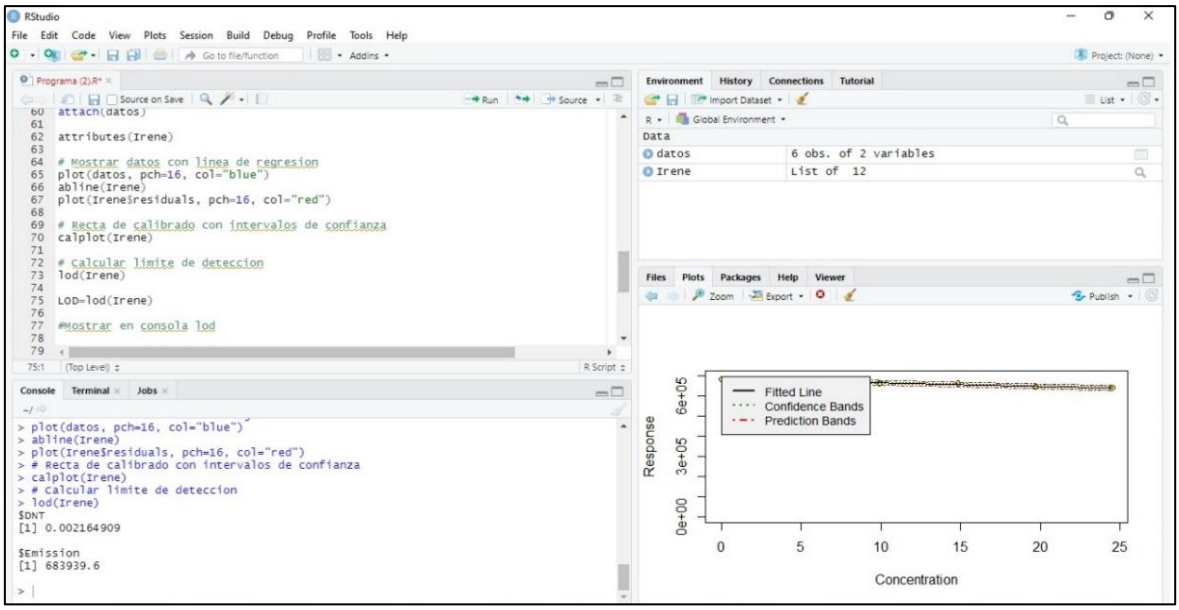

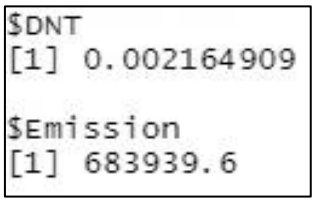

Figure 465. Calculation of the DNB limit of detection using the R software program and the emission values at 394 nm.

Previous solvent test of AR85 with trinitrophenol.

The effect of 2,4,6-trinitrophenol to AR85 was studied in 7 different solvents, to determine the best solvent to detect changes in the presence of TNP generated in the fluorescence emission of the probe. For this purpose, 14 vials were prepared, 7 with a 10 µM AR85 solution and 7 with a 10 µM AR85 solution + TNP excess (2 mg in each vial). All test were performed at room temperature and the photographs were taken immediately after their preparation under visible and 366 nm UV light.

	MeOH	DMSO	Acetone	THF	$CHCl_3$	DCM	Tol. + 5% DMSO
AR85 vs TNP, visible light							
AR85 vs TNP, UV light (366 nm)	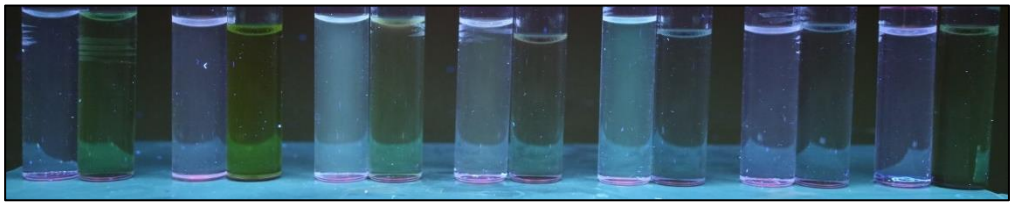						
AR85 vs TNP, visible light, after 24h	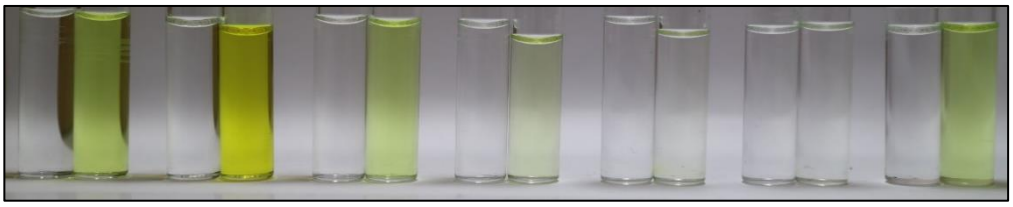						

AR85 vs TNP, UV light (366 nm), after 24h	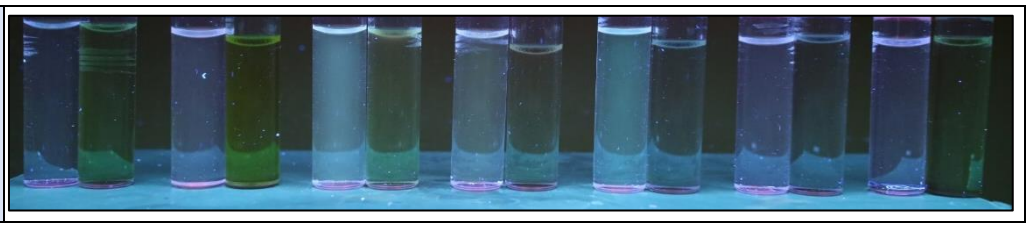

Figure 466. AR85 10 µM (left vial of each pair) and AR85 10 µM with 2 mg of TNP (right vial of each pair) in different solvents under visible light and 366 nm UV light.

AR85 was soluble in all tested solvents, 2,4,6-trinitrophenol was soluble in MeOH, DMSO, acetone and THF but not completely soluble in either DCM or CHCl3. Neither is it in pure toluene, but it is in toluene with an added 5% of DMSO. To keep the titration conditions as similar as possible to those previously carried out with 2,4,6-trinitrotoluene, 1,3,5-trinitrobenzene, nitrobenzene and 2,4-dinitrotoluene, the titration with TNP was performed in the mixture of solvents, toluene + 5% DMSO.

Titration of AR85 with 2,4,6-trinitrophenol in toluene + 5% DMSO and LOD calculations.

A solution of AR85 (2.5 µM) in toluene + 5% DMSO was prepared. The TNP concentration was increased by adding from a concentrated solution in the same solvent. Measurements were carried out immediately after the addition of TNP. λ_{exc} = 330 nm, λ_{em} = 365nm/397nm. Fluorescence changes were registered at 25ºC. Samples of the AR85 solution were taken before and after the titration and photographed under visible light and 366nm UV light.

2,4,6-trinitrophenol in toluene + 5% DMSO

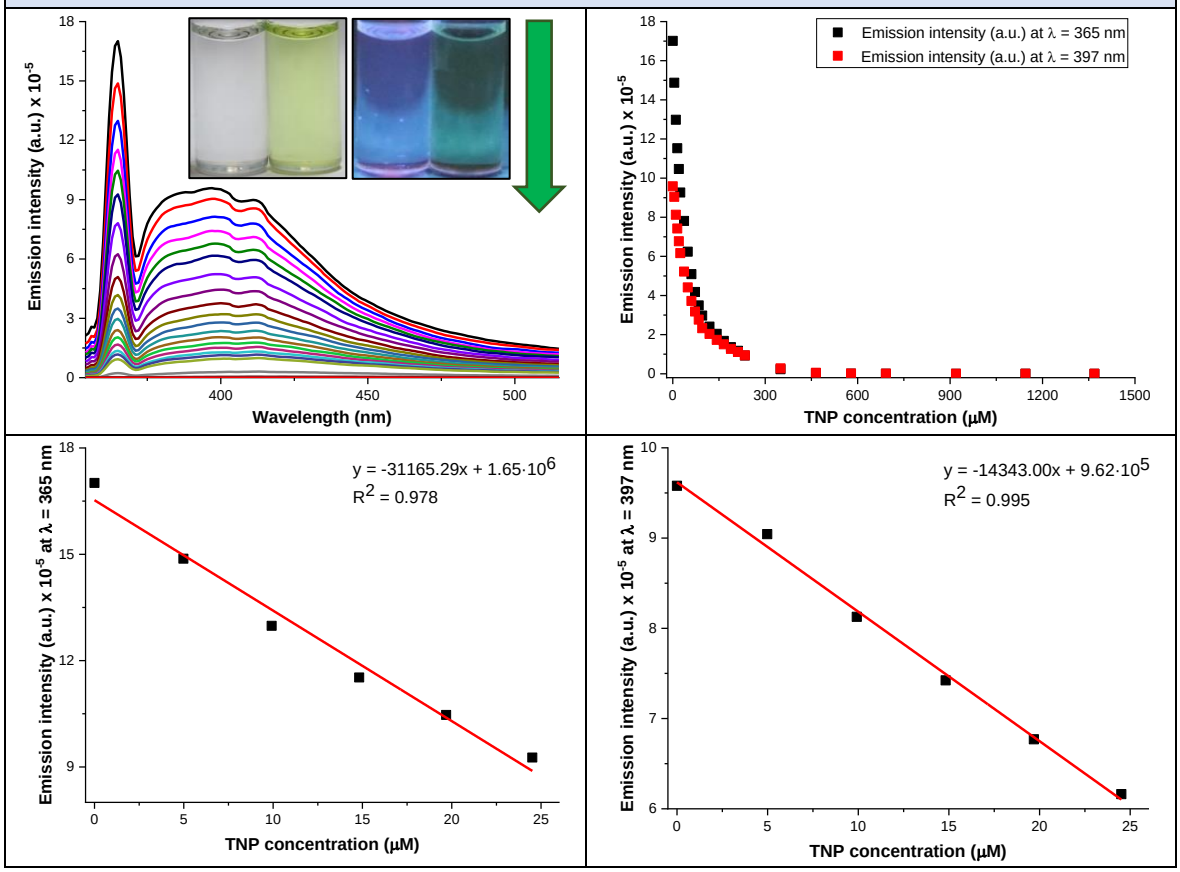

Figure 467. Titration (up left), fluorescence profile at 365 nm and 397 nm (up right), calibration for the LOD calculation using emission values at 365 nm (down left) and calibration for the LOD calculation using emission values at 397 nm (down right) of a AR85 solution in toluene under increasing concentrations of TNP.

In addition, the blank (sample only containing probe) was measured three times. The titration profile for TNP was obtained, and the limit of detection was calculated by linear regression + false positive and negative. By using the emission values at 365 nm, this methodm using “R” software, allowed to obtain a LOD = 2.16 nM.

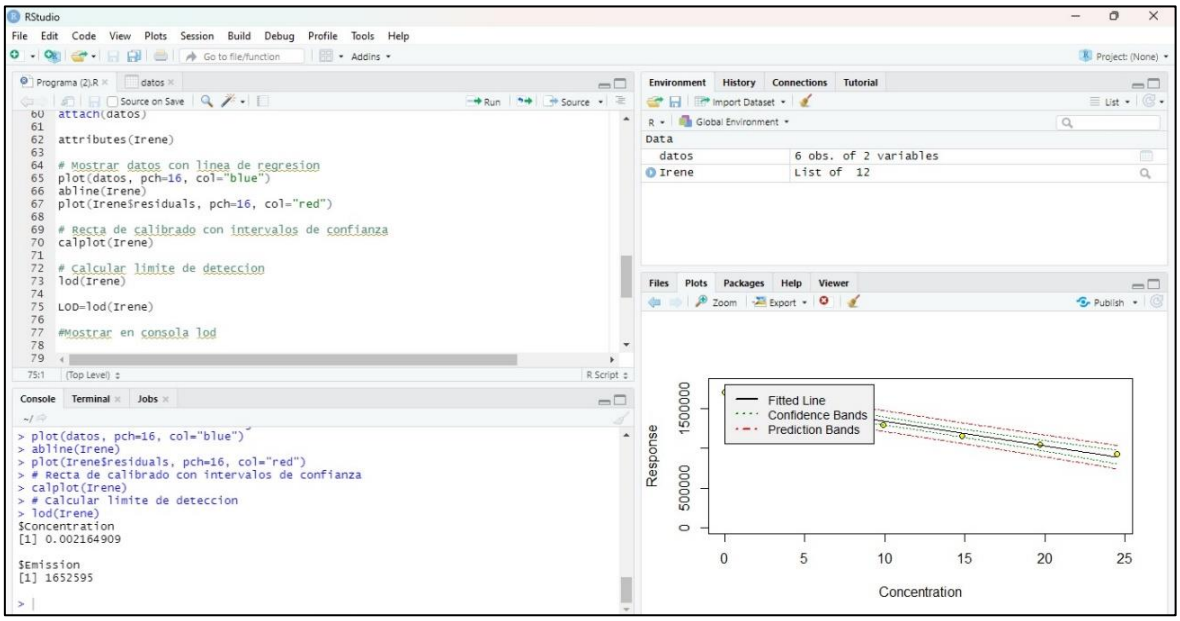

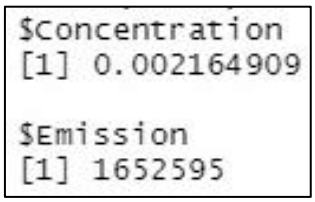

Figure 468. Calculation of the TNP limit of detection using the R software program and the emission values at 365 nm.

By using emission values at 397 nm, the LOD calculated by linear regression + false positive and negative was LOD = 2.19 nM.

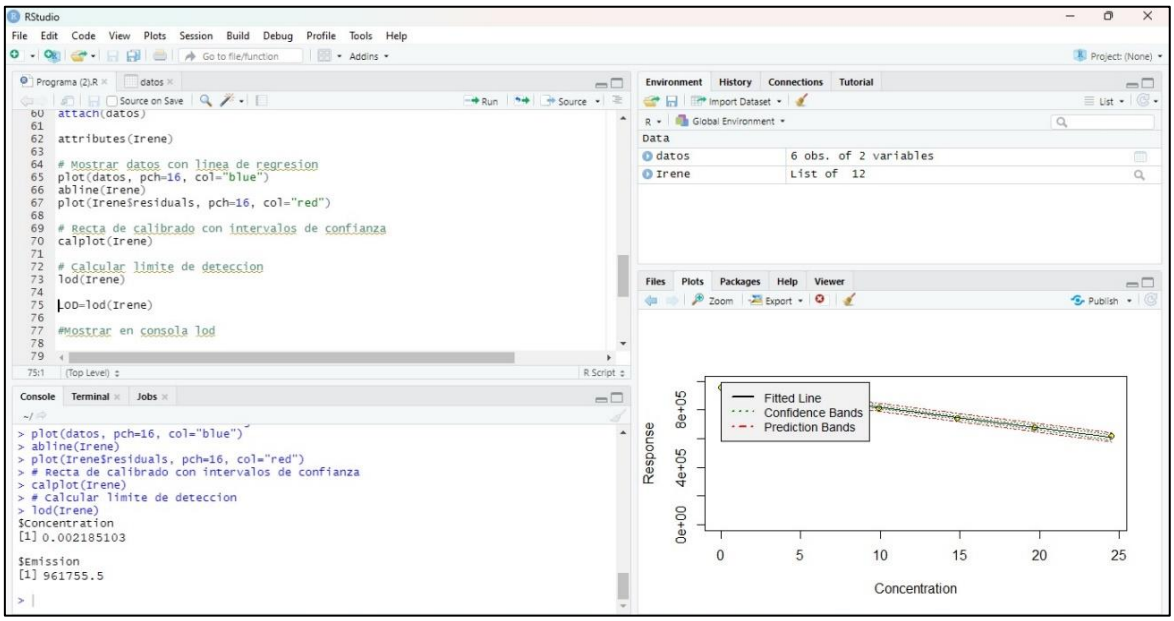

```
$Concentration
[1] 0.002185103

$Emission
[1] 961755.5
```

Figure 469. Calculation of the TNP limit of detection using the R software program and the emission values at 397 nm.

Previous solvent test AR85 with ammonium nitrate.

The effect of ammonium nitrate to AR85 was studied only in 5 different solvents (since the salt is not soluble in many organic solvents), in order to determine which one was the best to detect the change the presence of the explosive generates in the fluorescence emission of the probe.

Conditions were: 10 vials were prepared, 5 with a 10 µM AR85 solution and 5 with a 10 µM AR85 solution + an ammonium nitrate excess (2 mg in each vial) to ensure complete reaction with the probe. Photographs were taken immediately after their preparation under visible light and 366nm UV light and after 24 hours.

	H_2O	MeOH	DMSO	DCM	Tol. + 5% DMSO
AR85 vs NH_4NO_3, visible light					
AR85 vs NH_4NO_3, UV light (366 nm)	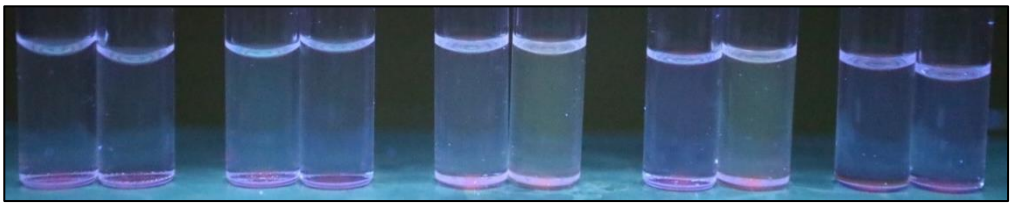				
AR85 vs NH_4NO_3, visible light, after 24 h					
AR85 vs NH_4NO_3, UV light (366 nm), after 24 h	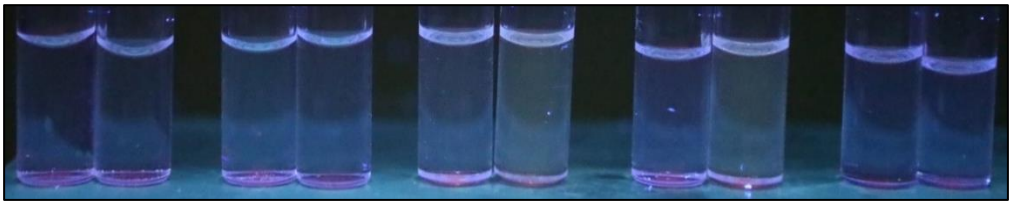				

Figure 470. AR85 10 µM (left vial of each pair) and AR85 10 µM with 2 mg of ammonium nitrate (right vial of each pair) indifferent solvents under visible light and under 366 nm UV light.

AR85 is soluble in all tested solvents but in water, a solvent in which the solubility of the salt would be optimal. Ammonium nitrate is soluble in all 5 solvents tested. The toluene - DMSO combination is especially interesting since it allows us to make this titration as comparable as possible with the previous ones. So, to make the titration conditions as similar as possible to those previously carried

out with TNT, TNB, NB, DNT and TNP, the titration with ammonium nitrate was performed in this last mixture of solvents.

Titration of AR85 with ammonium nitrate in toluene + 5% DMSO and LOD calculations.

A solution of AR85 (2.5 µM) in toluene + 5% DMSO was prepared. Conditions were: NH_4NO_3 was increased by adding from a concentrated solution in the same solvent. Measurements were carried out immediately after the addition of nitrate. λ_{exc} = 330 nm, λ_{em} = 365nm/397nm. Fluorescence changes were registered at 25ºC.

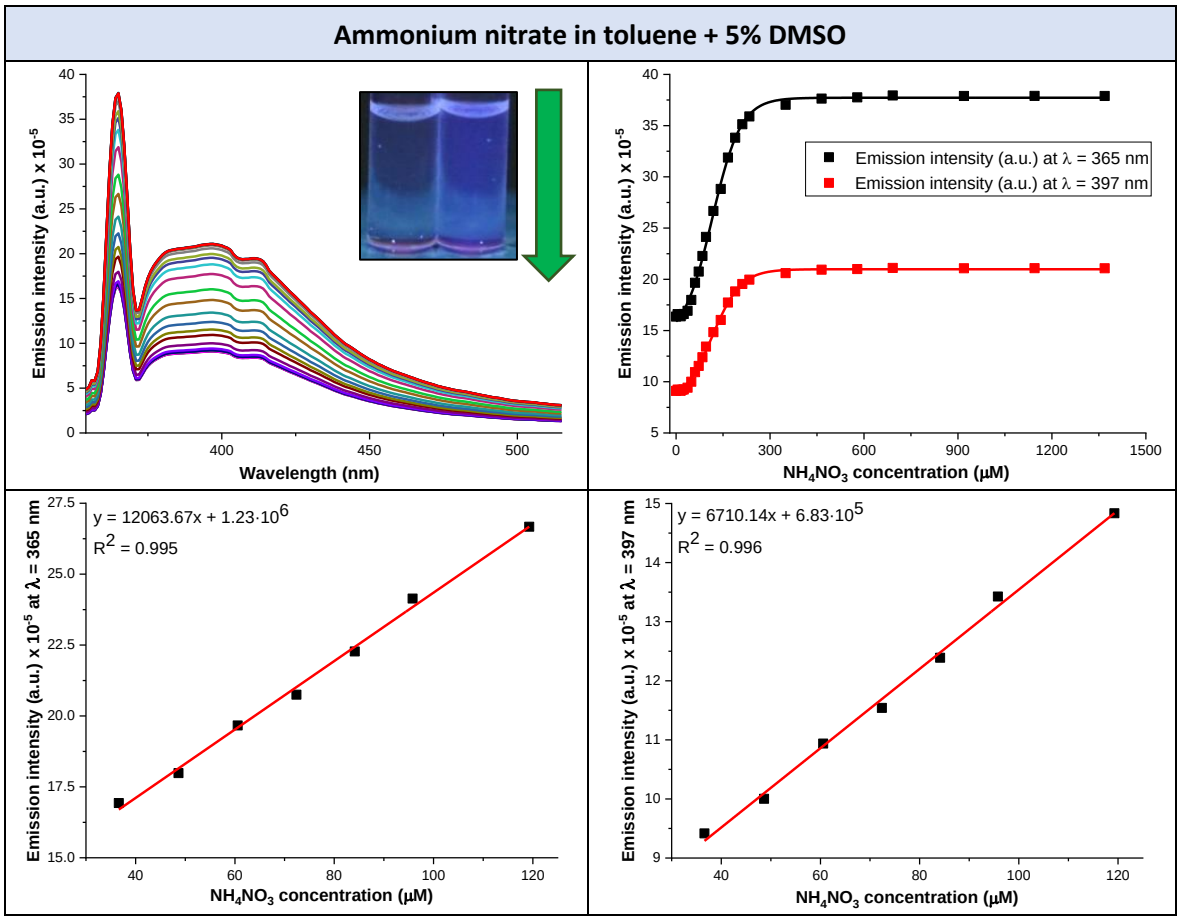

Figure 471. Titration (up left), fluorescence profile at 365 and 397 nm (up right), calibration for the limit of detection using emission values at 365 nm (down left) and calibration for the limit of detection using emission values at 397nm (down left) of a 2.5 µM AR85 solution in toluene + 5% DMSO, under increasing concentrations of nitrate.

The titration profile for NH_4NO_3 was obtained, and the limit of detection was calculated by linear regression + False positive and negative by using the emission values at 365 nm. This method gave a LOD = 11.31 µM.

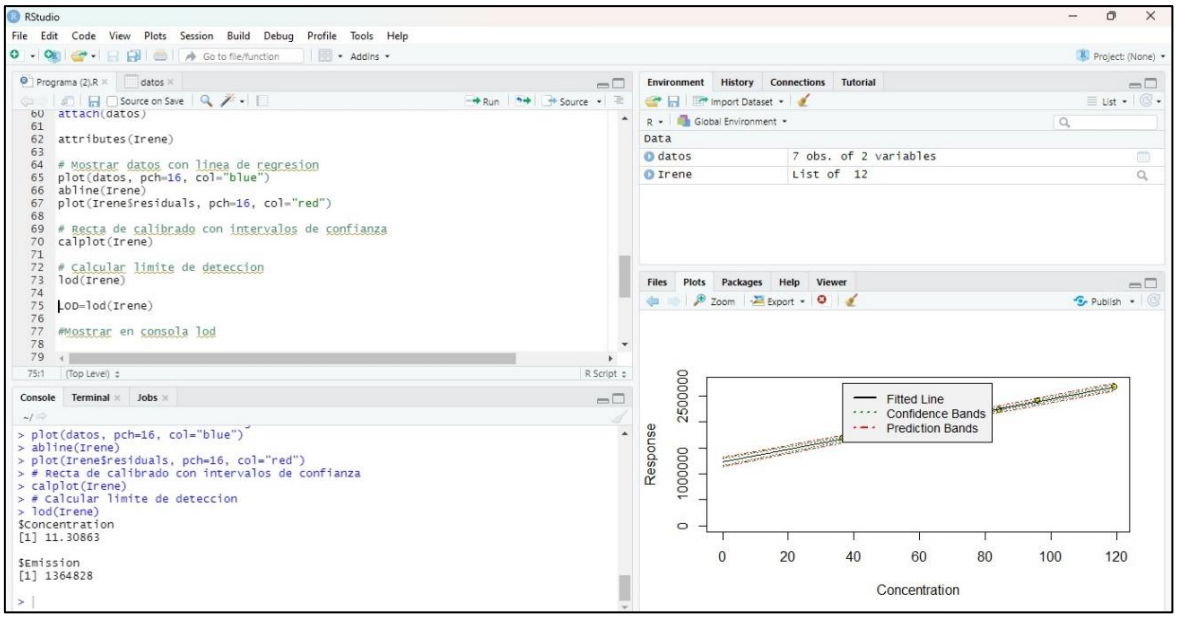

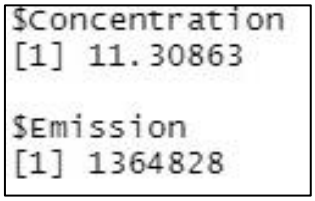

Figure 472. Calculation of the NH_4NO_3 limit of detection using the R software program and the emission values at 365 nm.

The LOD was calculated using emission values at 397 nm by linear regression + False positive and negative gave a value of LOD = 9.60 µM.

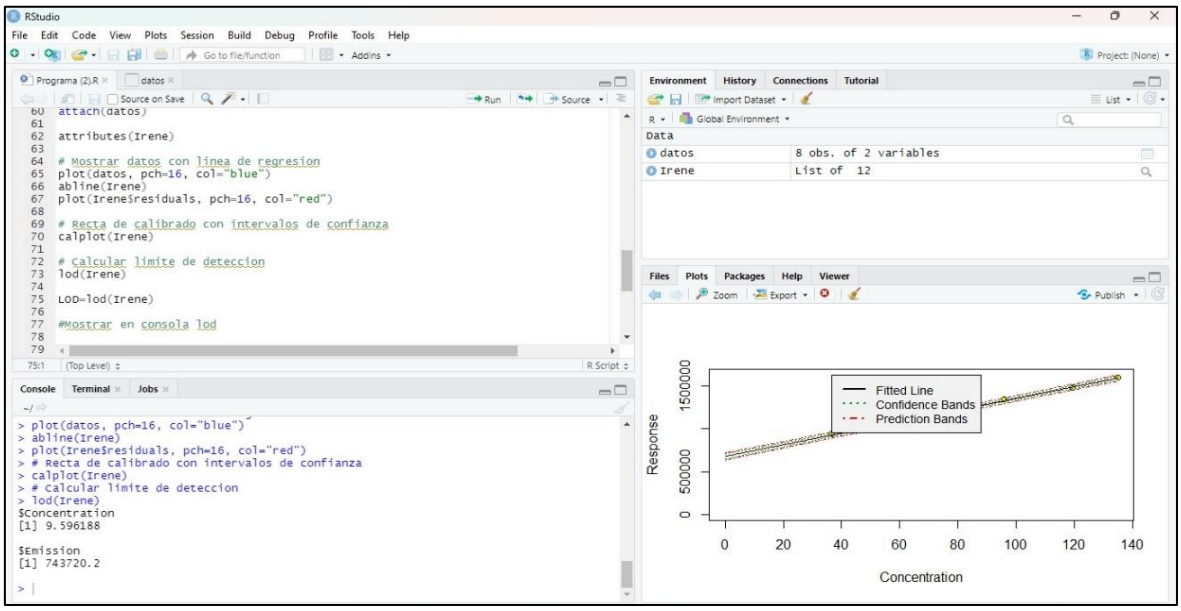

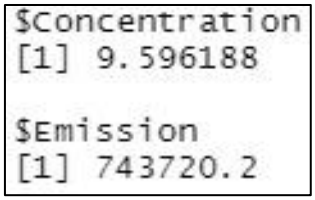

Figure 473. Calculation of NH_4NO_3 limit of detection using R software and emission values at 397 nm.

^{1}H-NMR titration of AR85 with TNT:

The ^{1}H-NMR was carried out used a dissolution of AR85 (4 mg in 0.5 ml of C_6D_6) as a reference. Increasing amounts of TNT was added to the NMR tube according to the following figure:

Addition number	TNT mass added (µg)	Total mass of TNT added (µg)	Addition number	TNT mass added (µg)	Total mass of TNT added (µg)
1	0	0	**10**	60	150
2	5	5	**11**	150	300
3	5	10	**12**	200	500
4	5	15	**13**	300	800
5	5	20	**14**	600	1400
6	10	30	**15**	1800	3200
7	10	40	**16**	3600	6800
8	20	60	**17**	3600	10400
9	30	90	**18**	5400	15800

Figure 474. Additions of TNT to the 1H-NMR titration fo AR85.

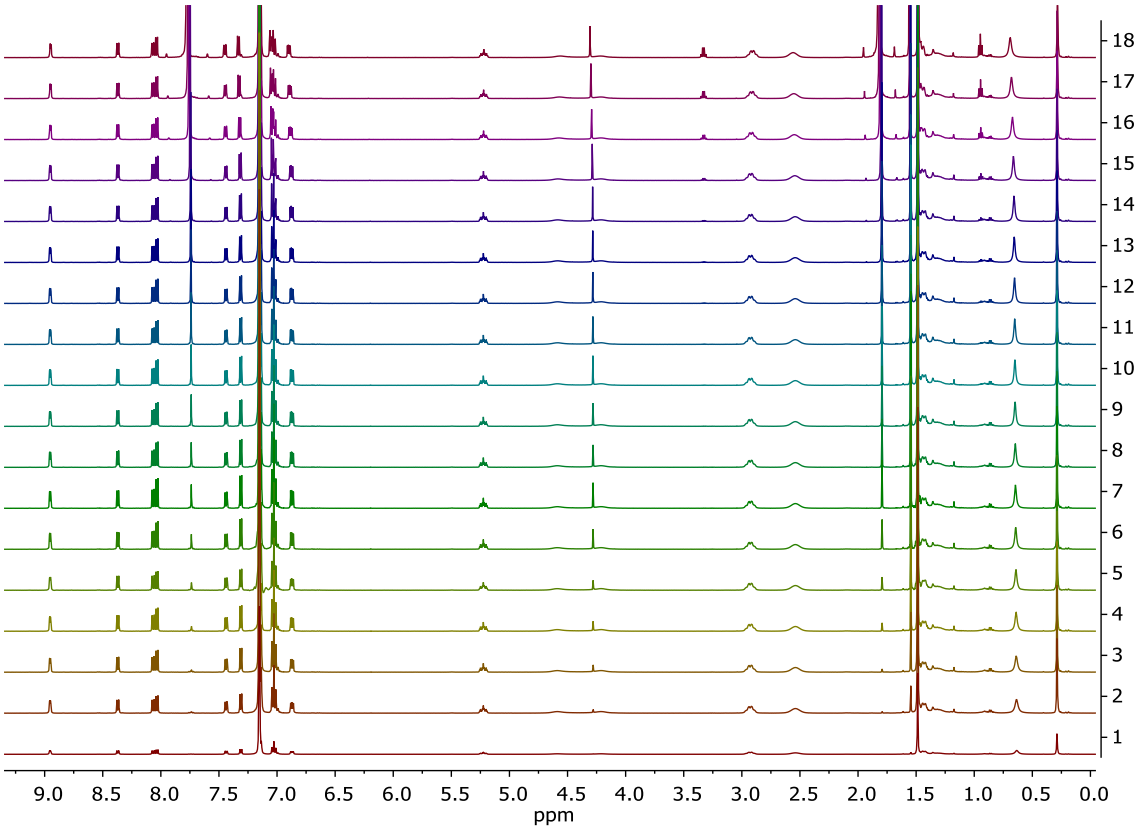

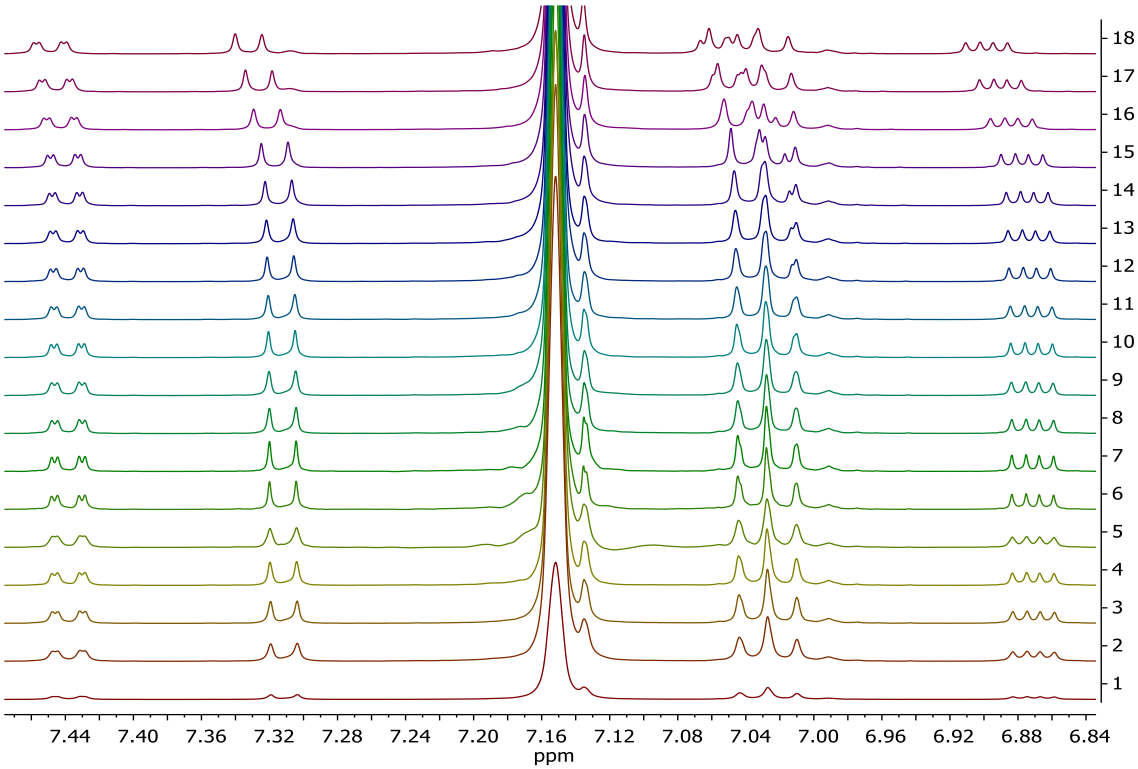

Figure 475. ^{1}H-NMR (C_6D_6, 500 MHz) titration of AR85 with increasing amounts of TNT and expansion of the aromatic region.

Titration of AR85 with TNT using a filter paper:

Increasing amounts of TNT was deposited on a watchglass. A fragment of filter paper (1 cm × 0.5 cm) was slided over them so that the TNT was retained in it. Each piece of filter paper was placed in a topaz vial to which 3 ml of MeOH was added. These vials were placed in an ultrasonic bath for a period of five minutes. After this, the filter paper was removed from tha vials and the content was brought to complete dryness. Finally, the probe AR85 and toluene were added to reach a final volume of 2.5 ml and the fluorescence emission spectra were measured.

Figure 476. TNT solutions used in the experiment (left) and TNT deposition process on the watch glass (right).

Figure 477. TNT sample after the air-drying process of the solution (left) and capture of the TNT with a piece of filter paper (right).

Figure 478. Insertion of filter paper into a topaz vial.

Figure 479. Process of sonication (left) and drying of the samples after removal of the filter paper (right).

The excitation wavelength was 330 nm and all the fluorescence changes were registered at 25ºC

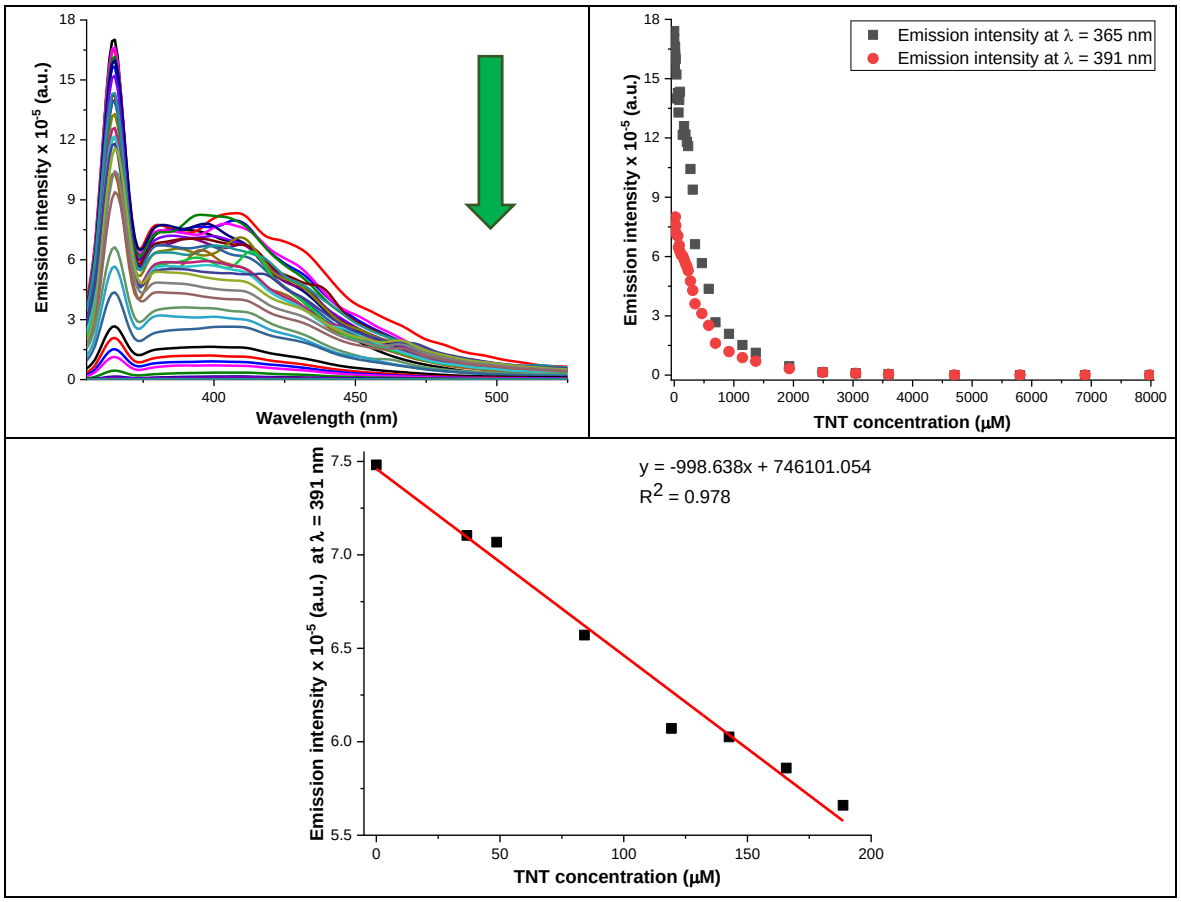

Figure 480. Titration (up left), fluorescence profile at 365 nm and 391 nm (up right) and calibration for the LOD using emission values al 391 nm (down) of a AR85 solution in toluene, in contact with increasing amounts of TNT collected on a physical support (filter).

A drop in emission intensity was observed as the amount of TNT in the physical support was increased followed by stabilizaton. The LOD was calculated by linear regression + false positive and negative at 365 nm. This method allowed to obtain a LOD = 17.31 µM.

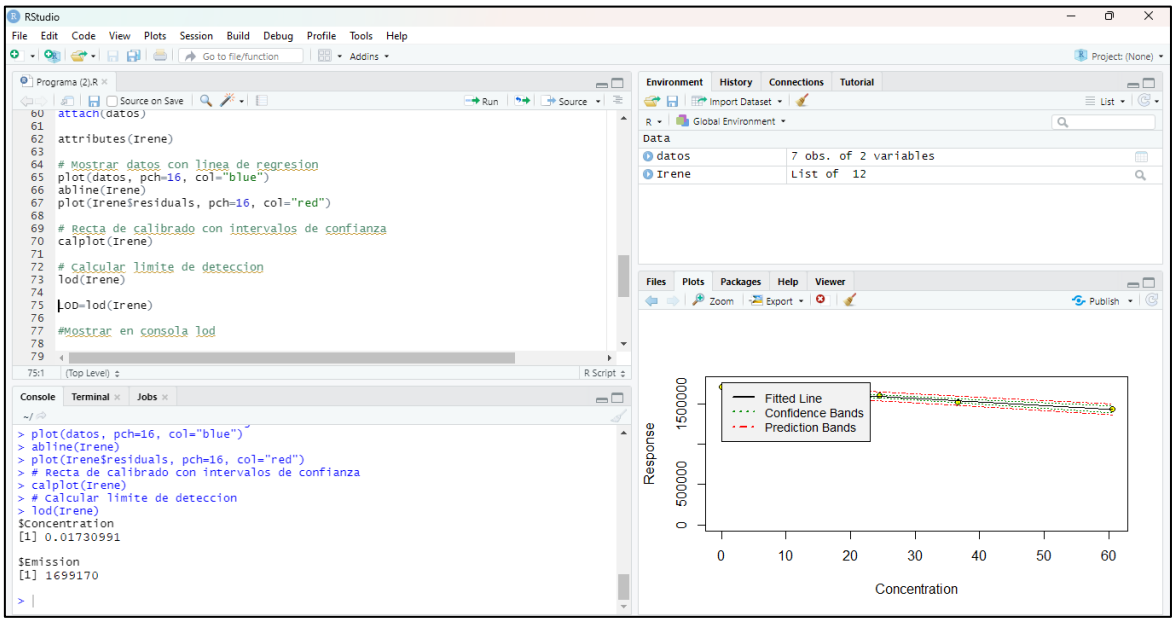

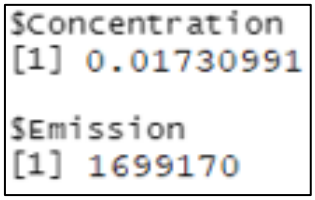

Figure 481. Calculation of the TNT limit of detection using the R software program and the emission values at 365 nm.

Then the LOD was calculated by linear regression + false positive and negative at 391 nm. For this method, the R software was used and the value of the LOD was 17.24 nM.

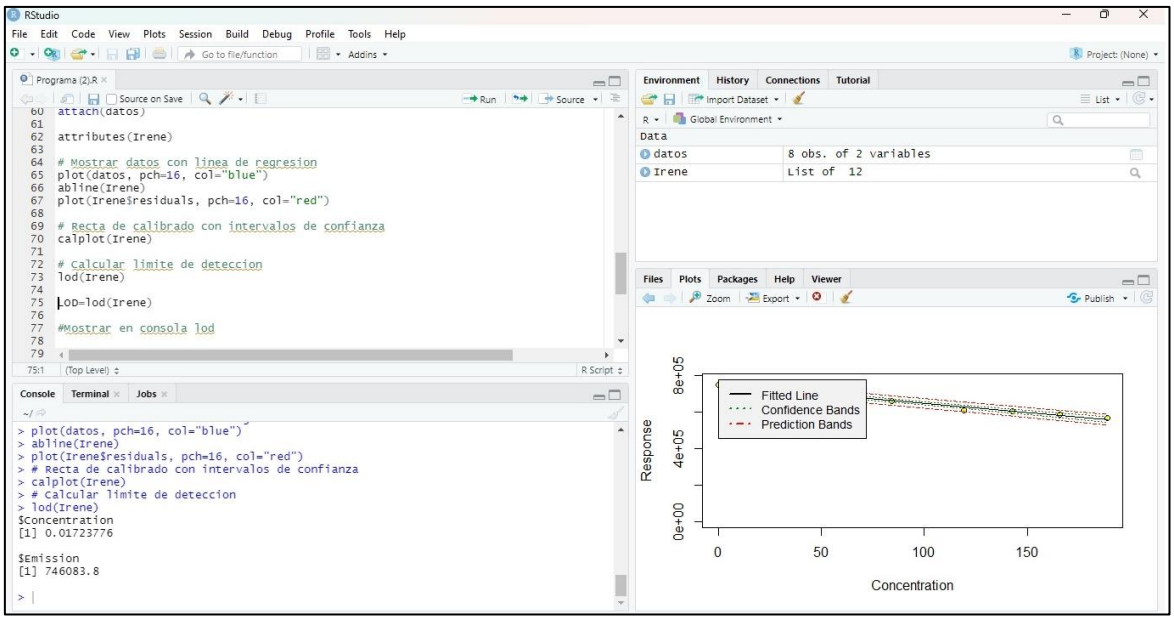

```
$Concentration
[1] 0.01723776

$Emission
[1] 746083.8
```

Figure 482. Calculation of the TNT limit of detection using the R software program and the emission values at 391 nm.

Synthesis of *N*-(*N*-Boc-piperidin-4-yl)-4-[(trimethylsilyl)ethynyl]naphthalene-1,8-dicarboxyl-monoimide (AR94p).

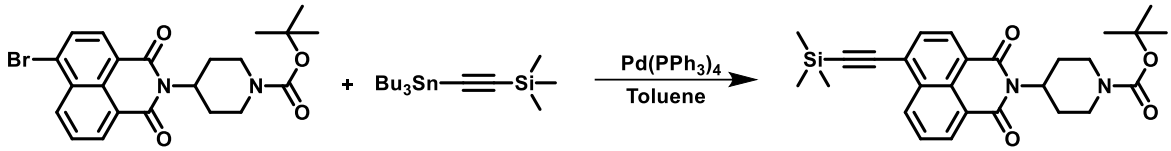

100 mg of *N*-piperidine-4-bromonaphthalene-1,8-dicarboxylmonoimide (AR43, 0.22 mmol) and 93 mg of tri-*N*-butyl(trimethylsilylethynyl)tin (0.24 mmol) were dissolved in 5 ml of dry toluene under argon atmosphere. Then, the $Pd(PPh_3)_4$ was added and the resulting mixture was stirred three days at 110°C. Afterwards, the solvent was evaporated under reduce pressure and the solid was dissolved in DCM and washed with water (3×100 ml). The organic extracts were combined, dried over anhidrous Na_2SO_4 and the solvent was evaporated under reduce pressure. The organic solid was purified by column chromatography (SiO_2, DCM:MeOH) getting 33 mg of a yellow solid, 32% yield.

m.p.: 159-161°C.

IR (ATR, cm^{-1}): 2958-2851, 1696 (C=O), 1650 (C=O), 1588, 1423 (C-O), 1348, 1235, 1142 (C-N), 1100, 1004, 938, 899, 839, 782, 753, 696, 454.

^{1}H-NMR (300 MHz, $CDCl_3$) δ (ppm): 8.65-8.57 (m, 2H, 2×$\mathbf{H_{Ar}}$), 8.48 (d, *J* = 7.6 Hz, 1H, $\mathbf{H_{Ar}}$), 7.88 (d, *J* = 7.6 Hz, 1H, $\mathbf{H_{Ar}}$), 7.81 (dd, *J* = 8.3, 7.6 Hz, 1H, $\mathbf{H_{Ar}}$), 5.22-5.12 (m, 1H, C**H**), 4.29 (s, 2H, C$\mathbf{H}_2$), 2.94-2.65 (m, 4H, 2×C$\mathbf{H}_2$), 1.67-1.60 (m, 2H, C$\mathbf{H}_2$), 1.49 (s, 9H, 3×C$\mathbf{H}_3$), 0.36 (s, 9H, 3×Si-C$\mathbf{H}_3$).

^{13}C-NMR (75MHz, $CDCl_3$) δ (ppm): 164.4 (**C**=O), 164.2 (**C**=O),154.8 (**C**=O), 132.5 ($\mathbf{C}_{Ar}$H), 131.8 ($\mathbf{C}_{Ar}$), 131.7 ($\mathbf{C}_{Ar}$H), 131.4 ($\mathbf{C}_{Ar}$H), 130.4 ($\mathbf{C}_{Ar}$H), 128.1 ($\mathbf{C}_{Ar}$), 127.7 ($\mathbf{C}_{Ar}$H), 127.3 ($\mathbf{C}_{Ar}$), 123.4 ($\mathbf{C}_{Ar}$), 122.8 ($\mathbf{C}_{Ar}$), 105.47 (-C≡**C**-Si(CH_3)$_3$), 101.36 (-**C**≡C-Si(CH_3)$_3$), 79.7 (**Cq**), 52.0 (**C**H), 44.2 (**C**H_2), 28.7 (**C**H_2), 28.41 (**C**H_3), 0.0 (Si(**C**H_3)$_3$).

HRMS (ESI, TOF+) m/z: calculated for $C_{27}H_{32}N_2O_4Si$: 499.2024 (M^++Na); found 499.2030.

UV-Vis ($CHCl_3$), λ_{max} nm (log ε): 353 (4.3).

Ø ($CHCl_3$, %): 33.72.

τ (280 nm, $CHCl_3$, ns): 1.362 (χ^2: 1.388).

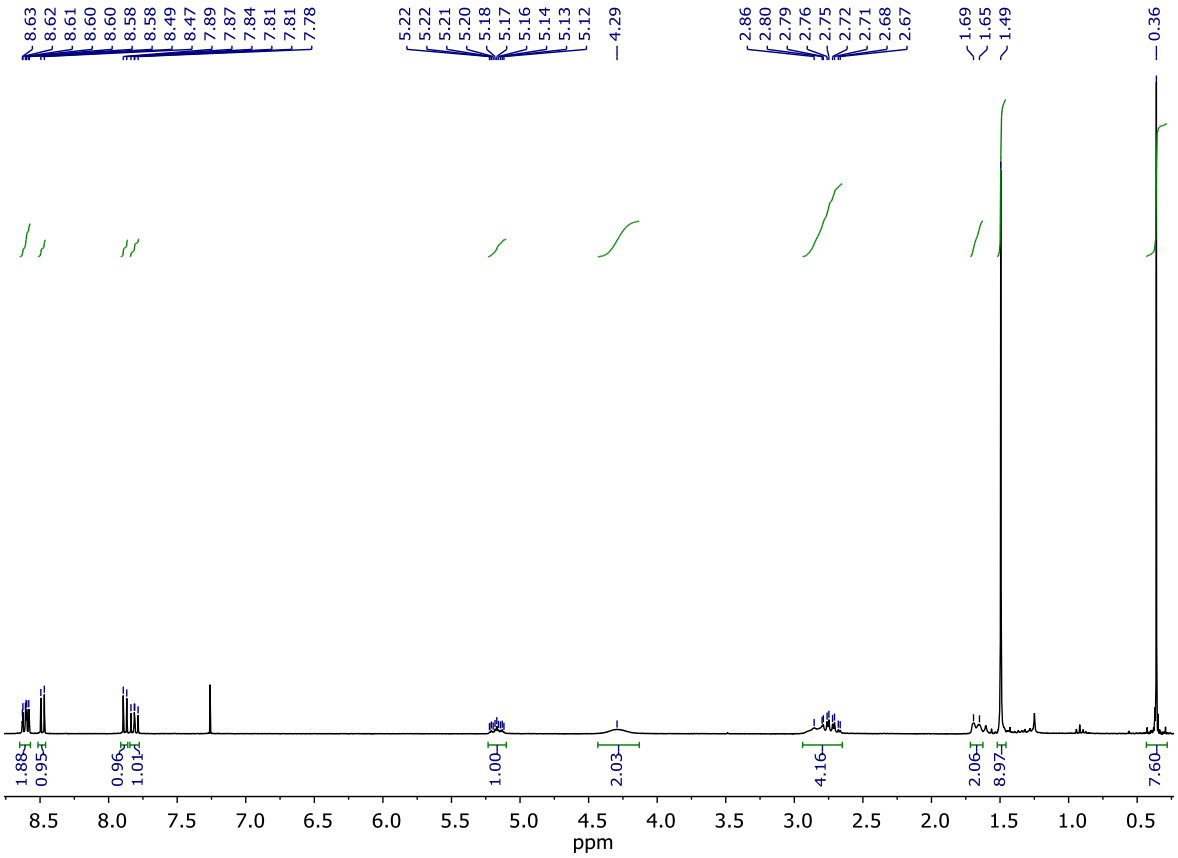

Figure 483. ^{1}H-NMR ($CDCl_3$, 300 MHz) of AR94p.

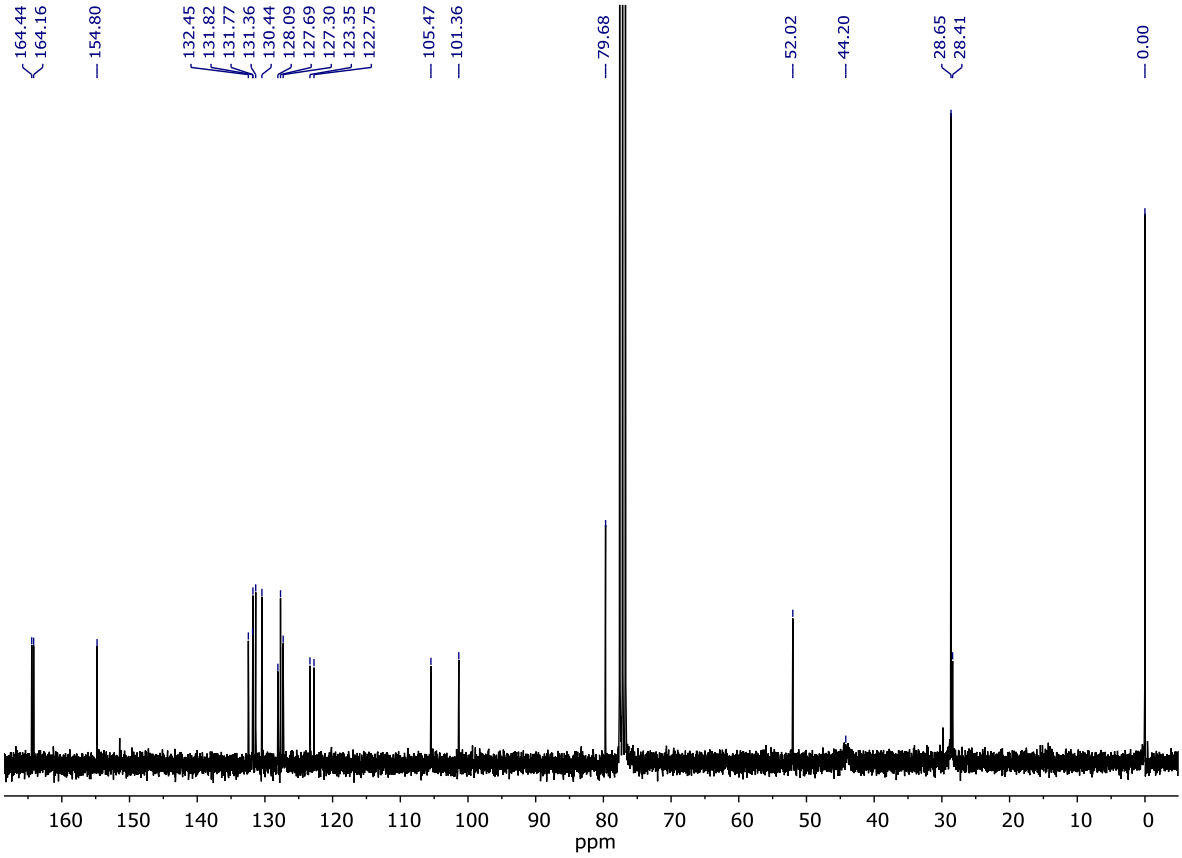

Figure 484. ^{13}C-NMR ($CDCl_3$, 75 MHz) of AR94p.

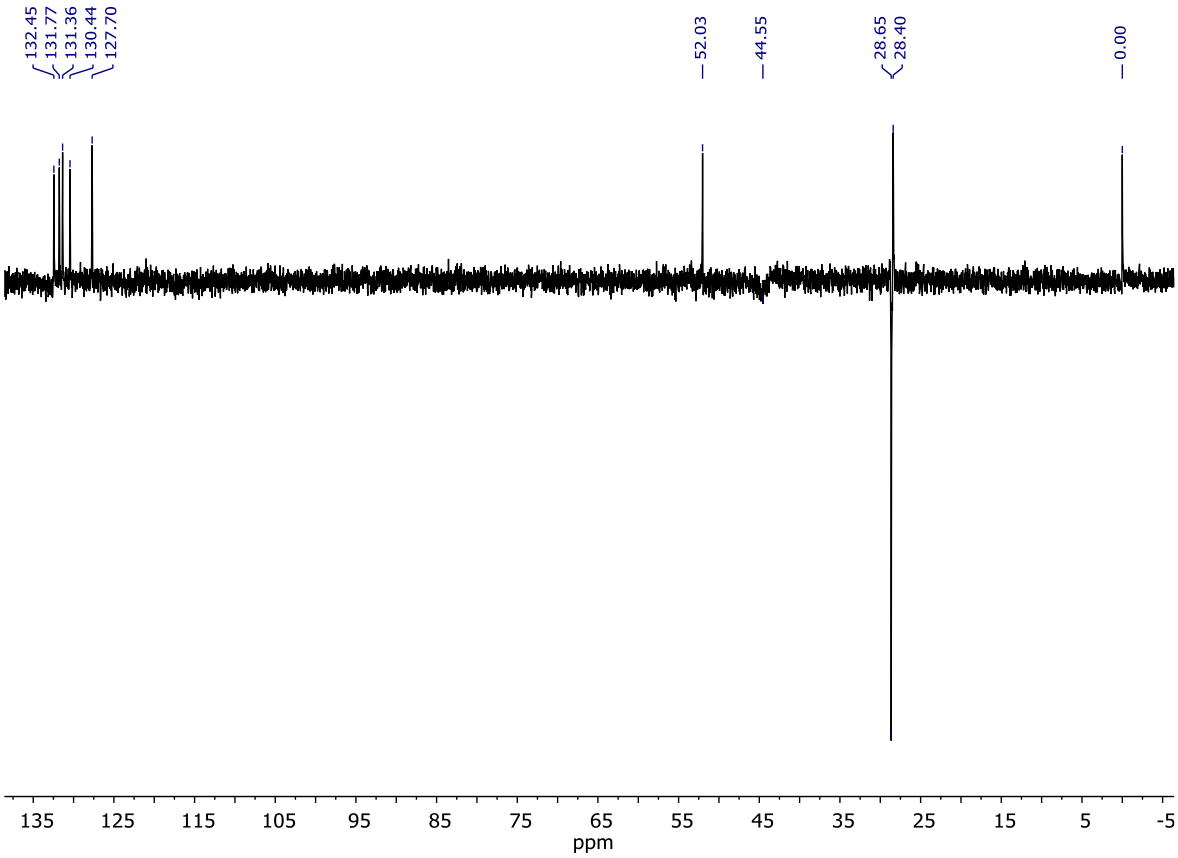

Figure 485. DEPT NMR ($CDCl_3$, 75 MHz) of AR94p.

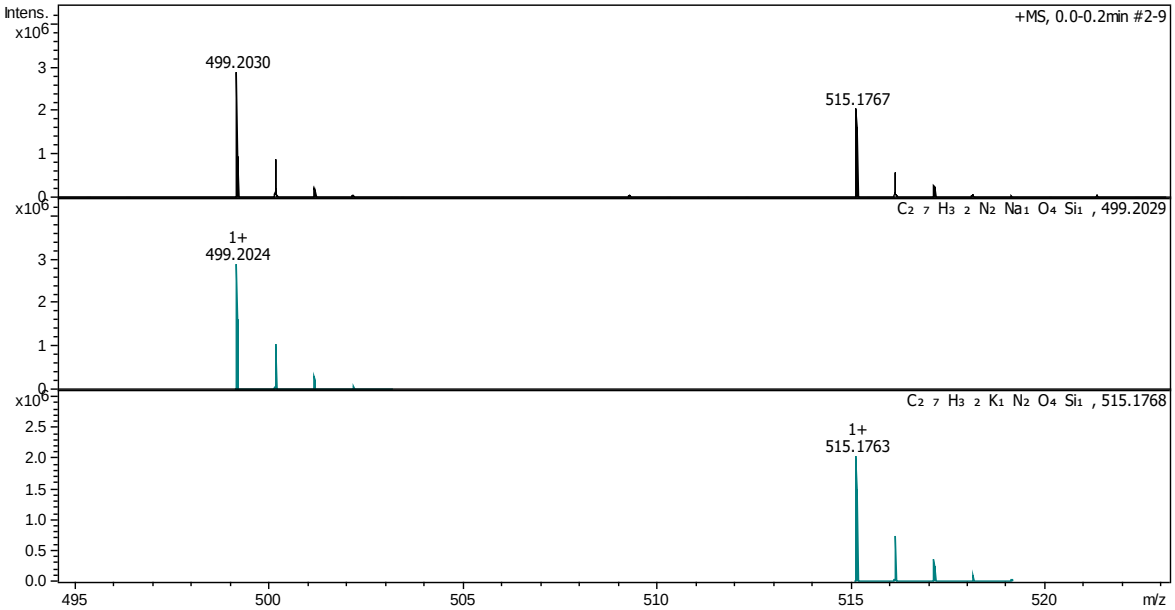

Meas. m/z	m/z	err [ppm]	mSigma	Ion Formula
499,2030	499,2024	-1.2	33.4	C27H32N2NaO4Si
515,1767	515,1763	-0.9	37.8	C27H32KN2O4Si

Figure 486. HRMS (ESI, TOF+) of AR94p.

Solvatochromism:

The concentration of the compound was 10 µM and the excitation wavelength was360 nm.

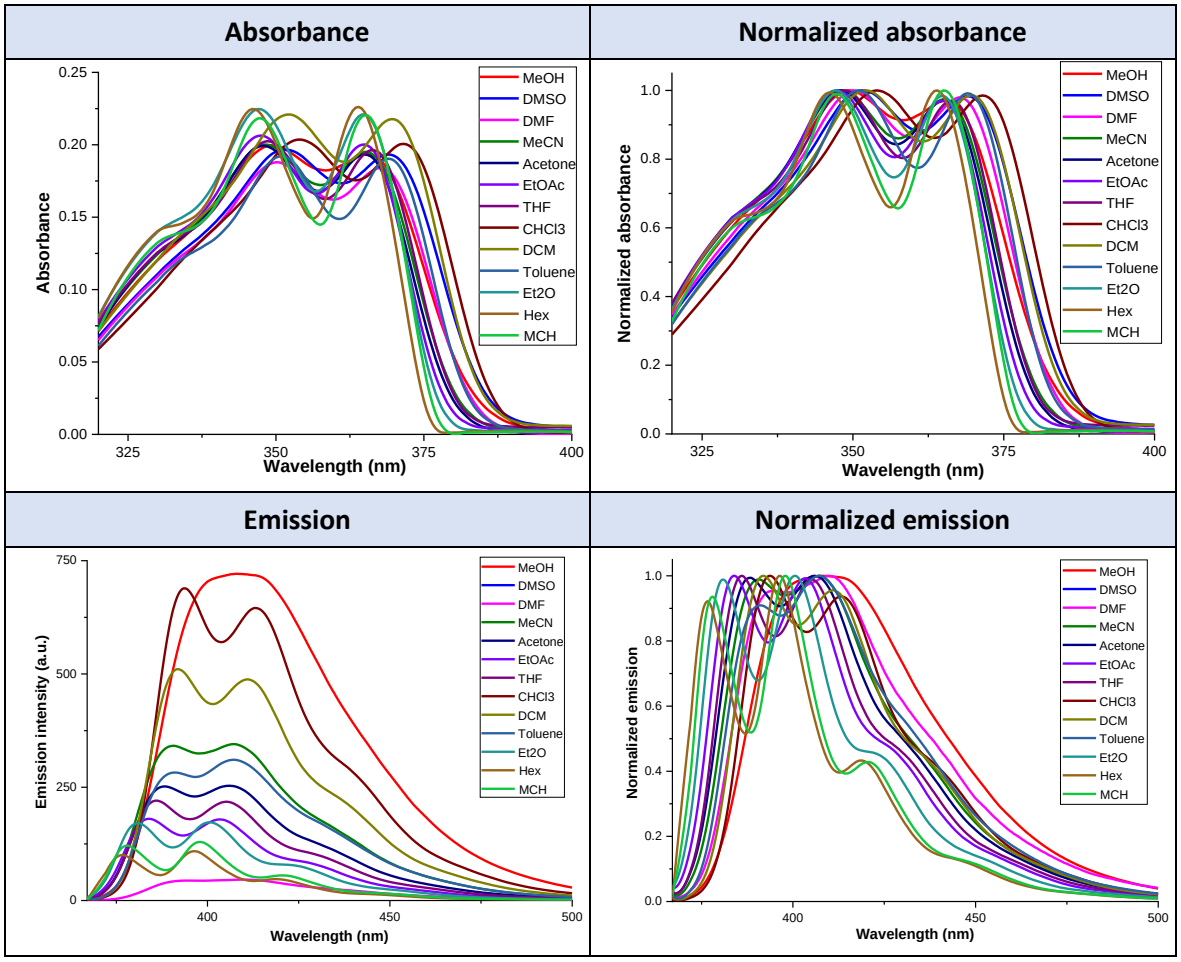

Figure 487. Solvatochromism of AR94p.

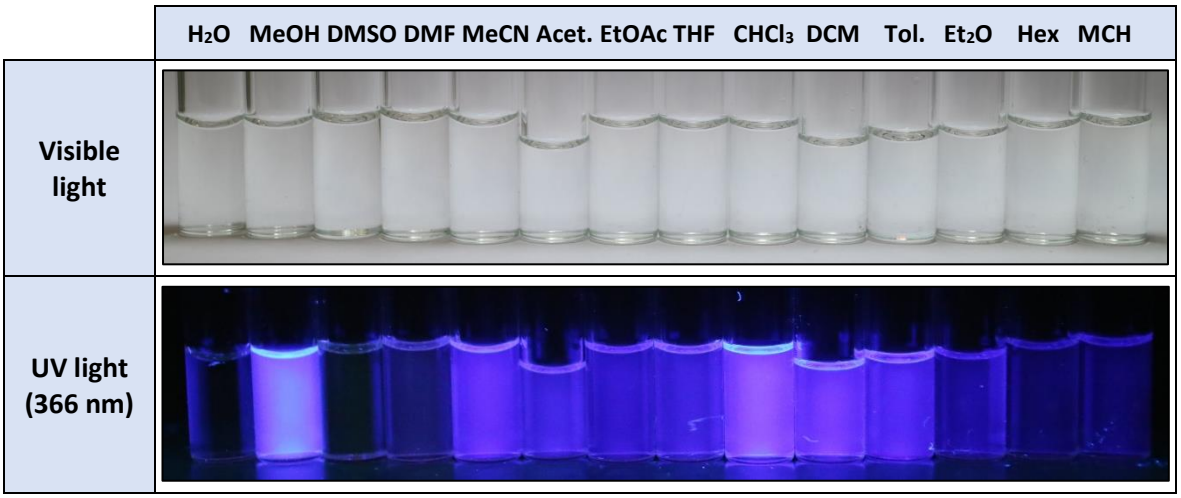

Figure 488. Solvatochromism of AR94p under visible and 366 nm light.

Fluorescence decay lifetime (τ):

The solvent used was chloroform. The concentration of the compound was 10 µM.

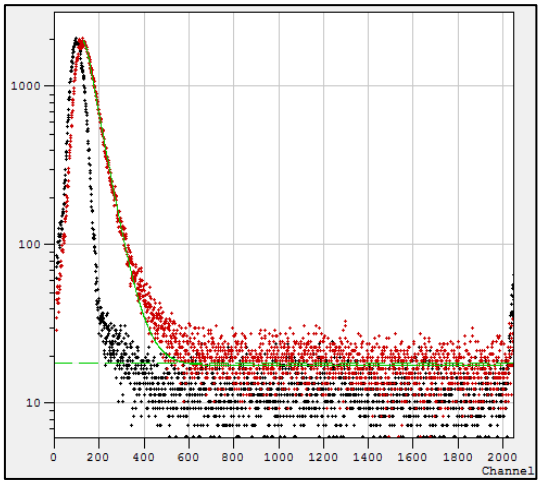

Figure 489. Fluorescence decay lifetime of AR94p.

Water acceptance test:

The solvent used was THF and the concentration of the compound was 10 µM.

	R	5%	10%	20%	30%	40%	50%	60%	70%	80%	90%
Visible light											
UV light (366 nm)	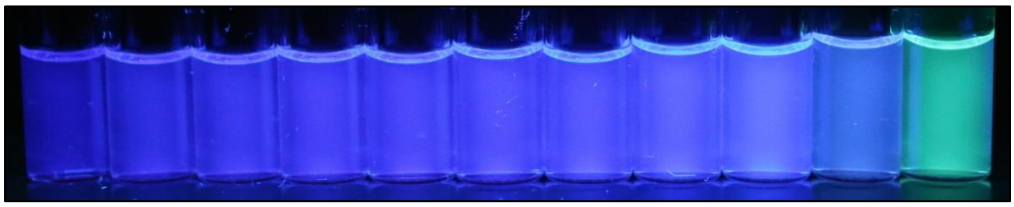										

Figure 490. Water acceptance test of AR94p under visible (up) and UV (down) light.

A slight increase in emission intensity was observed at higher percentages of water (50% - 60%), but at even higher percentages of water the emission intensity was droped noticeably.

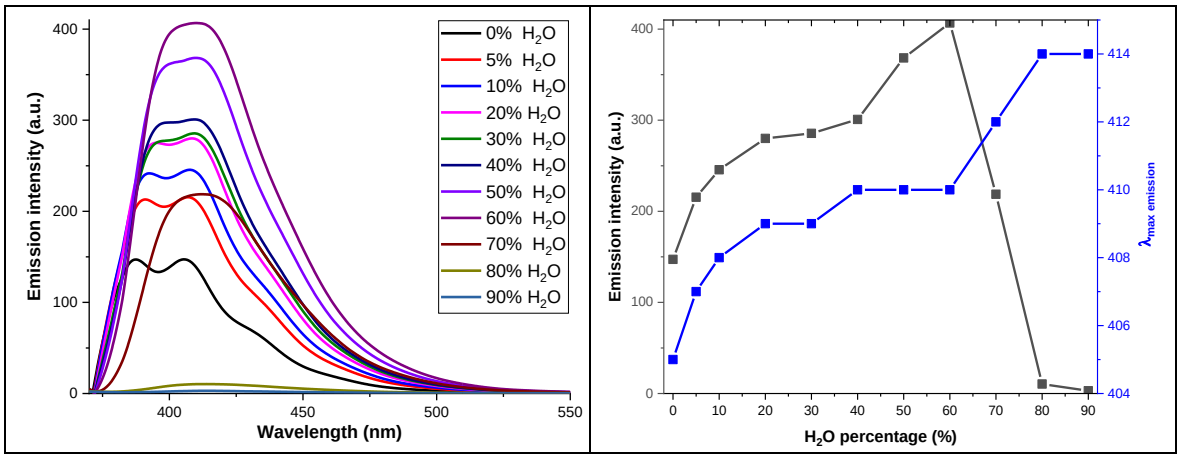

Figure 491. Emission intensity graph (left) and graph of relationship between the emission intensity and the wavelength of the maximum of emission (right) as a function of the amount of water added for AR94p.

pH test:

The pH was studied with a 70% of water and THF as a solvent. The concentration of the compound was 10 µM.

	R	HCl	3.4	4.8	6.4	7.4	7.9	10.5	KOH
Visible light	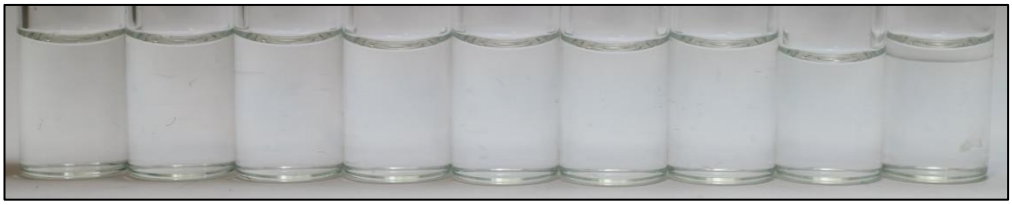								
UV light (366 nm)	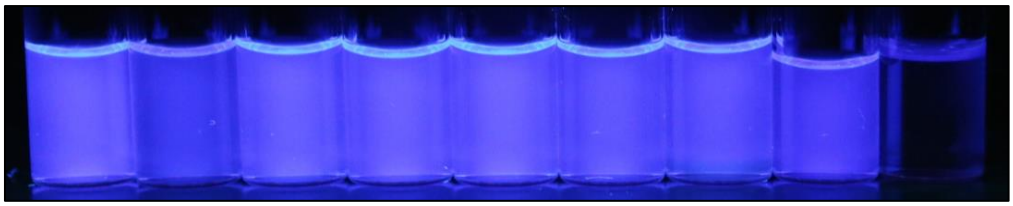								

Figure 492. pH test of AR94p at 70% of water under visible (up) and UV (down) light.

	R	HCl	3.4	4.8	6.4	7.4	7.9	10.5	KOH
Visible light									
UV light (366 nm)	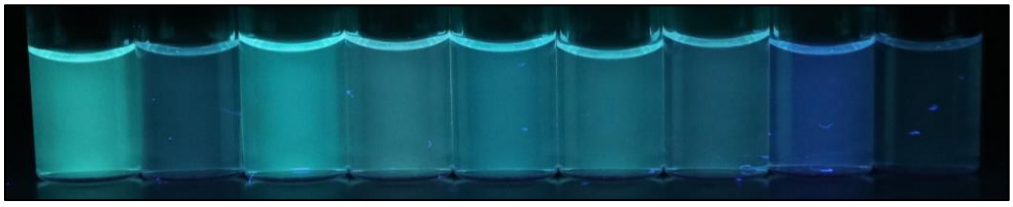								

Figure 493. pH test at 90% of water of AR94p under visible (up) and UV (down) light.

No significant changes were observed with amount of water at 70% but, when studying pH with 90% of water, fluorescence quenching was observed at very acidic and very basic pH and the colour of the fluorescence was changed from green to blue at pH 10.

Cations and anions test:

The concentration of the compound was 10 µM and the solvent used was THF.

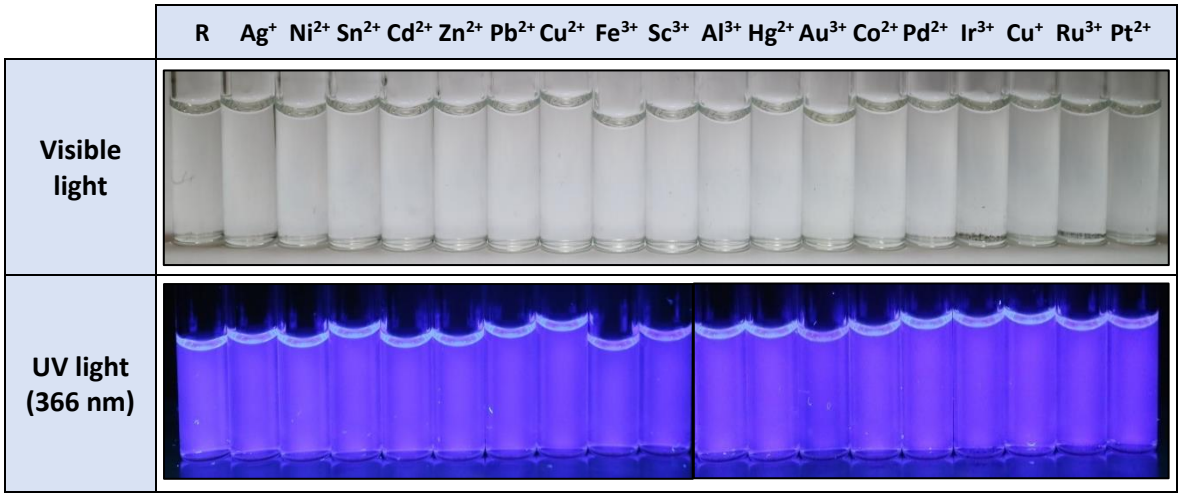

Figure 494. Cations test of AR94p under visible (up) and UV (down) light.

No significant changes were observed.

The concentration of the compound was 10 µM and the solvent used was THF.

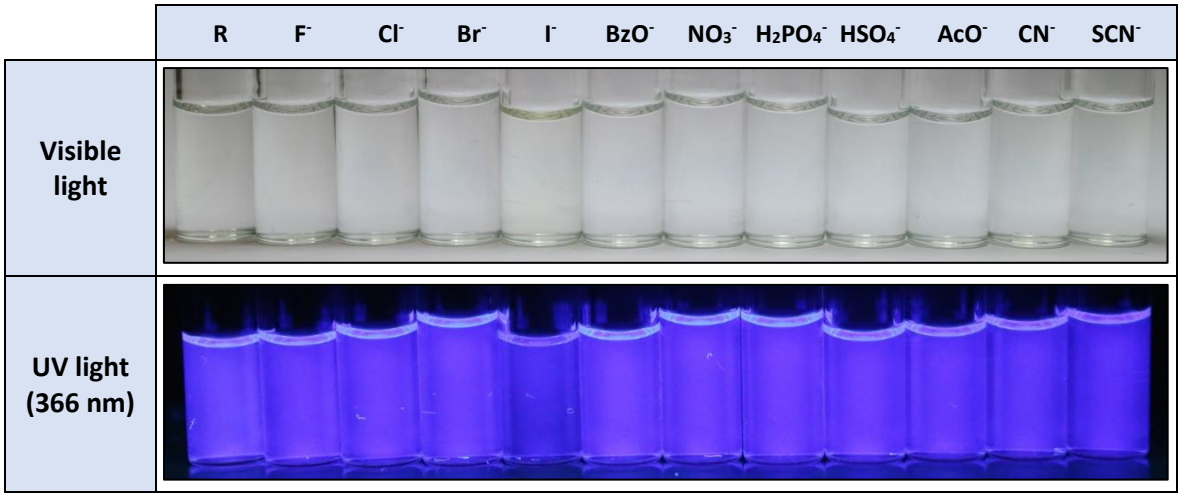

Figure 495. Anions test of AR94p under visible (up) and UV (down) light.

No significant changes were observed.

Oxidant and reductant reagents test:

The solvent used was THF and concentration of the compound was 10 µM.

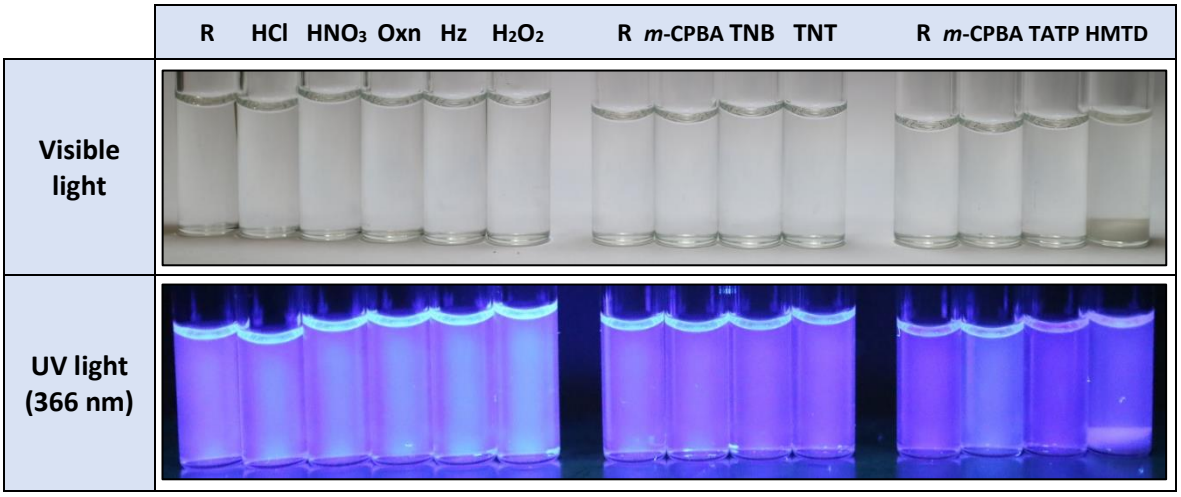

Figure 496. Oxidant and reductant reagents test of AR94p under visible (up) and UV (down) light.

No significan changes were observed.

Synthesis of *N*-(Boc-piperidine)-4-ethynylnaphthalene-1,8-dicarboxylmonoimide (AR94d)

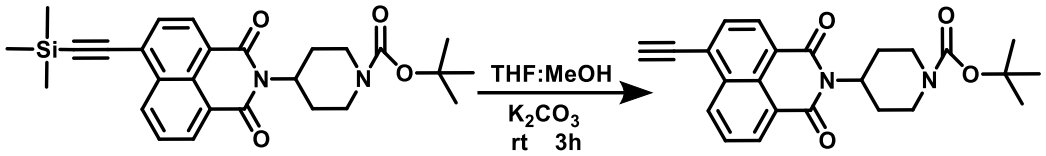

In a 100 ml flask, 27 mg of *N*-(*N'*-Boc-piperidin-4-yl)-4-[(trimethylsilyl)ethynyl]naphthalene-1,8-dicarboxylmonoimide (AR94p, 0.057 mmol) were dissolved in 10 ml of a mixture of THF:MeOH (1:1) and 1 g of potassium carbonate (7.25 mmol) were added. The mixture was stirred 3 hours at room temperature. Afterwards, the solvent was evaporated under reduce pressure and DCM was added to the flask. The solution was washed three times with water (3×100 ml) and the organic extracts was combined, dried over Na_2SO_4 and the solvent was evaporated under reduce pressure. The product is a yellow solid obtained with a 100% of yield (23 mg).

m.p.: 108-111°C (decomposition).

IR (ATR, cm^{-1}): 3238 (≡CH), 2974-2926 (C-H), 2860, 1692 (C=O), 1655, 1590, 1422 (C-O), 1401, 1347, 1244, 1160, 1140 (C-N), 1104, 1032, 999, 945, 900, 862, 783, 751, 693, 648, 538, 454.

^{1}H-NMR (300 MHz, $CDCl_3$) δ (ppm): 8.66-8.59 (m, 2H, 2×$\mathbf{H_{Ar}}$), 8.50 (d, *J* = 7.6 Hz, 1H, $\mathbf{H_{Ar}}$), 7.92 (d, *J* = 7.6 Hz, 1H, $\mathbf{H_{Ar}}$), 7.82 (t, *J* = 7.6 Hz, 1H, $\mathbf{H_{Ar}}$), 5.22-5.13 (m, 1H, C**H**), 4.30 (s, 2H, C$\mathbf{H}_2$), 3.73 (s, 1H, C**H**), 2.89-2.66 (m, 4H, 2×C$\mathbf{H}_2$), 1.67 (s, 2H, C$\mathbf{H}_2$), 1.49 (s, 9H, 3×C$\mathbf{H}_3$).

^{13}C-NMR (75MHz, $CDCl_3$) δ (ppm): 164.3 (**C**=O), 164.1 (**C**=O), 154.8 (**C**=O), 132.2 ($\mathbf{C}_{Ar}$H), 132.0 ($\mathbf{C}_{Ar}$H), 131.8 ($\mathbf{C}_{Ar}$H), 130.3 ($\mathbf{C}_{Ar}$H), 128.1 ($\mathbf{C}_{Ar}$), 127.9 ($\mathbf{C}_{Ar}$H), 126.2 ($\mathbf{C}_{Ar}$), 123.4 ($\mathbf{C}_{Ar}$), 123.3 ($\mathbf{C}_{Ar}$), 86.7 (**C**≡CH), 80.4 (C≡**C**H), 79.7 (**Cq**), 52.1 (**C**H), 44.1 (**C**H_2), 28.7 (**C**H_3) 28.4 (**C**H_2).

HRMS (Q-TOF, ESI+) m/z: calculated for $C_{24}H_{24}NaN_2O_4$: 427.1628 (M^++ Na^+); found 427.1633.

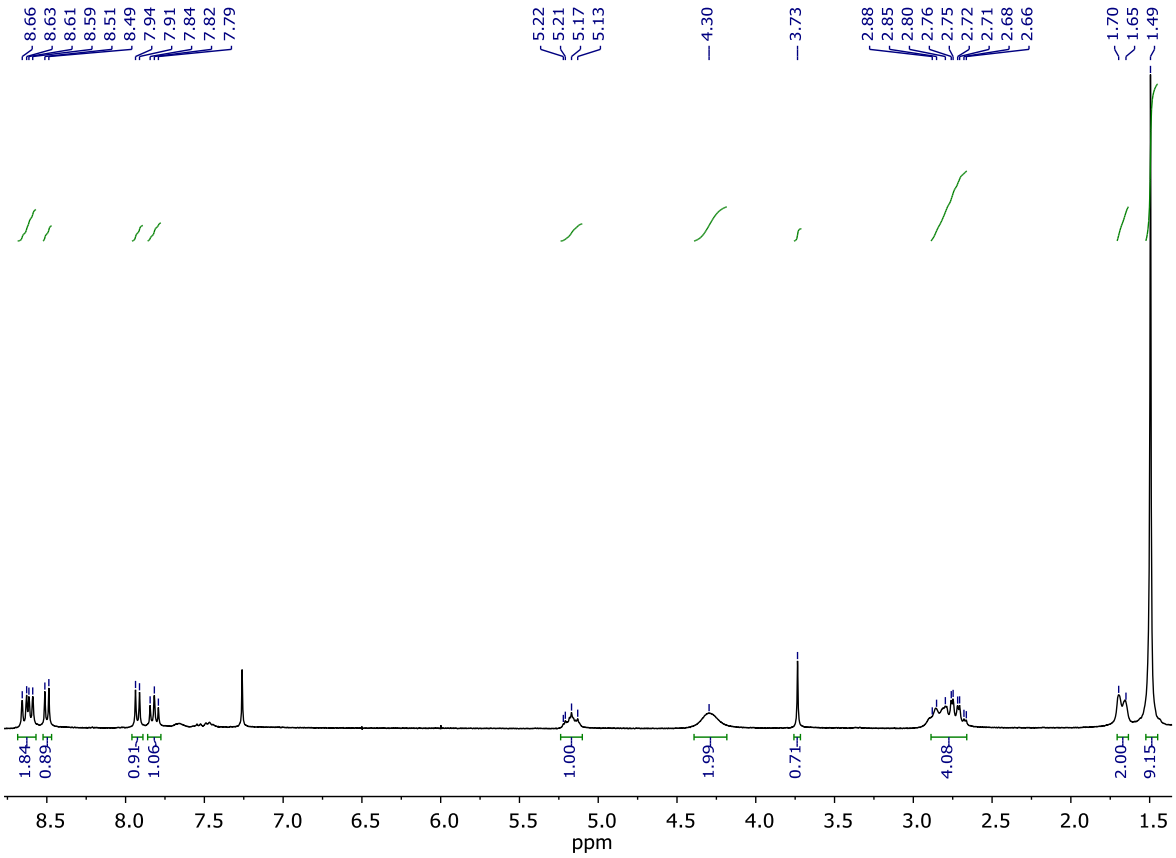

Figure 497. ^{1}H-NMR ($CDCl_3$, 300 MHz) of AR94d.

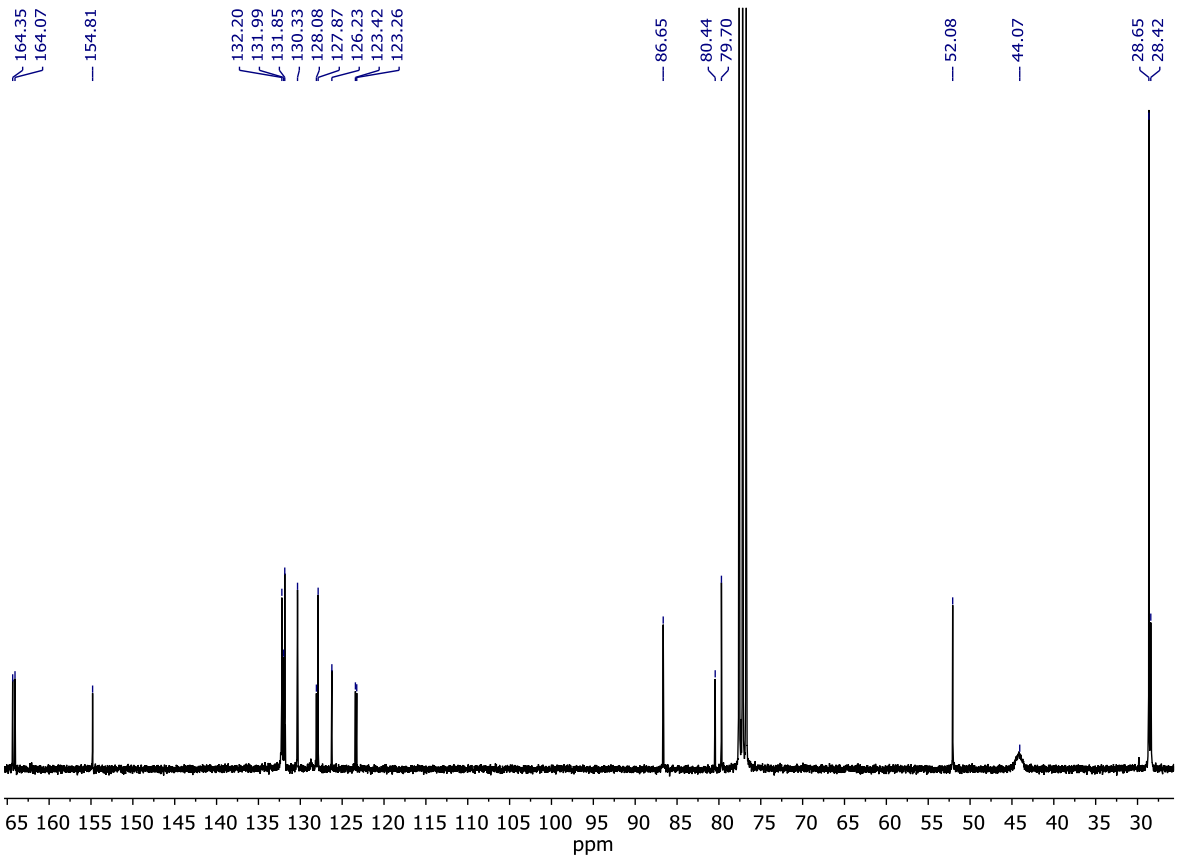

Figure 498. ^{13}C-NMR ($CDCl_3$, 75 MHz) of AR94d.

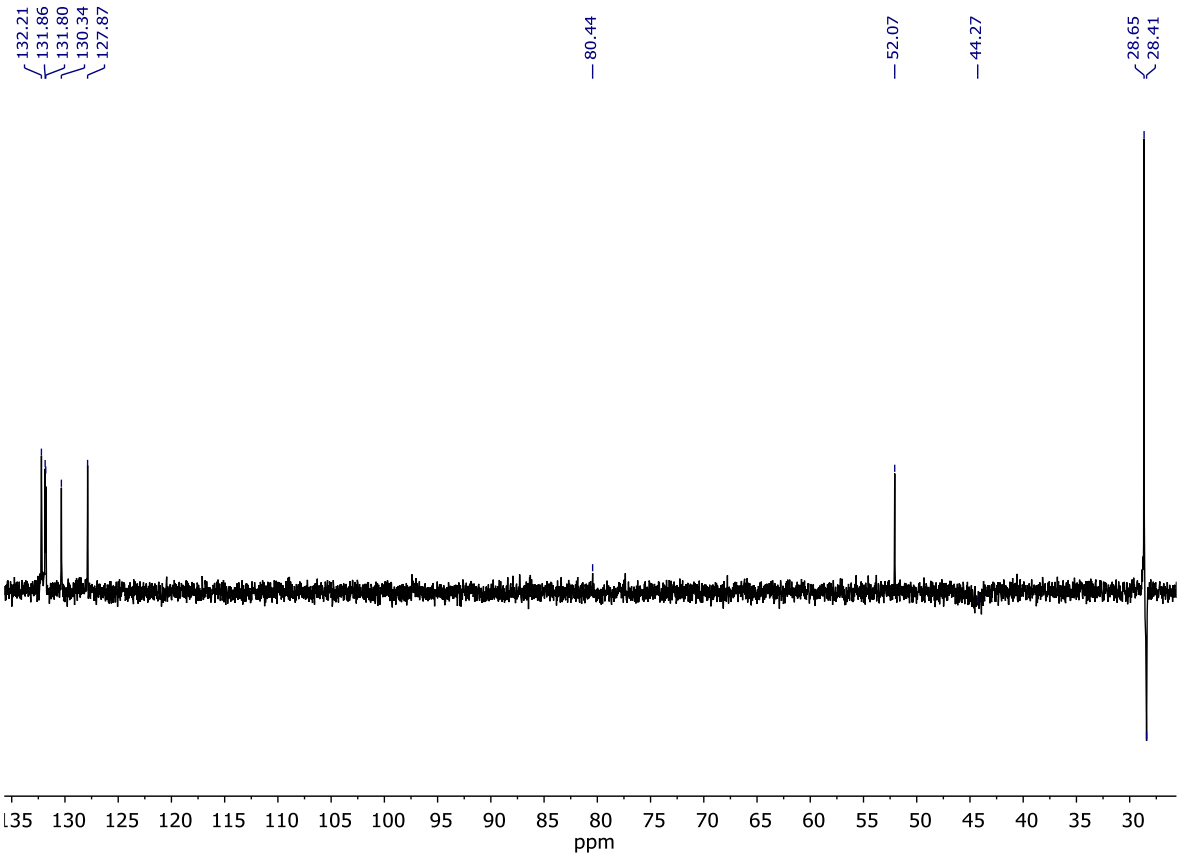

Figure 499. DEPT NMR ($CDCl_3$, 75 MHz) of AR94d.

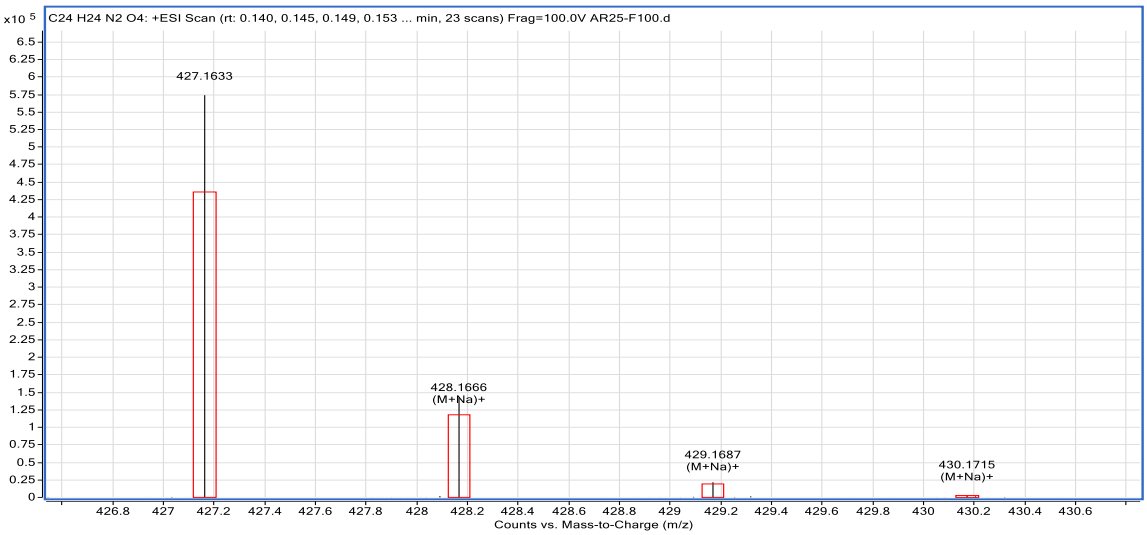

Meas. m/z	m/z	Err [ppm]	Ion Formula
427.1633	427.1628	1.09	$C_{24}H_{24}NaN_2O_4$

Figure 500. HRMS (Q-TOF, ESI+) of AR94d.

Synthesis of 2,2',7,7'-tetra(trimethylsilyl)ethynyl-9,9'-spirobi[9H-fluorene] (AR08p)

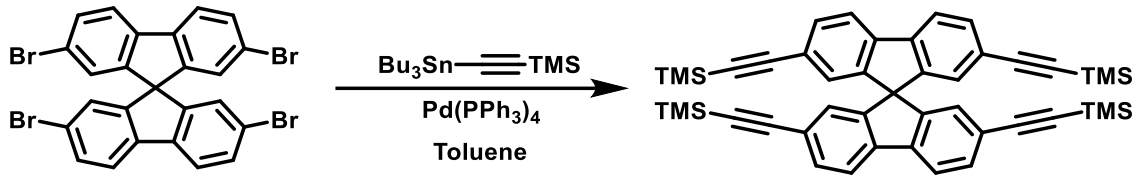

500 mg of 2,2',7,7'-tetrabromo-9,9'-spirobi[9H-fluorene] (0.79 mmol), 1.29 g of 1-tributylstannyl-2-tri methylsilylacetylene (3.3 mmol) and 9 mg of $Pd(PPh_3)_4$ (7.9 µmol) were dissolved in 10 ml of dry toluene and the resulting mixture were stirred at 110°C for 72 hours under nitrogen atmosphere. After that time, the reaction mixture was quenched and extracted with DCM. The organic layer was washed with brine (3×100 ml) and dried over anhydrous Na_2SO_4. After removal of solvent, the residue yellow oil was further purified by column chromatography (SiO_2, DCM:Hex 1:8) to afford the product (51 mg, 95% yield) as a yellow solid.

m.p.: 160-162°C.

^{1}H-NMR (300 MHz, $CDCl_3$) δ (ppm): 7.74 (dd, *J* = 8.0, 0.7 Hz, 4H, 4×$\mathbf{H_{Ar}}$), 7.49 (dd, *J* = 8.0, 1.4 Hz, 4H, 4×$\mathbf{H_{Ar}}$), 6.77 (dd, *J* = 1.4, 0.7 Hz, 4H, 4×$\mathbf{H_{Ar}}$), 0.16 (d, *J* = 1.2 Hz, 36H, 12×C$\mathbf{H}_3$).

^{13}C-NMR (75MHz, $CDCl_3$) δ (ppm): [148.7, 148.2, 142.2, 141.1, 132.1, 128.5, 128.1, 127.8, 124.3, 122.4, 120.5, 120.0] ($\mathbf{C}_{Ar}$ + $\mathbf{C}_{Ar}$H), 105.4 (**C**≡C-Si), 94.6 (C≡**C**-Si), 0.05 (**C**H_3).

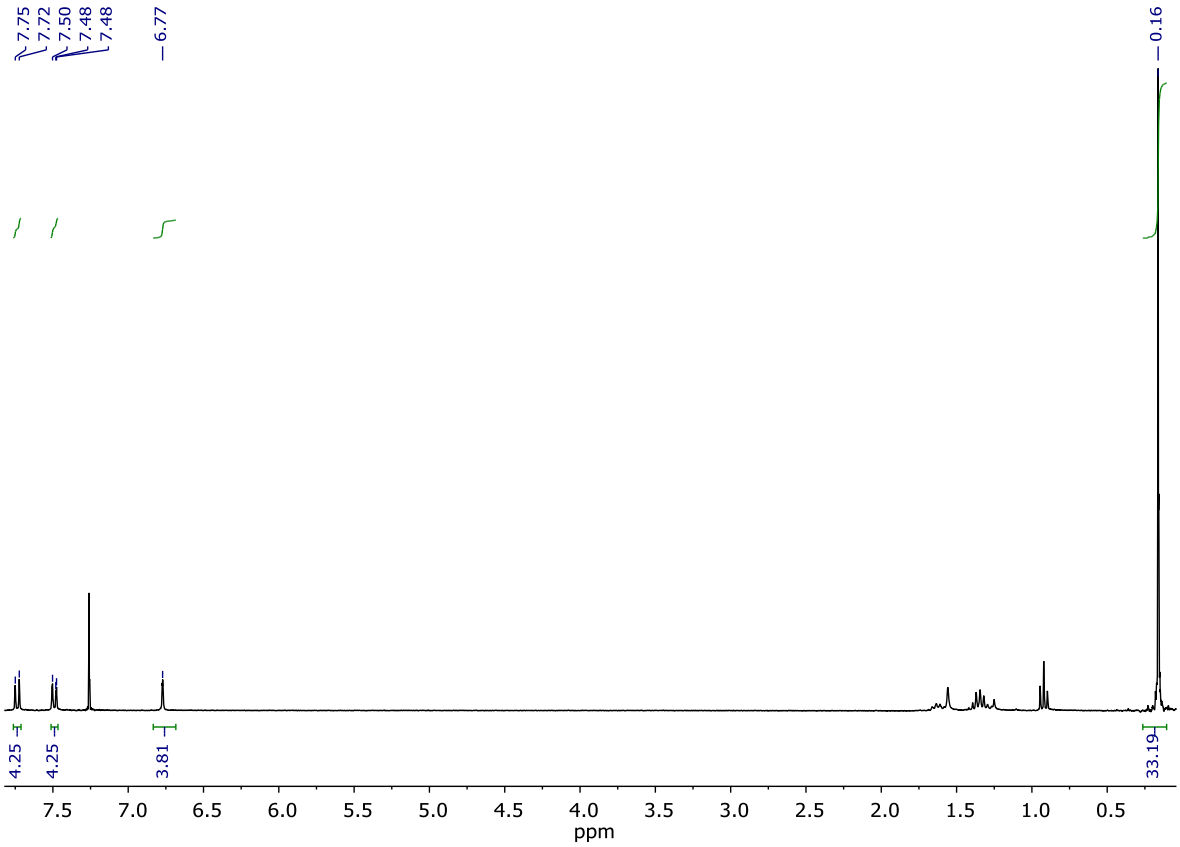

Figure 501. ^{1}H-NMR ($CDCl_3$, 300 MHz) of AR08p.

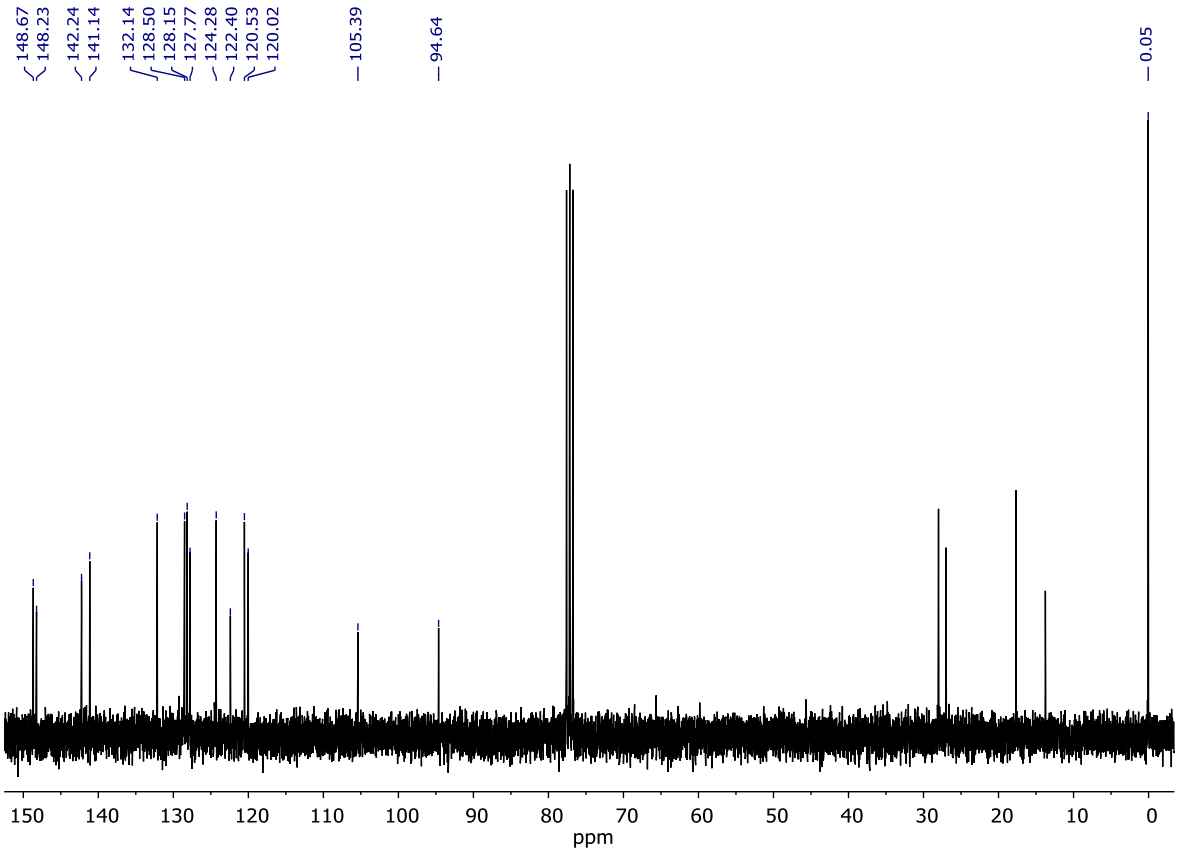

Figure 502. ^{13}C-NMR ($CDCl_3$, 75 MHz) of AR08p.

Synthesis of 2,2',7,7'-tetraethynyl-9,9'-spirobi[9H-fluorene] (AR08d)

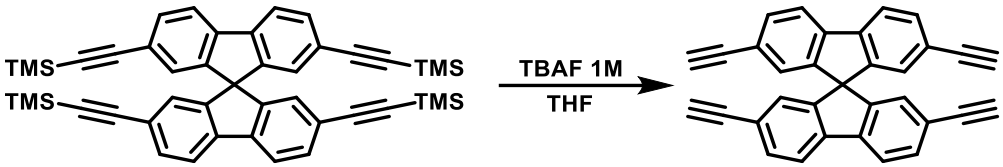

A solution of tetrabutylammonium fluoride in THF (1M, 9.60 ml, 260 µmol) was added to a solution of 124 mg of 2,2',7,7'-(trimethylsilyl)ethynyl-9,9'-spirobi[9H-fluorene] (AR08p, 0.26 mmol) in 5 ml of THF. The resulting reaction mixture was stirred for 30 minutes at room temperature. After the addition of 20 ml of water to quench the reactionthe aqueous layer was extracted with DCM (3×50 ml). The organic layers were combined, dried over anhydrous Na_2SO_4, filtered and concentrated under reduced pressure. Subsequent the product was purified with a column chromatography (SiO_2, DCM:Hex) to obtain the desired product (105 mg, 99% yield) as a white solid.

m.p.: 317-320°C (decomposition).

^{1}H-NMR (300 MHz, $CDCl_3$) δ (ppm): 7.79 (d, *J* = 7.9 Hz, 4H, 4×$\mathbf{H_{Ar}}$), 7.54 (dd, *J* = 7.9, 1.5 Hz, 5H, 5×$\mathbf{H_{Ar}}$), 6.85 (s, 4H, 4×$\mathbf{H_{Ar}}$), 3.01 (s, 4H, 4×C≡C**H**).

^{13}C-NMR (75MHz, $CDCl_3$) δ (ppm): 147.8 ($\mathbf{C}_{Ar}$), 141.4 ($\mathbf{C}_{Ar}$), 132.4 ($\mathbf{C}_{Ar}$H), 127.8 ($\mathbf{C}_{Ar}$H), 121.9 ($\mathbf{C}_{Ar}$), 120.5 ($\mathbf{C}_{Ar}$H), 83.5 (**C**≡CH), 78.1 (**C**≡**C**H), 53.5 (**Cq**).

HRMS (MALDI, DCTB+) m/z: calculated for $C_{33}H_{16}$: 412.1247 (M^+); found 412.1249.

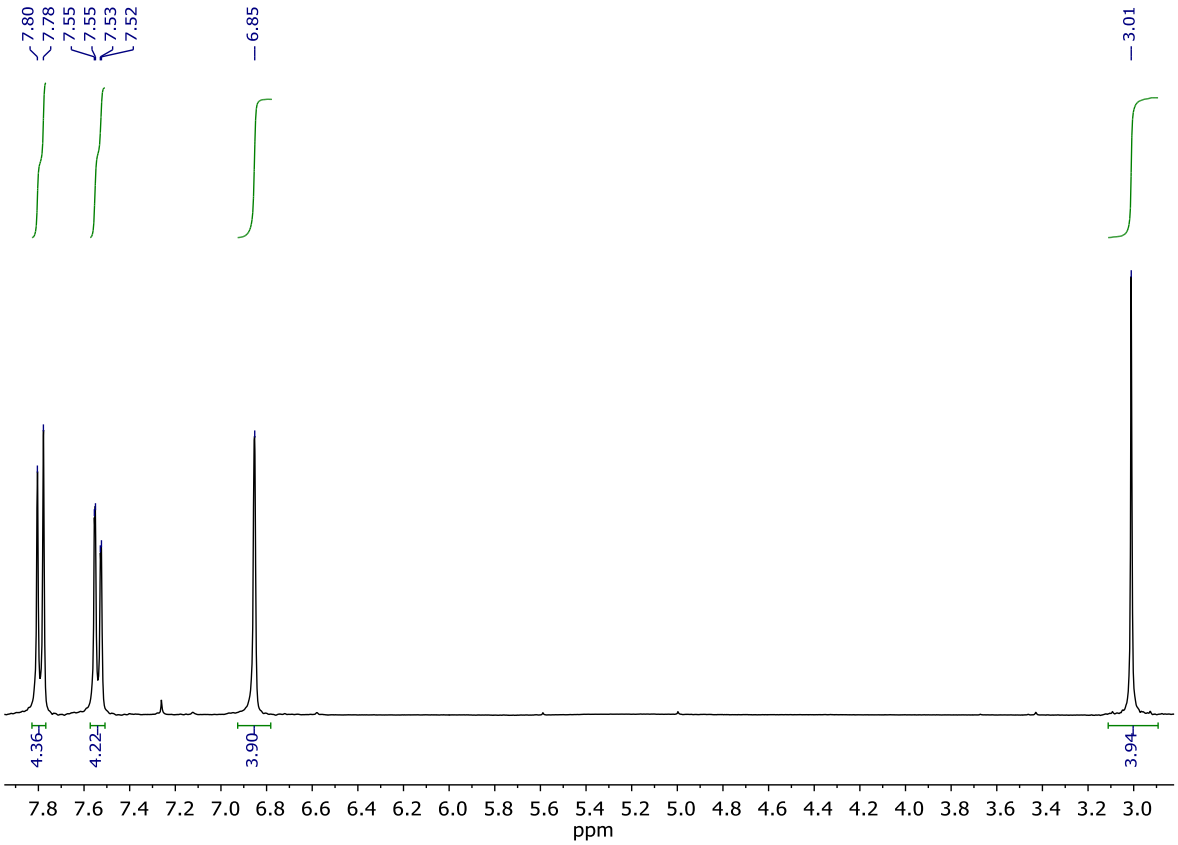

Figure 503. ^{1}H-NMR ($CDCl_3$, 300 MHz) of AR08d.

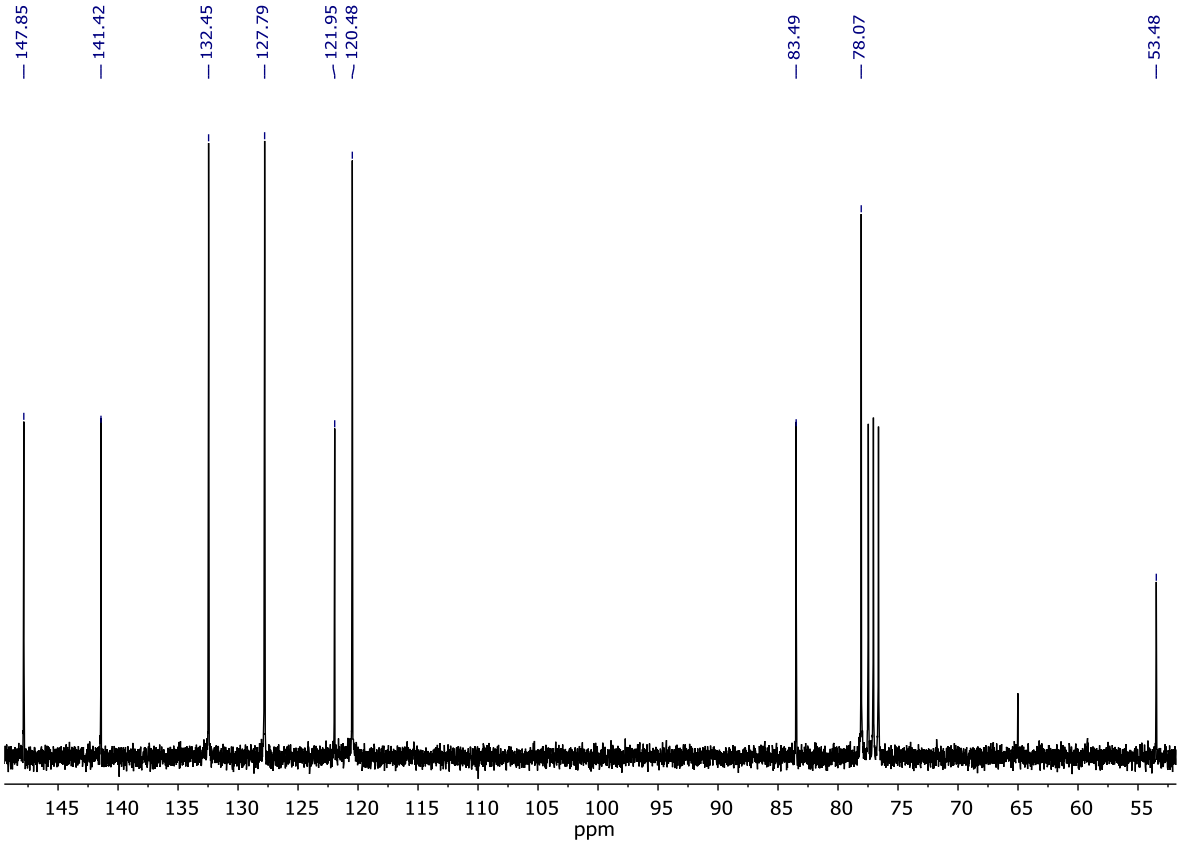

Figure 504. ^{13}C-NMR ($CDCl_3$, 75 MHz) of AR08d.

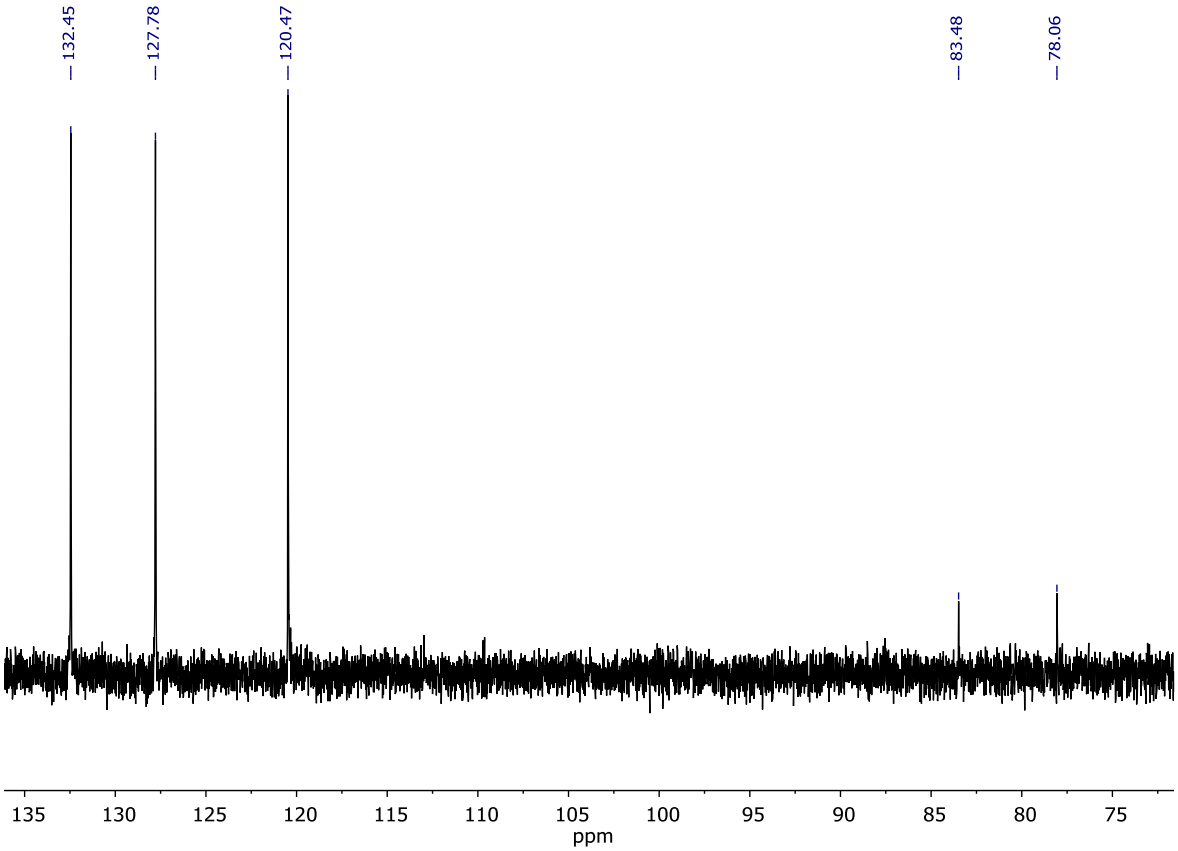

Figure 505. DEPT NMR ($CDCl_3$, 75 MHz) of AR08d.

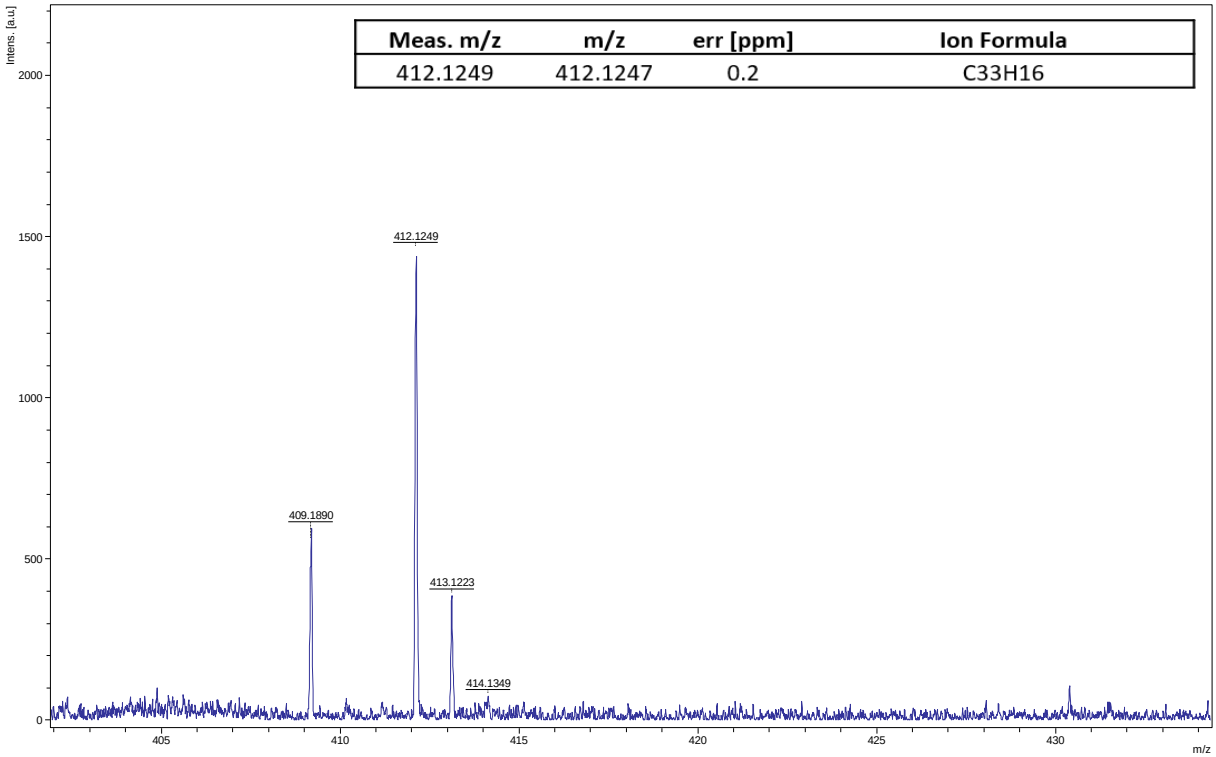

Meas. m/z	m/z	err [ppm]	Ion Formula
412.1249	412.1247	0.2	C33H16

Figure 506. HRMS (MALDI, DCTB+) of AR08d.

Synthesis of 2,2',7,7'-tetra(tributylstannyl)ethynyl-9,9'-spirobi[9H-fluorene] (AR09)

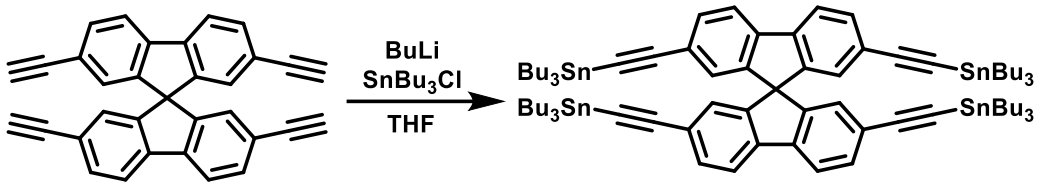

45 mg of 2,2',7,7'-tetraethynyl-9,9'-spirobi[9H-fluorene] (AR08d, 0.72 mmol) was dissolved in anhydrous THF and the mixture was cooled to -78°C to obtain a red solution. Next, BuLi (180 µl, 1.6 M hexanes, 0.29 mmol) were added drop by drop to give rise a purple dissolution and let it react for 30 minutes more. $SnBu_3Cl$ (78 µL, 0.29 mmol) were then added, lightening the color of the react mixture to red and it was stirred overnight. Afterwards, it was quenched with a dissolution of NH_4Cl, extracted 3 times with DCM (3×50 ml) and the organic layer was dried over anhydrous Na_2SO_4. Upon removal of the solvents in vacuo, getting the product in 99% yield (128 mg) without further purifications and, in these conditions, it was used for the following reaction.

^{1}H-NMR (300 MHz, $CDCl_3$) δ (ppm): 7.65-7.59 (m, 4H, 4×$\mathbf{H_{Ar}}$), 7.38 (m, 4H, 4×$\mathbf{H_{Ar}}$), 6.70 (s, 4H, 4×$\mathbf{H_{Ar}}$), 1.39 (s, 36H, 12×C$\mathbf{H}_3$), 0.82-0.79 (m, 72H, 36×C$\mathbf{H}_2$).

^{13}C-NMR (75MHz, $CDCl_3$) δ (ppm): [148.6, 148.2, 141.4, 141.2, 131.9, 128.1, 127.9, 127.6, 124.1, 123.2, 120.2, 119.7, 110.2, 93.7] ($\mathbf{C}_{Ar}$ + $\mathbf{C}_{Ar}$H), 65.6 (**Cq**), [29.3, 28.9, 27.9, 27.4, 27.0, 26.9] (**C**H_2), 13.6 (**C**H_3), 11.1 (**C**H_2), 8.8 (**C**H_2).

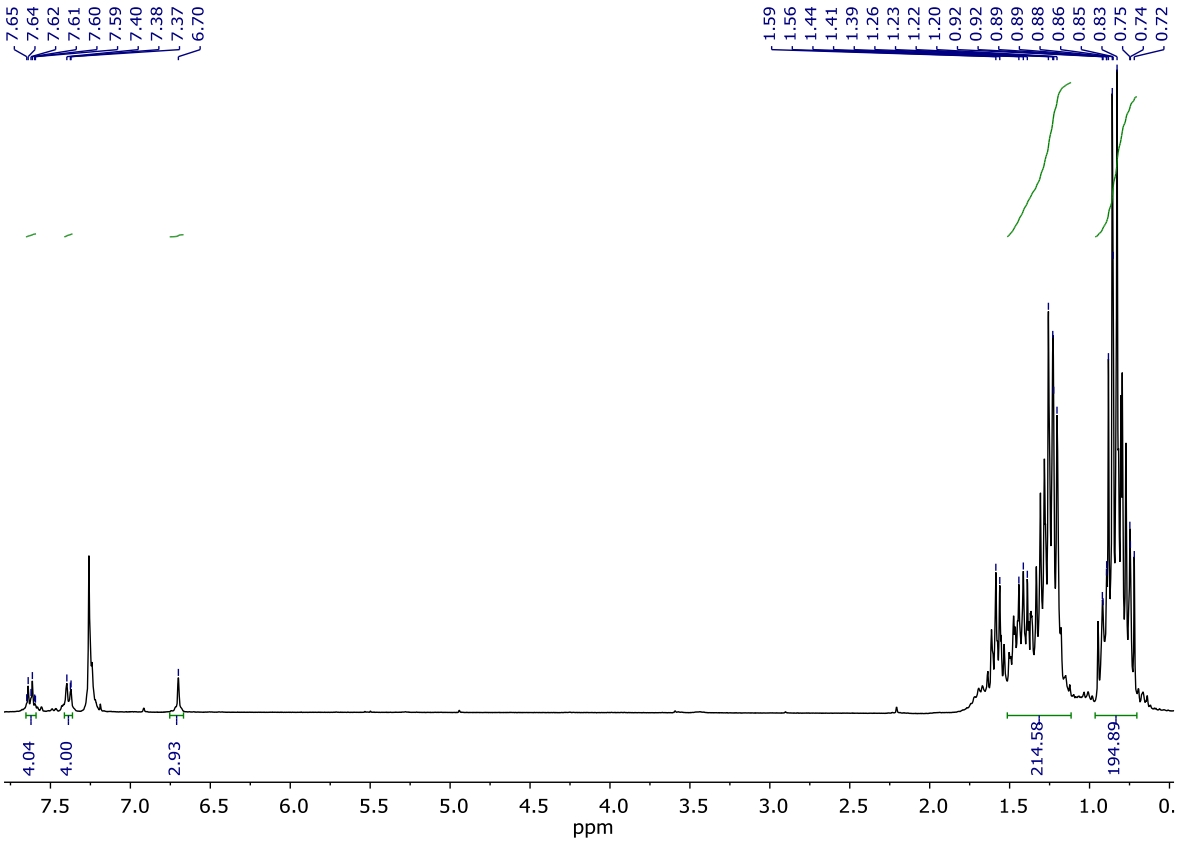

Figure 507. ^{1}H-NMR ($CDCl_3$, 300 MHz) of AR09.

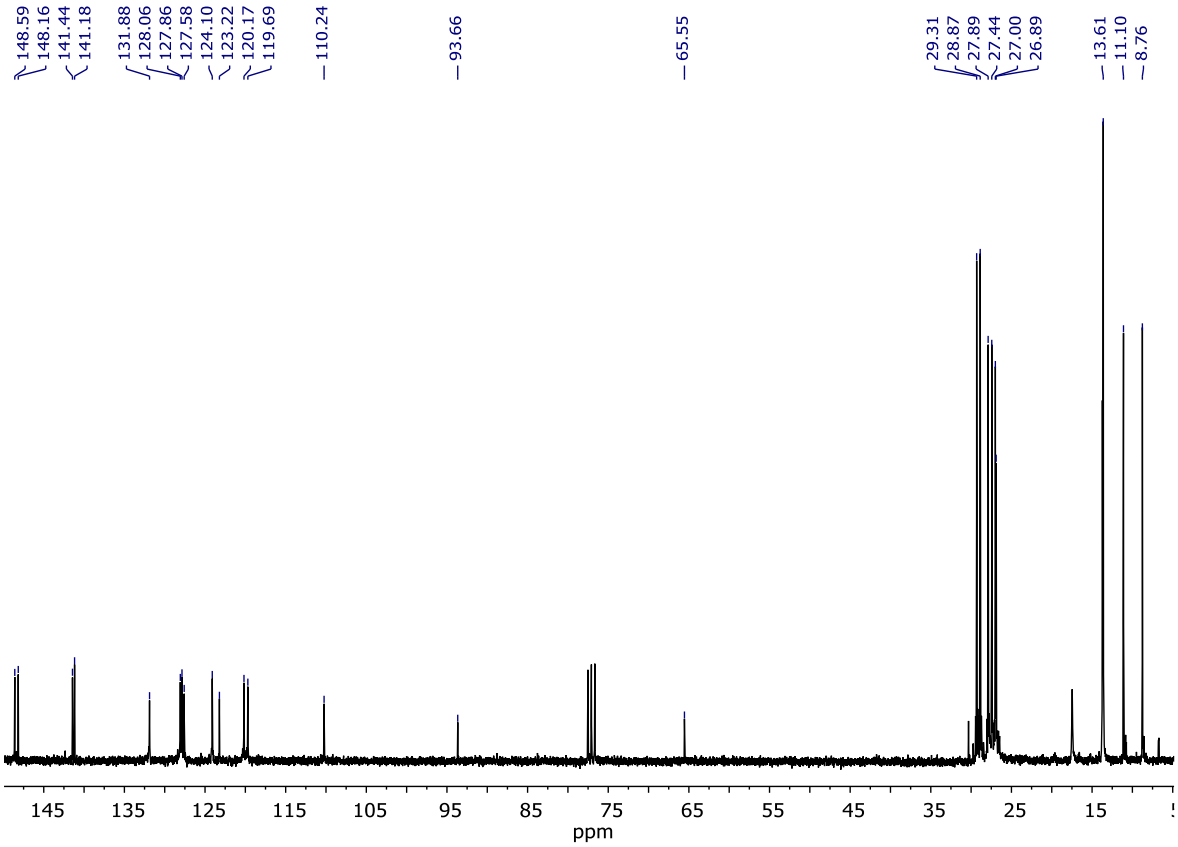

Figure 508. ^{13}C-NMR ($CDCl_3$, 75 MHz) of AR09.

Synthesis of 2,2',7,7'-tetra[*N*-(*N*-Boc-piperidin-4-yl)-4-(ethynyl)naphthalene-1,8-dicarboxyl-monoimide]-9,9'-spirobi[9H-fluorene] (AR80)

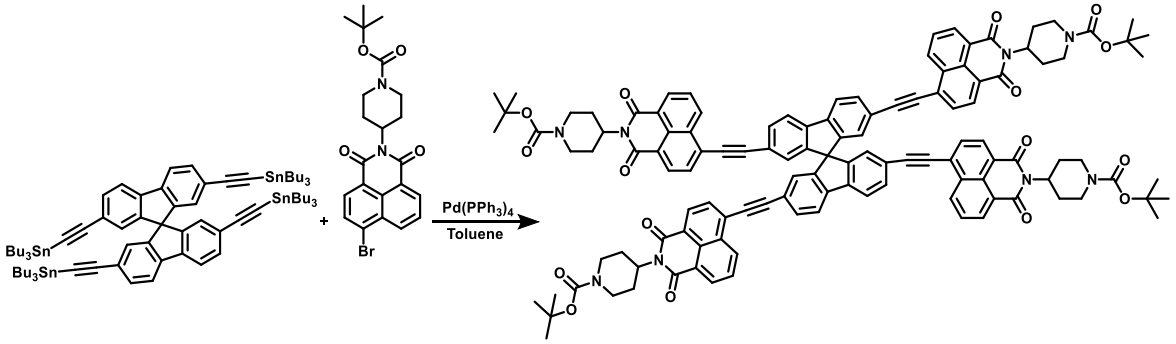

223 mg of *N*-(*N*-Boc-piperidin-4-yl)-4-bromonaphthalene-1,8-dicarboxylmonoimide (AR43p, 0.12 mmol), 190 mg of 2,2',7,7'-tetra(tributylstannyl)ethynyl-9,9'-spirobi[9H-fluorene] (AR09, 0.10 mmol) and a catalytic amount of $Pd(PPh_3)_4$ were dissolved in 3 ml of dry toluene and the resulting dark red solution was stirred at 110°C under nitrogen atmosphere. After stirring for 3 days, the reaction mixture was quenched with 50 ml of water and extracted three times with DCM (3×100 ml). The organic layer was washed with brine and dried over anhydrous Na_2SO_4. After removal of solvent, the residue was further purified by column chromatography (SiO_2, DCM) to obtain 134 mg of dark yellow solid, 57% yield.

m.p.: 238-240°C.

IR (ATR, cm^{-1}): 2973-2857 (C-H), 1689 (C=O), 1656 (C=O), 1582, 1504, 1420 (C-O), 1402, 1342, 1246, 1159 (C-N), 1142, 1103, 1031, 980, 893, 858, 777, 747, 693, 540, 457, 417.

^{1}H-NMR (300 MHz, $CDCl_3$) δ (ppm): 8.60-8.42 (m, 7H, 7×**H$_{Ar}$**), 8.32 (m, 2H, 2×**H$_{Ar}$**), 7.96 (m, 2H, 2×**H$_{Ar}$**), 7.79 (m, 4H, 4×**H$_{Ar}$**), 7.65 (m, 2H, 2×**H$_{Ar}$**), 7.46 (m, 7H, 7×**H$_{Ar}$**), 7.19 (m, 3H, 3×**H$_{Ar}$**), 7.12 (m, 5H, 5×**H$_{Ar}$**), 5.14 (m, 4H, 4×C**H**), 4.28 (s, 8H, 4×C**H**$_2$), 2.90-2.64 (m, 16H, 8×C**H**$_2$), 1.66 (m, 8H, 4×C**H**$_2$), 1.48 (s, 36H, 12×C**H**$_3$).

^{13}C-NMR (75MHz, $CDCl_3$) δ (ppm): 163.9 (**C**=O), 154.7 (**C**=O), 134.6 (**C**$_{Ar}$), 134.4 (**C**$_{Ar}$H), 134.3 (**C**$_{Ar}$H), 134.2 (**C**$_{Ar}$H), 133.1 (**C**$_{Ar}$H), 132.2 (**C**$_{Ar}$H), 132.1 (**C**$_{Ar}$H), 131.3 (**C**$_{Ar}$H), 131.1 (**C**$_{Ar}$H), 130.4 (**C**$_{Ar}$), 130.3 (**C**$_{Ar}$), 130.2 (**C**$_{Ar}$H), 130.1 (**C**$_{Ar}$), 128.6 (**C**$_{Ar}$H), 128.5 (**C**$_{Ar}$H), 128.1 (**C**$_{Ar}$H), 127.9 (**C**$_{Ar}$H), 127.8 (**C**$_{Ar}$H), 127.6 (**C**$_{Ar}$H), 123.4 (**C**$_{Ar}$), 122.5 (**C**$_{Ar}$), 79.6 (**Cq**), 52.0 (**C**H), 44.1 (**C**H$_2$), 28.6 (**C**H$_3$), 28.3 (**C**H$_2$).

HRMS (MALDI, DCTB-) m/z: calculated for $C_{121}H_{104}N_8O_{16}$: 1924.7565 (M^-); found 1924.7573.

UV-Vis ($CHCl_3$), λ_{max} nm (log ε): 355 (4.6).

Ø (Toluene, %): 20.19.

τ (280 nm, Toluene, ns): 1,296 (χ^2: 1.213).

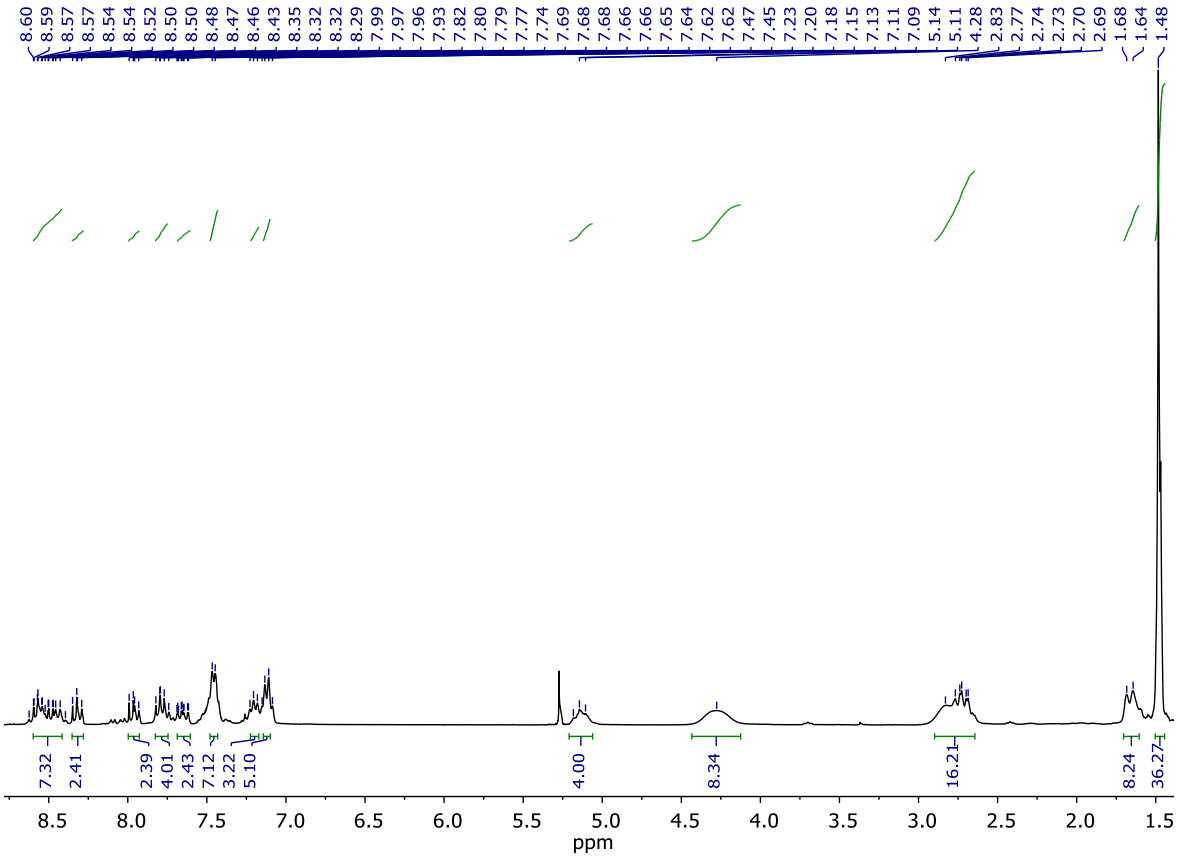

Figure 509. ^{1}H-NMR ($CDCl_3$, 300 MHz) of AR80.

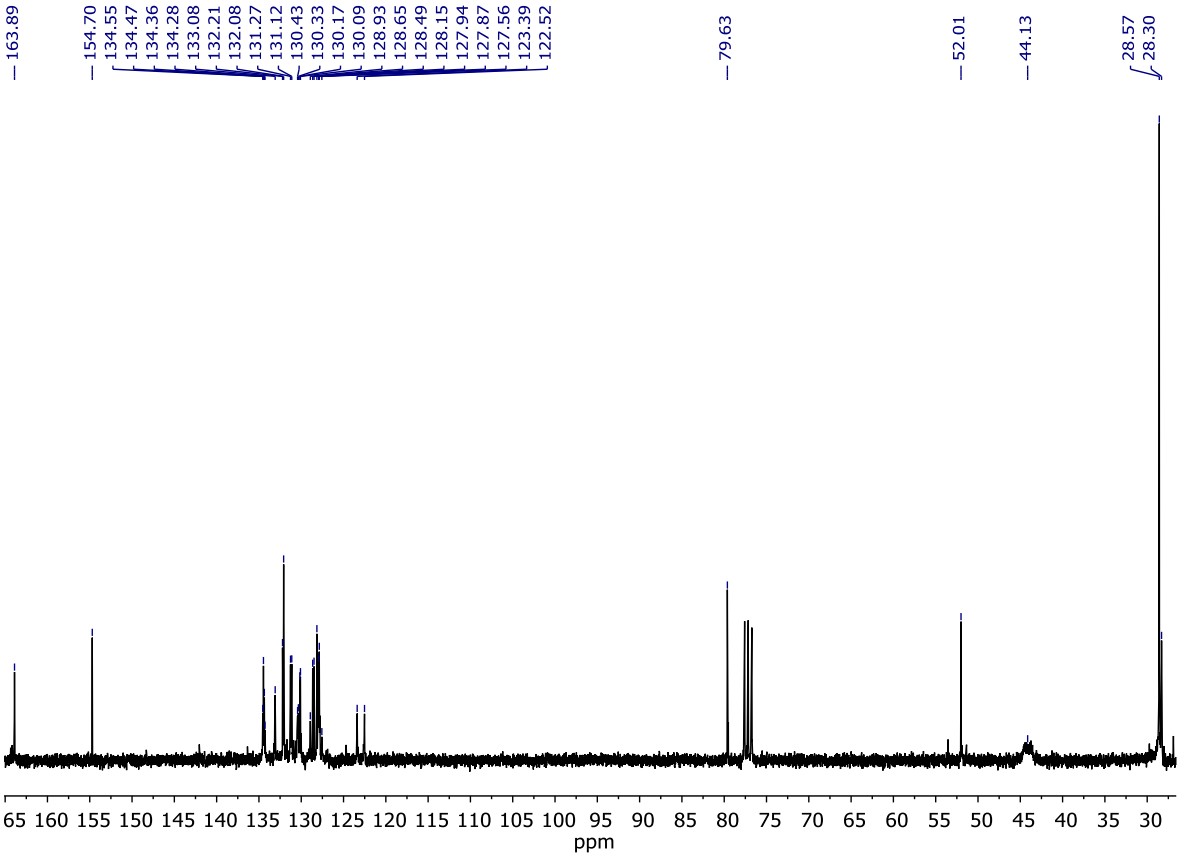

Figure 510. ^{13}C-NMR ($CDCl_3$, 75 MHz) of AR80.

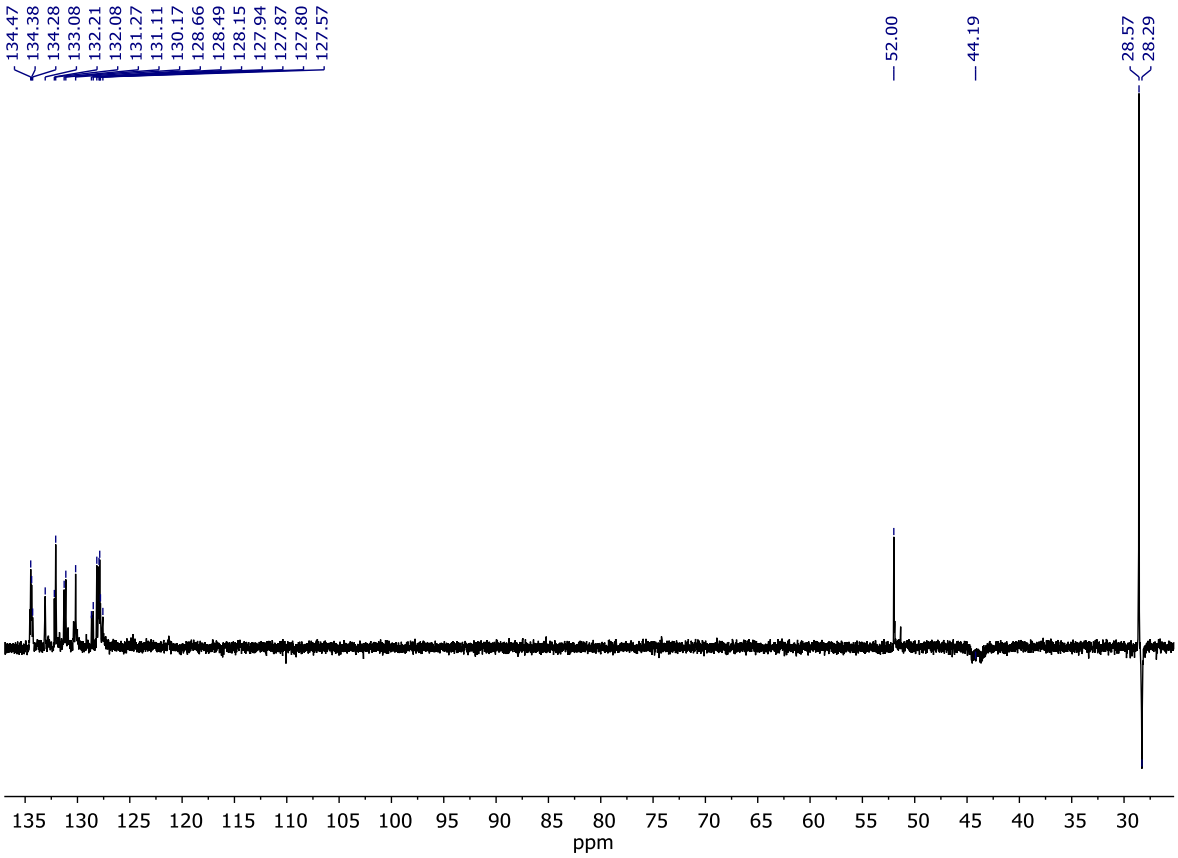

Figure 511. DEPT NMR ($CDCl_3$, 75 MHz) of AR80.

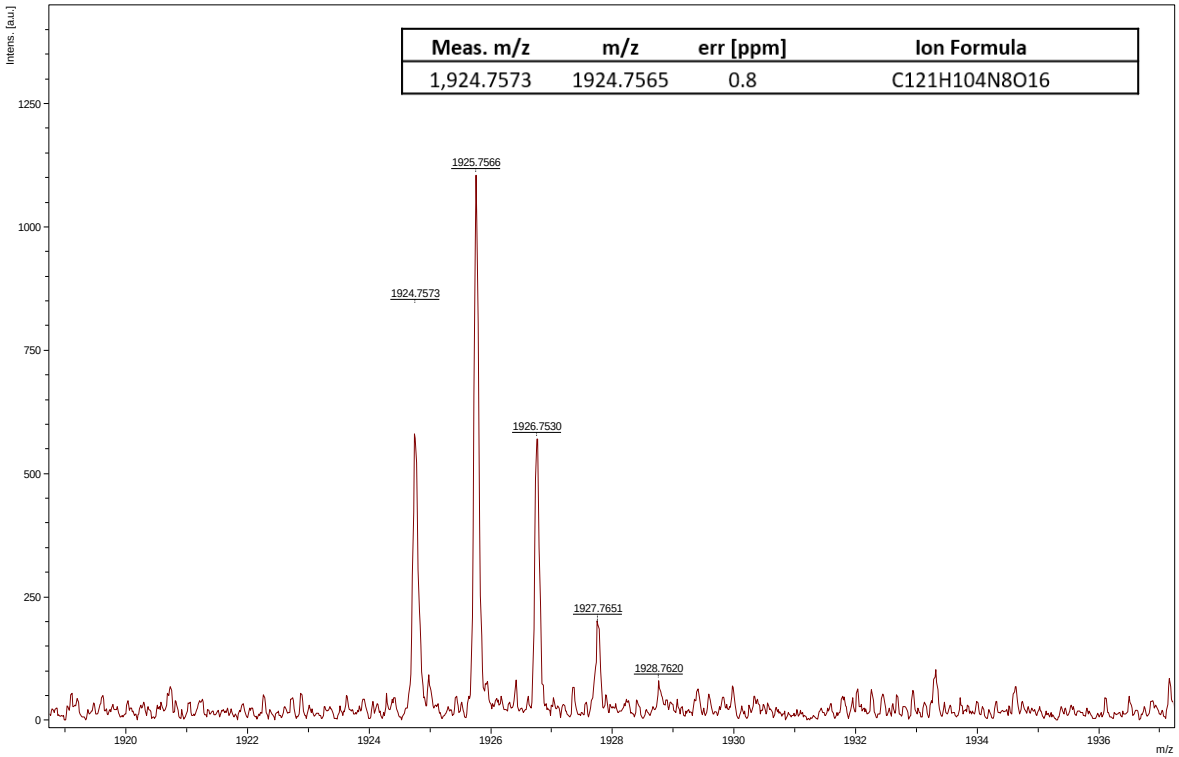

Meas. m/z	m/z	err [ppm]	Ion Formula
1,924.7573	1924.7565	0.8	C121H104N8O16

Figure 512. HRMS (MALDI, DCTB-) of AR80.

Solvatochromism:

The concentration of the compound was 20 µM and the excitation wavelength was 470 nm.

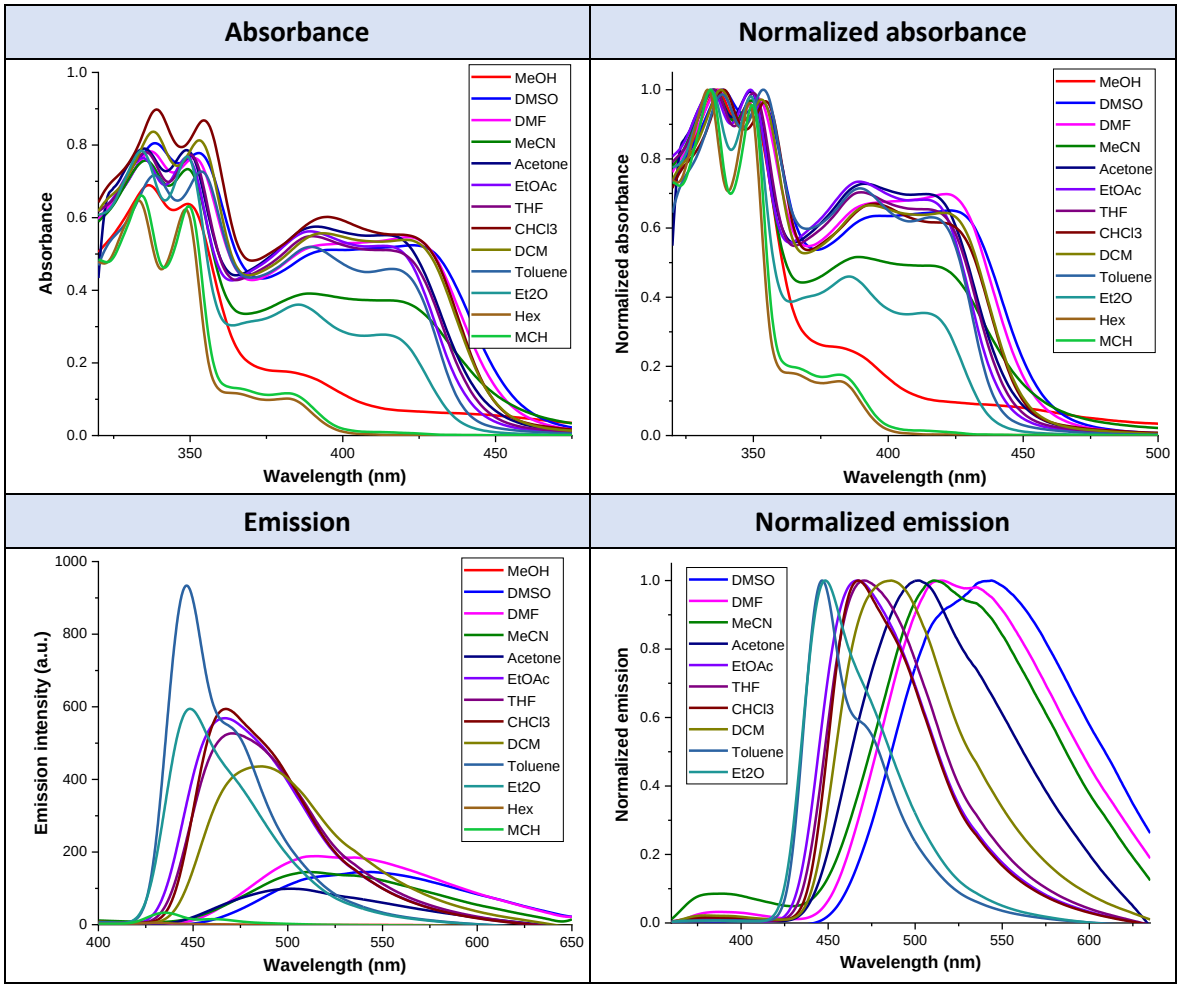

Figure 513. Solvatochromism of AR80.

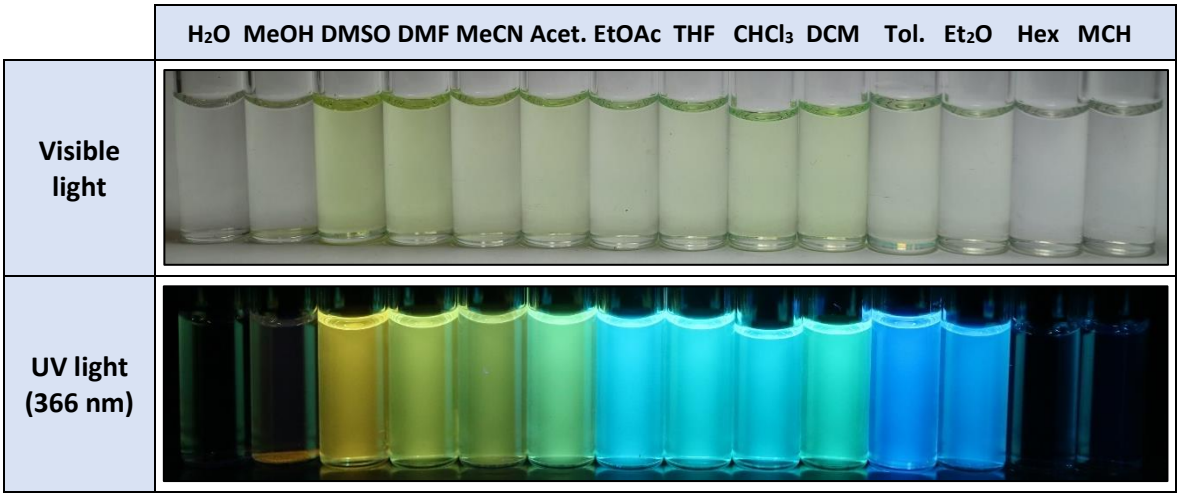

Figure 514. Solvatochromism of AR80 under visible and 366 nm light.

Fluorescence decay lifetime (τ):

The solvent used was toluene. The concentration of the compound was 20 µM.

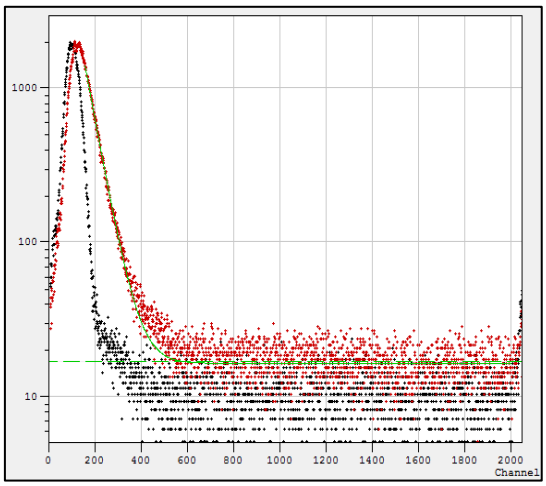

Figure 515. Fluorescence decay lifetime of AR80.

Water acceptance test:

The solvent used was THF and the concentration of the compound was 20 µM.

	R	5%	10%	20%	30%	40%	50%	60%	70%	80%	90%
Visible light											
UV light (366 nm)	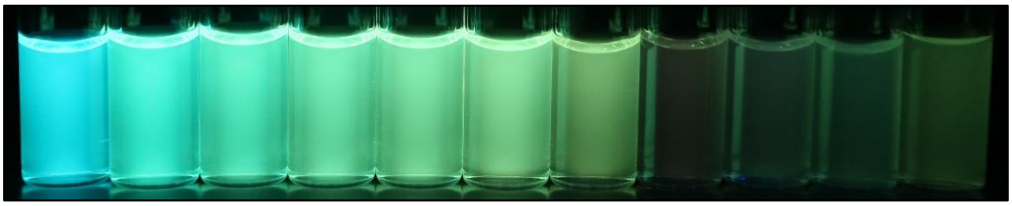										

Figure 516. Water acceptance test of AR80 under visible (up) and UV (down) light.

There was an AQC from 50% of water.

pH test:

The amount of water that the compound could accept was 50%. The concentration of the compound was 20 µM and the solvent used was THF.

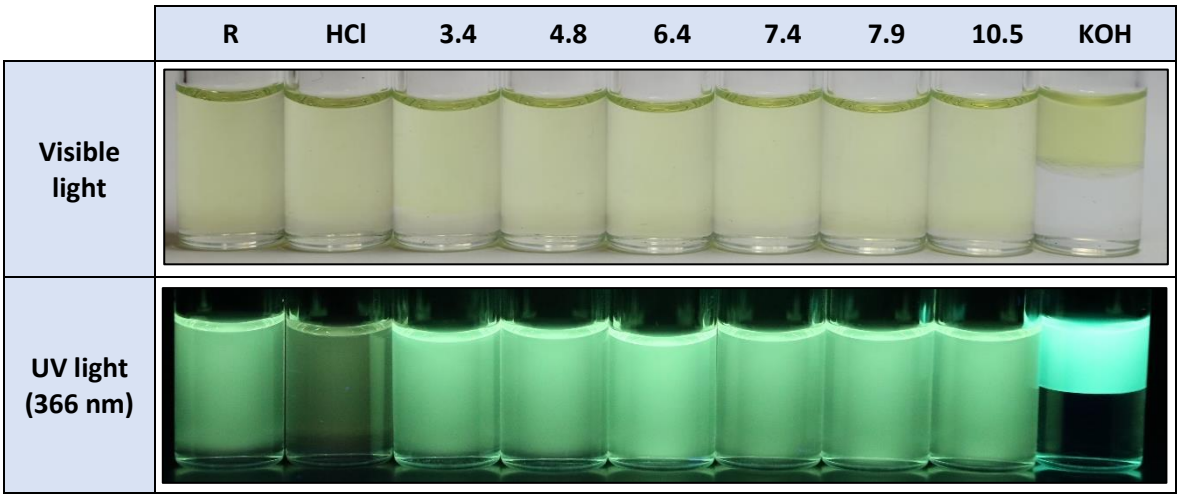

Figure 517. pH test of AR80 under visible (up) and UV (down) light.

The most significant change was the increase of the fluorescent emission at acidic environment.

Cations and anions test:

The concentration of the compound was 20 µM and the solvent used was THF.

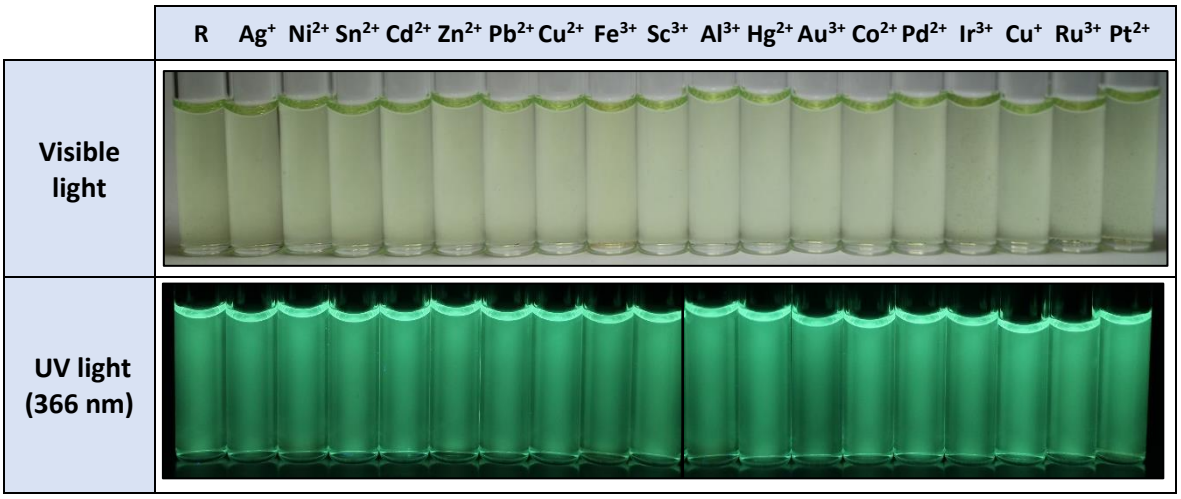

Figure 518. Cations test of AR80 under visible (up) and UV (down) light.

No significant changes were observed.

The concentration of the compound was 20 µM and the solvent used was THF.

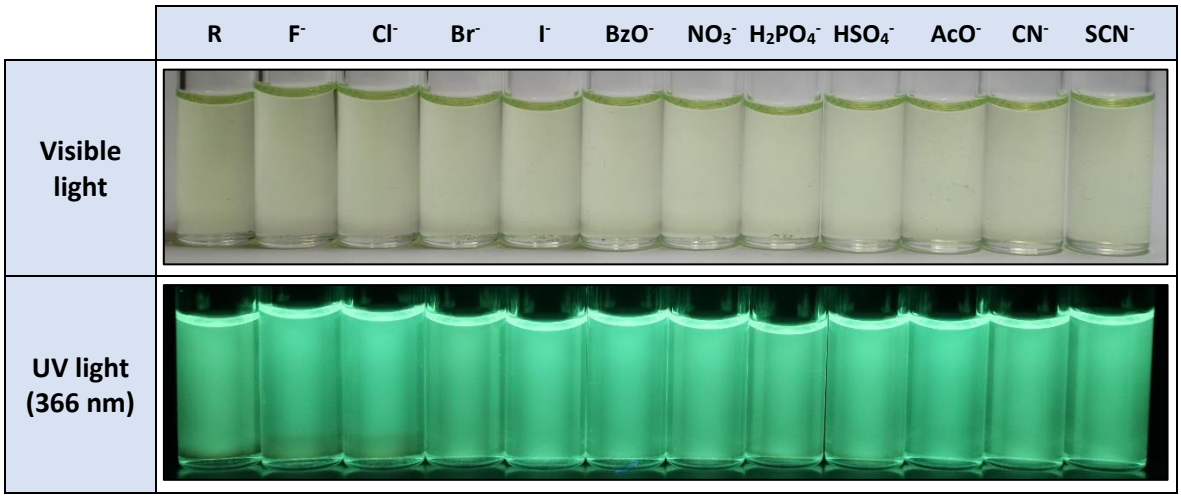

Figure 519. Anions test of AR80 under visible (up) and UV (down) light.

No significant changes were observed.

Oxidant and reductant reagents test:

The solvent used was THF and concentration of the compound was 20 µM.

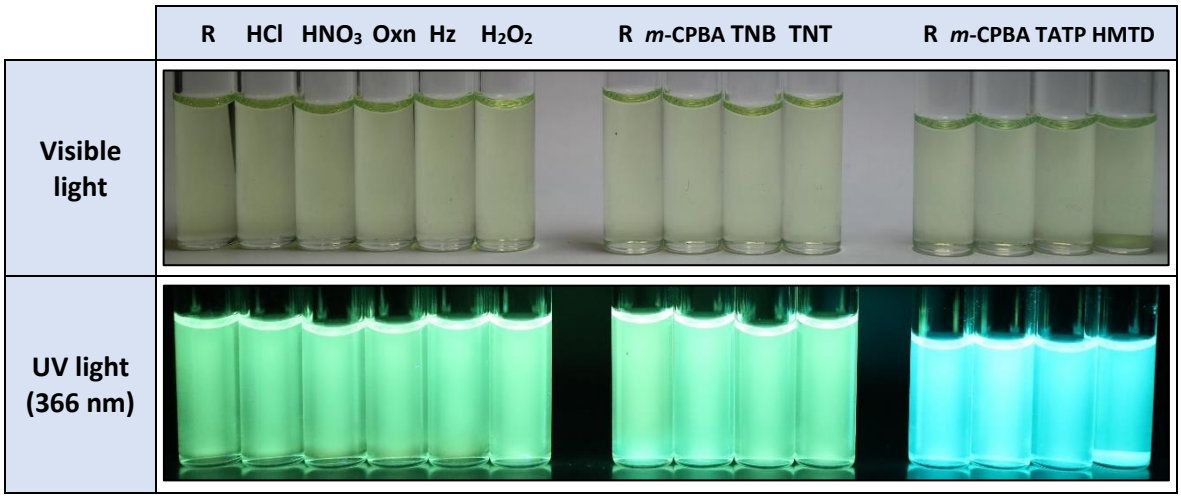

Figure 520. Oxidant and reductant reagents test of AR80 under visible (up) and UV (down) light.

No significant changes were observed.

ANNEX III:
PMI
DERIVATIVES

INDEX OF ANNEX III COMPOUNDS

Synthesis of **AR02** 547
Synthesis of **AR01** 550
Synthesis of **AR05** 553
Synthesis of **AR19** 560
Synthesis of **AR48** and **AR49** 567
Synthesis of **AR95** 583
Synthesis of **AR34** and **AR35** 595
Synthesis of **AR22p** 613
Synthesis of **AR22d** 620
Synthesis of **AR20** 623
Synthesis of **AR30** 631
Synthesis of **AR31** 632
Synthesis of **AR96** 635
Synthesis of **AR39** 644
Synthesis of **AR40** 647

Synthesis of *N*-(1-(1-adamantyl)ethyl)-9-bromoperylene-3,4-dicarboxylmonoimide (AR02)

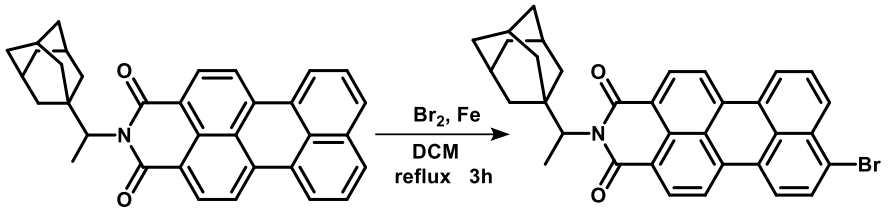

0.55 ml of a solution of Br_2 (10 mmol) in 10 ml of dichlorormethane were added dropwise to a mixture of 500 mg of *N*-(1-(1-adamantyl)ethyl)perylene-3,4-dicarboxylmonoimide (1.04 mmol) and 2.3 mg of Fe powder (0.04 mmol) in dichloromethane (150 ml) and the resulting solution was refluxed for three hours. Afterwards, the organic phase was washed three times (3×100 ml) with a saturated solution of sodium sulfite (Na_2SO_3) in water. The combined organic extracts were washed with 20 ml of water, dried over Na_2SO_4 and the solvent was evaporated under reduced pressure, getting 483 mg of a red solid, 95% yield.

m.p.: 338-339°C.

IR (ATR, cm^{-1}): 3090 – 3072, 2905, 2847, 1692 (C=O), 1658 (C=O), 1594, 1565, 1454, 1410, 1374, 1347, 1313, 1288, 1247, 1204, 1179 (C-N), 1114, 1099, 1058, 1036, 1017 (C-Br), 910, 841, 822, 803, 754, 684.

^{1}H-NMR (300 MHz, $CDCl_3$) δ (ppm): 8.62-8.50 (m, 2H, 2×**H_{Ar}**), 8.37 (ddd, *J* = 27.5, 16.8, 8.0 Hz, 4H, 4×**H_{Ar}**), 8.19 (d, *J* = 8.2 Hz, 1H, **H_{Ar}**), 7.88 (d, *J* = 8.2 Hz, 1H, **H_{Ar}**), 7.70 (t, *J* = 8.0 Hz, 1H, **H_{Ar}**), 5.10 (q, *J* = 7.3 Hz, 1H, C**H**), 1.98 (s, 3H, 3×C**H**), 1.85-1.62 (m, 15H, 6×C**H_2** + C**H_3**).

^{13}C-NMR (100 MHz, $CDCl_3$) δ (ppm): 165.6 (**C**=O), 164.9 (**C**=O), 136.3 (**C_{Ar}**), 133.2 (**C_{Ar}**), 132.2 (**C_{Ar}**H), 132.1 (**C_{Ar}**H), 131.5 (**C_{Ar}**H), 131.4 (**C_{Ar}**H), 130.0 (**C_{Ar}**), 130.0 (**C_{Ar}**), 129.9 (**C_{Ar}**), 129.5 (**C_{Ar}**H), 128.3 (**C_{Ar}**H), 126.4 (**C_{Ar}**), 124.3 (**C_{Ar}**), 123.7 (**C_{Ar}**), 123.7 (**C_{Ar}**H), 120.9 (**C_{Ar}**H), 120.6 (**C_{Ar}**H), 58.3 (**C**H), 40.5 (**C**H_2), 38.2 (**C_q**), 37.2 (**C**H_2), 29.0 (**C**H_2), 13.3 (**C**H_3).

HRMS (MALDI, DCTB+) m/z: calculated for $C_{34}H_{28}BrNO_2$: 561.1298 (M^+); found 561.1287.

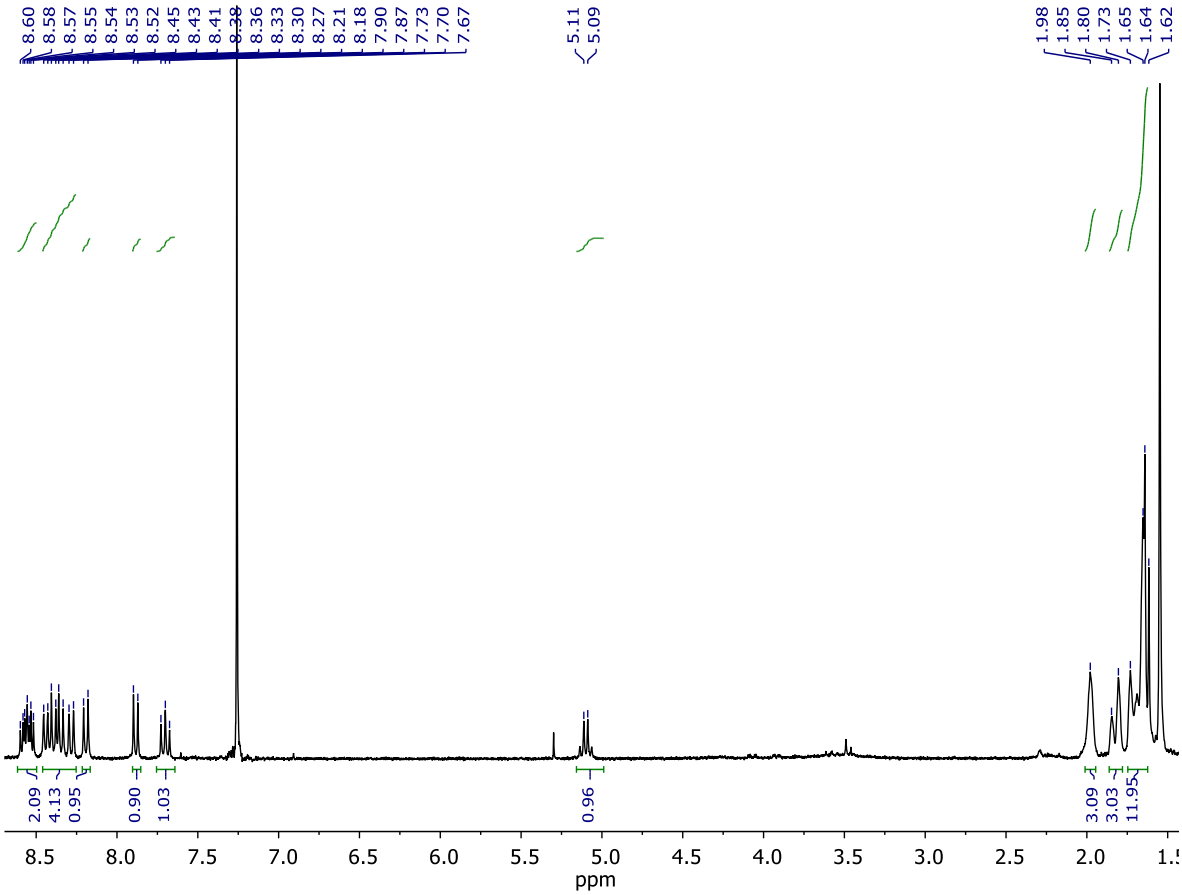

Figure 1. ^{1}H-NMR ($CDCl_3$, 300 MHz) of AR02.

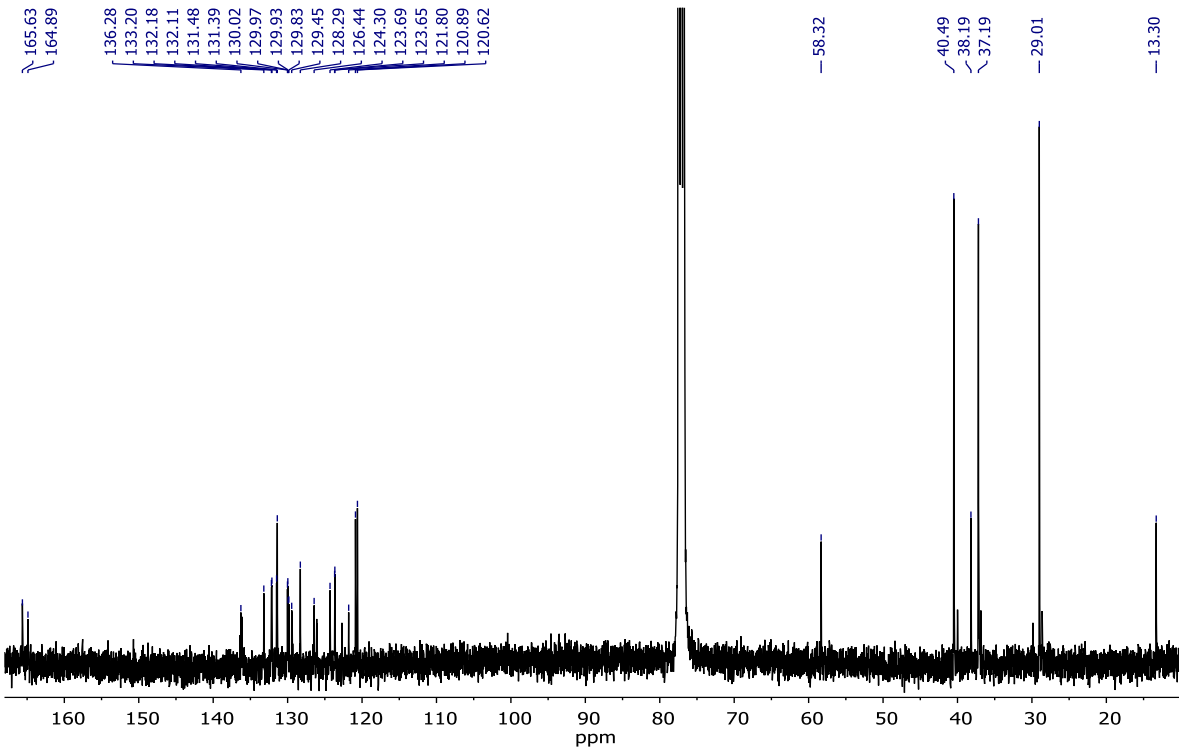

Figure 2. ^{13}C-NMR ($CDCl_3$, 75 MHz) of AR02.

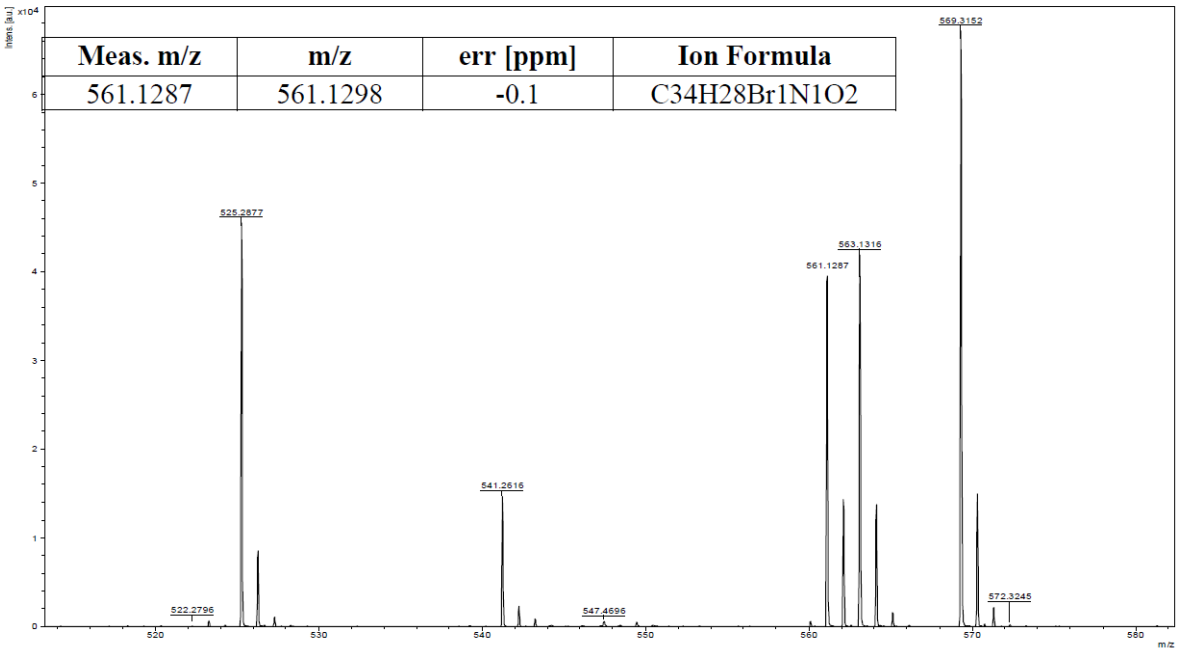

Meas. m/z	m/z	err [ppm]	Ion Formula
561.1287	561.1298	-0.1	C34H28Br1N1O2

Figure 3. HRMS (MALDI, DCTB+) of AR02.

Synthesis of *N*-(1-(1-adamantyl)ethyl)-9-(pinacolylboronate)perylene-3,4-dicarboxylmonoimide (AR01)

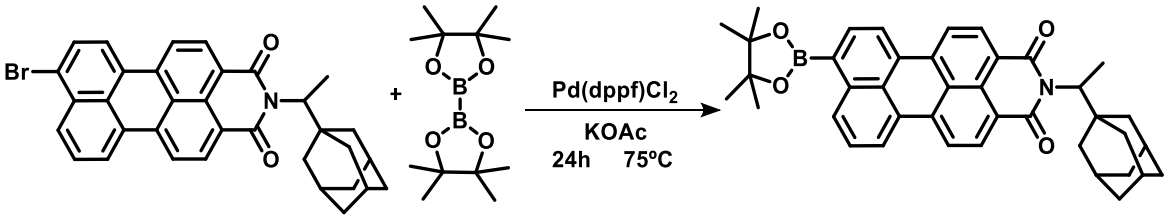

In a 100 ml Schlenk with a magnetic stirrer, 250 mg of *N*-(1-(1-adamantyl)ethyl)-9-bromoperylene-3,4-dicarboxylmonoimide (AR02, 0.52 mmol), 131 mg of potassium acetate (1.34 mmol) and 170 mg of bis(pinacolyl)boronate (0.55 mmol) were dissolved in 15 ml of dry 1,4-dioxane under nitrogen atmosphere. Then, 18 mg of Pd(dppf)Cl_2 (0.005 mmol), the catalyst, were added and the solution was stirred at 75°C for 24 hours. Afterwards, the solvent was evaporated under reduce pressure and 50 ml of water were added. The mixture was extracted three times with DCM (3×100 ml). Organic extracts were combined, dried over Na_2SO_4 and the solvent was evaporated under reduced pressure. The organic solid obtained was purified by column chromatographic (SiO_2, DCM), getting 108 mg of a red solid, 40% yield.

m.p.: 256-258°C.

IR (ATR, cm^{-1}): 2976-2849, 1694 (C=O), 1658 (C=O), 1592-1577, 1512, 1456, 1419, 1410, 1378, 1349, 1327 (B-O), 1276, 1241, 1206, 1170 (C-N), 1138, 1126, 1060, 1051, 1041, 966, 864, 847, 811, 755, 699, 667.

^{1}H-NMR (300 MHz, $CDCl_3$) δ (ppm): 8.77 (dd, *J* = 8.3, 2.6 Hz, 1H, **H_{Ar}**), 8.44 (q, *J* = 8.1 Hz, 2H, 2×**H_{Ar}**), 8.28-8.17 (m, 4H, 4×**H_{Ar}**), 8.10 (d, *J* = 7.2 Hz, 1H, **H_{Ar}**), 7.56 (td, *J* = 8.1, 2.6 Hz, 1H, **H_{Ar}**), 5.11 (q, *J* = 7.5 Hz, 1H, C**H**), 1.99 (s, 3H, 3x**CH**), 1.89-1.79 (m, 3H, C**H_3**), 1.77-1.62 (m, 12H, 6x**CH_2**), 1.48 (s, 12H, 4×C**H_3**).

^{13}C-NMR (75MHz, $CDCl_3$) δ (ppm): 165.7 (**C**=O), 165.0 (**C**=O), 138.0 (**C_{Ar}**), 137.1 (**C_{Ar}**), 136.9 (**C_{Ar}**), 136.6 (**C_{Ar}**), 136.4 (**C_{Ar}**), 136.2 (**C_{Ar}**H), 131.9 (**C_{Ar}**H), 131.8 (**C_{Ar}**H), 131.6 (**C_{Ar}**H), 131.5 (**C_{Ar}**), 131.2 (**C_{Ar}**H), 131.1 (**C_{Ar}**H), 129.5 (**C_{Ar}**), 129.0 (**C_{Ar}**), 127.7 (**C_{Ar}**), 127.2 (**C_{Ar}**H), 126.4 (**C_{Ar}**), 123.4 (**C_{Ar}**H), 122.4 (**C_{Ar}**H), 121.8 (**C_{Ar}**), 121.4 (**C_{Ar}**), 120.7 (**C_{Ar}**H), 120.2 (**C_{Ar}**H), 84.3 (**C**$(CH_3)_2$), 58.1 (**C**H), 40.4 (**C**H_2), 38.1 (**Cq**), 37.1 (**C**H_2), 28.9 (**C**H), 25.2 (**C**H_3), 13.3 (**C**H_3).

HRMS (MALDI, DCTB+) m/z: calculated for $C_{40}H_{40}BNO_4$: 608.3017 (M^+ + H); found 608.3081.

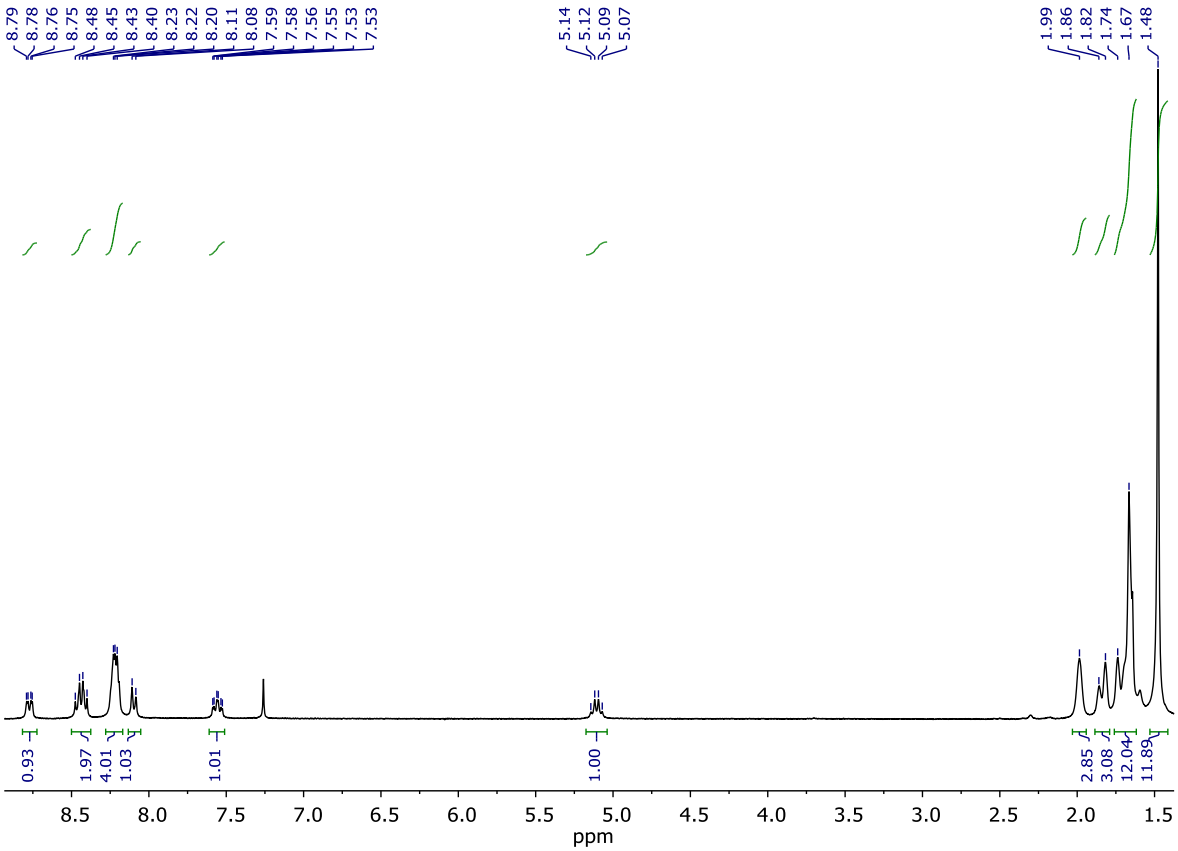

Figure 4. ^{1}H-NMR ($CDCl_3$, 300 MHz) of AR01.

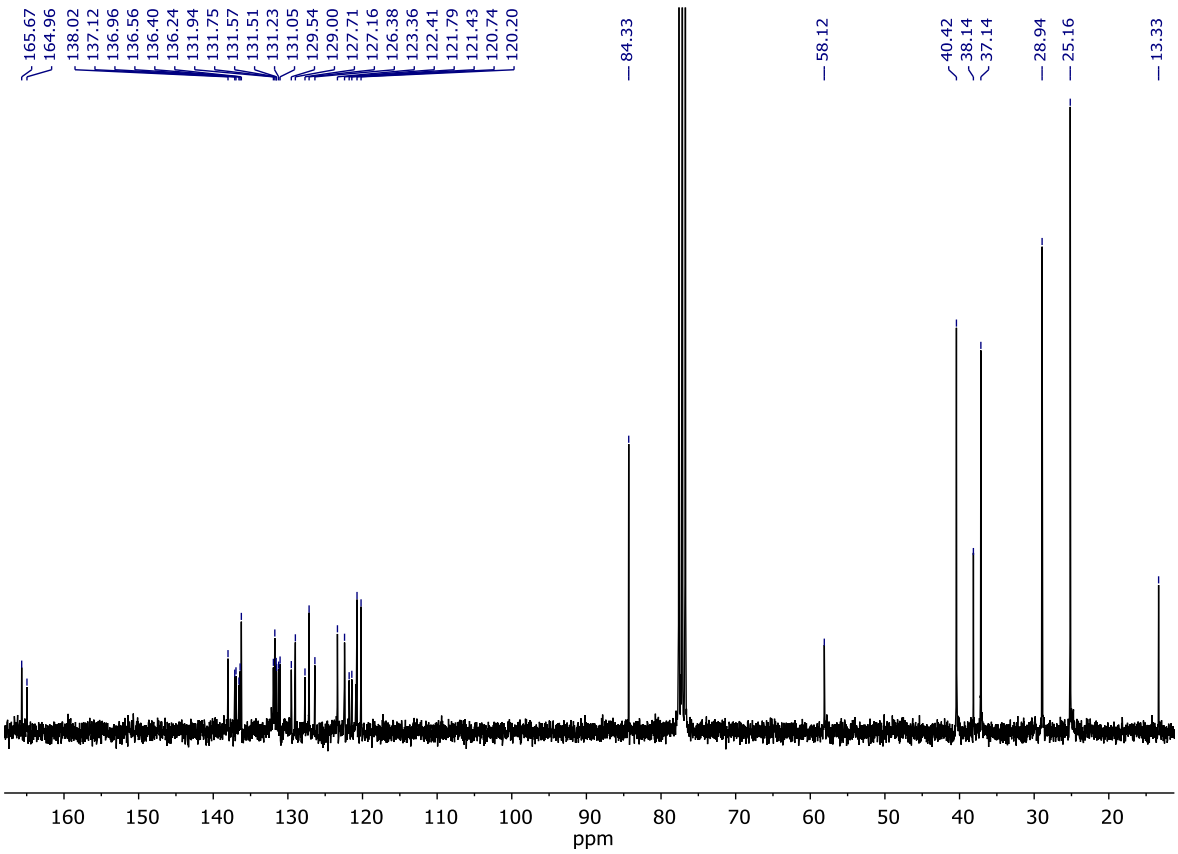

Figure 5. ^{13}C-NMR ($CDCl_3$, 75 MHz) of AR01.

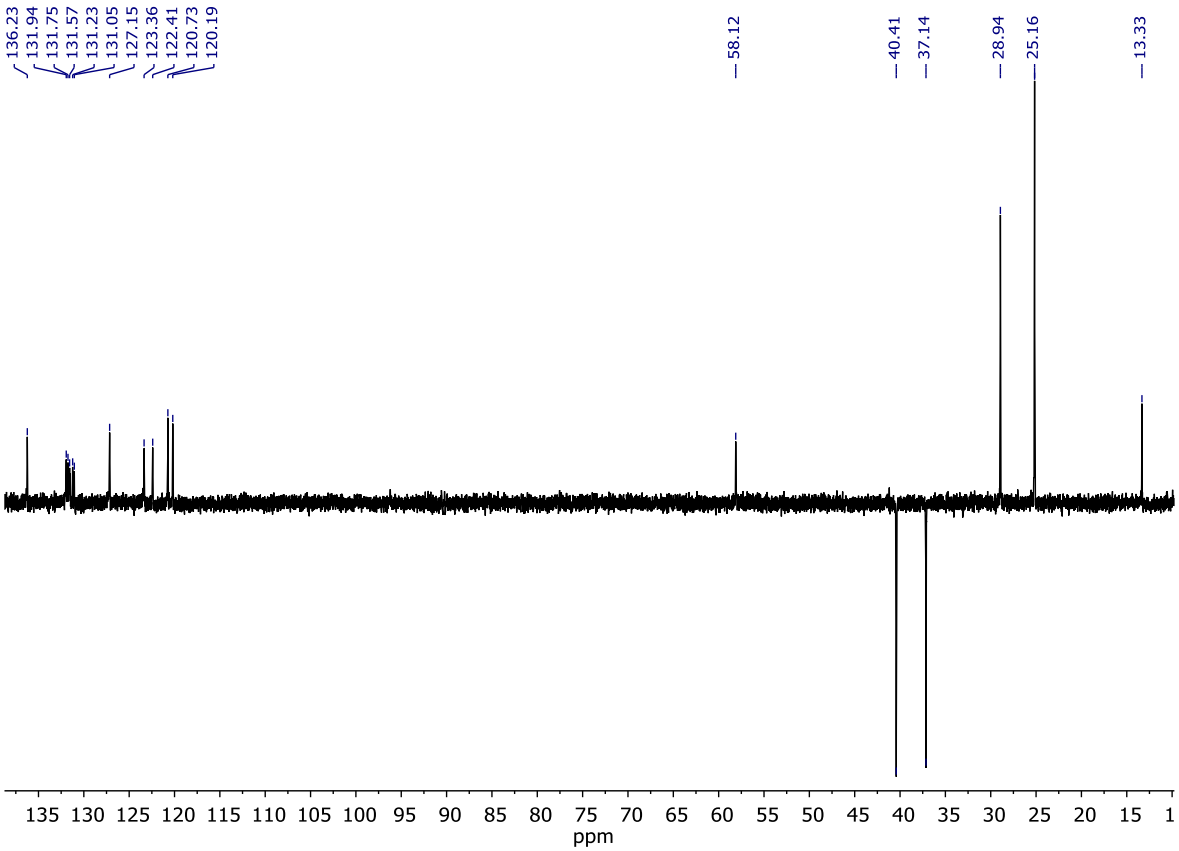

Figure 6. DEPT NMR ($CDCl_3$, 75 MHz) of AR01.

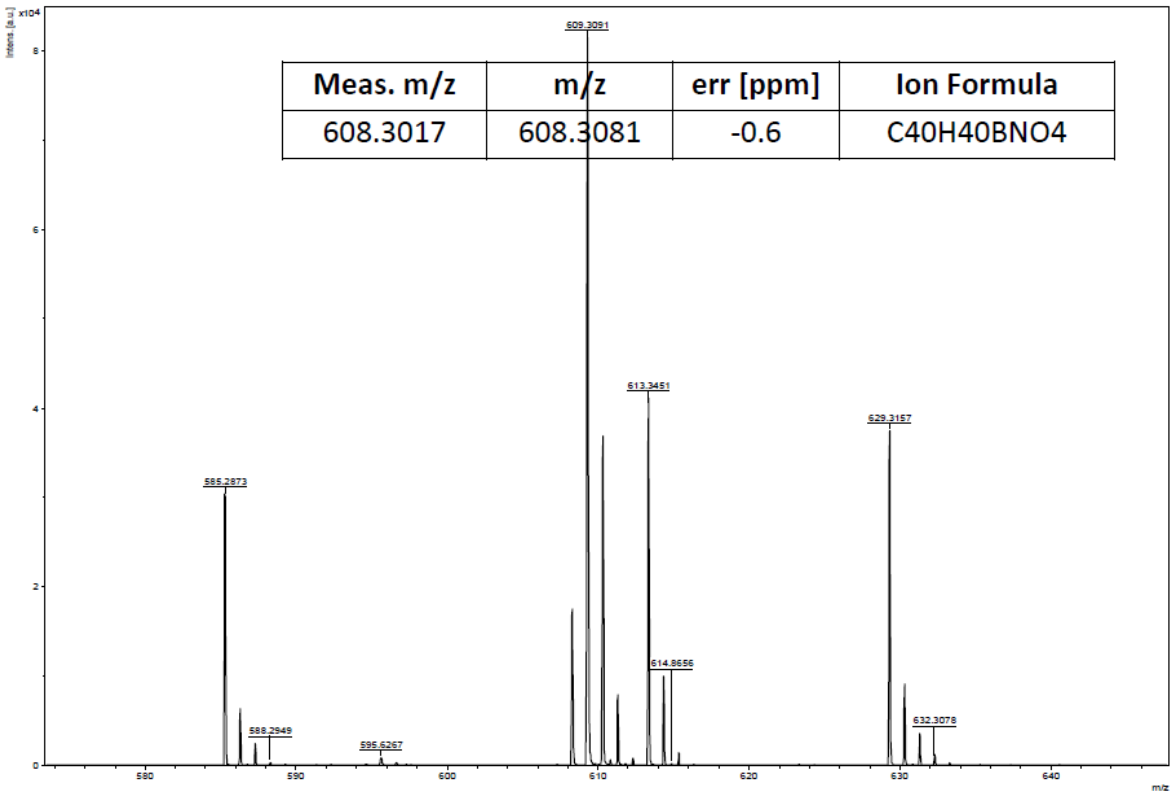

Meas. m/z	m/z	err [ppm]	Ion Formula
608.3017	608.3081	-0.6	C40H40BNO4

Figure 7. HRMS (MALDI, DCTB+) of AR01.

Synthesis of *N*-(1-(1-adamantyl)ethyl)-9-(1,10-phenanthrolin-3-yl)perylene-3,4-dicarboxylmonoimide (AR05)

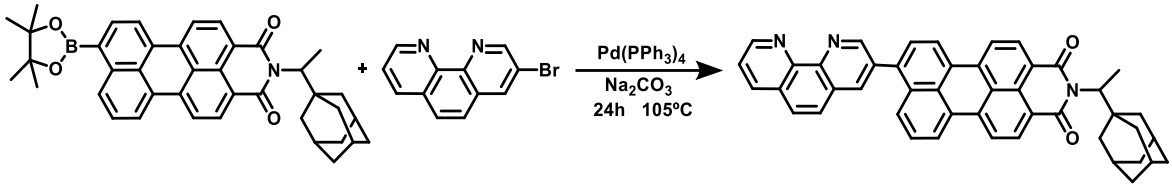

In a 100 ml Schlenk with a magnetic stirrer, 100 mg of *N*-(1-(1-adamantyl)ethyl)-9-(pinacolylboronate)perylene-3,4-dicarboxylmonoimide (AR01, 0.15 mmol), 39 mg of 3-bromo-1,10-phenanthroline (0.15 mmol), 105 mg of sodium carbonate (0.99 mmol) and 12 mg of $Pd(PPh_3)_4$ (0.01 mmol) were added under nitrogen atmosphere. Next, they were dissolved in a mixture of toluene:butanol:water (30.2:7.5:2.6 ml) and heated at 105°C for 24 hours. After that, 50 ml of water were added to the mixture and extracted three times with DCM (3×100 ml). The organic extracts were combined, dried over Na_2SO_4 and the solvent was evaporated under reduced pressure. As a result, the product was obtained and purified by column chromatographic (SiO_2, DCM:MeCN 50:1 v/v), obtaining 33 mg of orange solid, 30% yield.

m.p.: 232-234°C.

IR (ATR, cm^{-1}): 2896-2846, 1689 (C=O), 1646 (C=O), 1571, 1347, 1290, 1241, 1179 (C-N), 1056, 837, 808, 751, 735, 540, 424.

^{1}H-NMR (300 MHz, $CDCl_3$) δ (ppm): 9.34 (s, 1H, **H_{Ar}**), 9.25 (d, *J* = 3,4 Hz, 1H, **H_{Ar}**), 8.56-8.31 (m, 8H, 8×**H_{Ar}**), 7.93 (m, 3H, 3×**H_{Ar}**), 7,70 (t, *J* = 7.9 Hz, 2H, 2×**H_{Ar}**), 7.56 (t, *J* = 7.9 Hz, 1H, **H_{Ar}**), 5.11 (q, *J* = 7.3 Hz, 1H, C**H**), 1.98 (s, 3H, 3xC**H**), 1.84 (d, *J* = 12.3 Hz, 3H, C**H_3**), 1.74-1.62 (m, 12H, 6×C**H_2**).

^{13}C-NMR (75MHz, $CDCl_3$) δ (ppm): 165.6 (C=O), 164.9 (C=O), 151.3 (**C_{Ar}**H), 150.8 (**C_{Ar}**H), 146.2 (**C_{Ar}**H), 145.6 (**C_{Ar}**), 138.8 (**C_{Ar}**), 136.7 (**C_{Ar}**H), 136.3 (**C_{Ar}**H), 135.1 (**C_{Ar}**), 132.8 (**C_{Ar}**), 132.0 (**C_{Ar}**H), 131.3 (**C_{Ar}**H), 129.8 (**C_{Ar}**), 129.1 (**C_{Ar}**), 129.0 (**C_{Ar}**), 128.6 (**C_{Ar}**), 128.4 (**C_{Ar}**), 128.3 (**C_{Ar}**), 127.7 (**C_{Ar}**H), 127.5 (**C_{Ar}**H), 126.7 (**C_{Ar}**H), 126.6 (**C_{Ar}**), 123.9 (**C_{Ar}**H), 123.5 (**C_{Ar}**H), 123.1 (**C_{Ar}**H), 120.7 (**C_{Ar}**H), 120.5 (**C_{Ar}**H), 58.2 (**C**H), 40.4 (**C**H_2), 37.1 (**C**H_2), 29.8 (**Cq**), 28.9 (**C**H), 13.3 (**C**H_3).

HRMS (MALDI, DIT+) m/z: calculated for $C_{46}H_{35}N_3O_2$: 662.2802 (M^++H); found 662.2830.

UV-Vis ($CHCl_3$), λ_{max} nm (log ε): 514 (4.5).

Ø (THF, %): 93.53.

τ (475 nm, THF, ns): 4.110 (χ^2: 1.046).

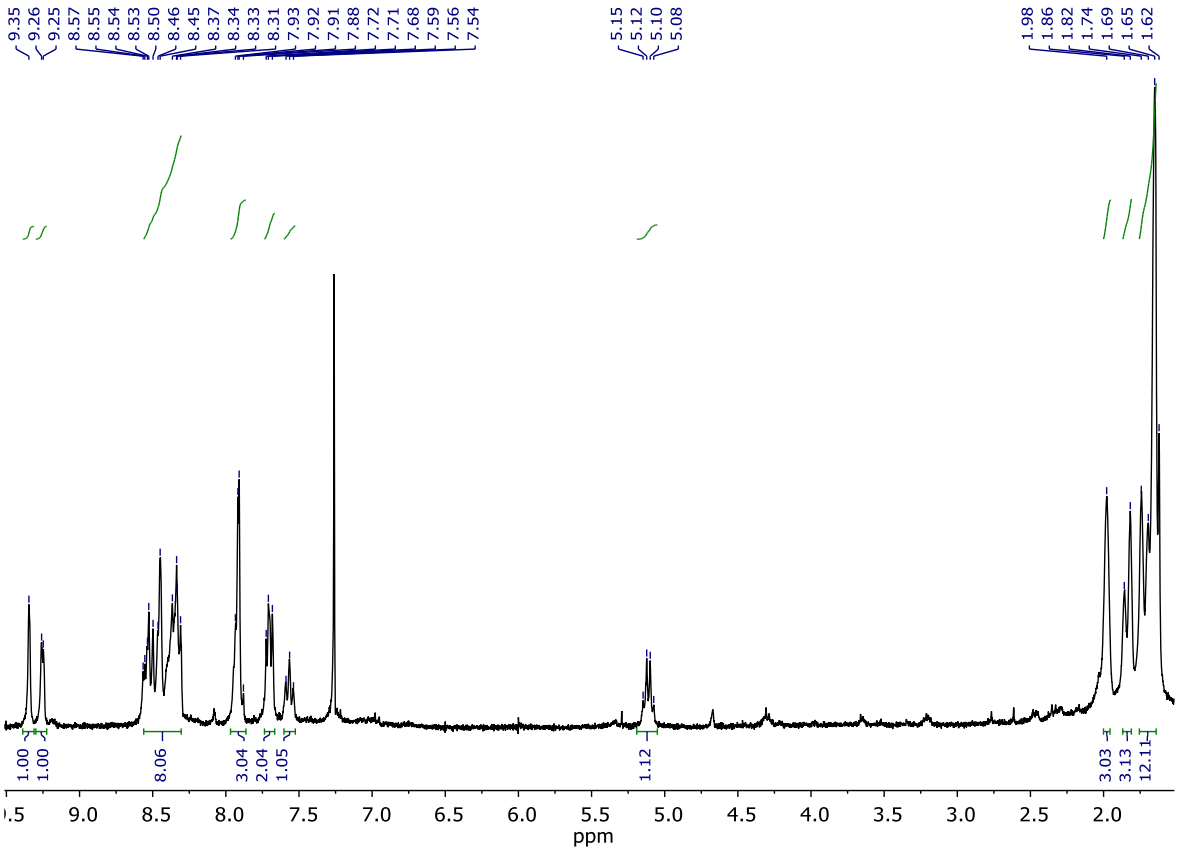

Figure 8. ^{1}H-NMR ($CDCl_3$, 300 MHz) of AR05

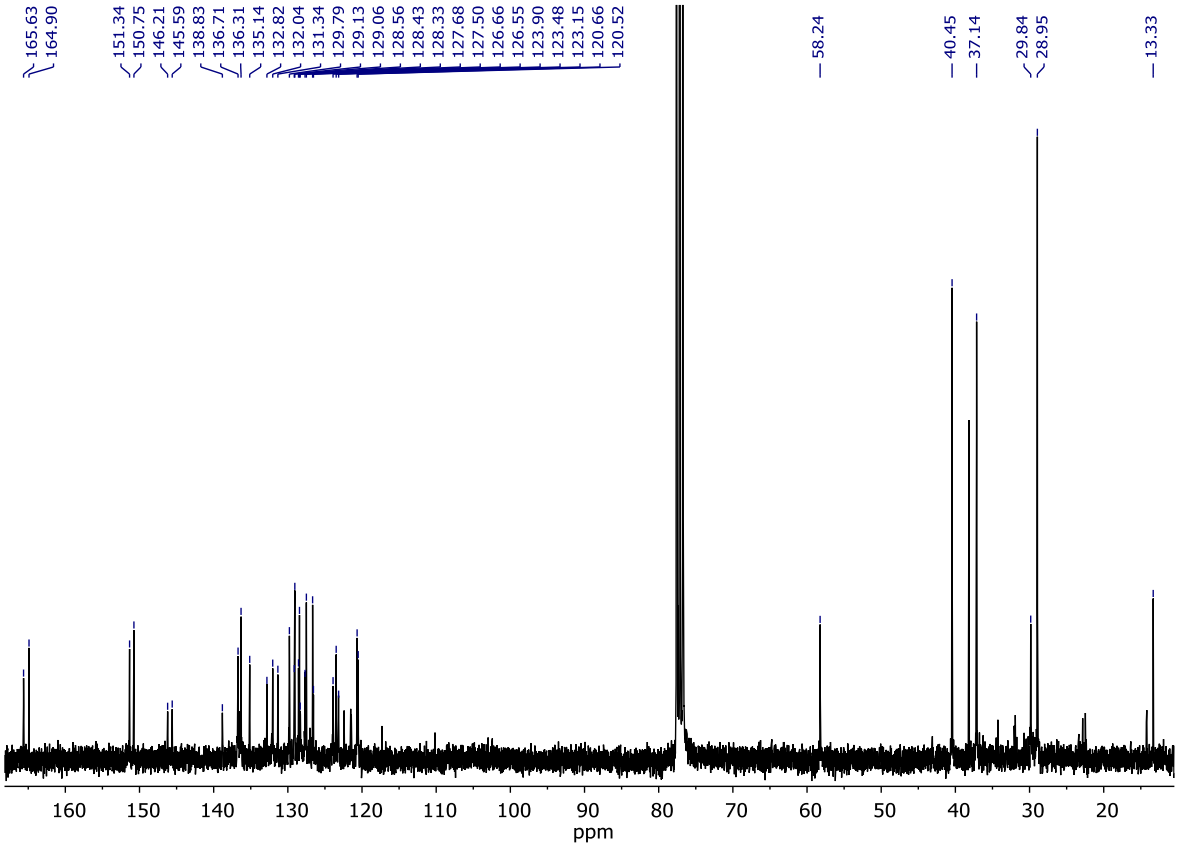

Figure 9. ^{13}C-NMR ($CDCl_3$, 75 MHz) of AR05

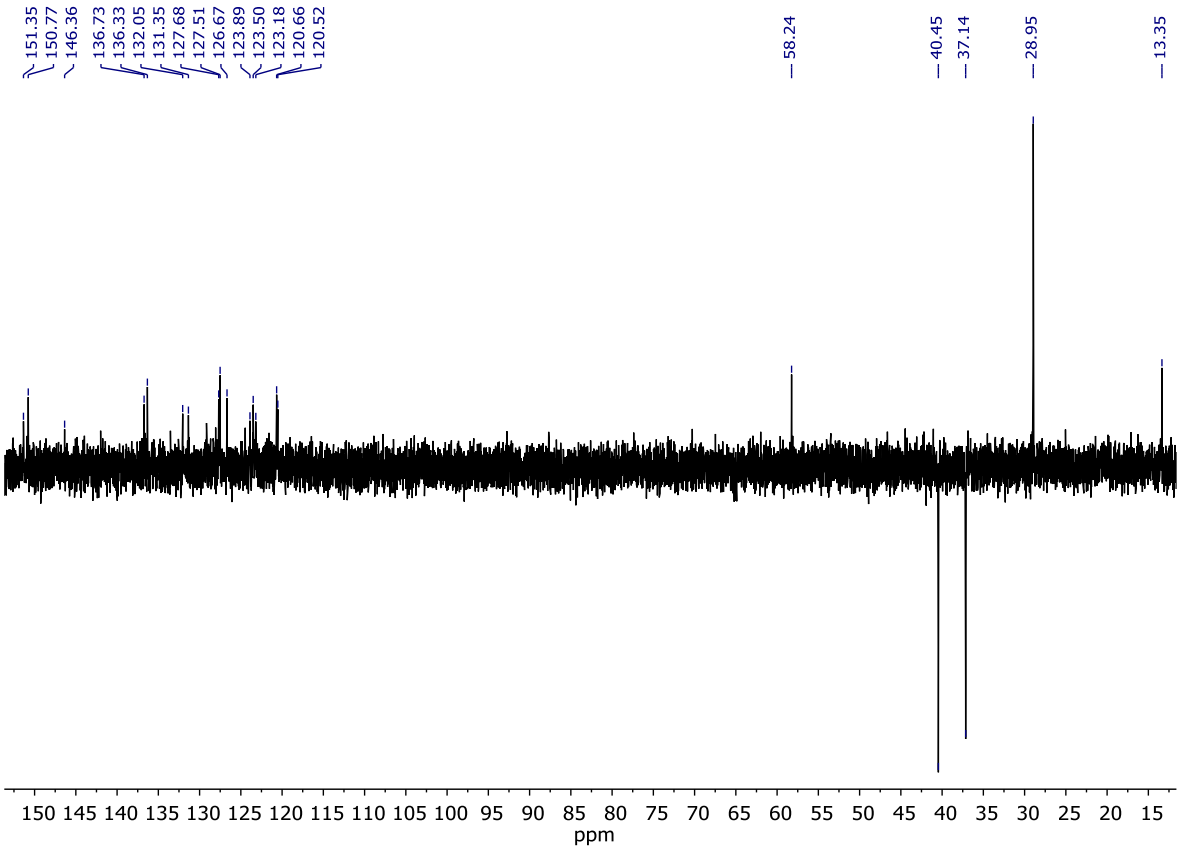

Figure 10. DEPT NMR ($CDCl_3$, 75 MHz) of AR05

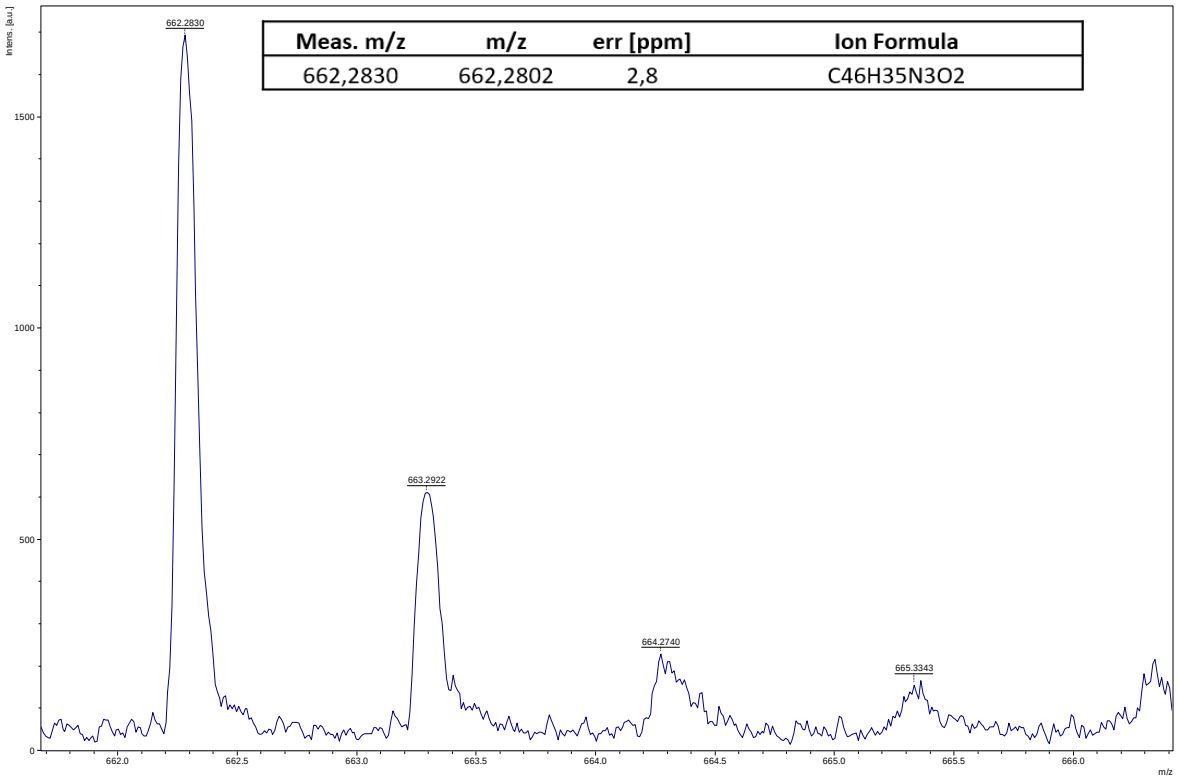

Meas. m/z	m/z	err [ppm]	Ion Formula
662,2830	662,2802	2,8	C46H35N3O2

Figure 11. HRMS (MALDI, DIT+) of AR05

Solvatochromism:

The concentration of the compound was 10 µM and the excitation wavelength was 480 nm.

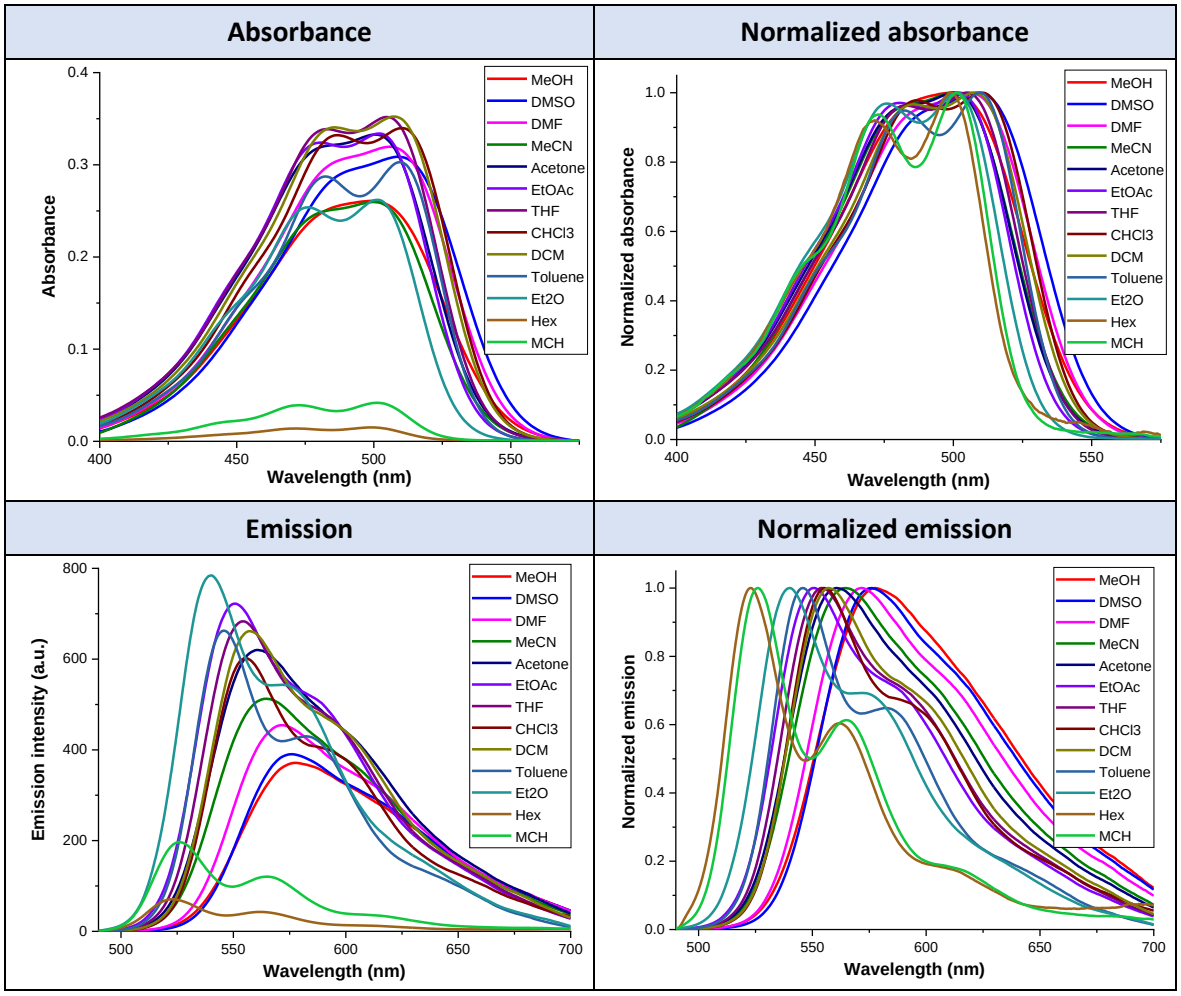

Figure 12. Solvatochromism of AR05.

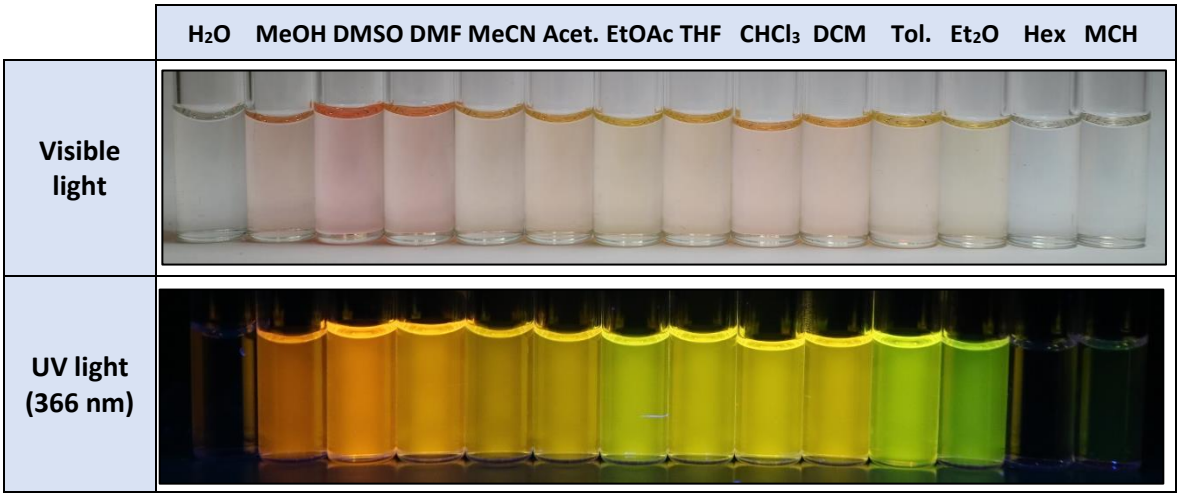

Figure 13. Solvatochromism of AR05 under visible and 366 nm light.

Fluorescence decay lifetime (τ):

The solvent used was THF. The concentration of the compound was 10 µM.

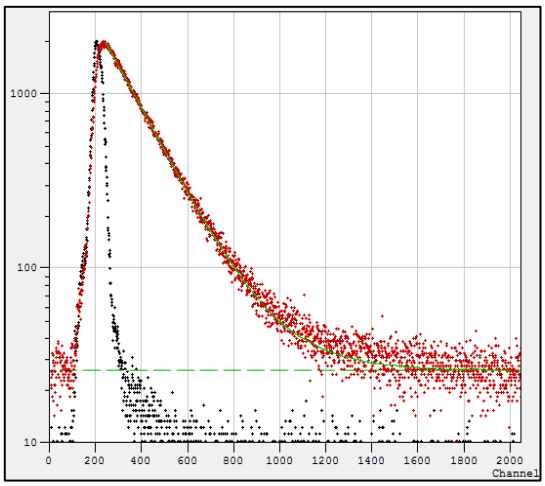

Figure 14. Fluorescence decay lifetime of AR05.

Water acceptance test:

The solvent used was THF and the concentration of the compound was 10 µM.

	R	5%	10%	20%	30%	40%	50%	60%	70%	80%	90%
Visible light	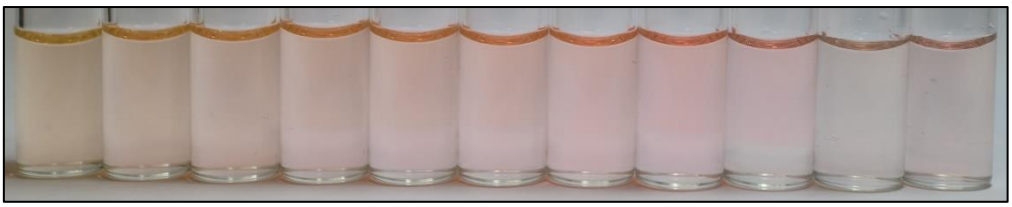										
UV light (366 nm)	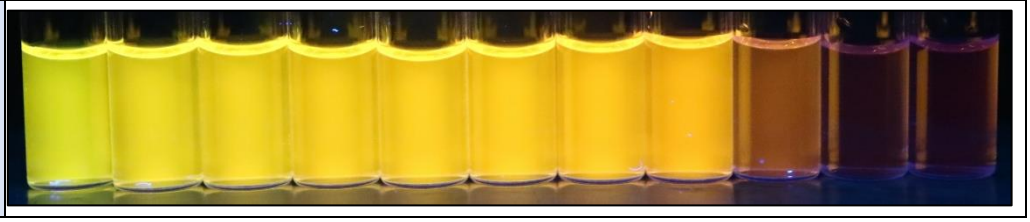										

Figure 15. Water acceptance test of AR05 under visible (up) and UV (down) light.

The maximum aumount of water that was admitted by the product was 60%. At this amount of water, fluorescence quenching was occurred (ACQ), the typical behavior of PMI derivatives.

pH test:

For this test, the proportion of water that the compound could accept according to the previous water acceptance test was 60%. The concentration of the compound was 10 µM and the solvent used was THF.

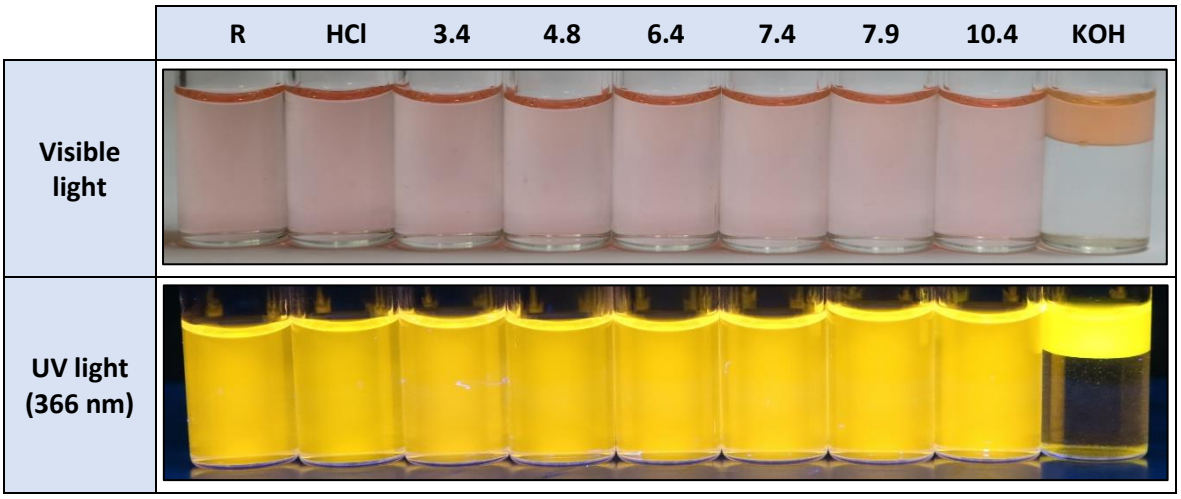

Figure 16. pH test of AR05 under visible (up) and UV (down) light.

No significant changes were observed.

Cations and anions test:

The concentration of the compound was 10 µM and the solvent used was THF.

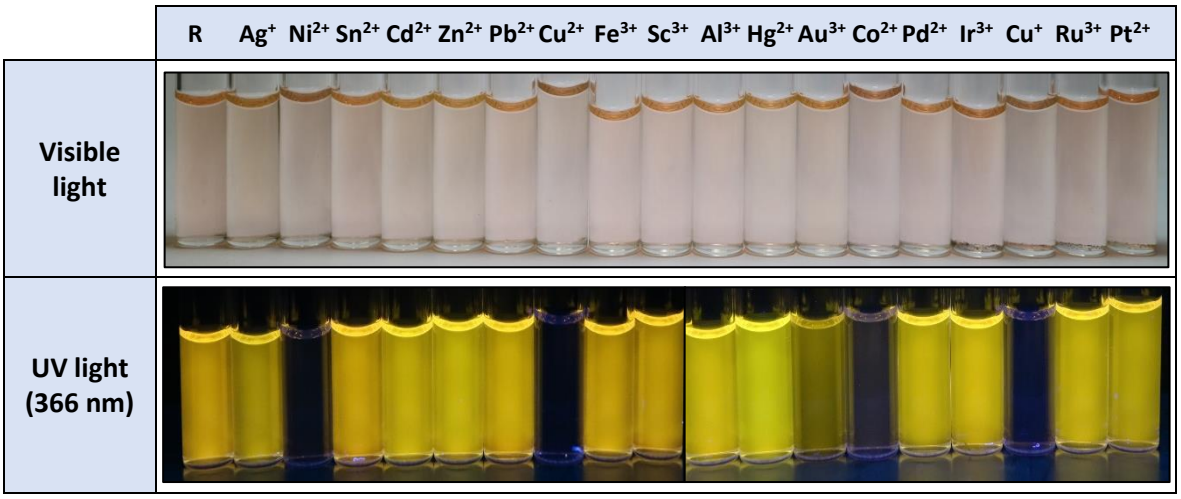

Figure 17. Cations test of AR05 under visible (up) and UV (down) light.

Fluorescence quenching was observed against Ni^{2+}, Cu^{2+}, Co^{2+} and Cu^{+}, while a green shift was observed for Au^{3+}.

For the anion test, the concentration of the compound was 10 µM and the solvent used was THF.

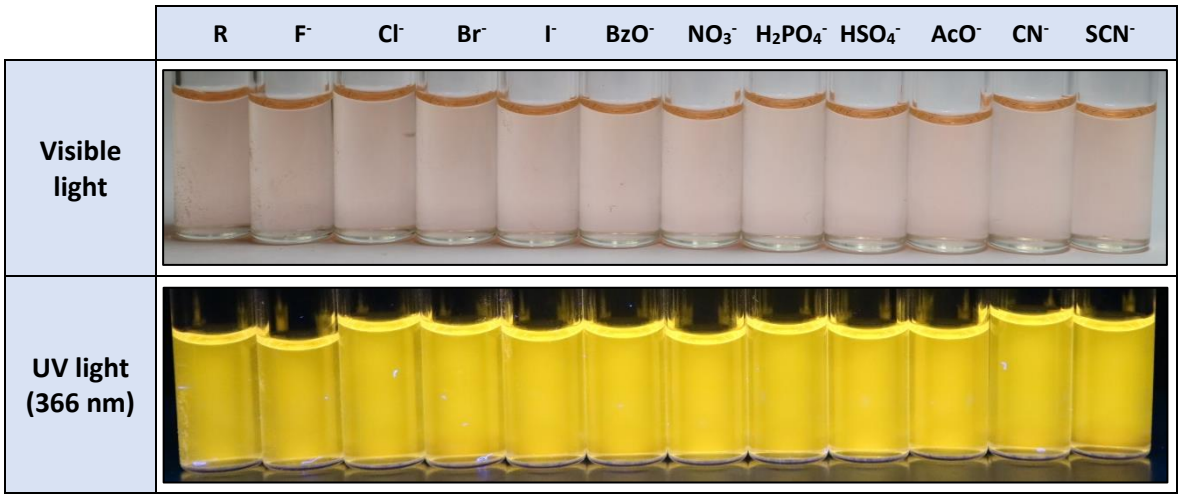

Figure 18. Anions test of AR05 under visible (up) and UV (down) light.

No significant changes was observed.

Oxidant and reductant reagents test:

The solvent used was THF and concentration of the compound was 10 µM.

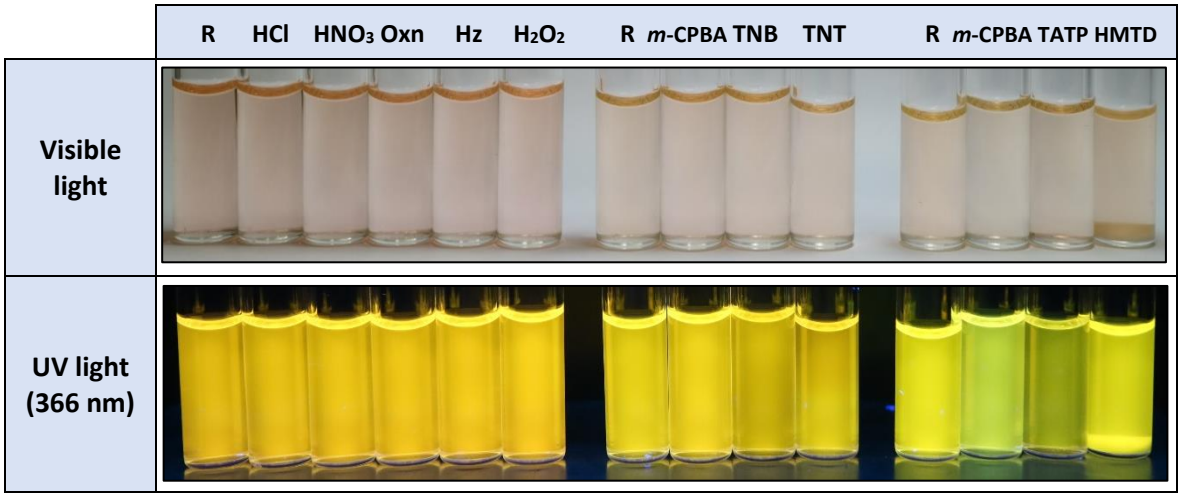

Figure 19. Oxidant and reductant reagents test of AR05 under visible (up) and UV (down) light.

The most significat change was observed against TATP, because the solution was turned green.

Synthesis of *N*-(1-(1adamantyl)ethyl)-9-(1',3',3'-trimethylindolin-6-benzopirylspiranyl)perylen-3,4-dicarboxylmonoimide (AR19)

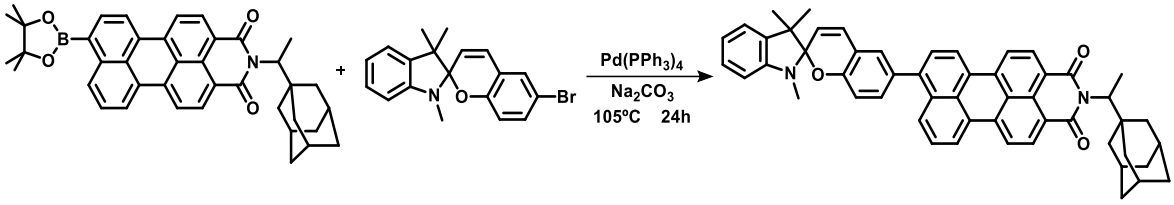

100 mg of *N*-(1-(1-adamantyl)ethyl)-9-bis(pinacolyl)boronateperylene-3,4-dicarboxylmonoimide (AR01, 0.16 mmol), 58 mg of 1,3,3-trimethylindoline-6'-bromobenzopirylspyrane (0.16 mmol), 105 mg of sodium carbonate (0.99 mmol) and 12 mg of $Pd(PPh_3)_4$ (0.01 mmol) were dissolved in a mixture of toluene:butanol:water (30.2:7.5:2.6 ml) under nitrogen atmosphere and the resulting solution was stirred at 105ºC for 24 hours. Afterwards, the solvent was evaporated under reduce pressure, the solid was dissolved in DCM and washed three times with water (3×100 ml). The organic extracts were combined, dry over Na_2SO_4 and the solvent was evaporated under reduce pressure. The organic solid was purified by column chromatography (SiO_2, DCM:MeOH 5%) getting 110 mg of a red solid, 88% yield.

m.p.: 264-265ºC.

IR (ATR, cm^{-1}): 2896-2846 (C-H), 1689 (C=O), 1646 (C=O), 1590, 1568, 1484, 1452 (C-O), 1344, 1241, 1170 (C-N), 1116, 1101, 1056, 1017, 960, 840, 805, 751, 693, 427.

^{1}H-NMR (300 MHz, $CDCl_3$) δ (ppm): 8.60-8.43 (m, 4H, 4×**H$_{Ar}$**), 8.38-8.30 (m, 3H, 3×**H$_{Ar}$**), 8.24 (d, *J* = 7.5 Hz, 1H, **H$_{Ar}$**), 8.00 (d, *J* = 8.5 Hz, 1H, **H$_{Ar}$**), 7.72-7.64 (m, 1H, **H$_{Ar}$**), 7.55-7.47 (m, 2H, 2×**H$_{Ar}$**), 7.23 (m, 1H, **H$_{Ar}$**), 7.13 (d, *J* = 7.7 Hz, 1H, **H$_{Ar}$**), 6.97 (d, *J* = 10.2 Hz, 1H, **H$_{Ar}$**), 6.91-6.86 (m, 1H, **H$_{Ar}$**), 6.59 (d, *J* = 7.7 Hz, 1H, **H$_{Ar}$**), 5.80 (d, *J* = 10.2 Hz, 1H, **H$_{Ar}$**), 5.14-5.09 (m, 1H, C**H**), 1.99 (s, 6H, 3×**CH** y C**H$_3$**), 1.91-1.70 (m, 15H, 6×C**H$_2$** y C**H$_3$**), 1.66 (s, 6H, 2×C**H$_3$**).

^{13}C-NMR (75MHz, $CDCl_3$) δ (ppm): 165.7 (**C**=O), 164.9 (**C**=O), 154.6 (**C**$_{Ar}$), 154.1 (**C**$_{Ar}$), 136.8 (**C**$_{Ar}$H), 136.4 (**C**$_{Ar}$), 133.7 (**C**$_{Ar}$), 132.1 (**C**$_{Ar}$), 131.4 (**C**$_{Ar}$H), 129.7 (**C**$_{Ar}$H), 129.4 (**C**$_{Ar}$H**)**, 129.2 (**C**$_{Ar}$), 128.3 (**C**$_{Ar}$H), 128.2 (**C**$_{Ar}$H), 127.8 (**C**$_{Ar}$), 127.4 (**C**$_{Ar}$H), 126.6 (**C**$_{Ar}$H), 123.8 (**C**$_{Ar}$), 123.4 (**C**$_{Ar}$), 123.2 (**C**$_{Ar}$H), 122.4 (**C**$_{Ar}$H), 121.7 (**C**$_{Ar}$H), 120.6 (**C**$_{Ar}$H), 120.5 (**C**$_{Ar}$H), 119.4 (**C**$_{Ar}$), 119.0 (**C**$_{Ar}$H), 115.3 (**C**$_{Ar}$), 107.0 (**C**$_{Ar}$), 104.9 (**Cq**), 58.3 (**C**H), 52.1 (**Cq**), 40.4 (**C**H$_2$), 38.2 (**C**H), 37.1 (**C**H$_2$), 29.9 (**C**H), 28.9 (**C**H$_3$), 13.3 (**C**H$_3$).

HRMS (MALDI, DIT+) m/z: calculated for $C_{53}H_{46}N_2O_3$: 759.3581 (M^++H); found 759.3617.

UV-Vis ($CHCl_3$), λ_{max} nm (log ε): 520 (4.6).

Ø (MCH, %): 96.78.

τ (475 nm, MCH, ns): 2.442/3.998 (χ^2: 1.080).

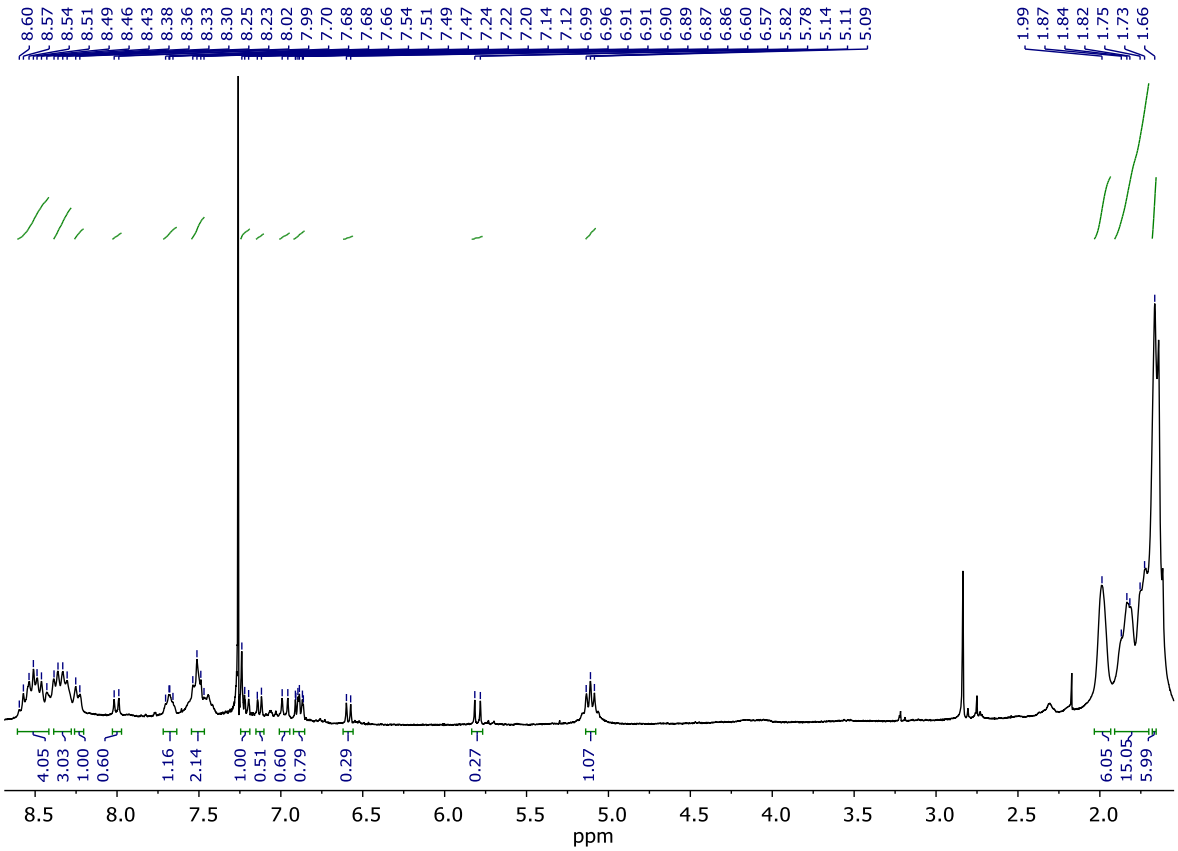

Figure 20. ^{1}H-NMR ($CDCl_3$, 300 MHz) of AR19.

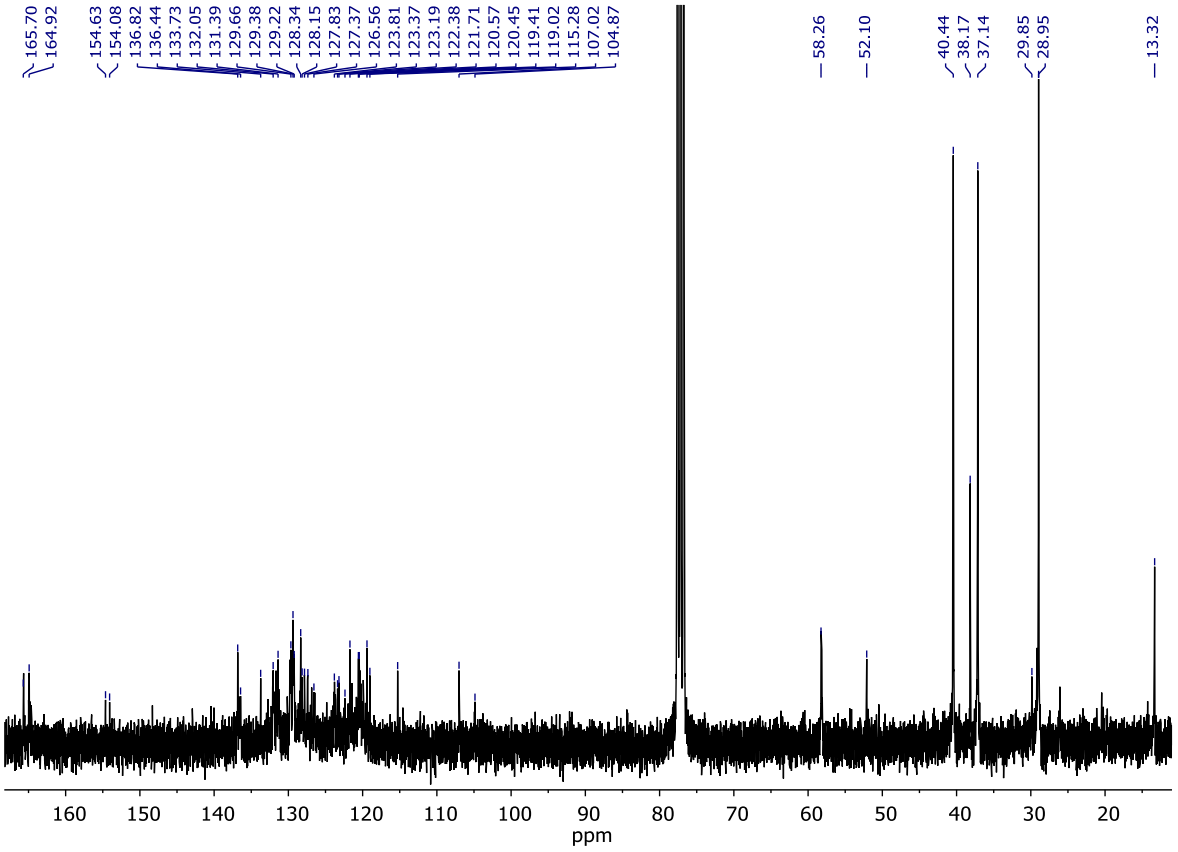

Figure 21. ^{13}C-NMR ($CDCl_3$, 75 MHz) of AR19.

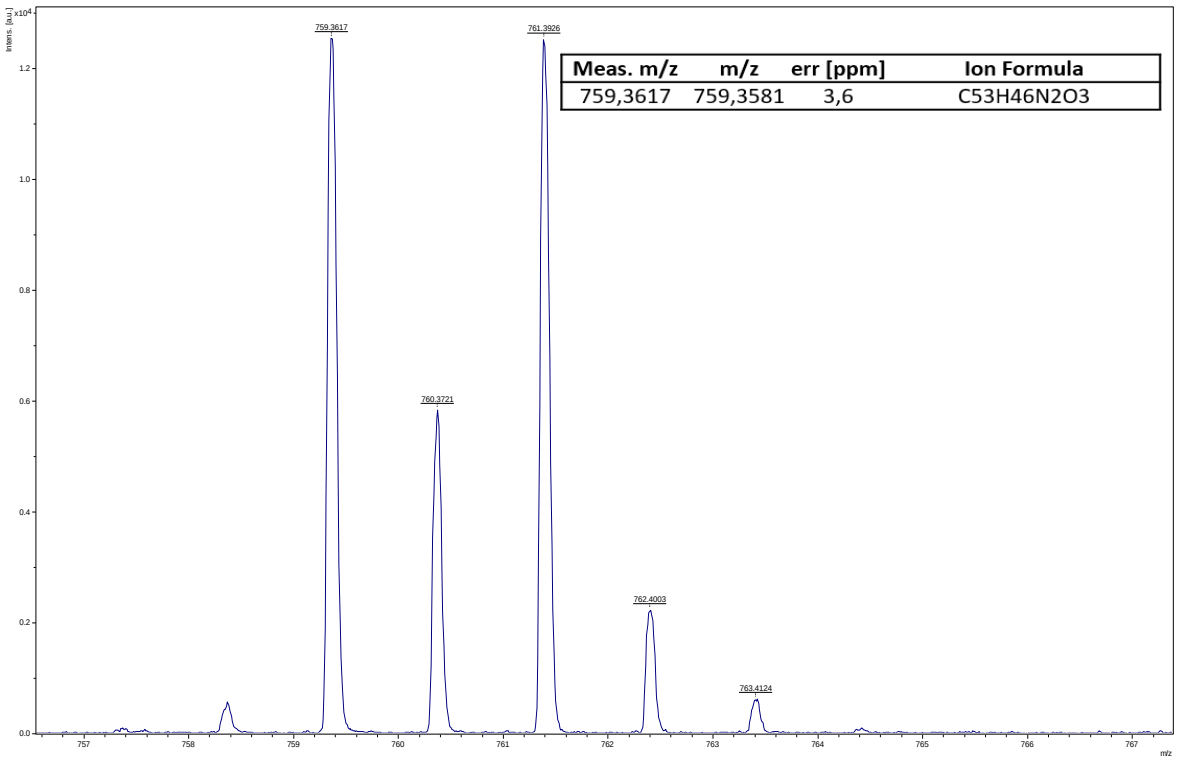

Figure 22. HRMS (MALDI, DIT+) of AR19.

Fluorescence decay lifetime (τ):

The solvent used was MCH. The concentration of the compound was 20 µM.

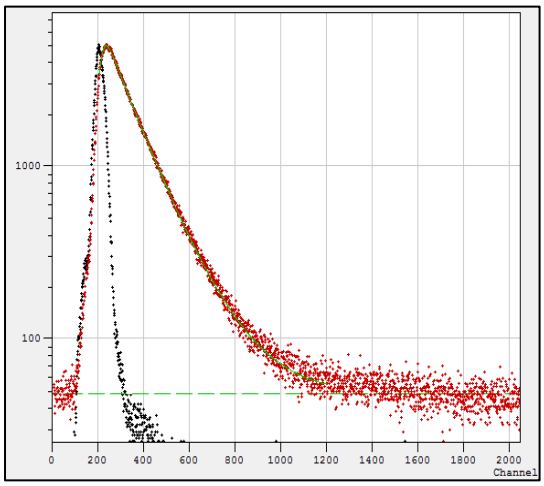

Figure 23. Fluorescence decay lifetime of AR19.

Solvatochromism:

The concentration of the compound was 20 µM and the excitatin wavelength was 490 nm.

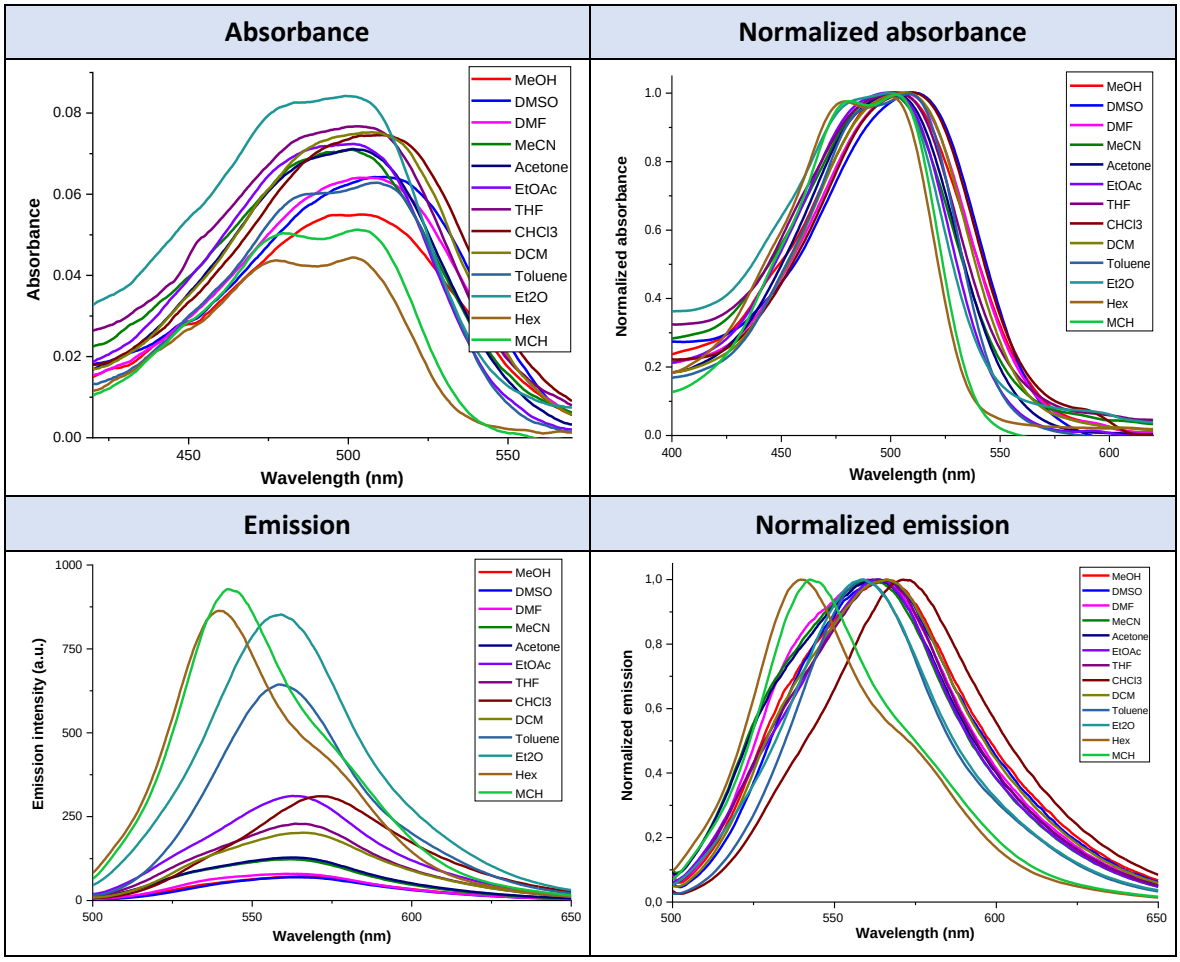

Figure 24. Solvatochromism of AR19.

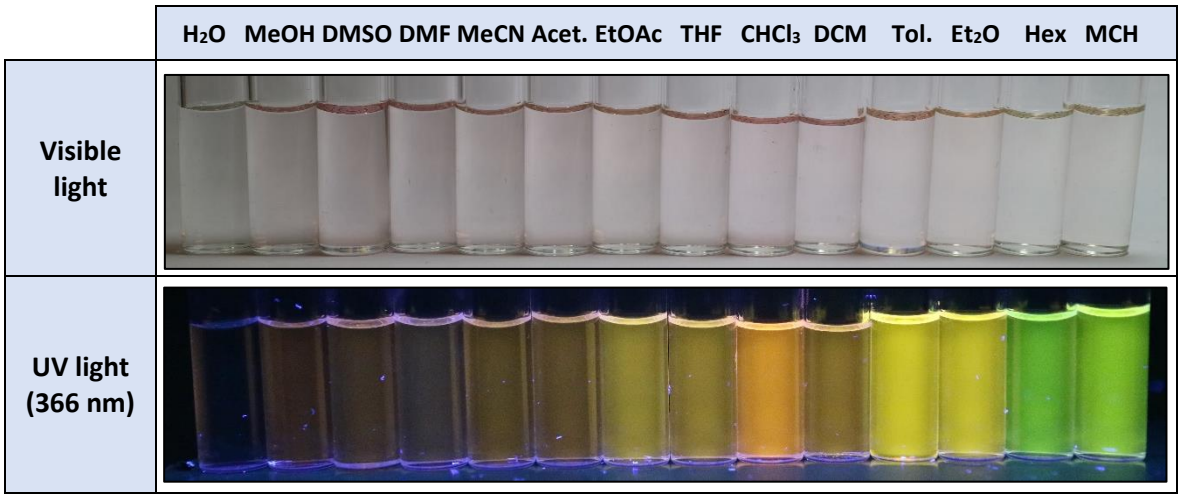

Figure 25. Solvatochromism of AR19 under visible and 366 nm light.

Water acceptance test:

The solvent used was MeCN and the concentration of the compound was 20 µM.

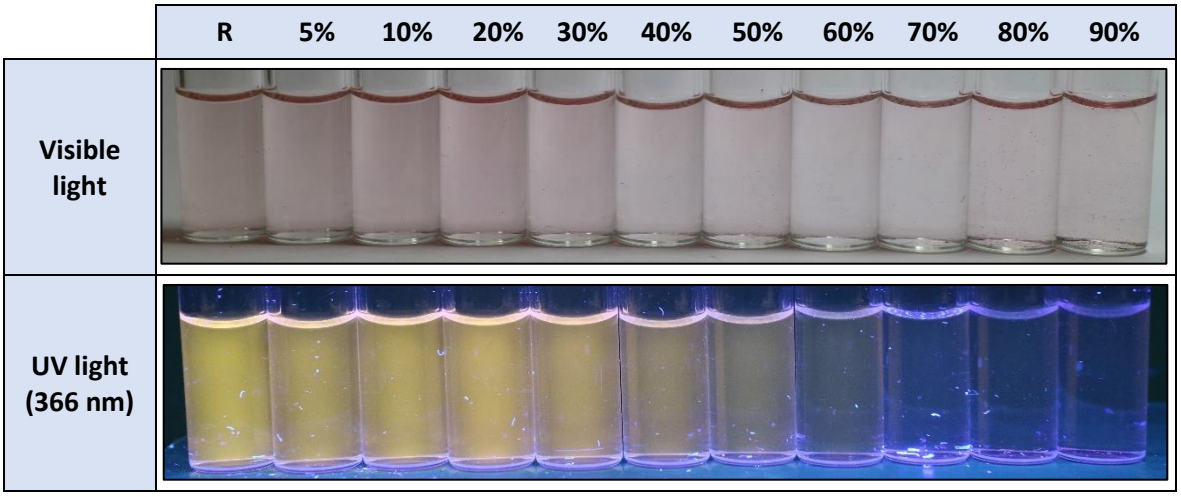

Figure 26. Water acceptance test of AR19 under visible (up) and UV (down) light.

The maximum aumount of water that was admitted by the product was 20%. At 50% of water, fluorescence quenching was occurred (ACQ), the typical behavior of PMI.

pH test:

For this test, the proportion of water that the compound could accept according to the previous water acceptance test was 20%. The concentration of the compound was 20 µM and the solvent used was MeCN.

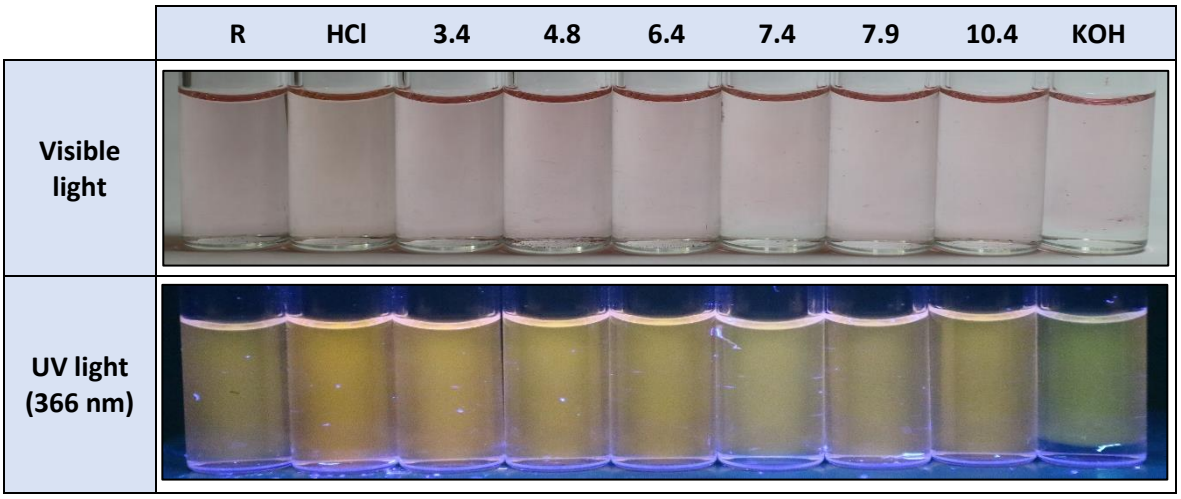

Figure 27. pH test of AR19 under visible (up) and UV (down) light.

No significant changes were observed except that, at very basic pH, the colour of the fluorescence was turned slightly greenish.

Cations and anions test:

The concentration of the compound was 20 µM and the solvent used was MeCN.

	R	Ag^+	Ni^{2+}	Sn^{2+}	Cd^{2+}	Zn^{2+}	Pb^{2+}	Cu^{2+}	Fe^{3+}	Sc^{3+}	Al^{3+}	Hg^{2+}	Au^{3+}	Co^{2+}	Pd^{2+}	Ir^{3+}	Cu^+	Ru^{3+}	Pt^{2+}
Visible light	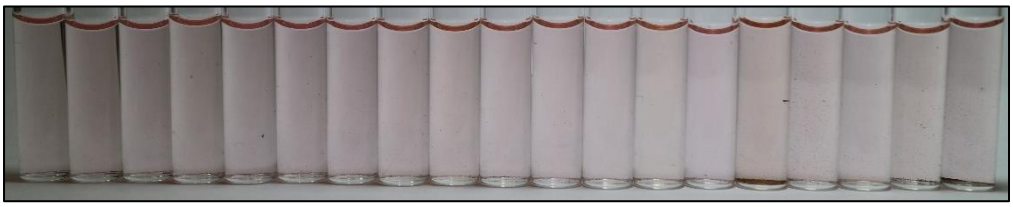																		
UV light (366 nm)	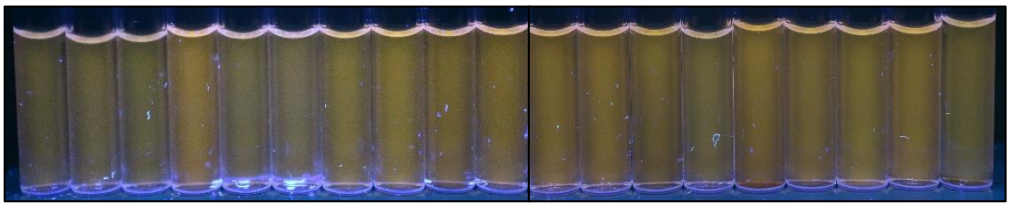																		

Figure 28. Cations test of AR19 under visible (up) and UV (down) light.

No significant changes were observed.

For the anion test, the concentration of the compound was 20 µM and the solvent used was acetonitrile.

	R	F^-	Cl^-	Br^-	I^-	BzO^-	NO_3^-	$H_2PO_4^-$	HSO_4^-	AcO^-	CN^-	SCN^-
Visible light	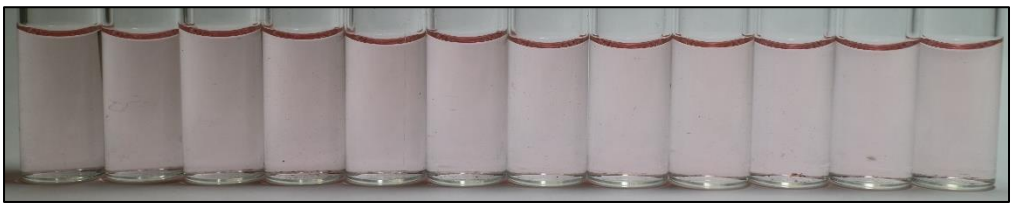											
UV light (366 nm)	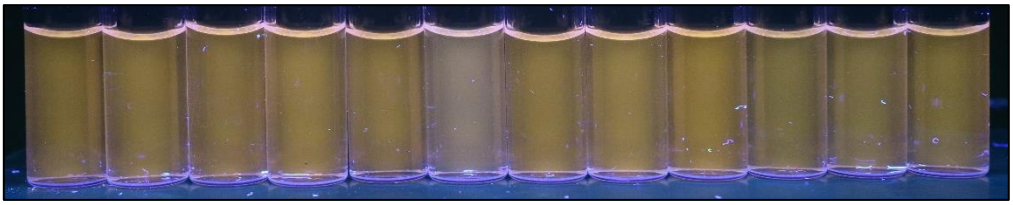											

Figure 29. Anions test of AR19 under visible (up) and UV (down) light.

The only positive response was against benzoate (BzO^-).

Oxidant and reductant reagents test:

The solvent used was acetonitrile and concentration of the compound was 20 µM.

	R	HCl	HNO_3	*m*-CPBA	Oxn	Hz	H_2O_2	TNB	TNT	TATP
Visible light	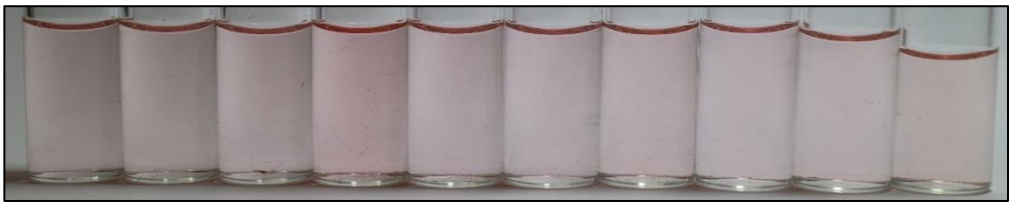									
UV light (366 nm)	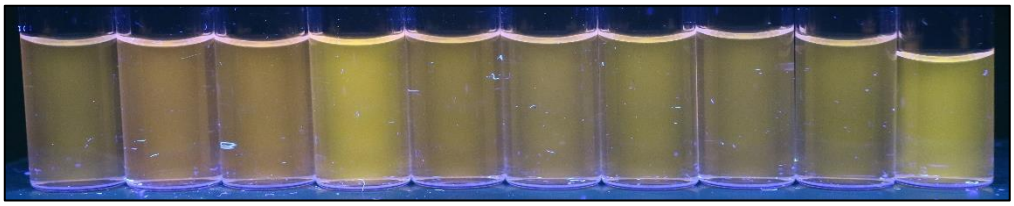									

Figure 30. Oxidant and reductant reagents test of AR19 under visible (up) and UV (down) light.

No significat changes were observed.

Synthesis of 1,6-bis(*N*-(1-(1-adamantyl)ethyl)-9-perylene-3,4-dicarboxylmonoimide)-3,8-diisopropyl pyrene (AR48) and 1-(*N*-(1-(1-adamantyl)ethyl)-9-perylene-3,4-dicarboxylmonoimide)-3,8-diisopropyl pyrene (AR49)

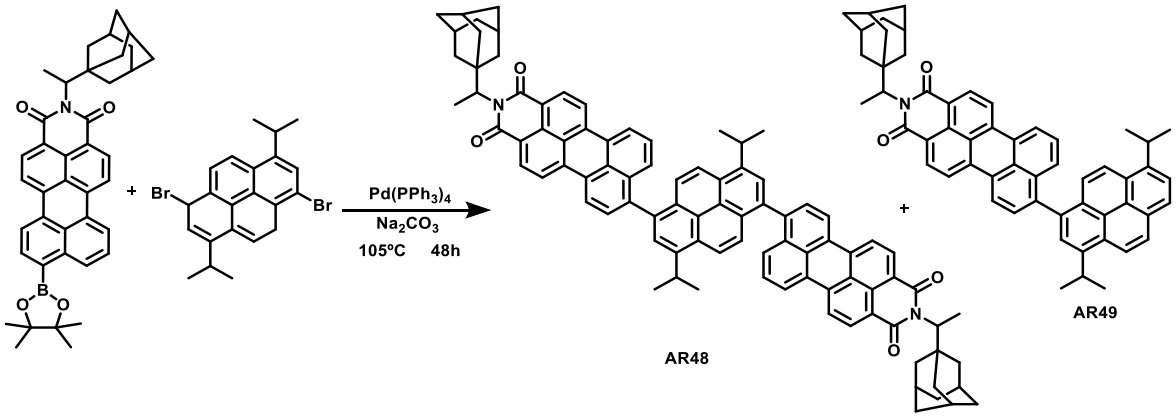

In a 100 ml Schlenk with a magnetic stirrer, 100 mg of 1,6-dibromo-3,8-diisopropylpyrene (0.23 mmol), 274 mg of *N*-(1-(1-adamantyl)ethyl)-8-bis(pinacolyl)boronateperylene-3,4-dicarboxylmono imide (AR01, 0.45 mmol) and 105 mg of sodium carbonate (0.99 mmol) were dissolved in a mixture of toluene:butanol:water (30.2:7.5:2.6 ml) under nitrogen atmosphere. The catalyst, 12 mg of $Pd(PPh_3)_4$ (0.01 mmol), was added and the resulting solution was stirred at 105ºC for 48 hours. Afterwards, the solvent was evaporated under reduce pressure, the solid was dissolved in DCM and washed three times with water (3×100 ml). The organic extracts were combined, dry over anhidrous Na_2SO_4 and the solvent was evaporated under reduce pressure. The organic solid was purified by column chromatography (SiO_2, DCM) to obtain two red solid with the next yields:

- AR48 was obtained with a 56% yield (158 mg).
- AR49 was obtained with a 23% yield (40 mg).

AR48

m.p.: >390ºC.

IR (ATR, cm^{-1}): 2960-2846, 1692 (C=O), 1649 (C=O), 1590 (C_{Ar}-C_{Ar}), 1568, 1503, 1449, 1409, 1347, 1311, 1287, 1241, 1176 (C-N), 1050, 903, 840, 808, 754, 603, 432.

^{1}H-NMR (300 MHz, $CDCl_3$) δ (ppm): 8.53 (m, 6H, 6×$\mathbf{H_{Ar}}$), 8.35 (m, 8H, 8×$\mathbf{H_{Ar}}$), 8.10 (m, 2H, 2×$\mathbf{H_{Ar}}$), 7.81 (m, 4H, 4×$\mathbf{H_{Ar}}$), 7.53 (d, *J* = 8.3 Hz, 2H, 2×$\mathbf{H_{Ar}}$), 7.42 (td, *J* = 8.3, 2.7 Hz, 2H, 2×$\mathbf{H_{Ar}}$), 5.15 (q, *J* = 7.0 Hz, 2H, 2×C**H**), 4.08 (hept, *J* = 7.8 Hz, 2H, 2×C**H**), 2.00 (s, 6H, 6×C**H**), 1.88 (d, *J* = 12.0 Hz, 6H, 2×C$\mathbf{H_3}$), 1.71 (m, 24H, 12×C$\mathbf{H_2}$), 1.53 (dd, *J* = 6.2, 2.5 Hz, 12H, 4×C$\mathbf{H_3}$).

^{13}C-NMR (75MHz, $CDCl_3$) δ (ppm): 165.8 (**C**=O), 165.0 (**C**=O), 142.7 ($\mathbf{C}_{Ar}$), 137.1 ($\mathbf{C}_{Ar}$), 135.0 ($\mathbf{C}_{Ar}$), 134.3 ($\mathbf{C}_{Ar}$), 132.2 ($\mathbf{C}_{Ar}$H), 131.5 ($\mathbf{C}_{Ar}$H), 129.9 ($\mathbf{C}_{Ar}$H), 129.7 ($\mathbf{C}_{Ar}$), 129.2 ($\mathbf{C}_{Ar}$), 128.4 ($\mathbf{C}_{Ar}$), 128.3 ($\mathbf{C}_{Ar}$), 128.2 ($\mathbf{C}_{Ar}$), 127.3 ($\mathbf{C}_{Ar}$H), 126.7 ($\mathbf{C}_{Ar}$), 125.9 ($\mathbf{C}_{Ar}$), 125.8 ($\mathbf{C}_{Ar}$H), 125.5 ($\mathbf{C}_{Ar}$H), 123.8 ($\mathbf{C}_{Ar}$H), 123.3 ($\mathbf{C}_{Ar}$H), 122.6 ($\mathbf{C}_{Ar}$H),122.26, 121.33, 120.5 ($\mathbf{C}_{Ar}$H), 120.3 ($\mathbf{C}_{Ar}$H), 58.2 (**C**H), 40.5 (**C**H_2), 38.2 (**Cq**), 37.2 (**C**H_2), 29.0 (**C**H), 24.2 (**C**H_3), 13.3 (**C**H_3).

HRMS (MALDI, DCTB+) m/z: calculated for $C_{90}H_{76}N_2O_4$: 1248.5800 (M^+); found 1248.5811.

UV-Vis ($CHCl_3$), λ_{max} nm (log ε): 522 (4.9).

Ø (MCH, %): 94.52.

τ (475 nm, MCH, ns): 2.788 (χ^2: 1.058).

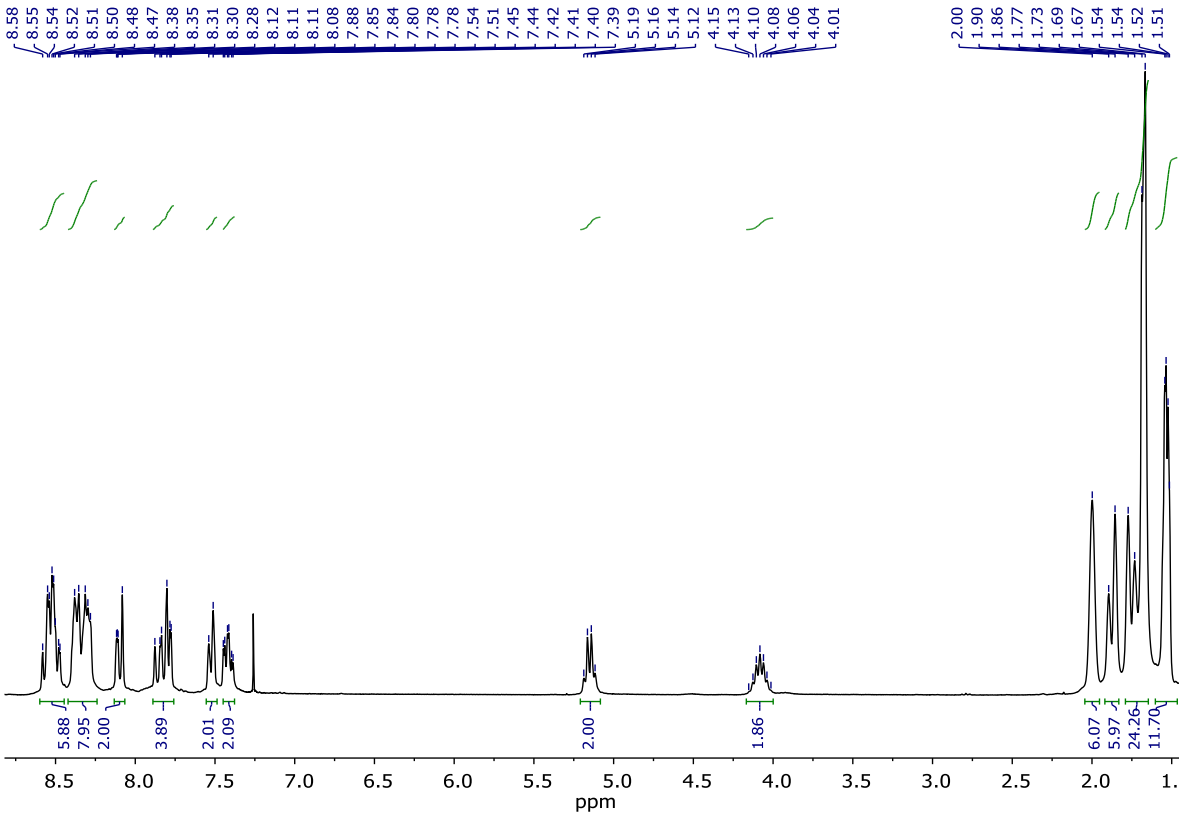

Figure 31. ^{1}H-NMR ($CDCl_3$, 300 MHz) of AR48.

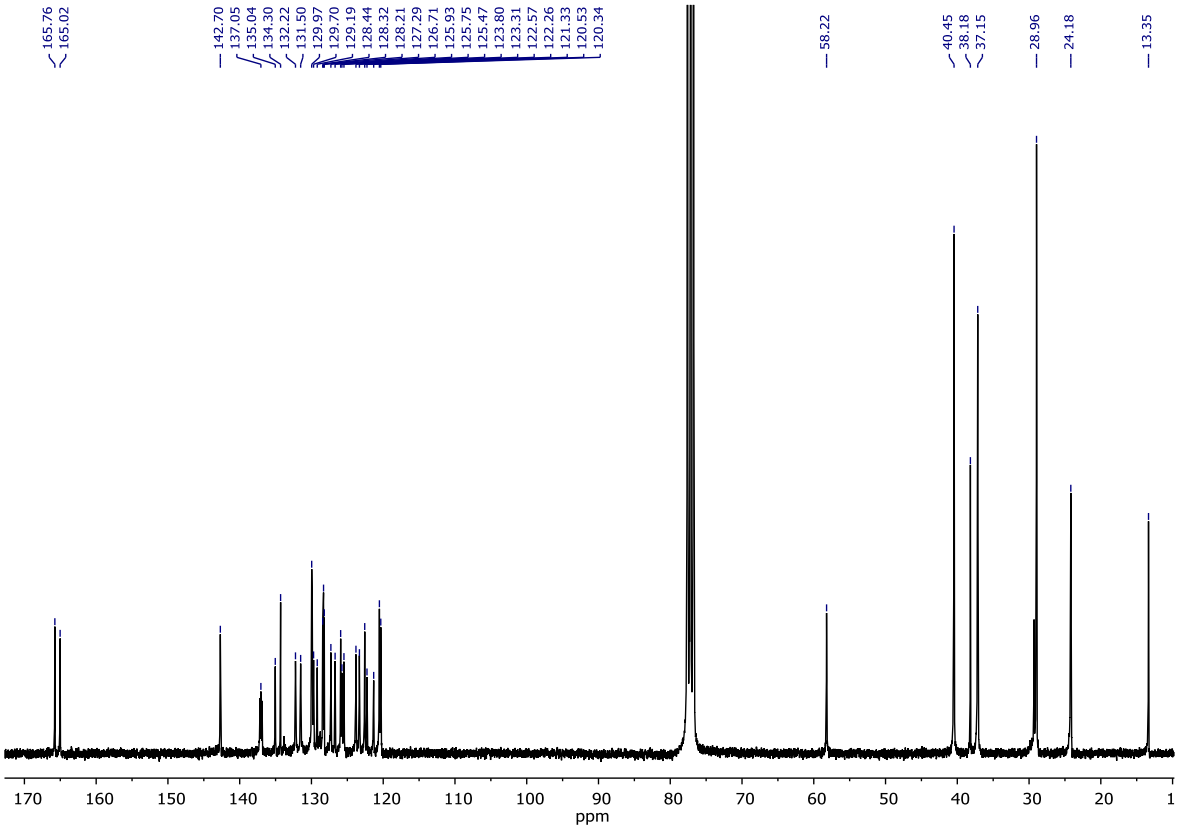

Figure 32. ^{13}C-NMR ($CDCl_3$, 75 MHz) of AR48.

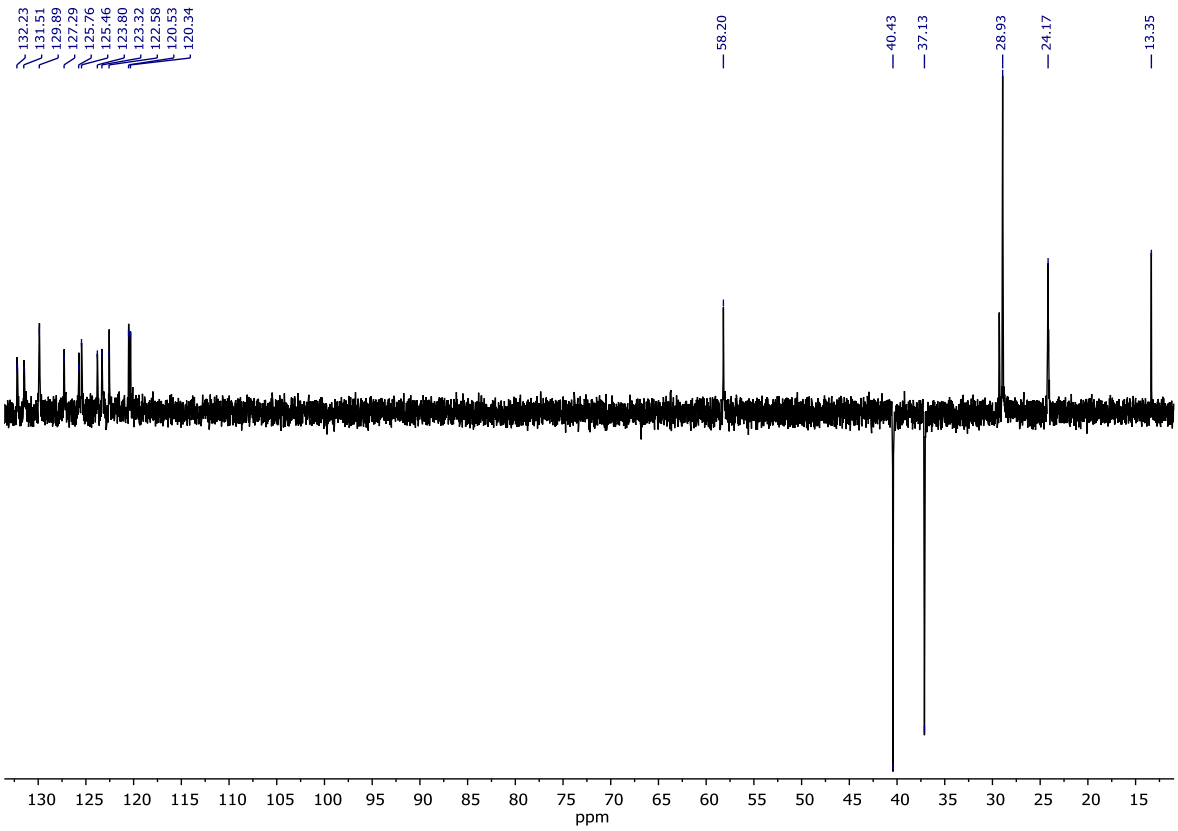

Figure 33. DEPT NMR ($CDCl_3$, 75 MHz) of AR48.

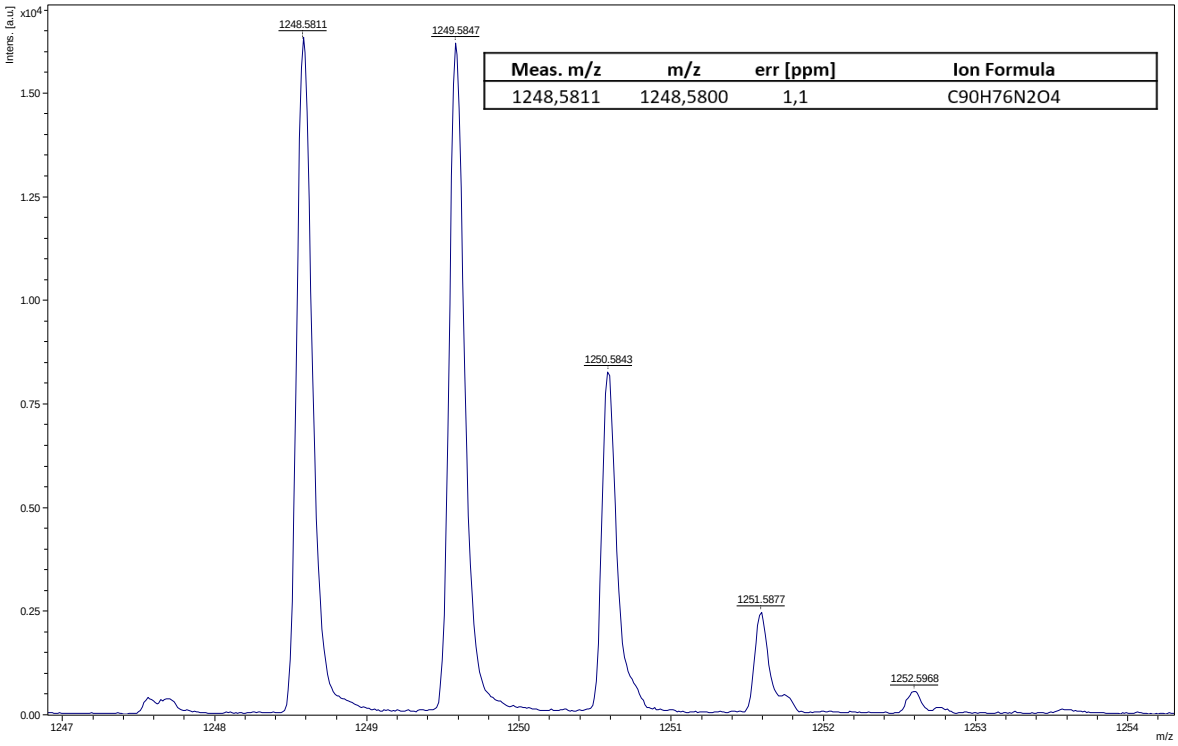

Meas. m/z	m/z	err [ppm]	Ion Formula
1248,5811	1248,5800	1,1	C90H76N2O4

Figure 34. HRMS (MALDI, DCTB+) of AR48.

Solvatochromism:

The concentration of the compound was 20 µM and the excitation wavelength was 480 nm.

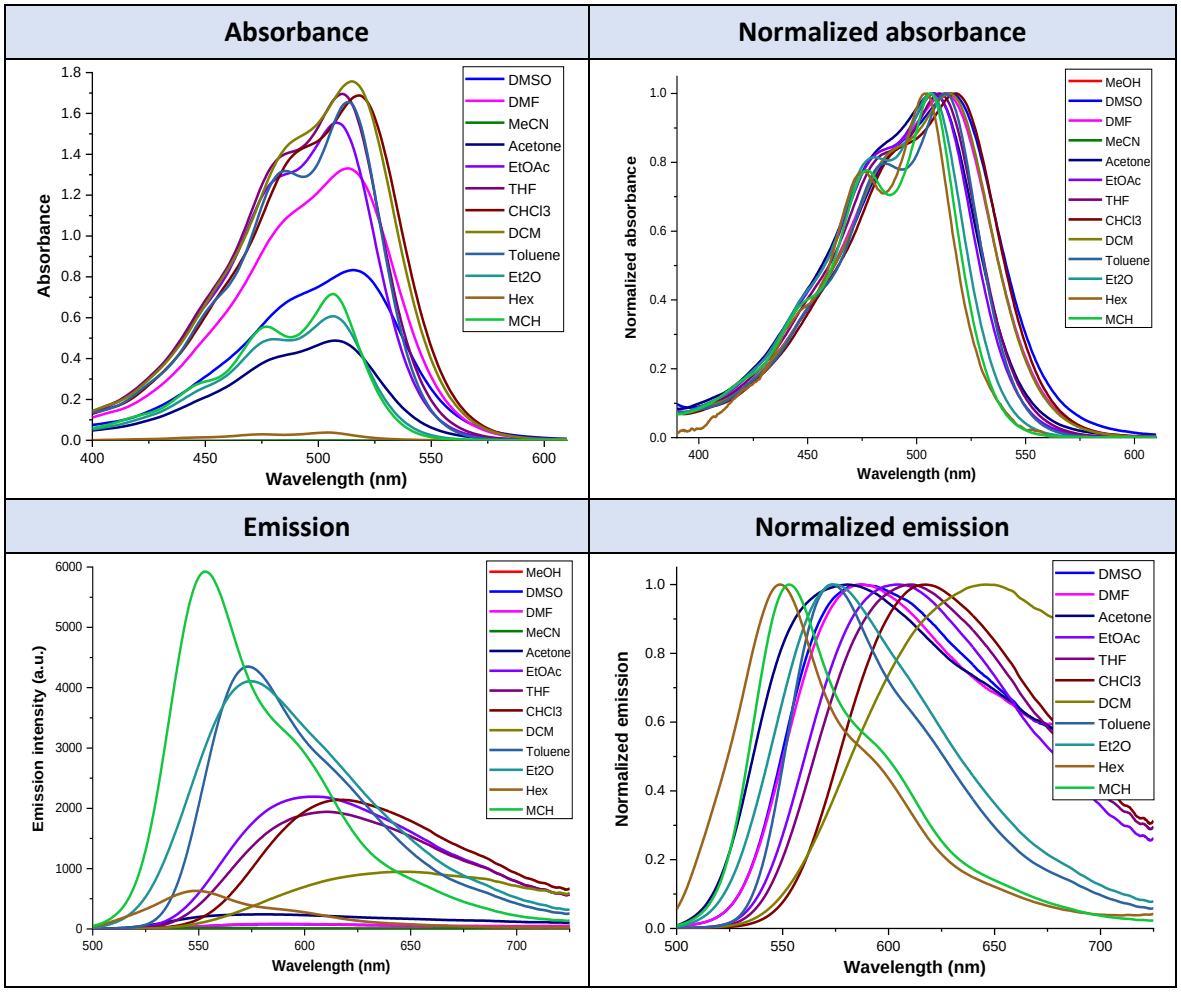

Figure 35. Solvatochromism of AR48.

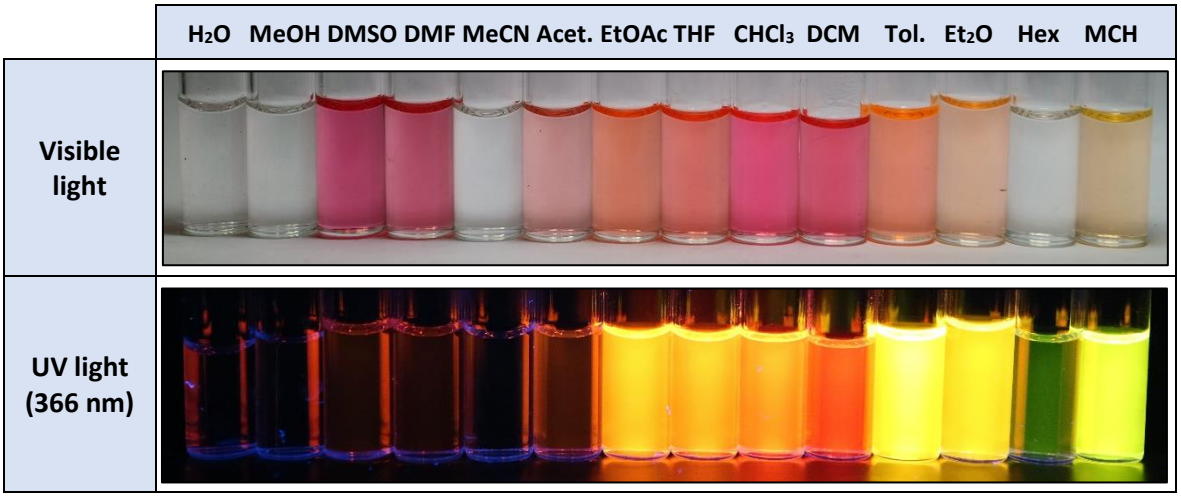

Figure 36. Solvatochromism of AR48 under visible and 366 nm light.

Fluorescence decay lifetime (τ):

The solvent used was hexane. The concentration of the compound was 20 µM.

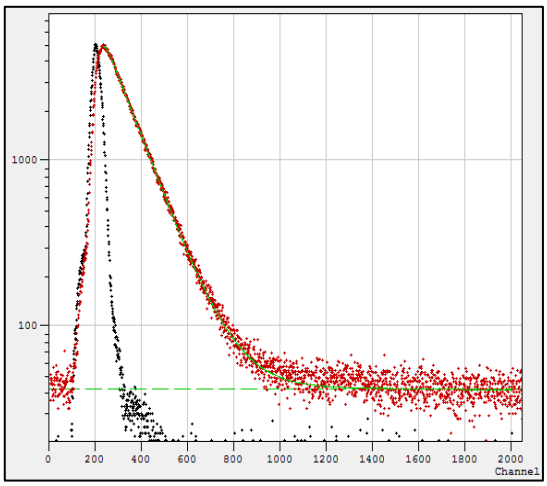

Figure 37. Fluorescence decay lifetime of AR48.

Water acceptance test:

The amount of water was increasing from 0% (R) to 90%. The solvent used was THF and the concentration of the compound was 20 µM.

	R	5%	10%	20%	30%	40%	50%	60%	70%	80%	90%
Visible light											
UV light (366 nm)	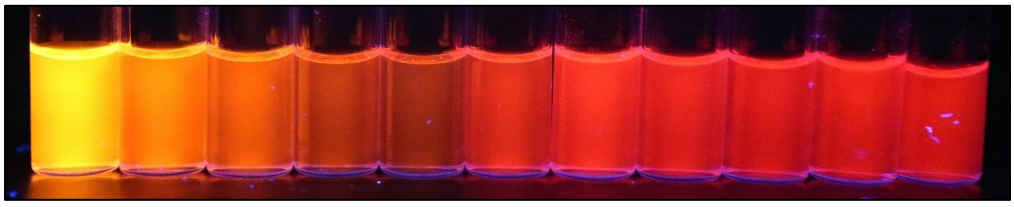										

Figure 38. Water acceptance test of AR48 under visible (up) and UV (down) light.

There was a quenching of fluorescence up to 40% of water, after which red fluorescence was observed due to the formation of nanoparticles (AIE). The emission maximum was shifted from the orange (615-625 nm) to the red (630-640 nm) region, while the intensity of fluorescence was remained constant.

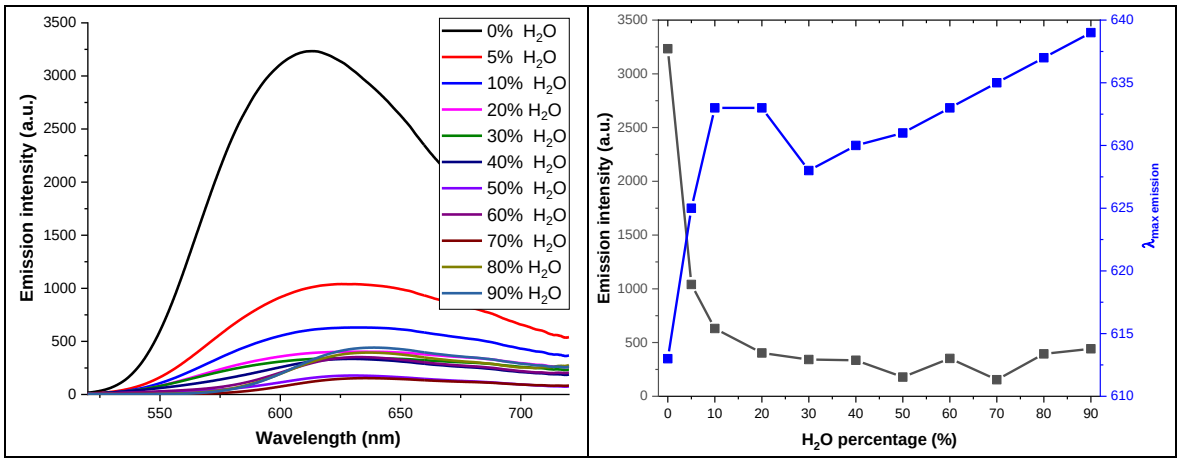

Figure 39. Emission intensity graph (left) and graph of relationship between the emission intensity and the wavelenght of the maximum of emission (right) as a function of the amount of water added for AR48.

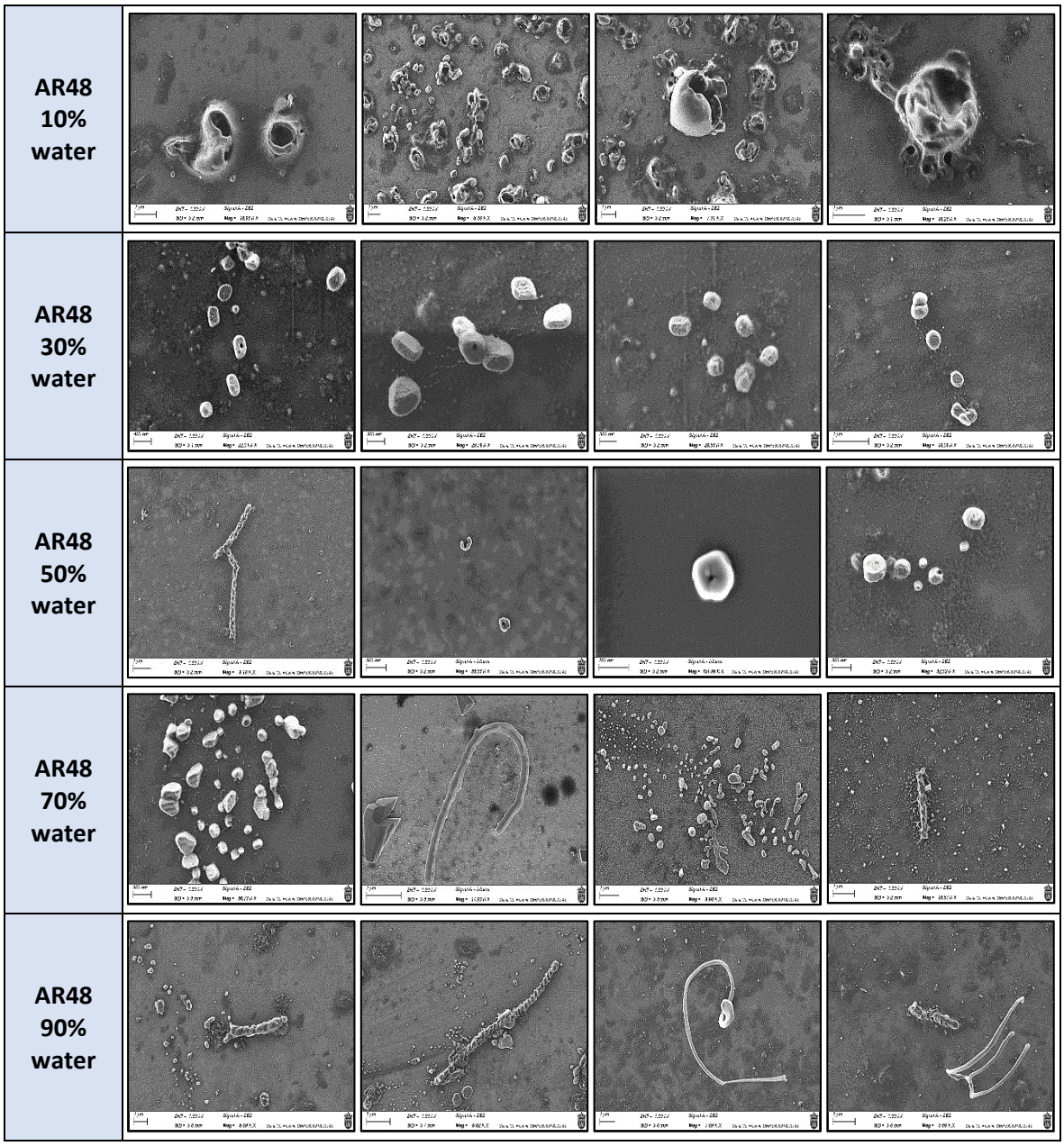

Figure 40. SEM nanoparticles of AR48 in different mixtures of THF-H_2O.

pH test:

For this test, the proportion of water that the compound could accept according to the previous water acceptance test was 10% The concentration of the compound was 20 µM and the solvent used was THF.

	R	HCl	3.4	4.8	6.4	7.4	7.9	10.5	KOH
Visible light									
UV light (366 nm)	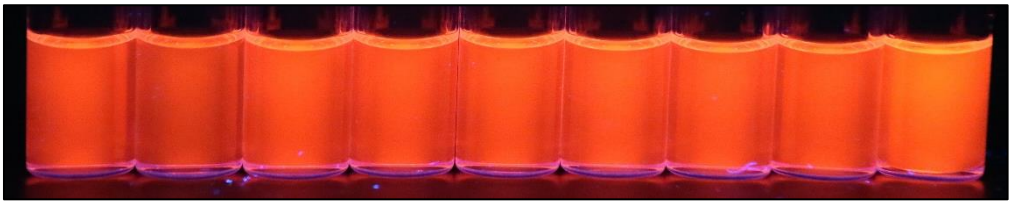								

Figure 41. pH test of AR48 under visible (up) and UV (down) light.

No significant changes were observed.

Cations and anions test:

The concentration of the compound was 20 µM and the solvent used was THF.

	R	Ag^{+}	Ni^{2+}	Sn^{2+}	Cd^{2+}	Zn^{2+}	Pb^{2+}	Cu^{2+}	Fe^{3+}	Sc^{3+}	Al^{3+}	Hg^{2+}	Au^{3+}	Co^{2+}	Pd^{2+}	Ir^{3+}	Cu^{+}	Ru^{3+}	Pt^{2+}
Visible light																			
UV light (366 nm)	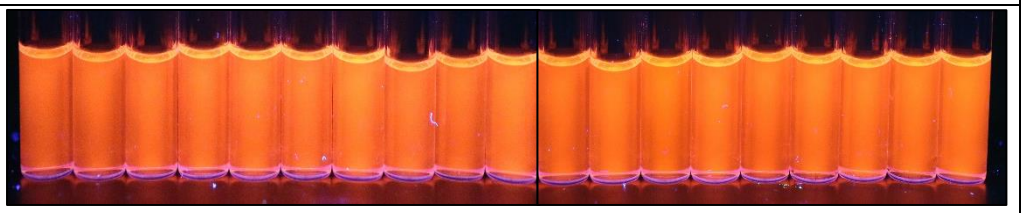																		

Figure 42. Cations test of AR48 under visible (up) and UV (down) light.

No significant changes were observed.

The concentration of the compound was 20 µM and the solvent used was THF.

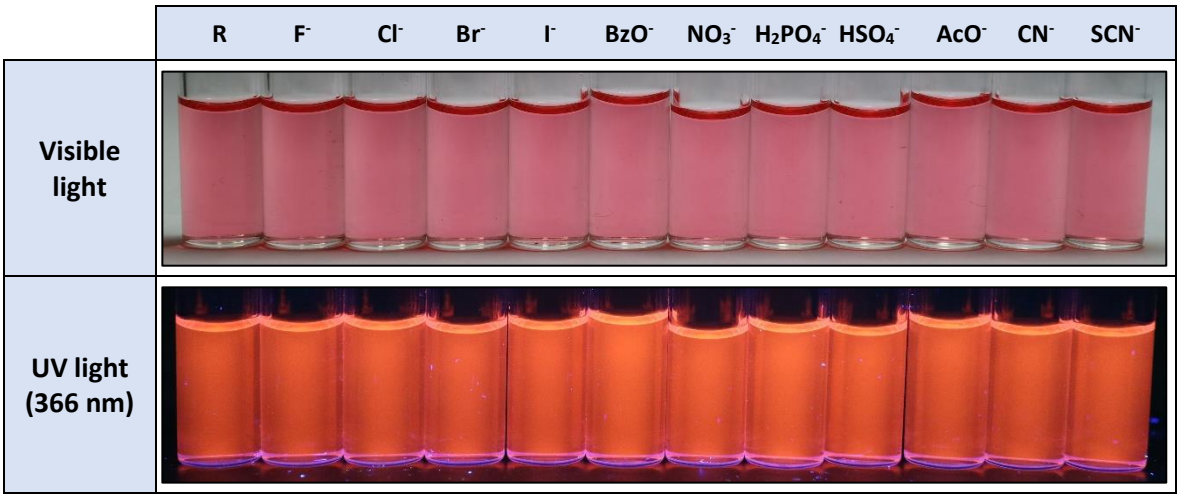

Figure 43. Anions test of AR48 under visible (up) and UV (down) light.

No significant changes were observed.

Oxidant and reductant reagents test:

The solvent used was THF and concentration of the compound was 20 µM.

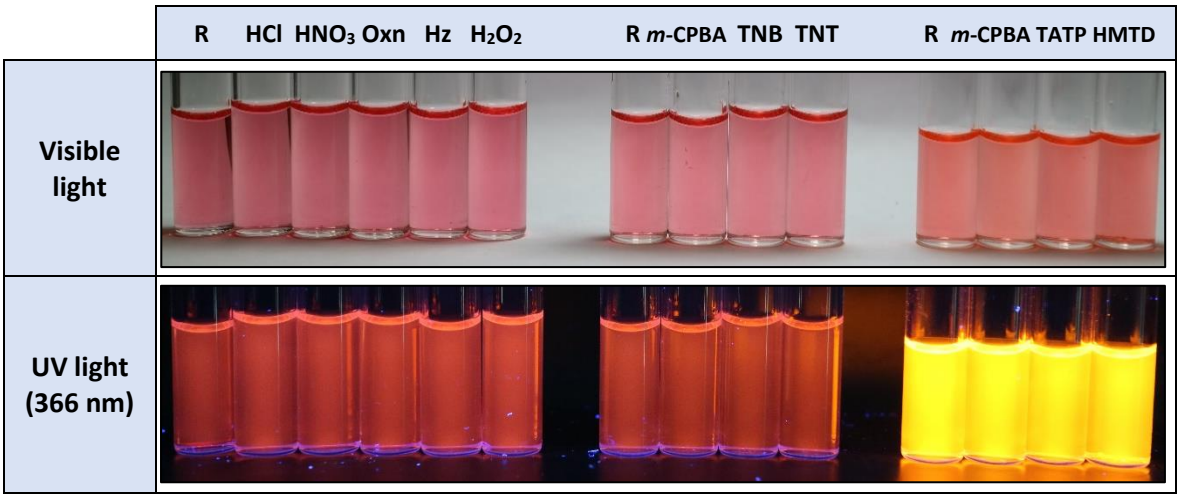

Figure 44. Oxidant and reductant reagents test of AR48 under visible (up) and UV (down) light.

No significant changes were observed.

AR49

m.p.: 230-231°C (decomposition).

IR (ATR, cm^{-1}): 2957-2846, 1692 (C=O), 1652 (C=O), 1592, 1571, 1347, 1290, 1241, 1176 (C-N), 1095, 1050 (-CH_3), 837, 808, 751, 432.

^{1}H-NMR (300 MHz, $CDCl_3$) δ (ppm): 8.51 (m, 4H, 4×**H$_{Ar}$**), 8.32 (m, 3H, 3×**H$_{Ar}$**), 8.18 (m, 3H, 3×**H$_{Ar}$**), 8.03(m, 2H, 2×**H$_{Ar}$**), 7.72 (m, 2H, 2×**H$_{Ar}$**), 7.50 (d, *J* = 8.3 Hz, 1H, **H$_{Ar}$**), 7.37 (t, *J* = 7.8 Hz, 1H, **H$_{Ar}$**), 5.16 (q, *J* = 7.1 Hz, 1H, C**H**), 4.17 (hept, *J* = 6.8 Hz, 1H, C**H**), 3.95 (hept, *J* = 6.9 Hz, 1H, C**H**), 2.01 (s, 3H, 3×C**H**), 1.88 (d, *J* = 12.1 Hz, 3H, C**H**$_3$), 1.74 (m, 12H, 6×C**H**$_2$), 1.57 (d, *J* = 6.8 Hz, 6H, 2×C**H**$_3$), 1.47 (d, *J* = 6.9 Hz, 6H, 2×C**H**$_3$).

^{13}C-NMR (75MHz, $CDCl_3$) δ (ppm): 165.9 (**C**=O), 165.1 (**C**=O), 143.0 (**C**$_{Ar}$), 142.7 (**C**$_{Ar}$), 142.2 (**C**$_{Ar}$), 137.1 (**C**$_{Ar}$), 134.3 (**C**$_{Ar}$), 132.2 (**C**$_{Ar}$H), 131.4 (**C**$_{Ar}$H), 130.0 (**C**$_{Ar}$H), 129.8 (**C**$_{Ar}$H), 129.5 (**C**$_{Ar}$), 128.6 (**C**$_{Ar}$), 128.4 (**C**$_{Ar}$), 128.1 (**C**$_{Ar}$), 127.9 (**C**$_{Ar}$), 127.2 (**C**$_{Ar}$H), 126.7 (**C**$_{Ar}$), 125.9 (**C**$_{Ar}$), 125.7 (**C**$_{Ar}$), 125.5 (**C**$_{Ar}$H), 125.2 (**C**$_{Ar}$H), 125.1 (**C**$_{Ar}$H), 123.8 (**C**$_{Ar}$H), 123.3 (**C**$_{Ar}$H), 123.0 (**C**$_{Ar}$H), 122.6 (**C**$_{Ar}$H), 122.1 (**C**$_{Ar}$H), 121.3 (**C**$_{Ar}$), 120.5 (**C**$_{Ar}$H), 120.3 (**C**$_{Ar}$H), 58.2 (**C**H), 40.4 (**C**H$_2$), 38.2 (**Cq**), 37.2 (**C**H$_2$), 28.9 (**C**H), 24.3 (**C**H$_3$), 13.3 (**C**H$_3$).

HRMS (MALDI, DCTB+) m/z: calculated for $C_{56}H_{49}NO_2$: 767.3758 (M^+); found 767.3774.

UV-Vis ($CHCl_3$), λ_{max} nm (log ε): 514 (5.5).

Ø (Hex, %): 85.49.

τ (475 nm, Hex, ns): 3.461 (χ^2: 1.004).

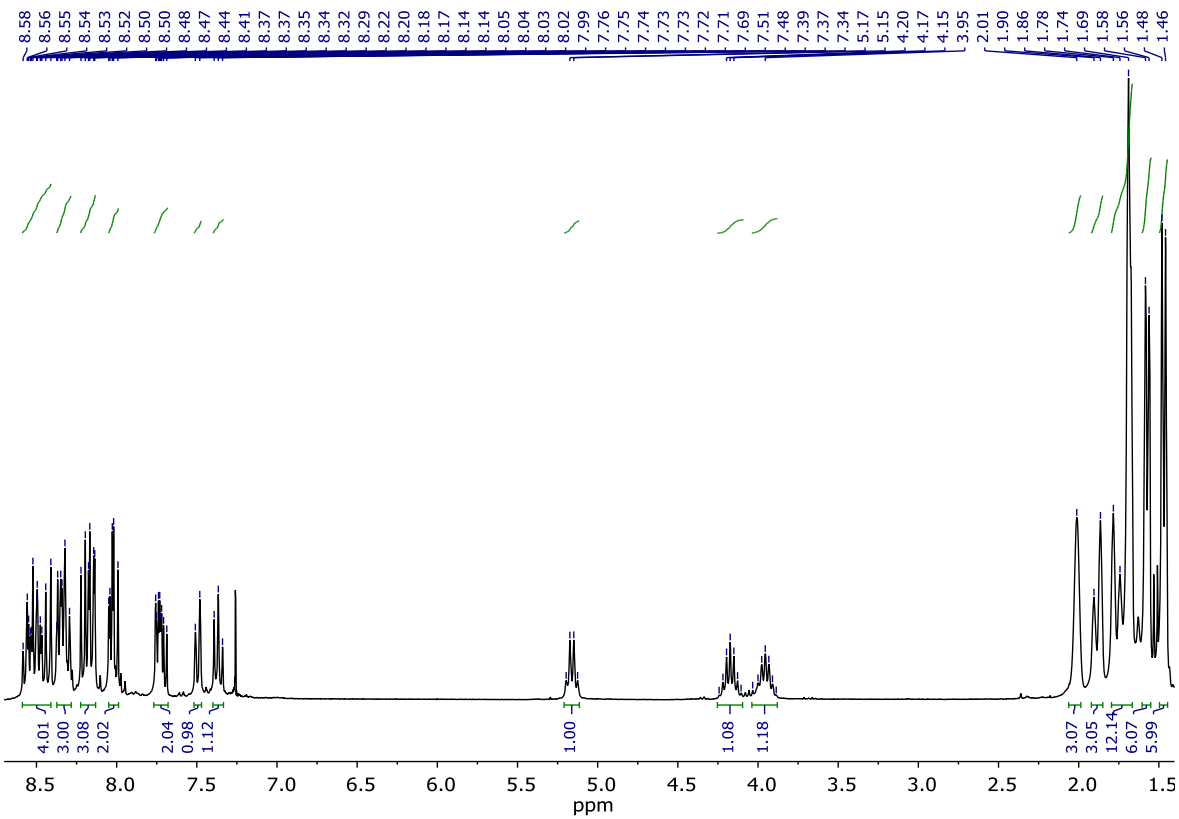

Figure 45. ^{1}H-NMR ($CDCl_3$, 300 MHz) of AR49.

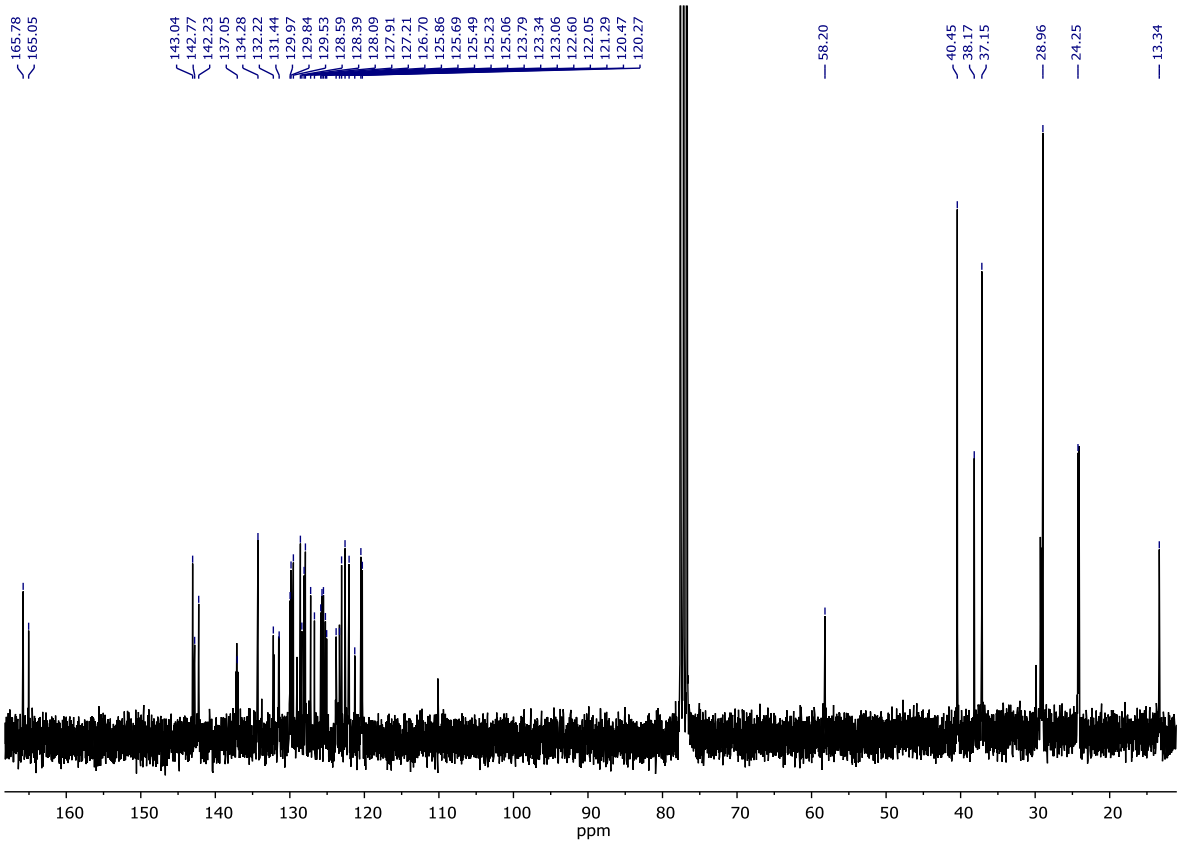

Figure 46. ^{13}C-NMR ($CDCl_3$, 75 MHz) of AR49.

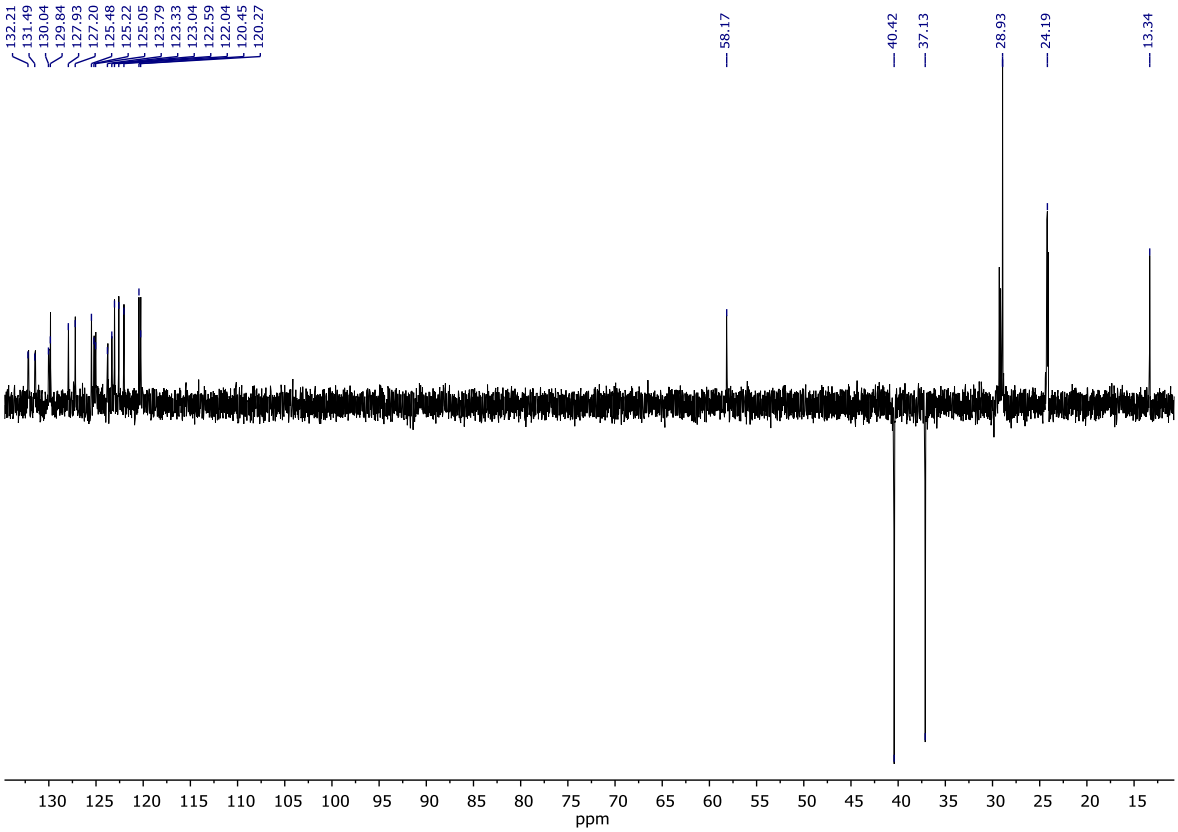

Figure 47. DEPT NMR ($CDCl_3$, 75 MHz) of AR49.

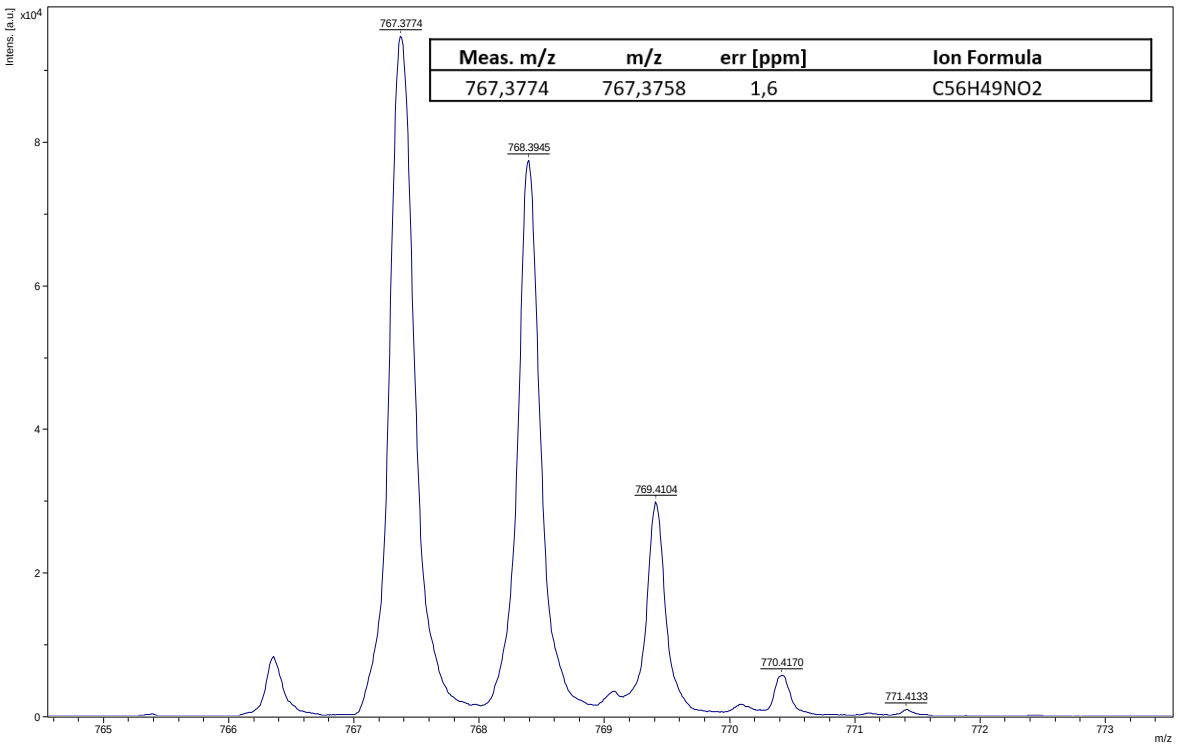

Meas. m/z	m/z	err [ppm]	Ion Formula
767,3774	767,3758	1,6	C56H49NO2

Figure 48. HRMS (MALDI, DCTB+) of AR49.

Fluorescence decay lifetime (τ):

The solvent used was hexane. The concentration of the compound was 20 µM.

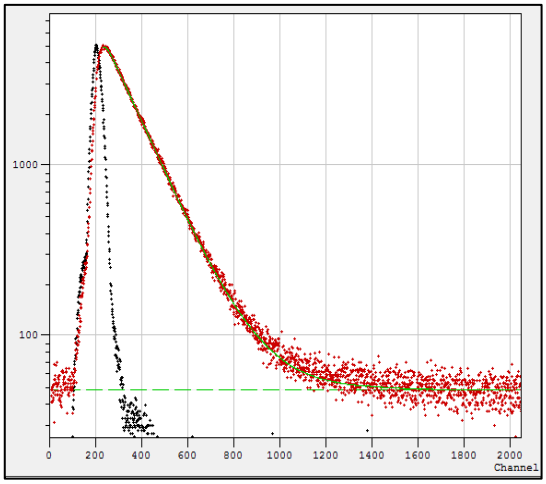

Figure 49. Fluorescence decay lifetime of AR49.

Solvatochromism:

The concentration of the compound was 20 µM and the excitation wavelength was 500 nm.

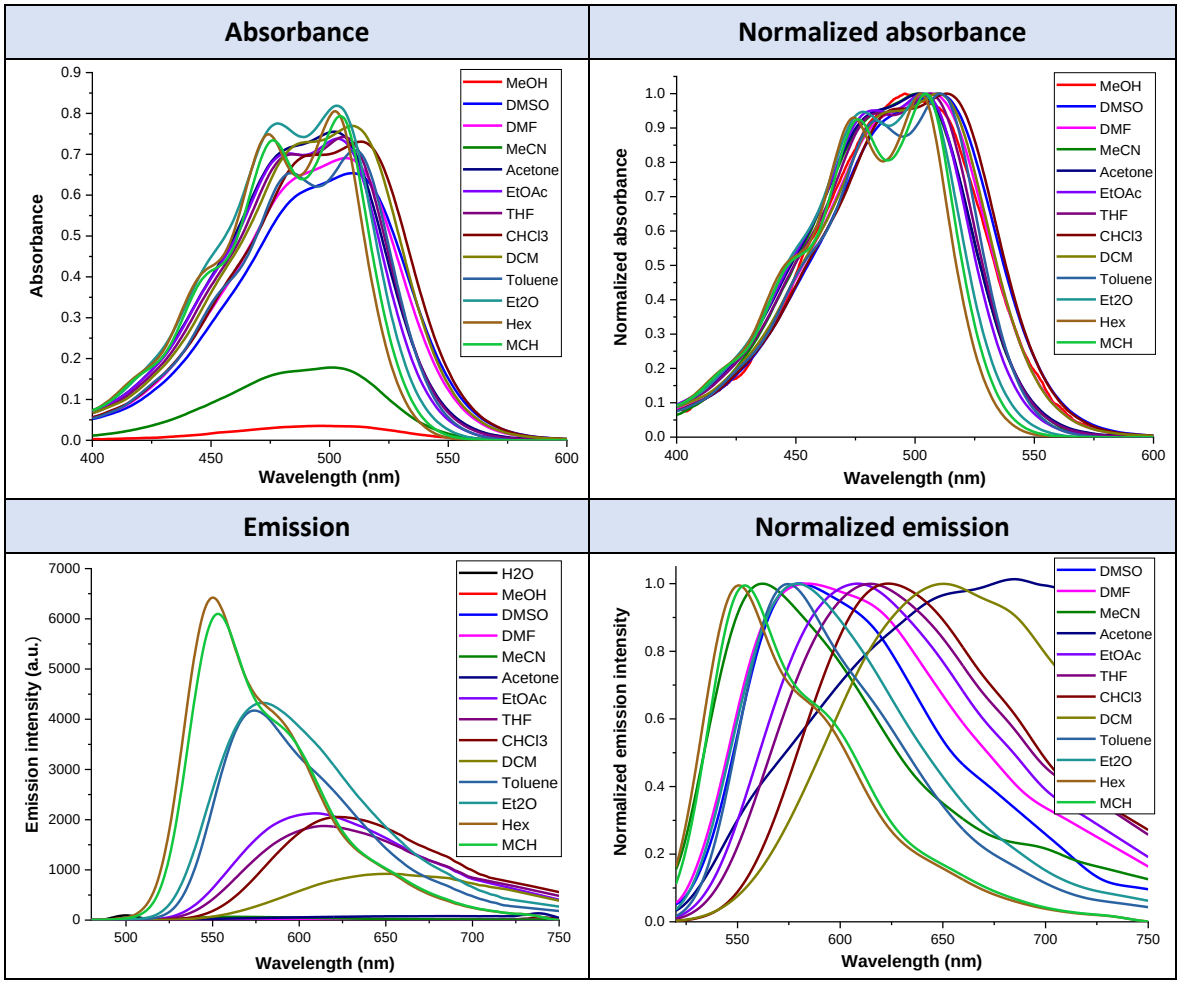

Figure 50. Solvatochromism of AR49.

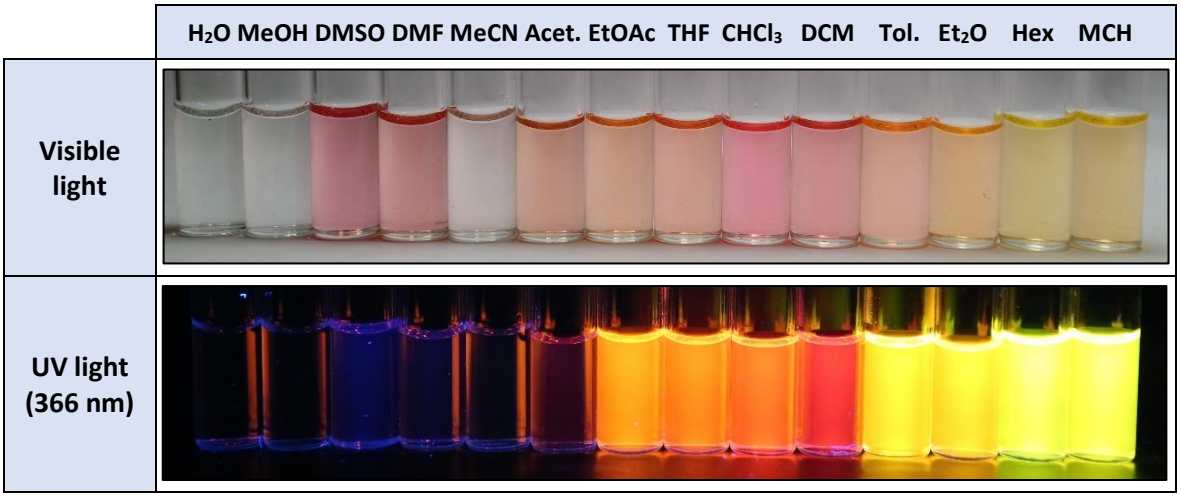

Figure 51. Solvatochromism of AR49 under visible and 366 nm light.

Water acceptance test:

The solvent used was THF and the concentration of the compound was 20 µM.

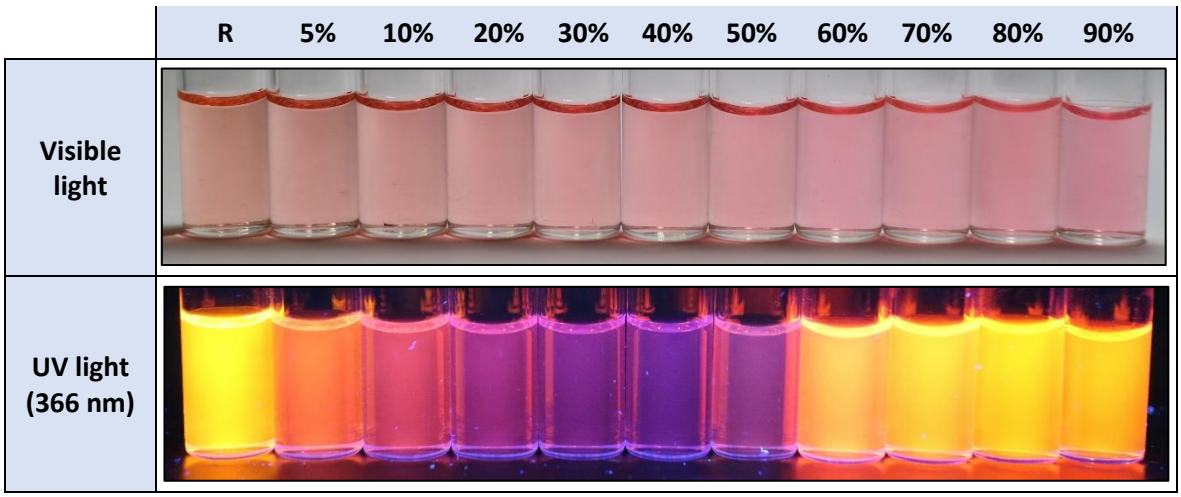

Figure 52. Water acceptance test of AR49 under visible (up) and UV (down) light.

There was a quenching of fluorescence up to 60% of water, after which a yellow fluorescence was turned on due to the formation of organic nanoparticles (AIE).

Figure 53.

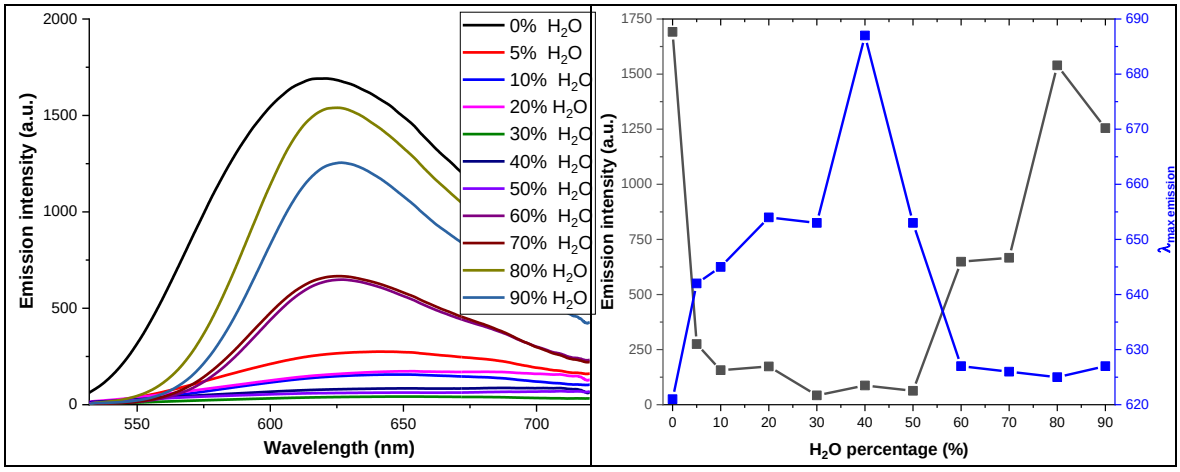

Figure 54. Emission intensity graph (left) and graph of relationship between the emission intensity and the wavelenght of the maximum of emission (right) as a function of the amount of water added for AR49.

The emission maximum was shifted from purple region (650-690 nm) to yellow region (620-630 nm). The fluorescence intensity was increased with a 60% of water.

SEM nanoparticles:

AR49 5% water	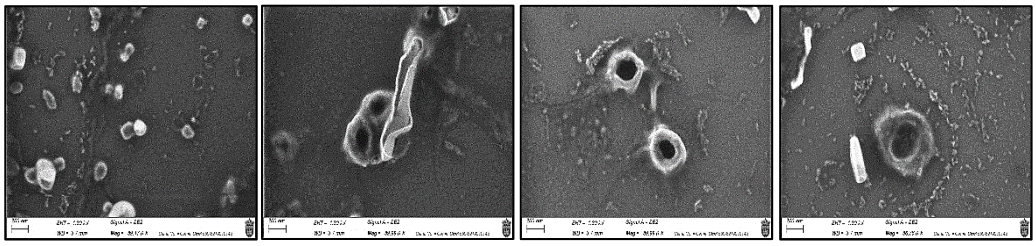
AR49 30% water	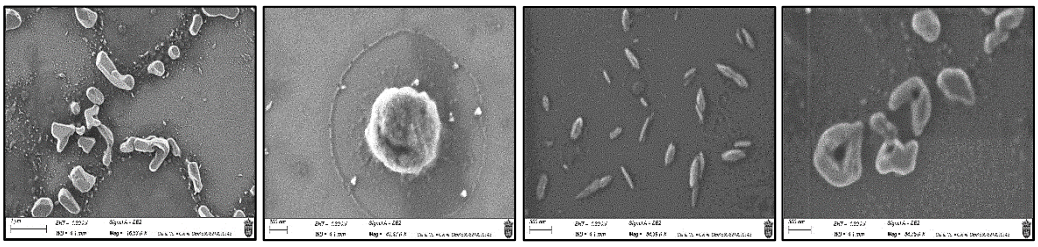
AR49 50% water	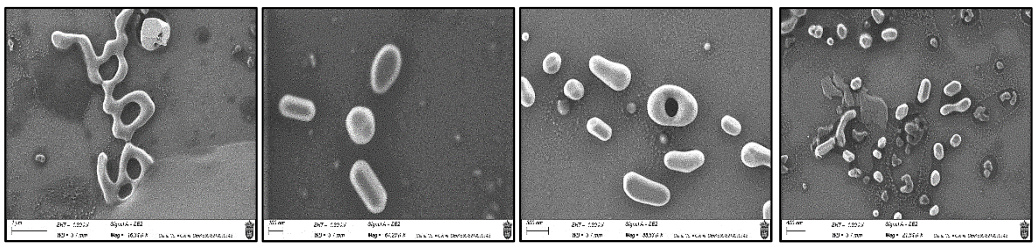
AR49 60% water	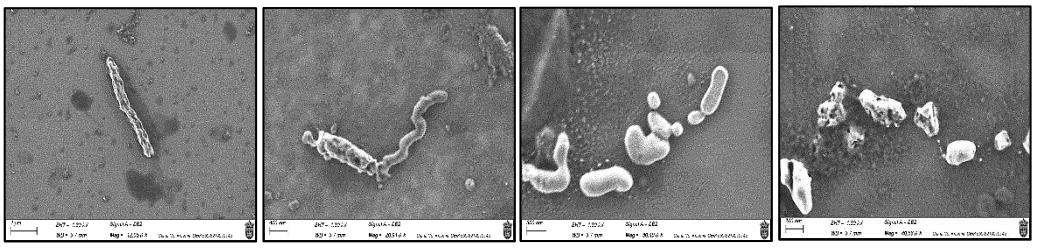
AR49 90% water	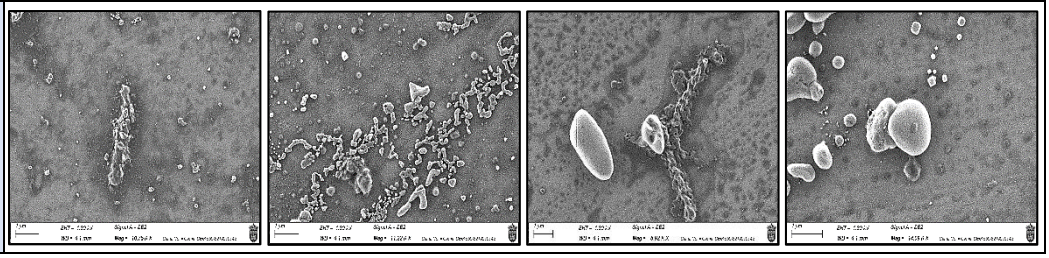

Figure 55. SEM nanoparticles of AR49 in different mixtures of THF-H_2O.

pH test:

For this test, the proportion of water that the compound could accept according to the previous water acceptance test was 10%. The concentration of the compound was 20 µM and the solvent used was THF.

	R	HCl	3.4	4.8	6.4	7.4	7.9	10.5	KOH
Visible light	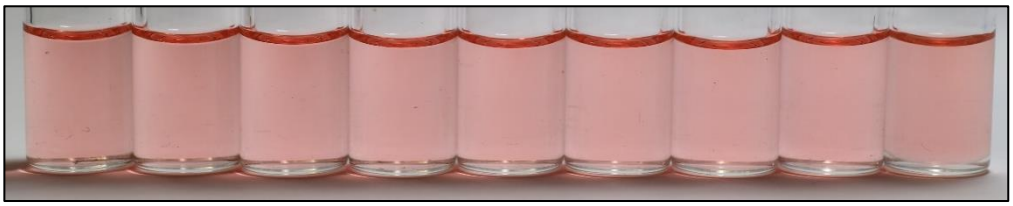								
UV light (366 nm)	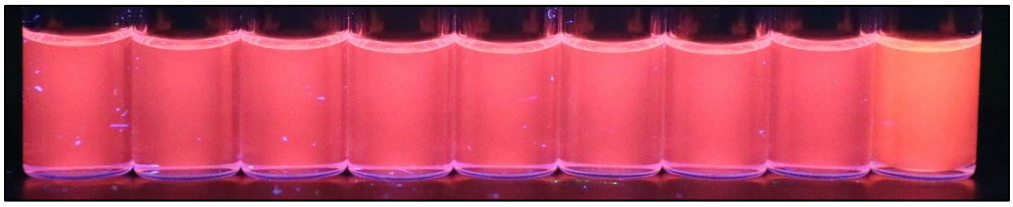								

Figure 56. pH test of AR49 under visible (up) and UV (down) light.

No significant changes were observed until very basic pH, where the fluorescence was turned orange.

Cations and anions test:

The concentration of the compound was 20 µM and the solvent used was THF.

	R	Ag^{+}	Ni^{2+}	Sn^{2+}	Cd^{2+}	Zn^{2+}	Pb^{2+}	Cu^{2+}	Fe^{3+}	Sc^{3+}	Al^{3+}	Hg^{2+}	Au^{3+}	Co^{2+}	Pd^{2+}	Ir^{3+}	Cu^{+}	Ru^{3+}	Pt^{2+}
Visible light																			
UV light (366 nm)	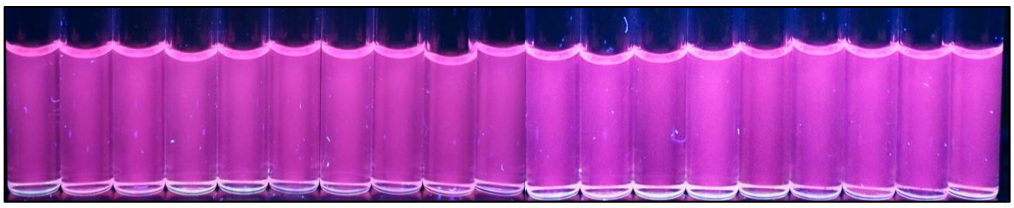																		

Figure 57. Cations test of AR49 under visible (up) and UV (down) light.

No significant changes were observed.

The concentration of the compound was 20 µM and the solvent used was THF.

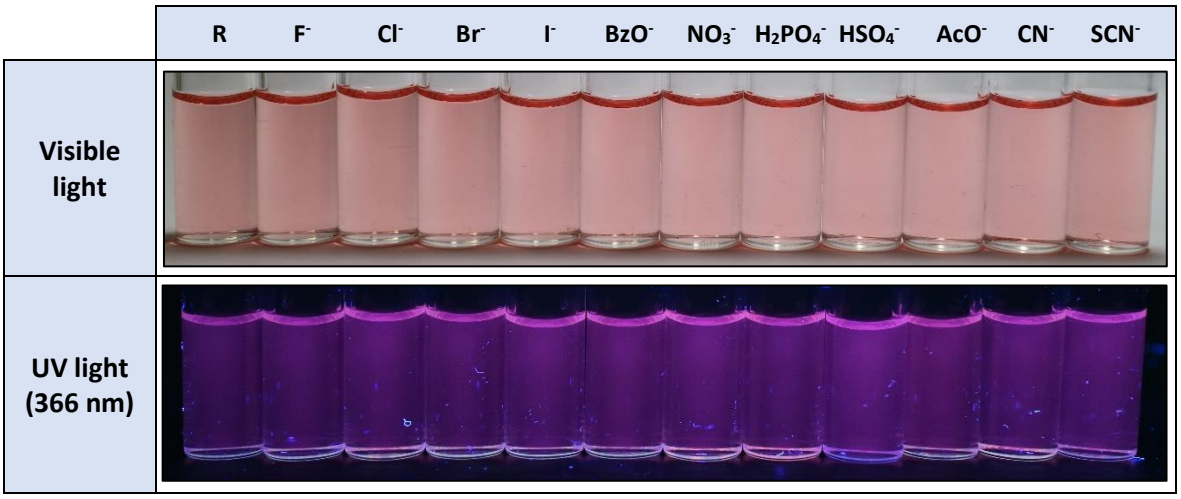

Figure 58. Anions test of AR49 under visible (up) and UV (down) light.

No significant changes were observed.

Oxidant and reductant reagents test:

The solvent used was THF and concentration of the compound was 20 µM.

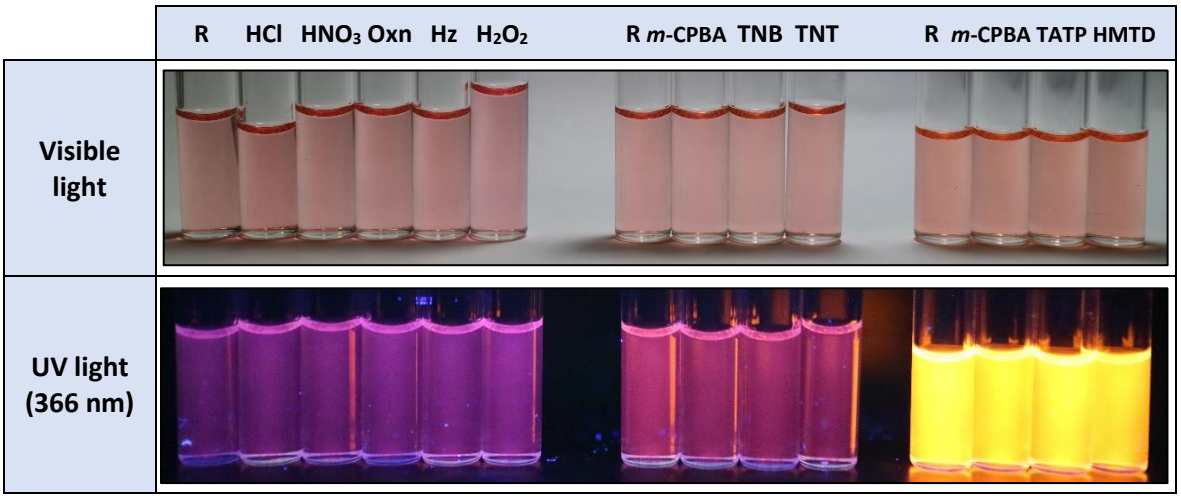

Figure 59. Oxidant and reductant reagents test of AR49 under visible (up) and UV (down) light.

No significant changes were observed.

Synthesis of *N*-(1-(1-adamantyl)ethyl)-9-[(4-phenyl)-2,2':6',2''-terpyridine]perylene-3,4-dicarboxylmonoimide (AR95).

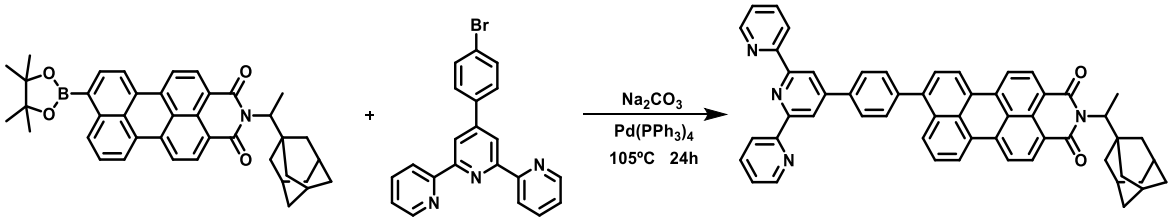

100 mg of *N*-(1-(1-adamantyl)ethyl)-9-(pinacolylboronate)perylene-3,4-dicarboxylmonoimide (AR01, 0.16 mmol), 76 mg of 4'-(4-bromophenyl)-2,2':6',2''-terpyridine (0.2 mmol), 105 mg of sodium carbonate (0.99 mmol) and 12 mg of $Pd(PPh_3)_4$ (0.01 mmol) were added under nitrogen atmosphere in a vial. Next, the solids were dissolved in a mixture of toluene:butanol:water (4:3:1 ml) and heated at 105°C for 24 hours. After that, the solvent was evaporated and the solid was dissolved in DCM and washed three times with water (3×100 ml). The organic extracts were combined, dried over Na_2SO_4 and the solvent was evaporated under reduced pressure. As a result, the product was obtained and purified by column chromatographic (SiO_2, DCM:MeOH), obtaining 21 mg of orange solid, 17% of purification yield.

m.p.: 211-213°C.

IR (ATR, cm^{-1}): 3051-2848, 1686 (C=O), 1650 (C=O), 1569, 1465, 1348, 1243, 1175 (C-N), 1037, 791, 755, 687, 657, 621.

^{1}H-NMR (300 MHz, $CDCl_3$) δ (ppm): 8.82 (s, 2H, 2×**H$_{Ar}$**), 8.76 – 8.72 (m, 2H, 2×**H$_{Ar}$**), 8.67 (d, *J* = 8.0 Hz, 2H, 2×**H$_{Ar}$**), 8.50-8.43 (m, 2H, 2×**H$_{Ar}$**), 8.33 (t, *J* = 8.4 Hz, 2H, 2×**H$_{Ar}$**), 8.24 (d, *J* = 8.2 Hz, 2H, 2×**H$_{Ar}$**), 8.06 (d, *J* = 8.2 Hz, 2H, 2×**H$_{Ar}$**), 7.97 (d, *J* = 8.4 Hz, 1H, **H$_{Ar}$**), 7.89 (td, *J* = 7.7, 1.8 Hz, 2H, 2×**H$_{Ar}$**), 7.67 (d, *J* = 8.2 Hz, 2H, 2×**H$_{Ar}$**), 7.59-7.50 (m, 2H, 2×**H$_{Ar}$**), 7.39-7.33 (m, 2H, 2×**H$_{Ar}$**), 5.12 (q, *J* = 7.3 Hz, 1H, C**H**), 1.99 (s, 3H, 3×C**H**), 1.86 (m, 3H, C**H**$_3$), 1.78-1.64 (m, 12H, 6×C**H**$_2$).

^{13}C-NMR (75MHz, $CDCl_3$) δ (ppm): 165.7 (**C**=O), 164.9 (**C**=O), 156.2 (**C**$_{Ar}$), 156.1 (**C**$_{Ar}$), 149.7 (**C**$_{Ar}$), 149.3 (**C**$_{Ar}$H), 142.4 (**C**$_{Ar}$), 140.7 (**C**$_{Ar}$), 138.2 (**C**$_{Ar}$), 137.0 (**C**$_{Ar}$H), 136.9 (**C**$_{Ar}$), 136.8 (**C**$_{Ar}$), 136.6 (**C**$_{Ar}$), 132.6 (**C**$_{Ar}$), 131.9 (**C**$_{Ar}$H), 131.2 (**C**$_{Ar}$H), 130.7 (**C**$_{Ar}$H), 129.7 (**C**$_{Ar}$), 129.5 (**C**$_{Ar}$), 129.0 (**C**$_{Ar}$), 128.8 (**C**$_{Ar}$), 128.4 (**C**$_{Ar}$), 128.3 (**C**$_{Ar}$H), 127.6 (**C**$_{Ar}$H), 127.1 (**C**$_{Ar}$H), 126.4 (**C**$_{Ar}$), 124.1 (**C**$_{Ar}$H), 123.7 (**C**$_{Ar}$H), 123.2 (**C**$_{Ar}$H), 122.0 (**C**$_{Ar}$), 121.9 (**C**$_{Ar}$), 121.5 (**C**$_{Ar}$H), 120.3 (**C**$_{Ar}$H), 120.1 (**C**$_{Ar}$H), 118.9 (**C**$_{Ar}$H), 58.1 (**C**$_{Ar}$H), 40.4 (**C**H$_2$), 38.2 (**Cq**), 37.2 (**C**H$_2$), 28.9 (**C**H), 13.4 (**C**H$_3$).

HRMS (MALDI, DIT+) m/z: calculated for $C_{55}H_{42}N_4O_2$: 791.3381 (M^++H); found 791.3371.

UV-Vis ($CHCl_3$), λ_{max} nm (log ε): 493 (4.5).

Ø ($CHCl_3$, %): 92.38.

τ (475 nm, $CHCl_3$, ns): 4.124 (χ^2: 1.046).

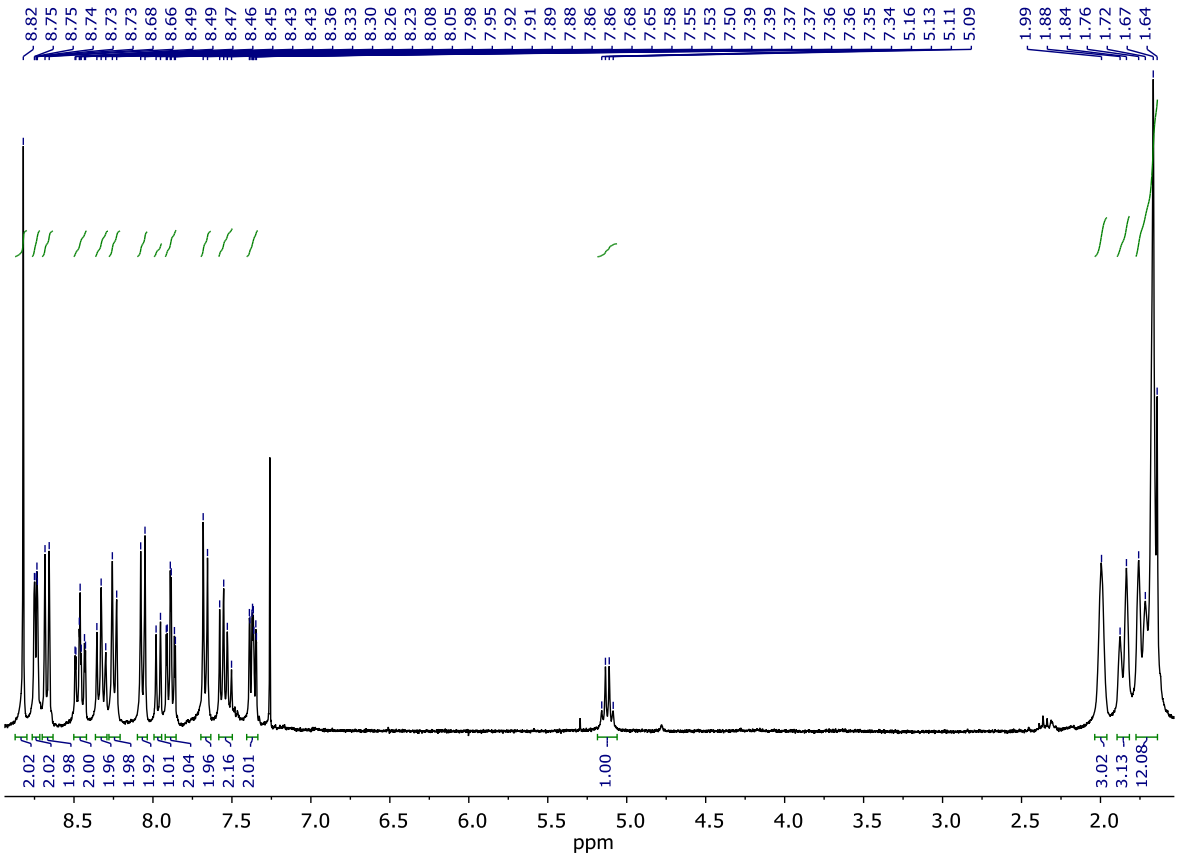

Figure 60. ^{1}H-NMR ($CDCl_3$, 300 MHz) of AR95.

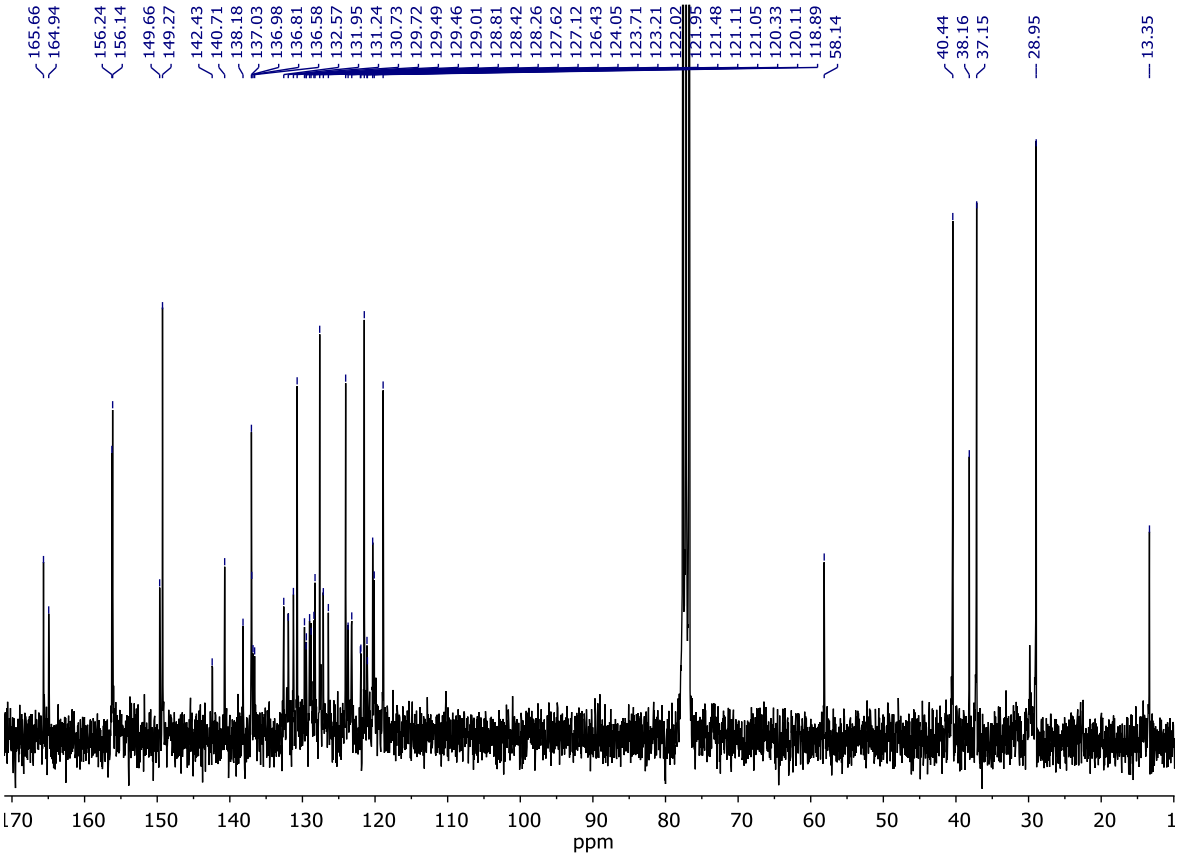

Figure 61. ^{13}C-NMR ($CDCl_3$, 75 MHz) of AR95.

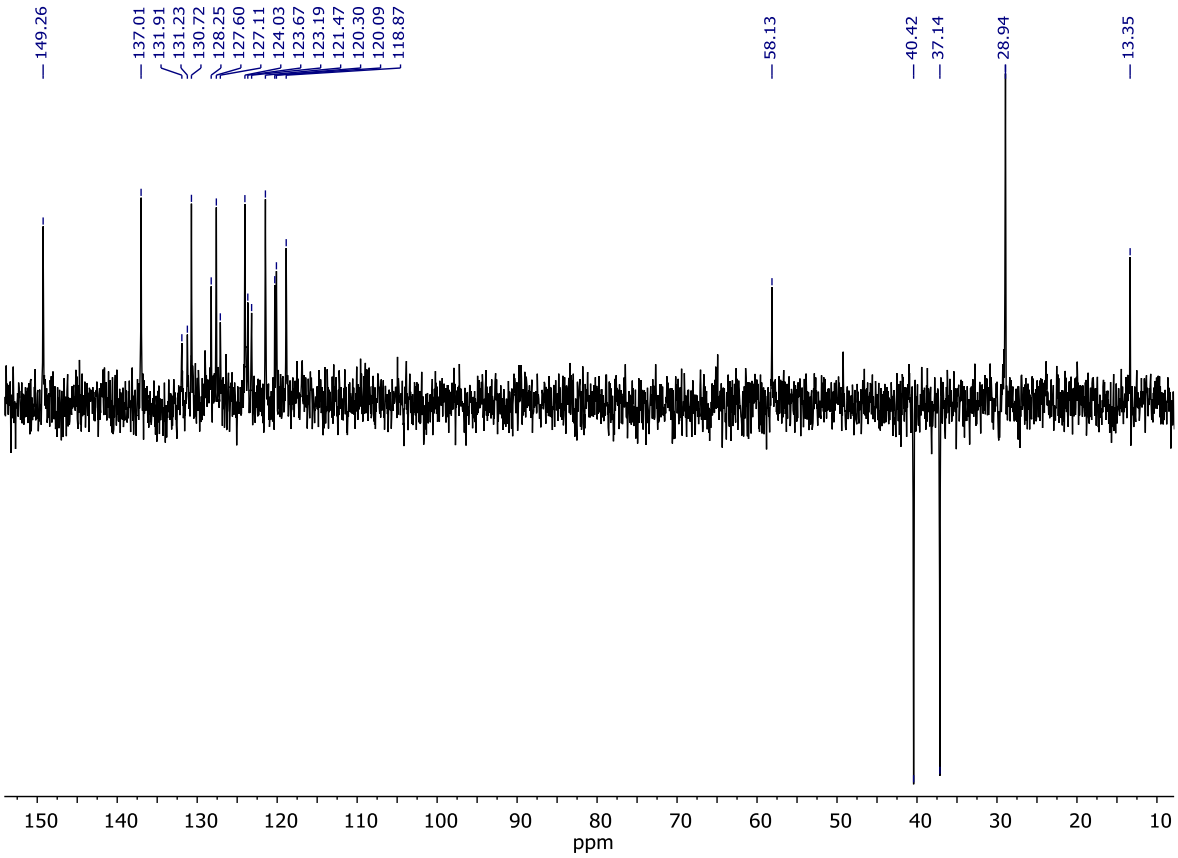

Figure 62. DEPT NMR ($CDCl_3$, 75 MHz) of AR95.

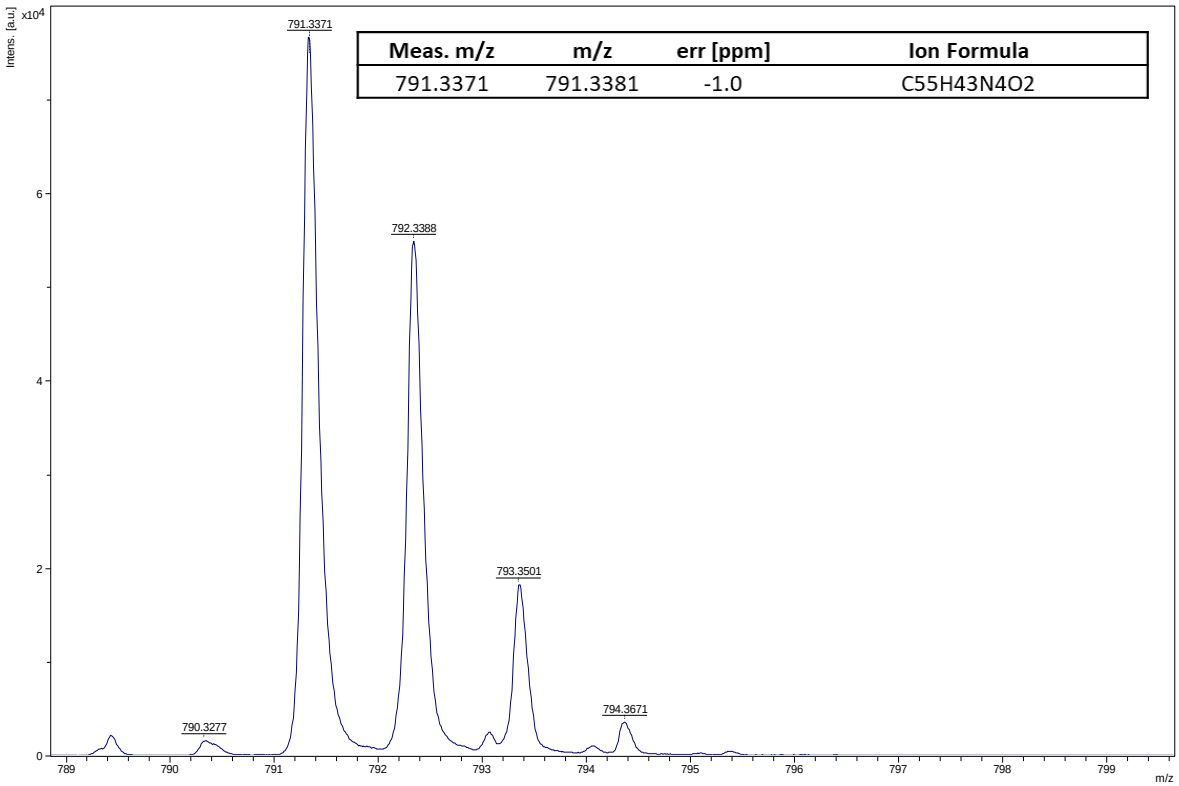

Meas. m/z	m/z	err [ppm]	Ion Formula
791.3371	791.3381	-1.0	C55H43N4O2

Figure 63. HRMS (MALDI, DIT+) of AR95.

Solvatochromism:

The concentration of the compound was 10 µM and the excitation wavelength was 480 nm.

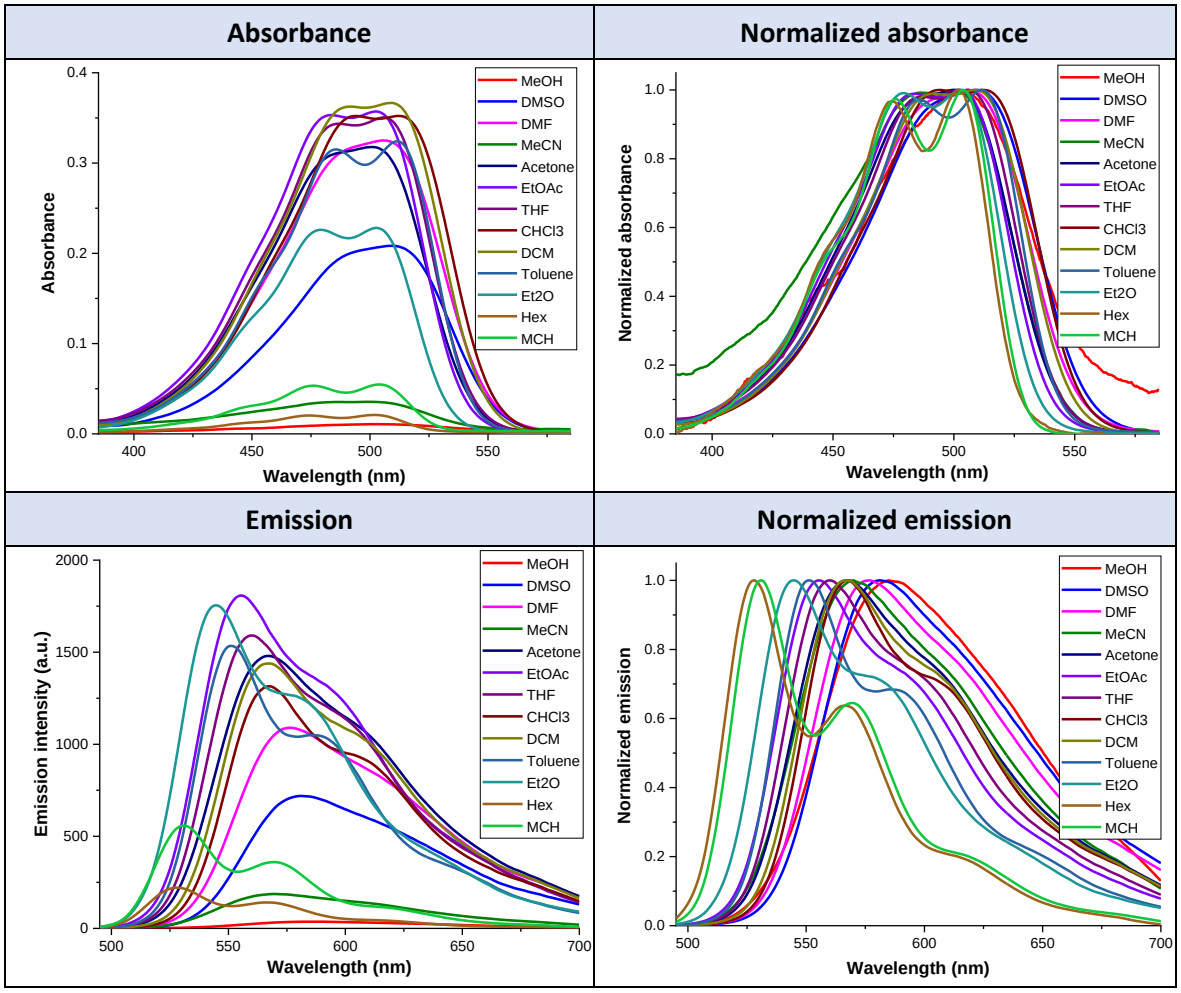

Figure 64. Solvatochromism of AR95.

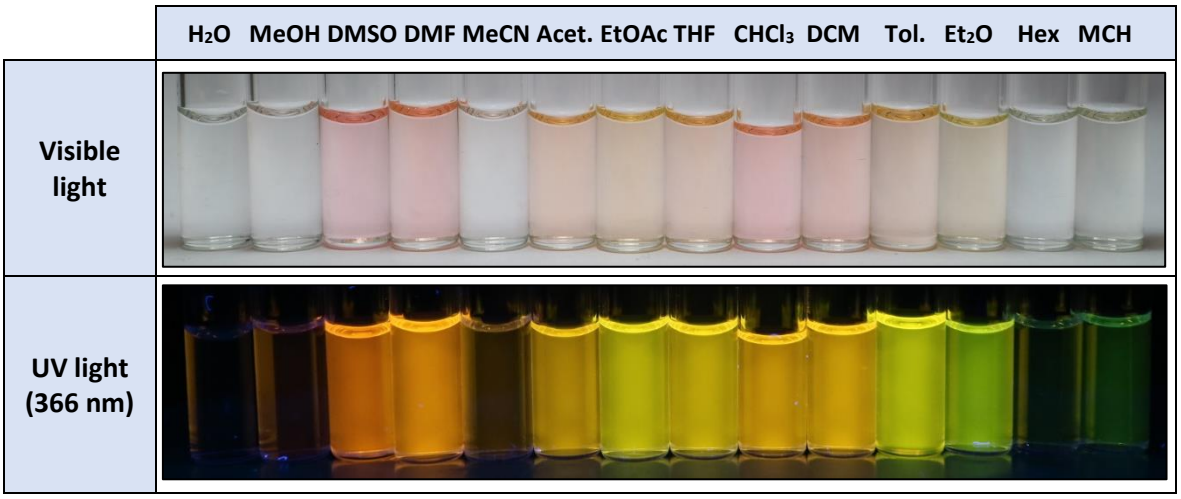

Figure 65. Solvatochromism of AR95 under visible and 366 nm light.

Fluorescence decay lifetime (τ):

The solvent used was chloroform. The concentration of the compound was 10 µM.

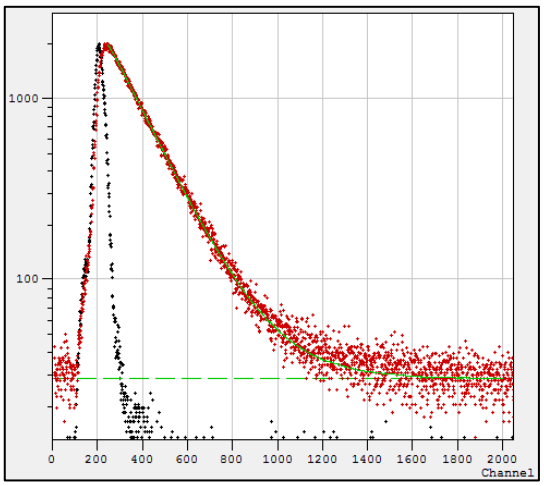

Figure 66. Fluorescence decay lifetime of AR95.

Water acceptance test:

The solvent used was THF and the concentration of the compound was 10 µM.

	R	5%	10%	20%	30%	40%	50%	60%	70%	80%	90%
Visible light	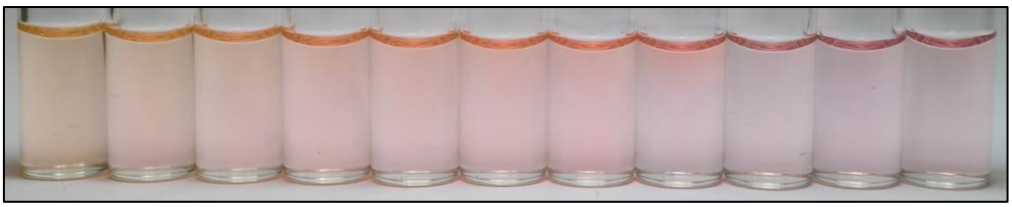										
UV light (366 nm)	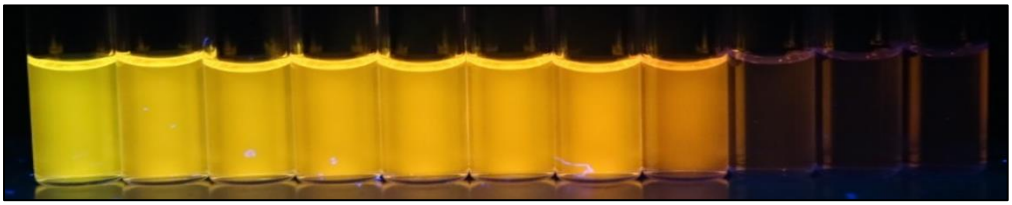										

Figure 67. Water acceptance test of AR95 under visible (up) and UV (down) light.

The maximum aumount of water that was admitted by the product was 60%. A quenching of fluorescence was ocurred due to the formation of aggregates (ACQ).

pH test:

For this test, the proportion of water that the compound could accept according to the previous water acceptance test was 60%. The concentration of the compound was 20 µM and the solvent used was THF.

	R	HCl	3.4	4.8	6.4	7.4	7.9	10.5	KOH
Visible light									
UV light (366 nm)									

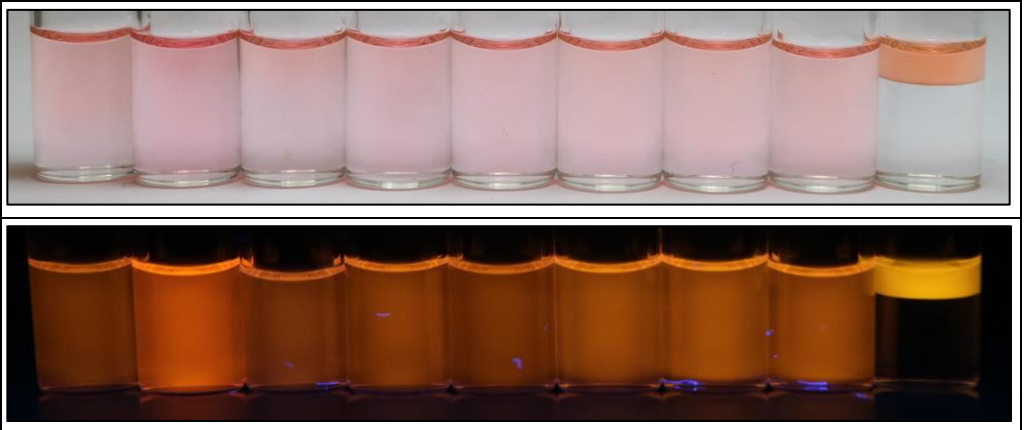

Figure 68. pH test of AR95 under visible (up) and UV (down) light.

The fluorescence of the product was been more orange at acidic pH, while it iwas been more yellowish in solutions with basic pH.

Cations and anions test:

The concentration of the compound was 10 µM and the solvent used was THF.

	R	Ag^{+}	Ni^{2+}	Sn^{2+}	Cd^{2+}	Zn^{2+}	Pb^{2+}	Cu^{2+}	Fe^{3+}	Sc^{3+}	Al^{3+}	Hg^{2+}	Au^{3+}	Co^{2+}	Pd^{2+}	Ir^{3+}	Cu^{+}	Ru^{3+}	Pt^{2+}
Visible light																			
UV light (366 nm)																			

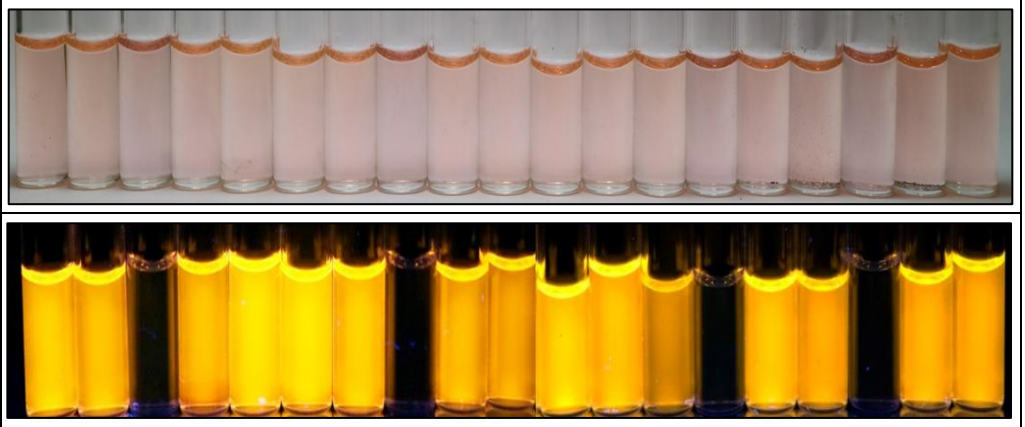

Figure 69. Cations test of AR95 under visible (up) and UV (down) light.

The product was experienced a quenching of fluorescence against the Ni^{2+}, Cu^{2+}, Co^{2+} and Cu^{+}.

The concentration of the compound was 20 µM and the solvent used was THF.

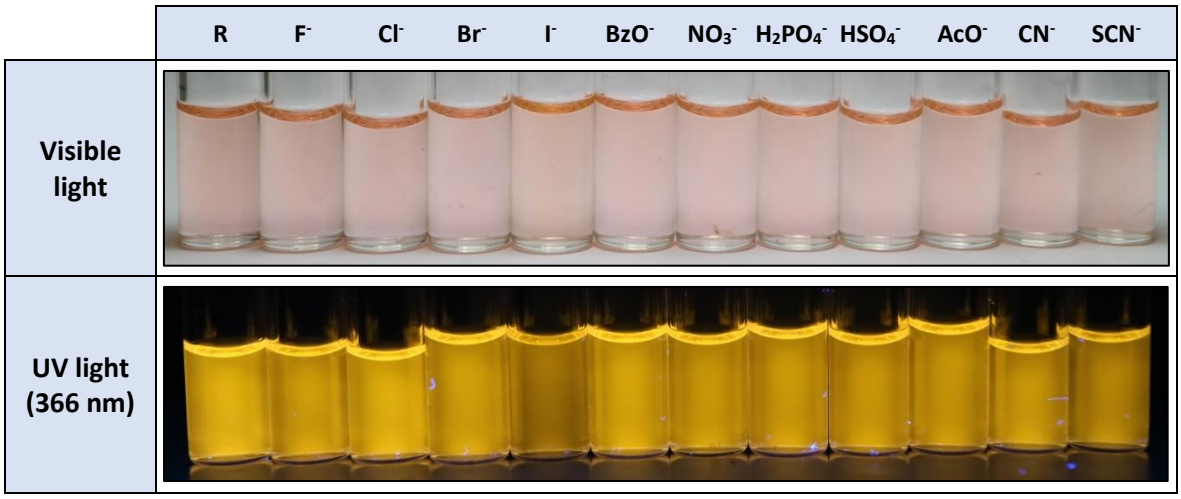

Figure 70. Anions test of AR95 under visible (up) and UV (down) light.

No significant changes were observed.

Oxidant and reductant reagents test:

The solvent used was THF and concentration of the compound was 10 µM.

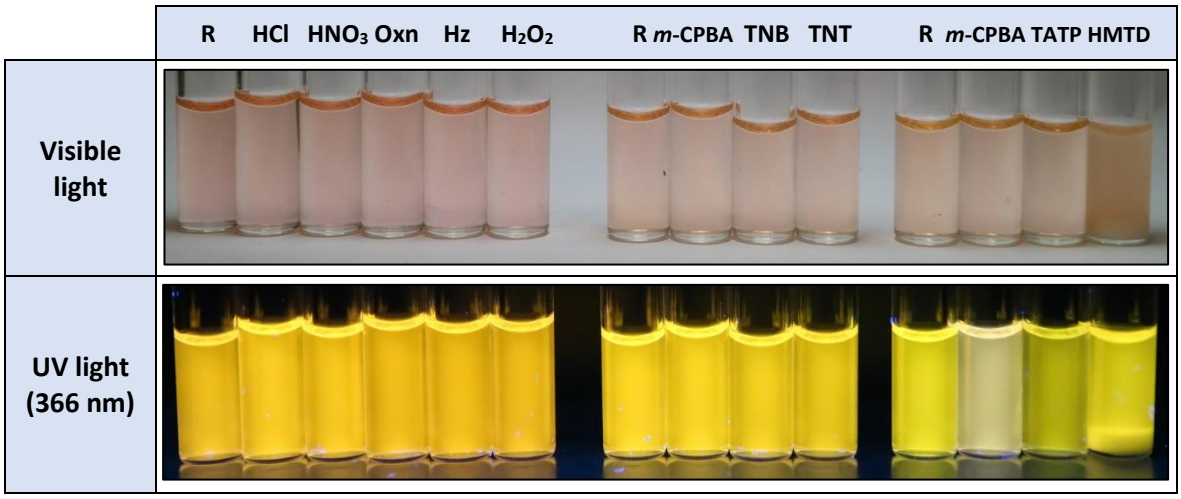

Figure 71. Oxidant and reductant reagents test of AR95 under visible (up) and UV (down) light.

The fluorescence of the product was turned green against TATP.

Previous solvents test:

In order to determine the fluorescence variation of the compound under study in the presence of TATP, some test were carried out for the probe in 9 different solvents. The AR95 concentration was 10 µM and the TATP was added in excess (7 mg in each vial). All the test were performed at room temperature and the photographs were taken immediately after the addition of the analyte and again after 24 hours.

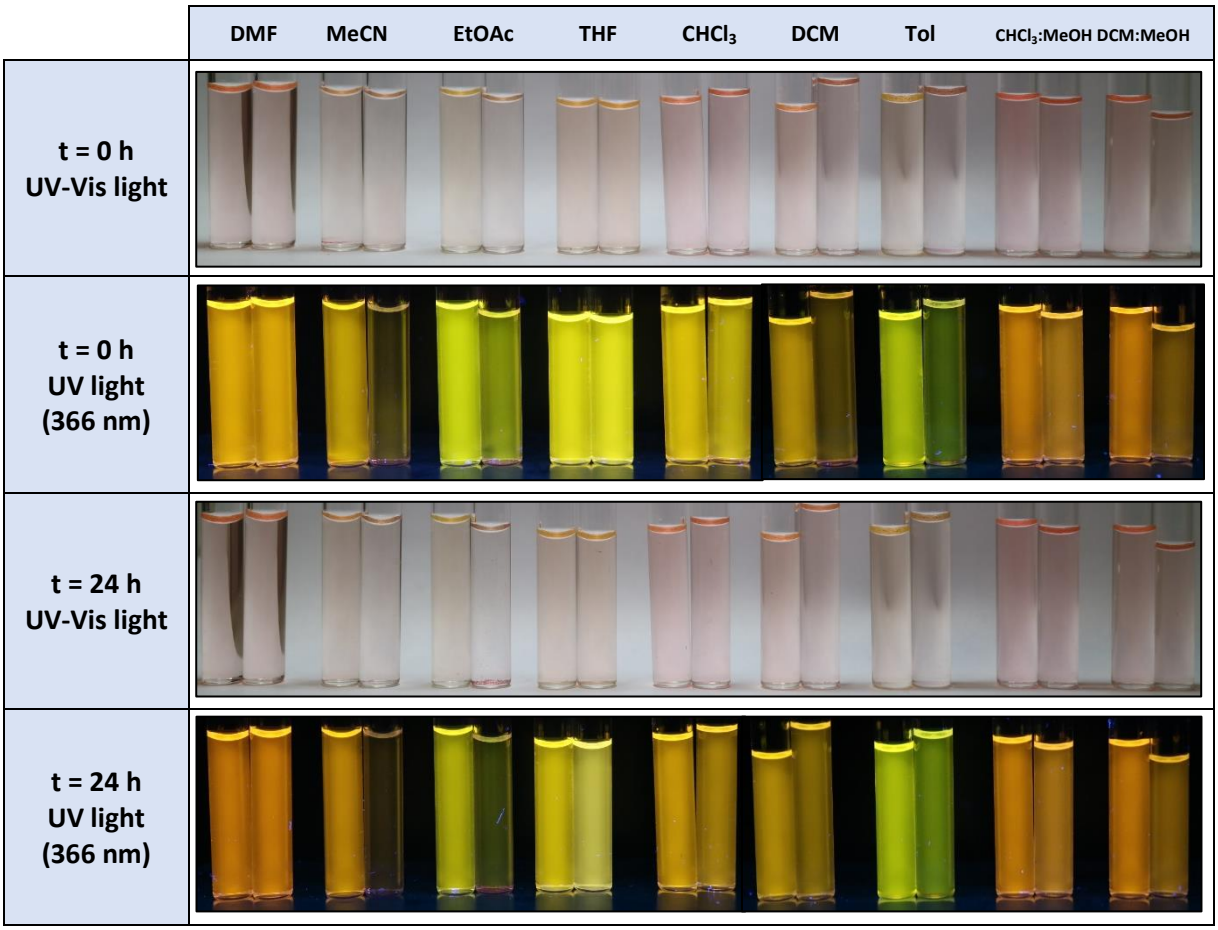

Figure 72. Pairs of AR95 (left) and AR95 with excess of TATP (right) in different solvents at time 0 h and 24 h.

The most significant changes were observed in MeCN, DCM and toluene.

Solvents test with TATP:

For all solvents, the working concentration of AR95 was 2.5 µM. In the kinetic studies, TATP was in excess but, in the titration, the TATP concentration was between 0 and 35000 µM. The excitation wavelenght was 480 nm for all experiments and the temperature for all test was 25°C.

Measurements were carried out immediately after the addition of TATP and the graphs were plotted at all emission maxima that were found.

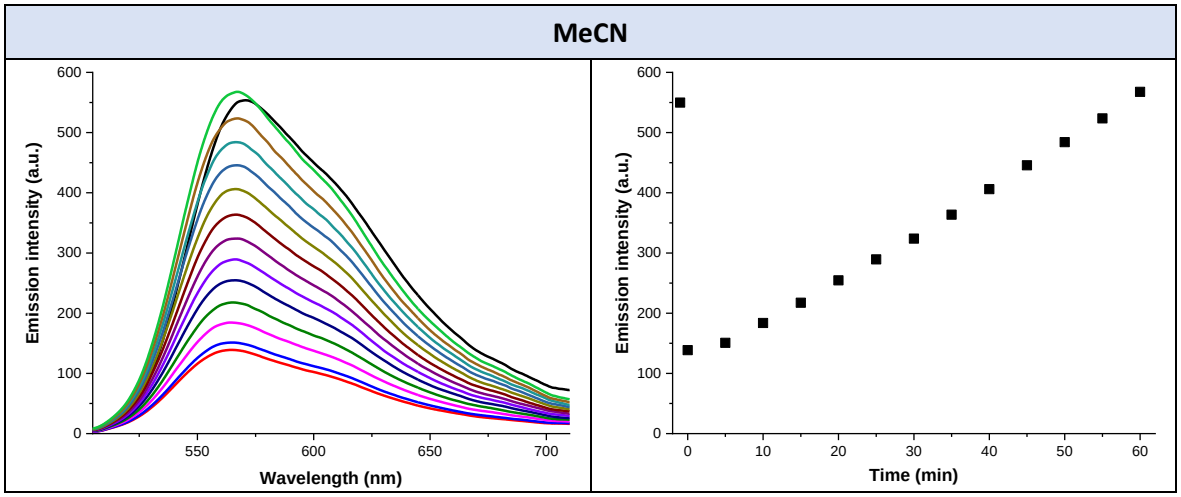

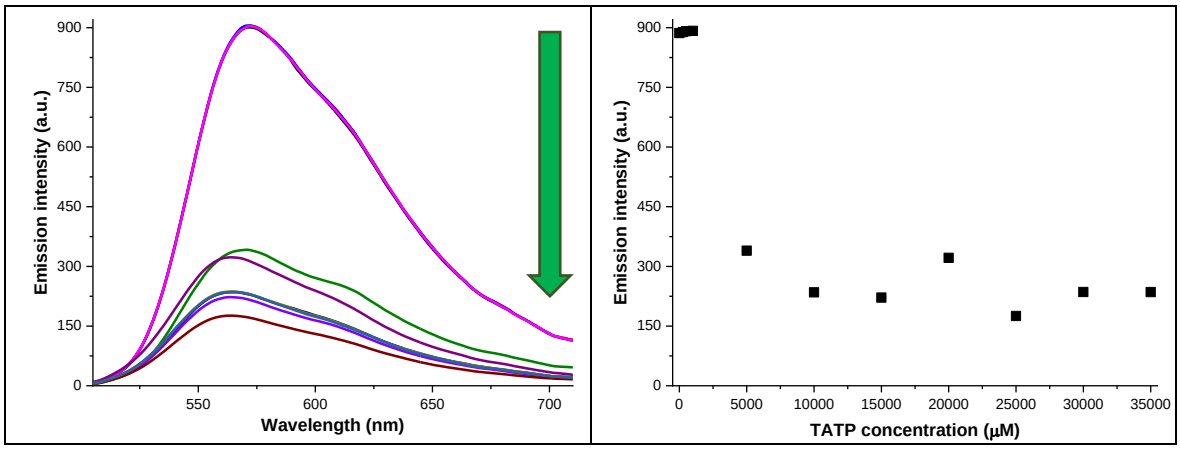

Figure 73. Study of AR95 with TATP in MeCN. Kinetic study (up left) and profile as function as time at 567 nm (up right) in presence of TATP excess. Titration (down left) and fluorescence profile at 567 nm (down right) under increasing concentrations of TATP.

There was a drop in the emission intensity immediately after adding TATP, following with a increase in the fluorescence emission The LOD of TATP was somewhere between 1000 and 5000 μM with a decrease in emission intensity.

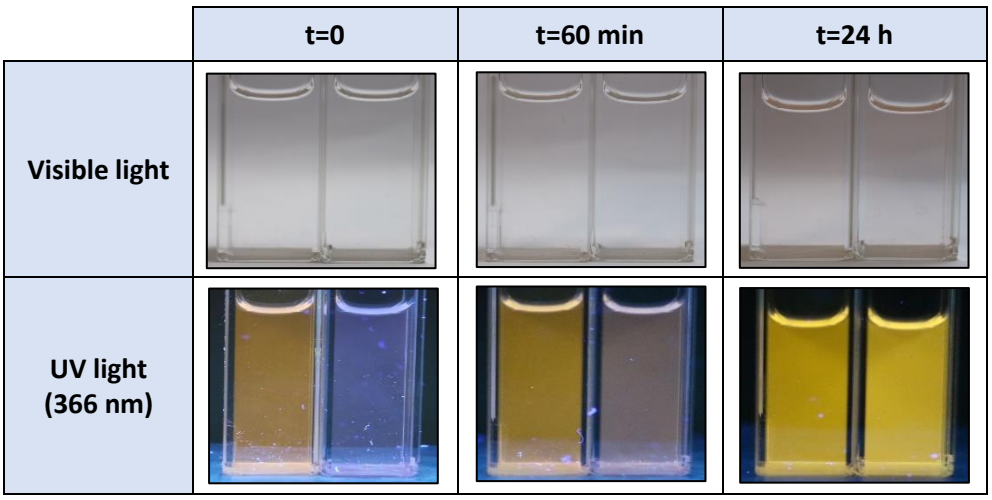

Figure 74. Kinetic study at different times under visible (up) and UV (down) light in MeCN. In each photo, left vial was contained the probe and right vial was contained the probe and an excess of TATP.

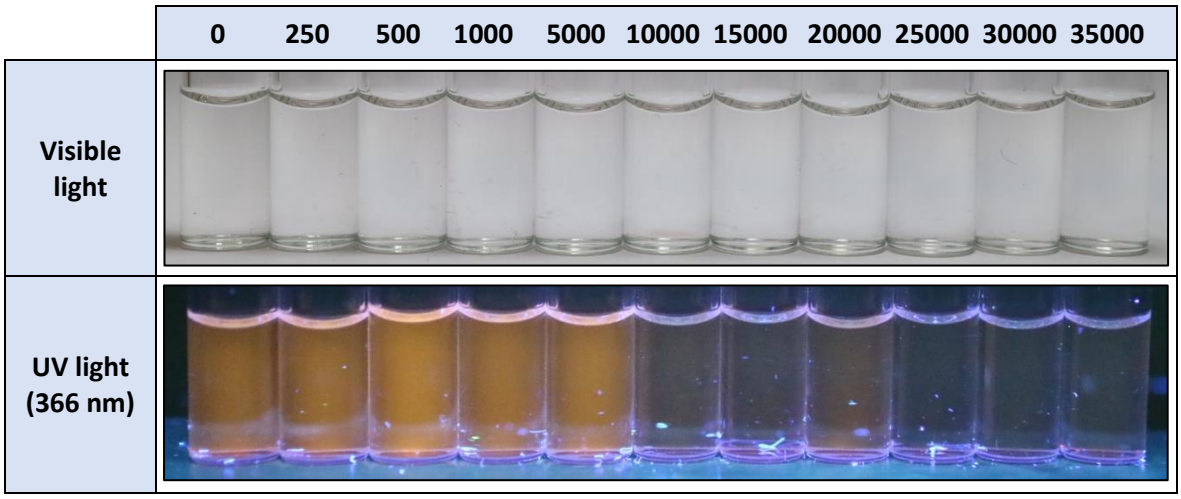

Figure 75. Titration of AR95 with an excess of TATP under visible (up) and UV (down) light in MeCN.

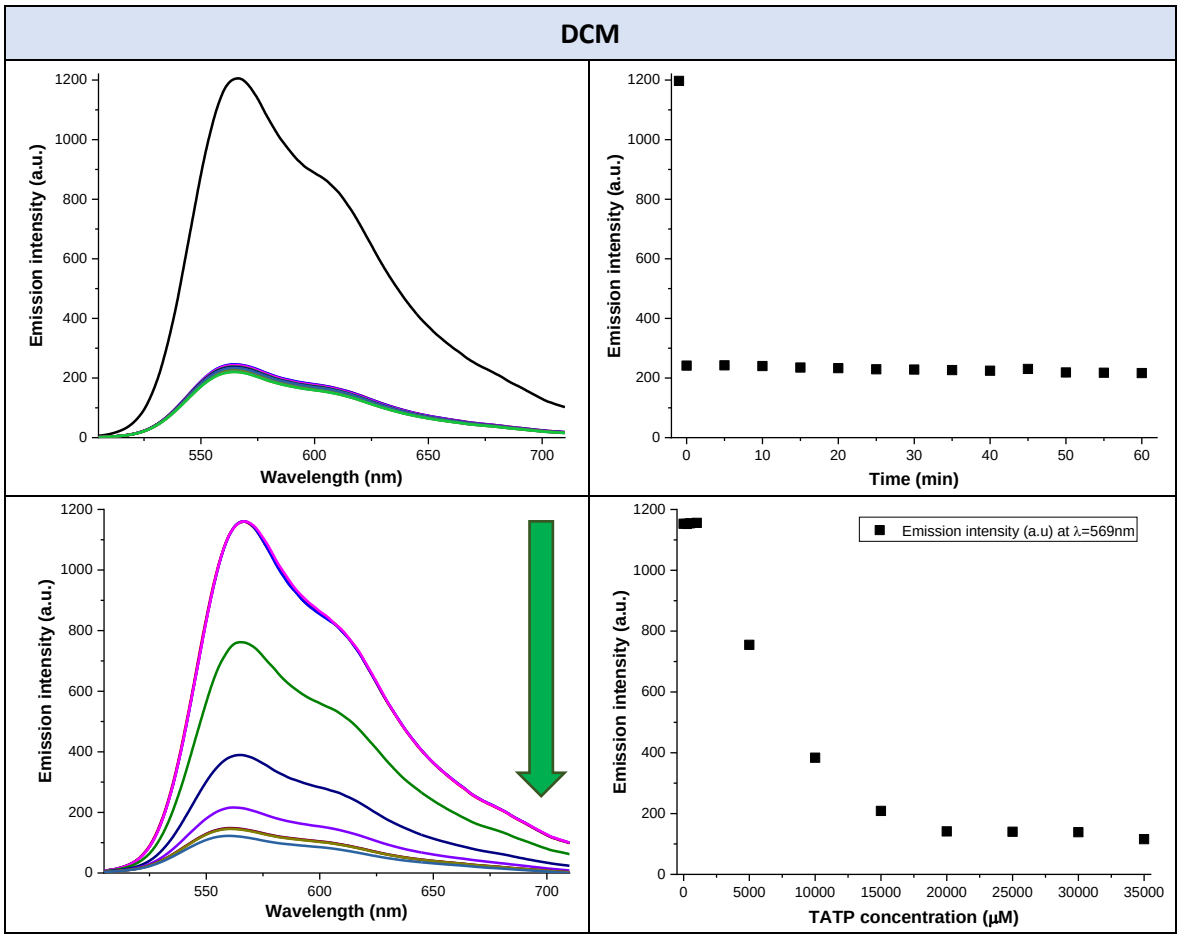

Figure 76. Study of AR95 with TATP in DCM. Kinetic study (up left) and profile as function as time at 569 nm (up right) in presence of TATP excess. Titration (down left) and fluorescence profile at 569 nm (down right) under increasing concentrations of TATP.

There was a drop in the emission intensity immediately after adding TATP, following with a increase in the fluorescence emission The LOD of TATP was somewhere between 1000 and 5000 µM with a decrease in emission intensity.

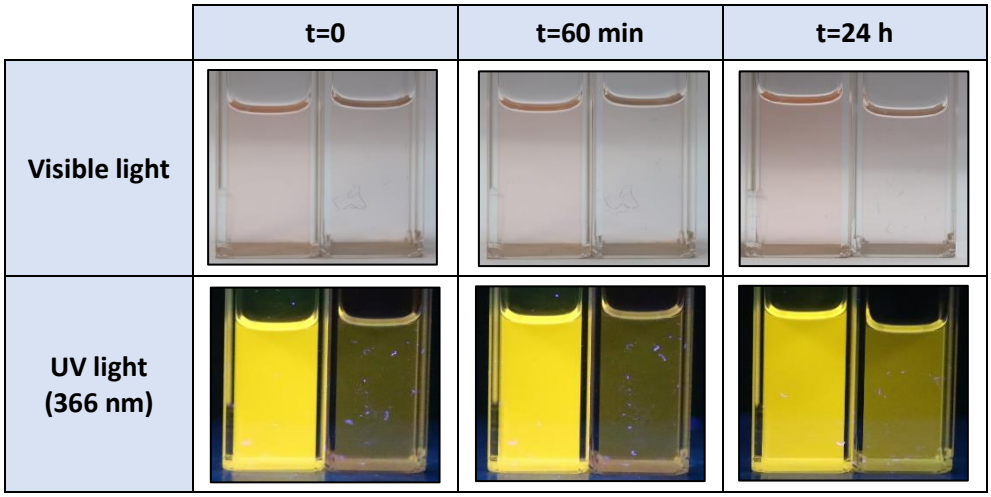

Figure 77. Kinetic study at different times under visible (up) and UV (down) light in DCM. In each photo, left vial was contained the probe and right vial was contained the probe and an excess of TATP.

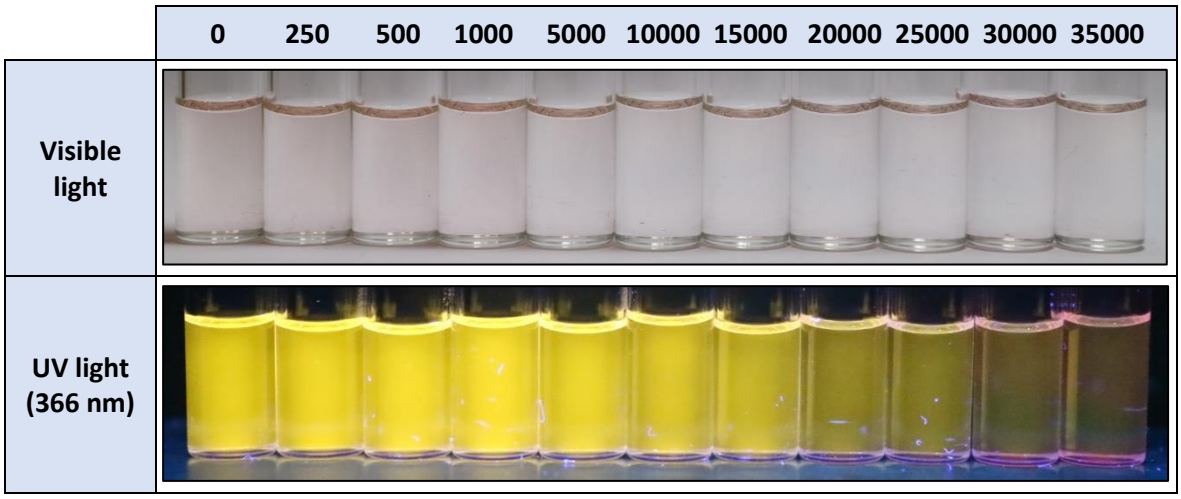

Figure 78. Titration of AR95 with an excess of TATP under visible (up) and UV (down) light in DCM.

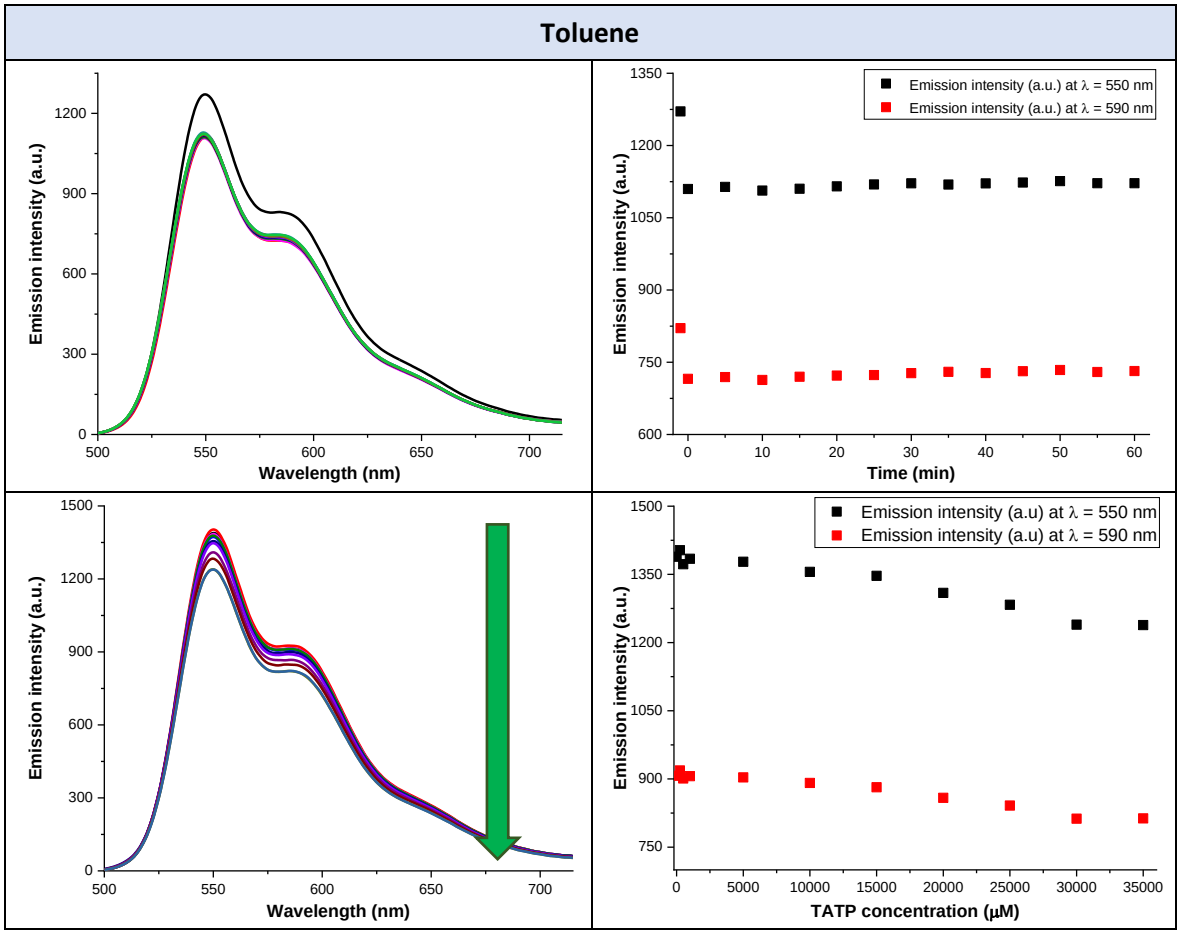

Figure 79. Study of AR95 with TATP in toluene. Kinetic study (up left) and profile as function as time at 550 nm and 590 nm simultaneously (up right) in presence of TATP excess. Titration (down left) and fluorescence profile at 550 nm and 590 nm simultaneously (down right) under increasing concentrations of TATP.

There was sligthly decrease in the emission intensity immediately after adding TATP, following with a increase in the fluorescence emission No significant changes were observed.

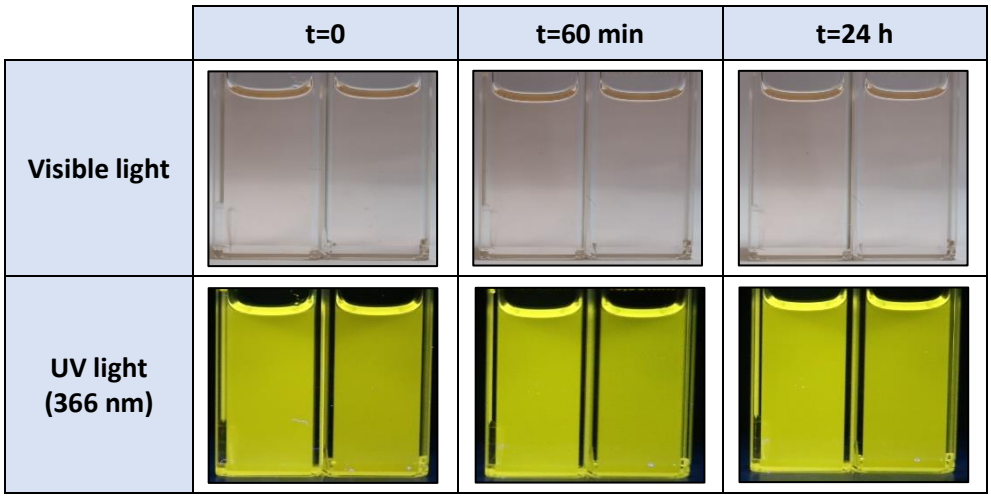

Figure 80. Kinetic study at different times under visible (up) and UV (down) light in toluene. In each photo, left vial was contained the probe and right vial was contained the probe and an excess of TATP.

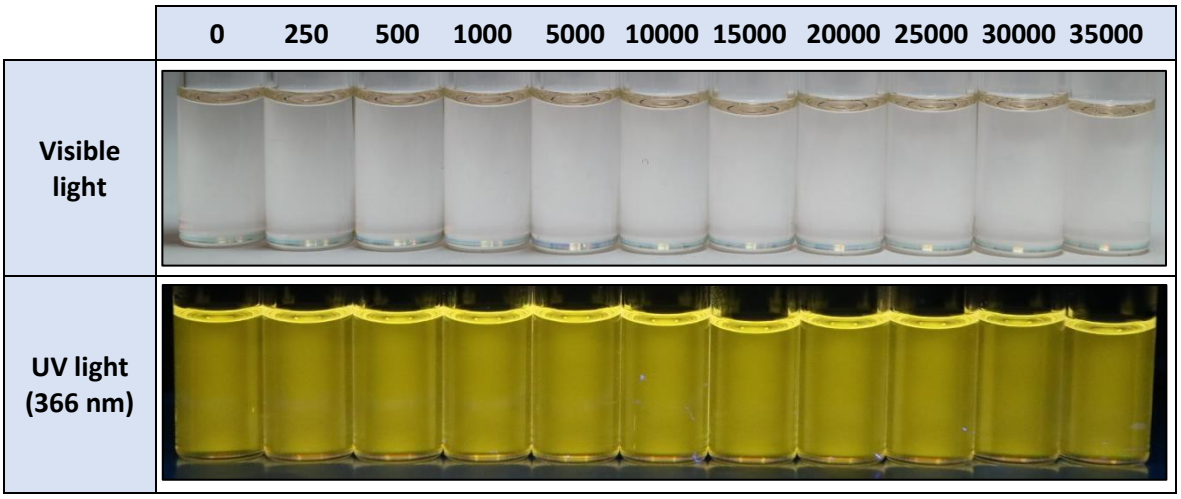

Figure 81. Titration of AR95 with an excess of TATP under visible (up) and UV (down) light in toluene.

Synthesis of 2,7-bis(*N*-(1-(1-adamantyl)ethyl)-9-perylene-3,4-dicarboxylmonoimide)-9,9'-spirobi-[9H-fluorene] (AR34) and 2-(*N*-(1-(1-adamantyl)ethyl)-9-perylene-3,4-dicarboxylmonoimide)-9,9'-spirobi[9H-fluorene] (AR35)

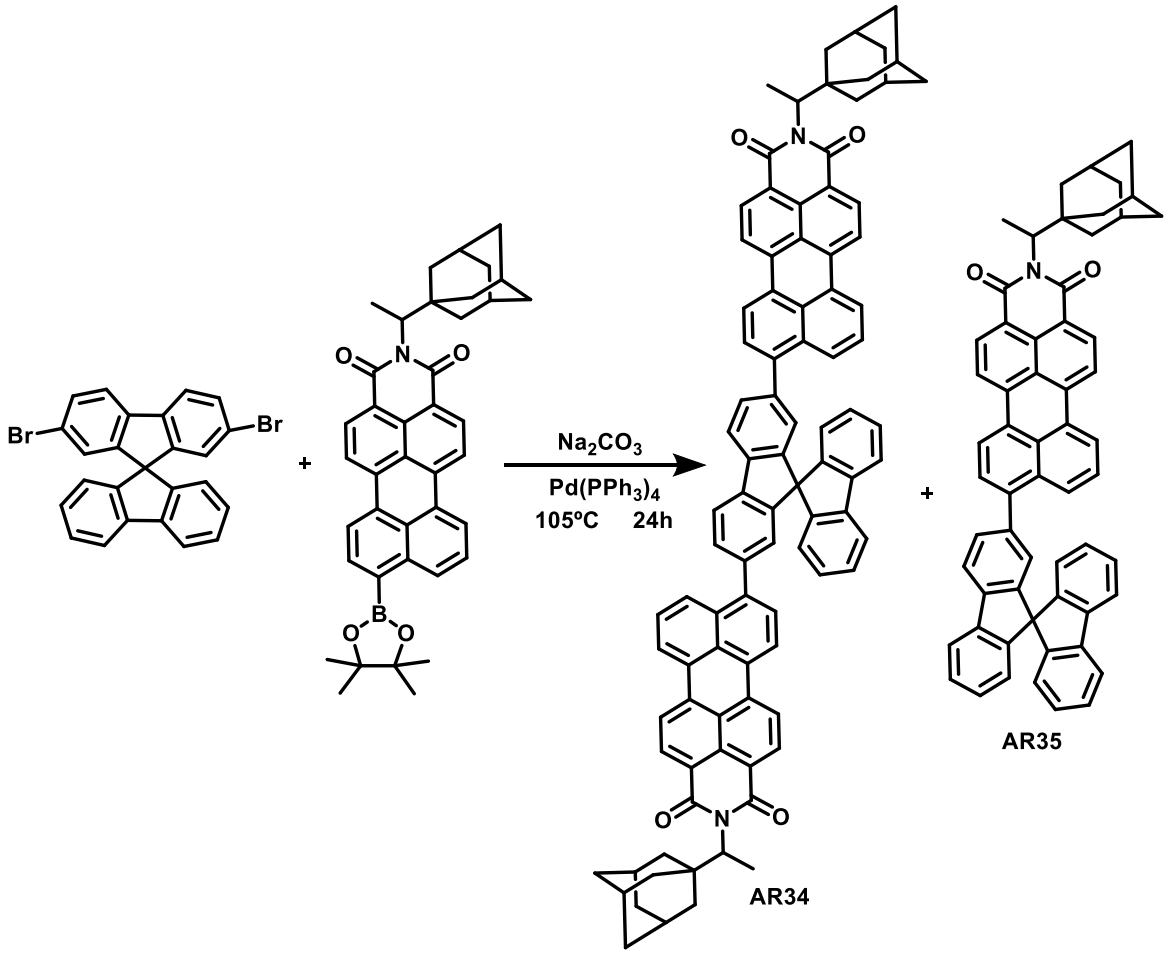

100 mg of 2,7-dibromo-9,9'-spirobi[9H-fluorene] (0.21 mmol), 257 mg of *N*-(1-(1-adamantyl)ethyl)-9-bis(pinacolyl)boronateperylene-3,4-dicarboxylmonoimide (AR01, 0.42 mmol), 105 mg of sodium carbonate (0.99 mmol) and 12 mg of $Pd(PPh_3)_4$ (0.01 mmol) were dissolved in a mixture of toluene:butanol:water (30.2:7.5:2.6 ml) under nitrogen atmosphere and the solution was stirred at 105°C for 48 hours. Later, the solvent was evaporated under reduce pressure, the solid was dissolved in DCM, washed three times with water (3×100 ml). The organic extracts were combined, dry over Na_2SO_4 and the solvent was evaporated under reduce pressure. The organic solid was purified by column chromatography (SiO_2, DCM) to obtain

- AR34 was obtained with a 8% yield (22.6 mg).
- AR35 was obtained with a 24% yield (39.9 mg).

AR34

m.p.: 350 – 353°C (decomposition).

IR (ATR, cm^{-1}): 2896 – 2846, 1692 (C=O), 1649 (C=O), 1592, 1568, 1446, 1347, 1314, 1287, 1241, 1176 (C-N), 1095, 1056, 1035, 906, 837, 808, 751, 729, 636, 609, 435, 424.

^{1}H-NMR (300 MHz, $CDCl_3$) δ (ppm): 8.41 (m, 4H, 4×**H$_{Ar}$**), 8.13 – 7.99 (m, 9H, 9×**H$_{Ar}$**), 7.86 (d, *J* = 7.5 Hz, 2H, 2×**H$_{Ar}$**), 7.71 (d, *J* = 8.4 Hz, 2H, 2×**H$_{Ar}$**), 7.57 (d, *J* = 7.8 Hz, 2H, 2×**H$_{Ar}$**), 7.39 (t, *J* = 7.5 Hz, 2H, 2×**H$_{Ar}$**), 7.27 (s, 1H, **H$_{Ar}$**), 7.23 (d, *J* = 7.8 Hz, 6H, 6×**H$_{Ar}$**), 7.02 (d, *J* = 7.5 Hz, 2H, 2×**H$_{Ar}$**), 6.90 (s, 2H, 2×**H$_{Ar}$**), 5.10 (q, *J* = 7.0 Hz, 2H, 2×C**H**), 1.98 (s, 6H, 6×C**H**), 1.83 (m, 6H, 2×C**H$_3$**), 1.69 (m, 24H, 12×C**H$_2$**).

^{13}C-NMR (75MHz, $CDCl_3$) δ (ppm): 165.7 (**C**=O),164.9 (**C**=O), 149.9 (**C$_{Ar}$**), 148.6 (**C$_{Ar}$**), 142.8 (**C$_{Ar}$**), 142.0 (**C$_{Ar}$**), 141.2 (**C$_{Ar}$**), 136.8 (**C$_{Ar}$**), 132.5 (**C$_{Ar}$**), 132.0 (**C$_{Ar}$**H), 131.3 (**C$_{Ar}$**H), 130.2 (**C$_{Ar}$**H), 129.8 (**C$_{Ar}$**), 129.3 (**C$_{Ar}$**), 128.9 (**C$_{Ar}$**), 128.2 (**C$_{Ar}$**H), 126.9 (**C$_{Ar}$**H), 125.9 (**C$_{Ar}$**H), 124.3 (**C$_{Ar}$**H), 123.5 (**C$_{Ar}$**H), 123.1 (**C$_{Ar}$**H), 120.4 (**C$_{Ar}$**H), 120.3 (**C$_{Ar}$**H), 120.1 (**C$_{Ar}$**H), 66.3 (**Cq**), 58.2 (**C**H), 40.5 (**C**H$_2$), 37.2 (**C**H$_2$), 29.9 (**Cq**), 28.9 (**C**H), 13.3 (**C**H$_3$).

HRMS (MALDI, DIT-) m/z: calculated for $C_{93}H_{70}N_2O_4$: 1279.5363 (M^-); found 1279.5367.

UV-Vis ($CHCl_3$), λ_{max} nm (log ε): 525 (4.9).

Ø (MCH, %): 80.41.

τ (510 nm, MCH, ns): 2.867 (χ^2: 1.036).

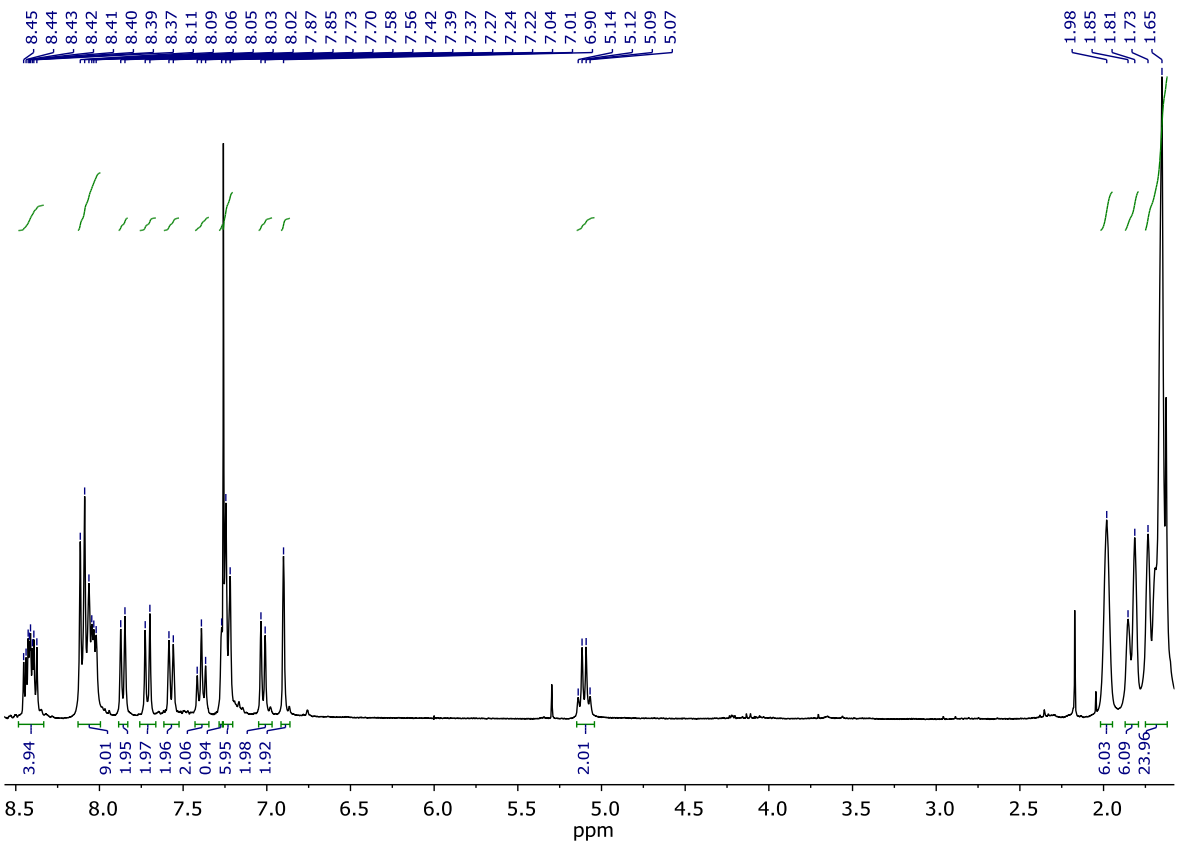

Figure 82. ^{1}H-NMR (CDCl3, 300 MHz) of AR34.

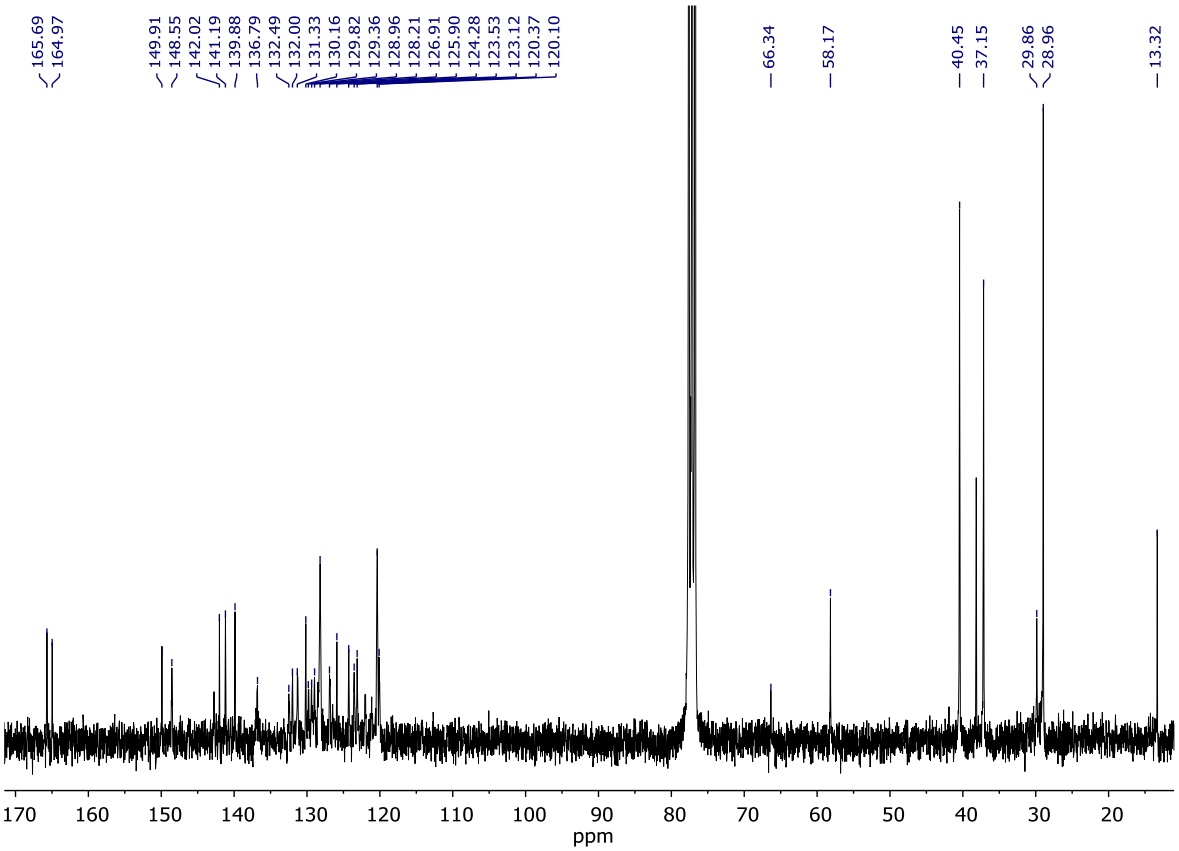

Figure 83. ^{13}C-NMR ($CDCl_3$, 75 MHz) of AR34.

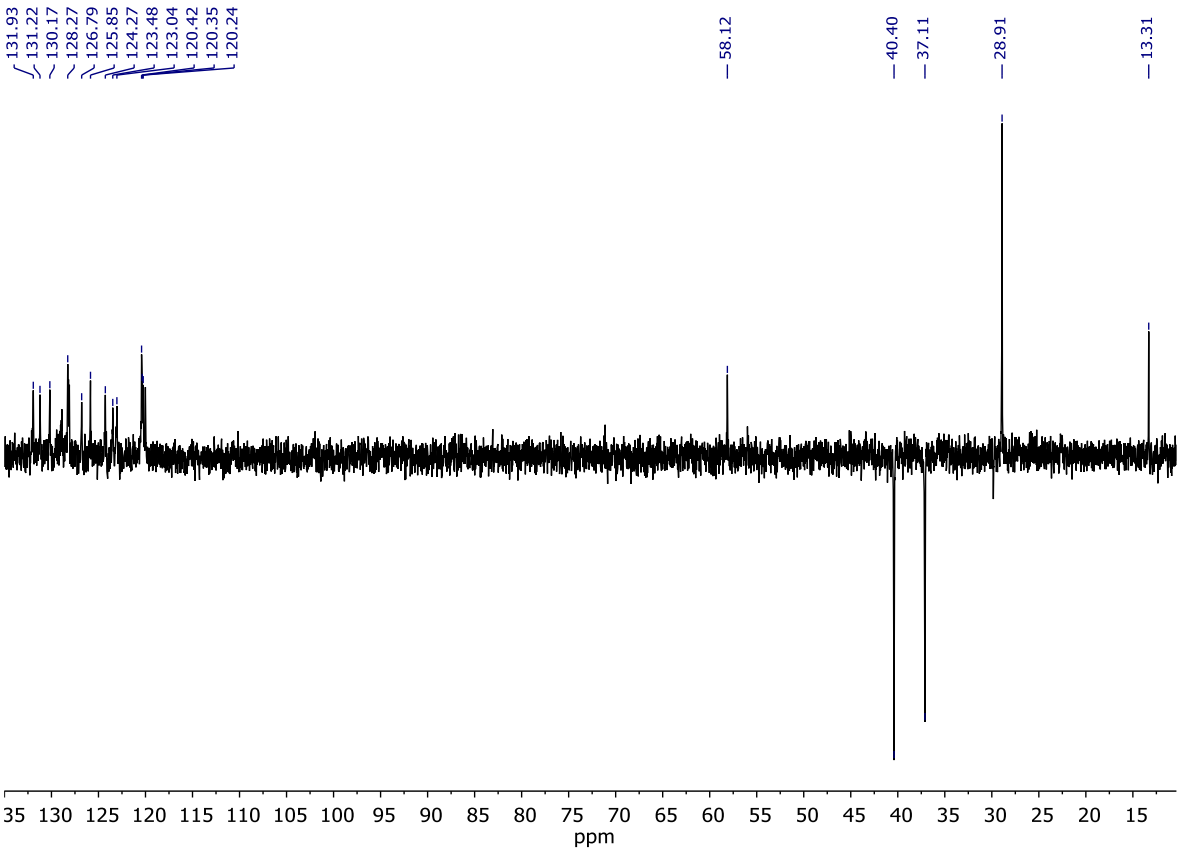

Figure 84. DEPT NMR ($CDCl_3$, 75 MHz) of AR34.

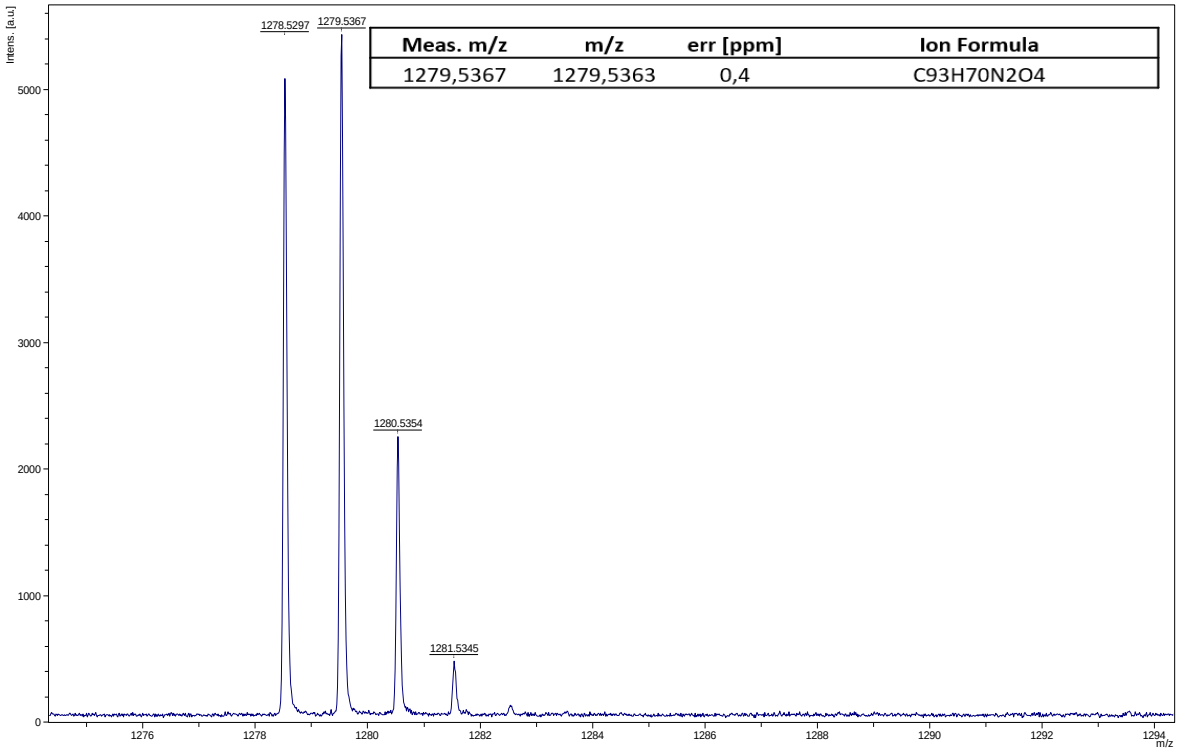

Meas. m/z	m/z	err [ppm]	Ion Formula
1279,5367	1279,5363	0,4	C93H70N2O4

Figure 85. HRMS (MALDI, DIT-) of AR34.

Fluorescence decay lifetime (τ):

The solvent used was MCH. The concentration of the compound was 20 µM.

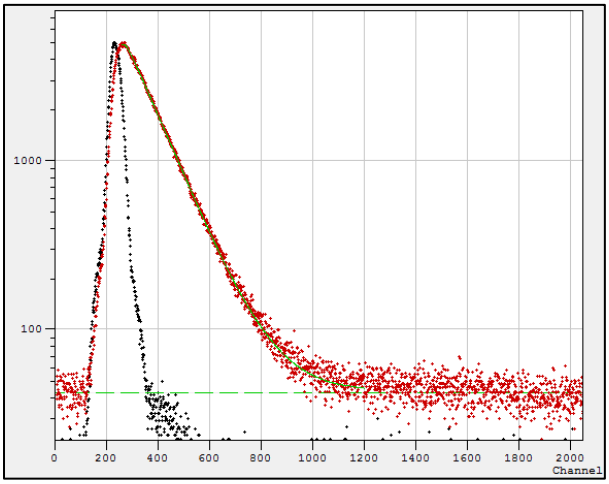

Figure 86. Fluorescence decay lifetime of AR34.

Solvatochromism:

The concentration of the compound was 20 µM and the excitation wavelength was 520 nm.

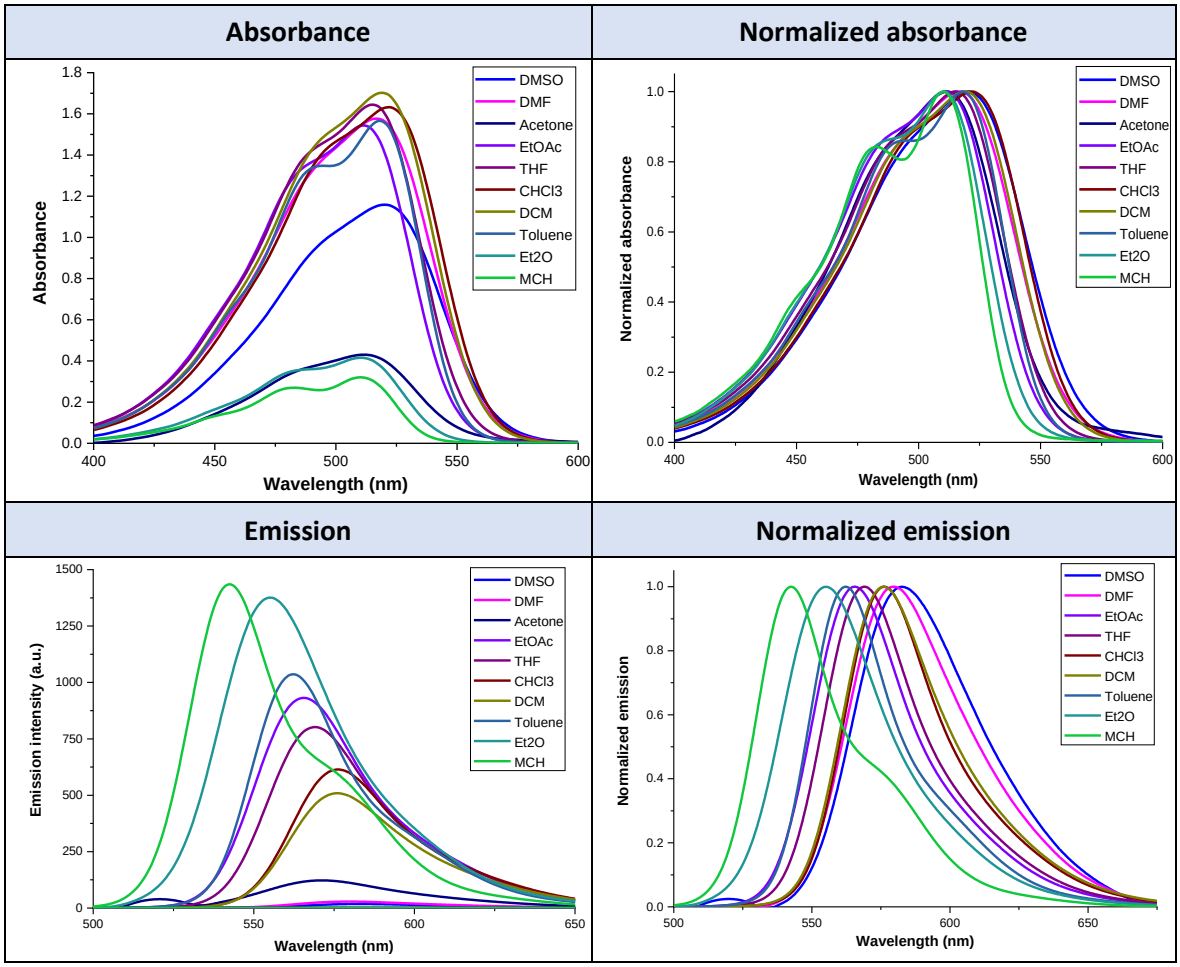

Figure 87. Solvatochromism of AR34.

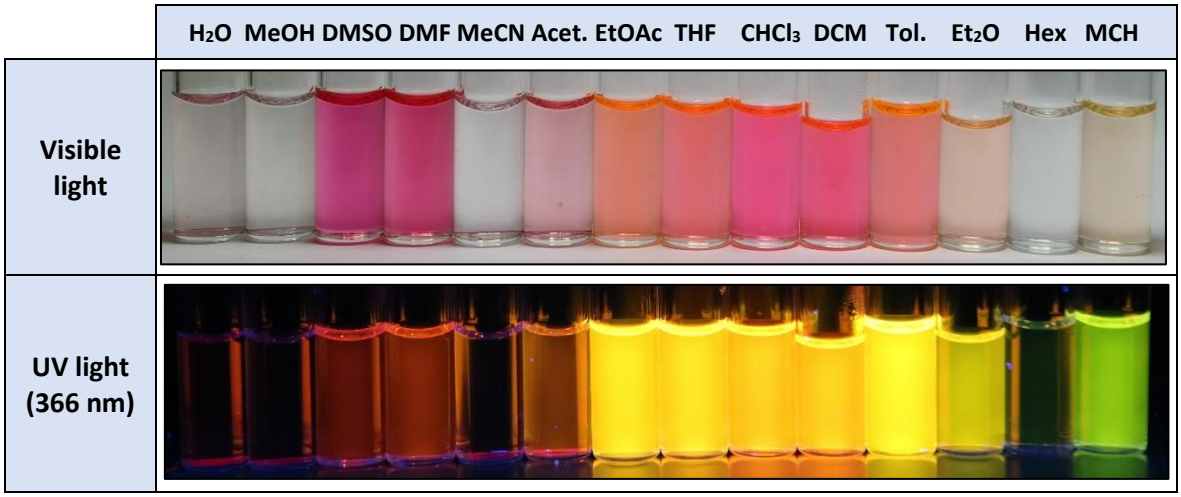

Figure 88. Solvatochromism of AR34 under visible and 366 nm light.

Water acceptance test:

The solvent used was THF and the concentration of the compound was 20 µM.

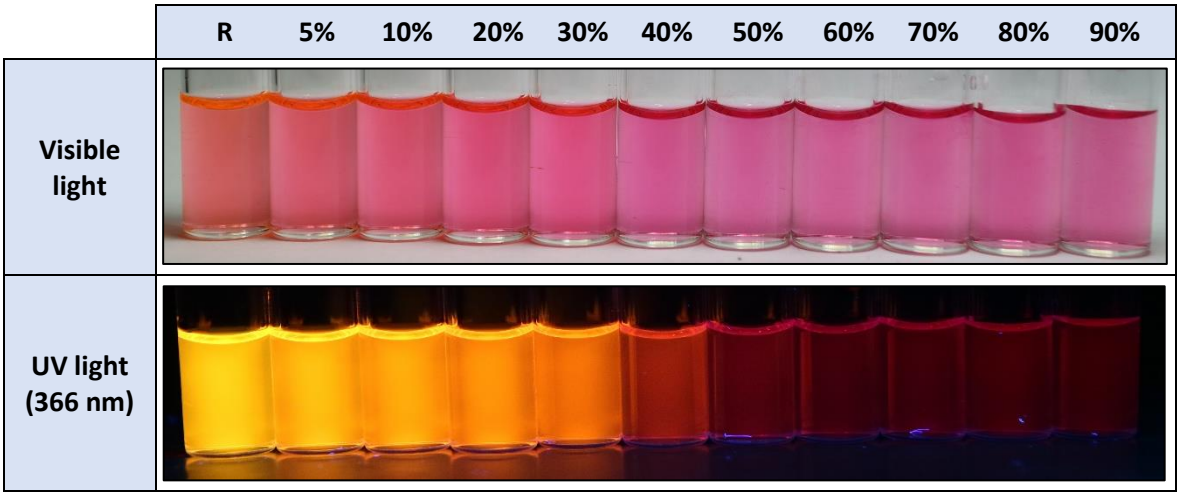

Figure 89. Water acceptance test of AR34 under visible (up) and UV (down) light.

The maximum aumount of water that was admitted by the product was 30%. Under visible light, the absorption maximum was shifted from pink (514-518 nm) to pinkish purple (525 nm) at 40% of water. At this percentage of water, there was also a shift of the emission maximum from the yellow-orange (570-585 nm) to the red (615-630 nm) region.

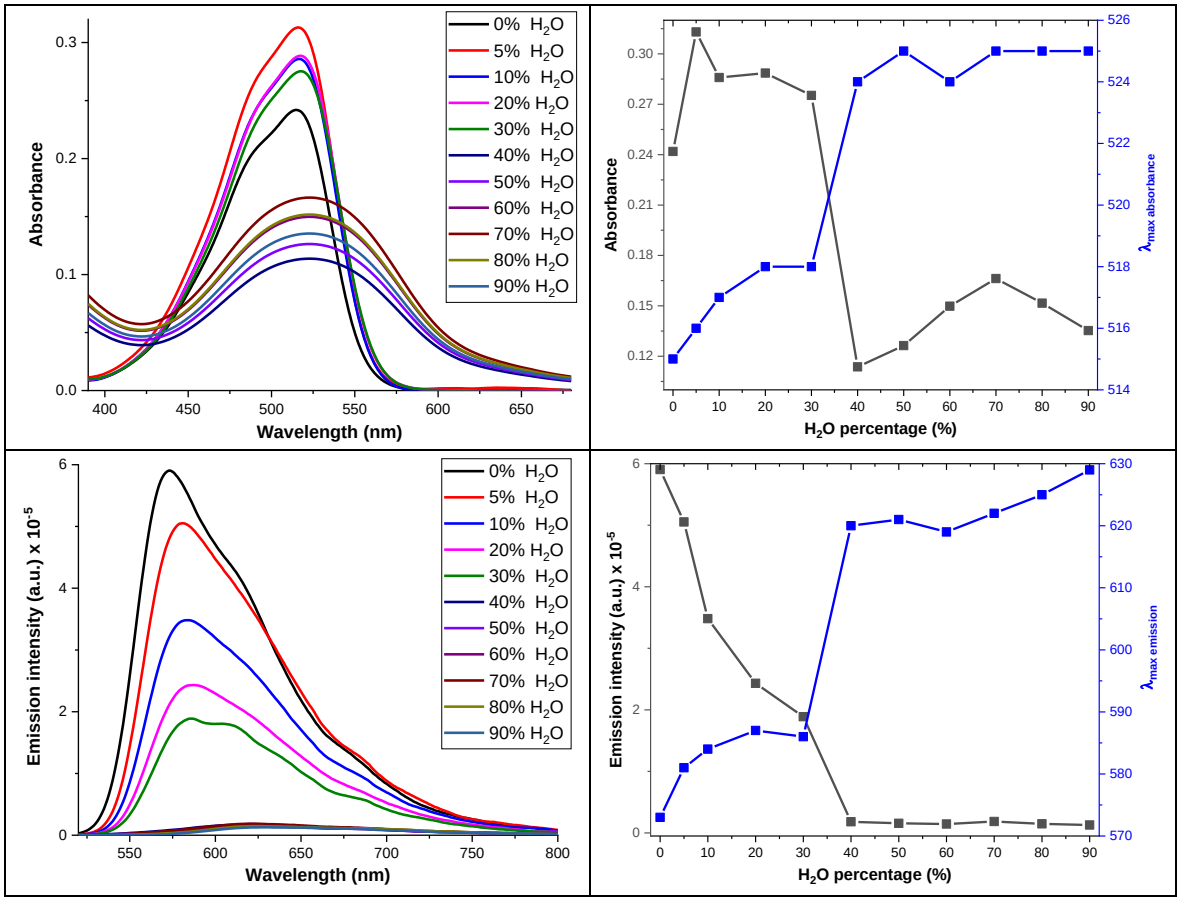

Figure 90. Absorbance graph (up left), graph of relationship between the intensity of emission and the wavelenght of the maximum of absorption as a function of the amount of water added (up right), emission intensity graph (down left) and graph of relationship between the intensity of emission and the wavelenght of the maximum of emission as a function of the amount of water added (down right) for AR34 in THF.

AR34 5% of water	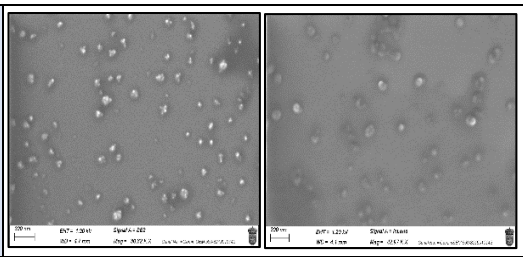
AR34 20% of water	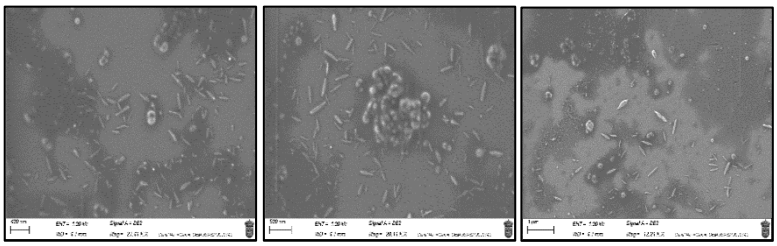
AR34 30% of water	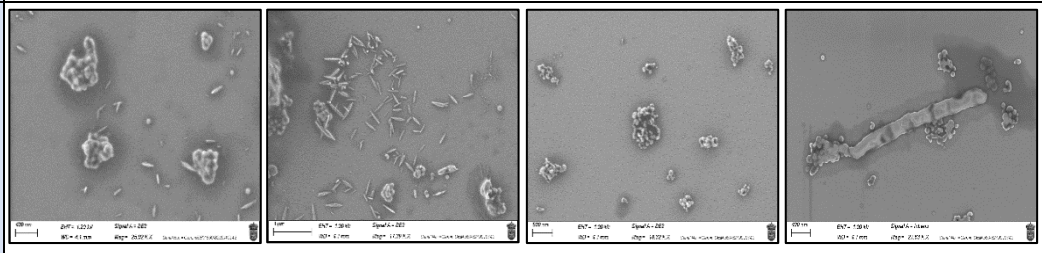
AR34 40% of water	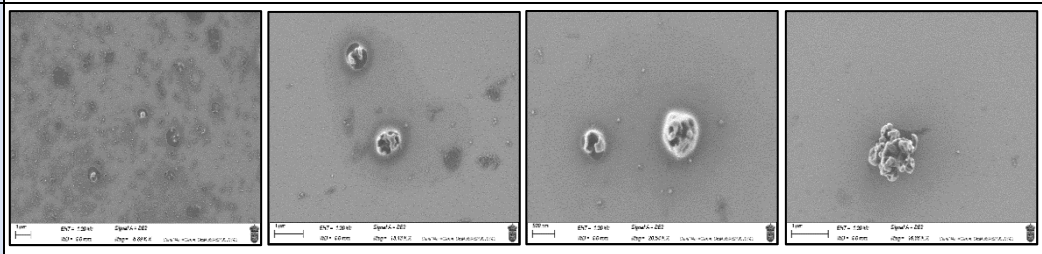
AR34 60% of water	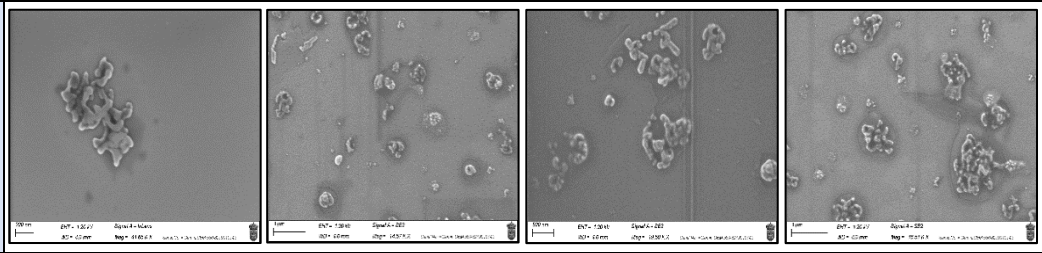
AR34 80% of water	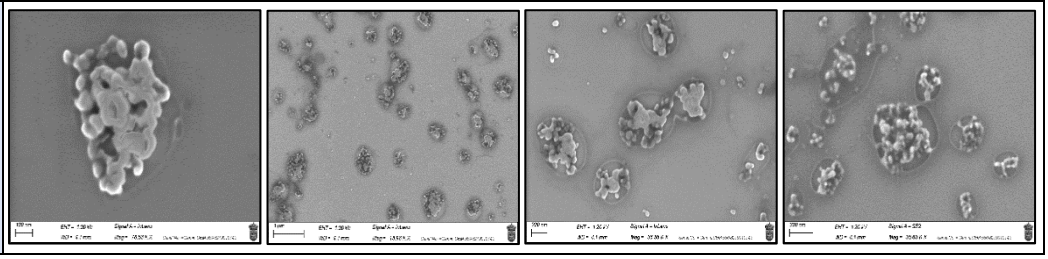

Figure 91. SEM nanoparticles of AR34 in different mixtures of water and THF.

pH test:

For this test, the proportion of water that the compound could accept according to the previous water acceptance test was 30%. The concentration of the compound was 20 µM and the solvent used was THF.

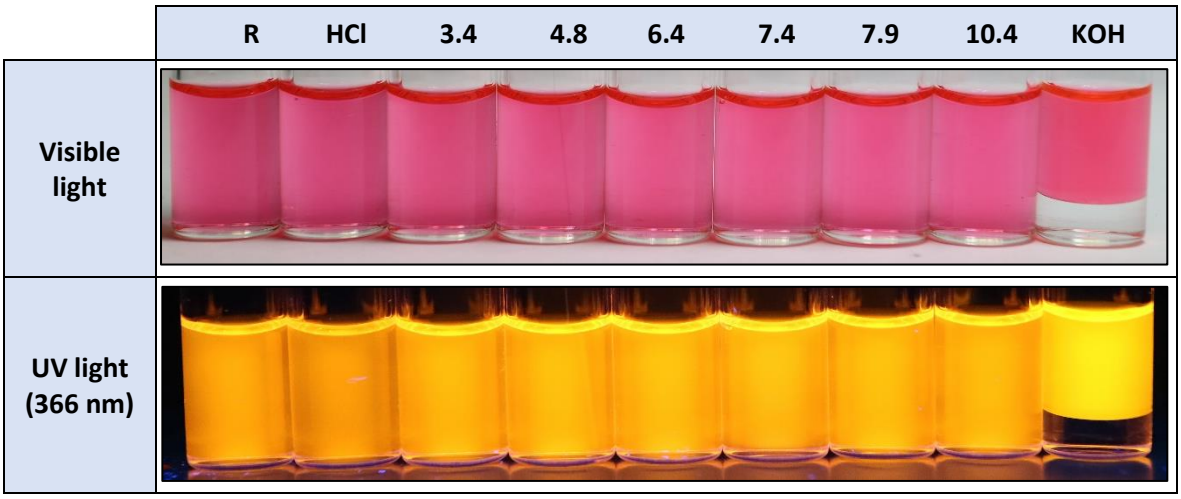

Figure 92. pH test of AR34 under visible (up) and UV (down) light.

No significant changes were observed.

Cations and anions test:

The concentration of the compound was 20 µM and the solvent used was THF.

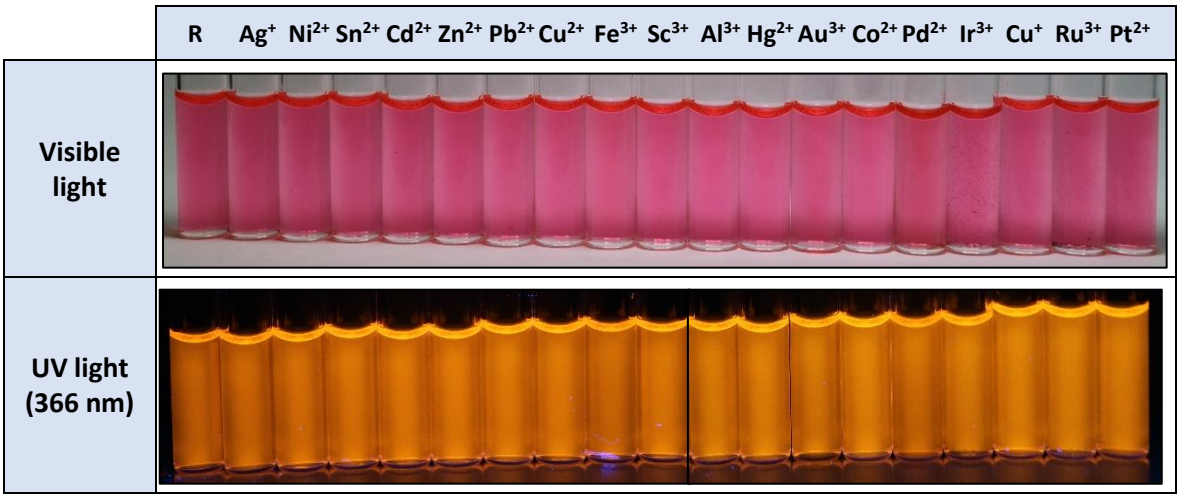

Figure 93. Cations test of AR34 under visible (up) and UV (down) light.

No significant changes were observed.

For the anion test, the concentration of the compound was 20 µM and the solvent used was THF.

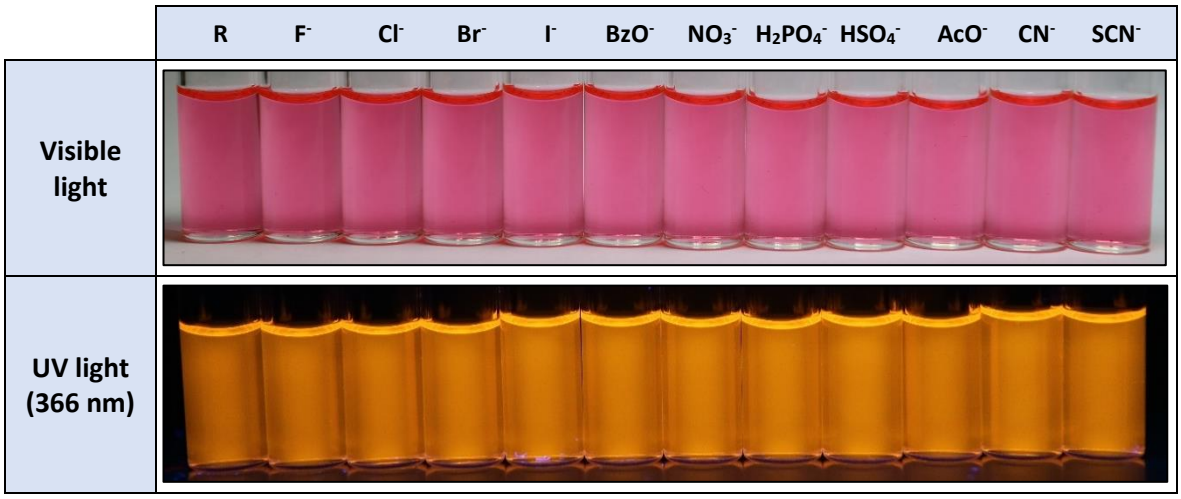

Figure 94. Anions test of AR34 under visible (up) and UV (down) light.

No significant changes were observed.

Oxidant and reductant reagents test:

The solvent used was THF and concentration of the compound was 20 µM.

Figure 95. Oxidant and reductant reagents test of AR34 under visible (up) and UV (down) light.

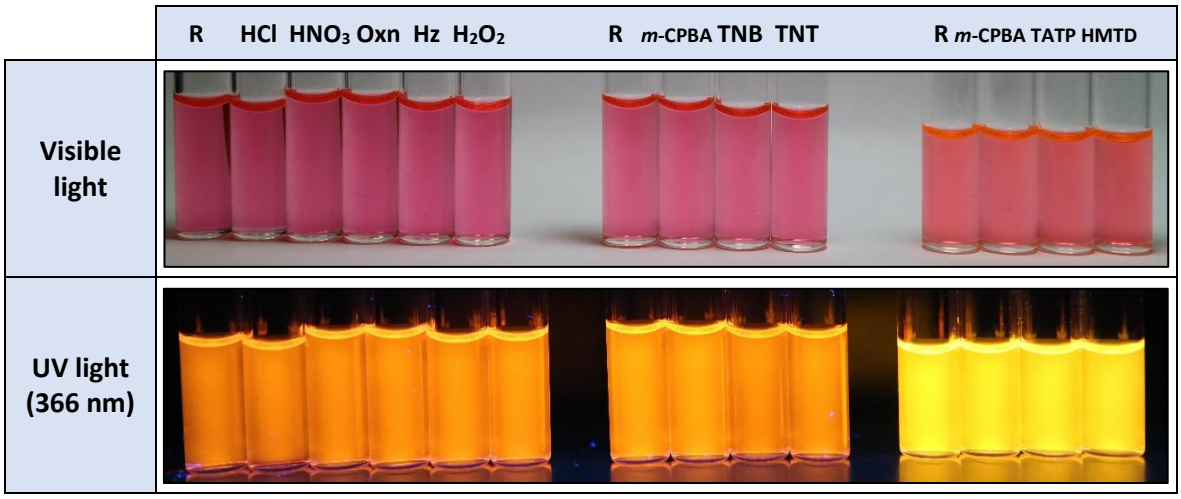

The most significant changes were observed respect *m*-CPBA, H_2O_2, TNT and TATP.

AR35

m.p.: 348-351°C (decomposition).

IR (ATR, cm^{-1}): 2899-2846, 1689 (C=O), 1652 (C=O), 1590, 1571, 1443, 1347, 1314, 1290, 1244, 837, 805, 751, 729, 697, 619, 421.

^{1}H-NMR (300 MHz, $CDCl_3$) δ (ppm): 8.36-8.27 (m, 2H, 2×**H_{Ar}**), 8.11 (m, 1H, **H_{Ar}**), 8.04-7.74 (m, 8H, 8×**H_{Ar}**), 7.62-7.28 (m, 8H, 8×**H_{Ar}**), 7.18 (t, *J* = 7.5 Hz, 2H, 2×**H_{Ar}**), 7.07 (m, 1H, **H_{Ar}**), 6.88 (d, *J* = 7.5 Hz, 1H, **H_{Ar}**), 6.81 (m, 1H, **H_{Ar}**), 5.10 (q, *J* = 7.0 Hz, 1H, C**H**), 1.99 (s, 3H, 3×C**H**), 1.84 (d, *J* = 12.1 Hz, 3H, C**H**$_3$), 1.70 (d, *J* = 23.9 Hz, 12H, 6×C**H**$_2$).

^{13}C-NMR (75MHz, $CDCl_3$) δ (ppm): 165.7 (**C**=O), 165.0 (**C**=O), 149.5 (**C**$_{Ar}$), 149.2 (**C**$_{Ar}$), 148.7 (**C**$_{Ar}$), 142.0 (**C**$_{Ar}$), 141.7 (**C**$_{Ar}$), 141.4 (**C**$_{Ar}$), 140.0 (**C**$_{Ar}$), 139.4 (**C**$_{Ar}$), 136.8 (**C**$_{Ar}$), 132.4 (**C**$_{Ar}$), 131.9 (**C**$_{Ar}$H), 131.3 (**C**$_{Ar}$H), 131.2 (**C**$_{Ar}$), 130.1 (**C**$_{Ar}$H), 129.9 (**C**$_{Ar}$), 129.2 (**C**$_{Ar}$), 128.7 (**C**$_{Ar}$H), 128.3 (**C**$_{Ar}$H), 128.0 (**C**$_{Ar}$H), 126.7 (**C**$_{Ar}$H), 125.7 (**C**$_{Ar}$H), 124.3 (**C**$_{Ar}$H), 124.2 (**C**$_{Ar}$H), 123.6 (**C**$_{Ar}$), 123.5 (**C**$_{Ar}$), 123.3 (**C**$_{Ar}$), 123.1 (**C**$_{Ar}$), 121.9 (**C**$_{Ar}$), 120.3 (**C**$_{Ar}$H), 120.1 (**C**$_{Ar}$), 66.2 (**Cq**), 58.1 (**C**H$_2$), 40.4 (**C**H), 38.1 (**Cq**), 37.1 (**C**H$_3$), 28.9 (**C**H$_2$), 13.3 (**C**H$_2$).

HRMS (MALDI, DIT-) m/z: calculated for $C_{59}H_{43}NO_2$: 797.3288 (M^-); found 797.3286.

UV-Vis ($CHCl_3$), λ_{max} nm (log ε): 500 (4.6).

Ø (MCH, %): 94.25.

τ (510 nm, MCH, ns): 4.020 (χ^2: 1.021).

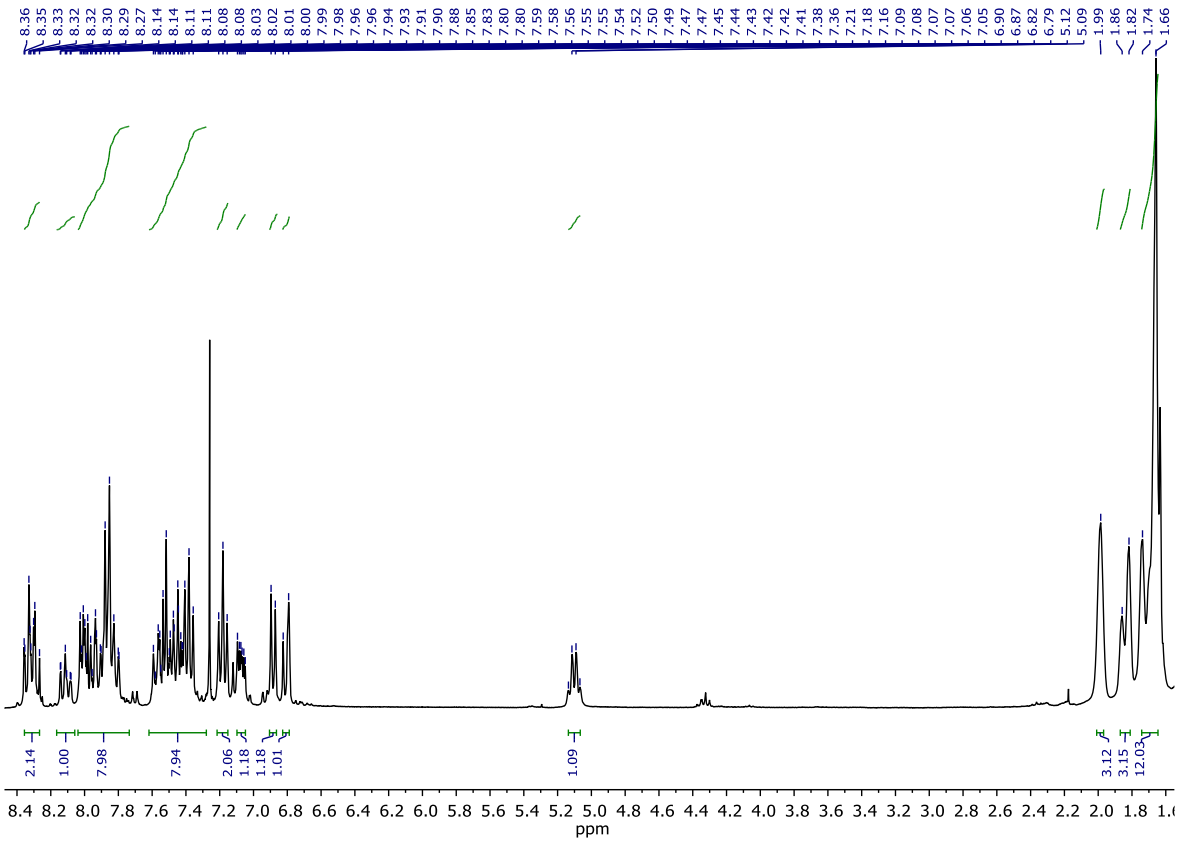

Figure 96. ^{1}H-NMR ($CDCl_3$, 300 MHz) of AR35.

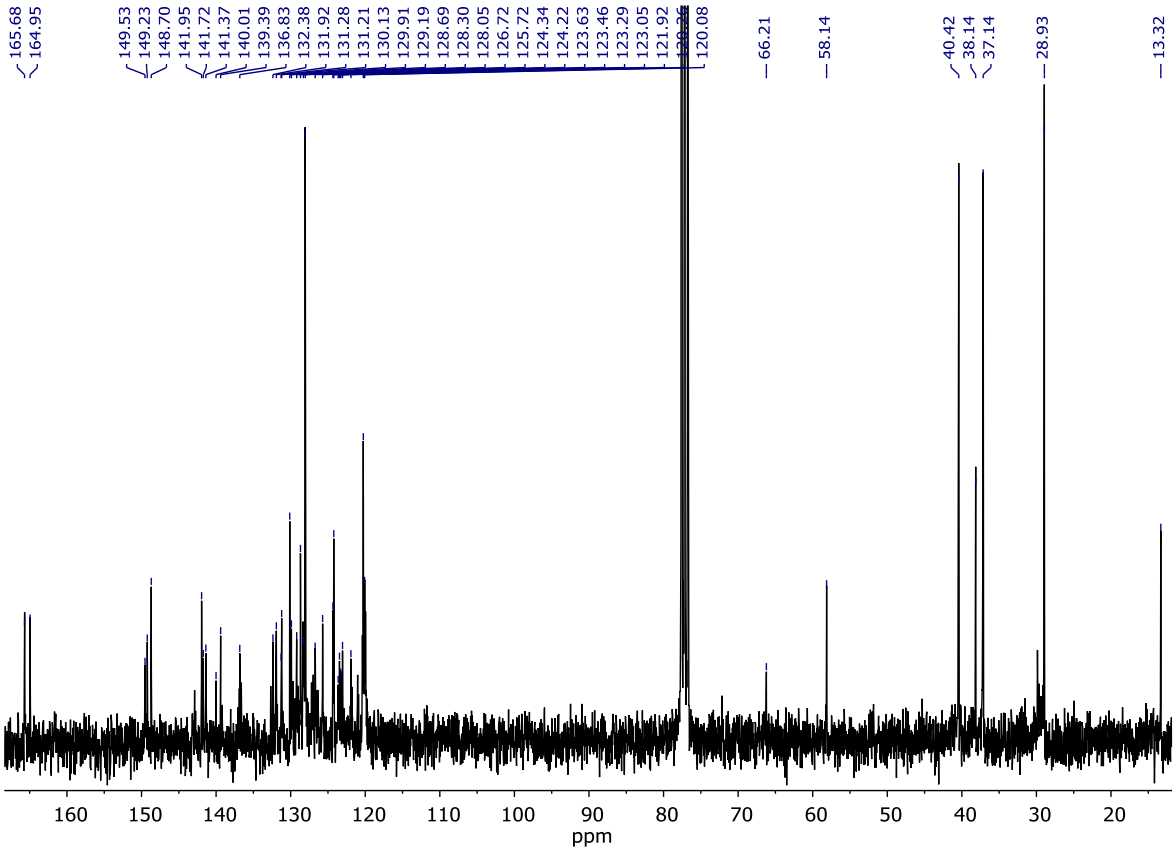

Figure 97. ^{13}C-NMR ($CDCl_3$, 75 MHz) of AR35.

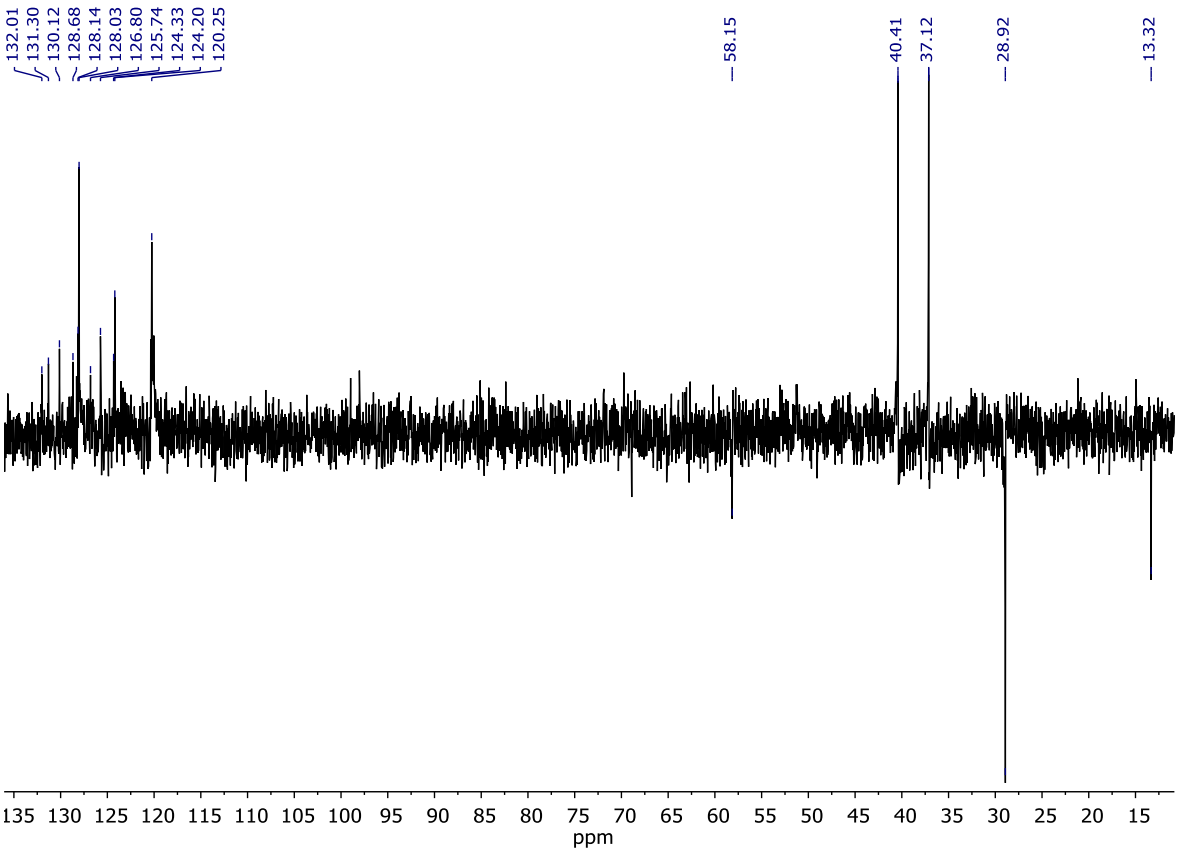

Figure 98. DEPT NMR ($CDCl_3$, 75 MHz) of AR35.

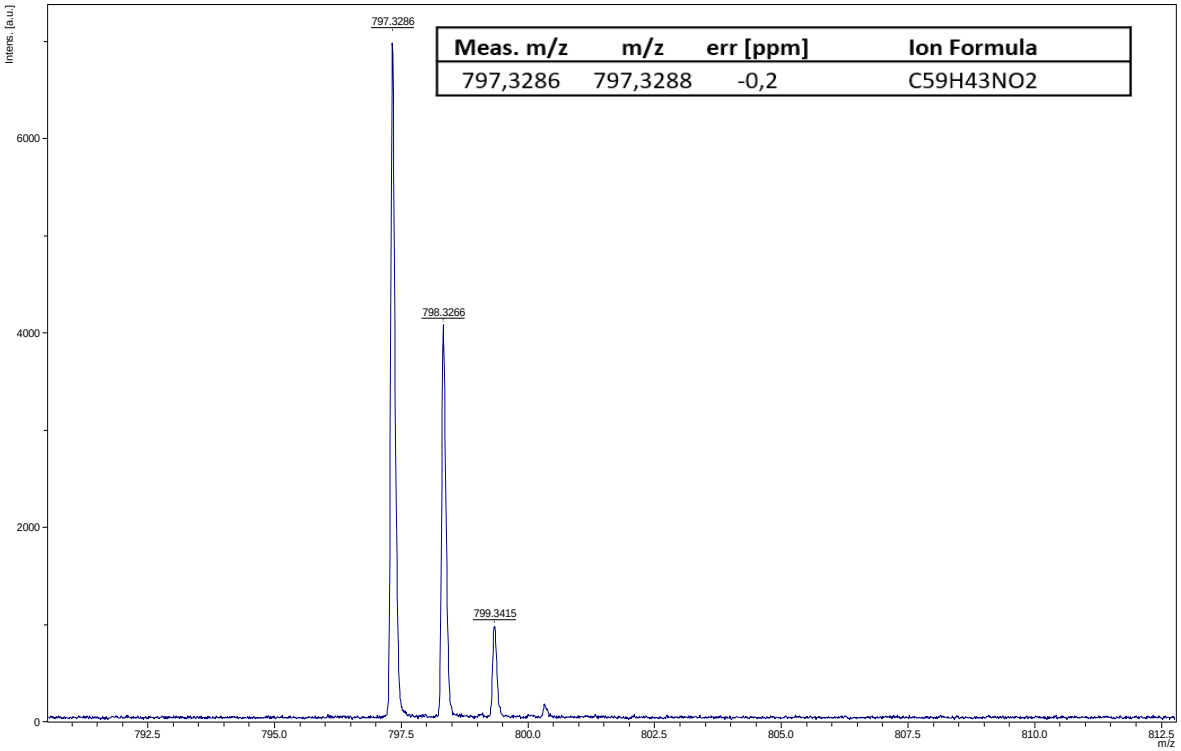

Meas. m/z	m/z	err [ppm]	Ion Formula
797,3286	797,3288	-0,2	C59H43NO2

Figure 99. HRMS (MALDI, DIT-) of AR35.

Fluorescence decay lifetime (τ):

The solvent used was methylcyclohexane. The concentration of the compound was 20 µM.

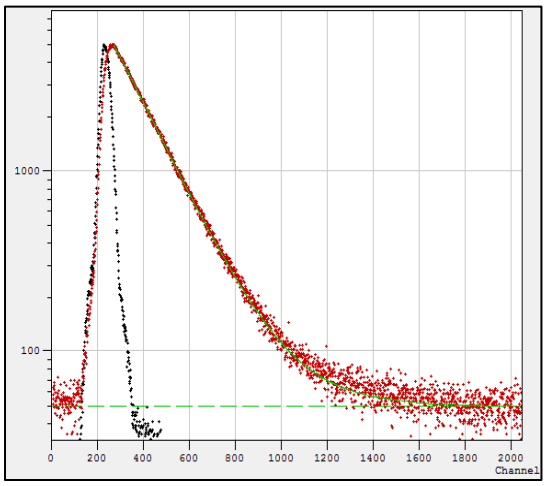

Figure 100. Fluorescence decay lifetime of AR35.

Solvatochromism:

The concentration of the compound was 20 µM and the excitation wavekength was 500 nm.

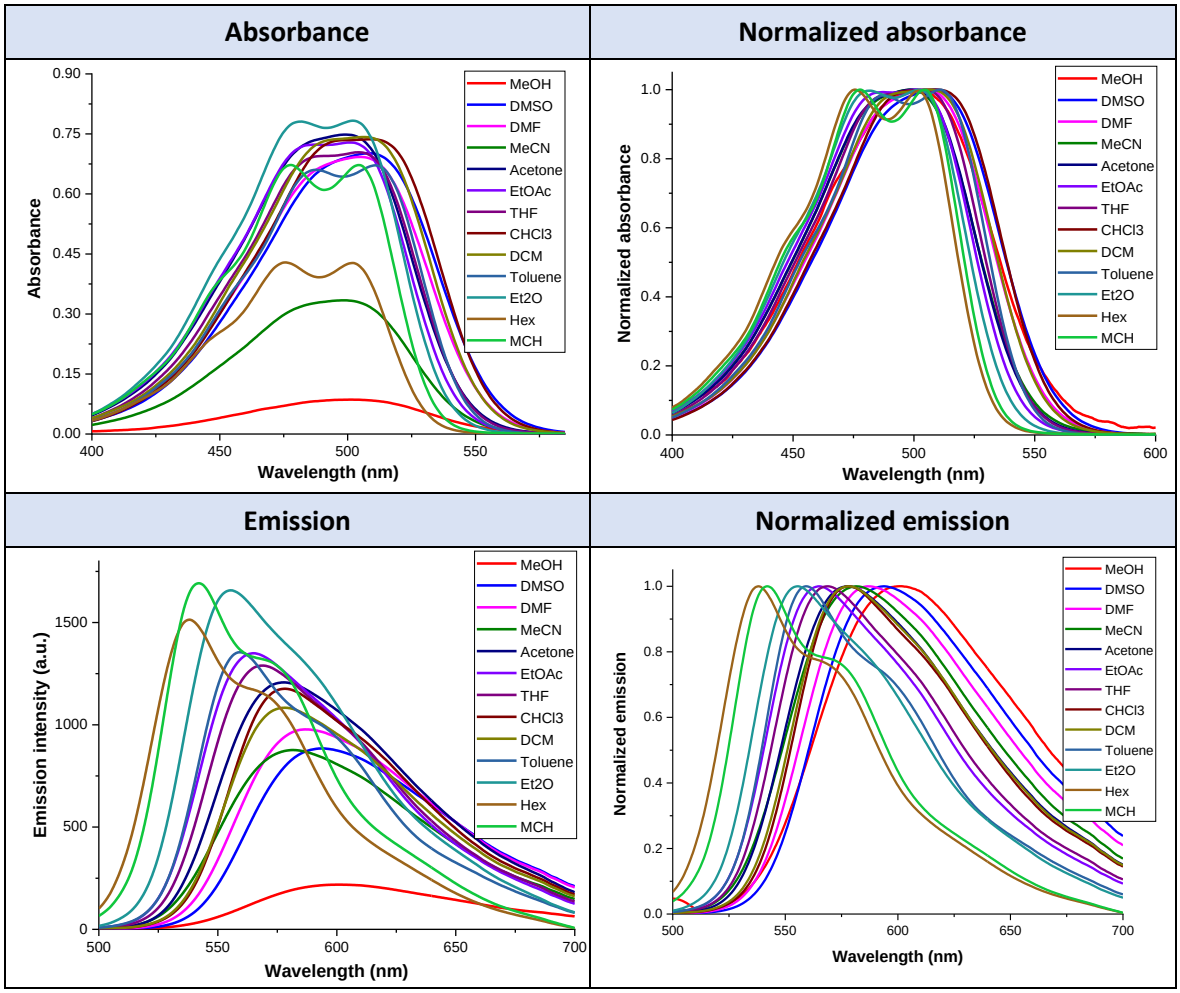

Figure 101. Solvatochromism of AR35.

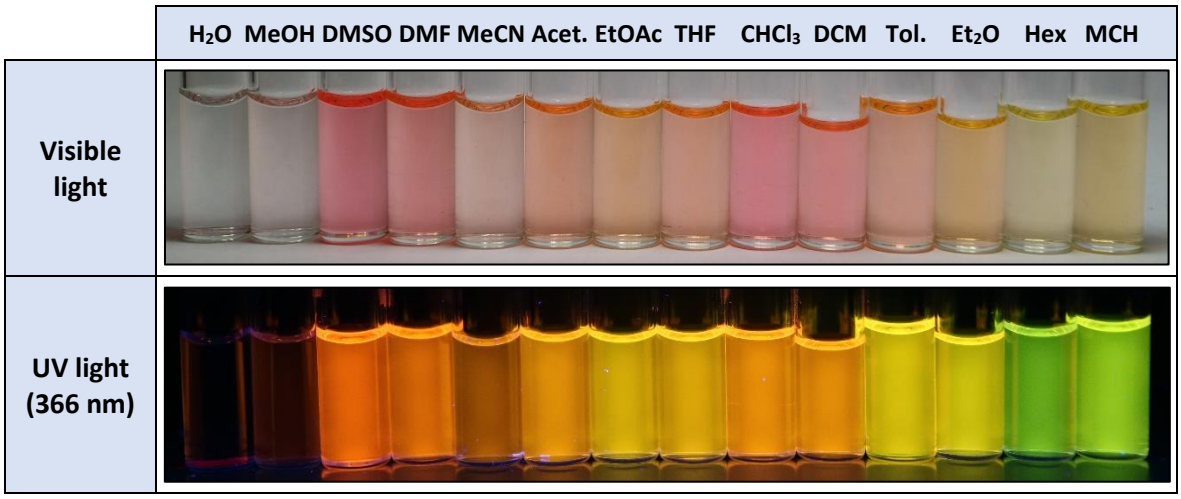

Figure 102. Solvatochromism of AR35 under visible and 366 nm light.

Water acceptance test:

The solvent used was acetone and THF and the concentration of the compound was 20 µM in both cases.

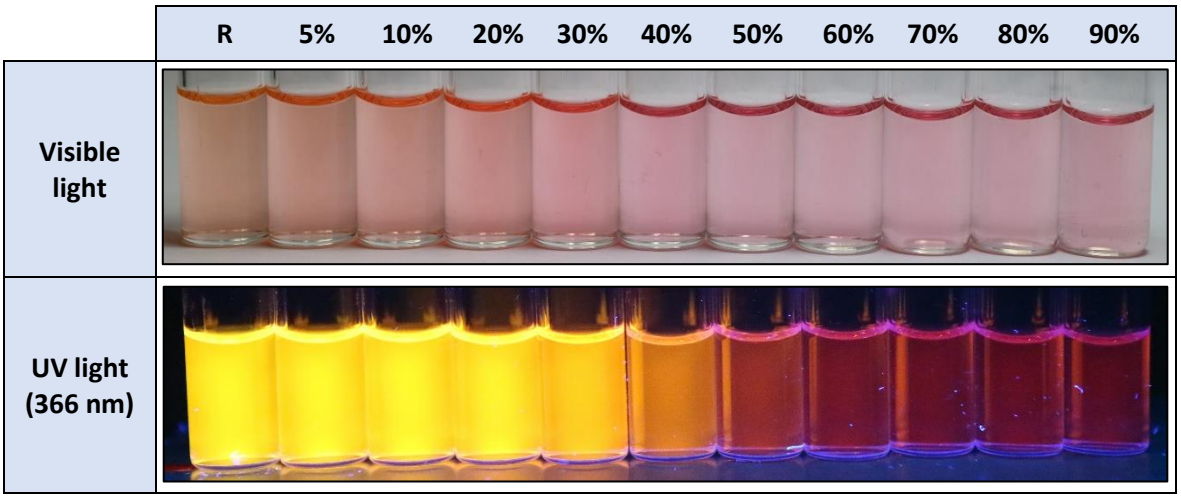

Figure 103. Water acceptance test of AR35 in acetone under visible (up) and UV (down) light.

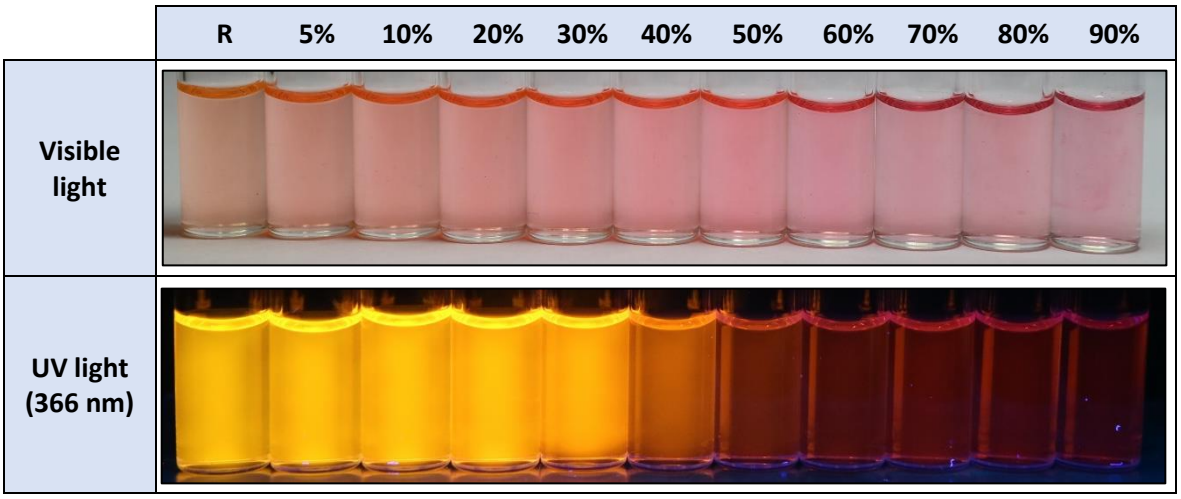

Figure 104. Water acceptance test of AR35 in THF under visible (up) and UV (down) light.

The result obtained was the same with two solvents. The maximum aumount of water that was admitted by the product was 30%. Under visible light, the shift of the absorption maximum from the orange region (504-508 nm) to the pink region (490-492 nm) was observed from 40% water. Under UV light, as the amount of water increased, the emission intensity was decreased considerably while the emission maximum was shifted from the yellow region (620-640 nm) to the red region (above 580 nm) also from 40% water.

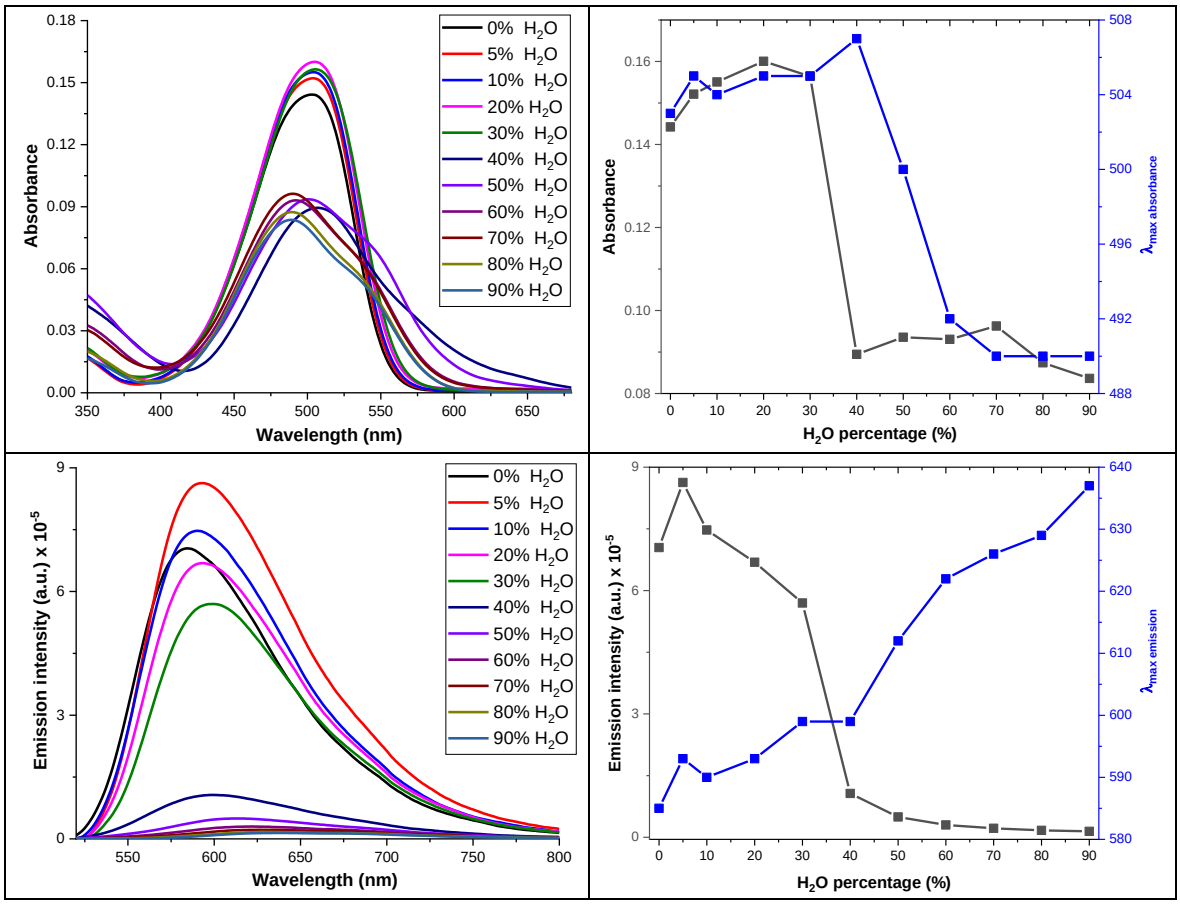

Figure 105. Absorbance graph (up left), graph of relationship between the intensity of emission and the wavelenght of the maximum of absorption as a function of the amount of water added (up right), emission intensity graph (down left) and graph of relationship between the intensity of emission and the wavelenght of the maximum of emission as a function of the amount of water added (down right) for AR35 in THF.

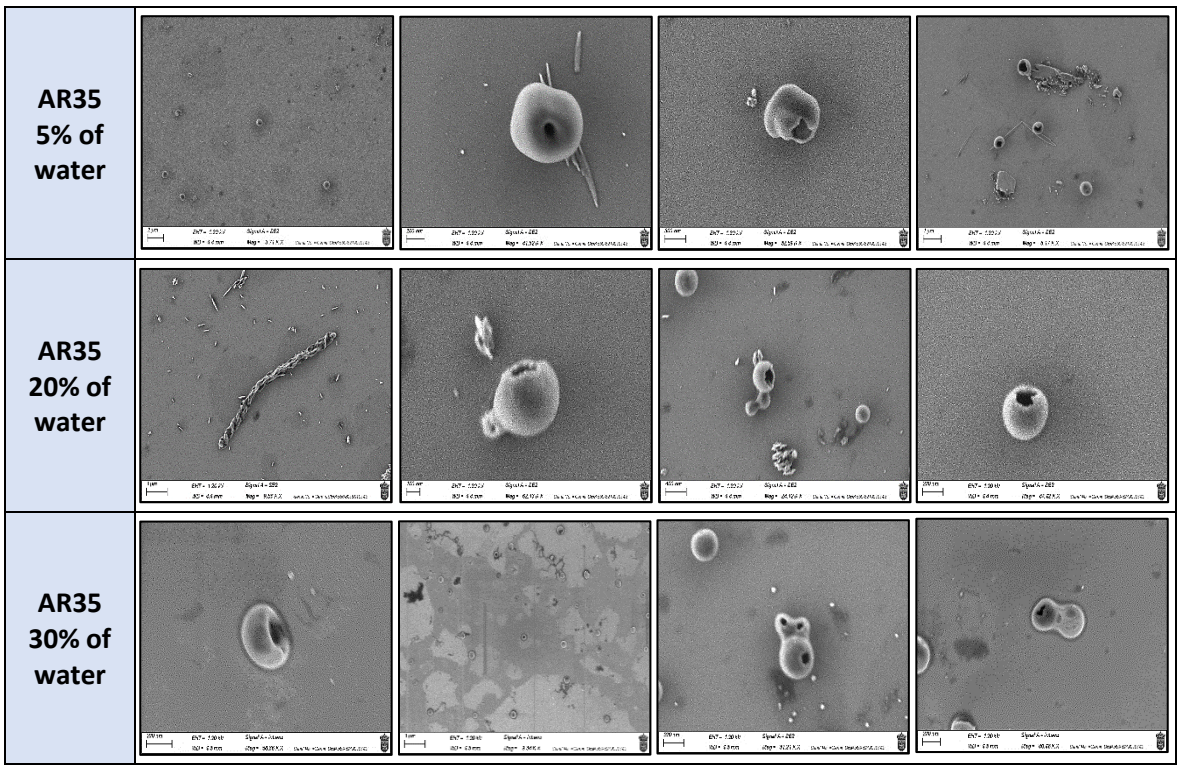

AR35 40% of water	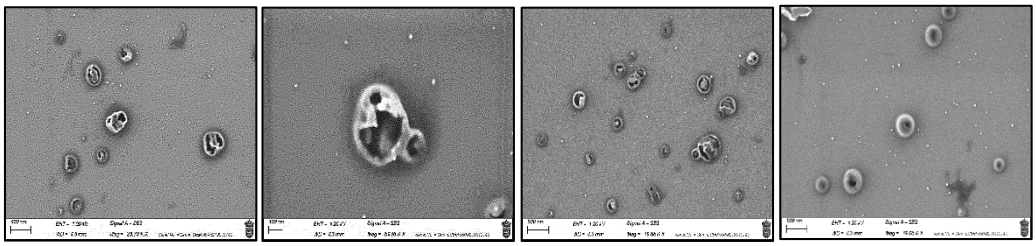
AR35 60% of water	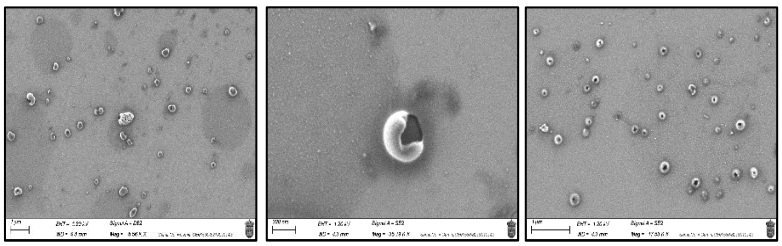
AR35 80% of water	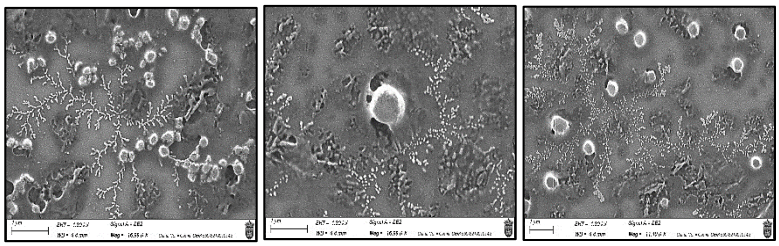

Figure 106. SEM nanoparticles of AR35 in different mixtures of water and THF.

pH test:

For this test, the proportion of water that the compound could accept according to the previous water acceptance test was 30%. The concentration of the compound was 20 µM and the solvent used was acetone.

	R	HCl	3.4	4.8	6.4	7.4	7.9	10.4	KOH
Visible light	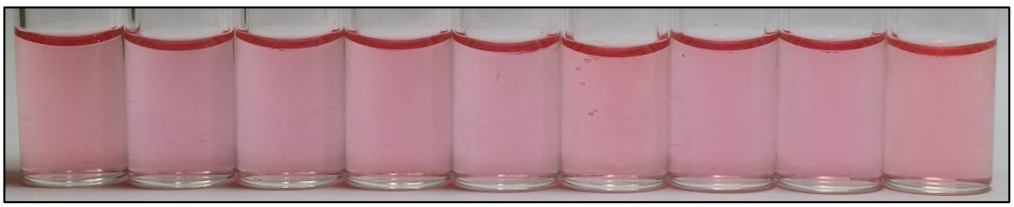								
UV light (366 nm)	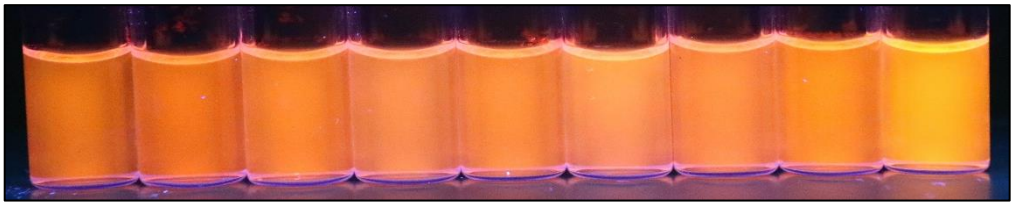								

Figure 107.pH test of AR35 under visible (up) and UV (down) light.

No significant changes were observed.

Cations and anions test:

The concentration of the compound was 20 µM and the solvent used was acetone.

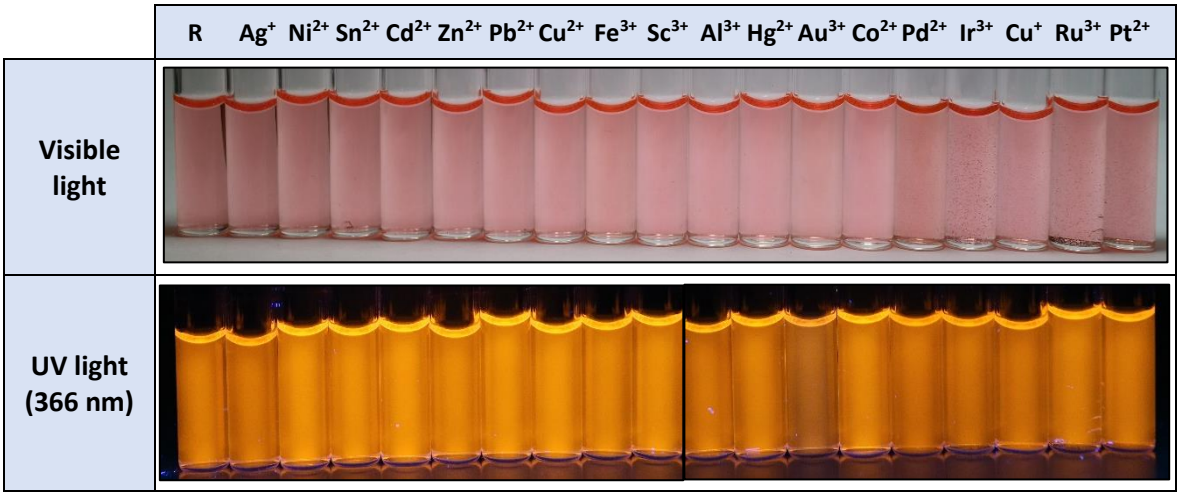

Figure 108. Cations test of AR35 under visible (up) and UV (down) light.

No significant changes were observed.

For the anion test, the concentration of the compound was 20 µM and the solvent used was acetone.

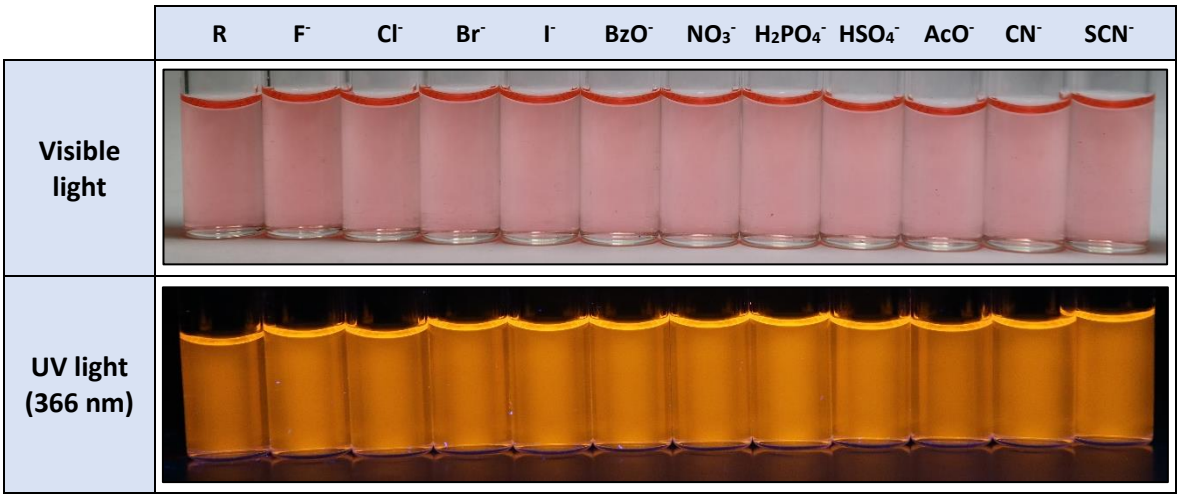

Figure 109. Anions test of AR35 under visible (up) and UV (down) light.

No significant changes were observed.

Oxidant and reductant reagents test:

The solvent used was acetone and concentration of the compound was 20 µM.

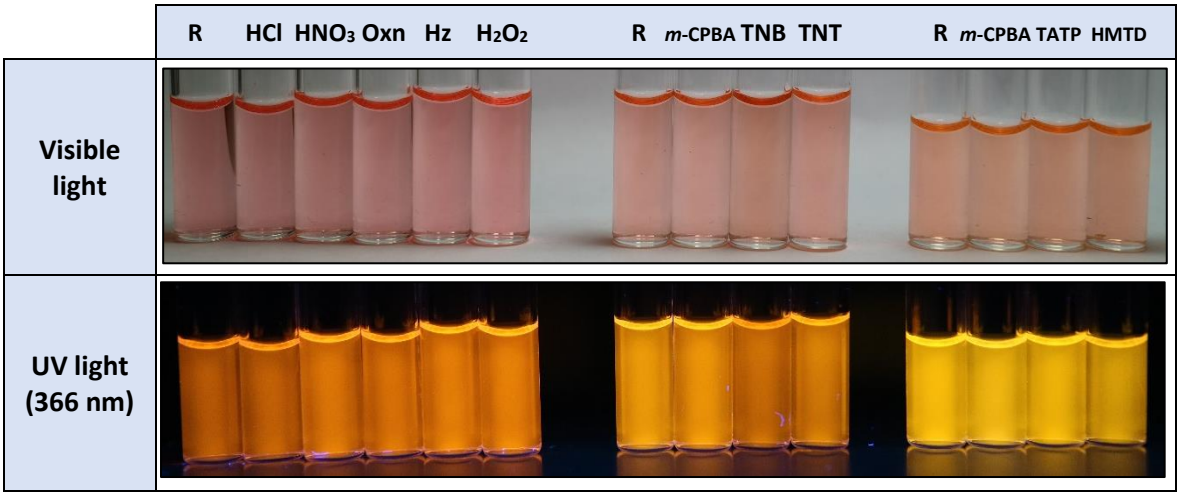

Figure 110.. Oxidant and reductant reagents test of AR35 under visible (up) and UV (down) light.

No significant changes were observed.

Synthesis of *N*-(1-(1-adamantyl)ethyl)-9-(trimethylsilyl)ethynylperylene-3,4-dicarboxylmonoimide (AR22p)

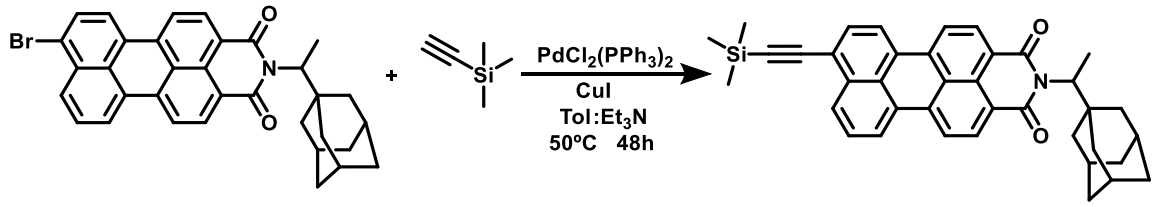

In a 100 ml Schlenk with a magnetic stirrer, 272 mg of *N*-(1-(1-adamantyl)ethyl)-9-bromoperylen-3,4-dicarboxylmonoimide (0.484 mmol), 17 mg of $PdCl_2(PPh_3)_2$ (0.02 mmol) and 10 mg of copper iodide (0.05 mmol) were disolved in 45 ml of toluene under nitrogen atmosphere. Later, 9 ml of triethylamine (0.06 mmol) was added to the solution and, then, 0.4 ml of TMSA (2.89 mmol) was added. The mixture was stirred 48 hours at 50ºC. Afterwards, 50 ml of water were added and the mixture was extracted three times with DCM (3×100 ml). The combined organic extracts were dried over Na_2SO_4 and the solvent was evaporated under reduce pressure. The solid obtained was purified with a column chromatographic (SiO_2, DCM:Hex 30%) to obtain 155 mg of a red solid, 55% yield.

m.p.: 240-243ºC (decomposition).

IR (ATR, cm^{-1}): 2898-2844, 1693 (C=O), 1647 (C=O), 1590, 1572, 1501, 1453, 1408, 1348, 1316, 1289, 1243, 1178 (C-N), 1151 (-CH_3), 1127, 1097, 1055, 962, 893, 836, 804, 750, 666, 627, 597, 538, 441.

^{1}H-NMR (300 MHz, $CDCl_3$) δ (ppm): 8.24-8.14 (m, 2H, 2×**H_{Ar}**), 8.08 (dd, *J* = 8.2, 1.9 Hz, 1H, **H_{Ar}**), 7.88-7.76 (m, 2H, 2×**H_{Ar}**), 7.71 (dd, *J* = 8.2, 4.4 Hz, 2H, 2×**H_{Ar}**), 7.45 (dd, *J* = 7.9, 2.7 Hz, 1H, **H_{Ar}**), 7.35 (td, *J* = 7.9, 3.0 Hz, 1H, **H_{Ar}**), 5.08 (q, *J* = 7.2 Hz, 1H, C**H**), 2.00 (s, 3H, 3×C**H**), 1.88-1.78 (m, 3H, C**H_3**), 1.75-1.65 (m, 12H, 6×C**H_2**), 0.41 (s, 9H, 3×C**H_3**).

^{13}C-NMR (75MHz, $CDCl_3$) δ (ppm): 165.3 (**C**=O) , 164.6 (**C**=O), 135.9 (**C_{Ar}**), 135.7 (**C_{Ar}**), 135.4 (**C_{Ar}**), 135.2 (**C_{Ar}**), 134.0 (**C_{Ar}**), 131.5 (**C_{Ar}**H), 131.3 (**C_{Ar}**H), 131.2 (**C_{Ar}**H), 130.7 (**C_{Ar}**H), 130.6 (**C_{Ar}**H), 129.1 (**C_{Ar}**), 129.0 (**C_{Ar}**), 128.9 (**C_{Ar}**), 128.7 (**C_{Ar}**H), 128.6 (**C_{Ar}**H), 127.2 (**C_{Ar}**H), 125.6 (**C_{Ar}**), 123.4 (**C_{Ar}**H), 123.1 (**C_{Ar}**), 123.0 (**C_{Ar}**), 122.2 (**C_{Ar}**H), 122.0 (**C_{Ar}**), 121.8 (**C_{Ar}**), 121.1 (**C_{Ar}**), 120.3 (**C_{Ar}**), 120.2 (**C_{Ar}**H), 120.0 (**C_{Ar}**H), 103.2 (**C**≡CH), 102.6 (C≡**C**Si(CH_3)$_3$), 58.1 (**C**H), 40.4 (**C**H_2), 38.1 (**Cq**), 37.2 (**C**H_2), 28.9 (**C**H), 13.3 (**C**H), 0.2 (**C**H_3).

UV-Vis ($CHCl_3$), λ_{max} nm (log ε): 560 (3.8).

Ø ($CHCl_3$, %): 85.56.

τ (475 nm, $CHCl_3$, ns): 4.390 (χ^2: 1.112).

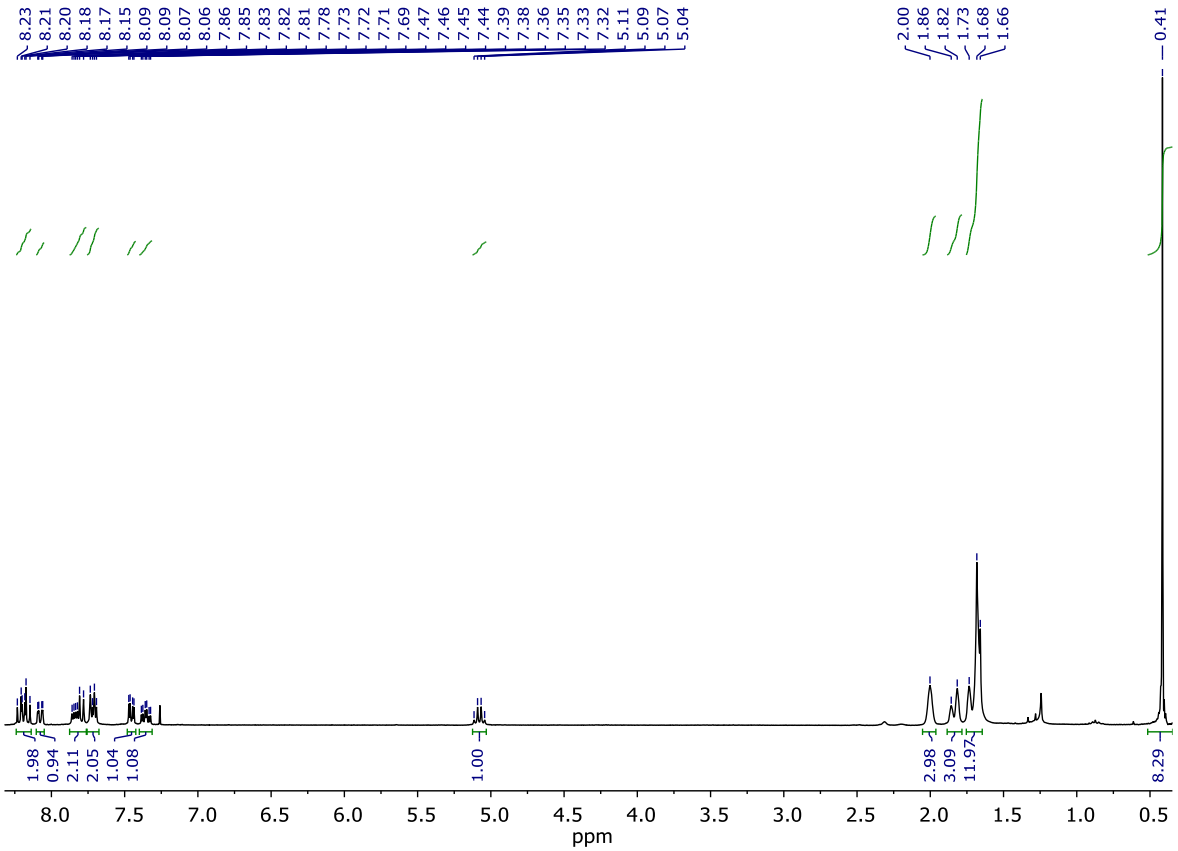

Figure 111. ¹H-NMR ($CDCl_3$, 300 MHz) of AR22p.

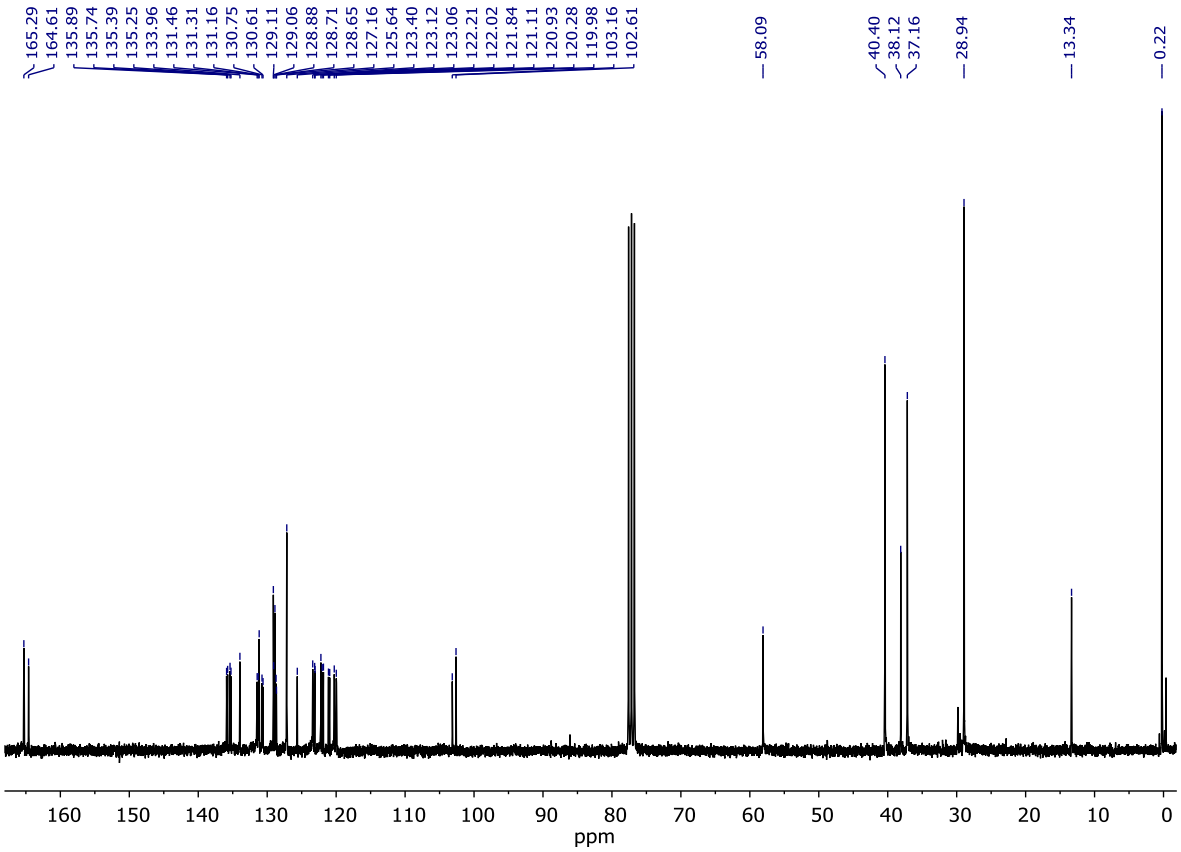

Figure 112. ¹³C-NMR ($CDCl_3$, 75 MHz) of AR22p.

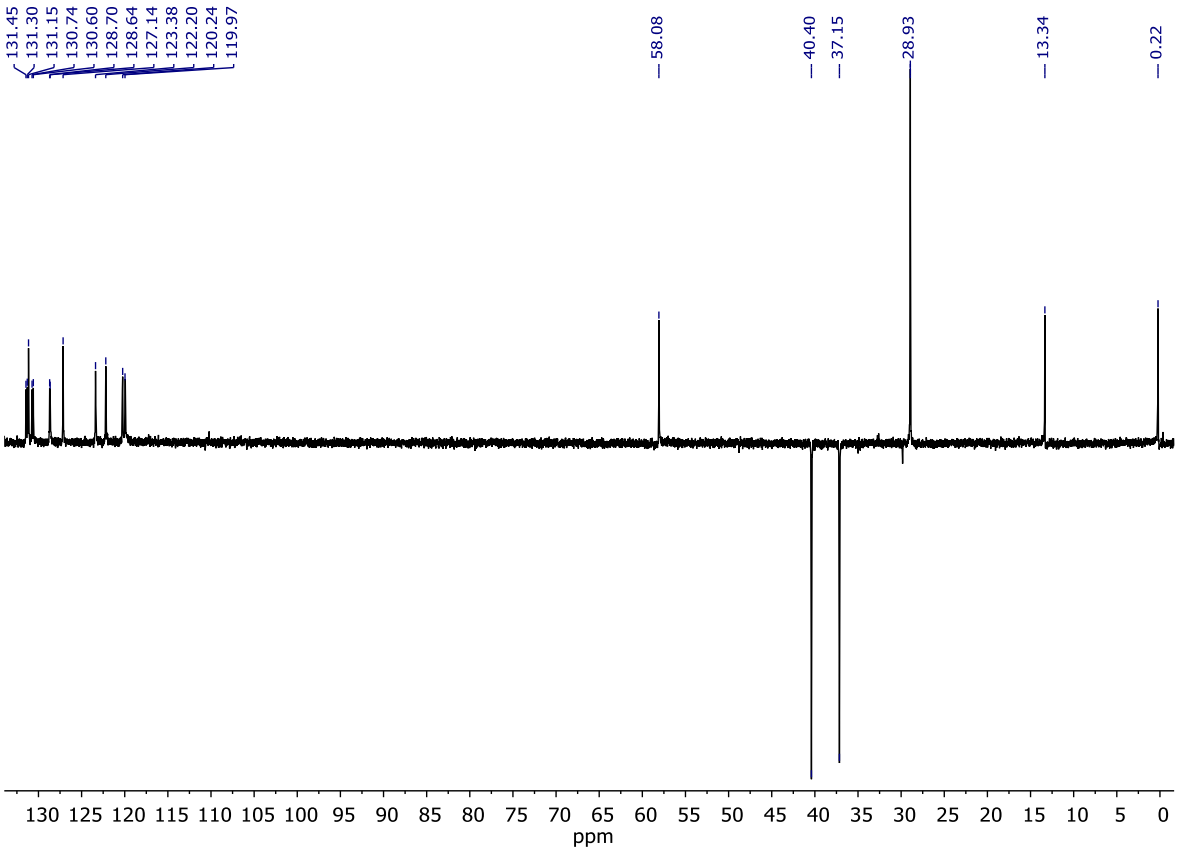

Figure 113. DEPT NMR ($CDCl_3$, 75 MHz) of AR22p.

Fluorescence decay lifetime (τ):

The solvent used was $CHCl_3$. The concentration of the compound was 10 µM.

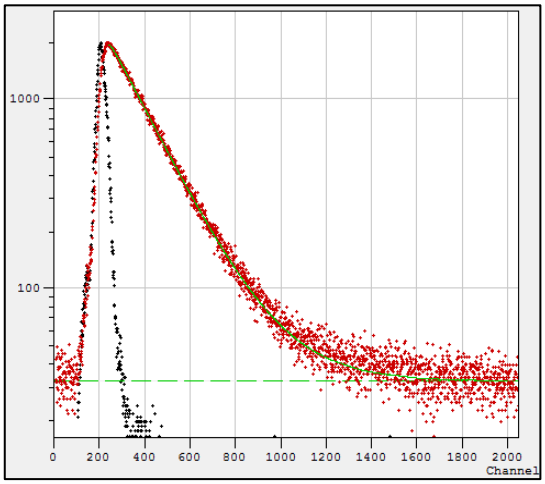

Figure 114. Fluorescence decay lifetime of AR22p.

Solvatochromism:

The concentration of the compound was 10 µM and the excitation wavelength was 490 nm.

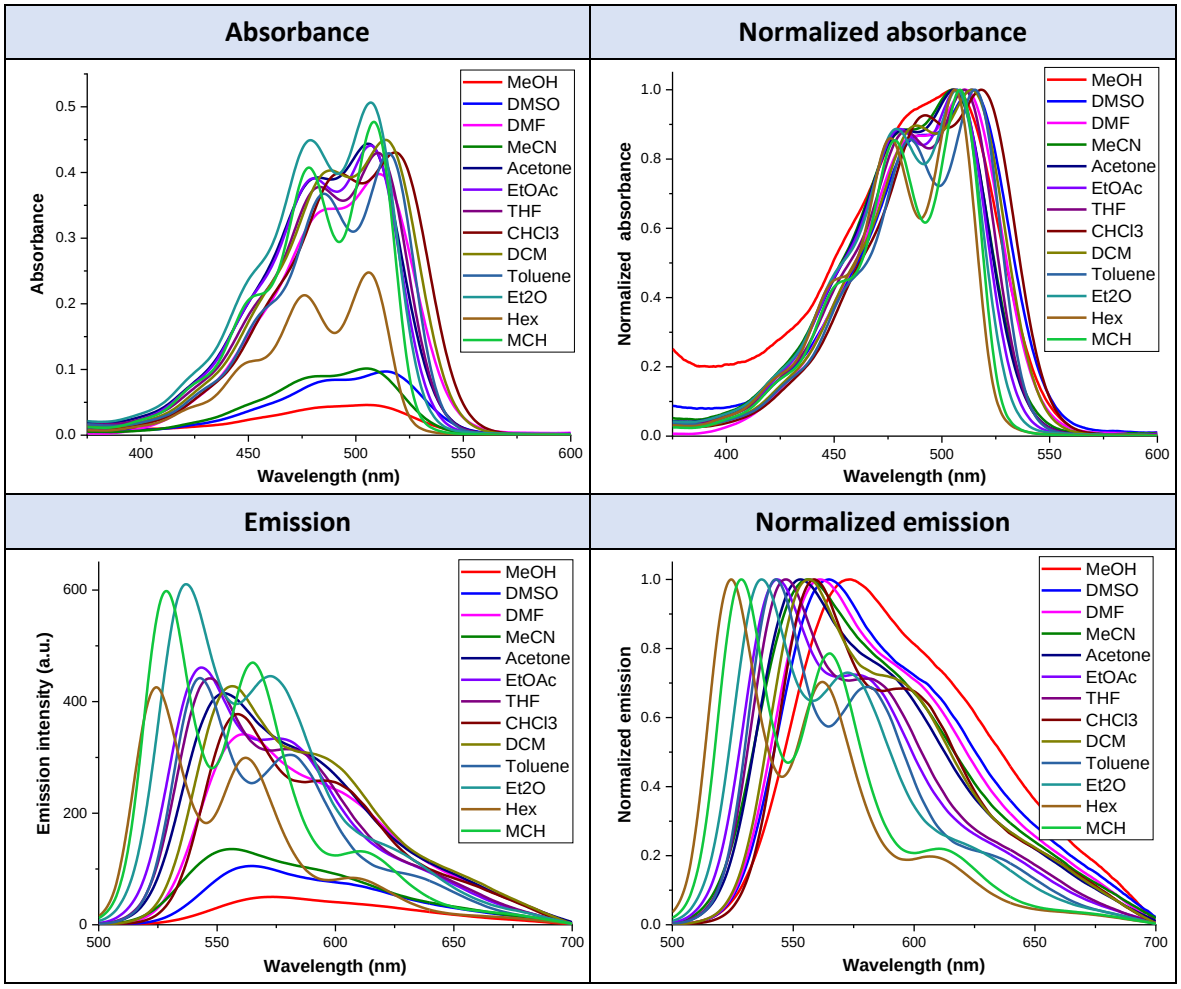

Figure 115. Solvatochromism of AR22p.

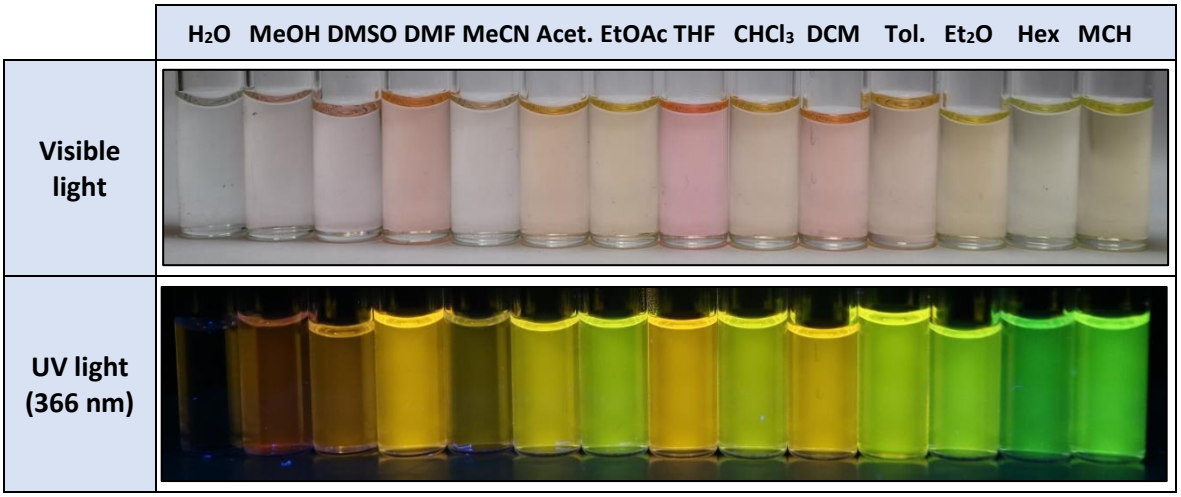

Figure 116. Solvatochromism of AR22p under visible and 366 nm light.

Water acceptance test:

The solvent used was THF and the concentration of the compound was 10 µM.

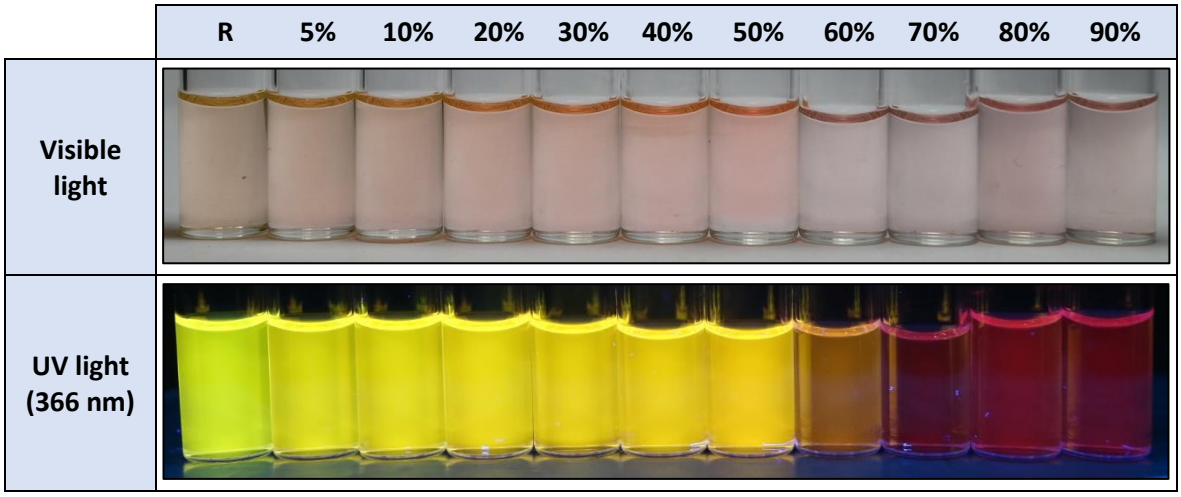

Figure 117. Water acceptance test of AR22p under visible (up) and UV (down) light.

The maximum aumount of water that was admitted by the product was 50%. At 50% of water, the maximum of emission was changed from yellow to dark red.

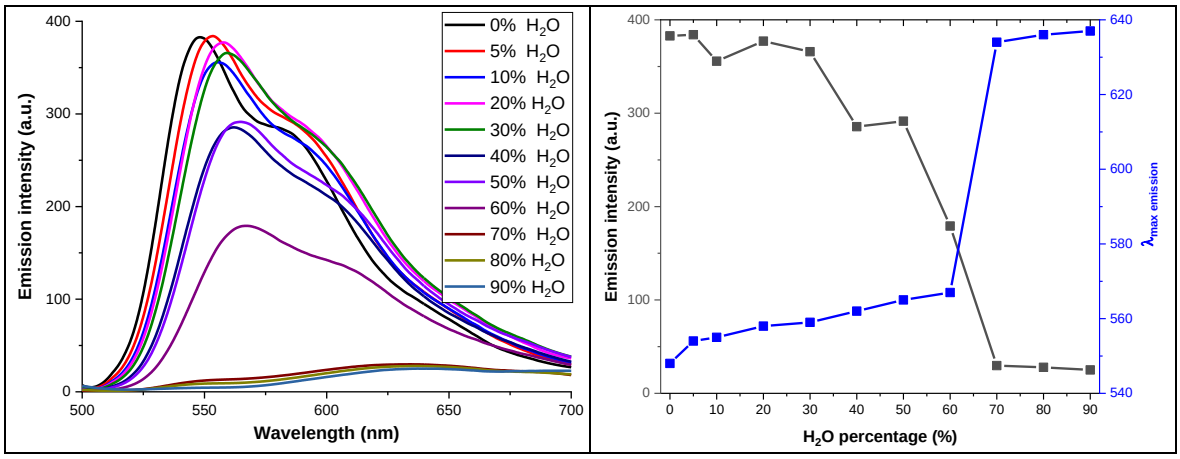

Figure 118. Emission intensity graph (left) and graph of relationship between the intensity of emission and the wavelenght of the maximum of emission (right) as a function of the amount of water added for AR22p.

pH test:

For this test, the proportion of water that the compound could accept according to the previous water acceptance test was 30%. The concentration of the compound was 10 µM and the solvent used was THF.

	R	HCl	3.4	4.8	6.4	7.4	7.9	10.4	KOH
Visible light									
UV light (366 nm)	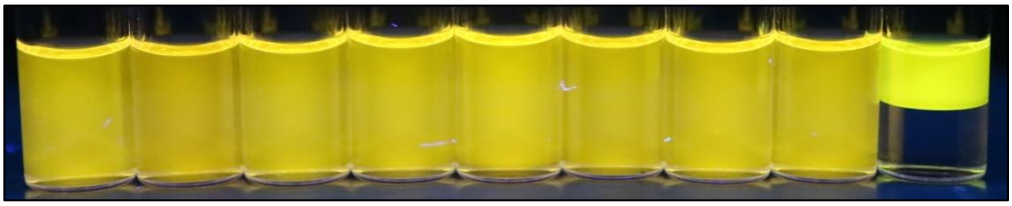								

Figure 119. pH test of AR22p under visible (up) and UV (down) light.

No significant changes were observed.

Cations and anions test:

The concentration of the compound was 10 µM and the solvent used was THF.

	R	Ag^{+}	Ni^{2+}	Sn^{2+}	Cd^{2+}	Zn^{2+}	Pb^{2+}	Cu^{2+}	Fe^{3+}	Sc^{3+}	Al^{3+}	Hg^{2+}	Au^{3+}	Co^{2+}	Pd^{2+}	Ir^{3+}	Cu^{+}	Ru^{3+}	Pt^{2+}
Visible light																			
UV light (366 nm)	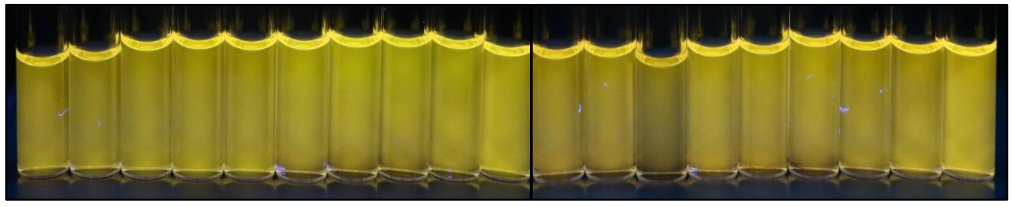																		

Figure 120. Cations test of AR22p under visible (up) and UV (down) light.

There was a slight decrease in fluorescence against Au^{3+}.

For the anion test, the concentration of the compound was 10 µM and the solvent used was THF.

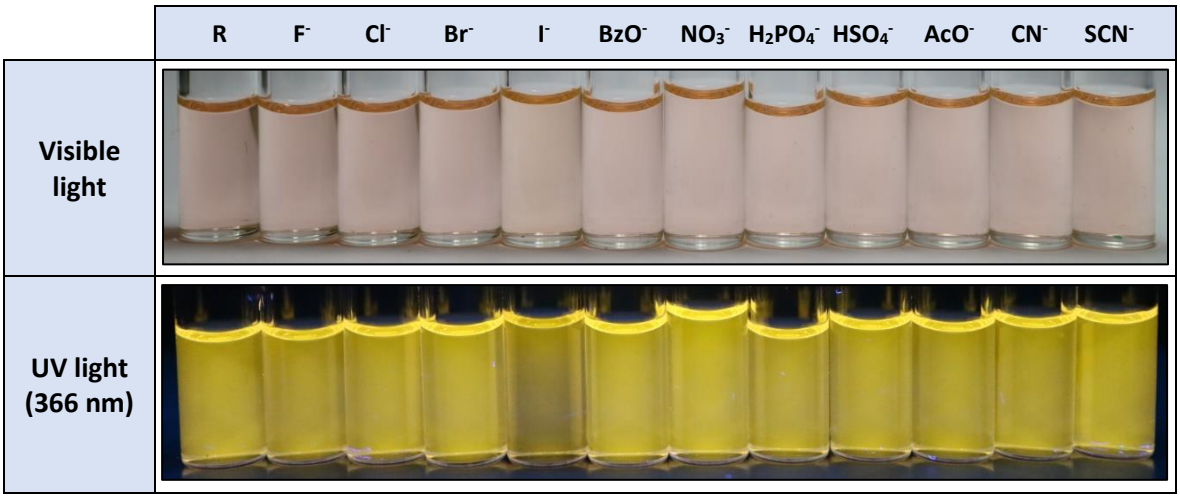

Figure 121. Anions test of AR22p under visible (up) and UV (down) light.

No significant changes were observed.

Oxidant and reductant reagents test:

The solvent used was THF and concentration of the compound was 10 µM.

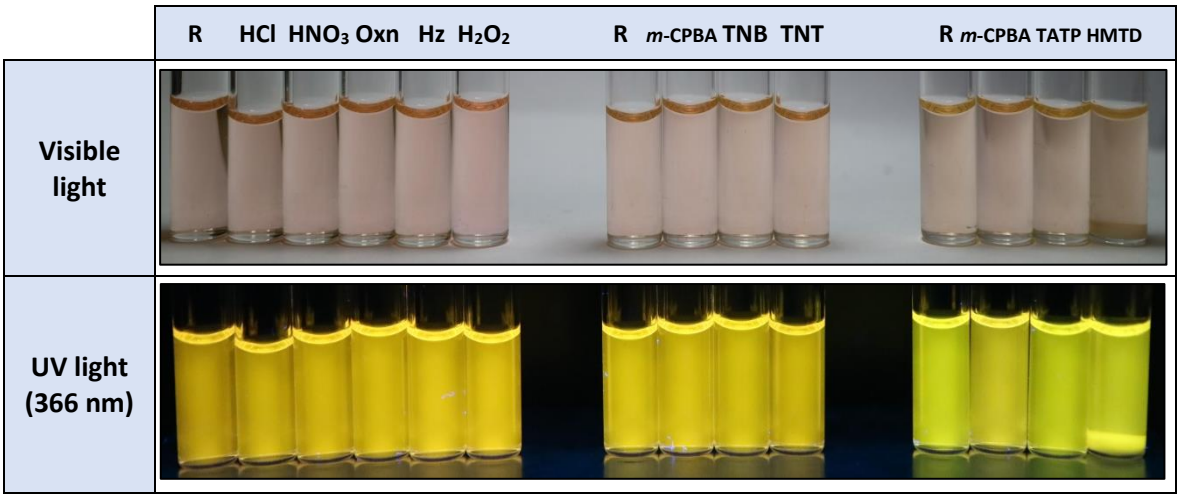

Figure 122. Oxidant and reductant reagents test of AR22p under visible (up) and UV (down) light.

No significant changes were observed.

Synthesis of *N*-(1-(1-adamantyl)ethyl)-9-ethynylperylene-3,4-dicarboxylmonoimide (AR22d)

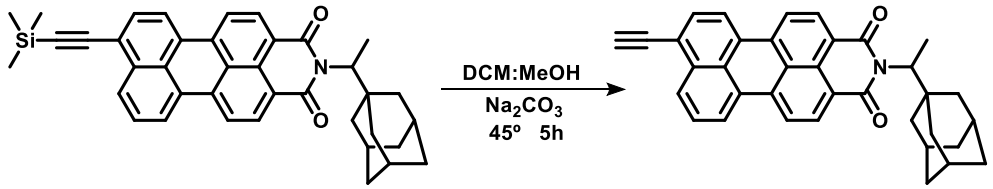

In a 250 ml flask, 155 mg of AR22p (0.28 mmol) were dissolved in 10 ml of a mixture of DCM:MeOH (1:1) and 1 g of sodium carbonate (9.43 mmol) was added. The mixture was stirred 5 hours at 45°C and later, the solvent was evaporated under reduce pressure. DCM was added to the flask and the solution was washed three times with water (3×100 ml). The organic extracts was combined, dried over Na_2SO_4 and the solvent was evaporated under reduce pressure. The product is a red solid obtained with a 100% of yield (136 mg).

m.p.: >390°C.

IR (ATR, cm^{-1}): 3301 (≡CH), 2899-2842 (C-H), 1689 (C=O), 1641 (C=O), 1590 (C_{Ar}-C_{Ar}), 1574, 1344, 1241, 1176 (C-N), 1053, 837, 805, 751, 597, 468.

^{1}H-NMR (300 MHz, $CDCl_3$) δ (ppm): 8.49-8.37 (m, 2H, 2×**H_{Ar}**), 8.30-8.04 (m, 5H, 5×**H_{Ar}**), 7.69 (dd, *J* = 12.4, 7.3 Hz, 1H, **H_{Ar}**), 7.58-7.53 (m, 1H, **H_{Ar}**), 5.10 (q, *J* = 7.3 Hz, 1H, C**H**), 3.65 (s, 1H, C**H**), 1.99 (s, 3H, 3×C**H**), 1.84 (d, *J* = 12.4 Hz, 3H, C**H_3**), 1.76-1.63 (m, 12H, 6×C**H_2**).

^{13}C-NMR (75MHz, $CDCl_3$) δ (ppm): 165.5 (**C**=O), 164.8 (**C**=O), 136.2 (**C_{Ar}**), 136.1 (**C_{Ar}**), 135.8 (**C_{Ar}**), 135.6 (**C_{Ar}**), 134.4 (**C_{Ar}**), 131.9 (**C_{Ar}**H), 131.7 (**C_{Ar}**H), 131.2 (**C_{Ar}**H), 131.0 (**C_{Ar}**H), 129.5 (**C_{Ar}**H), 127.6 (**C_{Ar}**H), 126.1 (**C_{Ar}**), 123.8 (**C_{Ar}**H), 122.4 (**C_{Ar}**H), 122.2 (**C_{Ar}**), 120.7 (**C_{Ar}**H), 120.4 (**C_{Ar}**H), 84.9 (**C**≡CH), 81.5 (C≡**C**H), 58.2 (**C**H), 40.4 (**C**H_2), 38.2 (**Cq**), 37.1 (**C**H_2), 28.9 (**C**H), 13.4 (**C**H_3).

HRMS (MALDI, DCTB+) m/z: calculated for $C_{36}H_{29}NO_2$: 507.2193 (M^+); found 507.2220.

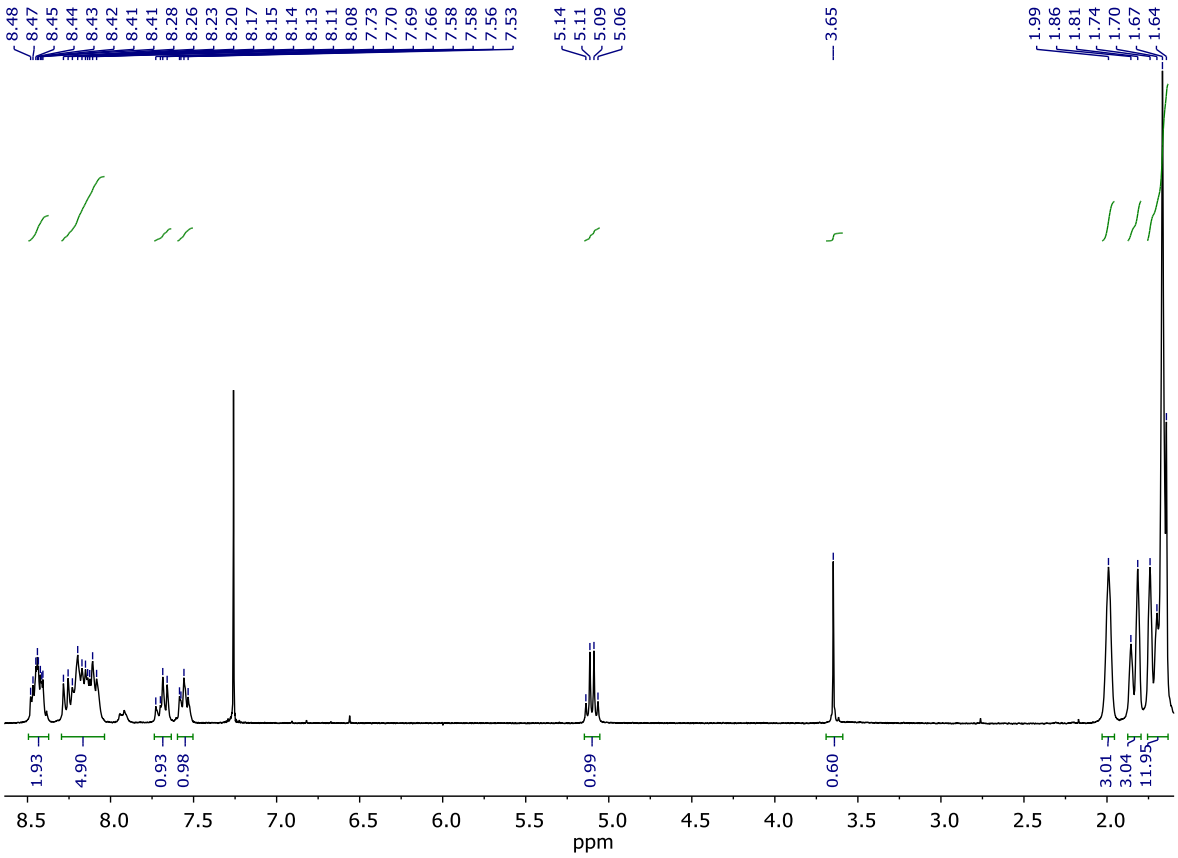

Figure 123. ^{1}H-NMR ($CDCl_3$, 300 MHz) of AR22d.

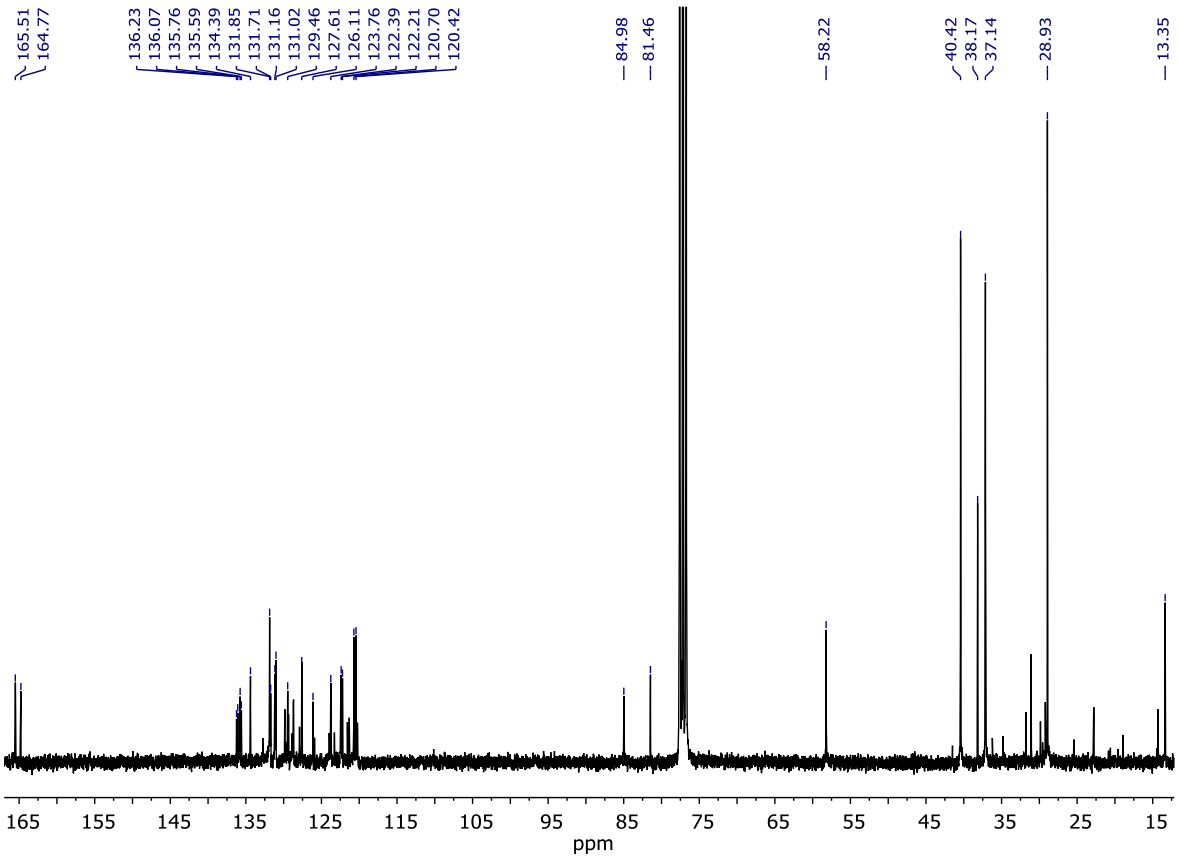

Figure 124. ^{13}C-NMR ($CDCl_3$, 75 MHz) of AR22d.

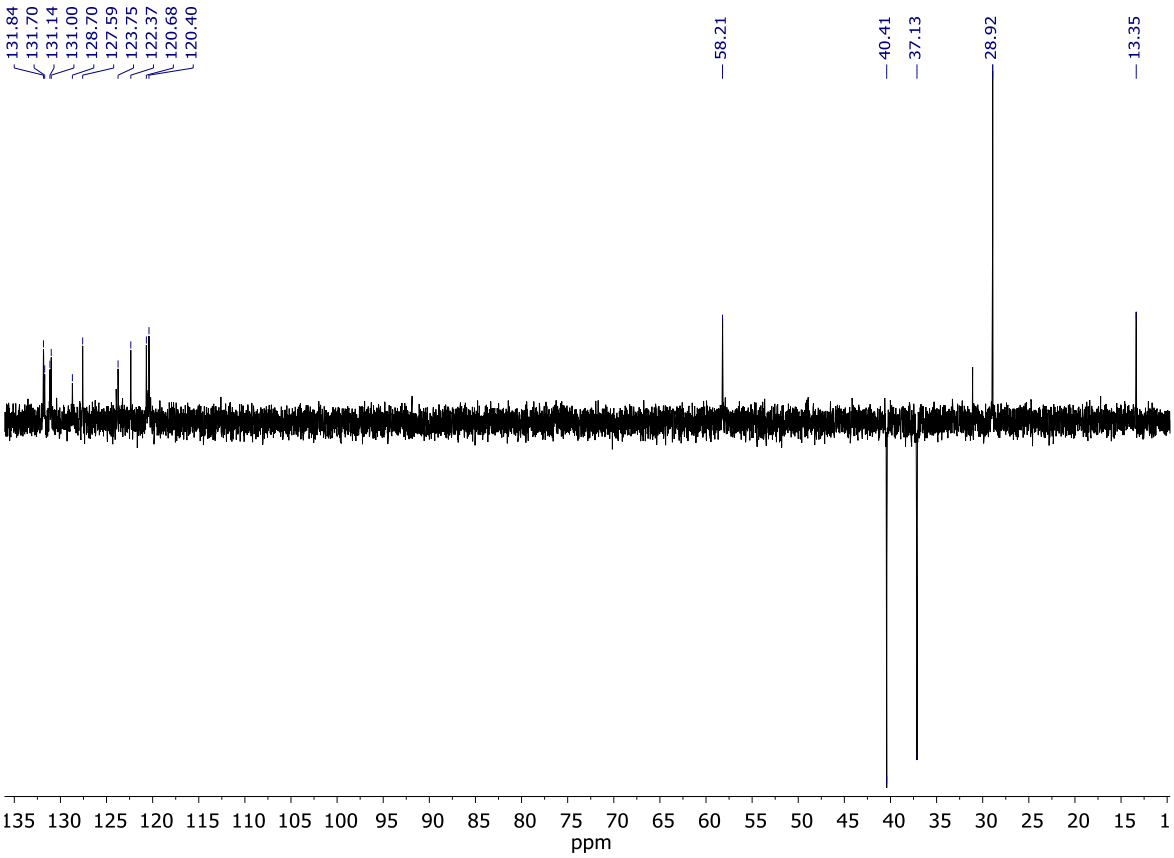

Figure 125. DEPT NMR ($CDCl_3$, 75 MHz) of AR22d.

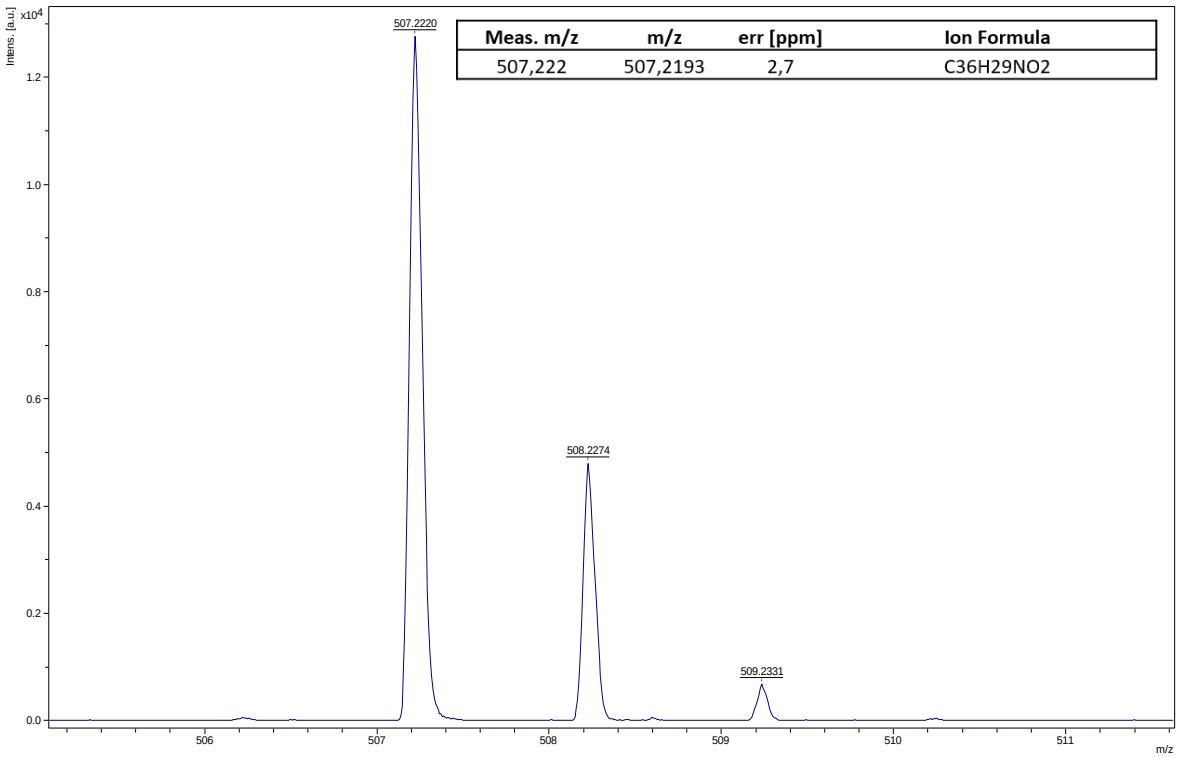

Meas. m/z	m/z	err [ppm]	Ion Formula
507,222	507,2193	2,7	C36H29NO2

Figure 126. HRMS (MALDI, DCTB+) of AR22d.

Synthesis of *N,N'*-bis(1-(1-adamantyl)ethyl)-9-diethynyldiperylen-3,3',4,4'-tetracarboxylmonoimide (AR20)

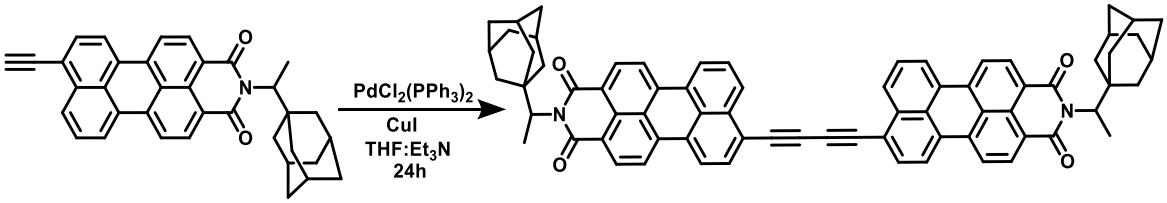

In a 100 ml Schlenk, 100 mg of *N*-(1-(1-adamantyl)ethyl)-9-ethynylperylene-3,4-dicarboxylmonoimide (AR22d, 0.2 mmol), 26 mg of cooper iodide (0.14 mmol) and 17 mg of $PdCl_2(PPh_3)_2$ (0.02 mmol) were dissolved en 45 ml of THF under nitrogen atmosphere and, later, 5 ml of triethylamine (0.03 mmol) were added and the mixture was refluxed overnight. Afterwards, 50 ml of water were added and the mixture was extracted three times with DCM (3×100 ml) and the organic extracts were combined, dried over Na_2SO_4 and the solvent was evaporated under reduce pressure. The organic solid was purified with a column chromatographic (SiO_2, DCM).getting 133 mg of a purple solid, 67% yield.

m.p.: >390°C.

IR (ATR, cm^{-1}): 2903 (C-H), 2846, 1689 (C=O), 1649 (C=O), 1590 (C_{Ar}-C_{Ar}), 1565, 1406, 1349, 1314, 1287, 1244, 1176 (C-N), 1098, 1056, 906, 837, 805, 754, 597, 471, 459, 424.

^{1}H-NMR (300 MHz, $CDCl_3$) δ (ppm): 8.69-8.34 (m, 14H, 14×**H_{Ar}**), 8.02-7.87 (m, 2H, 2×**H_{Ar}**), 7.83-7.78 (m, 2H, 2×**H_{Ar}**), 5.19-5.08 (m, 2H, 2×C**H**), 1.99 (s, 6H, 6×C**H**), 1.80-1.68 (m, 30H, 12×C**H_2** y 2×C**H_3**).

^{13}C-NMR (75MHz, $CDCl_3$) δ (ppm): 167.5 (**C**=O), 167.2 (**C**=O), 138.3 (**C_{Ar}**), 135.1 (**C_{Ar}**), 134.1 (**C_{Ar}**), 133.7 (**C_{Ar}**H), 133.6 (**C_{Ar}**), 133.3 (**C_{Ar}**H), 132.9 (**C_{Ar}**), 130.2 (**C_{Ar}**H), 129.9 (**C_{Ar}**H), 129.4 (**C_{Ar}**), 128.6 (**C_{Ar}**H), 127.8 (**C_{Ar}**), 126.4 (**C_{Ar}**), 125.5 (**C_{Ar}**H), 124.0 (**C_{Ar}**), 123.1 (**C_{Ar}**), 121.7 (**C_{Ar}**), 121.3 (**C_{Ar}**H), 120.7 (**C_{Ar}**H), 82.3 (**Cq**), 60.2 (**Cq**), 58.1 (**C**H), 40.4 (**C**H_2), 38.5 (**C**H_2), 37.0 (**C**H), 28.9 (**Cq**), 13.4 (**C**H_3).

HRMS (MALDI, DIT-) m/z: calculated for $C_{72}H_{56}N_2O_4$: 1012.4235 (M^-); found 1012.4245.

UV-Vis ($CHCl_3$), λ_{max} nm (log ε): 560 (4.4).

Ø ($CHCl_3$, %): 38.99.

τ (510 nm, $CHCl_3$, ns): 0.970/4.466 (χ^2: 1.074).

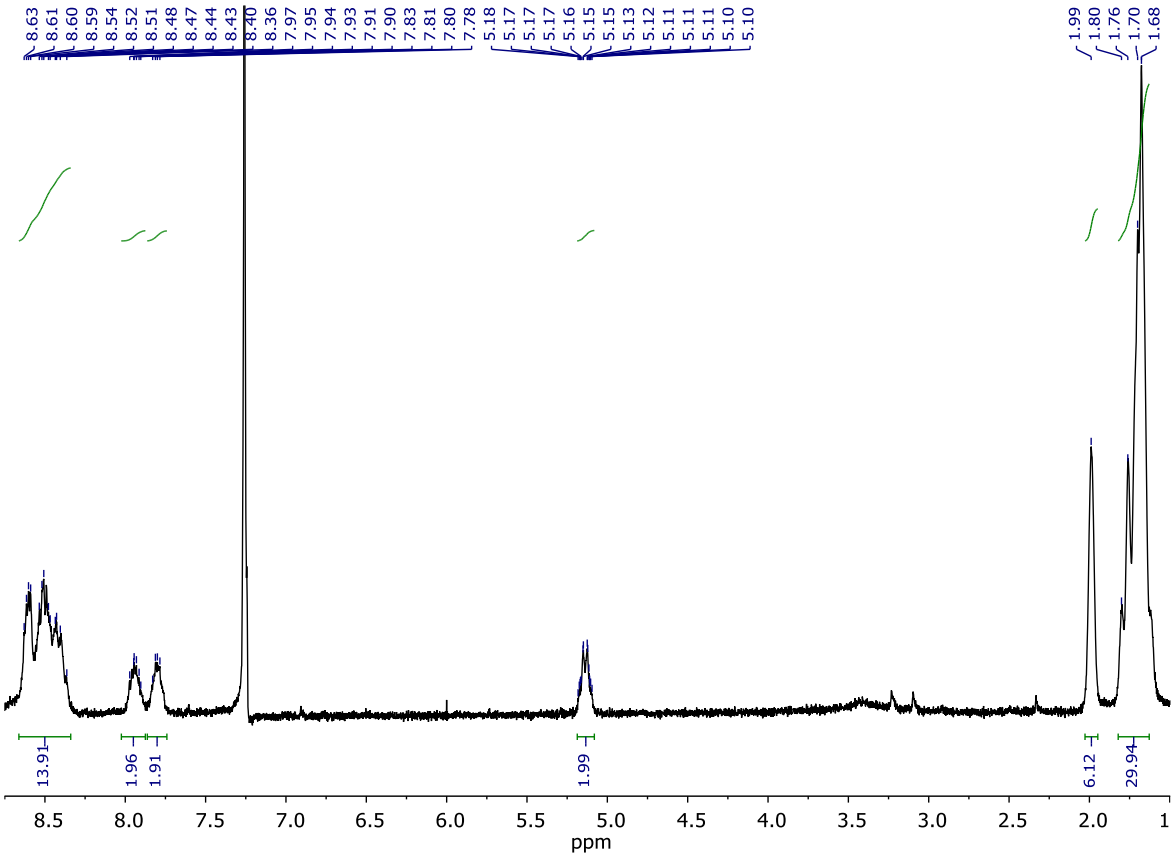

Figure 127. ^{1}H-NMR ($CDCl_3$, 300 MHz) of AR20.

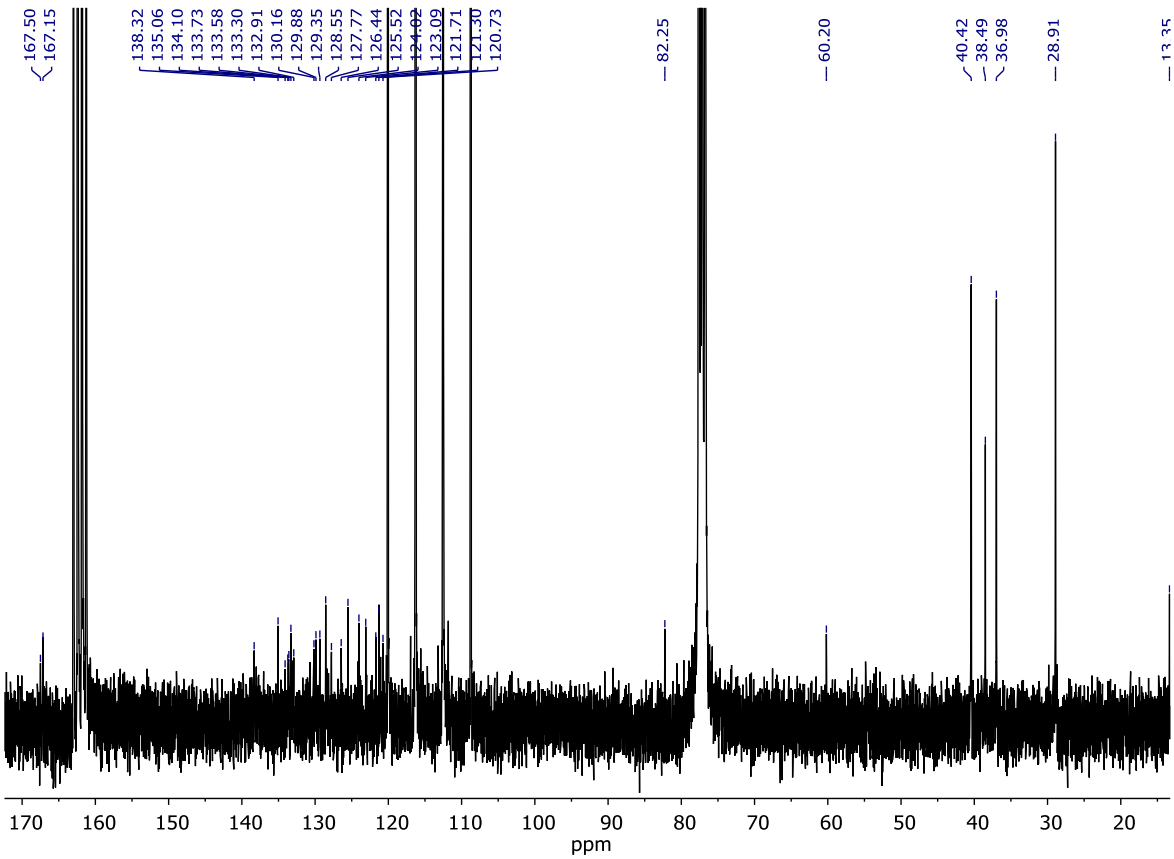

Figure 128. ^{13}C-NMR ($CDCl_3$, 75 MHz) of AR20.

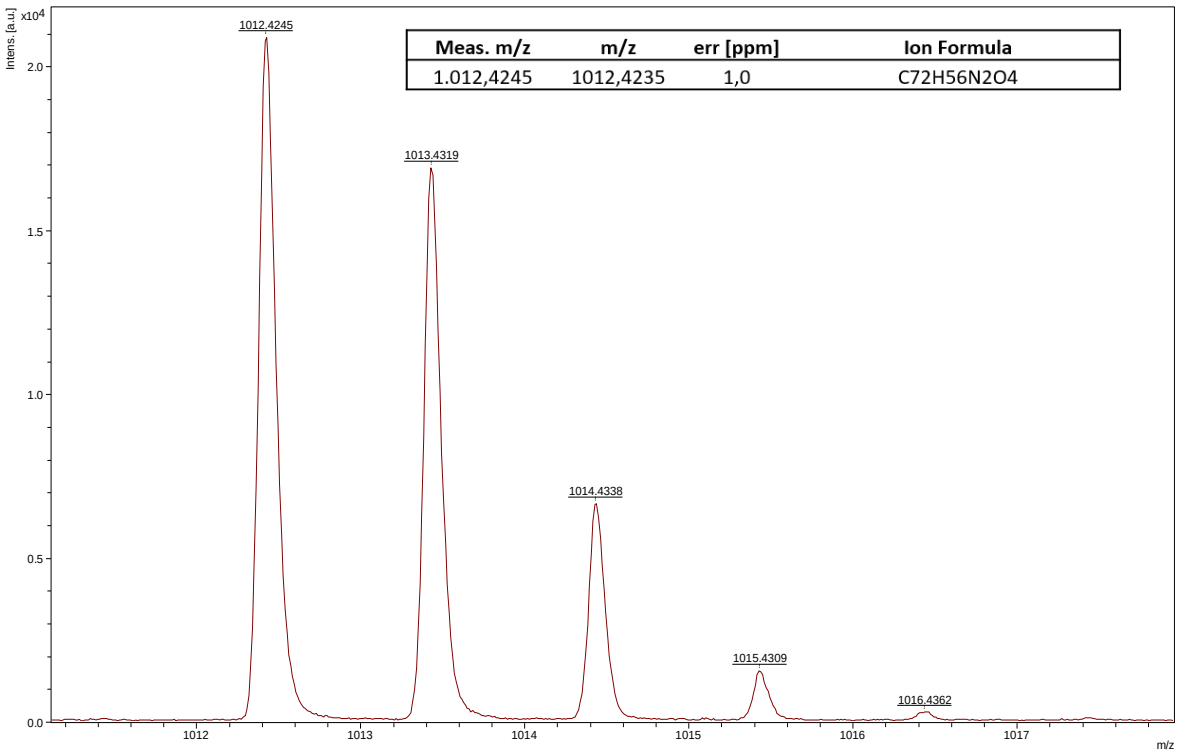

Meas. m/z	m/z	err [ppm]	Ion Formula
1.012,4245	1012,4235	1,0	C72H56N2O4

Figure 129. HRMS (MALDI, DIT-) of AR20.

Fluorescence decay lifetime (τ):

The solvent used was $CHCl_3$. The concentration of the compound was 20 µM.

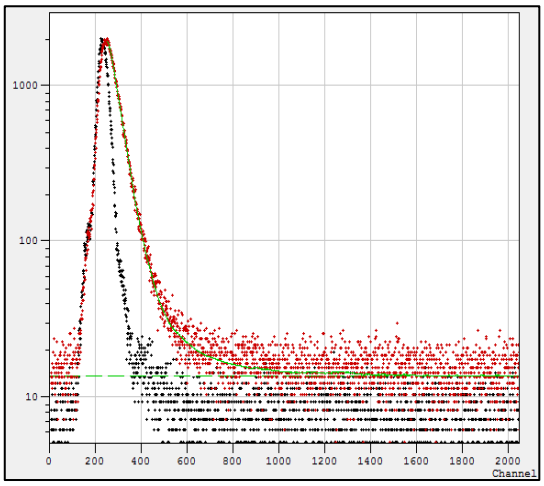

Figure 130. Fluorescence decay lifetime of AR20.

Solvatochromism:

The concentration of the compound was 20 µM and the excitation wavelength was 530 nm.

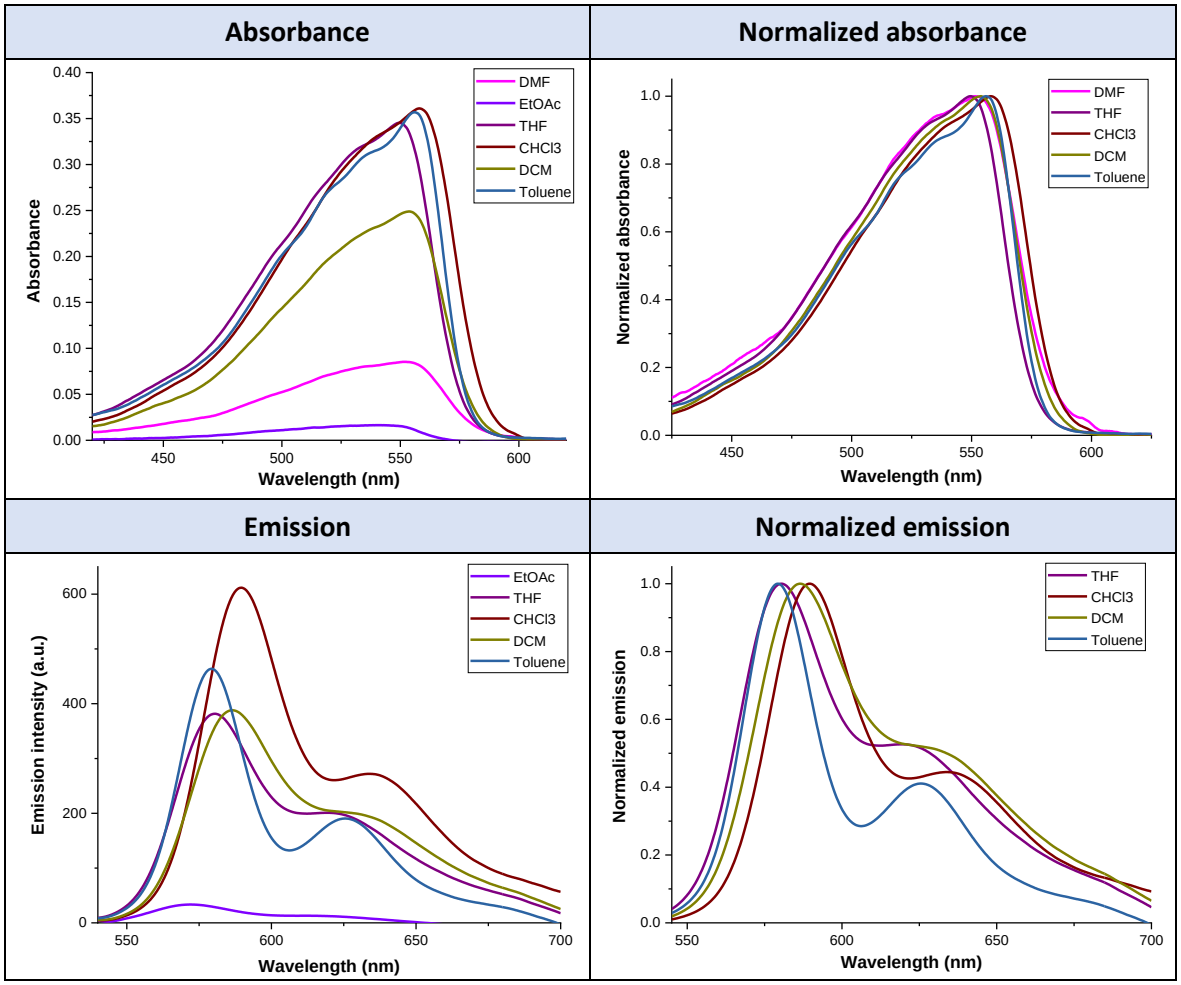

Figure 131. Solvatochromism of AR20.

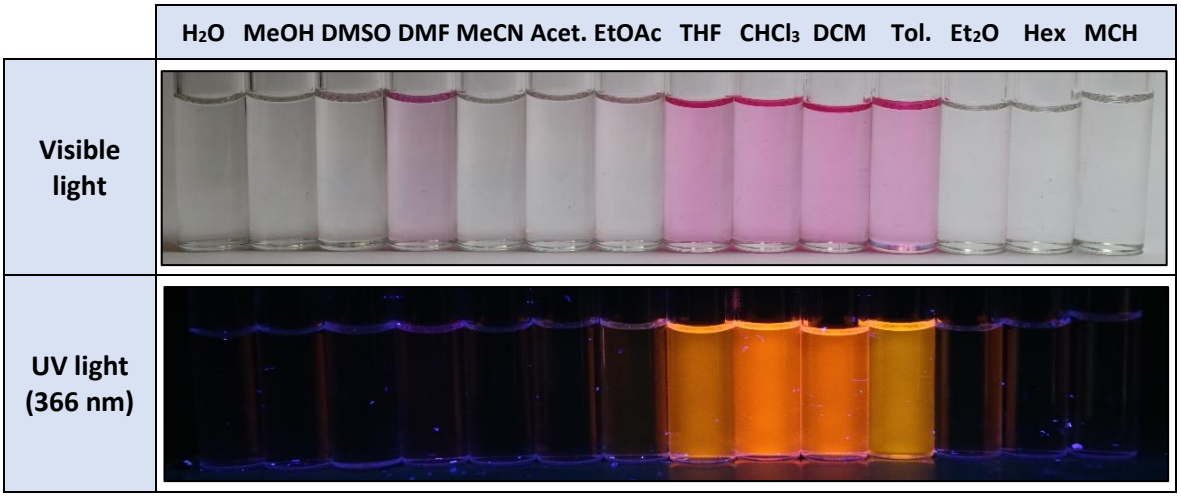

Figure 132. Solvatochromism of AR20 under visible and 366 nm light.

Water acceptance test:

The solvent used was THF and the concentration of the compound was 20 µM.

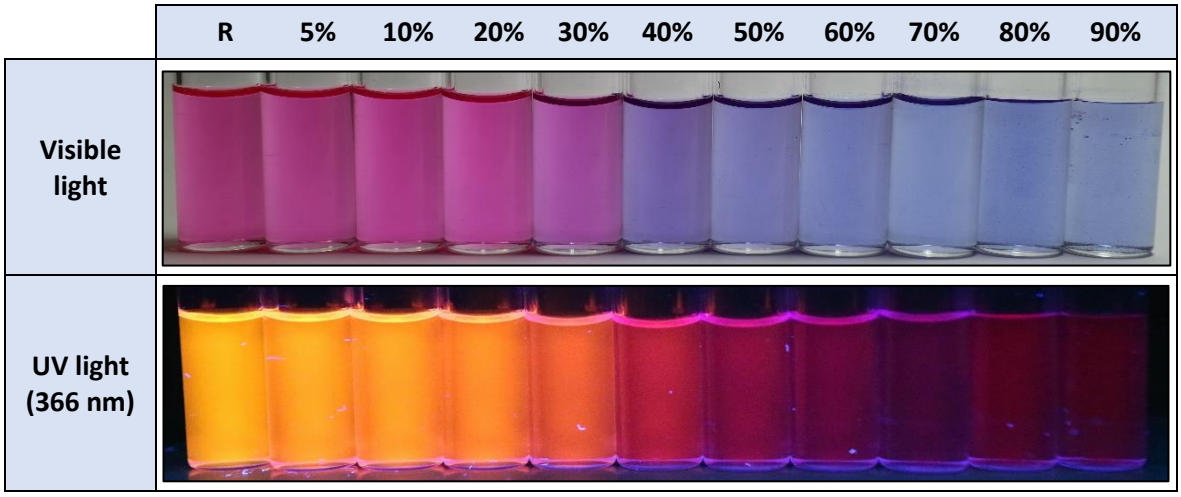

Figure 133. Water acceptance test of AR20 under visible (up) and UV (down) light.

The maximum aumount of water that was admitted by the product was 20%. Under visible light, at 30% of water, the maximum of absortion was changed from pink (about 550 nm) to purple. Under UV light, the emission intensity was decreased up to 50% water, stabilizing for higher percentages while, the emission maximum was shifted towards the red region (620-720 nm).

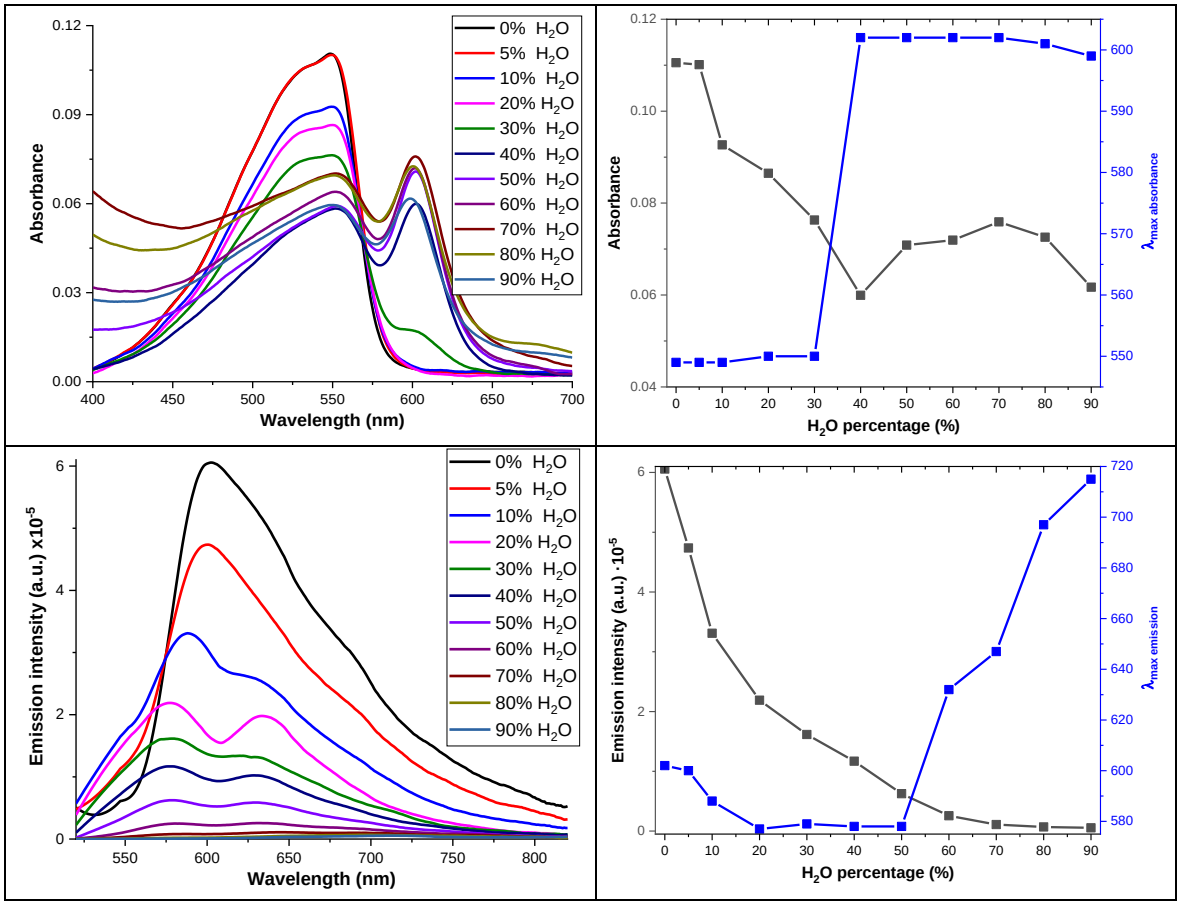

Figure 134. Absorbance graph (up left) and graph of relationship between the absorbance and the wavelength of the maximum of absorbance (up right) as a function of the amount of water, emission intensity graph (down left) and graph of relationship between the emission intensity and the wavelength of the maximum of emission (down right) as a function of the amount of water added for AR20 in THF.

AR20 5% of water	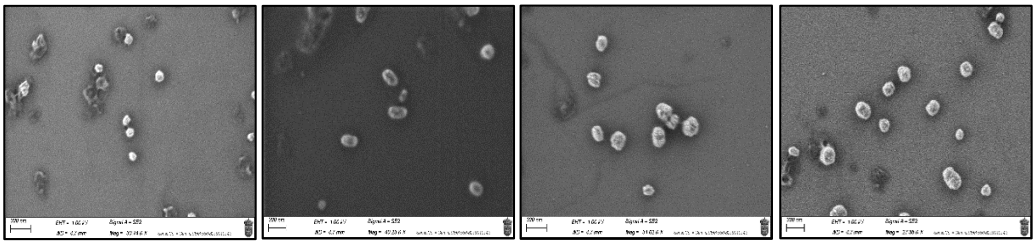
AR20 20% of water	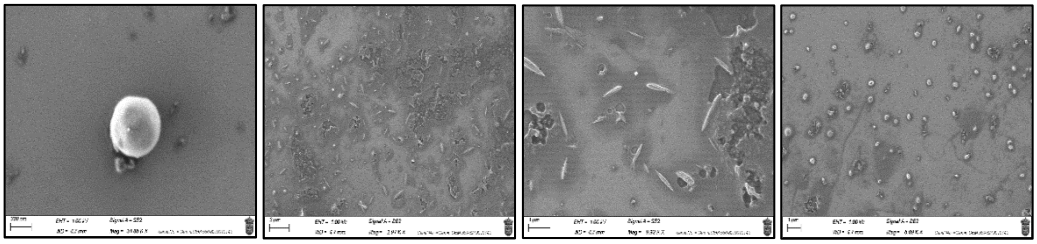
AR20 30% of water	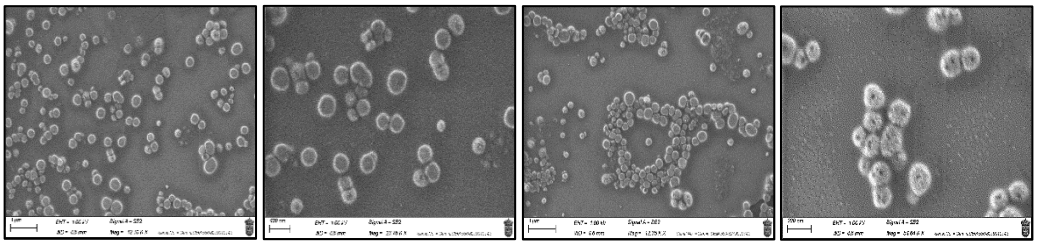
AR20 40% of water	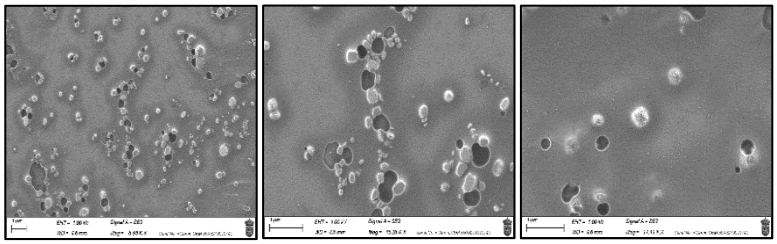
AR20 60% of water	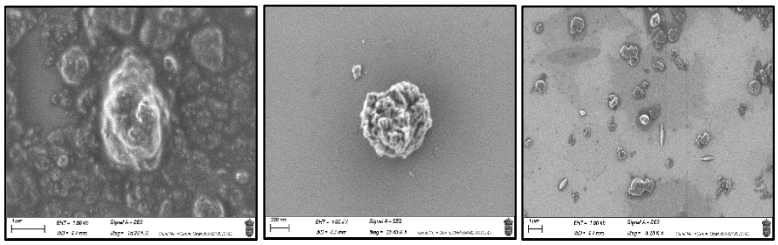
AR20 80% of water	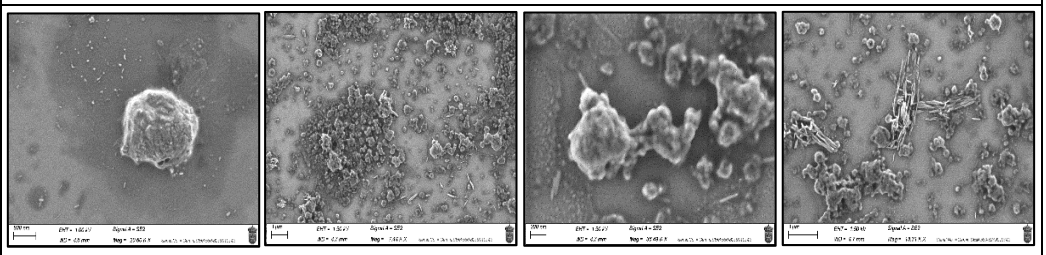

Figure 135. SEM nanoparticles of AR20 in different mixtures of water and THF.

pH test:

For this test, the proportion of water that the compound could accept according to the previous water acceptance test was 30%. The concentration of the compound was 20 µM and the solvent used was THF.

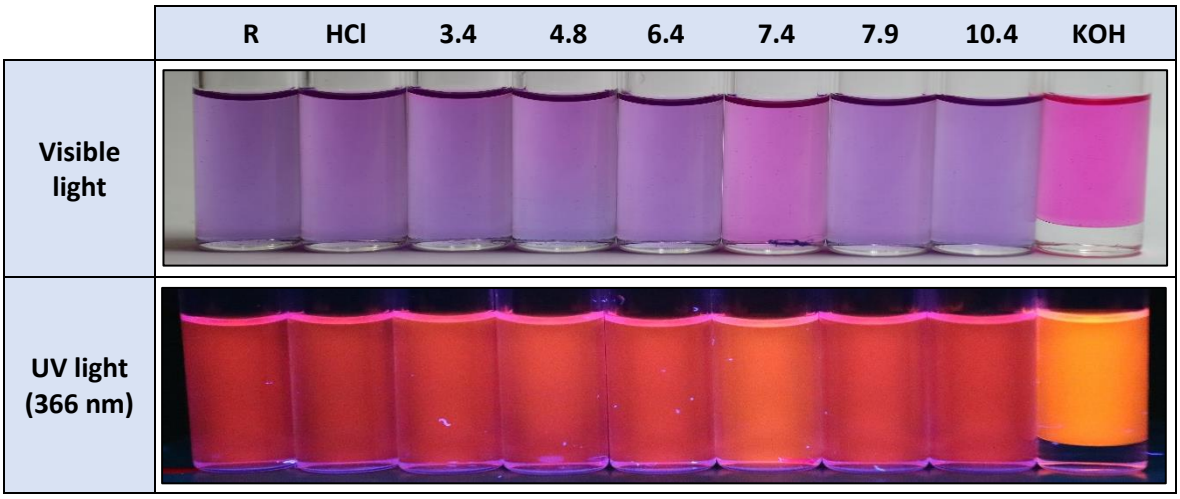

Figure 136. pH test of AR20 under visible (up) and UV (down) light.

The fluorescent emmision was become slightly orangish at physiological pH. At a wery basic pH, the fluorescence was turned orange.

Cations and anions test:

The concentration of the compound was 20 µM and the solvent used was THF.

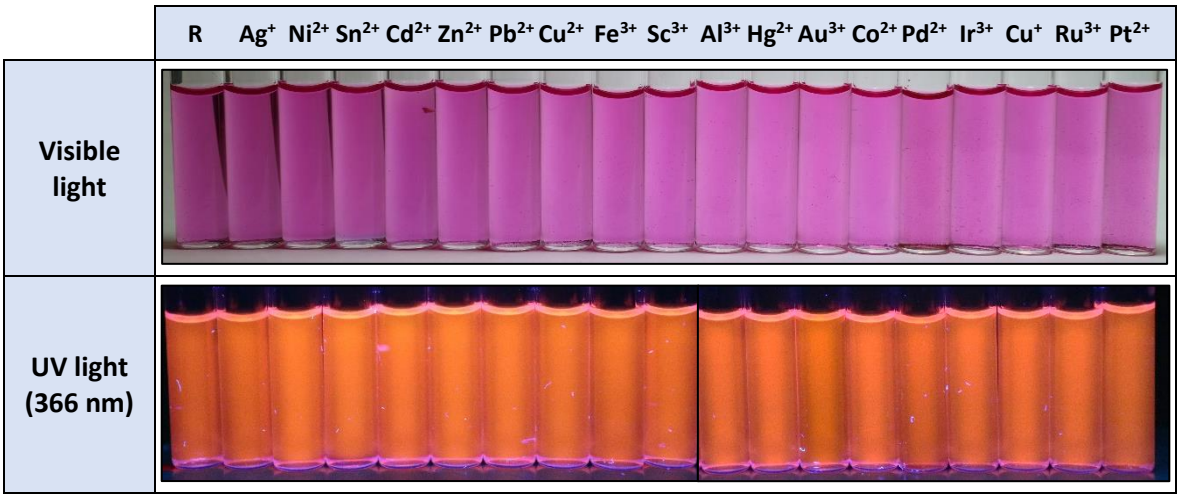

Figure 137. Cations test of AR20 under visible (up) and UV (down) light.

No significant changes were observed.

For the anion test, the concentration of the compound was 20 µM and the solvent used was THF.

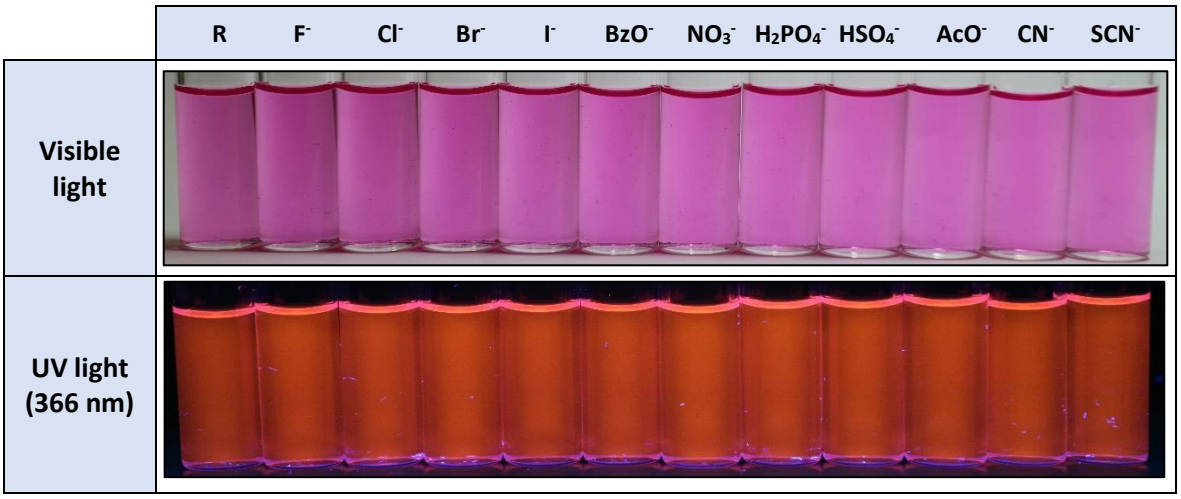

Figure 138. Anions test of AR20 under visible (up) and UV (down) light.

No significant changes were observed.

Oxidant and reductant reagents test:

The solvent used was THF and concentration of the compound was 20 µM.

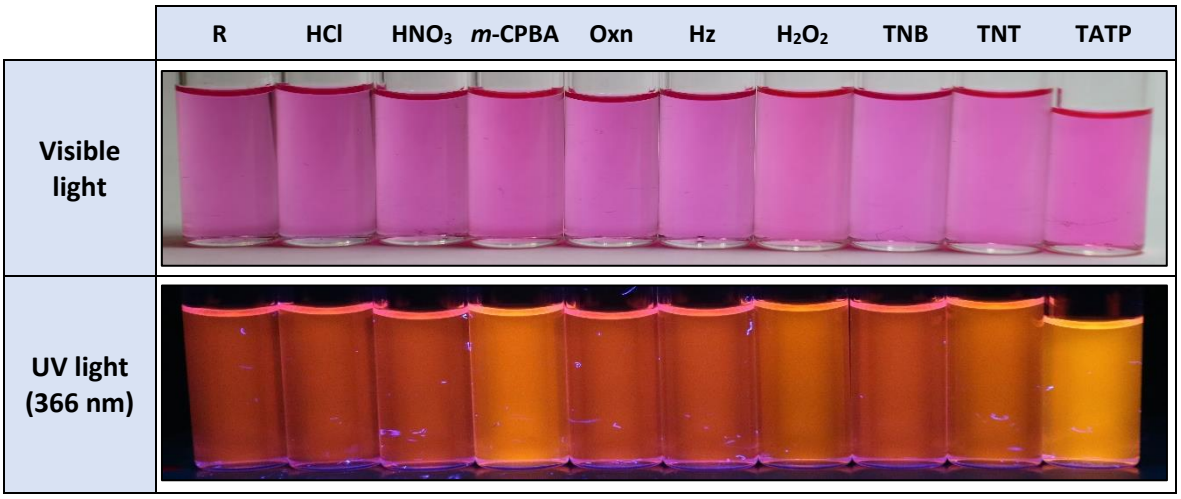

Figure 139. Oxidant and reductant reagents test of AR20 under visible (up) and UV (down) light.

The most significant changes were observed respect *m*-CPBA, H_2O_2, TNT and TATP.

Synthesis of 9-bromoperylene-3,4-dicarboxylic anhydride (AR30)

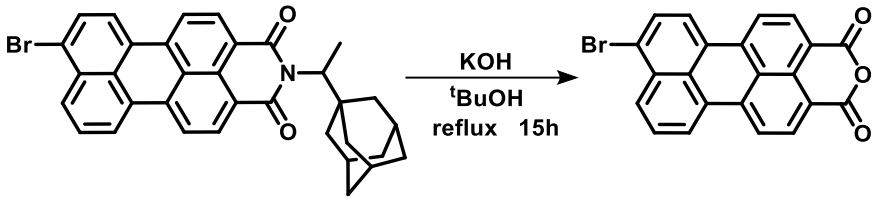

In a 100 ml flask with a magnetic stirrer, 250 mg of *N*-(1-(1-adamantyl)ethyl)-9-bromoperylene-3,4-dicarboxylmonoimide (AR02, 0.44 mmol) and 249 mg of potassium hydroxide (4.44 mmol) were dissolved in ^{t}BuOH and the mixture was refluxed for 15 hours. Afterwards, the resulting hot yellow suspension was poured into 50 ml of acetic acid and it was stirred at room temperature for two hours. The precipitate was filtered and washed with MeOH. The red solid was obtained with a 81% of yield (144 mg).

m.p.: >390°C.

IR (ATR, cm^{-1}): 2950-2849, 1749 (C=O), 1712 (C=O), 1590 (C_{Ar}-C_{Ar}), 1563, 1329, 1278, 1230, 1152, 1023 (C-Br), 1002, 805, 735, 673.

HRMS (MALDI, DIT-) m/z: calculated for $C_{22}H_9BrO_3$: 399.9730 (M^-); found 399.9760.

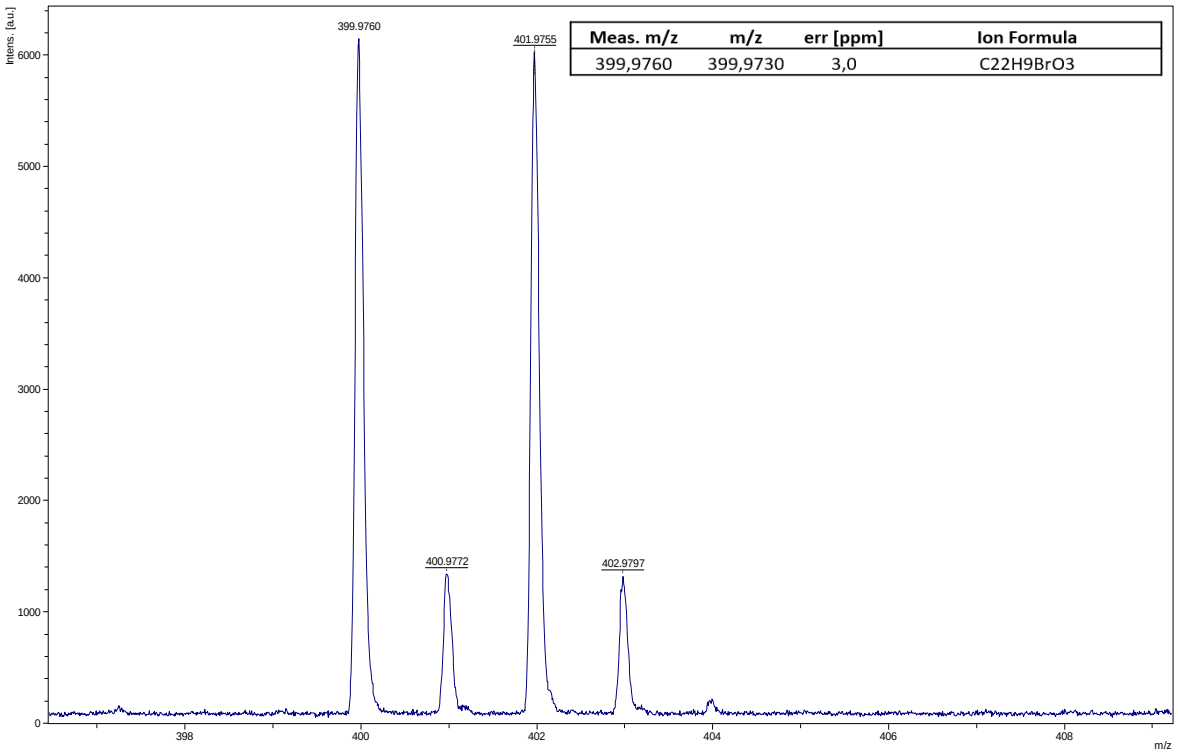

Figure 140. HRMS (MALDI, DIT-) of AR30.

Synthesis of *N*-(*N*-Boc-piperidin-4-yl)-9-bromoperylene-3,4-dicarboxylmonoimide (AR31)

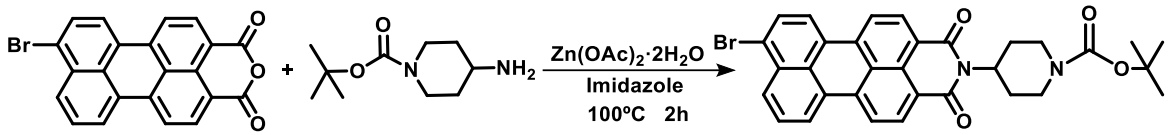

In a 100 ml flask, provided with a magnetic stirrer, 119 mg of 4-amino-1-Boc-piperidine (0.60 mmol) and 14 mg of $Zn(OAc)_2{\cdot}2H_2O$ (64 µmol) were added to a solution of 200 mg of 9-bromoperylene-3,4-dicarboxylic anhydride (AR30, 0.49 mmol) in imidazole and stirred two hours at 100ºC. Later, it was cooled to room temperature and 50 ml of water were added. The mixture was extracted three times with DCM (3×100 ml) and the combined organic extracts were dried over Na_2SO_4 and the solvent was evaporated under reduce pressure. The solid obtained was purified with a column chromatographic (SiO_2, DCM:MeOH 0.5%) to obtain 273 mg of red solid, 94% yield.

m.p.: >390ºC.

IR (ATR, cm^{-1}): 2920-2849, 1689 (C=O), 1638 (C=O), 1595 (C_{Ar}-C_{Ar}), 1557, 1401 (C-O), 1356, 1241, 1176 (C-N), 1146, 1106, 1026 (C-Br), 805, 744, 421.

^{1}H-NMR (300 MHz, $CDCl_3$) δ (ppm): 8.45 (t, *J* = 8.1 Hz, 2H, 2×$\mathbf{H_{Ar}}$), 8.30 (d, *J* = 7.5 Hz, 1H, $\mathbf{H_{Ar}}$), 8.27-8.14 (m, 3H, 3×$\mathbf{H_{Ar}}$), 8.03 (d, *J* = 8.3 Hz, 1H, $\mathbf{H_{Ar}}$), 7.80 (d, *J* = 8.3 Hz, 1H, $\mathbf{H_{Ar}}$), 7.63 (t, *J* = 8.1 Hz, 1H, $\mathbf{H_{Ar}}$), 5.22 (m, 1H, C**H**), 4.33 (s, 2H, C$\mathbf{H_2}$), 2.98-2.70 (m, 4H, 2×C$\mathbf{H_2}$), 1.74 (m, 2H, C$\mathbf{H_2}$), 1.52 (s, 9H, 3×C$\mathbf{H_3}$).

^{13}C-NMR (75MHz, $CDCl_3$) δ (ppm): 164.1 (**C**=O), 154.8 (**C**=O), 135.9 ($\mathbf{C}_{Ar}$), 131.4 ($\mathbf{C}_{Ar}$), 131.3 ($\mathbf{C}_{Ar}$H), 131.0 ($\mathbf{C}_{Ar}$), 129.9 ($\mathbf{C}_{Ar}$H), 128.8 ($\mathbf{C}_{Ar}$), 127.9 ($\mathbf{C}_{Ar}$H), 126.1 ($\mathbf{C}_{Ar}$H), 124.1 ($\mathbf{C}_{Ar}$), 123.4 ($\mathbf{C}_{Ar}$), 121.5 (2×$\mathbf{C}_{Ar}$H), 120.5 ($\mathbf{C}_{Ar}$), 120.2 ($\mathbf{C}_{Ar}$H), 79.7 (**Cq**), 51.9 (**C**H), 32.1 (**C**H_2), 29.9 (**C**H_3), 28.7 (**C**H_2).

HRMS (MALDI, DIT-) m/z: calculated for $C_{32}H_{27}BrN_2O_4$: 582.1149 (M^-); found 582.1184.

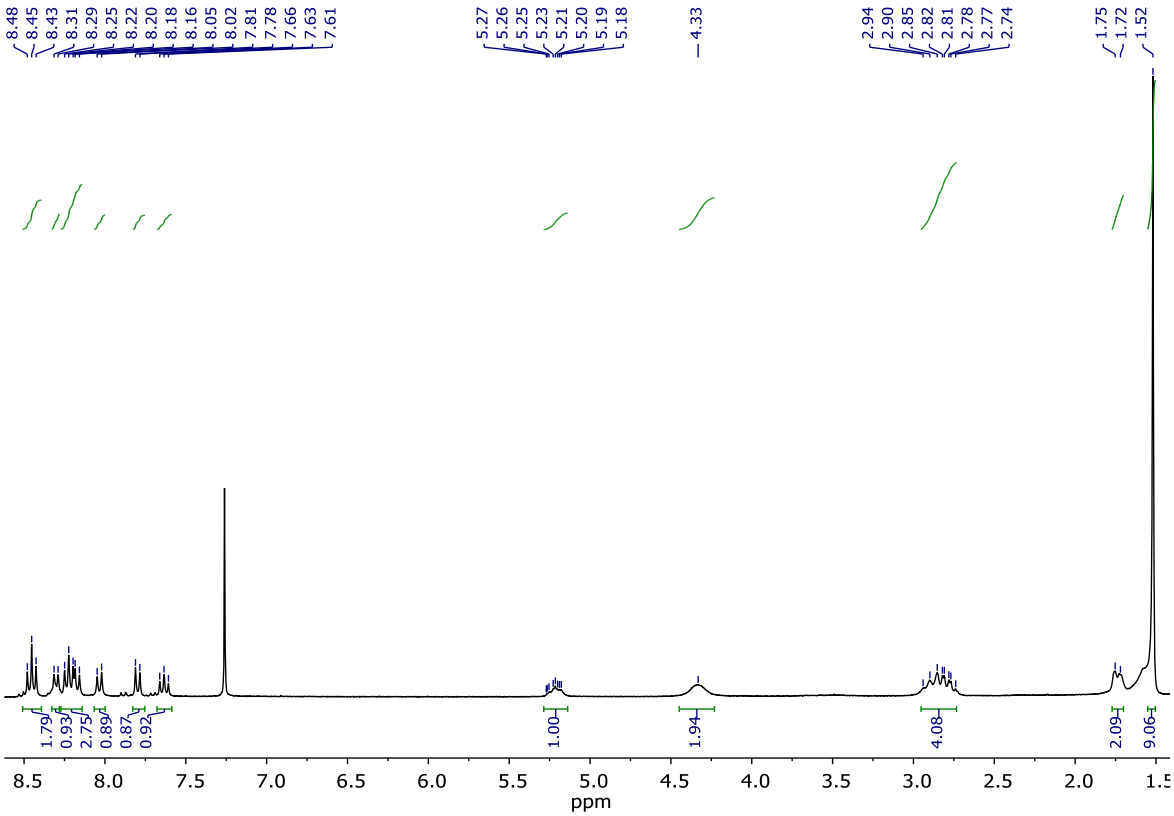

Figure 141. ^{1}H-NMR ($CDCl_3$, 300 MHz) of AR31.

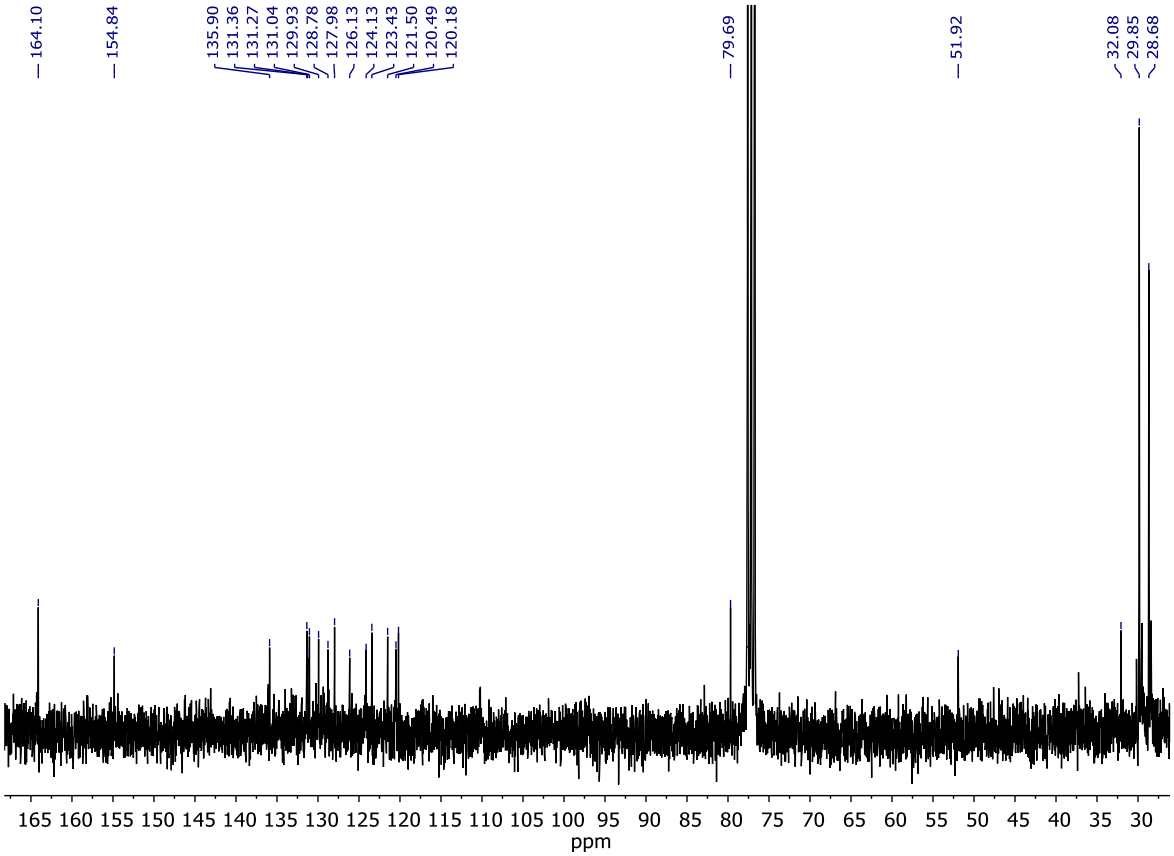

Figure 142. ^{13}C-NMR ($CDCl_3$, 75 MHz) of AR31.

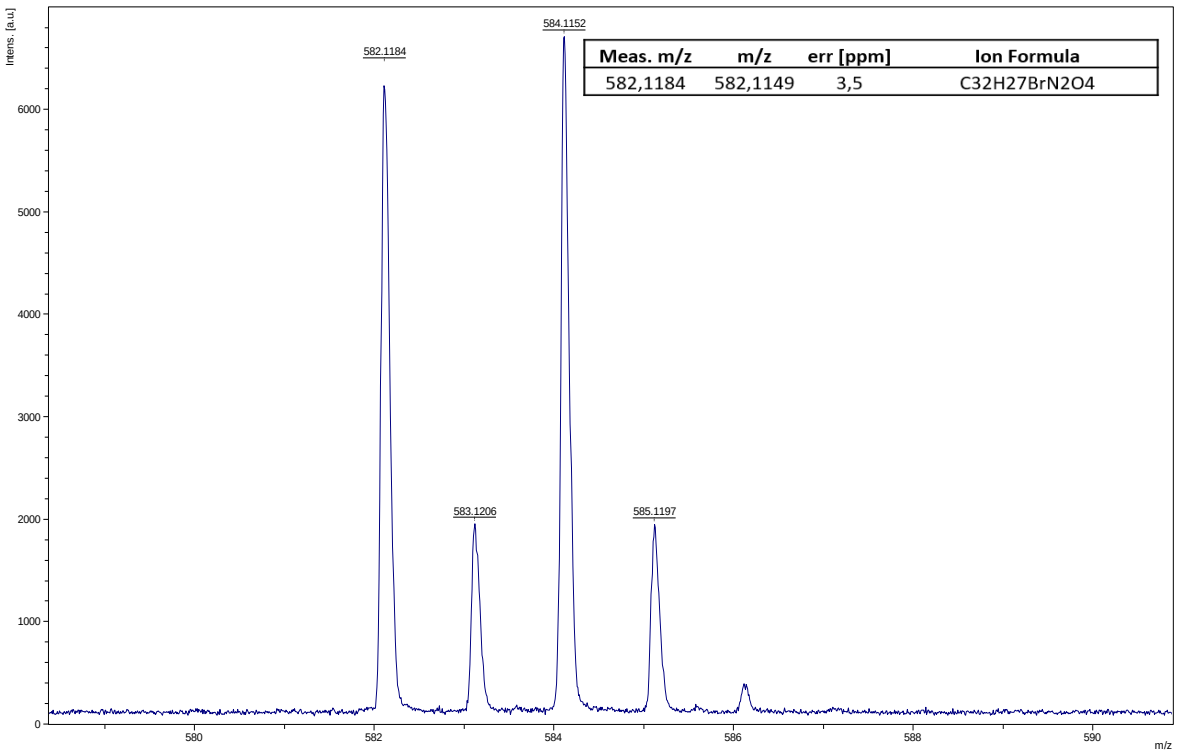

Figure 143. HRMS (MALDI, DIT-) of AR31.

Synthesis of *N*-(*N*-Boc-piperidin-4-yl)-9-[(trimethylsilyl)ethynyl]perylene-3,4-dicarboxylmonoimide (AR96).

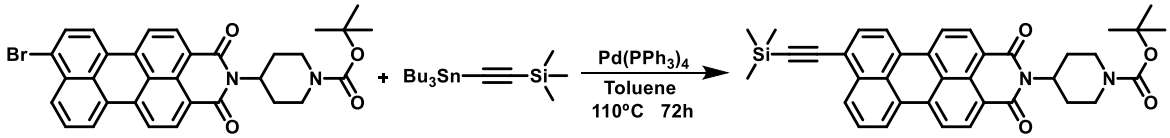

100 mg of *N*-(4-piperidine-*N'*-Boc)-9-bromoperylene-3,4-dicarboxylmonoimide (AR31, 0.17 mmol) and 73 mg of tri-*N*-butyl(trimethylsilylethynyl)tin (0.19 mmol) were dissolved in 5 ml of dry toluene under argon atmosphere and the catalyst, $Pd(PPh_3)_4$, was added. The resulting mixture was stirred three days at 110ºC and then, the solvent was evaporated under reduce pressure. The solid was dissolved in DCM and washed three times with destilled water (3×100 ml). The organic extracts were combined, dried over anhidrous Na_2SO_4 and the solvent was evaporated under reduce pressure. The organic solid was purified by column chromatography (SiO_2, DCM:MeOH) getting 46 mg of a yellow solid, 45% yield.

m.p.: 312-315ºC (decomposition).

IR (ATR, cm^{-1}): 2958-2854 (C-H), 1686 (C=O), 1644 (C=O), 1590, 1572, 1408 (C-O), 1351, 1243, 1165 (-CH_3), 1148, 1105, 1016, 942, 855, 836, 807, 747, 720, 624, 538, 448.

^{1}H-NMR (300 MHz, $CDCl_3$) δ (ppm): 8.28-8.14 (m, 3H, 3×$\mathbf{H_{Ar}}$), 7.97 (d, *J* = 7.5 Hz, 1H, $\mathbf{H_{Ar}}$), 7.93-7.79 (m, 3H, 3×$\mathbf{H_{Ar}}$), 7.55 (d, *J* = 7.9 Hz, 1H, $\mathbf{H_{Ar}}$), 7.46 (t, *J* = 7.9 Hz, 1H, $\mathbf{H_{Ar}}$), 5.25-5.12 (m, 1H, C**H**), 4.35 (s, 2H, C$\mathbf{H}_2$), 2.99-2.71 (m, 4H, 2×C$\mathbf{H}_2$), 1.83-1.70 (m, 2H, C$\mathbf{H}_2$), 1.53 (s, 9H, 3×C$\mathbf{H}_3$), 0.41 (s, 9H, Si-(C$\mathbf{H}_3$)$_3$).

^{13}C-NMR (75MHz, $CDCl_3$) δ (ppm): 164.0 (**C**=O), 163.9 (**C**=O), 154.8 (**C**=O), 136.2 ($\mathbf{C}_{Ar}$), 135.8 ($\mathbf{C}_{Ar}$), 134.1 ($\mathbf{C}_{Ar}$), 132.3 ($\mathbf{C}_{Ar}$), 132.1 ($\mathbf{C}_{Ar}$), 132.0 ($\mathbf{C}_{Ar}$), 131.3 ($\mathbf{C}_{Ar}$H), 131.1 ($\mathbf{C}_{Ar}$H), 130.9 ($\mathbf{C}_{Ar}$H), 129.1 ($\mathbf{C}_{Ar}$), 129.1 ($\mathbf{C}_{Ar}$), 129.0 ($\mathbf{C}_{Ar}$H), 128.9 ($\mathbf{C}_{Ar}$), 128.7 ($\mathbf{C}_{Ar}$), 128.5 ($\mathbf{C}_{Ar}$), 127.4 ($\mathbf{C}_{Ar}$H), 127.2 ($\mathbf{C}_{Ar}$), 125.8 ($\mathbf{C}_{Ar}$), 123.7 ($\mathbf{C}_{Ar}$H), 123.4, 122.5 ($\mathbf{C}_{Ar}$H), 121.3 ($\mathbf{C}_{Ar}$), 121.1 ($\mathbf{C}_{Ar}$), 120.4 ($\mathbf{C}_{Ar}$H), 120.1 ($\mathbf{C}_{Ar}$H), 103.5 (-C≡**C**-Si(CH_3)$_3$), 102.6 (-**C**≡C-Si(CH_3)$_3$), 79.7 (**Cq**), 51.8 (**C**H), 44.0 (**C**H_2), 28.7 (**C**H_3), 28.4 (**C**H_2), 0.2 (Si(**C**H_3)$_3$).

HRMS (MALDI, DIT-) m/z: calculated for $C_{37}H_{36}N_2O_4Si$: 600.2439 (M^-); found 600.2468.

UV-Vis ($CHCl_3$), λ_{max} nm (log ε): 565 (7.6).

Ø ($CHCl_3$, %): 94.33.

τ (475 nm, $CHCl_3$, ns): 4.457 (χ^2: 1.061).

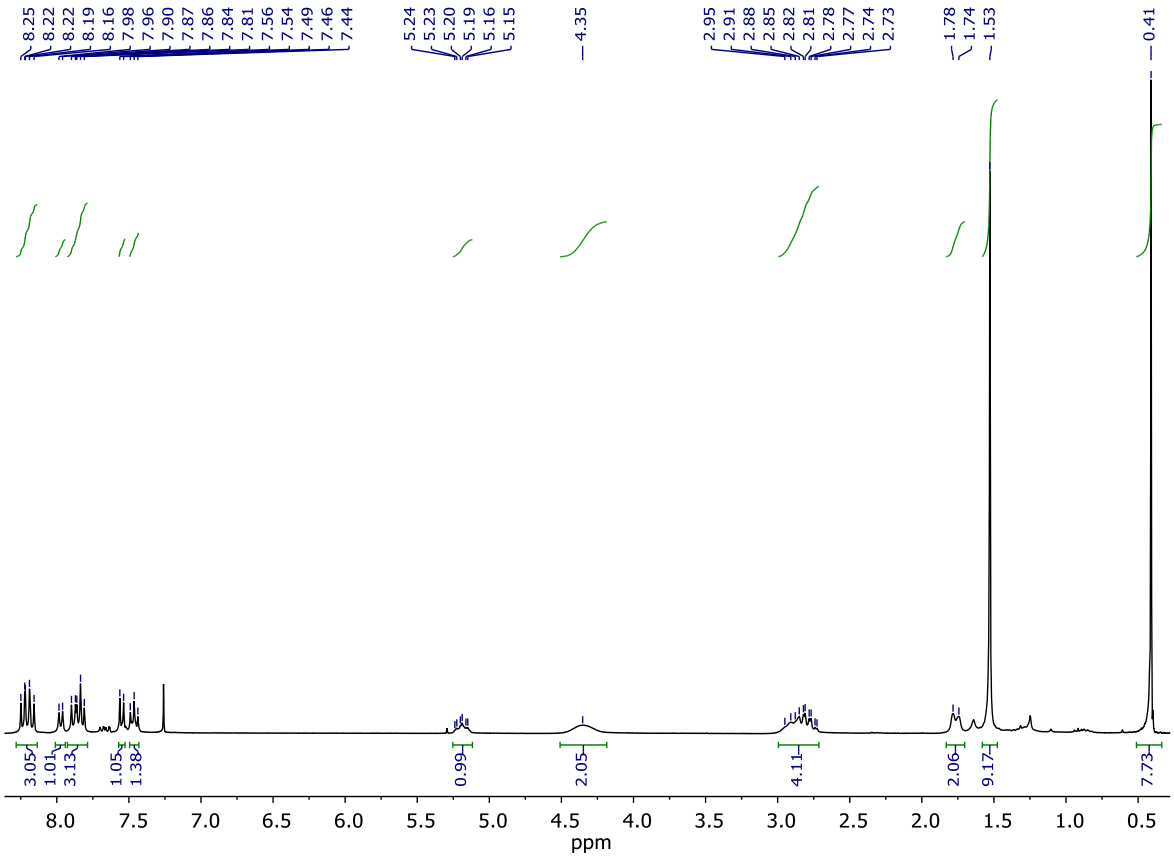

Figure 144. ^{1}H-NMR ($CDCl_3$, 300 MHz) of AR96.

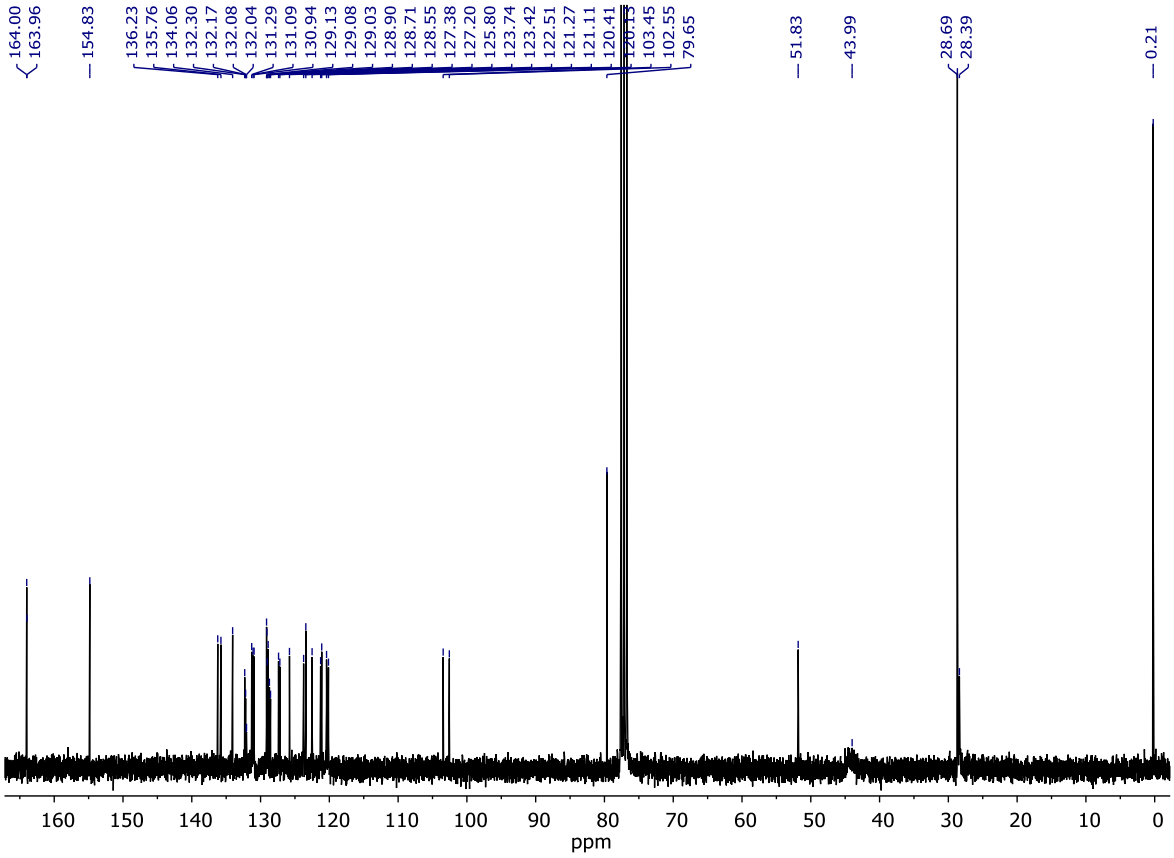

Figure 145. ^{13}C-NMR ($CDCl_3$, 75 MHz) of AR96.

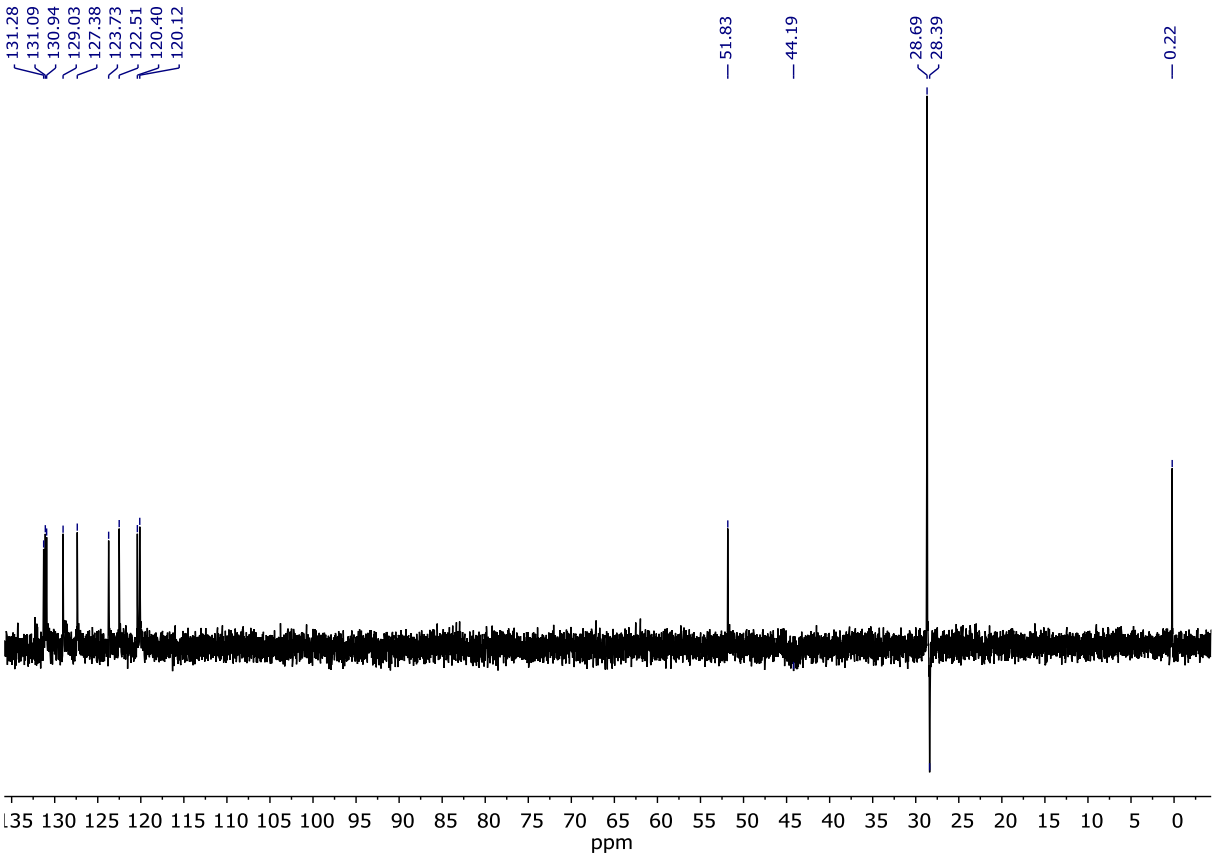

Figure 146. DEPT NMR ($CDCl_3$, 75 MHz) of AR96.

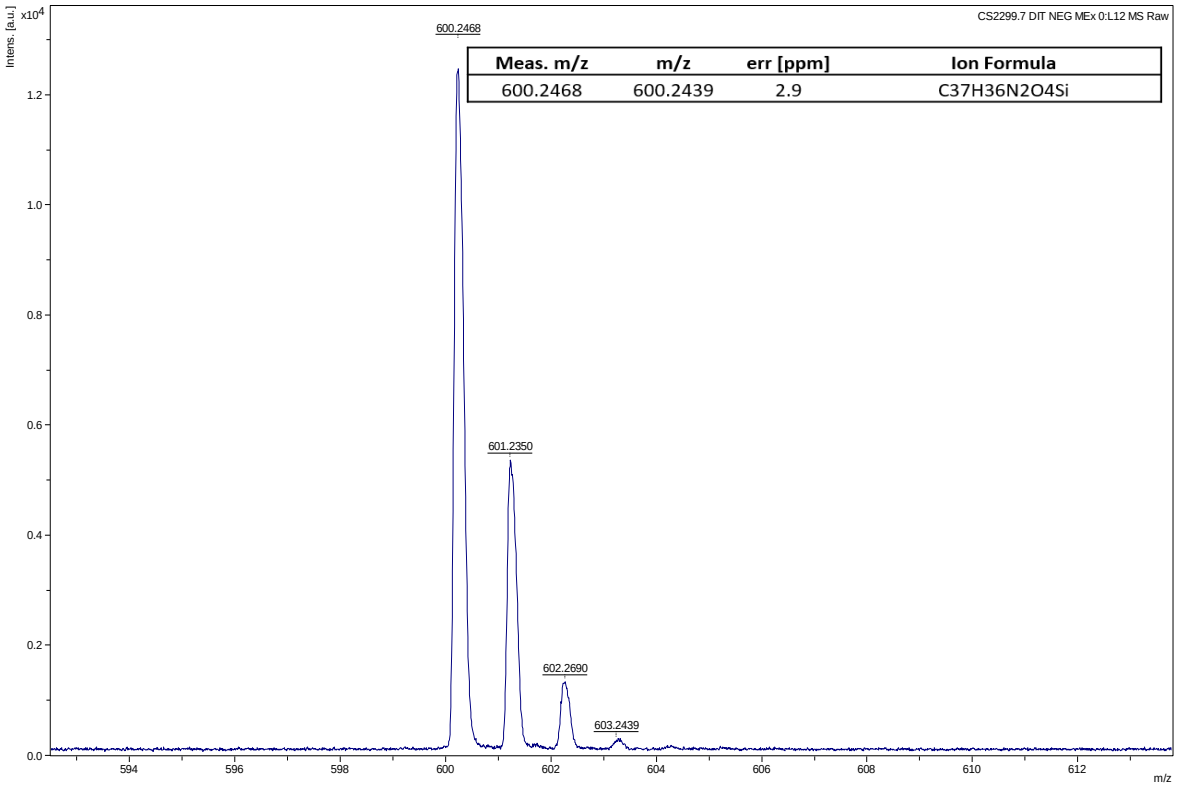

Figure 147. HRMS (MALDI, DIT-) of AR96.

Solvatochromism:

The concentration of the compound was 10 µM and the excitation wavelength was 500 nm.

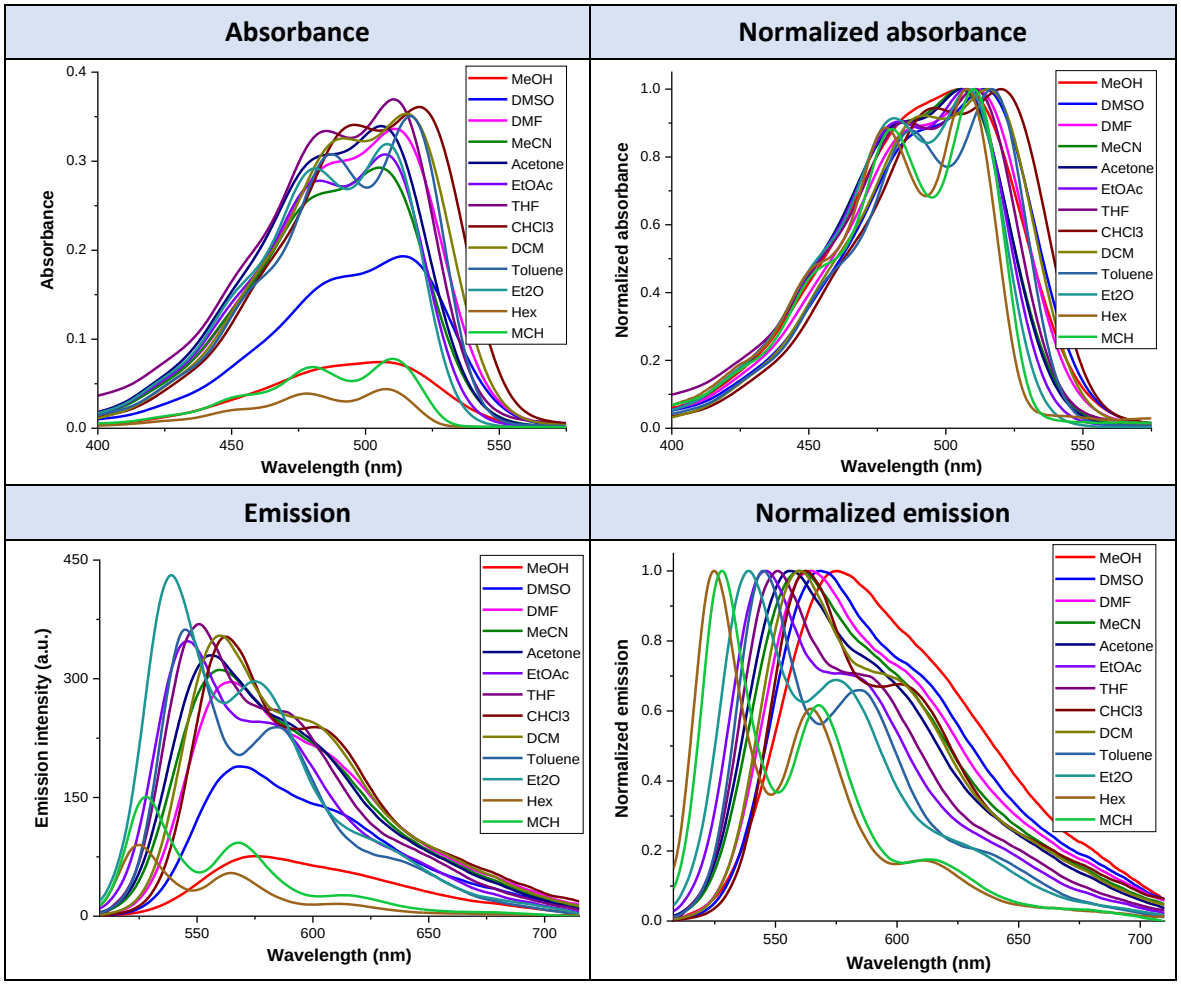

Figure 148. Solvatochromism of AR96.

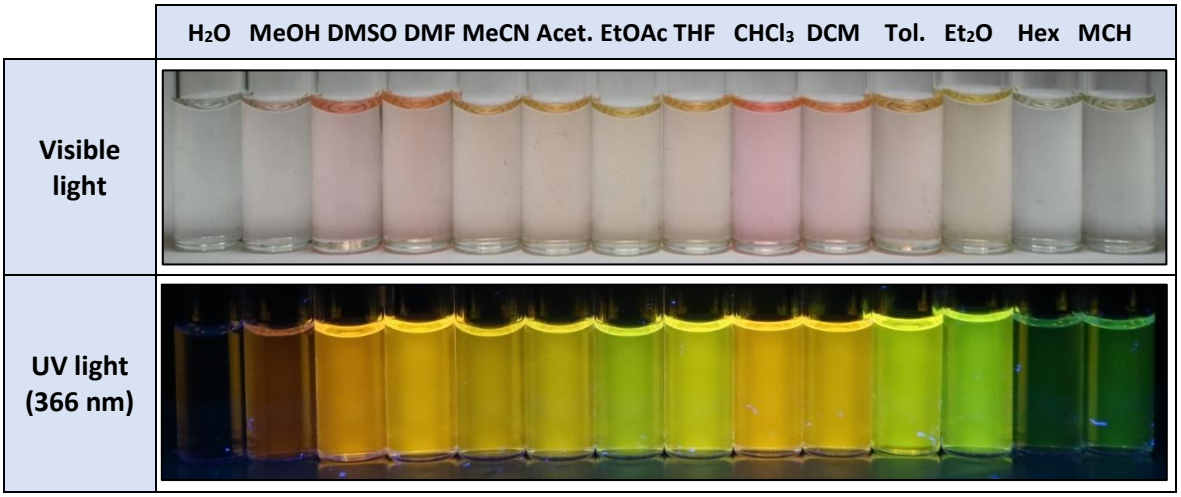

Figure 149. Solvatochromism of AR96 under visible and 366 nm light.

Fluorescence decay lifetime (τ):

The solvent used was $CHCl_3$. The concentration of the compound was 10 µM.

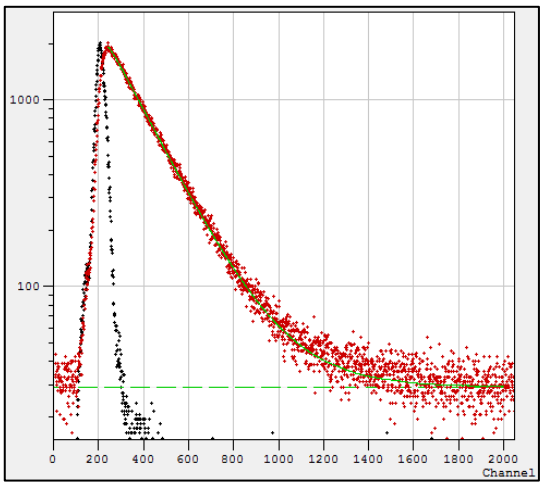

Figure 150. Fluorescence decay lifetime of AR96.

Water acceptance test:

The solvent used was THF and the concentration of the compound was 10 µM.

	R	5%	10%	20%	30%	40%	50%	60%	70%	80%	90%
Visible light											
UV light (366 nm)	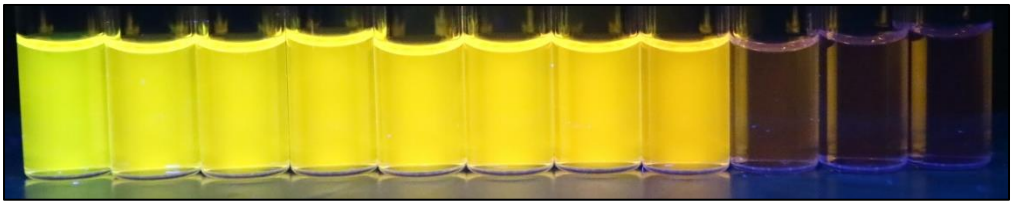										

Figure 151. Water acceptance test of AR96 under visible (up) and UV (down) light.

The fluorescence was quenched at 60% (ACQ), this was the maximum amount of water that was admitted by the product.

pH test:

The proportion of water that the compound could accept, according to the previous water acceptance test, was 60% The concentration of the compound was 10 µM and the solvent used was THF.

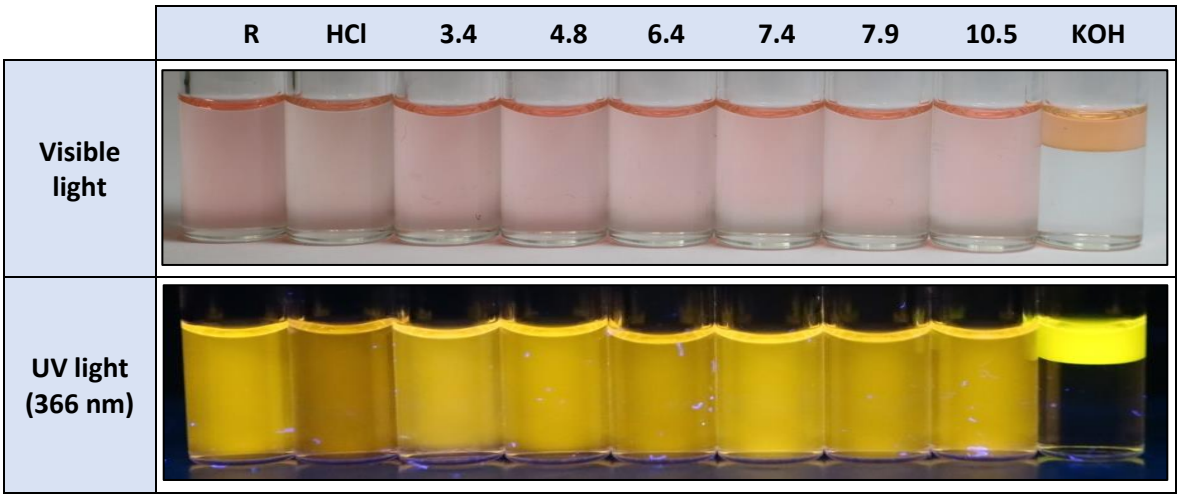

Figure 152. pH test of AR96 under visible (up) and UV (down) light.

No significant changes was observed with the exception that, at very acidic pH, the fluorescence darkens.

Cations and anions test:

The concentration of the compound was 10 µM and the solvent used was THF.

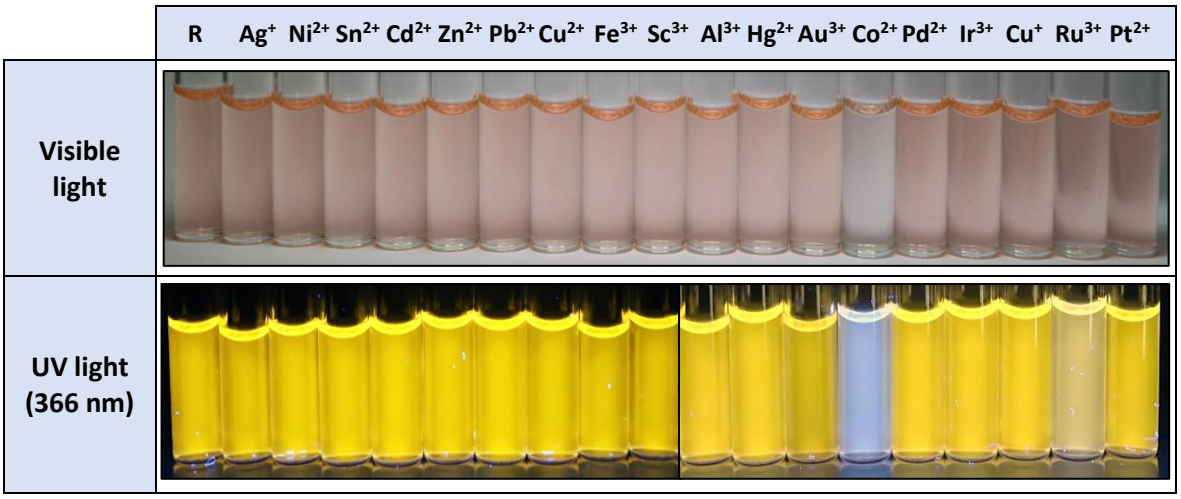

Figure 153. Cations test of AR96 under visible (up) and UV (down) light.

The colour of the florescence was changed from yellow to blue for Co^{2+} and to pale yellow for Ru^{3+}.

The concentration of the compound was 10 µM and the solvent used was THF.

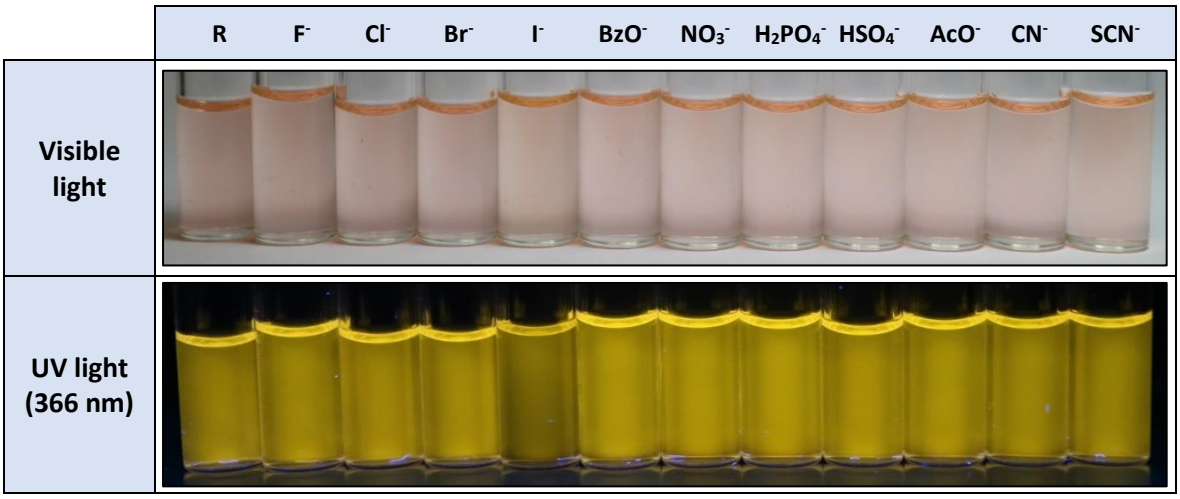

Figure 154. Anions test of AR96 under visible (up) and UV (down) light.

No significant changes were observed.

Oxidant and reductant agents test:

The solvent used was THF and concentration of the compound was 10 µM.

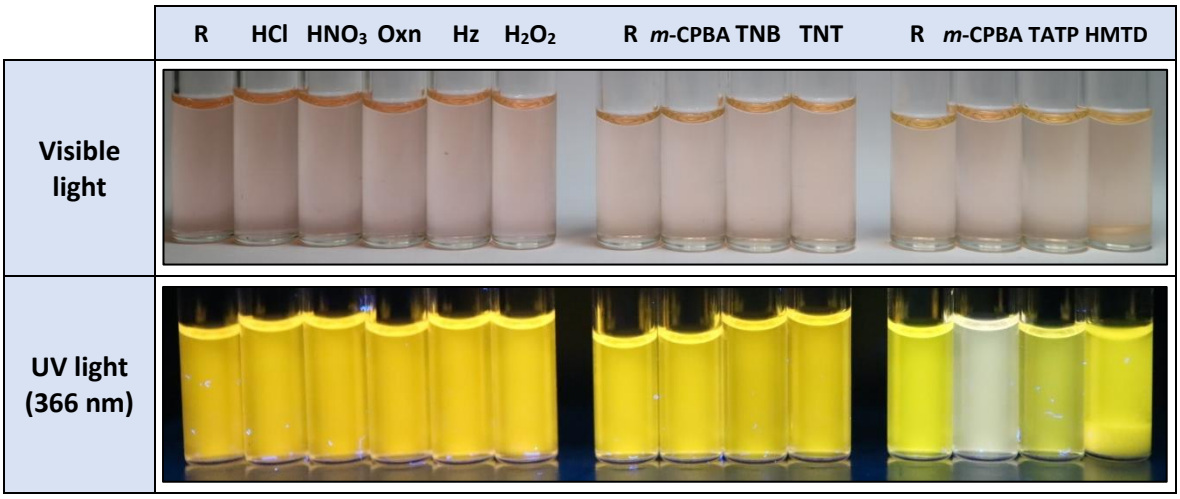

Figure 155. Oxidant and reductant reagents test of AR96 under visible (up) and UV (down) light.

The positive response was given for TATP, with which the fluorescence was turned green, and for *m*-CPBA, with a white fluorescence.

In the same solvent, THF, a kinetic study was carried out. The concentration of the probe was 10 µM while TATP was added in excess. The excitation wavelength was 375 nm and measurements were taken even 5 minutes for 3 hours at room temperature. It was noted that as the emission maximum in the yellow region (554 nm) was decreased, the emission maximum in the blue region (455 nm) was increased.

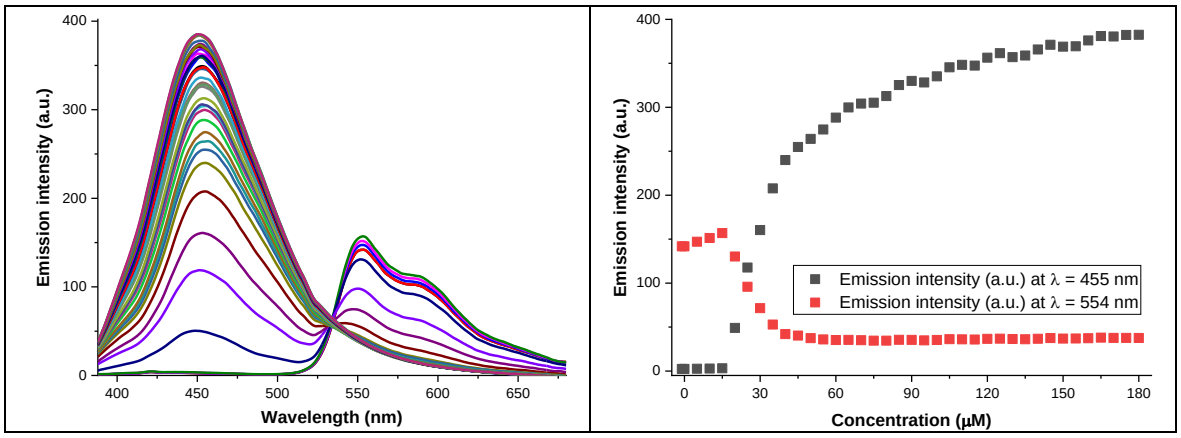

Figure 156. Kinetic response of AR96 (10 µM) to an excess of TATP in THF. Emission intensity graph (right) and profile as function as time at 455 nm and 554 nm (left).

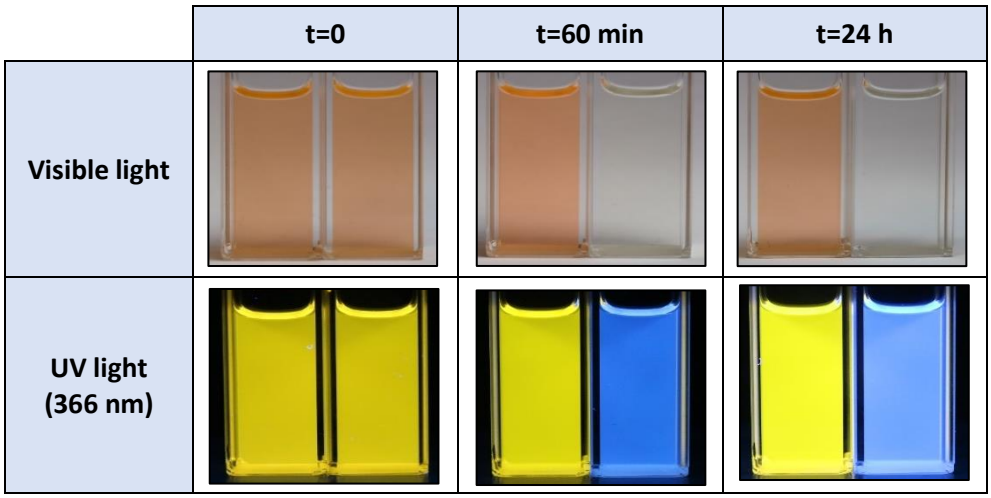

Figure 157. Kinetic study at different times under visible (up) and UV (down) light in THF. In each photo, left vial was contained the probe and right vial was contained the probe and an excess of TATP.

Behaviour under light:

The kinetics study of the AR96 alone were carried out. The working concentration of the probe was 2.5 µM and the excitation wavelength was 375 nm. Measurements were carried out every five minutes for five hours and the temperature for the test was 25ºC. It was observed that, under 366 nm light, the fluorescence was changed from yellow to blue.

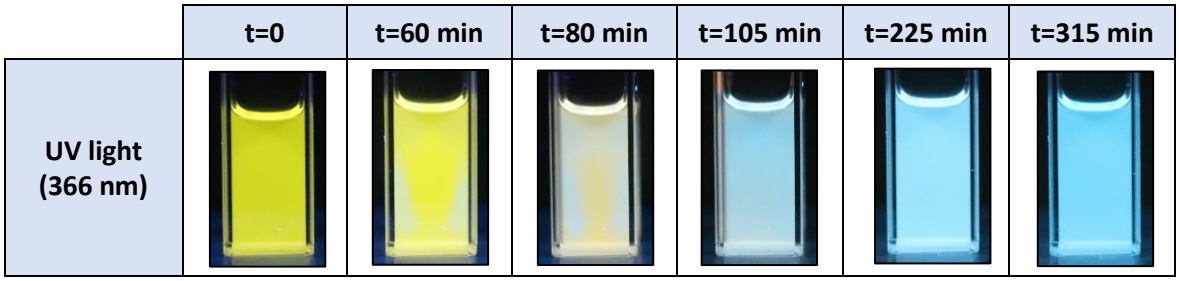

Figure 158. Kinetic study at different times under and UV light in THF of AR96 (2.5 µM).

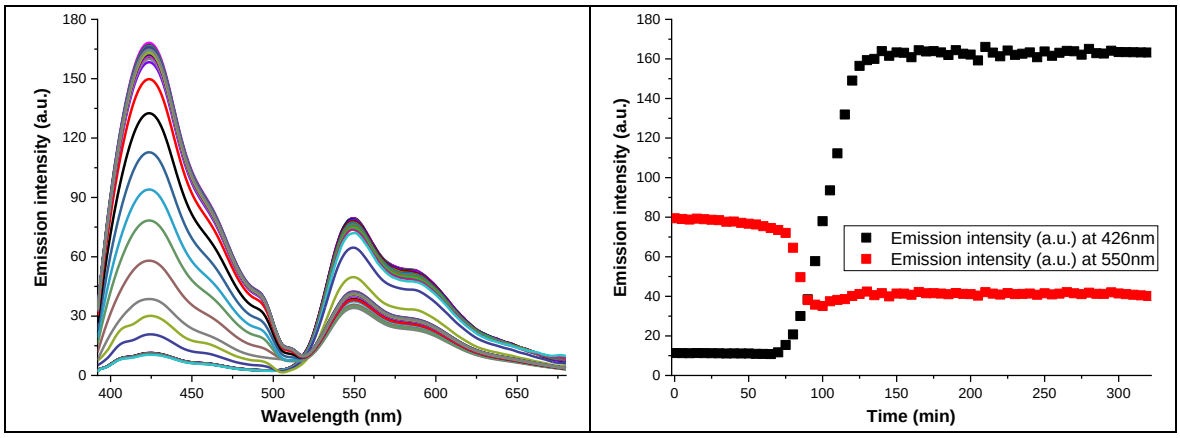

Figure 159. Kinetic response of AR96 (2.5 µM) in THF. Emission intensity graph (right) and profile as function as time at 426 nm and 550 nm (left).

Synthesis of tridecan-7-amine (AR39)

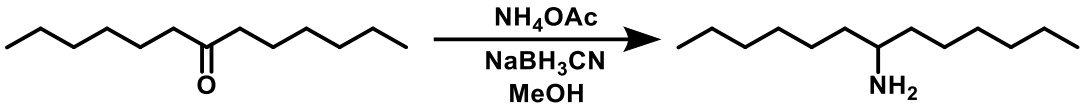

In a 100 ml Schlenk with a magnetic stirrer, 2.54 g of 7-tridecanone (12.8 mmol), 9.75 g of ammonium acetate (126 mmol) and 0.57 g of sodium cyanoborohydride (9.08 mmol) were dissolved in 30 ml of methanol under nitrogen atmosphere and stirred at room temperature for 48 hours. Afterwards, the mixture was quenched by adding 2 ml 2M hydrochloric acid and concentrated under reduce pressure. Later, the compound was disspersed in 200 ml of water, adjusted to pH 10 with potassium hidroxide and extracted with $CHCl_3$ (3×150 ml). The organic extracts were combined, dried over Na_2SO_4 and the solvent was evaporated under reduce pressure. The product was a pale yellow oil obtained with a 90% of yield (2.29 g).

m.p.: 22-25°C (rt).

IR (ATR, cm^{-1}): 3322 (N-H), 2957 – 2852, 1622, 1571, 1476, 1376, 1302, 1149 (C-N), 810, 717, 597, 511.

^{1}H-NMR (300 MHz, $CDCl_3$) δ (ppm): 2.29 (s, 1H, C**H**), 1.29 (s, 2H, C**H**$_2$), 0.92 (s, 16H, 8×C**H**$_2$), 0.51 (m, 6H, 2×C**H**$_3$).

^{13}C-NMR (75MHz, $CDCl_3$) δ (ppm): 50.4 (**C**H), 37.4 (**C**H$_2$), 31.1 (**C**H$_2$), 28.8 (**C**H$_2$), 25.4 (**C**H$_2$), 21.9 (**C**H$_2$), 13.2 (**C**H$_3$).

HRMS (ESI, TOF+) m/z: calculated for $C_{13}H_{29}N$: 200.2373 (M^++H); found 200.2372.

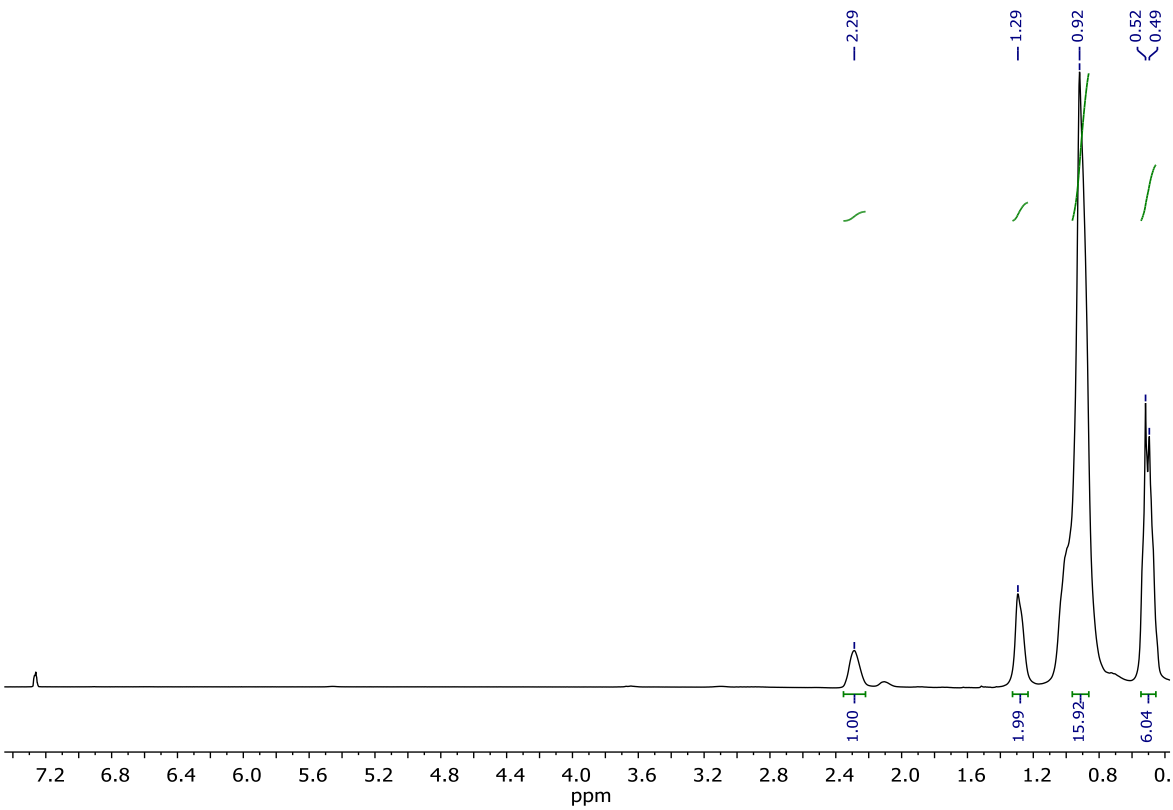

Figure 160. ^{1}H-NMR ($CDCl_3$, 300 MHz) of AR39.

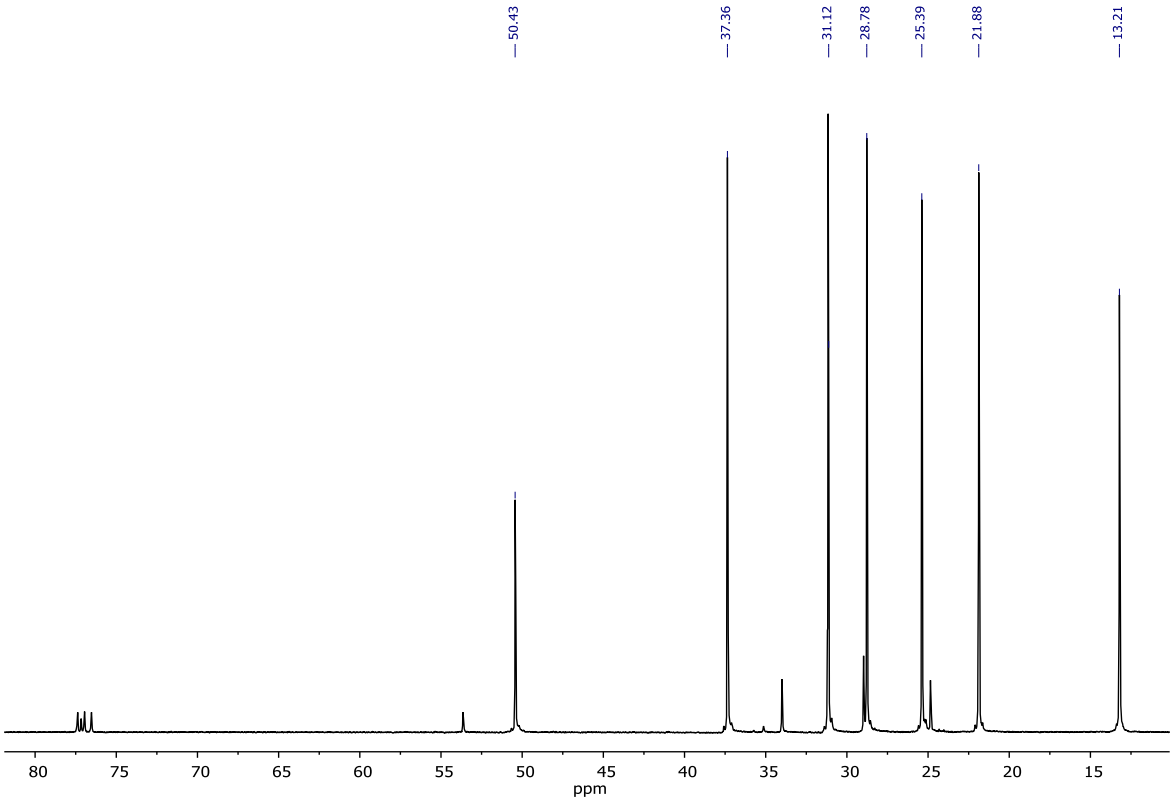

Figure 161. ^{13}C-NMR ($CDCl_3$, 75 MHz) of AR39.

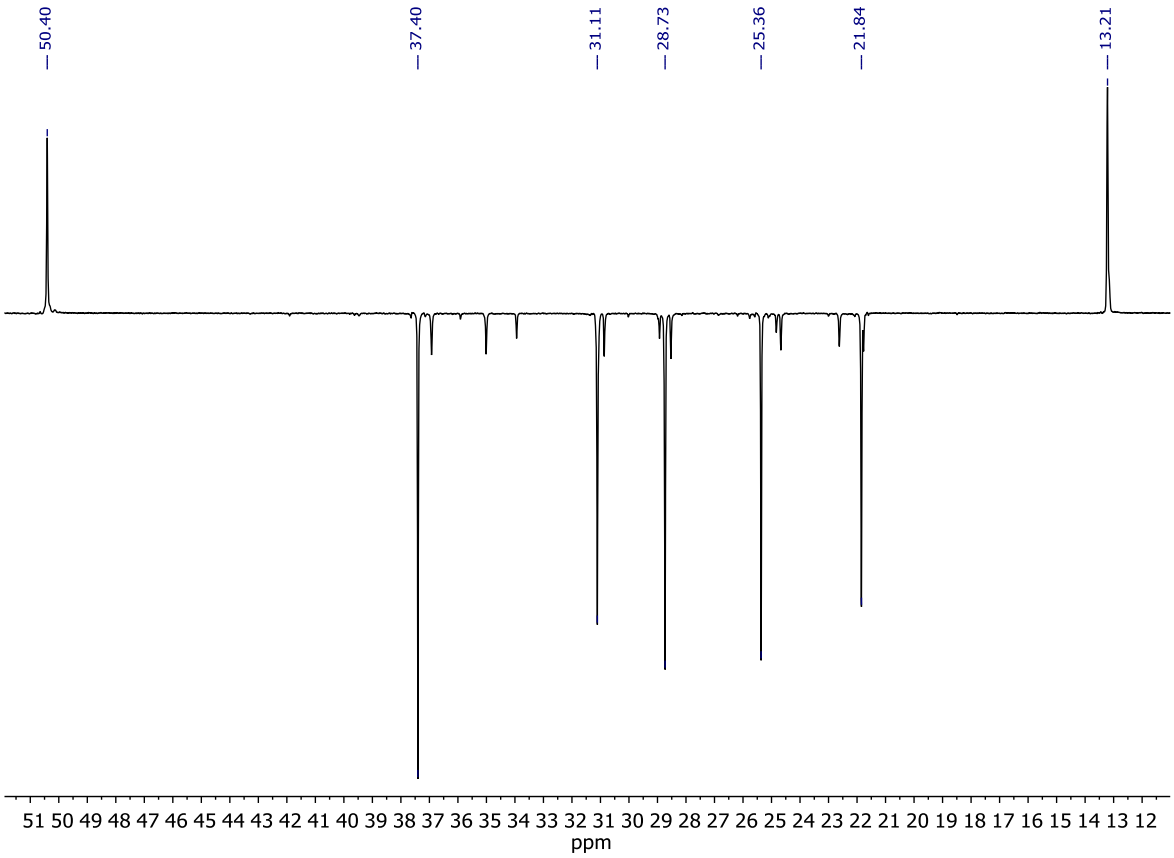

Figure 162. DEPT NMR (CDCl3, 75 MHz) of AR39.

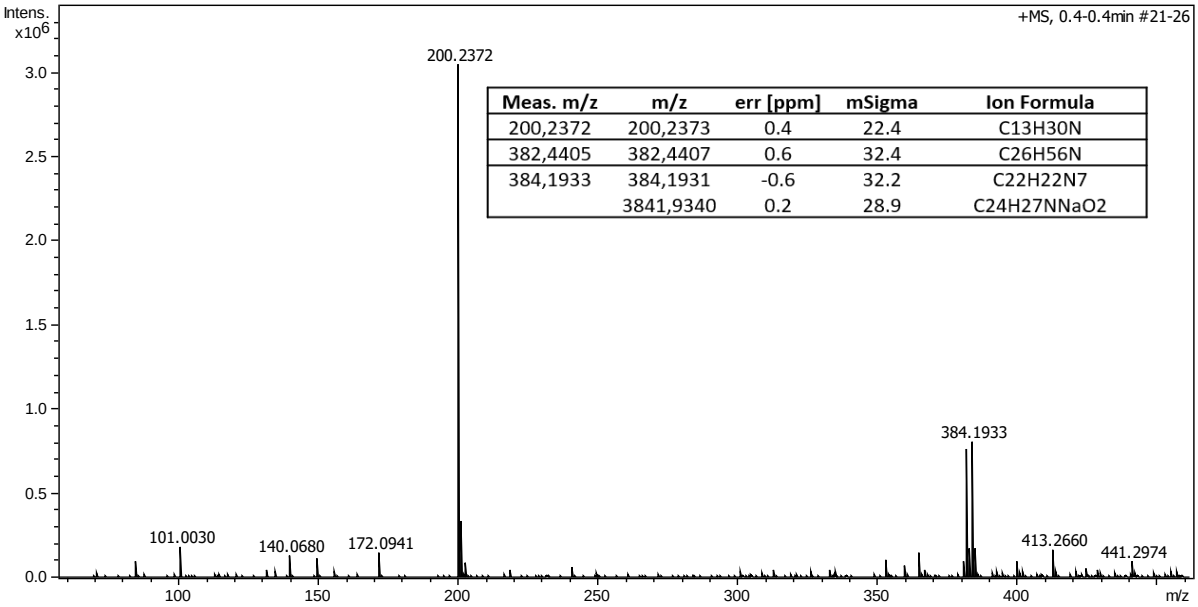

Meas. m/z	m/z	err [ppm]	mSigma	Ion Formula
200,2372	200,2373	0.4	22.4	C13H30N
382,4405	382,4407	0.6	32.4	C26H56N
384,1933	384,1931	-0.6	32.2	C22H22N7
	3841,9340	0.2	28.9	C24H27NNaO2

Figure 163. HRMS (ESI, TOF+) of AR39.

Synthesis of *N,N'*-bis(tridecanyl)perylene-3,4,9,10-tetracarboxylicdiimide (AR40)

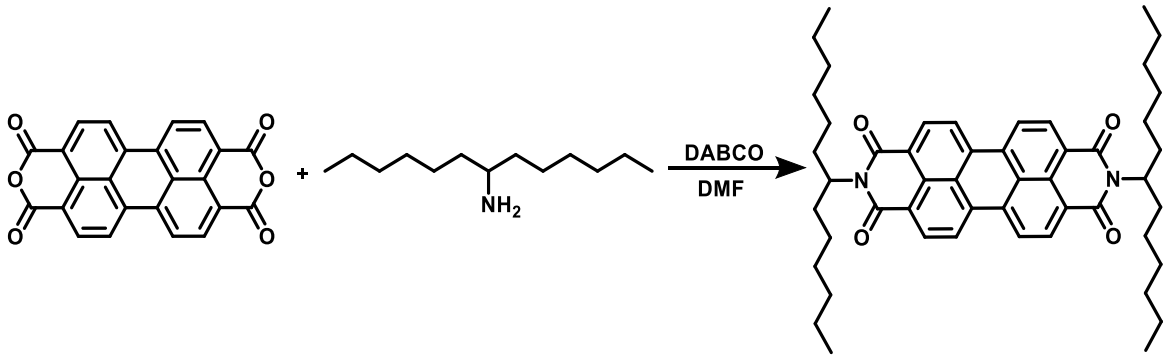

0.5 g of PDA (1.27 mmol), 1.02 g of tridecan-7-amine (AR39, 5.09 mmol) and 0.9 g of DABCO (8.02 mmol) were dissolved in anhydrous DMF (20 ml) under nitrogen atmosphere and the mixure was irradiated in a microwave device at 200°C for one hour. Then, it was poured over 15 ml of aqueous solution of hydrochloric acid, stirred for one hour, filtered and washed with water (30 ml). The organic solid was purified with a column chromatography (SiO_2, DCM), getting 654 mg of a red solid, 68% yield.

m.p.: 144-147°C.

IR (ATR, cm^{-1}): 2949-2854 (C-H), 1696 (C=O), 1653 (C=O), 1590 (C_{Ar}-C_{Ar}), 1572, 1458, 1402, 1336, 1246, 1208, 1168 (C-N), 1103, 848, 804, 741, 615.

^{1}H-NMR (300 MHz, $CDCl_3$) δ (ppm): 8.63 (m, 8H, 8×**H_{Ar}**), 5.18 (tt, *J* = 9.4, 5.8 Hz, 2H, 2×C**H**), 2.24 (m, 4H, 2×C**H_2**), 1.87 (m, 4H, 2×C**H_2**), 1.41 – 1.14 (m, 32H, 16×C**H_2**), 0.82 (m, 12H, 4×C**H_3**).

^{13}C-NMR (75MHz, $CDCl_3$) δ (ppm): 164.8 (**C**=O), 163.8 (**C**=O), 134.7 (**C_{Ar}**), 132.0 (**C_{Ar}**H), 131.4 (**C_{Ar}**H), 129.8 (**C_{Ar}**), 126.6 (**C_{Ar}**), 123.2 (**C_{Ar}**H) , 54.9 (**C**H), 32.6 (**C**H_2), 31.9 (**C**H_2), 29.4 (**C**H_2), 27.1(**C**H_2), 22.7 (**C**H_2), 14.2 (**C**H_3).

HRMS (MALDI, DIT-) m/z: calculated for $C_{50}H_{52}N_2O_4$: 754.4704 (M^-); found 754.4732.

UV-Vis ($CHCl_3$), λ_{max} nm (log ε): 365 (5.1).

Ø (Hex, %): 90.08.

τ (475 nm, Hex, ns): 4.869 (χ^2: 1.053).

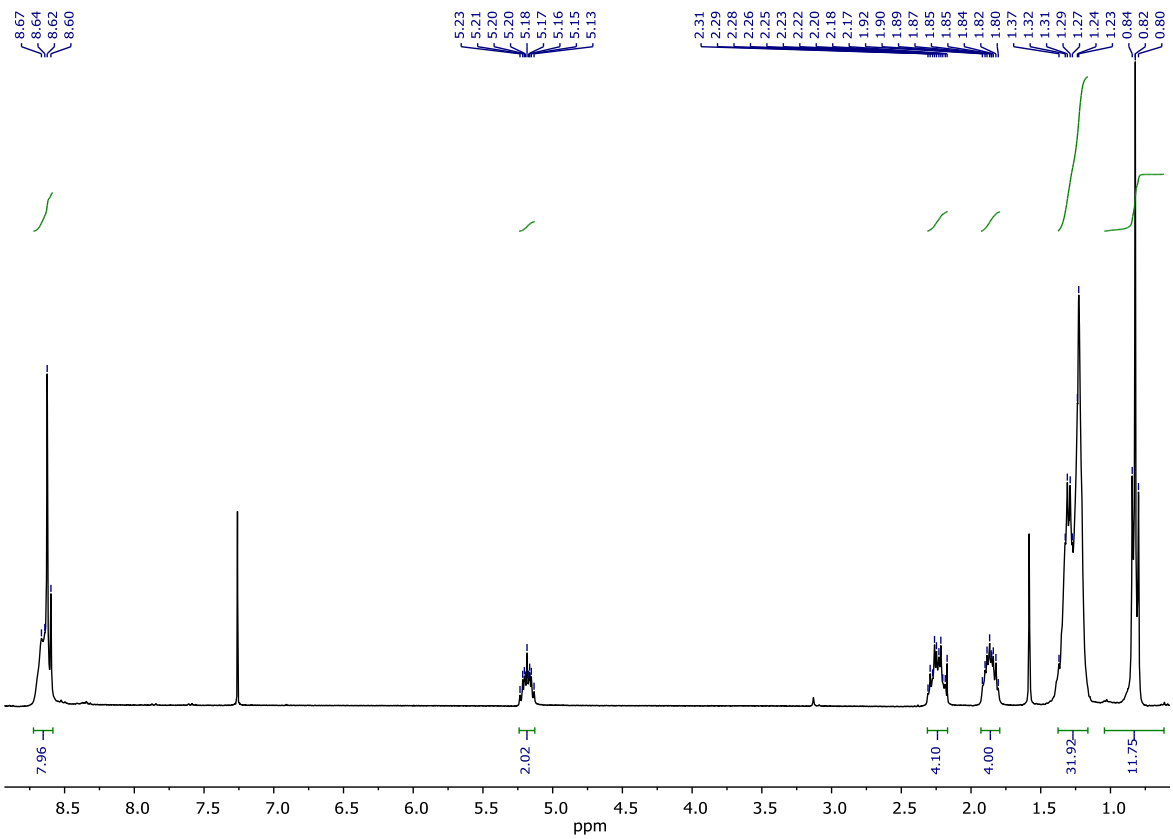

Figure 164. ^{1}H-NMR ($CDCl_3$, 300 MHz) of AR40.

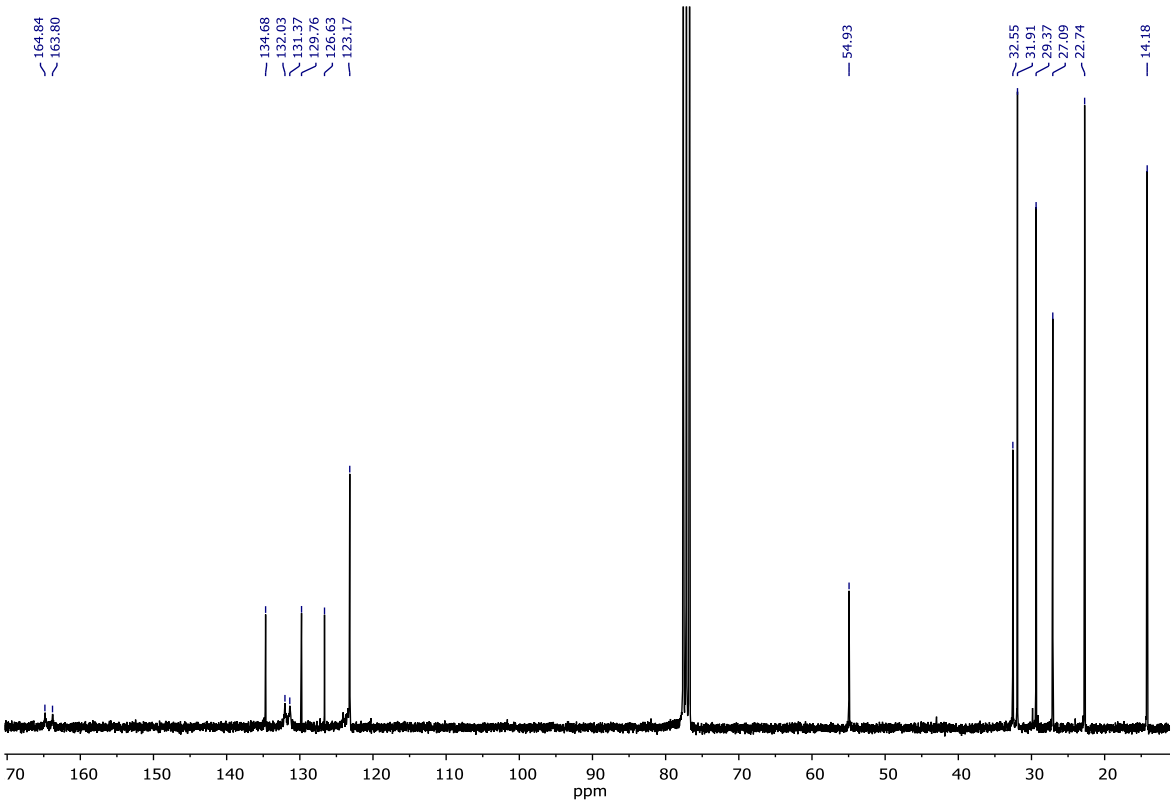

Figure 165. ^{13}C-NMR ($CDCl_3$, 75 MHz) of AR40.

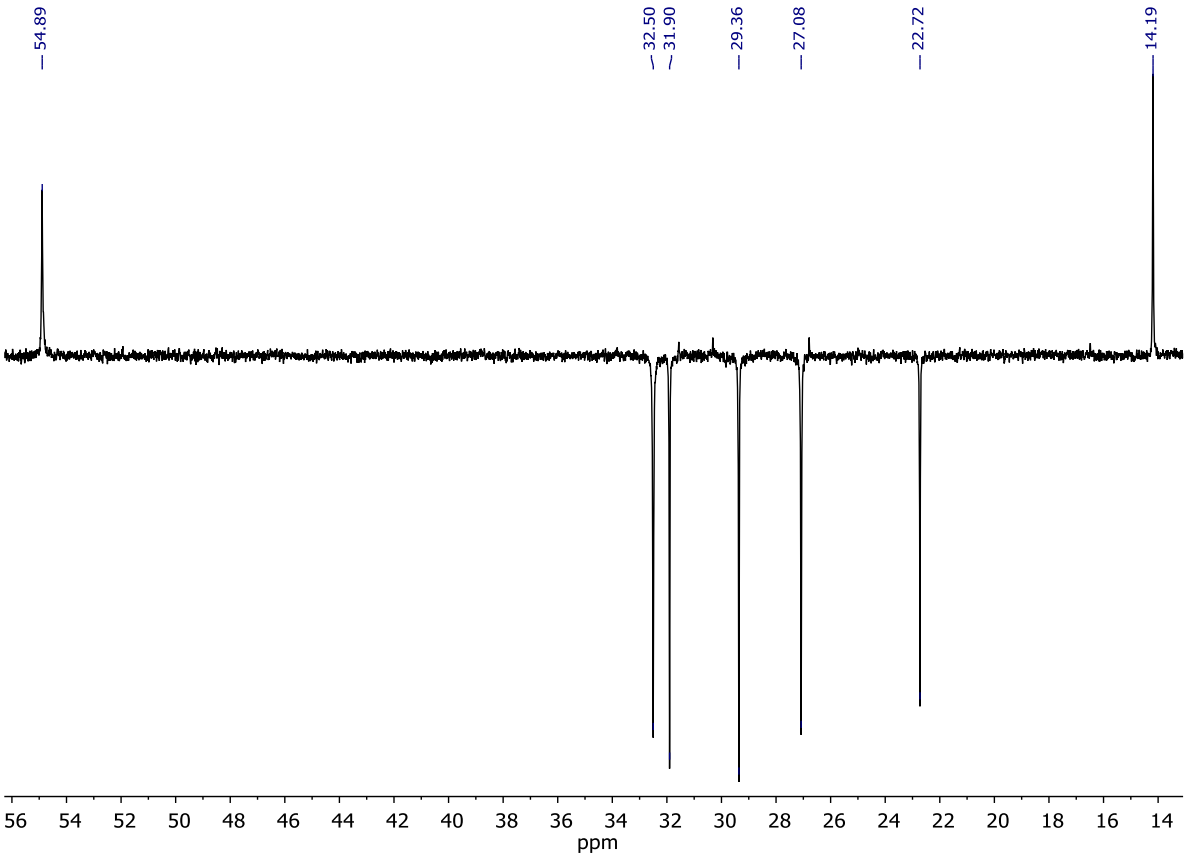

Figure 166. DEPT NMR ($CDCl_3$, 75 MHz) of AR40.

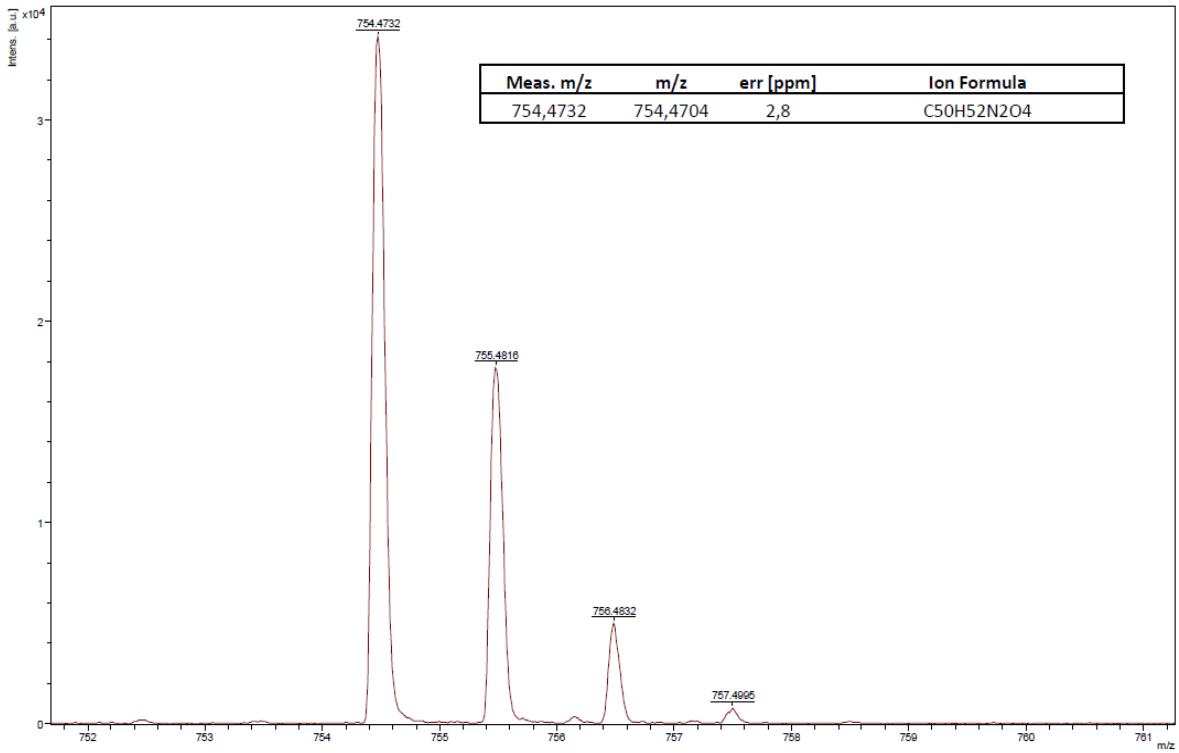

Meas. m/z	m/z	err [ppm]	Ion Formula
754,4732	754,4704	2,8	C50H52N2O4

Figure 167. HRMS (MALDI, DIT-) of AR40.

Solvatochromism:

The concentration of the compound was 20 µM and the excitation wavelength was 480 nm.

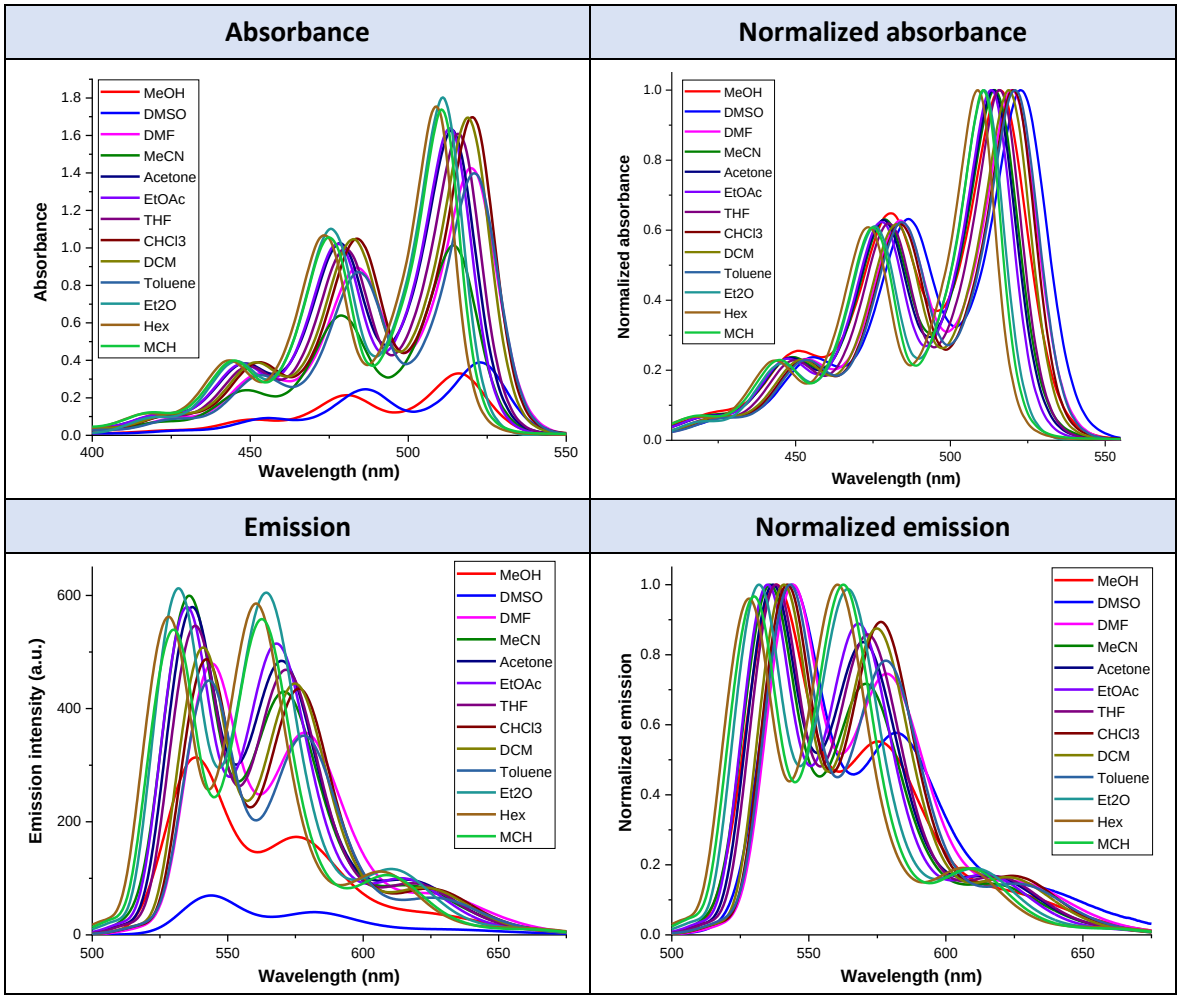

Figure 168. Solvatochromism of AR40.

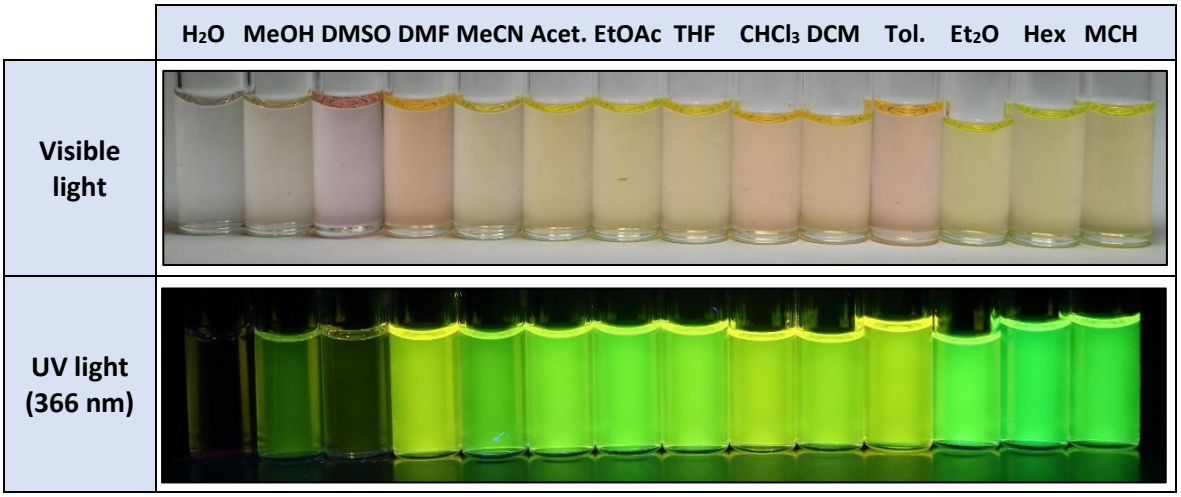

Figure 169. Solvatochromism of AR40 under visible and 366 nm light.

Fluorescence decay lifetime (τ):

The solvent used was hexane. The concentration of the compound was 20 µM.

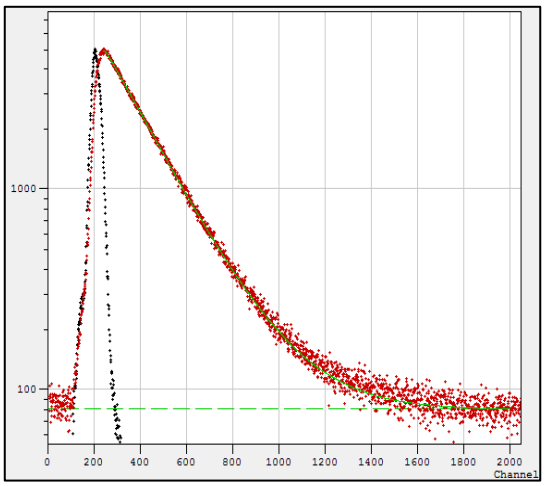

Figure 170. Fluorescence decay lifetime of AR40.